



Vrije Universiteit Brussel
Pleinlaan 2
1050 Brussel

Rectoraat
R&D DEPARTEMENT

Tel. : +32 (0)2 629 21 08
Fax : +32 (0)2 629 36 40

OPROEP 2016 tot indiening van een
aanvraag tot SRP-verlenging, voorafgegaan door
suggesties inzake experts in het domein van de aanvraag

Bijlage VI. STRAMIEN VOOR HET AANVRAAGDOSSIER

Goedgekeurd OZR 08.06.2016
Versie 08.06.2016

VUB Strategic Research Programme
Application for renewal for a 2nd term

1. Application identification details

TITLE	
High-Energy Physics at the VUB	
Coordinator and other group leaders	
Name of the coordinator	Affiliation (research group or department)
- Jorgen D'Hondt	ELEM/IIHE
Name(s) of the other group leader(s)	Affiliation (research group or department)
- Nick van Eijndhoven	ELEM/IIHE
- Ben Craps	TENA
- Stijn Buitink	AARG
Envisaged Scientific Advisory Board members for the 2nd term	
Name	Affiliation (institute)
- Guido Tonelli	University of Pisa
- Dieter Lust	Max-Planck-Institute for Physics (Munich)
- Francis Halzen	University of Wisconsin-Madison
-	
-	

Application in succession of: (Report on past activities and achievements in APPENDIX A.)

PROJECT-ID (SRP...)	
SRP08	
TITLE	
High-Energy Physics at the VUB	
Current 1st term coordinator and other group leaders	
Name of the coordinator	Affiliation (research group or department)
- Jorgen D'Hondt	ELEM/IIHE
Name(s) of the other group leader(s)	Affiliation (research group or department)
- Nick van Eijndhoven	ELEM/IIHE
- Ben Craps	TENA
Former group leaders (if any)	
Name(s) of the succeeded group leader(s)	Affiliation (research group or department)
-	
-	
IF NOT SUCCEEDED AS A WHOLE IN THE PRESENT APPLICATION: Indicate the part succeeded	



Current Scientific Advisory Board members	
Name	Affiliation
- Guido Tonelli	University of Pisa
- Dieter Lust	Max-Planck-Institute for Physics (Munich)
- Francis Halzen	University of Wisconsin-Madison
-	
-	

2. Overall vision and strategic plan

Vision: With about 50 researchers in HEP@VUB we perform fundamental research towards a profound and comprehensive understanding of both the largest and smallest structures around us. By combining theoretical and experimental research of high-energy phenomena in the universe and on the quantum scale we are convinced that we will be able to consolidate at the VUB our flourishing HEP@VUB research centre and continue to excel internationally. To achieve a coherent global picture of the reality around us, puzzling features that challenge the underlying basic principles in physics on large and small scales have to be studied and understood. The foundations of the Standard Models of particle physics and cosmology face problems to explain for example the omnipresence of dark matter and dark energy, as well as the apparent need for fine-tuning in several corners of our models and the difficulty to unite all forces. Novel theoretical reasoning and further experimental explorations will provide insights towards solutions. The recent creation and now further consolidation of our phenomenological research activities are essential to optimally connect theory and experiment, as well as large-scale and small-scale features.

Overall strategy: Three formal research groups in the physics department are included in the HEP@VUB centre: AARG (Astronomy and Astrophysics Research Group), ELEM/IIHE (Elementary Particles), TENA (Theoretical Physics). The research is organised in four groups: Theoretical Physics, Particle Physics Experiments (CMS and SoLid), Astro-Particle Physics (IceCube, ARA and Auger) and High-Energy Astrophysics (LOFAR and SKA). An optimal setting for phenomenological research is created explicitly to facilitate links and collaboration among these groups.

Scientific questions and objectives: The overall scientific questions relate to for example our understanding of dark matter, the origin and nature of high-energy phenomena in the universe, the fine-tuning problems in the Standard Model of particle physics, very early universe cosmology and the unification of the forces into one theory. These questions induce specific objectives for each of the four groups of which many are shared through inter-group phenomenological research:

- **Theoretical Physics:** Holography (entanglement and spacetime; AdS instability; holographic thermalization); Strings, Supergravity, Geometry and Duality (the geometric nature of spacetime invoked by string theory and its dualities)
- **Particle Physics Experiments:** CMS experiment (precise measurements in the top quark and Higgs boson sectors and related searches for new physics phenomena, dark matter and supersymmetry searches, searches for displaced signatures of long-lived particles, development of efficient and robust b/c-tagging methods, towards the construction of one of the two new Outer Tracker endcaps for the Upgraded CMS Detector) and SoLid experiment (measurement of the energy spectrum from antineutrinos at a Uranium-235 reactor, confirmation or exclusion of the reactor antineutrino anomaly and potential discovery of neutrino oscillations at very-short baseline)
- **Astro-Particle Physics:** IceCube experiment (search for cosmic sources of high-energy neutrinos; indirect search for dark matter; detection of neutrinos from supernovae, solar flares and gravitational wave events; study of neutrino oscillations at high energies, including sterile



neutrinos; development of new detection/analysis techniques for the IceCube-Gen2 detector upgrade), ARA experiment (search for ultra-high-energy (GZK) neutrinos) and Auger experiment (search for correlations between arrival directions of cosmic neutrinos and highest-energy cosmic rays)

- **High-Energy Astrophysics:** LOFAR observatory (mass composition of galactic and extragalactic cosmic rays, search for ultra-high-energy neutrinos, interactions between air showers and thunderstorms), simulation (acceleration and propagation of extragalactic cosmic rays)

With phenomenological research we develop methods and tools towards an inter-group interpretation of the experimental results in existing theories and to build novel models to be confronted with experimental observations. The explicit phenomenological research will focus on beyond the Standard Model physics related to supersymmetry, dark matter, cosmology and inflation, and collider physics.

Essential and unique impact of the SRP in reaching these objectives: Fostering a dynamic research environment where in the interplay between theory and experiment on large and small scales, novel ideas are created, is essential to reach our objectives. The diversity of research topics embraced within the centre is unique for Belgium. Although our groups are very successful at attracting external funding and at creating a clear leverage using the available university funds, it remains important to consolidate our knowledge over generations of young researchers, which might be considered a risk element. The SRP budget is therefore typically deployed as seed investment towards the application for external funds related to individual grants or project oriented funding programs. In total AARG+ELEM+TENA in the physics department worked with 16.5M Euro external funds and 39 working years of pre- and post-doctoral grants directly from the FWO funding agency, compared to 1.3M Euro from the SRP in the same period (2013-2017). The SRP funds mitigate the risks related to such funding applications and allow us to reach sustainable research strength as well as to react fast on worldwide scientific opportunities and developments. Additionally the SRP management creates incentives to seek joint PhD projects within HEP@VUB and deploys an attractive visitors program to strengthen our research with external partners.

3. Team structure, members and group leaders

Since the initial GOA (from 2010) and its transition to an SRP (from 2013) the High-Energy Physics research at the VUB expanded in size, depth and broadness. Over the years the team expanded due to three successful Odysseus applicants and one successful ERC Starting Grant applicant. Due to our increased scientific impact, strategic choices at the department level were made possible to hire in total 9 part-time professors and 1 full-time professor. Compared to the initial SRP (2013-2017) with researchers from ELEM and TENA, the new SRP (2018-2022) is extended to include the AARG research group of the physics department as well. This follows a scientific and strategic choice of the physics department in 2014 to refocus the research in astrophysics towards its high-energy part. The organogram on the next page shows the structure of our new team. To visualise our growth, the few professors present at the start of the GOA project in 2010 are indicated in red. Group leaders are underlined. The Phenomenology team is embedded in all three formal VUB research groups of the physics department, namely AARG, ELEM and TENA, and to avoid unnecessary division is not considered a separate group.

In total we have on October 1st, 2016, 12.8 post-doctoral researchers and 24 PhD students. Averaged since 2013, 37% of the effective postdoc years have been obtained via individual fellowships at the FWO (Flemish funding agency) and 20% of the effective PhD student years have been obtained via individual scholarships at the FWO. In absolute numbers these are respectively 8 and 7 obtained mandates since 2013 (i.e. in four annual funding cycles), or respectively 2 and 1.75 per funding cycle. These numbers are respectively 40% and 35% of the on average about 5 postdoc fellowships and about 5 PhD scholarships available per funding cycle at the FWO in the overall field of physics research in Flanders. Therefore, our numbers significantly

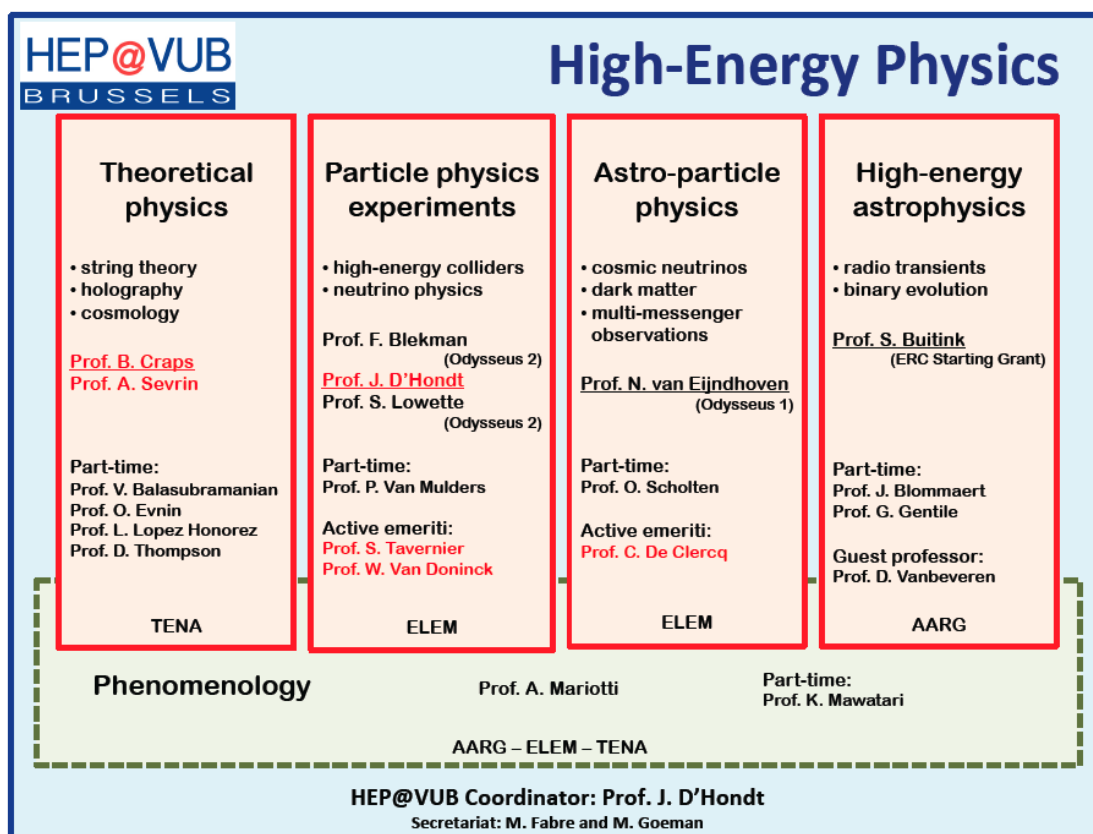


exceed our VUB “fair share” in the Flemish academic landscape (i.e. 10%). The SRP program was essential to reach these impressive numbers.

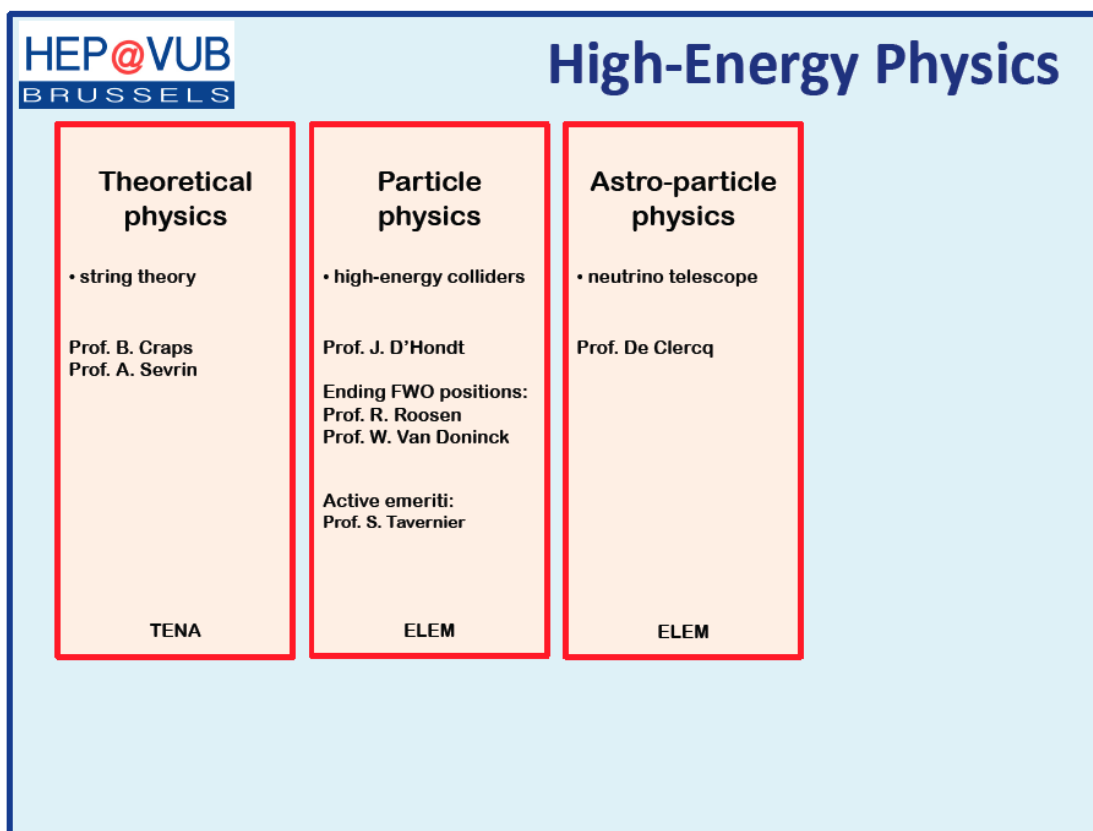
The full breakdown of the groups on October 1st, 2016, is shown in the table below (excluding three active emeriti in experimental (astro)particle physics). Based on our numbers since 2013 (with the High-Energy Astrophysics part only included since 2016) we plan to continue to have on average 16 postdocs and 20 PhD students in HEP@VUB. Today’s postdoc dip in phenomenology is due to a strategic choice to allow the newly hired professor in phenomenology (whose position started in October 2016) to steer future hirings. Since 2010 we have had in total about 12 postdoc years and about 11 PhD student years in phenomenology, hence an average of about 2 postdocs and 2 PhD students per year.

FTE per group	Theoretical Physics	Particle Physics Experiment	Astro-Particle Physics	High-Energy Astrophysics	Phenomenology
Faculty	2.4	3.1	1.1	1.2	1.1
Postdoc	3.9	4.9	2	2	0
PhD students	7	13	2	1	1
Support	2.5 (2 FTE related to IT, 0.5 FTE related to technical work)				
Secretaries	2				

Situation of faculty in HEP@VUB anno 2016:



Situation in 2010 at the start of the initiatives to bring the research groups in HEP closer to each other:





4. Concrete planning and funding allocations [± 2 pages]

In each of the four HEP@VUB groups objectives are defined and dedicated methodologies are used to reach them. The global picture emerges when the results and insights from different groups are combined. Research methods in phenomenology are developed to facilitate these bridges towards potentially revolutionary discoveries in fundamental physics at large and small scales. Below we first describe the research plans (with focus on the innovative aspects) in the four HEP@VUB groups, followed by the plans in phenomenology. Our exploratory research combines the search for novel knowledge towards major breakthroughs (i.e. high risk) with incremental aspects towards more in-depth understanding of a particular topic (i.e. low risk). We mitigate the overall risk by balancing the human and instrumental investments in both strategies.

Theoretical Physics: One theme in our research will be holography, also known as gauge/gravity duality. Our main interests are in far-from-equilibrium aspects and in the role played by quantum entanglement in the emergence of spacetime. First, we will study how novel forms of quantum entanglement give insight in the interior of a holographically dual spacetime. Second, using an analytic approach we have recently introduced, we will investigate the conjectured instability of anti-de Sitter spacetime, in particular the associated turbulent transfer of energy. Third, we will study thermalization using holographic techniques, on the one hand to test holography in far-from-equilibrium regimes, on the other hand to model ultrafast pump-probe spectroscopy.

Another theme will be the continuing investigation of the geometric nature of spacetime invoked by string theory and its dualities. We will carry on the development of a systematic treatment of supersymmetric doubled string using techniques of superspace and its applications to e.g. mirror symmetry. Using this we will elucidate the underlying mathematical structures behind the doubled formalism and its connection to Hitchin's generalized complex geometry. Another point will be the establishment of the connection between non-Abelian T-duality and DFT and the further exploitation of non-Abelian T-duality in the context of holography. Finally, we will develop a holographic understanding of integrable deformations based on non-Abelian T-duality.

Particle Physics Experiments: We continue to participate and observe leadership in CMS. Based on our recognized experience in measurements and searches in the top quark sector with the CMS experiment, our focus will turn to the mostly unexplored interplay between top quark physics and the Higgs sector (e.g. the top Yukawa coupling), as well as the interplay between top quarks and the searches for supersymmetry and dark matter. Precision reconstruction (e.g. b/c-tagging and boosted objects) and measurements of top quark processes will help the searches in those regions of the parameter space that are difficult to probe with traditional search strategies (e.g. the compressed spectra regions). The synergy with phenomenological interpretations in novel models with new physics phenomena is natural and will continue to be pro-actively explored. For the construction of the upgraded CMS Tracker we have expressed the ambition of taking the leadership to construct one Outer Tracker Endcap. The budget of about 10M euro in core cost is being secured by Jorgen D'Hondt as the PI of our successful Hercules application in Flanders with third party contributions from our Walloon colleagues. A new 120m² clean room is being installed at ELEM/IIHE for this purpose (funded with an additional 250k euro budget from the VUB research council) and we are training our researchers and technicians to engage in this ambitious project.

In the SoLid experiment we take the coordination role in the oscillation analysis, which is the main objective in the coming years and relates directly to the search for sterile neutrinos. Also Petra Van Mulders takes the coordination of the most important element for success, namely the precise estimation of all background contributions. With a first publication soon, the SoLid experiment is very well positioned to take the lead worldwide in this search for neutrino oscillations at a very short baseline.



Astro-Particle Physics: The main mission of the IceCube experiment is the observation of high-energy (TeV-PeV) neutrinos from astrophysical objects. In 2013 IceCube discovered these cosmic neutrinos, but so far no sources could yet be resolved. We will continue our IceCube analyses on the detection of neutrinos from Gamma Ray Bursts (GRBs) and Active Galactic Nuclei (AGN) as source candidates for both cosmic neutrinos and very energetic cosmic rays (CRs). In previous studies IceCube obtained upper limits on the GRB/AGN neutrino flux, but these apply only to the prompt emission of GRBs and a subclass of AGN. Our HEP@VUB team is developing an innovative analysis to investigate also the GRB precursor c.q. afterglow phases and we have proposed a new class of AGN to search for associated neutrino production. The HEP@VUB team is developing a dedicated analysis for GeV neutrinos to obtain sensitivity for solar flares and for this a special data-taking mode is currently being implemented at the South Pole. We will use this new data-taking mode also to develop a search for neutrinos related to gravitational wave events. At higher energies (i.e. EeV scale) our interest goes to the detection of GZK neutrinos produced in CR interactions with the cosmic microwave background photons. These neutrinos would indicate that the CR flux drop around 100 EeV, as detected by Auger, is indeed due to this GZK effect. The flux of these GZK neutrinos will also uniquely provide insight in the composition of the energetic CRs. The very low flux at GZK-scale energies calls for extensions of the current detector and even new detection techniques. Our HEP@VUB team will remain involved in both the feasibility studies of the so-called IceCube-Gen2 high-energy upgrade as well as in the development of radio detection techniques for extremely high-energy neutrinos. The latter allows a detector area expansion of about two orders of magnitude, needed to obtain sufficient event statistics.

High-Energy Astrophysics: We use the LOFAR radio telescope to detect signal from particle cascades in the atmosphere and the lunar surface. The main focus is the measurement of the mass composition of cosmic rays, a crucial step in understanding the origin of galactic and extragalactic cosmic rays. Planned activities include an expansion of the triggering array and improvement of the triggering strategies to increase statistics and lower the energy threshold. This will allow high-precision composition measurement at energies below 10^{17} eV, a regime that falls outside the reach of the more traditional fluorescence detection technique.

The second objective is the search for extremely energetic particles initiating cascades in the lunar regolith. The observation mode requires the formation of several LOFAR search beams on the Moon, a technique that is also used in pulsar searches. With these observations we will be sensitive to physics processes beyond the standard model like the decay of superheavy dark matter or cosmic strings.

Our HEP@VUB group is also part of the Cosmic Lightning project, a collaboration with the University of Groningen and the CWI in Amsterdam that studies the interplay between atmospheric air showers and thunderstorms, and the SKA High-Energy Cosmic Particles Focus Group which is pursuing the use of the Square Kilometer Array to study cosmic particles using the techniques we developed at LOFAR and other observatories.

Phenomenology: In the absence of BSM physics signals at the LHC, we will revisit the current paradigms for naturalness and explore novel scenarios, e.g. in non-minimal formulations of supersymmetry or in models where naturalness is realized through the introduction of new neutral particles. Together with the theory group we will study the UV completion of this class of models, while distinctive phenomenological signatures will be explored with the CMS group. We will also continue the investigation of simplified extensions of the Standard Model which provide viable dark matter candidates, studying their phenomenology for collider, direct and indirect detection experiments, in collaboration with the CMS and IceCube groups. Furthermore, the pheno team together with the theory group will investigate the interplay between supersymmetry breaking and the dynamics of inflation, aiming also to relate inflationary observables with predictions for supersymmetric signatures at colliders. Lastly, we continue our research on neutrino production in astrophysical sources, in collaboration with the Astro-Particle group. In particular, to explain the high-energy neutrino flux observed by IceCube, alternatives to AGN and GRB will be studied. We



will model the neutrino production and spectrum of for example hidden sources with reduced photon emission, such as obscured blazars.

Allocation of SRP budgets: An annual budget of 297.5k euro is requested to support HEP@VUB with the allocation defined in the table below. The budget will continue to be used for collaborative events (20 seminars and 3 Crosstalk Workshops per year), for an attractive international visitors program (10 visitors per year), and as seed money to hire new researchers and to start with new research topics. In the spirit of good governance, a budget for logistics, outreach and coordination is embedded and this 10% fraction covers as well a contingency for unexpected costs. In the absence of unexpected costs, the contingency budget will be re-directed to other elements of the HEP@VUB program. We plan to invite our Advisory Board every two years for a site visit (average cost per year is quoted in the table). The annual budget of 27.5k euro for each of the 8 full-time staff members is used to hire PhD students and postdocs and as such stimulates staff members to collaborate for example via joint PhDs or joint postdoc projects with internal as well as external partners. With $2 \times 27.5k = 55k$ euro per year the salary cost of a researcher and an adequate bench-fee are on average covered (taking into account the fact that most of our postdocs and PhD students can be hired on essentially tax-exempt fellowships).

	Annual Budget (kEuro)
Seminars (20)	15
Crosstalk Workshops (3)	15
Visitor program (10)	15
Logistics, Outreach & Coordination	30
Advisory Board	2,5
Allocation per staff member (8)	27,5 (x 8)
	297,5

5. Position, collaboration, and networking in the field

Brussels region: Since 1972 the experimental groups in high-energy physics of both Brussels universities, the VUB and ULB, are united in the Interuniversity Institute for High Energies (IIHE) with today about 100 members (<http://w3.iihe.ac.be>). The institute has a leading role in Belgium for experimental particle and astro-particle physics. The theoretical groups of the VUB and ULB collaborate in the International Solvay Institutes (<http://www.solvayinstitutes.be>). On the VUB+ULB campus, more than 100 researchers are involved in high-energy physics. The HEP@VUB consortium might be a first step towards an institutionalized collaboration uniting all Brussels research in high-energy physics.

National collaborations and recognitions: HEP@VUB is the only consortium in Belgium where via phenomenological work theoretical research is confronted with experimental observations at collider experiments (CMS), neutrino experiments (SoLid), astro-particle (IceCube, ARA, Auger) and high-energy astrophysics (LOFAR) experiments or observations. The extension of the HEP@VUB research in depth and scope has consolidated this position, and with the continuation of the SRP program we can guarantee to remain strong and pro-active in driving or following new developments worldwide. On the national level, Jorgen D'Hondt is the promoter of the main funding programs related to the Flemish participation in the CMS experiment (i.e. the Big Science and Hercules funds). Similarly Nick van Eijndhoven acts as a (co)promotor for the main funding programs related to the Flemish participation in the IceCube experiment. The HEP@VUB group hosts three Odysseus grant holders (1 Odysseus-I grant of about 2M euro and 2 Odysseus-II grants of about 0.8M euro each). Alexander Sevrin is board member within the Inter-university Attraction Pole (IAP) network "Fundamental Interactions"; where Ben Craps is co-coordinator of the



"Deductive approach to Fundamental Interactions" working group, Freya Blekman of the "Beyond the Standard Model" working group, Nick van Eijndhoven of the "High-energy Cosmic Rays" working group and Jorgen D'Hondt of the "Flavour Physics" working group. Stijn Buitink, Ben Craps and Catherine De Clercq are board members of the FNRS/FWO "CosmoParticles" network.

International collaborations and recognitions: The characteristics of our research are such that international collaboration and mobility is natural as well as essential. Jorgen D'Hondt is the Belgian representative in RECFA (Restricted European Committee for Future Accelerators) and was in the period 2006-2014 the Belgian representative in IPPOG (International Particle Physics Outreach Group). In 2014 Alexander Sevrin was elected as member of the International Union of Pure and Applied Physics (IUPAP). Nick van Eijndhoven is the Belgian delegate of the High-Energy Physics board of the European Physical Society and a member of the Scientific Programme Committee of the International Cosmic Ray Conferences. Walter Van Doninck was elected as vice-president of CERN Council (2013-2016).

- **CMS:** The financial contribution of a country in the CMS Collaboration typically relates to the relative number of PhD-titled CMS members in the country (2.9% for Belgium). The VUB CMS team has always observed a leading role in Belgium, and the Belgian excellence in the CMS experiment can be illustrated with the following fractions of Belgium in CMS (numbers only available on the country level): we have 5.3% of the PhD students, 6.6% of the physics area conveners, 8.3% of the major conference talks, 33% of the Best PhD Thesis Awards. These recognitions are clearly above the relative size of Belgium in CMS. Jorgen D'Hondt is one of the few permanent members of the International Advisory Committee of the annual Top Quark conferences, illustrating our excellent recognition in top quark physics. Within the international CMS Collaboration of over 4400 members, he was elected Chairperson of the Collaboration Board (2014-2017) and is the Chairperson of the International Committee. Previously Jorgen D'Hondt was top quark convener (2007-2008), Freya Blekman was convener of the Beyond-two-Generation physics group (2012-2014) and Petra Van Mulders was convener of the Heavy Flavour Tagging and Vertex physics group (2014-2016). Steven Lowette is the CMS delegate to the CERN LHC Dark Matter group. Several postdocs as well as PhD students have been selected for (sub)convener roles as well.
- **SoLid:** Petra Van Mulders is responsible (convener) for all background estimations related to the experiment, which is the most critical part to reach a competitive sensitivity. Leonidas Kalousis (postdoc) is responsible (convener) for the oscillation analysis itself, which is the main result of the experiment. Petra Van Mulders acts as resources manager for the budgets related to the construction of the experiment from three countries (10 institutions).
- **IceCube:** Nick van Eijndhoven is co-PI for the Belgian groups in IceCube and member of the IceCube collaboration board. The HEP@VUB IceCube team has taken a lead in combining data from the IceCube, Pierre Auger and Telescope Array experiments. Concerning the studies of GRB precursor and afterglow emission as well as the investigations of Dust Obscured AGN, our team has developed the basic ideas and consequently represents the key investigators. The IceCube search for Earth WIMPs was lead by members of our HEP@VUB group and we also coordinate the studies concerning neutrinos related to solar flares. In view of future detector extensions, the VUB team is leading the InIce self-veto studies for the IceCube-Gen2 high-energy extension as well as the development of radio detection techniques.
- **LOFAR:** Stijn Buitink is co-PI of the LOFAR Cosmic Ray Key Science Program. The HEP@VUB LOFAR team takes the lead in simulation production, detector upgrade and analysis pipeline design. In 2016, LOFAR had a Nature publication with Stijn Buitink as first author. He is also a member of the International Astronomical Union.
- **Theory:** Alexander Sevrin is Deputy Director and Scientific Secretary and Ben Craps is Assistant to the Director of the International Solvay Institutes for Physics and Chemistry. Alexander Sevrin is



national coordinator of the EU COST network "MPNS COST Action MP1210: The String Theory Universe", http://www.cost.eu/COST_Actions/mpns/Actions/MP1210.

- **Pheno:** Kentarou Mawatari is a member of the LHC Higgs Cross Section working group.

For theory and phenomenology, the author lists of the publications illustrate their strong international collaboration. Several of our HEP@VUB doctoral and postdoctoral researchers obtained excellent and in many cases permanent positions abroad, for example at IN2P3 Lyon, Princeton, Harvard, Durham, Mainz, DESY, CERN, Perimeter Institute, ...

6. External funding

In the period 2013-2016 we obtained or had running projects for **a total of 16.5M euro of external funds, as well as obtained 7 doctoral and 8 postdoctoral mandates directly from funding agencies (equivalent with an additional about 2.7M euro)**. The annual 0.26M euro SRP funds, or 1.3M euro total fund over 5-year, have been used mainly to continue initiating our phenomenological work and as seed-budget for additional research in HEP@VUB. Recently we have been able to consolidate these investments with the hiring of a first faculty member in phenomenology. With 74 candidates applying we had a very strong short list including for example an ERC grant holder. A selection of key budgets provided to HEP@VUB members is mentioned below. Although in several cases we are the promoter of interuniversity projects, only budgets provided to the VUB part of the projects are quoted. Not mention are the VUB-internal budgets we received.

Jointly HEP@VUB is partner in the IUAP Fundamental Interactions

A total budget for pre-doc and post-doc hirings: 500k euro (total of 5 years, 2013-2017)

Funding obtained for the Phenomenology group

2 FWO 4-year PhD mandates (including a total bench fee of 30k euro)

1 FWO 1-year Pegasus postdoc mandate (including a total bench fee of 4k euro)

Funding obtained for the CMS experiment

Big Science program (2013-2017): 1950k euro (total of 5 years, 2013-2017)

Hercules equipment for the CMS Tracker Upgrade (2016-2020): 5190k euro (2016-2020)

4 FWO 4-year projects: 1120k euro personnel, 316k euro running budget (total budgets of projects)

Odysseus 2 (Freya Blekman): 867k euro (2011-2015)

Odysseus 2 (Steven Lowette): 763k euro (2013-2017)

4 FWO 3-year post-doc mandates (including a total bench fee of 48k euro)

1 FWO 4-year PhD mandate (including a total bench fee of 15k euro)

Funding obtained for the SoLid experiment

2 FWO 4-year projects: 420k euro personnel, 15k euro running budget (total budgets of projects)

Hercules funding of 50k euro equipment (quoted VUB part only in a UA-UGent-VUB consortium)

Funding obtained for the IceCube, ARA and Auger experiment

Big Science program (2013-2017): 366k euro (total of 5 years, 2013-2017)

2 FWO 4-year projects: 320k euro personnel, 60k euro running budget (total budgets of projects)

Odysseus 1 (Nick Van Eijndhoven): 2000k euro (2009-2014)

1 FWO 3-year post-doc mandate (including a total bench fee of 12k euro)

Funding obtained for the LOFAR observatory and the AARG research group

ERC Starting Grant (Stijn Buitink): 1500k euro (5 years, 2015-2020)



1 FWO 3-year post-doc mandate (including a total bench fee of 12k euro)

Funding obtained for theoretical high-energy physics research

2 FWO 4-year projects: 480k euro personnel, 80k euro running budget (total budget of projects)

5 FWO 4-year PhD mandates (including a total bench fee of 45k euro)

6 FWO postdoc mandates (a total of 21 person years, including a total bench fee of 84k euro)

Joint Groningen-VUB PhD position: 4 person years, of which two spent at the VUB

Solvay Institutes funding for PhD position: 2 person years

Some of the additional obtained external funding for networks

COSPA network funded by FWO (12k euro per year for the network) and FNRS: funding for organizing scientific meetings on cosmoparticle physics.

EU COST network "MPNS COST Action MP1210: The String Theory Universe", http://www.cost.eu/COST_Actions/mpns/Actions/MP1210: provides ad hoc travel funding for young scientists in our group and organizes regularly high level scientific meetings on topics closely related to our research interests. Budget for the network: 128k euro per year.

ESF HoloGrav network, <http://www.fc.up.pt/cfp/HoloGrav/>: encourages and promotes research in gauge/gravity duality, including its applications across particle, nuclear, condensed matter and gravitational physics. The network supports staff and student exchanges, workshops, conferences and summer schools. Budget for the network: 134k euro per year.

ERC funding requested by HEP@VUB researchers:

- Stijn Buitink (group leader): obtained an ERC starting grant
- Petra Van Mulders (FWO post-doc, and 3-year 10% ZAP, Collider Physics): applied for an ERC starting grant (reached the interview stage, not selected)
- Laura Lopez Honorez (FWO post-doc, and 3-year 10% ZAP, Theoretical Physics): applied for an ERC starting grant (not selected)
- Alexey Koshelev (FWO post-doc, Theoretical Physics): applied for an ERC consolidator grant (not selected)
- Alberto Mariotti (FWO post-doc, Theoretical Physics): applied for an ERC starting grant (not selected)
- Ben Craps (group leader): applied for an ERC advanced grant (result not yet known)

Future plans: In the Odysseus program we had in addition to the three successful candidates, six other candidates applying (of which one Odysseus-I position was approved but finally not taken by the candidate due to a competing offer in Germany, and one Odysseus-II was selected by the Odysseus jury but not funded by the university because of budget constraints). In the future the HEP@VUB staff members will continue to apply and to seek outstanding internal and external candidates to apply through these national and international channels. Several faculty members and researchers in HEP@VUB have indeed very concrete plans to apply soon for ERC grants.

7. Goals for added value outside the academic community

In the period 2013-2016 HEP@VUB initiated and was strongly involved in a vast range of successful valorisation projects, mostly in the science communication part of valorisation. Some recent highlights mentioned below provide us with an outstanding experience to continue to deliver also in the future prosperous valorisation outcomes. Some concrete plans are mentioned for the near future; other opportunities and activities will surely appear in the 2018-2022 period.



Jorgen D'Hondt was awarded the annual prize for Science Valorisation of the VUB in 2014 (value of 150k euro) as well as one of the year prizes in 2013 of the Royal Academy of Belgium (KVAB) for Science Communication. He obtained as well two external funds (2 x 5k euro) from the Brussels region dedicated to outreach events. One of these grants was to sponsor the documentary "[Kwantumrevolutie](#)" which was selected for the 360° Science Film Festival in Moscow. Petra Van Mulders is member of the jury of [CanSat Belgium](#) (2015-2017), and provided workshops for about 80 children aged 8 to 12 at [Technopolis](#) as well as a keynote speech on curiosity-driven research at the [first VUB conference](#) with over 600 participants. For her continuous science communication via social media Freya Blekman was awarded one of the year prizes in 2016 of the Royal Academy of Belgium (KVAB) for Science Communication. She organised as well a "Career in Industry" seminar for our PhD students and postdocs. Freya Blekman and Steven Lowette are regularly judges during the yearly wetenschaps-ExpoSciences Science fair in Brussels. Freya Blekman was the invited CERN speaker at the prestigious London International Youth Science Forum in 2013, 2015 and 2016 (<http://www.liysf.org.uk/>). In 2014, our HEP@VUB team in IceCube organised several presentations of an IceCube 3D movie at the Brussels planetarium. In the same year they produced as well a [short movie explaining our GRB research](#). Via the International Solvay Institutes, Ben Craps and Alexander Sevrin are involved in the organization of yearly high-profile Public Lectures attracting audiences of many hundreds. To celebrate the discovery of gravitational waves, Simona Toscano and Gwen de Wasseige organized in 2016 a public lecture (more than 200 participants), followed by a dedicated symposium. We organized an IceCube exhibition at the "Printemps des Sciences" in 2014. HEP@VUB members are active in valorisation activities on social media such as YouTube videos, Google hangouts and twitter, with particularly the video activities regularly reaching tens of thousands of views. Alexander Sevrin was and Ben Craps is a board member of the Belgian Physical Society, which among other things promotes physics in society. Stefaan Tavernier is member of and was previously spokesperson (1995-2010) of Crystal Clear, an international collaboration active on research and development on inorganic scintillation materials for novel ionizing radiation detectors, for high-energy physics, medical imaging and industrial applications. Recent publications are "Validation of a highly integrated SiPM readout system with a TOF-PET demonstrator" (just accepted in JINST) and "A new method for depth of interaction determination in PET detectors" (Phys.Med.Biol. 61(12):4679-98, 2016).

Towards the future we are committed to remain very active and successful in reaching out to the society at large with high-energy physics results and our achievements in general. A substantial and novel outreach program is planned in view of the South Pole trip of Gwen de Wasseige in the period Dec 2016 to Jan 2017. The program involves a scientific competition among classes at schools and pedagogical exhibitions illustrating life at the South Pole and scientific activities at the IceCube observatory. We will continue to participate in the International Masterclasses organised by IPPOG for LHC collisions physics as well as organise Masterclasses for IceCube related physics. We have advanced plans to refurbish the astrophysics observation dome on the roof of building E on the campus. The HEP@VUB group will organize observation nights for schools and general audiences that will include a telescope tour and lectures on topics in astronomy and cosmology.

On a national and international scale we are strongly involved in training (typically young) researchers in our methodologies. These skills can be used in academia as well as outside academia. Jorgen D'Hondt was the organiser of the 2016 CERN Computing School (Aug-Sept 2016, at Mol, Belgium) and is member of the advisory board of the CMS Data Analysis Schools of which the training model was published in conference proceedings. He was the president of the Young Academy of Belgium that initiates several new interactions between young academics and external stakeholders. Today he is member of the Art&Science steering group of the national Center for Fine Arts (BOZAR) exploring new cultural synergies between artists and scientists. He was invited to participate in a national (informal) steering group to explore the possibilities of initiating novel interdisciplinary research how physics and biology can unite to challenge the fundamentals of



cancer. This might soon result in joint projects where with our methodologies in physics (and our specialist use of distributed computing) we can seek valorisation in understanding a key component in public health.

8. SRP management

Management of SRP: HEP@VUB is managed by the coordinator who organises meetings, typically every 4 months, involving all HEP@VUB staff members (cfr. organogram). At these meetings we discuss the progress as well as reach consensus on how to act on novel opportunities in research and research funding. On an annual basis the SRP coordinator presents to the staff members the financial situation as well as the budget planning for the upcoming years. These HEP@VUB meetings are supplemented with frequent meetings within and across the various groups.

Scientific events with international visibility: To enhance our research opportunities we will continue to invest in stimuli for our researchers to reach new fundamental insights (seminars and workshops) and in attracting outstanding external researchers to work with us (visitors program).

- **Visitors program:** Typically once a month, an external colleague is invited and supported for a short visit of 2-5 days. In order to initiate new research all HEP@VUB members can propose visitors to be invited. The visit is widely announced in the HEP@VUB community (and potentially beyond) such that all interested researchers can participate in discussions with the invited visitor. We put special emphasis on visitors that help us making bridges among the different HEP@VUB groups. This is not only a scientifically sound but also a cost effective strategy to broaden our research potential. Recently we hosted one International Francqui Chair (Francis Halzen, 2013-2015) and one National Francqui Chair (Antoine Van Proeyen, 2014), and we will continue to explore these external opportunities.
- **Seminar program:** Every two weeks either a topical or general HEP@VUB seminar is organised, with invited speakers as well as HEP@VUB researchers presenting new developments. These meetings have been successful in initiating concrete collaborative research projects across groups, with results published in international journals.
- **International workshops:** Two or three times per year we foresee to organise one-day "HEP@VUB Crosstalk Workshops" with a focus on contemporary topics on the interplay between HEP@VUB groups. This is complementary to the typically mono-disciplinary workshops organised by each of the groups. The HEP@VUB Crosstalk Workshops will foster discussion among experts and help us to be pro-active and fast in our developments of new research on hot topics. They will bring major international researchers on the topic to Brussels. We expect to have about 50 (mostly expert and/or interested) participants per workshop. Previous workshops have been organised on the topics of Gauge-Mediated Supersymmetry Breaking (GMSB), and a near future HEP@VUB Crosstalk Workshop is being organised on the topic of sterile neutrinos. The recent results from IceCube will be presented and the Spokesperson of the SoLid experiment will highlight the expectations for very-short baseline neutrino oscillations. Additional phenomenological and theoretical talks will make the link with model building and dark matter, and stimulate new research at the HEP@VUB in collaboration with worldwide the most prominent scientists in the field of sterile neutrinos. Another HEP@VUB Crosstalk Workshop is being planned in 2017 on the status of naturalness after LHC13.

Hiring policy: Most of our PhD students are hired from outside our university, and at the postdoctoral level almost all are non-Belgian. Whenever possible, we make use of essentially tax-exempt fellowships. Over the years we achieved an excellent balance between junior postdocs and more independent senior postdoctoral researchers who typically start steering the research of a small team of PhD students. For each researcher an adequate bench-fee is budgeted which they can use to participate in conferences and workshops. Long-term stays at for example CERN, Wisconsin-Madison or the South Pole (IceCube) are options.



Gender: While we have a reasonable gender balance in our HEP@VUB cohort of PhD students (38% female), the balance is broken towards the postdoctoral level (23% female) and even further to the professor level (19% female, taking into account all staff members in our HEP@VUB organogram). We are aware that this is an international trend not unique to HEP@VUB. In the latest science-wide round of the prestigious Odysseus calls in Flanders, which when successful would lead to a staff position for the candidate, we submitted in total five candidates of which three were female. One of the female candidates was successful and received an offer in the highest grade, but accepted a competing offer from abroad.

Website: At the overall university level a new VUB logo and website design were very recently endorsed. We will take the opportunity to explore how we can further professionalize our HEP@VUB website: <https://we.vub.ac.be/en/HEPVUB> .

9. Concise SWOT analysis

Strengths:

- The field of high-energy physics research achieved groundbreaking discoveries
- We are very well recognized in this international community
- A broad scope of high-energy physics research is established in HEP@VUB
- Strong international focus for the recruitment of PhD students and postdoc researchers
- Leading position nationally to obtain external funding
- Established a dynamic environment with young faculty members
- Established a phenomenological link among all HEP@VUB groups
- For the experimental research the FWO funding agency has a Big Science program to support the participation in large international collaborations

Weaknesses:

- Given the recent strong increase in the number of faculty members in HEP@VUB, it becomes increasingly difficult to hire additional full-time faculty members. In order to facilitate additional research links in this context, we count in part on part-time faculty members, on our extensive visitors program and on Odysseus and ERC opportunities.

Opportunities:

- Our HEP@VUB consortium is an excellent basis to apply for Odysseus and ERC grants
- We do attract collaborators from nearby high-energy physics groups
- Research in high-energy physics faces many relevant scientific questions or problems, and the solutions might have a groundbreaking impact
- The SRP budget allows us to react fast on new developments, and this would not be possible if we first needed to apply for a specific research project at funding agencies
- With the participation of the High-Energy Astrophysics group we will be able to seek external funding from a broader set of funding agency panels and programs

Threats:

- Current individual grants (Odysseus and ERC) will run out, as well as the application eligibility for junior faculty, hence we will have to aim for the more advanced (ERC) grants
- A significant fraction of the technical staff retired over the last decade, but based on our scientific success and the recently obtained large construction budgets we are in a fortunate position to find new opportunities



10. Additional information

The international trend to evolve from community oriented funding with a long-term vision towards project oriented funding with a typically short-term vision does not fit the research in high-energy physics. Addressing the key scientific questions about fundamental interactions requires important investments in people and infrastructure, as well as a long-term management vision. The SRP program is the only funding program that provides continuity of our high-energy research at the VUB. It allows consolidating the knowledge over generations of young researchers and is the essential basis for further successful applications for external national and international funding.

11. Information per group leader

Provide a brief description of the career path and the lists below for each of the group leaders of the present SRP-application, starting with the coordinator.

- 10 most important scientific publications (any document type) from the five years preceding the application (five full years + year of application).
Clearly label the 5 most important scientific publications, and submit a hard copy or digital version of these together with the application.
- Most important scientific reviews (if applicable).
- Applications for international research funding (including ERC-grants), and VUB-promotorships of applications for Odysseus funding.
- Promotorships of awarded PhD's.
- Realisations of added value outside the academic community, and of technology transfer.

For each group leader, a research cv including scientific publications and research project funding from the five years preceding the application (five full years + year of application), drawn from the university research database (PURE), will be added to the submitted application by the R&D department.

ATTACHED TO THIS DOCUMENT:

- file of Jorgen D'Hondt (p42 of this PDF file)
- file of Ben Craps (p428 of this PDF file)
- file of Nick van Eijndhoven (p533 of this PDF file)
- file of Stijn Buitink (p597 of this PDF file)



APPENDIX A. Report on past activities and achievements

a. Major scientific results

In this section, as well as the remainder of this report, only publications are quoted in which HEP@VUB members are co-authors. Citations are taken from Spires, the High-Energy Physics information system, during the month of November 2016.

Our research is curiosity driven fundamental research. Scientific breakthroughs are therefore not planned on an exact timeline. Creating optimal opportunities and attracting excellent researchers to collaborate in our research is our main vision to stimulate global breakthroughs. At the first site visit of our Advisory Panel, Prof. Guido Tonelli mentioned that the success of the HEP@VUB program is to be gauged on our ability to create this setting, as well as our achievements to obtain crosstalk between disciplines in high-energy physics.

Our strategic extension of the HEP@VUB organogram since its start is an illustration of our successful deployment of SRP (and other) funding to reach this objective. This has not only extended the diversity of our research opportunities but also facilitated the creation of effective bridges among groups. In the paragraph below we briefly illustrate this diversity.

Shortly after the presentation of the HEP@VUB program to the selection committee we **discovered the Higgs particle** with the CMS experiment as well as the ATLAS experiment at CERN (Phys.Lett. B716 (2012) 30-61, 6448 citations). Since then, a vast new research in the scalar sector of particle physics opened quickly and strongly, including a strong **phenomenological exploration of the Higgs sector** (JHEP 1311 (2013) 043 with 89 citations). National and international prizes have been awarded to the experimentalists discovering the new scalar particle and to the theorists inventing the theoretical mechanism behind it (Nobel Physics 2013). At the same time this discovery imposed **important constraints on the diversity of supersymmetric models** in high-energy physics (JHEP 1307 (2013) 109 with 29 citations). This is very interesting and perfectly timed because supersymmetry was, based on this expectation, chosen as the main topic for which the SRP budgets were deployed. Despite this focus, our phenomenological research is **ready to act on new developments at the LHC** (JHEP 1603 (2016) 157 with 202 citations). With leadership in experimental research in amongst others **top quark physics** (Phys.Rev.Lett. 112 (2014) 23, 231802 with 105 citations), **dark matter searches** (Eur.Phys.J. C75 (2015) 5, 235 with 264 citations), **displaced supersymmetry searches** (Phys.Rev.Lett. 114 (2015) 6, 061801 with 33 citations) and **supersymmetry searches** (Eur.Phys.J. C73 (2013) 12, 2677 with 283 citations) we further marked our contributions with the CMS experiment. A year after the Higgs particle discovery this highlight was followed by the IceCube **discovery of cosmic high-energy neutrinos** (Science 342 (2013) 1242856 with 483 citations; Phys.Rev.Lett. 111 (2013) 021103 with 399 citations; Phys.Rev.Lett. 113 (2014) 101101 with 503 citations), which opened a new window on the Universe and triggered new research across various disciplines, in both theory and experiment. The year 2016 started with the announcement of the **discovery of gravitational waves**, for which the IceCube neutrino telescope is very well placed to discover the potential multi-messenger signals towards a more complete understanding of these high-energy cosmic phenomena (Phys.Rev. D93 (2016) 12, 122010 with 22 citations). Despite the fact that the 2015 Nobel Prize was awarded for the discovery of neutrino oscillations, an anomaly remains for these oscillations at very short distances. With the SoLid detector we successfully initiated a novel experiment to confirm or exclude for the first time this reactor antineutrino anomaly and to **potentially discover neutrino oscillations at very-short baseline**. This might be related to the presence of sterile neutrinos for which the IceCube experiment released world-leading results (Phys.Rev.Lett. 117 (2016) 7, 071801 with 25 citations). Our exploration of the Cosmic Microwave Background anisotropy made an important step with the **interpretation of the new Planck satellite data** in the framework of dark energy and dark matter



models (Phys.Rev. D88 (2013) 2, 023531 with 60 citations). Related to our High-Energy Astrophysics research at LOFAR, the first large-scale radio telescope, recently **opened a unique radio observation window for the study of cosmic rays** (Astron.Astrophys. 560 (2013) A98 with 41 citations) with first results on the mass composition of cosmic rays (Nature 531 (2016) 70-73 with 10 citations). In a key theoretical development, approaches have been developed in which **duality symmetries of string and M-theory are manifest** (JHEP 1301 064 with 95 citations; Phys. Rept. 566 (2014) 1 with 104 citations). Thermalization properties of various strongly coupled systems have been studied via a dual process of black hole formation; we have introduced an **analytic approach for investigating whether anti-de Sitter spacetime is unstable** to the formation of small black holes (JHEP 1410 (2014) 48 with 45 citations; JHEP 1501 (2015) 108 with 37 citations).

The significance of these highlighted discoveries and other achievements in our field (and beyond) cannot be overrated. Our contributions have been recognized and it opened new research lines for HEP@VUB at the forefront of science at an international level. The HEP@VUB research is situated in a very dynamic field where important breakthroughs are expected as well in the near future.

Since 2013 the HEP@VUB program worked simultaneously on three fronts: Collider Physics, Astro-Particle Physics and Theoretical Physics. A phenomenological team works at the interface of these three groups. As mentioned before, a natural extension was to incorporate also the field of High-Energy Astrophysics, which we now include and on which we report as well. We report in the section "*progress made*" on our successes in creating phenomenological bridges between all groups. Below we report on the research highlights since we initiated the joint HEP@VUB project.

Phenomenological research: The pheno team has been studying the Higgs particle and models beyond the standard model, including supersymmetry, dark matter and extra dimensions. The investigation deals with model formulations and new physics signatures at colliders as well as developments of simulation tools. Below we describe few exemplifying topics where the pheno team has accomplished high-impact achievements that have led to publications in peer-reviewed journals. For a complete list of publications we refer to the section "*progress made*".

- **Higgs particle characterization:** We introduced a framework, based on an effective field theory approach, allowing us to perform characterization studies of the Higgs boson recently discovered at the LHC. The ATLAS and CMS experimentalists now use the framework (JHEP 11 (2013) 043 with 89 citations, Eur.Phys.J. C74 (2014) 74 with 47 citations, Eur.Phys.J. C74 (2014) 1 with 31 citations). Kentarou Mawatari is currently part of the LHC Higgs Cross Sections working group.
- **Unconventional SUSY phenomenology:** The team has obtained important results in the study of supersymmetric models and their signatures at the LHC. This has been also the main topic of two PhD theses written in the team. We performed the first exploration of the full parameter space of general gauge mediation, classifying the possible supersymmetric spectra (JHEP 07 (2013) 109 with 29 citations). The possible excess over the SM background in the multi-lepton signature reported by the CMS collaboration in 2013 was explained as a consequence of collider signatures arising in some portion of this parameter space (Phys.Lett. B731 (2014) 7 with 11 citations). We have also obtained important results in the study of NLO calculations for supersymmetric processes at colliders (Phys.Rev. D85 (2012) 114024 with 45 citations and Phys.Rev. D87 (2013) with 39 citations). Our team has a leading role in the investigations of new LHC signatures in supersymmetric models with multiple goldstini (JHEP 06 (2012) 096 with 19 citations, JHEP 04 (2014) 126 with 13 citations, Phys.Lett. B750 (2015) 539-546 with 10 citations), including e.g. multi-photons plus missing energy signals.
- **Dark matter simplified models:** The pheno team of HEP@VUB has obtained important achievements in the study of simplified models for dark matter, highlighting the complementarity between collider searches and direct/indirect detection experiments. The phenomenology of a



minimal model of dark matter, the singlet doublet model, has been thoroughly investigated, including constraints from dark matter direct and indirect detection experiments, as well as some preliminary constraints from the LHC (JHEP 1510 (2015) 116 with 21 citations). A joint collaboration between the pheno team and the CMS group in HEP@VUB has studied models of dark matter that couples to the SM through flavour violating interactions involving the top quark (JHEP 1603 (2016) 060 with 4 citations). The prospects for the sensitivity at LHC at 13 TeV on such models have been presented in detail, and the possibility that they can also accommodate the galactic center excess reported by the Fermi-LAT collaboration discussed. Recently, the pheno team has been the first one to propose an interpretation of the apparent di-photon resonance presented by the LHC experiments as a simplified model of dark matter with a scalar mediator (JHEP 1603 (2016) 157 with 202 citations).

Collider Physics: Using the data of 7-8-13 TeV proton collisions recorded by the CMS experiment in 2011-2012-2015-2016, several studies were performed in the field of mainly top quark physics, new physics connected to the 3rd generation of fermions, supersymmetry and dark matter. Below we provide some highlights, with leadership from members of our team.

- Combining our discovery of the Higgs particle (Phys.Lett. B716 (2012) 30-61, 6448 citations) with our **direct searches for 4th generation quarks** (at the time of publication the best limits worldwide achieved with a novel analysis strategy, Phys.Rev. D86 (2012) 112003 with 41 citations), resulted in a clear exclusion of additional chiral quarks. A fruitful collaboration with local phenomenologists appeared on this fourth generation quark topic.
- New multi-variate **b-tagging algorithms** have been developed resulting in a 5-20% relative improvement in the b-tagging performance (JINST 8 (2013) P04013 with 578 citations; CMS-PAS-BTV-15-001 with 69 citations), and therefore with a direct impact on for example H->bb and t->bW physics studies. For the first time in the CMS Collaboration a **novel c-tagger** was developed by our researchers (CMS-PAS-BTV-16-001).
- Using innovative reconstruction techniques a first CMS paper on the **production of four top quarks** within the Standard Model was achieved (at the time of publication the strongest limits worldwide, JHEP 1411 (2014) 154 with 30 citations). In the spirit of HEP@VUB these limits were subsequently used to provide limits on the production of sGluons, scalar gluon particles that occur in many non-minimal supersymmetry models (Phys.Lett. B746 (2015) 48-52 with 7 citations).
- A substantial fraction of supersymmetry and other physics Beyond the Standard Model scenarios are expected to produce particles that will travel for a short distance before producing particles that can be detected by the LHC experiments. The novelty of such a **search for displaced leptons** that could be originating from such displaced supersymmetry resulted in a first experimental publication on the topic (Phys.Rev.Lett. 114 (2015) 6, 061801 with 33 citations).
- Grown out of a joint ATLAS/CMS working group that was setup with theorists to study the introduction of **simplified models for dark matter searches** (Phys.Dark Univ. 9-10 (2015) 8-23 with 71 citations), a successful transition to these simplified models was implemented in CMS, in particular in the context of the important monojet analysis (paper submitted to JHEP), where currently some of the most sensitive limits at the LHC on the direct production of dark-matter particles were obtained. This global effort at the LHC is co-led by Steven Lowette, and the project fits excellently in the vision of HEP@VUB.

Members of the HEP@VUB Collider Physics team contributed or have taken leadership in several other research efforts in the CMS collaboration; examples include: **top quark mass and mass difference measurements** (JHEP 1212 (2012) 105, 99 citations; JHEP 1206 (2012) 109, 37 citations), **top quark pair cross section measurements** (Phys.Lett. B695 (2011) 424-443, 150 citations; Phys.Lett. B728 (2014) 496-517, 150 citations; Eur.Phys.J. C71 (2011) 1721, 78 citations; Phys.Rev. D84 (2011) 092004, 126 citations), **single-top quark production in the Wt channel** (Phys.Rev.Lett. 110 (2013)



022003, 121 citations) and **search for excited bottom quarks decaying to tW** (JHEP 01 (2016) 166, 11 citations), **search for stop quark pairs** (Eur.Phys.J. C73 (2013) 12, 2677, 283 citations; Eur.Phys.J. C76 (2016) 8, 460, 12 citations), **measurement of anomalous top quark couplings** (JHEP 1310 (2013) 167, 46 citations), **leadership in Analysis Tools** (Taejeong Kim as co-convener), **Tracker Upgrade studies, jet energy calibration** (JINST 6 (2011) P11002, 835 citations), **new c-tagging development**, ... One of our postdoctoral researcher was based at CERN to participate and coordinate the CMS tracker commissioning efforts towards the Run-2 of the LHC.

Also a last combination publication from the LEP experiments appeared in 2013 on W physics (Phys.Rept. 532 (2013) 119-244, 205 citations, where Jorgen D'Hondt is a member of the LEP Electroweak Working Group).

Astro-Particle Physics: The HEP@VUB group is involved in the detection and study of (very) high-energy neutrinos to search for transient events, dark matter and cosmic point sources. Below a few highlights are listed in which HEP@VUB members take the lead or are among the key researchers.

- Concerning dark matter studies, we focus on neutrino signatures from WIMPs located in the center of the Sun or the Earth. One of the research highlights is the achievement of the **most stringent limits on Solar WIMPs** (Phys.Rev.Lett. 110 (2013) 131302 with 257 citations). This was made possible thanks to the excellent performance of the veto capabilities of the IceCube sensors surrounding DeepCore. More recently an analysis has been finalized on a search for WIMP signals from the center of the Earth, being the first study for Earth WIMPs performed with the IceCube observatory. This research has been reflected in the PhD thesis (2015) of Jan Kunnen and a paper (arXiv:1609.01492) has recently been submitted for publication to EPJ C which provides the **most stringent limits on Earth WIMPs to date**.
- In a study aimed at the identification of high-energy neutrino production in relation with Gamma Ray Bursts, **unexpected low flux limits on GRBs** have been obtained (Nature 484 (2012) 351 with 229 citations). This strengthens the mystery around the origin of the most energetic cosmic rays because either Gamma Ray Bursts are not the only sources of the very energetic cosmic rays that we observe at Earth or the associated high-energy neutrino production is well below theoretical expectations or the neutrino flux is (mainly) associated to the precursor and/or afterglow phases of the GRBs. This result ruled out a large number of theoretical models. Consequently, the search is now open for new (maybe yet unknown) candidates, among which are the Active Galactic Nuclei, or for an innovative analysis to address the GRB precursor and afterglow phases. Elaborating on the original idea by Nick van Eijndhoven (Astroparticle Physics 28 (2008) 540 with 7 citations) a novel analysis method for the study of the precursor and afterglow phases of these cataclysmic phenomena is being developed by our HEP@VUB team to exploit the arrival time spectra of neutrino induced muons. A first implementation of this new approach has been performed on short and long duration GRBs separately and the results are reflected in the PhD theses (2015) of Martin Casier and Lionel Brayeur, respectively, and were published in PoS ICRC2015 (2016) 1048. With additional data from the full IceCube observatory we aim to increase the sensitivity and observe neutrinos from these objects for the first time in history in the near future in a follow up analysis.
- Another highlight is the **discovery of cosmic very high-energy neutrinos** (Science 342 (2013) 1242856 with 484 citations) and a subsequent more detailed study of their characteristics (Phys.Rev.Lett. 113 (2014) 101101 with 505 citations), which marks the birth of neutrino astronomy. This achievement was awarded the title "Breakthrough of the year 2013" by the Physics World magazine. Beyond this discovery, our HEP@VUB group has taken the lead (by Geraldina Golup and Olaf Scholten) in a combined study of these very energetic cosmic neutrinos and the ultra-high energy cosmic ray (UHECR) events observed with the Pierre Auger and Telescope Array observatories. The aim is to identify the sources of the highest energy particles via



correlation studies and the initial results have recently been published (JCAP 1601 (2016) 037, with 12 citations).

In addition to the topics mentioned above, our HEP@VUB team has also taken the lead in studies related to neutrinos from Active Galactic Nuclei (AGN) and solar flares. Concerning the AGN we focus on the ones for which the relativistic jet is aligned along our line of sight, called Blazars. However, instead of selecting the sources which are brightest in gamma rays as was done in previous analyses, we search for dust obscured Blazars via a combined radio and gamma ray flux investigation. The dust provides an additional target for high-energy neutrino production, which will enhance the detection potential with IceCube. An initial investigation of radio and X-ray spectra of nearby Blazars has been performed by Giuliano Maggi et al. (PoS ICRC2015 (2016) 1050) and several potential candidates for these dust-obscured objects have recently been identified. The results of this study (arXiv:1608.00028) have been accepted for publication in Phys.Rev. D.

Triggered by indications of an apparent correlation between low-energy neutrino fluxes and major solar flares, we have proposed a new analysis to study the feasibility of using IceCube to search for neutrinos in coincidence with solar flares, using X-ray and gamma ray fluxes observed by satellites as a time window template (PoS ICRC2015 (2016) 1049). For this our HEP@VUB team (with Gwen de Wasseige as lead) is developing a dedicated analysis for which we also have proposed a special data-taking mode for the IceCube detector, which is currently being implemented at the South Pole. In doing so we realized that this new data taking mode would also be beneficial to a search for neutrinos related to gravitational wave events and consequently we will also pursue this approach in our analyses.

Concerning detector upgrades and commissioning, three of our team members (M. Casier (2013), L. Brayeur (2015) and G. de Wasseige (2016)) were selected by the IceCube collaboration to actually travel to the South Pole to install and test new detector hardware.

High-energy astrophysics: The high-energy astrophysics group started in October 2014. We use the LOFAR radio telescope to study the radio pulses of extended air showers. In recent years the following results have been achieved:

- **Mass composition of cosmic rays.** Radio detection of air showers is a rapidly developing technique that can be used to study the mass composition of cosmic rays, a crucial ingredient in understanding their origin. Using a novel reconstruction technique based on two-dimensional radiation profiles developed by Stijn Buitink (Phys.Rev. D 90 (2014) 082003 with 25 citations) it was shown that LOFAR achieves the same precision as the fluorescence detection technique employed by the Pierre Auger Observatory. The first composition results were published in Nature and are in agreement with existing world data (Nature 531 (2016) 70-73 with 10 citations). The LOFAR energy range (10^{17} eV – 10^{18} eV) is of particular interest as it may harbour a transition from galactic to extragalactic origin, which is reflected in the mass composition. Current research focuses on further studies of systematic effects (Astropart. Phys. (2016) submitted) and an extension to lower energies.
- **Properties of air shower radio signals.** The LOFAR core consists of hundreds of dipole antennas within an area of ~ 2 km². This allows a study of the characteristics of radio pulses from air showers in very high detail. LOFAR has demonstrated that the pulse polarization (JCAP 10 (2014) 14 with 18 citations) and frequency spectrum (Astropart. Phys. 65 (2015) 11 with 18 citations) are in agreement with state-of-the-art simulation codes. A new time calibration method for short raw voltage time-series data was developed (Astron. & Astrophys. 590 (2015) A41 with 1 citation) in order to be able to study the shape of the radiation front and to achieve a 0.1 degree angular resolution (Astropart. Phys. 61 (2015) 22 with 19 citations). The detailed knowledge was used to develop parameterizations (Astropart. Phys. 60 (2014) 13 with 21 citations) and fast reconstruction tools (JCAP 05 (2015) 018 with 7 citations).



- **Interaction between air showers and thunderstorms.** It has been known for some time that the radio signals of air showers can be amplified in the presence of an atmospheric electric field. Recently we have shown that the polarization and power profiles of the radio emission hold information on the strength and direction of such a field and can thus be used to probe thunderstorm fields (Phys.Rev.Lett. 114 (2015) 165001 with 14 citations, Phys.Rev. D 93 (2016) 70 with 3 citations). By studying the full Stokes parameters an additional component of circular polarization has been found offering new possibilities of localizing charge layers in clouds (Phys.Rev. D (2016) accepted). Together with the University of Groningen and the CWI in Amsterdam we have formed a "cosmic lightning" collaboration in which we also study the influence of the deposit of low-energy air shower electrons on electrical processes in thunderstorms – and possible the initiation of lightning (Phys.Rev.Lett 115 (2015) 015002 with 7 citations).

Theoretical Physics: Our work on theoretical high-energy physics has mainly focused on geometric aspects of string theory and supersymmetry, applications of gauge/gravity duality, and cosmology. A few selected highlights are discussed below.

- **Geometric aspects of string theory.** Recent years have seen rapid development in the ideas of duality symmetric formalisms of string and M-theory. These approaches promote U-dualities to manifest symmetries and refine our understanding of geometry from the point of view of a string. The HEP@VUB group played a key role in e.g. elucidating the gauge structure of these theories (JHEP 1301 064, 95 citations) and contributed an influential review (Phys.Rept. 566 (2014) 1, 104 citations). The theory of supersymmetric chiral bosons and their application to the duality symmetric string has been formulated (JHEP 1307 086, 6 citations; arXiv 1609.03315 submitted) and is currently further developed in realistic string backgrounds with the final aim to understand the role being played by generalized Kähler geometry. C. Blair joined the group in October 2015 and already made incisive contributions providing an F-theory interpretation of these ideas (CQG 33 (2016) no.19, 195009, 6 citations, and recent preprints applying these ideas to black hole thermodynamics and negative strings).

A key development has been notions of generalized T-duality and the HEP@VUB group has led the way in their applications in holography (NPB 873 (2013) 1, 47 citations). Critical recent progress has been made in the application of non-Abelian and Poisson Lie T-duality in the construction of new so-called eta and lambda integrable string theory supergravity backgrounds that are conjectured to holographically encode long sought quantum group deformations of gauge theories (JHEP 1412 164, 33 citations; JHEP 1507 019, 34 citations). Most recent progress has been in applying the ideas of resurgence analysis to examine the quantum behavior of these theories (JHEP 1607 088, 2 citations).

Together with two Cambridge University collaborators, Alexander Sevrin discovered a completely novel way ("the third way") to obtain consistent continuity relations in gauge theories. In addition, this elucidated the intricate relation between Yang-Mills theories and massive Chern-Simons theories in three dimensions (Phys.Rev.Lett. 114 (2015) 181603, 2 citations). This is currently being extended to higher dimensional field theories.

- **Applications of gauge/gravity duality.** Gauge/gravity duality refers to a remarkable equivalence between certain strongly coupled quantum field theories and weakly coupled gravity theories in a negatively curved Anti-de Sitter (AdS) spacetime with one extra dimension. In a series of papers that started with (Phys.Rev.Lett. 106 (2011) 191601, 196 citations; Phys.Rev. D84 (2011) 026010, 202 citations), Ben Craps and collaborators made use of holography to study the behavior of strongly coupled quantum systems when taken out of equilibrium and then allowed to thermalize. We have found that in these models thermalization happens very fast (which is encouraging from the point of view of heavy ion collisions) and short-wavelength modes thermalize first. Our HEP@VUB group wrote pioneering papers on the effects of confinement (JHEP 1402 (2014) 120, 27 citations; Phys.Rev. D90 (2014) no.8, 086004, 17 citations; JHEP 1512 (2015)



116, 6 citations) and inhomogeneities (Phys.Rev.Lett. 111 (2013) 231602, 29 citations; JHEP 1310 (2013) 082, 26 citations) in far-from-equilibrium holography. The thermalization of spectral functions (JHEP 1304 (2013) 069, 46 citations; JHEP 1410 (2014) 172, 5 citations) may lead to links with condensed matter physics. Further links with condensed matter theory, in particular with charge density waves, superfluids and superconductors, were studied in a series of papers by H. Zhang (including Phys.Rev.Lett. 113 (2014) 091602, 33 citations).

In a recent series of papers, we have introduced an analytic approach for studying whether AdS is nonlinearly stable to arbitrarily small perturbations. Numerical work from 2011 suggested that spherically symmetric scalar field perturbations of arbitrarily small amplitude could lead to black hole formation in global AdS, often after many reflections from the AdS boundary, and secular growth in weakly nonlinear perturbation theory was identified to be responsible for the onset of energy transfer to short-wavelength modes. It was later observed, however, that other initial profiles do not lead to collapse. We have resummed the secular terms that invalidate naive perturbation theory, leading to equations describing the energy flow between modes. Key results include, among others, the absence of most secular terms (JHEP 1410 (2014) 48, 45 citations) and the construction of three conserved charges of the flow equations (JHEP 1501 (2015) 108, 37 citations).

- **Cosmology.** In the year 2013 the Planck experiment released the data relevant for constraining cosmological scenarios including the dark matter and dark energy components. L. Lopez Honorez has been involved in providing new analyses using CMB experiments results (1) on the dark matter annihilation cross-section and life-time including for the first time realistic halo models from N-body simulations (JCAP 1307 (2013) 046, 47 citations & JCAP 1402 (2014) 017, 27 citations), and (2) on coupled dark matter-dark energy models (Phys.Rev. D88 (2013) 2, 023531, 60 citations). In addition, she has shown that the scalar nature of certain dark matter candidates could be of particular interest for dark matter searches (JHEP 1506 (2015) 154, 10 citations and JCAP 1602 (2016) no.02, 002, 12 citations) and has determined imprints of dark matter on future cosmological probes such as the 21cm line signal (JCAP 1608 (2016) no.08, 004, 2 citations). In a series of papers (including JCAP 1208 (2012) 024, 83 citations and CQG 31 (2014) 015022, 49 citations), A. Koshelev and collaborators have constructed string-field-theory-inspired nonlocal gravity models and applied them to various cosmological questions.

New directions:

The SoLid experiment based at SCK-CEN (Mol, Belgium) near the BR2 nuclear reactor studies very short baseline neutrino oscillations. The aim is to zoom in into the so-called reactor anomaly observed by other experiments for neutrino oscillations at very short distances. A novel technique was tested successfully on a proto-type setup, and in 2015 deployed in a larger detector placed between 5 meter and 10 meter from the reactor core. Together with a very dense and homogeneous reactor core this is unique worldwide. As a technical breakthrough we managed to collect in early 2015 the first rounds of reactor-on and reactor-off data. Early 2017 we will install the full-scale detector, and after 2-3 years of data taking we expect to either exclude or confirm the reactor anomaly. At the VUB the project is led by Petra Van Mulders (FWO post-doc and 3-year 10% professor), who is responsible in the collaboration for the estimation of all background contributions and acts as the resources manager. One of her postdocs takes the leadership and coordination role in the oscillation analysis itself. The first journal papers from this experiment will appear soon. After numerous conference contributions (e.g. ICHEP, IEEE and Neutrino) with preliminary results the national and international community attributes great attention to the project. Recently the 4th era (since the 1960s) of the BR2 reactor started and will run for at least 10 years.

The ARA experiment based on the South Pole deploys an innovative radio detection technique in order to detect showers of the extremely low flux of very energetic neutrinos beyond the reach of the current IceCube observatory. The most energetic cosmic ray particles will be destroyed by interactions with the Cosmic Microwave Background radiation on their journey through the Universe. These interactions should



be a source of very energetic (GZK) neutrinos and their flux will provide insight in the composition of the most energetic cosmic rays. However, on the basis of cosmic ray flux measurements by the Pierre Auger Observatory and the Telescope Array, the associated neutrino flux is expected to be extremely low and consequently large detector areas are required. The astro-particle physics group of HEP@VUB has taken the lead (by Olaf Scholten and Krijn de Vries) to investigate the opportunities using radio detection and radar reflection techniques in ice in order to detect a substantial amount of particles in the high-energy range which is currently not covered by any detector. In view of this, an initial study of several aspects of radio detection of particle showers has been performed by our HEP@VUB team and the results have recently been published (Astroparticle Physics 74 (2016) 96). With recent beam tests of prototype detectors and the commissioning of the first stations of the Askaryan Radio Array (ARA), initial data are now available for analysis.

The IceCube-Gen2 experiment will be an extension of the current IceCube observatory. Due to the very low particle flux at very high energies, extensions of the current detector volume and even new detection techniques have to be investigated. Our VUB team has taken the lead in both the feasibility studies of InIce self-veto procedures (by Simona Toscano and Nick van Eijndhoven) for the high-energy upgrade of the IceCube observatory as well as in the development of radio detection techniques (by Olaf Scholten and Krijn de Vries), as indicated above. The former studies are performed in order to reduce the energy threshold for the identification of cosmic neutrinos in the existing IceCube detector as well as to provide a clean environment for the event selection in the foreseen IceCube-Gen2 configuration. This will increase the efficiency for the detection of cosmic neutrinos and might also enable a hybrid InIce-radio analysis which could reduce the energy threshold for the radio detection. The radio detection techniques will allow an expansion of the current IceCube detector area by about two orders of magnitude, which is required to obtain sufficient event statistics at these high energies. It is the intention that the above-mentioned ARA experiment will become a radio component of the future IceCube-Gen2 observatory.

The Square Kilometer Array is an expansive radio telescope array for which construction will start in 2020. The low frequency component will be built in Australia and consists, like the LOFAR low-band antennas, of omni-directional receivers suitable for radio detection of air showers. Together with scientists from Germany, the UK, the Netherlands, and other countries we have formed a High Energy Cosmic Particle Focus Group that explores the possibility of detecting atmospheric air showers and particle cascades in the lunar surface with the SKA, building on the experience with LOFAR and other observatories. The SKA design team is currently considering engineering change proposals that will make it possible to install a particle triggering array and signal buffering capability for individual antennas. The high-energy astrophysics group in HEP@VUB is one of the driving forces of this effort.

b. External funding

Copied from Section 6 in the Application for Renewal (i.e. page 9-11 of this document)

In the period 2013-2016 we obtained or had running projects for **a total of 16.5M euro of external funds, as well as obtained 7 doctoral and 8 postdoctoral mandates directly from funding agencies (equivalent with an additional about 2.7M euro)**. The annual 0.26M euro SRP funds, or 1.3M euro total fund over 5-year, have been used mainly to continue initiating our phenomenological work and as seed-budget for additional research in HEP@VUB. Recently we have been able to consolidate these investments with the hiring of a first faculty member in phenomenology. With 74 candidates applying we had a very strong short list including for example an ERC grant holder. A selection of key budgets provided to HEP@VUB members is mentioned below. Although in several cases we are the promoter of interuniversity projects, only budgets provided to the VUB part of the projects are quoted. Not mention are the VUB-internal budgets we received.

Jointly HEP@VUB is partner in the IUAP Fundamental Interactions

A total budget for pre-doc and post-doc hirings: 500k euro (total of 5 years, 2013-2017)



Funding obtained for the Phenomenology group

2 FWO 4-year PhD mandates (including a total bench fee of 30k euro)
1 FWO 1-year Pegasus postdoc mandate (including a total bench fee of 4k euro)

Funding obtained for the CMS experiment

Big Science program (2013-2017): 1950k euro (total of 5 years, 2013-2017)
Hercules equipment for the CMS Tracker Upgrade (2016-2020): 5190k euro (2016-2020)
4 FWO 4-year projects: 1120k euro personnel, 316k euro running budget (total budgets of projects)
Odysseus 2 (Freya Blekman): 867k euro (2011-2015)
Odysseus 2 (Steven Lowette): 763k euro (2013-2017)
4 FWO 3-year post-doc mandates (including a total bench fee of 48k euro)
1 FWO 4-year PhD mandate (including a total bench fee of 15k euro)

Funding obtained for the SoLid experiment

2 FWO 4-year projects: 420k euro personnel, 15k euro running budget (total budgets of projects)
Hercules funding of 50k euro equipment (quoted VUB part only in a UA-UGent-VUB consortium)

Funding obtained for the IceCube, ARA and Auger experiment

Big Science program (2013-2017): 366k euro (total of 5 years, 2013-2017)
2 FWO 4-year projects: 320k euro personnel, 60k euro running budget (total budgets of projects)
Odysseus 1 (Nick Van Eijndhoven): 2000k euro (2009-2014)
1 FWO 3-year post-doc mandate (including a total bench fee of 12k euro)

Funding obtained for the LOFAR observatory and the AARG research group

ERC Starting Grant (Stijn Buitink): 1500k euro (5 years, 2015-2020)
1 FWO 3-year post-doc mandate (including a total bench fee of 12k euro)

Funding obtained for theoretical high-energy physics research

2 FWO 4-year projects: 480k euro personnel, 80k euro running budget (total budget of projects)
5 FWO 4-year PhD mandates (including a total bench fee of 45k euro)
6 FWO postdoc mandates (a total of 21 person years, including a total bench fee of 84k euro)
Joint Groningen-VUB PhD position: 4 person years, of which two will be spent at the VUB
Solvay Institutes funding for PhD position: 2 person years

Some of the additional obtained external funding for networks

COSPA network funded by FWO (12k euro per year for the network) and FNRS: funding for organizing scientific meetings on cosmoparticle physics.

EU COST network "MPNS COST Action MP1210: The String Theory Universe", http://www.cost.eu/COST_Actions/mpns/Actions/MP1210: provides ad hoc travel funding for young scientists in our group and organizes regularly high level scientific meetings on topics closely related to our research interests. Budget for the network: 128k euro per year.

ESF HoloGrav network, <http://www.fc.up.pt/cfp/HoloGrav/>: encourages and promotes research in gauge/gravity duality, including its applications across particle, nuclear, condensed matter and gravitational physics. The network supports staff and student exchanges, workshops, conferences and summer schools. Budget for the network: 134k euro per year.

ERC funding requested by HEP@VUB researchers:

- Stijn Buitink (group leader): obtained an ERC starting grant



- Petra Van Mulders (FWO post-doc, and 3-year 10% ZAP, Collider Physics): applied for an ERC starting grant (reached the interview stage, not selected)
- Laura Lopez Honorez (FWO post-doc, and 3-year 10% ZAP, Theoretical Physics): applied for an ERC starting grant (not selected)
- Alexey Koshelev (FWO post-doc, Theoretical Physics): applied for an ERC consolidator grant (not selected)
- Alberto Mariotti (FWO post-doc, Theoretical Physics): applied for an ERC starting grant (not selected)
- Ben Craps (group leader): applied for an ERC advanced grant (result not yet known)

Future plans: In the Odysseus program we had in addition to the three successful candidates, six other candidates applying (of which one Odysseus-I position was approved but finally not taken by the candidate due to a competing offer in Germany, and one Odysseus-II was selected by the Odysseus jury but not funded by the university because of budget constraints). In the future the HEP@VUB staff members will continue to apply and to seek outstanding internal and external candidates to apply through these national and international channels. Several faculty members and researchers in HEP@VUB have indeed very concrete plans to apply soon for ERC grants.

c. International mobility

Because of the international character of our research the HEP@VUB group leaders as well as all other members of HEP@VUB spend in general a significant fraction of their time at laboratories and institutions abroad. Group leaders finance this mobility on their research grants external to the SRP budget.

Jorgen D'Hondt: In his role as Chairperson of the CMS Collaboration Board, as well as national delegate in RECFA and as member of other boards, Jorgen D'Hondt will typically have one or two travels abroad per week. This allows him to participate in several management meetings and discussions of the CMS Collaboration with more than 4000 members, to act on the policy making and advisory level worldwide and to interact with CMS team leaders from more than 200 institutions.

Ben Craps: In the period 2013-2016, the international mobility of Ben Craps included several extended stays (including Visiting Professor at École Normale Supérieure, Paris, France, 1-31 May 2014, and the Nordita program on "Black Holes and Emergent Spacetime", Stockholm, Sweden, 7-21 August 2016), 10 invited conference talks, 11 invited seminars or colloquia, an invited lecture series as well as other conferences and collaboration visits.

Nick van Eijndhoven: In view of his role as Belgian representative in the HEP board of the European Physical Society, co-PI for the Belgian groups in IceCube, membership of international committees and various invitations to conferences, Nick van Eijndhoven spends a considerable fraction of his time abroad. However, this obviously is limited by his commitments at the home institute. On average in the period 2013-2016 Nick van Eijndhoven spent about 10% of his time abroad.

Only about 20% of our PhD students obtained their Master degree at the VUB, another 20% at another Belgian university and finally the remaining 60% obtained their Master degree abroad. Less than 10% of our postdocs did obtain a PhD at the VUB.

In the period 2013-2016, only for researchers in the phenomenological team was the mobility financed from the SRP budget. The SRP management has agreed on a general policy for our non-tenured researchers concerning mobility budgets. Those researchers with an individual FWO grant use their FWO bench fee, while those without an FWO grant are provided a budget equal to the FWO bench fee. This comes with the



agreement that for each trip and whenever applicable the individual researcher will explore the opportunities at the FWO, VUB, doctoral school, Erasmus, etc. We are typically very successful in these applications. Our policy is that PhD students will in general participate in at least two international schools in high-energy physics.

For the experimental groups mobility is intrinsic in the research program because the instrument is installed elsewhere. Our researchers within the CMS Collaboration will typically participate several weeks per year at CERN and work on detector related operations. Several of our IceCube researchers spent an extended time period at the South Pole. Our researchers typically participate in some of the international collaboration weeks of the CMS, SoLid, IceCube and LOFAR collaborations. The above costs related to the participating in large international experiments are covered by the research budgets of the corresponding group. Budgets for the operational travels are foreseen within the FWO Big Science program. On these same budgets, dedicated apartments have been rented since the 1980s for accommodation around CERN.

As mentioned above, the HEP@VUB project embeds a dedicated visitors program. This is to enhance strongly the incoming mobility to the VUB and to strengthen the international position of the HEP@VUB program. Therefore with a modest financial investment our researchers can join and initiate excellent projects leading to important journal publications and new insights that stimulate the whole HEP@VUB team of currently more than 50 individual researchers. Since the start of the visitors program we have had in total more than 25 short to medium term visits. For instance, in the last years, HEP@VUB was visited by world leading researchers such as Alejandro Ibarra (Munich, MPI), Giovanni Villadoro (Trieste, ICTP), Adam Falkowski (Orsay, LPT), Steven Abel (Durham, IPPP), Michael Spannowsky (Durham, IPPP). These visits were very fruitful also for boosting joint projects (Eur. Phys. J. C75 (2015) no.12, 583 with 14 citations; JHEP 1608 (2016) 018 with 3 citations). Other aspects of incoming mobility are the Francqui Chairs in Belgium. We were the host of the International Francqui Chair 2013-2015, Prof. Francis Halzen, as well as the National Francqui Chair 2014, Prof. Antoine Van Proeyen.

Several of the PhD students and postdoctoral fellows who joined our team, have found excellent permanent positions, often abroad. Some examples over the last years: Stephanie Beauceron (CNRS researcher at IN2P3-Lyon, France), Taejeong Kim (professor at Chonbuk National University, Korea), Stijn Buitink (professor at VUB, after postdoc positions at Lawrence Berkeley National Laboratory, VUB and Universiteit Nijmegen), Steven Lowette (professor at VUB, after a postdoc at UCSB, USA), Geraldina Golup (staff researcher at the Bariloche Atomic Center, Argentina), Jonathan Miller (professor at the University of Valparaiso, Chile), Laura Lopez Honorez (faculty ULB), Alberto Mariotti (professor at VUB, after a postdoc at Durham, UK), Daniel Thompson (faculty at Swansea, UK) and Hongbao Zhang (faculty at Beijing Normal University, China), ...

Also several have obtained excellent postdoctoral positions abroad. Some examples: Alice Bernamonti and Federico Galli obtained (3+2)-year postdoc positions at Perimeter Institute (Canada), Nele Callebaut a postdoc positions at Princeton University and Columbia University (USA), Piotr Surowka a postdoc position at Harvard (USA), Alexey Koshelev a 5-year postdoc position in Portugal, Wieland Staessens postdoc positions at Mainz (Germany) and Madrid (Spain), Alexis Kalogeropoulos a postdoc position at DESY (Germany), Rebeca Suarez a postdoc position at the University of Nebraska (USA), Nadjieh Jafari an FNRS postdoc position at the UCLouvain (Belgium) and a CERN fellowship, James Keaveney a postdoc position at DESY (Germany), ...

Examples of mobility of the phenomenological researchers hired on the SRP budget are noted below from a PhD student, Karen De Causmaecker (for the full period of her PhD project), and from a post-doctoral fellow, Kentarou Mawatari (for the period 2013-2014).



Karen De Causmaecker (PhD student, PhD started in October 2011, and defended in August 2016):

1. Research stay; Strasbourg, France; 3 days; 2012
2. FeynRules Workshop; Mont St-Odile, France; 1 week; 2012
3. MCnet-LPCC School; CERN, Geneva, Switzerland; 4 days; 2012
4. International School Cargese, Across the TeV Frontier with the LHC; Cargese, France; 2 weeks; 2012
5. Research stay; Strasbourg, France; 1 week; 2012
6. FeynRules/MadGraph School/Workshop; Natal, Brasil; 2 weeks; 2012
7. MC4BSM Workshop; DESY, Hamburg, Germany; 3 days; 2013
8. Theoretical Advanced Study Institute in Elementary Particle Physics (TASI); Boulder, Colorado; 4 weeks; 2013
- 9. Research stay; CERN, Geneva, Switzerland; 6 months; 2013-2014**
10. GDR Terascale Workshop; Paris, France; 3 days; 2014
11. FeynRules Workshop; Durham, UK; 1 week; 2014
12. SUSY2014 Conference; Manchester, UK; 1 week; 2014
13. PSI Zuoz Summerschool; Zuoz, Switzerland; 1 week; 2014
14. Research stay; CERN, Geneva, Switzerland; 1 week; 2014
15. MadAnalysis5 Workshop; Grenoble, France; 2 weeks; 2014
16. MadAnalysis5 Workshop; Grenoble, France; 1 week; 2015

Kentarou Mawatari (post-doctoral researcher, period 2013-2014):

1. Higgs as a Probe of New Physics 2013 / seminar / KEK Phenomenology meeting 2013; Toyama / Kobe / Tsukuba (Japan); 1 month; 2013
2. MC4BSM Workshop; DESY, Hamburg, Germany; 5 days; 2013
3. Seminar and research stay; Gothenburg, Sweden; 4 days; 2013
4. Seminar; Bonn Germany; 2 days; 2013
5. Kavli IPMU School on the Future of Collider Physics / Toyama ILC summer camp / Yukawa Institute PPP2013 / seminar; Kashiwa / Toyama / Kyoto / Osaka (Japan); 1 month; 2013
6. SUSY2013 Conference; Trieste, Italy; 1 week; 2013
7. HEFT2013 / Higgs couplings 2013; Geneva (Switzerland) / Freiburg (Germany); 1 week; 2013
8. SM@LHC2014; Madrid, Spain; 1 week; 2014
9. Research stay; Heidelberg, Germany; 1 week; 2014
10. MC4BSM2014 / seminar and research stay / seminar and research stay; Daejeon / Seoul / Suwon (Korea); 2 weeks; 2014
11. VBF Workshop; Warwick, UK; 1 day; 2014
12. FeynRules Workshop / SUSY2014; Durham / Manchester (UK); 2 weeks; 2014
13. CKM2014; Vienna, Austria; 1 week; 2014
14. Higgs couplings 2014; Torino, Italy; 1 week; 2014
15. ERC Meeting; Geneva, Switzerland; 3 days; 2014
16. FCC-ee (TLEP) Physics Workshop; Paris, France; 3 days; 2014
17. ILC Workshop; Grenoble, France; 3 days; 2014

Conference, workshop and school organization:

Members of HEP@VUB take part in the organization of national and international conferences, workshops and schools. Ben Craps is an organizer of the yearly Amsterdam-Brussels-Geneva-Paris 9-week doctoral school on "Quantum Field Theory, Strings and Gravity" for first-year PhD students, and of the yearly Solvay/APC/PI workshop on "Cosmological Frontiers in Fundamental Physics". Alexander Sevrin is an organizer of the yearly CERN Winter School on Supergravity, Strings, and Gauge Theory. Ben Craps and



Alexander Sevrin were organizers of "The String Theory Universe; 21st European string workshop", Leuven, Belgium (September 2015). Daniel Thompson was an organizer of the Simons workshop on "Generalized Geometry and T-dualities", Stony Brook, USA (May 2016). Hongbao Zhang was an organizer of the International Workshop on condensed matter physics and AdS/CFT, University of Tokyo, Japan (May 2015) and of a workshop on "Numerical Relativity and Holography", Santiago de Compostela, Spain (June 2016). Nick van Eijndhoven is coordinator of the neutrino section within the Science Program Committee of the International Cosmic Ray Conferences. As the Belgian representative in the High-Energy Physics board of the European Physical Society he is also involved in defining the program and organization of the related EPS conferences. Olaf Scholten is the chair of the 2016 issue of the international ARENA conference in Groningen, The Netherlands (June 2016). Jorgen D'Hondt is a permanent member in the International Advisory Board of the series of International Top Quark workshops. In his mandate as Chairperson of the CMS Collaboration Board, he also takes part in the organization and/or advisory boards of several schools and workshops, and is member of several research steering boards. He was the main co-organizer of the CERN School of Computing in Belgium (Aug-Sept 2016). Steven Lowette is coordinating for the VUB the annual international Netherlands-Belgium-Germany school on particle physics with typically around 50 participating PhD students. Freya Blekman was the co-organiser of the "Physics Beyond Precision workshop" at CERN, a workshop focusing on BSM sensitivity in Top and SM physics at the Future Circular Collider (Febr 2016). Petra Van Mulders organized the international SoLid collaboration days in Brussels in September 2014 and February 2016.

Key international representations:

Jorgen D'Hondt represents Belgium in the Restricted European Committee for Future Accelerators (RECFA) and until recently also in the International Particle Physics Outreach Group (IPPOG). He is the chairperson of the International Scientific Advisory Panel of the Institute of Physics at the University of Amsterdam. Jorgen D'Hondt is the FWO delegate in the International Oversight Funding Group of the IceCube experiment organized by the NSF (USA). Alexander Sevrin is Deputy Director and Scientific Secretary and Ben Craps is Assistant to the Director of the International Solvay Institutes for Physics and Chemistry. Alexander Sevrin is national coordinator of the EU COST network "MPNS COST Action MP1210: The String Theory Universe", http://www.cost.eu/COST_Actions/mpns/Actions/MP1210. Nick van Eijndhoven is the Belgian representative in the High-Energy Physics board of the European Physical Society. He also acts as Adviser for the National Research Foundation (NRF) of South Africa. Catherine De Clercq is the FWO representative in the ApPEC General Assembly as well as the FWO representative in the CERN Resources Review Board. In 2014 Alexander Sevrin was elected a member of the International Union of Pure and Applied Physics (IUPAP).

d. Progress made

The original goals of the HEP@VUB program were to bring together various physics disciplines at the VUB in a united effort to study the key fundamental questions in high-energy physics. The understanding and search for supersymmetry was highlighted in the original proposal as a first topic around which this cross-group research can be initiated. From the organisational point of view the main aim was to establish an additional research team on phenomenological studies that connects scientifically the existing groups in collider physics, astro-particle physics and theoretical physics, and makes them stronger to address the above-mentioned fundamental questions.

The phenomenology team has now been established, with since the start of the project in total 5 post-doctoral researchers (of whom 2 obtained a temporary 10% faculty position) and 3 PhD students. Two PhD students graduated successfully in the phenomenology research. This academic year, a new tenure-track professor has been hired (Alberto Mariotti) in this research area to consolidate the work and investment, and to further strengthen the applications for additional external funding for phenomenological research. This is a milestone in the evolution of our HEP@VUB project.



Having consolidated the phenomenological team, we have extended our scope by including high-energy astrophysics. It is considered rare in the field of high-energy physics to establish a research centre that incorporates about 50 researchers in: theoretical physics, astro-particle physics, High-Energy Astrophysics, phenomenology, neutrino physics, and collider physics. The HEP@VUB budget was adequate to create the phenomenology team, and will in the future be essential to guarantee the sustainability of our knowledge and skills. High-energy physics projects run over long periods beyond the typical timescale of regular research projects. With the HEP@VUB budget we will continue to be able to make bridges between research projects as well as continue to be able to react timely on new developments in the very dynamic and international field of high-energy physics.

We are convinced that the phenomenological research in HEP@VUB has evolved successfully on a solid and diverse platform of experimental and theoretical research. This has opened novel possibilities not only for the phenomenological research, but also for the established theoretical and experimental groups. Several aspects of our research would not have been possible without the direct or indirect crosstalk between the phenomenological, theoretical and experimental researchers. Some examples are highlighted below with links to the publication list further on.

- In Gauge Mediated Supersymmetry models we have investigated together the possible excess observed by the CMS experiment in multi-lepton channels ([1] a clear experimental/phenomenological/theoretical collaboration) and have studied the phenomenology in light of the 125 GeV Higgs discovery ([2] a theoretical/phenomenological collaboration).
- Currently new Dark Matter models are being investigated between experimental and phenomenological groups. Simplified models for SIMPs are defined for the new 13 TeV LHC run ([3] a clear experimental/phenomenological collaboration) as well as novel models in the top quarks sector involving flavour changing dark matter couplings (a further experimental/phenomenological collaboration [4]). Moreover, members of both the pheno team and the CMS group have contributed to the recent document about Dark Matter searches at LHC [5].
- A direct collaboration between phenomenological and experimental researchers made possible a novel interpretation of four-top quark searches at the LHC in supersymmetric models with top-philic gluons [6].
- For the development of new numerical tools it is important to collaborate between theoretical, phenomenological and experimental researchers. A clear example emerged from our HEP@VUB team in collaboration with international partners [7].
- In a recent collaboration between the pheno group and the IceCube group it has been proposed for the first time that obscured Active Galactic Nuclei are the astrophysical sources responsible for the observed high energy cosmic neutrino flux [8].

New research directions have been explored. Members of HEP@VUB have joined and initiated the SoLid experiment at SCK-CEN in Mol (Belgium) on very short baseline neutrino oscillations, we established a joint project with the Auger experiment on high energetic-cosmic rays (Argentina) and initiated our involvement in SKA (Australia and South Africa).

The full HEP@VUB realized about 750 publications since the start of 2012 (the year of application). Since 2012, the phenomenology group has pursued excellent research activity in beyond standard model physics and collider physics. The group has published 36 papers in peer-reviewed international journals as well as 14 preprints and proceedings, collecting in total around 920 citations. Data from SPIRES on November 4, 2016:

Papers Published in international peer reviewed journals



Cornering diphoton resonance models at the LHC

M. Backović, S. Kulkarni, A. Mariotti, E. M. Sessolo and M. Spannowsky

JHEP 1608 (2016) 018

3 citations

Characterising the 750 GeV diphoton excess

J. Bernon, A. Goudelis, S. Kraml, K. Mawatari and D. Sengupta

JHEP 1605 (2016) 128

25 citations

Diphoton excess in phenomenological spin-2 resonance scenarios

A. Martini, K. Mawatari and D. Sengupta

Phys. Rev. D 93 (2016) no.7, 075011

33 citations

Di-photon excess illuminates Dark Matter

M. Backovic, A. Mariotti and D. Redigolo

JHEP 1603 (2016) 157

202 citations

[4] Signatures of top flavour-changing dark matter

J. D'Hondt, A. Mariotti, K. Mawatari, S. Moortgat, P. Tziveloglou and G. Van Onsem

JHEP 1603 (2016) 060

4 citations

General squark flavour mixing: constraints, phenomenology and benchmarks

K. De Causmaecker, B. Fuks, B. Herrmann, F. Mahmoudi, B. O'Leary, W. Porod, S. Sekmen and N. Strobbe

JHEP 1511 (2015) 125

6 citations

Rosetta: an operator basis translator for Standard Model effective field theory

A. Falkowski, B. Fuks, K. Mawatari, K. Mimasu, F. Riva and V. Sanz

Eur.Phys. J. C 75 (2015) no.12, 583

14 citations

Higher-order QCD predictions for dark matter production at the LHC in simplified models with s channel mediators

M. Backović, M. Krämer, F. Maltoni, A. Martini, K. Mawatari and M. Pellen

Eur. Phys. J. C 75 (2015) no.10, 482

17 citations

Z-peaked excess in goldstini scenarios

S. P. Liew, A. Mariotti, K. Mawatari, K. Sakurai and M. Vereecken

Phys.Lett.B 750 (2015) 539

10 citations

Singlet-Doublet Model: Dark matter searches and LHC constraints

L. Calibbi, A. Mariotti and P. Tziveloglou

JHEP 1510 (2015) 116

21 citations



Signs of Tops from Highly Mixed Stops

M. Backović, A. Mariotti and M. Spannowsky

JHEP 1506 (2015) 122

13 citations

Higgs production in association with a single top quark at the LHC

F. Demartin, F. Maltoni, K. Mawatari and M. Zaro

Eur. Phys. J. C 75 (2015) no.6, 267

35 citations

Search for Kaluza-Klein gravitons in extra dimension models via forward detectors at the LHC

G. C. Cho, T. Kono, K. Mawatari and K. Yamashita

Phys. Rev. D 91 (2015) no.11, 115015

2 citations

Signals of a superlight gravitino at the LHC

F. Maltoni, A. Martini, K. Mawatari and B. Oexl

JHEP 1504 (2015) 021

4 citations

[6] Probing top-philic sgluons with LHC Run I data

L. Beck, F. Blekman, D. Dobur, B. Fuks, J. Keaveney and K. Mawatari

Phys. Lett. B 746 (2015) 48

7 citations

[3] Simplified SIMPs and the LHC

N. Daci, I. De Bruyn, S. Lowette, M. H. G. Tytgat and B. Zaldivar

JHEP 1511 (2015) 108

3 citations

Higgs characterisation at NLO in QCD: CP properties of the top-quark Yukawa interaction

F. Demartin, F. Maltoni, K. Mawatari, B. Page and M. Zaro

Eur.Phys.J.C 74 (2014) no.9, 3065

47 citations

Dirac Gauginos in Low Scale Supersymmetry Breaking

M. D. Goodsell and P. Tziveloglou

Nucl. Phys. B 889 (2014) 650

18 citations

Automated third generation squark production to next-to-leading order

D. Goncalves, D. Lopez-Val, K. Mawatari and T. Plehn

Phys. Rev. D 90 (2014) no.7, 075007

13 citations

Monophoton signals in light gravitino production at e+e- colliders

K. Mawatari and B. Oexl

Eur. Phys. J. C 74 (2014) no.6, 2909

4 citations



Flavour models with Dirac and fake gluinos

E. Dudas, M. Goodsell, L. Heurtier and P. Tziveloglou
Nucl. Phys. B 884 (2014) 632
30 citations

Multiphoton signatures of goldstini at the LHC

G. Ferretti, A. Mariotti, K. Mawatari and C. Petersson
JHEP 1404 (2014) 126
13 citations

Higgs characterisation via vector-boson fusion and associated production: NLO and parton-shower effects

F. Maltoni, K. Mawatari and M. Zaro
Eur. Phys. J. C 74 (2014) no.1, 2710
31 citations

[1] Multilepton signals of gauge mediated supersymmetry breaking at the LHC

J. D'Hondt, K. De Causmaecker, B. Fuks, A. Mariotti, K. Mawatari, C. Petersson and D. Redigolo
Phys. Lett. B 731 (2014) 7
11 citations

Simulating spin-3/2 particles at colliders

N. D. Christensen et al.
Eur. Phys. J. C 73 (2013) no.10, 2580
21 citations

A framework for Higgs characterisation

P. Artoisenet et al.
JHEP 1311 (2013) 043
89 citations

[2] Phenomenology of General Gauge Mediation in light of a 125 GeV Higgs

P. Grajek, A. Mariotti and D. Redigolo
JHEP 1307 (2013) 109
29 citations

Looking for leptogluons

D. Goncalves-Netto, D. Lopez-Val, K. Mawatari, I. Wigmore and T. Plehn
Phys. Rev. D 87 (2013) 094023
12 citations

[7] Automated mass spectrum generation for new physics

A. Alloul, J. D'Hondt, K. De Causmaecker, B. Fuks and M. Rausch de Traubenberg
Eur. Phys. J. C 73 (2013) no.2, 2325
21 citations

Negative Refractive Index in Hydrodynamical Systems

A. Amariti, D. Forcella and A. Mariotti
JHEP 1301 (2013) 105
13 citations



TauDecay: a library to simulate polarized tau decays via FeynRules and MadGraph5

K. Hagiwara, T. Li, K. Mawatari and J. Nakamura

Eur. Phys. J. C 73 (2013) 2489

11 citations

Higgs Quantum Numbers in Weak Boson Fusion

C. Englert, D. Goncalves-Netto, K. Mawatari and T. Plehn

JHEP 1301 (2013) 148

62 citations

Field Theory Interpretation of N=2 Stringy Instantons

R. Argurio, D. Forcella, A. Mariotti, D. Musso and C. Petersson

JHEP 1302 (2013) 002

5 citations

Automated Squark and Gluino Production to Next-to-Leading Order

D. Gonçalves-Netto, D. López-Val, K. Mawatari, T. Plehn and I. Wigmore

Phys. Rev. D 87 (2013) no.1, 014002

39 citations

Light Gravitino Production in Association with Gluinos at the LHC

P. de Aquino, F. Maltoni, K. Mawatari and B. Oehl

JHEP 1210 (2012) 008

14 citations

Sgluon Pair Production to Next-to-Leading Order

D. Goncalves-Netto, D. Lopez-Val, K. Mawatari, T. Plehn and I. Wigmore

Phys. Rev. D 85 (2012) 114024

45 citations

Integrability on the Master Space

A. Amariti, D. Forcella and A. Mariotti

JHEP 1206 (2012) 053

7 citations

Soft Spectrum in Yukawa-Gauge Mediation

F. Galli and A. Mariotti

JHEP 1206 (2012) 055

4 citations

Preprints and proceedings

Handbook of LHC Higgs Cross Sections: 4. Deciphering the Nature of the Higgs Sector

D. de Florian et al. [LHC Higgs Cross Section Working Group Collaboration]

arXiv:1610.07922 [hep-ph]

An MCMC Study of General Squark Flavour Mixing in the MSSM

B. Herrmann, K. De Causmaecker, B. Fuks, F. Mahmoudi, B. O'Leary, W. Porod, S. Sekmen and N. Strobbe

PoS EPS HEP2015 (2015) 576



Signs of Tops from Highly Mixed Stops

A. Mariotti, M. Backovic and M. Spannowsky

PoS PLANCK 2015 (2015) 080

[5] Dark Matter Benchmark Models for Early LHC Run-2 Searches: Report of the ATLAS/CMS Dark Matter Forum

D. Abercrombie et al.

102 citations

Higgs characterisation: NLO and parton-shower effects

F. Demartin, E. Vryonidou, K. Mawatari and M. Zaro

arXiv:1505.07081 [hep-ph]

Characterising a Higgs-like resonance at the LHC

P. de Aquino and K. Mawatari

arXiv:1307.5607 [hep-ph]

Handbook of LHC Higgs Cross Sections: 3. Higgs Properties

S. Heinemeyer et al. [LHC Higgs Cross Section Working Group Collaboration]

doi:10.5170/CERN-2013-004

782 citations

MadGolem: automating NLO calculations for New Physics

D. Lopez-Val, D. Goncalves-Netto, T. Plehn, K. Mawatari and I. Wigmore

PoS LL 2012 (2012) 048

MadGolem: automated NLO predictions for Beyond-the-Standard Model searches

D. Lopez-Val, D. Goncalves-Netto, T. Plehn, I. Wigmore and K. Mawatari

PoS CHARGED 2012 (2012) 025

Electroweak Higgs boson production in the standard model effective field theory beyond leading order in QCD

C. Degrande, B. Fuks, K. Mawatari, K. Mimasu and V. Sanz,

arXiv:1609.04833

Submitted

tWH associated production at the LHC

F. Demartin, B. Maier, F. Maltoni, K. Mawatari and M. Zaro,

arXiv:1607.05862

Submitted

A comprehensive approach to dark matter studies: exploration of simplified top-philic models

C. Arina et al.,

arXiv:1605.09242

Submitted

[8] *Obscured flat spectrum radio AGN as sources of high-energy neutrinos*

G. Maggi et al.

arXiv:1608.00028 [astro-ph.HE]

Submitted



Several of our non-tenured members have obtained national and international recognition; examples are best thesis prizes, best presentation prizes, top-level positions in our scientific community, etc. Some examples are listed below. Awards for the tenured HEP@VUB members are noted in Section (e) of this report, as well as in the short CVs of the group leaders.

- Saskia Demulder – received the Robert Brout Award (2015), the Prize of the Belgian Physical Society (2016) and the Solvay Award for her Master thesis “Integrability in the AdS/CFT correspondence”
- Sibylle Driezen – received the Prize of the Belgian Physical Society (2016) for her Master Thesis “T-dualiteit en $N = (4,4)$ supersymmetrie op het wereldvlak”
- Federico Galli – received the Solvay Award (2014) for his PhD Thesis “Applications of the AdS/CFT correspondence to non-equilibrium physics at strong coupling”
- Jonathan Lindgren – received the John Ericsson medal 2014 (awarded to the top 6 out of the 750 civil engineering students who graduated during year 2013 at Chalmers University of Technology)
- Annik Olbrechts – second prize for best poster presentation at the TOP2013 conference (Sept 2013, Durbach, Germany), “Measurement of the W polarization in $t\bar{t}$ production in lepton+jets events at 7 TeV” (2013)
- Jan Kunnen – second prize for best poster presentation at the Belgian Physics Society meeting “Search for Dark Matter in our Solar System with IceCube” (2012)
- Abideh Jafari (joint PhD VUB and IPM in Tehran, Iran) won the prestigious "Ali-Mohammadi Prize" for the most outstanding PhD dissertation in Iran (2012)
- Seth Moortgat – received the Robert Brout Award (2015)
- Dennis Diederix – received the Prize of the Belgian Physical Society for his Master thesis “Model Independent Search for Neutrinos from Gamma Ray Bursts with the IceCube Detector” (2012)
- Jan Kunnen – received the prize of the EuroPhysics Journal Best Poster Contest “Searching for neutrinos from Dark Matter annihilation in the Earth with the IceCube detector” (2012)
- Jan Kunnen – received the public award poster prize at the ISAPP Summer School “Search for Dark Matter Signatures with the IceCube detector”, Paris, France (2012)
- Lionel Brayeur - received the prize of the EuroPhysics Journal Best Poster Contest “Bayesian Approach for low counting experiments applied to a Neutrino Point Source Analysis” (2013)

e. Scientific output

Quantitative overview of the output (since January 1, 2012):

- Number of finished PhD projects in 2012-2016 (i.e. including the year of application): in total 15 PhDs defended in HEP@VUB since 2012, namely Alice Bernamonti, Stijn Blyweert, Michael Maes, Gerrit Van Onsem, Alexis Kalogeropoulos, Annik Olbrechts, Karen De Causmaecker, Bettina Oexl, Dimitri Terry, Federico Galli, Nele Callebaut, Martin Casier, Jan Kunnen, Lionel Brayeur, Joris Vanhoof
- Number of journal papers in 2012-2016 (i.e. including the year of application) from researchers today in HEP@VUB: about 750 peer-reviewed publications with over 47000 citations (together with preprints and publications in the reviewing process this becomes a total of above 900 citeable papers)
- The vast majority of these publications appeared in top-level international journals

All publications relate to topics in high-energy physics and as demonstrated in the recent past the collection of all insights might lead to novel knowledge and discoveries about the fundamental nature of the smallest and largest structures around us. Our HEP@VUB phenomenological work has been essential to integrate theoretical and experimental insights into general physics models. Most of our publications are within one group which is according to international practices. For example in large experimental collaborations firm



rules exist concerning the author lists of publications. Our HEP@VUB cross-group collaborations are not only reflected in joint publications, but also materialize in joint discussions towards a global experimental and theoretical understanding of the smallest and largest structures in nature.

Most of the publications can be found using the following links.

IceCube collaboration

http://inspirehep.net/search?ln=en&as=1&m1=o&p1=eindhoven&f1=&op1=a&m2=o&p2=Brussel&f2=&op2=a&m3=o&p3=2012+2013+2014+2015+2016&f3=&action_search=Search&sf=&so=d&rm=&rq=25&sc=0&of=hb

CMS collaboration

http://inspirehep.net/search?ln=en&as=1&m1=o&p1=CMS&f1=collaboration&op1=a&m2=o&p2=Vrije+U.&f2=&op2=a&m3=o&p3=2012+2013+2014+2015+2016&f3=&action_search=Search&sf=&so=d&rm=&rq=25&sc=0&of=hb

Theoretical High-Energy Physics

<http://inspirehep.net/search?p2=IIHE+Mawatari+CMS&p3=2012+2013+2014+2015+2016&p1=Vrije+U+B+Russels+Intl+Solvay+Inst+Brussels&jrec=76&op1=n&op2=a&ln=en&as=1&m1=a&m3=o&m2=o>

High-Energy Astrophysics

http://inspirehep.net/search?ln=en&as=1&m1=o&p1=s.buitink.1&f1=author&op1=a&m2=o&p2=Vrije+U.&f2=&op2=a&m3=o&p3=2013+2014+2015+2016&f3=&action_search=Search&sf=&so=d&rm=&rq=25&sc=0&of=hb

http://inspirehep.net/search?ln=en&as=1&m1=o&p1=g.gentile.4&f1=author&op1=a&m2=o&p2=&f2=&op2=a&m3=o&p3=2013+2014+2015+2016&f3=&action_search=Search&sf=&so=d&rm=&rq=25&sc=0&of=hb

http://adsabs.harvard.edu/cgi-bin/nph-abs_connect?return_req=no_params&author=Blommaert,%20J.%20A.%20D.%20L.&db_key=PRE

http://inspirehep.net/search?ln=en&as=1&m1=o&p1=D.Vanbeveren.1&f1=author&op1=a&m2=o&p2=&f2=&op2=a&m3=o&p3=2013+2014+2015+2016&f3=&action_search=Search&sf=&so=d&rm=&rq=25&sc=0&of=hb

Phenomenological High-Energy Physics

https://inspirehep.net/search?ln=en&ln=en&p=f+a+mariotti%2Ca+or+a+mawatari+or+a+de+causmaecker+or+a+tziveloglou+or+a+vereecken+and+aff+Brussels+and+date+after+2011+and+not+t+selectron+and+not+arxiv%3A1211.5609&of=hb&action_search=Search&sf=earliestdate&so=d&rm=&rq=100&sc=0

Publications related to the H1 and DELPHI experiments have appeared as well, as have publications by experimentalists outside the context of the large international collaborations.

Qualitative aspects of the output:

The level and impact of our research illustrated with highlights in the section on “*scientific breakthroughs*” reflects the quality. Our excellent visibility in the international research in High-Energy Physics resulted in a series of (typically invited and plenary) talks at conferences and workshops, of which several are published into conference proceedings. Below we highlight few of our most important presentations on experimental results by our HEP@VUB members.

- Jorgen D’Hondt, “Status of Top Quark Physics”, invited plenary talk presented during the 26th Rencontre de Blois, 18-13 May 2014, Blois, France



- Freya Blekman, "Standard Model measurements and general agreement SM predictions in CMS", invited plenary talk at SEARCH, August-Sept 2016, Oxford, UK
- Freya Blekman, "Searches for BSM in final states with 3rd Generation Particles", invited plenary talk presented during the 26th Rencontre de Blois, 18-13 May 2014, Blois, France
- Freya Blekman, "Non-resonant and unusual BSM signatures", invited plenary talk at EPS-HEPP 2013, Stockholm, Sweden
- Petra Van Mulders, "CMS status report", plenary talk presented during the open session of the 127th LHCC meeting, Sept 2016, CERN, Geneva (Switzerland)
- Petra Van Mulders, "Status and recent highlights from CMS", opening plenary talk of the LHCP2016 conference, June 2016, Lund University, Lund (Sweden).
- Petra Van Mulders, "Higgs at the LHC", opening plenary talk providing a full overview of Higgs physics shortly after its discovery at WIN2013, Sept 2013, Natal (Brazil).
- Steven Lowette, "Accelerator searches for new physics in the context of dark matter", invited plenary talk at the 14th International Conference on Topics in Astroparticle and Underground Physics (TAUP 2015), September 2015, Torino, Italy

- Nick van Eijndhoven, "The Birth of Neutrino Astronomy", invited plenary opening talk at the "4th Quantum Universe Symposium", Groningen, The Netherlands, April 2014.
- Olaf Scholten, "From the Earth to the Moon", invited plenary talk at the "5th International Conference on Acoustic and Radio EeV Neutrino Detection Activities (ARENA2014)", Annapolis MD, USA, June 2014.
- Nick van Eijndhoven, "Exploring the Universe with Neutrinos", invited plenary review talk at the "27th International Lepton-Photon Symposium", Ljubljana, Slovenia, Aug 2015.
- Olaf Scholten, "Cosmic rays as probes of atmospheric electric fields", invited plenary talk at the American Geophysical Union, San Francisco CA, USA, Dec 2015.
- Catherine De Clercq, "IceCube: Cosmic Neutrinos Caught in Ice", invited highlight talk at the Belgian Senate, March 2014.
- Geraldina Golup, "Latest results from the IceCube Neutrino Telescope", plenary talk at the "15th International conference on Frontier Objects in Astrophysics and Particle Physics (VULCANO2014)", Vulcano Island, Italy, May 2014.
- Geraldina Golup, "Towards a Joint Analysis of Data from the IceCube Neutrino Telescope, The Pierre Auger Observatory and Telescope Array", plenary talk at the "International conference on Ultra-High Energy Cosmic Rays (UHECR2014)", Springdale (Utah), USA, Oct 2014.
- Krijn de Vries, "On the radar detection of neutrino induced particle cascades in ice", plenary talk at the "7th International Conference on Acoustic and Radio EeV Neutrino Detection Activities (ARENA2016)", Groningen, The Netherlands, June 2016.
- Krijn de Vries, "Detecting High-Energy neutrinos with RADAR", plenary talk at the IPA conference, Madison WI, USA, May 2015.
- Simona Toscano, "Neutrino astronomy at the South Pole: latest results from the IceCube neutrino observatory and its future development", plenary talk at the "9th International conference on Ring Imaging Cherenkov Detectors (RICH2016)", Bled, Slovenia, Sept 2016.

- Stijn Buitink, "Radio detection of cosmic rays with LOFAR", invited plenary talk, TeV Particle Astrophysics, August 2013, Irvine California, USA
- Stijn Buitink, "Measuring the cosmic ray mass composition with LOFAR", talk presented at 34th International Cosmic Ray Conference, July 2015, The Hague, Netherlands
- Stijn Buitink, "Cosmic-ray mass composition with LOFAR", invited plenary talk, 7th International Conference on Acoustic and Radio EeV Neutrino Detection Activities, June 2016, Groningen, Netherlands



Additionally, HEP@VUB members provided numerous presentations on experimental results at ICHEP, ICRC, ARENA, RICAP, TAUP, EPS-HEPP, LHCP, Moriond, Lepton-Photon, Neutrino, Physics in Collision (PIC), SUSY, International Top Quark Workshop,... In his role as Chairperson of the CMS Collaboration Board, Jorgen D'Hondt was invited to present as well at several international workshops and conferences general status reports of the CMS experiment.

Based on our theoretical research we have been invited to present our results at several venues. Below we present a sample of the most important presentations.

- Ben Craps, "Entwinement in discretely gauged theories", invited talk at Nordita program on Black Holes and Emergent Spacetime, Stockholm, Sweden, 15 August 2016
- V. Balasubramanian, "Novel forms of entanglement and spacetime geometry", invited talk at Quantum Information in String Theory and Many-body Systems, YITP, Kyoto University, Japan, 24 June 2016
- Ben Craps, "AdS (in)stability: an analytic approach and its interplay with numeric", invited talk at Numerical Relativity and Holography, Santiago de Compostela, Spain, 27 June 2016
- Alexander Sevrin, "Supersymmetry and the Doubled Formalism from a Worldsheet Perspective", invited talk at International Workshop "Generalized Geometry & T-dualities", Simons Center for Geometry and Physics, Stony Brook, New York, 9 -13 May 2016
- C. Blair, "The $SL(2) \times R^+$ exceptional field theory and F-theory", invited talk at Duality and Novel Geometry in M-theory, Pohang University of Science and Technology, Pohang, South Korea, 3 February 2016
- Ben Craps, "AdS (in)stability: an analytic approach", invited talk at the String Theory Universe, 21st European String Workshop and 3rd COST MP1210 Meeting, Leuven, Belgium, 7 September 2015
- Hongbao Zhang, "Numerical holography", invited talk at 2015 International School on Numerical Relativity and Gravitational Waves, KISTI & KAIST, Daejeon, Korea, 31 July 2015
- O. Evnin, "Nonlinear perturbations of AdS spacetime: an analytic approach", invited talk at Solvay-Perimeter-APC Workshop on "Cosmological Frontiers in Fundamental Physics", Brussels, Belgium, July 2015
- Alexander Sevrin, "Physics in low dimensions", invited talk at Workshop "About Various Kinds of Interactions", Mons, Belgium, 4 June 2015
- Ben Craps, "Holographic thermalization and AdS (in)stability", invited talk at International Workshop on Condensed Matter Physics and AdS/CFT, Kavli IPMU, Kashiwa, Japan, 28 May 2015
- H. Zhang, "Metal insulator transition by holographic charge density waves", invited talk at CERN-CKC TH Institute on Numerical Holography, Geneva, Switzerland, 9 December 2014
- Ben Craps, "AdS (in)stability, secular term resummation and the renormalization group", invited talk at Holograv 2014, Reykjavik, Iceland, 20 August 2014
- Koshelev, "What does gravity learn from SFT", invited talk at String Field Theory and Related Aspects VI, SFT 2014, Trieste, Italy, 31 July 2014
- Ben Craps, "Infalling shells in hard wall models", invited talk at Workshop on holography, gauge theory and black holes, Southampton, UK, 9 April 2014
- Alexander Sevrin, "Towards a Supersymmetric Doubled Worldsheet Formalism", invited talk at EU-Russia-JINR@Dubna Round Table on Theoretical and Experimental Physics after the discovery of the Brout-Englert-Higgs boson, Dubna, Russia, 4 March 2014
- Alexander Sevrin, "A Walk on the Supersymmetric Worldsheet", invited talk at workshop Aspects of Supergravity, Simons Center for Geometry and Physics, Stony Brook, NY, USA, 10 January 2014
- Ben Craps, "Holographic entanglement entropy", invited lecture series at Nordic Network meeting on Strings, Fields and Branes, Stockholm, Sweden, 8-9 November 2013



- Anastasios Taliotis, "QGP in central collisions for sufficiently large energy", talk at Holography and QCD - Recent progress and challenges, Kavli IPMU, Tokyo, Japan, 26 September 2013
- Ben Craps, "Inhomogeneous Holographic Thermalization", invited talk at Gauge/Gravity Duality Conference, Munich, Germany, 29 July 2013
- Dan Thompson, "Duality invariant approaches to String Theory" invited talk at Strong Fields, Strings and Holography, Swansea, UK, 19 July 2013
- Ben Craps, "Strings in Compact Cosmological Spaces", invited talk at PI/APC/Solvay Workshop on Cosmological Frontiers in Fundamental Physics, Waterloo, Canada, 11 July 2013
- Ben Craps, "Inhomogeneous Holographic Thermalization", invited talk at Erasmus IP Non-Perturbative Quantum Field Theory, Heraklion, Greece, 28 April 2013
- Koshelev, "p-adic limit of SFT inspired non-local gravity models", invited talk at p-Adic Methods for Modelling of Complex Systems, Bielefeld, Germany, 18 April 2013
- Ben Craps, "Holographic thermalization and energy density fluctuations", invited talk at ESF Holograv 2013 Workshop Helsinki, Finland, 7 March 2013

Also the HEP@VUB phenomenological members presented their work at several international venues, of which a representative selection is listed below.

- Kentarou Mawatari, "BEH characterization with FeynRules and MadGraph5", MC4BSM (Monte Carlo for Physics Beyond Standard Model), DESY (2013)
- Kentarou Mawatari, "Effective models for spin and CP studies", HC2013 (Higgs Couplings 2013), Friburg U.
- Kentarou Mawatari, "Higgs characterisation -- beyond leading order", SUSY13, Trieste ICTP
- Karen De Causmaecker, "Multilepton signals of gauge mediated supersymmetry breaking at the LHC", SUSY14 Manchester
- Kentarou Mawatari, "CP violation in $t\bar{t}H$ ", CKM2014 Vienna
- Alberto Mariotti, "Gauge mediation of exact scale breaking", SUSY14 Manchester
- Pantelis Tzivelologu, "Indirect Searches Illuminate Singlet - Doublet Dark Matter", Invisibles15 Workshop, Madrid
- Kentarou Mawatari, "Higgs Characterisation at NLO in QCD", Pheno2015, Pittsburgh (USA)
- Alberto Mariotti, "Signs of tops in highly mixed stops", Planck 2015, Ioannina
- Kentarou Mawatari, "Dark matter study in the FeynRules/MadGraph5_aMC@NLO framework", DSU2015, Kyoto YITP
- Alberto Mariotti, "Goldstini and the Z-peaked ATLAS excess", "Gearing Up for LHC13" Workshop, GGI Florence (2015)
- Alberto Mariotti, "Diphoton excess illuminates dark matter", Planck 2016, Valencia

In the CMS collaboration our research involvement and achievements led to the selection or election of several top-level managerial positions. These are relevant indications of the quality of our research. In the CMS experiment our researchers are selected or elected for key managerial positions, for example: Freya Blekman as co-convenor of the Beyond-2-Generators (B2G) group (2012-2014), Petra Van Mulders as co-convenor of the b-tagging and vertexing (BTV) group (2014-2016), Steven Lowette as co-convenor of the joint ATLAS/CMS dark matter working group and of the CMS Exotica MET+X group, James Keaveny co-coordinates the top quark cross-section group (2014-2015), Natalie Heracleous co-coordinates in the Offline and Computing/Reconstruction group for Electrons and Photons (2014-2015), Jorgen D'Hondt has been elected as chairperson of the Collaboration Board (2014-2017) and therefore participates in all managerial and financial boards, committees and meetings of the CMS Collaboration.

In the IceCube experiment our colleagues Geraldina Golup (postdoctoral researcher in our team until 2015) and Olaf Scholten have taken a lead in combining data from the IceCube, Pierre Auger and Telescope Array



experiments. Concerning the studies of GRB precursor and afterglow emission Martin Casier, Lionel Brayeur and Nick van Eijndhoven are the leading investigators, whereas the project on dust obscured AGN is coordinated by Giuliano Maggi, Krijn de Vries and Nick van Eijndhoven. Concerning the lower energy studies, the leading investigators in the search for Earth WIMPs are Catherine De Clercq, Jan Luenemann and Jan Kunnen, whereas the coordination for Solar Flare studies is performed by Gwen de Wasseige and Nick van Eijndhoven. The InIce self-veto studies for the IceCube-Gen2 high-energy extension are led by Simona Toscano and Nick van Eijndhoven, whereas the development of radio detection techniques are coordinated by Krijn de Vries and Olaf Scholten. In addition to the above, Nick van Eijndhoven is co-PI for the Belgian groups in IceCube and member of the IceCube collaboration board, being the panel that coordinates the construction, physics research and policy of the experiment.

Since 2012, the Theoretical High-Energy Physics team (excluding the pheno group) has produced about 84 peer-reviewed papers in international journals (with about 1751 citations in total) and a number of proceedings articles and recent preprints, on a broad variety of topics. Some of the highlights were mentioned before, and a slightly more detailed overview of the research topics can be found at <http://we.vub.ac.be/nl/theoretical-particle-physics>.

Stijn Buitink is co-PI of the LOFAR Cosmic Ray Key Science Project. The ERC-funded group in HEP@VUB takes the lead in cosmic-ray mass composition analysis, detector upgrade (including a low energy extension) and the development of a new observation mode to search for cosmic particles hitting the Moon.

Awards and recognitions: Several of our tenured researchers received strong national and international recognition for their achievements, illustrating the quality of our research. Some examples are highlighted below.

- Jorgen D'Hondt – “Young Scientist 2013” by the World Economic Forum
- Jorgen D'Hondt – Annual prize in 2014 for Valorisation by the VUB
- Jorgen D'Hondt – Prize for Science Communication by the Royal Academy of Belgium (KVAB, 2013)
- Ben Craps – Guest professor at Ecole Normale Supérieure (Paris, France, May 2014)
- Nick van Eijndhoven – Guest professor at the University of Lund (Sweden)
- Nick van Eijndhoven – Guest professor at the University of Cape Town (South Africa)
- Freya Blekman – LPC Distinguished Researcher 2013 (Fermilab, USA)
- Freya Blekman – Prize for Science Communication by the Royal Academy of Belgium (KVAB, 2016)
- Alberto Mariotti – awarded in 2015 with a Rita Levi Montalcini Fellowship (equivalent to a permanent position in an Italian University, declined)

Valorisation:

In the period 2013-2016 HEP@VUB initiated and was strongly involved in a vast range of successful valorisation projects, mostly in the science communication part of valorisation. Some recent highlights mentioned below provide us with an outstanding experience to continue to deliver also in the future prosperous valorisation outcomes. Jorgen D'Hondt was awarded the annual prize for Science Valorisation of the VUB in 2014 (value of 150k euro) as well as one of the year prizes in 2013 of the Royal Academy of Belgium (KVAB) for Science Communication. He obtained as well two external funds (2 x 5k euro) from the Brussels region dedicated to outreach events. One of these grants was to sponsor the documentary “[Kwantumrevolutie](#)” selected for the 360° Science Film Festival in Moscow. Several HEP@VUB members collaborated to and appeared in this documentary. Petra Van Mulders is member of the jury of [CanSat Belgium](#) (2015-2017), and provided workshops for about 80 children aged 8 to 12 at [Technopolis](#) as well as a keynote speech on curiosity-driven research at the [first VUB conference](#) with over 600 participants. For her continuous science communication via social media Freya Blekman was awarded one of the year prizes in 2016 of the Royal Academy of Belgium (KVAB) for Science Communication. She organised as well a “Career in Industry” seminar for our PhD students and postdocs. Freya Blekman and Steven Lowette are



regularly judges during the yearly wetenschaps-ExpoSciences Science fair in Brussels. Freya Blekman was the invited CERN speaker at the prestigious London International Youth Science Forum in 2013, 2015 and 2016 (<http://www.liysf.org.uk/>). In 2014, our HEP@VUB team in IceCube organised several presentations of an IceCube 3D movie at the Brussels planetarium. In the same year they produced as well a [short movie explaining our GRB research](#). Via the International Solvay Institutes, Ben Craps and Alexander Sevrin are involved in the organization of yearly high-profile Public Lectures attracting audiences of many hundreds. To celebrate the discovery of gravitational waves, Simona Toscano and Gwen de Wasseige organized in 2016 a public lecture (more than 200 participants), followed by a dedicated symposium. Several of the HEP@VUB members have been highlighted in the Belgian and international press for their achievements, and featured in leading newspapers, national television news and programs, as well as on large stages for science outreach. On an almost monthly basis we receive classes from schools at the university and present them in a workshop our research. We also participate in the International Masterclasses organised by IPPOG for LHC collisions physics as well as for IceCube. We organized an IceCube exhibition at the "Printemps des Sciences" in 2014. HEP@VUB members are active in valorisation activities on social media such as YouTube videos, Google hangouts and twitter, with particularly the video activities regularly reaching tens of thousands of views. Jorgen D'Hondt, Freya Blekman and Steven Lowette participated to "Bright Club" or similar event bringing science to society via stand-up comedy. Alexander Sevrin was and Ben Craps is a board member of the Belgian Physical Society, which among other things promotes physics in society. Stefaan Tavernier is member of and was previously spokesperson (1995-2010) of Crystal Clear, an international collaboration active on research and development on inorganic scintillation materials for novel ionizing radiation detectors, for high-energy physics, medical imaging and industrial applications. Recent publications are "Validation of a highly integrated SiPM readout system with a TOF-PET demonstrator" (just accepted in JINST) and "A new method for depth of interaction determination in PET detectors" (Phys.Med.Biol. 61(12):4679-98, 2016). We made the initial steps to refurbish the astrophysics observation dome on the roof of building E on the campus. The HEP@VUB group will organize observation nights for schools and general audiences that will include a telescope tour and lectures on topics in astronomy and cosmology.

f. Additional information

N/A

Short CV of Prof. Dr. Jorgen D'Hondt Hoogleraar at Vrije Universiteit Brussel (Belgium)



Professor D'Hondt is the VUB-director of the Inter-University Institute for High Energies (IIHE) in Brussels. He is elected as chairperson of the collaboration board of the CMS experiment at the Large Hadron Collider at CERN (Geneva, Switzerland), an experiment with 4400 scientific collaborators from more than 200 institutions in 43 countries worldwide. With this experiment the Higgs particle was discovered in 2012, an achievement that was internationally recognised as one of the major discoveries of our times. Towards the start of the LHC he was as well the first coordinator of the top quark physics program for the CMS experiment, one of the key research lines in particle physics worldwide. For his contributions Professor D'Hondt was rewarded Young Scientist 2013 by the World Economic Forum, and received prizes for the communication and valorisation of these achievements. In Flanders he was the first president of the Young Academy, is promoter of several large-scale projects and promoted numerous PhD's that obtained international prizes. Internationally he serves in major panels and committees for scientific assessments, advises, reviews and/or organisations. He is also member of the SoLid collaboration to measure the properties of neutrinos with an experiment deployed at the BR2 reactor in SCK-CEN (Mol, Belgium).

CAREER PATH

IWT-Vlaanderen PhD scholarship (1999-2003), PhD obtained at the VUB in 2003 on W boson physics with the DELPHI experiment at LEP2
FWO Fellowship (1st term 2003-2006, 2nd term 2006-2009)
Professorship at the VUB, since 2006
Promotion to *Hoogleraar* at the VUB in 2014

FELLOWSHIPS AND AWARDS

“Young Scientist 2013” by the World Economic Forum (2013)
Prize for Science Communication by the Royal Flemish Academy of Belgium (2013, Belgium)
Annual Prize for Science Valorisation by the Vrije Universiteit Brussel (2014, Belgium)

IMPORTANT COLLECTIVE AWARDS:

Science Magazine quoted “Breakthrough of the Year 2012” the discovery of the Higgs boson
The European Physics Society HEPP prize was awarded to the CMS Collaboration in 2013

INSTITUTIONAL AND RESEARCH RESPONSIBILITIES, among others:

President of the Collaboration Board of the CMS experiment (2014-now, CERN), ~4300 members
Director of the Inter-university Institute for High Energies (2011-now, VUB part), ~100 members
President of the Young Academy of Belgium (Flanders) (2013-2015)
President of the Department of Physics (2012-2014 and 2016-now, VUB, Belgium)
President of the Education Council of the Faculty of Science and Bioengineering (2013-2015, VUB)
President of the CMS International Committee (2013-now, CERN)
Promoter of 19 PhD students and 13 master students, several winning international awards

COMMISSIONS OF TRUST, among others:

Belgian delegate to the Restricted European Committee for Future Accelerators (2013-now, CERN)
Belgian delegate to the International Particle Physics Outreach Group (2006-2014, CERN)
Member of the FWO Committee for International Collaboration (Belgium)
Member of the NWO Committee for selecting VICI individual grants (Netherlands)
Member and chairperson of the Scientific Advisory Committee of the Institute of Physics at the Universiteit van Amsterdam (Netherlands)
Member of the Scientific Advisory Committee of the Institute for Physics and Mathematics (Iran)
Representing the FWO-Flanders funding agency in the International Oversight and Finance Group of the IceCube Neutrino Observatory (NSF, USA)
Permanent member of the International Advisory Board of the annual series of Top Quark Conferences (typical 130-150 participants per year)
Member of the Advisory Board for CMS Data Analysis Schools (Italy, Germany, USA, India, Taiwan)
Invited to steering groups: Honours Program (VUB), Education for the Future (VUB), Workload balance academic staff (VUB), Science and Arts at BOZAR (Center for Fine Arts, Brussels), et al.
Member of several PhD committees local, national and international

SCIENTIFIC ACHIEVEMENTS, among others:

Participation in ALEPH, DELPHI, CMS, SoLid experiments
In total 716 papers of which 697 are citable (h-index 115) and 643 already published
In total more than 200 presentations at conferences, workshops, seminars, and international meetings
Co-author of more than 100 internal publications in large international collaborations
As first coordinator of the top quark study group in the CMS experiment at CERN (2007-2008) with ~150 members world-wide I was at the basis of ~60 publications directly on the topic by CMS, the first edited by myself has today 150 citations, and several publications are achieved on related topics

RESEARCH FUNDING AND MANAGEMENT, among others:

PI of the Hercules project for the CMS Phase-2 upgrade (construction of Silicon Tracker Endcap)
PI of the largest FWO Big Science project in Flanders (CMS experiment at CERN)
PI of a VUB Strategic Research Program uniting theoretical and experimental “High-Energy Physics”
PI (or co-PI) of many other projects, for in total 27.5 M euro funding obtained as co-PI of which 17.2 M euro as main PI (excluding individual grants for PhD and post-doc scholarships, as well as running budgets from the university)

SCIENCE COMMUNICATION AND VALORISATION, among others:

Several key articles/interviews appeared on myself in magazines (eg. New Scientist, EOS)
Keynote talks at academic, career, outreach and political events, debates, academic openings, et al.
In total more than 150 presentations on science for the general public
In total more than 100 media contacts/appearances (television, radio, national newspapers)

ORGANISATION OF SCIENTIFIC EVENTS, among others:

Organiser of the International Top Quark Conference in Bruges (Belgium, 2010, 130 participants)
Organiser of the International CMS Collaboration Week in Brussels (Belgium, 2011, 350 participants)
Organiser of about 10 sessions during international conferences or workshops
Organiser of about 5 topical workshops at CERN on different scientific themes
Organiser of 3 symposia at the university to celebrate individuals or scientific achievements
Member of the organising or advisory committee of ~15 other international conferences or workshop

Information from Prof. Dr. Jorgen D'Hondt (section 11)

Most important scientific publications (*: 5 most important publications):

- Precise determination of the mass of the Higgs boson and tests of compatibility of its couplings with the standard model predictions using proton collisions at 7 and 8 TeV, by CMS Collaboration (Vardan Khachatryan et al.), Eur.Phys.J. C75 (2015) no.5, 212.
- (*) Observation of the rare B^0_s to $\mu^+\mu^-$ decay from the combined analysis of CMS and LHCb data, by CMS and LHCb Collaborations (Vardan Khachatryan et al.), Nature 522 (2015) 68-72.
- Multilepton signals of gauge mediated supersymmetry breaking at the LHC
- By Jorgen D'Hondt, Karen De Causmaecker, Benjamin Fuks, Alberto Mariotti, Kentarou Mawatari, Christoffer Petersson, Diego Redigolo, Phys.Lett. B731 (2014) 7-12.
- Search for the associated production of the Higgs boson with a top-quark pair, by CMS Collaboration (Vardan Khachatryan et al.), JHEP 1409 (2014) 087, Erratum: JHEP 1410 (2014) 106.
- Description and performance of track and primary-vertex reconstruction with the CMS tracker, by CMS Collaboration (Serguei Chatrchyan et al.), JINST 9 (2014) no.10, P10009.
- (*) Electroweak Measurements in Electron-Positron Collisions at W-Boson-Pair Energies at LEP, by ALEPH and DELPHI and L3 and OPAL and LEP Electroweak Collaborations (S. Schael et al.), Phys.Rept. 532 (2013) 119-244.
- (*) Identification of b-quark jets with the CMS experiment, by CMS Collaboration (Serguei Chatrchyan et al.), JINST 8 (2013) P04013.
- Search for top-squark pair production in the single-lepton final state in pp collisions at 8 TeV, by CMS Collaboration (Serguei Chatrchyan et al.), Eur.Phys.J. C73 (2013) no.12, 2677.
- (*) Observation of a new boson at a mass of 125 GeV with the CMS experiment at the LHC, by CMS Collaboration (Serguei Chatrchyan et al.), Phys.Lett. B716 (2012) 30-61.
- (*) First Measurement of the Cross Section for Top-Quark Pair Production in Proton-Proton Collisions at 7 TeV, by CMS Collaboration (Vardan Khachatryan et al.), Phys.Lett. B695 (2011) 424-443.

Applications for international research funding:

In our field of experimental particle physics research we do apply together with our colleagues for the required budgets in our home country to establish together an experimental instrument. Based on the integral of these national/regional budgets we are able to construct and operate within an international collaboration a particle detector for example at CERN. Dedicated international committees and boards are setup to steer this process. Therefore most of our funding for experimental particle physics comes from the national/regional funding agencies and not from international programmes. Therefore all my funding is obtained through national programmes. As PI (or co-PI) obtained for in total 27.5M euro of which 17.2M euro as main PI (excluding individual grants for PhD and post-doc scholarships, as well as running budgets from the university).

The leverage factor of this national investment is enormous. Within the CMS Collaboration the Flemish investment is about 1,5 to 2%. Therefore with this investment the researchers at Flemish institutions have access to unique instruments that would require a budget at least 50 times larger than the Flemish investment. About 98% of the

total budget we have available within the CMS Collaboration is therefore indeed international.

VUB-promotorships of applications for Odysseus funding:

- Promoter for Freya Blekman, Odysseus-II, successful
- Promoter for Steven Lowette, Odysseus-II, successful
- Promoter for Sadia Khalil, Odysseus-II, not granted

Promotorships of awarded PhD's (last 5 years):

- Nadjieh Jafari, Measurement of the b-tagging efficiency in the CMS experiment with the first LHC collisions, Sept 2011
- Marya, Zeinali, Measurement of the Jet Energy Scale in the CMS experiment with the first LHC collisions, Sept 2011
- Stijn Blyweert, Measurement of the top-quark mass and the mass difference between top and antitop quarks at the LHC, 18/10/2013
- Michael Maes, Measurement of the top quark pair production cross section at the LHC with the CMS experiment, 23/10/2013
- Alexis Kalogeropoulos, Search for direct stop quark pair production at the LHC with the CMS experiment, 24/01/2014
- Gerrit Van Onsem, Search for new heavy quarks with the CMS detector at the Large Hadron Collider, 30/05/2014
- Annik Olbrechts, Measuring the anomalous couplings in the Wtb vertex using the Matrix Element Method at the LHC, 25/02/2016
- Karen De Causmaecker, Unconventional signatures of supersymmetry, 22/08/2016

Realisations of valorisation efforts, amongst others:

- Prize for Science Communication by the Royal Flemish Academy of Belgium (2013, Belgium)
- Annual Prize for Science Valorisation by the Vrije Universiteit Brussel (2014, Belgium)
- Belgian delegate to the International Particle Physics Outreach Group (2006-2014, CERN)
- Several key articles/interviews appeared on myself in magazines (eg. New Scientist, EOS)
- Keynote talks at academic, career, outreach and political events, debates, academic openings, et al.
- In total more than 150 presentations on science for the general public with audiences from 25 persons to very large audiences)
- In total more than 100 media contacts/appearances (television, radio, national newspapers)
- Organiser of national wide press conferences for the start of the LHC (2008) and the discovery of the Higgs boson (2012)
- Organiser of the *Terzake* reportage on the discovery of the Higgs boson, that won the "Diversity prize of the VRT" in 2014 (national television)
- Organiser of the first Bright Spark workshop on Quantum Physics, "The WOW! Of Quantum Physics" for children
- Organiser of Career events with >200 participants at CERN
- Chairperson of the CMS Career Committee at CERN (2012-2014)
- Organising visits to CERN of the Belgian King (May 2014), the Belgian Prime Minister (June 2013), the rectors of Flemish universities (June 2014), the Belgian Federal Secretary of State for Science (Sept 2016), et al.
- Organiser of several visits to CERN for interested (typically Belgian) groups

- Elected as first President of the Young Academy of Belgium (2013-2015)
- Member of the Scientific Advisory Board of ITERA Life-Science (International Tissue Engineering Research Association)

Observation of the rare $B_s^0 \rightarrow \mu^+ \mu^-$ decay from the combined analysis of CMS and LHCb data

The CMS and LHCb collaborations*

The standard model of particle physics describes the fundamental particles and their interactions via the strong, electromagnetic and weak forces. It provides precise predictions for measurable quantities that can be tested experimentally. The probabilities, or branching fractions, of the strange B meson (B_s^0) and the B^0 meson decaying into two oppositely charged muons (μ^+ and μ^-) are especially interesting because of their sensitivity to theories that extend the standard model. The standard model predicts that the $B_s^0 \rightarrow \mu^+ \mu^-$ and $B^0 \rightarrow \mu^+ \mu^-$ decays are very rare, with about four of the former occurring for every billion B_s^0 mesons produced, and one of the latter occurring for every ten billion B^0 mesons¹. A difference in the observed branching fractions with respect to the predictions of the standard model would provide a direction in which the standard model should be extended. Before the Large Hadron Collider (LHC) at CERN² started operating, no evidence for either decay mode had been found. Upper limits on the branching fractions were an order of magnitude above the standard model predictions. The CMS (Compact Muon Solenoid) and LHCb (Large Hadron Collider beauty) collaborations have performed a joint analysis of the data from proton–proton collisions that they collected in 2011 at a centre-of-mass energy of seven teraelectronvolts and in 2012 at eight teraelectronvolts. Here we report the first observation of the $B_s^0 \rightarrow \mu^+ \mu^-$ decay, with a statistical significance exceeding six standard deviations, and the best measurement so far of its branching fraction. Furthermore, we obtained evidence for the $B^0 \rightarrow \mu^+ \mu^-$ decay with a statistical significance of three standard deviations. Both measurements are statistically compatible with standard model predictions and allow stringent constraints to be placed on theories beyond the standard model. The LHC experiments will resume taking data in 2015, recording proton–proton collisions at a centre-of-mass energy of 13 teraelectronvolts, which will approximately double the production rates of B_s^0 and B^0 mesons and lead to further improvements in the precision of these crucial tests of the standard model.

Experimental particle physicists have been testing the predictions of the standard model of particle physics (SM) with increasing precision since the 1970s. Theoretical developments have kept pace by improving the accuracy of the SM predictions as the experimental results gained in precision. In the course of the past few decades, the SM has passed critical tests derived from experiment, but it does not address some profound questions about the nature of the Universe. For example, the existence of dark matter, which has been confirmed by cosmological data³, is not accommodated by the SM. It also fails to explain the origin of the asymmetry between matter and antimatter, which after the Big Bang led to the survival of the tiny amount of matter currently present in the Universe^{3,4}. Many theories have been proposed to modify the SM to provide solutions to these open questions.

The B_s^0 and B^0 mesons are unstable particles that decay via the weak interaction. The measurement of the branching fractions of the very rare decays of these mesons into a dimuon ($\mu^+ \mu^-$) final state is especially interesting.

At the elementary level, the weak force is composed of a ‘charged current’ and a ‘neutral current’ mediated by the W^\pm and Z^0 bosons,

respectively. An example of the charged current is the decay of the π^+ meson, which consists of an up (u) quark of electrical charge $+2/3$ of the charge of the proton and a down (d) antiquark of charge $+1/3$. A pictorial representation of this process, known as a Feynman diagram, is shown in Fig. 1a. The u and d quarks are ‘first generation’ or lowest mass quarks. Whenever a decay mode is specified in this Letter, the charge conjugate mode is implied.

The B^+ meson is similar to the π^+ , except that the light d antiquark is replaced by the heavy ‘third generation’ (highest mass quarks) beauty (b) antiquark, which has a charge of $+1/3$ and a mass of $\sim 5 \text{ GeV}/c^2$ (about five times the mass of a proton). The decay $B^+ \rightarrow \mu^+ \nu$, represented in Fig. 1b, is allowed but highly suppressed because of angular momentum considerations (helicity suppression) and because it involves transitions between quarks of different generations (CKM suppression), specifically the third and first generations of quarks. All b hadrons, including the B^+ , B_s^0 and B^0 mesons, decay predominantly via the transition of the b antiquark to a ‘second generation’ (intermediate mass quarks) charm (c) antiquark, which is less CKM suppressed, into final states with charmed hadrons. Many allowed decay modes, which typically involve charmed hadrons and other particles, have angular momentum configurations that are not helicity suppressed.

The neutral B_s^0 meson is similar to the B^+ except that the u quark is replaced by a second generation strange (s) quark of charge $-1/3$. The decay of the B_s^0 meson to two muons, shown in Fig. 1c, is forbidden at the elementary level because the Z^0 cannot couple directly to quarks of different flavours, that is, there are no direct ‘flavour changing neutral currents’. However, it is possible to respect this rule and still have this decay occur through ‘higher order’ transitions such as those shown in Fig. 1d and e. These are highly suppressed because each additional interaction vertex reduces their probability of occurring significantly. They are also helicity and CKM suppressed. Consequently, the branching fraction for the $B_s^0 \rightarrow \mu^+ \mu^-$ decay is expected to be very small compared to the dominant b antiquark to c antiquark transitions. The corresponding decay of the B^0 meson, where a d quark replaces the s quark, is even more CKM suppressed because it requires a jump across two quark generations rather than just one.

The branching fractions, \mathcal{B} , of these two decays, accounting for higher-order electromagnetic and strong interaction effects, and using lattice quantum chromodynamics to compute the B_s^0 and B^0 meson decay constants^{5–7}, are reliably calculated¹ in the SM. Their values are $\mathcal{B}(B_s^0 \rightarrow \mu^+ \mu^-)_{\text{SM}} = (3.66 \pm 0.23) \times 10^{-9}$ and $\mathcal{B}(B^0 \rightarrow \mu^+ \mu^-)_{\text{SM}} = (1.06 \pm 0.09) \times 10^{-10}$.

Many theories that seek to go beyond the standard model (BSM) include new phenomena and particles^{8,9}, such as in the diagrams shown in Fig. 1f and g, that can considerably modify the SM branching fractions. In particular, theories with additional Higgs bosons^{10,11} predict possible enhancements to the branching fractions. A significant deviation of either of the two branching fraction measurements from the SM predictions would give insight on how the SM should be extended. Alternatively, a measurement compatible with the SM could provide strong constraints on BSM theories.

*Lists of participants and their affiliations appear in the online version of the paper.

The ratio of the branching fractions of the two decay modes provides powerful discrimination among BSM theories¹². It is predicted in the SM (refs 1, 13 (updates available at <http://itpwiki.unibe.ch/>), 14, 15 (updated results and plots available at <http://www.slac.stanford.edu/xorg/hfag/>)) to be $\mathcal{R} \equiv \mathcal{B}(B^0 \rightarrow \mu^+ \mu^-)_{\text{SM}} / \mathcal{B}(B_s^0 \rightarrow \mu^+ \mu^-)_{\text{SM}} = 0.0295^{+0.0028}_{-0.0025}$. Notably, BSM theories with the property of minimal flavour violation¹⁶ predict the same value as the SM for this ratio.

The first evidence for the decay $B_s^0 \rightarrow \mu^+ \mu^-$ was presented by the LHCb collaboration in 2012¹⁷. Both CMS and LHCb later published results from all data collected in proton–proton collisions at centre-of-mass energies of 7 TeV in 2011 and 8 TeV in 2012. The measurements had comparable precision and were in good agreement^{18,19}, although neither of the individual results had sufficient precision to constitute the first definitive observation of the B_s^0 decay to two muons.

In this Letter, the two sets of data are combined and analysed simultaneously to exploit fully the statistical power of the data and to account for the main correlations between them. The data correspond to total integrated luminosities of 25 fb^{-1} and 3 fb^{-1} for the CMS and LHCb experiments, respectively, equivalent to a total of approximately 10^{12} B_s^0 and B^0 mesons produced in the two experiments together. Assuming the branching fractions given by the SM and accounting for the detection efficiencies, the predicted numbers of decays to be observed in the two experiments together are about 100 for $B_s^0 \rightarrow \mu^+ \mu^-$ and 10 for $B^0 \rightarrow \mu^+ \mu^-$.

The CMS²⁰ and LHCb²¹ detectors are designed to measure SM phenomena with high precision and search for possible deviations. The two collaborations use different and complementary strategies. In addition to performing a broad range of precision tests of the SM and studying the newly-discovered Higgs boson^{22,23}, CMS is designed to search for and study new particles with masses from about $100 \text{ GeV}/c^2$ to a few TeV/c^2 . Since many of these new particles would be able to decay into b quarks and many of the SM measurements also involve b quarks, the detection of b -hadron decays was a key element in the design of CMS. The LHCb collaboration has optimized its detector to study matter–antimatter asymmetries and rare decays of particles containing b quarks, aiming to detect deviations from precise SM predictions that would indicate BSM effects. These different approaches, reflected in the design of the detectors, lead to instrumentation of complementary angular regions with respect to the LHC beams, to operation at different proton–proton collision rates, and to selection of b quark events with different efficiency (for experimental details, see Methods). In general, CMS operates at a higher instantaneous luminosity than LHCb but has a lower efficiency for reconstructing low-mass particles, resulting in a similar sensitivity to LHCb for B^0 or B_s^0 (denoted hereafter by $B_{(s)}^0$) mesons decaying into two muons.

Muons do not have strong nuclear interactions and are too massive to emit a substantial fraction of their energy by electromagnetic

radiation. This gives them the unique ability to penetrate dense materials, such as steel, and register signals in detectors embedded deep within them. Both experiments use this characteristic to identify muons.

The experiments follow similar data analysis strategies. Decays compatible with $B_{(s)}^0 \rightarrow \mu^+ \mu^-$ (candidate decays) are found by combining the reconstructed trajectories (tracks) of oppositely charged particles identified as muons. The separation between genuine $B_{(s)}^0 \rightarrow \mu^+ \mu^-$ decays and random combinations of two muons (combinatorial background), most often from semi-leptonic decays of two different b hadrons, is achieved using the dimuon invariant mass, $m_{\mu^+ \mu^-}$, and the established characteristics of $B_{(s)}^0$ -meson decays. For example, because of their lifetimes of about 1.5 ps and their production at the LHC with momenta between a few GeV/c and $\sim 100 \text{ GeV}/c$, $B_{(s)}^0$ mesons travel up to a few centimetres before they decay. Therefore, the $B_{(s)}^0 \rightarrow \mu^+ \mu^-$ ‘decay vertex’, from which the muons originate, is required to be displaced with respect to the ‘production vertex’, the point where the two protons collide. Furthermore, the negative of the $B_{(s)}^0$ candidate’s momentum vector is required to point back to the production vertex.

These criteria, amongst others that have some ability to distinguish known signal events from background events, are combined into boosted decision trees (BDTs)^{24–26}. A BDT is an ensemble of decision trees each placing different selection requirements on the individual variables to achieve the best discrimination between ‘signal-like’ and ‘background-like’ events. Both experiments evaluated many variables for their discriminating power and each chose the best set of about ten to be used in its respective BDT. These include variables related to the quality of the reconstructed tracks of the muons; kinematic variables such as transverse momentum (with respect to the beam axis) of the individual muons and of the $B_{(s)}^0$ candidate; variables related to the decay vertex topology and fit quality, such as candidate decay length; and isolation variables, which measure the activity in terms of other particles in the vicinity of the two muons or their displaced vertex. A BDT must be ‘trained’ on collections of known background and signal events to generate the selection requirements on the variables and the weights for each tree. In the case of CMS, the background events used in the training are taken from intervals of dimuon mass above and below the signal region in data, while simulated events are used for the signal. The data are divided into disjoint sub-samples and the BDT trained on one sub-sample is applied to a different sub-sample to avoid any bias. LHCb uses simulated events for background and signal in the training of its BDT. After training, the relevant BDT is applied to each event in the data, returning a single value for the event, with high values being more signal-like. To avoid possible biases, both experiments kept the small mass interval that includes both the B_s^0 and B^0 signals blind until all selection criteria were established.

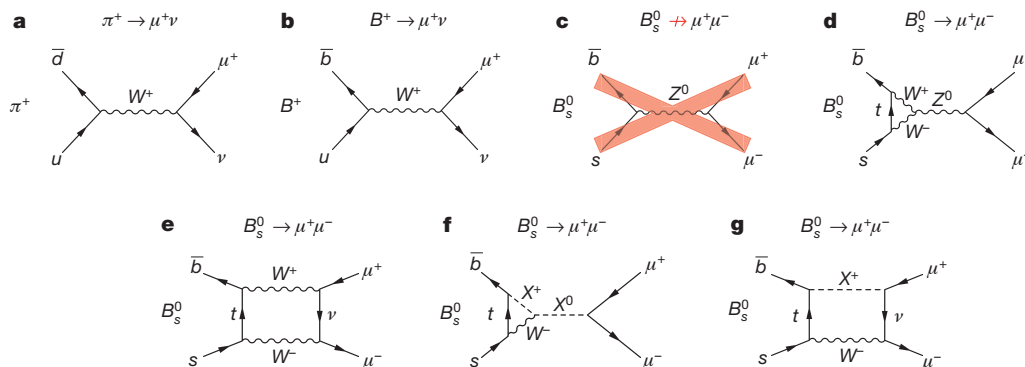


Figure 1 | Feynman diagrams related to the $B_s^0 \rightarrow \mu^+ \mu^-$ decay. **a**, π^+ meson decay through the charged-current process; **b**, B^+ meson decay through the charged-current process; **c**, a B_s^0 decay through the direct flavour changing neutral current process, which is forbidden in the SM, as indicated by a large red

‘X’; **d**, **e**, higher-order flavour changing neutral current processes for the $B_s^0 \rightarrow \mu^+ \mu^-$ decay allowed in the SM; and **f** and **g**, examples of processes for the same decay in theories extending the SM, where new particles, denoted X^0 and X^+ , can alter the decay rate.

In addition to the combinatorial background, specific b -hadron decays, such as $B^0 \rightarrow \pi^- \mu^+ \nu$ where the neutrino cannot be detected and the charged pion is misidentified as a muon, or $B^0 \rightarrow \pi^0 \mu^+ \mu^-$, where the neutral pion in the decay is not reconstructed, can mimic the dimuon decay of the $B_{(s)}^0$ mesons. The invariant mass of the reconstructed dimuon candidate for these processes (semi-leptonic background) is usually smaller than the mass of the $B_{(s)}^0$ or B^0 meson because the neutrino or another particle is not detected. There is also a background component from hadronic two-body $B_{(s)}^0$ decays (peaking background) as $B^0 \rightarrow K^+ \pi^-$, when both hadrons from the decay are misidentified as muons. These misidentified decays can produce peaks in the dimuon invariant-mass spectrum near the expected signal, especially for the $B^0 \rightarrow \mu^+ \mu^-$ decay. Particle identification algorithms are used to minimize the probability that pions and kaons are misidentified as muons, and thus suppress these background sources. Excellent mass resolution is mandatory for distinguishing between B^0 and $B_{(s)}^0$ mesons with a mass difference of about $87 \text{ MeV}/c^2$ and for separating them from backgrounds. The mass resolution for $B_{(s)}^0 \rightarrow \mu^+ \mu^-$ decays in CMS ranges from 32 to $75 \text{ MeV}/c^2$, depending on the direction of the muons relative to the beam axis, while LHCb achieves a uniform mass resolution of about $25 \text{ MeV}/c^2$.

The CMS and LHCb data are combined by fitting a common value for each branching fraction to the data from both experiments. The branching fractions are determined from the observed numbers, efficiency-corrected, of $B_{(s)}^0$ mesons that decay into two muons and the total numbers of $B_{(s)}^0$ mesons produced. Both experiments derive the latter from the number of observed $B^+ \rightarrow J/\psi K^+$ decays, whose branching fraction has been precisely measured elsewhere¹⁴. Assuming equal rates for B^+ and B^0 production, this gives the normalization for $B^0 \rightarrow \mu^+ \mu^-$. To derive the number of $B_{(s)}^0$ mesons from this B^+ decay mode, the ratio of b quarks that form (hadronize into) B^+ mesons to those that form $B_{(s)}^0$ mesons is also needed. Measurements of this ratio^{27,28}, for which there is additional discussion in Methods, and of the branching fraction $\mathcal{B}(B^+ \rightarrow J/\psi K^+)$ are used to normalize both sets of data and are constrained within Gaussian uncertainties in the fit. The use of these two results by both CMS and LHCb is the only significant source of correlation between their individual branching fraction measurements. The combined fit takes advantage of the larger data sample to increase the precision while properly accounting for the correlation.

In the simultaneous fit to both the CMS and LHCb data, the branching fractions of the two signal channels are common parameters of interest and are free to vary. Other parameters in the fit are considered as nuisance parameters. Those for which additional knowledge is available are constrained to be near their estimated values by using Gaussian penalties with their estimated uncertainties while the others are free to float in the fit. The ratio of the hadronization probability into B^+ and $B_{(s)}^0$ mesons and the branching fraction of the normalization channel $B^+ \rightarrow J/\psi K^+$ are common, constrained parameters. Candidate decays are categorized according to whether they were detected in CMS or LHCb and to the value of the relevant BDT discriminant. In the case of CMS, they are further categorized according to the data-taking period, and, because of the large variation in mass resolution with angle, whether the muons are both produced at large angles relative to the proton beams (central-region) or at least one muon is emitted at small angle relative to the beams (forward-region). An unbinned extended maximum likelihood fit to the dimuon invariant-mass distribution, in a region of about $\pm 500 \text{ MeV}/c^2$ around the $B_{(s)}^0$ mass, is performed simultaneously in all categories (12 categories from CMS and eight from LHCb). Likelihood contours in the plane of the parameters of interest, $\mathcal{B}(B^0 \rightarrow \mu^+ \mu^-)$ versus $\mathcal{B}(B_{(s)}^0 \rightarrow \mu^+ \mu^-)$, are obtained by constructing the test statistic $-2\Delta \ln L$ from the difference in log-likelihood ($\ln L$) values between fits with fixed values for the parameters of interest and the nominal fit. For each of the two branching fractions, a one-dimensional profile likelihood scan is likewise obtained by fixing only the single parameter of interest and allowing the other to vary during the fits. Additional fits are performed where the parameters under consideration are the ratio of the branching fractions relative to their SM predictions, $S_{\text{SM}}^{B_{(s)}^0} \equiv \mathcal{B}(B_{(s)}^0 \rightarrow \mu^+ \mu^-) / \mathcal{B}(B_{(s)}^0 \rightarrow \mu^+ \mu^-)_{\text{SM}}$, or the ratio \mathcal{R} of the two branching fractions.

The combined fit result is shown for all 20 categories in Extended Data Fig. 1. To represent the result of the fit in a single dimuon invariant-mass spectrum, the mass distributions of all categories, weighted according to values of $S/(S+B)$, where S is the expected number of $B_{(s)}^0$ signals and B is the number of background events under the $B_{(s)}^0$ peak in that category, are added together and shown in Fig. 2. The result of the simultaneous fit is overlaid. An alternative representation of the fit to the dimuon invariant-mass distribution for the six

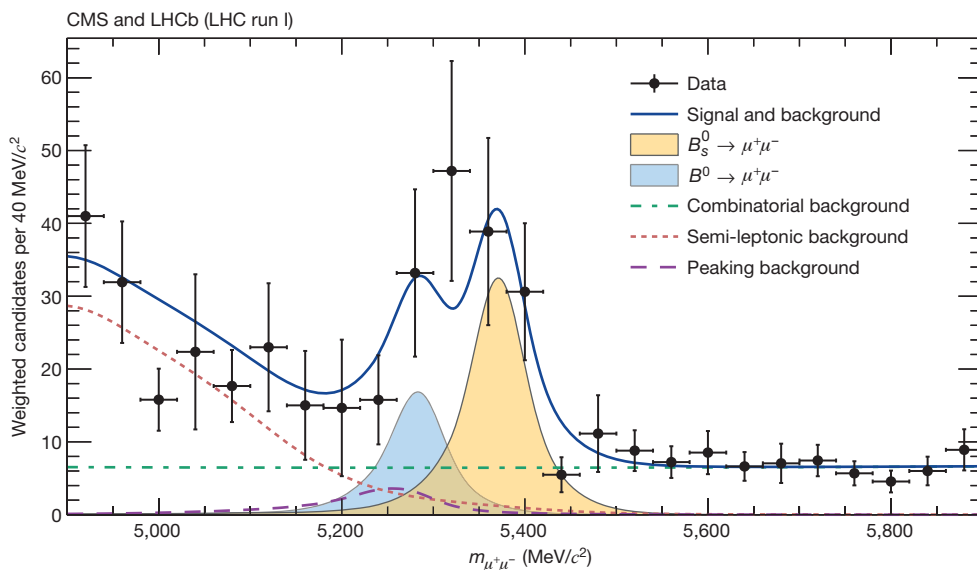


Figure 2 | Weighted distribution of the dimuon invariant mass, $m_{\mu^+\mu^-}$, for all categories. Superimposed on the data points in black are the combined fit (solid blue line) and its components: the $B_{(s)}^0$ (yellow shaded area) and B^0 (light-blue shaded area) signal components; the combinatorial background (dash-dotted green line); the sum of the semi-leptonic backgrounds (dotted salmon

line); and the peaking backgrounds (dashed violet line). The horizontal bar on each histogram point denotes the size of the binning, while the vertical bar denotes the 68% confidence interval. See main text for details on the weighting procedure.

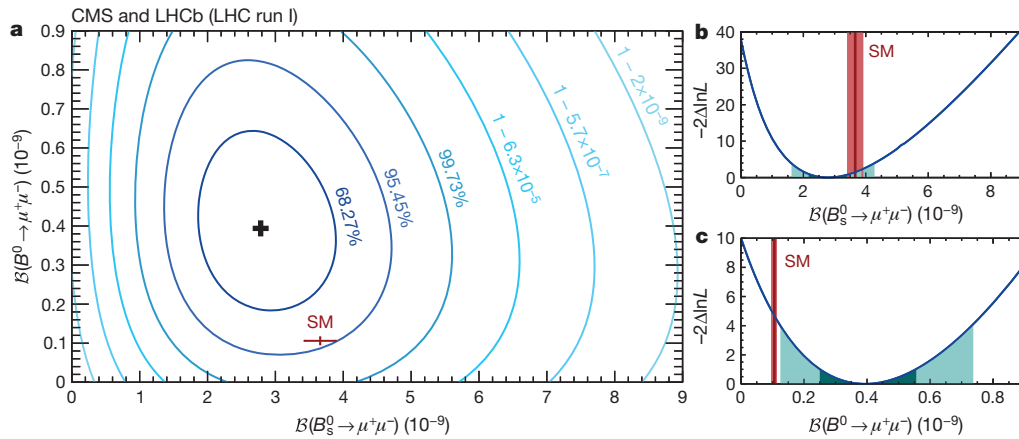


Figure 3 | Likelihood contours in the $\mathcal{B}(B^0 \rightarrow \mu^+ \mu^-)$ versus $\mathcal{B}(B_s^0 \rightarrow \mu^+ \mu^-)$ plane. The (black) cross in **a** marks the best-fit central value. The SM expectation and its uncertainty is shown as the (red) marker. Each contour encloses a region approximately corresponding to the reported confidence level. **b**, **c**, Variations of the test statistic $-2\Delta\ln L$ for $\mathcal{B}(B_s^0 \rightarrow \mu^+ \mu^-)$

(**b**) and $\mathcal{B}(B^0 \rightarrow \mu^+ \mu^-)$ (**c**). The dark and light (cyan) areas define the $\pm 1\sigma$ and $\pm 2\sigma$ confidence intervals for the branching fraction, respectively. The SM prediction and its uncertainty for each branching fraction is denoted with the vertical (red) band.

categories with the highest $S/(S+B)$ value for CMS and LHCb, as well as displays of events with high probability to be genuine signal decays, are shown in Extended Data Figs 2–4.

The combined fit leads to the measurements $\mathcal{B}(B_s^0 \rightarrow \mu^+ \mu^-) = (2.8_{-0.6}^{+0.7}) \times 10^{-9}$ and $\mathcal{B}(B^0 \rightarrow \mu^+ \mu^-) = (3.9_{-1.4}^{+1.6}) \times 10^{-10}$, where the uncertainties include both statistical and systematic sources, the latter contributing 35% and 18% of the total uncertainty for the B_s^0 and B^0 signals, respectively. Using Wilks' theorem²⁹, the statistical significance in unit of standard deviations, σ , is computed to be 6.2 for the $B_s^0 \rightarrow \mu^+ \mu^-$ decay mode and 3.2 for the $B^0 \rightarrow \mu^+ \mu^-$ mode. For each signal the null hypothesis that is used to compute the significance includes all background components predicted by the SM as well as the other signal, whose branching fraction is allowed to vary freely. The median expected significances assuming the SM branching fractions are 7.4σ and 0.8σ for the B_s^0 and B^0 modes, respectively. Likelihood contours for $\mathcal{B}(B^0 \rightarrow \mu^+ \mu^-)$ versus $\mathcal{B}(B_s^0 \rightarrow \mu^+ \mu^-)$ are shown in Fig. 3. One-dimensional likelihood scans for both decay modes are displayed in the same figure. In addition to the likelihood scan, the statistical significance and confidence intervals for the B^0 branching fraction are determined using simulated experiments. This determination yields a significance of 3.0σ for a B^0 signal with respect to the same null hypothesis described above. Following the Feldman–Cousins³⁰ procedure,

$\pm 1\sigma$ and $\pm 2\sigma$ confidence intervals for $\mathcal{B}(B^0 \rightarrow \mu^+ \mu^-)$ of $[2.5, 5.6] \times 10^{-10}$ and $[1.4, 7.4] \times 10^{-10}$ are obtained, respectively (see Extended Data Fig. 5).

The fit for the ratios of the branching fractions relative to their SM predictions yields $\mathcal{S}_{SM}^{B_s} = 0.76_{-0.18}^{+0.20}$ and $\mathcal{S}_{SM}^{B^0} = 3.7_{-1.4}^{+1.6}$. Associated likelihood contours and one-dimensional likelihood scans are shown in Extended Data Fig. 6. The measurements are compatible with the SM branching fractions of the $B_s^0 \rightarrow \mu^+ \mu^-$ and $B^0 \rightarrow \mu^+ \mu^-$ decays at the 1.2σ and 2.2σ level, respectively, when computed from the one-dimensional hypothesis tests. Finally, the fit for the ratio of branching fractions yields $\mathcal{R} = 0.14_{-0.06}^{+0.08}$, which is compatible with the SM at the 2.3σ level. The one-dimensional likelihood scan for this parameter is shown in Fig. 4.

The combined analysis of data from CMS and LHCb, taking advantage of their full statistical power, establishes conclusively the existence of the $B_s^0 \rightarrow \mu^+ \mu^-$ decay and provides an improved measurement of its branching fraction. This concludes a search that started more than three decades ago (see Extended Data Fig. 7), and initiates a phase of precision measurements of the properties of this decay. It also produces three standard deviation evidence for the $B^0 \rightarrow \mu^+ \mu^-$ decay. The measured branching fractions of both decays are compatible with SM predictions. This is the first time that the CMS and LHCb collaborations have performed a combined analysis of sets of their data in order to obtain a statistically significant observation.

Online Content Methods, along with any additional Extended Data display items and Source Data, are available in the online version of the paper; references unique to these sections appear only in the online paper.

Received 12 November 2014; accepted 31 March 2015.

Published online 13 May 2015.

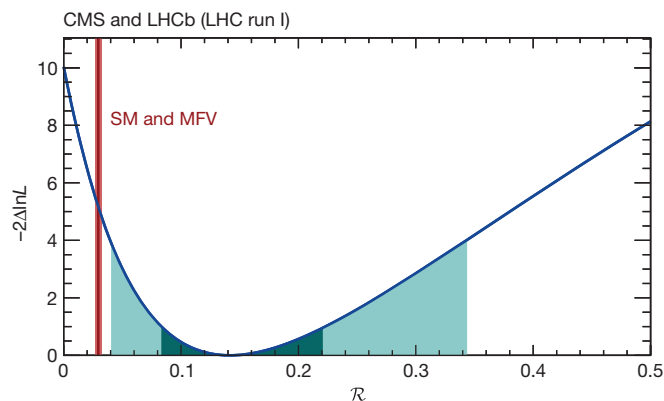


Figure 4 | Variation of the test statistic $-2\Delta\ln L$ as a function of the ratio of branching fractions $\mathcal{R} \equiv \mathcal{B}(B^0 \rightarrow \mu^+ \mu^-) / \mathcal{B}(B_s^0 \rightarrow \mu^+ \mu^-)$. The dark and light (cyan) areas define the $\pm 1\sigma$ and $\pm 2\sigma$ confidence intervals for \mathcal{R} , respectively. The value and uncertainty for \mathcal{R} predicted in the SM, which is the same in BSM theories with the minimal flavour violation (MFV) property, is denoted with the vertical (red) band.

- Bobeth, C. *et al.* $B_{s,d} \rightarrow l^+ l^-$ in the Standard Model with reduced theoretical uncertainty. *Phys. Rev. Lett.* **112**, 101801 (2014).
- Evans, L. & Bryant, P. LHC machine. *J. Instrum.* **3**, S08001 (2008).
- Planck Collaboration, Ade P. A. R. *et al.* Planck 2013 results. XVI. Cosmological parameters. *Astron. Astrophys.* **571**, A16 (2014).
- Gavela, M., Lozano, M., Orloff, J. & Pène, O. Standard model CP-violation and baryon asymmetry (I). Zero temperature. *Nucl. Phys. B* **430**, 345–381 (1994).
- RBC–UKQCD Collaborations, Witzel, O. B -meson decay constants with domain-wall light quarks and nonperturbatively tuned relativistic b -quarks. Preprint at <http://arXiv.org/abs/1311.0276> (2013).
- HPQCD Collaboration, Na, H. *et al.* B and B_s meson decay constants from lattice QCD. *Phys. Rev. D* **86**, 034506 (2012).
- Fermilab Lattice and MILC Collaborations, Bazavov A. *et al.* B - and D -meson decay constants from three-flavor lattice QCD. *Phys. Rev. D* **85**, 114506 (2012).
- Huang, C.-S., Liao, W. & Yan, Q.-S. The promising process to distinguish supersymmetric models with large $\tan\beta$ from the standard model: $B \rightarrow X_s \mu^+ \mu^-$. *Phys. Rev. D* **59**, 011701 (1998).


9. Rai Choudhury, S. & Gaur, N. Dileptonic decay of B_s meson in SUSY models with large $\tan \beta$. *Phys. Lett. B* **451**, 86–92 (1999).
10. Babu, K. & Kolda, C. F. Higgs-mediated $B^0 \rightarrow \mu^+ \mu^-$ in minimal supersymmetry. *Phys. Rev. Lett.* **84**, 228–231 (2000).
11. Bobeth, C., Ewerth, T., Kruger, F. & Urban, J. Analysis of neutral Higgs-boson contributions to the decays $B_s \rightarrow \ell^+ \ell^-$ and $B \rightarrow K \ell^+ \ell^-$. *Phys. Rev. D* **64**, 074014 (2001).
12. Buras, A. J. Relations between ΔM_{S_d} and $B_{S_d} \rightarrow \mu \bar{\mu}$ in models with minimal flavor violation. *Phys. Lett. B* **566**, 115–119 (2003).
13. Aoki, S. *et al.* Review of lattice results concerning low-energy particle physics. *Eur. Phys. J. C* **74**, 2890 (2014).
14. Particle Data Group, Beringer, J. *et al.* Review of particle physics. *Phys. Rev. D* **86**, 010001 (2012); 2013 partial update for the 2014 edition at <http://pdg.lbl.gov>.
15. Heavy Flavor Averaging Group, Amhis, Y. *et al.* Averages of b -hadron, c -hadron, and τ -lepton properties as of early 2012. Preprint at <http://arXiv.org/abs/1207.1158> (2012).
16. D'Ambrosio, G., Giudice, G. F., Isidori, G. & Strumia, A. Minimal flavour violation: an effective field theory approach. *Nucl. Phys. B* **645**, 155–187 (2002).
17. LHCb Collaboration, Aaij, R. *et al.* First evidence for the decay $B_s^0 \rightarrow \mu^+ \mu^-$. *Phys. Rev. Lett.* **110**, 021801 (2013).
18. CMS Collaboration, Chatrchyan, S. *et al.* Measurement of the $B_s^0 \rightarrow \mu^+ \mu^-$ branching fraction and search for $B^0 \rightarrow \mu^+ \mu^-$ with the CMS experiment. *Phys. Rev. Lett.* **111**, 101804 (2013).
19. LHCb Collaboration, Aaij, R. *et al.* Measurement of the $B_s^0 \rightarrow \mu^+ \mu^-$ branching fraction and search for $B^0 \rightarrow \mu^+ \mu^-$ decays at the LHCb experiment. *Phys. Rev. Lett.* **111**, 101805 (2013).
20. CMS Collaboration, Chatrchyan, S. *et al.* The CMS experiment at the CERN LHC. *J. Instrum.* **3**, S08004 (2008).
21. LHCb Collaboration, Alves, A. A. Jr *et al.* The LHCb detector at the LHC. *J. Instrum.* **3**, S08005 (2008).
22. ATLAS Collaboration, Aad, G. *et al.* Observation of a new particle in the search for the Standard Model Higgs boson with the ATLAS detector at the LHC. *Phys. Lett. B* **716**, 1–29 (2012).
23. CMS Collaboration, Chatrchyan, S. *et al.* Observation of a new boson at a mass of 125 GeV with the CMS experiment at the LHC. *Phys. Lett. B* **716**, 30–61 (2012).
24. Breiman, L., Friedman, J. H., Olshen, R. A. & Stone, C. J. *Classification and Regression Trees* (Wadsworth International Group, 1984).
25. Freund, Y. & Schapire, R. E. A decision-theoretic generalization of on-line learning and an application to boosting. *J. Comput. Syst. Sci.* **55**, 119–139 (1997).
26. Hoecker, A. *et al.* TMVA: Toolkit for Multivariate Data Analysis. *Proc. Sci. Adv. Comput. Anal. Techn. Phys. Res.* 040 http://pos.sissa.it/archive/conferences/050/040/ACAT_040.pdf (2007).
27. LHCb Collaboration, Aaij, R. *et al.* Measurement of b hadron production fractions in 7 TeV pp collisions. *Phys. Rev. D* **85**, 032008 (2012).
28. LHCb Collaboration, Aaij, R. *et al.* Measurement of the fragmentation fraction ratio f_s/f_d and its dependence on B meson kinematics. *J. High Energy Phys.* **4**, 1 (2013); updated in <https://cds.cern.ch/record/1559262/files/LHCb-CONF-2013-011.pdf>.
29. Wilks, S. S. The large-sample distribution of the likelihood ratio for testing composite hypotheses. *Ann. Math. Stat.* **9**, 60–62 (1938).
30. Feldman, G. J. & Cousins, R. D. Unified approach to the classical statistical analysis of small signals. *Phys. Rev. D* **57**, 3873–3889 (1998).

Acknowledgements We express our gratitude to colleagues in the CERN accelerator departments for the excellent performance of the LHC. We thank the technical and administrative staff at CERN, at the CMS institutes and at the LHCb institutes. In addition, we gratefully acknowledge the computing centres and personnel of the Worldwide LHC Computing Grid for delivering so effectively the computing infrastructure essential to our analyses. Finally, we acknowledge the enduring support

for the construction and operation of the LHC, the CMS and the LHCb detectors provided by CERN and by many funding agencies. The following agencies provide support for both CMS and LHCb: CAPES, CNPq, FAPERJ and FINEP (Brazil); NSFC (China); CNRS/IN2P3 (France); BMBF, DFG and HGF (Germany); SFI (Ireland); INFN (Italy); NASU (Ukraine); STFC (UK); and NSF (USA). Agencies that provide support for CMS only are BMWF and FWF (Austria); FNRS and FWO (Belgium); FAPESP (Brazil); MES (Bulgaria); CAS and MoST (China); COLCIENCIAS (Colombia); MSES and CSF (Croatia); RPF (Cyprus); MoER, ERC IUT and ERDF (Estonia); Academy of Finland, MEC, and HIP (Finland); CEA (France); GSRT (Greece); OTKA and NIH (Hungary); DAE and DST (India); IPM (Iran); NRF and WCU (Republic of Korea); LAS (Lithuania); MOE and UM (Malaysia); CINVESTAV, CONACYT, SEP, and UASLP-FAI (Mexico); MBIE (New Zealand); PAEC (Pakistan); MSHE and NSC (Poland); FCT (Portugal); JINR (Dubna); MON, RosAtom, RAS and RFBR (Russia); MESTD (Serbia); SEIDI and CPAN (Spain); Swiss Funding Agencies (Switzerland); MST (Taipei); ThEPCenter, IPST, STAR and NSTDA (Thailand); TUBITAK and TAEK (Turkey); SFFR (Ukraine); and DOE (USA). Agencies that provide support for only LHCb are: FINEP (Brazil); MPG (Germany); FOM and NWO (The Netherlands); MNiSW and NCN (Poland); MEN/IFA (Romania); MinES and FANO (Russia); MinEco (Spain); SNSF and SER (Switzerland). Individuals from the CMS collaboration have received support from the Marie-Curie programme and the European Research Council and EPLANET (European Union); the Leventis Foundation; the A. P. Sloan Foundation; the Alexander von Humboldt Foundation; the Belgian Federal Science Policy Office; the Fonds pour la Formation à la Recherche dans l'Industrie et dans l'Agriculture (FRIABelgium); the Agentschap voor Innovatie door Wetenschap en Technologie (IWT-Belgium); the Ministry of Education, Youth and Sports (MEYS) of the Czech Republic; the Council of Science and Industrial Research, India; the HOMING PLUS programme of Foundation for Polish Science, cofinanced from European Union, Regional Development Fund; the Compagnia di San Paolo (Torino); the Consorzio per la Fisica (Trieste); MIUR project 20108T4XTM (Italy); the Thales and Aristeia programmes cofinanced by EU-ESF and the Greek NSRF; and the National Priorities Research Program by Qatar National Research Fund. Individual groups or members of the LHCb collaboration have received support from EPLANET, Marie Skłodowska-Curie Actions and ERC (European Union), Conseil général de Haute-Savoie, Labex ENIGMASS and OCEVU, Région Auvergne (France), RFBR (Russia), XuntaGal and GENCAT (Spain), Royal Society and Royal Commission for the Exhibition of 1851 (UK). LHCb is also thankful for the computing resources and the access to software R&D tools provided by Yandex LLC (Russia). The CMS and LHCb collaborations are indebted to the communities behind the multiple open source software packages on which they depend.

Author Contributions All authors have contributed to the publication, being variously involved in the design and the construction of the detectors, in writing software, calibrating sub-systems, operating the detectors and acquiring data and finally analysing the processed data.

Author Information Reprints and permissions information is available at www.nature.com/reprints. The authors declare no competing financial interests. Readers are welcome to comment on the online version of the paper. Correspondence and requests for materials should be addressed to cms-publication-committee-chair@cern.ch and to lhc-editorial-board-chair@cern.ch.

 This work is licensed under a Creative Commons Attribution-NonCommercial-ShareAlike 3.0 Unported licence. The images or other third party material in this article are included in the article's Creative Commons licence, unless indicated otherwise in the credit line; if the material is not included under the Creative Commons licence, users will need to obtain permission from the licence holder to reproduce the material. To view a copy of this licence, visit <http://creativecommons.org/licenses/by-nc-sa/3.0>

METHODS

Experimental setup. At the Large Hadron Collider (LHC), two counter-rotating beams of protons, contained and guided by superconducting magnets spaced around a 27 km circular tunnel, located approximately 100 m underground near Geneva, Switzerland, are brought into collision at four interaction points (IPs). The study presented in this Letter uses data collected at energies of 3.5 TeV per beam in 2011 and 4 TeV per beam in 2012 by the CMS and LHCb experiments located at two of these IPs.

The CMS and LHCb detectors are both designed to look for phenomena beyond the SM (BSM), but using complementary strategies. The CMS detector²⁰, shown in Extended Data Fig. 3, is optimized to search for yet unknown heavy particles, with masses ranging from 100 GeV/ c^2 to a few TeV/ c^2 , which, if observed, would be a direct manifestation of BSM phenomena. Since many of the hypothesized new particles can decay into particles containing b quarks or into muons, CMS is able to detect efficiently and study B^0 (5,280 MeV/ c^2) and B_s^0 (5,367 MeV/ c^2) mesons decaying to two muons even though it is designed to search for particles with much larger masses. The CMS detector covers a very large range of angles and momenta to reconstruct high-mass states efficiently. To that extent, it employs a 13 m long, 6 m diameter superconducting solenoid magnet, operated at a field of 3.8 T, centred on the IP with its axis along the beam direction and covering both hemispheres. A series of silicon tracking layers, consisting of silicon pixel detectors near the beam and silicon strips farther out, organized in concentric cylinders around the beam, extending to a radius of 1.1 m and terminated on each end by planar detectors (disks) perpendicular to the beam, measures the momentum, angles, and position of charged particles emerging from the collisions. Tracking coverage starts from the direction perpendicular to the beam and extends to within 220 mrad from it on both sides of the IP. The inner three cylinders and disks extending from 4.3 to 10.7 cm in radius transverse to the beam are arrays of $100 \times 150 \mu\text{m}^2$ silicon pixels, which can distinguish the displacement of the b -hadron decays from the primary vertex of the collision. The silicon strips, covering radii from 25 cm to approximately 110 cm, have pitches ranging from 80 to 183 μm . The impact parameter is measured with a precision of 10 μm for transverse momenta of 100 GeV/ c and 20 μm for 10 GeV/ c . The momentum resolution, provided mainly by the silicon strips, changes with the angle relative to the beam direction, resulting in a mass resolution for $B_{(s)}^0 \rightarrow \mu^+ \mu^-$ decays that varies from 32 MeV/ c^2 for $B_{(s)}^0$ mesons produced perpendicularly to the proton beams to 75 MeV/ c^2 for those produced at small angles relative to the beam direction. After the tracking system, at a greater distance from the IP, there is a calorimeter that stops (absorbs) all particles except muons and measures their energies. The calorimeter consists of an electromagnetic section followed by a hadronic section. Muons are identified by their ability to penetrate the calorimeter and the steel return yoke of the solenoid magnet and to produce signals in gas-ionization particle detectors located in compartments within the steel yoke. The CMS detector has no capability to discriminate between charged hadron species, pions, kaons, or protons, that is effective at the typical particle momenta in this analysis.

The primary commitment of the LHCb collaboration is the study of particle-antiparticle asymmetries and of rare decays of particles containing b and c quarks. LHCb aims at detecting BSM particles indirectly by measuring their effect on b -hadron properties for which precise SM predictions exist. The production cross section of b hadrons at the LHC is particularly large at small angles relative to the colliding beams. The small-angle region also provides advantages for the detection and reconstruction of a wide range of their decays. The LHCb experiment²¹, shown in Extended Data Fig. 4, instruments the angular interval from 10 to 300 mrad with respect to the beam direction on one side of the interaction region. Its detectors are designed to reconstruct efficiently a wide range of b -hadron decays, resulting in charged pions and kaons, protons, muons, electrons, and photons in the final state. The detector includes a high-precision tracking system consisting of a silicon strip vertex detector, a large-area silicon strip detector located upstream of a dipole magnet characterized by a field integral of 4 T m, and three stations of silicon strip detectors and straw drift tubes downstream of the magnet. The vertex detector has sufficient spatial resolution to distinguish the slight displacement of the weakly decaying b hadron from the primary production vertex where the two protons collided and produced it. The tracking detectors upstream and downstream of the dipole magnet measure the momenta of charged particles. The combined tracking system provides a momentum measurement with an uncertainty that varies from 0.4% at 5 GeV/ c to 0.6% at 100 GeV/ c . This results in an invariant-mass resolution of 25 MeV/ c^2 for $B_{(s)}^0$ mesons decaying to two muons that is nearly independent of the angle with respect to the beam. The impact parameter resolution is smaller than 20 μm for particle tracks with large transverse momentum. Different types of charged hadrons are distinguished by information from two ring-imaging Cherenkov detectors. Photon, electron, and hadron candidates are identified by calorimeters. Muons are identified by a system composed of alternating layers of iron and multiwire proportional chambers.

Neither CMS nor LHCb records all the interactions occurring at its IP because the data storage and analysis costs would be prohibitive. Since most of the interactions are reasonably well characterized (and can be further studied by recording only a small sample of them) specific event filters (known as triggers) select the rare processes that are of interest to the experiments. Both CMS and LHCb implement triggers that specifically select events containing two muons. The triggers of both experiments have a hardware stage, based on information from the calorimeter and muon systems, followed by a software stage, consisting of a large computing cluster that uses all the information from the detector, including the tracking, to make the final selection of events to be recorded for subsequent analysis. Since CMS is designed to look for much heavier objects than $B_{(s)}^0$ mesons, it selects events that contain muons with higher transverse momenta than those selected by LHCb. This eliminates many of the $B_{(s)}^0$ decays while permitting CMS to run at a higher proton-proton collision rate to look for the more rare massive particles. Thus CMS runs at higher collision rates but with lower efficiency than LHCb for $B_{(s)}^0$ mesons decaying to two muons. The overall sensitivity to these decays turns out to be similar in the two experiments.

CMS and LHCb are not the only collaborations to have searched for $B_s^0 \rightarrow \mu^+ \mu^-$ and $B^0 \rightarrow \mu^+ \mu^-$ decays. Over three decades, a total of eleven collaborations have taken part in this search¹⁴, as illustrated by Extended Data Fig. 7. This plot gathers the results from CLEO^{21–25}, ARGUS²⁶, UA1^{27,28}, CDF^{29–34}, L3³⁵, DØ^{36–40}, Belle⁴¹, Babar^{42,43}, LHCb^{17,54–57}, CMS^{18,58,59} and ATLAS⁶⁰.

Analysis description. The analysis techniques used to obtain the results presented in this Letter are very similar to those used to obtain the individual result in each collaboration, described in more detail in refs 18, 19. Here only the main analysis steps are reviewed and the changes used in the combined analysis are highlighted. Data samples for this analysis were collected by the two experiments in proton-proton collisions at a centre-of-mass energy of 7 and 8 TeV during 2011 and 2012, respectively. These samples correspond to a total integrated luminosity of 25 and 3 fb⁻¹ for the CMS and LHCb experiments, respectively, and represent their complete data sets from the first running period of the LHC.

The trigger criteria were slightly different between the two experiments. The large majority of events were triggered by requirements on one or both muons of the signal decay: the LHCb detector triggered on muons with transverse momentum $p_T > 1.5$ GeV/ c while the CMS detector, because of its geometry and higher instantaneous luminosity, triggered on two muons with $p_T > 4$ (3) GeV/ c , for the leading (sub-leading) muon.

The data analysis procedures in the two experiments follow similar strategies. Pairs of high-quality oppositely charged particle tracks that have one of the expected patterns of hits in the muon detectors are fitted to form a common vertex in three dimensions, which is required to be displaced from the primary interaction vertex (PV) and to have a small χ^2 in the fit. The resulting $B_{(s)}^0$ candidate is further required to point back to the PV, for example, to have a small impact parameter, consistent with zero, with respect to it. The final classification of data events is done in categories of the response of a multivariate discriminant (MVA) combining information from the kinematics and vertex topology of the events. The type of MVA used is a boosted decision tree (BDT)^{24–26}. The branching fractions are then obtained by a fit to the dimuon invariant mass, $m_{\mu^+ \mu^-}$, of all categories simultaneously.

The signals appear as peaks at the B_s^0 and B^0 masses in the invariant-mass distributions, observed over background events. One of the components of the background is combinatorial in nature, as it is due to the random combinations of genuine muons. These produce a smooth dimuon mass distribution in the vicinity of the B_s^0 and B^0 masses, estimated in the fit to the data by extrapolation from the sidebands of the invariant-mass distribution. In addition to the combinatorial background, certain specific b -hadron decays can mimic the signal or contribute to the background in its vicinity. In particular, the semi-leptonic decays $B^0 \rightarrow \pi^- \mu^+ \nu$, $B_s^0 \rightarrow K^- \mu^+ \nu$, and $A_b^0 \rightarrow p \mu^- \bar{\nu}$ can have reconstructed masses that are near the signal if one of the hadrons is misidentified as a muon and is combined with a genuine muon. Similarly the dimuon coming from the rare $B^0 \rightarrow \pi^0 \mu^+ \mu^-$ and $B^+ \rightarrow \pi^+ \mu^+ \mu^-$ decays can also fake the signal. All these background decays, when reconstructed as a dimuon final state, have invariant masses that are lower than the masses of the B^0 and B_s^0 mesons, because they are missing one of the original decay particles. An exception is the decay $A_b^0 \rightarrow p \mu^- \bar{\nu}$, which can also populate, with a smooth mass distribution, higher-mass regions. Furthermore, background due to misidentified hadronic two-body decays $B_{(s)}^0 \rightarrow h^+ h'^-$, where $h^{(\prime)} = \pi$ or K , is present when both hadrons are misidentified as muons. These misidentified decays produce an apparent dimuon invariant-mass peak close to the B^0 mass value. Such a peak can mimic a $B^0 \rightarrow \mu^+ \mu^-$ signal and is estimated from control channels and added to the fit.

The distributions of signal in the invariant mass and in the MVA discriminant are derived from simulations with a detailed description of the detector response

for CMS and are calibrated using exclusive two-body hadronic decays in data for LHCb. The distributions for the backgrounds are obtained from simulation with the exception of the combinatorial background. The latter is obtained by interpolating from the data invariant-mass sidebands separately for each category, after the subtraction of the other background components.

To compute the signal branching fractions, the numbers of B_s^0 and B^0 mesons that are produced, as well as the numbers of those that have decayed into a dimuon pair, are needed. The latter numbers are the raw results of this analysis, whereas the former need to be determined from measurements of one or more ‘normalization’ decay channels, which are abundantly produced, have an absolute branching fraction that is already known with good precision, and that share characteristics with the signals, so that their trigger and selection efficiencies do not differ significantly. Both experiments use the $B^+ \rightarrow J/\psi K^+$ decay as a normalization channel with $\mathcal{B}(B^+ \rightarrow J/\psi (\mu^+ \mu^-) K^+) = (6.10 \pm 0.19) \times 10^{-5}$, and LHCb also uses the $B^0 \rightarrow K^+ \pi^-$ channel with $\mathcal{B}(B^0 \rightarrow K^+ \pi^-) = (1.96 \pm 0.05) \times 10^{-5}$. Both branching fraction values are taken from ref. 14. Hence, the $B_s^0 \rightarrow \mu^+ \mu^-$ branching fraction is expressed as a function of the number of signal events ($N_{B_s^0 \rightarrow \mu^+ \mu^-}$) in the data normalized to the numbers of $B^+ \rightarrow J/\psi K^+$ and $B^0 \rightarrow K^+ \pi^-$ events:

$$\mathcal{B}(B_s^0 \rightarrow \mu^+ \mu^-) = \frac{N_{B_s^0 \rightarrow \mu^+ \mu^-}}{N_{\text{norm.}}} \times \frac{f_d}{f_s} \times \frac{\varepsilon_{\text{norm.}}}{\varepsilon_{B_s^0 \rightarrow \mu^+ \mu^-}} \times \mathcal{B}_{\text{norm.}} = \alpha_{\text{norm.}} \times N_{B_s^0 \rightarrow \mu^+ \mu^-} \quad (1)$$

where the ‘norm.’ subscript refers to either of the normalization channels. The values of the normalization parameter $\alpha_{\text{norm.}}$ obtained by LHCb from the two normalization channels are found in good agreement and their weighted average is used. In this formula ε indicates the total event detection efficiency including geometrical acceptance, trigger selection, reconstruction, and analysis selection for the corresponding decay. The f_d/f_s factor is the ratio of the probabilities for a b quark to hadronize into a B^0 as compared to a B_s^0 meson; the probability to hadronize into a B^+ (f_u) is assumed to be equal to that into B^0 (f_d) on the basis of theoretical grounds, and this assumption is checked on data. The value of $f_d/f_s = 3.86 \pm 0.22$ measured by LHCb^{27,28,61} is used in this analysis. As the value of f_d/f_s depends on the kinematic range of the considered particles, which differs between LHCb and CMS, CMS checked this observable with the decays $B_s^0 \rightarrow J/\psi \phi$ and $B^+ \rightarrow J/\psi K^+$ within its acceptance, finding a consistent value. An additional systematic uncertainty of 5% was assigned to f_d/f_s to account for the extrapolation of the LHCb result to the CMS acceptance. An analogous formula to that in equation (1) holds for the normalization of the $B^0 \rightarrow \mu^+ \mu^-$ decay, with the notable difference that the f_d/f_s factor is replaced by $f_d/f_u = 1$.

The antiparticle \bar{B}^0 (\bar{B}_s^0) and the particle B^0 (B_s^0) can both decay into two muons and no attempt is made in this analysis to determine whether the antiparticle or particle was produced (untagged method). However, the B^0 and B_s^0 particles are known to oscillate, that is to transform continuously into their antiparticles and vice versa. Therefore, a quantum superposition of particle and antiparticle states propagates in the laboratory before decaying. This superposition can be described by two ‘mass eigenstates’, which are symmetric and antisymmetric in the charge-parity (CP) quantum number, and have slightly different masses. In the SM, the heavy eigenstate can decay into two muons, whereas the light eigenstate cannot without violating the CP quantum number conservation. In BSM models, this is not necessarily the case. In addition to their masses, the two eigenstates of the B_s^0 system also differ in their lifetime values¹⁴. The lifetimes of the light and heavy eigenstates are also different from the average B_s^0 lifetime, which is used by CMS and LHCb in the simulations of signal decays. Since the information on the displacement of the secondary decay with respect to the PV is used as a discriminant against combinatorial background in the analysis, the efficiency versus lifetime has a model-dependent bias⁶² that must be removed. This bias is estimated assuming SM dynamics. Owing to the smaller difference between the lifetime of its heavy and light mass eigenstates, no correction is required for the B^0 decay mode.

Detector simulations are needed by both CMS and LHCb. CMS relies on simulated events to determine resolutions and trigger and reconstruction efficiencies, and to provide the signal sample for training the BDT. The dimuon mass resolution given by the simulation is validated using data on J/ψ , Y , and Z -boson decays to two muons. The tracking and trigger efficiencies obtained from the simulation are checked using special control samples from data. The LHCb analysis is designed to minimize the impact of discrepancies between simulations and data. The mass resolution is measured with data. The distribution of the BDT for the signal and for the background is also calibrated with data using control channels and mass sidebands. The efficiency ratio for the trigger is also largely determined from data. The simulations are used to determine the efficiency ratios of selection and reconstruction processes between signal and normalization channels. As for the overall detector simulation, each experiment has a team dedicated to making the simulations as complete and realistic as possible. The simulated data are constantly being compared to the

actual data. Agreement between simulation and data in both experiments is quite good, often extending well beyond the cores of distributions. Differences occur because, for example, of incomplete description of the material of the detectors, approximations made to keep the computer time manageable, residual uncertainties in calibration and alignment, and discrepancies or limitations in the underlying theory and experimental data used to model the relevant collisions and decays. Small differences between simulation and data that are known to have an impact on the result are treated either by reweighting the simulations to match the data or by assigning appropriate systematic uncertainties.

Small changes are made to the analysis procedure with respect to refs 18, 19 in order to achieve a consistent combination between the two experiments. In the LHCb analysis, the $A_b^0 \rightarrow p \mu^- \bar{\nu}$ background component, which was not included in the fit for the previous result but whose effect was accounted for as an additional systematic uncertainty, is now included in the standard fit. The following modifications are made to the CMS analysis: the $A_b^0 \rightarrow p \mu^- \bar{\nu}$ branching fraction is updated to a more recent prediction^{63,64} of $\mathcal{B}(A_b^0 \rightarrow p \mu^- \bar{\nu}) = (4.94 \pm 2.19) \times 10^{-4}$; the phase space model of the decay $A_b^0 \rightarrow p \mu^- \bar{\nu}$ is changed to a more appropriate semi-leptonic decay model⁶³; and the decay time bias correction for the B_s^0 , previously absent from the analysis, is now calculated and applied with a different correction for each category of the multivariate discriminant.

These modifications result in changes in the individual results of each experiment. The modified CMS analysis, applied on the CMS data, yields

$$\mathcal{B}(B_s^0 \rightarrow \mu^+ \mu^-) = (2.8_{-0.9}^{+1.1}) \times 10^{-9} \quad \text{and} \quad \mathcal{B}(B^0 \rightarrow \mu^+ \mu^-) = (4.4_{-1.9}^{+2.2}) \times 10^{-10} \quad (2)$$

while the LHCb results change to

$$\mathcal{B}(B_s^0 \rightarrow \mu^+ \mu^-) = (2.7_{-0.9}^{+1.1}) \times 10^{-9} \quad \text{and} \quad \mathcal{B}(B^0 \rightarrow \mu^+ \mu^-) = (3.3_{-2.1}^{+2.4}) \times 10^{-10} \quad (3)$$

These results are only slightly different from the published ones and are in agreement with each other.

Simultaneous fit. The goal of the analysis presented in this Letter is to combine the full data sets of the two experiments to reduce the uncertainties on the branching fractions of the signal decays obtained from the individual determinations. A simultaneous unbinned extended maximum likelihood fit is performed to the data of the two experiments, using the invariant-mass distributions of all 20 MVA discriminant categories of both experiments. The invariant-mass distributions are defined in the dimuon mass ranges $m_{\mu^+ \mu^-} \in [4.9, 5.9] \text{ GeV}/c^2$ and $[4.9, 6.0] \text{ GeV}/c^2$ for the CMS and LHCb experiments, respectively. The branching fractions of the signal decays, the hadronization fraction ratio f_d/f_s , and the branching fraction of the normalization channel $B^+ \rightarrow J/\psi K^+$ are treated as common parameters. The value of the $B^+ \rightarrow J/\psi K^+$ branching fraction is the combination of results from five different experiments¹⁴, taking advantage of all their data to achieve the most precise input parameters for this analysis. The combined fit takes advantage of the larger data sample and proper treatment of the correlations between the individual measurements to increase the precision and reliability of the result, respectively.

Fit parameters, other than those of primary physics interest, whose limited knowledge affects the results, are called ‘nuisance parameters’. In particular, systematic uncertainties are modelled by introducing nuisance parameters into the statistical model and allowing them to vary in the fit; those for which additional knowledge is present are constrained using Gaussian distributions. The mean and standard deviation of these distributions are set to the central value and uncertainty obtained either from other measurements or from control channels. The statistical component of the final uncertainty on the branching fractions is obtained by repeating the fit after fixing all of the constrained nuisance parameters to their best fitted values. The systematic component is then calculated by subtracting in quadrature the statistical component from the total uncertainty. In addition to the free fit, a two-dimensional likelihood ratio scan in the plane $\mathcal{B}(B^0 \rightarrow \mu^+ \mu^-)$ versus $\mathcal{B}(B_s^0 \rightarrow \mu^+ \mu^-)$ is performed.

Feldman–Cousins confidence interval. The Feldman–Cousins likelihood ratio ordering procedure³⁰ is a unified frequentist method to construct single- and double-sided confidence intervals for parameters of a given model adapted to the data. It provides a natural transition between single-sided confidence intervals, used to define upper or lower limits, and double-sided ones. Since the single-experiment results^{18,19} showed that the $B^0 \rightarrow \mu^+ \mu^-$ signal is at the edge of the probability region customarily used to assert statistically significant evidence for a result, a Feldman–Cousins procedure is performed. This allows a more reliable determination of the confidence interval and significance of this signal without the assumptions required for the use of Wilks’ theorem. In addition, a prescription for the treatment of nuisance parameters has to be chosen because scanning the whole parameter space in the presence of more than a few parameters is computationally too intensive. In this case the procedure described by the ATLAS and CMS Higgs combination group⁶⁵ is adopted. For each point of the space of the relevant parameters, the nuisance parameters are fixed to their best value estimated by the mean

- of a maximum likelihood fit to the data with the value of $\mathcal{B}(B^0 \rightarrow \mu^+ \mu^-)$ fixed and all nuisance parameters profiled with Gaussian penalties. Sampling distributions are constructed for each tested point of the parameter of interest by generating simulated experiments and performing maximum likelihood fits in which the Gaussian mean values of the external constraints on the nuisance parameters are randomized around the best-fit values for the nuisance parameters used to generate the simulated experiments. The sampling distribution is constructed from the distribution of the negative log-likelihood ratio evaluated on the simulated experiments by performing one likelihood fit in which the value of $\mathcal{B}(B^0 \rightarrow \mu^+ \mu^-)$ is free to float and another with the $\mathcal{B}(B^0 \rightarrow \mu^+ \mu^-)$ fixed to the tested point value. This sampling distribution is then converted to a confidence level by evaluating the fraction of simulated experiments entries with a value for the negative log-likelihood ratio greater than or equal to the value observed in the data for each tested point. The results of this procedure are shown in Extended Data Fig. 5.
31. CLEO Collaboration, Giles R. *et al.* Two-body decays of B mesons. *Phys. Rev. D* **30**, 2279–2294 (1984).
 32. CLEO Collaboration, Avery P. *et al.* Limits on rare exclusive decays of B mesons. *Phys. Lett. B* **183**, 429–433 (1987).
 33. CLEO Collaboration, Avery P. *et al.* A search for exclusive penguin decays of B mesons. *Phys. Lett. B* **223**, 470–475 (1989).
 34. CLEO Collaboration, Ammar R. *et al.* Search for B^0 decays to two charged leptons. *Phys. Rev. D* **49**, 5701–5704 (1994).
 35. CLEO Collaboration, Bergfeld T. *et al.* Search for decays of B^0 mesons into pairs of leptons: $B^0 \rightarrow e^+ e^-$, $B^0 \rightarrow \mu^+ \mu^-$ and $B^0 \rightarrow e^\pm \mu^\mp$. *Phys. Rev. D* **62**, 091102 (2000).
 36. ARGUS Collaboration, Albrecht H. *et al.* B meson decays into charmonium states. *Phys. Lett. B* **199**, 451–456 (1987).
 37. UA1 Collaboration, Albajar C. *et al.* Low mass dimuon production at the CERN proton-antiproton collider. *Phys. Lett. B* **209**, 397–406 (1988).
 38. UA1 Collaboration, Albajar C. *et al.* A search for rare B meson decays at the CERN $SppS$ collider. *Phys. Lett. B* **262**, 163–170 (1991).
 39. CDF Collaboration, Abe F. *et al.* Search for flavor-changing neutral current B meson decays in $p\bar{p}$ collisions at $\sqrt{s} = 1.8$ TeV. *Phys. Rev. Lett.* **76**, 4675–4680 (1996).
 40. CDF Collaboration, Abe F. *et al.* Search for the decays $B_d^0 \rightarrow \mu^+ \mu^-$ and $B_s^0 \rightarrow \mu^+ \mu^-$ in $p\bar{p}$ collisions at $\sqrt{s} = 1.8$ TeV. *Phys. Rev. D* **57**, 3811–3816 (1998).
 41. CDF Collaboration, Acosta D. *et al.* Search for $B_s^0 \rightarrow \mu^+ \mu^-$ and $B_d^0 \rightarrow \mu^+ \mu^-$ decays in $p\bar{p}$ collisions at $\sqrt{s} = 1.96$ TeV. *Phys. Rev. Lett.* **93**, 032001 (2004).
 42. CDF Collaboration, Abulencia A. *et al.* Search for $B_s \rightarrow \mu^+ \mu^-$ and $B_d \rightarrow \mu^+ \mu^-$ decays in $p\bar{p}$ collisions with CDF II. *Phys. Rev. Lett.* **95**, 221805 (2005).
 43. CDF Collaboration, Aaltonen T. *et al.* Search for $B_s \rightarrow \mu^+ \mu^-$ and $B_d \rightarrow \mu^+ \mu^-$ decays with CDF II. *Phys. Rev. Lett.* **107**, 191801 (2011).
 44. CDF Collaboration, Aaltonen T. *et al.* Search for $B_s \rightarrow \mu^+ \mu^-$ and $B_d \rightarrow \mu^+ \mu^-$ decays with the full CDF Run II data set. *Phys. Rev. D* **87**, 072003 (2013).
 45. L3 Collaboration, Acciarri M. *et al.* Search for neutral B meson decays to two charged leptons. *Phys. Lett. B* **391**, 474–480 (1997).
 46. DØ Collaboration, Abbott B. *et al.* Search for the decay $b \rightarrow X_s \mu^+ \mu^-$. *Phys. Lett. B* **423**, 419–426 (1998).
 47. DØ Collaboration, Abazov V. *et al.* A search for the flavor-changing neutral current decay $B_s^0 \rightarrow \mu^+ \mu^-$ in $p\bar{p}$ collisions at $\sqrt{s} = 1.96$ TeV with the DØ detector. *Phys. Rev. Lett.* **94**, 071802 (2005).
 48. DØ Collaboration, Abazov V. M. *et al.* Search for $B_s^0 \rightarrow \mu^+ \mu^-$ at DØ. *Phys. Rev. D* **76**, 092001 (2007).
 49. DØ Collaboration, Abazov V. M. *et al.* Search for the rare decay $B_s^0 \rightarrow \mu^+ \mu^-$. *Phys. Lett. B* **693**, 539–544 (2010).
 50. DØ Collaboration, Abazov V. M. *et al.* Search for the rare decay $B_s^0 \rightarrow \mu^+ \mu^-$. *Phys. Rev. D* **87**, 072006 (2013).
 51. BELLE Collaboration, Chang M. *et al.* Search for $B^0 \rightarrow \ell^+ \ell^-$ at BELLE. *Phys. Rev. D* **68**, 111101 (2003).
 52. BaBar Collaboration, Aubert B. *et al.* Search for decays of B^0 mesons into pairs of charged leptons: $B^0 \rightarrow e^+ e^-$, $B^0 \rightarrow \mu^+ \mu^-$, $B^0 \rightarrow e^\pm \mu^\mp$. *Phys. Rev. Lett.* **94**, 221803 (2005).
 53. BaBar Collaboration, Aubert B. *et al.* Search for decays of B^0 mesons into $e^+ e^-$, $\mu^+ \mu^-$, and $e^\pm \mu^\mp$ final states. *Phys. Rev. D* **77**, 032007 (2008).
 54. LHCb Collaboration, Aaij R. *et al.* Search for the rare decays $B_s^0 \rightarrow \mu^+ \mu^-$ and $B^0 \rightarrow \mu^+ \mu^-$. *Phys. Lett. B* **699**, 330–340 (2011).
 55. LHCb Collaboration, Aaij R. *et al.* Strong constraints on the rare decays $B_s^0 \rightarrow \mu^+ \mu^-$ and $B^0 \rightarrow \mu^+ \mu^-$. *Phys. Rev. Lett.* **108**, 231801 (2012).
 56. LHCb Collaboration, Aaij R. *et al.* Search for the rare decays $B_s^0 \rightarrow \mu^+ \mu^-$ and $B^0 \rightarrow \mu^+ \mu^-$. *Phys. Lett. B* **708**, 55–67 (2012).
 57. LHCb Collaboration, Aaij R. *et al.* Measurement of the $B_s^0 \rightarrow \mu^+ \mu^-$ branching fraction and search for $B^0 \rightarrow \mu^+ \mu^-$ decays at the LHCb experiment. *Phys. Rev. Lett.* **111**, 101805 (2013).
 58. CMS Collaboration, Chatrchyan S. *et al.* Search for $B_s^0 \rightarrow \mu^+ \mu^-$ and $B^0 \rightarrow \mu^+ \mu^-$ decays in pp collisions at 7 TeV. *Phys. Rev. Lett.* **107**, 191802 (2011).
 59. CMS Collaboration, Chatrchyan S. *et al.* Search for $B_s^0 \rightarrow \mu^+ \mu^-$ and $B^0 \rightarrow \mu^+ \mu^-$ decays. *J. High Energy Phys.* **04**, 033 (2012).
 60. ATLAS Collaboration, Aad G. *et al.* Search for the decay $B_s^0 \rightarrow \mu^+ \mu^-$ with the ATLAS detector. *Phys. Lett. B* **713**, 387–407 (2012).
 61. LHCb Collaboration, Aaij R. *et al.* Updated average f_s/f_d b -hadron production fraction ratio for 7 TeV pp collisions. <http://cds.cern.ch/record/1559262> (LHCb-CONF-2013-011, 2013).
 62. De Bruyn, K. *et al.* Probing new physics via the $B_s^0 \rightarrow \mu^+ \mu^-$ effective lifetime. *Phys. Rev. Lett.* **109**, 041801 (2012).
 63. Khodjamirian, A., Klein, C., Mannel, T. & Wang, Y.-M. Form factors and strong couplings of heavy baryons from QCD light-cone sum rules. *J. High Energy Phys.* **09**, 106 (2011).
 64. LHCb Collaboration, Aaij R. *et al.* Precision measurement of the ratio of the A_0^0 to \bar{B}^0 lifetimes. *Phys. Lett. B* **734**, 122–130 (2014).
 65. ATLAS and CMS Collaborations. Procedure for the LHC Higgs boson search combination in summer 2011. <http://cds.cern.ch/record/1379837> (ATL-PHYS-PUB-2011-011, CMS NOTE 2011/005, 2011).

CMS Collaboration

V. Khachatryan¹, A.M. Sirunyan¹, A. Tumasyan¹, W. Adam², T. Bergauer², M. Dragicic², J. Ero², M. Friedl², R. Frühwirth^{2,204}, V.M. Ghete², C. Hartl², N. Hörmann², J. Hrubec², M. Jeitler^{2,204}, W. Kiesenhofer², V. Knünz², M. Krammer^{2,204}, I. Krätschmer², D. Liko², I. Mikulec², D. Rabady^{2,205}, B. Rabraner², H. Rohringer², R. Schöfbeck², J. Strauss², W. Treberer-Treberspurg², W. Waltenberger², C.-E. Wulz^{2,204}, V. Mossolov³, N. Shumeiko³, J. Suarez Gonzalez³, S. Alderweireldt⁴, S. Bansal⁴, T. Cornelis⁴, E.A. De Wolf⁴, X. Janssen⁴, A. Knutsson⁴, J. Lauwers⁴, S. Luycckx⁴, S. Ochesanu⁴, R. Rougny⁴, M. Van De Klundert⁴, H. Van Haevermaet⁴, P. Van Mechelen⁴, N. Van Remortel⁴, A. Van Spilbeeck⁴, F. Blekman⁵, S. Blyweert⁵, J. D'Hondt⁵, N. Daci⁵, N. Heracleous⁵, J. Keaveney⁵, S. Lowette⁵, M. Maes⁵, A. Olbrechts⁵, Q. Python⁵, D. Strom⁵, S. Tavernier⁵, W. Van Doninck⁵, P. Van Mulders⁵, G.P. Van Onsem⁵, I. Villella⁵, C. Caillol⁶, B. Clerbaux⁶, G. De Lentdecker⁶, D. Dobur⁶, L. Favart⁶, A.P.R. Gay⁶, A. Grebenyuk⁶, A. Léonard⁶, A. Mohammadi⁶, L. Pernie^{6,205}, A. Randle-conde⁶, T. Reis⁶, T. Seva⁶, L. Thomas⁶, C. Vander Velde⁶, P. Vanlaer⁶, J. Wang⁶, F. Zenoni⁶, V. Adler⁷, K. Beernaert⁷, L. Benucci⁷, A. Cimmino⁷, S. Costantini⁷, S. Crucy⁷, S. Dildick⁷, A. Fagot⁷, G. Garcia⁷, J. Mccartin⁷, A.A. Ocampo Rios⁷, D. Ryckbosch⁷, S. Salva Diben⁷, M. Sigamani⁷, N. Strobbe⁷, F. Thyssen⁷, M. Tytgat⁷, E. Yazgan⁷, N. Zaganidis⁷, S. Basegmez⁷, C. Beluffi^{8,206}, G. Bruno⁸, R. Castello⁸, A. Caudron⁸, L. Ceard⁸, G.G. Da Silva⁸, C. Delaere⁸, T. du Pree⁸, D. Favart⁸, L. Forthomme⁸, A. Giammanco^{8,207}, J. Hollar⁸, A. Jafari⁸, P. Jez⁸, M. Komm⁸, V. Lemaitre⁸, C. Nuttens⁸, D. Pagano⁸, L. Perrini⁸, A. Pin⁸, K. Piotrkowski⁸, A. Popov^{8,208}, L. Quertenmont⁸, M. Selvaggi⁸, M. Vidal Maron⁸, J.M. Vizan Garcia⁸, N. Belyi⁹, T. Caebergs⁹, E. Daubie⁹, G.H. Hamad⁹, W.L. Aldá Júnior⁹, G.A. Alves¹⁰, L. Brito¹⁰, M. Correa Martins Junior¹⁰, T. Dos Reis Martins¹⁰, C. Mora Herrera¹⁰, M.E. Pol¹⁰, P. Rebello Teles¹⁰, W. Carvalho¹¹, J. Chinellato^{11,209}, A. Custódio¹¹, E.M. Da Costa¹¹, D. De Jesus Damiao¹¹, C. De Oliveira Martins¹¹, S. Fonseca De Souza¹¹, H. Malbousson¹¹, D. Matos Figueiredo¹¹, L. Mundim¹¹, H. Nogima¹¹, W.L. Prado Da Silva¹¹, J. Santaolalla¹¹, A. Santoro¹¹, A. Sznajder¹¹, E.J. Tonelli Manganote^{11,209}, A. Vilela Pereira¹¹, C.A. Bernardes¹⁴, S. Dogra¹³, T.R. Fernandez Perez Tomei¹³, E.M. Gregores¹⁴, P.G. Mercadante¹⁴, S.F. Novaes¹³, S. Sandra S. Padula¹³, A. Aleksandrov¹⁵, V. Genchev^{15,205}, R. Hadjiiska¹⁵, P. Iaydjiev¹⁵, A. Marinov¹⁵, S. Piperov¹⁵, M. Rodozov¹⁵, G. Sultanov¹⁵, M. Vutova¹⁵, A. Dimitrov¹⁶, I. Glushkov¹⁶, L. Litov¹⁶, B. Pavlov¹⁶, P. Petkov¹⁶, J.G. Bian¹⁷, G.M. Chen¹⁷, H.S. Chen¹⁷, M. Chen¹⁷, T. Cheng¹⁷, R. Du¹⁷, C.H. Jiang¹⁷, R. Plestina^{17,210}, F. Romeo¹⁷, J. Tao¹⁷, Z. Wang¹⁷, C. Asawatangtrakuldee¹⁸, Y. Ban¹⁸, Q. Li¹⁸, S. Liu¹⁸, Y. Mao¹⁸, S.J. Qian¹⁸, D. Wang¹⁸, Z. Xu¹⁸, W. Zou¹⁸, C. Avila¹⁹, A. Cabrera¹⁹, L.F. Chaparro Sierra¹⁹, C. Florez¹⁹, J.P. Gomez¹⁹, B. Gomez Moreno¹⁹, J.C. Sanabria¹⁹, N. Godinovic²⁰, D. Lelas²⁰, D. Polic²⁰, I. Puljak²⁰, Z. Antunovic²¹, M. Kovac²¹, V. Brigljevic²², K. Kadija²², J. Luetic²², D. Mekterovic²², L. Sudic²², A. Atkitis²³, G. Mavromanolakis²³, J. Mousa²³, C. Nicolaou²³, F. Ptochos²³, P.A. Raziš²³, M. Bodlak²⁴, M. Finger²⁴, M. Finger Jr.^{24,211}, Y. Assran^{25,212}, A. Ellithi Kamel^{25,213}, M.A. Mahmoud^{25,214}, A. Radi^{25,215,216}, M. Kadastik²⁶, M. Murašev²⁶, M. Raidal²⁶, A. Tiko²⁶, P. Eerola²⁷, G. Fed²⁷, M. Voutilainen²⁷, J. Härkönen²⁸, V. Karimäki²⁸, R. Kinnunen²⁸, M.J. Kortelainen²⁸, T. Lampén²⁸, K. Lassila-Perini²⁸, S. Lehti²⁸, T. Lindén²⁸, P. Luukka²⁸, T. Mäenpää²⁸, T. Peltola²⁸, E. Tuominen²⁸, J. Tuominiemi²⁸, E. Tuovinen²⁸, L. Wendland²⁸, J. Talvitie²⁸, T. Tuuva²⁹, M. Besancon³⁰, F. Couderc³⁰, M. DeJardin³⁰, D. Denegri³⁰, B. Fabbro³⁰, J.L. Faure³⁰, C. Favaro³⁰, F. Ferri³⁰, S. Ganjour³⁰, A. Givernaud³⁰, P. Gras³⁰, G. Hamel de Monchenault³⁰, P. Jarry³⁰, E. Locci³⁰, J. Malcles³⁰, J. Rander³⁰, A. Rosowsky³⁰, M. Titov³⁰, S. Baffioni³¹, F. Beaudette³¹, P. Busson³¹, C. Charlot³¹, T. Dahms³¹, M. Dalchenko³¹, L. Dobrzynski³¹, N. Filipovic³¹, A. Florent³¹, R. Granier de Cassagnac³¹, L. Mastrolorenzo³¹, P. Miné³¹, C. Mirouze³¹, I.N. Naranjo³¹, M. Nguyen³¹, C. Ochando³¹, G. Ortona³¹, P. Paganini³¹, S. Regnard³¹, R. Salerno³¹, J.B. Sauvan³¹, Y. Sirois³¹, C. Veelken³¹, Y. Yilmaz³¹, A. Zabi³¹, J.-L. Agram^{32,217}, J. Andrea³², A. Aubin³², D. Bloch³², J.-M. Brom³², E.C. Chabert³², C. Collard³², E. Conte^{32,217}, J.-C. Fontaine^{32,217}, D. Gelé³², U. Goerlach³², C. Goetzmann³², A.-C. Le Bihan³², K. Skovpen³², P. Van Hove³², S. Gadrat³³, S. Beauceron³⁴, N. Beaupere³⁴, G. Boudoul^{34,205}, E. Bouvier³⁴, S. Brochet³⁴, C.A. Carrillo Montoya³⁴, J. Chasserat³⁴, R. Chierici³⁴, D. Contardo³⁴, P. Depasse³⁴, H. El Mamouni³⁴, J. Fan³⁴, J. Fay³⁴, S. Gascon³⁴, M. Gouzevitch³⁴, B. Ille³⁴, T. Kurca³⁴, M. Lethuillier³⁴, L. Mirabito³⁴, S. Perries³⁴, J.D. Ruiz Alvarez³⁴, D. Sabes³⁴, L. Sgandurra³⁴, V. Sordini³⁴, M. Vander Donck³⁴, P. Verdier³⁴, S. Viret³⁴, H. Xiao³⁴, Z. Tsalalaidze^{35,211}, C. Autermann³⁶, S. Beranek³⁶, M. Bontenackels³⁶, M. Edelhoff³⁶, L. Feld³⁶, A. Heister³⁶, O. Hindrichs³⁶, K. Klein³⁶, A. Ostapchuk³⁶, F. Raupach³⁶, J. Sammet³⁶, S. Schael³⁶, J.F. Schulte³⁶, H. Weber³⁶, B. Wittmer³⁶, V. Zhukov³⁶, M. Ata³⁷, M. Brodski³⁷, E. Dietz-Laurson³⁷, D. Duchard³⁷, M. Erdmann³⁷, R. Fischer³⁷, A. Gith³⁷, T. Hebbeker³⁷, C. Heidemann³⁷, K. Hoepfner³⁷, D. Klingebiel³⁷, S. Knutzen³⁷, P. Kreuzer³⁷, M. Merschmeyer³⁷, A. Meyer³⁷, P. Millet³⁷, M. Olschewski³⁷, K. Padeken³⁷, P. Papacz³⁷, H. Reithler³⁷, S.A. Schmitz³⁷, L. Sonnenschein³⁷, D. Teyssier³⁷, S. Thüer³⁷, M. Weber³⁷, V. Cherepanov³⁷, S. Erdogan³⁸, G. Flügge³⁸, H. Geenen³⁸, M. Geisler³⁸, W. Haj Ahmad³⁸, F. Hoehle³⁸, B. Kargoli³⁸, T. Kress³⁸, Y. Kuesel³⁸, A. Künsken³⁸, J. Lingemann³⁸, A. Nowack³⁸, I.M. Nugent³⁸, O. Pooth³⁸, A. Stahl³⁸, M. Aldaya Martin³⁹, I. Asin³⁹, N. Bartosik³⁹, J. Behr³⁹, U. Behrens³⁹, A.J. Bell³⁹, A. Bethan³⁹, K. Borras³⁹, A. Burgmeier³⁹, A. Cakir³⁹, L. Calligaris³⁹, A. Campbell³⁹, S. Choudhury³⁹, F. Costanza³⁹, C. Diez Pardo³⁹, G. Dolinska³⁹, S. Dooling³⁹, T. Dorland³⁹, G. Eckerlin³⁹, D. Eckstein³⁹, T. Eichhorn³⁹, G. Flucke³⁹, J. Garay Garcia³⁹, A. Geiser³⁹, P. Gunnellini³⁹, J. Hauk³⁹, M. Hempel^{39,218}, H. Jung³⁹, A. Kalogeropoulos³⁹, M. Kasemann³⁹, P. Katsas³⁹, J. Kieseler³⁹, C. Kleinwort³⁹, D. Krücker³⁹, W. Lange³⁹, J. Leonard³⁹, K. Lipka³⁹, A. Lobanov³⁹, W. Lohmann^{39,218}, B. Lutz³⁹, R. Mankel³⁹, I. Marfin^{39,218}, I.-A. Melzer-Pellmann³⁹, A.B. Meyer³⁹, G. Mittag³⁹, J. Mnich³⁹, A. Mussgiller³⁹, S. Naumann-Pempe³⁹, A. Nayak³⁹, E. Notarni³⁹, H. Perrey³⁹, D. Pitz³⁹, R. Placakyte³⁹, A. Raspereza³⁹, P.M. Ribeiro Cipriano³⁹, B. Roland³⁹, E. Ron³⁹, M.O. Sahin³⁹, J. Salfeld-Nebgen³⁹, P. Saxena³⁹, T. Schoerner-Sadenius³⁹, M. Schröder³⁹, C. Seitz³⁹, S. Spannagel³⁹, A.D.R. Vargas Trevino³⁹, R. Walsh³⁹, C. Wissing³⁹, V. Blobel⁴⁰, M. Centis Vignali⁴⁰, A.R. Draeger⁴⁰, J. Erle⁴⁰, E. Garutti⁴⁰, K. Goebel⁴⁰, M. Görner⁴⁰, J. Haller⁴⁰, M. Hoffmann⁴⁰, R.S. Höing⁴⁰, A. Junkes⁴⁰, H. Kirschenmann⁴⁰, R. Klanner⁴⁰, R. Kogler⁴⁰, J. Lange⁴⁰, T. Lapsien⁴⁰, T. Lenz⁴⁰, I. Marchesini⁴⁰, J. Ott⁴⁰, T. Peiffer⁴⁰, A. Perianu⁴⁰, N. Pietsch⁴⁰, J. Poehls⁴⁰, T. Poehlsen⁴⁰, D. Rathjens⁴⁰, C. Sander⁴⁰,

H. Schettler⁴⁰, P. Schleper⁴⁰, E. Schlieckau⁴⁰, A. Schmidt⁴⁰, M. Seidel⁴⁰, V. Solo⁴⁰, H. Stadio⁴⁰, G. Steinbrück⁴⁰, D. Troendle⁴⁰, E. Usai⁴⁰, L. Vanelderen⁴⁰, A. Vanhoefer⁴⁰, C. Barth⁴¹, C. Baus⁴¹, J. Berger⁴¹, C. Böser⁴¹, E. Butz⁴¹, T. Chwalek⁴¹, W. De Boer⁴¹, A. Descroix⁴¹, A. Dierlamm⁴¹, M. Feindt⁴¹, F. Frensch⁴¹, M. Giffels⁴¹, A. Gilbert⁴¹, F. Hartmann^{41,205}, T. Hauth⁴¹, U. Husemann⁴¹, I. Katkov^{41,208}, A. Kornmayer^{41,205}, E. Kuznetsova⁴¹, P. Lobelle Pardo⁴¹, M.U. Mozer⁴¹, T. Müller⁴¹, Th. Müller⁴¹, A. Nürnberg⁴¹, G. Quast⁴¹, K. Rabbertz⁴¹, S. Röcker⁴¹, H.J. Simonis⁴¹, F.M. Stobe⁴¹, R. Ulrich⁴¹, J. Wagner-Kuhr⁴¹, S. Wayand⁴¹, T. Weiler⁴¹, R. Wolf⁴¹, G. Anagnostou⁴², G. Daskalakis⁴², T. Geralis⁴², V.A. Giakoumopoulou⁴², A. Kyriakis⁴², D. Loukas⁴², A. Markou⁴², C. Markou⁴², A. Psallidas⁴², I. Topsis-Giotis⁴², A. Agapitos⁴², S. Kesisoglou⁴², A. Panagiotou⁴², N. Saoulidou⁴², E. Stiliaris⁴², X. Aslanoglou⁴⁴, I. Evangelou⁴⁴, G. Flouris⁴⁴, C. Foudas⁴⁴, P. Kokkas⁴⁴, N. Manthos⁴⁴, I. Papadopoulos⁴⁴, E. Paradas⁴⁴, J. Strologas⁴⁴, G. Bencze⁴⁵, C. Hajdu⁴⁵, P. Hidas⁴⁵, D. Horvath^{45,219}, F. Sikler⁴⁵, V. Veszpremi⁴⁵, G. Vesztergombi^{45,220}, A.J. Zsigmond⁴⁵, N. Beni⁴⁶, S. Czellar⁴⁶, J. Karancsi^{46,221}, J. Molnar⁴⁶, J. Palinkas⁴⁶, Z. Szillasi⁴⁶, A. Makovec⁴⁷, P. Raics⁴⁷, Z.L. Trocsanyi⁴⁷, B. Ujvari⁴⁷, N. Sahoo⁴⁸, S.K. Swain⁴⁸, S.B. Beri⁴⁹, V. Bhatnagar⁴⁹, R. Gupta⁴⁹, U. Bhawandeep⁴⁹, A.K. Kalsi⁴⁹, M. Kaur⁴⁹, R. Kumar⁴⁹, M. Mittal⁴⁹, N. Nishu⁴⁹, J.B. Singh⁴⁹, Ashok Kumar⁵⁰, Arun Kumar⁵⁰, S. Ahuja⁵⁰, A. Bhardwaj⁵⁰, B.C. Choudhary⁵⁰, A. Kumar⁵⁰, S. Malhotra⁵⁰, M. Naimuddin⁵⁰, K. Ranjan⁵⁰, V. Sharma⁵⁰, S. Banerjee⁵¹, S. Bhattacharya⁵¹, K. Chatterjee⁵¹, S. Dutta⁵¹, B. Gomber⁵¹, Sa. Jain⁵¹, Sh. Jain⁵¹, R. Khurana⁵¹, A. Modak⁵¹, S. Mukherjee⁵¹, D. Roy⁵¹, S. Sarkar⁵¹, M. Sharan⁵¹, A. Abdulsalam⁵², D. Dutta⁵², S. Kailas⁵², V. Kumar⁵², A.K. Mohanty^{52,205}, L.M. Pant⁵², P. Shukla⁵², A. Topkar⁵², T. Aziz⁵³, S. Banerjee⁵³, S. Bhowmik^{53,222}, R.M. Chatterjee⁵³, R.K. Dewanjee⁵³, S. Dugad⁵³, S. Ganguly^{53,222}, S. Ghosh⁵³, M. Guchait⁵³, A. Gurtu^{53,223}, G. Kole⁵³, S. Kumar⁵³, M. Maity^{53,222}, G. Majumder⁵³, K. Mazumdar⁵³, G.B. Mohanty⁵³, B. Parida⁵³, S.K. Sudhakar⁵³, N. Wickramage^{53,224}, H. Bakhshiansohi⁵⁴, H. Behnamian⁵⁴, S.M. Etesami^{54,225}, A. Fahim^{54,226}, R. Goldouzian⁵⁴, M. Khakzad⁵⁴, M. Mohammadi Najafabadi⁵⁴, M. Naseri⁵⁴, S. Pakhtin Mehdiabadi⁵⁴, F. Rezaei Hosseiniabadi⁵⁴, B. Safarzadeh^{54,227}, M. Zeinali⁵⁴, M. Felcini⁵⁵, M. Grunewald⁵⁵, M. Abbrescia^{57,58}, C. Calabria^{57,58}, S.S. Chhibra^{57,58}, A. Colaleo⁵⁷, D. Creanza⁵⁷, M. De Filippo^{57,59}, M. De Palma^{57,58}, L. Fiore⁵⁷, G. Iaselli^{57,59}, G. Maggi^{57,59}, M. Maggi^{57,59}, S. Nuzzo^{57,58}, A. Pompili^{57,58}, G. Pugliese^{57,59}, R. Radogna^{57,58,205}, G. Selvaggi^{57,58}, A. Sharma⁵⁷, L. Silvestri^{57,205}, R. Venditti^{57,58}, P. Verwilligen⁵⁷, G. Abbiendi⁶¹, A.C. Benvenuti⁶¹, D. Bonacorsi^{61,62}, S. Braibant-Giacomelli^{61,62}, L. Brigliadori^{61,62}, R. Campanini^{61,62}, P. Capiluppi^{61,62}, A. Castro^{61,62}, F.R. Cavallo⁶¹, G. Codispoti^{61,62}, M. Cuffiani^{61,62}, G.M. Dallavalle⁶¹, F. Fabbri⁶¹, A. Fanfani^{61,62}, D. Fasanella^{61,62}, P. Giacomelli⁶¹, C. Grandi⁶¹, L. Guiducci^{61,62}, S. Marcellini⁶¹, G. Masetti⁶¹, A. Montanari⁶¹, F.L. Navarria^{61,62}, A. Perrotta⁶¹, F. Primavera^{61,62}, A.M. Rossi^{61,62}, T. Rovelli^{61,62}, G.P. Siroli^{61,62}, N. Tosi^{61,62}, R. Travaglini^{61,62}, S. Albergo^{64,65}, G. Cappello⁶⁴, M. Chiorboli^{64,65}, S. Costa^{64,65}, F. Giordano^{64,205}, R. Potenza^{64,65}, A. Tricomi^{64,65}, C. Tuve^{64,65}, G. Barbagli⁶⁸, V. Ciulli^{68,69}, C. Ciminini⁶⁸, R. D'Alessandro^{68,69}, E. Focardi^{68,69}, E. Gallo⁶⁸, S. Gozzi^{68,69}, V. Gori^{68,69}, P. Lenzi^{68,69}, M. Meschini⁶⁸, S. Paoletti⁶⁸, G. Sguazzaroni⁶⁸, A. Troiano^{68,69}, L. Benussi⁷⁰, S. Bianco⁷⁰, F. Fabbri⁷⁰, D. Piccolo⁷⁰, R. Ferretti^{72,73}, F. Ferro⁷², M. Lo Vetere^{72,73}, E. Robutti⁷², S. Tosi^{72,73}, M.E. Dinardo^{75,76}, S. Fiorendi^{75,76}, S. Genna^{75,205}, R. Gerosa^{75,205}, A. Ghezzi^{75,76}, P. Govoni^{75,76}, M.T. Lucchini^{75,76,205}, S. Malvezzi⁷⁵, R.A. Manzoni^{75,76}, A. Martelli^{75,76}, B. Marzocchi^{75,76,205}, D. Menasce⁷⁵, L. Moroni⁷⁵, M. Paganoni^{75,76}, D. Pedrini⁷⁵, S. Ragazzi^{75,76}, N. Redaelli⁷⁵, T. Tabarelli di Fatis^{75,76}, S. Buontempo⁷⁸, N. Cavallo^{78,80}, S. Di Guida^{78,81,205}, F. Fabozzi^{78,80}, A.O.M. Iorio⁷⁸, L. Lista⁷⁸, S. Meola^{78,81,205}, M. Merola⁷⁸, P. Paolucci^{78,205}, P. Azzi⁸³, N. Bacchetta⁸³, D. Bisello^{83,84}, A. Branca^{83,84}, R. Carli^{83,84}, P. Checchia⁸³, M. Dall'Oso^{83,84}, T. Dorigo⁸³, U. Dosselli⁸³, M. Galanti^{83,84}, F. Gasparini^{83,84}, U. Gasparini^{83,84}, P. Giubilato^{83,84}, A. Gozzelino⁸³, K. Kanishch^{83,85}, S. Lacaprarà⁸³, M. Margoni^{83,84}, A.T. Meneguzzo^{83,84}, J. Pazzini^{83,84}, N. Pozzobon^{83,84}, P. Ronchese^{83,84}, F. Simonetto^{83,84}, E. Torassa⁸³, M. Tosi^{83,84}, P. Zotto^{83,84}, A. Zucchetta^{83,84}, G. Zumerle^{83,84}, M. Gabusi^{87,88}, S.P. Ratti⁸⁷, V. Re⁸⁷, C. Riccardi^{87,88}, P. Salvini⁸⁷, P. Vitulo^{87,88}, M. Biasini^{90,91}, G.M. Bilei⁹⁰, D. Ciangottini^{90,91,205}, L. Fano^{90,91}, P. Laricci^{90,91}, G. Mantovani^{90,91}, M. Menichelli⁹⁰, A. Saha⁹⁰, A. Santocchia^{90,91}, A. Spiezia^{90,91,205}, K. Androsova^{93,228}, P. Azzurri⁹³, G. Bagliesi⁹³, J. Bernardini⁹³, T. Boccali⁹³, G. Broccolo^{93,95}, R. Castaldi⁹³, M.A. Ciocci^{93,228}, R. Dell'Orso⁹³, S. Donato^{93,95,205}, F. Fiori^{93,95}, L. Foà^{93,95}, A. Giassi⁹³, M.T. Grippo^{93,228}, F. Ligabue^{93,95}, T. Lomtadze⁹³, L. Martin⁹³, A. Messineo⁹³, C.S. Moon⁹³, R. F. F. Palla^{93,229}, A. Rizzi^{93,94}, A. Savoy-Navarro^{93,230}, A.T. Serban⁹³, P. Spagnolo⁹³, P. Squillacioti⁹³, R. Tenchini⁹³, G. Tonelli^{93,94}, A. Venturi⁹³, P.G. Verdini⁹³, C. Vernieri^{93,95}, L. Barone^{97,98}, F. Cavallari⁹⁷, G. D'imperio⁹⁷, D. Del Re⁹⁷, M. Diemoz⁹⁷, C. Jorda⁹⁷, E. Longo^{97,98}, F. Margaroli^{97,98}, P. Meridiani⁹⁷, F. Micheli^{97,98,205}, S. Nourbakhsh^{97,98}, G. Organtini^{97,98}, R. Paramatti⁹⁷, S. Rahatlou^{97,98}, C. Rovelli⁹⁷, F. Santanastasio^{97,98}, L. Soffi^{97,98}, P. Traczyk^{97,98,205}, N. Amapane^{100,101}, R. Arcidiacono^{100,102}, S. Argiro^{100,101}, M. Arneodo^{100,102}, R. Bellan^{100,101}, C. Biino¹⁰⁰, N. Cartiglia¹⁰⁰, S. Casasso^{100,101,205}, M. Costa^{100,101}, A. Degano^{100,101}, N. Demaria¹⁰⁰, L. Finco^{100,101,205}, C. Mariotti¹⁰⁰, S. Maselli¹⁰⁰, E. Migliore^{100,101}, V. Monaco^{100,101}, M. Musich¹⁰⁰, M.M. Oberino^{100,102}, L. Pacher^{100,101}, N. Pastrone¹⁰⁰, M. Pelliccioni¹⁰⁰, G.L. Pinna Angioni^{100,101}, A. Potenza^{100,101}, A. Romero^{100,101}, M. Ruspai^{100,102}, R. Sacchi^{100,101}, A. Solano^{100,101}, A. Staiano¹⁰⁰, U. Tamponi¹⁰⁰, S. Belforte¹⁰⁴, V. Candeliere^{104,105,205}, M. Casarsa¹⁰⁴, F. Cossutti¹⁰⁴, G. Della Ricca^{104,105}, B. Gobbo¹⁰⁴, C. La Licata^{104,105}, M. Marone^{104,105}, A. Schizzi^{104,105}, T. Umer^{104,105}, A. Zanetti¹⁰⁴, S. Chang¹⁰⁶, A. Kropivnitskaya¹⁰⁶, S.K. Nam¹⁰⁶, D.H. Kim¹⁰⁷, G.N. Kim¹⁰⁷, M.S. Kim¹⁰⁷, D.Y. Kim¹⁰⁷, S. Lee¹⁰⁷, Y.D. Oh¹⁰⁷, H. Park¹⁰⁷, A. Sakharov¹⁰⁷, D.C. Son¹⁰⁷, T.J. Kim¹⁰⁸, J.J. Kim¹⁰⁹, S. Song¹⁰⁹, S. Choi¹¹⁰, D. Gyun¹¹⁰, B. Hong¹¹⁰, M. Jo¹¹⁰, H. Kim¹¹⁰, Y. Kim¹¹⁰, B. Lee¹¹⁰, K.S. Lee¹¹⁰, S.K. Park¹¹⁰, Y. Roh¹¹⁰, H.D. Yoo¹¹¹, M. Choi¹¹², J.H. Kim¹¹², I.C. Park¹¹², G. Ryu¹¹², M.S.

H. Bialkowska¹²³, M. Bluj¹²³, B. Boimska¹²³, T. Frueboes¹²³, M. Górski¹²³, M. Kazana¹²³, K. Nawrocki¹²³, K. Romanowska-Rybinska¹²³, M. Szeleper¹²³, P. Zalewski¹²³, G. Brona¹²⁴, K. Bunkowski¹²⁴, M. Cwiok¹²⁴, W. Dominik¹²⁴, K. Doroba¹²⁴, A. Kalinowski¹²⁴, M. Konecki¹²⁴, J. Krolkowski¹²⁴, M. Misiura¹²⁴, M. Olszewski¹²⁴, W. Wolszczak¹²⁴, P. Bargassa¹²⁵, C. Beirão Da Cruz E Silva¹²⁵, P. Faccioli¹²⁵, P.G. Ferreira Parrachó¹²⁵, M. Gallinaro¹²⁵, L. Lloret Iglesias¹²⁵, F. Nguyen¹²⁵, J. Rodrigues Antunes¹²⁵, J. Seixas¹²⁵, J. Varela¹²⁵, P. Vischia¹²⁵, S. Afanasiev¹²⁶, P. Bunin¹²⁶, M. Gavrilenko¹²⁶, I. Golutvin¹²⁶, I. Gorbunov¹²⁶, A. Kamenev¹²⁶, V. Karjavin¹²⁶, V. Konoplyanikov¹²⁶, A. Lanev¹²⁶, A. Malakhov¹²⁶, V. Matveev^{126,232}, P. Moiseev¹²⁶, V. Palchik¹²⁶, V. Perelygin¹²⁶, S. Shmatov¹²⁶, N. Skatchkov¹²⁶, V. Smirnov¹²⁶, A. Zarubin¹²⁶, V. Golovtsov¹²⁷, Y. Ivanov¹²⁷, V. Kim^{127,233}, P. Levchenko¹²⁷, V. Murzin¹²⁷, V. Oreshkin¹²⁷, I. Smirnov¹²⁷, V. Sulimov¹²⁷, L. Uvarov¹²⁷, S. Vavilov¹²⁷, A. Vorobyev¹²⁷, An. Vorobyev¹²⁷, Yu. Andreev¹²⁸, A. Dermenev¹²⁸, S. Gninenko¹²⁸, N. Golubev¹²⁸, M. Kirsanov¹²⁸, N. Krasnikov¹²⁸, A. Pashchenko¹²⁸, D. Tlisov¹²⁸, A. Toropin¹²⁸, V. Epshteyn¹²⁹, V. Gavrilov¹²⁹, N. Lychkovskaya¹²⁹, V. Popov¹²⁹, I. Pozdnyakov¹²⁹, G. Safronov¹²⁹, S. Semenov¹²⁹, A. Spiridonov¹²⁹, V. Stolin¹²⁹, E. Vlasov¹²⁹, A. Zhokin¹²⁹, V. Andreev¹³⁰, M. Azarkin¹³⁰, I. Dremin¹³⁰, M. Kirakosyan¹³⁰, A. Leonidov¹³⁰, G. Mesyats¹³⁰, S.V. Rusakov¹³⁰, A. Vinogradov¹³⁰, A. Belyaev¹³¹, E. Boos¹³¹, M. Dubinin^{131,234}, L. Dudko¹³¹, A. Ershov¹³¹, A. Griubshin¹³¹, V. Klyukhin¹³¹, O. Kodolova¹³¹, I. Lokhtin¹³¹, S. Obraztsov¹³¹, S. Petrushanko¹³¹, V. Savrin¹³¹, A. Snigirev¹³¹, I. Azhgirev¹³², I. Bayshev¹³², S. Bitoukov¹³², V. Kachanov¹³², A. Kalinin¹³², D. Konstantinov¹³², V. Krychkin¹³², V. Petrov¹³², R. Rytin¹³², A. Sobol¹³², L. Tourchanovitch¹³², S. Troshin¹³², N. Tyurin¹³², A. Uzunian¹³², A. Volkov¹³², P. Adzic^{133,235}, M. Ekmedzic¹³³, J. Milosevic¹³³, V. Rekovic¹³³, J. Alcaraz Maestre¹³⁴, C. Battilana¹³⁴, E. Calvo¹³⁴, M. Cerrada¹³⁴, M. Chamizo Llatas¹³⁴, N. Colino¹³⁴, B. De La Cruz¹³⁴, A. Delgado Peris¹³⁴, D. Domínguez Vázquez¹³⁴, A. Escalante Del Valle¹³⁴, C. Fernandez Bedoya¹³⁴, J.P. Fernández Ramos¹³⁴, J. Flix¹³⁴, M.C. Fouz¹³⁴, P. Garcia-Abia¹³⁴, O. Gonzalez Lopez¹³⁴, S. Goy Lopez¹³⁴, J.M. Hernandez¹³⁴, M.L. Josa¹³⁴, E. Navarro De Martino¹³⁴, A. Pérez-Calero Yzquierdo¹³⁴, J. Puerta Pelayo¹³⁴, A. Quintario Olmeda¹³⁴, I. Redondo¹³⁴, L. Romero¹³⁴, M.S. Soares¹³⁴, C. Albajar¹³⁵, J.F. de Trocóniz¹³⁵, M. Missiroli¹³⁵, D. Moran¹³⁵, H. Brun¹³⁵, J.A. Cuevas¹³⁵, J. Fernandez Menendez¹³⁵, S. Folgueras¹³⁵, I. Gonzalez Caballero¹³⁵, J.A. Brochero Cifuentes¹³⁷, I.J. Cabrillo¹³⁷, A. Calderon¹³⁷, J. Duarte Campderros¹³⁷, M. Fernandez¹³⁷, G. Gomez¹³⁷, A. Graziano¹³⁷, A. Lopez Virto¹³⁷, J. Marco¹³⁷, R. Marco¹³⁷, C. Martinez Rivero¹³⁷, F. Mattozza¹³⁷, F.J. Munoz Sanchez¹³⁷, J. Piedra Gomez¹³⁷, T. Rodrigo¹³⁷, A.Y. Rodríguez-Marrero¹³⁷, A. Ruiz-Jimeno¹³⁷, L. Scodellaro¹³⁷, I. Vila¹³⁷, R. Vilar Cortabitarte¹³⁷, D. Abbaneo¹³⁸, E. Auffray¹³⁸, G. Auzinger¹³⁸, M. Bachtis¹³⁸, P. Baillon¹³⁸, A.H. Ball¹³⁸, D. Barney¹³⁸, A. Benaglia¹³⁸, J. Bendavid¹³⁸, L. Benhabib¹³⁸, J.F. Benitez¹³⁸, C. Berner^{138,210}, P. Bloch¹³⁸, A. Bocchi¹³⁸, A. Bonato¹³⁸, O. Bondu¹³⁸, C. Botta¹³⁸, H. Breuker¹³⁸, T. Camporesi¹³⁸, G. Cerminara¹³⁸, S. Colafranceschi^{138,236}, M. D'Alfonso¹³⁸, D. d'Enterria¹³⁸, A. Dabrowski¹³⁸, A. David¹³⁸, F. De Guio¹³⁸, A. De Roeck¹³⁸, S. De Visser¹³⁸, E. Di Marco¹³⁸, M. Dobson¹³⁸, M. Dordevic¹³⁸, N. Dupont-Sagorin¹³⁸, A. Elliott-Peisert¹³⁸, G. Franzoni¹³⁸, W. Funk¹³⁸, D. Gig¹³⁸, K. Gill¹³⁸, D. Giordano¹³⁸, M. Girone¹³⁸, F. Glege¹³⁸, R. Guida¹³⁸, S. Gundacker¹³⁸, M. Guthoff¹³⁸, J. Hammer¹³⁸, M. Hansen¹³⁸, P. Harris¹³⁸, J. Hegeman¹³⁸, V. Innocente¹³⁸, P. Janot¹³⁸, K. Kousouris¹³⁸, K. Krajcarz¹³⁸, P. Lecoq¹³⁸, C. Lourenco¹³⁸, N. Magin¹³⁸, L. Malgeri¹³⁸, M. Mannelli¹³⁸, J. Marrouche¹³⁸, L. Masetti¹³⁸, F. Meijers¹³⁸, S. Mersi¹³⁸, E. Meschi¹³⁸, F. Moortgat¹³⁸, S. Morovic¹³⁸, M. Mulders¹³⁸, L. Orsini¹³⁸, L. Pape¹³⁸, E. Perez¹³⁸, L. Perrozzi¹³⁸, A. Petrilli¹³⁸, G. Petrucciari¹³⁸, A. Pfeiffer¹³⁸, M. Pimià¹³⁸, D. Piparo¹³⁸, M. Plagge¹³⁸, A. Racz¹³⁸, G. Rolandi^{138,237}, M. Rovere¹³⁸, H. Sakulin¹³⁸, C. Schäfer¹³⁸, C. Schwick¹³⁸, A. Sharma¹³⁸, P. Siegart¹³⁸, P. Silva¹³⁸, M. Simon¹³⁸, P. Spiccas^{138,238}, D. Spiga¹³⁸, J. Steggemann¹³⁸, B. Stieger¹³⁸, M. Stoye¹³⁸, Y. Takahashi¹³⁸, D. Treille¹³⁸, A. Tsiros¹³⁸, G.L. Veres^{138,220}, N. Wardle¹³⁸, H.K. Wöhri¹³⁸, H. Wolny¹³⁸, W.D. Zeuner¹³⁸, W. Bertl¹³⁹, K. Deiters¹³⁹, W. Erdmann¹³⁹, R. Horisberger¹³⁹, Q. Ingram¹³⁹, H.C. Kaestli¹³⁹, D. Kotlinski¹³⁹, D. Renker¹³⁹, T. Rohe¹³⁹, F. Bachmair¹⁴⁰, L. Bäni¹⁴⁰, L. Bianchini¹⁴⁰, M.A. Buchmann¹⁴⁰, B. Casal¹⁴⁰, N. Chanon¹⁴⁰, G. Dissertori¹⁴⁰, M. Dittmar¹⁴⁰, M. Donega¹⁴⁰, M. Dünser¹⁴⁰, P. Eller¹⁴⁰, C. Grab¹⁴⁰, D. Hits¹⁴⁰, J. Hoss¹⁴⁰, W. Lustermann¹⁴⁰, B. Mangano¹⁴⁰, A.C. Marinin¹⁴⁰, M. Marionneau¹⁴⁰, P. Martinez Ruiz del Arbol¹⁴⁰, M. Masciovecchio¹⁴⁰, D. Meister¹⁴⁰, N. Mohr¹⁴⁰, P. Musella¹⁴⁰, C. Nageli¹⁴⁰, F. Nessi-Tedaldi¹⁴⁰, F. Pandolfi¹⁴⁰, F. Pauss¹⁴⁰, M. Peruzzi¹⁴⁰, M. Quittnat¹⁴⁰, L. Rebane¹⁴⁰, M. Rossini¹⁴⁰, A. Starodumov^{140,240}, M. Takahashi¹⁴⁰, K. Theofilatos¹⁴⁰, R. Wallny¹⁴⁰, H.A. Weber¹⁴⁰, C. AMSLER^{141,241}, M.F. Canelli¹⁴¹, V. Chiochia¹⁴¹, A. De Cosa¹⁴¹, A. Hinzmann¹⁴¹, T. Hreus¹⁴¹, B. Kilminster¹⁴¹, C. Lange¹⁴¹, B. Millan Mejias¹⁴¹, J. Ngadiubi¹⁴¹, D. Pinna¹⁴¹, P. Robmann¹⁴¹, F.J. Ronga¹⁴¹, S. Taroni¹⁴¹, M. Verzetti¹⁴¹, Y. Yang¹⁴¹, M. Cardaci¹⁴², K.H. Chen¹⁴², C. Ferro¹⁴², C.M. Kuo¹⁴², W. Lin¹⁴², Y. Liu¹⁴², R. Volpe¹⁴², S.S. Yu¹⁴², P. Chang¹⁴³, Y.H. Chang¹⁴³, Y.W. Chang¹⁴³, Y. Chao¹⁴³, K.F. Chen¹⁴³, P.H. Chen¹⁴³, C. Dietz¹⁴³, U. Grondler¹⁴³, W.-S. Hou¹⁴³, K.Y. Kao¹⁴³, Y.F. Liu¹⁴³, R.-S. Lu¹⁴³, D. Majumder¹⁴³, E. Petrakou¹⁴³, Y.M. Tzeng¹⁴³, R. Wilken¹⁴³, B. Asavapibhop¹⁴⁴, G. Singh¹⁴⁴, N. Srimanobhas¹⁴⁴, N. Suwonjanadee¹⁴⁴, A. Adiguzel¹⁴⁵, M.N. Bakirci^{145,242}, S. Cerci^{145,243}, C. Dozen¹⁴⁵, I. Dumanoglu¹⁴⁵, E. Eskut¹⁴⁵, S. Girgis¹⁴⁵, G. Gokbulut¹⁴⁵, E. Gurpinar¹⁴⁵, I. Hos¹⁴⁵, E.E. Kangal¹⁴⁵, A. Kayis Topaksu¹⁴⁵, G. Onengut^{145,244}, K. Ozdemir¹⁴⁵, S. Ozturk^{145,242}, A. Polatovic¹⁴⁵, D. Sunar Cerci^{145,243}, B. Tali^{145,243}, H. Topakli^{145,242}, M. Vergili¹⁴⁵, I.V. Akin¹⁴⁶, B. Bilin¹⁴⁶, S. Bilmis¹⁴⁶, H. Gamsizkan^{146,245}, B. Isildak¹⁴⁶, G. Karapinar^{146,247}, K. Ocalan^{146,248}, S. Sekmen¹⁴⁶, U.E. Surar¹⁴⁶, M. Yalvac¹⁴⁶, M. Zeyrek¹⁴⁶, E.A. Albayrak^{147,249}, E. Gülmez¹⁴⁷, M. Kaya^{147,250}, O. Kaya^{147,251}, T. Yetkin^{147,252}, K. Cankocak¹⁴⁸, F.I. Vardarli¹⁴⁸, L. Levchenko¹⁴⁹, P. Sorokin¹⁴⁹, J.J. Brooke¹⁵⁰, E. Clement¹⁵⁰, D. Cussans¹⁵⁰, H. Flache¹⁵⁰, J. Goldstein¹⁵⁰, M. Grimes¹⁵⁰, G.P. Heath¹⁵⁰, H.F. Heath¹⁵⁰, J. Jacob¹⁵⁰, L. Kreczko¹⁵⁰, C. Lucas¹⁵⁰, Z. Meng¹⁵⁰, D.M. Newbold^{150,253}, S. Parmar¹⁵⁰, A. Poll¹⁵⁰, T. Sakuma¹⁵⁰, S. Senkin¹⁵⁰, V.J. Smith¹⁵⁰, K.W. Bell¹⁵¹, A. Belyaev^{151,254}, C. Brew¹⁵¹, R.M. Brown¹⁵¹, D.J.A. Cockerill¹⁵¹, J.A. Coughlan¹⁵¹, K. Harder¹⁵¹, S. Harper¹⁵¹, E. Olaiya¹⁵¹, D. Petyt¹⁵¹, C.H. Shepherd-Themistocleous¹⁵¹, A. Thea¹⁵¹, I.R. Tomalin¹⁵¹, T. Williams¹⁵¹, W.J. Womersley¹⁵¹, S.D. Worm¹⁵¹, M.I. Baber¹⁵², R. Bainbridge¹⁵², O. Buchmüller¹⁵², D. Burton¹⁵², D. Colling¹⁵², N. Cripps¹⁵², P. Dauncey¹⁵², G. Davies¹⁵², M. Della Negra¹⁵², P. Dunne¹⁵², W. Ferguson¹⁵², J. Fulcher¹⁵², D. Futyan¹⁵², G. Hall¹⁵², G. Iles¹⁵², M. Jarvis¹⁵², G. Karapostoli¹⁵², M. Kenzie¹⁵², R. Lane¹⁵², R. Lucas^{152,253}, L. Lyons¹⁵², A.-M. Magnan¹⁵², S. Malik¹⁵², B. Mathias¹⁵², J. Nash¹⁵², A. Nikitenko^{152,240}, J. Pela¹⁵², M. Pesaresi¹⁵², K. Petridis¹⁵², D.M. Raymond¹⁵², S. Rogerson¹⁵², A. Rose¹⁵², C. Seez¹⁵², P. Sharp¹⁵², A. Tapper¹⁵², M. Vazquez Acosta¹⁵², T. Virdee¹⁵², S.C. Zenz¹⁵², J.E. Cole¹⁵³, P.R. Hobson¹⁵³, A. Khan¹⁵³, P. Kyberd¹⁵³, D. Leggat¹⁵³, D. Leslie¹⁵³, I.D. Reid¹⁵³, P. Symonds¹⁵³, L. Teodorescu¹⁵³, M. Turner¹⁵³, J. Dittmann¹⁵⁴, K. Hatakeyama¹⁵⁴, A. Kasmi¹⁵⁴, H. Liu¹⁵⁴, T. Scarborough¹⁵⁴, O. Charaf¹⁵⁵, S.I. Cooper¹⁵⁵, C. Henderson¹⁵⁵, P. Rumerio¹⁵⁵, A. Avetisyan¹⁵⁶, T. Bose¹⁵⁶, C. Fantasia¹⁵⁶, P. Lawson¹⁵⁶, C. Richardson¹⁵⁶, J. Rohlf¹⁵⁶, J. St. John¹⁵⁶, L. Sulak¹⁵⁶, J. Alimena¹⁵⁷, E. Berry¹⁵⁷, S. Bhattacharya¹⁵⁷, G. Christopher¹⁵⁷, D. Cutts¹⁵⁷, Z. Demiragli¹⁵⁷, N. Dhir¹⁵⁷, A. Ferapontov¹⁵⁷, A. Garabedian¹⁵⁷, U. Heintz¹⁵⁷, G. Kukartsev¹⁵⁷, E. Laird¹⁵⁷, G. Landsberg¹⁵⁷, M. Luk¹⁵⁷, M. Narain¹⁵⁷, M. Segala¹⁵⁷, T. Sinthuprasith¹⁵⁷, S. Speer¹⁵⁷, J. Swanson¹⁵⁷, R. Breedon¹⁵⁸, G. Breto¹⁵⁸, M. Calderon De La Barca Sanchez¹⁵⁸, S. Chauhan¹⁵⁸, M. Chertok¹⁵⁸, J. Conway¹⁵⁸, R. Conway¹⁵⁸, P.T. Cox¹⁵⁸, R. Erbacher¹⁵⁸, M. Gardner¹⁵⁸, W. Ko¹⁵⁸, R. Lander¹⁵⁸, M. Mulharen¹⁵⁸, D. Pellett¹⁵⁸, J. Pilot¹⁵⁸, F. Ricci-Tam¹⁵⁸, S. Shalhout¹⁵⁸, J. Smith¹⁵⁸, M. Squires¹⁵⁸, D. Stolp¹⁵⁸, M. Tripathi¹⁵⁸, S. Wilbur¹⁵⁸, R. Yohay¹⁵⁸, R. Cousins¹⁵⁹, P. Everaerts¹⁵⁹, C. Farrell¹⁵⁹, J. Haupt¹⁵⁹, M. Ignatenko¹⁵⁹, G. Raknes¹⁵⁹, E. Takasigi¹⁵⁹, V. Valuev¹⁵⁹, M. Weber¹⁵⁹, K. Burk¹⁶⁰, R. Clare¹⁶⁰, J. Ellison¹⁶⁰, J.W. Gary¹⁶⁰, G. Hanson¹⁶⁰, J. Heilmann¹⁶⁰, M. Iovanna¹⁶⁰, P. Jandir¹⁶⁰, E. Kennedy¹⁶⁰, F. Lacroix¹⁶⁰, O.R. Long¹⁶⁰, A. Luthra¹⁶⁰, M. Malberti¹⁶⁰, M. Olmedo Negrete¹⁶⁰, A. Shrinivas¹⁶⁰, S. Sumowidagat¹⁶⁰, S. Wimpenny¹⁶⁰, J.G. Branson¹⁶¹, G.B. Cerati¹⁶¹, S. Cittolin¹⁶¹, R.T. D'Agnoletto¹⁶¹, A. Holzner¹⁶¹, R. Kelley¹⁶¹, D. Klein¹⁶¹, D. Kovalsky¹⁶¹, J. Letts¹⁶¹, I. Macneil¹⁶¹, D. Olivito¹⁶¹, S. Padhi¹⁶¹, C. Palmer¹⁶¹, M. Pieri¹⁶¹, M. Sani¹⁶¹, V. Sharma¹⁶¹, S. Simon¹⁶¹, Y. Tu¹⁶¹, A. Vartak¹⁶¹, C. Welke¹⁶¹, F. Würthwein¹⁶¹, A. Yagci¹⁶¹, D. Barge¹⁶², J. Bradmiller-Feld¹⁶², C. Campagnari¹⁶², T. Danielson¹⁶², A. Dishaw¹⁶², V. Dutta¹⁶², K. Flowers¹⁶², M. Franco Sevilla¹⁶², P. Geffert¹⁶², C. George¹⁶², F. Golf¹⁶², L. Gouskos¹⁶², J. Incandella¹⁶², C. Justus¹⁶², N. Mccoll¹⁶², J. Richman¹⁶², D. Stuart¹⁶², W. To¹⁶², C. West¹⁶², J. Yoo¹⁶², A. Apresyan¹⁶³, A. Bornheim¹⁶³, J. Bunn¹⁶³, Y. Chen¹⁶³, J. Duarte¹⁶³, A. Mott¹⁶³, H.B. Newman¹⁶³, C. Pena¹⁶³, M. Pierini¹⁶³, M. Spiropulu¹⁶³, J.R. Vlimant¹⁶³, R. Wilkinson¹⁶³, S. Xie¹⁶³, R.Y. Zhu¹⁶³, V. Zolotarev¹⁶³, A. Calamba¹⁶⁴, M. Carlson¹⁶⁴, T. Ferguson¹⁶⁴, Y. Iiyama¹⁶⁴, M. Paulini¹⁶⁴, J. Russ¹⁶⁴, H. Vogel¹⁶⁴, I. Vorobiev¹⁶⁴, J.P. Cumalat¹⁶⁵, W.T. Ford¹⁶⁵, A. Gaz¹⁶⁵, M. Krohn¹⁶⁵, E. Luiggi Lopez¹⁶⁵, U. Nauen¹⁶⁵, J.G. Smith¹⁶⁵, K. Stenson¹⁶⁵, S.R. Wagner¹⁶⁵, J. Alexander¹⁶⁶, A. Chatterjee¹⁶⁶, J. Chaves¹⁶⁶, J. Chu¹⁶⁶, S. Dittmer¹⁶⁶, N. Eggert¹⁶⁶, N. Mirman¹⁶⁶, G. Nicolas Kaufman¹⁶⁶, J.R. Patterson¹⁶⁶, A. Ryd¹⁶⁶, E. Salvati¹⁶⁶, L. Skinnari¹⁶⁶, W. Sun¹⁶⁶, W.D. Teo¹⁶⁶, J. Thom¹⁶⁶, J. Thompson¹⁶⁶, J. Tucker¹⁶⁶, Y. Weng¹⁶⁶, L. Winstrom¹⁶⁶, P. Wittich¹⁶⁶, D. Winn¹⁶⁶, S. Abdullin¹⁶⁶, M. Albrow¹⁶⁶, J. Anderson¹⁶⁶, G. Apollinari¹⁶⁶, L.A.T. Bauerick¹⁶⁶, A. Beres¹⁶⁶, J. Berryhill¹⁶⁶, P.C. Bhat¹⁶⁶, G. Bolla¹⁶⁶, K. Burkett¹⁶⁶, J.N. Butler¹⁶⁶, H.W. Chung¹⁶⁶, F. Chlebana¹⁶⁶, S. Cihangir¹⁶⁶, V.D. Elvira¹⁶⁶, I. Fisk¹⁶⁶, J. Freeman¹⁶⁶, Y. Gao¹⁶⁶, E. Gottschalk¹⁶⁶, L. Gray¹⁶⁶, D. Green¹⁶⁶, S. Grünendahl¹⁶⁶, O. Gutsche¹⁶⁶, J. Hanlon¹⁶⁶, D. Hare¹⁶⁶, R.M. Harris¹⁶⁶, J. Hirschauer¹⁶⁶, B. Hooperman¹⁶⁶, S. Jindariani¹⁶⁶, M. Johnson¹⁶⁶, U. Joshi¹⁶⁶, K. Kaadze¹⁶⁶, B. Klima¹⁶⁶, B. Kreis¹⁶⁶, S. Kwan¹⁶⁶, J. Linac¹⁶⁶, D. Lincoln¹⁶⁶, R. Lipton¹⁶⁶, T. Liu¹⁶⁶, J. Lykken¹⁶⁶, K. Maeshima¹⁶⁶, J.M. Marraffino¹⁶⁶, V.I. Martinez Outschoorn¹⁶⁶, S. Maruyama¹⁶⁶, D. Mason¹⁶⁶, P. McBride¹⁶⁶, P. Merkel¹⁶⁶, K. Mishra¹⁶⁶, S. Mrenna¹⁶⁶, S. Nahn¹⁶⁶, C. Newman-Holmes¹⁶⁶, V. O'Dell¹⁶⁶, O. Prokofyev¹⁶⁶, E. Sexton-Kennedy¹⁶⁶, S. Sharma¹⁶⁶, A. Saha¹⁶⁶, H.W. S. Spalding¹⁶⁶, L. Spiegel¹⁶⁶, L. Taylor¹⁶⁶, S. Tkaczyk¹⁶⁶, N.V. Tran¹⁶⁶, L. Uplegger¹⁶⁶, E.W. Vaandering¹⁶⁶, R. Vidal¹⁶⁶, A. Whitbeck¹⁶⁶, J. Whitmore¹⁶⁶, F. Yang¹⁶⁶, D. Acosta¹⁶⁹, P. Avery¹⁶⁹, P. Bortignon¹⁶⁹, D. Bourlikov¹⁶⁹, M. Carver¹⁶⁹, D. Curry¹⁶⁹, S. Das¹⁶⁹, M. De Gruttola¹⁶⁹, G.P. Di Giovanni¹⁶⁹, R.D. Field¹⁶⁹, M. Fisher¹⁶⁹, I.K. Furrer¹⁶⁹, J. Hugon¹⁶⁹, J. Konigsberg¹⁶⁹, A. Korytov¹⁶⁹, T. Kyreos¹⁶⁹, J.F. Low¹⁶⁹, K. Matchev¹⁶⁹, H. Mei¹⁶⁹, P. Milenovic^{169,255}, G. Mitselmakher¹⁶⁹, L. Muniz¹⁶⁹, A. Rinkevicius¹⁶⁹, L. Shchutska¹⁶⁹, M. Snowball¹⁶⁹, D. Sperka¹⁶⁹, J. Yelton¹⁶⁹, M. Zakaria¹⁶⁹, S. Hewamanage¹⁷⁰, S. Linn¹⁷⁰, P. Markowitz¹⁷⁰, G. Martinez¹⁷⁰, J.L. Rodriguez¹⁷⁰, T. Adams¹⁷¹, A. Askew¹⁷¹, J. Bochenek¹⁷¹, B. Diamond¹⁷¹, J. Haas¹⁷¹, S. Hagopian¹⁷¹, V. Hagopian¹⁷¹, K.F. Johnson¹⁷¹, H. Prosper¹⁷¹, V. Veeraraghavan¹⁷¹, M. Weinberg¹⁷¹, M.M. Baarmand¹⁷², M. Hohmann¹⁷², H. Kalakhety¹⁷², F. Yumiceva¹⁷², M.R. Adams¹⁷³, L. Apanasovich¹⁷³, D. Berry¹⁷³, R.R. Betts¹⁷³, I. Bucinskaite¹⁷³, R. Cavanaugh¹⁷³, O. Evdokimov¹⁷³, L. Gauthier¹⁷³, C.E. Gerber¹⁷³, D.J. Hofman¹⁷³, P. Kurt¹⁷³, D.H. Moon¹⁷³, C. O'Brien¹⁷³, I.D. Sandova Gonzalez¹⁷³, C. Silkworth¹⁷³, P. Turner¹⁷³, N. Varelas¹⁷³, B. Bilk^{174,256}, W. Clarida¹⁷⁴, K. Dilsiz¹⁷⁴, M. Haytmyradov¹⁷⁴, J.-P. Merlo¹⁷⁴, H. Mermerkaya^{174,257}, A. Mestvirishvili¹⁷⁴, A. Moeller¹⁷⁴, J. Nachtman¹⁷⁴, H. Ogul¹⁷⁴, Y. Onel¹⁷⁴, F. Ozok¹⁷⁴, A. Penzo¹⁷⁴, R. Rahmat¹⁷⁴, S. Sen¹⁷⁴, P. Tan¹⁷⁴, E. Tiras¹⁷⁴, J. Wetzel¹⁷⁴, K. Yi¹⁷⁴, B.A. Barnett¹⁷⁵, B. Blumenfeld¹⁷⁵, S. Bolognesi¹⁷⁵, D. Fehling¹⁷⁵, A.V. Gritsan¹⁷⁵, P. Maksimovic¹⁷⁵, C. Martin¹⁷⁵, M. Swartz¹⁷⁵, P. Baringer¹⁷⁶, A. Bean¹⁷⁶, G. Benelli¹⁷⁶, C. Bruner¹⁷⁶, R.P. Kenny III¹⁷⁶, M. Malek¹⁷⁶, M. Murray¹⁷⁶, D. Noonan¹⁷⁶, S. Sanders¹⁷⁶, J. Sekaric¹⁷⁶, R. Stringer¹⁷⁶, Q. Wang¹⁷⁶, J.S. Wood¹⁷⁶, I. Chakaberia¹⁷⁷, A. Ivanov¹⁷⁷, S. Khalil¹⁷⁷, M. Makouski¹⁷⁷, Y. Maravin¹⁷⁷, L.K. Saini¹⁷⁷, N. Skhirtladze¹⁷⁷, I. Svintradze¹⁷⁷, J. Gronberg¹⁷⁸, D. Lange¹⁷⁸, F. Rebassoo¹⁷⁸, D. Wright¹⁷⁸, A. Baden¹⁷⁹, A. Belloni¹⁷⁹, B. Calvert¹⁷⁹, S.C. Eno¹⁷⁹, J.A. Gomez¹⁷⁹, N.J. Hadley¹⁷⁹, R.G. Kellogg¹⁷⁹, T. Kolberg¹⁷⁹, Y. Lu¹⁷⁹, A.C. Mignerey¹⁷⁹, K. Pedro¹⁷⁹, A. Skuja¹⁷⁹, M.B. Tonjes¹⁷⁹, S.C. Tonwar¹⁷⁹, A. Apyan¹⁸⁰, R. Barbieri¹⁸⁰, G. Bauer¹⁸⁰, W. Busza¹⁸⁰, I.A. Calhoun¹⁸⁰, M. Chan¹⁸⁰, L. Di Matteo¹⁸⁰, G. Gomez Ceballos¹⁸⁰, M. Goncharov¹⁸⁰, D. Gulhan¹⁸⁰, M. Klute¹⁸⁰, Y.S. Lai¹⁸⁰, Y.-J. Lee¹⁸⁰, A. Levin¹⁸⁰, P.D. Luckey¹⁸⁰, T. Ma¹⁸⁰, C. Paus¹⁸⁰, D. Ralph¹⁸⁰, C. Roland¹⁸⁰, G. Roland¹⁸⁰, G.S.F. Stephens¹⁸⁰, K. Sumorok¹⁸⁰, D. Velicanu¹⁸⁰, J. Veverka¹⁸⁰, B. Wyslouch¹⁸⁰, M. Yang¹⁸⁰, M. Zanetti¹⁸⁰, V. Zhukova¹⁸⁰, B. Dahmes¹⁸¹, A. Gude¹⁸¹, S.C. Kao¹⁸¹, K. Klapöetke¹⁸¹, Y. Kubota¹⁸¹, J. Mans¹⁸¹, N. Pastika¹⁸¹, R. Rusack¹⁸¹, A. Singovsky¹⁸¹, N. Tamba¹⁸¹, J. Turkewitz¹⁸¹, J.G. Acosta¹⁸², S. Oliveros¹⁸²

A. Brinkerhoff¹⁸⁷, K.M. Chan¹⁸⁷, A. Drozdetskiy¹⁸⁷, M. Hildreth¹⁸⁷, C. Jessop¹⁸⁷, D.J. Karmgard¹⁸⁷, N. Kellams¹⁸⁷, K. Lannon¹⁸⁷, S. Lynch¹⁸⁷, N. Marinelli¹⁸⁷, Y. Musienko^{187,232}, T. Pearson¹⁸⁷, M. Planer¹⁸⁷, R. Ruchti¹⁸⁷, G. Smith¹⁸⁷, N. Valls¹⁸⁷, M. Wayne¹⁸⁷, M. Wolf¹⁸⁷, A. Woodard¹⁸⁷, L. Antonelli¹⁸⁸, J. Brinson¹⁸⁸, B. Bylsma¹⁸⁸, L.S. Durkin¹⁸⁸, S. Flowers¹⁸⁸, A. Hart¹⁸⁸, C. Hill¹⁸⁸, R. Hughes¹⁸⁸, K. Kotov¹⁸⁸, T.Y. Ling¹⁸⁸, W. Luo¹⁸⁸, D. Pugh¹⁸⁸, M. Rodenburg¹⁸⁸, B.L. Winer¹⁸⁸, H. Wolfe¹⁸⁸, H.W. Wulsin¹⁸⁸, O. Driga¹⁸⁹, P. Elmer¹⁸⁹, J. Hardenbrook¹⁸⁹, P. Hebda¹⁸⁹, A. Hunt¹⁸⁹, S.A. Koay¹⁸⁹, P. Lujan¹⁸⁹, D. Marlow¹⁸⁹, T. Medvedeva¹⁸⁹, M. Mooney¹⁸⁹, J. Olsen¹⁸⁹, P. Piroué¹⁸⁹, X. Quan¹⁸⁹, H. Saka¹⁸⁹, D. Stickland^{189,205}, C. Tully¹⁸⁹, J.S. Werner¹⁸⁹, A. Zuranski¹⁸⁹, E. Brownson¹⁹⁰, S. Malik¹⁹⁰, H. Mendez¹⁹⁰, J.E. Ramirez Vargas¹⁹⁰, V.E. Barnes¹⁹¹, D. Benedetto¹⁹¹, D. Bortoletto¹⁹¹, M. De Mattia¹⁹¹, L. Gutay¹⁹¹, Z. Hu¹⁹¹, M.K. Jha¹⁹¹, M. Jones¹⁹¹, K. Jung¹⁹¹, M. Kress¹⁹¹, N. Leonardo¹⁹¹, D.H. Miller¹⁹¹, N. Neumeister¹⁹¹, B.C. Radburn-Smith¹⁹¹, X. Shi¹⁹¹, I. Shipsey¹⁹¹, D. Silvers¹⁹¹, A. Svyatkovskiy¹⁹¹, F. Wang¹⁹¹, W. Xie¹⁹¹, L. Xu¹⁹¹, J. Zablocki¹⁹¹, N. Parashar¹⁹², J. Stupak¹⁹², A. Adair¹⁹³, B. Akgun¹⁹³, K.M. Ecklund¹⁹³, F.J.M. Geurts¹⁹³, W. Li¹⁹³, B. Michlin¹⁹³, B.P. Padley¹⁹³, R. Redjimi¹⁹³, J. Roberts¹⁹³, J. Zabel¹⁹³, B. Betchart¹⁹⁴, A. Bodek¹⁹⁴, R. Covarelli¹⁹⁴, P. de Barbaro¹⁹⁴, R. Demina¹⁹⁴, Y. Eshaq¹⁹⁴, T. Ferbel¹⁹⁴, A. Garcia-Bellido¹⁹⁴, P. Goldenzweig¹⁹⁴, J. Han¹⁹⁴, A. Harel¹⁹⁴, A. Khukhunaishvili¹⁹⁴, S. Korjenevski¹⁹⁴, G. Petrillo¹⁹⁴, D. Vishnevskiy¹⁹⁴, R. Ciesielski¹⁹⁵, L. Demortier¹⁹⁵, K. Goulianos¹⁹⁵, C. Mesropian¹⁹⁵, S. Arora¹⁹⁶, A. Barker¹⁹⁶, J.P. Chou¹⁹⁶, C. Contreras-Campana¹⁹⁶, E. Contreras-Campana¹⁹⁶, D. Duggan¹⁹⁶, D. Ferencek¹⁹⁶, Y. Gershtein¹⁹⁶, R. Gray¹⁹⁶, E. Halkiadakis¹⁹⁶, D. Hidas¹⁹⁶, S. Kaplan¹⁹⁶, A. Lath¹⁹⁶, S. Panwalkar¹⁹⁶, M. Park¹⁹⁶, R. Patel¹⁹⁶, S. Salur¹⁹⁶, S. Schnetzer¹⁹⁶, S. Somalwar¹⁹⁶, R. Stone¹⁹⁶, S. Thomas¹⁹⁶, P. Thomassen¹⁹⁶, M. Walker¹⁹⁶, K. Rose¹⁹⁷, S. Spanier¹⁹⁷, A. York¹⁹⁷, O. Bouhali^{198,258}, A. Castaneda Hernandez¹⁹⁸, R. Eusebi¹⁹⁸, W. Flanagan¹⁹⁸, J. Gilmore¹⁹⁸, T. Kamon^{198,259}, V. Khotilovich¹⁹⁸, V. Krutelyov¹⁹⁸, R. Montalvo¹⁹⁸, I. Osipenko¹⁹⁸, Y. Pakhotin¹⁹⁸, A. Perloff¹⁹⁸, J. Roe¹⁹⁸, A. Rose¹⁹⁸, A. Safonov¹⁹⁸, I. Suarez¹⁹⁸, A. Tatarinov¹⁹⁸, K.A. Ulmer¹⁹⁸, N. Akchurin¹⁹⁹, C. Cowden¹⁹⁹, J. Damgov¹⁹⁹, C. Drougou¹⁹⁹, P.R. Dudero¹⁹⁹, J. Faulkner¹⁹⁹, K. Kovitanggoon¹⁹⁹, S. Kunori¹⁹⁹, S.W. Lee¹⁹⁹, T. Libeiro¹⁹⁹, I. Volobouev¹⁹⁹, E. Appelt²⁰⁰, A.G. Delannoy²⁰⁰, S. Greene²⁰⁰, A. Gurrola²⁰⁰, W. Johns²⁰⁰, C. Maguire²⁰⁰, Y. Mao²⁰⁰, A. Melo²⁰⁰, M. Sharma²⁰⁰, P. Sheldon²⁰⁰, B. Snook²⁰⁰, S. Tuo²⁰⁰, J. Velkovska²⁰⁰, M.W. Arenton²⁰¹, S. Boutle²⁰¹, B. Cox²⁰¹, B. Francis²⁰¹, J. Goodell²⁰¹, R. Hirosky²⁰¹, A. Ledovskoy²⁰¹, H. Li²⁰¹, C. Lin²⁰¹, C. Neul²⁰¹, J. Wood²⁰¹, C. Clarke²⁰², R. Harr²⁰², P.E. Karchin²⁰², C. Kottachchi Kankanamge Don²⁰², P. Lamichhane²⁰², J. Sturdy²⁰², D.A. Belknap²⁰³, D. Carlsmith²⁰³, M. Cepeda²⁰³, S. Dasu²⁰³, L. Dodd²⁰³, S. Duric²⁰³, E. Friis²⁰³, R. Hall-Wilton²⁰³, M. Herndon²⁰³, A. Hervé²⁰³, P. Klabbers²⁰³, A. Lanaro²⁰³, C. Lazaridis²⁰³, A. Levine²⁰³, R. Loveless²⁰³, A. Mohapatra²⁰³, I. Ojalvo²⁰³, T. Perry²⁰³, G.A. Pierro²⁰³, G. Polese²⁰³, I. Ross²⁰³, T. Sarangi²⁰³, A. Savin²⁰³, W.H. Smith²⁰³, D. Taylor²⁰³, C. Vuosalo²⁰³ & N. Woods²⁰³

Primary affiliations

¹Yerevan Physics Institute, Yerevan, Armenia. ²Institut für Hochenergiephysik der OeAW, Wien, Austria. ³National Centre for Particle and High Energy Physics, Minsk, Belarus. ⁴Universiteit Antwerpen, Antwerpen, Belgium. ⁵Vrije Universiteit Brussel, Brussel, Belgium. ⁶Université Libre de Bruxelles, Bruxelles, Belgium. ⁷Ghent University, Ghent, Belgium. ⁸Université Catholique de Louvain, Louvain-la-Neuve, Belgium. ⁹Université de Mons, Mons, Belgium. ¹⁰Centro Brasileiro de Pesquisas Físicas, Rio de Janeiro, Brazil. ¹¹Universidade do Estado do Rio de Janeiro, Rio de Janeiro, Brazil. ¹²Universidade Estadual Paulista, Universidade Federal do ABC, São Paulo, Brazil. ¹³Universidade Estadual Paulista. ¹⁴Universidade Federal do ABC. ¹⁵Institute for Nuclear Research and Nuclear Energy, Sofia, Bulgaria. ¹⁶University of Sofia, Sofia, Bulgaria. ¹⁷Institute of High Energy Physics, Beijing, China. ¹⁸State Key Laboratory of Nuclear Physics and Technology, Peking University, Beijing, China. ¹⁹Universidad de Los Andes, Bogota, Colombia. ²⁰University of Split, Faculty of Electrical Engineering, Mechanical Engineering and Naval Architecture, Split, Croatia. ²¹University of Split, Faculty of Science, Split, Croatia. ²²Institute Rudjer Boskovic, Zagreb, Croatia. ²³University of Cyprus, Nicosia, Cyprus. ²⁴Charles University, Prague, Czech Republic. ²⁵Academy of Scientific Research and Technology of the Arab Republic of Egypt, Egyptian Network of High Energy Physics, Cairo, Egypt. ²⁶National Institute of Chemical Physics and Biophysics, Tallinn, Estonia. ²⁷Department of Physics, University of Helsinki, Helsinki, Finland. ²⁸Helsinki Institute of Physics, Helsinki, Finland. ²⁹Lappeenranta University of Technology, Lappeenranta, Finland. ³⁰DSM/IRFU, CEA/Saclay, Gif-sur-Yvette, France. ³¹Laboratoire Leprince-Ringuet, Ecole Polytechnique, IN2P3-CNRS, Palaiseau, France. ³²Institut Pluridisciplinaire Hubert Curie, Université de Strasbourg, Université de Haute Alsace Mulhouse, CNRS/IN2P3, Strasbourg, France. ³³Centre de Calcul de l'Institut National de Physique Nucléaire et de Physique des Particules, CNRS/IN2P3, Villeurbanne, France. ³⁴Université de Lyon, Université Claude Bernard Lyon 1, CNRS-IN2P3, Institut de Physique Nucléaire de Lyon, Villeurbanne, France. ³⁵Institute of High Energy Physics and Informatization, Tbilisi State University, Tbilisi, Georgia. ³⁶RWTH Aachen University, I. Physikalisches Institut, Aachen, Germany. ³⁷RWTH Aachen University, III. Physikalisches Institut A, Aachen, Germany. ³⁸RWTH Aachen University, III. Physikalisches Institut B, Aachen, Germany. ³⁹Deutsches Elektronen-Synchrotron, Hamburg, Germany. ⁴⁰University of Hamburg, Hamburg, Germany. ⁴¹Institut für Experimentelle Kernphysik, Karlsruhe, Germany. ⁴²Institute of Nuclear and Particle Physics (INPP), NCSR Demokritos, Aghia Paraskevi, Greece. ⁴³University of Athens, Athens, Greece. ⁴⁴University of Ioánnina, Ioánnina, Greece. ⁴⁵Wigner Research Centre for Physics, Budapest, Hungary. ⁴⁶Institute of Nuclear Research ATOMKI, Debrecen, Hungary. ⁴⁷University of Debrecen, Debrecen, Hungary. ⁴⁸National Institute of Science Education and Research, Bhubaneswar, India. ⁴⁹Panjab University, Chandigarh, India. ⁵⁰University of Delhi, Delhi, India. ⁵¹Saha Institute of Nuclear Physics, Kolkata, India. ⁵²Bhabha Atomic Research Centre, Mumbai, India. ⁵³Tata Institute of Fundamental Research, Mumbai, India. ⁵⁴Institute for Research in Fundamental Sciences (IPM), Tehran, Iran. ⁵⁵University College Dublin, Dublin, Ireland. ⁵⁶INFN Sezione di Bari, Università di Bari, Politecnico di Bari, Bari, Italy. ⁵⁷INFN Sezione di Bari. ⁵⁸Università di Bari. ⁵⁹Politecnico di Bari. ⁶⁰INFN Sezione di Bologna, Università

di Bologna, Bologna, Italy. ⁶¹INFN Sezione di Bologna. ⁶²Università di Bologna. ⁶³INFN Sezione di Catania, Università di Catania, CSFNSM, Catania, Italy. ⁶⁴INFN Sezione di Catania. ⁶⁵Università di Catania. ⁶⁶CSFNSM. ⁶⁷INFN Sezione di Firenze, Università di Firenze, Firenze, Italy. ⁶⁸INFN Sezione di Firenze. ⁶⁹Università di Firenze. ⁷⁰INFN Laboratori Nazionali di Frascati, Frascati, Italy. ⁷¹INFN Sezione di Genova, Università di Genova, Genova, Italy. ⁷²INFN Sezione di Genova. ⁷³Università di Genova. ⁷⁴INFN Sezione di Milano-Bicocca, Università di Milano-Bicocca, Milano, Italy. ⁷⁵INFN Sezione di Milano-Bicocca. ⁷⁶Università di Milano-Bicocca. ⁷⁷INFN Sezione di Napoli, Università di Napoli 'Federico II', Università della Basilicata (Potenza), Università G. Marconi (Roma), Napoli, Italy. ⁷⁸INFN Sezione di Napoli. ⁷⁹Università di Napoli 'Federico II'. ⁸⁰Università della Basilicata (Potenza). ⁸¹Università G. Marconi (Roma). ⁸²INFN Sezione di Padova, Università di Padova, Università di Trento (Trento), Padova, Italy. ⁸³INFN Sezione di Padova. ⁸⁴Università di Padova. ⁸⁵Università di Trento (Trento). ⁸⁶INFN Sezione di Pavia, Università di Pavia, Pavia, Italy. ⁸⁷INFN Sezione di Pavia. ⁸⁸Università di Pavia. ⁸⁹INFN Sezione di Perugia, Università di Perugia, Perugia, Italy. ⁹⁰INFN Sezione di Perugia. ⁹¹Università di Perugia. ⁹²INFN Sezione di Pisa, Università di Pisa, Scuola Normale Superiore di Pisa, Pisa, Italy. ⁹³INFN Sezione di Pisa. ⁹⁴Università di Pisa. ⁹⁵Scuola Normale Superiore di Pisa. ⁹⁶INFN Sezione di Roma, Università di Roma, Roma, Italy. ⁹⁷INFN Sezione di Roma. ⁹⁸Università di Roma. ⁹⁹INFN Sezione di Torino, Università di Torino, Università del Piemonte Orientale (Novara), Torino, Italy. ¹⁰⁰INFN Sezione di Torino. ¹⁰¹Università di Torino. ¹⁰²Università del Piemonte Orientale (Novara). ¹⁰³INFN Sezione di Trieste, Università di Trieste, Trieste, Italy. ¹⁰⁴INFN Sezione di Trieste. ¹⁰⁵Università di Trieste. ¹⁰⁶Kangwon National University, Chunchon, Korea. ¹⁰⁷Kyungpook National University, Daegu, Korea. ¹⁰⁸Chonbuk National University, Jeonju, Korea. ¹⁰⁹Chonnam National University, Institute for Universe and Elementary Particles, Kwangju, Korea. ¹¹⁰Korea University, Seoul, Korea. ¹¹¹Seoul National University, Seoul, Korea. ¹¹²University of Seoul, Seoul, Korea. ¹¹³Sungkyunkwan University, Suwon, Korea. ¹¹⁴Vilnius University, Vilnius, Lithuania. ¹¹⁵National Centre for Particle Physics, Universiti Malaysia, Kuala Lumpur, Malaysia. ¹¹⁶Centro de Investigación y de Estudios Avanzados del IPN, Mexico City, Mexico. ¹¹⁷Universidad Iberoamericana, Mexico City, Mexico. ¹¹⁸Benemerita Universidad Autónoma de Puebla, Puebla, Mexico. ¹¹⁹Universidad Autónoma de San Luis Potosí, San Luis Potosí, Mexico. ¹²⁰University of Auckland, Auckland, New Zealand. ¹²¹University of Canterbury, Christchurch, New Zealand. ¹²²National Centre for Physics, Quaid-I-Azam University, Islamabad, Pakistan. ¹²³National Centre for Nuclear Research, Swierk, Poland. ¹²⁴Institute of Experimental Physics, Faculty of Physics, University of Warsaw, Warsaw, Poland. ¹²⁵Laboratório de Instrumentação e Física Experimental de Partículas, Lisboa, Portugal. ¹²⁶Joint Institute for Nuclear Research, Dubna, Russia. ¹²⁷Petersburg Nuclear Physics Institute, Gatchina (St. Petersburg), Russia. ¹²⁸Institute for Nuclear Research, Moscow, Russia. ¹²⁹Institute for Theoretical and Experimental Physics, Moscow, Russia. ¹³⁰P.N. Lebedev Physical Institute, Moscow, Russia. ¹³¹Skobeltsyn Institute of Nuclear Physics, Lomonosov Moscow State University, Moscow, Russia. ¹³²State Research Center of Russian Federation, Institute for High Energy Physics, Protvino, Russia. ¹³³University of Belgrade, Faculty of Physics and Vinca Institute of Nuclear Sciences, Belgrade, Serbia. ¹³⁴Centro de Investigaciones Energéticas Medioambientales y Tecnológicas (CIEMAT), Madrid, Spain. ¹³⁵Universidad Autónoma de Madrid, Madrid, Spain. ¹³⁶Universidad de Oviedo, Oviedo, Spain. ¹³⁷Instituto de Física de Cantabria (IFCA), CSIC-Universidad de Cantabria, Santander, Spain. ¹³⁸CERN, European Organization for Nuclear Research, Geneva, Switzerland. ¹³⁹Paul Scherrer Institut, Villigen, Switzerland. ¹⁴⁰Institute for Particle Physics, ETH Zurich, Zurich, Switzerland. ¹⁴¹Universität Zürich, Zurich, Switzerland. ¹⁴²National Central University, Chung-Li, Taiwan. ¹⁴³National Taiwan University (NTU), Taipei, Taiwan. ¹⁴⁴Chulalongkorn University, Faculty of Science, Department of Physics, Bangkok, Thailand. ¹⁴⁵Cukurova University, Adana, Turkey. ¹⁴⁶Middle East Technical University, Physics Department, Ankara, Turkey. ¹⁴⁷Bogazici University, Istanbul, Turkey. ¹⁴⁸Istanbul Technical University, Istanbul, Turkey. ¹⁴⁹National Scientific Center, Kharkov Institute of Physics and Technology, Kharkov, Ukraine. ¹⁵⁰University of Bristol, Bristol, United Kingdom. ¹⁵¹Rutherford Appleton Laboratory, Didcot, United Kingdom. ¹⁵²Imperial College, London, United Kingdom. ¹⁵³Brunel University, Uxbridge, United Kingdom. ¹⁵⁴Baylor University, Waco, USA. ¹⁵⁵The University of Alabama, Tuscaloosa, USA. ¹⁵⁶Boston University, Boston, USA. ¹⁵⁷Brown University, Providence, USA. ¹⁵⁸University of California, Davis, Davis, USA. ¹⁵⁹University of California, Los Angeles, USA. ¹⁶⁰University of California, Riverside, Riverside, USA. ¹⁶¹University of California, San Diego, La Jolla, USA. ¹⁶²University of California, Santa Barbara, Santa Barbara, USA. ¹⁶³California Institute of Technology, Pasadena, USA. ¹⁶⁴Carnegie Mellon University, Pittsburgh, USA. ¹⁶⁵University of Colorado at Boulder, Boulder, USA. ¹⁶⁶Cornell University, Ithaca, USA. ¹⁶⁷Fairfield University, Fairfield, USA. ¹⁶⁸Fermi National Accelerator Laboratory, Batavia, USA. ¹⁶⁹University of Florida, Gainesville, USA. ¹⁷⁰Florida International University, Miami, USA. ¹⁷¹Florida State University, Tallahassee, USA. ¹⁷²Florida Institute of Technology, Melbourne, USA. ¹⁷³University of Illinois at Chicago (UIC), Chicago, USA. ¹⁷⁴The University of Iowa, Iowa City, USA. ¹⁷⁵Johns Hopkins University, Baltimore, USA. ¹⁷⁶The University of Kansas, Lawrence, USA. ¹⁷⁷Kansas State University, Manhattan, USA. ¹⁷⁸Lawrence Livermore National Laboratory, Livermore, USA. ¹⁷⁹University of Maryland, College Park, USA. ¹⁸⁰Massachusetts Institute of Technology, Cambridge, USA. ¹⁸¹University of Minnesota, Minneapolis, USA. ¹⁸²University of Mississippi, Oxford, USA. ¹⁸³University of Nebraska-Lincoln, Lincoln, USA. ¹⁸⁴State University of New York at Buffalo, Buffalo, USA. ¹⁸⁵Northeastern University, Boston, USA. ¹⁸⁶Northwestern University, Evanston, USA. ¹⁸⁷University of Notre Dame, Notre Dame, USA. ¹⁸⁸The Ohio State University, Columbus, USA. ¹⁸⁹Princeton University, Princeton, USA. ¹⁹⁰University of Puerto Rico, Mayaguez, USA. ¹⁹¹Purdue University, West Lafayette, USA. ¹⁹²Purdue University Calumet, Hammond, USA. ¹⁹³Rice University, Houston, USA. ¹⁹⁴University of Rochester, Rochester, USA. ¹⁹⁵The Rockefeller University, New York, USA. ¹⁹⁶Rutgers, The State University of New Jersey, Piscataway, USA. ¹⁹⁷University of Tennessee, Knoxville, USA. ¹⁹⁸Texas A&M University, College Station, USA. ¹⁹⁹Texas Tech University, Lubbock, USA. ²⁰⁰Vanderbilt University, Nashville, USA. ²⁰¹University of Virginia, Charlottesville, USA. ²⁰²Wayne State University, Detroit, USA. ²⁰³University of Wisconsin, Madison, USA.

Secondary affiliations

²⁰⁴Vienna University of Technology, Vienna, Austria. ²⁰⁵CERN, European Organization for Nuclear Research, Geneva, Switzerland. ²⁰⁶Institut Pluridisciplinaire Hubert Curien, Université de Strasbourg, Université de Haute Alsace Mulhouse, CNRS/IN2P3, Strasbourg, France. ²⁰⁷National Institute of Chemical Physics and Biophysics, Tallinn, Estonia. ²⁰⁸Skobeltsyn Institute of Nuclear Physics, Lomonosov Moscow State University, Moscow, Russia. ²⁰⁹Universidade Estadual de Campinas, Campinas, Brazil. ²¹⁰Laboratoire Leprince-Ringuet, Ecole Polytechnique, IN2P3-CNRS, Palaiseau, France. ²¹¹Joint Institute for Nuclear Research, Dubna, Russia. ²¹²Suez University, Suez, Egypt. ²¹³Cairo University, Cairo, Egypt. ²¹⁴Fayoum University, El-Fayoum, Egypt. ²¹⁵Ain Shams University, Cairo, Egypt. ²¹⁶Now at Sultan Qaboos University, Muscat, Oman. ²¹⁷Université de Haute Alsace, Mulhouse, France. ²¹⁸Brandenburg University of Technology, Cottbus, Germany. ²¹⁹Institute of Nuclear Research ATOMKI, Debrecen, Hungary. ²²⁰Eötvös Loránd University, Budapest, Hungary. ²²¹University of Debrecen, Debrecen, Hungary. ²²²University of Visva-Bharati, Santiniketan, India. ²²³Now at King Abdulaziz University, Jeddah, Saudi Arabia. ²²⁴University of Ruhuna, Matara, Sri Lanka. ²²⁵Isfahan University of Technology, Isfahan, Iran. ²²⁶University of Tehran, Department of Engineering Science, Tehran, Iran. ²²⁷Plasma Physics Research Center, Science and Research Branch, Islamic Azad University, Tehran, Iran. ²²⁸Università degli Studi di Siena, Siena, Italy. ²²⁹Centre National de la Recherche Scientifique (CNRS) - IN2P3, Paris, France. ²³⁰Purdue University, West Lafayette, USA. ²³¹Universidad Michoacana de San Nicolas de Hidalgo, Morelia, Mexico. ²³²Institute for Nuclear Research, Moscow, Russia. ²³³St. Petersburg State Polytechnical University, St. Petersburg, Russia. ²³⁴California Institute of Technology, Pasadena, USA. ²³⁵Faculty of Physics, University of Belgrade, Belgrade, Serbia. ²³⁶Facoltà Ingegneria, Università di Roma, Roma, Italy. ²³⁷Scuola Normale e Sezione dell'INFN, Pisa, Italy. ²³⁸University of Athens, Athens, Greece. ²³⁹Paul Scherrer Institut, Villigen, Switzerland. ²⁴⁰Institute for Theoretical and Experimental Physics, Moscow, Russia. ²⁴¹Albert Einstein Center for Fundamental Physics, Bern, Switzerland. ²⁴²Gaziosmanpaşa University, Tokat, Turkey. ²⁴³Adiyaman University, Adiyaman, Turkey. ²⁴⁴Çag University, Mersin, Turkey. ²⁴⁵Anadolu University, Eskisehir, Turkey. ²⁴⁶Ozyegin University, Istanbul, Turkey. ²⁴⁷Izmir Institute of Technology, Izmir, Turkey. ²⁴⁸Necmettin Erbakan University, Konya, Turkey. ²⁴⁹Mimar Sinan University, Istanbul, Turkey. ²⁵⁰Marmara University, Istanbul, Turkey. ²⁵¹Kafkas University, Kars, Turkey. ²⁵²Yildiz Technical University, Istanbul, Turkey. ²⁵³Rutherford Appleton Laboratory, Didcot, United Kingdom. ²⁵⁴School of Physics and Astronomy, University of Southampton, Southampton, United Kingdom. ²⁵⁵University of Belgrade, Faculty of Physics and Vinca Institute of Nuclear Sciences, Belgrade, Serbia. ²⁵⁶Argonne National Laboratory, Argonne, USA. ²⁵⁷Erzincan University, Erzincan, Turkey. ²⁵⁸Texas A&M University at Qatar, Doha, Qatar. ²⁵⁹Kyungpook National University, Daegu, Korea. †Deceased.

LHCb Collaboration

I. Bediaga¹, J.M. De Miranda¹, F. Ferreira Rodrigues¹, A. Gomes^{1,79}, A. Massafferri¹, A.C. dos Reis¹, A.B. Rodrigues¹, S. Amato², K. Carvalho Akiba², L. De Paula², O. Francisco², M. Gandelman², A. Hicheur², J.H. Lopes², D. Martins Tostes², I. Nasteva², J.M. Otalora Goicochea², E. Polycarpo², C. Potterat², M.S. Rangel², V. Salustino Guimaraes², B. Souza De Paula², D. Vieira², L. An³, Y. Gao³, F. Jing³, Y. Li³, Z. Yang³, X. Yuan³, Y. Zhang³, L. Zhong³, L. Beaucourt⁴, M. Chefeldt⁴, D. Decamp⁴, N. Déleage⁴, Ph. Ghez⁴, J.-P. Lees⁴, J.F. Marchand⁴, M.-N. Minard⁴, B. Pietrzyk⁴, W. Qian⁴, S. T'Jampens⁴, V. Tisserand⁴, E. Tournier⁴, Z. Ajaltouni⁵, M. Baalouch⁵, E. Cogneras⁵, O. Deschamps⁵, I. El Rifai⁵, M. Grabalosa Gándara⁵, P. Henrard⁵, M. Hoballah⁵, R. Lefevre⁵, J. Maratas⁵, S. Monteil⁵, V. Niess⁵, P. Perret⁵, C. Adrover⁶, S. Akar⁶, E. Aslanides⁶, J. Cogan⁶, W. Kansa⁶, R. Le Gac⁶, O. Leroy⁶, G. Mancinelli⁶, A. Mordà⁶, M. Perrin-Terrin⁶, J. Ferraro⁶, A. Tsaregorodtsev⁶, Y. Amhis⁷, S. Barsuk⁷, M. Borsato⁷, O. Kochebina⁷, J. Lefrançois⁷, F. Machefert⁷, A. Martín Sánchez⁷, M. Nicol⁷, P. Robbe⁷, M.-H. Schune⁷, M. Teklishyn⁷, A. Vallier⁷, B. Viaud⁷, G. Wormser⁷, E. Ben-Haim⁸, M. Charles⁸, S. Coquereau⁸, P. David⁸, L. Del Buono⁸, L. Henry⁸, F. Polci⁸, J. Albrecht⁹, T. Brambach⁹, Ch. Calet⁹, M. Deckenhoff⁹, U. Eitschberger⁹, R. Ekelhof⁹, L. Gauthier⁹, F. Kruse⁹, F. Meier⁹, R. Niet⁹, C.J. Parkinson^{9,45}, M. Schlupp⁹, A. Shires⁹, B. Spaan⁹, S. Swientek⁹, J. Wishahi⁹, O. Aquines Gutierrez¹⁰, J. Blouw¹⁰, M. Britsch¹⁰, M. Fontana¹⁰, D. Popov¹⁰, M. Schmelling¹⁰, D. Volynskiy¹⁰, M. Zavertyaev^{10,89}, S. Bachmann¹¹, A. Bien¹¹, A. Comerma-Montells¹¹, M. De Cian¹¹, F. Dordei¹¹, S. Esen¹¹, C. Färber¹¹, E. Gersabeck¹¹, L. Grillo¹¹, X. Han¹¹, S. Hansmann-Menzemer¹¹, A. Jaeger¹¹, M. Kolpin¹¹, K. Kreplin¹¹, G. Krocker¹¹, B. Leverington¹¹, J. Marks¹¹, M. Meissner¹¹, M. Neuner¹¹, T. Nikodem¹¹, P. Seyfert¹¹, M. Stahl¹¹, S. Stahl¹¹, U. Uwer¹¹, M. Vesterinen¹¹, S. Wandernoth¹¹, D. Wiedner¹¹, A. Zhelezov¹¹, R. McNulty¹², R. Wallace¹², W.C. Zhang¹², A. Palano^{13,84}, A. Carbone^{14,74}, A. Falabella¹⁴, D. Galli^{14,74}, U. Marconi¹⁴, N. Moggi¹⁴, M. Mussini¹⁴, S. Perazzini^{14,74}, V. Vagnoni¹⁴, G. Valenti¹⁴, M. Zangoli¹⁴, W. Bonivento^{15,38}, S. Cadeddu¹⁵, A. Cardini¹⁵, V. Cogoni¹⁵, A. Contu^{15,38}, A. Lai¹⁵, B. Liu¹⁵, G. Manca^{15,82}, R. Oldeman^{15,82}, B. Saïta^{15,82}, C. Vacca¹⁵, M. Andreotti^{16,69}, W. Baldini¹⁶, C. Bozzi¹⁶, R. Calabrese^{16,69}, M. Corvo^{16,69}, M. Fiore^{16,69}, M. Fiorini^{16,69}, E. Lupp^{16,69}, L.L. Pappalardo^{16,69}, I. Shapoval^{16,69}, G. Tellarini^{16,69}, L. Tomassetti¹⁶, S. Vecchi¹⁶, L.L. Anderlini^{17,68}, A. Bizzeti^{17,71}, M. Frosini^{17,68}, G. Graziani¹⁷, G. Passaleva¹⁷, M. Veltri^{18,88}, G. Bencivenni¹⁸, P. Campana¹⁸, P. De Simone¹⁸, G. Lanfranchi¹⁸, M. Palutan¹⁸, M. Rama¹⁸, A. Sarti^{18,88}, B. Sciacca¹⁸, R. Vazquez Gomez¹⁸, R. Cardinale^{19,38,76}, F. Fontaneli^{19,76}, S. Gambetta^{19,76}, C. Patrignani^{19,76}, A. Petrolini^{19,76}, A. Pistone¹⁹, M. Calvi^{20,72}, L. Cassina^{20,72}, C. Gotti^{20,72}, B. Khanji^{20,38,72}, M. Kucharczyk^{20,26,72}, C. Matteuzzi²⁰, J. Fu^{21,38}, A. Geraci^{21,78}, N. Neri²¹, F. Palombo^{21,85}, S. Amerio²², G. Collazuol²², S. Gallorini^{22,38}, A. Gianelle²², D. Lucchesi^{22,81}, A. Lupato²², M. Morandini²², M. Rotondo²², L. Sestini²², G. Simi²², R. Stroili²², F. Bedeschi²³, R. Cenci^{23,77}, S. Leo²³, P. Marino^{23,77}, M.J. Morello^{23,77}, G. Punzi^{23,87}, S. Stracka^{23,77}, J. Walsh²³, G. Carboni^{24,75}, E. Furfaro^{24,75}, E. Santovetti^{24,75}, A. Satta²⁴, A.A. Alves Jr^{25,38}, G. Auriemma^{25,70}, V. Bocci²⁵, G. Martellotti²⁵, G. Penso^{25,86}, D. Pinci²⁵, R. Santacesaria²⁵, C. Satriano^{25,70}, A. Sciubba^{25,86}, A. Dziuza²⁶, W. Kucewicz^{26,80}, T. Lesiak²⁶, B. Rachwal²⁶, M. Witek²⁶, M. Frlje²⁷, T. Fiuatowski²⁷, M. Idzik²⁷, P. Morawski²⁷,

J. Moron²⁷, A. Oblakowska-Mucha^{27,38}, K. Swientek²⁷, T. Szumlak²⁷, V. Batzokskaya²⁸, K. Klimaszewski²⁸, K. Kurek²⁸, M. Szczekowski²⁸, A. Ukleja²⁸, W. Wislicki²⁸, L. Cojocariu²⁹, L. Giubega²⁹, A. Grecu²⁹, F. Maciuc²⁹, M. Orlandea²⁹, B. Popovici²⁹, S. Stoica²⁹, M. Straticu²⁹, G. Alkhazov³⁰, N. Bondar^{30,38}, A. Dzyuba³⁰, O. Maev³⁰, N. Sagidova³⁰, Y. Shcheglov³⁰, A. Vorobyev³⁰, S. Belogurov³¹, I. Belyaev³¹, V. Egorychev³¹, D. Golubkov³¹, T. Kvaratskheliya³¹, I.V. Machikhiliyan³¹, I. Polyakov³¹, D. Savrina^{31,32}, A. Semennikov³¹, A. Zhokhov³¹, A. Berezhnoy³², M. Korolev³², A. Leflat³², N. Nikitin³², S. Filippov³², E. Gushchin³², L. Kravchuk³², A. Bondar³⁴, S. Eidelman³⁴, P. Krokovny³⁴, V. Kudryavtsev³⁴, L. Shekhtman³⁴, V. Vorobyev³⁴, A. Artamonov³⁵, K. Belous³⁵, R. Dzhelelyadin³⁵, Yu. Guz^{35,38}, A. Novoselov³⁵, V. Obraztsov³⁵, A. Popov³⁵, V. Romanovsky³⁵, M. Shapkin³⁵, O. Stenyagin³⁵, O. Yushchenko³⁵, A. Badalov³⁶, M. Calvo Gomez^{36,73}, L. Garrido³⁶, D. Gascon³⁶, R. Graciani Diaz³⁶, E. Graugés³⁶, C. Marin Benito³⁶, E. Picaatoste Olloqui³⁶, V. Rives Molina³⁶, H. Ruiz³⁶, X. Vilasis-Cardona^{36,73}, B. Adeva³⁷, P. Alvarez Cartelle³⁷, A. Dosil Suárez³⁷, V. Fernandez Albor³⁷, A. Gallas Torreira³⁷, J. García Pardiñas³⁷, J.A. Hernandez Morata³⁷, M. Pio Casasus³⁷, A. Romero Vidal³⁷, J.J. Saborido Silva³⁷, B. Sanmartin Sedes³⁷, C. Santamarina Rios³⁷, P. Vazquez Real³⁷, R. Vázquez Sierra³⁷, M. Viteles Diaz³⁷, F. Alessio³⁸, F. Archilli³⁸, C. Barschel³⁸, S. Benson³⁸, J. Buytaert³⁸, D. Campora Perez³⁸, L. Castillo Garcia³⁸, M. Cattaneo³⁸, Ph. Charpentier³⁸, X. Cid Vidal³⁸, M. Clemencic³⁸, J. Closier³⁸, V. Coco³⁸, P. Collins³⁸, G. Corti³⁸, B. Couturier³⁸, C. D'Ambrosio³⁸, F. Dettori³⁸, A. Di Canto³⁸, H. Dijkstra³⁸, P. Durante³⁸, M. Ferro-Luzzi³⁸, R. Forby³⁸, M. Frank³⁸, C. Frei³⁸, C. Gaspar³⁸, V.V. Gligorov³⁸, L.A. Granado Cardoso³⁸, T. Gys³⁸, C. Haen³⁸, J. He³⁸, T. Head³⁸, E. van Herwijnen³⁸, R. Jacobsson³⁸, D. Johnson³⁸, C. Joram³⁸, B. Jost³⁸, M. Karacson³⁸, T.M. Karbach³⁸, D. Lacarrere³⁸, B. Langhans³⁸, R. Lindner³⁸, C. Linn³⁸, S. Lohm³⁸, A. Mappel³⁸, R. Matev³⁸, Z. Mathe³⁸, S. Neuber³⁸, N. Neufeld³⁸, A. Otto³⁸, J. Panman³⁸, M. Pepe Altarelli³⁸, N. Rauschmayr³⁸, M. Rih³⁸, S. Roiser³⁸, T. Ruf³⁸, H. Schindler³⁸, B. Schmidt³⁸, A. Schopper³⁸, R. Schwemmer³⁸, S. Sridharan³⁸, F. Stagni³⁸, V.K. Subbiah³⁸, F. Teubert³⁸, E. Thomas³⁸, D. Tonelli³⁸, A. Trisovic³⁸, M. Ubeda Garcia³⁸, J. Wicht³⁸, K. Yellie³⁸, V. Battista³⁹, A. Bay³⁹, F. Bianco³⁹, M. Dorigo³⁹, F. Dupertuis³⁹, C. Fitzpatrick³⁹, S. Giani³⁹, G. Haefeli³⁹, P. Jaton³⁹, C. Khurwathanakul³⁹, I. Komarov³⁹, V.N. La Thi³⁹, N. Lopez-March³⁹, R. Märki³⁹, M. Martinelli³⁹, B. Muster³⁹, T. Nakada³⁹, A.D. Nguyen³⁹, T.D. Nguyen³⁹, C. Nguyen-Mau^{39,83}, J. Prisciandaro³⁹, A. Puig Navarro³⁹, B. Rakotomiaramanana³⁹, J. Rouvinet³⁹, O. Schneider³⁹, F. Soomro³⁹, P. Szczypka^{39,38}, M. Tobin³⁹, S. Tournear³⁹, M.T. Tran³⁹, G. Veneziano³⁹, Z. Xu³⁹, J. Anderson⁴⁰, R. Bernet⁴⁰, E. Bowen⁴⁰, A. Bursche⁴⁰, N. Chhipolani⁴⁰, M. Chrzasczcz^{40,26}, Ch. Elsassler⁴⁰, E. Graverin⁴⁰, F. Lionetto⁴⁰, P. Lowdon⁴⁰, K. Müller⁴⁰, N. Serra⁴⁰, O. Steinkamp⁴⁰, B. Stora⁴⁰, U. Straumann⁴⁰, M. Tresch⁴⁰, A. Vollhardt⁴⁰, R. Aaij⁴¹, S. Ali⁴¹, M. van Beuzekom⁴¹, P.N.Y. David⁴¹, K. De Bruyn⁴¹, C. Farinelli⁴¹, V. Heijne⁴¹, W. Hulsbergen⁴¹, E. Jans⁴¹, P. Koppenburg^{41,38}, A. Kozlinskiy⁴¹, J. van Leerdam⁴¹, M. Merk⁴¹, S. Oggero⁴¹, A. Pellegrino⁴¹, H. Snoek⁴¹, J. van Tilburg⁴¹, P. Tsopelas⁴¹, N. Tuning⁴¹, J.A. de Vries⁴¹, T. Ketel⁴², R.F. Koopman⁴², R.W. Lambert⁴², D. Martinez Santos^{42,38}, G. Raven⁴², M. Schiller⁴², V. Syropoulos⁴², S. Tolk⁴², A. Dovbnya⁴³, S. Kandybe⁴³, I. Raniuk⁴³, O. Okhrimenko⁴⁴, V. Pugatch⁴⁴, S. Bifani⁴⁵, N. Farley⁴⁵, P. Griffith⁴⁵, I.R. Kenyon⁴⁵, C. Lazzeroni⁴⁵, A. Mazurov⁴⁵, J. McCarthy⁴⁵, L. Pescatore⁴⁵, N.K. Watson⁴⁵, M.P. Williams⁴⁵, M. Adinolfi⁴⁶, J. Benton⁴⁶, N.H. Brook⁴⁶, A. Cook⁴⁶, M. Coombes⁴⁶, J. Dalseno⁴⁶, T. Hampson⁴⁶, S.T. Harnwell⁴⁶, P. Naik⁴⁶, E. Price⁴⁶, C. Prouve⁴⁶, J.H. Rademacker⁴⁶, S. Richards⁴⁶, D.M. Saunders⁴⁶, N. Skidmore⁴⁶, D. Souza⁴⁶, J.J. Velthuis⁴⁶, D. Voong⁴⁶, W. Barter⁴⁷, M.-O. Bettler⁴⁷, H.V. Cliff⁴⁷, H.-M. Evans⁴⁷, J. Garra Tico⁴⁷, V. Gibson⁴⁷, S. Gregson⁴⁷, S.C. Haines⁴⁷, C.R. Jones⁴⁷, M. Sirendi⁴⁷, J. Smith⁴⁷, D.R. Ward⁴⁷, S.A. Wotton⁴⁷, S. Wright⁴⁷, J.J. Back⁴⁸, T. Blake⁴⁸, D.C. Craik⁴⁸, A.C. Croombe⁴⁸, D. Dosssett⁴⁸, T. Gershon⁴⁸, M. Kreps⁴⁸, C. Langenbruch⁴⁸, T. Latham⁴⁸, D.P. O'Hanlon⁴⁸, T. Pila⁴⁸, A. Poluektov^{48,34}, M.M. Reid⁴⁸, A. Ripa Coutinho⁴⁸, C. Wallace⁴⁸, M. Whitehead⁴⁸, S. Easo^{49,38}, R. Nandakumar⁴⁹, A. Pananestis^{49,38}, S. Ricciardi⁴⁹, F.F. Wilson⁴⁹, L. Carson⁵⁰, P.E.L. Clarke⁵⁰, G.A. Cowan⁵⁰, S. Eisenhardt⁵⁰, D. Ferguson⁵⁰, D. Lambert⁵⁰, H. Luo⁵⁰, A.-B. Morris⁵⁰, F. Muheim⁵⁰, M. Needham⁵⁰, S. Player⁵⁰, M. Alexander⁵¹, J. Beddow⁵¹, C.-T. Dean⁵¹, L. Eklund⁵¹, D. Hynds⁵¹, S. Karodia⁵¹, I. Longstaff⁵¹, S. Ogilvy⁵¹, M. Pappagallo⁵¹, P. Sail⁵¹, I. Skillicorn⁵¹, F.J.P. Soller⁵¹, Spradlin⁵¹, A. Affolder⁵², T.J.V. Bowcock⁵², H. Brown⁵², G. Casse⁵², S. Donleavy⁵², K. Dreimanis⁵², S. Farr⁵², R. Fay⁵², K. Hennessy⁵², D. Hutchcroft⁵², M. Liles⁵², B. McKelvey⁵², G.D. Patel⁵², J.D. Preece⁵², A. Pritchard⁵², K. Rinnert⁵², T. Shears⁵², N.A. Smith⁵², G. Ciezarek⁵³, S. Cunliffe⁵³, R. Currie⁵³, P. Egede⁵³, P. Fol⁵³, A. Golutin^{53,31,38}, S. Hall⁵³, M. McCann⁵³, P. Owen⁵³, M. Patel⁵³, K. Petridis⁵³, F. Redi⁵³, I. Sepp⁵³, E. Smith⁵³, W. Sutcliffe⁵³, D. Websdale⁵³, R.B. Appleby⁵⁴, R.J. Barlow⁵⁴, T. Bird⁵⁴, P.M. Bjørnstad⁵⁴, S. Borgh⁵⁴, D. Brett⁵⁴, J. Brodzicka⁵⁴, L. Capriotti⁵⁴, S. Chen⁵⁴, S. De Capua⁵⁴, G. Dujany⁵⁴, M. Gersabeck⁵⁴, J. Harrison⁵⁴, C. Hornbach⁵⁴, S. Klaver⁵⁴, G. Lafferty⁵⁴, A. McNab⁵⁴, C. Parkes⁵⁴, A. Pearce⁵⁴, S. Reichert⁵⁴, E. Rodrigues⁵⁴, P. Rodriguez Perez⁵⁴, M. Smith⁵⁴, S.-F. Cheung⁵⁵, D. Derkach⁵⁵, T. Evans⁵⁵, R. Gauld⁵⁵, E. Greening⁵⁵, N. Harnwell⁵⁵, D. Hill⁵⁵, P. Hunt⁵⁵, N. Hussain⁵⁵, J. Jalocha⁵⁵, M. John⁵⁵, O. Lupton⁵⁵, S. Malde⁵⁵, E. Smith⁵⁵, S. Stevenson⁵⁵, C. Thomas⁵⁵, S. Topp-Joergensen⁵⁵, N. Torr⁵⁵, G. Wilkinson^{55,38}, I. Counts⁵⁶, P. Iten⁵⁶, M. Williams⁵⁶, R. Andressen⁵⁷, A. Davis⁵⁷, W. De Silva⁵⁷, B. Meadows⁵⁷, W.M. Sokoloff⁵⁷, L. Sun⁵⁷, J. Todd⁵⁷, J.E. Andrews⁵⁸, B. Hamilton⁵⁸, A. Jawahery⁵⁸, J. Wimmerly⁵⁸, M. Artuso⁵⁹, S. Blusk⁵⁹, A. Borgia⁵⁹, T. Britton⁵⁹, S. El⁵⁹, P. Gandini⁵⁹, J. Garofalo⁵⁹, B. Gui⁵⁹, C. Hadjivasiliou⁵⁹, N. Jurik⁵⁹, M. Kelsey⁵⁹, R. Mountain⁵⁹, B.K. Pal⁵⁹, T. Skwarnicki⁵⁹, S. Stone⁵⁹, J. Wang⁵⁹, Z. Xing⁵⁹, L. Zhang⁵⁹, C. Baesso⁶⁰, M. Cruz Torres⁶⁰, C. Göbel⁶⁰, J. Molina Rodriguez⁶⁰, Y. Xie⁶¹, D.A. Milanes⁶², O. Grünberg⁶³, M. Heß⁶³, C. Voß⁶³, R. Waldi⁶³, T. Likhomanenko⁶⁴, A. Malinin⁶⁴, V. Shevchenko⁶⁴, A. Ustyuzhanin⁶⁴, F. Martinez Vidal⁶⁵, A. Oyangueren⁶⁵, P. Ruiz Valls⁶⁵, C. Sanchez Mayordomo⁶⁵, C.J.G. Onderwater⁶⁶, H.W. Wilschut⁶⁶ & E. Pesen⁶⁷

Primary affiliations

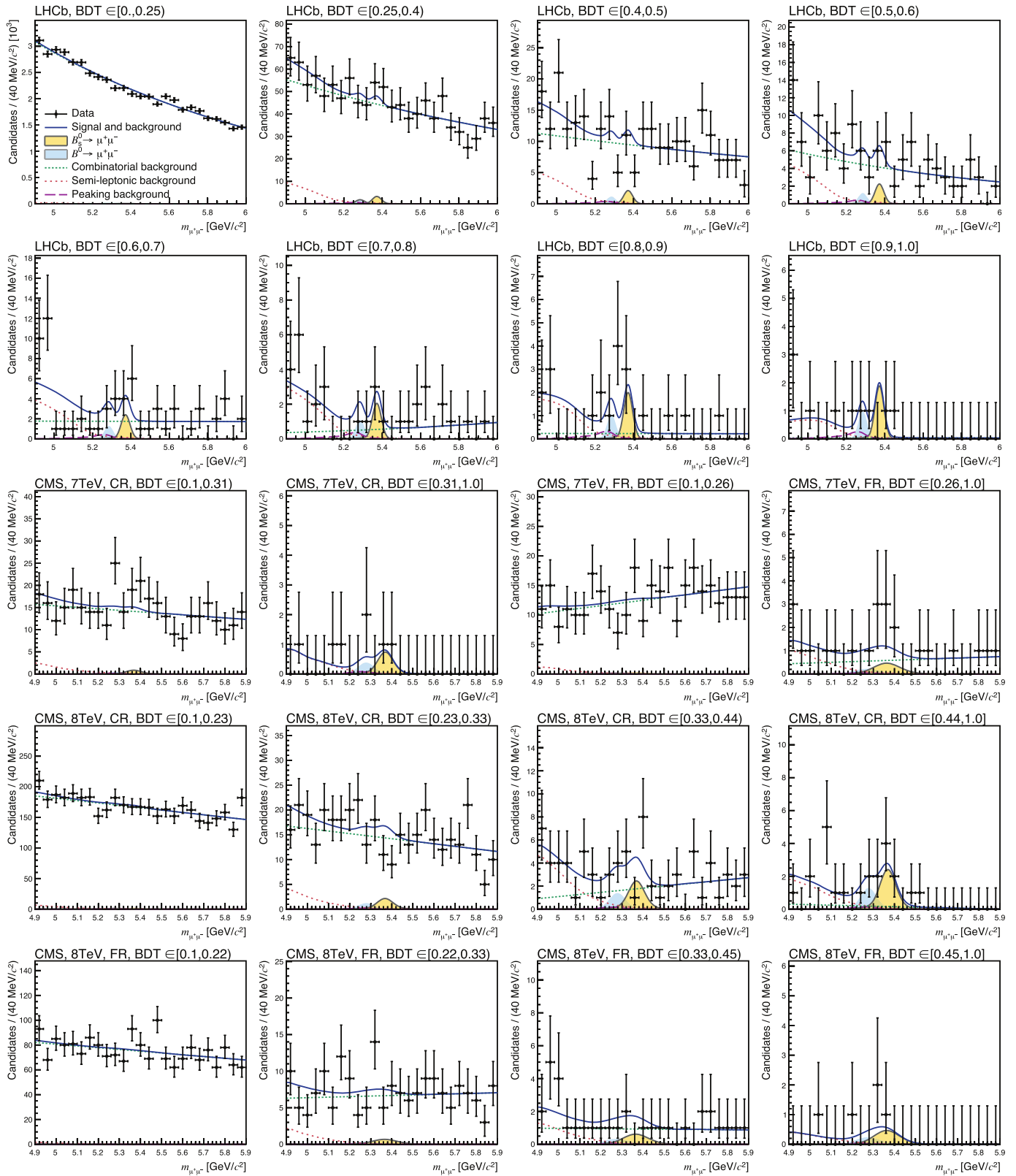
¹Centro Brasileiro de Pesquisas Físicas (CBPF), Rio de Janeiro, Brazil. ²Universidade Federal do Rio de Janeiro (UFRJ), Rio de Janeiro, Brazil. ³Center for High Energy Physics, Tsinghua University, Beijing, China. ⁴LAPP, Université de Savoie, CNRS/IN2P3, Annecy-Le-Vieux, France. ⁵Clermont Université, Université Blaise Pascal, CNRS/IN2P3, LPC, Clermont-Ferrand, France. ⁶CPPM, Aix-Marseille Université, CNRS/IN2P3, Marseille,

France. ⁷LAL, Université Paris-Sud, CNRS/IN2P3, Orsay, France. ⁸LPNHE, Université Pierre et Marie Curie, Université Paris Diderot, CNRS/IN2P3, Paris, France. ⁹Fakultät Physik, Technische Universität Dortmund, Dortmund, Germany. ¹⁰Max-Planck-Institut für Kernphysik (MPIK), Heidelberg, Germany. ¹¹Physikalisches Institut, Ruprecht-Karls-Universität Heidelberg, Heidelberg, Germany. ¹²School of Physics, University College Dublin, Dublin, Ireland. ¹³Sezione INFN di Bari, Bari, Italy. ¹⁴Sezione INFN di Bologna, Bologna, Italy. ¹⁵Sezione INFN di Cagliari, Cagliari, Italy. ¹⁶Sezione INFN di Ferrara, Ferrara, Italy. ¹⁷Sezione INFN di Firenze, Firenze, Italy. ¹⁸Laboratori Nazionali dell'INFN di Frascati, Frascati, Italy. ¹⁹Sezione INFN di Genova, Genova, Italy. ²⁰Sezione INFN di Milano Bicocca, Milano, Italy. ²¹Sezione INFN di Milano, Milano, Italy. ²²Sezione INFN di Padova, Padova, Italy. ²³Sezione INFN di Pisa, Pisa, Italy. ²⁴Sezione INFN di Roma Tor Vergata, Roma, Italy. ²⁵Sezione INFN di Roma La Sapienza, Roma, Italy. ²⁶Henryk Niewodniczanski Institute of Nuclear Physics Polish Academy of Sciences, Kraków, Poland. ²⁷AGH - University of Science and Technology, Faculty of Physics and Applied Computer Science, Kraków, Poland. ²⁸National Center for Nuclear Research (NCBJ), Warsaw, Poland. ²⁹Horia Hulubei National Institute of Physics and Nuclear Engineering, Bucharest-Magurele, Romania. ³⁰Petersburg Nuclear Physics Institute (PNPI), Gatchina, Russia. ³¹Institute of Theoretical and Experimental Physics (ITEP), Moscow, Russia. ³²Institute of Nuclear Physics, Moscow State University (SINP MSU), Moscow, Russia. ³³Institute for Nuclear Research of the Russian Academy of Sciences (INR RAN), Moscow, Russia. ³⁴Budker Institute of Nuclear Physics (SB RAS) and Novosibirsk State University, Novosibirsk, Russia. ³⁵Institute for High Energy Physics (IHEP), Protvino, Russia. ³⁶Universitat de Barcelona, Barcelona, Spain. ³⁷Universidad de Santiago de Compostela, Santiago de Compostela, Spain. ³⁸European Organization for Nuclear Research (CERN), Geneva, Switzerland. ³⁹Ecole Polytechnique Fédérale de Lausanne (EPFL), Lausanne, Switzerland. ⁴⁰Physik-Institut, Universität Zürich, Zürich, Switzerland. ⁴¹Nikhef National Institute for Subatomic Physics, Amsterdam, The Netherlands. ⁴²Nikhef National Institute for Subatomic Physics and VU University Amsterdam, Amsterdam, The Netherlands. ⁴³NSC Kharkiv Institute of Physics and Technology (NSC KIPT), Kharkiv, Ukraine. ⁴⁴Institute for Nuclear Research of the National Academy of Sciences (KINR), Kyiv, Ukraine. ⁴⁵University of Birmingham, Birmingham, United Kingdom. ⁴⁶H.H. Wills Physics Laboratory, University of Bristol, Bristol, United Kingdom. ⁴⁷Cavendish Laboratory, University of Cambridge, Cambridge, United Kingdom. ⁴⁸Department of Physics, University of Warwick, Coventry, United Kingdom. ⁴⁹STFC Rutherford Appleton Laboratory, Didcot, United Kingdom. ⁵⁰School of Physics and Astronomy, University of Edinburgh, Edinburgh, United Kingdom. ⁵¹School of Physics and Astronomy, University of Glasgow, Glasgow, United Kingdom. ⁵²Oliver Lodge

Laboratory, University of Liverpool, Liverpool, United Kingdom. ⁵³Imperial College London, London, United Kingdom. ⁵⁴School of Physics and Astronomy, University of Manchester, Manchester, United Kingdom. ⁵⁵Department of Physics, University of Oxford, Oxford, United Kingdom. ⁵⁶Massachusetts Institute of Technology, Cambridge, MA, United States. ⁵⁷University of Cincinnati, Cincinnati, OH, United States. ⁵⁸University of Maryland, College Park, MD, United States. ⁵⁹Syracuse University, Syracuse, NY, United States. ⁶⁰Pontificia Universidade Católica do Rio de Janeiro (PUC-Rio), Rio de Janeiro, Brazil; Universidade Federal do Rio de Janeiro (UFRJ), Rio de Janeiro, Brazil. ⁶¹Institute of Particle Physics, Central China Normal University, Wuhan, Hubei, China; Center for High Energy Physics, Tsinghua University, Beijing, China. ⁶²Departamento de Física, Universidad Nacional de Colombia, Bogotá, Colombia; LPNHE, Université Pierre et Marie Curie, Université Paris Diderot, CNRS/IN2P3, Paris, France. ⁶³Institut für Physik, Universität Rostock, Rostock, Germany; Physikalisches Institut, Ruprecht-Karls-Universität Heidelberg, Heidelberg, Germany. ⁶⁴National Research Centre Kurchatov Institute, Moscow, Russia; Institute of Theoretical and Experimental Physics (ITEP), Moscow, Russia. ⁶⁵Instituto de Física Corpuscular (IFIC), Universitat de Valencia-CSIC, Valencia, Spain; Universitat de Barcelona, Barcelona, Spain. ⁶⁶Van Swinderen Institute, University of Groningen, Groningen, The Netherlands; Nikhef National Institute for Subatomic Physics, Amsterdam, The Netherlands. ⁶⁷Celal Bayar University, Manisa, Turkey; European Organization for Nuclear Research (CERN), Geneva, Switzerland.

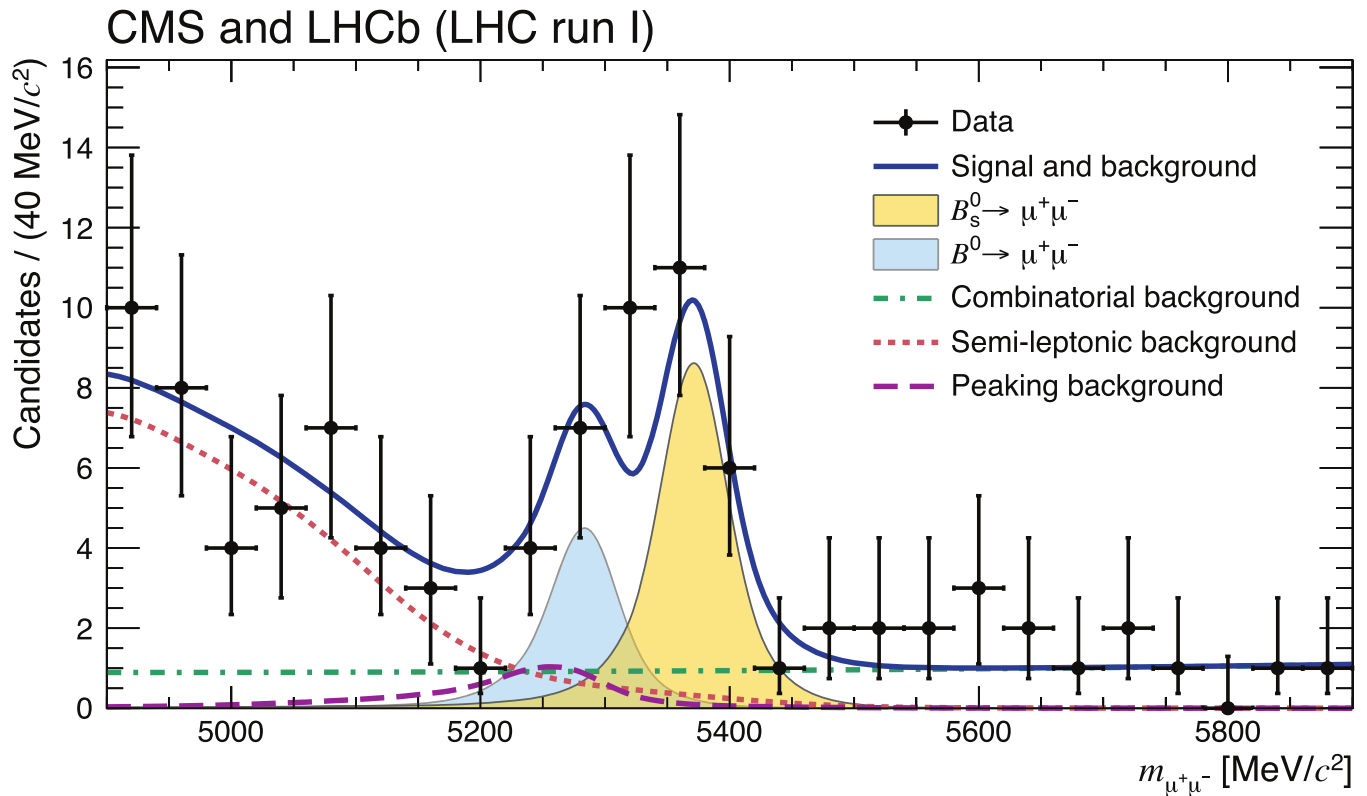
Secondary affiliations

⁶⁸Università di Firenze, Firenze, Italy. ⁶⁹Università di Ferrara, Ferrara, Italy. ⁷⁰Università della Basilicata, Potenza, Italy. ⁷¹Università di Modena e Reggio Emilia, Modena, Italy. ⁷²Università di Milano Bicocca, Milano, Italy. ⁷³LIFAELS, La Salle, Universitat Ramon Llull, Barcelona, Spain. ⁷⁴Università di Bologna, Bologna, Italy. ⁷⁵Università di Roma Tor Vergata, Roma, Italy. ⁷⁶Università di Genova, Genova, Italy. ⁷⁷Scuola Normale Superiore, Pisa, Italy. ⁷⁸Politecnico di Milano, Milano, Italy. ⁷⁹Universidade Federal do Triângulo Mineiro (UFMT), Uberaba-MG, Brazil. ⁸⁰AGH - University of Science and Technology, Faculty of Computer Science, Electronics and Telecommunications, Kraków, Poland. ⁸¹Università di Padova, Padova, Italy. ⁸²Università di Cagliari, Cagliari, Italy. ⁸³Hanoi University of Science, Hanoi, Viet Nam. ⁸⁴Università di Bari, Bari, Italy. ⁸⁵Università degli Studi di Milano, Milano, Italy. ⁸⁶Università di Roma La Sapienza, Roma, Italy. ⁸⁷Università di Pisa, Pisa, Italy. ⁸⁸Università di Urbino, Urbino, Italy. ⁸⁹P.N. Lebedev Physical Institute, Russian Academy of Science (LPI RAS), Moscow, Russia.



Extended Data Figure 1 | Distribution of the dimuon invariant mass $m_{\mu^+\mu^-}$ in each of the 20 categories. Superimposed on the data points in black are the combined fit (solid blue) and its components: the B_s^0 (yellow shaded) and B^0 (light-blue shaded) signal components; the combinatorial background (dash-dotted green); the sum of the semi-leptonic backgrounds (dotted salmon); and the peaking backgrounds (dashed violet). The categories are defined by the

range of BDT values for LHCb, and for CMS, by centre-of-mass energy, by the region of the detector in which the muons are detected, and by the range of BDT values. Categories for which both muons are detected in the central region of the CMS detector are denoted with CR, those for which at least one muon was detected into the forward region with FR.



Extended Data Figure 2 | Distribution of the dimuon invariant mass $m_{\mu^+\mu^-}$ for the best six categories. Categories are ranked according to values of $S/(S+B)$ where S and B are the numbers of signal events expected assuming the SM rates and background events under the B_s^0 peak for a given category, respectively. The mass distribution for the six highest-ranking categories, three

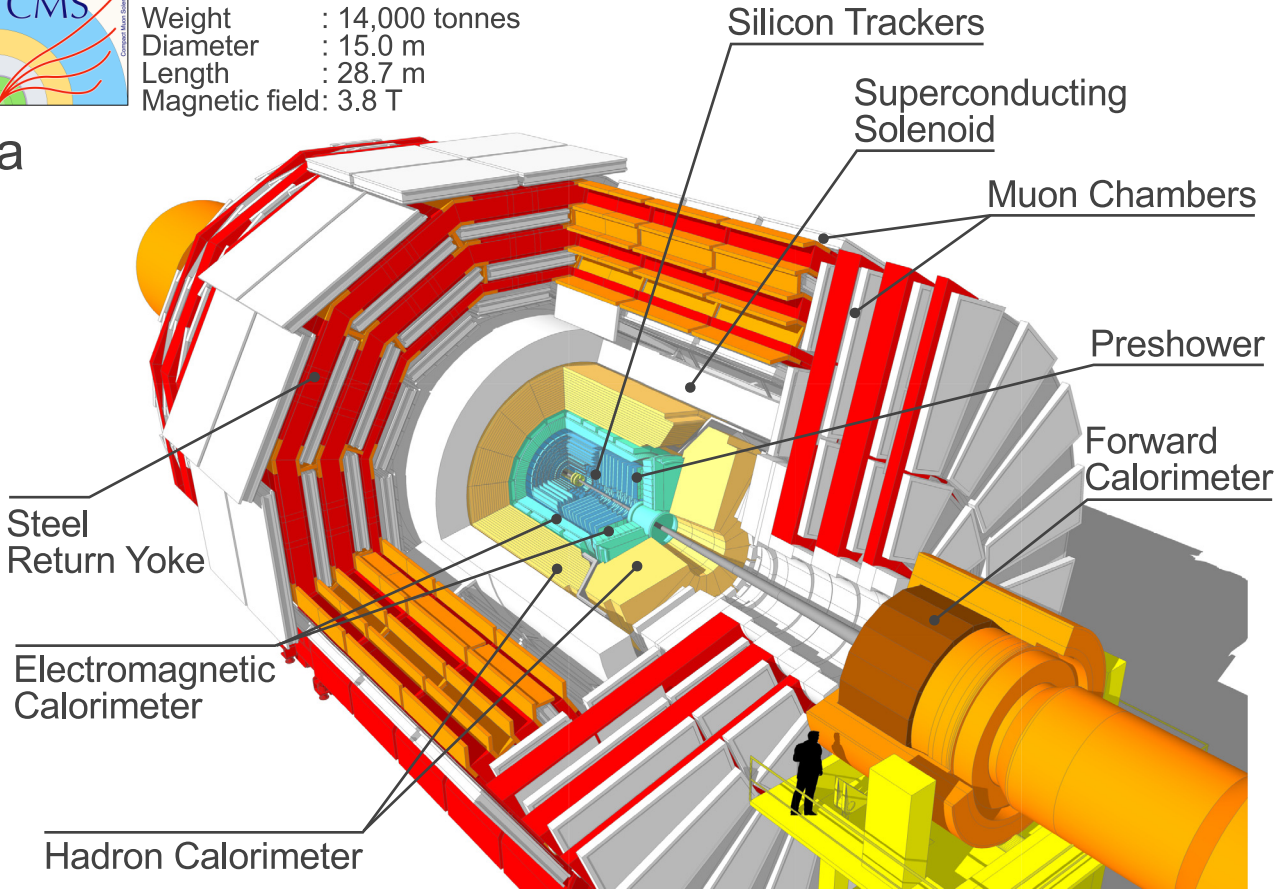
per experiment, is shown. Superimposed on the data points in black are the combined full fit (solid blue) and its components: the B_s^0 (yellow shaded) and B^0 (light-blue shaded) signal components; the combinatorial background (dash-dotted green); the sum of the semi-leptonic backgrounds (dotted salmon); and the peaking backgrounds (dashed violet).



CMS Detector

Weight : 14,000 tonnes
 Diameter : 15.0 m
 Length : 28.7 m
 Magnetic field: 3.8 T

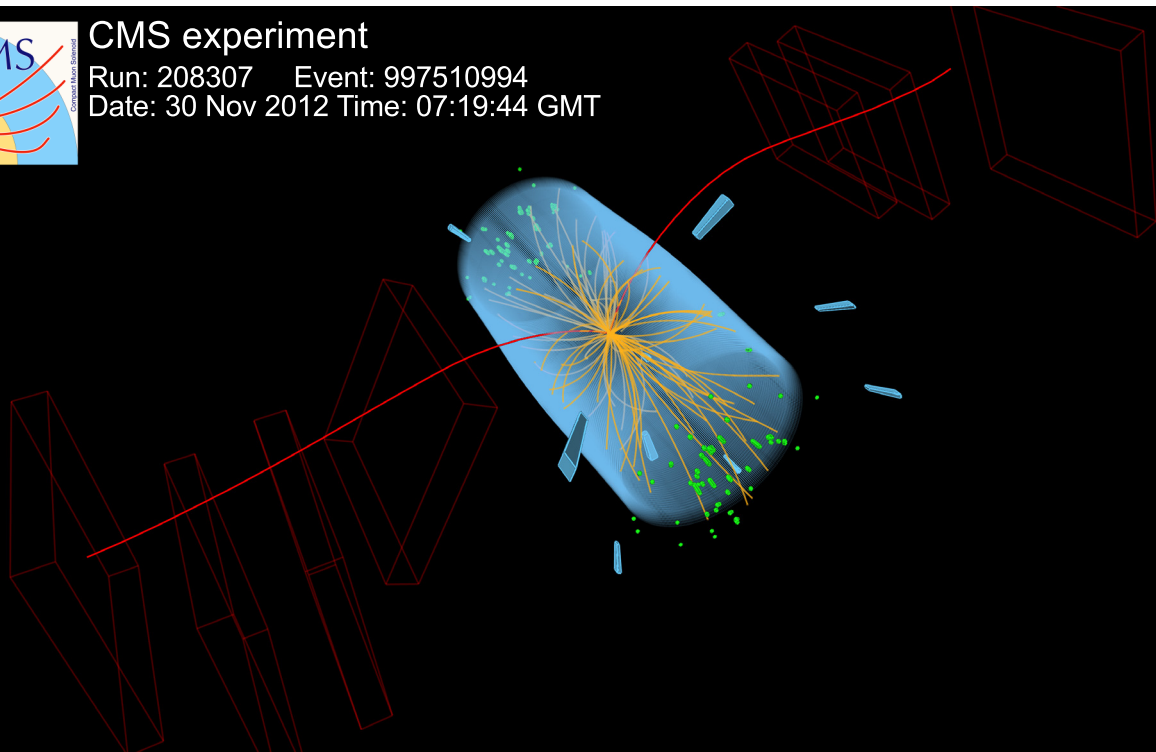
a



CMS experiment

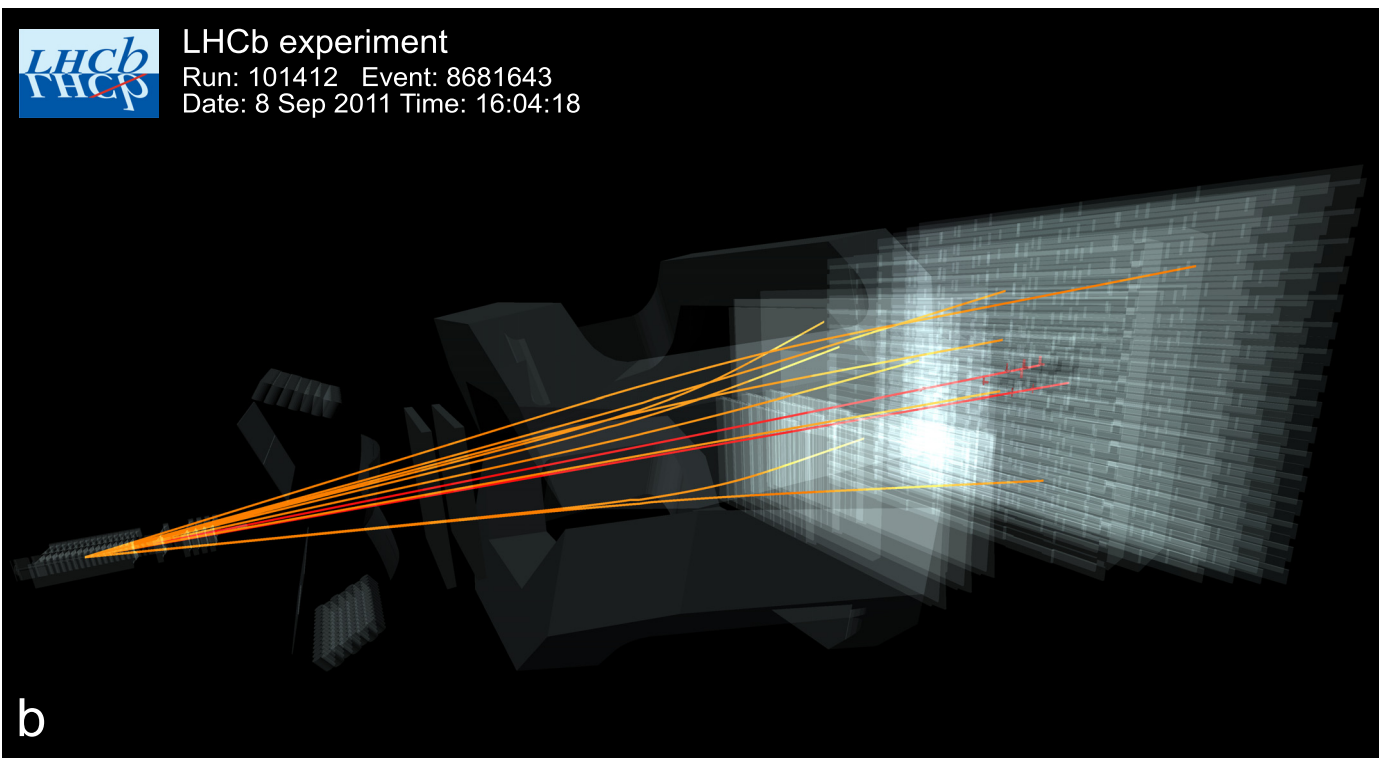
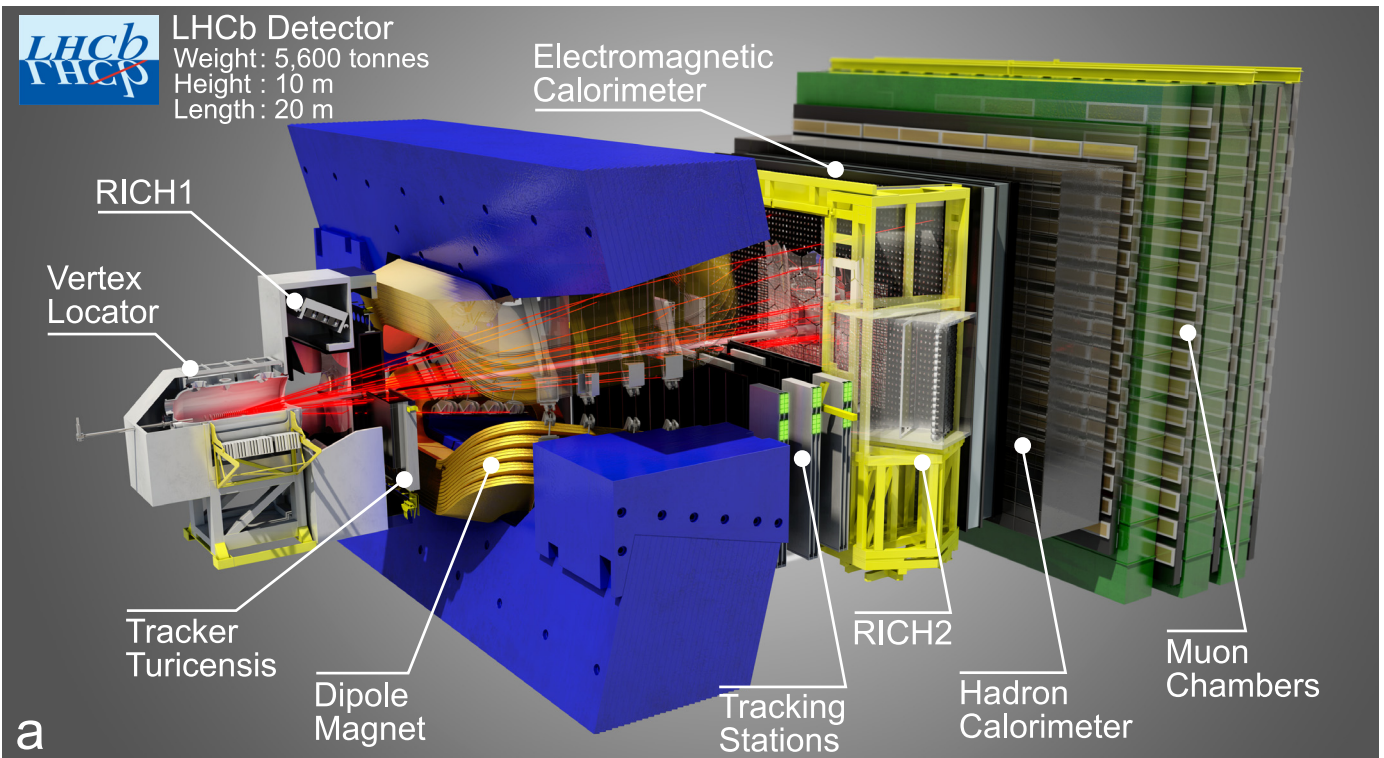
Run: 208307 Event: 997510994
 Date: 30 Nov 2012 Time: 07:19:44 GMT

b



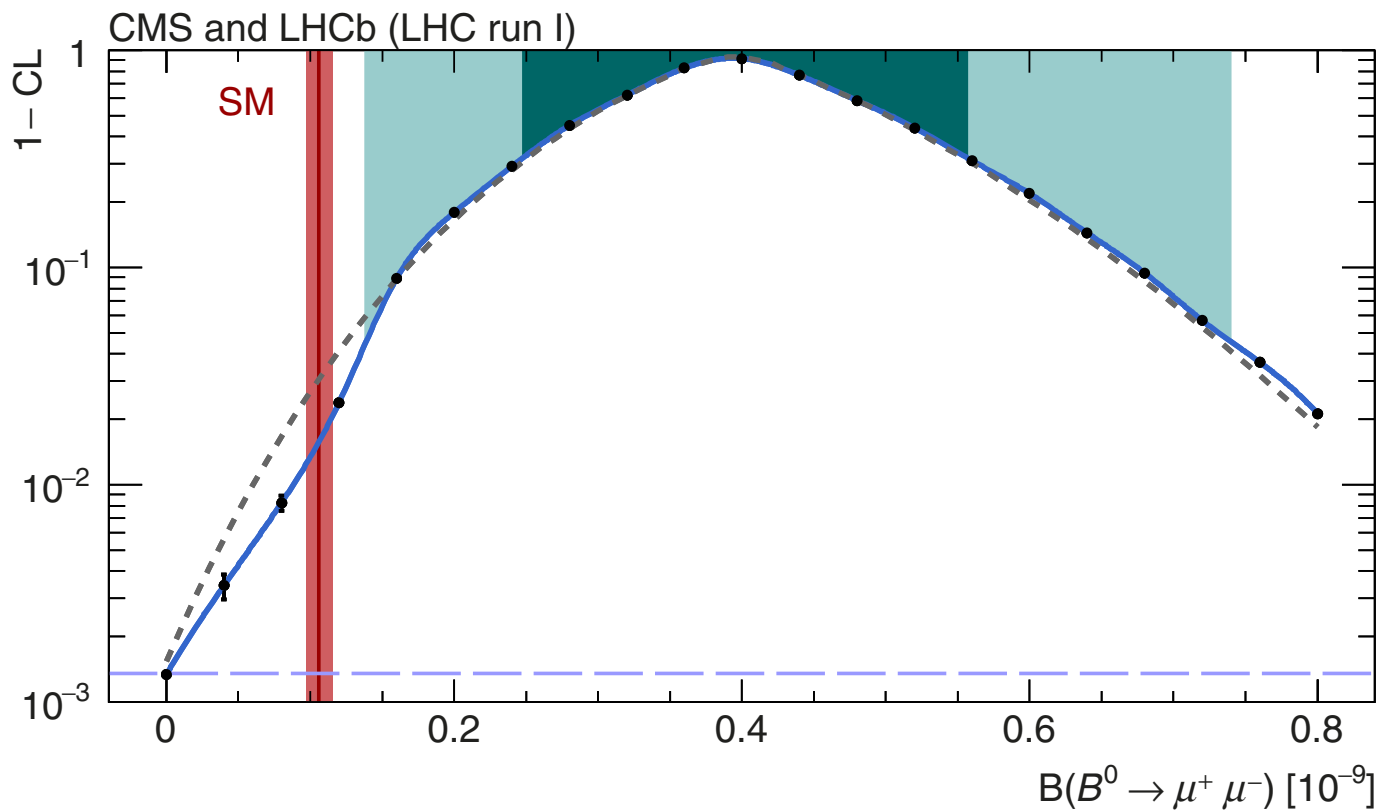
Extended Data Figure 3 | Schematic of the CMS detector and event display for a candidate $B_s^0 \rightarrow \mu^+ \mu^-$ decay at CMS. **a**, The CMS detector and its components; see ref. 20 for details. **b**, A candidate $B_s^0 \rightarrow \mu^+ \mu^-$ decay produced

in proton–proton collisions at 8 TeV in 2012 and recorded in the CMS detector. The red arched curves represent the trajectories of the muons from the B_s^0 decay candidate.



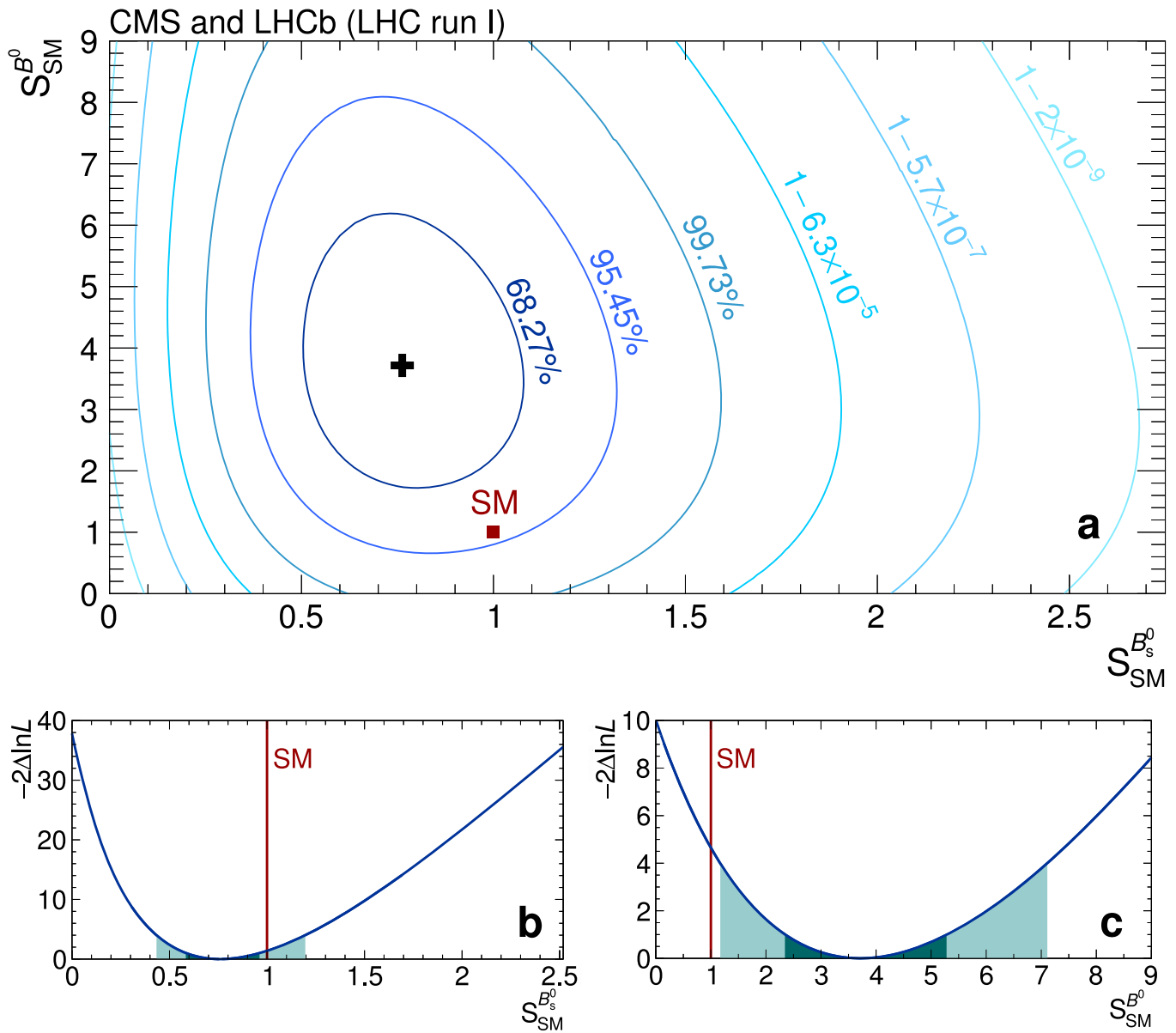
Extended Data Figure 4 | Schematic of the LHCb detector and event display for a candidate $B_s^0 \rightarrow \mu^+ \mu^-$ decay at LHCb. **a**, The LHCb detector and its components; see ref. 21 for details. **b**, A candidate $B_s^0 \rightarrow \mu^+ \mu^-$ decay produced in proton–proton collisions at 7 TeV in 2011 and recorded in the LHCb

detector. The proton–proton collision occurs on the left-hand side, at the origin of the trajectories depicted with the orange curves. The red curves represent the trajectories of the muons from the B_s^0 candidate decay.



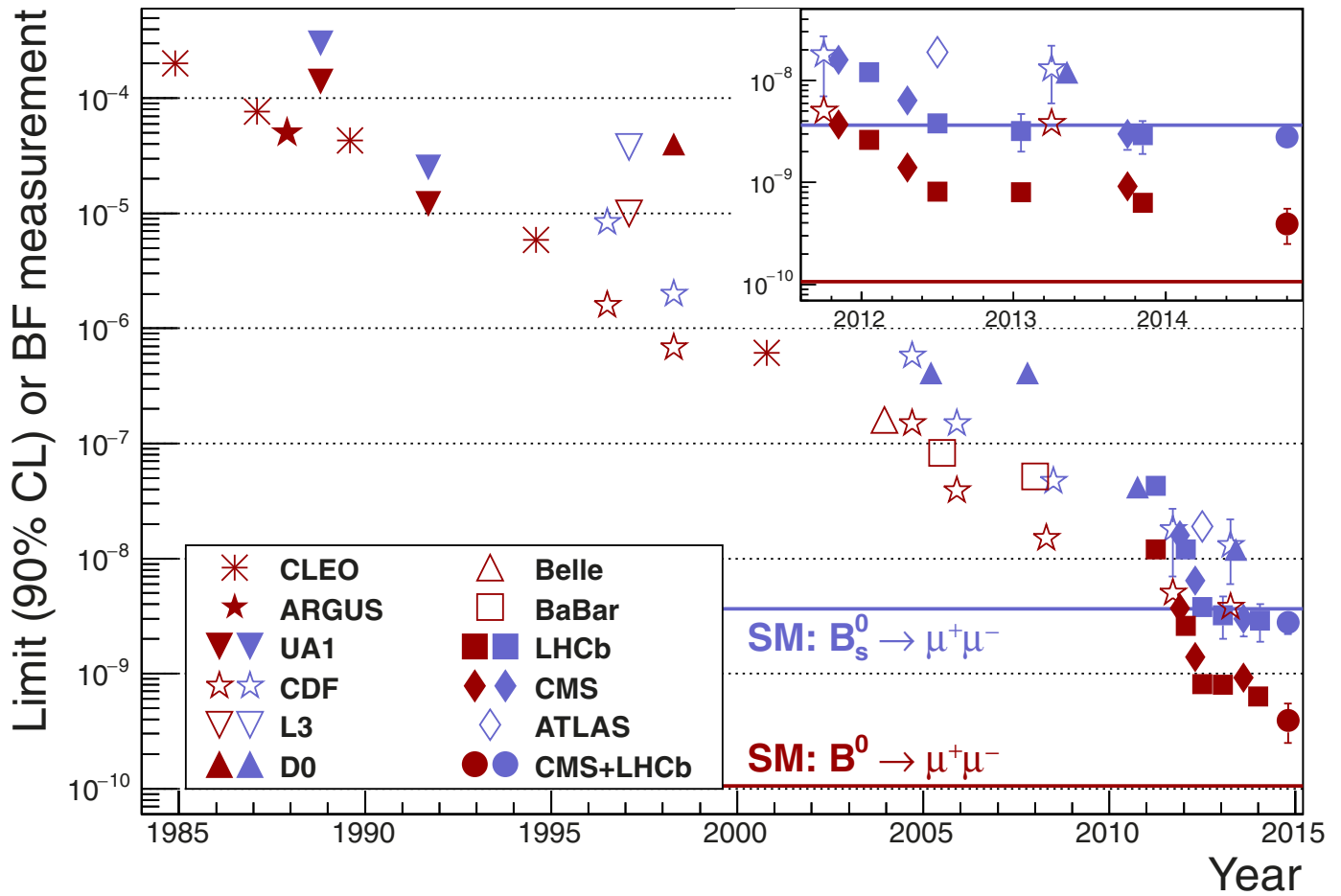
Extended Data Figure 5 | Confidence level as a function of the $B(B^0 \rightarrow \mu^+ \mu^-)$ hypothesis. The value of $1 - \text{CL}$, where CL is the confidence level obtained with the Feldman–Cousins procedure, as a function of $B(B^0 \rightarrow \mu^+ \mu^-)$ is shown in logarithmic scale. The points mark the computed $1 - \text{CL}$ values and the curve is their spline interpolation. The dark and light (cyan) areas define the two-sided $\pm 1\sigma$ and $\pm 2\sigma$ confidence intervals for the branching fraction, while

the dashed horizontal line defines the confidence level for the 3σ one-sided interval. The dashed (grey) curve shows the $1 - \text{CL}$ values computed from the one-dimensional $-2\Delta\ln L$ test statistic using Wilks’ theorem. Deviations between these confidence level values and those from the Feldman–Cousins procedure³⁰ illustrate the degree of approximation implied by the asymptotic assumptions inherent to Wilks’ theorem²⁹.



Extended Data Figure 6 | Likelihood contours for the ratios of the branching fractions with respect to their SM prediction, in the $S_{SM}^{B_s^0}$ versus $S_{SM}^{B^0}$ plane. **a**, The (black) cross marks the central value returned by the fit. The SM point is shown as the (red) square located, by construction, at $S_{SM}^{B_s^0} = S_{SM}^{B^0} = 1$. Each contour encloses a region approximately corresponding to the reported confidence level. The SM branching fractions are assumed

uncorrelated to each other, and their uncertainties are accounted for in the likelihood contours. **b**, **c**, Variations of the test statistic $-2\Delta\ln L$ for $S_{SM}^{B_s^0}$ and $S_{SM}^{B^0}$ are shown in **b** and **c**, respectively. The SM is represented by the (red) vertical lines. The dark and light (cyan) areas define the $\pm 1\sigma$ and $\pm 2\sigma$ confidence intervals, respectively.



Extended Data Figure 7 | Search for the $B_s^0 \rightarrow \mu^+\mu^-$ and $B^0 \rightarrow \mu^+\mu^-$ decays, reported by 11 experiments spanning more than three decades, and by the present results. Markers without error bars denote upper limits on the branching fractions at 90% confidence level, while measurements are denoted with error bars delimiting 68% confidence intervals. The solid horizontal lines

represent the SM predictions for the $B_s^0 \rightarrow \mu^+\mu^-$ and $B^0 \rightarrow \mu^+\mu^-$ branching fractions¹; the blue (red) lines and markers relate to the $B_s^0 \rightarrow \mu^+\mu^-$ ($B^0 \rightarrow \mu^+\mu^-$) decay. Data (see key) are from refs 17, 18, 31–60; for details see Methods. Inset, magnified view of the last period in time.

EUROPEAN ORGANIZATION FOR NUCLEAR RESEARCH

CERN-PH-EP/2013-022

arXiv:1302.3415 [hep-ex]

February 14th, 2013

**Electroweak Measurements in
Electron-Positron Collisions
at W-Boson-Pair Energies at LEP**

**The ALEPH Collaboration
The DELPHI Collaboration
The L3 Collaboration
The OPAL Collaboration
The LEP Electroweak Working Group¹**

Submitted to PHYSICS REPORTS

February 14th, 2013

¹ Web access at <http://www.cern.ch/LEPEWWG>

Abstract

Electroweak measurements performed with data taken at the electron-positron collider LEP at CERN from 1995 to 2000 are reported. The combined data set considered in this report corresponds to a total luminosity of about 3 fb^{-1} collected by the four LEP experiments ALEPH, DELPHI, L3 and OPAL, at centre-of-mass energies ranging from 130 GeV to 209 GeV.

Combining the published results of the four LEP experiments, the measurements include total and differential cross-sections in photon-pair, fermion-pair and four-fermion production, the latter resulting from both double-resonant WW and ZZ production as well as singly resonant production. Total and differential cross-sections are measured precisely, providing a stringent test of the Standard Model at centre-of-mass energies never explored before in electron-positron collisions. Final-state interaction effects in four-fermion production, such as those arising from colour reconnection and Bose-Einstein correlations between the two W decay systems arising in WW production, are searched for and upper limits on the strength of possible effects are obtained. The data are used to determine fundamental properties of the W boson and the electroweak theory. Among others, the mass and width of the W boson, m_W and Γ_W , the branching fraction of W decays to hadrons, $B(W \rightarrow \text{had})$, and the trilinear gauge-boson self-couplings g_1^Z , κ_γ and λ_γ are determined to be:

$$\begin{aligned} m_W &= 80.376 \pm 0.033 \text{ GeV} \\ \Gamma_W &= 2.195 \pm 0.083 \text{ GeV} \\ B(W \rightarrow \text{had}) &= 67.41 \pm 0.27 \% \\ g_1^Z &= 0.984_{-0.020}^{+0.018} \\ \kappa_\gamma &= 0.982 \pm 0.042 \\ \lambda_\gamma &= -0.022 \pm 0.019. \end{aligned}$$

Keywords: Electron-positron physics, electroweak interactions, decays of heavy intermediate gauge bosons, fermion-antifermion production, precision measurements at W-pair energies, tests of the Standard Model, radiative corrections, effective coupling constants, neutral weak current, Z boson, W boson, top quark, Higgs boson.

PACS: 12.15.-y, 13.38.-b, 13.66.-a, 14.60.-z, 14.65.-q, 14.70.-e, 14.80.-j.

Author Lists

The ALEPH, DELPHI, L3, OPAL collaborations have provided the inputs for the combined results presented in this Report. The LEP Electroweak Working Group has performed the combinations. The Working Group consists of members of the four LEP collaborations. The lists of authors from the collaborations follow.

The ALEPH Collaboration

S. Schael,¹ R. Barate,² R. Brunelière,² D. Buskulic,² I. De Bonis,² D. Decamp,² P. Ghez,² C. Goy,² S. Jézéquel,² J.-P. Lees,² A. Lucotte,² F. Martin,² E. Merle,² M.-N. Minard,² J.-Y. Nief,² P. Odier,² B. Pietrzyk,² B. Trocmé,² S. Bravo,³ M.P. Casado,³ M. Chmeissani,³ P. Comas,³ J.M. Crespo,³ E. Fernandez,³ M. Fernandez-Bosman,³ Ll. Garrido,^{3,a15} E. Grauges,³ A. Juste,³ M. Martinez,³ G. Merino,³ R. Miquel,³ Ll.M. Mir,³ S. Orteu,³ A. Pacheco,³ I.C. Park,³ J. Perlas,³ I. Riu,³ H. Ruiz,³ F. Sanchez,³ A. Colaleo,⁴ D. Creanza,⁴ N. De Filippis,⁴ M. de Palma,⁴ G. Iaselli,⁴ G. Maggi,⁴ M. Maggi,⁴ S. Nuzzo,⁴ A. Ranieri,⁴ G. Raso,^{4,a24} F. Ruggieri,⁴ G. Selvaggi,⁴ L. Silvestris,⁴ P. Tempesta,⁴ A. Tricomi,^{4,a3} G. Zito,⁴ X. Huang,⁵ J. Lin,⁵ Q. Ouyang,⁵ T. Wang,⁵ Y. Xie,⁵ R. Xu,⁵ S. Xue,⁵ J. Zhang,⁵ L. Zhang,⁵ W. Zhao,⁵ D. Abbaneo,⁶ A. Bazarko,⁶ U. Becker,⁶ G. Boix,^{6,a33} F. Bird,⁶ E. Blucher,⁶ B. Bonvicini,⁶ P. Bright-Thomas,⁶ T. Barklow,^{6,a26} O. Buchmüller,^{6,a26} M. Cattaneo,⁶ F. Cerutti,⁶ V. Ciulli,⁶ B. Clerbaux,^{6,a23} H. Drevermann,⁶ R.W. Forty,⁶ M. Frank,⁶ T.C. Greening,⁶ R. Hagelberg,⁶ A.W. Halley,⁶ F. Gianotti,⁶ M. Girone,⁶ J.B. Hansen,⁶ J. Harvey,⁶ R. Jacobsen,⁶ D.E. Hutchcroft,^{6,a30} P. Janot,⁶ B. Jost,⁶ J. Knobloch,⁶ M. Kado,^{6,a26} I. Lehraus,⁶ P. Lazeyras,⁶ P. Maley,⁶ P. Mato,⁶ J. May,⁶ A. Moutoussi,⁶ M. Pepe-Altarelli,⁶ F. Ranjard,⁶ L. Rolandi,⁶ D. Schlatter,⁶ B. Schmitt,⁶ O. Schneider,⁶ W. Tejessy,⁶ F. Teubert,⁶ I.R. Tomalin,⁶ E. Tournefier,⁶ R. Veenhof,⁶ A. Valassi,⁶ W. Wiedenmann,⁶ A.E. Wright,⁶ Z. Ajaltouni,⁷ F. Badaud,⁷ G. Chazelle,⁷ O. Deschamps,⁷ S. Dessagne,⁷ A. Falvard,^{7,a20} C. Ferdi,⁷ D. Fayolle,⁷ P. Gay,⁷ C. Guicheney,⁷ P. Henrard,⁷ J. Jousset,⁷ B. Michel,⁷ S. Monteil,⁷ J.C. Montret,⁷ D. Pallin,⁷ J.M. Pascolo,⁷ P. Perret,⁷ F. Podlyski,⁷ H. Bertelsen,⁸ T. Fernley,⁸ J.D. Hansen,⁸ J.R. Hansen,⁸ P.H. Hansen,⁸ A.C. Kraan,⁸ A. Lindahl,⁸ R. Mollerud,⁸ B.S. Nilsson,⁸ B. Rensch,⁸ A. Waananen,⁸ G. Daskalakis,⁹ A. Kyriakis,⁹ C. Markou,⁹ E. Simopoulou,⁹ I. Siotis,⁹ A. Vayaki,⁹ K. Zachariadou,⁹ A. Blondel,^{10,a12} G. Bonneaud,¹⁰ J.-C. Brient,¹⁰ F. Machefert,¹⁰ A. Rougé,¹⁰ M. Rumpf,¹⁰ M. Swynghedauw,¹⁰ R. Tanaka,¹⁰ M. Verderi,¹⁰ H. Videau,¹⁰ V. Ciulli,¹¹ E. Focardi,¹¹ G. Parrini,¹¹ K. Zachariadou,¹¹ M. Corden,¹² C. Georgiopoulos,¹² A. Antonelli,¹³ M. Antonelli,¹³ G. Bencivenni,¹³ G. Bologna,^{13,a34} F. Bossi,¹³ P. Campana,¹³ G. Capon,¹³ F. Cerutti,¹³ V. Chiarella,¹³ G. Felici,¹³ P. Laurelli,¹³ G. Mannocchi,^{13,a5} G.P. Murtas,¹³ L. Passalacqua,¹³ P. Picchi,¹³ P. Colrain,¹⁴ I. ten Have,¹⁴ I.S. Hughes,¹⁴ J. Kennedy,¹⁴ I.G. Knowles,¹⁴ J.G. Lynch,¹⁴ W.T. Morton,¹⁴ P. Negus,¹⁴ V. O'Shea,¹⁴ C. Raine,¹⁴ P. Reeves,¹⁴ J.M. Scarr,¹⁴ K. Smith,¹⁴ A.S. Thompson,¹⁴ R.M. Turnbull,¹⁴ S. Wasserbaech,¹⁵ O. Buchmüller,¹⁶ R. Cavanaugh,^{16,a4} S. Dhamotharan,^{16,a21} C. Geweniger,¹⁶ P. Hanke,¹⁶ G. Hansper,¹⁶ V. Hepp,¹⁶ E.E. Kluge,¹⁶

A. Putzer,¹⁶ J. Sommer,¹⁶ H. Stenzel,¹⁶ K. Tittel,¹⁶ W. Werner,¹⁶ M. Wunsch,^{16,a19} R. Beuselinck,¹⁷
 D.M. Binnie,¹⁷ W. Cameron,¹⁷ G. Davies,¹⁷ P.J. Dornan,¹⁷ S. Goodsir,¹⁷ N. Marinelli,¹⁷
 E.B. Martin,¹⁷ J. Nash,¹⁷ J. Nowell,¹⁷ S.A. Rutherford,¹⁷ J.K. Sedgbeer,¹⁷ J.C. Thompson,^{17,a14}
 R. White,¹⁷ M.D. Williams,¹⁷ V.M. Ghete,¹⁸ P. Girtler,¹⁸ E. Kneringer,¹⁸ D. Kuhn,¹⁸
 G. Rudolph,¹⁸ E. Bouhova-Thacker,¹⁹ C.K. Bowdery,¹⁹ P.G. Buck,¹⁹ D.P. Clarke,¹⁹ G. Ellis,¹⁹
 A.J. Finch,¹⁹ F. Foster,¹⁹ G. Hughes,¹⁹ R.W.L. Jones,¹⁹ N.R. Keemer,¹⁹ M.R. Pearson,¹⁹
 N.A. Robertson,¹⁹ T. Sloan,¹⁹ M. Smizanska,¹⁹ S.W. Snow,¹⁹ M.I. Williams,¹⁹ O. van der Aa,²⁰
 C. Delaere,^{20,a28} G. Leibenguth,^{20,a31} V. Lemaître,^{20,a29} L.A.T. Bauerdick,²¹ U. Blumenschein,²¹
 P. van Gemmeren,²¹ I. Giehl,²¹ F. Hölldorfer,²¹ K. Jakobs,²¹ M. Kasemann,²¹ F. Kayser,²¹
 K. Kleinknecht,²¹ A.-S. Müller,²¹ G. Quast,²¹ B. Renk,²¹ E. Rohne,²¹ H.-G. Sander,²¹
 S. Schmeling,²¹ H. Wachsmuth,²¹ R. Wanke,²¹ C. Zeitnitz,²¹ T. Ziegler,²¹ J.J. Aubert,²²
 C. Benchouk,²² A. Bonissent,²² J. Carr,²² P. Coyle,²² C. Curtil,²² A. Ealet,²² F. Etienne,²²
 D. Fouchez,²² F. Motsch,²² P. Payre,²² D. Rousseau,²² A. Tilquin,²² M. Talby,²² M. Thulasidas,²²
 M. Aleppo,²³ M. Antonelli,²³ F. Ragusa,²³ V. Büscher,²⁴ A. David,²⁴ H. Dietl,^{24,a32} G. Ganis,^{24,a27}
 K. Hüttmann,²⁴ G. Lütjens,²⁴ C. Mannert,²⁴ W. Männer,^{24,a32} H.-G. Moser,²⁴ R. Settles,²⁴
 H. Seywerd,²⁴ H. Stenzel,²⁴ M. Villegas,²⁴ W. Wiedenmann,²⁴ G. Wolf,²⁴ P. Azzurri,²⁵ J. Boucrot,²⁵
 O. Callot,²⁵ S. Chen,²⁵ A. Cordier,²⁵ M. Davier,²⁵ L. Duflot,²⁵ J.-F. Grivaz,²⁵ Ph. Heusse,²⁵
 A. Jacholkowska,^{25,a6} F. Le Diberder,²⁵ J. Lefrançois,²⁵ A.M. Mutz,²⁵ M.H. Schune,²⁵ L. Serin,²⁵
 J.-J. Veillet,²⁵ I. Videau,²⁵ D. Zerwas,²⁵ P. Azzurri,²⁶ G. Bagliesi,²⁶ S. Bettarini,²⁶ T. Boccali,²⁶
 C. Bozzi,²⁶ G. Calderini,²⁶ R. Dell’Orso,²⁶ R. Fantechi,²⁶ I. Ferrante,²⁶ F. Fidecaro,²⁶ L. Foà,²⁶
 A. Giammanco,²⁶ A. Giassi,²⁶ A. Gregorio,²⁶ F. Ligabue,²⁶ A. Lusiani,²⁶ P.S. Marrocchesi,²⁶
 A. Messineo,²⁶ F. Palla,²⁶ G. Rizzo,²⁶ G. Sanguinetti,²⁶ A. Sciabà,²⁶ G. Sguazzoni,²⁶ P. Spagnolo,²⁶
 J. Steinberger,²⁶ R. Tenchini,²⁶ C. Vannini,²⁶ A. Venturi,²⁶ P.G. Verdini,²⁶ O. Awunor,²⁷
 G.A. Blair,²⁷ G. Cowan,²⁷ A. Garcia-Bellido,²⁷ M.G. Green,²⁷ T. Medcalf,²⁷ A. Misiejuk,²⁷
 J.A. Strong,²⁷ P. Teixeira-Dias,²⁷ D.R. Botterill,²⁸ R.W. Clift,²⁸ T.R. Edgecock,²⁸ M. Edwards,²⁸
 S.J. Haywood,²⁸ P.R. Norton,²⁸ I.R. Tomalin,²⁸ J.J. Ward,²⁸ B. Bloch-Devau,²⁹ D. Boumediene,²⁹
 P. Colas,²⁹ S. Emery,²⁹ B. Fabbro,²⁹ W. Kozanecki,²⁹ E. Lançon,²⁹ M.-C. Lemaire,²⁹ E. Locci,²⁹
 P. Perez,²⁹ J. Rander,²⁹ J.F. Renardy,²⁹ A. Roussarie,²⁹ J.P. Schuller,²⁹ J. Schwindling,²⁹
 B. Tuchming,²⁹ B. Vallage,²⁹ S.N. Black,³⁰ J.H. Dann,³⁰ H.Y. Kim,³⁰ N. Konstantinidis,³⁰
 A.M. Litke,³⁰ M.A. McNeil,³⁰ G. Taylor,³⁰ C.N. Booth,³¹ S. Cartwright,³¹ F. Combley,^{31,a25}
 P.N. Hodgson,³¹ M. Lehto,³¹ L.F. Thompson,³¹ K. Affholderbach,³² E. Barberio,³² A. Böhrer,³²
 S. Brandt,³² H. Burkhardt,³² E. Feigl,³² C. Grupen,³² J. Hess,³² G. Lutters,³² H. Meinhard,³²
 J. Minguet-Rodriguez,³² L. Mirabito,³² A. Misiejuk,³² E. Neugebauer,³² A. Ngac,³² G. Prange,³²
 F. Rivera,³² P. Saraiva,³² U. Schäfer,³² U. Sieler,³² L. Smolik,³² F. Stephan,³² H. Trier,³²
 M. Apollonio,³³ C. Borean,³³ L. Bosisio,³³ R. Della Marina,³³ G. Giannini,³³ B. Gobbo,³³
 G. Musolino,³³ L. Pitis,³³ H. He,³⁴ H. Kim,³⁴ J. Putz,³⁴ J. Rothberg,³⁴ S.R. Armstrong,³⁵
 L. Bellantoni,³⁵ K. Berkelman,³⁵ D. Cinabro,³⁵ J.S. Conway,³⁵ K. Cranmer,³⁵ P. Elmer,³⁵ Z. Feng,³⁵
 D.P.S. Ferguson,³⁵ Y. Gao,^{35,a13} S. González,³⁵ J. Grahl,³⁵ J.L. Harton,³⁵ O.J. Hayes,³⁵ H. Hu,³⁵
 S. Jin,³⁵ R.P. Johnson,³⁵ J. Kile,³⁵ P.A. McNamara III,³⁵ J. Nielsen,³⁵ W. Orejudos,³⁵ Y.B. Pan,³⁵
 Y. Saadi,³⁵ I.J. Scott,³⁵ V. Sharma,³⁵ A.M. Walsh,³⁵ J. Walsh,³⁵ J. Wear,³⁵
 J.H. von Wimmersperg-Toeller,³⁵ W. Wiedenmann,³⁵ J. Wu,³⁵ S.L. Wu,³⁵ X. Wu,³⁵
 J.M. Yamartino,³⁵ G. Zobernig,³⁵ G. Dissertori.³⁶

¹ Physikalisches Institut der RWTH-Aachen, D-52056 Aachen, Germany

² Laboratoire de Physique des Particules (LAPP), IN²P³-CNRS, F-74019
Annecy-le-Vieux Cedex, France

³ Institut de Física d’Altes Energies, Universitat Autònoma de Barcelona, E-08193
Bellaterra (Barcelona), Spain^{a7}

- ⁴ Dipartimento di Fisica, INFN Sezione di Bari, I-70126 Bari, Italy
- ⁵ Institute of High Energy Physics, Academia Sinica, Beijing, The People's Republic of China^{a8}
- ⁶ European Laboratory for Particle Physics (CERN), CH-1211 Geneva 23, Switzerland
- ⁷ Laboratoire de Physique Corpusculaire, Université Blaise Pascal, IN²P³-CNRS, Clermont-Ferrand, F-63177 Aubière, France
- ⁸ Niels Bohr Institute, 2100 Copenhagen, DK-Denmark^{a9}
- ⁹ Nuclear Research Center Demokritos (NRC), GR-15310 Attiki, Greece
- ¹⁰ Laboratoire Leprince-Ringuet, Ecole Polytechnique, IN²P³-CNRS, F-91128 Palaiseau Cedex, France
- ¹¹ Dipartimento di Fisica, Università di Firenze, INFN Sezione di Firenze, I-50125 Firenze, Italy
- ¹² Supercomputer Computations Research Institute, Florida State University, Tallahassee, FL-32306-4052, USA
- ¹³ Laboratori Nazionali dell'INFN (LNF-INFN), I-00044 Frascati, Italy
- ¹⁴ Department of Physics and Astronomy, University of Glasgow, Glasgow G12 8QQ, United Kingdom^{a10}
- ¹⁵ Utah Valley State College, Orem, UT 84058, U.S.A.
- ¹⁶ Kirchhoff-Institut für Physik, Universität Heidelberg, D-69120 Heidelberg, Germany^{a16}
- ¹⁷ Department of Physics, Imperial College, London SW7 2BZ, United Kingdom^{a10}
- ¹⁸ Institut für Experimentalphysik, Universität Innsbruck, A-6020 Innsbruck, Austria^{a18}
- ¹⁹ Department of Physics, University of Lancaster, Lancaster LA1 4YB, United Kingdom^{a10}
- ²⁰ Institut de Physique Nucléaire, Département de Physique, Université Catholique de Louvain, 1348 Louvain-la-Neuve, Belgium
- ²¹ Institut für Physik, Universität Mainz, D-55099 Mainz, Germany^{a16}
- ²² Centre de Physique des Particules de Marseille, Univ Méditerranée, IN²P³-CNRS, F-13288 Marseille, France
- ²³ Dipartimento di Fisica, Università di Milano e INFN Sezione di Milano, I-20133 Milano, Italy.
- ²⁴ Max-Planck-Institut für Physik, Werner-Heisenberg-Institut, D-80805 München, Germany^{a16}
- ²⁵ Laboratoire de l'Accélérateur Linéaire, Université de Paris-Sud, IN²P³-CNRS, F-91898 Orsay Cedex, France
- ²⁶ Dipartimento di Fisica dell'Università, INFN Sezione di Pisa, e Scuola Normale Superiore, I-56010 Pisa, Italy
- ²⁷ Department of Physics, Royal Holloway & Bedford New College, University of London, Egham, Surrey TW20 OEX, United Kingdom^{a10}
- ²⁸ Particle Physics Dept., Rutherford Appleton Laboratory, Chilton, Didcot, Oxon OX11 0QX, United Kingdom^{a10}
- ²⁹ CEA, DAPNIA/Service de Physique des Particules, CE-Saclay, F-91191 Gif-sur-Yvette Cedex, France^{a17}
- ³⁰ Institute for Particle Physics, University of California at Santa Cruz, Santa Cruz, CA 95064, USA^{a22}
- ³¹ Department of Physics, University of Sheffield, Sheffield S3 7RH, United Kingdom^{a10}
- ³² Fachbereich Physik, Universität Siegen, D-57068 Siegen, Germany^{a16}

- ³³ Dipartimento di Fisica, Università di Trieste e INFN Sezione di Trieste, I-34127 Trieste, Italy
- ³⁴ Experimental Elementary Particle Physics, University of Washington, Seattle, WA 98195 U.S.A.
- ³⁵ Department of Physics, University of Wisconsin, Madison, WI 53706, USA^{a11}
- ³⁶ Institute for Particle Physics, ETH Hönggerberg, 8093 Zürich, Switzerland.
- ^{a1} Also at CERN, 1211 Geneva 23, Switzerland.
- ^{a2} Now at Fermilab, PO Box 500, MS 352, Batavia, IL 60510, USA
- ^{a3} Also at Dipartimento di Fisica di Catania and INFN Sezione di Catania, 95129 Catania, Italy.
- ^{a4} Now at University of Florida, Department of Physics, Gainesville, Florida 32611-8440, USA
- ^{a5} Also IFSI sezione di Torino, INAF, Italy.
- ^{a6} Also at Groupe d'Astroparticules de Montpellier, Université de Montpellier II, 34095, Montpellier, France.
- ^{a7} Supported by CICYT, Spain.
- ^{a8} Supported by the National Science Foundation of China.
- ^{a9} Supported by the Danish Natural Science Research Council.
- ^{a10} Supported by the UK Particle Physics and Astronomy Research Council.
- ^{a11} Supported by the US Department of Energy, grant DE-FG0295-ER40896.
- ^{a12} Now at Departement de Physique Corpusculaire, Université de Genève, 1211 Genève 4, Switzerland.
- ^{a13} Also at Department of Physics, Tsinghua University, Beijing, The People's Republic of China.
- ^{a14} Supported by the Leverhulme Trust.
- ^{a15} Permanent address: Universitat de Barcelona, 08208 Barcelona, Spain.
- ^{a16} Supported by Bundesministerium für Bildung und Forschung, Germany.
- ^{a17} Supported by the Direction des Sciences de la Matière, C.E.A.
- ^{a18} Supported by the Austrian Ministry for Science and Transport.
- ^{a19} Now at SAP AG, 69185 Walldorf, Germany
- ^{a20} Now at Groupe d' Astroparticules de Montpellier, Université de Montpellier II, 34095 Montpellier, France.
- ^{a21} Now at BNP Paribas, 60325 Frankfurt am Mainz, Germany
- ^{a22} Supported by the US Department of Energy, grant DE-FG03-92ER40689.
- ^{a23} Now at Institut Inter-universitaire des hautes Energies (IIHE), CP 230, Université Libre de Bruxelles, 1050 Bruxelles, Belgique
- ^{a24} Now at Dipartimento di Fisica e Tecnologia Relative, Università di Palermo, Palermo, Italy.
- ^{a25} Deceased.
- ^{a26} Now at SLAC, Stanford, CA 94309, U.S.A
- ^{a27} Now at CERN, 1211 Geneva 23, Switzerland
- ^{a28} Research Fellow of the Belgium FNRS
- ^{a29} Research Associate of the Belgium FNRS
- ^{a30} Now at Liverpool University, Liverpool L69 7ZE, United Kingdom
- ^{a31} Supported by the Federal Office for Scientific, Technical and Cultural Affairs through the Interuniversity Attraction Pole P5/27

^{a32} Now at Henryk Niewodnicznski Institute of Nuclear Physics, Polish Academy of Sciences, Cracow, Poland

^{a33} Supported by the Commission of the European Communities, contract ERBFMBICT982894

^{a34} Also Istituto di Fisica Generale, Università di Torino, 10125 Torino, Italy

The DELPHI Collaboration

J. Abdallah,²⁷ P. Abreu,²⁴ W. Adam,⁵⁶ P. Adzic,¹³ T. Albrecht,¹⁹ R. Alemany-Fernandez,¹⁰ T. Allmendinger,¹⁹ P.P. Allport,²⁵ U. Amaldi,³¹ N. Amapane,⁴⁹ S. Amato,⁵³ E. Anashkin,³⁸ A. Andreatza,³⁰ S. Andringa,²⁴ N. Anjos,²⁴ P. Antilogus,²⁷ W-D. Apel,¹⁹ Y. Arnoud,¹⁶ S. Ask,¹⁰ B. Asman,⁴⁸ J.E. Augustin,²⁷ A. Augustinus,¹⁰ P. Baillon,¹⁰ A. Ballestrero,⁵⁰ P. Bambade,²² R. Barbier,²⁹ D. Bardin,¹⁸ G.J. Barker,⁵⁸ A. Baroncelli,⁴¹ M. Battaglia,¹⁰ M. Baubillier,²⁷ K-H. Becks,⁵⁹ M. Begalli,⁸ A. Behrmann,⁵⁹ K. Belous,⁴⁴ E. Ben-Haim,²⁷ N. Benekos,³⁴ A. Benvenuti,⁶ C. Berat,¹⁶ M. Berggren,²⁷ L. Berntzon,⁴⁸ D. Bertrand,³ M. Besancon,⁴² N. Besson,⁴² D. Bloch,¹¹ M. Blom,³³ M. Bluj,⁵⁷ M. Bonesini,³¹ M. Boonekamp,⁴² P.S.L. Booth[†],²⁵ G. Borisov,²³ O. Botner,⁵⁴ B. Bouquet,²² T.J.V. Bowcock,²⁵ I. Boyko,¹⁸ M. Bracko,⁴⁵ R. Brenner,⁵⁴ E. Brodet,³⁷ P. Bruckman,²⁰ J.M. Brunet,⁹ L. Bugge,³⁵ B. Buschbeck,⁵⁶ P. Buschmann,⁵⁹ M. Calvi,³¹ T. Camporesi,¹⁰ V. Canale,⁴⁰ F. Carena,¹⁰ N. Castro,²⁴ F. Cavallo,⁶ M. Chapkin,⁴⁴ Ph. Charpentier,¹⁰ P. Checchia,³⁸ R. Chierici,²⁹ P. Chliapnikov,⁴⁴ J. Chudoba,¹⁴ K. Cieslik,²⁰ P. Collins,¹⁰ R. Contri,¹⁵ G. Cosme,²² F. Cossutti,⁵¹ M.J. Costa,⁵⁵ B. Crawley,¹ D. Crennell,³⁹ J. Cuevas,³⁶ J. D'Hondt,³ J. Dalmau,⁴⁸ T. da Silva,⁵³ W. Da Silva,²⁷ G. Della Ricca,⁵¹ A. De Angelis,⁵² W. De Boer,¹⁹ C. De Clercq,³ B. De Lotto,⁵² N. De Maria,⁴⁹ A. De Min,³⁸ L. de Paula,⁵³ L. Di Ciaccio,⁴⁰ A. Di Simone,⁴⁰ K. Doroba,⁵⁷ J. Drees,⁵⁹ M. Dris,³⁴ A. Duperrin,²⁹ G. Eigen,⁵ T. Ekelof,⁵⁴ M. Ellert,⁵⁴ M. Elsing,¹⁰ M.C. Espirito Santo,²⁴ G. Fanourakis,¹³ D. Fassouliotis,^{13,4} M. Feindt,¹⁹ J. Fernandez,⁴³ A. Ferrer,⁵⁵ F. Ferro,¹⁵ U. Flagmeyer,⁵⁹ H. Foeth,¹⁰ E. Fokitis,³⁴ F. Fulda-Quenzer,²² J. Fuster,⁵⁵ M. Gandelman,⁵³ C. Garcia,⁵⁵ Ph. Gavillet,¹⁰ E. Gazis,³⁴ D. Gele,¹¹ R. Gokieli[†],⁵⁷ B. Golob,^{45,47} G. Gomez-Ceballos,⁴³ P. Gonçaves,²⁴ E. Graziani,⁴¹ G. Grosdidier,²² K. Grzelak,⁵⁷ J. Guy,³⁹ C. Haag,¹⁹ A. Hallgren,⁵⁴ K. Hamacher,⁵⁹ K. Hamilton,³⁷ S. Haug,³⁵ F. Hauler,¹⁹ V. Hedberg,²⁸ M. Henneke,¹⁹ H. Herr[†],¹⁰ J. Hoffman,⁵⁷ S-O. Holmgren,⁴⁸ P.J. Holt,¹⁰ M.A. Houlden,²⁵ K. Hultqvist,⁴⁸ J.N. Jackson,²⁵ G. Jarlskog,²⁸ P. Jarry,⁴² D. Jeans,³⁷ E.K. Johansson,⁴⁸ P.D. Johansson,⁴⁸ P. Jonsson,²⁹ C. Joram,¹⁰ L. Jungermann,¹⁹ F. Kapusta,²⁷ S. Katsanevas,²⁹ E. Katsoufis,³⁴ G. Kernel,⁴⁵ B.P. Kersevan,^{45,47} U. Kerzel,¹⁹ A. Kiiskinen,¹⁷ B.T. King,²⁵ N.J. Kjaer,¹⁰ P. Kluit,³³ P. Kokkinias,¹³ V. Kostioukhine,¹⁵ C. Kourkoumelis,⁴ O. Kouznetsov,¹⁸ Z. Krumstein,¹⁸ M. Kucharczyk,²⁰ J. Lamsa,¹ G. Leder,⁵⁶ F. Ledroit,¹⁶ L. Leinonen,⁴⁸ R. Leitner,³² J. Lemonne,³ V. Lepeltier[†],²² T. Lesiak,²⁰ J. Libby,³⁷ W. Liebig,⁵⁹ D. Liko,⁵⁶ A. Lipniacka,⁵ J.H. Lopes,⁵³ J.M. Lopez,³⁶ D. Loukas,¹³ P. Lutz,⁴² L. Lyons,³⁷ J. MacNaughton,⁵⁶ A. Malek,⁵⁹ S. Maltezos,³⁴ F. Mandl,⁵⁶ J. Marco,⁴³ R. Marco,⁴³ B. Marechal,⁵³ M. Margoni,³⁸ J-C. Marin,¹⁰ C. Mariotti,¹⁰ A. Markou,¹³ C. Martinez-Rivero,⁴³ J. Masik,¹⁴ N. Mastroiannopoulos,¹³ F. Matorras,⁴³ C. Matteuzzi,³¹ F. Mazzucato,³⁸ M. Mazzucato,³⁸ R. Mc Nulty,²⁵ C. Meroni,³⁰ W.T. Meyer,¹ E. Migliore,⁴⁹ W. Mitaroff,⁵⁶ U. Mjoernmark,²⁸ T. Moa,⁴⁸ M. Moch,¹⁹ K. Moenig,¹² R. Monge,¹⁵ J. Montenegro,³³ D. Moraes,⁵³ P. Morettini,¹⁵ U. Mueller,⁵⁹ K. Muenich,⁵⁹ M. Mulders,³³ L. Mundim,⁸ W. Murray,³⁹ B. Muryn,²¹ G. Myatt,³⁷ T. Myklebust,³⁵ M. Nassiakou,¹³ F. Navarria,⁶ K. Nawrocki,⁵⁷ S. Nemecek,¹⁴ R. Nicolaidou,⁴² V. Nikolaenko,¹¹ M. Nikolenko,^{18,11} A. Oblakowska-Mucha,²¹ V. Obraztsov,⁴⁴ A. Olshevski,¹⁸ A. Onofre,²⁴ R. Orava,¹⁷ K. Osterberg,¹⁷ A. Ouraou,⁴² A. Oyanguren,⁵⁵ M. Paganoni,³¹ S. Paiano,⁶ J.P. Palacios,²⁵ H. Palka[†],²⁰ Th.D. Papadopoulou,³⁴

L. Pape,¹⁰ C. Parkes,²⁶ F. Parodi,¹⁵ U. Parzefall,¹⁰ A. Passeri,⁴¹ O. Passon,⁵⁹ V. Perepelitsa,⁵⁵ A. Perrotta,⁶ A. Petrolini,¹⁵ J. Piedra,⁴³ L. Pieri,³⁸ F. Pierre[†],⁴² M. Pimenta,²⁴ T. Podobnik,^{45,47} V. Poireau,¹⁰ M.E. Pol,⁷ G. Polok,²⁰ P. Poropat[†],⁵¹ V. Pozdniakov,¹⁸ N. Pukhaeva,¹⁸ A. Pullia,³¹ D. Radojicic,³⁷ J. Rames,¹⁴ L. Ramler,¹⁹ A. Read,³⁵ P. Rebecchi,¹⁰ J. Rehn,¹⁹ D. Reid,³³ R. Reinhardt,⁵⁹ P. Renton,³⁷ F. Richard,²² J. Ridky,¹⁴ I. Ripp-Baudot,¹¹ M. Rivero,⁴³ D. Rodriguez,⁴³ A. Romero,⁴⁹ P. Ronchese,³⁸ E. Rosenberg,¹ P. Roudeau,²² T. Rovelli,⁶ V. Ruhlmann-Kleider,⁴² D. Ryabtchikov,⁴⁴ A. Sadovsky,¹⁸ L. Salmi,¹⁷ J. Salt,⁵⁵ C. Sander,¹⁹ A. Savoy-Navarro,²⁷ U. Schwickerath,¹⁰ A. Segar[†],³⁷ R. Sekulin,³⁹ M. Siebel,⁵⁹ L. Simard,⁴² A. Sisakian[†],¹⁸ G. Smadja,²⁹ O. Smirnova,²⁸ A. Sokolov,⁴⁴ A. Sopczak,²³ R. Sosnowski,⁵⁷ T. Spassov,¹⁰ M. Stanitzki,¹⁹ A. Stocchi,²² J. Strauss,⁵⁶ B. Stugu,⁵ M. Szczekowski,⁵⁷ M. Szeptycka,⁵⁷ T. Szumlak,²¹ T. Tabarelli,³¹ A.C. Taffard,²⁵ F. Tegenfeldt,⁵⁴ F. Terranova,³¹ J. Thomas,³⁷ J. Timmermans,³³ L. Tkatchev,¹⁸ M. Tobin,⁶⁰ S. Todorovova,¹⁴ B. Tomé,²⁴ A. Tonazzo,³¹ P. Tortosa,⁵⁵ P. Travnicek,¹⁴ D. Treille,¹⁰ G. Tristram,⁹ M. Trochimczuk,⁵⁷ C. Troncon,³⁰ M-L. Turluer,⁴² I.A. Tyapkin,¹⁸ P. Tyapkin,¹⁸ S. Tzamarias,¹³ V. Uvarov,⁴⁴ G. Valenti,⁶ P. Van Dam,³³ J. Van Eldik,¹⁰ A. Van Lysebetten,³ N. van Remortel,² I. Van Vulpen,³³ G. Vegni,³⁰ F. Veloso,²⁴ W. Venus,³⁹ F. Verbeure[†],² P. Verdier,²⁹ V. Verzi,⁴⁰ D. Vilanova,⁴² L. Vitale,⁵¹ V. Vrba,¹⁴ H. Wahlen,⁵⁹ A.J. Washbrook,²⁵ C. Weiser,¹⁹ D. Wicke,⁵⁹ J. Wickens,³ G. Wilkinson,³⁷ M. Winter,¹¹ M. Witek,²⁰ O. Yushchenko,⁴⁴ A. Zalewska,²⁰ P. Zalewski,⁵⁷ D. Zavrtanik,⁴⁶ V. Zhuravlov,¹⁸ N.I. Zimin,¹⁸ A. Zintchenko,¹⁸ M. Zupan.¹³

¹ Department of Physics and Astronomy, Iowa State University, Ames IA 50011-3160, USA

² Physics Department, Universiteit Antwerpen, Universiteitsplein 1, B-2610 Antwerpen, Belgium

³ IIHE, ULB-VUB, Pleinlaan 2, B-1050 Brussels, Belgium

⁴ Physics Laboratory, University of Athens, Solonos Str. 104, GR-10680 Athens, Greece

⁵ Department of Physics, University of Bergen, Allégaten 55, NO-5007 Bergen, Norway

⁶ Dipartimento di Fisica, Università di Bologna and INFN, Viale C. Berti Pichat 6/2, IT-40127 Bologna, Italy

⁷ Centro Brasileiro de Pesquisas Físicas, rua Xavier Sigaud 150, BR-22290 Rio de Janeiro, Brazil

⁸ Inst. de Física, Univ. Estadual do Rio de Janeiro, rua São Francisco Xavier 524, Rio de Janeiro, Brazil

⁹ Collège de France, Lab. de Physique Corpusculaire, IN2P3-CNRS, FR-75231 Paris Cedex 05, France

¹⁰ CERN, CH-1211 Geneva 23, Switzerland

¹¹ Institut Pluridisciplinaire Hubert Curien, Université de Strasbourg, IN2P3-CNRS, BP28, FR-67037 Strasbourg Cedex 2, France

¹² Now at DESY-Zeuthen, Platanenallee 6, D-15735 Zeuthen, Germany

¹³ Institute of Nuclear Physics, N.C.S.R. Demokritos, P.O. Box 60228, GR-15310 Athens, Greece

¹⁴ FZU, Inst. of Phys. of the C.A.S. High Energy Physics Division, Na Slovance 2, CZ-182 21, Praha 8, Czech Republic

¹⁵ Dipartimento di Fisica, Università di Genova and INFN, Via Dodecaneso 33, IT-16146 Genova, Italy

¹⁶ Laboratoire de Physique Subatomique et de Cosmologie, Université Joseph Fourier Grenoble 1, CNRS/IN2P3, Institut Polytechnique de Grenoble, FR-38026 Grenoble Cedex, France

- ¹⁷ Helsinki Institute of Physics and Department of Physics, P.O. Box 64, FIN-00014
University of Helsinki, Finland
- ¹⁸ Joint Institute for Nuclear Research, Dubna, Head Post Office, P.O. Box 79, RU-101 000
Moscow, Russian Federation
- ¹⁹ Institut für Experimentelle Kernphysik, Universität Karlsruhe, Postfach 6980, DE-76128
Karlsruhe, Germany
- ²⁰ Institute of Nuclear Physics PAN, Ul. Radzikowskiego 152, PL-31142 Krakow, Poland
- ²¹ Faculty of Physics and Nuclear Techniques, University of Mining and Metallurgy,
PL-30055 Krakow, Poland
- ²² LAL, Univ Paris-Sud, CNRS/IN2P3, Orsay, France
- ²³ School of Physics and Chemistry, University of Lancaster, Lancaster LA1 4YB, UK
- ²⁴ LIP, IST, FCUL - Av. Elias Garcia, 14-1º, PT-1000 Lisboa Codex, Portugal
- ²⁵ Department of Physics, University of Liverpool, P.O. Box 147, Liverpool L69 3BX, UK
- ²⁶ Dept. of Physics and Astronomy, Kelvin Building, University of Glasgow, Glasgow G12
8QQ, UK
- ²⁷ LPNHE, IN2P3-CNRS, Univ. Paris VI et VII, 4 place Jussieu, FR-75252 Paris Cedex
05, France
- ²⁸ Department of Physics, University of Lund, Sölvegatan 14, SE-223 63 Lund, Sweden
- ²⁹ Université Claude Bernard de Lyon, IPNL, IN2P3-CNRS, FR-69622 Villeurbanne
Cedex, France
- ³⁰ Dipartimento di Fisica, Università di Milano and INFN-MILANO, Via Celoria 16,
IT-20133 Milan, Italy
- ³¹ Dipartimento di Fisica, Univ. di Milano-Bicocca and INFN-MILANO, Piazza della
Scienza 3, IT-20126 Milan, Italy
- ³² IPNP of MFF, Charles Univ., Areal MFF, V Holesovickach 2, CZ-180 00, Praha 8,
Czech Republic
- ³³ NIKHEF, Postbus 41882, NL-1009 DB Amsterdam, The Netherlands
- ³⁴ National Technical University, Physics Department, Zografou Campus, GR-15773
Athens, Greece
- ³⁵ Physics Department, University of Oslo, Blindern, NO-0316 Oslo, Norway
- ³⁶ Dpto. Fisica, Univ. Oviedo, Avda. Calvo Sotelo s/n, ES-33007 Oviedo, Spain
- ³⁷ Department of Physics, University of Oxford, Keble Road, Oxford OX1 3RH, UK
- ³⁸ Dipartimento di Fisica, Università di Padova and INFN, Via Marzolo 8, IT-35131
Padua, Italy
- ³⁹ Rutherford Appleton Laboratory, Chilton, Didcot OX11 0QX, UK
- ⁴⁰ Dipartimento di Fisica, Università di Roma II and INFN, Tor Vergata, IT-00173 Rome,
Italy
- ⁴¹ Dipartimento di Fisica, Università di Roma III and INFN, Via della Vasca Navale 84,
IT-00146 Rome, Italy
- ⁴² DAPNIA/Service de Physique des Particules, CEA-Saclay, FR-91191 Gif-sur-Yvette
Cedex, France
- ⁴³ Instituto de Fisica de Cantabria (CSIC-UC), Avda. los Castros s/n, ES-39006
Santander, Spain
- ⁴⁴ Institute for high energy physics, 142281 Protvino, Moscow region, Russian Federation
- ⁴⁵ J. Stefan Institute, Jamova 39, SI-1000 Ljubljana, Slovenia
- ⁴⁶ Laboratory for Astroparticle Physics, University of Nova Gorica, Kostanjevska 16a,
SI-5000 Nova Gorica, Slovenia

- ⁴⁷ Department of Physics, University of Ljubljana, SI-1000 Ljubljana, Slovenia
- ⁴⁸ Fysikum, Stockholm University, Box 6730, SE-113 85 Stockholm, Sweden
- ⁴⁹ Dipartimento di Fisica Sperimentale, Università di Torino and INFN, Via P. Giuria 1, IT-10125 Turin, Italy
- ⁵⁰ INFN, Sezione di Torino and Dipartimento di Fisica Teorica, Università di Torino, Via Giuria 1, IT-10125 Turin, Italy
- ⁵¹ Dipartimento di Fisica, Università di Trieste and INFN, Via A. Valerio 2, IT-34127 Trieste, Italy
- ⁵² Istituto di Fisica, Università di Udine and INFN, IT-33100 Udine, Italy
- ⁵³ Univ. Federal do Rio de Janeiro, C.P. 68528 Cidade Univ., Ilha do Fundão BR-21945-970 Rio de Janeiro, Brazil
- ⁵⁴ Department of Radiation Sciences, University of Uppsala, P.O. Box 535, SE-751 21 Uppsala, Sweden
- ⁵⁵ IFIC, Valencia-CSIC, and D.F.A.M.N., U. de Valencia, Avda. Dr. Moliner 50, ES-46100 Burjassot (Valencia), Spain
- ⁵⁶ Institut für Hochenergiephysik, Österr. Akad. d. Wissensch., Nikolsdorfergasse 18, AT-1050 Vienna, Austria
- ⁵⁷ Inst. Nuclear Studies and University of Warsaw, Ul. Hoza 69, PL-00681 Warsaw, Poland
- ⁵⁸ Now at University of Warwick, Coventry CV4 7AL, UK
- ⁵⁹ Fachbereich Physik, University of Wuppertal, Postfach 100 127, DE-42097 Wuppertal, Germany
- ⁶⁰ Now at Physik-Institut der Universität Zürich, Zürich, Switzerland
- † Deceased

The L3 Collaboration

P.Achard,²⁰ O.Adriani,¹⁷ M.Aguilar-Benitez,²⁵ J.Alcaraz,²⁵ G.Alemanni,²³ J.Allaby,¹⁸ A.Aloisio,²⁹ M.G.Alvigi,²⁹ H.Anderhub,⁴⁹ V.P.Andreev,^{6,34} F.Anselmo,⁸ A.Arefiev,²⁸ T.Azemoon,³ T.Aziz,⁹ P.Bagnaia,³⁹ A.Bajo,²⁵ G.Baksay,²⁶ L.Baksay,²⁶ S.V.Baldew,² S.Banerjee,⁹ Sw.Banerjee,⁴ A.Barczyk,^{49,47} R.Barillère,¹⁸ P.Bartalini,²³ M.Basile,⁸ N.Batalova,⁴⁶ R.Battiston,³³ A.Bay,²³ U.Becker,¹³ F.Behner,⁴⁹ L.Bellucci,¹⁷ R.Berbeco,³ J.Berdugo,²⁵ P.Berges,¹³ B.Bertucci,³³ B.L.Betev,⁴⁹ M.Biasini,³³ M.Biglietti,²⁹ A.Biland,⁴⁹ J.J.Blaising,⁴ S.C.Blyth,³⁵ G.J.Bobbink,² A.Böhm,¹ L.Boldizsar,¹² B.Borgia,³⁹ S.Bottai,¹⁷ D.Bourilkov,⁴⁹ M.Bourquin,²⁰ S.Braccini,²⁰ J.G.Branson,⁴¹ F.Brochu,⁴ J.D.Burger,¹³ W.J.Burger,³³ X.D.Cai,¹³ M.Capell,¹³ G.Cara Romeo,⁸ G.Carlino,²⁹ A.Cartacci,¹⁷ J.Casaus,²⁵ F.Cavallari,³⁹ N.Cavallo,³⁶ C.Cecchi,³³ M.Cerrada,²⁵ M.Chamizo,²⁰ Y.H.Chang,⁴⁴ M.Chemarin,²⁴ A.Chen,⁴⁴ G.Chen,⁷ G.M.Chen,⁷ H.F.Chen,²² H.S.Chen,⁷ G.Chiefari,²⁹ L.Cifarelli,⁴⁰ F.Cindolo,⁸ I.Clare,¹³ R.Clare,³⁸ G.Coignet,⁴ N.Colino,²⁵ S.Costantini,³⁹ B.de la Cruz,²⁵ S.Cucciarelli,³³ R.de Asmundis,²⁹ P.Déglon,²⁰ J.Debreczeni,¹² A.Degré,⁴ K.Dehmelt,²⁶ K.Deiters,⁴⁷ D.della Volpe,²⁹ E.Delmeire,²⁰ P.Denes,³⁷ F.DeNotaristefani,³⁹ A.De Salvo,⁴⁹ M.Diemoz,³⁹ M.Dierckxsens,² C.Dionisi,³⁹ M.Dittmar,⁴⁹ A.Doria,²⁹ M.T.Dova,^{10,#} D.Duchesneau,⁴ M.Duda,¹ B.Echenard,²⁰ A.Eline,¹⁸ A.El Hage,¹ H.El Mamouni,²⁴ A.Engler,³⁵ F.J.Eppling,¹³ P.Extermann,²⁰ M.A.Falagan,²⁵ S.Falciano,³⁹ A.Favara,³² J.Fay,²⁴ O.Fedin,³⁴ M.Felcini,⁴⁹ T.Ferguson,³⁵ H.Fesefeldt,¹ E.Fiandrini,³³ J.H.Field,²⁰ F.Filthaut,³¹ P.H.Fisher,¹³ W.Fisher,³⁷ G.Forconi,¹³ K.Freudenreich,⁴⁹ C.Furetta,²⁷ Yu.Galaktionov,^{28,13} S.N.Ganguli,⁹ P.Garcia-Abia,²⁵ M.Gataullin,³² S.Gentile,³⁹ S.Giagu,³⁹ Z.F.Gong,²² G.Grenier,²⁴ O.Grimm,⁴⁹ M.W.Gruenewald,¹⁶ V.K.Gupta,³⁷ A.Gurtu,⁹ L.J.Gutay,⁴⁶ D.Haas,⁵ D.Hatzifotiadou,⁸ T.Hebbeker,¹ A.Hervé,¹⁸ J.Hirschfelder,³⁵ H.Hofer,⁴⁹ M.Hohlmann,²⁶

G.Holzner,⁴⁹ S.R.Hou,⁴⁴ B.N.Jin,⁷ P.Jindal,¹⁴ L.W.Jones,³ P.de Jong,² I.Josa-Mutuberría,²⁵ M.Kaur,¹⁴ M.N.Kienzle-Focacci,²⁰ J.K.Kim,⁴³ J.Kirkby,¹⁸ W.Kittel,³¹ A.Klimentov,^{13,28} A.C.König,³¹ M.Kopal,⁴⁶ V.Koutsenko,^{13,28} M.Kräber,⁴⁹ R.W.Kraemer,³⁵ A.Krüger,⁴⁸ A.Kunin,¹³ P.Ladron de Guevara,²⁵ I.Laktineh,²⁴ G.Landi,¹⁷ M.Lebeau,¹⁸ A.Lebedev,¹³ P.Lebzun,²⁴ P.Lecomte,⁴⁹ P.Lecoq,¹⁸ P.Le Coultre,⁴⁹ J.M.Le Goff,¹⁸ R.Leiste,⁴⁸ M.Levtchenko,²⁷ P.Levtchenko,³⁴ C.Li,²² S.Likhoded,⁴⁸ C.H.Lin,⁴⁴ W.T.Lin,⁴⁴ F.L.Linde,² L.Lista,²⁹ Z.A.Liu,⁷ W.Lohmann,⁴⁸ E.Longo,³⁹ Y.S.Lu,⁷ C.Luci,³⁹ L.Luminari,³⁹ W.Lustermann,⁴⁹ W.G.Ma,²² L.Malgeri,¹⁸ A.Malinin,²⁸ C.Maña,²⁵ J.Mans,³⁷ J.P.Martin,²⁴ F.Marzano,³⁹ K.Mazumdar,⁹ R.R.McNeil,⁶ S.Mele,^{18,29} L.Merola,²⁹ M.Meschini,¹⁷ W.J.Metzger,³¹ A.Mihul,¹¹ H.Milcent,¹⁸ G.Mirabelli,³⁹ J.Mnich,¹ G.B.Mohanty,⁹ G.S.Muanza,²⁴ A.J.M.Muijs,² M.Musy,³⁹ S.Nagy,¹⁵ S.Natale,²⁰ M.Napolitano,²⁹ F.Nessi-Tedaldi,⁴⁹ H.Newman,³² A.Nisati,³⁹ T.Novak,³¹ H.Nowak,⁴⁸ R.Ofierzynski,⁴⁹ G.Organtini,³⁹ I.Pal,⁴⁶ C.Palomares,²⁵ P.Paolucci,²⁹ R.Paramatti,³⁹ G.Passaleva,¹⁷ S.Patricelli,²⁹ T.Paul,¹⁰ M.Pauluzzi,³³ C.Paus,¹³ F.Pauss,⁴⁹ M.Pedace,³⁹ S.Pensotti,²⁷ D.Perret-Gallix,⁴ D.Piccolo,²⁹ F.Pierella,⁸ M.Pieri,⁴¹ M.Pioppi,³³ P.A.Piroué,³⁷ E.Pistolesi,²⁷ V.Plyaskin,²⁸ M.Pohl,²⁰ V.Pojidaev,¹⁷ J.Pothier,¹⁸ D.Prokofiev,³⁴ G.Rahal-Callot,⁴⁹ M.A.Rahaman,⁹ P.Raics,¹⁵ N.Raja,⁹ R.Ramelli,⁴⁹ P.G.Rancoita,²⁷ R.Ranieri,¹⁷ A.Raspereza,⁴⁸ P.Razis,³⁰ S.Rembeczki,²⁶ D.Ren,⁴⁹ M.Rescigno,³⁹ S.Reucroft,¹⁰ S.Riemann,⁴⁸ K.Riles,³ B.P.Roe,³ L.Romero,²⁵ A.Rosca,⁴⁸ C.Rosemann,¹ C.Rosenbleck,¹ S.Rosier-Lees,⁴ S.Roth,¹ J.A.Rubio,¹⁸ G.Ruggiero,¹⁷ H.Rykaczewski,⁴⁹ A.Sakharov,⁴⁹ S.Saremi,⁶ S.Sarkar,³⁹ J.Salicio,¹⁸ E.Sanchez,²⁵ C.Schäfer,¹⁸ V.Schegelsky,³⁴ H.Schopper,²¹ D.J.Schotanus,³¹ C.Sciacca,²⁹ L.Servoli,³³ S.Shevchenko,³² N.Shivarov,⁴² V.Shoutko,¹³ E.Shumilov,²⁸ A.Shvorob,³² D.Son,⁴³ C.Souga,²⁴ P.Spillantini,¹⁷ M.Steuer,¹³ D.P.Stickland,³⁷ B.Stoyanov,⁴² A.Straessner,²⁰ K.Sudhakar,⁹ G.Sultanov,⁴² L.Z.Sun,²² S.Sushkov,¹ H.Suter,⁴⁹ J.D.Swain,¹⁰ Z.Szillasi,^{26,¶} X.W.Tang,⁷ P.Tarjan,¹⁵ L.Tauscher,⁵ L.Taylor,¹⁰ B.Tellili,²⁴ D.Teyssier,²⁴ C.Timmermans,³¹ S.C.C.Ting,¹³ S.M.Ting,¹³ S.C.Tonwar,⁹ J.Tóth,¹² C.Tully,³⁷ K.L.Tung,⁷ J.Ulbricht,⁴⁹ E.Valente,³⁹ R.T.Van de Walle,³¹ R.Vasquez,⁴⁶ G.Vesztergombi,¹² I.Vetlitsky,²⁸ G.Viertel,⁴⁹ M.Vivargent,⁴ S.Vlachos,⁵ I.Vodopianov,²⁶ H.Vogel,³⁵ H.Vogt,⁴⁸ I.Vorobiev,^{35,28} A.A.Vorobyov,³⁴ M.Wadhwa,⁵ Q.Wang,³¹ X.L.Wang,²² Z.M.Wang,²² M.Weber,¹⁸ S.Wynhoff,^{37,†} L.Xia,³² Z.Z.Xu,²² J.Yamamoto,³ B.Z.Yang,²² C.G.Yang,⁷ H.J.Yang,³ M.Yang,⁷ S.C.Yeh,⁴⁵ An.Zalite,³⁴ Yu.Zalite,³⁴ Z.P.Zhang,²² J.Zhao,²² G.Y.Zhu,⁷ R.Y.Zhu,³² H.L.Zhuang,⁷ A.Zichichi,^{8,18,19} B.Zimmermann,⁴⁹ M.Zöller.¹

¹ III. Physikalisches Institut, RWTH, D-52056 Aachen, Germany[§]

² National Institute for High Energy Physics, NIKHEF, and University of Amsterdam, NL-1009 DB Amsterdam, The Netherlands

³ University of Michigan, Ann Arbor, MI 48109, USA

⁴ Laboratoire d'Annecy-le-Vieux de Physique des Particules, LAPP,IN2P3-CNRS, BP 110, F-74941 Annecy-le-Vieux CEDEX, France

⁵ Institute of Physics, University of Basel, CH-4056 Basel, Switzerland

⁶ Louisiana State University, Baton Rouge, LA 70803, USA

⁷ Institute of High Energy Physics, IHEP, 100039 Beijing, China[△]

⁸ University of Bologna and INFN-Sezione di Bologna, I-40126 Bologna, Italy

⁹ Tata Institute of Fundamental Research, Mumbai (Bombay) 400 005, India

¹⁰ Northeastern University, Boston, MA 02115, USA

¹¹ Institute of Atomic Physics and University of Bucharest, R-76900 Bucharest, Romania

¹² Central Research Institute for Physics of the Hungarian Academy of Sciences, H-1525 Budapest 114, Hungary[‡]

¹³ Massachusetts Institute of Technology, Cambridge, MA 02139, USA

¹⁴ Panjab University, Chandigarh 160 014, India

- ¹⁵ KLTE-ATOMKI, H-4010 Debrecen, Hungary[¶]
- ¹⁶ UCD School of Physics, University College Dublin, Belfield, Dublin 4, Ireland
- ¹⁷ INFN Sezione di Firenze and University of Florence, I-50125 Florence, Italy
- ¹⁸ European Laboratory for Particle Physics, CERN, CH-1211 Geneva 23, Switzerland
- ¹⁹ World Laboratory, FBLJA Project, CH-1211 Geneva 23, Switzerland
- ²⁰ University of Geneva, CH-1211 Geneva 4, Switzerland
- ²¹ University of Hamburg, D-22761 Hamburg, Germany
- ²² Chinese University of Science and Technology, USTC, Hefei, Anhui 230 029, China[△]
- ²³ University of Lausanne, CH-1015 Lausanne, Switzerland
- ²⁴ Institut de Physique Nucléaire de Lyon, IN2P3-CNRS, Université Claude Bernard, F-69622 Villeurbanne, France
- ²⁵ Centro de Investigaciones Energéticas, Medioambientales y Tecnológicas, CIEMAT, E-28040 Madrid, Spain^b
- ²⁶ Florida Institute of Technology, Melbourne, FL 32901, USA
- ²⁷ INFN-Sezione di Milano, I-20133 Milan, Italy
- ²⁸ Institute of Theoretical and Experimental Physics, ITEP, Moscow, Russia
- ²⁹ INFN-Sezione di Napoli and University of Naples, I-80125 Naples, Italy
- ³⁰ Department of Physics, University of Cyprus, Nicosia, Cyprus
- ³¹ Radboud University and NIKHEF, NL-6525 ED Nijmegen, The Netherlands
- ³² California Institute of Technology, Pasadena, CA 91125, USA
- ³³ INFN-Sezione di Perugia and Università Degli Studi di Perugia, I-06100 Perugia, Italy
- ³⁴ Nuclear Physics Institute, St. Petersburg, Russia
- ³⁵ Carnegie Mellon University, Pittsburgh, PA 15213, USA
- ³⁶ INFN-Sezione di Napoli and University of Potenza, I-85100 Potenza, Italy
- ³⁷ Princeton University, Princeton, NJ 08544, USA
- ³⁸ University of California, Riverside, CA 92521, USA
- ³⁹ INFN-Sezione di Roma and University of Rome, “La Sapienza”, I-00185 Rome, Italy
- ⁴⁰ University and INFN, Salerno, I-84100 Salerno, Italy
- ⁴¹ University of California, San Diego, CA 92093, USA
- ⁴² Bulgarian Academy of Sciences, Central Lab. of Mechatronics and Instrumentation, BU-1113 Sofia, Bulgaria
- ⁴³ The Center for High Energy Physics, Kyungpook National University, 702-701 Taegu, Republic of Korea
- ⁴⁴ National Central University, Chung-Li, Taiwan, China
- ⁴⁵ Department of Physics, National Tsing Hua University, Taiwan, China
- ⁴⁶ Purdue University, West Lafayette, IN 47907, USA
- ⁴⁷ Paul Scherrer Institut, PSI, CH-5232 Villigen, Switzerland
- ⁴⁸ DESY, D-15738 Zeuthen, Germany
- ⁴⁹ Eidgenössische Technische Hochschule, ETH Zürich, CH-8093 Zürich, Switzerland

[§] Supported by the German Bundesministerium für Bildung, Wissenschaft, Forschung und Technologie.

[‡] Supported by the Hungarian OTKA fund under contract numbers T019181, F023259 and T037350.

[¶] Also supported by the Hungarian OTKA fund under contract number T026178.

^b Supported also by the Comisión Interministerial de Ciencia y Tecnología.

[#] Also supported by CONICET and Universidad Nacional de La Plata, CC 67, 1900 La

Plata, Argentina.

△ Supported by the National Natural Science Foundation of China.

† Deceased.

The OPAL Collaboration

G. Abbiendi², K. Ackerstaff⁷, C. Ainsley⁵, P.F. Åkesson⁷, G. Alexander²¹, J. Allison¹⁵, N. Altekamp⁵, K. Ametewee²⁵, G. Anagnostou¹, K.J. Anderson⁸, S. Anderson¹¹, S. Arcelli², S. Asai²², S.F. Ashby¹, D. Axen²⁶, G. Azuelos¹⁷, A.H. Ball⁷, I. Bailey²⁵, E. Barberio^{7,p}, T. Barillari³¹, R.J. Barlow¹⁵, R. Bartoldus³, R.J. Batley⁵, S. Baumann³, P. Bechtel²⁴, J. Bechtluft¹³, C. Beeston¹⁵, T. Behnke²⁴, K.W. Bell¹⁹, P.J. Bell¹, G. Bella²¹, A. Bellerive⁶, G. Benelli⁴, S. Bentvelsen^{7,aa}, P. Berlich⁹, S. Bethke³¹, O. Biebel³⁰, O. Boeriu⁹, V. Blobel²⁴, I.J. Bloodworth¹, J.E. Bloomer¹, M. Bobinski⁹, P. Bock¹⁰, O. Boeriu⁹, D. Bonacorsi², H.M. Bosch¹⁰, M. Boutemeur³⁰, B.T. Bouwens¹¹, S. Braibant², P. Bright-Thomas¹, L. Brigliadori², R.M. Brown¹⁹, H.J. Burckhart⁷, C. Burgard⁷, R. Bürgin⁹, J. Cammin³, S. Campana⁴, P. Capiluppi², R.K. Carnegie⁶, A.A. Carter¹², J.R. Carter⁵, C.Y. Chang¹⁶, D.G. Charlton¹, D. Chrisman⁴, C. Ciocca², P.E.L. Clarke^{14,bb}, E. Clay¹⁴, I. Cohen²¹, J.E. Conboy¹⁴, O.C. Cooke¹⁵, J. Couchman¹⁴, C. Couyoumtzelis¹², R.L. Coxe⁸, A. Csilling²⁸, M. Cuffiani², S. Dado²⁰, C. Dallapiccola¹⁶, M. Dallavalle², S. Dallison¹⁵, S. De Jong^{11,cc}, A. De Roeck⁷, P. Dervan¹⁴, E.A. De Wolf^{7,s}, L.A. del Pozo⁷, K. Desch²⁴, B. Dienes²⁹, M.S. Dixit⁶, E. do Couto e Silva¹¹, M. Donkers⁶, M. Doucet¹⁷, J. Dubbert³⁰, E. Duchovni²³, G. Duckeck³⁰, I.P. Duerdoth¹⁵, J.E.G. Edwards¹⁵, P.G. Estabrooks⁶, E. Etzion²¹, H.G. Evans^{8,dd}, M. Evans¹², F. Fabbri², M. Fanti², P. Fath¹⁰, L. Feld⁹, P. Ferrari⁷, F. Fiedler³⁰, M. Fierro², H.M. Fischer³, I. Fleck⁹, R. Folman^{23,kk}, D.G. Fong¹⁶, M. Ford¹⁵, M. Foucher¹⁷, A. Frey⁷, A. Fürties⁷, D.I. Futyan¹⁵, P. Gagnon¹¹, J.W. Gary⁴, J. Gascon¹⁷, S.M. Gascon-Shotkin^{16,ee}, G. Gaycken²⁴, N.I. Geddes¹⁹, C. Geich-Gimbel³, T. Gerasis¹⁹, G. Giacomelli², P. Giacomelli², R. Giacomelli², V. Gibson⁵, W.R. Gibson¹², D.M. Gingrich²⁷, M. Giunta⁴, D. Glenzinski^{8,ff}, J. Goldberg²⁰, M.J. Goodrick⁵, W. Gorn⁴, K. Graham²⁵, C. Grandi², E. Gross²³, J. Grunhaus²¹, M. Gruwé⁷, P.O. Günther³, A. Gupta⁸, C. Hajdu²⁸, M. Hamann²⁴, G.G. Hanson⁴, M. Hansroul⁷, M. Hapke¹², K. Harder²⁴, A. Harel²⁰, C.K. Hargrove⁶, M. Harin-Dirac⁴, P.A. Hart⁸, C. Hartmann³, A. Hauke³, M. Hauschild⁷, C.M. Hawkes¹, R. Hawkings⁷, R.J. Hemingway³, C. Hensel²⁴, M. Herndon¹⁶, G. Herten⁹, R.D. Heuer^{24,y}, M.D. Hildreth^{7,gg}, J.C. Hill⁵, S.J. Hillier¹, T. Hilse⁹, P.R. Hobson³³, A. Hocker⁸, K. Hoffman⁷, R.J. Homer¹, A.K. Honma⁷, D. Horváth^{28,c}, K.R. Hossain²⁷, R. Howard²⁶, R.E. Hughes-Jones¹⁵, P. Hüntemeyer²⁴, D.E. Hutchcroft⁵, P. Igo-Kemenes¹⁰, D.C. Imrie²⁵, M.R. Ingram¹⁵, K. Ishii²², F.R. Jacob¹⁹, A. Jawahery¹⁶, P.W. Jeffreys¹⁹, H. Jeremie¹⁷, M. Jimack¹, A. Joly¹⁷, C.R. Jones⁵, G. Jones¹⁵, M. Jones⁶, R.W.L. Jones^{7,hh}, U. Jost¹⁰, P. Jovanovic¹, T.R. Junk^{6,i}, N. Kanaya²², J. Kanzaki^{22,u}, G. Karapetian¹⁷, D. Karlen²⁵, V. Kartvelishvili¹⁵, K. Kawagoe²², T. Kawamoto²², R.K. Keeler²⁵, R.G. Kellogg¹⁶, B.W. Kennedy¹⁹, D.H. Kim¹⁸, B.J. King⁷, J. Kirk²⁶, K. Klein¹⁰, A. Klier²³, S. Kluth³¹, T. Kobayashi²², M. Kobel^{3,t}, D.S. Koetke⁶, T.P. Kokott³, M. Kolrep⁹, S. Komamiya²², R.V. Kowalewski²⁵, T. Krämer²⁴, A. Krasznahorkay Jr.^{29,e}, T. Kress¹⁰, P. Krieger^{6,l}, J. von Krogh¹⁰, T. Kuhl²⁴, M. Kupper²³, P. Kyberd¹², G.D. Lafferty¹⁵, R. Lahmann¹⁶, W.P. Lai¹⁸, H. Landsman²⁰, D. Lanske^{13,*}, J. Lauber¹⁴, S.R. Lautenschlager³⁴, I. Lawson²⁵, J.G. Layter⁴, D. Lazic²⁰, A.M. Lee³⁴, E. Lefebvre¹⁷, A. Leins³⁰, D. Lellouch²³, J. Letts^o, L. Levinson²³, C. Lewis¹⁴, R. Liebisch¹⁰, J. Lillich⁹, B. List²⁴, J. List²⁴, C. Littlewood⁵, A.W. Lloyd¹, S.L. Lloyd¹², F.K. Loebinger¹⁵, G.D. Long¹⁶, M.J. Losty^{6,*}, J. Lu^{26,b}, A. Ludwig^{3,t}, J. Ludwig⁹, A. Macchiolo¹⁷, A. Macpherson^{27,y}, W. Mader^{3,t}, M. Mannelli⁷, S. Marcellini², T.E. Marchant¹⁵, C. Markus³, A.J. Martin¹², J.P. Martin¹⁷, G. Martinez¹⁶, T. Mashimo²², W. Matthews²⁵, P. Mättig^{23,m}, W.J. McDonald²⁷, J. McKenna²⁶, E.A. Mckigney¹⁴, T.J. McMahon¹, A.I. McNab¹², R.A. McPherson²⁵, P. Mendez-Lorenzo³⁰, F. Meijers⁷, W. Menges²⁴, S. Menke³, F.S. Merritt⁸, H. Mes^{6,a}, N. Meyer²⁴, J. Meyer²⁴, A. Michelini², S. Mihara²², G. Mikenberg²³, D.J. Miller¹⁴, R. Mir^{23,ii}, W. Mohr⁹, A. Montanari²,

T. Mori²², M. Morii^{22,jj}, U. Müller³, A. Mutter⁹, K. Nagai¹², I. Nakamura^{22,v}, H. Nanjo²², H.A. Neal³², B. Nellen³, B. Nijjhar¹⁵, R. Nisius³¹, S.W. O’Neale^{1,*}, F.G. Oakham⁶, F. Odorici², H.O. Ogren¹¹, A. Oh⁷, A. Okpara¹⁰, N.J. Oldershaw¹⁵, T. Omori²², M.J. Oreglia⁸, S. Orito^{22,*}, C. Pahl³¹, J. Pálinkás²⁹, G. Pásztor^{4,g}, J.R. Pater¹⁵, G.N. Patrick¹⁹, J. Patt⁹, M.J. Pearce¹, S. Petzold²⁴, P. Pfeifenschneider^{13,*}, J.E. Pilcher⁸, J. Pinfold²⁷, D.E. Plane⁷, P. Poffenberger²⁵, J. Polok⁷, B. Poli², O. Pooth¹³, A. Posthaus³, M. Przybycien^{7,n}, H. Przysiezniak²⁷, A. Quadt³¹, K. Rabbertz^{7,r}, D.L. Rees¹, C. Rembser⁷, P. Renkel²³, H. Rick⁴, D. Rigby¹, S. Robertson²⁵, S.A. Robins¹², N. Rodning²⁷, J.M. Roney²⁵, A. Rooke¹⁴, E. Ros⁷, S. Rosati³, K. Roscoe¹⁵, A.M. Rossi², M. Rosvick²⁵, P. Routenburg²⁷, Y. Rozen²⁰, K. Runge⁹, O. Runolfsson⁷, U. Ruppel¹³, D.R. Rust¹¹, R. Rylko²⁵, K. Sachs⁶, T. Saeki²², O. Sahr³⁰, E.K.G. Sarkisyan^{7,j}, M. Sasaki²², C. Sbarra², A.D. Schaile³⁰, O. Schaile³⁰, P. Scharff-Hansen⁷, P. Schenk²⁴, J. Schieck³¹, B. Schmitt⁷, S. Schmitt¹⁰, T. Schörner-Sadenius^{7,z}, M. Schröder⁷, H.C. Schultz-Coulon⁹, M. Schulz⁷, M. Schumacher³, P. Schütz³, C. Schwick⁷, W.G. Scott¹⁹, R. Seuster^{13,f}, T.G. Shears^{7,h}, B.C. Shen^{4,*}, C.H. Shepherd-Themistocleous¹⁹, P. Sherwood¹⁴, G.P. Siroli², A. Sittler²⁴, A. Skillman¹⁴, A. Skuja¹⁶, A.M. Smith⁷, T.J. Smith²⁵, G.A. Snow^{16,*}, R. Sobie²⁵, S. Söldner-Rembold¹⁵, S. Spagnolo¹⁹, F. Spano^{8,x}, R.W. Springer²⁷, M. Sproston¹⁹, A. Stahl¹³, M. Steiert¹⁰, K. Stephens¹⁵, J. Steuerer²⁴, B. Stockhausen³, K. Stoll⁹, D. Strom¹⁸, R. Ströhmer³⁰, F. Strumia⁷, L. Stumpf²⁵, B. Surrow⁷, P. Szymanski¹⁹, R. Tafirout¹⁷, S.D. Talbot¹, S. Tanaka²², P. Taras¹⁷, S. Tarem²⁰, R.J. Taylor¹⁴, M. Tasevsky^{7,d}, R. Teuscher⁸, M. Thiergen⁹, J. Thomas¹⁴, M.A. Thomson⁵, E. von Törne³, E. Torrence¹⁸, S. Towers⁶, D. Toya²², T. Trefzger³⁰, I. Trigger^{7,w}, Z. Trócsányi^{29,e}, T. Tsukamoto²², E. Tsur²¹, A.S. Turcot⁸, M.F. Turner-Watson¹, I. Ueda²², B. Ujvári^{29,e}, P. Utzat¹⁰, B. Vachon²⁵, R. Van Kooten¹¹, P. Vannerem⁹, R. Vértesi^{29,e}, M. Verzocchi¹⁶, P. Vikas¹⁷, M. Vincker²⁵, E.H. Vokurka¹⁵, C.F. Vollmer³⁰, H. Voss^{7,q}, J. Vosseveld^{7,h}, F. Wackerle⁹, A. Wagner²⁴, D. Waller⁶, C.P. Ward⁵, D.R. Ward⁵, J.J. Ward¹⁴, P.M. Watkins¹, A.T. Watson¹, N.K. Watson¹, P.S. Wells⁷, T. Wengler⁷, N. Wormes³, D. Wetterling¹⁰, J.S. White²⁵, B. Wilkens⁹, G.W. Wilson^{15,k}, J.A. Wilson¹, G. Wolf²³, S. Wotton⁵, T.R. Wyatt¹⁵, S. Yamashita²², G. Yekutieli²³, V. Zacek¹⁷, D. Zer-Zion⁴, L. Zivkovic²⁰

¹School of Physics and Astronomy, University of Birmingham, Birmingham B15 2TT, UK

²Dipartimento di Fisica dell’ Università di Bologna and INFN, I-40126 Bologna, Italy

³Physikalisches Institut, Universität Bonn, D-53115 Bonn, Germany

⁴Department of Physics, University of California, Riverside CA 92521, USA

⁵Cavendish Laboratory, Cambridge CB3 0HE, UK

⁶Ottawa-Carleton Institute for Physics, Department of Physics, Carleton University, Ottawa, Ontario K1S 5B6, Canada

⁷CERN, European Organisation for Nuclear Research, CH-1211 Geneva 23, Switzerland

⁸Enrico Fermi Institute and Department of Physics, University of Chicago, Chicago IL 60637, USA

⁹Fakultät für Physik, Albert-Ludwigs-Universität Freiburg, D-79104 Freiburg, Germany

¹⁰Physikalisches Institut, Universität Heidelberg, D-69120 Heidelberg, Germany

¹¹Indiana University, Department of Physics, Bloomington IN 47405, USA

¹²Queen Mary and Westfield College, University of London, London E1 4NS, UK

¹³Technische Hochschule Aachen, III Physikalisches Institut, Sommerfeldstrasse 26-28, D-52056 Aachen, Germany

¹⁴University College London, London WC1E 6BT, UK

¹⁵School of Physics and Astronomy, Schuster Laboratory, The University of Manchester M13 9PL, UK

¹⁶Department of Physics, University of Maryland, College Park, MD 20742, USA

¹⁷Laboratoire de Physique Nucléaire, Université de Montréal, Montréal, Québec H3C 3J7, Canada

- ¹⁸University of Oregon, Department of Physics, Eugene OR 97403, USA
¹⁹Rutherford Appleton Laboratory, Chilton, Didcot, Oxfordshire OX11 0QX, UK
²⁰Department of Physics, Technion-Israel Institute of Technology, Haifa 32000, Israel
²¹Department of Physics and Astronomy, Tel Aviv University, Tel Aviv 69978, Israel
²²International Centre for Elementary Particle Physics and Department of Physics, University of Tokyo, Tokyo 113-0033, and Kobe University, Kobe 657-8501, Japan
²³Particle Physics Department, Weizmann Institute of Science, Rehovot 76100, Israel
²⁴Universität Hamburg/DESY, Institut für Experimentalphysik, Notkestrasse 85, D-22607 Hamburg, Germany
²⁵University of Victoria, Department of Physics, P O Box 3055, Victoria BC V8W 3P6, Canada
²⁶University of British Columbia, Department of Physics, Vancouver BC V6T 1Z1, Canada
²⁷University of Alberta, Department of Physics, Edmonton AB T6G 2J1, Canada
²⁸Research Institute for Particle and Nuclear Physics, H-1525 Budapest, P O Box 49, Hungary
²⁹Institute of Nuclear Research, H-4001 Debrecen, P O Box 51, Hungary
³⁰Ludwig-Maximilians-Universität München, Sektion Physik, Am Coulombwall 1, D-85748 Garching, Germany
³¹Max-Planck-Institute für Physik, Föhringer Ring 6, D-80805 München, Germany
³²Yale University, Department of Physics, New Haven, CT 06520, USA
³³Brunel University, Uxbridge, Middlesex UB8 3PH, UK
³⁴Duke University, Dept of Physics, Durham, NC 27708-0305, USA

- a* and at TRIUMF, Vancouver, Canada V6T 2A3
b now at University of Alberta
c and Institute of Nuclear Research, Debrecen, Hungary
d now at Institute of Physics, Academy of Sciences of the Czech Republic 18221 Prague, Czech Republic
e and Department of Experimental Physics, University of Debrecen, Hungary
f and MPI München
g and Research Institute for Particle and Nuclear Physics, Budapest, Hungary
h now at University of Liverpool, Dept of Physics, Liverpool L69 3BX, U.K.
i now at Fermilab, Illinois, U.S.A.
j and University of Texas at Arlington, USA
k now at University of Kansas, Dept of Physics and Astronomy, Lawrence, KS 66045, U.S.A.
l now at University of Toronto, Dept of Physics, Toronto, Canada
m current address Bergische Universität, Wuppertal, Germany
n now at University of Mining and Metallurgy, Cracow, Poland
o now at University of California, San Diego, U.S.A.
p now at The University of Melbourne, Victoria, Australia
q now at IPHE Université de Lausanne, CH-1015 Lausanne, Switzerland
r now at IEKP Universität Karlsruhe, Germany
s now at University of Antwerpen, Physics Department, B-2610 Antwerpen, Belgium; supported by Interuniversity Attraction Poles Programme – Belgian Science Policy
t now at Technische Universität, Dresden, Germany
u and High Energy Accelerator Research Organisation (KEK), Tsukuba, Ibaraki, Japan
v now at University of Pennsylvania, Philadelphia, Pennsylvania, USA
w now at TRIUMF, Vancouver, Canada
x now at Columbia University
y now at CERN

- aa* now at Nikhef, the Netherlands
bb now at University of Edinburgh, United Kingdom
cc now at University of Nijmegen, the Netherlands
dd now at Indiana University, USA
ee now at IPN Lyon, France
ff now at Fermilab, USA
gg now at University of Notre Dame, USA
hh now at University of Lancaster, United Kingdom
ii now at Technion, Haifa, Israel
jj now at Harvard University, USA
kk now at Ben-Gurion University of the Negev, Beersheba, Israel
* Deceased

In addition to the support staff at our own institutions we are pleased to acknowledge the Department of Energy, USA, National Science Foundation, USA, Particle Physics and Astronomy Research Council, UK, Natural Sciences and Engineering Research Council, Canada, Israel Science Foundation, administered by the Israel Academy of Science and Humanities, Benozio Center for High Energy Physics, Japanese Ministry of Education, Culture, Sports, Science and Technology (MEXT) and a grant under the MEXT International Science Research Program, Japanese Society for the Promotion of Science (JSPS), German Israeli Bi-national Science Foundation (GIF), Bundesministerium für Bildung und Forschung, Germany, National Research Council of Canada, Hungarian Foundation for Scientific Research, OTKA T-038240, and T-042864, The NWO/NATO Fund for Scientific Research, the Netherlands.

Contents

1	Introduction	20
1.1	LEP-II Data	20
1.2	Standard-Model Processes	21
2	Photon-Pair Production	26
2.1	Introduction	26
2.2	Event Selection	26
2.3	Theory	27
2.3.1	QED Born Cross-Section	27
2.3.2	Non-QED Models	27
2.3.3	Radiative Corrections	29
2.3.4	Theory Uncertainty	29
2.4	Combination of the Differential Cross-Section	30
2.5	Combined Total Cross-Section	31
2.6	Interpretation	31
2.7	Conclusion	37
3	Fermion-Pair Production	39
3.1	Introduction	39
3.2	Averages for Cross-Sections and Asymmetries	40
3.3	Differential Cross-Sections for Muon- and Tau-Pair Final States	43
3.4	Differential Cross-Sections for Electron-Positron Final States	48
3.5	Interpretation	53
3.5.1	Models with Z' Bosons	53
3.5.2	Contact Interactions	58
3.5.3	Large Extra Dimensions	61
3.5.4	Leptoquarks	64
3.6	Summary	64
4	Final-State Interconnection Effects	66
4.1	Colour Reconnection	66
4.1.1	Introduction	66
4.1.2	Particle-Flow Measurements	67
4.1.3	Determination of CR Effects Using W Mass Estimators	70
4.1.4	Combination of LEP CR Measurements	73
4.1.5	Summary	74
4.2	Bose-Einstein Correlations	74
4.2.1	Introduction	74

4.2.2	Methods	76
4.2.3	Distributions	76
4.2.4	Results	78
4.2.5	Conclusions	80
5	Boson-Pair and Four-Fermion Processes	86
5.1	Introduction and Signal Definitions	86
5.2	W-Pair Production	88
5.2.1	Total Cross-Section Measurement	89
5.2.2	Derived Quantities	93
5.2.3	W Angular Distribution	96
5.3	Z-Pair Production	97
5.4	Z- γ^* Production	100
5.5	Single-Boson Production	100
5.5.1	$W e \nu$ Cross-Section Measurement	105
5.5.2	Zee Cross-Section Measurement	105
5.6	WW γ Production	112
5.7	Summary	112
6	Electroweak Gauge Boson Self Couplings	114
6.1	Introduction	114
6.1.1	Charged Triple Gauge Boson Couplings	114
6.1.2	Neutral Triple Gauge Boson Couplings	115
6.2	Combination Procedure	116
6.3	Measurements	118
6.4	Results	119
6.4.1	Charged Triple Gauge Boson Couplings	119
6.4.2	Neutral Triple Gauge Boson Couplings	121
6.5	Summary and Conclusions	127
7	Mass and Width of the W Boson	128
7.1	Introduction	128
7.2	Determination of the W Mass at the W-Pair Production Threshold	128
7.3	Measurement of Mass and Width by Direct Reconstruction	129
7.3.1	Mass Reconstruction	129
7.3.2	Kinematic Fitting	130
7.3.3	Techniques for Determining the W-Boson Mass and Width	131
7.3.4	Combination Procedure	133
7.3.5	Overview of Systematic Uncertainties	134
7.4	LEP Combined W-Boson Mass	139
7.5	Consistency Checks	140
7.6	LEP Combined W-Boson Width	140
7.7	Summary	141
8	Summary and Conclusions	145
	Acknowledgements	146

A	S-Matrix	147
A.1	Introduction	147
A.2	The S-Matrix Ansatz	148
A.3	LEP-I Combination	149
A.4	Discussion	150
A.5	S-Matrix Combination Tables	157
B	Two-Fermion Combination Details	162
B.1	Input Measurements	163
B.2	Differential Cross-Section for Muon- and Tau-Pair Final States	174
B.3	Differential Cross-Section for Electron-Positron Final States	178
C	Determination of the LEP Centre-of-Mass Energy Using Radiative-Return Events	181
D	Tests of the Colour-Reconnection Combination Procedure	186
E	Detailed Inputs and Results of LEP Four-Fermion Averages	191
F	Constraints on the Standard Model	211
F.1	Introduction	211
F.2	Measurements	211
F.3	Theoretical Uncertainties	214
F.4	Standard-Model Analyses	214

Chapter 1

Introduction

The electron-positron collider LEP at CERN increased its collision centre-of-mass energy, \sqrt{s} , from the Z pole (LEP-I) up to 209 GeV during its second running phase (LEP-II) from 1995 to 2000. The four LEP experiments ALEPH, DELPHI, L3 and OPAL collected a combined total integrated luminosity of about 3 fb^{-1} in the LEP-II centre-of-mass energy range above the Z pole, 130 GeV to 209 GeV. This large data set explores the new energy regime accessed by LEP-II with high precision, allowing new tests of the electroweak Standard Model of particle physics [1] (SM), and searches for new physics effects at higher mass scales.

Combinations of electroweak measurements performed in electron-positron collisions at Z-pole centre-of-mass energies, at LEP-I and the SLC, are reported in Reference [4]. Here, the measurements in the electroweak sector of the SM at LEP-II centre-of-mass energies are discussed, including, where necessary, studies of strong-interaction effects. Photon-pair, fermion-pair and four-fermion production processes are analysed and the results are presented in the form of total and differential cross-sections. Final-state interactions between the decay products in W-boson pair production are investigated for signals of colour reconnection and Bose-Einstein correlations. Pair-production of W bosons yields measurements of the mass, total decay width and decay branching fractions of the W boson. Together with other reactions such as single-W, single-Z, $WW\gamma$, Z-pair, $Z\gamma$ and $Z\gamma\gamma$ production, the data sample allows stringent tests of the non-Abelian structure of the electroweak gauge group, by measuring triple and quartic electroweak gauge boson couplings.

1.1 LEP-II Data

In a circular accelerator such as LEP, the energy loss of the beam particles due to synchrotron radiation increases with the fourth power of the Lorentz γ factor. In order to push the LEP centre-of-mass energy beyond the Z-pole, the warm copper RF cavities used at LEP-I were replaced by superconducting RF cavities to increase the available RF power. In parallel the LEP-II centre-of-mass energy increased in steps up to a maximum of 209 GeV, reached in 2000, the final year of LEP operation. The centre-of-mass energies and the corresponding integrated luminosities collected per experiment are reported in Table 1.1. For some of the analyses described in this report, the data have been combined in different slices of centre-of-mass energies. About 0.75 fb^{-1} of integrated luminosity was recorded by each LEP experiment, for a total of about 3 fb^{-1} .

Year	Mean energy \sqrt{s} [GeV]	Luminosity [pb ⁻¹]
1995, 1997	130.3	6
	136.3	6
	140.2	1
1996	161.3	12
	172.1	12
1997	182.7	60
1998	188.6	180
1999	191.6	30
	195.5	90
	199.5	90
	201.8	40
2000	204.8	80
	206.5	130
	208.0	8
Total	130 – 209	745

Table 1.1: Centre-of-mass energies and integrated luminosities recorded by each experiment at LEP-II.

1.2 Standard-Model Processes

The various SM processes occurring at high centre-of-mass energies in electron-positron collisions and their cross-sections are shown as a function of the centre-of-mass energy in Figure 1.1.

Photon-Pair Production

The photon-pair production process, $e^+e^- \rightarrow \gamma\gamma(\gamma)$, is dominated by QED interactions. The corresponding Feynman diagrams at Born level are shown in Figure 1.2. Higher-order QED effects play a significant role but the weak interaction is negligible for the present data set. Therefore this reaction is different from the other processes discussed in this report as it provides a clean test of QED, independent of other parts of the SM.

Fermion-Pair Production

Pair-production of fermions proceeds mainly via s -channel exchange of a photon or a Z boson as shown in Figure 1.3. For energies above the Z resonance, QED radiative corrections are very large, up to several 100% of the Born cross-section. This is caused by hard initial-state radiation of photons, which lowers the centre-of-mass energy, \sqrt{s} , of the hard interaction down to values $\sqrt{s'}$ close to the Z mass, called radiative return to the Z. In order to probe the hard interaction at the nominal energy scale \sqrt{s} , cuts are applied to remove the radiative return to

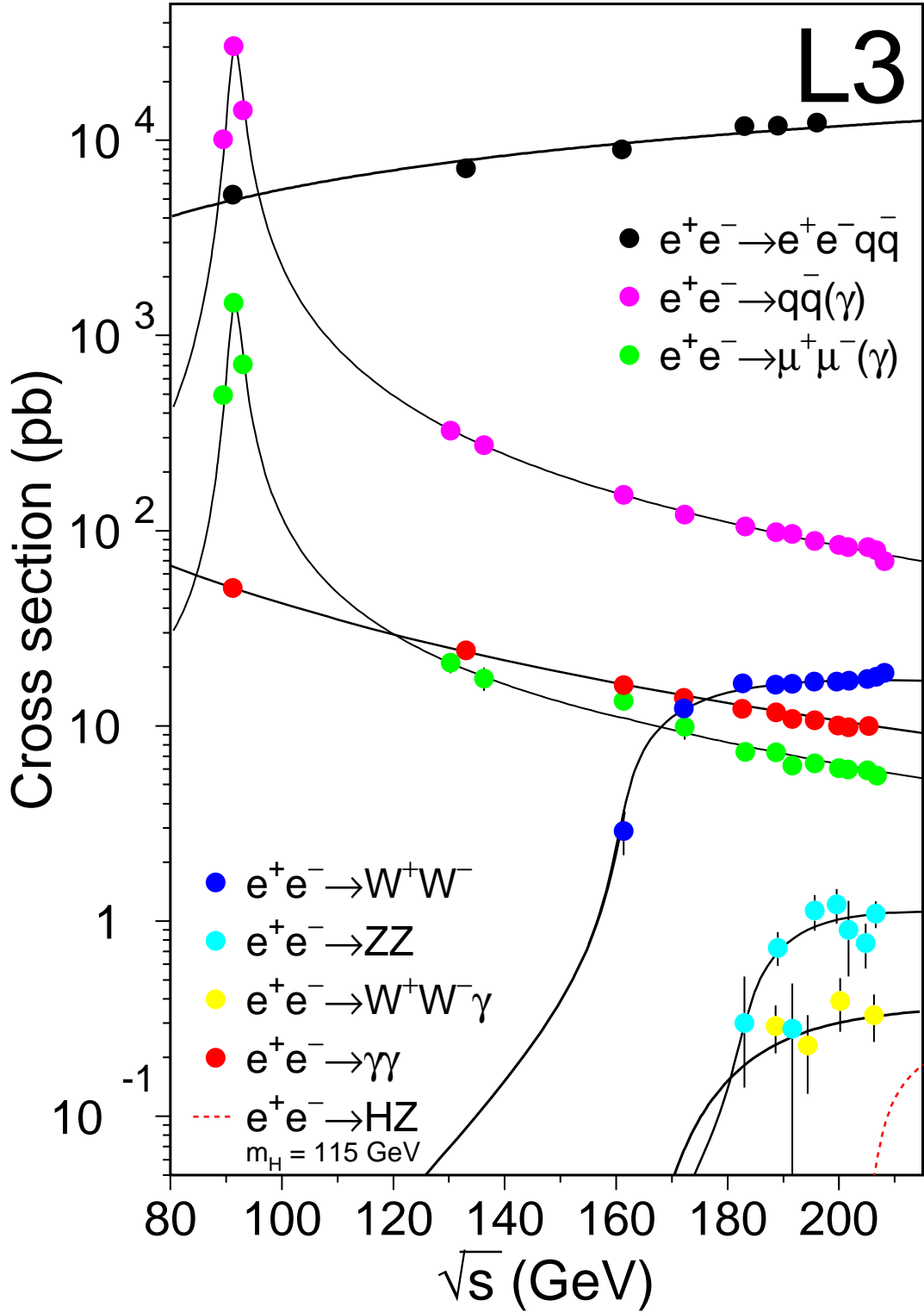


Figure 1.1: Cross-sections of electroweak SM processes. The dots with error bars show the measurements, while the continuous curves show the theoretical predictions based on the SM.

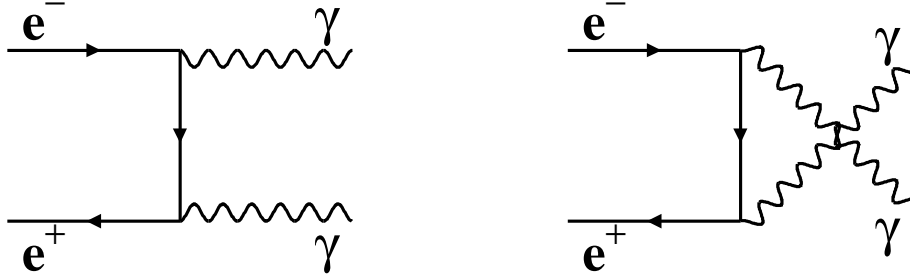


Figure 1.2: Feynman diagrams for the process $e^+e^- \rightarrow \gamma\gamma$ at the Born level.

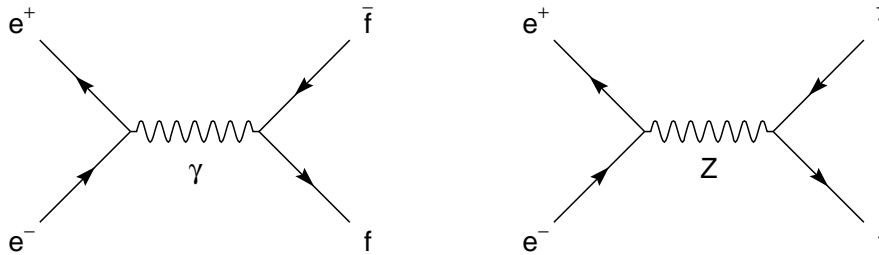


Figure 1.3: Feynman diagrams for the process $e^+e^- \rightarrow f\bar{f}$ at the Born level. For e^+e^- final states additional t -channel diagrams contribute.

the Z and only keep the high- Q^2 events. Further cuts remove non-resonant pair corrections arising from four-fermion production not included in the signal definition.

WW and ZZ Production

One of the most important processes at LEP-II consists of pair production of on-shell W bosons as shown in Figure 1.4. These events allow a determination of the mass and total decay width of the W boson. The non-Abelian nature of the electroweak gauge theory, leading to triple and quartic gauge-boson vertices such as those appearing in the two s -channel WW production diagrams, is studied and the gauge couplings are measured. Each W boson decays to a quark-antiquark pair, hadronising into jets, or to a lepton-neutrino pair, resulting in a four-fermion final state. The WW events are thus classified into fully hadronic, semileptonic and purely leptonic events. At higher centre-of-mass energies, four-fermion final states are also produced via Z-pair production, as shown in Figure 1.5.

Final-state corrections arising from the interaction between the two W decay systems, such as colour reconnection and Bose-Einstein correlations, may lead to a cross-talk effect. Such an effect potentially spoils the assignment of decay products to decaying weak bosons in terms of four-momentum, with consequences in the measurement of the W-boson mass and width in the all-hadronic channel.

Radiative corrections to W-pair production are particularly interesting as they allow the study of quartic-gauge-boson vertices as shown in Figure 1.6.

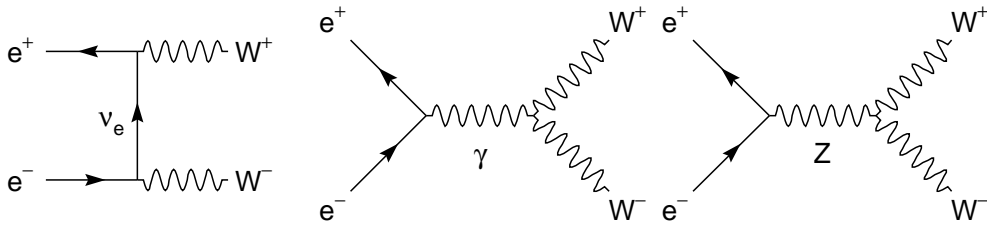


Figure 1.4: Feynman diagrams (CC03) for the process $e^+e^- \rightarrow W^+W^-$ at the Born level.



Figure 1.5: Feynman diagrams (NC02) for the process $e^+e^- \rightarrow ZZ$ at the Born level.

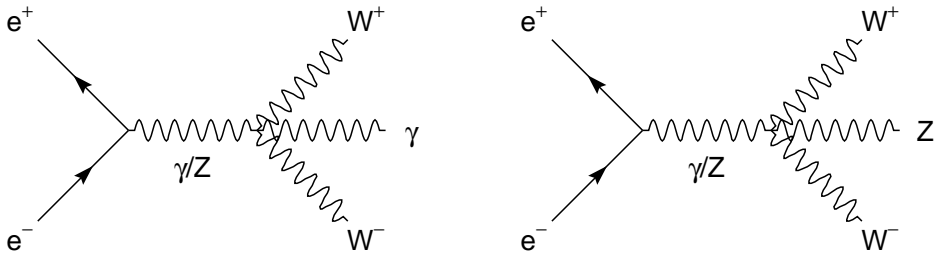


Figure 1.6: Feynman diagrams for the process $e^+e^- \rightarrow WW\gamma$ and WWZ at the Born level involving quartic electroweak-gauge-boson vertices.

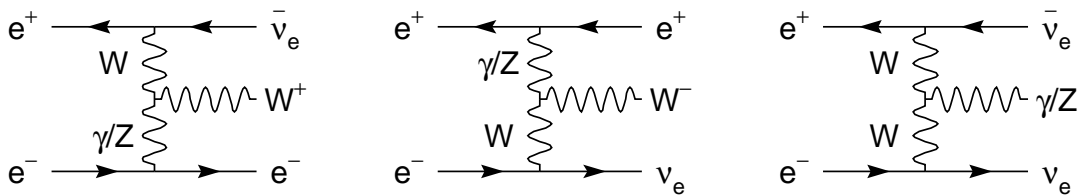


Figure 1.7: Vector-boson fusion diagrams for the single $W/Z/\gamma$ process at the Born level.

Four-Fermion Production

Besides the double-resonant WW and ZZ processes, single-resonant boson production channels such as those shown in Figure 1.7, as well as non-resonant diagrams also contribute to four-fermion production. Selections are devised to separate the various four-fermion processes, in particular WW , ZZ , single- W and single- Z production. Single- W production is sensitive to the electromagnetic gauge couplings of the W boson, as the t -channel photon exchange diagram dominates over the t -channel Z exchange diagram at LEP-II energies. Bremsstrahlung diagrams with radiation of an on-shell Z boson off an initial- or final-state fermion leg in Bhabha scattering contribute to single- Z production in the form of Zee final states.

Chapter 2

Photon-Pair Production

2.1 Introduction

The differential cross-section for the photon-pair production process $e^+e^- \rightarrow \gamma\gamma(\gamma)$ is presented here for centre-of-mass energies above 183 GeV. This process is one of the few channels at LEP energies with negligible contribution from the weak interaction. Therefore it provides a clean test of quantum electrodynamics, QED, at high energies. The combination is based on the publications [5, 6, 7, 8].

Section 2.2 gives a short overview on the event selections of the four experiments as far as they are relevant for the determination of the theory uncertainty, which is described in Section 2.3. Also the expected cross-sections from QED and other models are given. In Section 2.4 the combination of the differential cross-section is presented. The total cross-section given in Section 2.5 is derived from the differential cross-section. The results are summarised in Section 2.6.

2.2 Event Selection

The topology of this channel is very clean and the event selection, which is similar for all experiments, is based on the presence of at least two energetic clusters in the electromagnetic calorimeters (ECAL). A minimum energy of the two highest-energy ECAL clusters is required. Restrictions are made either on the acollinearity, ξ_{acol} , or on the missing longitudinal momentum, p_z . The cuts and the allowed range in polar angle, θ_i , of the observed clusters are listed in Table 2.1. The clusters are ordered by decreasing energy. In order to remove background, especially from Bhabha events, charged tracks are in general not allowed except when they can be associated to a photon conversion in one hemisphere.

Besides limited coverage of the ECAL, selection cuts to reject events with charged tracks are the main reason for a reduced signal efficiency. The effect of the different cuts depends strongly on the detector geometry. Therefore experimental systematic errors are considered uncorrelated between the experiments.

Experiment	polar angles	energies	acollinearity
ALEPH	$ \cos \theta_i < 0.95$	$E_1, E_2 > 0.5 \cdot E_{\text{beam}}$	$\xi_{\text{acol}} < 20^\circ$
DELPHI	$25^\circ < \theta_i < 155^\circ$	$E_1, E_2 > 0.3 \cdot E_{\text{beam}}$	$\xi_{\text{acol}} < 50^\circ$
L3	$16^\circ < \theta_i < 164^\circ$	$E_1 + E_2 > E_{\text{beam}}$	$\xi_{\text{acol}} < 165^\circ$
OPAL	$ \cos \theta_i < 0.93$	$E_1, E_2 > p_z$	–

Table 2.1: Simplified phase-space definition for the selection of $e^+e^- \rightarrow \gamma\gamma(\gamma)$ events. DELPHI does not select clusters in the range $[35^\circ, 42^\circ]$, $[88^\circ, 92^\circ]$ and $[138^\circ, 145^\circ]$. OPAL is sensitive to additional clusters up to $|\cos \theta_i| < 0.97$ ($i \geq 3$).

2.3 Theory

2.3.1 QED Born Cross-Section

The differential cross-section for the QED process $e^+e^- \rightarrow \gamma\gamma$ in lowest order is known since a long time [9]:

$$\left(\frac{d\sigma}{d\Omega}\right)_{\text{Born}} = \frac{\alpha^2}{s} \left[\frac{1 + \beta^2 + \beta^2 \sin^2 \theta}{1 - \beta^2 \cos^2 \theta} - \frac{2\beta^4 \sin^4 \theta}{(1 - \beta^2 \cos^2 \theta)^2} \right], \quad (2.1)$$

where \sqrt{s} is the centre-of-mass energy. Since the emitted photons are real, with a vanishing invariant mass, the relevant scale for the fine-structure constant α is zero momentum transfer. In the following the relativistic limit for the velocity of the electron $\beta = p/E \rightarrow 1$ will be used. Since the final-state particles are identical the polar angle θ is defined such that $\cos \theta > 0$ to avoid double counting. This results in a full phase space of $\int d\Omega = 2\pi$.

Higher-order QED corrections are relevant but the lowest-order contribution involving weak couplings is negligible compared to the current experimental precision of about 1%. There is no resonance effect for this process at energies around the Z mass (LEP-I) since a spin-one vector or axial-vector particle cannot couple to two real photons. However, at the W-pair threshold there is a resonance-like effect, since the photons can be radiated off an on-shell W loop, with a dominating contribution from the triangle diagram with WW $\gamma\gamma$ coupling [10]. At such energies, corrections of up to 1.2% are expected for $\cos \theta = 0$. At the energies considered here the corrections are smaller, *e.g.*, for a centre-of-mass energy of 200 GeV they are below 0.2% at all angles, and will be neglected.

2.3.2 Non-QED Models

Various models predict deviations from the QED expectation. The simplest ansatz is the introduction of cut-off parameters Λ_\pm as used for Bhabha and Møller scattering [12, 13]. With this formalism a short range exponential deviation is added to the Coulomb potential resulting in a differential cross-section of the form:

$$\left(\frac{d\sigma}{d\Omega}\right)_{\Lambda_\pm} = \left(\frac{d\sigma}{d\Omega}\right)_{\text{Born}} \pm \frac{\alpha^2 s}{2\Lambda_\pm^4} (1 + \cos^2 \theta). \quad (2.2)$$

New effects can also be described by effective Lagrangian theory [14]. Here dimension-6 terms lead to anomalous $ee\gamma$ couplings. The resulting deviations in the differential cross-section are similar in form to those for cut-off parameters, but with a slightly different definition of the parameter: $\Lambda_6^4 = \frac{2}{\alpha}\Lambda_+^4$. Dimension 7 and 8 Lagrangians introduce $ee\gamma\gamma$ contact interactions and result in an angular-independent term added to the Born cross-section:

$$\left(\frac{d\sigma}{d\Omega}\right)_{\Lambda'} = \left(\frac{d\sigma}{d\Omega}\right)_{\text{Born}} + \frac{s^2}{32\pi} \frac{1}{\Lambda'^6}. \quad (2.3)$$

The associated parameters are given by $\Lambda_7 = \Lambda'$ and $\Lambda_8^4 = m_e\Lambda'^3$ for dimension 7 and dimension 8 couplings, respectively.

Theories of quantum gravity in extra spatial dimensions might solve the hierarchy problem since gravitons would propagate in a compactified higher dimensional space, while other Standard Model (SM) particles are confined to the usual $3 + 1$ space-time dimensions [15]. While in these models the Planck mass M_D in $D = n + 4$ dimensions is chosen to be at the electroweak scale, the usual Planck mass M_{Pl} in four dimensions would be $M_{\text{Pl}}^2 = R^n M_D^{n+2}$, where R is the compactification radius of the additional dimensions. Since gravitons couple to the energy-momentum tensor, their interaction with photons is as weak as that with fermions. However, the huge number of Kaluza-Klein excitation modes in the extra dimensions may give rise to observable effects. These effects depend on the scale $M_s (\sim M_D)$ which may be as low as $\mathcal{O}(\text{TeV})$. Model dependences are absorbed in the parameter λ which is expected to be of order 1. For this analysis it is assumed that $\lambda = \pm 1$. The expected differential cross-section is given by [16]:

$$\left(\frac{d\sigma}{d\Omega}\right)_{M_s} = \left(\frac{d\sigma}{d\Omega}\right)_{\text{Born}} - \frac{\alpha s}{2\pi} \frac{\lambda}{M_s^4} (1 + \cos^2\theta) + \frac{s^3}{16\pi^2} \frac{\lambda^2}{M_s^8} (1 - \cos^4\theta), \quad \lambda = \pm 1. \quad (2.4)$$

Instead of an ordinary electron an excited electron e^* coupling to electron and photon could be exchanged in the t-channel of the process [13, 17]. In the most general case $e^*e\gamma$ couplings would lead to a large anomalous magnetic moment of the electron on which strong experimental limits exist [18]. This effect can be prevented by a chiral magnetic coupling of the form:

$$\mathcal{L} = \frac{1}{2\Lambda} \bar{e}^* \sigma^{\mu\nu} \left[g f \frac{\tau}{2} W_{\mu\nu} + g' f' \frac{Y}{2} B_{\mu\nu} \right] e_L + \text{h.c.}, \quad (2.5)$$

where τ are the Pauli matrices and Y is the hypercharge. The model parameters are the compositeness scale Λ and the relative couplings f and f' to the gauge fields W and B with SM couplings g and g' . For the process $e^+e^- \rightarrow \gamma\gamma(\gamma)$, effects vanish in the case of $f = -f'$. For $f_\gamma = -\frac{1}{2}(f + f')$ the following cross-section results [20]:

$$\left(\frac{d\sigma}{d\Omega}\right)_{e^*} = \left(\frac{d\sigma}{d\Omega}\right)_{\text{Born}} + \frac{\alpha^2 f_\gamma^4}{16 \Lambda^4} s \sin^2\theta \left[\frac{p^4}{(p^2 - M_{e^*}^2)^2} + \frac{q^4}{(q^2 - M_{e^*}^2)^2} \right] - \frac{\alpha^2 f_\gamma^2}{2s \Lambda^2} \left[\frac{p^4}{(p^2 - M_{e^*}^2)} + \frac{q^4}{(q^2 - M_{e^*}^2)} \right], \quad (2.6)$$

with $p^2 = -\frac{s}{2}(1 - \cos\theta)$ and $q^2 = -\frac{s}{2}(1 + \cos\theta)$. In the following it is assumed that $\Lambda = M_{e^*}$ unless stated otherwise.

2.3.3 Radiative Corrections

Radiative corrections, *i.e.*, the ratio of the next-to-leading order QED to Born level, are shown in Figure 2.1. They are determined from Monte-Carlo simulations [22], implementing a full third-order calculation including electron-mass effects. In case the third photon is below an energy cut-off, only two back-to-back photons are generated. Fourth-order effects are not included. The event angle θ is calculated as:

$$\cos \theta = \left| \sin \left(\frac{\theta_1 - \theta_2}{2} \right) \right| / \sin \left(\frac{\theta_1 + \theta_2}{2} \right), \quad (2.7)$$

to minimise higher order effects, where $\theta_{1,2}$ are the polar angles of the two highest-energy photons.

The correction labelled RADCOR shown in Figure 2.1 is determined from the angles $\theta_{1,2}$ of the two highest-energy photons generated without restriction on the angle. The radiative corrections depend on the selected phase space, which differs between the four experiments as listed in Table 2.1. For OPAL the radiative corrections are identical to the RADCOR distribution, apart from the edge effect, since events with a high energy photon having $|\cos \theta_i| > 0.93$ are rejected due to the cut on the longitudinal momentum. Radiative corrections for DELPHI are moderate and similar to OPAL due to the intermediate restriction on the acollinearity angle. L3 on the other hand has a very loose cut on the acollinearity angle. Thus events with only one hard photon in the accepted angle range $|\cos \theta_{2/1}| < 0.96$, the other hard photon having $0.96 < |\cos \theta_{1/2}| \simeq 1$, are selected. The event angle is calculated from the angle $\cos \theta_3$ of an observed soft photon leading to a smaller $\cos \theta$. Especially in the central region, where the cross-section is small, this leads to large corrections of up to 30%. ALEPH has a very tight cut on the acollinearity angle leading to a cross-section smaller than the Born cross-section in the central region.

2.3.4 Theory Uncertainty

For the $\gamma\gamma(\gamma)$ channel, no detailed study of the theory uncertainty, *i.e.*, the uncertainty of the third-order Monte-Carlo prediction, exists. For a QED process the higher-order effect can be estimated to be 10% ($\simeq \sqrt{\alpha}$) of the correction due to the highest calculated order. For each experiment the theory uncertainty is estimated as 10% of the radiative correction, with a minimum of 0.5%.

A Monte-Carlo study shows that despite different selections the overlap in the selected phase space is very high, for example, at $\cos \theta = 0.7$ where the third-order DELPHI cross-section is larger than the OPAL cross-section, all events in the phase space selected by OPAL are also in the phase space selected by DELPHI. This means that the common part of the correction is correlated between experiments.

For each $\cos \theta$ bin the theory error is calculated as the luminosity weighted average over the four experiments taking the correlation into account. The resulting error, listed in Tables 2.2 and 2.3, varies between 0.5% and 1.0%. The first $\cos \theta$ bin shows a larger error because DELPHI's analysis does not cover this region and thus the L3 measurements get a larger weight.

To determine limits on non-QED models these correlations are taken into account in the following way. Obviously the radiative corrections in neighbouring bins are due to the same effects and hence correlated. Forward and central region on the other hand are uncorrelated. A

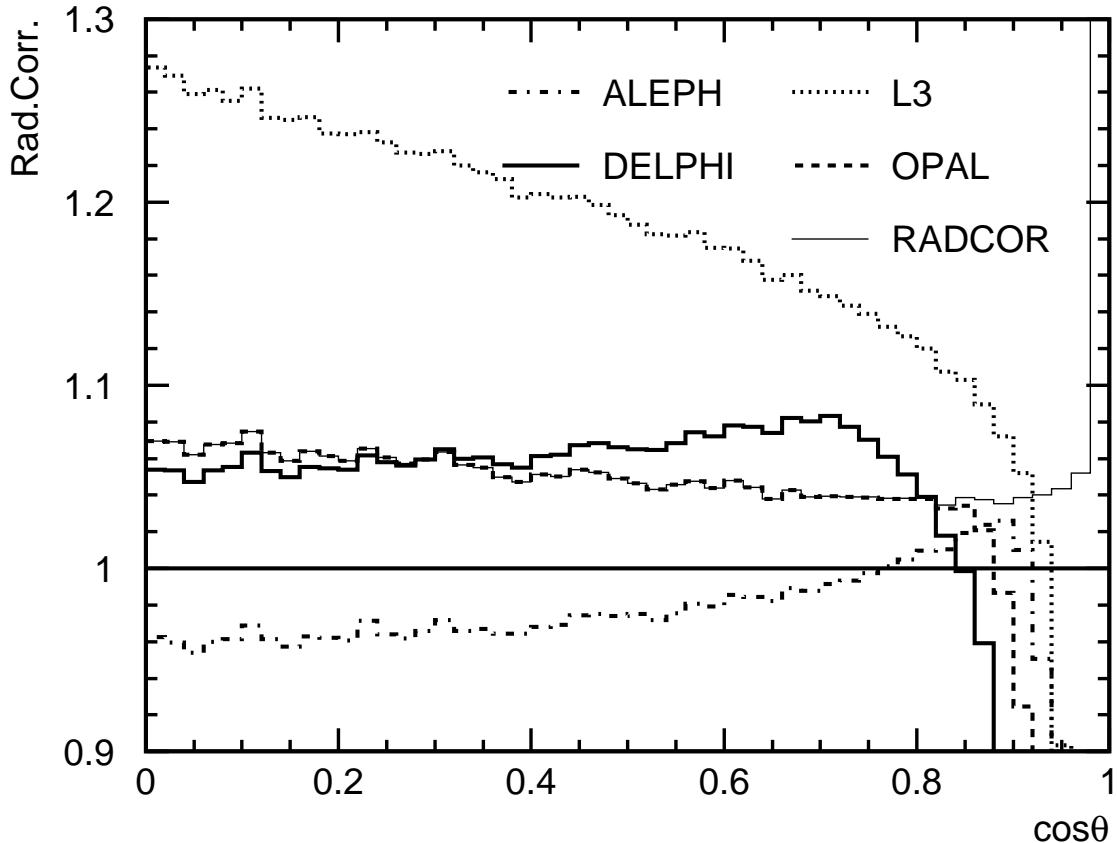


Figure 2.1: Radiative corrections for the four experiments: shown is the ratio of the full third-order RADCOR Monte-Carlo cross-section calculation with the phase-space cuts used by each experiment to the Born cross-section. The line labelled RADCOR is the ratio determined without any phase-space cuts.

detailed correlation matrix describing this situation properly is difficult to implement with a log-likelihood fit while for a χ^2 fit the available statistics are too small. To keep the log-likelihood fits of the non-QED models simple, just two independent regions are defined: barrel ($\cos\theta < 0.75$) and endcap ($\cos\theta > 0.75$). Within each region the theory error is 100% correlated, whereas the two regions are treated as uncorrelated. This simplified treatment is possible, since the theory uncertainty is smaller than the experimental systematic and statistical uncertainties.

2.4 Combination of the Differential Cross-Section

Apart from ALEPH at 183 GeV, all experiments provide the measured angular distributions in bins of $\cos\theta$, with a bin-width $B = 0.05$ for all bins except for the last one which has $B = 0.0113$. Only the $\cos\theta$ -range covered differs. Besides the centre-of-mass energy $\sqrt{s_k}$ and luminosity \mathcal{L}_k of each experiment k , the information includes the number of observed events N_k^{obs} , the number of expected events N_k^{QED} or equivalently the correction C_k with $N_k^{\text{QED}} = C_k \left(\frac{d\sigma}{d\cos\theta} \right)_{\text{Born}} \mathcal{L}_k B$, as well as the experimental systematic error δ_k^{exp} . The experiment-dependent terms C_k correct for the different phase-space cuts reported in Table 2.1. All experiments assume an experimental systematic error which does not depend on $\cos\theta$ and hence is correlated between all bins. The

OPAL experiment introduces an additional uncorrelated experimental error δ^{unc} for some bins. As explained above the experimental systematic error is uncorrelated between experiments. The resulting errors on the LEP combination are reported in Tables 2.2 and 2.3.

The effective centre-of-mass energy, \sqrt{s} , is determined as the luminosity weighted average, taking into account that the cross-section is proportional to $1/s$:

$$s = \mathcal{L} \left/ \sum_k \frac{\mathcal{L}_k}{s_k} \right., \quad (2.8)$$

where $\mathcal{L} = \sum_k \mathcal{L}_k$. The average correction C at a given angle and energy is calculated as:

$$C = \sum_k \frac{d\sigma}{d\cos\theta}(\cos\theta_k, s_k) \mathcal{L}_k C_k \left/ \frac{d\sigma}{d\cos\theta}(\cos\theta, s) \mathcal{L} \right. . \quad (2.9)$$

Similarly the systematic errors are calculated, adding the contributions in quadrature. The results are given in Tables 2.2 and 2.3. The combined differential cross-section in each bin, corrected to Born level, is then calculated as:

$$\frac{d\sigma}{d\cos\theta} = \frac{N}{CB\mathcal{L}} \quad (2.10)$$

where $N = \sum_k N_k^{\text{obs}}$. The ratio of the combined cross-section and the expected Born cross-section is shown in Figure 2.2. For illustration the differential cross-section combined for all energies is shown in Figure 2.3. On average, the cross-section is slightly below the QED expectation.

2.5 Combined Total Cross-Section

The total cross-section is derived by integrating the combined differential cross-section. Since the coverage in the scattering angle varies between experiments, the total cross-section is given for two ranges, $\cos\theta < 0.9613$ and $\cos\theta < 0.90$. The latter range is covered by all four experiments. The results are shown in Figure 2.4 and are summarised in Table 2.4. For the theory error the contributions in barrel and endcap are added in quadrature. The total cross-section (especially for $\cos\theta < 0.9613$) is dominated by the very forward region, where the cross-section is strongly increasing.

2.6 Interpretation

Limits on the parameters describing the non-QED models discussed in Section 2.3.2 are determined from log-likelihood fits to the combined differential cross-section. Where possible the fit parameters are chosen such that the likelihood function is approximately Gaussian. The results of the fits are given in Table 2.5. The values of the fit parameters are about 1.5 standard deviations below the expectation, reflecting the low cross-section in the central region.

Since no significant deviations with respect to the QED expectations are found – all the parameters are compatible with zero – 95% confidence level limits are obtained by renormalising

$\cos \theta'$	N	C	theo	exp	unc	$\frac{d\sigma}{d\cos\theta}$	N	C	theo	exp	unc	$\frac{d\sigma}{d\cos\theta}$
	$\sqrt{s} = 182.692$ GeV $\mathcal{L} = 159.4/\text{pb}$						$\sqrt{s} = 188.609$ GeV $\mathcal{L} = 682.6/\text{pb}$					
0.029	23	0.7860	1.00	1.18	1.10	3.7	92	0.7853	1.00	1.00	0.84	3.4
0.076	39	1.0257	0.79	1.03	0.00	4.8	108	0.9321	0.79	0.80	0.00	3.4
0.126	32	0.9147	0.78	1.00	0.00	4.4	132	0.9718	0.78	0.83	0.00	4.0
0.176	32	1.0743	0.76	1.04	0.00	3.7	129	0.9473	0.76	0.81	0.00	4.0
0.226	33	0.9297	0.74	0.98	0.00	4.5	147	0.9210	0.74	0.80	0.00	4.7
0.275	41	0.9982	0.72	1.01	0.00	5.2	142	0.9539	0.72	0.82	0.00	4.4
0.326	44	0.9907	0.71	1.01	0.00	5.6	162	0.9308	0.71	0.81	0.00	5.1
0.375	37	0.9726	0.69	1.01	0.00	4.8	152	0.9207	0.69	0.82	0.00	4.8
0.426	39	0.9265	0.67	0.99	0.00	5.3	159	0.9301	0.67	0.81	0.00	5.0
0.475	37	0.9747	0.65	1.01	0.00	4.8	190	0.9351	0.65	0.80	0.00	6.0
0.525	55	0.9360	0.64	0.98	0.00	7.4	214	0.9523	0.64	0.79	0.00	6.6
0.576	55	0.9476	0.62	0.99	0.00	7.3	213	0.9380	0.62	0.80	0.00	6.7
0.626	73	0.9274	0.60	0.98	0.00	9.9	224	0.9240	0.60	0.79	0.00	7.1
0.676	70	0.9120	0.59	0.97	0.00	9.6	299	0.9198	0.59	0.79	0.00	9.5
0.726	44	0.4260	0.57	0.58	1.69	13.0	223	0.5398	0.57	0.88	1.01	12.1
0.776	53	0.4109	0.55	0.56	1.73	16.2	275	0.5295	0.55	0.89	1.02	15.2
0.826	104	0.5469	0.53	0.84	1.28	23.8	399	0.6400	0.53	0.89	0.83	18.3
0.877	197	0.7874	0.52	0.95	0.88	31.4	743	0.7959	0.52	0.82	0.66	27.4
0.928	133	0.3628	0.50	1.29	1.17	46.0	682	0.4409	0.50	1.10	0.73	45.3
0.956	35	0.2010	0.50	2.10	0.00	99.2	78	0.1426	0.50	2.10	0.00	72.8
	$\sqrt{s} = 191.597$ GeV $\mathcal{L} = 111.8/\text{pb}$						$\sqrt{s} = 195.506$ GeV $\mathcal{L} = 314.0/\text{pb}$					
0.029	13	0.6903	1.00	0.92	0.93	3.4	35	0.7437	1.00	1.00	0.80	3.0
0.076	22	0.9613	0.79	0.81	0.00	4.1	51	0.9882	0.79	0.84	0.00	3.3
0.126	14	0.9154	0.78	0.78	0.00	2.7	45	0.9061	0.78	0.79	0.00	3.2
0.176	18	0.9117	0.76	0.79	0.00	3.5	68	0.9401	0.76	0.84	0.00	4.6
0.226	12	0.9529	0.74	0.83	0.00	2.3	47	1.0174	0.74	0.83	0.00	2.9
0.275	30	0.9242	0.72	0.79	0.00	5.8	54	0.8987	0.72	0.80	0.00	3.8
0.326	21	0.9212	0.71	0.78	0.00	4.1	53	0.9260	0.71	0.82	0.00	3.6
0.375	26	0.9950	0.69	0.84	0.00	4.7	72	0.9005	0.69	0.80	0.00	5.1
0.426	28	0.9054	0.67	0.79	0.00	5.5	65	0.8896	0.67	0.81	0.00	4.7
0.475	29	0.9181	0.65	0.81	0.00	5.7	79	0.9573	0.65	0.81	0.00	5.3
0.525	27	0.8903	0.64	0.77	0.00	5.4	97	0.9172	0.64	0.80	0.00	6.7
0.576	29	0.9808	0.62	0.83	0.00	5.3	93	0.9437	0.62	0.82	0.00	6.3
0.626	46	0.9386	0.60	0.82	0.00	8.8	116	0.9216	0.60	0.81	0.00	8.0
0.676	41	0.9026	0.59	0.80	0.00	8.1	129	0.8611	0.59	0.78	0.00	9.5
0.726	34	0.5506	0.57	0.93	0.97	11.0	82	0.5200	0.57	0.92	0.96	10.0
0.776	43	0.5032	0.55	0.89	1.05	15.3	120	0.4941	0.55	0.92	1.00	15.5
0.826	75	0.6263	0.53	0.88	0.83	21.4	178	0.6082	0.53	0.91	0.80	18.6
0.877	108	0.7951	0.52	0.79	0.65	24.3	350	0.7900	0.52	0.79	0.61	28.2
0.928	117	0.4165	0.50	1.08	0.76	50.3	276	0.4203	0.50	1.11	0.70	41.8
0.956	16	0.1459	0.50	2.10	0.00	89.2	33	0.1492	0.50	2.10	0.00	64.0

Table 2.2: Combined differential cross-sections for $e^+e^- \rightarrow \gamma\gamma(\gamma)$. The first two numbers of each block are the centre-of-mass energy, \sqrt{s} , and the total luminosity, \mathcal{L} . The following rows list for each bin: weighted $\cos\theta$, total number of events N , correction C , theory error (theo), experimental systematic error (exp) and systematic uncorrelated error (unc). The errors are relative and given in %. The differential cross-section (in pb) is: $d\sigma/d\cos\theta(\cos\theta, \sqrt{s}) = N/C/B/\mathcal{L}$. The value listed for $\cos\theta'$ corresponds to $d\sigma/d\cos\theta(\cos\theta') \cdot B = \int_{\text{bin}} d\sigma/d\cos\theta d\cos\theta$.

$\cos \theta'$	N	C	theo	exp	unc	$\frac{d\sigma}{d\cos\theta}$	N	C	theo	exp	unc	$\frac{d\sigma}{d\cos\theta}$
	$\sqrt{s} = 199.504$ GeV $\mathcal{L} = 315.2/\text{pb}$						$\sqrt{s} = 201.631$ GeV $\mathcal{L} = 157.1/\text{pb}$					
0.029	43	0.6607	1.00	0.92	0.93	4.1	23	0.7240	1.00	0.99	0.80	4.0
0.076	44	0.8989	0.79	0.76	0.00	3.1	25	0.8865	0.79	0.78	0.00	3.6
0.126	38	0.9171	0.78	0.78	0.00	2.6	25	0.8697	0.78	0.78	0.00	3.7
0.176	38	0.9480	0.76	0.78	0.00	2.5	18	0.9562	0.76	0.84	0.00	2.4
0.226	50	0.9385	0.74	0.76	0.00	3.4	23	0.9482	0.74	0.79	0.00	3.1
0.275	57	0.9574	0.72	0.80	0.00	3.8	19	0.8910	0.72	0.76	0.00	2.7
0.326	64	0.9220	0.71	0.78	0.00	4.4	31	0.8263	0.71	0.75	0.00	4.8
0.375	64	0.9122	0.69	0.80	0.00	4.5	38	0.9389	0.69	0.81	0.00	5.2
0.426	64	0.9186	0.67	0.80	0.00	4.4	36	0.9471	0.67	0.86	0.00	4.8
0.475	67	0.9311	0.65	0.77	0.00	4.6	28	0.9213	0.65	0.79	0.00	3.9
0.525	77	0.9137	0.64	0.78	0.00	5.3	43	0.8979	0.64	0.80	0.00	6.1
0.576	94	0.9057	0.62	0.77	0.00	6.6	48	0.9472	0.62	0.82	0.00	6.5
0.626	104	0.9226	0.60	0.80	0.00	7.2	52	0.9153	0.60	0.81	0.00	7.2
0.676	111	0.8897	0.59	0.77	0.00	7.9	62	0.8703	0.59	0.78	0.00	9.1
0.726	70	0.5447	0.57	0.96	0.94	8.2	52	0.5281	0.57	0.98	0.91	12.5
0.776	108	0.5174	0.55	0.94	0.98	13.2	53	0.5151	0.55	0.97	0.93	13.1
0.826	160	0.5807	0.53	0.90	0.86	17.5	92	0.5886	0.53	0.93	0.80	19.9
0.877	307	0.8001	0.52	0.77	0.62	24.3	152	0.7988	0.52	0.79	0.58	24.2
0.928	279	0.4092	0.50	1.10	0.74	43.3	115	0.4240	0.50	1.12	0.67	34.5
0.956	28	0.1231	0.50	2.10	0.00	65.6	11	0.1197	0.50	2.10	0.00	53.2
	$\sqrt{s} = 205.279$ GeV $\mathcal{L} = 393.3/\text{pb}$						$\sqrt{s} = 206.671$ GeV $\mathcal{L} = 462.9/\text{pb}$					
0.029	44	0.5596	1.00	0.96	0.89	4.0	59	0.8530	1.00	0.99	0.85	3.0
0.076	64	0.9151	0.79	0.74	0.00	3.6	68	1.0029	0.79	0.89	0.00	2.9
0.126	53	0.9524	0.78	0.72	0.00	2.8	70	1.0074	0.78	0.91	0.00	3.0
0.176	51	0.9325	0.76	0.75	0.00	2.8	66	0.9777	0.76	0.87	0.00	2.9
0.226	65	0.9267	0.74	0.72	0.00	3.6	74	1.0103	0.74	0.88	0.00	3.2
0.275	50	0.9477	0.72	0.73	0.00	2.7	67	0.9818	0.72	0.87	0.00	2.9
0.326	71	0.8851	0.71	0.72	0.00	4.1	94	0.9437	0.71	0.87	0.00	4.3
0.375	63	0.9136	0.69	0.75	0.00	3.5	72	0.9200	0.69	0.92	0.00	3.4
0.426	72	0.9104	0.67	0.72	0.00	4.0	88	0.9542	0.67	0.90	0.00	4.0
0.475	62	0.9108	0.65	0.72	0.00	3.5	98	0.9776	0.65	0.88	0.00	4.3
0.525	91	0.8862	0.64	0.71	0.00	5.2	122	0.9286	0.64	0.87	0.00	5.7
0.576	97	0.9212	0.62	0.72	0.00	5.4	126	0.9500	0.62	0.88	0.00	5.7
0.626	102	0.8721	0.60	0.72	0.00	5.9	144	0.9281	0.60	0.87	0.00	6.7
0.676	150	0.8650	0.59	0.71	0.00	8.8	206	0.9089	0.59	0.86	0.00	9.8
0.726	89	0.4266	0.57	0.92	0.97	10.6	147	0.6288	0.57	0.92	0.97	10.1
0.776	105	0.3995	0.55	0.89	1.03	13.4	166	0.5891	0.55	0.90	1.02	12.2
0.826	154	0.4833	0.53	0.89	0.84	16.2	227	0.7137	0.53	0.89	0.83	13.7
0.877	345	0.7747	0.52	0.71	0.52	22.6	431	0.8173	0.52	0.86	0.72	22.8
0.928	252	0.3169	0.50	1.07	0.77	40.4	418	0.4780	0.50	1.09	0.75	37.8
0.956	24	0.0960	0.50	2.10	0.00	57.8	61	0.1490	0.50	2.10	0.00	80.4

Table 2.3: Combined differential cross-sections for $e^+e^- \rightarrow \gamma\gamma(\gamma)$. The first two numbers of each block are the centre-of-mass energy, \sqrt{s} , and the total luminosity, \mathcal{L} . The following rows list for each bin: weighted $\cos \theta$, total number of events N , correction C , theory error (theo), experimental systematic error (exp) and systematic uncorrelated error (unc). The errors are relative and given in %. The differential cross-section (in pb) is: $d\sigma/d\cos\theta(\cos\theta, \sqrt{s}) = N/C/B/\mathcal{L}$. The value listed for $\cos \theta'$ corresponds to $d\sigma/d\cos\theta(\cos\theta') \cdot B = \int_{\text{bin}} d\sigma/d\cos\theta d\cos\theta$.

$e^+e^- \rightarrow \gamma\gamma(\gamma)$ LEP combined
 $d\sigma_{\text{LEP}}/d\cos\theta / d\sigma_{\text{QED}}/d\cos\theta$

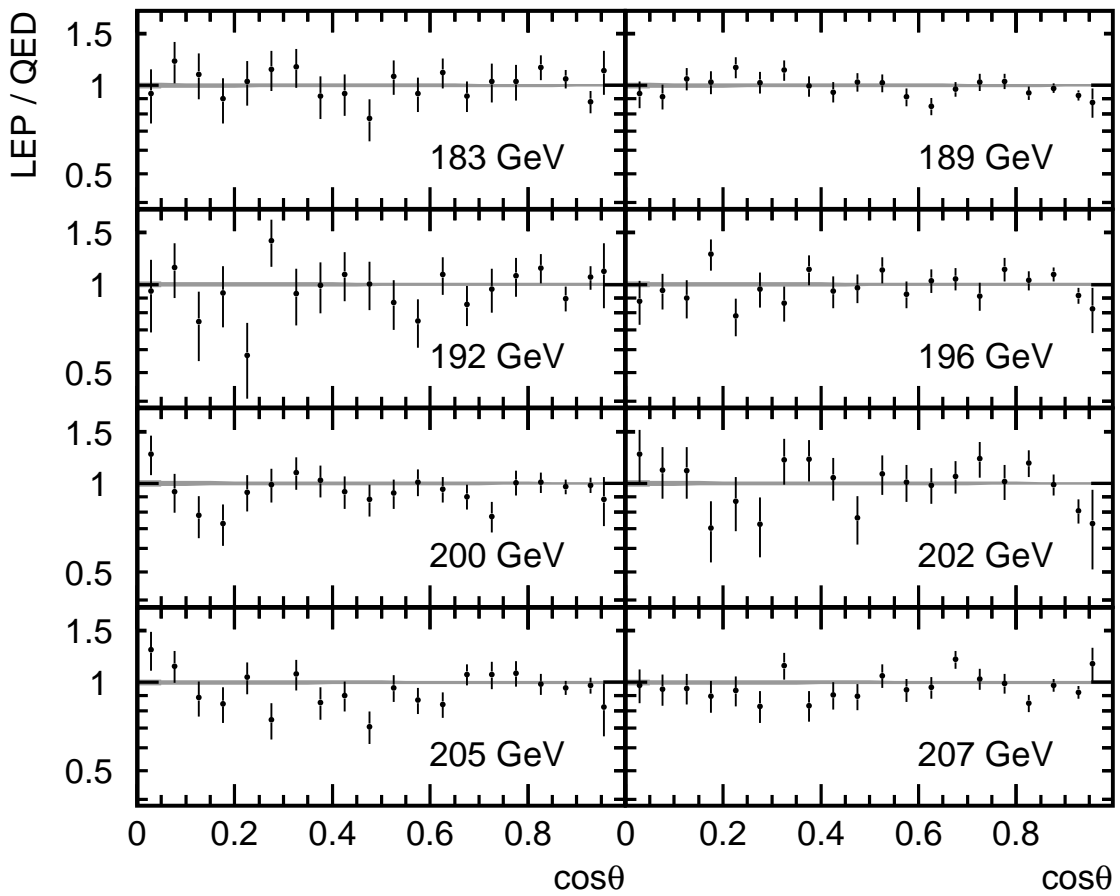


Figure 2.2: Combined differential cross-sections relative to the QED expectation. The error bars shown include the statistical and systematic experimental errors. The theory uncertainty is small, decreasing from 1.0% to 0.5% for increasing $|\cos\theta|$.

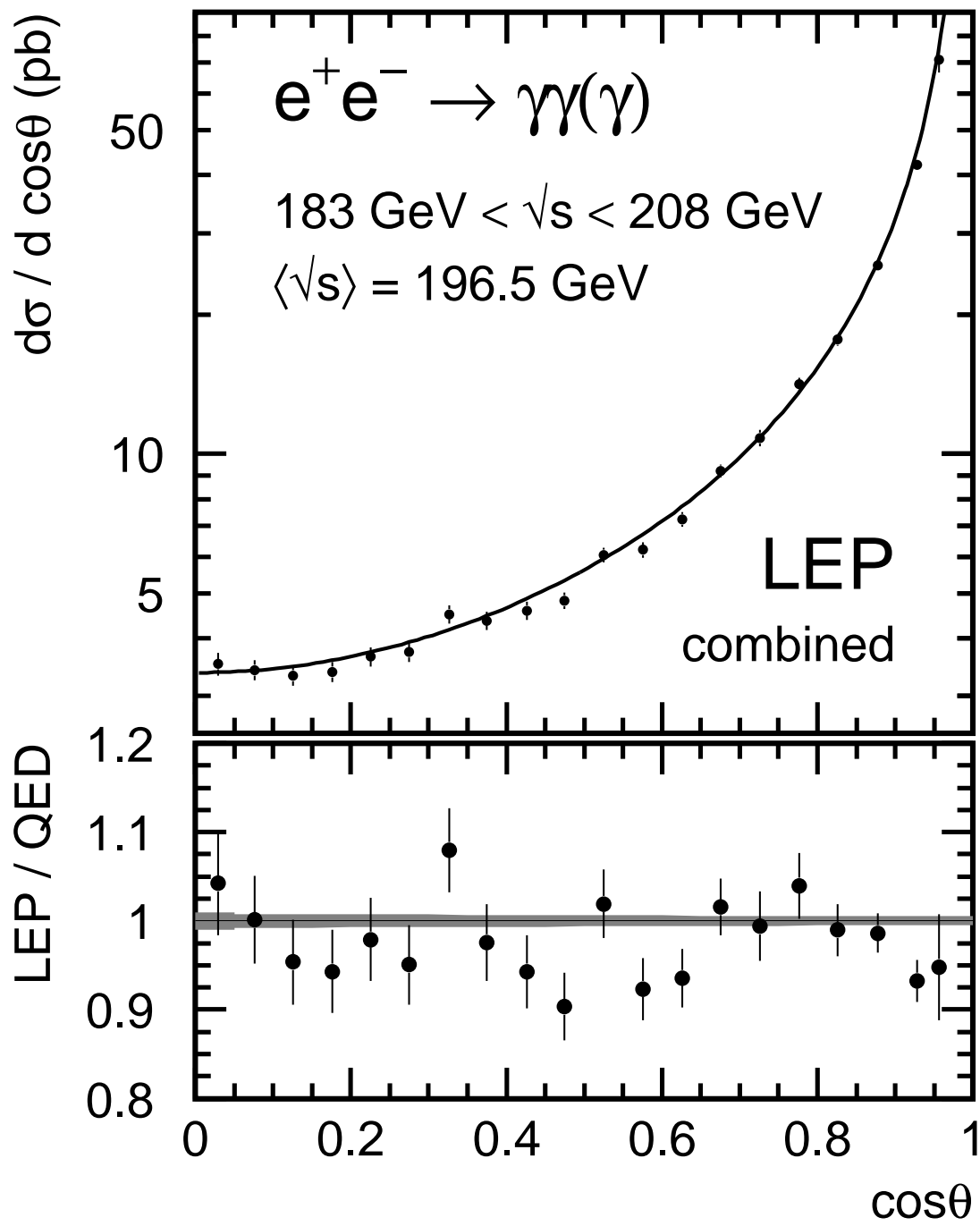


Figure 2.3: The differential cross-section combined for all energies compared to the expectation from QED. The lower plot shows the ratio of measured and expected cross-section, with the band indicating the theory error.

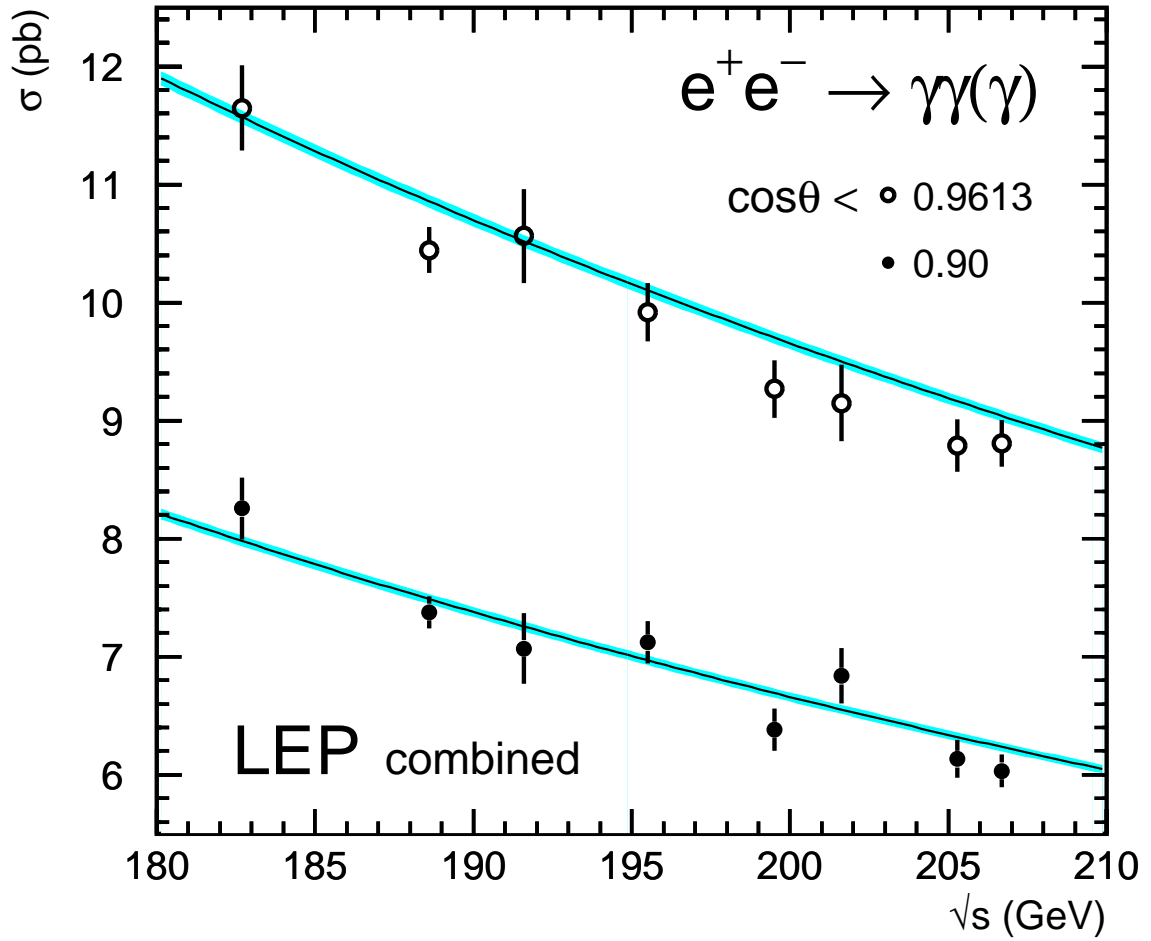


Figure 2.4: The total cross-section as a function of energy for two regions in $\cos\theta$. The error includes statistical and systematic experimental error. The theory error is shown as the band on the QED prediction.

\sqrt{s} (GeV)	$\cos\theta < 0.90$		$\cos\theta < 0.9613$	
	LEP	QED	LEP	QED
182.7	$8.26 \pm 0.26 \pm 0.08$	7.98 ± 0.04	$11.65 \pm 0.34 \pm 0.13$	11.57 ± 0.05
188.6	$7.38 \pm 0.12 \pm 0.06$	7.49 ± 0.03	$10.44 \pm 0.15 \pm 0.11$	10.86 ± 0.04
191.6	$7.07 \pm 0.28 \pm 0.06$	7.26 ± 0.03	$10.56 \pm 0.39 \pm 0.11$	10.52 ± 0.04
195.5	$7.12 \pm 0.17 \pm 0.06$	6.97 ± 0.03	$9.92 \pm 0.22 \pm 0.10$	10.10 ± 0.04
199.5	$6.38 \pm 0.16 \pm 0.06$	6.69 ± 0.03	$9.27 \pm 0.21 \pm 0.10$	9.70 ± 0.04
201.6	$6.84 \pm 0.24 \pm 0.06$	6.55 ± 0.03	$9.15 \pm 0.30 \pm 0.10$	9.50 ± 0.04
205.3	$6.13 \pm 0.15 \pm 0.05$	6.32 ± 0.03	$8.79 \pm 0.20 \pm 0.09$	9.16 ± 0.04
206.7	$6.03 \pm 0.13 \pm 0.06$	6.24 ± 0.03	$8.81 \pm 0.17 \pm 0.10$	9.04 ± 0.04

Table 2.4: The total cross-section (in pb) for $e^+e^- \rightarrow \gamma\gamma(\gamma)$. For the measured cross-sections (LEP) the statistical and systematic errors are given. The theory error of 0.45% (0.41%) for $\cos\theta < 0.90$ (0.9613) is quoted for the QED expectation.

Model and Fit parameter	Fit result	95% CL limit (GeV)
Cut-off parameters Λ_{\pm}^{-4}	$(-37_{-23}^{+24}) \cdot 10^{-12} \text{ GeV}^{-4}$	$\Lambda_+ > 431$ $\Lambda_- > 339$
effective Lagrangian dimension 7 Λ_7^{-6}	$(-2.8_{-1.7}^{+1.8}) \cdot 10^{-18} \text{ GeV}^{-6}$	$\Lambda_7 > 880$
effective Lagrangian dimension 6 and 8	derived from Λ_+ derived from Λ_7	$\Lambda_6 > 1752$ $\Lambda_8 > 24.3$
quantum gravity λ/M_s^4	$(-0.85_{-0.55}^{+0.54}) \cdot 10^{-12} \text{ GeV}^{-4}$	$\lambda = +1: M_s > 868$ $\lambda = -1: M_s > 1108$
excited electrons $M_{e^*}(f_\gamma = 1)$ $f_\gamma^2(M_{e^*} = 200 \text{ GeV})$	see Figure 2.6 $-0.17_{-0.12}^{+0.12}$	$M_{e^*} > 366$ $f_\gamma/\Lambda < 7.0 \text{ TeV}^{-1}$

Table 2.5: Results of the fits to the differential cross-section for $e^+e^- \rightarrow \gamma\gamma(\gamma)$ and the 95% confidence level limits on the model parameters.

the probability distribution of the fit parameter to the physically allowed region, $\epsilon \geq 0$ for each Λ^+ limit and $\epsilon \leq 0$ for Λ^- limits. For limits on the coupling of an excited electron f_γ/Λ a scan over the mass M_{e^*} is performed and presented in Figure 2.5. The cross-section is nonlinear in the fit parameter only for M_{e^*} . The obtained negative log likelihood distribution is shown in Figure 2.6 and the limit is determined at 1.92 units above the minimum.

2.7 Conclusion

The differential cross-section for the photon-pair production process $e^+e^- \rightarrow \gamma\gamma(\gamma)$ was measured and found in agreement with the expectation from QED. Limits on new physics were obtained for various models. They supersede by large factors previous limits on cut-off parameters obtained from data collected at electron-positron colliders of lower centre-of-mass energies [23].

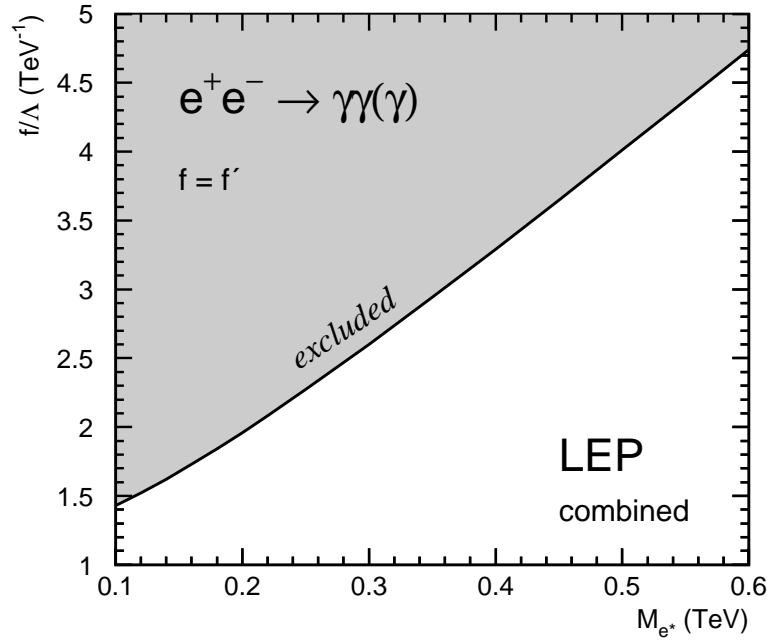


Figure 2.5: 95% CL limits on f_γ/Λ as a function of M_{e^*} . In the case of $f = f'$ it follows that $f_\gamma = -f$. It is assumed that $\Lambda = M_{e^*}$.

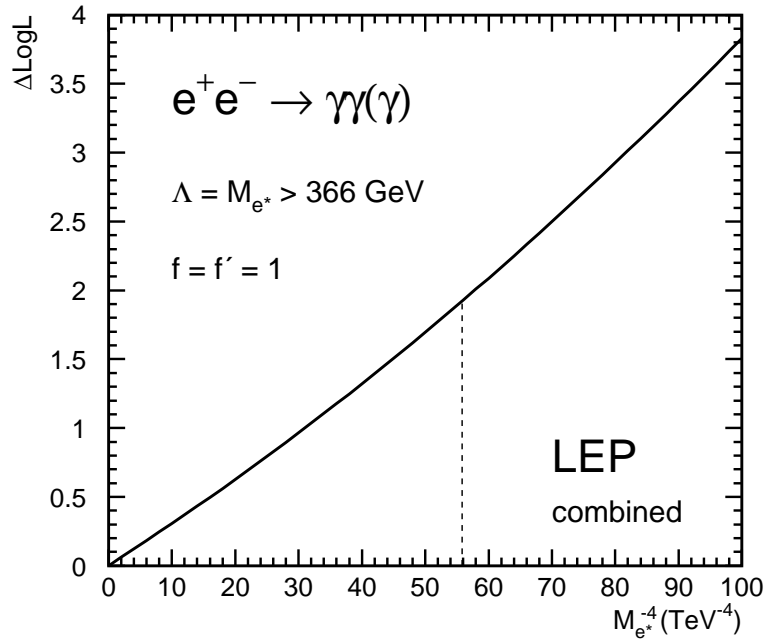


Figure 2.6: Log likelihood difference $\Delta\text{LogL} = -\ln \mathcal{L} + \ln \mathcal{L}_{\max}$ as a function of $M_{e^*}^{-4}$. The coupling is fixed at $f = f' = 1$. The value corresponding to $\Delta\text{LogL} = 1.92$ is $M_{e^*}^{-4} = 55.8 \text{ TeV}^{-4} \rightarrow M_{e^*} = 366 \text{ GeV}$.

Chapter 3

Fermion-Pair Production

3.1 Introduction

The LEP-II data were taken at centre-of-mass energies, \sqrt{s} , increasing from 130 GeV to 209 GeV. These energies are well above the Z-pole and the cross-sections for $e^+e^- \rightarrow f\bar{f}$ are significantly smaller than those at the Z-pole. The four LEP experiments have made measurements of the $e^+e^- \rightarrow f\bar{f}$ process over this range of energies [32, 33, 34, 35], and a combination of these data is discussed in this section.

Initial-state photon radiation is very important in analysing $e^+e^- \rightarrow f\bar{f}$. If an initial-state photon (or photons) is emitted then the effective e^+e^- centre-of-mass energy is reduced from \sqrt{s} to a lower value $\sqrt{s'}$. The rate of events at a given effective energy is given by the probability to emit photons times the cross-section of $e^+e^- \rightarrow f\bar{f}$ at the reduced centre-of-mass energy $\sqrt{s'}$. For the case when $\sqrt{s'} \simeq m_Z$, corresponding to a photon energy of $E_\gamma = (s - m_Z^2)/(2\sqrt{s})$, the rate becomes very large. This part, which is called radiative return to the Z, is thus important in both the event selection and the analysis of $e^+e^- \rightarrow f\bar{f}$. For the studies reported in this section only events with a small amount of initial state radiation, *i.e.*, large $\sqrt{s'}/s$, are retained.

The cross-section for $e^+e^- \rightarrow e^+e^-$ is considerably larger than those of $e^+e^- \rightarrow \mu^+\mu^-$ and $e^+e^- \rightarrow \tau^+\tau^-$ because of the additional Feynman diagrams involving t -channel photon and Z exchange. The low angle $e^+e^- \rightarrow e^+e^-$ Bhabha scattering process is used to determine the luminosity.

In the years 1995 through 1999 LEP delivered luminosity at a number of distinct centre-of-mass energy points. In 2000 most of the luminosity was delivered close to two distinct energies, but there was also a significant fraction of the luminosity delivered in more or less a continuum of energies. To facilitate the combination of the fermion-pair measurements, the four LEP experiments divided the data collected in 2000 into two energy bins: from 202.5 to 205.5 GeV, and above 205.5 GeV. The nominal and actual centre-of-mass energies to which the LEP data are averaged for each year are given in Table 3.1.

A number of measurements of the process $e^+e^- \rightarrow f\bar{f}$ exist and are combined. The averages of cross-section and forward-backward asymmetry measurements are discussed in Section 3.2. In Section 3.3 the averages of the differential cross-section measurements, $\frac{d\sigma}{d\cos\theta}$, for the channels $e^+e^- \rightarrow \mu^+\mu^-$ and $e^+e^- \rightarrow \tau^+\tau^-$ are presented; similar averages for differential cross-sections for $e^+e^- \rightarrow e^+e^-$ are given in Section 3.4. In Section 3.5 the combined results are interpreted in terms of contact interactions, the exchange of Z' bosons, the exchange of leptoquarks or squarks and the exchange of gravitons in large-extra-dimensions scenarios. The results are summarised in Section 3.6.

Year	Nominal Energy GeV	Actual Energy GeV	Luminosity pb ⁻¹
1995	130	130.1	3
	136	136.1	3
1996	161	161.3	10
	172	172.1	10
1997	130	130.1	2
	136	136.1	2
	183	182.7	50
1998	189	188.6	170
1999	192	191.6	30
	196	195.5	80
	200	199.5	80
	202	201.7	40
2000	205	204.9	80
	207	206.5	140

Table 3.1: The nominal and actual average centre-of-mass energies for data collected during LEP-II operation in each year. The approximate average integrated luminosity analysed per experiment at each energy is also shown.

The uncorrelated systematic errors on the input measurements have been separated from the statistical errors, allowing the decomposition of the errors on the averages into statistical and systematic components. Multiplicative corrections have been used to correct measurements to the full solid angle or full s' region of the common signal definition. Additional errors have been included to account for uncertainties in these corrections.

Where comparisons with Standard Model (SM) predictions are performed, the predictions are calculated using ZFITTER [36] version 6.36 with the following input parameters:

$$m_Z = 91.1875 \text{ GeV} \quad (3.1)$$

$$m_t = 170.9 \text{ GeV} \quad (3.2)$$

$$m_H = 150 \text{ GeV} \quad (3.3)$$

$$\Delta\alpha_{\text{had}}^{(5)}(m_Z^2) = 0.02758 \quad (3.4)$$

$$\alpha_S(m_Z) = 0.118. \quad (3.5)$$

3.2 Averages for Cross-Sections and Asymmetries

In this section the results of the combination of cross-sections and asymmetries are given. The individual experiments' analyses of cross-sections and forward-backward asymmetries are presented in a number of publications [46, 48, 51, 54]. Cross-section results are combined for the $e^+e^- \rightarrow q\bar{q}$, $e^+e^- \rightarrow \mu^+\mu^-$ and $e^+e^- \rightarrow \tau^+\tau^-$ channels, forward-backward asymmetry measurements are combined for the $\mu^+\mu^-$ and $\tau^+\tau^-$ final states. Events are classified according to the effective centre-of-mass energy, $\sqrt{s'}$. The averages are made for the samples of events with high effective centre-of-mass energies.

Individual experiments study different $f\bar{f}$ signal definitions; corrections are applied to bring the measurements to the common signal definition:¹

- $\sqrt{s'}$ is taken to be the mass of the s -channel propagator, with the $f\bar{f}$ signal being defined by the cut $\sqrt{s'}/s > 0.85$.
- ISR-FSR photon interference is subtracted to render the propagator mass unambiguous.
- Results are given for the full 4π angular acceptance.
- Initial state non-singlet diagrams [59], see for example Figure 3.1, which lead to events containing additional fermion pairs are considered as part of the two-fermion signal. In such events, the additional fermion pairs are typically lost down the beampipe of the experiments, such that the visible event topologies are usually similar to difermion events with photons radiated from the initial state.

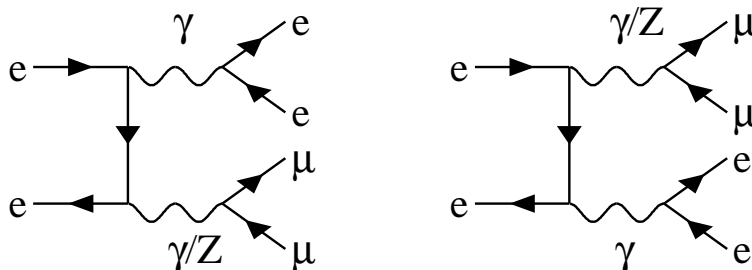


Figure 3.1: Diagrams leading to the production of initial state non-singlet electron-positron pairs in $e^+e^- \rightarrow \mu^+\mu^-$, which are considered as signal in the common signal definition.

The corrections to the common signal definition were applied in two stages. First, for any measurement which used a restricted angular range or s' cut different from the default, a multiplicative correction was applied to the measurement, the associated errors, and the associated SM prediction to correct the acceptance to 4π and to the common s' cut. These corrections were calculated with ZFITTER for each centre-of-mass energy value. Although these corrections are sizeable, up to 14%, they are expected to be well modelled. In the second stage an additive correction was used to correct for any other differences in signal definition (*e.g.*, use of a different s' definition, inclusion of interference between initial- and final-state radiation, treatment of four-fermion contribution) and centre-of-mass energy. The additive correction is simply the difference between the SM prediction calculated using the common signal definition, at the mean centre-of-mass energy of the measurements, and that provided by the experiment (corrected for acceptance where necessary).

Uncertainties derived from a comparison of ZFITTER with KK2f [60] are included; these are shown in Table 3.2. Additional errors are also included to account for those cases where the SM prediction provided by the experiment had used a version of ZFITTER other than the default one, or different parameters; these are shown in Table 3.3. The inclusion of these errors has a very small effect on the averages. The hadronic cross-sections change by less than 0.02%, the leptonic cross-sections by less than 0.1% and typically 0.05% and the lepton asymmetries by 0.001.

	$\sigma(q\bar{q})$	$\sigma(\mu^+\mu^-)$	$\sigma(\tau^+\tau^-)$	$A_{\text{FB}}(\mu^+\mu^-)$	$A_{\text{FB}}(\tau^+\tau^-)$
cos θ cut	0.0005	0.0005	0.0005	–	–
s' cut	0.0015	0.0005	0.0005	–	–
s' definition	0.002	0.001	0.001	0.0002	0.0002
ISR-FSR interference	0.002	0.002	0.002	0.005	0.005

Table 3.2: Errors derived from a comparison between ZFITTER and KK2f for variations on the standard signal definition. Values for cross-sections are given as a fraction of the corresponding cross-section; those for asymmetries are absolute.

Expt.	Energies	$\sigma(q\bar{q})$	$\sigma(\mu^+\mu^-)$	$\sigma(\tau^+\tau^-)$	$A_{\text{FB}}(\mu^+\mu^-)$	$A_{\text{FB}}(\tau^+\tau^-)$
ALEPH	130–183	0.002	0.005	0.005	0.001	0.001
	189–207	0.002	0.003	0.003	0.0006	0.0006
DELPHI	130–207	0.00015	0.00007	0.00007	0.00002	0.00002
L3	130–189	0.002	0.005	0.005	0.005	0.005
	192–207	0.002	0.003	0.003	0.002	0.002
OPAL	130–207	0.00005	0.00005	0.00005	–	–

Table 3.3: Errors applied to account for uncertainties on the ZFITTER predictions quoted by each experiment, depending on ZFITTER version and parameter settings used by each experiment. Values for cross-sections are given as a fraction of the corresponding cross-section; those for asymmetries are absolute.

Theoretical uncertainties associated with the SM predictions for each of the measurements are not included during the averaging procedure, but must be included when assessing the compatibility of the data with theoretical predictions. The theoretical uncertainties on the SM predictions amount to 0.26% on $\sigma(q\bar{q})$, 0.4% on $\sigma(\mu^+\mu^-)$ and $\sigma(\tau^+\tau^-)$, 2% on $\sigma(e^+e^-)$, and 0.004 on the leptonic forward-backward asymmetries [59].

The average is performed using the best linear unbiased estimator technique (BLUE) [62], which is equivalent to a χ^2 minimisation. All data from the nominal centre-of-mass energy points are averaged at the same time.

Particular care is taken to ensure that the correlations between the hadronic cross-sections are reasonably estimated. The errors are broken down into six categories, with the ensuing correlations accounted for in the combinations:

- The statistical uncertainty.
- The systematic uncertainty for the final state X which is fully correlated between energy points for that experiment.
- The systematic uncertainty for experiment Y which is fully correlated between different final states for this energy point.
- The systematic uncertainty for the final state X which is fully correlated between energy points and between different experiments.

¹ZFITTER flags BOXD=2, CONV=2, FINR=0, INTF=0, ALEM=2.

- The systematic uncertainty which is fully correlated between energy points and between different experiments for all final states.
- The uncorrelated systematic uncertainty.

The measurements used in the combination are presented in Appendix B.1, using this decomposition of the uncertainties. Uncertainties in the hadronic cross-sections arising from fragmentation models and modelling of ISR are treated as fully correlated between experiments. Despite some differences between the models used and the methods of evaluating the errors in the different experiments, there are significant common elements in the estimation of these sources of uncertainty.

Table 3.4 gives the averaged cross-sections and forward-backward asymmetries for all energies. The χ^2/dof for the average of the LEP-II $f\bar{f}$ data is 163/180, corresponding to a χ^2 probability of 81%. Most correlations are rather small, with the largest components at any given pair of energies being those between the hadronic cross-sections. The other off-diagonal terms in the correlation matrix are smaller than 10%. The correlation matrix between the averaged hadronic cross-sections at different centre-of-mass energies is given in Table 3.5.

Figures 3.2 and 3.3 show the LEP averaged cross-sections and asymmetries, respectively, as a function of the centre-of-mass energy, together with the SM predictions. There is good agreement between the SM expectations and the measurements of the individual experiments and the combined averages. The ratios of the measured cross-sections and asymmetries to the SM expectations, averaged over all energies and taking into account the correlations between the data points and the theoretical errors on the SM predictions, are given in Table 3.6. It is concluded that there is no evidence in the results of the combinations of the cross-sections and lepton forward-backward asymmetries for physics beyond the SM in the process $e^+e^- \rightarrow f\bar{f}$, for $f = q, \mu$ or τ .

3.3 Differential Cross-Sections for Muon- and Tau-Pair Final States

The LEP experiments have measured the differential cross-section, $\frac{d\sigma}{d\cos\theta}$, for the $e^+e^- \rightarrow \mu^+\mu^-$ and $e^+e^- \rightarrow \tau^+\tau^-$ channels for samples of events with high effective centre-of-mass energy, $\sqrt{s'/s} > 0.85$. A combination of these results is made using the BLUE technique. For some bins the number of observed events is very small, so the statistical error associated with each measurement is taken as the expected statistical error on the differential cross-section, computed from the expected number of events in each bin for each experiment. Using a Monte-Carlo simulation it has been shown that this method provides a good approximation to the exact likelihood method based on Poisson statistics.

The combination includes data from 183 GeV to 207 GeV from DELPHI and OPAL, data at 189 GeV from L3 and data from 189 GeV to 207 GeV from ALEPH. Each experiment's data are binned in 10 bins of $\cos\theta$ at each energy, using their own signal definition. The polar scattering angle, θ , is the angle of the outgoing negative lepton with respect to the incoming electron direction in the detector coordinate system. The outer acceptances of the most forward and most backward bins for which the experiments present their data are different. This was accounted for as part of the correction to a common signal definition. The ranges in $\cos\theta$ for the measurements of the individual experiments and the average are given in Table 3.7. The signal definition used corresponded to the definition given in Section 3.2.

Quantity	\sqrt{s} (GeV)	Average value	SM	\sqrt{s} (GeV)	Average value	SM
$\sigma(q\bar{q})$	130	$82.445 \pm 2.197 \pm 0.766$	83.090	192	$22.064 \pm 0.507 \pm 0.107$	21.259
$\sigma(\mu^+\mu^-)$	130	$8.606 \pm 0.699 \pm 0.131$	8.455	192	$2.926 \pm 0.181 \pm 0.018$	3.096
$\sigma(\tau^+\tau^-)$	130	$9.020 \pm 0.944 \pm 0.175$	8.452	192	$2.860 \pm 0.246 \pm 0.032$	3.096
$A_{\text{fb}}(\mu^+\mu^-)$	130	$0.694 \pm 0.059 \pm 0.012$	0.705	192	$0.551 \pm 0.051 \pm 0.007$	0.566
$A_{\text{fb}}(\tau^+\tau^-)$	130	$0.682 \pm 0.079 \pm 0.016$	0.705	192	$0.590 \pm 0.067 \pm 0.008$	0.565
$\sigma(q\bar{q})$	136	$66.984 \pm 1.954 \pm 0.630$	66.787	196	$20.307 \pm 0.294 \pm 0.096$	20.148
$\sigma(\mu^+\mu^-)$	136	$8.325 \pm 0.692 \pm 0.109$	7.292	196	$2.994 \pm 0.110 \pm 0.018$	2.961
$\sigma(\tau^+\tau^-)$	136	$7.167 \pm 0.851 \pm 0.143$	7.290	196	$2.961 \pm 0.152 \pm 0.029$	2.961
$A_{\text{fb}}(\mu^+\mu^-)$	136	$0.707 \pm 0.061 \pm 0.011$	0.684	196	$0.592 \pm 0.030 \pm 0.005$	0.562
$A_{\text{fb}}(\tau^+\tau^-)$	136	$0.761 \pm 0.089 \pm 0.013$	0.684	196	$0.464 \pm 0.044 \pm 0.008$	0.561
$\sigma(q\bar{q})$	161	$37.166 \pm 1.063 \pm 0.398$	35.234	200	$19.170 \pm 0.283 \pm 0.095$	19.105
$\sigma(\mu^+\mu^-)$	161	$4.580 \pm 0.376 \pm 0.062$	4.610	200	$3.072 \pm 0.108 \pm 0.018$	2.833
$\sigma(\tau^+\tau^-)$	161	$5.715 \pm 0.553 \pm 0.139$	4.610	200	$2.952 \pm 0.148 \pm 0.029$	2.832
$A_{\text{fb}}(\mu^+\mu^-)$	161	$0.542 \pm 0.069 \pm 0.012$	0.610	200	$0.519 \pm 0.031 \pm 0.005$	0.558
$A_{\text{fb}}(\tau^+\tau^-)$	161	$0.764 \pm 0.061 \pm 0.013$	0.610	200	$0.539 \pm 0.041 \pm 0.007$	0.558
$\sigma(q\bar{q})$	172	$29.350 \pm 0.989 \pm 0.336$	28.775	202	$18.873 \pm 0.408 \pm 0.098$	18.569
$\sigma(\mu^+\mu^-)$	172	$3.562 \pm 0.331 \pm 0.058$	3.950	202	$2.709 \pm 0.146 \pm 0.017$	2.766
$\sigma(\tau^+\tau^-)$	172	$4.053 \pm 0.469 \pm 0.092$	3.950	202	$2.838 \pm 0.208 \pm 0.022$	2.765
$A_{\text{fb}}(\mu^+\mu^-)$	172	$0.673 \pm 0.077 \pm 0.012$	0.591	202	$0.547 \pm 0.045 \pm 0.005$	0.556
$A_{\text{fb}}(\tau^+\tau^-)$	172	$0.357 \pm 0.098 \pm 0.013$	0.591	202	$0.535 \pm 0.058 \pm 0.009$	0.556
$\sigma(q\bar{q})$	183	$24.599 \pm 0.393 \pm 0.182$	24.215	205	$18.137 \pm 0.282 \pm 0.087$	17.832
$\sigma(\mu^+\mu^-)$	183	$3.505 \pm 0.145 \pm 0.042$	3.444	205	$2.464 \pm 0.098 \pm 0.015$	2.673
$\sigma(\tau^+\tau^-)$	183	$3.367 \pm 0.174 \pm 0.049$	3.444	205	$2.783 \pm 0.149 \pm 0.028$	2.672
$A_{\text{fb}}(\mu^+\mu^-)$	183	$0.564 \pm 0.034 \pm 0.008$	0.576	205	$0.556 \pm 0.034 \pm 0.004$	0.553
$A_{\text{fb}}(\tau^+\tau^-)$	183	$0.604 \pm 0.044 \pm 0.011$	0.576	205	$0.618 \pm 0.040 \pm 0.008$	0.553
$\sigma(q\bar{q})$	189	$22.492 \pm 0.206 \pm 0.119$	22.184	207	$17.316 \pm 0.212 \pm 0.083$	17.482
$\sigma(\mu^+\mu^-)$	189	$3.150 \pm 0.075 \pm 0.016$	3.207	207	$2.618 \pm 0.078 \pm 0.014$	2.628
$\sigma(\tau^+\tau^-)$	189	$3.204 \pm 0.107 \pm 0.032$	3.206	207	$2.502 \pm 0.109 \pm 0.029$	2.628
$A_{\text{fb}}(\mu^+\mu^-)$	189	$0.571 \pm 0.020 \pm 0.005$	0.569	207	$0.535 \pm 0.028 \pm 0.004$	0.552
$A_{\text{fb}}(\tau^+\tau^-)$	189	$0.590 \pm 0.026 \pm 0.007$	0.569	207	$0.590 \pm 0.034 \pm 0.010$	0.552

Table 3.4: Combined LEP results for the $e^+e^- \rightarrow f\bar{f}$ cross-sections (in pb) and forward-backward asymmetries; in each case the first error is statistical and the second systematic. The SM predictions are from ZFITTER.

\sqrt{s} (GeV)	\sqrt{s} (GeV)											
	130	136	161	172	183	189	192	196	200	202	205	207
130	1.000	0.060	0.065	0.058	0.104	0.112	0.043	0.065	0.065	0.045	0.061	0.076
136	0.060	1.000	0.061	0.055	0.098	0.104	0.040	0.061	0.061	0.042	0.057	0.071
161	0.065	0.061	1.000	0.060	0.108	0.117	0.044	0.067	0.068	0.047	0.063	0.078
172	0.058	0.055	0.060	1.000	0.096	0.103	0.039	0.060	0.060	0.041	0.056	0.069
183	0.104	0.098	0.108	0.096	1.000	0.205	0.078	0.120	0.121	0.084	0.114	0.140
189	0.112	0.104	0.117	0.103	0.205	1.000	0.097	0.149	0.151	0.105	0.141	0.174
192	0.043	0.040	0.044	0.039	0.078	0.097	1.000	0.060	0.061	0.042	0.057	0.071
196	0.065	0.061	0.067	0.060	0.120	0.149	0.060	1.000	0.094	0.066	0.089	0.110
200	0.065	0.061	0.068	0.060	0.121	0.151	0.061	0.094	1.000	0.067	0.090	0.112
202	0.045	0.042	0.047	0.041	0.084	0.105	0.042	0.066	0.067	1.000	0.063	0.079
205	0.061	0.057	0.063	0.056	0.114	0.141	0.057	0.089	0.090	0.063	1.000	0.106
207	0.076	0.071	0.078	0.069	0.140	0.174	0.071	0.110	0.112	0.079	0.106	1.000

Table 3.5: The correlation coefficients between averaged hadronic cross-sections at different energies.

Channel	Ratio	Deviation
$\sigma(q\bar{q})$	1.0092 ± 0.0076	+1.21
$\sigma(\mu^+\mu^-)$	0.9936 ± 0.0141	-0.45
$\sigma(\tau^+\tau^-)$	1.0005 ± 0.0203	+0.02
$A_{\text{FB}}(\mu^+\mu^-)$	0.9925 ± 0.0212	-0.35
$A_{\text{FB}}(\tau^+\tau^-)$	1.0246 ± 0.0274	+0.90

Table 3.6: Comparison of measurements to SM predictions for each channel. The second column gives the mean ratio of data to prediction; the third column gives the numbers of standard deviations of the ratio from unity.

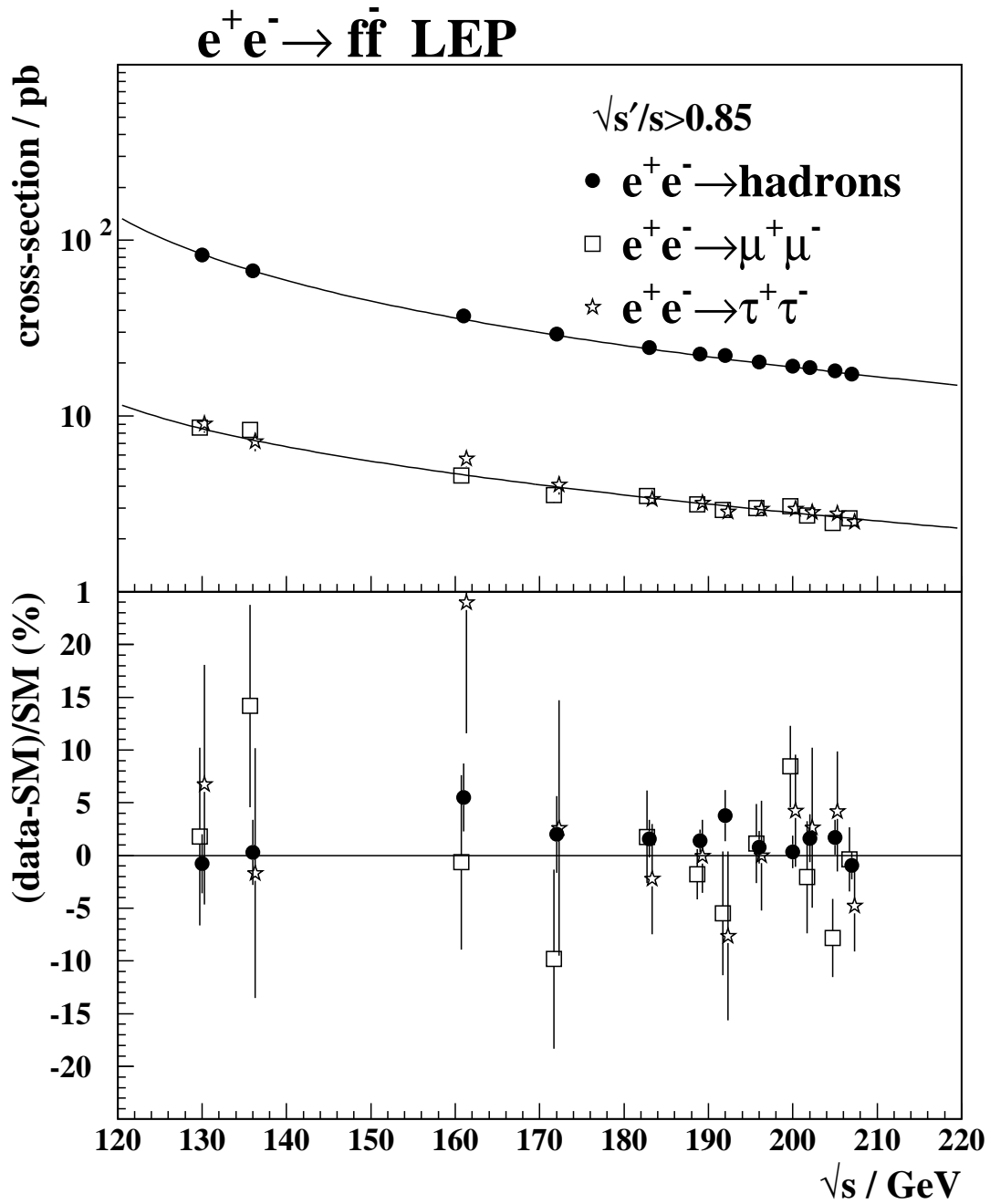


Figure 3.2: Combined LEP results on the cross-sections for $q\bar{q}$, $\mu^+\mu^-$ and $\tau^+\tau^-$ final states, as a function of centre-of-mass energy. The expectations of the SM, computed with ZFITTER, are shown as curves. The lower plot shows the difference between the data and the SM.

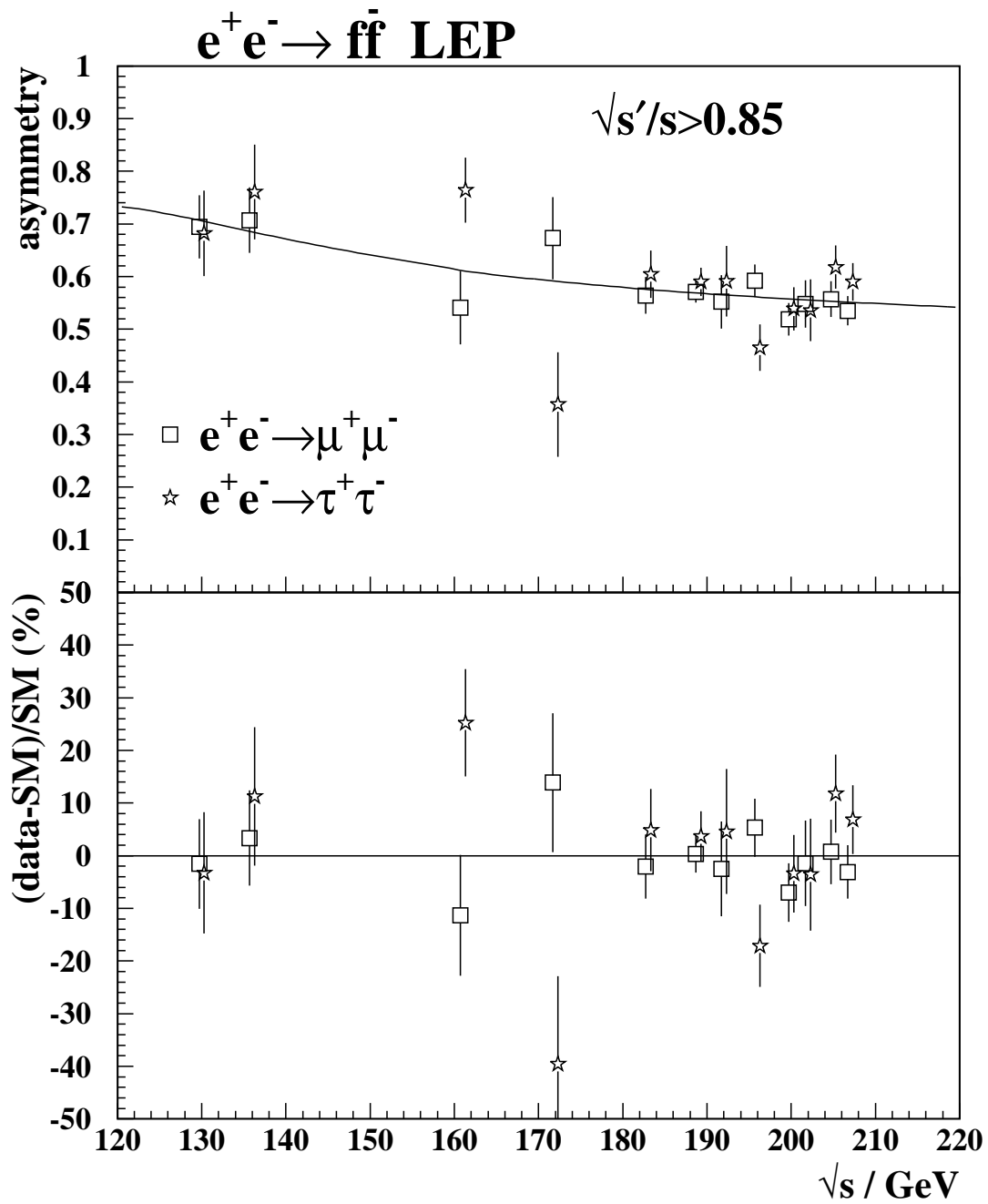


Figure 3.3: Combined LEP results on the forward-backward asymmetry for $\mu^+\mu^-$ and $\tau^+\tau^-$ final states as a function of centre-of-mass energy. The expectations of the SM computed with ZFITTER, are shown as curves. The lower plot shows differences between the data and the SM.

Experiment	$\cos \theta_{min}$	$\cos \theta_{max}$
ALEPH	-0.95	0.95
DELPHI ($e^+e^- \rightarrow \mu^+\mu^-$)	-0.97	0.97
DELPHI ($e^+e^- \rightarrow \tau^+\tau^-$)	-0.96	0.96
L3	-0.90	0.90
OPAL	-1.00	1.00
Average	-1.00	1.00

Table 3.7: The acceptances in $\cos \theta$ for which the experimental measurements at all energies are presented for combination, and the acceptance for the LEP average. For DELPHI the acceptance is shown for the different channels. For ALEPH, L3 and OPAL the acceptance is the same for muon and tau-lepton channels.

Correlated systematic errors between different experiments, channels and energies, arising from uncertainties on the overall normalisation, are considered in the averaging procedure. All data from all energies are combined in a single fit to obtain averages at each centre-of-mass energy.

The results of the averages are reported in Tables 3.8 and 3.9 and shown in Figures 3.4 and 3.5, with more details summarised in Appendix B.2. The correlations between bins in the average are less than 2% of the total error on the averages in each bin. The combination results in a χ^2 of 352.2 for 320 degrees of freedom, corresponding to a probability of 10.4%.

3.4 Differential Cross-Sections for Electron-Positron Final States

The LEP experiments have measured the differential cross-section, $\frac{d\sigma}{d\cos\theta}$ for the process $e^+e^- \rightarrow e^+e^-$ with different acollinearity cuts [32, 33, 34, 35]. The results are combined using a χ^2 fit to the measured differential cross-sections, using the experimental errors as given by the experiments. In contrast to the muon and tau-lepton channels, the higher statistics makes the use of expected errors, as discussed in Section 3.3, unnecessary here.

The combination includes data from 189 to 207 GeV, provided by ALEPH, DELPHI and OPAL. Each experiment's data are binned according to an agreed common definition, which takes into account the large forward peak of Bhabha scattering:

- 10 bins for $\cos \theta$ between 0.0 and 0.90 and
- 5 bins for $\cos \theta$ between -0.90 and 0.0

at each energy, where the polar scattering angle, θ , is the angle of the outgoing electron with respect to the incoming electron direction in the lab coordinate system. Apart from the common binning in $\cos \theta$, each experiment uses its own signal definition. The ranges in $\cos \theta$ covered by the individual experiments and the range used for the combination are given in Table 3.10. The signal definition used for the LEP average corresponds to an acollinearity cut of 10° .

Correlated systematic errors between different experiments, energies and bins at the same energy, arising from uncertainties on the overall normalisation, and from migration of events between forward and backward bins with the same absolute value of $\cos \theta$ due to uncertainties in the corrections for charge confusion, were considered in the averaging procedure.

$\cos \theta$ bin	\sqrt{s} (GeV)	Average value	SM	\sqrt{s} (GeV)	Average value	SM
[-1.00, -0.80]	183	0.197±0.183	0.547	200	0.558±0.113	0.501
[-0.80, -0.60]	183	0.589±0.163	0.534	200	0.376±0.098	0.478
[-0.60, -0.40]	183	0.807±0.174	0.627	200	0.799±0.105	0.541
[-0.40, -0.20]	183	1.033±0.197	0.823	200	0.817±0.118	0.689
[-0.20, 0.00]	183	1.178±0.236	1.121	200	1.105±0.139	0.922
[0.00, 0.20]	183	1.778±0.276	1.521	200	1.462±0.162	1.239
[0.20, 0.40]	183	2.143±0.315	2.020	200	1.849±0.185	1.640
[0.40, 0.60]	183	2.690±0.367	2.619	200	2.122±0.211	2.126
[0.60, 0.80]	183	2.916±0.420	3.314	200	2.947±0.239	2.694
[0.80, 1.00]	183	4.368±0.529	4.096	200	3.474±0.306	3.336
[-1.00, -0.80]	189	0.614±0.080	0.532	202	1.137±0.162	0.495
[-0.80, -0.60]	189	0.420±0.065	0.514	202	0.295±0.139	0.471
[-0.60, -0.40]	189	0.530±0.069	0.595	202	0.506±0.149	0.531
[-0.40, -0.20]	189	0.651±0.077	0.772	202	0.455±0.169	0.674
[-0.20, 0.00]	189	1.064±0.089	1.044	202	0.860±0.197	0.900
[0.00, 0.20]	189	1.313±0.111	1.411	202	1.010±0.230	1.208
[0.20, 0.40]	189	2.038±0.123	1.872	202	1.749±0.264	1.599
[0.40, 0.60]	189	2.158±0.139	2.426	202	1.844±0.299	2.072
[0.60, 0.80]	189	2.954±0.158	3.072	202	2.268±0.339	2.627
[0.80, 1.00]	189	3.795±0.216	3.799	202	3.396±0.435	3.254
[-1.00, -0.80]	192	0.481±0.198	0.524	205	0.621±0.113	0.485
[-0.80, -0.60]	192	0.384±0.173	0.504	205	0.385±0.098	0.461
[-0.60, -0.40]	192	0.788±0.186	0.579	205	0.382±0.104	0.517
[-0.40, -0.20]	192	0.581±0.212	0.748	205	0.443±0.118	0.654
[-0.20, 0.00]	192	1.324±0.248	1.008	205	0.891±0.137	0.870
[0.00, 0.20]	192	1.187±0.292	1.360	205	1.205±0.160	1.166
[0.20, 0.40]	192	1.932±0.334	1.803	205	1.614±0.183	1.542
[0.40, 0.60]	192	2.080±0.379	2.337	205	1.663±0.209	1.998
[0.60, 0.80]	192	3.003±0.429	2.960	205	2.097±0.237	2.534
[0.80, 1.00]	192	3.083±0.552	3.662	205	3.318±0.306	3.140
[-1.00, -0.80]	196	0.535±0.119	0.512	207	0.518±0.087	0.481
[-0.80, -0.60]	196	0.485±0.103	0.491	207	0.496±0.075	0.456
[-0.60, -0.40]	196	0.668±0.111	0.560	207	0.473±0.079	0.510
[-0.40, -0.20]	196	0.484±0.126	0.718	207	0.781±0.089	0.643
[-0.20, 0.00]	196	0.802±0.147	0.964	207	0.795±0.104	0.855
[0.00, 0.20]	196	1.507±0.172	1.298	207	0.995±0.121	1.145
[0.20, 0.40]	196	1.657±0.197	1.720	207	1.630±0.139	1.515
[0.40, 0.60]	196	2.303±0.223	2.229	207	2.247±0.159	1.963
[0.60, 0.80]	196	2.949±0.253	2.824	207	2.491±0.179	2.489
[0.80, 1.00]	196	3.272±0.325	3.495	207	2.995±0.231	3.086

Table 3.8: Combined LEP results for the $e^+e^- \rightarrow \mu^+\mu^-$ differential cross-sections, in pb divided by $\Delta(\cos \theta)$. The combined statistical and systematic error is shown. The SM predictions are from ZFITTER.

$\cos \theta$ bin	\sqrt{s} (GeV)	Average value	SM	\sqrt{s} (GeV)	Average value	SM
[-1.00, -0.80]	183	0.302±0.351	0.548	200	0.489±0.201	0.501
[-0.80, -0.60]	183	0.206±0.240	0.535	200	0.619±0.141	0.478
[-0.60, -0.40]	183	0.198±0.230	0.627	200	0.528±0.137	0.541
[-0.40, -0.20]	183	0.542±0.254	0.823	200	0.628±0.155	0.689
[-0.20, 0.00]	183	1.364±0.302	1.121	200	1.067±0.186	0.922
[0.00, 0.20]	183	1.519±0.350	1.521	200	1.130±0.214	1.239
[0.20, 0.40]	183	1.583±0.389	2.020	200	1.871±0.240	1.640
[0.40, 0.60]	183	2.296±0.450	2.619	200	2.043±0.274	2.125
[0.60, 0.80]	183	3.954±0.574	3.313	200	2.777±0.339	2.694
[0.80, 1.00]	183	4.156±0.919	4.095	200	3.437±0.523	3.336
[-1.00, -0.80]	189	0.389±0.123	0.532	202	0.968±0.287	0.495
[-0.80, -0.60]	189	0.379±0.093	0.515	202	0.322±0.189	0.471
[-0.60, -0.40]	189	0.485±0.089	0.595	202	0.420±0.194	0.531
[-0.40, -0.20]	189	0.809±0.100	0.772	202	0.731±0.220	0.674
[-0.20, 0.00]	189	0.848±0.118	1.044	202	0.922±0.263	0.900
[0.00, 0.20]	189	1.323±0.139	1.411	202	0.789±0.300	1.208
[0.20, 0.40]	189	1.989±0.154	1.872	202	1.953±0.341	1.599
[0.40, 0.60]	189	2.445±0.179	2.426	202	1.838±0.386	2.072
[0.60, 0.80]	189	2.467±0.225	3.071	202	3.129±0.479	2.626
[0.80, 1.00]	189	4.111±0.357	3.798	202	3.186±0.747	3.254
[-1.00, -0.80]	192	0.014±0.325	0.524	205	0.363±0.203	0.486
[-0.80, -0.60]	192	0.355±0.247	0.505	205	0.562±0.137	0.461
[-0.60, -0.40]	192	0.479±0.245	0.580	205	0.603±0.135	0.517
[-0.40, -0.20]	192	0.762±0.278	0.748	205	0.443±0.154	0.654
[-0.20, 0.00]	192	0.816±0.331	1.008	205	0.397±0.179	0.870
[0.00, 0.20]	192	1.609±0.385	1.360	205	1.242±0.209	1.166
[0.20, 0.40]	192	1.810±0.433	1.803	205	1.522±0.237	1.542
[0.40, 0.60]	192	2.059±0.491	2.337	205	1.846±0.268	1.998
[0.60, 0.80]	192	2.643±0.599	2.959	205	2.045±0.330	2.533
[0.80, 1.00]	192	2.575±0.935	3.661	205	4.671±0.520	3.140
[-1.00, -0.80]	196	0.810±0.211	0.513	207	0.272±0.145	0.481
[-0.80, -0.60]	196	0.738±0.147	0.491	207	0.412±0.106	0.456
[-0.60, -0.40]	196	0.524±0.141	0.560	207	0.534±0.104	0.510
[-0.40, -0.20]	196	0.688±0.162	0.718	207	0.563±0.118	0.644
[-0.20, 0.00]	196	0.976±0.195	0.964	207	0.683±0.140	0.855
[0.00, 0.20]	196	0.977±0.225	1.298	207	1.443±0.161	1.145
[0.20, 0.40]	196	1.648±0.252	1.719	207	1.351±0.181	1.514
[0.40, 0.60]	196	1.965±0.289	2.228	207	1.761±0.207	1.962
[0.60, 0.80]	196	2.269±0.357	2.823	207	1.655±0.255	2.489
[0.80, 1.00]	196	3.346±0.557	3.494	207	3.597±0.399	3.085

Table 3.9: Combined LEP results for the $e^+e^- \rightarrow \tau^+\tau^-$ differential cross-sections, in pb divided by $\Delta(\cos \theta)$. The combined statistical and systematic error is shown. The SM predictions are from ZFITTER.

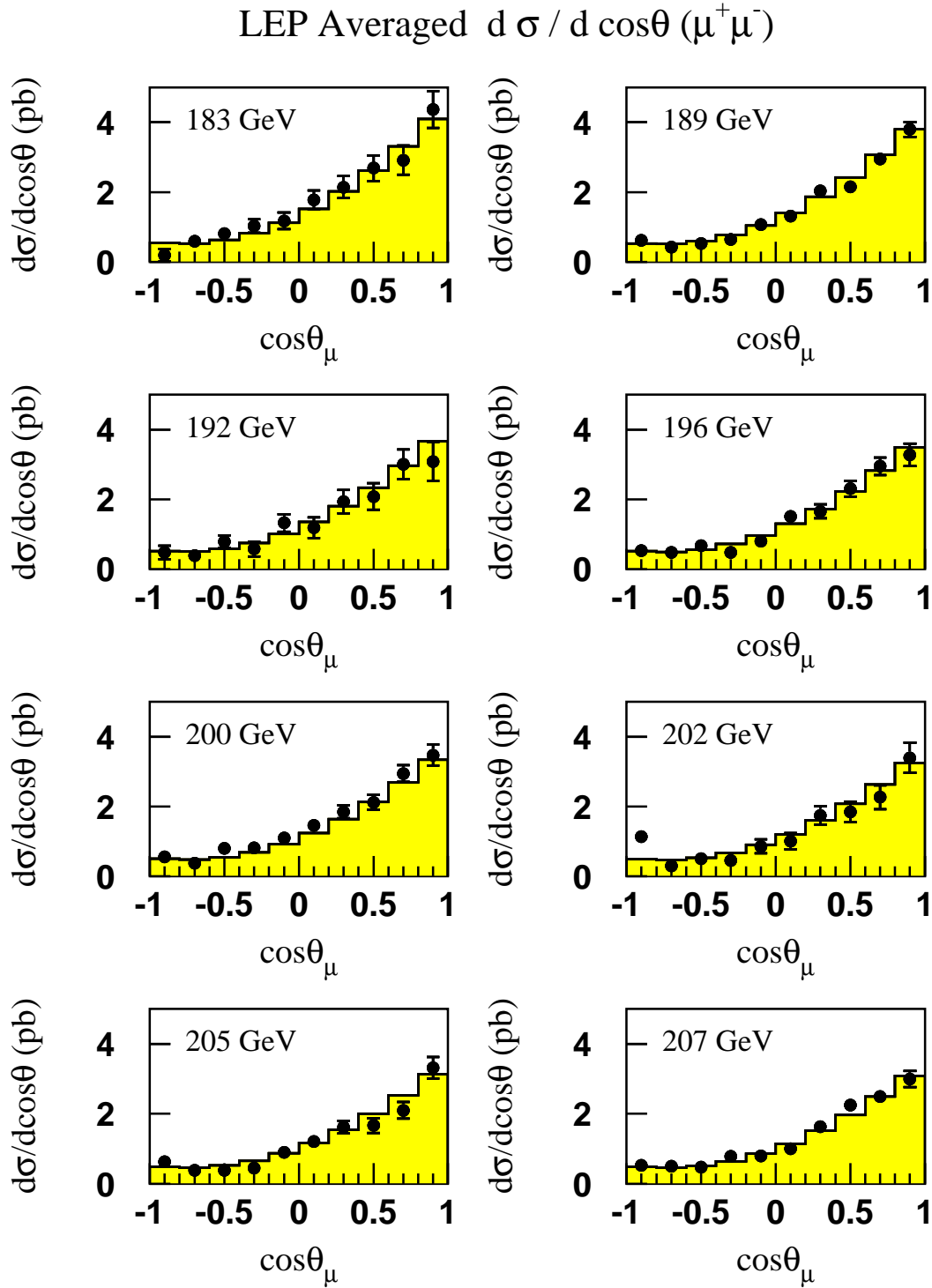


Figure 3.4: LEP averaged differential cross-sections for $e^+e^- \rightarrow \mu^+\mu^-$ at energies of 183–207 GeV. The SM predictions, shown as solid histograms, are computed with ZFITTER.

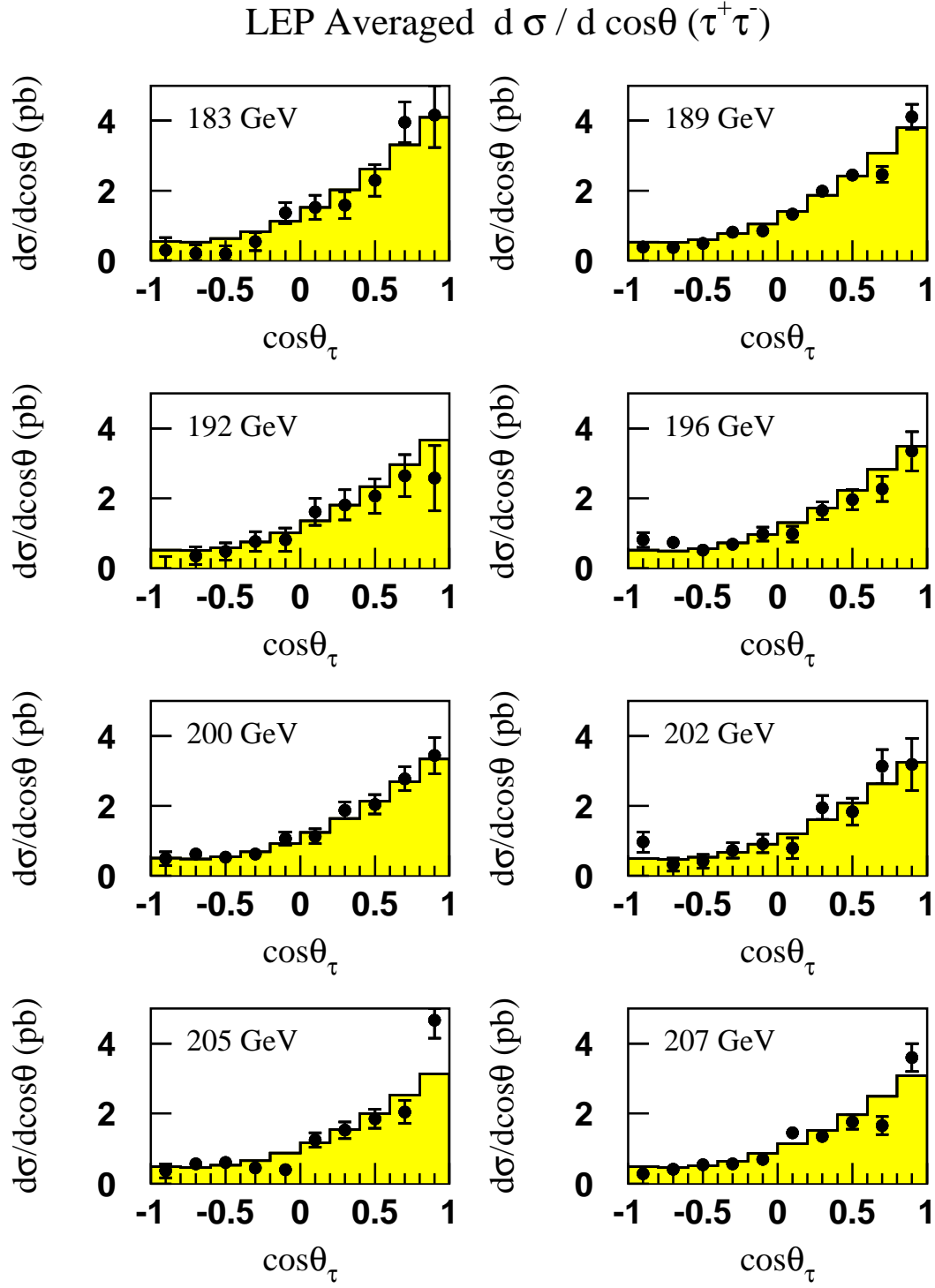


Figure 3.5: LEP averaged differential cross-sections for $e^+e^- \rightarrow \tau^+\tau^-$ at energies of 183–207 GeV. The SM predictions, shown as solid histograms, are computed with ZFITTER.

Experiment	$\cos \theta_{min}$	$\cos \theta_{max}$
ALEPH ($\sqrt{s'}/s > 0.85$)	-0.90	0.90
DELPHI (acol. $< 20^\circ$)	-0.72	0.72
OPAL (acol. $< 10^\circ$)	-0.90	0.90
Average (acol. $< 10^\circ$)	-0.90	0.90

Table 3.10: The acceptances for which experimental data are presented for the $e^+e^- \rightarrow e^+e^-$ channel and the acceptance for the LEP average.

An average for all energies between 189 and 207 GeV was performed. The results of the averages are reported in Tables 3.11 and 3.12 and shown in Figures 3.6 and 3.7, with more details summarised in Appendix B.3. The χ^2/dof for the average is 199.4/189, corresponding to a probability of 28.8%.

The correlations between bins in the average are well below 5% of the total error on the averages in each bin for most of the cases, and around 10% for bins close to the edges of the acceptance. The agreement between the averaged data and the predictions from the Monte-Carlo generator BHWIDE [64] is good, with a χ^2 of 85 for 90 degrees of freedom, corresponding to a probability of 63%. In conclusion, the combined results for the $e^+e^- \rightarrow e^+e^-$ channel are compatible with the SM.

3.5 Interpretation

The combined cross-section and asymmetry results are interpreted in a variety of models. They are used to place limits on the mass of a possible additional heavy neutral boson, Z' , under different assumptions. Limits on contact interactions between leptons and between leptons and quarks are obtained. The former results are of particular interest since they are inaccessible to $p\bar{p}$, pp or ep colliders. Limits are also provided on the masses of leptoquarks. The $e^+e^- \rightarrow e^+e^-$ channel is used to constrain the scale of gravity in models with extra dimensions.

3.5.1 Models with Z' Bosons

The combined hadronic and leptonic cross-sections and the leptonic forward-backward asymmetries are used to fit the data to models including an additional, heavy, neutral boson, Z' .

New gauge bosons in the intermediate TeV scale are motivated by several theoretical approaches [65]. For instance, the breaking of Grand Unifying Theories (GUTs) based on $SO(10)$ or E_6 symmetries may leave one or several $U(1)$ remnants unbroken down to TeV energies, before the symmetry reduces to the SM symmetry. In the case of the E_6 model, one has the possible breaking pattern:

$$E_6 \rightarrow SO(10) \times U(1)_\psi \rightarrow SU(5) \times U(1)_\chi \times U(1)_\psi \rightarrow SM \times U(1)', \quad (3.6)$$

and the new Z' boson corresponding to the final $U(1)'$ remnant is a linear combination of the gauge bosons of the two $U(1)$ groups, $U(1)_\chi$ and $U(1)_\psi$, generated in the two-step symmetry breaking, $Z' = Z'_\chi \cos \beta + Z'_\psi \sin \beta$. The value $\beta = \arctan(-\sqrt{5/3})$ would correspond to a Z'_η originating from the direct breaking of E_6 to a rank-5 group in superstring inspired models.

$\cos\theta$ bin	\sqrt{s} (GeV)	Average value	SM	\sqrt{s} (GeV)	Average value	SM
$[-0.90, -0.72]$	189	1.401 ± 0.161	1.590	196	1.470 ± 0.261	1.483
$[-0.72, -0.54]$	189	2.030 ± 0.160	1.816	196	1.527 ± 0.221	1.695
$[-0.54, -0.36]$	189	2.162 ± 0.170	2.162	196	2.058 ± 0.250	2.000
$[-0.36, -0.18]$	189	2.298 ± 0.186	2.681	196	2.788 ± 0.284	2.498
$[-0.18, 0.00]$	189	4.321 ± 0.230	3.906	196	3.646 ± 0.318	3.610
$[0.00, 0.09]$	189	4.898 ± 0.348	5.372	196	5.887 ± 0.521	4.999
$[0.09, 0.18]$	189	6.090 ± 0.404	6.892	196	6.233 ± 0.591	6.406
$[0.18, 0.27]$	189	8.838 ± 0.476	9.610	196	9.016 ± 0.694	8.832
$[0.27, 0.36]$	189	12.781 ± 0.576	13.345	196	13.444 ± 0.856	12.326
$[0.36, 0.45]$	189	19.586 ± 0.707	19.445	196	18.568 ± 0.977	18.039
$[0.45, 0.54]$	189	30.598 ± 0.895	30.476	196	27.056 ± 1.223	28.300
$[0.54, 0.63]$	189	50.488 ± 1.135	51.012	196	49.391 ± 1.619	47.362
$[0.63, 0.72]$	189	95.178 ± 1.520	95.563	196	88.163 ± 2.154	88.473
$[0.72, 0.81]$	189	211.427 ± 2.900	212.390	196	197.369 ± 4.121	198.250
$[0.81, 0.90]$	189	679.146 ± 5.773	689.989	196	637.846 ± 8.003	642.688
$[-0.90, -0.72]$	192	1.300 ± 0.364	1.539	200	1.483 ± 0.245	1.420
$[-0.72, -0.54]$	192	2.099 ± 0.419	1.754	200	1.638 ± 0.214	1.623
$[-0.54, -0.36]$	192	1.871 ± 0.385	2.091	200	2.068 ± 0.227	1.885
$[-0.36, -0.18]$	192	1.808 ± 0.422	2.604	200	2.362 ± 0.250	2.409
$[-0.18, 0.00]$	192	3.800 ± 0.519	3.778	200	4.251 ± 0.313	3.435
$[0.00, 0.09]$	192	5.015 ± 0.891	5.205	200	5.244 ± 0.506	4.770
$[0.09, 0.18]$	192	5.695 ± 0.976	6.692	200	5.888 ± 0.571	6.157
$[0.18, 0.27]$	192	9.239 ± 1.175	9.242	200	8.244 ± 0.667	8.471
$[0.27, 0.36]$	192	12.941 ± 1.414	12.800	200	9.506 ± 0.736	11.773
$[0.36, 0.45]$	192	20.761 ± 1.807	18.776	200	16.376 ± 0.920	17.262
$[0.45, 0.54]$	192	26.466 ± 2.074	29.471	200	27.000 ± 1.214	27.117
$[0.54, 0.63]$	192	49.382 ± 2.671	49.338	200	44.614 ± 1.537	45.607
$[0.63, 0.72]$	192	89.676 ± 3.615	92.079	200	86.454 ± 2.060	85.143
$[0.72, 0.81]$	192	204.579 ± 6.760	206.087	200	190.962 ± 3.941	190.786
$[0.81, 0.90]$	192	655.724 ± 12.588	669.173	200	604.986 ± 7.608	617.718

Table 3.11: Combined LEP results for the $e^+e^- \rightarrow e^+e^-$ differential cross-sections, in pb divided by $\Delta(\cos\theta)$, for \sqrt{s} between 189 GeV and 200 GeV. The combined statistical and systematic error is shown. The SM predictions are from BHWIDE

$\cos\theta$ bin	\sqrt{s} (GeV)	Average value	SM	\sqrt{s} (GeV)	Average value	SM
[-0.90, -0.72]	202	1.568± 0.368	1.401	207	1.440±0.196	1.339
[-0.72, -0.54]	202	1.344± 0.276	1.579	207	1.426±0.163	1.517
[-0.54, -0.36]	202	2.107± 0.345	1.836	207	1.889±0.177	1.745
[-0.36, -0.18]	202	3.240± 0.406	2.361	207	2.156±0.198	2.240
[-0.18, 0.00]	202	2.911± 0.394	3.356	207	3.215±0.233	3.194
[0.00, 0.09]	202	4.603± 0.628	4.669	207	4.434±0.357	4.380
[0.09, 0.18]	202	6.463± 0.861	6.017	207	6.393±0.463	5.729
[0.18, 0.27]	202	7.457± 0.957	8.320	207	6.951±0.481	7.972
[0.27, 0.36]	202	11.032± 1.113	11.554	207	11.221±0.615	11.019
[0.36, 0.45]	202	16.428± 1.338	16.891	207	15.933±0.739	16.053
[0.45, 0.54]	202	27.153± 1.643	26.583	207	25.676±0.923	25.254
[0.54, 0.63]	202	46.490± 2.214	44.786	207	42.075±1.188	42.456
[0.63, 0.72]	202	87.253± 2.887	83.473	207	77.611±1.569	79.639
[0.72, 0.81]	202	189.026± 5.516	186.904	207	173.825±3.002	178.042
[0.81, 0.90]	202	599.860±10.339	605.070	207	573.637±6.024	576.688
[-0.90, -0.72]	205	1.102± 0.205	1.355			
[-0.72, -0.54]	205	1.470± 0.195	1.539			
[-0.54, -0.36]	205	2.050± 0.231	1.786			
[-0.36, -0.18]	205	2.564± 0.255	2.280			
[-0.18, 0.00]	205	3.410± 0.300	3.253			
[0.00, 0.09]	205	5.308± 0.472	4.479			
[0.09, 0.18]	205	5.836± 0.571	5.820			
[0.18, 0.27]	205	7.996± 0.635	8.077			
[0.27, 0.36]	205	10.607± 0.764	11.200			
[0.36, 0.45]	205	14.729± 0.874	16.322			
[0.45, 0.54]	205	26.189± 1.157	25.722			
[0.54, 0.63]	205	43.124± 1.497	43.217			
[0.63, 0.72]	205	79.255± 1.976	80.939			
[0.72, 0.81]	205	179.842± 3.838	180.878			
[0.81, 0.90]	205	587.999± 7.527	586.205			

Table 3.12: Combined LEP results for the $e^+e^- \rightarrow e^+e^-$ differential cross-sections (continued), in pb divided by $\Delta(\cos\theta)$, for \sqrt{s} larger than 200 GeV. The combined statistical and systematic error is shown. The SM predictions are from BHWIDE.

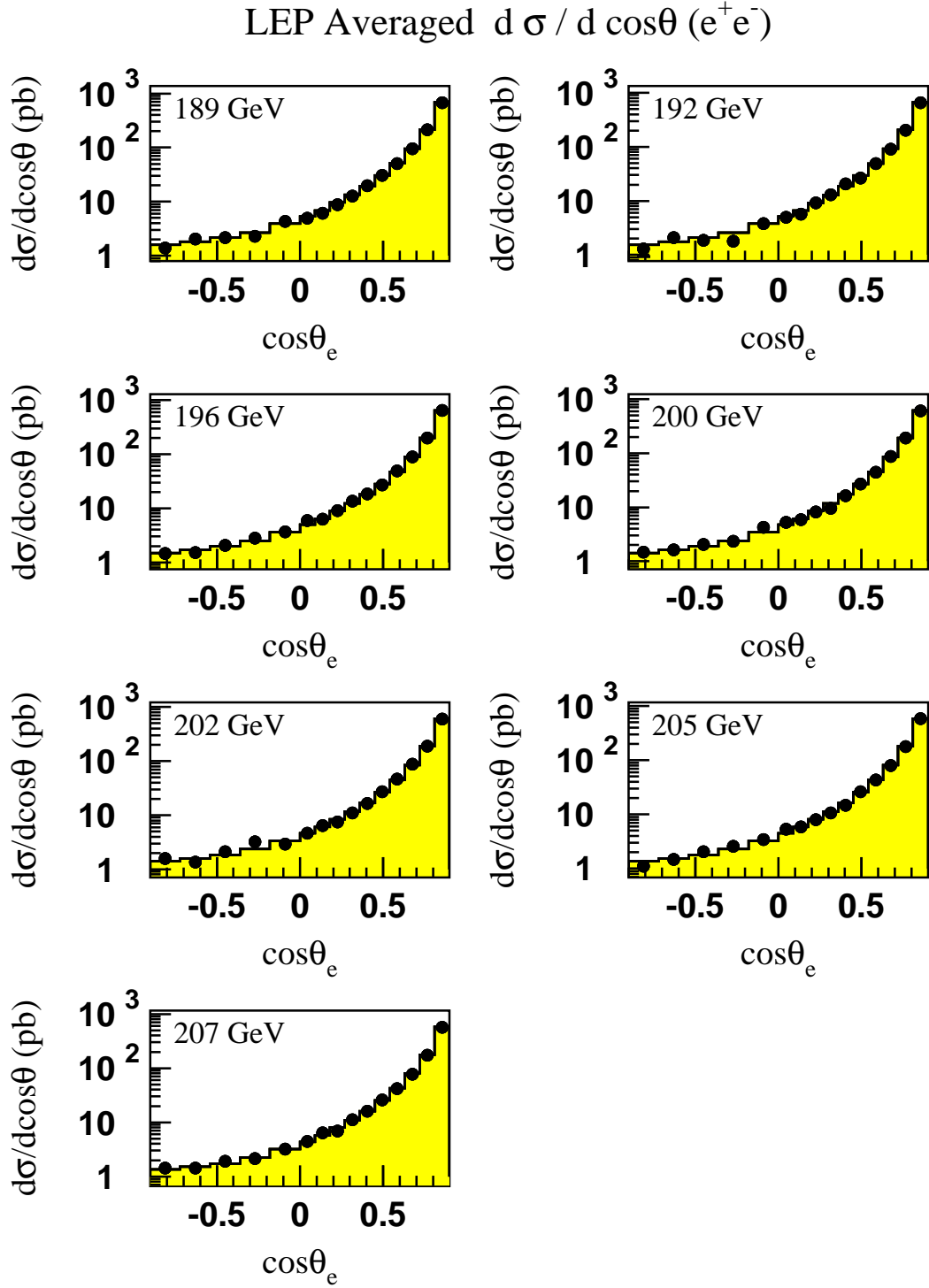


Figure 3.6: LEP averaged differential cross-sections for $e^+e^- \rightarrow e^+e^-$ at energies of 189–207 GeV. The SM predictions, shown as solid histograms, are computed with BHWIDE.

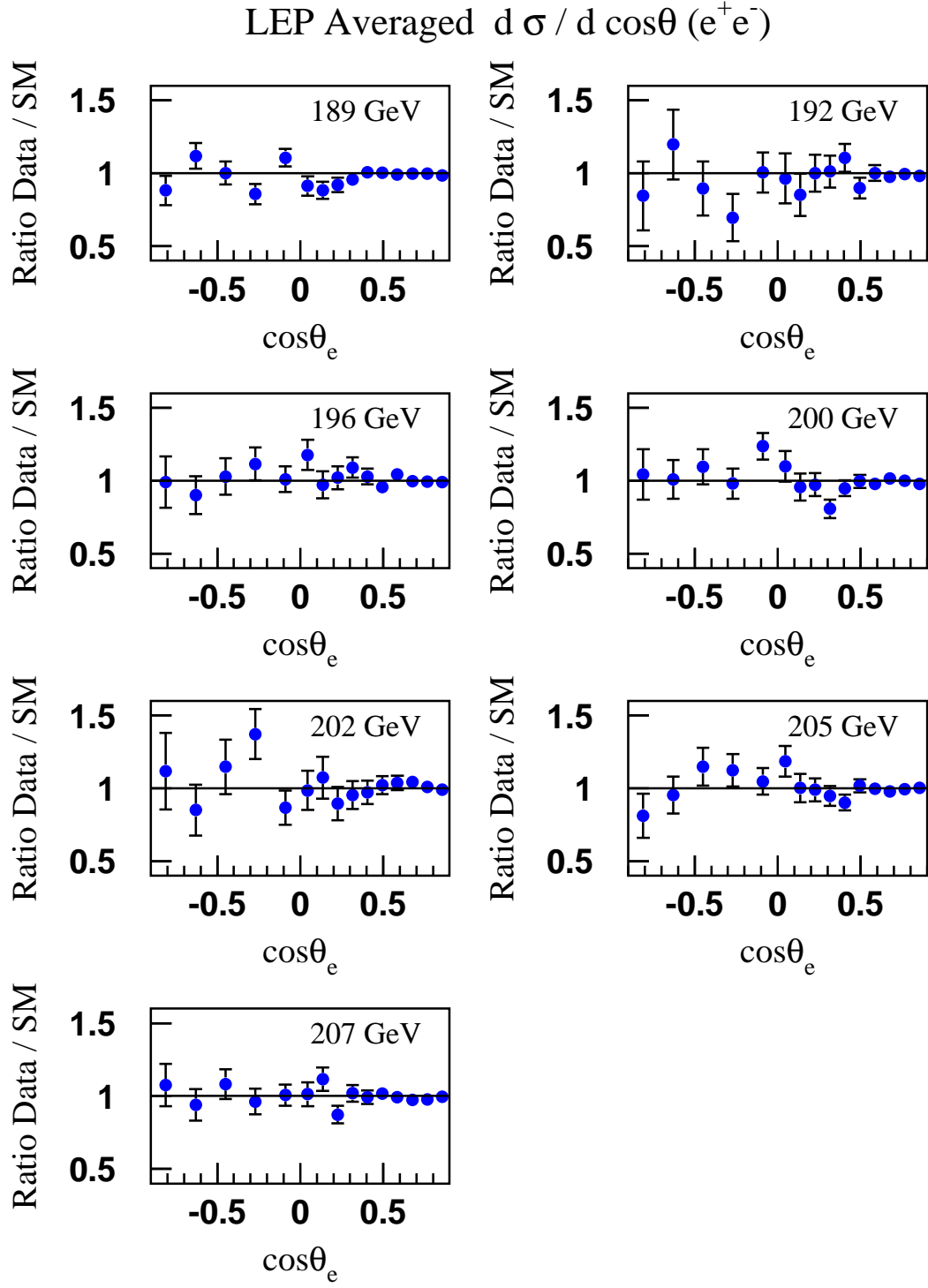


Figure 3.7: Ratio of the LEP averaged differential cross-sections for $e^+e^- \rightarrow e^+e^-$ at energies of 189–207 GeV to the SM predictions, as computed with BHWIDE.

Other options are left-right (L-R) models, based on the group $SU(2)_R \times SU(2)_L \times U(1)_{B-L}$ in which the new Z'_{LR} will couple to a linear combination of the right-handed and B-L currents with a parameter:

$$\alpha_{LR}^2 = \frac{\sin^2 \theta_W g_R^2}{\cos^2 \theta_W g_L^2} - 1. \quad (3.7)$$

Below the resonance, new gauge bosons appear as deviations from the SM predictions due to $\gamma - Z'$ and $Z - Z'$ interference terms. Fits are made to the mass of a Z' , $M_{Z'}$, for Z' models varying the parameters β and α_{LR} including four special models referred to as χ , ψ , η and L-R [69] and the Sequential Standard Model (SSM) [74], which proposes the existence of a Z' with exactly the same coupling to fermions as the standard Z.

The LEP-II data alone do not significantly constrain the mixing angle between the Z and Z' fields, $\Theta_{ZZ'}$. However, results from a single experiment in which LEP-I data are used in the fit show that the mixing is consistent with zero (see for example Reference [76], giving limits of 30 mrad or less depending on the model). Hence, for these fits $\Theta_{ZZ'}$ is fixed to zero. The calculation of Z' contributions is implemented in an extension of the ZFITTER program [77].

The predictions from the Z' models are fitted to the combined LEP-II cross-section and forward-backward asymmetry measurements. In this approach the absence of Z' bosons is equivalent to infinite Z' mass or zero coupling.

No significant evidence is found for the existence of a Z' boson in any of the models. In its absence, 95% confidence level lower limits on $M_{Z'}$ are obtained with a Bayesian method with the assumption of a flat prior in the physically allowed region. The lower limits on the Z' mass are summarised in Table 3.13 and shown in Figure 3.8.

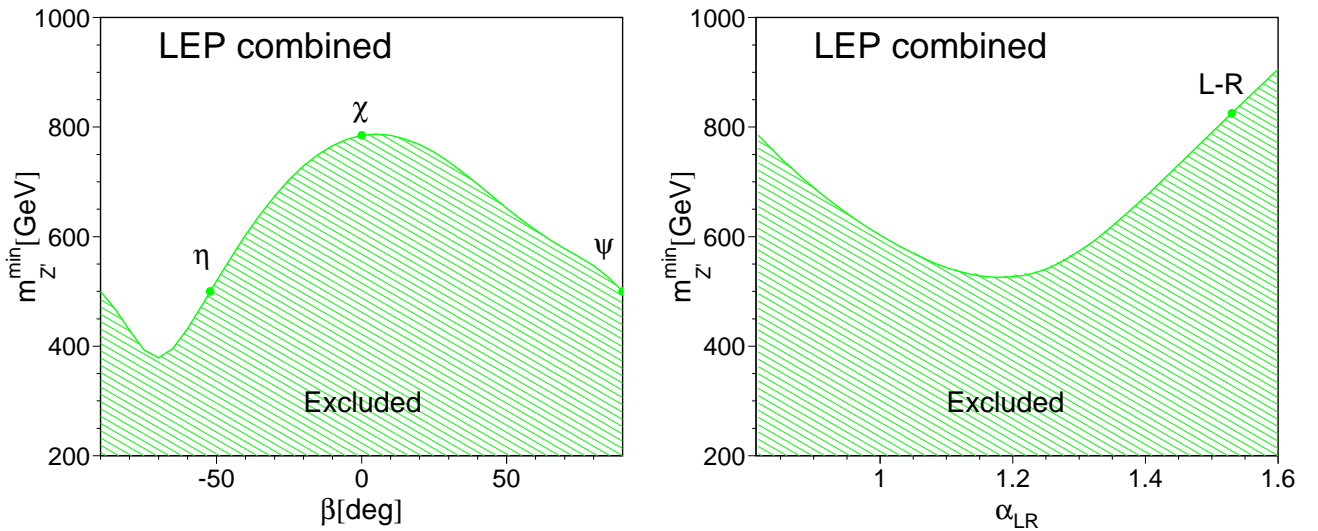


Figure 3.8: Lower limits on the Z' mass at the 95% C.L. for Z' models based on the symmetry breaking of E_6 GUT models (left plot) and on left-right models (right plot).

3.5.2 Contact Interactions

The averaged differential cross-sections for electron-pairs, the averaged cross-sections and forward-backward asymmetries for muon-pairs and tau-lepton pairs, and the hadron cross-sections are

Model	χ	ψ	η	L-R	SSM
$M_{Z'}^{limit}$ (GeV)	785	500	500	825	1760

Table 3.13: The 95% confidence level lower limits on the Z' mass in the χ , ψ , η , L-R and SSM models.

used to search for contact interactions between leptons and between leptons and quarks.

Following Reference [79], contact interactions are parametrised by an effective Lagrangian, \mathcal{L}_{eff} , which is added to the SM Lagrangian and has the form:

$$\mathcal{L}_{\text{eff}} = \frac{g^2}{(1+\delta)\Lambda_{\pm}^2} \sum_{i,j=L,R} \eta_{ij} \bar{e}_i \gamma_{\mu} e_i \bar{f}_j \gamma^{\mu} f_j, \quad (3.8)$$

where $g^2/4\pi$ is taken to be 1 by convention, $\delta = 1(0)$ for $f = e$ ($f \neq e$), $\eta_{ij} = \pm 1$ or 0, Λ_{\pm} is the scale of the contact interactions, e_i and f_j are left or right-handed spinors. By assuming different helicity coupling between the initial state and final state currents, a set of different models can be defined from this Lagrangian [80], with either constructive (+) or destructive (−) interference between the SM process and the contact interactions. The models and corresponding choices of η_{ij} are given in Table 3.14. The models LL, RR, VV, AA, LR, RL, V0, A0, A1 are considered here since these models lead to large deviations in the $e^+e^- \rightarrow \mu^+\mu^-$ and $e^+e^- \rightarrow \tau^+\tau^-$ channels. Potential deviations between SM predictions and measurements of the hadronic cross-section can be interpreted as new interactions occurring between electrons and a single quark flavour only, or as interaction between electrons and all quark flavours at the same time. In the former case the scale of the contact interaction is denoted by Λ_{uu} for a flavour of up type (u,c) and by Λ_{dd} for a flavour of down type (d,s,b), while for the latter the scale of the single contact interaction is denoted by Λ_{qq} .

For the purpose of fitting contact interaction models to the data, a new parameter $\varepsilon_{\pm} = 1/\Lambda_{\pm}^2$ is defined; $\varepsilon = 0$ in the limit that there are no contact interactions. This parameter is allowed to take both positive and negative values in the fits. Theoretical uncertainties on the SM predictions are taken from Reference [59], see above.

The values of ε extracted for each model are all compatible with the SM expectation $\varepsilon = 0$ within at most two standard deviations. The fitted values of ε are converted into 95% confidence level lower limits on Λ_{\pm} . The limits are obtained with a Bayesian method with the assumption of a flat prior in the physically allowed region, $\varepsilon \geq 0$ for each Λ_+ limit and $\varepsilon \leq 0$ for Λ_- limits. The results are shown in Table 3.15 and illustrated in Figure 3.9. The parameters Λ given in the last column of Table 3.15 are derived from the $\Lambda_{e^+e^-}$ values combined with the results on Λ from a combined fit to the $\mu^+\mu^-$ and $\tau^+\tau^-$ cross-sections and asymmetries.

The full correlation matrix of the differential cross-sections for electron pairs, obtained in the averaging procedure, is used in the fits. Some aspects of the combination of the LEP data on Bhabha scattering are discussed in References [81, 82, 83]). For the VV model with positive interference and assuming electromagnetic coupling strength instead of $g^2/4\pi = 1$ [82], the scale Λ can be converted to an upper limit on the electron size:

$$r_e < 1.1 \cdot 10^{-19} \text{ m}. \quad (3.9)$$

Models with stronger couplings will make this upper limit even stronger.

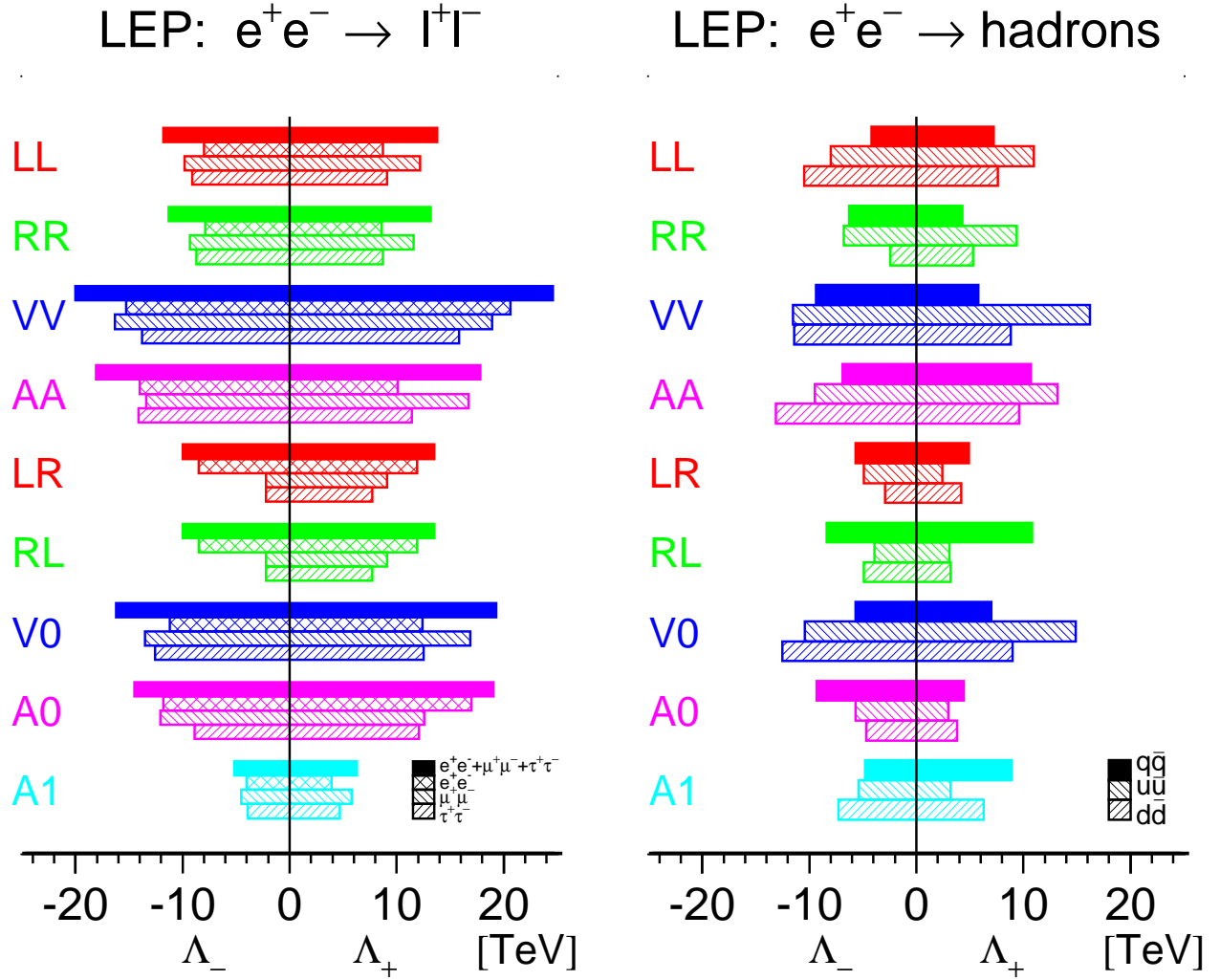


Figure 3.9: The 95% confidence limits on Λ_{\pm} , for constructive (+) and destructive interference (-) with the SM, for the contact interaction models discussed in the text. Results are shown for $e^+e^- \rightarrow e^+e^-$, $e^+e^- \rightarrow \mu^+\mu^-$, and $e^+e^- \rightarrow \tau^+\tau^-$ as well as for $e^+e^- \rightarrow u\bar{u}$, $e^+e^- \rightarrow d\bar{d}$ and $e^+e^- \rightarrow q\bar{q}$. For $e^+e^- \rightarrow \ell^+\ell^-$, universality in the contact interactions between leptons is assumed.

Model	η_{LL}	η_{RR}	η_{LR}	η_{RL}
LL $^\pm$	± 1	0	0	0
RR $^\pm$	0	± 1	0	0
VV $^\pm$	± 1	± 1	± 1	± 1
AA $^\pm$	± 1	± 1	∓ 1	∓ 1
LR $^\pm$	0	0	± 1	0
RL $^\pm$	0	0	0	± 1
V0 $^\pm$	± 1	± 1	0	0
A0 $^\pm$	0	0	± 1	± 1
A1 $^\pm$	± 1	∓ 1	0	0

Table 3.14: Choices of η_{ij} for different contact interaction models.

3.5.3 Large Extra Dimensions

An approach to the solution of the hierarchy problem has been proposed in [84], which brings close the electroweak scale $m_{EW} \sim 1$ TeV and the Planck scale $M_{Pl} = \frac{1}{\sqrt{G_N}} \sim 10^{15}$ TeV. In this framework the effective 4 dimensional M_{Pl} is connected to a new $M_{Pl(4+n)}$ scale in a $(4+n)$ dimensional theory:

$$M_{Pl}^2 \sim M_{Pl(4+n)}^{2+n} R^n, \quad (3.10)$$

where there are n extra compact spatial dimensions of radius R .

In the production of fermion- or boson-pairs in e^+e^- collisions this class of models can manifest itself through virtual effects due to the exchange of gravitons (Kaluza-Klein excitations). As discussed in [87, 88, 89, 90], the exchange of spin-2 gravitons modifies in a unique way the differential cross-sections for fermion pairs, providing clear signatures. These models introduce an effective scale (ultraviolet cut-off). We will adopt the notation from [87] and call the gravitational mass scale M_s . The cut-off scale is supposed to be of the order of the fundamental gravity scale in $4+n$ dimensions.

The parameter ε is defined as:

$$\varepsilon = \frac{\lambda}{M_s^4}, \quad (3.11)$$

where the coefficient λ is of order 1 and cannot be calculated explicitly without knowledge of the full quantum gravity theory. In the following analysis we will assume that $\lambda = \pm 1$ in order to study both the cases of positive and negative interference. To compute the deviations from the SM due to virtual graviton exchange we use the calculations [89, 88].

A fit to the $e^+e^- \rightarrow e^+e^-$ differential cross-section is performed; this channel has by far the highest sensitivity. The fitted values of ε agree well with the SM expectation, and are used to derive limits on the gravitational mass scale M_s at 95 % CL:

$$M_s > 1.09 \text{ TeV for } \lambda = +1, \quad (3.12)$$

$$M_s > 1.25 \text{ TeV for } \lambda = -1. \quad (3.13)$$

$e^+e^- \rightarrow \ell^+\ell^-$								
Model	Λ_{ee}^- (TeV)	Λ_{ee}^+	$\Lambda_{\mu\mu}^-$ (TeV)	$\Lambda_{\mu\mu}^+$	$\Lambda_{\tau\tau}^-$ (TeV)	$\Lambda_{\tau\tau}^+$	$\Lambda_{\ell^+\ell^-}^-$ (TeV)	$\Lambda_{\ell^+\ell^-}^+$
LL	8.0	8.7	9.8	12.2	9.1	9.1	11.8	13.8
RR	7.9	8.6	9.3	11.6	8.7	8.7	11.3	13.2
VV	15.3	20.6	16.3	18.9	13.8	15.8	20.0	24.6
AA	14.0	10.1	13.4	16.7	14.1	11.4	18.1	17.8
LR	8.5	11.9	2.2	9.1	2.2	7.7	10.0	13.5
RL	8.5	11.9	2.2	9.1	2.2	7.7	10.0	13.5
V0	11.2	12.4	13.5	16.9	12.6	12.5	16.2	19.3
A0	11.8	17.0	12.1	12.6	8.9	12.1	14.5	19.0
A1	4.0	3.9	4.5	5.8	3.9	4.7	5.2	6.3

$e^+e^- \rightarrow q\bar{q}$						
Model	$\Lambda_{u\bar{u}}^-$ (TeV)	$\Lambda_{u\bar{u}}^+$ (TeV)	$\Lambda_{d\bar{d}}^-$ (TeV)	$\Lambda_{d\bar{d}}^+$ (TeV)	$\Lambda_{q\bar{q}}^-$ (TeV)	$\Lambda_{q\bar{q}}^+$ (TeV)
LL	8.0	11.0	10.5	7.6	4.2	7.2
RR	6.8	9.4	2.4	5.3	6.3	4.3
VV	11.5	16.2	11.4	8.8	9.4	5.8
AA	9.5	13.2	13.1	9.6	6.9	10.7
LR	4.9	2.4	2.9	4.2	5.7	4.9
RL	3.9	3.1	4.9	3.2	8.4	10.8
V0	10.4	14.9	12.5	9.0	5.7	7.0
A0	5.7	3.0	4.7	3.8	9.3	4.4
A1	5.4	3.2	7.3	6.3	4.8	8.9

Table 3.15: The 95% confidence limits on the scale, Λ^\pm , for constructive (+) and destructive interference (-) with the SM, for the contact interaction models discussed in the text. Results are given for $e^+e^- \rightarrow \mu^+\mu^-$, $e^+e^- \rightarrow \tau^+\tau^-$ and $e^+e^- \rightarrow e^+e^-$ as well as for $e^+e^- \rightarrow u\bar{u}$, $e^+e^- \rightarrow d\bar{d}$ and $e^+e^- \rightarrow q\bar{q}$. For $e^+e^- \rightarrow \ell^+\ell^-$, universality in the contact interactions between leptons is assumed.

LEP Averaged $d\sigma/d\cos\theta$ (e^+e^-)

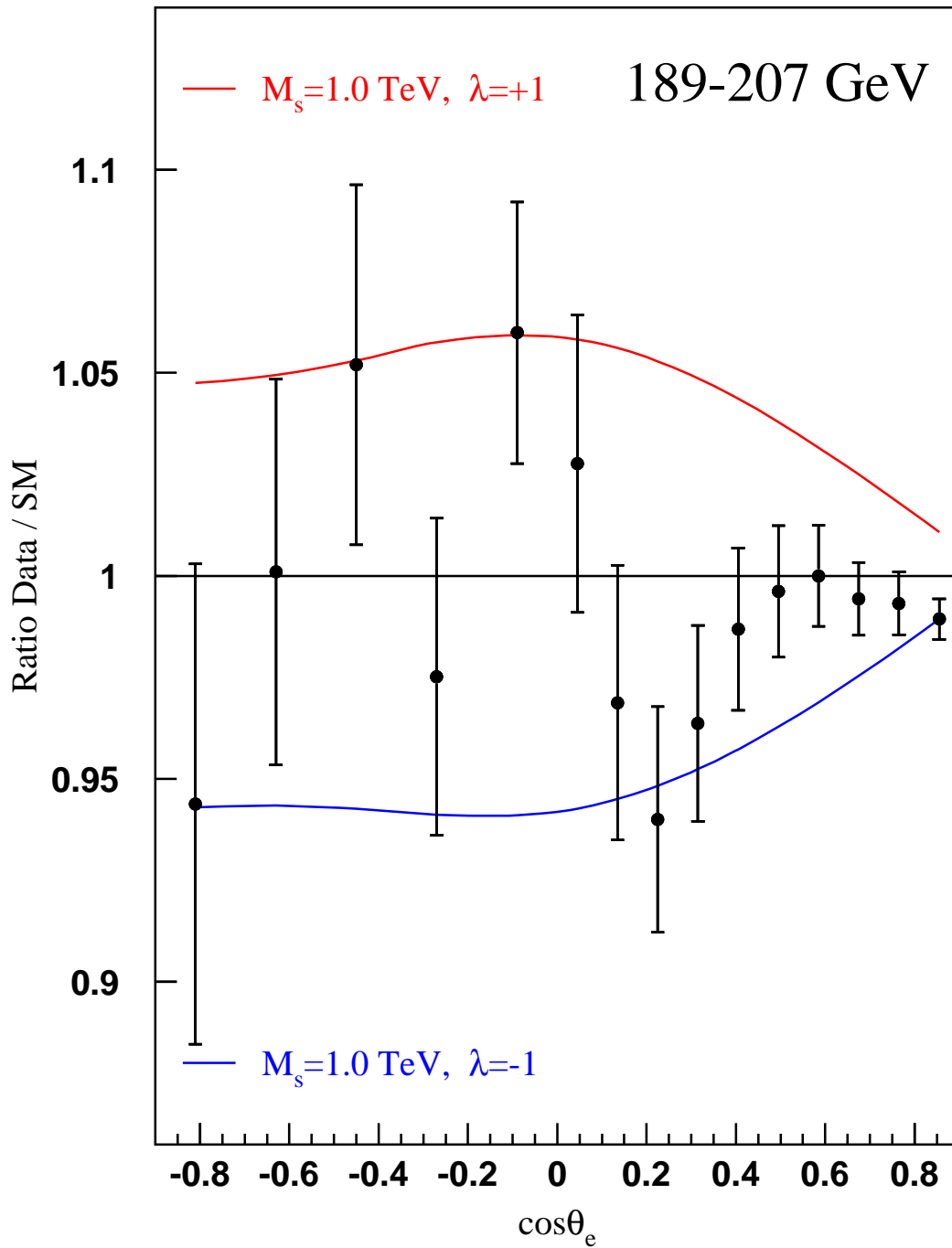


Figure 3.10: Ratio of the LEP averaged differential cross-section for $e^+e^- \rightarrow e^+e^-$ compared to the SM prediction. The effects expected from virtual graviton exchange are also shown.

An example of the analysis is shown in Figure 3.10.

The interference of virtual graviton exchange amplitudes with both t -channel and s -channel Bhabha scattering amplitudes makes this the most sensitive search channel at LEP. The results obtained here would not be strictly valid if the luminosity measurements of the LEP experiments, based on the very same process, is also be affected by graviton exchange. However, as shown in [81], the effect on the cross-section in the luminosity angular range is so small that it can safely be neglected in this analysis.

3.5.4 Leptoquarks

Leptoquarks (LQ) mediate quark-lepton transitions. They carry fermion numbers, $F = L + 3B$. Following the notations in References [92] and [94], scalar leptoquarks, S_I , and vector leptoquarks, V_I , are indicated based on spin and isospin I . Isomultiplets with different hypercharges are denoted by an additional tilde. It is assumed that leptoquark couplings to quark-lepton pairs are flavour-diagonal and preserve baryon- and lepton-number. The couplings refer to g_L , g_R , according to the chirality of the lepton. In the process $e^+e^- \rightarrow q\bar{q}$ leptoquarks can be exchanged in u - or t -channel, with $F = 0$ or $|F| = 2$.

For convenience, one type of leptoquarks is assumed to be much lighter than the others. Further, experimental constraints on the product $g_L g_R$ allow separate studies of $g_L \neq 0$ or $g_R \neq 0$.

Assuming a coupling of electromagnetic strength, $g = \sqrt{4\pi\alpha}$, where α is the fine structure constant, limits on the masses of leptoquarks coupling to electrons and the first generation of quarks are derived with a Bayesian method with the assumption of a flat prior in the physically allowed region from comparisons of the theoretical predictions for the total hadronic cross-section to the LEP-II averaged measurements.

The 95% confidence level lower limits on masses m_{LQ} are summarised in Table 3.16.

LQ type	m_{LQ}^{min} (GeV)	LQ type	m_{LQ}^{min} (GeV)
$S_0(L) \rightarrow eu$	646	$V_{1/2}(L) \rightarrow ed$	348
$S_0(R) \rightarrow eu$	516	$V_{1/2}(R) \rightarrow eu, ed$	238
$\tilde{S}_0(R) \rightarrow ed$	256	$\tilde{V}_{1/2}(L) \rightarrow eu$	186
$S_1(L) \rightarrow eu, ed$	429	$V_0(L) \rightarrow e\bar{d}$	897
$S_{1/2}(L) \rightarrow e\bar{u}$	228	$V_0(R) \rightarrow e\bar{d}$	482
$S_{1/2}(R) \rightarrow e\bar{u}, e\bar{d}$	285	$\tilde{V}_0(R) \rightarrow e\bar{u}$	577
$\tilde{S}_{1/2}(L) \rightarrow e\bar{d}$	–	$V_1(L) \rightarrow e\bar{u}, e\bar{d}$	765

Table 3.16: The 95% confidence level lower limits on the LQ mass assuming $g_{L,R} = \sqrt{4\pi\alpha}$. For $\tilde{S}_{1/2}(L)$ no limit can be set because the contribution from this leptoquark type to the hadronic cross-section is not observable with the precision of the measurements.

3.6 Summary

A combination of the LEP-II $e^+e^- \rightarrow f\bar{f}$ cross-sections (for hadron, muon and tau-lepton final states) and forward-backward asymmetries (for muon and tau-lepton final states) from LEP

running at energies from 130 to 209 GeV is made. The results from the four LEP experiments are in good agreement with each other. The averages for all energies are shown in Table 3.4. The use of the combined fermion-pair results in an S-Matrix analysis is discussed in Appendix A. Differential cross-sections, $\frac{d\sigma}{d\cos\theta}$, for $e^+e^- \rightarrow \mu^+\mu^-$, $e^+e^- \rightarrow \tau^+\tau^-$ and $e^+e^- \rightarrow e^+e^-$ are also combined. Results are shown in Figures 3.4, 3.5 and 3.6. All results are in good agreement with the predictions of the SM.

The averaged cross-section, forward-backward asymmetry and differential cross-section results are interpreted in a variety of models. The LEP-II averaged cross-sections and lepton asymmetries are used to obtain lower limits on the mass of a possible Z' boson in different models. Limits range from 500 to 1760 GeV depending on the model. Limits on the scale of contact interactions between leptons and between electrons and quarks are determined. A full set of limits are reported in Table 3.15. Limits on the scale of gravity in models with extra dimensions ranging from 1.09 to 1.25 TeV are obtained. Limits on the masses of leptoquarks are derived from the hadronic cross-sections. The limits range from 186 to 897 GeV depending on the type of leptoquark.

Chapter 4

Final-State Interconnection Effects

At LEP-II, Final-State Interconnection (FSI) effects may exist when two colourless W or Z bosons decay hadronically, close in space-time to one another. Two phenomena are considered: Colour Reconnection (CR) and Bose-Einstein Correlations (BEC). The former is expected to appear as a consequence of the strong interaction described by non-perturbative QCD, while the latter is due to the quantum mechanical properties of those particles in the hadronic final state which follow Bose statistics. Both were observed in other physical systems [95, 99]. An additional motivation for the study of FSI effects is that they introduce potentially large systematic uncertainties in the measurement of the mass of the W boson using fully hadronic W-pair decays. The studies described here allow a better understanding of CR and BEC at LEP-II and, by constraining models and their parameters, impose limits on their quantitative effect in the W-boson mass measurement.

4.1 Colour Reconnection

4.1.1 Introduction

In $W^+W^- \rightarrow q\bar{q}q\bar{q}$ events, the products of the two colour singlet W decays have in general a significant space-time overlap, because the separation of their decay vertices, $\tau_W \sim 1/\Gamma_W \approx 0.1$ fm, is small compared to characteristic hadronic distance scales of ~ 1 fm. Colour reconnection, also known as colour rearrangement (CR), was first introduced in [101] and refers to a reorganisation of the colour flow between the decay products of the two W bosons. A precedent for such effects is set by colour suppressed B meson decays, *e.g.* $B \rightarrow J/\psi K$, where there is “cross-talk” between the two original colour singlets, $\bar{c}+s$ and $c+s$ spectator [101, 102].

QCD interference effects between the colour singlets in W^+W^- decays during the perturbative phase are expected to be small, affecting the W mass by $\sim (\frac{\alpha_s}{\pi N_{\text{colours}}})^2 \Gamma_W \sim \mathcal{O}(1 \text{ MeV})$ [102]. In contrast, non-perturbative effects involving soft gluons with energies less than Γ_W may be significant, with effects on m_W of $\sim \mathcal{O}(10 \text{ MeV})$. To estimate the impact of this phenomenon, a variety of phenomenological models have been developed [102, 103, 104, 105, 106, 107]. These models differ mainly in the detailed mechanism of CR and hadronisation, and in the fraction of reconnected events.

Some of the models can also be tested at the Z peak in three-jet events. The analyses [108, 109, 110] showed that the ARIADNE model type 1 [103], and similar the Rathman/GAL model [107] with default parameter settings, is not consistent with the data. Colour rearrangement in W-pair events could, however, also be caused by additional reconnection

mechanisms. The combination presented here concentrates on the SK1 model [102] in which the probability for reconnection to occur in an event is given by $p_{\text{reco}} = 1 - \exp(-\mathcal{I}k_I)$. The quantity \mathcal{I} is the space-time overlap integral between the colour flux tubes that are stretched between quarks and gluons originating from the perturbative phase of the two hadronic W decays, and k_I is an adjustable parameter of the SK1 model, thus allowing to vary the fraction of reconnected events in the Monte-Carlo simulation. Figure 4.1 shows the reconnection probability, p_{reco} as a function of the model parameter k_I , for an SK1 Monte-Carlo event sample generated at a centre-of-mass energy of 189 GeV, and used by all LEP experiments as part of the combination procedure. By varying k_I , the SK1 model results can be compared to other models which have a fixed reconnection probability, such as the ARIADNE model type 2 [103] and HERWIG [104]. In the context of W mass measurements, it is observed [111, 112, 113, 114] that all models behave similarly when adjusted to the same reconnection fraction. The HERWIG CR model assumes a reconnection probability of 1/9 counting the possible colour rearrangements, while the ARIADNE-2 reconnection probability is about 22% at a centre-of-mass energy of 189 GeV.

Many observables have been studied in the search for an experimental signature of colour reconnection. The inclusive properties of events such as the mean charged particle multiplicity, distributions of thrust, rapidity, transverse momentum and $\ln(1/x_p)$, where x_p is the scaled particle momentum, are found to have limited sensitivity [115, 116]. The effects of CR are predicted to be numerically larger in these observables when only higher mass hadrons such as kaons and protons are considered [117]. However, experimental investigations [116] find no significant gain in sensitivity due to the low production rate of such particles in W decays.

Eventually, two methods were developed which yield a sensitive handle on CR effects in hadronic W decays: the so-called “particle-flow” method [118, 120], and the influence of CR on the W-boson mass reconstructed as a function of the particle momentum threshold and when applying different jet algorithms. These two are described in the following and their combined results are presented.

4.1.2 Particle-Flow Measurements

In the analogy with the “string effect” analysis in 3-jet $e^+e^- \rightarrow q\bar{q}g$ events [121], the particle-flow method has been investigated by the DELPHI, L3 and OPAL collaborations [128, 129, 115]. In these analyses, pairs of jets in $W^+W^- \rightarrow q\bar{q}q\bar{q}$ events are associated with the decay of a W, after which four jet-jet regions are chosen: two corresponding to jets sharing the same W parent (intra-W), and two in which the parents differ (inter-W). As there is a two-fold ambiguity in the assignment of inter-W regions, the configuration having the smaller sum of inter-W angles is chosen.

Particles are projected onto the planes defined by these jet pairs and the particle density constructed as a function of ϕ , the projected angle relative to one jet in each plane. To account for the variation in the opening angles, ϕ_0 , of the jet-jet pairs defining each plane, the particle densities in ϕ are constructed as functions of normalised angles, $\phi_r = \phi/\phi_0$, by a simple rescaling of the projected angles for each particle, event by event. Particles having projected angles ϕ smaller than ϕ_0 in at least one of the four planes are considered further. This gives particle densities, $\frac{1}{N_{\text{event}}} \frac{dn}{d\phi_r}$, in four regions with ϕ_r in the range from 0 to 1, and where n and N_{event} are the number of particles and events, respectively.

As the particle density reflects the colour flow in an event, CR models predict a change in the relative particle densities between inter-W and intra-W regions. On average, colour

reconnection is expected to affect the particle densities of both inter-W regions in the same way and so they are added together, as are the two intra-W regions. The observable used to quantify such changes, R_N , is defined:

$$R_N = \frac{\frac{1}{N_{\text{event}}} \int_{0.2}^{0.8} \frac{dn}{d\phi_r} (\text{intra} - W) d\phi_r}{\frac{1}{N_{\text{event}}} \int_{0.2}^{0.8} \frac{dn}{d\phi_r} (\text{inter} - W) d\phi_r}. \quad (4.1)$$

As the effects of CR are expected to be enhanced for low momentum particles far from the jet axes, the range of integration excludes jet cores ($\phi_r \approx 0$ and $\phi_r \approx 1$). The precise upper and lower limits are optimised by model studies of predicted sensitivity.

The DELPHI, L3 and OPAL experiments have developed their own variation on this analysis, differing primarily in the selection of $W^+W^- \rightarrow q\bar{q}q\bar{q}$ events. In DELPHI [128] and L3 [129], events are selected in a very particular configuration (“topological selection”) by imposing restrictions on the jet-jet angles and on the jet-resolution parameter for the three- to four-jet transition (Durham [130] or Luclus [134] schemes). This leads to more planar events than those in an inclusive $W^+W^- \rightarrow q\bar{q}q\bar{q}$ sample and the association between jet pairs and W bosons is given by the relative angular separation of the jets. The overall efficiency for selecting signal events ranges between 12% and 22% with purities of 70-85%. The efficiency to assign the correct jets to the parent W’s amounts to 70-91%. Data samples with small signal efficiency typically have the highest purity and best efficiency for correct jet assignment. The OPAL [115] event selection is based on their W mass analysis. Assignment of pairs of jets to W’s follows the procedure used in measuring m_W , using a multivariate algorithm [114] with an overall efficiency for selecting $W^+W^- \rightarrow q\bar{q}q\bar{q}$ events of 40%, a signal purity of 86%, and an efficiency for correctly assigning jets to parent W’s of 90%, albeit with a less planar topology and hence a more complicated colour flow.

The data are corrected bin-by-bin for background contamination in the inter-W and intra-W regions separately. The possibility of CR effects existing in background processes is neglected because the background is dominated by $e^+e^- \rightarrow q\bar{q}$ events and the $ZZ \rightarrow q\bar{q}q\bar{q}$ background, in which CR effects may also be present, is at the level of 2% only.

The measured values of R_N are compared after they have been normalised using a common sample of Monte-Carlo events, processed using the detector simulation and particle-flow analysis of each experiment. The ratio, r , is constructed:

$$r = \frac{R_N^{\text{data}}}{R_N^{\text{no-CR}}}, \quad (4.2)$$

where R_N^{data} and $R_N^{\text{no-CR}}$ are the values of R_N measured by each experiment in data and in a common sample of events simulated without CR. In the absence of CR, all experiments should find r consistent with unity. The default no-CR sample used for this normalisation consists of $e^+e^- \rightarrow W^+W^-$ events produced using the KORALW [139] event generator and hadronised using the JETSET [140] model.

The common Monte-Carlo samples used in the combination are only available at a single centre-of-mass energy, E_{cm} , of 188.6 GeV. The R_N are however measured at each centre-of-mass energy separately, in both real data and Monte-Carlo simulations. The predicted variation of R_N with centre-of-mass energy is determined by each experiment using its own samples of simulated $e^+e^- \rightarrow W^+W^-$ events, with hadronisation performed using the no-CR JETSET

	Experiment	
R_N	L3	OPAL
Data	0.8436 ± 0.0217	1.2426 ± 0.0248
JETSET	0.8622 ± 0.0037	1.2910 ± 0.0028
SK1 (100%)	0.7482 ± 0.0033	1.0780 ± 0.0028
HERWIG	0.8822 ± 0.0038	1.3110 ± 0.0029
ARIADNE	0.8754 ± 0.0037	1.2860 ± 0.0028
Systematics	L3	OPAL
Intra-W BEC	0.0017	0.0017
$e^+e^- \rightarrow q\bar{q}$ shape	0.0086	0.0104
$\sigma(e^+e^- \rightarrow q\bar{q})$	0.0071	0.0024
$ZZ \rightarrow q\bar{q}q\bar{q}$ shape	} 0.0020	0.0018
$\sigma(ZZ \rightarrow q\bar{q}q\bar{q})$		0.0009
Detector effects	0.0016	0.0142
E_{cm} dependence	0.0020	0.0005

Table 4.1: Particle-flow measurements compared to Monte-Carlo predictions for the SK1 CR model and different hadronisation models, together with systematic uncertainties, provided by L3 and OPAL for the CR combination.

model. The evolutions of R_N are parametrised by second order polynomial functions in E_{cm} and are detailed in References [128, 129, 115]. The R_N measured in data are subsequently extrapolated by each experiment to the reference energy of 188.6 GeV.

Input from a particle-flow measurement is provided by L3 and OPAL in terms of measured R_N and corresponding ΔR_N for different systematic variations of the analysis or different Monte Carlo modelling [129, 115]. They are shown in Table 4.1. DELPHI provides their results in terms of likelihood functions, which are discussed below. Systematic uncertainties due to Bose-Einstein correlations are limited to the level which is compatible with the LEP measurement of BEC (see Chapter 4.2). Scale uncertainties on the main background processes $e^+e^- \rightarrow q\bar{q}$ and $ZZ \rightarrow q\bar{q}q\bar{q}$, and hadronisation uncertainties, which are derived from the spread of R_N for the JETSET, ARIADNE and HERWIG hadronisation models are also taken into account. For these uncertainties the smallest of each systematic uncertainty of L3 and OPAL is taken as correlated, the remaining part as uncorrelated. Detector effects and the extrapolation to a single centre-of-mass energy, as well as the uncertainty of the 4-jet background shape of $e^+e^- \rightarrow q\bar{q}$ events with multi-gluon emission, are assumed to be uncorrelated.

The scaled measurements of L3 and OPAL, $r_1^{\text{data}} = r_L^{\text{data}}$ and $r_2^{\text{data}} = r_O^{\text{data}}$, are combined by minimising a χ^2 function which depends on the model parameter k_I through the model dependence of $r_i(k_I)$:

$$\begin{aligned}
\chi_r^2(k_I, c_1, c_2) = & \sum_{i,j=1,2} \left\{ (r_i^{\text{data}} - r_i(k_I) + c_i \delta_{i,r}) (C_r^{-1})_{ij} \right. \\
& \left. \cdot (r_j^{\text{data}} - r_j(k_I) + c_j \delta_{j,r}) \right\} \\
& + \sum_{m,n=1,2} c_m (C_c^{-1})_{mn} c_n.
\end{aligned} \tag{4.3}$$

The covariance matrix, C_r , is constructed from only the uncorrelated uncertainties and is ac-

tually diagonal. Correlated uncertainties are introduced by varying each measurement r_i^{data} with an additive term $c_i \delta_{i,r}$, where $\delta_{i,r}$ is the correlated part of the uncertainty on r_i^{data} , and c_i are auxiliary variables. The second term in the χ_r^2 function introduces correlations between the auxiliary variables, so that the systematic uncertainties $\delta_{i,r}$ also become effectively correlated. This procedure is equivalent to the so-called profile likelihood method with correlated nuisance parameters, see, *e.g.*, [141] and references therein. The correlation matrix $(C_c^{-1})_{mn}$ is constructed such that the uncertainty and central value of k_I is exactly identical to the result obtained with a classical and full covariance matrix C_r . The best agreement is found for a correlation coefficient of 0.50 between the auxiliary parameters. This more complicated prescription is used to combine this result with other CR inputs, which are provided in terms of likelihood functions.

To be able to vary k_I continuously in the minimisation, the SK1 model predictions of $r_i(k_I)$ are described by a parametrised, phenomenological function:

$$r_i(k_I) = 1 + a_{i,1} \frac{k_I}{k_I + b_i} + a_{i,2} \left(\frac{k_I}{k_I + b_i} \right)^2 + a_{i,3} \left(\frac{k_I}{k_I + b_i} \right)^4 + \frac{a_{i,4}}{(1 + k_I)} - a_{i,4} . \quad (4.4)$$

By construction, $r_i(k_I)$ is equal to 1 in the limit $k_I \rightarrow 0$, *i.e.*, when no CR effects are present. The parameters, $a_{i,j}$ and b_i ($i = 1, 2, j = 1, \dots, 4$), of the function are adjusted to fit the $r_i(k_I)$ dependence determined in the SK1 Monte-Carlo simulation by L3 and OPAL, which are shown in Table D.1 of Appendix D. The terms $\frac{k_I}{k_I + b}$ are motivated by the approximate description of the functional shape of the reconnection probability, $p_{\text{reco}}(k_I)$.

With this parameter set, the function and the Monte-Carlo simulations agree within less than one statistical standard deviation, as shown in Figure 4.1. The best fitting parameter values are listed in Table D.2.

The DELPHI experiment also performed a particle-flow analysis [128]. The result is represented in terms of two likelihood functions, $L_{\text{p-flow},D,\text{full}}(k_I)$ and $L_{\text{p-flow},D,\text{uncorr}}(k_I)$, where the former contains all systematic uncertainties and the latter only uncorrelated systematic uncertainties. These likelihoods are transformed into $\Delta\chi^2(k_I) = -2 \log L(k_I)$ values, which are smoothed by cubic splines and then used in the combination. To treat correlations with other inputs properly, a systematic variation, $\delta_{\text{p-flow},D}(k_I)$, of k_I is introduced such that the full $\Delta\chi_{\text{p-flow},D,\text{full}}^2(k_I)$ can be reproduced in the following way from the uncorrelated $\Delta\chi_{\text{p-flow},D,\text{uncorr}}^2(k_I)$ using an auxiliary variable c_3 :

$$\Delta\chi_{\text{p-flow},D,\text{corr}}^2(k_I) = \min_{c_3} \{ \Delta\chi_{\text{p-flow},D,\text{uncorr}}^2(k_I + c_3 \delta_{\text{p-flow},D}(k_I)) + c_3^2 \} . \quad (4.5)$$

The combined minimisation of $\Delta\chi_{\text{p-flow},D,\text{corr}}^2(k_I, c_3)$ with respect to k_I and c_3 is equivalent to a minimisation of $\Delta\chi_{\text{p-flow},D,\text{full}}^2(k_I)$ with respect to k_I only. The best agreement between the full description and this procedure is obtained for $\delta_{\text{p-flow},D}(k_I) = 0.246 + (0.754)^2 k_I$, which is shown in Figure 4.2. The advantage of this method is again the possibility to correlate c_3 with systematic uncertainties from other CR inputs.

4.1.3 Determination of CR Effects Using W Mass Estimators

A second very sensitive observable for CR is the variation of the reconstructed W-boson mass in fully hadronic events when applying different particle momentum thresholds and jet algorithms

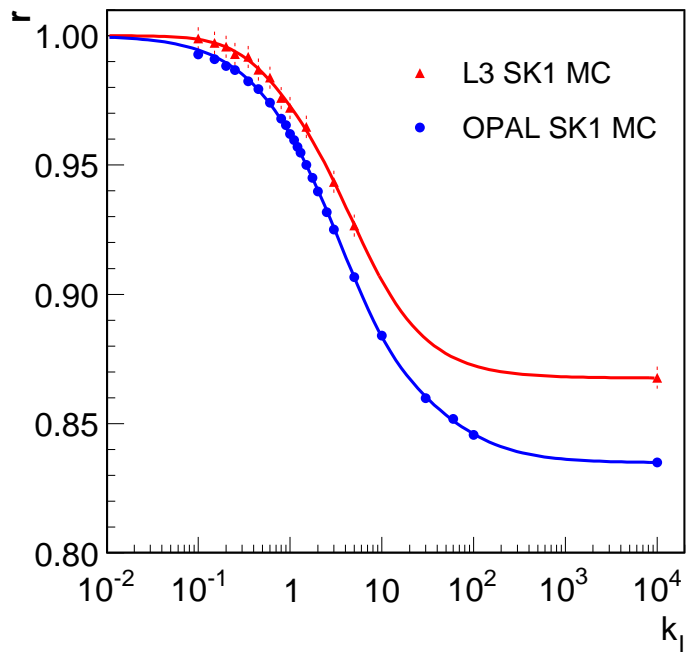
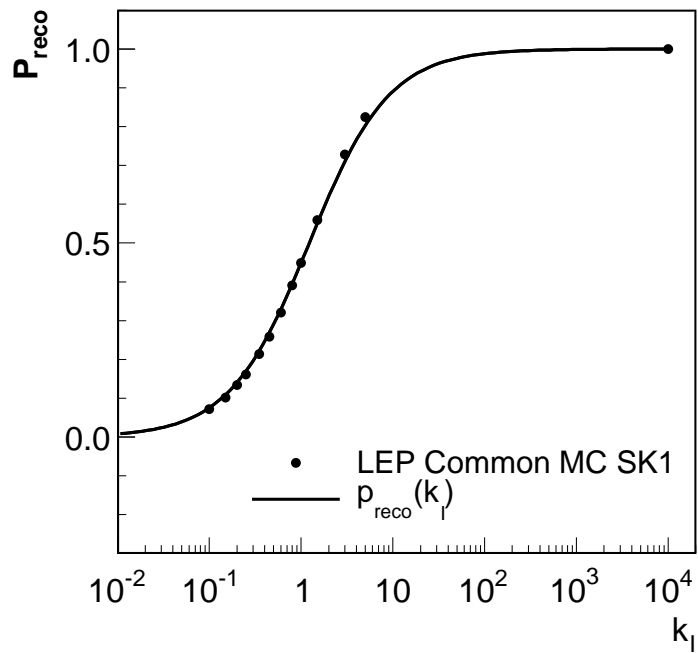


Figure 4.1: Top: Reconnection probability as a function of the SK1 model parameter, k_I , together with an approximate curve $p_{\text{reco}}(k_I)$ to guide the eye. Bottom: Monte-Carlo calculation and parametrisation of the particle-flow ratio, $r(k_I)$, for L3 and OPAL, shown as triangles and circles, respectively.

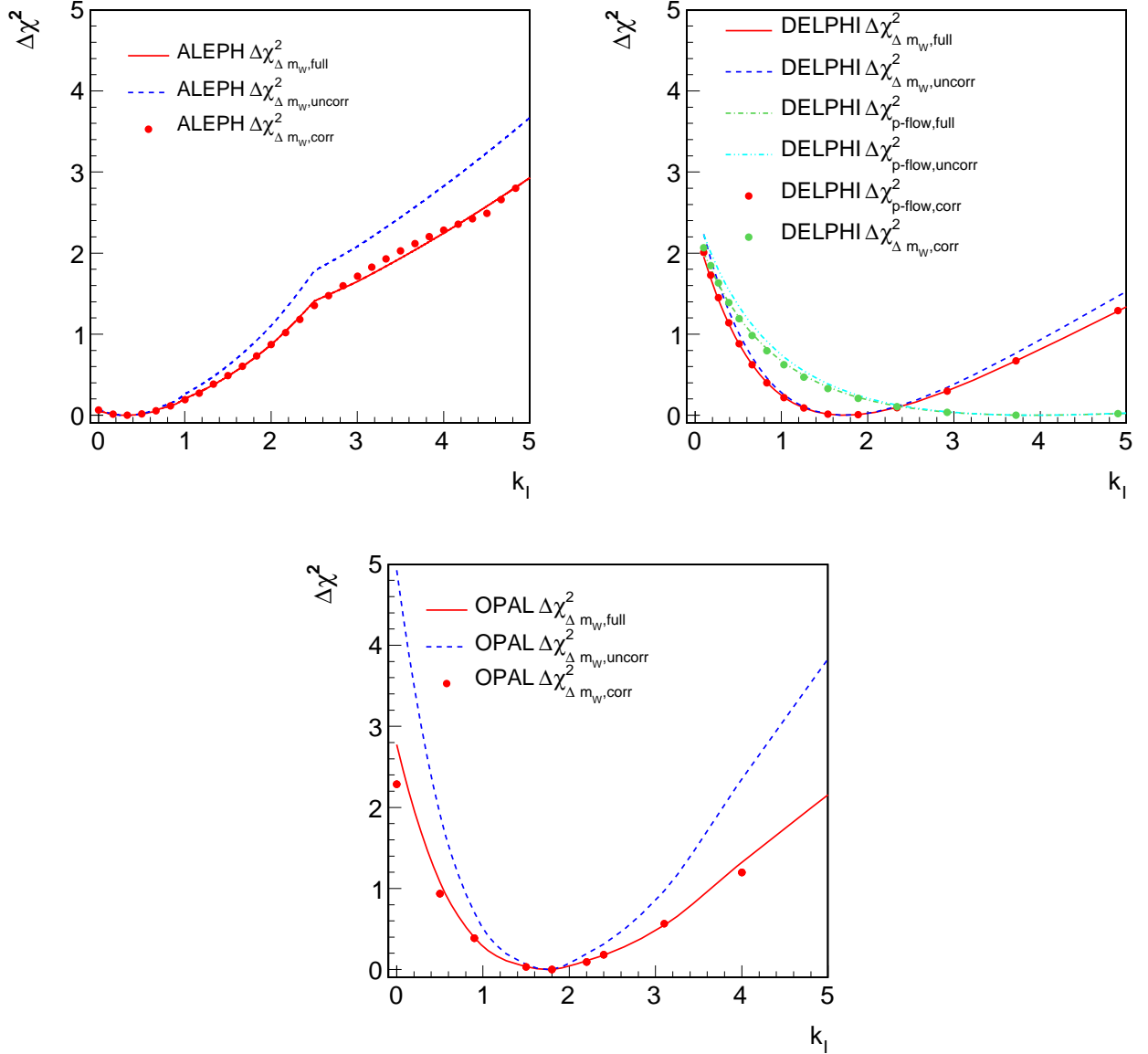


Figure 4.2: Comparison of $\Delta\chi^2$ distributions for CR measurements from particle-flow and mass estimator differences, Δm_W , by the ALEPH, DELPHI and OPAL experiments. Distributions are shown when all uncertainties (continuous lines) and only uncorrelated uncertainties (dashed lines) are taken into account. The full-uncertainty curves are compared to the $\Delta\chi^2$ distribution when the variation of the parametrised uncertainty $\delta(k_I)$ is used to introduce the correlated part of the systematic uncertainties (circles).

at event reconstruction. As pointed out before, CR influences mostly the particle-flow between jets and hence the low momentum component of the hadronic jets. Thus, estimators of m_W in which the jet-defining parameters are chosen to enhance or reduce the weight given to such low momentum particles allow an observable to be constructed which is sensitive to the presence or absence of CR. To measure the effect of CR, the mass difference, Δm_W , of two estimators is determined in data and compared to the mass difference predicted by a certain CR model. Since only mass *differences* are used to measure CR, the correlation with the actual W mass measurement is small, in the order of 10% [111, 128, 114].

The ALEPH experiment studied the dependence of m_W as a function of a momentum threshold, p_{cut} , of the jet particles and of the cone radius R of the jets, which were constructed using the Durham-PE algorithm [130]. The p_{cut} thresholds were varied between 1 GeV and 3 GeV and the radius between 0.4 rad and 1.0 rad. DELPHI compared the m_W value from the standard W mass analysis with alternative estimators applying a cone cut at $R = 0.5$ rad and a particle momentum cut at 2 GeV, applying again the Durham jet clustering algorithm [130] in combination with an iterative cone algorithm in order to estimate the direction of the modified jets. OPAL found that their optimal CR sensitivity is for the comparison between an analysis with a particle momentum cut at 2.5 GeV and an alternative one in which the jet particles are weighted according to a factor p^κ , with $\kappa = -0.5$. The Durham jet clustering algorithm [130] is used to calculate the modified jet directions.

The ALEPH, DELPHI and OPAL inputs are provided in terms of $\Delta\chi^2$ curves with complete systematic uncertainties and with only the uncorrelated part, $\Delta\chi_{\Delta m_W, i, \text{full}}^2(k_I)$ and $\Delta\chi_{\Delta m_W, i, \text{uncorr}}^2(k_I)$, respectively. Cubic splines are used to interpolate between the provided data points. Correlations are again not taken directly from the input function, $\Delta\chi_{\Delta m_W, i, \text{full}}^2(k_I)$, but are introduced by varying k_I with additional uncertainties $\pm\delta(k_I)$ using auxiliary variables c_i :

$$\Delta\chi_{\Delta m_W, A, \text{corr}}^2(k_I) = \min_{c_4} \{ \Delta\chi_{\Delta m_W, A, \text{uncorr}}^2(k_I + c_4\delta_{\Delta m_W, A}(k_I)) + c_4^2 \}, \quad (4.6)$$

$$\Delta\chi_{\Delta m_W, D, \text{corr}}^2(k_I) = \min_{c_5} \{ \Delta\chi_{\Delta m_W, D, \text{uncorr}}^2(k_I + c_5\delta_{\Delta m_W, D}(k_I)) + c_5^2 \}, \quad (4.7)$$

$$\Delta\chi_{\Delta m_W, O, \text{corr}}^2(k_I) = \min_{c_6} \{ \Delta\chi_{\Delta m_W, O, \text{uncorr}}^2(k_I + c_6\delta_{\Delta m_W, O}(k_I)) + c_6^2 \}. \quad (4.8)$$

The parametrisations of $\delta_{\Delta m_W, i}(k_I)$ follow step-wise linear functions and are listed in Appendix D. The original input of ALEPH, DELPHI and OPAL is shown in Figure 4.2 and compared to the $\Delta\chi_{\Delta m_W, i, \text{corr}}^2(k_I)$ functions using the prescription described above. Good agreement is observed.

The main correlated systematic uncertainties which are taken into account are from comparisons of hadronisation models, background scale and shape uncertainties, as well as Bose-Einstein correlations. Detector effects and corrections of the 4-jet background are taken as uncorrelated. The original ALEPH analysis [111] does not consider uncertainties due to the BEC effect. Therefore, the corresponding $\delta_{\Delta m_W, A}(k_I)$ values are scaled up by 11%, which is derived from an additional dedicated systematic study.

4.1.4 Combination of LEP CR Measurements

The LEP measurements of CR using the particle-flow method and the mass estimator differences are combined using the following total $\Delta\chi^2$ function:

$$\begin{aligned}
\Delta\chi^2(k_I, c_1, \dots, c_6) = & \sum_{i,j=1,2} \left\{ (r_i^{\text{data}} - r_i(k_I) + c_i\delta_{i,r}) (C_r^{-1})_{ij} (r_j^{\text{data}} - r_j(k_I) + c_j\delta_{j,r}) \right\} \\
& + \Delta\chi_{\text{p-flow},D,\text{uncorr}}^2(k_I + c_3\delta_{\text{p-flow},D}(k_I)) \\
& + \Delta\chi_{\Delta m_W,A,\text{uncorr}}^2(k_I + c_4\delta_{\Delta m_W,A}(k_I)) \\
& + \Delta\chi_{\Delta m_W,D,\text{uncorr}}^2(k_I + c_5\delta_{\Delta m_W,D}(k_I)) \\
& + \Delta\chi_{\Delta m_W,O,\text{uncorr}}^2(k_I + c_6\delta_{\Delta m_W,O}(k_I)) \\
& + \sum_{m,n=1}^6 c_m (C_c^{-1})_{mn} c_n, \tag{4.9}
\end{aligned}$$

which is constructed from the ingredients presented above. It is minimised with respect to k_I and the auxiliary parameters c_1, \dots, c_6 , which are correlated through the covariance matrix C_c . In the LEP combination, the correlation coefficients are set to 0.5, motivated by the full covariance matrix of the R_N measurements, where the correlated systematic uncertainties are reduced to only the common part in each pair of measurements.

As a cross-check, the CR measurements of each collaboration are combined, and the best k_I values as well as their uncertainties are extracted using the procedure described above. All results of the individual experiments [111, 128, 129, 114] could be adequately reproduced, with small deviations being attributed to known systematic effects covered by the assigned uncertainties. More details can be found in the Appendix D.

The $\Delta\chi^2$ curves obtained for each experiment are shown in Figure 4.3, together with the LEP result. Combining all LEP data yields:

$$k_I = 1.26_{-0.64}^{+0.84}. \tag{4.10}$$

This result corresponds to a preferred reconnection probability of 51% at a centre-of-mass energy of 189 GeV in the SK1 model. Absence of CR cannot be excluded, but is disfavoured by LEP at more than two standard deviations.

4.1.5 Summary

A combination of the LEP particle-flow and W-mass estimator results is presented, using the entire LEP-II data sample. The data exclude with 6.9 standard deviations an extreme version of the SK-I model in which colour reconnection has been forced to occur in essentially all events. The combination procedure has been generalised to the SK-I model as a function of its reconnection probability. The combined data are described best by the model in which 51% of events at 189 GeV are reconnected, corresponding to $k_I = 1.26$. The LEP data disfavour the no-CR hypothesis at 99.5% confidence level, deviating from it by 2.8 standard deviations. The 68% confidence level range for k_I is determined to be $0.62 \leq k_I \leq 2.10$.

4.2 Bose-Einstein Correlations

4.2.1 Introduction

The LEP experiments have studied the strength of particle correlations between two hadronic systems obtained from W-pair decays occurring close in space-time at LEP-II. The work

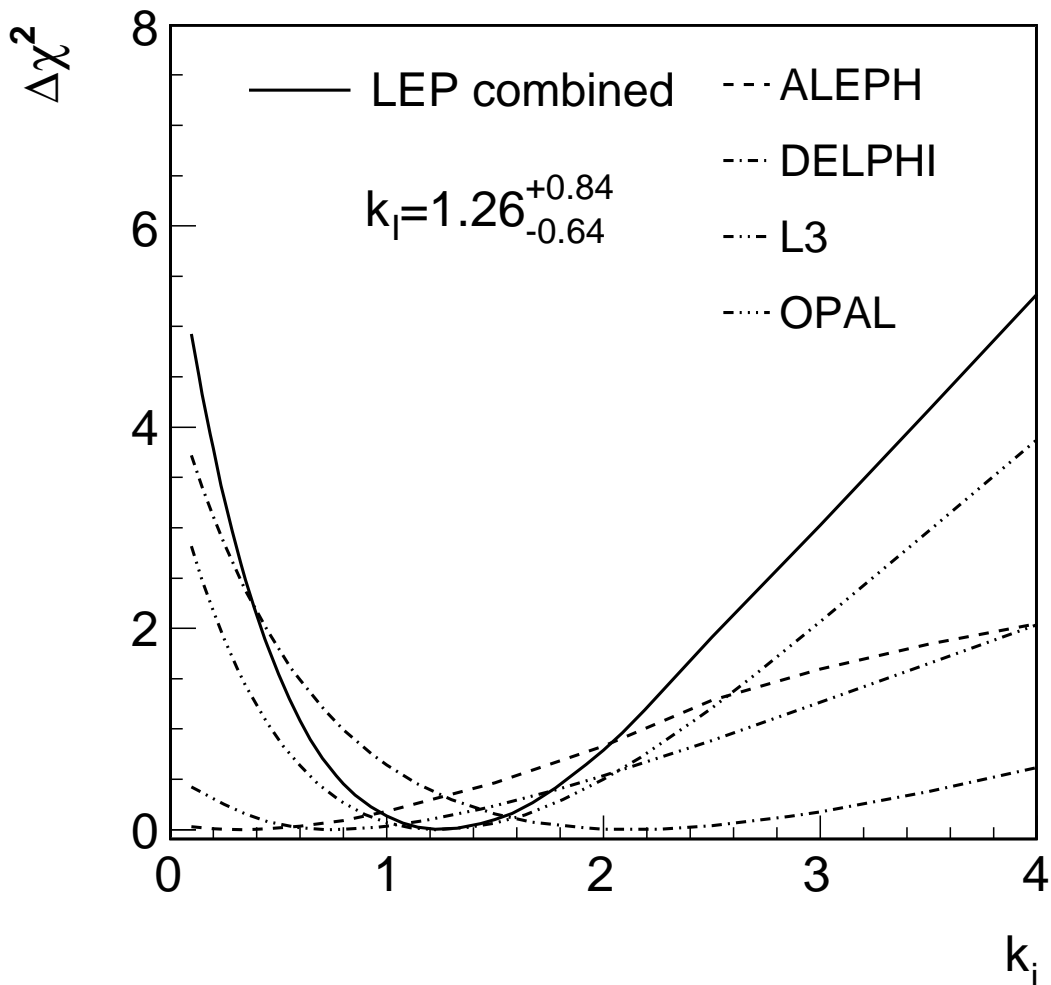


Figure 4.3: Individual and LEP combined $\Delta\chi^2$ curves for the measurement of the CR parameter k_I in the SK1 model.

presented in this section is focused on so-called Bose-Einstein correlations (BEC), *i.e.*, the enhanced probability of production of pairs (multiplets) of identical mesons close together in phase space. The effect is readily observed in particle physics, in particular in hadronic decays of the Z boson, and is qualitatively understood as a result of quantum-mechanical interference originating from the symmetry of the amplitude of the particle production process under exchange of identical mesons.

The presence of correlations between hadrons coming from the decay of a W-pair, in particular those between hadrons originating from different W bosons, can affect the direct reconstruction of the mass of the initial W bosons. The measurement of the strength of these correlations can be used to constrain the corresponding systematic uncertainty in the W mass measurement.

4.2.2 Methods

The principal method [142], called ‘‘mixing method’’, used in the measurement is based on the direct comparison of 2-particle spectra from genuine hadronic W-pair events, $WW \rightarrow q\bar{q}q\bar{q}$, and from mixed WW events. The latter are constructed by mixing the hadronic sides of two semileptonic W-pair events, $WW \rightarrow q\bar{q}\ell\nu$, first used in [143]. Such a reference sample has the advantage of reproducing the correlations between particles belonging to the same W boson, while the particles from different W bosons are uncorrelated by construction.

This method gives a model-independent estimate of the interplay between the two hadronic systems, for which BEC and also colour reconnection are considered as dominant sources. The possibility of establishing the strength of inter-W correlations in a model-independent way is rather unique; most correlations do carry an inherent model dependence on the reference sample. In the present measurement, the model dependence is limited to the background subtraction.

4.2.3 Distributions

The two-particle correlations are evaluated using two-particle densities defined in terms of the 4-momentum transfer $Q = \sqrt{-(p_1 - p_2)^2}$, where p_1, p_2 are the 4-momenta of the two particles:

$$\rho_2(Q) = \frac{1}{N_{ev}} \frac{dn_{pairs}}{dQ}. \quad (4.11)$$

Here n_{pairs} stands for the number of like-sign (unlike-sign) 2-particle permutations.¹ In the case of two stochastically independent hadronically decaying W bosons the two-particle inclusive density is given by:

$$\rho_2^{WW} = \rho_2^{W^+} + \rho_2^{W^-} + 2\rho_2^{mix}, \quad (4.12)$$

where ρ_2^{mix} can be expressed via the single-particle inclusive density $\rho_1(p)$ as:

$$\rho_2^{mix}(Q) = \int d^4p_1 d^4p_2 \rho^{W^+}(p_1) \rho^{W^-}(p_2) \delta(Q^2 + (p_1 - p_2)^2) \delta(p_1^2 - m_\pi^2) \delta(p_2^2 - m_\pi^2). \quad (4.13)$$

Assuming further that:

$$\rho_2^{W^+}(Q) = \rho_2^{W^-}(Q) = \rho_2^W(Q), \quad (4.14)$$

one obtains for the case of two stochastically independent hadronically decaying W bosons:

$$\rho_2^{WW}(Q) = 2\rho_2^W(Q) + 2\rho_2^{mix}(Q). \quad (4.15)$$

¹For historical reasons, the number of particle permutations rather than combinations is used in formulas, leading to a factor 2 in front of ρ_2^{mix} in Equation 4.12. The experimental statistical errors are, however, based on the number of particle pairs, *i.e.*, 2-particle combinations.

In the mixing method, ρ_2^{mix} is obtained by combining two hadronic W systems from two different semileptonic W-pair events. The direct search for inter-W BEC is done using the difference of 2-particle densities:

$$\Delta\rho(Q) = \rho_2^{WW}(Q) - 2\rho_2^W(Q) - 2\rho_2^{mix}(Q), \quad (4.16)$$

or, alternatively, their ratio:

$$D(Q) = \frac{\rho_2^{WW}(Q)}{2\rho_2^W(Q) + 2\rho_2^{mix}(Q)} = 1 + \frac{\Delta\rho(Q)}{2\rho_2^W(Q) + 2\rho_2^{mix}(Q)}. \quad (4.17)$$

Given the definition of the genuine inter-W correlations function $\delta_I(Q)$ [144], it can be shown that

$$\delta_I(Q) = \frac{\Delta\rho(Q)}{2\rho_2^{mix}(Q)}. \quad (4.18)$$

To disentangle the BEC effects from other possible correlation sources (such as energy-momentum conservation or colour reconnection), which are supposed to be the same for like-sign and unlike-sign charge pairs, the double difference:

$$\delta\rho(Q) = \Delta\rho^{like-sign}(Q) - \Delta\rho^{unlike-sign}(Q), \quad (4.19)$$

or the double ratio,

$$d(Q) = D^{like-sign}(Q)/D^{unlike-sign}(Q), \quad (4.20)$$

is analysed.

The event mixing procedure may introduce artificial distortions, or may not fully account for some detector effects or for correlations other than BEC. Most of these possible effects are treated in the Monte-Carlo simulation without inter-W BEC. Therefore they are reduced by using the double ratio or the double difference:

$$D'(Q) = \frac{D(Q)_{data}}{D(Q)_{MC,nointer}}, \quad \Delta\rho'(Q) = \Delta\rho(Q)_{data} - \Delta\rho(Q)_{MC,nointer}, \quad (4.21)$$

where $D(Q)_{MC,nointer}$ and $\Delta\rho(Q)_{MC,nointer}$ are derived from a MC without inter-W BEC.

In addition to the mixing method, ALEPH [145] also uses the double ratio of like-sign pairs ($N_{\pi^{++},--}(Q)$) and unlike-sign pairs $N_{\pi^{+-}}(Q)$ corrected with Monte-Carlo simulations without BEC effects:

$$R^*(Q) = \left(\frac{N_{\pi^{++},--}(Q)}{N_{\pi^{+-}}(Q)} \right)^{data} \bigg/ \left(\frac{N_{\pi^{++},--}(Q)}{N_{\pi^{+-}}(Q)} \right)_{noBEC}^{MC}. \quad (4.22)$$

In analyses based on $\Delta\rho(Q)$, $\delta\rho(Q)$ or $\delta_I(Q)$, a deviation from zero indicates the presence of inter-W correlations, whereas for studies of $D(Q)$, $D'(Q)$ or $d(Q)$, the corresponding signature is a deviation from unity. For $R^*(Q)$, a difference between data and the Monte-Carlo prediction excluding inter-W BEC is studied.

4.2.4 Results

The four LEP experiments have published results applying the mixing method to the full LEP-II data sample. As examples, the distributions of $\Delta\rho'$ measured by ALEPH [146], δ_I measured by DELPHI [147], D and D' measured by L3 [148] and D measured by OPAL [149] are shown in Figures 4.4, 4.5, 4.6 and 4.7, respectively. In addition ALEPH have published results using R^* [145]. The centre-of-mass energies, luminosities and the number of events used for the different measurements are listed in Table 4.2.

	\sqrt{s} [GeV]	Luminosity [pb ⁻¹]	Number of events	
			WW \rightarrow q \bar{q} q \bar{q}	WW \rightarrow q \bar{q} $\ell\nu$
ALEPH	183-209	683	6155	4849
DELPHI	189-209	550	3252	2567
L3	189-209	629	5100	3800
OPAL	183-209	680	4470	4533
ALEPH R*	172-189	242	2021	-

Table 4.2: The centre-of-mass energies, luminosities and the number of events used for the different measurements.

A simple combination procedure is available through a χ^2 average of the numerical results of each experiment [145, 146, 147, 148, 149] with respect to a specific BEC model under study, here based on comparisons with various tuned versions of the LUBOEI model [140, 150]. The tuning is performed by adjusting the parameters of the model to reproduce correlations in samples of Z and semileptonic W decays, and applying identical parameters to the modelling of inter-W correlations (so-called “fullBE” scenario). In this way the tuning of each experiment takes into account detector systematic uncertainties in the track measurements.

An important advantage of the combination procedure used here is that it allows the combination of results obtained using different analyses. The combination procedure assumes a linear dependence of the observed size of BEC on various estimators used to analyse the different distributions. It is also verified that there is a linear dependence between the measured W mass shift and the values of these estimators [113]. The estimators are: the integral of the $\Delta\rho(Q)$ distribution (ALEPH, L3, OPAL); the parameter Λ when fitting the function $N(1 + \delta Q)(1 + \Lambda \exp(-k^2 Q^2))$ to the $D'(Q)$ distribution, with N fixed to unity (L3), or δ fixed to zero and k fixed to the value obtained from a fit to the full BEC sample (ALEPH); the parameter Λ when fitting the function $N(1 + \delta Q)(1 + \Lambda \exp(-Q/R))$ to the $D(Q)$, $D(Q)'$ and d distributions, with R fixed to the value obtained from a fit to the full BEC sample (OPAL); the parameter Λ when fitting the function $\Lambda \exp(-RQ)(1 + \epsilon RQ) + \delta(1 + \frac{\rho_2^W}{\rho_2^{mix}})$ to the δ_I distribution, with R and ϵ fixed to the value obtained from a fit to the full BEC sample (DELPHI); and finally the integral of the term describing the BEC part, $\int \lambda \exp(-\sigma^2 Q^2)$, when fitting the function $\kappa(1 + \epsilon Q)(1 + \lambda \exp(-\sigma^2 Q^2))$ to the $R^*(Q)$ distribution (ALEPH).

The size of the correlations for like-sign pairs of particles measured in terms of these estimators is compared with the values expected in the model with and without inter-W correlations in Table 4.3. Table 4.4 summarises the normalised fractions of the model seen.

For the combination of the above measurements one has to take into account correlations between them. Correlations between results of the same experiment are strong and are not

Analysis	Data–noBE	stat.	syst.	corr. syst.	fullBE–noBE	Ref.
ALEPH (fit to D')	−0.004	0.011	0.014	0.003	0.081	[146]
ALEPH (integral of $\Delta\rho$)	−0.127	0.143	0.199	0.044	0.699	[146]
ALEPH (fit to R^*)	−0.004	0.0062	0.0036	negligible	0.0177	[145]
DELPHI (fit to δ_I)	+0.72	0.29	0.17	0.070	1.40	[147]
L3 (fit to D')	+0.008	0.018	0.012	0.0042	0.103	[148]
L3 (integral of $\Delta\rho$)	+0.03	0.33	0.15	0.055	1.38	[148]
OPAL (integral of $\Delta\rho$)	−0.01	0.27	0.23	0.06	0.77	[149]
OPAL (fit to D)	+0.040	0.038	0.038	0.017	0.120	[149]
OPAL (fit to D')	+0.042	0.042	0.047	0.019	0.123	[149]
OPAL (fit to d)	−0.017	0.055	0.050	0.003	0.133	[149]

Table 4.3: An overview of the results from different measurements described in Section 4.2.3: the difference between the measured correlations and the model without inter-W correlations (data–noBE), the corresponding statistical (stat.) and total systematic (syst.) errors, the correlated systematic error contribution (corr. syst.), and the difference between “fullBE” and “noBE” scenario. The measurements used in the combination are highlighted.

Analysis	Fraction of model	stat.	syst.
ALEPH (fit to D')	−0.05	0.14	0.17
ALEPH (integral of $\Delta\rho$)	−0.18	0.20	0.28
ALEPH (fit to R^*)	−0.23	0.35	0.20
DELPHI (fit to δ_I)	+0.51	0.21	0.12
L3 (fit to D')	+0.08	0.17	0.12
L3 (integral of $\Delta\rho$)	+0.02	0.24	0.11
OPAL (integral of $\Delta\rho$)	−0.01	0.35	0.30
OPAL (fit to D)	+0.33	0.32	0.32
OPAL (fit to D')	+0.34	0.34	0.38
OPAL (fit to d)	−0.13	0.41	0.38

Table 4.4: The measured size of BEC expressed as the relative fraction of the model with inter-W correlations (see Equation 4.23 and Table 4.3). The measurements used in the combination are highlighted.

available. Varying these correlations and combining the three ALEPH measurements, for example, one obtains normalised fractions of the model seen very close to those of the most precise measurement. Therefore, for simplicity, the combination of the most precise measurements of each experiment is made here: D' from ALEPH, δ_I from DELPHI, D' from L3 and D from OPAL. In this combination only the uncertainties in the understanding of the background contribution in the data are treated as correlated between experiments (denoted as “corr. syst.” in Table 4.3). The combination via a fit using MINUIT gives:

$$\frac{\text{data} - \text{model}(\text{noBE})}{\text{model}(\text{fullBE}) - \text{model}(\text{noBE})} = 0.17 \pm 0.095(\text{stat.}) \pm 0.085(\text{sys.}) = 0.17 \pm 0.13, \quad (4.23)$$

where “noBE” includes correlations between decay products of each W, but not the ones between decay products of different Ws and “fullBE” includes all the correlations. A $\chi^2/\text{dof} = 3.5/3$ of the fit is observed. The measurements and their average are shown in Figure 4.8. The measurements used in the combination are marked with an arrow. The results of LEP experiments are in good agreement.

4.2.5 Conclusions

The LUBOEI model of BEC between pions from different W bosons is disfavoured. The 68% confidence level (CL) upper limit on these correlations is $0.17 + 0.13 = 0.30$. This result can be translated into a 68% CL upper limit on the shift of the W mass measurements due to the BEC between particles from different Ws, Δm_W , assuming a linear dependence of Δm_W on the size of the correlation. For the specific BE model investigated, LUBOEI, a shift of -35 MeV in the W mass is obtained at full BEC strength. The W mass analysis techniques applied are, however, optimised to reduce colour reconnection effects on m_W which also has the effect of reducing the mass shift due to BEC. A combination of the reduced shifts reported by the LEP experiments [151, 152, 153, 154] gives a shift of -23 MeV in the W mass at full BEC strength. Thus the 68% CL upper limit on the magnitude of the mass shift within the LUBOEI model is: $|\Delta m_W| = 0.30 \times 23 \text{ MeV} = 7 \text{ MeV}$.

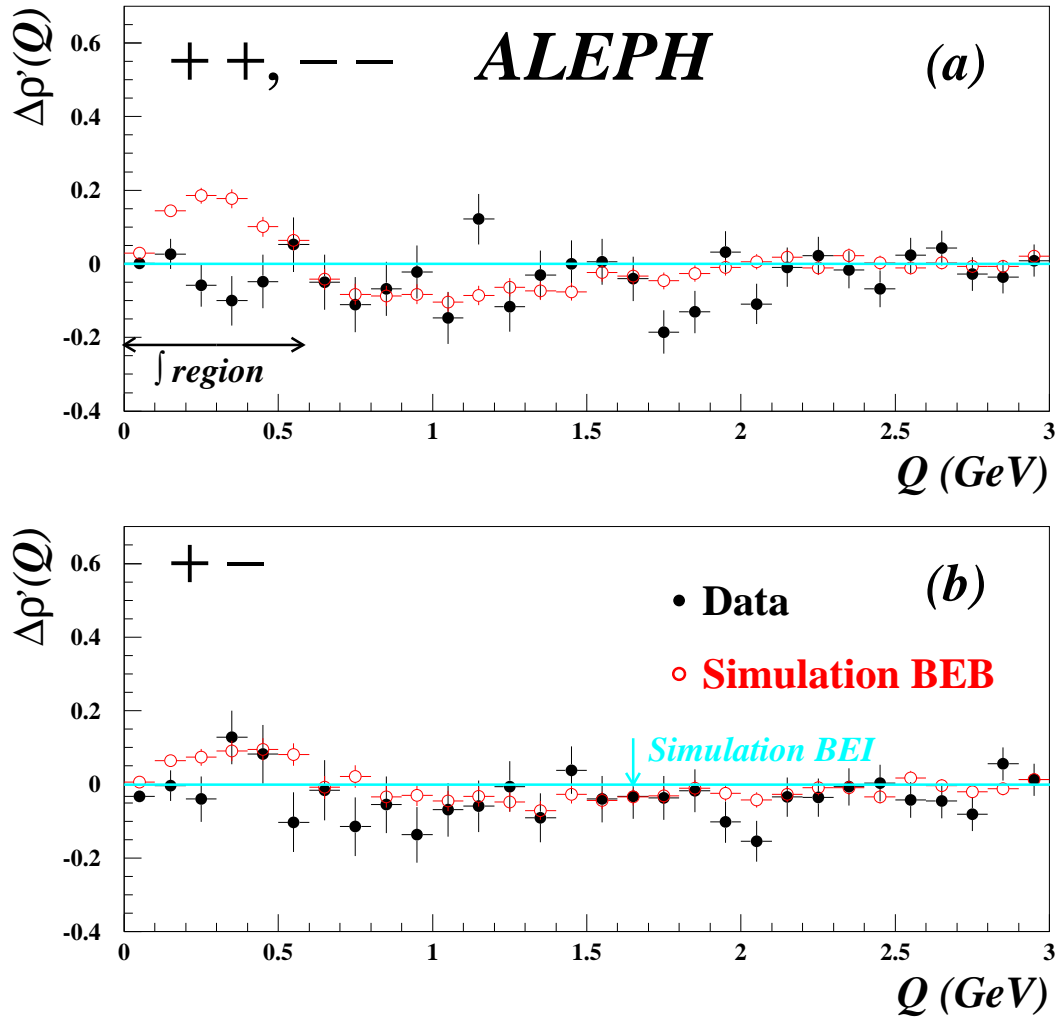


Figure 4.4: Distribution of the quantity $\Delta\rho'$ for like- and unlike-sign pairs as a function of Q as measured by the ALEPH collaboration [146]. BEI stands for the case in which Bose-Einstein correlations do not occur between decay products of different W bosons, and BEB if they do.

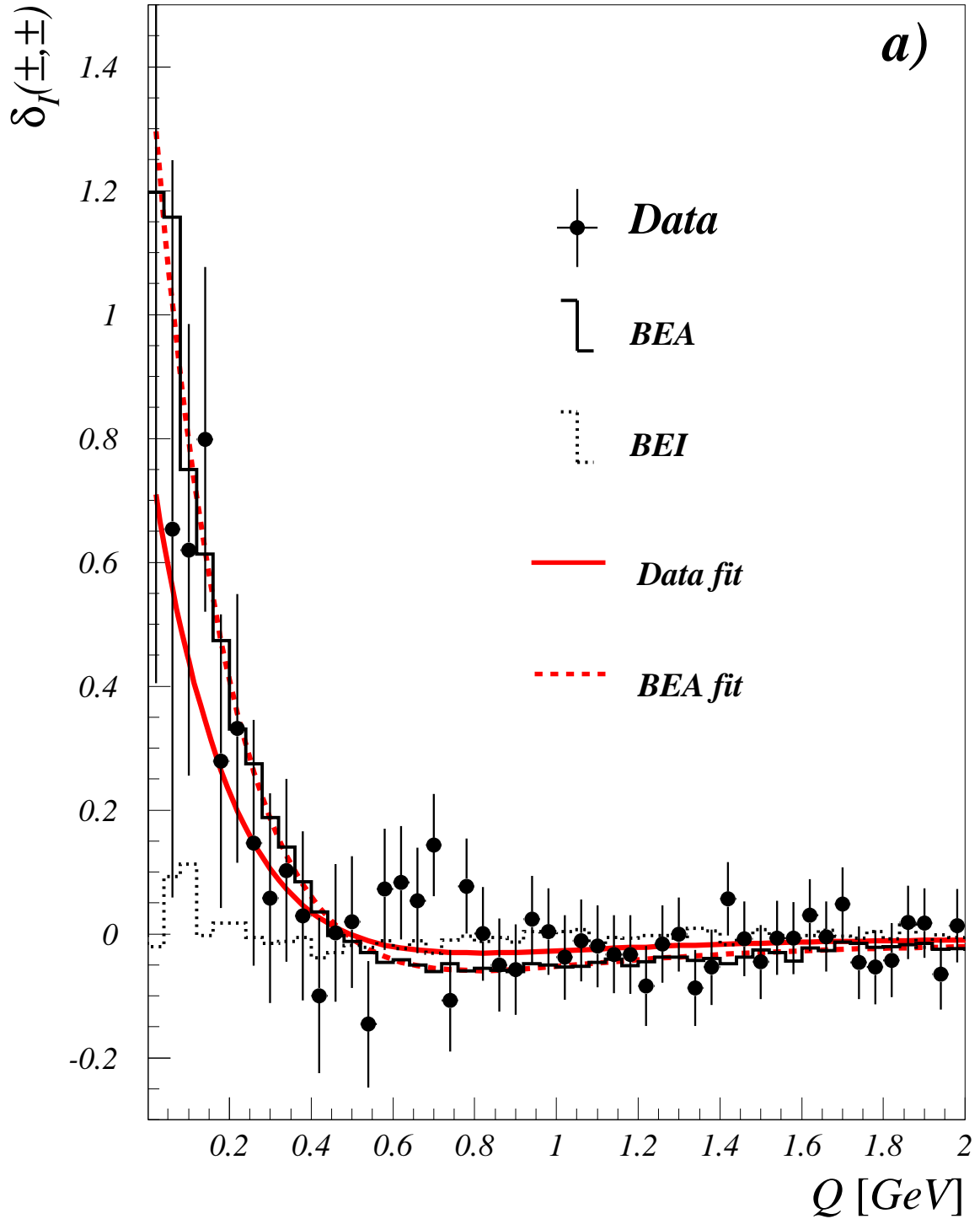


Figure 4.5: Distributions of the quantity δ_I for like-sign pairs as a function of Q as measured by the DELPHI collaboration [147]. The solid line shows the fit results. BEI stands for the case in which Bose-Einstein correlations do not occur between decay products of different W bosons, and BEA if they do.

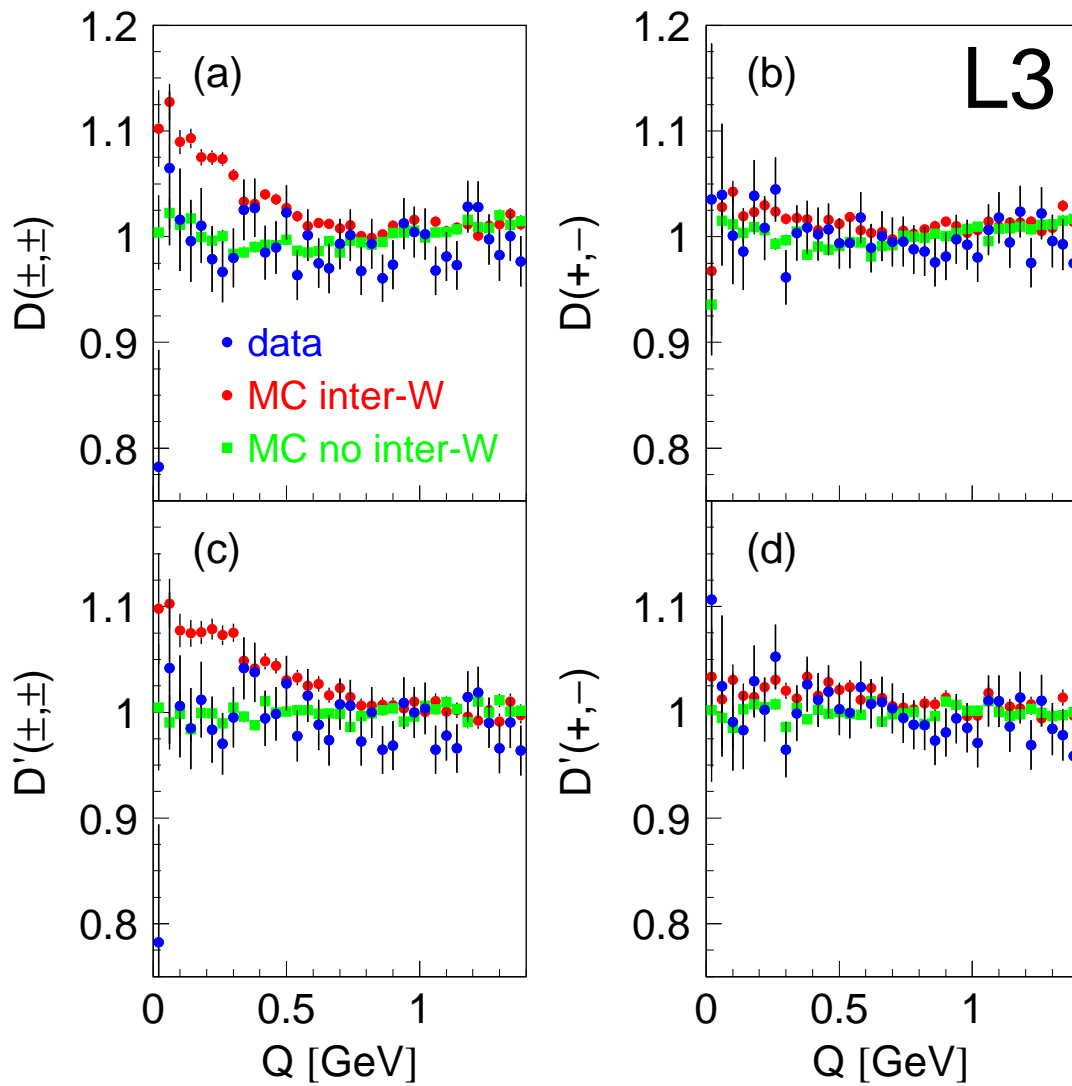


Figure 4.6: Distributions of the quantity D and D' for like- and unlike-sign pairs as a function of Q as measured by the L3 collaboration [148].

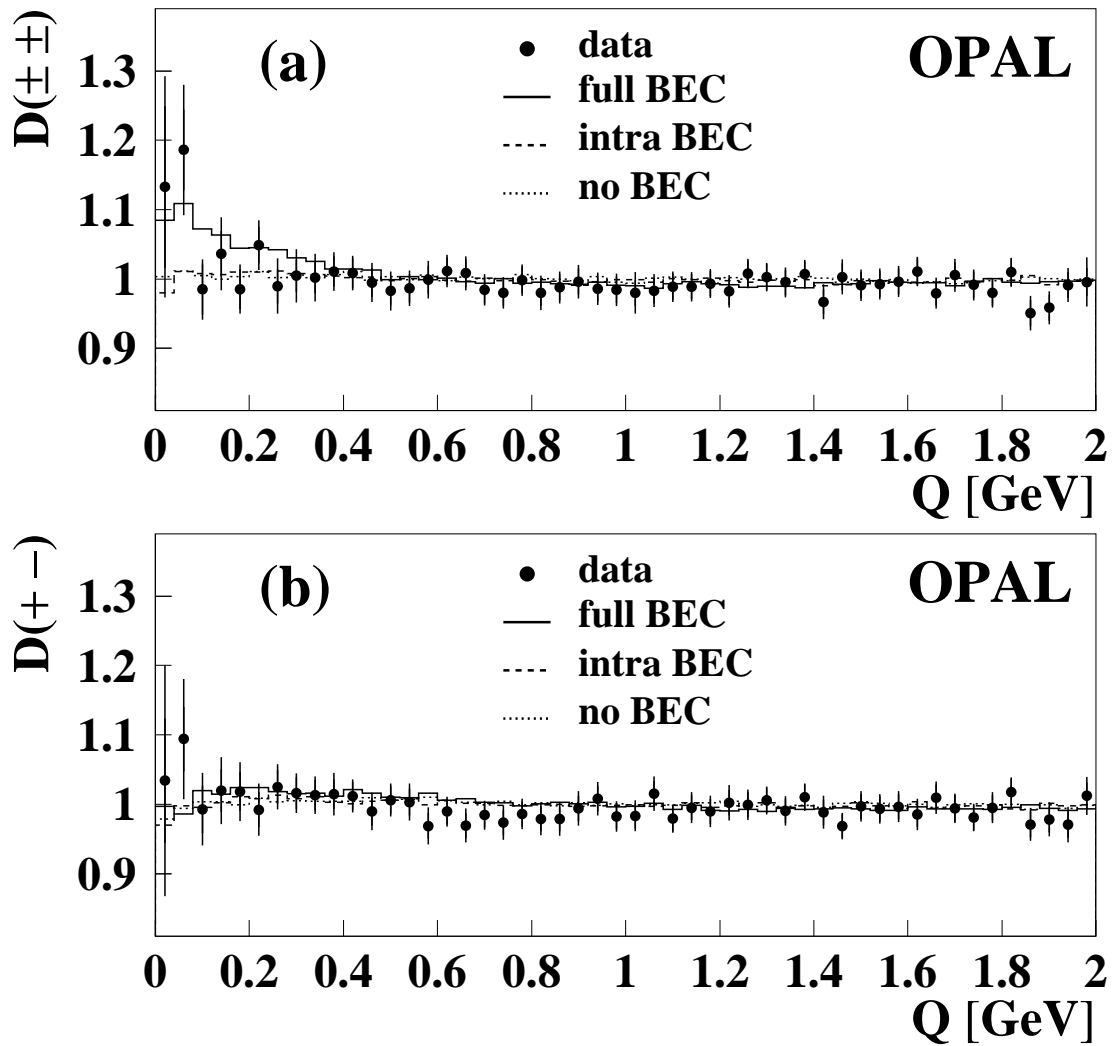


Figure 4.7: Distribution of the quantity D for like- and unlike-sign pairs as a function of Q as measured by the OPAL collaboration [149].

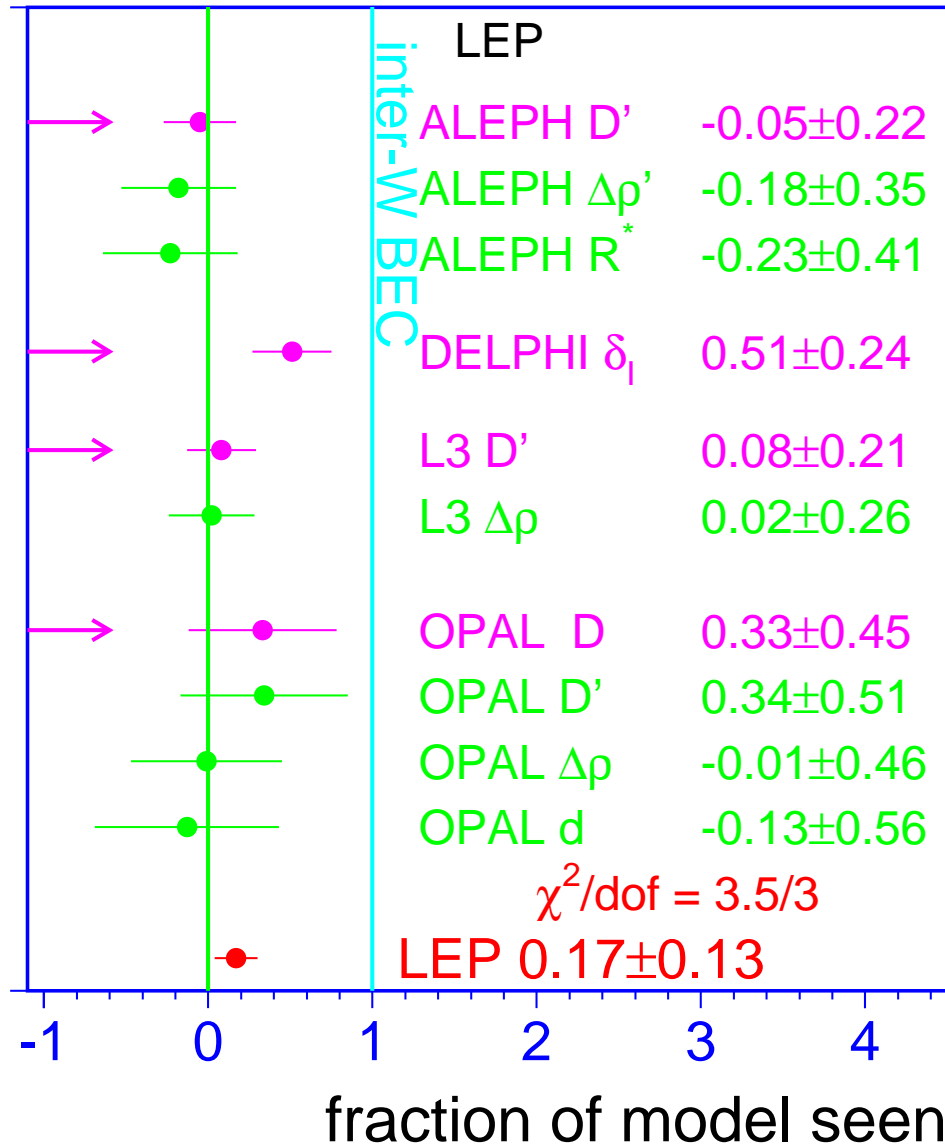


Figure 4.8: Measured BEC expressed as the relative fraction of the model with inter-W correlations. The arrows indicate the measurements used in the combination. The LEP combination is shown at the bottom.

Chapter 5

Boson-Pair and Four-Fermion Processes

5.1 Introduction and Signal Definitions

Cross-section measurements at LEP-II are essential because they allow many direct and indirect tests of the Standard Model (SM). W -pair production and decay, certainly the most interesting manifestation of four-fermion production, is directly related to fundamental parameters of the model, such as the W -boson mass at the production threshold energy and to the non-Abelian gauge structure of the theory. The W -decay branching fractions and the value of $|V_{cs}|$ can be directly extracted from a cross-section measurement. A broader investigation of four-fermion production in several regions of phase space also brings additional information on the boson-fermion coupling structure, on the effect of radiative corrections and on the possible presence of new physics.

This chapter summarises the combination of final results of the four LEP experiments on four-fermion production cross-sections. The signals, with the exception of WW and ZZ , are defined on the basis of their final states together with cuts to enhance certain regions of phase space. For WW and ZZ , a diagrammatic definition is used for the sake of simplicity, even though this corresponds to a non gauge invariant definition. In what follows we will use terms such as “singly resonant” or “doubly resonant”, indicating regions of the phase space rather than a process itself.

The most interesting regions of the four-fermion phase space that are measured at LEP and for which a combination is performed, are summarised as:

- **WW:** defined as the CC03 component of the four-fermion processes, involving s -channel γ and Z exchange and t -channel ν exchange (see Figure 1.4).
- **ZZ:** in analogy with the definition of W -pair production, Z -pair production is defined as the subset of NC02 Feynman diagrams having two resonant Z bosons (see Figure 1.5).
- **$Z\gamma^*$:** defined for final states with two fermion-antifermion pairs, at least one being leptonic (electrons or muons). To properly consider only singly resonant regions, it is required that one and only one of the invariant masses of the couples satisfies: $|m_{ff'} - m_Z| < 2\Gamma_Z$, where $m_{ff'}$ is the invariant mass of the two same-flavour fermions. In case of four identical leptons all oppositely charged couples have to be considered. Moreover the following final state dependent phase-space cuts have been introduced:

- eeqq, $\mu\mu$ qq: $|\cos\theta_\ell| < 0.95$, $m_{\ell\ell} > 5$ GeV, $m_{qq} > 10$ GeV, $\ell = e, \mu$
 - $\nu\nu$ qq: $m_{qq} > 10$ GeV
 - $\nu\nu\ell\ell$: $m_{\ell\ell} > 10$ GeV, $m_{\ell\nu} > 90$ GeV or $m_{\ell\nu} < 70$ GeV, $\ell = e, \mu$
 - $\ell_1\ell_1\ell_2\ell_2$: $|\cos\theta_{\ell_1\ell_2}| < 0.95$, $m_{\ell_1\ell_1} > 5$ GeV, $m_{\ell_2\ell_2} > 5$ GeV, $\ell = e, \mu$
- **We ν** : considered as the complete t -channel subset of Feynman diagrams contributing to $e\nu_e\bar{f}f'$ final states, with additional cuts to exclude the regions of phase space dominated by multiperipheral diagrams, where the cross-section calculation is affected by large uncertainties. The phase space cuts are (charge conjugation is implicit): $m_{q\bar{q}} > 45$ GeV for the $e\nu q\bar{q}$ final states, $E_\ell > 20$ GeV for the $e\nu\ell\nu$ final states with $\ell = \mu$ or τ , and finally $|\cos\theta_{e-}| > 0.95$, $|\cos\theta_{e+}| < 0.95$ and $E_{e+} > 20$ GeV for the $e\nu e\nu$ final states (see Figure 1.7).
 - **Zee**: defined considering only the $eeq\bar{q}$ and $ee\mu\mu$ final states. The following phase space cuts are applied to enhance the signal: $m_{q\bar{q}}(m_{\mu\mu}) > 60$ GeV, and in addition: $\theta_{e-} < 12^\circ$, $12^\circ < \theta_{e+} < 120^\circ$ and $E_{e+} > 3$ GeV when the positron is visible, or $\theta_{e+} > 168^\circ$, $60^\circ < \theta_{e-} < 168^\circ$ and $E_{e-} > 3$ GeV when the electron is visible. This definition assumes the electron direction to be $+z$ and the positron direction to be $-z$.
 - **WW γ** : it is defined as the part of the $e^+e^- \rightarrow W^+W^-\gamma$ process compatible with charged currents, *i.e.*, including the final states $udud\gamma$, $cscs\gamma$, $udcs\gamma$, $udlv\gamma$, $cslv\gamma$, $\ell\nu\ell\nu\gamma$, assuming a diagonal CKM matrix. The following phase-space cuts are applied to enhance the signal: $E_\gamma > 5$ GeV, $|\cos\theta_\gamma| < 0.95$, $\cos\theta_{\gamma,f} < 0.9$, the invariant mass of the W-decay fermion pairs between $m_W - 2\Gamma_W$ and $m_W + 2\Gamma_W$ (see Figure 1.6).

The cross-sections are determined from a fit to the number of observed events in data, knowing the signal efficiencies corresponding to the above signal definitions, and the expected accepted backgrounds, from Monte-Carlo simulations.

The LEP cross-section combination is performed in a fit to the $N=N_{exp}\times N_{\sqrt{s}}$ experimental inputs, where N_{exp} identifies the number of LEP experiments providing input for the measurement and $N_{\sqrt{s}}$ is the number of energy points provided. The method used is the Best Linear Unbiased Estimate method (BLUE) described in [62]. In the fits, inter-experiment and inter-energy correlations of the systematic errors are taken into account, dividing the sources according to their correlation and assuming for each either 0% or 100% correlation strength for simplicity. After building the appropriate $N\times N$ correlation matrix for the measurements, the χ^2 minimisation fit is performed by matrix algebra and is cross-checked with the use of Minuit [155].

The numbers shown here represent the combination of cross-section values and derived quantities such as branching fractions or differential distributions. For each measurement, the collaborations provided input in agreement with the conventions used to define the signal and to split the systematic uncertainties: small differences may therefore appear between the values quoted here and those published by the experiments. The combinations are performed for the whole LEP-II period, that includes data from e^+e^- collisions from $\sqrt{s} = 183$ GeV up to $\sqrt{s} = 207$ GeV. The energy binning chosen and the corresponding average integrated luminosity per experiment at each energy point are shown in Table 5.1; they result from a combination of the luminosity in the hadronic and leptonic channels, therefore small changes from the values published by individual experiments may be present.

Year	ALEPH		DELPHI		L3		OPAL		LEP
	\sqrt{s}	\mathcal{L}	\sqrt{s}	\mathcal{L}	\sqrt{s}	\mathcal{L}	\sqrt{s}	\mathcal{L}	\sqrt{s}
	[GeV]	[pb ⁻¹]	[GeV]	[pb ⁻¹]	[GeV]	[pb ⁻¹]	[GeV]	[pb ⁻¹]	[GeV]
1997	182.66	56.81	182.65	52.08	182.68	55.46	182.68	57.38	182.67
1998	188.63	174.21	188.63	154.07	188.64	176.77	188.63	183.04	188.63
1999	191.58	28.93	191.58	24.84	191.60	29.83	191.61	29.33	191.59
1999	195.52	79.86	195.51	74.04	195.54	84.15	195.54	76.41	195.53
1999	199.52	86.28	199.51	82.31	199.54	83.31	199.54	76.58	199.52
1999	201.63	41.89	201.64	40.01	201.75	37.18	201.65	37.68	201.67
2000	204.86	81.41	204.86	75.66	204.82	79.01	204.88	81.91	204.85
2000	206.53	133.21	206.55	129.95	206.57	139.12	206.56	138.54	206.55

Table 5.1: Summary of luminosity and luminosity-weighted centre-of-mass energies, per year, of the four LEP experiments, and final LEP averaged energy.

The structure of this chapter is as follows: in Section 5.2 the W-pair production is described and the combined results on cross-sections, W branching fractions, $|V_{cs}|$ and W polar-angle distributions are presented. Sections 5.3 and 5.4 concern neutral current boson production and present combined results on ZZ and $Z\gamma^*$ cross-sections, respectively. The combination of single boson production cross-sections is reported in Section 5.5. All the presented results are compared to recent theoretical predictions, many of which were developed in the framework of the LEP-II Monte-Carlo workshop [156].

5.2 W-Pair Production

The signal definition has been given in Section 5.1. W-pair production is investigated via all possible final states arising in the decay of the two W bosons. According to the different decays, three topologically different final states can arise: the fully hadronic, where both W bosons decay into quarks, characterised by high multiplicity of the final state; the mixed hadronic-leptonic, also called semileptonic, with the presence of an isolated and energetic lepton and hadronic decay products of the second W; and the fully leptonic, with the production of two acoplanar leptons. The SM branching fractions for these final states are, respectively, 0.456, 0.349, and 0.105 [36]. There are ten experimentally distinguishable final states: $q\bar{q}q\bar{q}$, $q\bar{q}\mu^+\nu$, $q\bar{q}e^+\nu$, $q\bar{q}\tau^+\nu$, $\mu^+\nu\tau^-\nu$, $e^+\nu\tau^-\nu$, $\tau^+\nu\tau^-\nu$, $\mu^+\nu e^-\nu$, $\mu^+\nu\mu^-\nu$, $e^+\nu e^-\nu$. Charge conjugation is assumed everywhere.

Event selections are generally based on Neural Network approaches to separate the signals from the major backgrounds, which arise mainly from $q\bar{q}(\gamma)$ events in the fully hadronic final state, while four-fermion backgrounds are also important in the other channels. Typical selection efficiencies range from 80% to 90% in the fully hadronic channel, from 70% to 90% in the various semileptonic channels and about 70% in the fully leptonic ones. The purest channels (95%) are the semileptonic ones with electrons or muons in the final state. Details on the event selections and experimental performances can be found in [157, 158, 159, 160].

5.2.1 Total Cross-Section Measurement

From the number of WW selected events in data, knowing the expected background and the efficiency on the signal, the production cross-section is extracted through likelihood fits. Cross-sections are then combined, accounting for the correlation of the systematic errors as shown in Table 5.2. The inputs used for the combinations are given in Table E.1, with the details on the composition of the systematic error in terms of correlated components shown in Table E.2. For this analysis, the SM W-decay branching fractions are assumed; see Section 5.2.2 for the measurement of these branching fractions.

Source	LEP correlation	Energy correlation
Theory uncertainties on signal	Yes	Yes
Theory uncertainties on backgrounds	Yes	Yes
Theory uncertainty on luminosity	Yes	Yes
Experimental uncertainties on luminosity	No	Yes
Detector effects	No	Yes
Monte-Carlo statistics	No	No

Table 5.2: Grouping of systematic uncertainties into those correlated among experiments and those correlated among different energies. The theory uncertainties on the signal include fragmentation effects, radiative corrections and final state interaction effects.

The measured statistical errors are used for the combination; after building the full 32×32 covariance matrix for the measurements, the χ^2 minimisation fit is performed by matrix algebra, as described in Ref. [62], and is cross-checked using Minuit [155].

The results from each experiment for the W-pair production cross-section are shown in Table 5.3, together with the LEP combination at each energy. All measurements assume SM values for the W decay branching fractions. The combined LEP cross-sections at the eight energies are all positively correlated, see Table E.3, with correlations ranging from 6% to 19%.

Figure 5.1 shows the combined LEP W-pair cross-section measured as a function of the centre-of-mass energy. The experimental results are compared with the theoretical calculations from YFSWW [161, 167] and RACOONWW [168] between 155 and 215 GeV using $m_W = 80.35$ GeV. The two programs have been extensively compared and agree at a level better than 0.5% at the LEP-II energies [156]. The calculations above 170 GeV, based for the two programs on the so-called leading-pole (LPA) or double-pole (DPA) approximations [156], have theoretical uncertainties decreasing from 0.7% at 170 GeV to about 0.4% at centre-of-mass energies larger than 200 GeV¹, while in the threshold region, where the programs use an improved Born approximation, a larger theoretical uncertainty of 2% is assigned. This theoretical uncertainty is represented by the blue band in the figure. The cross-sections are sensitive to the W-boson mass, such that an error of 50 MeV on the W mass would translate into additional errors of 0.1% (3.0%) on the cross-section predictions at 200 GeV (161 GeV), respectively. All results, up to the highest centre-of-mass energies, are in agreement with the two theoretical predictions

¹ The theoretical uncertainty $\Delta\sigma/\sigma$ on the W-pair production cross-section calculated in the LPA/DPA above 170 GeV can be parametrised as $\Delta\sigma/\sigma = (0.4 \oplus 0.072 \cdot t_1 \cdot t_2)\%$, where $t_1 = (200 - 2 \cdot m_W)/(\sqrt{s} - 2 \cdot m_W)$ and $t_2 = (1 - (\frac{2 \cdot M_W}{200})^2)/(1 - (\frac{2 \cdot M_W}{\sqrt{s}})^2)$.

\sqrt{s} [GeV]	WW Cross-Section [pb]				
	ALEPH	DELPHI	L3	OPAL	LEP
161.3	4.23 ± 0.75	$3.61^{+0.99}_{-0.87}$	$2.89^{+0.82}_{-0.71}$	$3.62^{+0.94}_{-0.84}$	3.69 ± 0.45
172.1	11.7 ± 1.3	11.4 ± 1.4	12.3 ± 1.4	12.3 ± 1.3	12.0 ± 0.7
182.7	15.86 ± 0.63	16.07 ± 0.70	16.53 ± 0.72	15.45 ± 0.62	15.92 ± 0.34
188.6	15.78 ± 0.36	16.09 ± 0.42	16.17 ± 0.41	16.24 ± 0.37	16.05 ± 0.21
191.6	17.10 ± 0.90	16.64 ± 1.00	16.11 ± 0.92	15.93 ± 0.86	16.42 ± 0.47
195.5	16.60 ± 0.54	17.04 ± 0.60	16.22 ± 0.57	18.27 ± 0.58	16.99 ± 0.29
199.5	16.93 ± 0.52	17.39 ± 0.57	16.49 ± 0.58	16.29 ± 0.55	16.77 ± 0.29
201.6	16.63 ± 0.71	17.37 ± 0.82	16.01 ± 0.84	18.01 ± 0.82	16.98 ± 0.40
204.9	16.84 ± 0.54	17.56 ± 0.59	17.00 ± 0.60	16.05 ± 0.53	16.81 ± 0.29
206.6	17.42 ± 0.43	16.35 ± 0.47	17.33 ± 0.47	17.64 ± 0.44	17.20 ± 0.24

Table 5.3: W-pair production cross-section from the four LEP experiments and combined values at all recorded centre-of-mass energies. The measurements above 175 GeV have been combined in a single fit, taking into account inter-experiment as well as inter-energy correlations of systematic errors, with a χ^2/dof of 26.6/24. The fit at 161.3 GeV (172.1 GeV) has a χ^2/dof of 1.3/3 (0.22/3).

considered and listed in Table E.4. In the lower part of the figure, the data are also compared with hypothetical predictions for which W-pair production happens in absence of one or two of the CC03 diagrams. The need for the diagram with a ZWW vertex is a spectacular confirmation of the non-Abelian nature of the electroweak SM.

The agreement between the measured W-pair cross-section, $\sigma_{\text{WW}}^{\text{meas}}$, and its expectation according to a given theoretical model, $\sigma_{\text{WW}}^{\text{theo}}$, can be expressed quantitatively in terms of their ratio:

$$\mathcal{R}_{\text{WW}} = \frac{\sigma_{\text{WW}}^{\text{meas}}}{\sigma_{\text{WW}}^{\text{theo}}}, \quad (5.1)$$

averaged over the measurements performed by the four experiments at different energies in the LEP-II region. The above procedure has been used to compare the measurements at the eight energies between 183 GeV and 207 GeV with the predictions of GENTLE [173], KORALW [174, 167], YFSWW [161, 167] and RACOONWW [168]. The measurements at 161 GeV and 172 GeV have not been used in the combination because they were performed using data samples of low statistics and because of the high sensitivity of the cross-section to the value of the W mass at these energies.

The combination of the ratio \mathcal{R}_{WW} is performed using as input from the four experiments the 32 cross-sections measured at each of the eight energies. These are then converted into 32 ratios by dividing them by the theoretical predictions listed in Table E.4. The full 32×32 covariance matrix for the ratios is built taking into account the same sources of systematic errors used for the combination of the W-pair cross-sections at these energies.

The small statistical errors on the theoretical predictions at the various energies, taken as fully correlated for the four experiments and uncorrelated between different energies, are

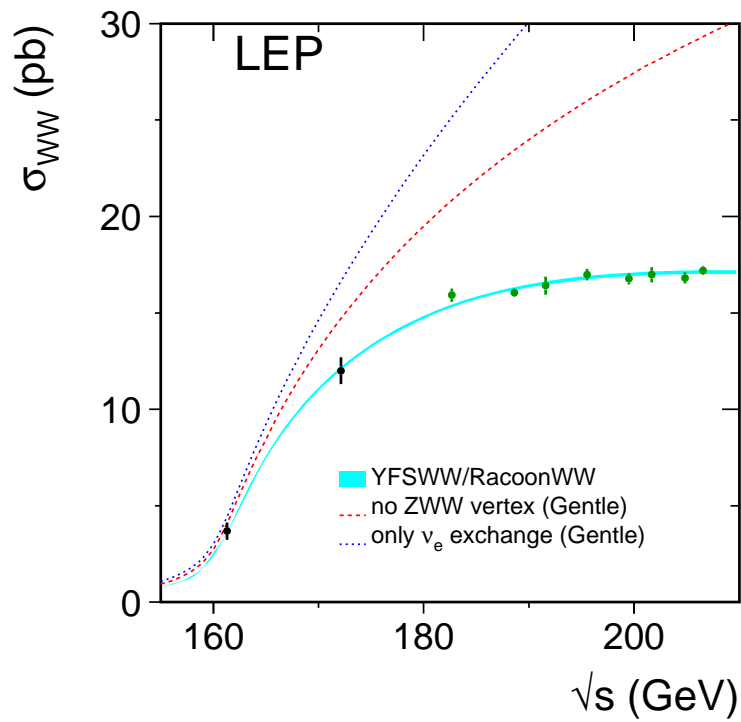
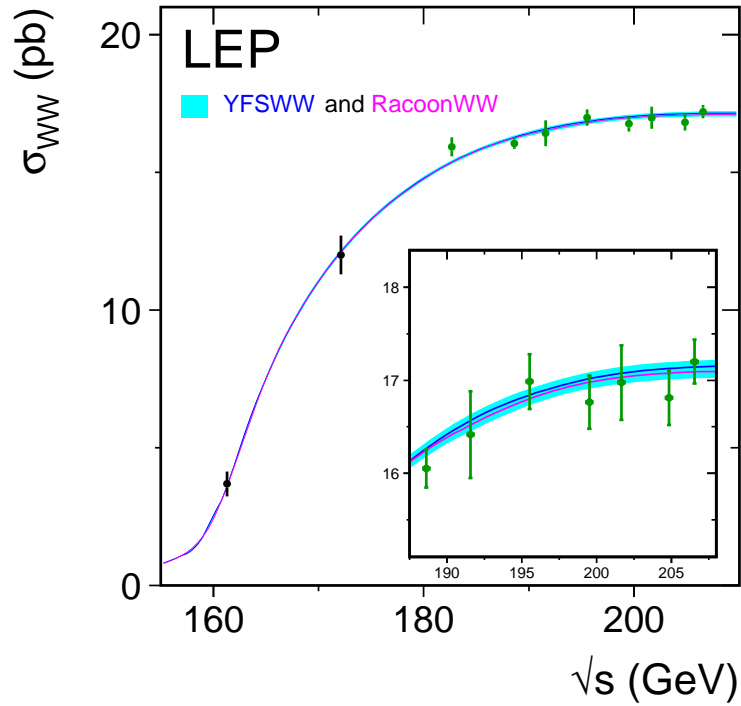


Figure 5.1: Measurements of the W-pair production cross-section, compared to the predictions of RACOONWW [168] and YFSWW [161, 167]. The shaded area represents the uncertainty on the theoretical predictions, estimated as $\pm 2\%$ for $\sqrt{s} < 170$ GeV and ranging from 0.7 to 0.4% above 170 GeV. The W mass is fixed at 80.35 GeV; its uncertainty is expected to give a significant contribution only at threshold energies.

\sqrt{s} [GeV]	$\mathcal{R}_{\text{WW}}^{\text{YFSWW}}$	$\mathcal{R}_{\text{WW}}^{\text{RACOONWW}}$
182.7	1.037 ± 0.022	1.036 ± 0.023
188.6	0.987 ± 0.013	0.988 ± 0.013
191.6	0.991 ± 0.028	0.994 ± 0.029
195.5	1.009 ± 0.018	1.011 ± 0.019
199.5	0.985 ± 0.017	0.987 ± 0.018
201.6	0.994 ± 0.023	0.997 ± 0.024
204.9	0.982 ± 0.017	0.984 ± 0.018
206.6	1.003 ± 0.014	1.007 ± 0.015
χ^2/dof	26.6/24	26.6/24
Average	0.995 ± 0.008	0.997 ± 0.008
χ^2/dof	32.2/31	32.0/31

Table 5.4: Ratios of LEP combined W-pair cross-section measurements to the expectations according to YFSWW [161, 167] and RACOONWW [168]. For each of the two models, two fits are performed, one to the LEP combined values of \mathcal{R}_{WW} at the eight energies between 183 GeV and 207 GeV, and another to the LEP combined average of \mathcal{R}_{WW} over all energies. The results of the fits are given in the table together with the resulting χ^2/dof . The fits take into account inter-experiment as well as inter-energy correlations of systematic errors.

also translated into errors on the individual measurements of \mathcal{R}_{WW} . The theoretical errors on the predictions, due to the physical and technical precision of the generators used, are not propagated to the individual ratios but are used when comparing the combined values of \mathcal{R}_{WW} to unity. For each of the four models considered, two fits are performed: in the first, eight values of \mathcal{R}_{WW} at the different energies are extracted, averaged over the four experiments; in the second, only one value of \mathcal{R}_{WW} is determined, representing the global agreement of measured and predicted cross-sections over the whole energy range.

The results of the fits to \mathcal{R}_{WW} for YFSWW and RACOONWW are given in Table 5.4, with more details given in Table E.5. As already qualitatively noted from Figure 5.1, the LEP measurements of the W-pair cross-section above threshold are in very good agreement with the predictions and can test the theory at the level of better than 1%. In contrast, the predictions from GENTLE and KORALW are about 3% too high with respect to the measurements due to the lack of LPA/DPA corrections; the equivalent values of \mathcal{R}_{WW} in those cases are, respectively, 0.970 ± 0.008 and 0.976 ± 0.008 . The results of the fits for YFSWW and RACOONWW are also shown in Figure 5.2, where relative errors of 0.5% on the cross-section predictions have been assumed. For simplicity the energy dependence of the theory error on the W-pair cross-section has been neglected in the figure. The main differences between the predictions of YFSWW/RACOONWW and GENTLE/KORALW arise from non-leading $\mathcal{O}(\alpha)$ electroweak radiative corrections to the W-pair production process and non-factorisable corrections, which are included (in the LPA/DPA leading-pole/double-pole approximation [156]) in both YFSWW and RACOONWW, but not in GENTLE and KORALW. The data clearly prefer the computations which more precisely include $\mathcal{O}(\alpha)$ radiative corrections.

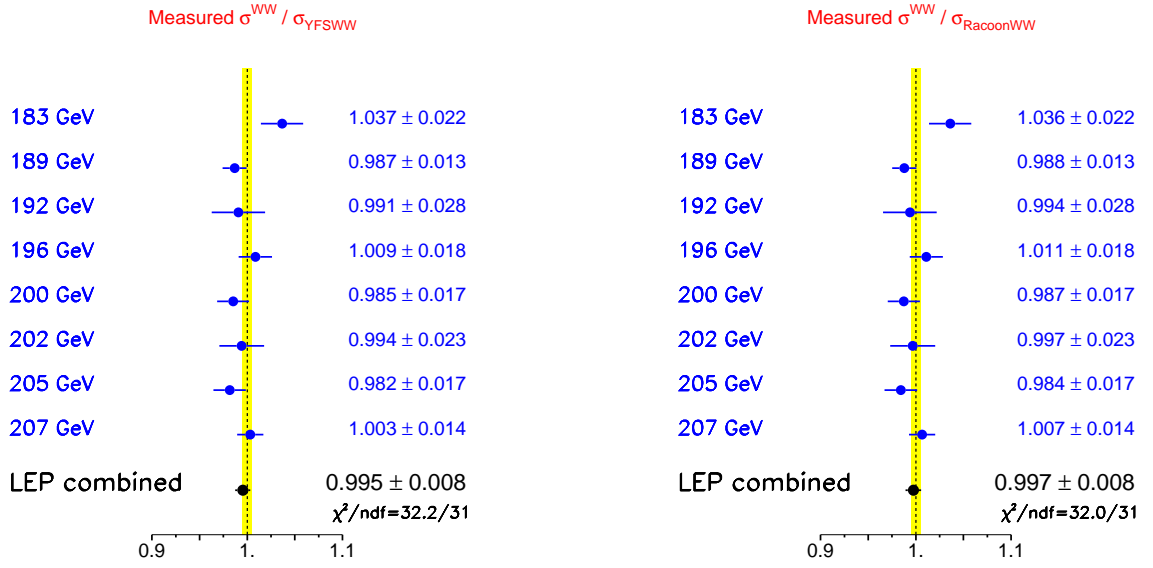


Figure 5.2: Ratios of LEP combined W-pair cross-section measurements to the expectations calculated with YFSWW [161, 167] and RACOONWW [168] The yellow bands represent constant relative errors of 0.5% on the two cross-section predictions.

5.2.2 Derived Quantities

From the cross-sections of the individual WW decay channels, each experiment determined the values of the W branching fractions, with and without the assumption of lepton universality². In the fit with lepton universality, the branching fraction to hadrons is determined from that to leptons by constraining the sum to unity. In building the full 12×12 covariance matrix, the same correlations of the systematic errors as used for the cross-section measurements are assumed. The detailed inputs to LEP and the correlation matrices are reported in Table E.6.

The results from each experiment are reported in Table 5.5 together with the LEP combination and shown in Figure 5.3. The results of the fit which does not assume lepton universality show a negative correlation of 20.1% (12.2%) between the $W \rightarrow \tau\bar{\nu}_\tau$ and $W \rightarrow e\bar{\nu}_e$ ($W \rightarrow \mu\bar{\nu}_\mu$) branching fractions, while between the electron and muon decay channels there is a positive correlation of 13.5%.

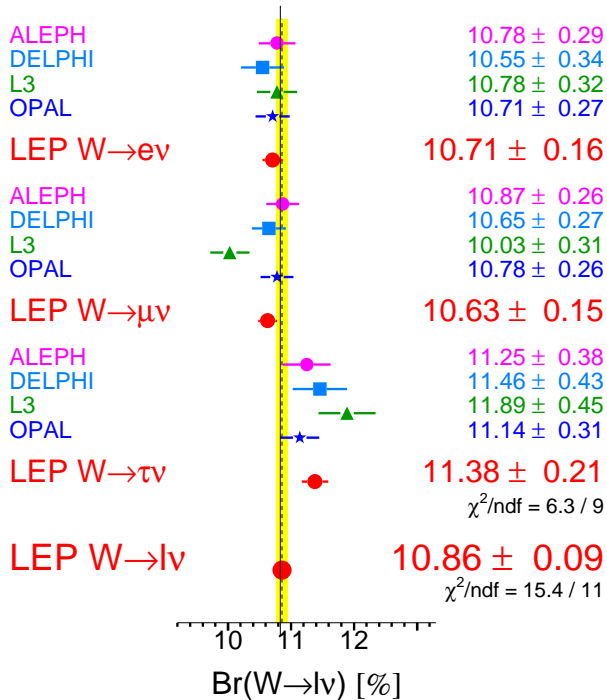
From the results on the leptonic branching fractions an excess of the branching fraction $W \rightarrow \tau\bar{\nu}_\tau$ with respect to the other leptons is evident. The excess can be quantified by the pair-wise ratios of the branching fractions, which represent a test of lepton universality in the decay of on-shell W bosons:

²In what follows any effects from lepton masses on W partial widths are neglected given their small size.

Experiment	Lepton non-universality			Lepton universality
	$\mathcal{B}(W \rightarrow e\bar{\nu}_e)$ [%]	$\mathcal{B}(W \rightarrow \mu\bar{\nu}_\mu)$ [%]	$\mathcal{B}(W \rightarrow \tau\bar{\nu}_\tau)$ [%]	$\mathcal{B}(W \rightarrow \text{hadrons})$ [%]
ALEPH	10.78 ± 0.29	10.87 ± 0.26	11.25 ± 0.38	67.13 ± 0.40
DELPHI	10.55 ± 0.34	10.65 ± 0.27	11.46 ± 0.43	67.45 ± 0.48
L3	10.78 ± 0.32	10.03 ± 0.31	11.89 ± 0.45	67.50 ± 0.52
OPAL	10.71 ± 0.27	10.78 ± 0.26	11.14 ± 0.31	67.41 ± 0.44
LEP	10.71 ± 0.16	10.63 ± 0.15	11.38 ± 0.21	67.41 ± 0.27
χ^2/dof	6.3/9			15.4/11

Table 5.5: Summary of W branching fractions derived from W-pair production cross-sections measurements up to 207 GeV centre-of-mass energy.

W Leptonic Branching Ratios



W Hadronic Branching Ratio

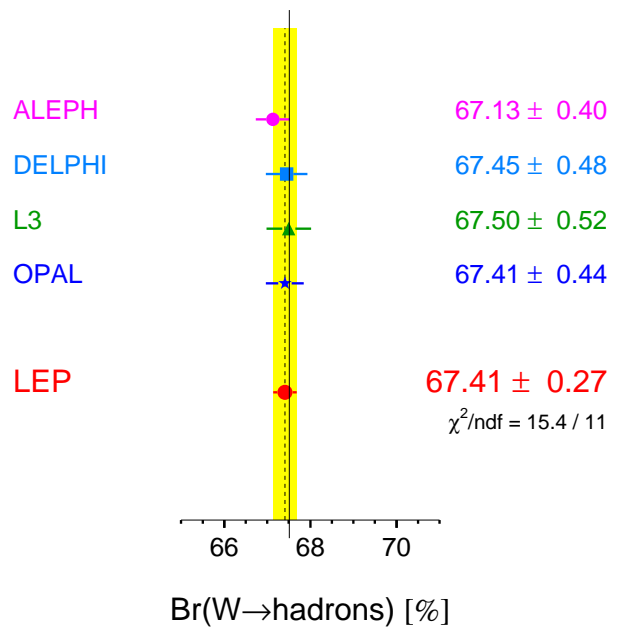


Figure 5.3: Leptonic and hadronic W branching fractions, as measured by the experiments, and the LEP combined values according to the procedures described in the text.

$$\mathcal{B}(W \rightarrow \mu\bar{\nu}_\mu) / \mathcal{B}(W \rightarrow e\bar{\nu}_e) = 0.993 \pm 0.019, \quad (5.2)$$

$$\mathcal{B}(W \rightarrow \tau\bar{\nu}_\tau) / \mathcal{B}(W \rightarrow e\bar{\nu}_e) = 1.063 \pm 0.027, \quad (5.3)$$

$$\mathcal{B}(W \rightarrow \tau\bar{\nu}_\tau) / \mathcal{B}(W \rightarrow \mu\bar{\nu}_\mu) = 1.070 \pm 0.026. \quad (5.4)$$

The branching fraction of W into taus with respect to that into electrons and muons differs by more than two standard deviations, where the correlations have been taken into account. The branching fractions of W into electrons and into muons agree well. Assuming only partial lepton universality the ratio between the tau fractions and the average of electrons and muons can also be computed:

$$2\mathcal{B}(W \rightarrow \tau\bar{\nu}_\tau) / (\mathcal{B}(W \rightarrow e\bar{\nu}_e) + \mathcal{B}(W \rightarrow \mu\bar{\nu}_\mu)) = 1.066 \pm 0.025 \quad (5.5)$$

resulting in an agreement at the level of 2.6 standard deviations only, with all correlations included.

If overall lepton universality is assumed (in the massless assumption), the hadronic branching fraction is determined to be $67.41 \pm 0.18(\text{stat.}) \pm 0.20(\text{syst.})\%$, while the leptonic branching fraction is $10.86 \pm 0.06(\text{stat.}) \pm 0.07(\text{syst.})\%$. These results are consistent with the SM expectations of 67.51% and 10.83% [36], respectively. The systematic error receives equal contributions from the correlated and uncorrelated sources.

Within the SM, the branching fractions of the W boson depend on the six matrix elements $|V_{qq'}|$ of the Cabibbo–Kobayashi–Maskawa (CKM) quark mixing matrix not involving the top quark. In terms of these matrix elements, the leptonic branching fraction of the W boson $\mathcal{B}(W \rightarrow \ell\bar{\nu}_\ell)$ is given by

$$\frac{1}{\mathcal{B}(W \rightarrow \ell\bar{\nu}_\ell)} = 3 \left\{ 1 + \left[1 + \frac{\alpha_s(M_W^2)}{\pi} \right] \sum_{\substack{i=(u,c) \\ j=(d,s,b)}} |V_{ij}|^2 \right\}, \quad (5.6)$$

where $\alpha_s(M_W^2)$ is the strong coupling constant and fermion mass effects are negligible. Taking $\alpha_s(M_W^2) = 0.119 \pm 0.002$ [178], and using the experimental knowledge of the sum $|V_{ud}|^2 + |V_{us}|^2 + |V_{ub}|^2 + |V_{cd}|^2 + |V_{cb}|^2 = 1.0544 \pm 0.0051$ [178], the above result can be interpreted as a measurement of $|V_{cs}|$ which is the least well determined of these matrix elements:

$$|V_{cs}| = 0.969 \pm 0.013.$$

The error includes a contribution of 0.0006 from the uncertainty on α_s and a 0.003 contribution from the uncertainties on the other CKM matrix elements, the largest of which is that on $|V_{cd}|$. These uncertainties are negligible in the error of this determination of $|V_{cs}|$, which is dominated by the experimental error of 0.013 arising from the measurement of the W branching fractions.

5.2.3 W Angular Distribution

In addition to measuring the total W^+W^- cross-section, the LEP experiments produce results for the differential cross-section, $d\sigma_{WW}/d\cos\theta_W$, where θ_W is the polar angle of the produced W^- with respect to the e^- beam direction. The LEP combination of these measurements will allow future theoretical models which predict deviations in this distribution to be tested against the LEP data in a direct and, as far as possible, model-independent manner. To reconstruct the $\cos\theta_W$ distribution it is necessary to identify the charges of the decaying W bosons. This can only be performed without significant ambiguity when one of W-boson decays via $W \rightarrow e\nu$ or $W \rightarrow \mu\nu$, in which case the lepton provides the charge tag. Consequently, the combination of the differential cross-section measurements is performed for the $q\bar{q}e\nu$ and $q\bar{q}\mu\nu$ channels combined. Selected $q\bar{q}\tau\nu$ events are not considered due to the larger backgrounds and difficulties in determining the tau lepton charge in the case where not all charged decay products are detected.

The measured $q\bar{q}e\nu$ and $q\bar{q}\mu\nu$ differential cross-sections are corrected to correspond to the CC03 set of diagrams with the additional constraint that the charged lepton is more than 20° away from the e^+e^- beam direction, $|\theta_{\ell^\pm}| > 20^\circ$. This angular requirement corresponds approximately to the experimental acceptance of the four LEP experiments and also greatly reduces the difference between the full $4f$ cross-section and the CC03 cross-section by reducing the contribution of t -channel diagrams in the $q\bar{q}e\nu$ final state³. The angle $\cos\theta_W$ is reconstructed from the four-momenta of the fermions from the W^- decay using the ECALO5 photon recombination scheme[156], a prescription for combining photons to a close-by charged fermion.

The LEP combination is performed in ten bins of $\cos\theta_W$. Because the differential cross-section distribution evolves with \sqrt{s} , reflecting the changing relative s - and t - channel contributions, the LEP data are divided into four \sqrt{s} ranges: 180 GeV – 184 GeV, 184 GeV – 194 GeV, 194 GeV – 204 GeV, and 204 GeV – 210 GeV. It has been verified for each \sqrt{s} range that the differences in the differential cross-sections at the mean value of \sqrt{s} compared to the luminosity-weighted sum of the differential cross-sections reflecting the actual distribution of the data across \sqrt{s} are negligible compared to the statistical errors.

The experimental resolution in LEP on the reconstructed values of $\cos\theta_W$ is typically 0.15-0.20. When simulating W-pair production, a significant migration between generated and reconstructed bins of $\cos\theta_W$ is observed. The effects of bin-to-bin migration are not explicitly unfolded, instead each experiment obtains the cross-section in the i th bin of the differential distribution, σ_i , from

$$\sigma_i = \frac{N_i - b_i}{\epsilon_i \mathcal{L}}, \quad (5.7)$$

where:

N_i is the observed number of $q\bar{q}e\nu/q\bar{q}\mu\nu$ events reconstructed in the i th bin of the $\cos\theta_W$ distribution.

b_i is the expected number of background events in bin i . The contribution from four-fermion background is treated as in each of the experiments' W^+W^- cross-section analyses.

³With this requirement the difference between the total four-fermion (CC20 [156]) and double-resonant (CC03) $q\bar{q}e\nu$ cross-section is approximately 3.5%, as opposed to 24.0% without the lepton angle requirement. For the $q\bar{q}\mu\nu$ channel the difference between the total four-fermion (CC10 [156]) and double-resonant (CC03) cross-section is less than 1% in both cases.

ϵ_i is the Monte-Carlo efficiency in bin i , defined as $\epsilon_i = S_i/G_i$ where S_i is the number of selected CC03 MC $q\bar{q}\ell\nu_\ell$ events reconstructed in bin i and G_i is the number of MC CC03 $q\bar{q}e\nu/q\bar{q}\mu\nu$ events with generated $\cos\theta_W$ (calculated using the ECALO5 recombination scheme) lying in the i th bin ($|\theta_{\ell^\pm}| > 20^\circ$). Selected $q\bar{q}\tau\nu$ events are included in the numerator of the efficiency.

This bin-by-bin efficiency correction method has the advantages of simplicity and that the resulting σ_i are uncorrelated. The main disadvantage of this procedure is that bin-by-bin migrations between generated and reconstructed $\cos\theta_W$ are corrected purely on the basis of the SM expectation and may potentially be biased. The validity of the simple correction procedure was tested by considering a range of deviations from the SM. Specifically, the SM $\cos\theta_W$ distribution was reweighted, in turn, by factors of $1 + 0.1(\cos\theta_W - 1)$, $1 - 0.2\cos^2\theta_W$, $1 + 0.2\cos^2\theta_W$ and $1 - 0.4\cos^8\theta_W$, and data samples generated corresponding to the combined LEP luminosity. These reweighting functions represent deviations which are large compared to the statistics of the combined LEP measurements. The bin-by-bin correction method was found to result in good χ^2 distributions when the extracted $\cos\theta_W$ distributions were compared with the underlying generated distribution (*e.g.* the worst case gave a mean χ^2 of 11.3 for the 10 degrees of freedom corresponding to the ten $\cos\theta_W$ bins), and no significant bias was found in these tests.

For the LEP combination the systematic uncertainties on measured differential cross-sections are broken down into two terms: uncertainties which are fully correlated between bins and experiments and errors which are correlated between bins but uncorrelated between experiments. This procedure reflects the fact that the dominant systematic errors affect the overall normalisation of the measured distributions rather than the shape.

The detailed inputs provided by the four LEP experiments are reported in Tables E.7, E.8, E.9 and E.10. Table 5.6 presents the combined LEP results. In the table the bin-by-bin error breakdown is also reported. The result is also shown in Figure 5.4, where the combined data are superimposed on the four-fermion theory predictions calculated with Kandy [167] and RACOONWW [168], which are indistinguishable on the plot scale. The agreement of data and calculations is generally very good, with an apparent under-fluctuation of data with respect to the central values of the theory predictions in the last bin of the 194 GeV – 204 GeV energy range.

5.3 Z-Pair Production

The signal definition has been given in Section 5.1. Z-pair production shows several similarities to W-pair production. The different final states depend on the decay of the heavy bosons: it is possible to have four quarks, two quarks and two leptons or four leptons in the final state. The signatures are very clean and the main background is represented by WW production.

The approaches used by the experiments for the selection are based on Neural Network techniques. The final states studied involve both the hadronic and leptonic decays of the Z boson, where invisible decays are included when accompanied by a charged decay. The selection efficiencies depend significantly on the final state, ranging from 25% to 60%, with purities from 30% to 70% [179, 180, 181, 182]. The main backgrounds include four-fermion production, di-leptonic and QCD final states.

The LEP combination is performed applying the same technique as used for the WW cross-section measurement. The symmetrised expected statistical error of each analysis is used, to

$\cos\theta_{W^-}$ bin i	1	2	3	4	5	6	7	8	9	10
\sqrt{s} range: 180 – 184 GeV $\mathcal{L} = 163.90 \text{ pb}^{-1}$ Weighted $\sqrt{s} = 182.66 \text{ GeV}$										
σ_i (pb)	0.502	0.705	0.868	1.281	1.529	2.150	2.583	2.602	4.245	5.372
$\delta\sigma_i$ (pb)	0.114	0.129	0.143	0.203	0.195	0.244	0.270	0.254	0.367	0.419
$\delta\sigma_i(\text{stat})$ (pb)	0.112	0.128	0.142	0.202	0.194	0.241	0.267	0.249	0.362	0.413
$\delta\sigma_i(\text{syst})$ (pb)	0.016	0.017	0.018	0.023	0.024	0.036	0.040	0.049	0.059	0.073
\sqrt{s} range: 184 – 194 GeV $\mathcal{L} = 587.95 \text{ pb}^{-1}$ Weighted $\sqrt{s} = 189.09 \text{ GeV}$										
σ_i (pb)	0.718	0.856	1.009	1.101	1.277	1.801	2.215	2.823	4.001	5.762
$\delta\sigma_i$ (pb)	0.074	0.079	0.086	0.088	0.094	0.123	0.140	0.151	0.179	0.223
$\delta\sigma_i(\text{stat})$ (pb)	0.073	0.078	0.084	0.085	0.091	0.119	0.135	0.144	0.169	0.208
$\delta\sigma_i(\text{syst})$ (pb)	0.015	0.015	0.018	0.023	0.023	0.031	0.035	0.046	0.060	0.081
\sqrt{s} range: 194 – 204 GeV $\mathcal{L} = 605.05 \text{ pb}^{-1}$ Weighted $\sqrt{s} = 198.38 \text{ GeV}$										
σ_i (pb)	0.679	0.635	0.991	1.087	1.275	1.710	2.072	2.866	4.100	6.535
$\delta\sigma_i$ (pb)	0.079	0.065	0.084	0.088	0.096	0.116	0.126	0.158	0.185	0.236
$\delta\sigma_i(\text{stat})$ (pb)	0.078	0.064	0.083	0.085	0.094	0.112	0.122	0.152	0.175	0.220
$\delta\sigma_i(\text{syst})$ (pb)	0.012	0.013	0.016	0.021	0.021	0.029	0.033	0.043	0.059	0.085
\sqrt{s} range: 204 – 210 GeV $\mathcal{L} = 630.51 \text{ pb}^{-1}$ Weighted $\sqrt{s} = 205.92 \text{ GeV}$										
σ_i (pb)	0.495	0.602	0.653	1.057	1.240	1.707	2.294	2.797	4.481	7.584
$\delta\sigma_i$ (pb)	0.058	0.066	0.069	0.094	0.093	0.115	0.140	0.143	0.187	0.262
$\delta\sigma_i(\text{stat})$ (pb)	0.057	0.065	0.068	0.091	0.090	0.111	0.137	0.136	0.175	0.244
$\delta\sigma_i(\text{syst})$ (pb)	0.012	0.013	0.015	0.021	0.022	0.030	0.033	0.045	0.064	0.096

Table 5.6: Combined W^- differential angular cross-section in the 10 angular bins for the four chosen energy intervals. For each energy range, the sum of the measured integrated luminosities and the luminosity-weighted centre-of-mass energy is reported. The results per angular bin in each of the energy interval are then presented: σ_i indicates the average of $d[\sigma_{WW}(\text{BR}_{e\nu} + \text{BR}_{\mu\nu})]/d\cos\theta_{W^-}$ in the i -th bin of $\cos\theta_{W^-}$, with a bin width of 0.2. For each bin, the values of the total, statistical and systematic errors are reported. All values are given in pb.

LEP (ADLO)

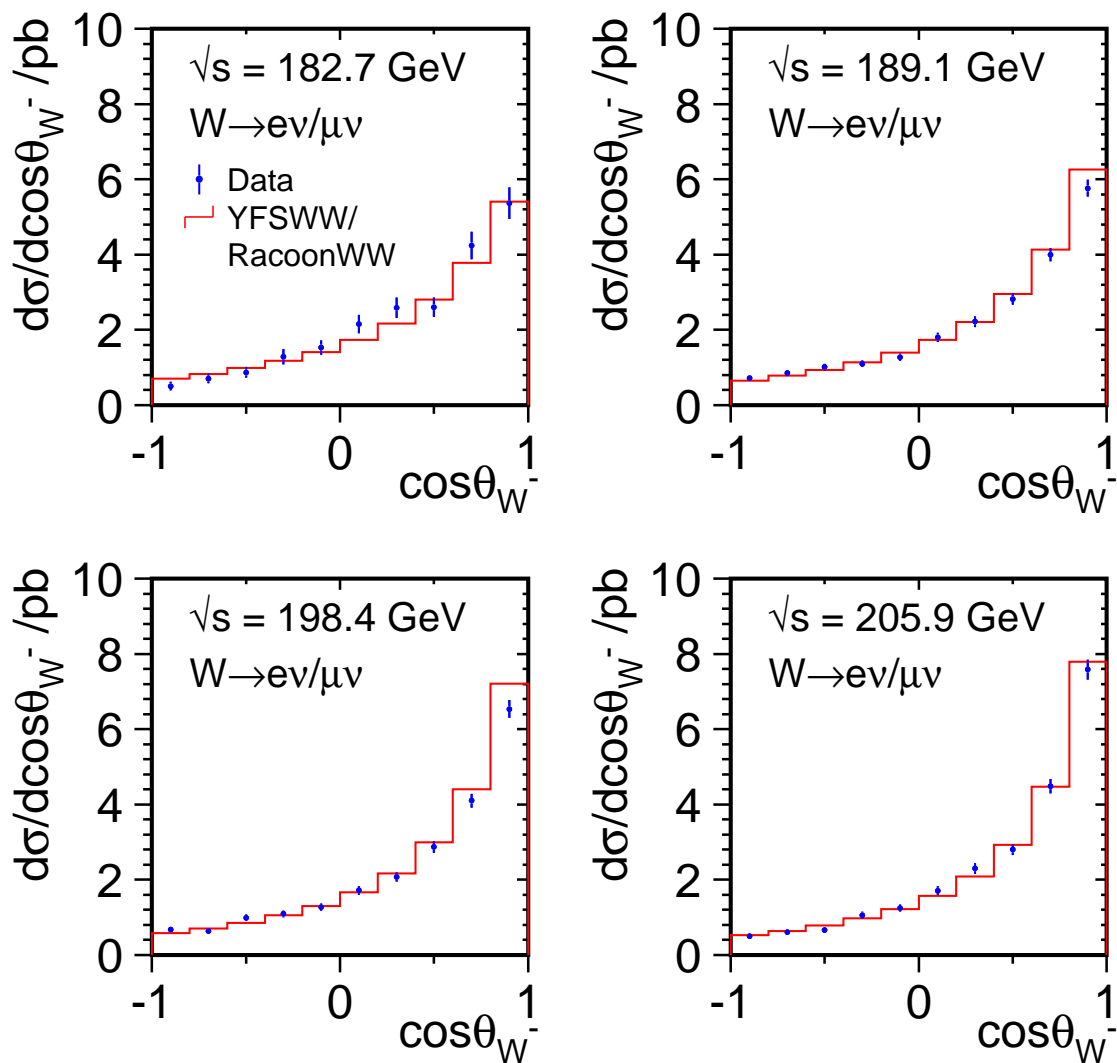


Figure 5.4: LEP combined $d[\sigma_{WW}(\text{BR}_{e\nu} + \text{BR}_{\mu\nu})]/d\cos\theta_{W^-}$ distributions for the four chosen energy intervals. The combined values (points) are superimposed on the four-fermion predictions from KandY and RACOONWW.

avoid biases due to the limited number of selected events. The detailed inputs from the experiments are reported in Table E.11. The results of the individual experiments are summarised in Table 5.7, together with the LEP averages. The composition of the systematic error in terms of correlated components is shown in Table E.12. The cross-sections used for the combination are determined by the experiments using the frequentist approach, without assuming any prior for the value of the cross-section itself.

The measurements are shown in Figure 5.5 as a function of the LEP centre-of-mass energy, where they are compared to the YFSZZ [183] and ZZTO [184] predictions as listed in Table E.13. Both these calculations have an estimated uncertainty of 2% [156]. The data do not show any significant deviation from the theoretical expectations.

In analogy with the W-pair cross-section, a value for \mathcal{R}_{ZZ} can also be determined: its definition and the procedure of the combination follows those described for \mathcal{R}_{WW} . The data are compared with the YFSZZ and ZZTO predictions; Table 5.8, with more details given in Table E.14, reports the combined values of \mathcal{R}_{ZZ} at each energy and combined, and Figure 5.6 shows them in comparison to unity, where the $\pm 2\%$ error on the theoretical ZZ cross-section is shown as a yellow band. The experimental accuracy on the combined value of \mathcal{R}_{ZZ} is about 5%.

5.4 Z- γ^* Production

The signal definition has been given in Section 5.1. The study of these final states is also relevant for the measurement of neutral gauge couplings. The LEP collaborations did not provide a complete analysis of all possible $Z\gamma^*$ final states. While ALEPH and OPAL did not present any results on $Z\gamma^*$, DELPHI provided results for the $\nu\nu q\bar{q}$, $l\bar{l}q\bar{q}$, $l\bar{l}l\bar{l}$ and $q\bar{q}q\bar{q}$ final states [185], and L3 provided results for the $\nu\nu q\bar{q}$, $l\bar{l}q\bar{q}$, $l\bar{l}\nu\nu$, and $l\bar{l}l\bar{l}$ channels [186], where $l = e, \mu$. Final states containing τ leptons were not studied. The combination reported here has been performed using data from the final states provided by both DELPHI and L3, namely $\nu\nu q\bar{q}$, $\mu\mu q\bar{q}$ and $e\bar{e}q\bar{q}$.

To increase the statistics the cross-sections were determined using the full data sample at an average LEP-II centre-of-mass energy. Table 5.9 presents the measured cross-sections, where the expected statistical errors were used for the combination. As noted in Section 5.1, the $Z\gamma^*$ signal has been defined by mass and angular cuts specific to each of the contributing channels, and the comparison of the combined LEP cross-section with the theoretical prediction, calculated with `grc4f` [187] and shown in the last section of Table 5.9, has been made by imposing the same cuts on each of the experimental and simulated samples included in the combination. The results agree well with the expectations.

5.5 Single-Boson Production

The study of singly resonant final states finds its motivations in the comparison with SM calculations in a delicate region of the $4-f$ phase space, where the treatment of ISR or fermion loop corrections can induce large corrections, up to several percent, to the total cross-section. These processes are also very sensitive to the value of α_{QED} . Moreover, single W production also brings information on possible anomalous $WW\gamma$ couplings.

Single boson production at LEP is mostly realised via t -channel processes, where either the incident electron or positron maintains its direction, escaping undetected along the beam

\sqrt{s} (GeV)	ZZ cross-section [pb]				
	ALEPH	DELPHI	L3	OPAL	LEP
182.7	$0.11^{+0.16}_{-0.12}$	$0.35^{+0.20}_{-0.15}$	0.31 ± 0.17	$0.12^{+0.20}_{-0.18}$	0.22 ± 0.08
188.6	$0.67^{+0.14}_{-0.13}$	$0.52^{+0.12}_{-0.11}$	0.73 ± 0.15	$0.80^{+0.15}_{-0.14}$	0.66 ± 0.07
191.6	$0.62^{+0.40}_{-0.33}$	$0.63^{+0.36}_{-0.30}$	0.29 ± 0.22	$1.29^{+0.48}_{-0.41}$	0.67 ± 0.18
195.5	$0.73^{+0.25}_{-0.22}$	$1.05^{+0.25}_{-0.22}$	1.18 ± 0.26	$1.13^{+0.27}_{-0.25}$	1.00 ± 0.12
199.5	$0.91^{+0.25}_{-0.22}$	$0.75^{+0.20}_{-0.18}$	1.25 ± 0.27	$1.05^{+0.26}_{-0.23}$	0.95 ± 0.12
201.6	$0.71^{+0.32}_{-0.27}$	$0.85^{+0.33}_{-0.28}$	0.95 ± 0.39	$0.79^{+0.36}_{-0.30}$	0.81 ± 0.18
204.9	$1.20^{+0.28}_{-0.26}$	$1.03^{+0.23}_{-0.20}$	$0.77^{+0.21}_{-0.19}$	$1.07^{+0.28}_{-0.25}$	0.98 ± 0.13
206.6	$1.05^{+0.22}_{-0.21}$	$0.96^{+0.16}_{-0.15}$	$1.09^{+0.18}_{-0.17}$	$0.97^{+0.20}_{-0.19}$	1.00 ± 0.09

Table 5.7: Z-pair production cross-sections from the four LEP experiments and combined values for the eight centre-of-mass energies between 183 GeV and 207 GeV. The χ^2/dof of the combined fit is 14.5/24.

$\sqrt{s}(\text{GeV})$	$\mathcal{R}_{ZZ}^{\text{ZZTO}}$	$\mathcal{R}_{ZZ}^{\text{YFSZZ}}$
182.7	0.857 ± 0.320	0.857 ± 0.320
188.6	1.017 ± 0.113	1.007 ± 0.111
191.6	0.865 ± 0.226	0.859 ± 0.224
195.5	1.118 ± 0.134	1.118 ± 0.134
199.5	0.974 ± 0.126	0.970 ± 0.126
201.6	0.805 ± 0.174	0.800 ± 0.174
204.9	0.934 ± 0.122	0.928 ± 0.121
206.6	0.948 ± 0.092	0.938 ± 0.091
χ^2/dof	14.5/24	14.5/24
Average	0.966 ± 0.052	0.960 ± 0.052
χ^2/dof	17.4/31	17.4/31

Table 5.8: Ratios of LEP combined Z-pair cross-section measurements to the expectations according to ZZTO [184] and YFSZZ [183]. The results of the combined fits are given together with the resulting χ^2/dof . Both fits take into account inter-experiment as well as inter-energy correlations of systematic errors.

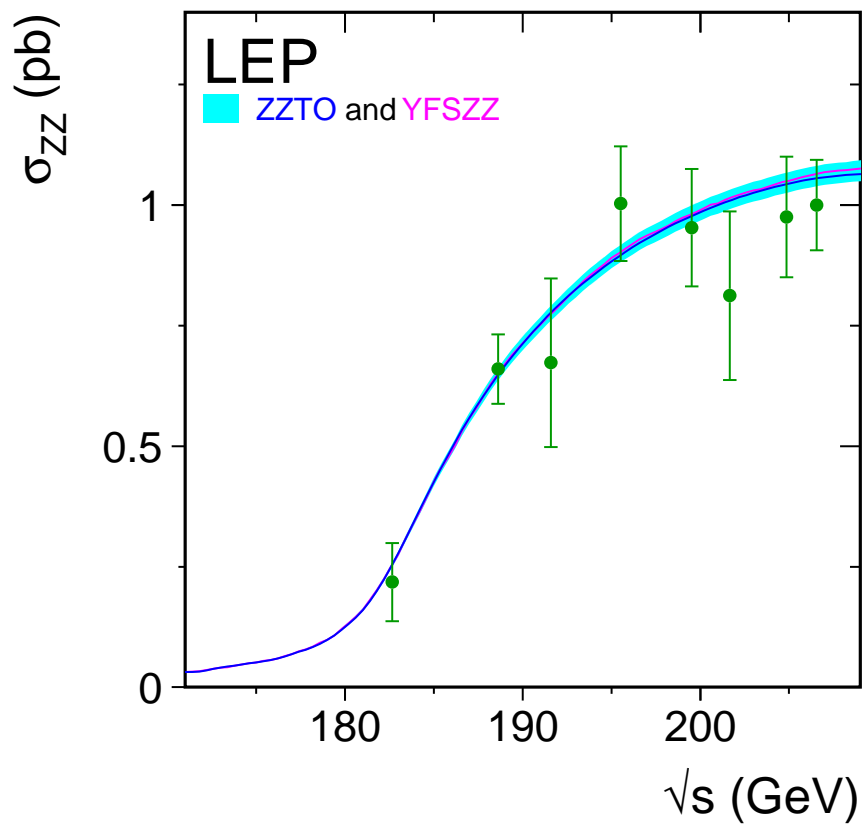


Figure 5.5: Measurements of the Z-pair production cross-section, compared to the predictions of YFSZZ [183] and ZZTO [184]. The shaded area represents the $\pm 2\%$ uncertainty on the predictions.

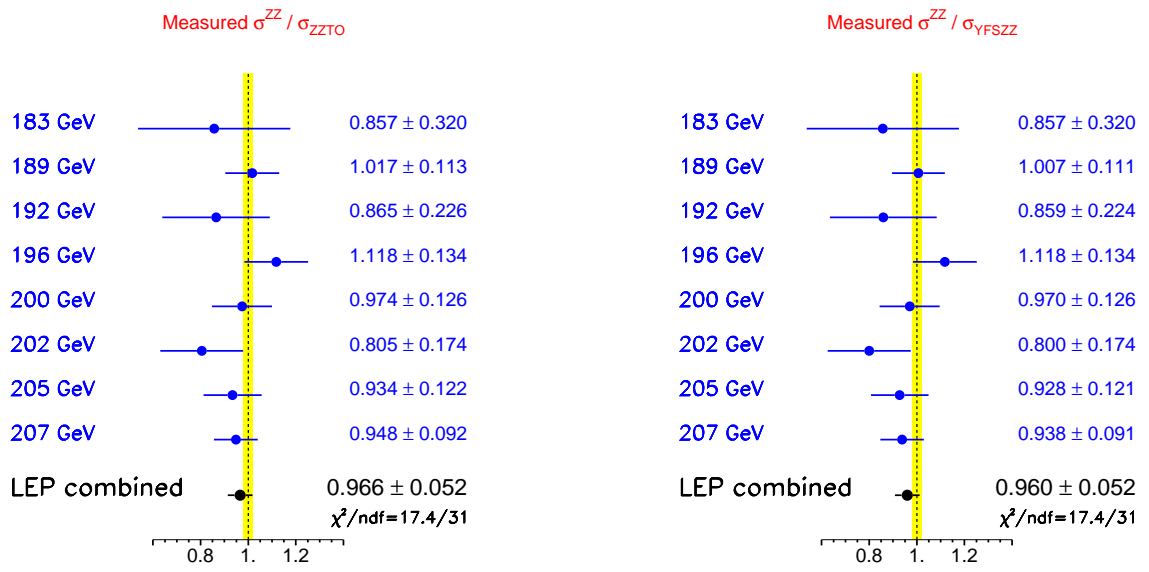


Figure 5.6: Ratios of LEP combined Z-pair cross-section measurements to the expectations according to ZZTO [184] and YFSZZ [183]. The yellow bands represent constant relative errors of 2% on the two cross-section predictions.

Channel	\sqrt{s} [GeV]	L [pb ⁻¹]	σ [pb]	$\delta\sigma_{\text{stat}}$ [pb]	$\delta\sigma_{\text{syst}}^{\text{unc}}$ [pb]	$\delta\sigma_{\text{syst}}^{\text{cor}}$ [pb]	$\delta\sigma_{\text{MC}}$ [pb]
DELPHI							
$\nu\nu q\bar{q}$	197.1	666.7	0.042	+0.022 -0.014	0.008	0.002	0.042
$\mu\mu q\bar{q}$	197.1	666.7	0.031	+0.013 -0.011	0.004	0.001	0.016
$ee q\bar{q}$	197.1	666.7	0.063	+0.018 -0.016	0.009	0.001	0.016
L3							
$\nu\nu q\bar{q}$	196.7	679.4	0.072	+0.047 -0.041	0.004	0.016	0.046
$\mu\mu q\bar{q}$	196.7	681.9	0.040	+0.018 -0.016	0.002	0.003	0.017
$ee q\bar{q}$	196.7	681.9	0.100	+0.024 -0.022	0.004	0.007	0.020
LEP combined							
Channel	\sqrt{s} [GeV]	L [pb ⁻¹]	σ [pb]	$\delta\sigma_{\text{stat}}$ [pb]	$\delta\sigma_{\text{syst}}$ [pb]	$\delta\sigma_{\text{tot}}$ [pb]	σ_{theory} [pb]
$\nu\nu q\bar{q}$	196.9	679.4	0.055	0.031	0.008	0.032	0.083
$\mu\mu q\bar{q}$	196.9	681.9	0.035	0.012	0.003	0.012	0.042
$ee q\bar{q}$	196.9	681.9	0.079	0.012	0.005	0.013	0.059

Table 5.9: $Z\gamma^*$ measurements by the experiments and combined LEP measurements. The columns show, respectively, the channel, the luminosity-weighted centre-of-mass energy, the luminosity, the measured cross-section, the measured statistical error, the systematic contribution uncorrelated between experiments, the systematic contribution correlated between experiments and the expected statistical error from the simulation. For the LEP combination the full systematic error and the total error are given and the last column presents the theory expectation with `grc4f` [187].

and thus generating missing momentum along the z axis. Single W and single Z production then proceed dominantly via the vector boson fusion process illustrated in Figure 1.7 or via Bremsstrahlung processes. In the case of single W production in the $W \rightarrow e\bar{\nu}_e$ final state, the W is detected either by its hadronic decay producing two jets, or by its leptonic decay producing a single charged lepton; single Z production in the $Z \rightarrow e^+e^-$ final state is identified from an electron recoiling against two fermions (quarks or leptons) coming from the Z decay.

The selection of these events is particularly difficult because of the relatively low cross-section of the signal and because of the presence of large backgrounds in these phase space regions. Particularly large backgrounds arise from radiative $q\bar{q}$ production or $\gamma\gamma$ scattering. The analyses, mostly based on sequential cuts on kinematic variables, have an efficiency which depends on the considered final state and ranges typically from 35% to 60% [190, 191, 192, 193, 194]. These references describe results on single-boson production using selection criteria which are specific to the individual experiments. The results shown below are derived from a common selection procedure using the criteria listed in Section 5.1.

5.5.1 $We\nu$ Cross-Section Measurement

The signal definition has been given in Section 5.1. The LEP combination of the single-W production cross-section is performed using the expected statistical errors, given the limited statistical precision of the single measurements. The correlation of the systematic errors in energy and among experiments is properly taken into account. The hadronic and the total single-W cross-sections are combined independently, as the former is less contaminated by $\gamma\gamma$ interaction contributions. The details on the input measurements are summarised in Tables E.15 and E.16.

The hadronic single-W results and combinations are reported in Table 5.10 and Figure 5.7. The total single-W results, for all decay modes and combinations are listed in Table 5.11 and Figure 5.8. In the two figures, the measurements are compared with the expected values from WPHACT [195] and `grc4f` [187], listed in Table E.17. In Figure 5.7, the predictions of WTO [198], which includes fermion-loop corrections for the hadronic final states, have also been included. As discussed more in detail in [156], the theoretical predictions are scaled upward to correct for the implementation of QED radiative corrections at the wrong energy scale s . The full correction of 4%, derived from comparison with the theoretical predictions from SWAP [202], is conservatively taken as a systematic error. This uncertainty dominates the $\pm 5\%$ theoretical error currently assigned to these predictions, represented by the shaded area in Figures 5.7 and 5.8. All results, up to the highest centre-of-mass energies, are in agreement with the theoretical predictions.

The agreement can also be appreciated in Table 5.12, where the values of the ratio between measured and expected cross-section values according to the computations of `grc4f` and WPHACT are reported, with additional details listed in Table E.18. The combination is performed accounting for the energy and experiment correlations of the systematic sources. The results are also presented in Figure 5.9.

5.5.2 Zee Cross-Section Measurement

The signal definition has been given in Section 5.1. The combination of results is performed with the same technique used for the other channels. The results include the hadronic and the leptonic channels and all the centre-of-mass energies from 183 to 209 GeV from the ALEPH [190], DELPHI [191] and L3 [203] Collaborations. The OPAL results [204] are not included in the combination as they were not provided according to the common signal definition.

Tables 5.13 and 5.14, with details summarised in Table E.19, present the inputs from the experiments and the corresponding LEP combinations in the muon and hadronic channel, respectively. The $ee\mu\mu$ cross-section is already combined in energy by the individual experiments to increase the statistics of the data. The combination takes into account the correlation of the energy and experimental systematic errors. The results in the hadronic channel are compared with the predictions of WPHACT and `grc4f`, listed in Table E.20, in Figure 5.10 as a function of the centre-of-mass energy.

The same data are expressed as ratios of the measured to the predicted cross-section, listed in Table 5.15, with details on the decomposition of the systematic error reported in Table E.21, and shown in Figure 5.11. The accuracy of the combined ratio is about 7% with three experiments contributing to the average.

\sqrt{s} (GeV)	Single-W hadronic cross-section (pb)			
	ALEPH	DELPHI	L3	LEP
182.7	$0.44^{+0.29}_{-0.24}$	$0.11^{+0.31}_{-0.14}$	$0.58^{+0.23}_{-0.20}$	0.42 ± 0.15
188.6	$0.33^{+0.16}_{-0.15}$	$0.57^{+0.21}_{-0.20}$	$0.52^{+0.14}_{-0.13}$	0.47 ± 0.09
191.6	$0.52^{+0.52}_{-0.40}$	$0.30^{+0.48}_{-0.31}$	$0.84^{+0.44}_{-0.37}$	0.56 ± 0.25
195.5	$0.61^{+0.28}_{-0.25}$	$0.50^{+0.30}_{-0.27}$	$0.66^{+0.25}_{-0.23}$	0.60 ± 0.14
199.5	$1.06^{+0.30}_{-0.27}$	$0.57^{+0.28}_{-0.26}$	$0.37^{+0.22}_{-0.20}$	0.65 ± 0.14
201.6	$0.72^{+0.39}_{-0.33}$	$0.67^{+0.40}_{-0.36}$	$1.10^{+0.40}_{-0.35}$	0.82 ± 0.20
204.9	$0.34^{+0.24}_{-0.21}$	$0.99^{+0.33}_{-0.31}$	$0.42^{+0.25}_{-0.21}$	0.54 ± 0.15
206.6	$0.64^{+0.21}_{-0.19}$	$0.81^{+0.23}_{-0.22}$	$0.66^{+0.20}_{-0.18}$	0.69 ± 0.12

Table 5.10: Single-W hadronic production cross-section from the LEP experiments and combined values for the eight energies between 183 and 207 GeV, in the hadronic decay channel of the W boson. The χ^2/dof of the combined fit is 13.2/16.

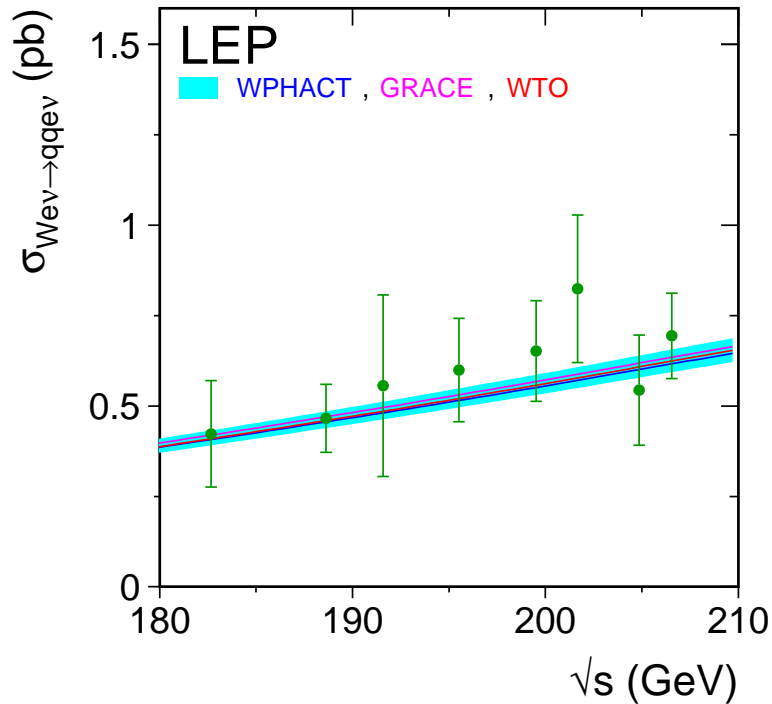


Figure 5.7: Measurements of the single-W production cross-section in the hadronic decay channel of the W boson, compared to the predictions of WTO [198], WPHACT [195] and grc4f [187]. The shaded area represents the $\pm 5\%$ uncertainty on the predictions.

\sqrt{s} (GeV)	Single-W total cross-section (pb)			
	ALEPH	DELPHI	L3	LEP
182.7	$0.60^{+0.32}_{-0.26}$	$0.69^{+0.42}_{-0.25}$	$0.80^{+0.28}_{-0.25}$	0.70 ± 0.17
188.6	$0.55^{+0.18}_{-0.16}$	$0.75^{+0.23}_{-0.22}$	$0.69^{+0.16}_{-0.15}$	0.66 ± 0.10
191.6	$0.89^{+0.58}_{-0.44}$	$0.40^{+0.55}_{-0.33}$	$1.11^{+0.48}_{-0.41}$	0.81 ± 0.28
195.5	$0.87^{+0.31}_{-0.27}$	$0.68^{+0.34}_{-0.38}$	$0.97^{+0.27}_{-0.25}$	0.85 ± 0.16
199.5	$1.31^{+0.32}_{-0.29}$	$0.95^{+0.34}_{-0.30}$	$0.88^{+0.26}_{-0.24}$	1.05 ± 0.16
201.6	$0.80^{+0.42}_{-0.35}$	$1.24^{+0.52}_{-0.43}$	$1.50^{+0.45}_{-0.40}$	1.17 ± 0.23
204.9	$0.65^{+0.27}_{-0.23}$	$1.06^{+0.37}_{-0.32}$	$0.78^{+0.29}_{-0.25}$	0.80 ± 0.17
206.6	$0.81^{+0.22}_{-0.20}$	$1.14^{+0.28}_{-0.25}$	$1.08^{+0.21}_{-0.20}$	1.00 ± 0.14

Table 5.11: Single-W total production cross-section from the LEP experiments and combined values for the eight energies between 183 and 207 GeV. The χ^2/dof of the combined fit is 8.1/16.

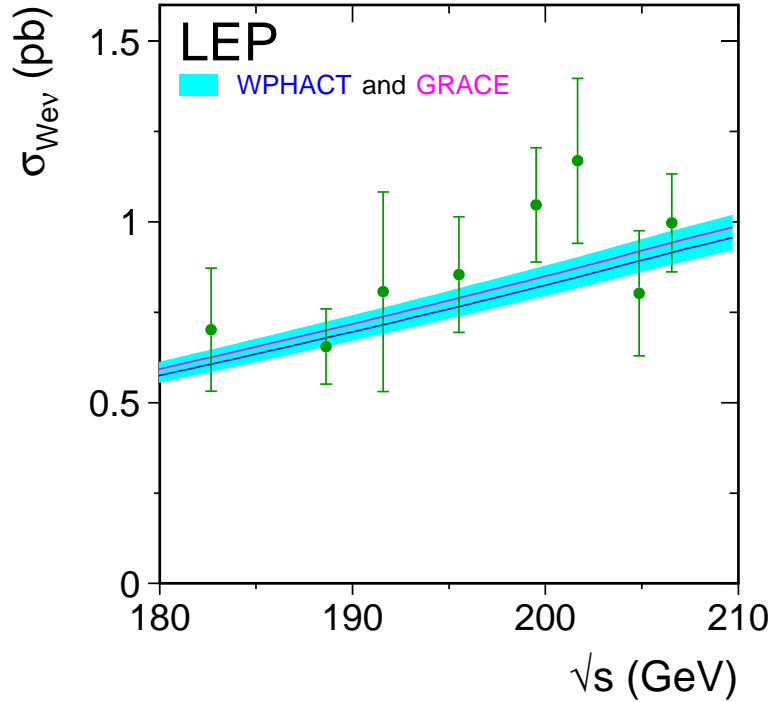


Figure 5.8: Measurements of the single-W total production cross-section, compared to the predictions of WPHACT [195] and grc4f [187]. The shaded area represents the $\pm 5\%$ uncertainty on the predictions.

$\sqrt{s}(\text{GeV})$	$\mathcal{R}_{W_{e\nu}}^{\text{grc4f}}$	$\mathcal{R}_{W_{e\nu}}^{\text{WPHACT}}$
182.7	1.122 ± 0.272	1.157 ± 0.281
188.6	0.936 ± 0.149	0.965 ± 0.154
191.6	1.094 ± 0.373	1.128 ± 0.385
195.5	1.081 ± 0.203	1.115 ± 0.210
199.5	1.242 ± 0.187	1.280 ± 0.193
201.6	1.340 ± 0.261	1.380 ± 0.269
204.9	0.873 ± 0.189	0.899 ± 0.195
206.6	1.058 ± 0.143	1.089 ± 0.148
χ^2/dof	8.1/16	8.1/16
Average	1.058 ± 0.078	1.090 ± 0.080
χ^2/dof	12.1/23	12.1/23

Table 5.12: Ratios of LEP combined total single-W cross-section measurements to the expectations according to `grc4f` [187] and `WPHACT` [195]. The resulting averages over energies are also given. The averages take into account inter-experiment as well as inter-energy correlations of systematic errors.

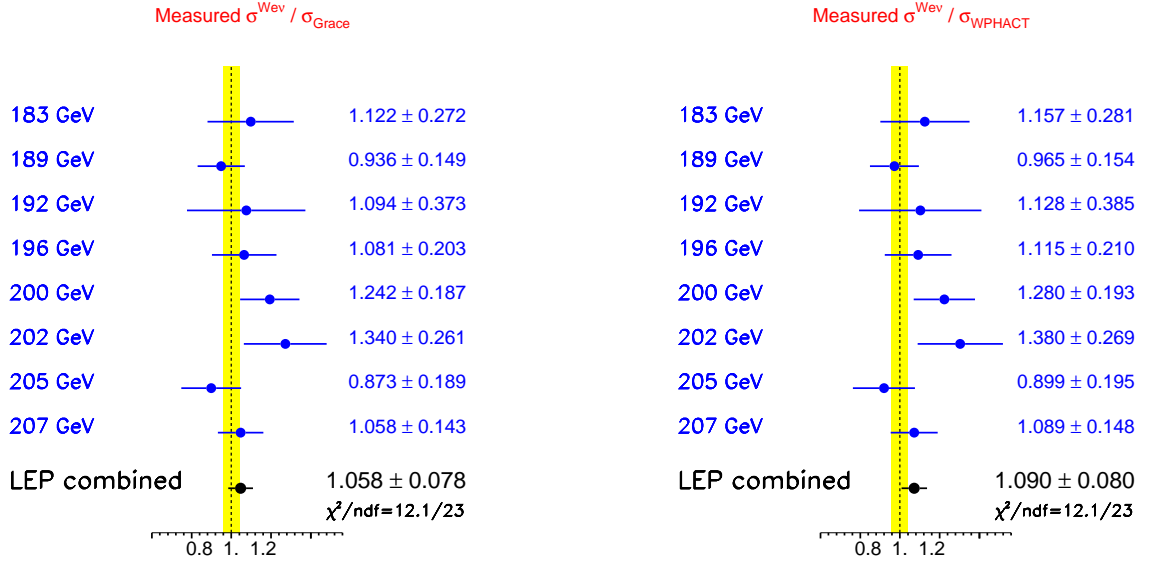


Figure 5.9: Ratios of LEP combined total single-W cross-section measurements to the expectations according to `grc4f` [187] and `WPHACT` [195]. The yellow bands represent constant relative errors of 5% on the two cross-section predictions.

	Single-Z cross-section into muons(pb)			
	ALEPH	DELPHI	L3	LEP
Av. \sqrt{s} (GeV)	196.67	197.10	196.60	196.79
$\sigma_{Zee \rightarrow \mu\mu ee}$	0.055 ± 0.016	$0.070 \begin{smallmatrix} + 0.023 \\ - 0.019 \end{smallmatrix}$	0.043 ± 0.013	0.057 ± 0.009

Table 5.13: Energy averaged single-Z production cross-section into muons from the LEP experiments and the LEP combined value.

\sqrt{s} (GeV)	Single-Z hadronic cross-section (pb)			
	ALEPH	DELPHI	L3	LEP
182.7	$0.27 \begin{smallmatrix} + 0.21 \\ - 0.16 \end{smallmatrix}$	$0.56 \begin{smallmatrix} + 0.28 \\ - 0.23 \end{smallmatrix}$	$0.51 \begin{smallmatrix} + 0.19 \\ - 0.16 \end{smallmatrix}$	0.45 ± 0.11
188.6	$0.42 \begin{smallmatrix} + 0.14 \\ - 0.12 \end{smallmatrix}$	$0.64 \begin{smallmatrix} + 0.16 \\ - 0.14 \end{smallmatrix}$	$0.55 \begin{smallmatrix} + 0.11 \\ - 0.10 \end{smallmatrix}$	0.53 ± 0.07
191.6	$0.61 \begin{smallmatrix} + 0.39 \\ - 0.29 \end{smallmatrix}$	$0.63 \begin{smallmatrix} + 0.40 \\ - 0.30 \end{smallmatrix}$	$0.60 \begin{smallmatrix} + 0.26 \\ - 0.21 \end{smallmatrix}$	0.61 ± 0.15
195.5	$0.72 \begin{smallmatrix} + 0.24 \\ - 0.20 \end{smallmatrix}$	$0.66 \begin{smallmatrix} + 0.22 \\ - 0.19 \end{smallmatrix}$	$0.40 \begin{smallmatrix} + 0.13 \\ - 0.11 \end{smallmatrix}$	0.55 ± 0.10
199.5	$0.60 \begin{smallmatrix} + 0.21 \\ - 0.18 \end{smallmatrix}$	$0.57 \begin{smallmatrix} + 0.20 \\ - 0.17 \end{smallmatrix}$	$0.33 \begin{smallmatrix} + 0.13 \\ - 0.11 \end{smallmatrix}$	0.47 ± 0.10
201.6	$0.89 \begin{smallmatrix} + 0.35 \\ - 0.28 \end{smallmatrix}$	$0.19 \begin{smallmatrix} + 0.21 \\ - 0.16 \end{smallmatrix}$	$0.81 \begin{smallmatrix} + 0.27 \\ - 0.23 \end{smallmatrix}$	0.67 ± 0.13
204.9	$0.42 \begin{smallmatrix} + 0.17 \\ - 0.15 \end{smallmatrix}$	$0.37 \begin{smallmatrix} + 0.18 \\ - 0.15 \end{smallmatrix}$	$0.56 \begin{smallmatrix} + 0.16 \\ - 0.14 \end{smallmatrix}$	0.47 ± 0.10
206.6	$0.70 \begin{smallmatrix} + 0.17 \\ - 0.15 \end{smallmatrix}$	$0.69 \begin{smallmatrix} + 0.16 \\ - 0.14 \end{smallmatrix}$	$0.59 \begin{smallmatrix} + 0.12 \\ - 0.11 \end{smallmatrix}$	0.65 ± 0.08

Table 5.14: Single-Z hadronic production cross-section from the LEP experiments and combined values for the eight energies between 183 and 207 GeV. The χ^2/dof of the combined fit is 13.0/16.

\sqrt{s} (GeV)	$\mathcal{R}_{Zee}^{\text{grc4f}}$	$\mathcal{R}_{Zee}^{\text{WPHACT}}$
182.7	0.871 ± 0.219	0.876 ± 0.220
188.6	0.982 ± 0.126	0.990 ± 0.127
191.6	1.104 ± 0.275	1.112 ± 0.277
195.5	0.964 ± 0.167	0.972 ± 0.168
199.5	0.809 ± 0.165	0.816 ± 0.167
201.6	1.126 ± 0.222	1.135 ± 0.224
204.9	0.769 ± 0.160	0.776 ± 0.162
206.6	1.062 ± 0.124	1.067 ± 0.125
χ^2/dof	13.0/16	13.0/16
Average	0.955 ± 0.065	0.962 ± 0.065
χ^2/dof	17.1/23	17.0/23

Table 5.15: Ratios of LEP combined single-Z hadronic cross-section measurements to the expectations according to grc4f [187] and WPHACT [195]. The resulting averages over energies are also given. The averages take into account inter-experiment as well as inter-energy correlations of systematic errors.

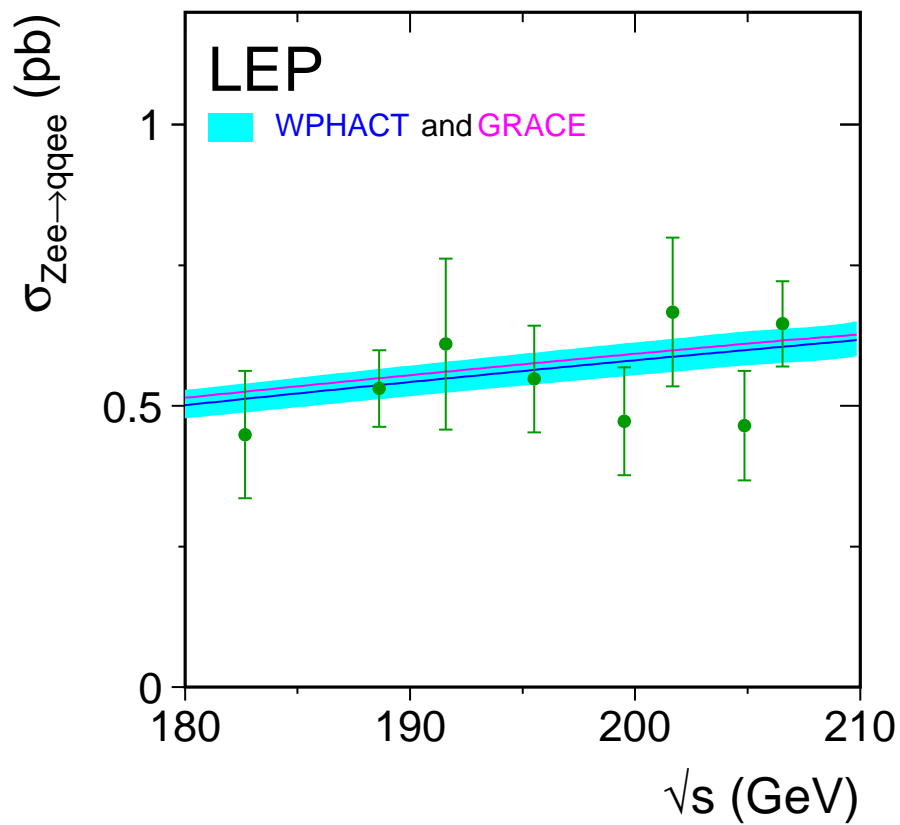


Figure 5.10: Measurements of the single-Z hadronic production cross-section, compared to the predictions of WPHACT [195] and `grc4f` [187]. The shaded area represents the $\pm 5\%$ uncertainty on the predictions.

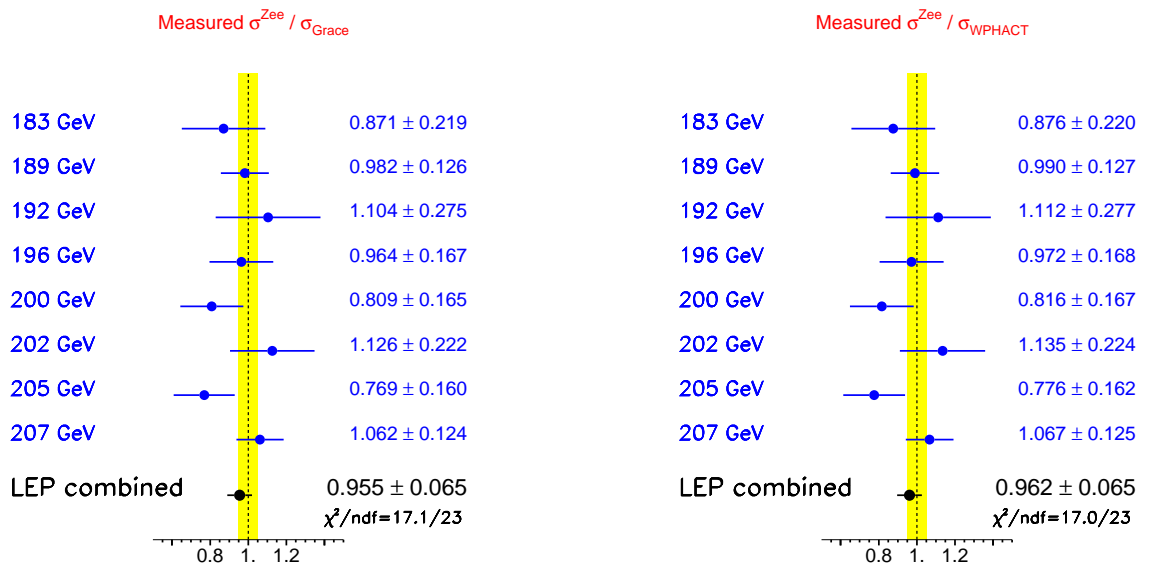


Figure 5.11: Ratios of LEP combined single-Z hadronic cross-section measurements to the expectations according to `grc4f` [187] and WPHACT [195]. The yellow bands represent constant relative errors of 5% on the two cross-section predictions.

5.6 $WW\gamma$ Production

The signal definition has been given in Section 5.1. The study of photon production in association with a W-boson pair is important for testing the sector of quartic gauge couplings. In order to increase the statistical accuracy, the LEP combination is performed in energy intervals rather than at each energy point; they are defined according to the LEP-II running periods where more statistics were accumulated. The luminosity-weighted centre-of-mass energy per interval is determined in each experiment and then combined to obtain the corresponding value for each energy interval. Table 5.16 reports those energies and the cross-sections measured by the experiments that are used in this combination [206, 207, 208], together with the combined LEP values.

Figure 5.12 shows the combined data points compared with the cross-section calculated with EEWWG [209] and RACOONWW. The RACOONWW prediction is shown in the figure without any theory error band.

5.7 Summary

This chapter has summarised the final LEP results in terms of four-fermion cross-sections and derived quantities. The WW cross-section has been measured precisely at LEP-II energies. The measurements clearly favour those theoretical predictions which properly include $O(\alpha)$ electroweak corrections, thus showing that the SM can be tested at the loop level at LEP-II.

In general the results are in good agreement with the SM predictions, both in the charged current and in the neutral current sector. A small anomaly in the W decay branching fractions, favouring W decays into $\tau\nu_\tau$ compared to the other lepton families, is observed in the data. This excess is above two standard deviations in the measured branching fractions into both $e\nu_e$ and $\mu\nu_\mu$.

\sqrt{s} (GeV)	WW γ cross-section (pb)			
	DELPHI	L3	OPAL	LEP
188.6	0.05 ± 0.08	0.20 ± 0.09	0.16 ± 0.04	0.15 ± 0.03
194.4	0.17 ± 0.12	0.17 ± 0.10	0.17 ± 0.06	0.17 ± 0.05
200.2	0.34 ± 0.12	0.43 ± 0.13	0.21 ± 0.06	0.27 ± 0.05
206.1	0.18 ± 0.08	0.13 ± 0.08	0.30 ± 0.05	0.24 ± 0.04

Table 5.16: WW γ production cross-section from the LEP experiments and combined values for the four energy bins.

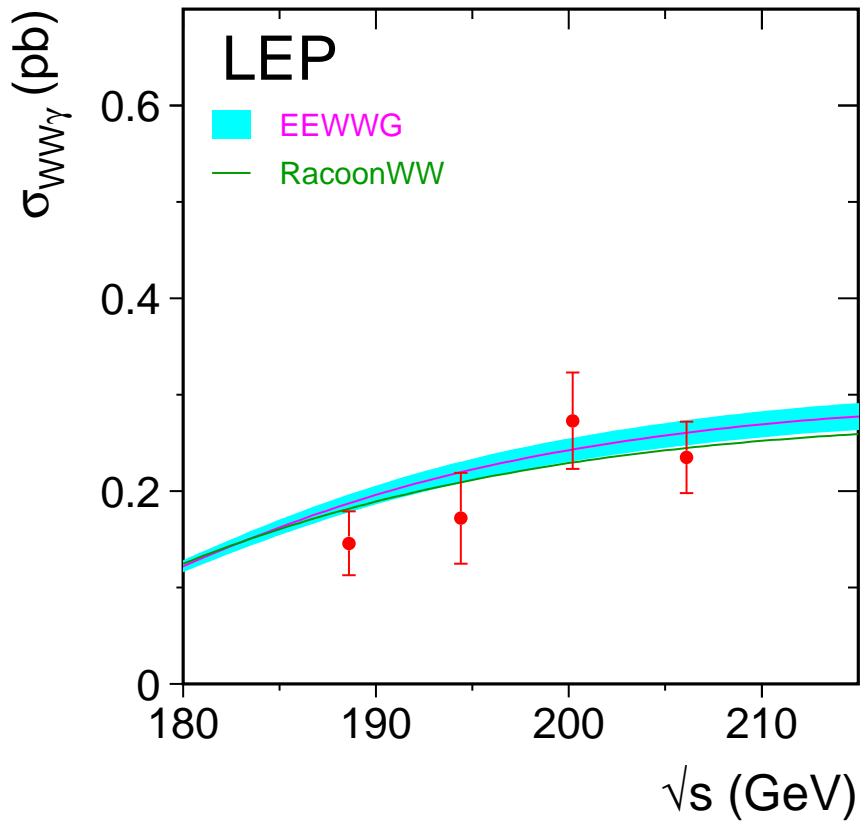


Figure 5.12: Measurements of the WW γ production cross-section, compared to the predictions of EEWWG [209] and RACOONWW [168]. The shaded area in the EEWWG curve represents the $\pm 5\%$ uncertainty on the predictions.

Chapter 6

Electroweak Gauge Boson Self Couplings

6.1 Introduction

The measurement of gauge boson couplings and the search for possible anomalous contributions due to the effects of new physics beyond the Standard Model (SM) are among the principal physics aims at LEP-II [210]. Combined results on triple gauge boson couplings are presented here.

The W -pair production process, $e^+e^- \rightarrow W^+W^-$, involves the charged triple gauge boson vertices between the W^+W^- and the Z or photon shown in Figure 1.4. During LEP-II operation, about 10,000 W -pair events were collected by each experiment. Single W ($e\nu W$) and single photon ($\nu\bar{\nu}\gamma$) production at LEP are also sensitive to the $WW\gamma$ vertex, see Figure 1.7. Results from these channels are also included in the combination for some experiments; the individual references should be consulted for details. The Monte-Carlo calculations, *RacoonWW* [168] and *YFSWW* [161, 167], incorporate an improved treatment of $O(\alpha_{em})$ corrections to WW production. The corrections affect the measurements of the charged TGCs in W -pair production. Results including these $O(\alpha_{em})$ corrections have been submitted from all four LEP collaborations ALEPH [211], DELPHI [212], L3 [213] and OPAL [214].

At centre-of-mass energies exceeding twice the Z boson mass, pair production of Z bosons is kinematically allowed. Here, one searches for the possible existence of triple vertices involving only neutral electroweak gauge bosons. Such vertices could also contribute to $Z\gamma$ production. In contrast to triple gauge boson vertices with two charged gauge bosons, purely neutral gauge boson vertices do not occur at tree level in the SM of electroweak interactions.

The expected total and differential cross-sections of these processes depend on the values of the triple gauge couplings, allowing their measurements by comparing Monte-Carlo simulations to the data. In contrast to the analysis of electroweak gauge boson self-couplings performed at hadron colliders, no form-factor term scaling the bare couplings is applied in the analysis of the LEP data.

6.1.1 Charged Triple Gauge Boson Couplings

The parametrisation of the charged triple gauge boson vertices is described in References [210, 215, 216, 217]. The most general Lorentz invariant Lagrangian which describes the triple gauge boson interaction has fourteen independent complex couplings, seven describing the $WW\gamma$

vertex and seven describing the WWZ vertex. Assuming electromagnetic gauge invariance as well as C and P conservation, the number of independent TGCs reduces to five. A common set is $\{g_1^Z, \kappa_\gamma, \kappa_Z, \lambda_\gamma, \lambda_Z\}$, with SM values of $g_1^Z = \kappa_\gamma = \kappa_Z = 1$ and $\lambda_\gamma = \lambda_Z = 0$. The parameters proposed in [210] and used by the LEP experiments are g_1^Z , κ_γ and λ_γ with the gauge constraints:

$$\kappa_Z = g_1^Z - (\kappa_\gamma - 1) \tan^2 \theta_W, \quad (6.1)$$

$$\lambda_Z = \lambda_\gamma, \quad (6.2)$$

where θ_W is the weak mixing angle. In an effective Lagrangian approach, all three of the remaining independent couplings, g_1^Z , κ_γ and λ_γ , receive contributions from operators of dimension six or greater. The couplings are considered as real, with the imaginary parts fixed to zero. Note that the measured coupling values themselves and not their deviation from the SM values are quoted. LEP combinations are made in single-parameter fits, in each case setting the other TGCs to their SM value.

The coupling g_1^Z describes the overall strength of the WWZ coupling. The photonic couplings κ_γ and λ_γ are related to the magnetic and electric properties of the W boson. One can write the lowest order terms for a multipole expansion describing the W- γ interaction as a function of κ_γ and λ_γ . For the magnetic dipole moment, μ_W , and the electric quadrupole moment, q_W , one obtains:

$$\mu_W = \frac{e}{2m_W} (1 + \kappa_\gamma + \lambda_\gamma), \quad (6.3)$$

$$q_W = -\frac{e}{m_W^2} (\kappa_\gamma - \lambda_\gamma). \quad (6.4)$$

The inclusion of $O(\alpha_{em})$ corrections in the Monte-Carlo calculations has a considerable effect on the charged TGC measurement. Both the total cross-section and the differential distributions are affected. The cross-section is reduced by 1–2% depending on the energy. For the differential distributions, the effects are naturally more complex. The polar W^- production angle carries most of the information on the TGC parameters; its shape is modified to be more forwardly peaked. In a fit to data, the $O(\alpha_{em})$ effect manifests itself as a negative shift of the obtained TGC values with a magnitude of typically -0.015 for λ_γ and g_1^Z and -0.04 for κ_γ .

6.1.2 Neutral Triple Gauge Boson Couplings

There are two classes of Lorentz invariant structures associated with neutral TGC vertices which preserve $U(1)_{em}$ and Bose symmetry, as described in [216, 224].

The first class refers to anomalous $Z\gamma\gamma^*$ and $Z\gamma Z^*$ couplings which are accessible at LEP in the process $e^+e^- \rightarrow Z\gamma$. The parametrisation contains eight couplings: h_i^V with $i = 1, \dots, 4$ and $V = \gamma, Z$. The superscript $V = \gamma$ refers to $Z\gamma\gamma^*$ couplings and superscript $V = Z$ refers to $Z\gamma Z^*$ couplings. The photon and the Z boson in the final state are considered as on-shell particles, while the third boson at the vertex, the s -channel internal propagator, is off shell. The couplings h_1^V and h_2^V are CP-odd while h_3^V and h_4^V are CP-even.

The second class refers to anomalous $ZZ\gamma^*$ and ZZZ^* couplings which are accessible at LEP-II in the process $e^+e^- \rightarrow ZZ$. This anomalous vertex is parametrised in terms of four couplings: f_i^V with $i = 4, 5$ and $V = \gamma, Z$. The superscript $V = \gamma$ refers to $ZZ\gamma^*$ couplings and

the superscript $V = Z$ refers to ZZZ^* couplings. Both Z bosons in the final state are assumed to be on-shell, while the third boson at the triple vertex, the s -channel internal propagator, is off-shell. The couplings f_4^V are CP-odd whereas f_5^V are CP-even.

In an effective Lagrangian approach, the couplings $h_1^V, h_3^V, f_4^V, f_5^V$ receive contributions from operators of dimension six or greater, while the lowest-dimension operators contributing to h_2^V and h_4^V have dimension eight. Note that the h_i^V and the f_i^V couplings are independent of each other. They are assumed to be real and they vanish at tree level in the SM. Results on neutral gauge boson couplings are reported for single- and two-parameter fits.

6.2 Combination Procedure

The combination is based on the individual likelihood functions from the four LEP experiments. Each experiment provides the negative log likelihood, $\log \mathcal{L}$, as a function of the coupling parameters to be combined. The single-parameter analyses are performed fixing all other parameters to their SM values. For the charged TGCs, the gauge constraints listed in Section 6.1.1 are always enforced. Either the $\log \mathcal{L}$ curves were available in numerical form or they have been treated as parabolic according to the respective publication. Details of the individual measurements entering the combination are summarised below.

The $\log \mathcal{L}$ functions from each experiment include statistical as well as those systematic uncertainties which are considered as uncorrelated between experiments. In all combinations, the individual $\log \mathcal{L}$ functions are combined. It is necessary to use the $\log \mathcal{L}$ functions directly in the combination, since in some cases they are not parabolic, and hence it is not possible to properly combine the results by simply taking weighted averages of the measurements.

The main contributions to the systematic uncertainties that are uncorrelated between experiments arise from detector effects, background in the selected signal samples, limited Monte-Carlo statistics and the fitting method. Their importance varies for each experiment and the individual references should be consulted for details.

In the neutral TGC sector, the main correlated systematic uncertainties arise from the theoretical cross-section prediction in ZZ and $Z\gamma$ -production, about 2% for ZZ and about 1% (2%) in the $q\bar{q}\gamma$ ($\nu\bar{\nu}\gamma$) channel. The effect of a correlated treatment has been estimated in earlier measurements to be negligible. Hence this and all other correlated sources of systematic errors, such as those arising from the LEP beam energy, are for simplicity treated as uncorrelated. The combination is performed by adding the $\log \mathcal{L}$ curves of the individual experiments.

In the charged TGC sector, systematic uncertainties considered correlated between the experiments are summarised in Table 6.1: the theoretical cross-section prediction, σ , which is 0.5% for W -pair production and 5% for single W production, hadronisation effects (HAD), the final state interactions, namely Bose-Einstein correlations (BEC) and colour reconnection (CR), and the uncertainty in the radiative corrections themselves (LPA). The latter was the dominant systematic error in previous combinations, where we used a conservative estimate, namely the full effect from applying the $O(\alpha_{em})$ corrections. Analyses on the subject are available from several LEP experiments, based on comparisons of fully simulated events using two different leading-pole approximation schemes (LPA-A and LPA-B, [225] and references therein). In addition, the availability of comparisons of the generators incorporating $O(\alpha_{em})$ corrections, RacoonWW and YFSWW [168, 161, 167], makes it possible to perform a more realistic estimation of this effect and its uncertainty. In general, the TGC shift measured in the comparison of the two generators is found to be larger than the effect from the different LPA schemes. This improved estimation, while still being conservative, reduces the systematic

Source	g_1^Z	κ_γ	λ_γ
σ_{WW} prediction	0.003	0.018	0.002
σ_W prediction	-	0.003	0.001
Hadronisation	0.003	0.005	0.004
Bose-Einstein Correlation	0.002	0.003	0.002
Colour Reconnection	0.003	0.005	0.002
$O(\alpha_{em})$ correction	0.002	0.014	0.002

Table 6.1: The systematic uncertainties considered correlated between the LEP experiments in the charged TGC combination and their effect on the combined fit results for the charged TGC parameters.

uncertainty from $O(\alpha_{em})$ corrections by about a third for g_1^Z and λ_γ and roughly halves it for κ_γ , compared to the full $O(\alpha_{em})$ correction. The application of this reduced systematic error renders the charged TGC measurements statistics dominated. In case of the charged TGCs, the systematic uncertainties considered correlated between the experiments amount to 32% of the combined statistical and uncorrelated uncertainties for λ_γ and g_1^Z , while for κ_γ they amount to 57%, indicating again that the measurements of λ_γ , g_1^Z and κ_γ are limited by data statistics.

The combination procedure [226] used for the charged TGCs allows the combination of statistical and correlated systematic uncertainties, independently of the analysis method chosen by the individual experiments. The combination uses the likelihood curves and correlated systematic errors submitted by each of the four experiments. The procedure is based on the introduction of an additional free parameter to take into account the systematic uncertainties, which are treated as shifts on the fitted TGC value, and are assumed to have a Gaussian distribution. A simultaneous minimisation of both parameters, TGC and systematic error, is performed.

In detail, the combination proceeds in the following way: the set of measurements from the LEP experiments ALEPH, DELPHI, OPAL and L3 is given with statistical and uncorrelated systematic uncertainties in terms of likelihood curves: $-\log \mathcal{L}_{stat}^A(x)$, $-\log \mathcal{L}_{stat}^D(x)$, $-\log \mathcal{L}_{stat}^L(x)$ and $-\log \mathcal{L}_{stat}^O(x)$, respectively, where x is the coupling parameter in question. Also given are the shifts for each of the five totally correlated sources of uncertainty mentioned above; each source S leads to systematic errors σ_A^S , σ_D^S , σ_L^S and σ_O^S .

Additional parameters Δ^S are included in order to take into account a Gaussian distribution for each of the systematic uncertainties. The procedure then consists in minimising the function:

$$-\log \mathcal{L}_{total} = \sum_{E=A,D,L,O} \log \mathcal{L}_{stat}^E(x - \sum_S (\sigma_E^S \Delta^S)) + \sum_S \frac{(\Delta^S)^2}{2} \quad (6.5)$$

where x and Δ_S are the free parameters, and the sums run over the four experiments E and the correlated systematic errors S discussed above and listed in Table 6.1. The resulting uncertainty on x takes into account all sources of uncertainty, yielding a measurement of the coupling with the error representing statistical and systematic sources. The projection of the minima of

the log-likelihood as a function of x gives the combined log-likelihood curve including statistical and systematic uncertainties. The advantage over the scaling method used previously is that it treats systematic uncertainties that are correlated between the experiments correctly, while not forcing the averaging of these systematic uncertainties into one global LEP systematic uncertainties scaling factor. In other words, the (statistical) precision of each experiment gets reduced by its own correlated systematic errors, instead of an averaged LEP systematic error. The method has been cross-checked against the scaling method, and was found to give comparable results. The inclusion of the systematic uncertainties leads to small differences, as expected by the improved treatment of correlated systematic errors. A similar behaviour is seen in Monte-Carlo comparisons of these two combination methods [227]. Furthermore, it was shown that the minimisation-based combination method used for the charged TGCs agrees with the method based on optimal observables, where systematic effects are included directly in the mean values of the optimal observables (see [227]), for any realistic ratio of statistical to systematic uncertainties. Further details on the combination method can be found in [226].

In the following, single-parameter fits are presented for the TGC parameters g_1^Z , κ_γ , λ_γ , h_i^V and f_i^V , while results from two-parameter fits are also given for (f_4^γ, f_4^Z) and (f_5^γ, f_5^Z) . For results quoted in numerical form, the one standard deviation uncertainties (68% confidence level) are obtained by taking the coupling values for which $\Delta \log \mathcal{L} = +0.5$ above the minimum. The 95% confidence level (C.L.) limits are given by the coupling values for which $\Delta \log \mathcal{L} = +1.92$ above the minimum. For multi-parameter analyses, the two dimensional 68% C.L. contour curves for any pair of couplings are obtained by requiring $\Delta \log \mathcal{L} = +1.15$, while for the 95% C.L. contour curves $\Delta \log \mathcal{L} = +3.0$ is required. Since the results on the different parameters and parameter sets are obtained from the same data sets, they cannot themselves be combined when looking at models establishing additional relations between these couplings.

6.3 Measurements

The combined results presented here are obtained from charged and neutral electroweak gauge boson coupling measurements as discussed above. The individual references should be consulted for details about the data samples used.

The charged TGC analyses of ALEPH, DELPHI, L3 and OPAL use data collected at LEP-II with centre-of-mass energies up to 209 GeV. These analyses use different channels, typically the semileptonic and fully hadronic W -pair decays [211, 212, 228, 229, 230, 213, 214]. The full data set is analysed by all four experiments. Anomalous TGCs affect both the total production cross-section and the shape of the differential cross-section as a function of the polar W^- production angle. The relative contributions of each helicity state of the W bosons are also changed, which in turn affects the distributions of their decay products. The analyses presented by each experiment make use of different combinations of each of these quantities. In general, however, all analyses use at least the expected variations of the total production cross-section and the W^- production angle. Results from $e\nu W$ and $\nu\bar{\nu}\gamma$ production are included by some experiments. Single- W production is particularly sensitive to κ_γ , thus providing information complementary to that from W -pair production.

The h -coupling analyses of ALEPH, DELPHI and L3 use data collected at LEP-II with centre-of-mass energies of up to 209 GeV. The OPAL measurements use the data at 189 GeV only. The results of the f -couplings are obtained from the whole data set above the ZZ -production threshold by all experiments. The experiments already pre-combine different processes and final states for each of the couplings. All analyses use measurements of the total

cross-sections of $Z\gamma$ and ZZ production and the differential distributions in the determination of the h_i^V couplings [231, 232, 233, 234] and the f_i^V couplings [231, 232, 235, 236], while DELPHI also includes $Z\gamma^*$ data in the determination of both sets of couplings.

6.4 Results

We present results from the four LEP experiments on the various electroweak gauge boson couplings, and their combination. The results quoted for each individual experiment are calculated using the methods described in Section 6.2. Therefore they may differ slightly from those reported in the individual references, as the experiments in general use other methods to combine the data from different channels and to include systematic uncertainties. In particular for the charged couplings, experiments using a combination method based on optimal observables (ALEPH, OPAL) obtain results with small differences compared to the values given by our combination technique. These small differences have been studied in Monte-Carlo tests and are well understood [227]. For the h -coupling results from OPAL and DELPHI, a slightly modified estimate of the systematic uncertainty due to the theoretical cross-section prediction is responsible for slightly different limits compared to the published results.

6.4.1 Charged Triple Gauge Boson Couplings

The individual analyses and results of the experiments for the charged couplings are described in [211, 212, 228, 229, 230, 214]. The results of single-parameter fits from each experiment are shown in Table 6.2, where the errors include both statistical and systematic effects. The individual $\log \mathcal{L}$ curves and their sum are shown in Figure 6.1. The results of the combination are given in Table 6.3. A list of the systematic errors treated as fully correlated between the LEP experiments, and their shift on the combined fit result were given in Table 6.1. The combined results agree well with the SM expectation.

Parameter	ALEPH	DELPHI	L3	OPAL	SM
g_1^Z	$0.996^{+0.030}_{-0.028}$	$0.975^{+0.035}_{-0.032}$	$0.965^{+0.038}_{-0.037}$	$0.985^{+0.035}_{-0.034}$	1
κ_γ	$0.983^{+0.060}_{-0.060}$	$1.022^{+0.082}_{-0.084}$	$1.020^{+0.075}_{-0.069}$	$0.899^{+0.090}_{-0.084}$	1
λ_γ	$-0.014^{+0.029}_{-0.029}$	$0.001^{+0.036}_{-0.035}$	$-0.023^{+0.042}_{-0.039}$	$-0.061^{+0.037}_{-0.036}$	0

Table 6.2: The measured central values and one standard deviation errors obtained by the four LEP experiments for the charged TGC parameters. In each case the parameter listed is varied while the remaining two are fixed to their SM values (also shown). Both statistical and systematic errors are included. The values given here differ slightly from the ones quoted in the individual contributions from the four LEP experiments, as a different combination method is used. See text in section 6.2 for details.

Parameter	68% C.L.	95% C.L.	SM
g_1^Z	$+0.984^{+0.018}_{-0.020}$	[0.946, 1.021]	1
κ_γ	$+0.982^{+0.042}_{-0.042}$	[0.901, 1.066]	1
λ_γ	$-0.022^{+0.019}_{-0.019}$	[-0.059, 0.017]	0

Table 6.3: The combined results for the 68% C.L. errors and 95% C.L. intervals obtained for the charged TGC parameters from the four LEP experiments. In each case the parameter listed is varied while the other two are fixed to their SM values (also shown). Both statistical and systematic errors are included.

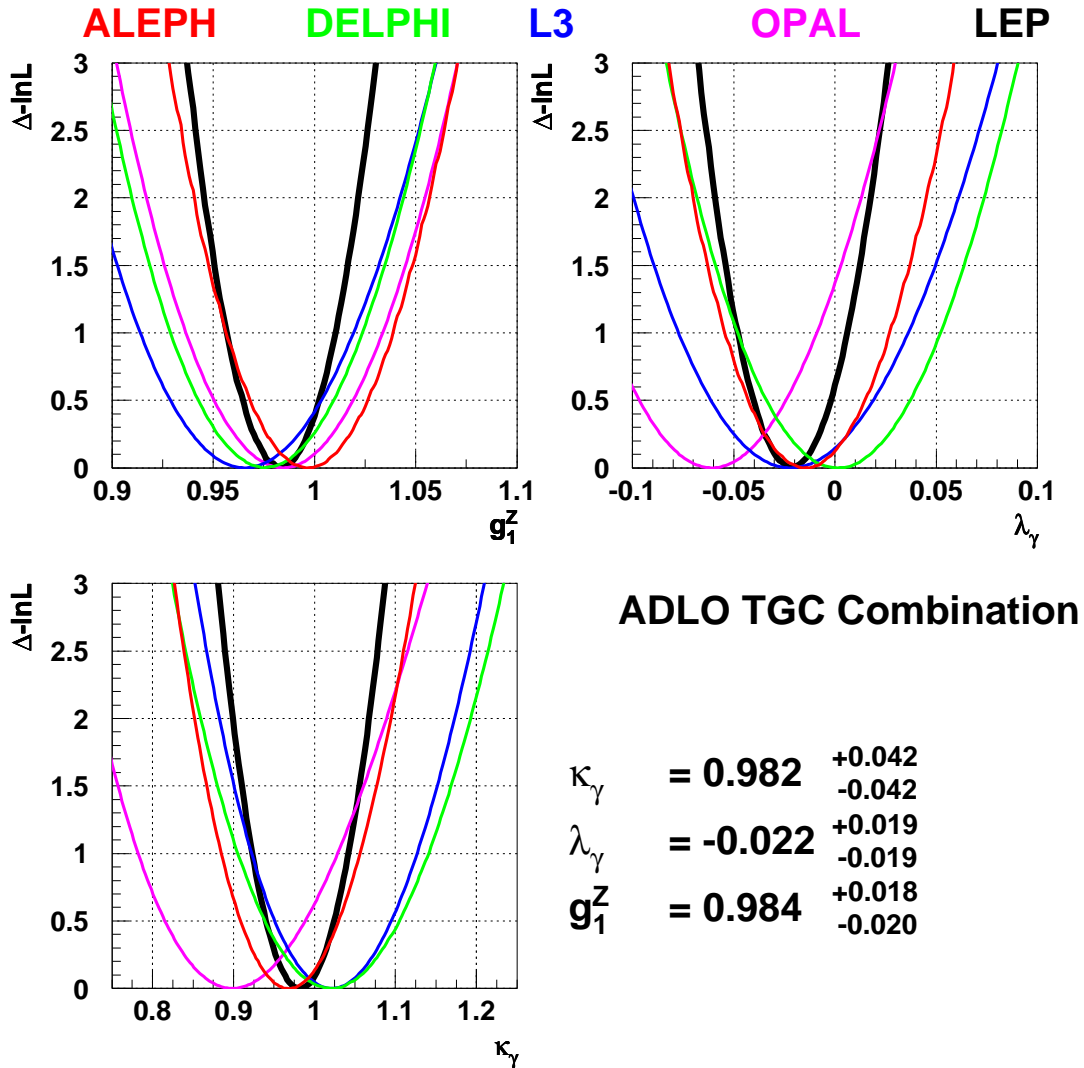


Figure 6.1: The log \mathcal{L} curves of the four experiments (thin lines) and the LEP combined curve (black line) for the three charged TGCs g_1^Z , κ_γ and λ_γ . In each case, the minimal log \mathcal{L} value is subtracted.

6.4.2 Neutral Triple Gauge Boson Couplings

The individual analyses and results of the experiments for the h -couplings are described in [232, 233, 234]. The results from DELPHI, L3 and OPAL, and the LEP combination, are shown in Table 6.4, where the errors include both statistical and systematic uncertainties. The individual $\log \mathcal{L}$ curves and their sum are shown in Figures 6.2 and 6.3. The results agree with the SM expectation.

Parameter	DELPHI	L3	OPAL	LEP
h_1^γ	[-0.14, 0.14]	[-0.06, 0.06]	[-0.11, 0.11]	[-0.05, 0.05]
h_2^γ		[-0.05, 0.02]	[-0.08, 0.08]	[-0.04, 0.02]
h_3^γ	[-0.05, 0.04]	[-0.06, 0.00]	[-0.16, -0.01]	[-0.05, -0.00]
h_4^γ		[-0.00, 0.04]	[0.01, 0.13]	[0.01, 0.05]
h_1^Z	[-0.23, 0.23]	[-0.15, 0.14]	[-0.19, 0.19]	[-0.12, 0.11]
h_2^Z		[-0.09, 0.08]	[-0.13, 0.13]	[-0.07, 0.07]
h_3^Z	[-0.30, 0.16]	[-0.22, 0.11]	[-0.27, 0.12]	[-0.19, 0.06]
h_4^Z		[-0.07, 0.15]	[-0.08, 0.17]	[-0.04, 0.13]

Table 6.4: The 95% C.L. intervals ($\Delta \log \mathcal{L} = 1.92$) in the neutral TGC parameters h_i^V measured by the DELPHI, L3 and OPAL, and the LEP combined values. In each case the parameter listed is varied while the remaining ones are fixed to their SM values ($h_i^V = 0$). Both statistical and systematic uncertainties are included. DELPHI did not interpret its measurements in terms of neutral gauge couplings of dimension 8 operators, hence does not enter in the combination for $h_{2/4}^V$.

The individual analyses and results of the experiments for the f -couplings are described in [231, 232, 235, 236]. The single-parameter results for each experiment and the LEP combination are shown in Table 6.5, where the errors include both statistical and systematic uncertainties. The individual $\log \mathcal{L}$ curves and their sum are shown in Figure 6.4. Three experiments, ALEPH, L3 and OPAL, contributed data to two-parameter fits to the TGC pairs (f_4^γ, f_4^Z) and (f_5^γ, f_5^Z) . The two-parameter results including the LEP combination are shown in Table 6.6, where the errors include both statistical and systematic uncertainties. The 68% C.L. and 95% C.L. contour curves resulting from the combinations of the two-dimensional likelihood curves are shown in Figures 6.5 and 6.6. The couplings agree with the SM expectation.

LEP **DELPHI+ L3+OPAL**

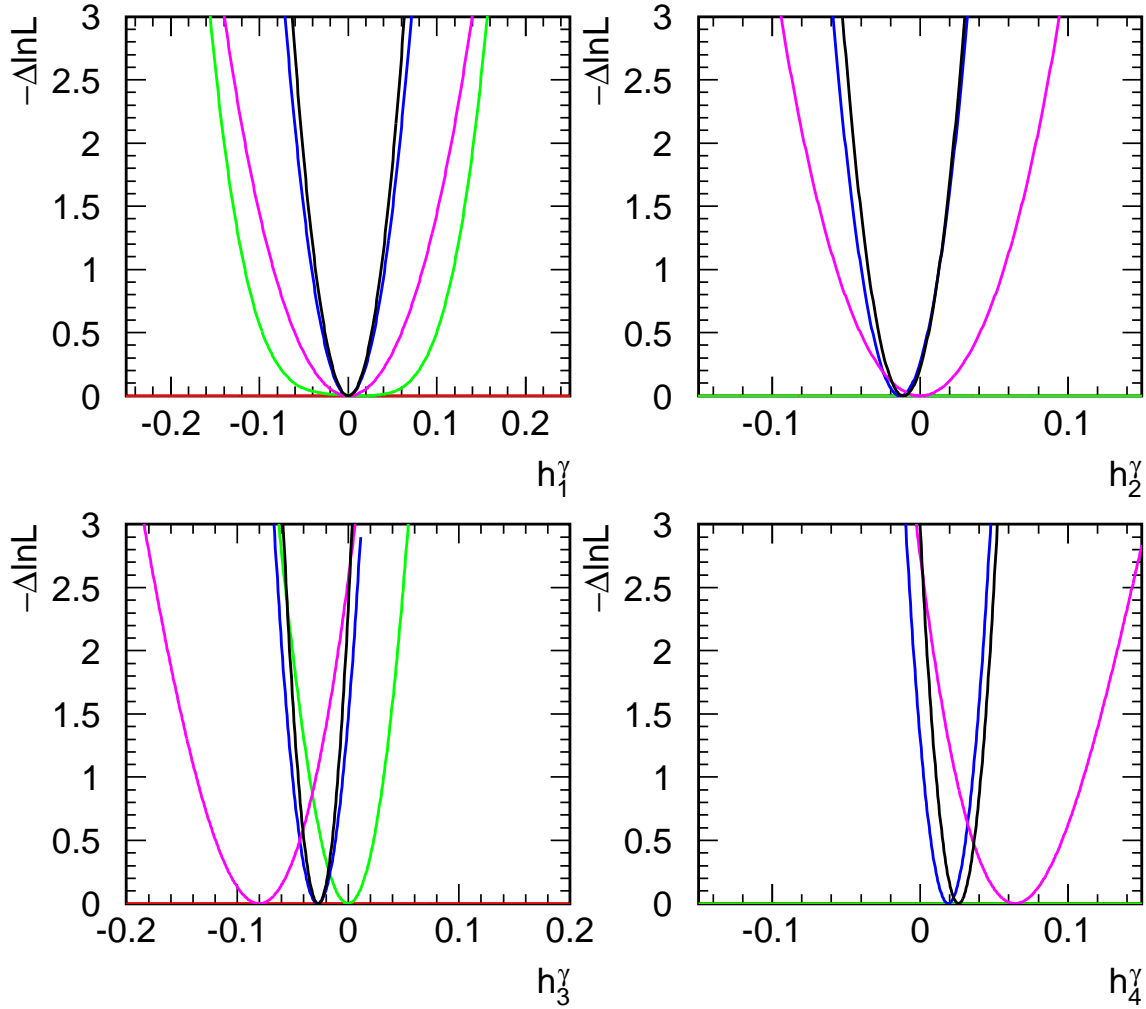


Figure 6.2: The $\log \mathcal{L}$ curves of DELPHI, L3, and OPAL experiments and the LEP combined curve for the four neutral TGCs h_i^γ , $i = 1, 2, 3, 4$. In each case, the minimal value is subtracted. Note, DELPHI did not interpret its measurements in terms of neutral gauge couplings of dimension 8 operators, hence does not enter in the combination for $h_{2/4}^\gamma$.

LEP **DELPHI+ L3+OPAL**

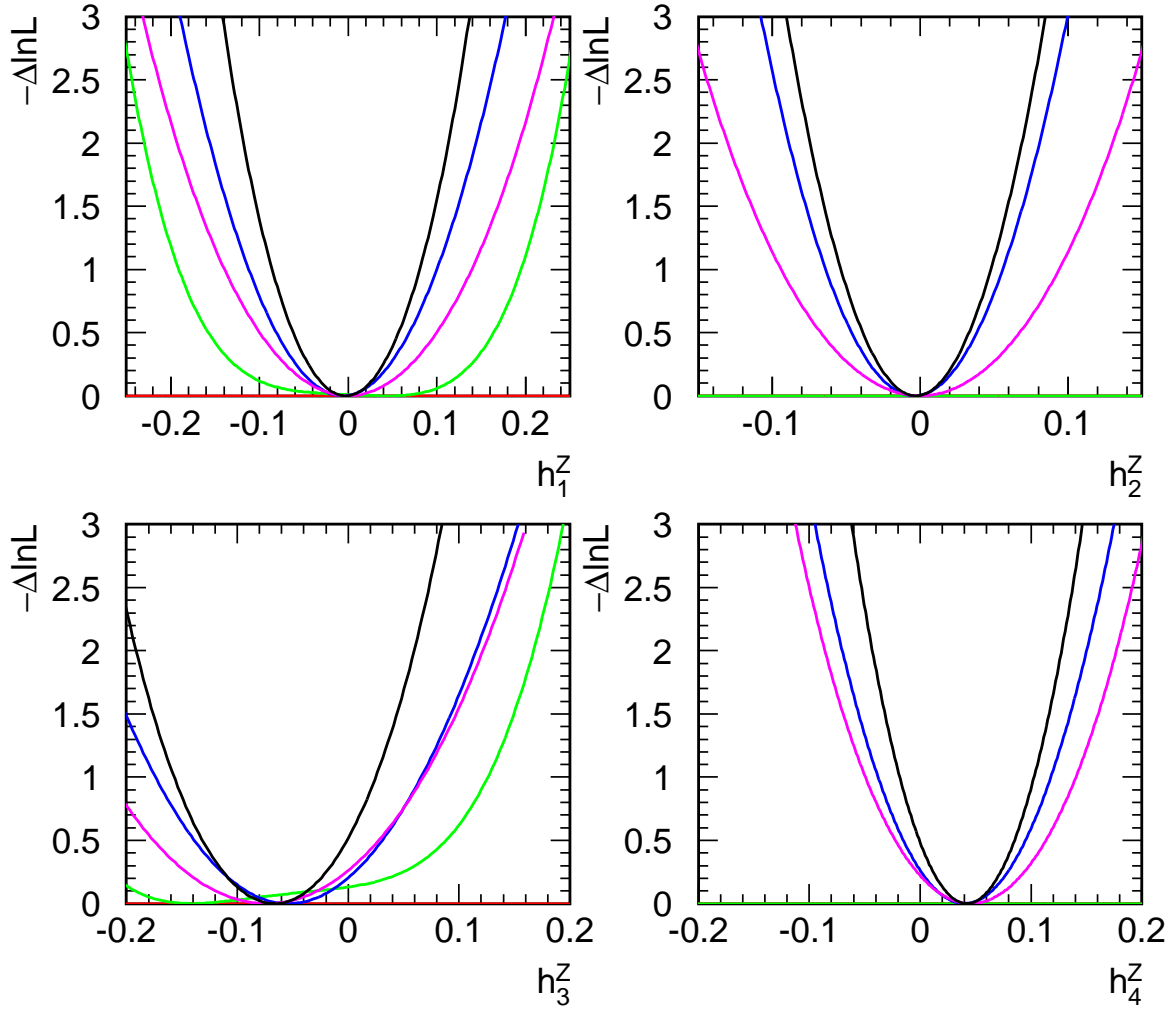


Figure 6.3: The $\log \mathcal{L}$ curves of the DELPHI, L3, OPAL experiments and the LEP combined curve for the four neutral TGCs h_i^Z , $i = 1, 2, 3, 4$. In each case, the minimal value is subtracted. Note, DELPHI did not interpret its measurements in terms of neutral gauge couplings of dimension 8 operators, hence does not enter in the combination for $h_{2/4}^V$.

Parameter	ALEPH	DELPHI	L3	OPAL	LEP
f_4^γ	[-0.32, 0.33]	[-0.23, 0.25]	[-0.28, 0.28]	[-0.32, 0.33]	[-0.17, 0.19]
f_4^Z	[-0.53, 0.54]	[-0.40, 0.42]	[-0.48, 0.46]	[-0.45, 0.58]	[-0.28, 0.32]
f_5^γ	[-0.73, 0.74]	[-0.52, 0.48]	[-0.39, 0.47]	[-0.71, 0.59]	[-0.35, 0.32]
f_5^Z	[-1.18, 1.19]	[-0.38, 0.62]	[-0.35, 1.03]	[-0.94, 0.25]	[-0.34, 0.35]

Table 6.5: The 95% C.L. intervals ($\Delta \log \mathcal{L} = 1.92$) in the neutral TGC parameters f_i^V measured by ALEPH, DELPHI, L3 and OPAL, and the LEP combined values. In each case the parameter listed is varied while the remaining ones are fixed to their SM values ($f_i^V = 0$). Both statistical and systematic uncertainties are included.

Parameter	ALEPH	L3	OPAL	LEP	Correlations
f_4^γ	[-0.29, 0.25]	[-0.28, 0.28]	[-0.32, 0.33]	[-0.20, 0.18]	1.00 -0.33
f_4^Z	[-0.43, 0.44]	[-0.48, 0.46]	[-0.47, 0.58]	[-0.29, 0.32]	-0.33 1.00
f_5^γ	[-0.59, 0.57]	[-0.53, 0.62]	[-0.67, 0.62]	[-0.40, 0.38]	1.00 -0.20
f_5^Z	[-0.90, 0.78]	[-0.47, 1.39]	[-0.95, 0.33]	[-0.56, 0.36]	-0.20 1.00

Table 6.6: The 95% C.L. intervals ($\Delta \log \mathcal{L} = 1.92$) in the neutral TGC parameters f_i^V in two-parameter fits measured by ALEPH, L3 and OPAL, and the LEP combined values. In each case the two parameters listed are varied while the remaining ones are fixed to their SM values ($f_i^V = 0$). Both statistical and systematic uncertainties are included. Since the shape of the log-likelihood is not parabolic, there is some ambiguity in the definition of the correlation coefficients and the values quoted here are approximate.

LEP **ALEPH+DELPHI+ L3+OPAL**

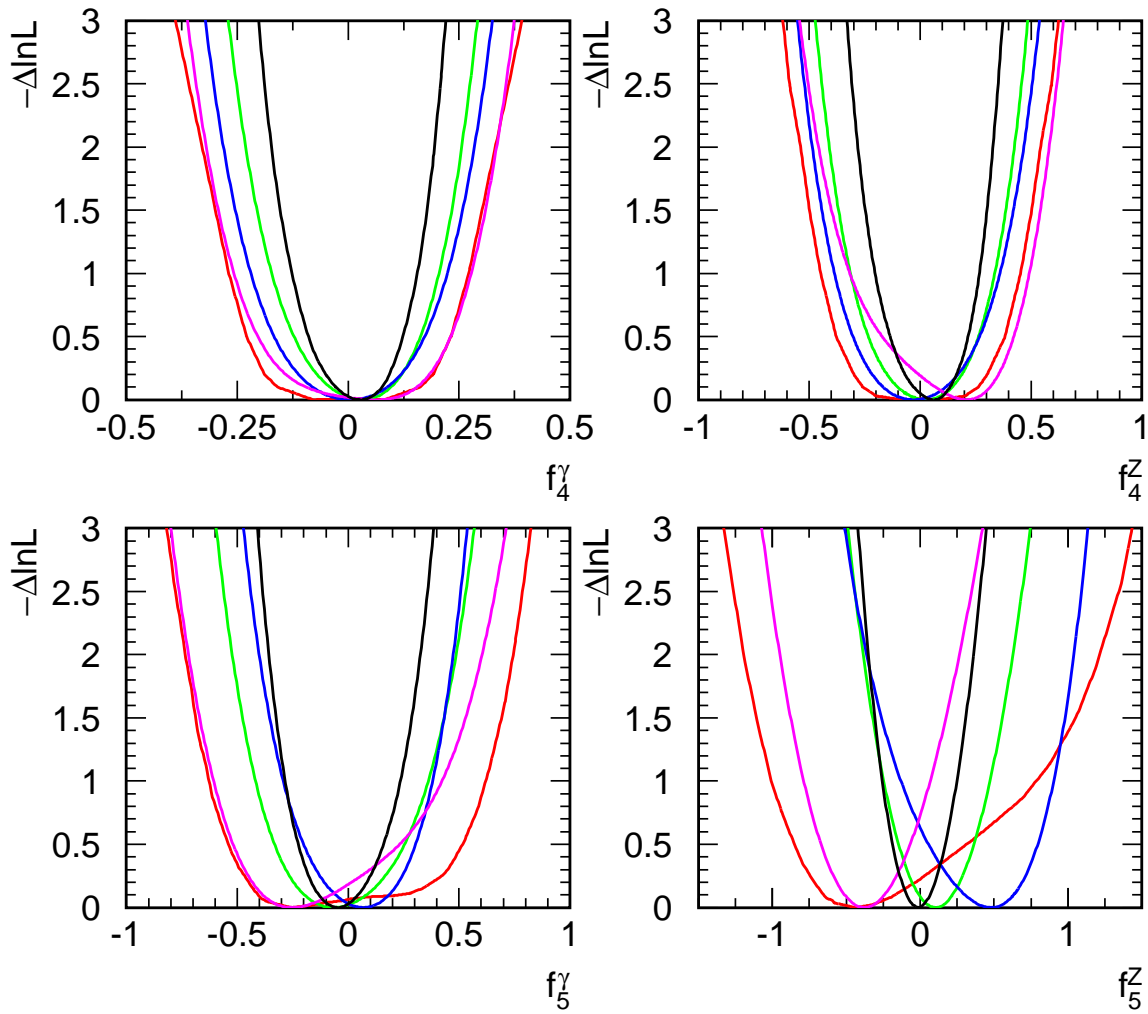


Figure 6.4: The $\log \mathcal{L}$ curves of the four experiments, and the LEP combined curve for the four neutral TGCs f_i^V , $V = \gamma, Z$, $i = 4, 5$. In each case, the minimal value is subtracted.

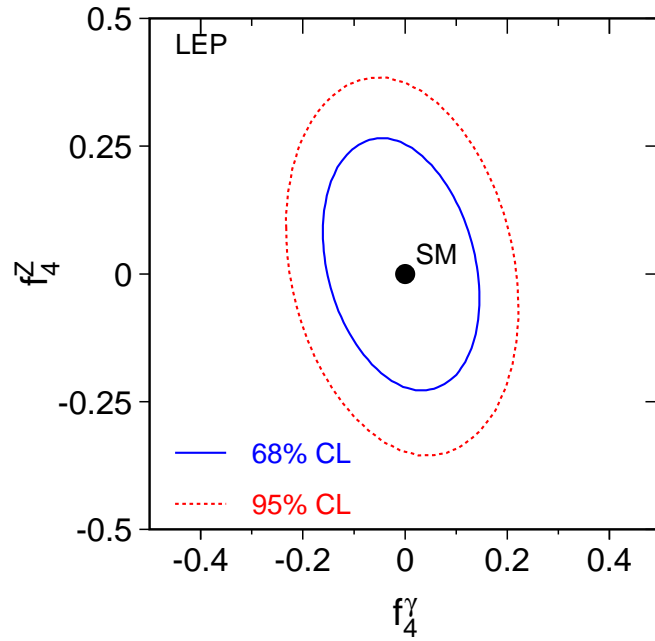


Figure 6.5: Contour curves of 68% C.L. and 95% C.L. in the plane of the neutral TGC parameters (f_4^γ, f_4^Z) showing the LEP combined result to which ALEPH, L3 and OPAL contributed.

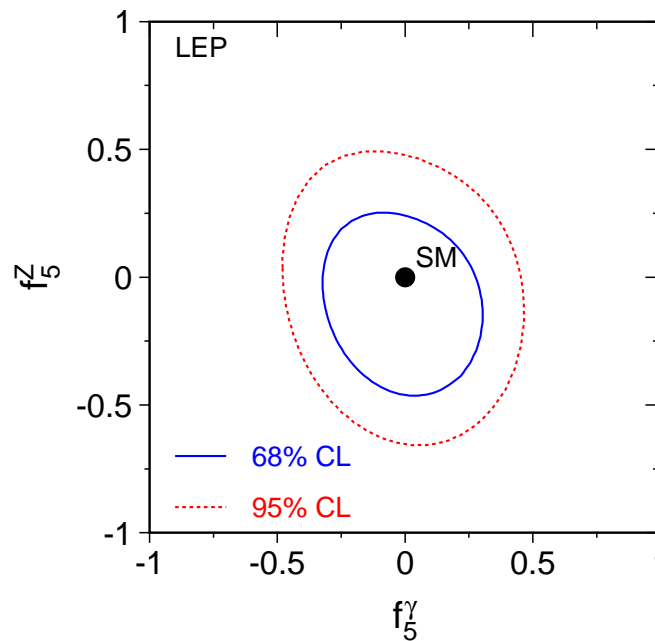


Figure 6.6: Contour curves of 68% C.L. and 95% C.L. in the plane of the neutral TGC parameters (f_5^γ, f_5^Z) showing the LEP combined result to which ALEPH, L3 and OPAL contributed.

6.5 Summary and Conclusions

Combinations of charged and neutral triple gauge boson couplings were made, based on results from the four LEP experiments ALEPH, DELPHI, L3 and OPAL. No deviation from the SM prediction is seen for any of the electroweak gauge boson couplings studied. While the existence of charged TGCs was experimentally verified already early on by the measurement of the total WW cross-section, see also Chapter 5, their values have now been measured with an accuracy of 0.02 to 0.04, and found to be in agreement with the SM expectation. As an example, these data allow the Kaluza-Klein theory [237], in which $\kappa_\gamma = -2$, to be excluded [238]. No evidence of the existence of neutral TGCs are found, limiting their magnitude to less than 0.05 to 0.35 depending on coupling.

Chapter 7

Mass and Width of the W Boson

7.1 Introduction

The mass of the W boson is a fundamental parameter in particle physics. Together with the Z-boson mass, it sets the energy scale of electroweak symmetry breaking. Both masses are closely related to the weak mixing angle. At LEP, the W-boson mass is determined by measuring the cross-section of W-boson pairs at the production threshold, from the leptonic decay spectrum of the W boson, and by directly reconstructing W boson decays. The latter method is the more precise one. It also allows a determination of the total decay width of the W boson. Direct measurements of W-boson mass and width are also performed at the Tevatron $p\bar{p}$ collider [239, 240, 241, 242].

7.2 Determination of the W Mass at the W-Pair Production Threshold

The SM cross-section of the reaction $e^+e^- \rightarrow W^+W^-$ shows a typical threshold behaviour close to a centre-of-mass energy that corresponds to twice the W mass. In the threshold region the cross-section rises in proportion to the velocity of the W bosons produced, which is approximately given by $\beta = \sqrt{1 - 4m_W^2/s}$, neglecting radiative corrections and finite width effects. Thus, a measurement of the production cross-section at a given centre-of-mass energy is directly related to the W boson mass. The intrinsic precision of this method is similar to the direct-reconstruction method, described below. However, since LEP predominantly operated at higher centre-of-mass energies in order to search for new physics as well as to make precise electroweak measurements, the data collected at threshold energies corresponds to only 3% of the full data set (see Table 1.1).

Using Monte-Carlo simulations, the centre-of-mass energy where the cross-section is most sensitive to m_W was determined to be $\sqrt{s} = 161$ GeV, but data at 172-183 GeV were also analysed to extract m_W from the measured cross-section. Each LEP experiment compared the measured cross-sections at each centre-of-mass energy to the m_W dependent SM prediction calculated using the GENTLE program [173]. The results of the four LEP experiments combined for the different centre-of-mass energies [243, 152, 244, 245] are shown in Table 7.1. Owing to the dependence of the theory cross-section on the mass for a given centre-of-mass energy, both the extracted mass and its uncertainty decrease with increasing measured cross-sections.

Systematic uncertainties from hadronisation and fragmentation effects in hadronically de-

Threshold Analysis	
Experiment	m_W [GeV]
ALEPH	80.20 ± 0.34
DELPHI	$80.45^{+0.45}_{-0.41}$
L3	$80.78^{+0.48}_{-0.42}$
OPAL	$80.40^{+0.46}_{-0.43}$

Table 7.1: W mass measurements from the W^+W^- threshold cross-section at $\sqrt{s} = 161 - 183$ GeV [243, 152, 244, 245]. The uncertainties include statistical and systematic contributions.

caying W bosons, radiative corrections, final-state interactions are all negligible compared to the statistical uncertainty of the measurement. Combining all LEP W -pair threshold data yields:

$$m_W(\text{threshold}) = 80.42 \pm 0.20 \pm 0.03(E_{\text{LEP}}) \text{ GeV} , \quad (7.1)$$

where the uncertainty due to the LEP centre-of-mass energy [246] is given separately. The treatment of systematic uncertainties is further detailed below.

7.3 Measurement of Mass and Width by Direct Reconstruction

7.3.1 Mass Reconstruction

The mass and total decay width of the W boson is determined with high precision by reconstructing directly the decay products of the two W bosons, mainly in the fully hadronic, $W^+W^- \rightarrow q\bar{q}q\bar{q}$, and semi-leptonic, $W^+W^- \rightarrow q\bar{q}l\nu_\ell$, decay channels.

The $W^+W^- \rightarrow l\nu_\ell l\nu_\ell$ decay also contains information on m_W when analysing the leptonic energy spectrum or reconstructing an approximated mass of the decaying W bosons, as performed by the OPAL collaboration [248]. However, the intrinsic statistical precision dominates the total uncertainty and OPAL determines a value of:

$$m_W(l\nu_\ell l\nu_\ell) = 80.41 \pm 0.41(\text{stat.}) \pm 0.13(\text{syst.}) \text{ GeV} , \quad (7.2)$$

analysing data at centre-of-mass energies between 183 GeV and 209 GeV. It is interesting to compare this result with those from the other decay channels, since systematic uncertainties from hadronic W decays are absent. Within the given precision it agrees well with the W mass measurements in $W^+W^- \rightarrow q\bar{q}q\bar{q}$ and $W^+W^- \rightarrow q\bar{q}l\nu_\ell$ events discussed below. For the purpose of the LEP combination, OPAL combines the measurements in the fully leptonic channel at each run period with the semi-leptonic results.

The $W^+W^- \rightarrow q\bar{q}q\bar{q}$ decays are reconstructed from hadronic jets observed in the final state, formed from measured particle tracks and energy depositions in the calorimeters. Different jet

clustering algorithms are applied, *e.g.*, the Durham [130], Dicus [249], and Cambridge [250] algorithms. Depending on the choice of clustering parameters, additional gluon radiation may be resolved, so that not only pairs of jets, but also five-jet topologies are reconstructed. Similarly, initial-state photon radiation (ISR) and final-state photon radiation (FSR) may be detected by a calorimetric cluster consistent with an electromagnetic shower shape and without a matched track in a given angular cone around the photon candidate. Such reconstruction methods improve the detailed knowledge of the event kinematics and therefore the resolution in the reconstructed masses of the decaying W bosons. The correct reconstruction of the fully hadronic final state is further complicated by combinatorial ambiguities to pair the reconstructed jets to the W decays. In case of four jets there are three possible combinations. For five-jet topologies this number increases to 15. The ambiguity is treated differently by the four LEP experiments. ALEPH selects only one combination in their analyses, using a pairing probability that is based on the CC03 matrix element evaluated for the reconstructed jets [151]. The other experiments use a W-mass estimator which combines all pairings that have a high probability to be correct [152, 153, 154]. The pairings are weighted accordingly in the combined mass likelihood. In this way, a maximum of information is retained for the subsequent mass extraction method. For DELPHI, the weights are based on the polar angle of the reconstructed W boson, the sum of jet charges of each jet combination and the transverse momentum of the gluon jet in five-jet events [152]. L3 exploits the probability of a kinematic fit [153], while OPAL uses a neural network trained with the above-mentioned variables and the reconstructed mass differences of the W bosons [154]. The fully hadronic data samples are furthermore separated into 4-jet and 5-jet sub-samples (L3), or all possible jet configurations, also with different clustering schemes, and properly weighted in the final m_W and Γ_W analysis.

Semi-leptonic W-pair decays, $W^+W^- \rightarrow q\bar{q}e\nu_e$, $W^+W^- \rightarrow q\bar{q}\mu\nu_\mu$ and $W^+W^- \rightarrow q\bar{q}\tau\nu_\tau$, are reconstructed as a pair of hadronic jets, possibly with a third jet from gluon radiation, and an isolated electron, muon or tau lepton. Photons from initial state radiation are detected in about 5% of the events and excluded from the jet clustering. The mass of the hadronically decaying W is determined directly from the jet system. In the leptonic $W \rightarrow e\nu_e$ and $W \rightarrow \mu\nu_\mu$ decays, the missing momentum vector is calculated applying total momentum conservation and is assigned to the momentum of the neutrino. The masses of both W decays can thus be reconstructed. In case of the $q\bar{q}\tau\nu_\tau$ final state, only the hadronically decaying W contains useable W-mass information due to the presence of a second neutrino from the tau decay.

7.3.2 Kinematic Fitting

The di-jet mass resolution is mainly determined by the precision of jet energy measurements. The jet energy is carried by charged particles ($\sim 62\%$ on average), photons ($\sim 27\%$) and neutral hadrons ($\sim 10\%$), which are measured using the tracking and calorimetric devices of the detectors. Even with the help of sophisticated energy-flow algorithms which combine tracks and calorimetric clusters in order to reduce effects of double counting of particles, the best jet energy resolutions achieved are typically $\Delta E/E \approx 60 - 80\%/\sqrt{E/\text{GeV}}$. The corresponding di-jet mass resolution for W-boson decays is in the order of 8 – 9 GeV.

The mass resolution is substantially improved by imposing the constraint that the total energy in the event should equal the known LEP centre-of-mass energy [246], or that the energy of each W boson should be equal to the LEP beam energy. In practice, this is most commonly implemented by means of a kinematic fit. In such a fit, the measured parameters of the jets and leptons are adjusted, taking account of their measurement uncertainties in such a

way as to satisfy the constraints of energy and momentum conservation. In case of hadronic jets, the jet three-momenta are varied while keeping the jet velocity constant, as systematic effects cancel in the ratio of jet momentum and jet energy. For leptons, the energy for electrons and momentum for muons, together with the polar and azimuthal angles, are considered in the fit. The lepton masses are set to their nominal values. For $q\bar{q}\tau\nu_\tau$ final states, an energy rescaling of the hadronic system to the beam energy is practically equivalent to a kinematic fit, due to the lack of further kinematic constraints.

In the $q\bar{q}q\bar{q}$ case, the improved kinematic reconstruction is referred to as a 4C fit, because there are four energy and momentum constraints. In the $q\bar{q}e\nu$ and $q\bar{q}\mu\nu_\mu$ channels it is referred to as a 1C or one constraint fit, because the three momentum components of the neutrino have to be determined, eliminating three of the constraints. It is often useful to impose the additional constraint that the masses of the two W bosons are equal, leading to a 5C or 2C fit, in which case the kinematic fit provides a single estimate of the average W mass in each event. Although the equal-mass assumption is not fulfilled in an individual event, it is valid on average. Since the intrinsic total width of the W is much smaller than the mass resolution, the equal-mass assumption further improves the mass resolution. The corresponding probabilities of fits in terms of a χ^2 variable are used to reject background and to resolve combinatorial ambiguities in the $q\bar{q}q\bar{q}$ channel.

The resolution on the W-boson mass varies slightly from experiment to experiment. Typical values¹, after use of kinematic fitting, are 2.5 GeV for the $W^+W^- \rightarrow q\bar{q}e\nu_e$ and $W^+W^- \rightarrow q\bar{q}\mu\nu_\mu$ channels, 3.1 GeV for the $W^+W^- \rightarrow q\bar{q}\tau\nu_\tau$ channel and 1.5 GeV for the $W^+W^- \rightarrow q\bar{q}q\bar{q}$ channel, at $\sqrt{s} = 189$ GeV. These resolutions increase to 2.9 GeV, 3.4 GeV and 1.7 GeV, respectively, at $\sqrt{s} = 207$ GeV.

The use of a kinematic fit or an equivalent kinematic constraint implies that the scale of the W mass measurement is directly linked to the knowledge of the LEP beam energy. Checks on the determination of the LEP energy are discussed in Appendix C. It should also be emphasised that the kinematic fit technique neglects the effects of initial-state radiation (ISR) if it is not measured directly in the detector. The average energy radiated in ISR in $e^+e^- \rightarrow W^+W^-$ events is 2.2 GeV at $\sqrt{s} = 189$ GeV, rising to ~ 3.5 GeV at $\sqrt{s} = 207$ GeV, which is substantially smaller than the intrinsic resolution of the jet energies and hence of the W mass, and therefore cannot be resolved by kinematic fitting. Any remaining bias due to unmeasured ISR photons is taken into account in the W mass and width extraction methods based on MC simulations of radiative effects.

7.3.3 Techniques for Determining the W-Boson Mass and Width

In the direct reconstruction method, the mass of the W boson is obtained by comparing data to simulated $e^+e^- \rightarrow W^+W^-$ event samples generated with known values of m_W and Γ_W , in order to obtain those which describe the data best. These Monte-Carlo samples are of large statistics, typically 10^6 events. Since the generation of event samples for all possible parameter values is very computing time intensive, different methods are used to perform the m_W and Γ_W extraction in a more efficient, but still precise way.

¹The resolutions quoted here are estimated from the distributions of the difference between the fitted W mass and the average of the two true W masses in each event. These resolution functions are not Gaussian, and the values quoted represent RMS values computed in a range ± 10 GeV around zero. In order to estimate the intrinsic mass resolution, events with significant ISR are excluded, and Monte-Carlo information is used to identify the correct jet-pairings in the $q\bar{q}q\bar{q}$ channel.

The Monte-Carlo simulation programs used to generate the signal process, Kandy [167], RACOONWW [168], and WPHACT [195], include all relevant diagrams leading to the same 4-fermion final state and full $O(\alpha)$ electroweak radiative corrections. Real ISR photons are calculated in $O(\alpha^3)$, and FSR photons to higher order leading-log approximation. The underlying mass and width of the W boson are defined using a relativistic Breit-Wigner propagator with s -dependent width which is also the convention adopted to quote the measured values. Tau decays are simulated using the TAUOLA [252] package. The fragmentation and hadronisation of quark and gluon jets is described by the JETSET [140], HERWIG [104], and ARIADNE [254] programs, which are compared to estimate the corresponding systematic uncertainties. The default fragmentation parameters exclude any FSI effects from Bose-Einstein correlations (BEC) or colour reconnection (CR). For the latter, a dedicated procedure is developed to suppress mass biases in the $W^+W^- \rightarrow q\bar{q}q\bar{q}$ channel, which is detailed below.

The background, mainly from $e^+e^- \rightarrow q\bar{q}(\gamma)$ with additional gluon radiation and pair production of Z bosons, amounts to 2 – 15% in the $q\bar{q}\ell\nu_\ell$ channels, depending on the selected W^+W^- final state, and about 30% in the $q\bar{q}q\bar{q}$ channel. The background is simulated using Monte-Carlo programs which include radiative corrections with higher order ISR and FSR. Dedicated control samples of 2-fermion and 4-fermion events are studied by the LEP experiments to ensure the agreement of the Monte-Carlo simulations with data, concerning jet and lepton resolutions, event shape variables, and detector response. Any remaining differences are taken into account as systematic uncertainties.

The methods that are applied to extract the W mass and width results are based on unbinned maximum likelihood fits to the measured data. Different procedures are employed to construct the likelihood functions and to describe their dependence on the underlying m_W and Γ_W values. For the final results, ALEPH and L3 apply a reweighting method, while OPAL and DELPHI use a convolution technique. The OPAL collaboration also performs fits of an analytical description of the Breit-Wigner resonance curves and background shapes to data, in order to access systematic uncertainties of the mass and width extraction method. Since the W-boson width, Γ_W , depends on the mass m_W , the SM dependence of Γ_W on m_W is assumed when performing the fit to the data to determine m_W . In fits for Γ_W , both m_W and Γ_W are varied independently. The m_W values obtained in the two-parameter fits are consistent within the given uncertainty with the one-parameter fit for m_W only. The methods used are described in the following.

Monte-Carlo reweighting

In the reweighting method, a multi-dimensional probability density is calculated using different mass estimators. These estimators are the masses from the 5C and 4C kinematic fit in the $q\bar{q}q\bar{q}$ channel, and those of the 2C and 1C fit for $q\bar{q}e\nu_e$ and $q\bar{q}\mu\nu_\mu$ events. To further improve the sensitivity, ALEPH also includes the uncertainty on the 5C and 2C masses. The $q\bar{q}\tau\nu_\tau$ sample contributes only with the rescaled hadronic mass. The probability densities are determined from distributions of the corresponding multi-differential cross-sections, including m_W and Γ_W dependent signal predictions and background contributions. This is done either using binned distributions or a local sampling of the phase-space density determined from Monte-Carlo simulations. Since the signal Monte-Carlo sample is generated with pre-defined underlying W mass and width values, the m_W and Γ_W dependence is introduced by reweighting of Monte-Carlo events. Each signal event is given a weight according to the ratio of the absolute values of the matrix element squared for the $e^+e^- \rightarrow W^+W^- \rightarrow f\bar{f}f\bar{f}(\gamma)$ process, calculated for the m_W and Γ_W values that are to be determined and for the nominal m_W and Γ_W used in the

simulation. The total likelihood functions of the different data samples are maximised with respect to m_W and Γ_W . This method is applied for the final ALEPH and L3 results, and by the OPAL collaboration to evaluate systematic uncertainties of the extraction method.

Convolution method

In this method, a probability density function is computed for each event, giving the probability that this event, with a set of reconstructed mass estimators $m_{i,\text{rec}}$ ($i = 1, \dots, n$), originated from a sample with true W mass and width, m_W and Γ_W , of the following schematic form:

$$P_s(m_W, \Gamma_W, m_{i,\text{rec}}) = S(m_W, \Gamma_W, m_i, s') \otimes ISR(s', s) \otimes R(m_i, m_{i,\text{rec}}) \quad (7.3)$$

In this expression, $S(m_W, \Gamma_W, m_i, s')$ is the true distribution of the mass estimators, folded with the radiator function $ISR(s', s)$ and the detector resolution function, $R(m, m_{\text{rec}})$, which is determined from Monte-Carlo simulations and describes the probability that an event of true mass estimator m_i would be reconstructed with mass estimators $m_{i,\text{rec}}$. The likelihood for the data is then constructed as the product of $f_s P_s(m_W, \Gamma_W, m_{i,\text{rec}}) + f_b P_b(m_{i,\text{rec}})$ over all events, where f_s and f_b are the probabilities that the event originates from signal and background processes, respectively, and $P_b(m_{i,\text{rec}})$ is a parametrisation of the background distribution. The parameters of interest, m_W and Γ_W , are estimated by maximising the total likelihood. In this approach, the resolution function may take account of the uncertainties in the reconstructed mass, which are likely to vary from event to event, and thus better measured events are given greater weight. This procedure is used for the final OPAL and DELPHI results.

7.3.4 Combination Procedure

The maximum likelihood fits are performed for each of the data sets at the different centre-of-mass energies and for each W-pair decay channel separately. Table 7.2 shows the final results on m_W obtained by the four LEP experiments with the direct reconstruction method in the $W^+W^- \rightarrow q\bar{q}\ell\nu_\ell$ and $W^+W^- \rightarrow q\bar{q}q\bar{q}$ final states. For the LEP combination, each experiment individually combines the results of the three $q\bar{q}\ell\nu_\ell$ channels. The OPAL collaboration also includes the $\ell\nu_\ell\ell\nu_\ell$ measurements in these results. Input to the combination procedure are thus the m_W and Γ_W central values and uncertainties from the four LEP experiments in the $q\bar{q}q\bar{q}$ (4q) and $q\bar{q}\ell\nu_\ell + \ell\nu_\ell\ell\nu_\ell$ (non-4q) final states for five centre-of-mass energy bins corresponding to the five years of data taking. These inputs combine the data collected in 1996 at 172 GeV, in 1997 at 183 GeV, in 1998 at 189 GeV, in 1999 at 192 – 202 GeV, and in 2000 at 205 – 209 GeV.

The combination of the measurements is performed and the evaluation of the components of the total measurement uncertainty is assessed using the Best Linear Unbiased Estimate (BLUE) technique [62]. In this way, statistical and systematic uncertainties of each measurement are properly taken into account, including correlations between them. The LEP combination procedure as described here is also applied to combine the measurements of each LEP experiment for comparison with the combined measurement published by each experiment in Table 7.2. The observed differences are mainly due to a different assessment of FSI uncertainties, which affects the fully hadronic channel, as discussed below. The changes of the semi-leptonic results are due to systematic uncertainties correlated between the $q\bar{q}q\bar{q}$ and $q\bar{q}\ell\nu_\ell$ channels.

Direct Reconstruction			
Experiment	$W^+W^- \rightarrow q\bar{q}l\nu_\ell$ $m_W[\text{GeV}]$	$W^+W^- \rightarrow q\bar{q}q\bar{q}$ $m_W[\text{GeV}]$	Combined $m_W[\text{GeV}]$
Published			
ALEPH	80.429 ± 0.060	80.475 ± 0.080	80.444 ± 0.051
DELPHI	80.339 ± 0.075	80.311 ± 0.137	80.336 ± 0.067
L3	80.212 ± 0.071	80.325 ± 0.080	80.270 ± 0.055
OPAL	80.449 ± 0.063	80.353 ± 0.083	80.416 ± 0.053
LEP combination			
ALEPH	80.429 ± 0.059	80.477 ± 0.082	80.444 ± 0.051
DELPHI	80.339 ± 0.076	80.310 ± 0.101	80.330 ± 0.064
L3	80.217 ± 0.071	80.324 ± 0.090	80.254 ± 0.058
OPAL	80.449 ± 0.062	80.353 ± 0.081	80.415 ± 0.052

Table 7.2: W mass measurements from direct reconstruction ($\sqrt{s} = 172 - 209$ GeV). Results are given for the semi-leptonic, fully-hadronic channels and the combined value. The top part of the table shows the results as published by the experiments [151, 152, 153, 154], using their individual evaluations of FSI effects; these results are final. The bottom part of the table shows the results of the experiments when propagating the common LEP estimates of FSI effects to the mass, which also affects the $W^+W^- \rightarrow q\bar{q}l\nu_\ell$ results through correlations due to other systematic uncertainties. The $W^+W^- \rightarrow q\bar{q}l\nu_\ell$ results from the OPAL collaboration include mass information from the $W^+W^- \rightarrow l\nu_\ell l\nu_\ell$ channel.

7.3.5 Overview of Systematic Uncertainties

There are several sources of systematic uncertainties affecting the measurements of m_W and Γ_W . Table 7.3 summarises the systematic and statistical uncertainties on the W mass and width measurements evaluated for the combined LEP data using the direct reconstruction method. For the W mass determination, the uncertainties are also given separately for the $q\bar{q}l\nu_\ell$ and $q\bar{q}q\bar{q}$ final states, and for their combination. The main contributions are discussed in the following.

LEP centre-of-mass energy

Since the LEP centre-of-mass energy is used as a constraint in order to improve the W mass resolution, uncertainties in the centre-of-mass energy translate directly into uncertainties on m_W . These can approximately be obtained by scaling the LEP centre-of-mass energy uncertainties with the ratio $m_W/(\sqrt{s}/2)$. The W width is less affected. At W -pair threshold energies, the calibration of the LEP centre-of-mass energy yields precisions of 25 – 27 MeV, and at energies between 182.7 GeV up to 201.6 GeV the uncertainty is 20 – 24 MeV. Since in the last LEP runs in the year 2000 horizontal corrector magnets were used to spread the magnetic field over a larger bending section in order to eventually increase the LEP beam energy to its absolute maximum, the related additional systematic effects reduced the centre-of-mass energy precision

Source	Systematic Uncertainty in MeV			
	on m_W			on Γ_W
	$q\bar{q}\ell\nu_\ell$	$q\bar{q}q\bar{q}$	Combined	
ISR/FSR	8	5	7	6
Hadronisation	13	19	14	40
Detector effects	10	8	9	23
LEP energy	9	9	9	5
Colour reconnection	–	35	8	27
Bose-Einstein Correlations	–	7	2	3
Other	3	10	3	12
Total systematic	21	44	22	55
Statistical	30	40	25	63
Statistical in absence of systematics	30	31	22	48
Total	36	59	34	83

Table 7.3: Error decomposition for the combined LEP W mass and width results using the direct reconstruction method. Information from cross-section measurements at the W-pair production threshold are not included in the W-mass uncertainties. Detector effects include uncertainties in the jet and lepton energy scales and resolution. The ‘Other’ category refers to errors, all of which are uncorrelated between experiments, arising from: simulation statistics, background estimation, four-fermion treatment, fitting method and event selection. The error decomposition in the $q\bar{q}\ell\nu_\ell$ and $q\bar{q}q\bar{q}$ channels refers to the independent fits to the results from the two channels separately. Large correlated uncertainties, mainly from FSI, lead to a reduced weight of measurements contributing to the average result and thus an increased statistical uncertainty both in the $q\bar{q}q\bar{q}$ channel and for the LEP combination.

to 37 – 42 MeV.

A cross-check of the LEP energy determination is performed by analysing $e^+e^- \rightarrow Z + \gamma \rightarrow f\bar{f} + \gamma$ events with hard ISR photons, mostly emitted at small polar angles with respect to the beam directions. In these events with a so-called radiative return to the Z, the mass of the 2-fermion system is calculated from the fermion production angles only, assuming energy-momentum conservation. The mass spectrum exhibits a peak around the Z mass value. Comparing the Z mass, m_Z^{ff} , determined from this spectrum with the precise value of m_Z measured at Z pole energies [4] is equivalent to a test of the LEP centre-of-mass energy (see Appendix C for further details):

$$\Delta\sqrt{s} = \sqrt{s} - \sqrt{s}_{LEP} = \sqrt{s} \frac{m_Z^{\text{ff}} - m_Z}{m_Z}, \quad (7.4)$$

with the nominal value of \sqrt{s}_{LEP} [246] provided by the LEP energy working group. When combining all available LEP data [151, 255, 256, 257] with Z decays to hadrons, and to electron,

	LEP energy correlations					
\sqrt{s} [GeV]	161	172	183	189	192-202	205-209
161	1.00	1.00	0.57	0.56	0.58	0.36
172	1.00	1.00	0.58	0.57	0.58	0.37
183	0.57	0.58	1.00	0.94	0.95	0.53
189	0.56	0.57	0.94	1.00	0.94	0.53
192-202	0.58	0.58	0.95	0.94	1.00	0.55
205-209	0.36	0.37	0.53	0.53	0.55	1.00

Table 7.4: Correlation between the LEP centre-of-mass energy measurements in the six run periods [246].

muon, and tau pairs, the difference is found to be

$$\Delta\sqrt{s} = -54 \pm 54 \text{ MeV}, \quad (7.5)$$

in good agreement with no shift with respect to the more precise standard LEP energy calibration.

The properly calibrated LEP centre-of-mass energy is used in the W mass and width analysis on event-by-event basis. Uncertainties on m_W and Γ_W are determined by detailed Monte-Carlo studies, and also the effect of the LEP energy spread is taken into account. When combining the LEP W mass and width results the correlations between the LEP energy uncertainties at the different energies are properly included. They are derived from the LEP energy model [246] and listed in Table 7.4. The overall LEP energy uncertainty is 9 MeV on m_W and 5 MeV on Γ_W .

Detector effects

The effects of detector performance as well as of identification and reconstruction efficiencies for final state leptons, jets and photons are studied in dedicated control data samples. Energy and momentum calibration, as well as detector alignment and angular measurements, very important for the mass reconstructed, were studied [151, 152, 153, 154]. Since Monte-Carlo samples are compared to data to extract m_W and Γ_W , all effects are modelled in detail in the simulation and remaining differences to data result in corresponding systematic uncertainties. The LEP experiments provide separate uncertainties for lepton and jet measurements. These are considered uncorrelated between measurements from different experiments, but correlated for m_W and Γ_W measurements from the same experiment at different LEP energy points. The total systematic uncertainty from detector effects is 10 MeV and 8 MeV on m_W in the $q\bar{q}l\nu_\ell$ and $q\bar{q}q\bar{q}$ channels. The W width systematic uncertainties due to finite precision in modelling jet and lepton measurements is 23 MeV, combining all final states.

Fragmentation and hadronisation

Since the m_W and Γ_W extraction methods rely on the comparison of Monte-Carlo simulations to data the modelling of the fragmentation and hadronisation process subsequent to the $W \rightarrow q\bar{q}$

decay is essential. The calibration of the reconstructed jets is very sensitive to the fractions of the different final state hadrons inside the jets. Furthermore, the jet reconstruction usually cannot resolve each individual hadron, so that the same particle masses are assumed (usually the pion mass) when tracks and clusters are combined to form quark and gluon jets. To assess systematic uncertainties due to fragmentation and hadronisation, different Monte-Carlo models are compared, whose parameters are adjusted to describe high-statistic data samples of $Z \rightarrow q\bar{q}$ decays at the Z pole. These Z decays are depleted in b -quarks, to resemble the hadronic decays of W bosons. The systematic uncertainty is derived from the relative shifts in W mass and width values determined in Monte-Carlo samples using the JETSET/PYTHIA [140], HERWIG [258], and ARIADNE [254] fragmentation models. In addition, the fraction of certain hadrons, like kaons and protons, is directly measured in $W \rightarrow q\bar{q}$ decays and compared to the fragmentation models. The measurement uncertainties on these fractions are also taken into account in the fragmentation and hadronisation systematic uncertainties for the m_W and Γ_W determination.

Since all four LEP experiments study the same fragmentation models, the systematic uncertainty is taken as fully correlated for all measurements of the W mass and width. Eventually, the systematic effect on m_W is estimated to be 13 MeV and 19 MeV in the $q\bar{q}\ell\nu_\ell$ and $q\bar{q}q\bar{q}$ final states. In the W width determination, the corresponding systematic uncertainties contribute with 40 MeV to the combined W width measurement.

Colour reconnection

A particular systematic uncertainty arises in the $W^+W^- \rightarrow q\bar{q}q\bar{q}$ channel, where the two W bosons decay close in phase space so that FSI effects may play a significant role. Indeed, colour reconnection (CR) effects leads to shifts of the extracted W mass up to about 100 MeV [151, 152, 153, 154] if nominal jet reconstruction is applied and data are compared to Monte-Carlo models with and without colour reconnection. These large shifts are observed even if the measured constraints on the reconnection parameters, which are discussed in section 4, are applied. The LEP collaborations therefore developed new techniques in the $q\bar{q}q\bar{q}$ channel. It is observed that colour reconnection effects on m_W as implemented in the ARIADNE [103], SK [102], and HERWIG [104] models are reduced when the jet reconstruction is modified. This is achieved by either rejecting particles inside jets with energies or momenta lower than a given threshold or by reweighting their energies and momenta to suppress soft particles, which are mainly in the inter-jet and reconnection-sensitive region. The four LEP experiments applied thresholds and weights which are optimised individually for the colour reconnection constraints of the SK-I model [102] which are measured by each experiment separately. In the optimisation process the overall uncertainty on m_W is minimised, again individually, trading a reduced statistical precision due to a modified jet reconstruction for an improved FSI systematic uncertainty. For the LEP combined analysis, the threshold values and weights of each experiment are however not always optimal when the LEP combined upper limit on the SK-I parameter, $k_I < 2.10$, is used as reference for the CR uncertainty in the LEP m_W combination. Although this reduces the relative weight of some m_W measurements in the LEP combination, a further optimisation is not performed.

For the final LEP combination, the central value of the W mass is determined using Monte-Carlo samples without colour reconnection. The systematic uncertainties are evaluated from the mass differences observed when data is compared to the SK-I model with $k_I = 2.10$. The systematic uncertainties are evaluated at each centre-of-mass energy independently since the colour reconnection effects are energy dependent. The systematic uncertainties are taken as symmetric in the combination procedure and correlated between all measurements in the

$q\bar{q}q\bar{q}$ channel at the different centre-of-mass energies and by the four LEP experiments. They contribute 35 MeV to the total uncertainty in the fully hadronic final state.

When the W width is extracted, the optimisation of the jet reconstruction is not applied by the LEP collaborations, and the standard jet measurement is used. The reason is the relatively large statistical uncertainty of the W width measurement, which does not require a modification of the standard $q\bar{q}q\bar{q}$ analysis. The corresponding CR uncertainty is evaluated using the LEP upper limit on the SK-I parameter, $k_I < 2.10$, like in the W mass determination, and corresponds to 27 MeV on the combined width result.

Bose-Einstein correlations

A further source of uncertainty connected with FSI in the $W^+W^- \rightarrow q\bar{q}q\bar{q}$ channel is the possibility of Bose-Einstein correlations (BEC) between identical mesons in the decay of different W bosons. The measurement of these correlations is discussed in detail in section 4. For the final LEP results, Bose-Einstein correlations between particles from inside each hadronically decaying W are implemented in the Monte-Carlo simulation according to the BE_{32} model [140], which describes $W^+W^- \rightarrow q\bar{q}\ell\nu_\ell$ data well. However, the combined analysis of LEP data yields an upper limit on the strength of Bose-Einstein correlations between mesons from different W bosons of 30% of the full correlation in the BE_{32} model. The systematic effect on the W mass and width in the $W^+W^- \rightarrow q\bar{q}q\bar{q}$ channel is effectively reduced by the modified jet reconstruction algorithms, which were originally introduced for controlling systematic uncertainties from CR. Therefore, the uncertainties due to Bose-Einstein correlations on the W mass in $W^+W^- \rightarrow q\bar{q}q\bar{q}$ events is 7 MeV, while it is just 3 MeV on the combined width result.

Initial state radiation and $\mathcal{O}(\alpha)$ effects

Photon radiation influences the reconstructed W mass spectra. The Monte-Carlo programs used to extract m_W and Γ_W , Kandy, RACOONWW and WPHACT, include ISR effects in the YFS exponentiation scheme to $\mathcal{O}(\alpha^3)$, full $\mathcal{O}(\alpha)$ electroweak corrections, including interference between ISR, FSR and photon radiation of the W boson, as well as screened Coulomb corrections. These describe Coulomb interactions between the W bosons, which are potentially large but screened due to the limited lifetime of the W bosons. Higher-order leading-log FSR corrections are included using PHOTOS for leptons and PYTHIA for quarks. ISR effects on m_W are estimated by comparing the $\mathcal{O}(\alpha^3)$ with the $\mathcal{O}(\alpha^2)$ calculation, yielding small shifts of about 1 MeV [259]. The effect of Coulomb screening are estimated by taking half of the difference between Monte-Carlo samples with screened Coulomb effect and without any Coulomb effect, which amounts to about 7 MeV. To evaluate the uncertainty on the non-leading $\mathcal{O}(\alpha)$ electroweak corrections, a direct comparison of the RACOONWW and the Kandy generators is performed. The observed differences are in the order of 10 MeV for $q\bar{q}\ell\nu_\ell$ and 5 MeV for $q\bar{q}q\bar{q}$. Some systematic studies overlap, however, and the experiments apply different strategies to assess them. The total LEP uncertainty on the W mass due to radiative corrections is 8 MeV in the semi-leptonic channel and 5 MeV in the fully hadronic channel. Full correlation between all data sets is assumed. In case of the W width, the corresponding uncertainties amount to 6 MeV when combining all final states.

Other sources of systematic uncertainties

The contribution of background to the selected W -pair samples arises mainly from 4-fermion and hadronic 2-fermion events. All LEP experiments study the event shapes of the different background contributions using control samples to best describe the data. The systematic effect of the background on m_W and Γ_W are derived by varying the overall scale on the production cross-sections of the background processes, mainly $e^+e^- \rightarrow q\bar{q}(\gamma, g)$ and $e^+e^- \rightarrow ZZ$, within the measured uncertainty. Effects on the mass spectrum which do not scale with the overall production rate are studied by varying, for example, the slope of the background spectra.

In addition, uncertainties due to limited Monte-Carlo statistics, from the mass and width extraction techniques, and due to the event selection are considered. Early analyses at LEP-II used Monte-Carlo simulations based on CC03 matrix elements to simulate W^+W^- production. In this case, systematic biases of the W mass and width may arise because four-fermion diagrams are neglected which might interfere with W -pair production.

All these categories of systematic uncertainties are taken as uncorrelated in the LEP combination and contribute on the mass with 3 MeV in the semi-leptonic channel and 10 MeV in the fully hadronic channel, and 12 MeV on Γ_W .

7.4 LEP Combined W-Boson Mass

The combined LEP W mass from direct reconstruction data alone is:

$$m_W(\text{direct}) = 80.375 \pm 0.025(\text{stat.}) \pm 0.022(\text{syst.}) \text{ GeV}, \quad (7.6)$$

with a total uncertainty of 34 MeV. The combination has a χ^2/dof of 47.7/37, corresponding to a probability of 11.1%. The weight of the fully-hadronic channel in the combination amounts to just 22% due to significant FSI systematic uncertainties.

The largest contribution to the systematic error originates from hadronisation uncertainties, which are fully correlated between all measurements. In the absence of any systematic effects the current LEP statistical precision on m_W would be 22 MeV. The statistical error contribution in the LEP combination is larger than this, 25 MeV, due to the reduced weight of the fully-hadronic channel, mainly due to FSI systematic uncertainties.

When the threshold measurements (Section 7.2) are combined with the precise results obtained from direct reconstruction one achieves a W mass measurement of:

$$m_W = 80.376 \pm 0.025(\text{stat.}) \pm 0.022(\text{syst.}) \text{ GeV}, \quad (7.7)$$

with a slightly improved total uncertainty of 33 MeV. The combination has a χ^2/dof of 48.9/41, corresponding to a probability of 18.5%. The LEP energy uncertainty is the only correlated systematic error source between the threshold and direct reconstruction measurements. The threshold measurements have a weight of only 2% in the combined fit. This LEP combined result is compared with the final results of the four LEP experiments in Figure 7.1.

7.5 Consistency Checks

The masses from the two channels with all uncertainties and correlations included are:

$$m_W(W^+W^- \rightarrow q\bar{q}\ell\nu_\ell) = 80.372 \pm 0.030(\text{stat.}) \pm 0.021(\text{syst.}) \text{ GeV}, \quad (7.8)$$

$$m_W(W^+W^- \rightarrow q\bar{q}q\bar{q}) = 80.387 \pm 0.040(\text{stat.}) \pm 0.044(\text{syst.}) \text{ GeV}. \quad (7.9)$$

The two results are correlated with a correlation coefficient of 0.20. These results and the correlation between them can be used to combine the two measurements or to form the mass difference. The LEP combined results from the two channels are compared with those quoted by the individual experiments in Figure 7.2. When combining the m_W measurements in the $q\bar{q}\ell\nu_\ell$ and $q\bar{q}q\bar{q}$ channels separately and neglecting any correlations between these final states, results consistent within 2 MeV with the correlated averages above are obtained.

The difference between the combined W-boson mass measurements obtained from the fully-hadronic and semi-leptonic channels, $\Delta m_W(q\bar{q}q\bar{q} - q\bar{q}\ell\nu_\ell)$ is also determined. Since Δm_W is primarily of interest as a check of the possible effects of final state interactions, the uncertainties from Bose-Einstein correlation and colour reconnection are set to zero in its determination. A fit imposing otherwise the same correlations as those for the results given in the previous sections yields:

$$\Delta m_W(q\bar{q}q\bar{q} - q\bar{q}\ell\nu_\ell) = -12 \pm 45 \text{ MeV}. \quad (7.10)$$

Note that this mass difference has a different value and opposite sign compared to the difference between the $q\bar{q}q\bar{q}$ and $q\bar{q}\ell\nu_\ell$ mass values presented above, because the BEC and CR uncertainties are not included in its determination. A significant non-zero value for Δm_W could indicate that such Bose-Einstein correlation or colour reconnection effects are biasing the value of m_W determined from $W^+W^- \rightarrow q\bar{q}q\bar{q}$ events. The consistency of the mass difference with zero shows that such FSI effects are well suppressed by the modified jet reconstruction in the fully hadronic channel.

7.6 LEP Combined W-Boson Width

The method of direct reconstruction is also well suited to the direct measurement of the total decay width of the W boson. The published results of the four LEP experiments are shown in Table 7.5 and in Figure 7.3.

For the LEP combination, each experiment provided a W width measurement for both $W^+W^- \rightarrow q\bar{q}\ell\nu_\ell$ and $W^+W^- \rightarrow q\bar{q}q\bar{q}$ channels for each of the data taking periods that were analysed, and using the same error categories as for the mass. The BEC and CR uncertainties supplied by the experiments were based on studies of phenomenological models of these effects, using the same estimates of such FSI effects as for the mass and propagating them to the width. Note that the W width results of the experiments do not use the techniques introduced to reduce sensitivity to FSI effects used for the mass analysis. A simultaneous fit to the results of the four LEP collaborations is performed in the same way as for the m_W measurement. Correlated systematic uncertainties are taken into account and the combination yields:

$$\Gamma_W = 2.195 \pm 0.063(\text{stat.}) \pm 0.055(\text{syst.}) \text{ GeV}, \quad (7.11)$$

Experiment	Published	LEP combination
	Γ_W [GeV]	Γ_W [GeV]
ALEPH	2.14 ± 0.11	2.14 ± 0.11
DELPHI	2.40 ± 0.17	2.39 ± 0.17
L3	2.18 ± 0.14	2.24 ± 0.15
OPAL	2.00 ± 0.14	2.00 ± 0.14

Table 7.5: W width measurements ($\sqrt{s} = 172 - 209$ GeV) from the individual experiments. The column labelled “published” shows the results as published by the experiments, using their individual evaluations of FSI effects. The column labelled “LEP combination” shows the results of the experiments when propagating the LEP measurements of FSI effects to the W width.

for a total error of 83 MeV. The combination has a χ^2/dof of 37.4/33, corresponding to a probability of 27.3%.

7.7 Summary

The final results of the four LEP experiments on the mass and width of the W boson are combined taking into account correlated systematic uncertainties, with the result:

$$m_W = 80.376 \pm 0.033 \text{ GeV}, \quad (7.12)$$

$$\Gamma_W = 2.195 \pm 0.083 \text{ GeV}. \quad (7.13)$$

The correlations between mass and width are found to be less than 5% and thus negligible. These values correspond to the theoretical definition of a W-boson propagator with s -dependent width. The results of the mass and width determined by the LEP collaborations are in good agreement with the measurements at hadron colliders [239, 240, 241, 242]. Updated constraints on SM parameters using the mass and width results are presented in Appendix F.

LEP W-Boson Mass

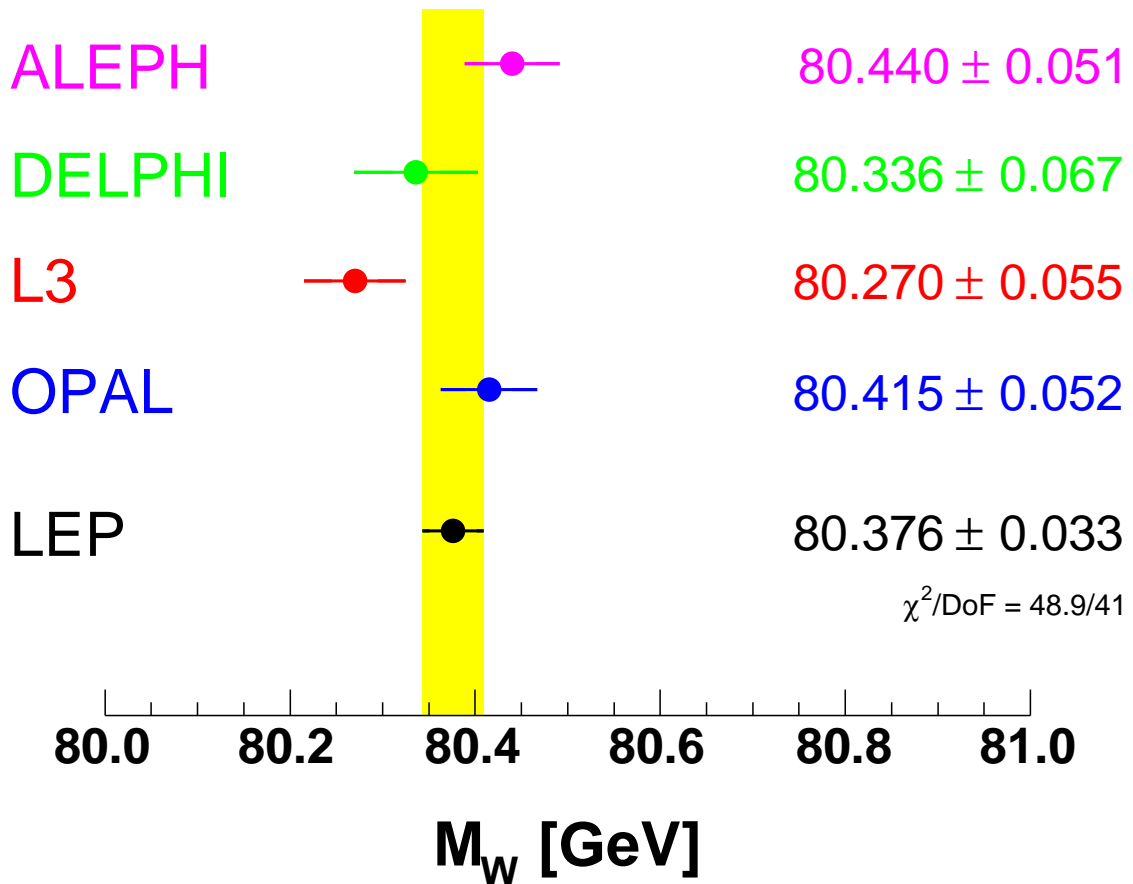


Figure 7.1: The measurements of the W-boson mass obtained by the four LEP collaborations (as published) together with the LEP combined result. The combined value includes correlations between experiments, between different energy points, and between the $q\bar{q}\ell\nu_\ell$ and $q\bar{q}q\bar{q}$ channels. A revised estimation of systematic uncertainties due to colour reconnection and Bose-Einstein correlations is applied to the input of the individual measurements to the LEP combined results in order to take the direct determination of FSI parameters into account.

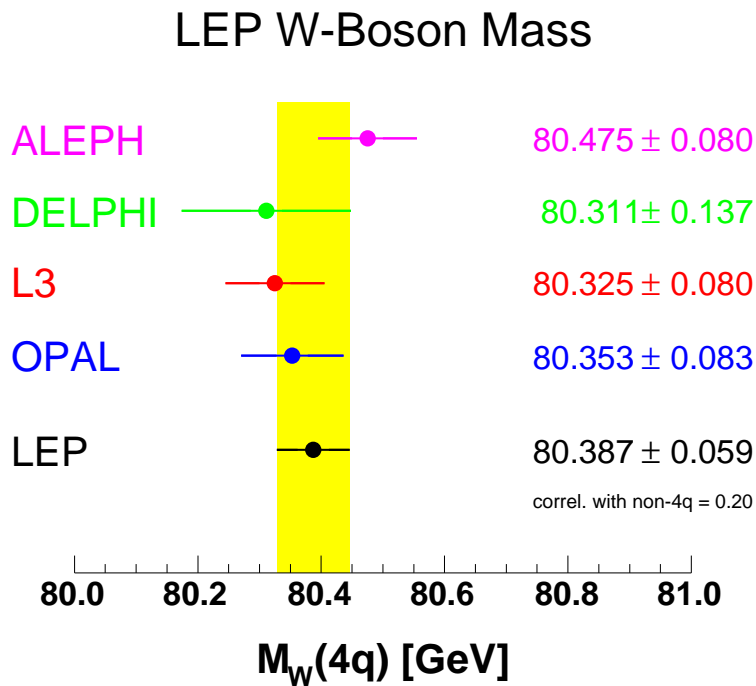
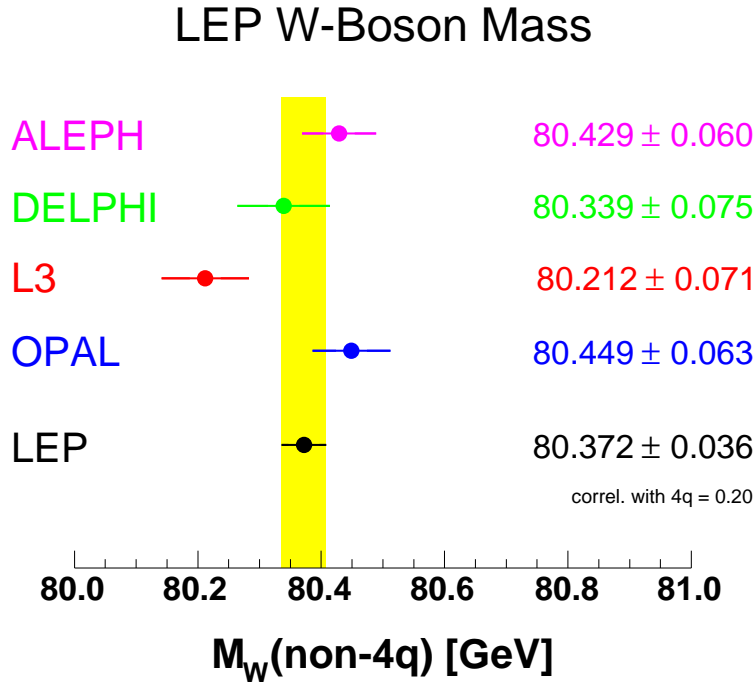


Figure 7.2: The W mass measurements in the $W^+W^- \rightarrow q\bar{q}\ell\nu_\ell$ channels (top), and the $W^+W^- \rightarrow q\bar{q}q\bar{q}$ channel (bottom) obtained by the four LEP collaborations (as published) compared to the combined value. Correlations between experiments and between measurements at different energy points are properly taken into account. The combined non-4q and 4q results are correlated since they are obtained from a fit to both channels taking into account inter-channel correlations. For the LEP combination, the assessment of systematic uncertainties due to colour reconnection and Bose-Einstein correlations for the individual measurements of the four experiments is revised with respect to the direct LEP measurements of FSI.

LEP W-Boson Width

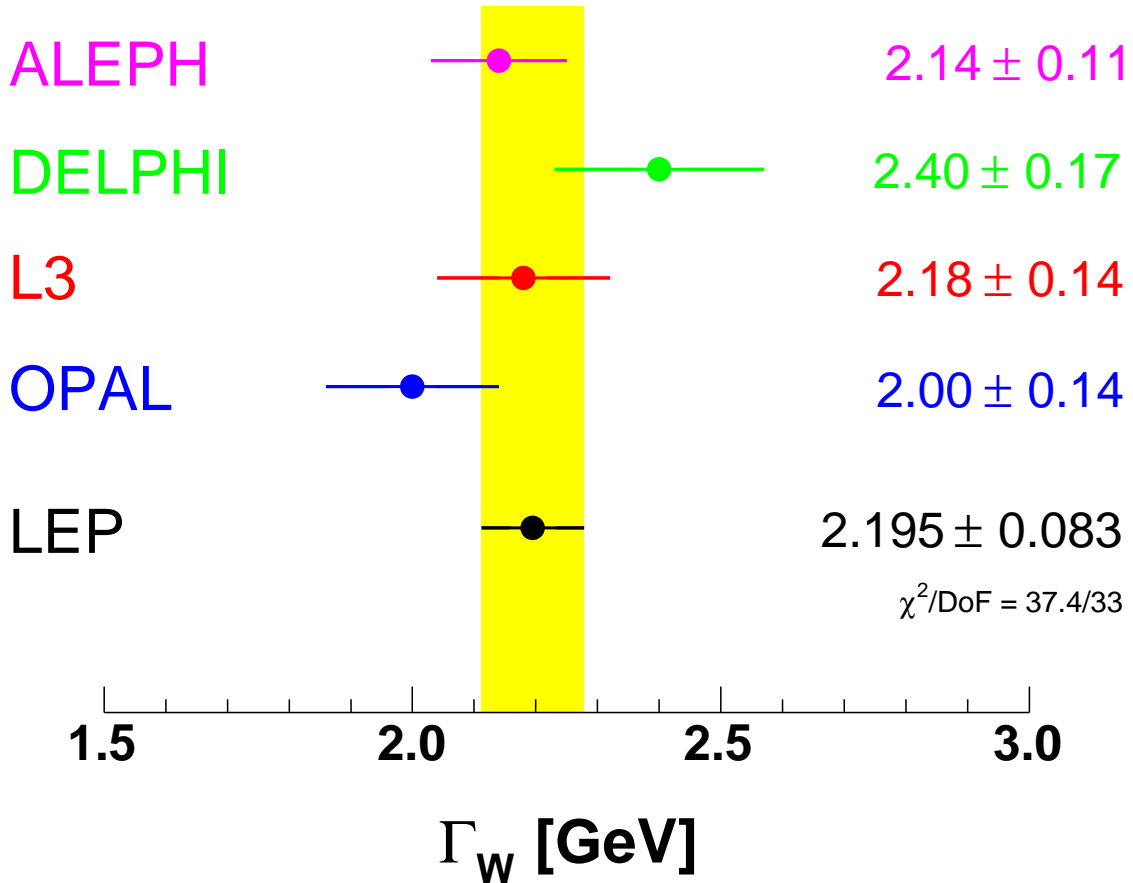


Figure 7.3: The measurements of the W-boson width obtained by the four LEP collaborations (as published) together with the LEP combined result. The combined value includes correlations between experiments, between different energy points, and between the $q\bar{q}\ell\nu_\ell$ and $q\bar{q}q\bar{q}$ channels. A revised estimation of systematic uncertainties due to colour reconnection and Bose-Einstein correlations is applied to the input of the individual measurements to the LEP combined results in order to take the direct determination of FSI parameters into account.

Chapter 8

Summary and Conclusions

The four LEP experiments ALEPH, DELPHI, L3 and OPAL performed measurements in electron-positron collisions at centre-of-mass energies above the mass of the Z boson, ranging from 130 GeV, crossing the W-pair production threshold at 160 GeV, up to 209 GeV. Based on about 0.75 fb^{-1} of luminosity collected by each experiment, yielding a total of 3 fb^{-1} , many precision measurements are summarised in this report.

The combinations of precise electroweak results yield stringent constraints on the Standard Model (SM) and its free parameters, for example:

$$\begin{aligned} m_W &= 80.376 \pm 0.033 \text{ GeV} \\ \Gamma_W &= 2.195 \pm 0.083 \text{ GeV} \\ B(W \rightarrow \text{had}) &= 67.41 \pm 0.27 \% \\ g_1^Z &= 0.984_{-0.020}^{+0.018} \\ \kappa_\gamma &= 0.982 \pm 0.042 \\ \lambda_\gamma &= -0.022 \pm 0.019. \end{aligned}$$

The results, together with measurements performed in electron-positron collisions at the Z-pole and in hadron collider experiments, test the SM with unprecedented precision at the highest interaction energies. The measurements agree well with the SM predictions.

Overall, the SM is verified to be a good theory up to the 200 GeV scale, see also the studies presented in Appendix F. The data impose very tight constraints on any new physics beyond the SM, and are well compatible with a 125 – 126 GeV SM Higgs boson [260]. Any extended theory must be consistent with the SM or one or more Higgs doublet models such as super-symmetry.

Acknowledgements

We would like to thank the CERN accelerator divisions for the efficient operation of the LEP accelerator, the precise information on the beam energy scale and their close cooperation with the four experiments. We would also like to thank members of the SLD, CDF, DØ, NuTeV and E-158 collaborations for making results available to us and for useful discussions concerning their combination. Finally, the results and their interpretation within the SM would not have been possible without the close collaboration of many theorists.

Appendix A

S-Matrix

A.1 Introduction

The S-Matrix ansatz provides a coherent way of describing the measurements of the cross-section and forward-backward asymmetries in s -channel $e^+e^- \rightarrow f\bar{f}$ processes at centre-of-mass energies around the Z resonance and the measurements at centre-of-mass energies from 130 GeV to 209 GeV from the LEP-II program. This chapter describes the combination of results from the full LEP-I data sets of the four LEP experiments, to obtain a LEP combined result on the parameters of the S-Matrix ansatz describing the Z lineshape.

The standard description of the measurements at the Z resonance [4] makes use of nine parameters ($m_Z, \Gamma_Z, \sigma_{\text{had}}^0, R_\ell^0, A_{\text{FB}}^{0,\ell}$, for $\ell = e, \mu, \tau$) which are reduced to five in case lepton universality is assumed. The S-Matrix formalism utilises an extra three parameters (assuming lepton universality) or seven parameters (not assuming lepton universality). The additional parameters describe the contributions to the cross-sections and forward-backward asymmetries of the interference between the exchange of a Z and a photon. The Z-pole data alone cannot tightly constrain these interference terms, in particular the interference term for cross-sections, since their contributions are small around the Z resonance and change sign at the pole. Owing to strong correlations between the size of the hadronic cross-section interference term and the mass of the Z, this leads to a larger error on the extracted mass of the Z compared to the standard five and nine parameter analyses where the hadronic interference term is fixed to the value predicted in the Standard Model (SM). However, using the LEP-II data leads to a significant improvement in the constraints on the interference terms and a corresponding reduction in the uncertainty on the mass of the Z, expected to result in a measurement of m_Z which is almost as precise but without having to constrain the γ/Z interference to the SM prediction.

The LEP combination is a two-step procedure: first a combination of the LEP-I based results, and then including the LEP-II data. For the LEP-I data, an average of the individual experiments' results on the S-Matrix parameters is made. Such a combination at parameter level, similar to the method used to combine the Z lineshape results in terms of the five and nine parameters [4], is presented here. To include the LEP-II data, a fit of the S-Matrix parameters to the combined LEP-II measurements of cross-sections and asymmetries as presented in Chapter 3 is envisaged, including in the χ^2 the LEP-I based combination of S-Matrix parameters with uncertainties and correlations as additional constraints.¹

¹Based on preliminary LEP measurements, Reference [262] contains a partial LEP-I+LEP-II combination along these lines, which shows the vast improvement made possible by including the LEP-II measurements.

In Section A.2 the parameters of the S-Matrix ansatz are explained in detail. In Section A.3 the average of the LEP-I data is described, preparing for the inclusion of the LEP-II measurements in the future. The results are discussed in Section A.4 while the detailed combination tables are listed in Section A.5.

A.2 The S-Matrix Ansatz

The S-Matrix ansatz [263] is a rigorous approach to describe the cross-sections and forward-backward asymmetries in s -channel e^+e^- annihilations under the basic assumption that the processes can be parametrised as the exchange of a massless and a massive vector boson, in which the couplings of the bosons including their interference are treated as free and independent parameters. In this model, the cross-sections are parametrised as follows:

$$\sigma_{\text{tot},f}^0(s) = \frac{4}{3}\pi\alpha^2 \left[\frac{g_f^{\text{tot}}}{s} + \frac{j_f^{\text{tot}}(s - \overline{m}_Z^2) + r_f^{\text{tot}} s}{(s - \overline{m}_Z^2)^2 + \overline{m}_Z^2 \overline{\Gamma}_Z^2} \right] \quad \text{with } f = \text{had}, e, \mu, \tau, \quad (\text{A.1})$$

while the forward-backward asymmetries are given by:

$$A_{\text{fb},f}^0(s) = \pi\alpha^2 \left[\frac{g_f^{\text{fb}}}{s} + \frac{j_f^{\text{fb}}(s - \overline{m}_Z^2) + r_f^{\text{fb}} s}{(s - \overline{m}_Z^2)^2 + \overline{m}_Z^2 \overline{\Gamma}_Z^2} \right] / \sigma_{\text{tot},f}^0(s), \quad (\text{A.2})$$

where \sqrt{s} is the centre-of-mass energy. The parameters r_f and j_f scale the Z exchange and the γ/Z interference contributions to the total cross-section and forward-backward asymmetries. The contribution g_f of the pure γ exchange is fixed to the value predicted by QED. Neither the hadronic charge asymmetry nor the flavour-tagged quark forward-backward asymmetries are considered here, which leaves 16 S-Matrix parameters to describe the LEP data: the mass and total width of the Z resonance, and 14 r_f and j_f parameters. Applying the constraint of neutral-current lepton universality reduces the number of parameters from 16 to 8.

In the SM the Z exchange term, the γ/Z interference term and the photon exchange term are given in terms of the fermion charges and their effective vector and axial-vector couplings to the Z by:

$$r_f^{\text{tot}} = \kappa^2 \left[g_{Ae}^2 + g_{Ve}^2 \right] \left[g_{Af}^2 + g_{Vf}^2 \right] - 2\kappa g_{Ve} g_{Vf} C_{Im} \quad (\text{A.3})$$

$$j_f^{\text{tot}} = 2\kappa g_{Ve} g_{Vf} (C_{Re} + C_{Im}) \quad (\text{A.4})$$

$$g_f^{\text{tot}} = Q_e^2 Q_f^2 \left| F_A(m_Z) \right|^2 \quad (\text{A.5})$$

$$r_f^{\text{fb}} = 4\kappa^2 g_{Ae} g_{Ve} g_{Af} g_{Vf} - 2\kappa g_{Ae} g_{Af} C_{Im} \quad (\text{A.6})$$

$$j_f^{\text{fb}} = 2\kappa g_{Ae} g_{Af} (C_{Re} + C_{Im}) \quad (\text{A.7})$$

$$g_f^{\text{fb}} = 0, \quad (\text{A.8})$$

with the following definitions:

$$\kappa = \frac{G_F m_Z^2}{2\sqrt{2}\pi\alpha} \approx 1.50 \quad (\text{A.9})$$

$$C_{Im} = \frac{\Gamma_Z}{m_Z} Q_e Q_f \text{Im} \{F_A(m_Z)\} \quad (\text{A.10})$$

$$C_{Re} = Q_e Q_f \text{Re} \{F_A(m_Z)\} \quad (\text{A.11})$$

$$F_A(m_Z) = \frac{\alpha(m_Z)}{\alpha}, \quad (\text{A.12})$$

where $\alpha(m_Z)$ is the complex fine-structure constant, and $\alpha \equiv \alpha(0)$. The expressions of the S-Matrix parameters in terms of the effective vector and axial-vector couplings given above neglect the imaginary parts of the effective couplings. The photonic virtual and bremsstrahlung corrections are included through the convolution of Equations A.1 and A.2 with the same radiator functions as used in the five and nine parameter Z-lineshape fits [4].

In the S-Matrix framework, the parameters mass (\bar{m}_Z) and total width ($\bar{\Gamma}_Z$) of the Z boson are defined in terms of a relativistic Breit-Wigner with s -independent width. These definitions are related to the usual definitions of the mass m_Z and width Γ_Z of a Breit-Wigner resonance with s -dependent width, used in [4], as follows:

$$m_Z \equiv \bar{m}_Z \sqrt{1 + \bar{\Gamma}_Z^2 / \bar{m}_Z^2} \approx \bar{m}_Z + 34.20 \text{ MeV}, \quad (\text{A.13})$$

$$\Gamma_Z \equiv \bar{\Gamma}_Z \sqrt{1 + \bar{\Gamma}_Z^2 / \bar{m}_Z^2} \approx \bar{\Gamma}_Z + 0.94 \text{ MeV}. \quad (\text{A.14})$$

The predictions of the S-Matrix ansatz for cross-sections and asymmetries are calculated using SMATASY [267], which in turn uses ZFITTER [36] to calculate the QED convolution of the electroweak kernel. In case of the e^+e^- final state, t -channel and s/t interference contributions are added to the s -channel ansatz [4].

A.3 LEP-I Combination

The LEP experiments have determined the 16 S-Matrix parameters using their full LEP-I data set [268, 269, 270, 271]. These results are averaged using the BLUE technique [62]. Sources of systematic uncertainty correlated between the experiments have been investigated using techniques described in Reference [4] and are accounted for in the averaging procedure.

The main problem in the combination is the proper treatment of the common systematic uncertainties. The LEP experiments provide their results in terms of the standard S-Matrix parametrisation. This parameter set is not well suited for the determination of common systematic uncertainties since common errors such as the theory error for luminosity affect many parameters. Using a transformed parameter set, which is defined as similar as possible to the standard LEP nine parameter set, facilitates the study of common systematic errors as well as cross checks with the LEP nine-parameter combination [4]. The experiments' results are transformed to this parameter set, combined, and the final results transformed back to the standard S-Matrix parameter set. The transformed S-Matrix parameters are defined as follows:

$$S_{\text{had}} \equiv \frac{r_{\text{had}}^{\text{tot}}}{\Gamma_Z^2} \quad (\text{A.15})$$

$$R_e^{\text{smx}} \equiv \frac{r_{\text{had}}^{\text{tot}}}{r_e^{\text{tot}}} \quad (\text{A.16})$$

$$R_\mu^{\text{smx}} \equiv \frac{r_{\text{had}}^{\text{tot}}}{r_\mu^{\text{tot}}} \quad (\text{A.17})$$

$$R_\tau^{\text{smx}} \equiv \frac{r_{\text{had}}^{\text{tot}}}{r_\tau^{\text{tot}}} \quad (\text{A.18})$$

$$A_{\text{FB}}^{\text{smx},e} \equiv \frac{3 r_e^{\text{fb}}}{4 r_e^{\text{tot}}} \quad (\text{A.19})$$

$$A_{\text{FB}}^{\text{smx},\mu} \equiv \frac{3 r_\mu^{\text{fb}}}{4 r_\mu^{\text{tot}}} \quad (\text{A.20})$$

$$A_{\text{FB}}^{\text{smx},\tau} \equiv \frac{3 r_\tau^{\text{fb}}}{4 r_\tau^{\text{tot}}} \quad (\text{A.21})$$

Table A.1 gives the input of the four LEP experiments for the 16 transformed S-Matrix parameters. The corresponding correlation matrices are given in Tables A.8, A.9, A.10 and A.11.

Table A.2 shows the common systematic uncertainty of the transformed S-Matrix parameters due to the uncertainties in the LEP centre-of-mass energy. The parameters m_Z and $j_{\text{had}}^{\text{tot}}$ are the most sensitive of all 16 S-Matrix parameters to the inclusion of the LEP-II data, and are also the most interesting ones in comparison to the five and nine parameter fits. For these parameters the most significant source of systematic error correlated between experiments arises from the uncertainty on the e^+e^- centre-of-mass energy. These errors amount to ± 3.2 MeV on m_Z and ± 0.16 on $j_{\text{had}}^{\text{tot}}$, with a correlation coefficient of -0.86 . Table A.3 specifies the common uncertainties due to theoretical uncertainties in the calculation of the t -channel contributions for Bhabha scattering. In this case the determination of the common error was complicated by the fact that the experiments choose different procedures for the t -channel correction, which yield different common errors. We used the common t -channel errors as determined by ALEPH [4] as basis for the combination since these result in the smallest common errors. As a cross-check the combination was repeated with common t -channel errors based on OPAL's analysis which yields the largest common errors. The effect on the combined result is small, the shift of central values is below 20% of its uncertainty. In this parametrisation, the luminosity theory uncertainty affects only the parameter S_{had} . The uncertainties are 0.061% for ALEPH, DELPHI and L3, and 0.054% for OPAL.

The result of the LEP-I combination in terms of the transformed S-Matrix parameters is listed in Table A.4, Table A.5 shows the corresponding correlation matrix. Transforming this result back to the standard S-Matrix parameter set, the combination is reported in Tables A.6 and A.7. The χ^2/dof for the average of all 16 parameters is 59.8/48, corresponding to a probability of 12%.

A.4 Discussion

In the LEP-I combination the measured values of the Z boson mass $m_Z = 91.1929 \pm 0.0059$ GeV agrees well with the results of the standard nine parameter fit, 91.1876 ± 0.0021 GeV, albeit

with a significantly larger error, resulting from the correlation with the large uncertainty on $j_{\text{had}}^{\text{tot}}$. This uncertainty is the dominant source of uncertainty on m_Z in the S-Matrix fits. The measured value of $j_{\text{had}}^{\text{tot}} = -0.10 \pm 0.33$ also agrees with the prediction of the SM, $0.2201_{-0.0137}^{+0.0032}$.

Parameter	ALEPH	DELPHI	L3	OPAL
m_Z (GeV)	91.2143 ± 0.0120	91.1939 ± 0.0112	91.1893 ± 0.0112	91.1903 ± 0.0114
Γ_Z (GeV)	2.4900 ± 0.0052	2.4861 ± 0.0048	2.5028 ± 0.0046	2.4935 ± 0.0047
S_{had}	0.47736 ± 0.00068	0.47713 ± 0.00080	0.47660 ± 0.00063	0.47629 ± 0.00064
$j_{\text{had}}^{\text{tot}}$	-1.2618 ± 0.6500	-0.2067 ± 0.6364	0.2109 ± 0.6370	0.0017 ± 0.6419
R_e^{smx}	20.8010 ± 0.0830	20.9270 ± 0.1200	20.8528 ± 0.0977	20.9718 ± 0.0945
R_μ^{smx}	20.8360 ± 0.0580	20.6600 ± 0.0773	20.8790 ± 0.0982	20.8484 ± 0.0589
R_τ^{smx}	20.6860 ± 0.0640	20.8250 ± 0.1277	20.7546 ± 0.1339	20.8255 ± 0.0918
j_e^{tot}	-0.0531 ± 0.0500	-0.0939 ± 0.0750	-0.0293 ± 0.0542	-0.0856 ± 0.0528
j_μ^{tot}	-0.0646 ± 0.0430	0.0561 ± 0.0421	0.0355 ± 0.0459	-0.0131 ± 0.0415
j_τ^{tot}	-0.0449 ± 0.0440	0.0040 ± 0.0464	0.0729 ± 0.0476	-0.0073 ± 0.0442
$A_{\text{FB}}^{\text{smx},e}$	0.0164 ± 0.0034	0.0163 ± 0.0048	0.0091 ± 0.0059	0.0071 ± 0.0046
$A_{\text{FB}}^{\text{smx},\mu}$	0.0178 ± 0.0027	0.0145 ± 0.0026	0.0179 ± 0.0034	0.0140 ± 0.0024
$A_{\text{FB}}^{\text{smx},\tau}$	0.0180 ± 0.0030	0.0215 ± 0.0038	0.0238 ± 0.0049	0.0126 ± 0.0031
j_e^{fb}	0.8599 ± 0.0570	0.8021 ± 0.0748	0.6983 ± 0.0797	0.7640 ± 0.0715
j_μ^{fb}	0.8196 ± 0.0400	0.7110 ± 0.0366	0.8192 ± 0.0474	0.7319 ± 0.0363
j_τ^{fb}	0.8481 ± 0.0430	0.7070 ± 0.0472	0.7536 ± 0.0550	0.7394 ± 0.0420

Table A.1: Transformed LEP-I S-Matrix input parameters of the four LEP experiments

Parameters										
	1	2	3	4	5	8	9	10	11	14
	m_Z	Γ_Z	S_{had}	$j_{\text{had}}^{\text{tot}}$	R_e^{smx}	j_e^{tot}	j_μ^{tot}	j_τ^{tot}	$A_{\text{FB}}^{\text{smx},e}$	j_e^{fb}
1	3.2e-03	-1.4e-03	1.2e-04	-2.1e-02	5.1e-03	-4.4e-03	-4.4e-03	-4.5e-03	-8.3e-04	1.3e-03
2	-1.4e-03	1.4e-03	-3.2e-04	9.2e-03	-3.0e-03	1.8e-03	2.0e-03	2.0e-03	4.4e-04	-6.9e-04
3	1.2e-04	-3.2e-04	1.3e-04	-1.2e-03	9.7e-04	8.4e-05	-2.2e-04	-2.5e-04	-1.2e-04	2.0e-04
4	-2.1e-02	9.2e-03	-1.2e-03	1.6e-01	-3.6e-02	3.3e-02	3.3e-02	3.4e-02	5.7e-03	-9.3e-03
5	5.1e-03	-3.0e-03	9.7e-04	-3.6e-02	1.6e-02	-7.3e-03	-7.5e-03	-7.6e-03	-2.6e-03	3.5e-03
8	-4.4e-03	1.8e-03	8.4e-05	3.3e-02	-7.3e-03	7.0e-03	7.1e-03	7.2e-03	1.2e-03	-1.8e-03
9	-4.4e-03	2.0e-03	-2.2e-04	3.3e-02	-7.5e-03	7.1e-03	7.0e-03	7.2e-03	1.2e-03	-2.0e-03
10	-4.5e-03	2.0e-03	-2.5e-04	3.4e-02	-7.6e-03	7.2e-03	7.2e-03	7.3e-03	1.2e-03	-2.0e-03
11	-8.3e-04	4.4e-04	-1.2e-04	5.7e-03	-2.6e-03	1.2e-03	1.2e-03	1.2e-03	4.3e-04	-5.4e-04
14	1.3e-03	-6.9e-04	2.0e-04	-9.3e-03	3.5e-03	-1.8e-03	-2.0e-03	-2.0e-03	-5.4e-04	1.4e-03

Table A.2: Signed square-root of LEP-I covariance matrix for common energy errors

Parameters	5	8	11	14
5 R_e^{smx}	2.4e-02	-3.20e-03	-5.00e-03	-3.20e-03
8 j_e^{tot}	-3.20e-03	0.89e-02	0.00000	0.99e-02
11 $A_{\text{FB}}^{\text{smx,e}}$	-5.00e-03	0.00000	1.00e-03	-0.32e-03
14 j_e^{fb}	-3.20e-03	0.99e-02	-0.32e-03	1.10e-02

Table A.3: Signed square-root of LEP-I covariance matrix for common t -channel errors

Parameter	LEP-I
m_Z (GeV)	91.1929 ± 0.0059
Γ_Z (GeV)	2.4940 ± 0.0026
S_{had}	0.47676 ± 0.00043
$j_{\text{had}}^{\text{tot}}$	-0.10 ± 0.33
R_e^{smx}	20.865 ± 0.052
R_μ^{smx}	20.811 ± 0.034
R_τ^{smx}	20.746 ± 0.045
j_e^{tot}	-0.054 ± 0.029
j_μ^{tot}	0.013 ± 0.022
j_τ^{tot}	0.014 ± 0.023
$A_{\text{FB}}^{\text{smx,e}}$	0.0132 ± 0.0023
$A_{\text{FB}}^{\text{smx},\mu}$	0.0153 ± 0.0014
$A_{\text{FB}}^{\text{smx},\tau}$	0.0170 ± 0.0017
j_e^{fb}	0.792 ± 0.037
j_μ^{fb}	0.763 ± 0.020
j_τ^{fb}	0.766 ± 0.023
χ^2/dof	$59.96/48$

Table A.4: LEP-I combination result for transformed S-Matrix parameters

Parameters																
	1	2	3	4	5	6	7	8	9	10	11	12	13	14	15	16
	m_Z	Γ_Z	S_{had}	$j_{\text{had}}^{\text{tot}}$	R_e^{smx}	R_μ^{smx}	R_τ^{smx}	j_e^{tot}	j_μ^{tot}	j_τ^{tot}	$A_{\text{FB}}^{\text{smx},e}$	$A_{\text{FB}}^{\text{smx},\mu}$	$A_{\text{FB}}^{\text{smx},\tau}$	j_e^{fb}	j_μ^{fb}	j_τ^{fb}
1	1.000	-0.435	0.083	-0.936	0.330	-0.007	-0.006	-0.597	-0.665	-0.630	-0.128	0.221	0.182	-0.009	-0.006	0.005
2	-0.435	1.000	-0.307	0.442	-0.164	0.006	0.004	0.254	0.319	0.301	0.062	-0.096	-0.079	0.011	0.041	0.030
3	0.083	-0.307	1.000	-0.081	0.134	0.130	0.093	-0.056	-0.065	-0.063	-0.013	0.026	0.022	-0.003	-0.004	-0.002
4	-0.936	0.442	-0.081	1.000	-0.317	0.014	0.011	0.604	0.679	0.645	0.121	-0.221	-0.182	0.010	0.007	-0.004
5	0.330	-0.164	0.134	-0.317	1.000	0.053	0.035	-0.276	-0.228	-0.215	-0.407	0.082	0.067	-0.020	-0.002	0.002
6	-0.007	0.006	0.130	0.014	0.053	1.000	0.059	0.005	-0.128	0.005	0.002	-0.008	-0.002	-0.000	-0.045	-0.000
7	-0.006	0.004	0.093	0.011	0.035	0.059	1.000	0.005	0.005	-0.109	0.002	-0.002	0.000	0.000	-0.000	-0.057
8	-0.597	0.254	-0.056	0.604	-0.276	0.005	0.005	1.000	0.433	0.408	0.084	-0.148	-0.123	0.221	0.003	-0.004
9	-0.665	0.319	-0.065	0.679	-0.228	-0.128	0.005	0.433	1.000	0.460	0.086	-0.137	-0.131	0.007	-0.034	-0.003
10	-0.630	0.301	-0.063	0.645	-0.215	0.005	-0.109	0.408	0.460	1.000	0.081	-0.150	-0.107	0.007	0.005	-0.046
11	-0.128	0.062	-0.013	0.121	-0.407	0.002	0.002	0.084	0.086	0.081	1.000	-0.024	-0.019	0.092	0.001	-0.001
12	0.221	-0.096	0.026	-0.221	0.082	-0.008	-0.002	-0.148	-0.137	-0.150	-0.024	1.000	0.061	-0.005	0.198	0.002
13	0.182	-0.079	0.022	-0.182	0.067	-0.002	0.000	-0.123	-0.131	-0.107	-0.019	0.061	1.000	-0.004	-0.001	0.181
14	-0.009	0.011	-0.003	0.010	-0.020	-0.000	0.000	0.221	0.007	0.007	0.092	-0.005	-0.004	1.000	0.001	0.000
15	-0.006	0.041	-0.004	0.007	-0.002	-0.045	-0.000	0.003	-0.034	0.005	0.001	0.198	-0.001	0.001	1.000	0.002
16	0.005	0.030	-0.002	-0.004	0.002	-0.000	-0.057	-0.004	-0.003	-0.046	-0.001	0.002	0.181	0.000	0.002	1.000

Table A.5: Correlation matrix for transformed LEP-I S-Matrix parameters

Parameter	LEP-I
m_Z (GeV)	91.1929 ± 0.0059
Γ_Z (GeV)	2.4940 ± 0.0026
$r_{\text{had}}^{\text{tot}}$	2.9654 ± 0.0060
$j_{\text{had}}^{\text{tot}}$	-0.10 ± 0.33
r_e^{tot}	0.14214 ± 0.00049
r_μ^{tot}	0.14249 ± 0.00036
r_τ^{tot}	0.14294 ± 0.00042
j_e^{tot}	-0.054 ± 0.029
j_μ^{tot}	0.013 ± 0.022
j_τ^{tot}	0.014 ± 0.023
r_e^{fb}	0.00251 ± 0.00045
r_μ^{fb}	0.00291 ± 0.00026
r_τ^{fb}	0.00324 ± 0.00033
j_e^{fb}	0.792 ± 0.036
j_μ^{fb}	0.763 ± 0.020
j_τ^{fb}	0.766 ± 0.023
χ^2/dof	$59.84/48$

Table A.6: LEP-I combination result for standard S-Matrix parameters

Parameters																
	1	2	3	4	5	6	7	8	9	10	11	12	13	14	15	16
	m_Z	Γ_Z	$r_{\text{had}}^{\text{tot}}$	$j_{\text{had}}^{\text{tot}}$	r_e^{tot}	r_μ^{tot}	r_τ^{tot}	j_e^{tot}	j_μ^{tot}	j_τ^{tot}	r_e^{fb}	r_μ^{fb}	r_τ^{fb}	j_e^{fb}	j_μ^{fb}	j_τ^{fb}
1	1.000	-0.434	-0.416	-0.936	-0.493	-0.330	-0.285	-0.597	-0.664	-0.630	-0.138	0.212	0.174	-0.008	-0.006	0.005
2	-0.434	1.000	0.905	0.441	0.660	0.725	0.628	0.254	0.319	0.300	0.076	-0.075	-0.060	0.012	0.041	0.030
3	-0.416	0.905	1.000	0.424	0.678	0.764	0.663	0.240	0.303	0.285	0.073	-0.066	-0.053	0.011	0.041	0.031
4	-0.936	0.441	0.424	1.000	0.488	0.332	0.287	0.605	0.678	0.645	0.131	-0.212	-0.174	0.009	0.007	-0.004
5	-0.493	0.660	0.678	0.488	1.000	0.546	0.472	0.347	0.349	0.329	0.356	-0.098	-0.079	0.022	0.026	0.017
6	-0.330	0.725	0.764	0.332	0.546	1.000	0.534	0.190	0.327	0.226	0.058	-0.037	-0.041	0.009	0.062	0.025
7	-0.285	0.628	0.663	0.287	0.472	0.534	1.000	0.163	0.207	0.280	0.049	-0.045	-0.021	0.007	0.028	0.064
8	-0.597	0.254	0.240	0.605	0.347	0.190	0.163	1.000	0.433	0.408	0.091	-0.143	-0.118	0.219	0.003	-0.004
9	-0.664	0.319	0.303	0.678	0.349	0.327	0.207	0.433	1.000	0.460	0.093	-0.128	-0.125	0.007	-0.034	-0.003
10	-0.630	0.300	0.285	0.645	0.329	0.226	0.280	0.408	0.460	1.000	0.087	-0.143	-0.099	0.007	0.005	-0.046
11	-0.138	0.076	0.073	0.131	0.356	0.058	0.049	0.091	0.093	0.087	1.000	-0.025	-0.020	0.093	0.001	-0.000
12	0.212	-0.075	-0.066	-0.212	-0.098	-0.037	-0.045	-0.143	-0.128	-0.143	-0.025	1.000	0.059	-0.005	0.200	0.003
13	0.174	-0.060	-0.053	-0.174	-0.079	-0.041	-0.021	-0.118	-0.125	-0.099	-0.020	0.059	1.000	-0.004	0.000	0.183
14	-0.008	0.012	0.011	0.009	0.022	0.009	0.007	0.219	0.007	0.007	0.093	-0.005	-0.004	1.000	0.001	0.000
15	-0.006	0.041	0.041	0.007	0.026	0.062	0.028	0.003	-0.034	0.005	0.001	0.200	0.000	0.001	1.000	0.002
16	0.005	0.030	0.031	-0.004	0.017	0.025	0.064	-0.004	-0.003	-0.046	-0.000	0.003	0.183	0.000	0.002	1.000

Table A.7: Correlation matrix for standard LEP-I S-Matrix parameters

A.5 S-Matrix Combination Tables

See Tables A.8–A.11.

		Parameters															
	1	2	3	4	5	6	7	8	9	10	11	12	13	14	15	16	
	m_Z	Γ_Z	S_{had}	$j_{\text{had}}^{\text{tot}}$	R_e^{smx}	R_μ^{smx}	R_τ^{smx}	j_e^{tot}	j_μ^{tot}	j_τ^{tot}	$A_{\text{FB}}^{\text{smx},e}$	$A_{\text{FB}}^{\text{smx},\mu}$	$A_{\text{FB}}^{\text{smx},\tau}$	j_e^{fb}	j_μ^{fb}	j_τ^{fb}	
1	1.000	-0.537	0.243	-0.963	0.449	-0.004	-0.015	-0.592	-0.685	-0.676	-0.209	0.313	0.296	0.005	-0.023	0.003	
2	-0.537	1.000	-0.436	0.547	-0.234	0.008	0.008	0.324	0.391	0.385	0.106	-0.169	-0.160	0.014	0.056	0.040	
3	0.243	-0.436	1.000	-0.225	0.219	0.160	0.143	-0.144	-0.171	-0.168	-0.041	0.087	0.082	0.000	-0.012	-0.005	
4	-0.963	0.547	-0.225	1.000	-0.426	0.011	0.021	0.593	0.685	0.676	0.197	-0.307	-0.290	-0.003	0.024	-0.002	
5	0.449	-0.234	0.219	-0.426	1.000	0.070	0.051	-0.400	-0.307	-0.301	-0.413	0.139	0.131	-0.047	-0.011	0.001	
6	-0.004	0.008	0.160	0.011	0.070	1.000	0.089	0.002	-0.171	0.003	0.001	-0.008	-0.001	-0.001	-0.036	0.000	
7	-0.015	0.008	0.143	0.021	0.051	0.089	1.000	0.011	0.011	-0.142	0.003	-0.005	-0.007	0.000	0.000	-0.038	
8	-0.592	0.324	-0.144	0.593	-0.400	0.002	0.011	1.000	0.422	0.411	0.133	-0.189	-0.179	0.159	0.014	-0.002	
9	-0.685	0.391	-0.171	0.685	-0.307	-0.171	0.011	0.422	1.000	0.481	0.141	-0.198	-0.206	-0.002	-0.015	-0.002	
10	-0.676	0.385	-0.168	0.676	-0.301	0.003	-0.142	0.411	0.481	1.000	0.139	-0.215	-0.193	-0.002	0.017	-0.050	
11	-0.209	0.106	-0.041	0.197	-0.413	0.001	0.003	0.133	0.141	0.139	1.000	-0.055	-0.053	0.159	0.005	0.000	
12	0.313	-0.169	0.087	-0.307	0.139	-0.008	-0.005	-0.189	-0.198	-0.215	-0.055	1.000	0.105	0.000	0.231	0.002	
13	0.296	-0.160	0.082	-0.290	0.131	-0.001	-0.007	-0.179	-0.206	-0.193	-0.053	0.105	1.000	0.000	-0.006	0.202	
14	0.005	0.014	0.000	-0.003	-0.047	-0.001	0.000	0.159	-0.002	-0.002	0.159	0.000	0.000	1.000	0.001	0.001	
15	-0.023	0.056	-0.012	0.024	-0.011	-0.036	0.000	0.014	-0.015	0.017	0.005	0.231	-0.006	0.001	1.000	0.003	
16	0.003	0.040	-0.005	-0.002	0.001	0.000	-0.038	-0.002	-0.002	-0.050	0.000	0.002	0.202	0.001	0.003	1.000	

Table A.8: Correlation matrix of transformed LEP-I S-Matrix input parameters for ALEPH.

		Parameters															
	1	2	3	4	5	6	7	8	9	10	11	12	13	14	15	16	
	m_Z	Γ_Z	S_{had}	$j_{\text{had}}^{\text{tot}}$	R_e^{smx}	R_μ^{smx}	R_τ^{smx}	j_e^{tot}	j_μ^{tot}	j_τ^{tot}	$A_{\text{FB}}^{\text{smx},e}$	$A_{\text{FB}}^{\text{smx},\mu}$	$A_{\text{FB}}^{\text{smx},\tau}$	j_e^{fb}	j_μ^{fb}	j_τ^{fb}	
1	1.000	-0.504	0.123	-0.966	0.034	-0.030	0.002	-0.804	-0.702	-0.640	0.133	0.253	0.173	-0.029	-0.002	-0.003	
2	-0.504	1.000	-0.285	0.528	-0.018	0.008	-0.004	0.403	0.385	0.350	-0.069	-0.125	-0.086	0.040	0.043	0.034	
3	0.123	-0.285	1.000	-0.112	0.124	0.185	0.113	-0.098	-0.092	-0.085	0.018	0.033	0.022	-0.003	0.003	0.002	
4	-0.966	0.528	-0.112	1.000	-0.027	0.037	0.002	0.786	0.695	0.634	-0.131	-0.247	-0.169	0.030	0.004	0.005	
5	0.034	-0.018	0.124	-0.027	1.000	0.053	0.033	-0.061	-0.023	-0.021	-0.100	0.009	0.006	-0.066	-0.000	-0.000	
6	-0.030	0.008	0.185	0.037	0.053	1.000	0.051	0.025	-0.086	0.019	-0.005	-0.013	-0.006	0.001	-0.056	-0.000	
7	0.002	-0.004	0.113	0.002	0.033	0.051	1.000	-0.002	-0.001	-0.089	0.000	0.000	-0.002	-0.000	-0.000	-0.079	
8	-0.804	0.403	-0.098	0.786	-0.061	0.025	-0.002	1.000	0.571	0.521	-0.081	-0.205	-0.140	0.102	0.001	0.003	
9	-0.702	0.385	-0.092	0.695	-0.023	-0.086	-0.001	0.571	1.000	0.461	-0.095	-0.158	-0.123	0.022	-0.038	0.004	
10	-0.640	0.350	-0.085	0.634	-0.021	0.019	-0.089	0.521	0.461	1.000	-0.086	-0.164	-0.090	0.020	0.003	-0.035	
11	0.133	-0.069	0.018	-0.131	-0.100	-0.005	0.000	-0.081	-0.095	-0.086	1.000	0.044	0.029	0.087	0.001	-0.000	
12	0.253	-0.125	0.033	-0.247	0.009	-0.013	0.000	-0.205	-0.158	-0.164	0.044	1.000	0.053	-0.008	0.196	-0.000	
13	0.173	-0.086	0.022	-0.169	0.006	-0.006	-0.002	-0.140	-0.123	-0.090	0.029	0.053	1.000	-0.005	0.001	0.176	
14	-0.029	0.040	-0.003	0.030	-0.066	0.001	-0.000	0.102	0.022	0.020	0.087	-0.008	-0.005	1.000	0.002	0.001	
15	-0.002	0.043	0.003	0.004	-0.000	-0.056	-0.000	0.001	-0.038	0.003	0.001	0.196	0.001	0.002	1.000	0.002	
16	-0.003	0.034	0.002	0.005	-0.000	-0.000	-0.079	0.003	0.004	-0.035	-0.000	-0.000	0.176	0.001	0.002	1.000	

Table A.9: Correlation matrix of transformed LEP-I S-Matrix input parameters for DELPHI.

		Parameters															
	1	2	3	4	5	6	7	8	9	10	11	12	13	14	15	16	
	m_Z	Γ_Z	S_{had}	$j_{\text{had}}^{\text{tot}}$	R_e^{smx}	R_μ^{smx}	R_τ^{smx}	j_e^{tot}	j_μ^{tot}	j_τ^{tot}	$A_{\text{FB}}^{\text{smx},e}$	$A_{\text{FB}}^{\text{smx},\mu}$	$A_{\text{FB}}^{\text{smx},\tau}$	j_e^{fb}	j_μ^{fb}	j_τ^{fb}	
1	1.000	-0.378	0.024	-0.959	0.418	-0.010	-0.013	-0.528	-0.627	-0.600	-0.200	0.226	0.150	0.011	-0.006	0.008	
2	-0.378	1.000	-0.331	0.410	-0.165	0.002	0.006	0.196	0.271	0.262	0.076	-0.087	-0.057	-0.009	0.042	0.028	
3	0.024	-0.331	1.000	-0.020	0.076	0.079	0.055	-0.029	-0.025	-0.025	0.010	0.011	0.007	-0.008	-0.002	-0.001	
4	-0.959	0.410	-0.020	1.000	-0.403	0.015	0.017	0.528	0.627	0.600	0.195	-0.220	-0.146	-0.009	0.007	-0.006	
5	0.418	-0.165	0.076	-0.403	1.000	0.024	0.016	-0.274	-0.267	-0.256	-0.202	0.107	0.070	0.027	-0.003	0.003	
6	-0.010	0.002	0.079	0.015	0.024	1.000	0.021	0.006	-0.104	0.006	0.002	-0.007	-0.002	0.000	-0.068	-0.001	
7	-0.013	0.006	0.055	0.017	0.016	0.021	1.000	0.007	0.008	-0.078	0.002	-0.003	-0.004	0.000	-0.000	-0.080	
8	-0.528	0.196	-0.029	0.528	-0.274	0.006	0.007	1.000	0.346	0.331	0.097	-0.121	-0.080	0.166	0.002	-0.005	
9	-0.627	0.271	-0.025	0.627	-0.267	-0.104	0.008	0.346	1.000	0.393	0.127	-0.119	-0.096	-0.006	-0.041	-0.004	
10	-0.600	0.262	-0.025	0.600	-0.256	0.006	-0.078	0.331	0.393	1.000	0.122	-0.138	-0.075	-0.006	0.005	-0.039	
11	-0.200	0.076	0.010	0.195	-0.202	0.002	0.002	0.097	0.127	0.122	1.000	-0.051	-0.034	0.026	0.001	-0.002	
12	0.226	-0.087	0.011	-0.220	0.107	-0.007	-0.003	-0.121	-0.119	-0.138	-0.051	1.000	0.038	0.003	0.170	0.002	
13	0.150	-0.057	0.007	-0.146	0.070	-0.002	-0.004	-0.080	-0.096	-0.075	-0.034	0.038	1.000	0.002	-0.001	0.150	
14	0.011	-0.009	-0.008	-0.009	0.027	0.000	0.000	0.166	-0.006	-0.006	0.026	0.003	0.002	1.000	-0.001	-0.000	
15	-0.006	0.042	-0.002	0.007	-0.003	-0.068	-0.000	0.002	-0.041	0.005	0.001	0.170	-0.001	-0.001	1.000	0.002	
16	0.008	0.028	-0.001	-0.006	0.003	-0.001	-0.080	-0.005	-0.004	-0.039	-0.002	0.002	0.150	-0.000	0.002	1.000	

Table A.10: Correlation matrix of transformed LEP-I S-Matrix input parameters for L3.

Parameters																
	1	2	3	4	5	6	7	8	9	10	11	12	13	14	15	16
	m_Z	Γ_Z	S_{had}	$j_{\text{had}}^{\text{tot}}$	R_e^{smx}	R_μ^{smx}	R_τ^{smx}	j_e^{tot}	j_μ^{tot}	j_τ^{tot}	$A_{\text{FB}}^{\text{smx},e}$	$A_{\text{FB}}^{\text{smx},\mu}$	$A_{\text{FB}}^{\text{smx},\tau}$	j_e^{fb}	j_μ^{fb}	j_τ^{fb}
1	1.000	-0.446	0.120	-0.963	0.442	0.012	0.013	-0.525	-0.703	-0.651	-0.244	0.299	0.262	0.025	0.001	0.013
2	-0.446	1.000	-0.360	0.462	-0.194	0.008	0.001	0.224	0.338	0.315	0.110	-0.131	-0.114	-0.012	0.043	0.032
3	0.120	-0.360	1.000	-0.110	0.188	0.221	0.141	-0.067	-0.090	-0.084	-0.018	0.039	0.037	-0.002	-0.007	-0.004
4	-0.963	0.462	-0.110	1.000	-0.428	-0.005	-0.009	0.525	0.701	0.650	0.239	-0.293	-0.256	-0.024	0.000	-0.012
5	0.442	-0.194	0.188	-0.428	1.000	0.085	0.043	-0.278	-0.315	-0.292	-0.298	0.151	0.131	0.023	0.001	0.008
6	0.012	0.008	0.221	-0.005	0.085	1.000	0.056	-0.006	-0.133	-0.007	-0.004	-0.002	0.004	0.001	-0.037	0.002
7	0.013	0.001	0.141	-0.009	0.043	0.056	1.000	-0.008	-0.009	-0.100	-0.003	0.004	0.017	-0.000	0.001	-0.060
8	-0.525	0.224	-0.067	0.525	-0.278	-0.006	-0.008	1.000	0.383	0.354	0.125	-0.160	-0.140	0.218	-0.002	-0.008
9	-0.703	0.338	-0.090	0.701	-0.315	-0.133	-0.009	0.383	1.000	0.473	0.174	-0.193	-0.187	-0.017	-0.041	-0.009
10	-0.651	0.315	-0.084	0.650	-0.292	-0.007	-0.100	0.354	0.473	1.000	0.161	-0.198	-0.157	-0.016	0.001	-0.056
11	-0.244	0.110	-0.018	0.239	-0.298	-0.004	-0.003	0.125	0.174	0.161	1.000	-0.083	-0.072	0.056	-0.000	-0.004
12	0.299	-0.131	0.039	-0.293	0.151	-0.002	0.004	-0.160	-0.193	-0.198	-0.083	1.000	0.090	0.008	0.179	0.005
13	0.262	-0.114	0.037	-0.256	0.131	0.004	0.017	-0.140	-0.187	-0.157	-0.072	0.090	1.000	0.007	0.001	0.175
14	0.025	-0.012	-0.002	-0.024	0.023	0.001	-0.000	0.218	-0.017	-0.016	0.056	0.008	0.007	1.000	-0.000	0.000
15	0.001	0.043	-0.007	0.000	0.001	-0.037	0.001	-0.002	-0.041	0.001	-0.000	0.179	0.001	-0.000	1.000	0.002
16	0.013	0.032	-0.004	-0.012	0.008	0.002	-0.060	-0.008	-0.009	-0.056	-0.004	0.005	0.175	0.000	0.002	1.000

Table A.11: Correlation matrix of transformed LEP-I S-Matrix input parameters for OPAL.

Appendix B

Two-Fermion Combination Details

B.1 Input Measurements

In this section, the experimental measurements of total cross-sections and forward-backward asymmetries as used in the combination are reported. For each result, the ZFITTER prediction, followed by the measured value and the six error components as described in Section 3.2, are listed. The results are extrapolated to 4π acceptance ($|\cos\theta| \leq 1$) except for ALEPH ($|\cos\theta| < 0.95$).

ALEPH

ALEPH results at 130 GeV

* E_CM = 130.200 GeV

*

XSEC_QQ	71.15	71.6	3.8	0.64	0.82	0.29	0.19	0.22
XSEC_MUMU	6.987	7.9	1.22	0.041	0.008	0.04	0.02	0.077
XSEC_TAUTAU	7.234	10.9	1.79	0.152	0.22	0.29	0.03	0.137
AFB_MUMU	0.698	0.83	0.09	0.004	0.026	0.004	0.0	0.01
AFB_TAUTAU	0.697	0.56	0.12	0.011	0.035	0.004	0.0	0.01

ALEPH results at 136 GeV

* E_CM = 136.200 GeV

*

XSEC_QQ	57.64	58.8	3.5	0.53	0.67	0.23	0.15	0.18
XSEC_MUMU	6.053	6.9	1.1	0.04	0.007	0.034	0.02	0.076
XSEC_TAUTAU	6.267	5.6	1.3	0.073	0.11	0.15	0.01	0.1
AFB_MUMU	0.678	0.63	0.105	0.004	0.024	0.004	0.0	0.01
AFB_TAUTAU	0.677	0.65	0.14	0.009	0.028	0.004	0.0	0.012

ALEPH results at 161 GeV

* E_CM = 161.314 GeV

*

XSEC_QQ	30.88	29.9	1.8	0.21	0.29	0.16	0.08	0.09
XSEC_MUMU	3.857	4.5	0.69	0.03	0.008	0.027	0.01	0.06
XSEC_TAUTAU	3.992	5.75	0.94	0.08	0.13	0.17	0.01	0.17
AFB_MUMU	0.609	0.63	0.11	0.004	0.026	0.004	0.0	0.009
AFB_TAUTAU	0.608	0.48	0.14	0.009	0.029	0.004	0.0	0.008

ALEPH results at 172 GeV

* E_CM = 172.086 GeV

*

XSEC_QQ	25.22	26.4	1.7	0.18	0.30	0.18	0.06	0.08
XSEC_MUMU	3.30	2.64	0.53	0.042	0.008	0.021	0.006	0.04
XSEC_TAUTAU	3.415	3.26	0.74	0.04	0.07	0.04	0.008	0.07
AFB_MUMU	0.593	0.72	0.14	0.005	0.034	0.005	0.0	0.01
AFB_TAUTAU	0.592	0.44	0.16	0.009	0.029	0.004	0.0	0.01

ALEPH results at 183 GeV

* E_CM = 183.00 GeV

*

XSEC_QQ	21.24	21.71	0.70	0.13	0.12	0.126	0.06	0.07
XSEC_MUMU	2.871	2.98	0.24	0.045	0.004	0.019	0.012	0.05
XSEC_TAUTAU	2.974	2.90	0.29	0.048	0.067	0.011	0.012	0.06
AFB_MUMU	0.579	0.54	0.06	0.02	0.01	0.004	0.0	0.008
AFB_TAUTAU	0.579	0.52	0.08	0.03	0.02	0.004	0.0	0.009

ALEPH results at 189 GeV

* E_CM = 189 GeV

*

XSEC_QQ	20.580	20.800	0.380	0.156	0.108	0.021	0.052	0.021
XSEC_MUMU	2.831	2.879	0.134	0.007	0.014	0.000	0.007	0.004
XSEC_TAUTAU	2.910	2.787	0.198	0.020	0.014	0.000	0.007	0.020
AFB_MUMU	0.570	0.576	0.036	0.001	0.000	0.000	0.000	0.009
AFB_TAUTAU	0.570	0.598	0.046	0.007	0.000	0.000	0.000	0.010

ALEPH results at 192 GeV

* E_CM = 192 GeV

*

XSEC_QQ	19.720	20.070	0.920	0.151	0.111	0.020	0.050	0.040
XSEC_MUMU	2.729	2.862	0.333	0.008	0.013	0.000	0.004	0.004
XSEC_TAUTAU	2.811	2.600	0.467	0.062	0.011	0.000	0.003	0.020
AFB_MUMU	0.567	0.580	0.088	0.001	0.000	0.000	0.000	0.009
AFB_TAUTAU	0.567	0.490	0.124	0.006	0.000	0.000	0.000	0.009

ALEPH results at 196 GeV

* E_CM = 196 GeV

*

XSEC_QQ	18.670	18.930	0.540	0.144	0.115	0.015	0.047	0.038
XSEC_MUMU	2.611	2.704	0.193	0.014	0.012	0.000	0.003	0.004
XSEC_TAUTAU	2.69	2.551	0.289	0.012	0.012	0.000	0.003	0.020
AFB_MUMU	0.563	0.553	0.057	0.001	0.000	0.000	0.000	0.006
AFB_TAUTAU	0.563	0.543	0.075	0.007	0.000	0.000	0.000	0.010

ALEPH results at 200 GeV

* E_CM = 200 GeV

*

XSEC_QQ	17.690	17.940	0.510	0.138	0.113	0.014	0.045	0.036
XSEC_MUMU	2.502	2.991	0.195	0.015	0.012	0.000	0.004	0.005
XSEC_TAUTAU	2.571	2.881	0.293	0.012	0.012	0.000	0.003	0.021
AFB_MUMU	0.560	0.442	0.056	0.003	0.000	0.000	0.000	0.006
AFB_TAUTAU	0.560	0.445	0.073	0.005	0.000	0.000	0.000	0.009

ALEPH results at 202 GeV

*E_CM = 202 GeV

*

XSEC_QQ	17.210	17.560	0.710	0.137	0.133	0.012	0.044	0.035
XSEC_MUMU	2.442	2.639	0.262	0.015	0.011	0.000	0.003	0.005
XSEC_TAUTAU	2.512	2.832	0.411	0.012	0.011	0.000	0.003	0.021
AFB_MUMU	0.558	0.573	0.078	0.001	0.000	0.000	0.000	0.010
AFB_TAUTAU	0.557	0.654	0.090	0.008	0.000	0.000	0.000	0.012

ALEPH results at 205 GeV

*E_CM = 205 GeV

*

XSEC_QQ	16.510	16.940	0.520	0.129	0.100	0.012	0.042	0.034
XSEC_MUMU	2.358	1.918	0.162	0.014	0.011	0.000	0.003	0.005
XSEC_TAUTAU	2.434	2.430	0.290	0.016	0.010	0.000	0.003	0.020
AFB_MUMU	0.555	0.572	0.066	0.003	0.000	0.000	0.000	0.008
AFB_TAUTAU	0.555	0.593	0.075	0.007	0.000	0.000	0.000	0.011

ALEPH results at 207 GeV

*E_CM = 207 GeV

*

XSEC_QQ	16.160	16.340	0.380	0.124	0.087	0.011	0.041	0.033
XSEC_MUMU	2.318	2.458	0.143	0.014	0.010	0.000	0.003	0.005
XSEC_TAUTAU	2.383	2.101	0.212	0.015	0.010	0.000	0.003	0.021
AFB_MUMU	0.554	0.572	0.066	0.001	0.000	0.000	0.000	0.009
AFB_TAUTAU	0.554	0.568	0.062	0.007	0.000	0.000	0.000	0.011

DELPHI

DELPHI results at 130 GeV

* Centre-of-mass energy used: 130.200 GeV

*

XSEC_QQ	82.506	82.400	5.200	0.411	0.296	0.000	0.098	2.509
XSEC_MUMU	8.107	9.700	1.900	0.015	0.000	0.000	0.000	0.359
XSEC_TAUTAU	8.312	10.200	3.100	0.009	0.037	0.000	0.012	0.714
AFB_MUMU	0.719	0.670	0.150	0.000	0.000	0.000	0.000	0.003
AFB_TAUTAU	0.719	0.730	0.170	0.000	0.000	0.000	0.000	0.020

DELPHI results at 136 GeV

* Centre-of-mass energy used: 136.20 GeV

*

XSEC_QQ	66.362	65.300	4.700	0.326	0.241	0.000	0.078	2.010
XSEC_MUMU	6.997	6.600	1.600	0.010	0.000	0.000	0.000	0.244
XSEC_TAUTAU	7.173	8.800	3.000	0.008	0.033	0.000	0.011	0.616

AFB_MUMU	0.699	0.740	0.160	0.000	0.000	0.000	0.000	0.003
AFB_TAUTAU	0.699	0.490	0.230	0.000	0.000	0.000	0.000	0.020

DELPHI results at 161 GeV

* Centre-of-mass energy used: 161.30 GeV

*

XSEC_QQ	35.119	41.000	2.100	0.215	0.162	0.000	0.051	1.223
XSEC_MUMU	4.426	3.600	0.700	0.019	0.000	0.000	0.000	0.126
XSEC_TAUTAU	4.538	5.100	1.200	0.025	0.016	0.000	0.006	0.357
AFB_MUMU	0.629	0.430	0.160	0.000	0.000	0.000	0.000	0.003
AFB_TAUTAU	0.628	0.920	0.080	0.000	0.000	0.000	0.000	0.020

DELPHI results at 172 GeV

* Centre-of-mass energy used: 172.10 GeV

*

XSEC_QQ	28.745	30.400	1.900	0.176	0.159	0.000	0.042	0.932
XSEC_MUMU	3.790	3.600	0.700	0.019	0.000	0.000	0.000	0.122
XSEC_TAUTAU	3.886	4.500	1.100	0.023	0.020	0.000	0.005	0.315
AFB_MUMU	0.610	0.940	0.140	0.000	0.000	0.000	0.000	0.003
AFB_TAUTAU	0.610	0.130	0.200	0.000	0.000	0.000	0.000	0.020

DELPHI results at 183 GeV

* Centre-of-mass energy used: 182.65 GeV

*

XSEC_QQ	24.154	25.500	0.796	0.272	0.057	0.026	0.137	0.056
XSEC_MUMU	3.304	3.605	0.284	0.027	0.000	0.000	0.000	0.011
XSEC_TAUTAU	3.387	3.292	0.376	0.071	0.006	0.011	0.013	0.000
AFB_MUMU	0.596	0.588	0.064	0.001	0.000	0.000	0.000	0.001
AFB_TAUTAU	0.596	0.671	0.080	0.011	0.000	0.002	0.002	0.000

DELPHI results at 189 GeV

* Centre-of-mass energy used: 188.63 GeV

*

XSEC_QQ	22.099	22.630	0.452	0.257	0.034	0.023	0.136	0.040
XSEC_MUMU	3.072	3.071	0.150	0.023	0.000	0.000	0.000	0.008
XSEC_TAUTAU	3.150	3.105	0.215	0.065	0.003	0.011	0.013	0.000
AFB_MUMU	0.589	0.600	0.039	0.001	0.000	0.000	0.000	0.001
AFB_TAUTAU	0.589	0.697	0.048	0.011	0.000	0.002	0.002	0.000

DELPHI results at 192 GeV

* Centre-of-mass energy used: 191.58 GeV

*

XSEC_QQ	21.191	22.140	1.119	0.255	0.098	0.022	0.136	0.072
XSEC_MUMU	2.967	2.822	0.357	0.021	0.000	0.000	0.000	0.006

XSEC_TAUTAU	3.042	2.497	0.479	0.053	0.007	0.008	0.011	0.000
AFB_MUMU	0.586	0.636	0.098	0.001	0.000	0.000	0.000	0.001
AFB_TAUTAU	0.586	0.578	0.150	0.011	0.000	0.002	0.002	0.000

DELPHI results at 196 GeV

* Centre-of-mass energy used: 195.51 GeV

*

XSEC_QQ	20.075	21.180	0.634	0.249	0.058	0.021	0.136	0.053
XSEC_MUMU	2.837	2.763	0.207	0.020	0.000	0.000	0.000	0.006
XSEC_TAUTAU	2.908	2.895	0.301	0.062	0.006	0.010	0.012	0.000
AFB_MUMU	0.582	0.586	0.061	0.001	0.000	0.000	0.000	0.000
AFB_TAUTAU	0.582	0.465	0.083	0.011	0.000	0.002	0.002	0.000

DELPHI results at 200 GeV

* Centre-of-mass energy used: 199.51 GeV

*

XSEC_QQ	19.035	19.450	0.591	0.240	0.054	0.020	0.135	0.051
XSEC_MUMU	2.713	3.080	0.207	0.023	0.000	0.000	0.000	0.007
XSEC_TAUTAU	2.781	2.614	0.270	0.056	0.005	0.009	0.011	0.000
AFB_MUMU	0.578	0.548	0.056	0.001	0.000	0.000	0.000	0.000
AFB_TAUTAU	0.578	0.540	0.080	0.011	0.000	0.002	0.002	0.000

DELPHI results at 202 GeV

* Centre-of-mass energy used: 201.64 GeV

*

XSEC_QQ	18.517	18.880	0.843	0.237	0.077	0.019	0.135	0.066
XSEC_MUMU	2.650	2.464	0.268	0.018	0.000	0.000	0.000	0.005
XSEC_TAUTAU	2.717	2.550	0.380	0.054	0.007	0.009	0.011	0.000
AFB_MUMU	0.577	0.544	0.090	0.001	0.000	0.000	0.000	0.001
AFB_TAUTAU	0.576	0.464	0.122	0.011	0.000	0.002	0.002	0.000

DELPHI results at 205 GeV

* Centre-of-mass energy used: 204.87 GeV

*

XSEC_QQ	17.775	17.670	0.580	0.230	0.053	0.018	0.135	0.042
XSEC_MUMU	2.560	2.345	0.188	0.017	0.000	0.000	0.000	0.005
XSEC_TAUTAU	2.625	2.803	0.282	0.059	0.006	0.010	0.012	0.000
AFB_MUMU	0.574	0.642	0.061	0.001	0.000	0.000	0.000	0.001
AFB_TAUTAU	0.574	0.709	0.068	0.011	0.000	0.002	0.002	0.000

DELPHI results at 207 GeV

* Centre-of-mass energy used: 206.55 GeV

*

XSEC_QQ	17.408	17.040	0.444	0.228	0.040	0.017	0.135	0.033
---------	--------	--------	-------	-------	-------	-------	-------	-------

XSEC_MUMU	2.515	2.475	0.145	0.018	0.000	0.000	0.000	0.004
XSEC_TAUTAU	2.578	2.534	0.210	0.055	0.004	0.009	0.011	0.000
AFB_MUMU	0.573	0.558	0.048	0.001	0.000	0.000	0.000	0.001
AFB_TAUTAU	0.572	0.666	0.059	0.011	0.000	0.002	0.002	0.000

L3

L3 results at 130 GeV

* Exact centre-of-mass energy: 130.0 GeV

*

XSEC_QQ	83.5	84.2	4.4	0.96	0.05	0.27	0.03	0.0
XSEC_MUMU	8.5	8.2	1.4	0.200	0.006	0.012	0.004	0.0
XSEC_TAUTAU	8.5	9.8	1.9	0.300	0.006	0.010	0.004	0.0
AFB_MUMU	0.707	0.67	0.11	0.020	0.0	0.004	0.0	0.0
AFB_TAUTAU	0.707	0.78	0.16	0.020	0.0	0.004	0.0	0.0

L3 results at 136 GeV

* Exact centre-of-mass energy: 136.1 GeV

*

XSEC_QQ	66.9	66.6	3.9	0.77	0.05	0.22	0.03	0.0
XSEC_MUMU	7.3	6.9	1.4	0.300	0.006	0.012	0.004	0.0
XSEC_TAUTAU	7.3	7.5	1.8	0.300	0.006	0.010	0.004	0.0
AFB_MUMU	0.686	0.75	0.11	0.050	0.0	0.004	0.0	0.0
AFB_TAUTAU	0.686	0.96	0.17	0.030	0.0	0.004	0.0	0.0

L3 results at 161 GeV

* Exact centre-of-mass energy: 161.3 GeV

*

XSEC_QQ	35.4	37.3	2.2	0.69	0.05	0.12	0.03	0.0
XSEC_MUMU	4.70	4.59	0.84	0.180	0.006	0.012	0.004	0.0
XSEC_TAUTAU	4.7	4.6	1.1	0.300	0.006	0.010	0.004	0.0
AFB_MUMU	0.619	0.59	0.15	0.050	0.0	0.004	0.0	0.0
AFB_TAUTAU	0.619	0.97	0.25	0.020	0.0	0.004	0.0	0.0

L3 results at 172 GeV

* Exact centre-of-mass energy: 172.1 GeV

*

XSEC_QQ	28.8	28.2	2.2	0.59	0.05	0.09	0.03	0.0
XSEC_MUMU	4.00	3.60	0.75	0.140	0.006	0.012	0.004	0.0
XSEC_TAUTAU	4.0	4.3	1.1	0.300	0.006	0.010	0.004	0.0
AFB_MUMU	0.598	0.31	0.195	0.050	0.0	0.004	0.0	0.0
AFB_TAUTAU	0.598	0.18	0.27	0.020	0.0	0.004	0.0	0.0

L3 results at 183 GeV

* Exact centre-of-mass energy: 182.7 GeV

*

XSEC_QQ	24.3	24.7	0.8	0.38	0.05	0.08	0.03	0.0
XSEC_MUMU	3.47	3.09	0.35	0.059	0.006	0.012	0.004	0.0
XSEC_TAUTAU	3.47	3.62	0.40	0.059	0.006	0.010	0.004	0.0
AFB_MUMU	0.582	0.62	0.08	0.020	0.0	0.004	0.0	0.0
AFB_TAUTAU	0.582	0.53	0.105	0.020	0.0	0.004	0.0	0.0

L3 results at 189 GeV

* Exact centre-of-mass energy: 188.7 GeV

*

XSEC_QQ	22.2	23.1	0.4	0.28	0.05	0.07	0.03	0.0
XSEC_MUMU	3.22	2.92	0.16	0.059	0.006	0.012	0.004	0.0
XSEC_TAUTAU	3.22	3.18	0.21	0.069	0.006	0.010	0.004	0.0
AFB_MUMU	0.573	0.58	0.04	0.020	0.0	0.004	0.0	0.0
AFB_TAUTAU	0.573	0.44	0.06	0.020	0.0	0.004	0.0	0.0

L3 results at 192 GeV

* Exact centre-of-mass energy: 191.6 GeV

*

XSEC_QQ	21.334	22.38	1.020	0.180	0.032	0.045	0.019	0.010
XSEC_MUMU	3.112	2.54	0.390	0.087	0.009	0.018	0.006	0.004
XSEC_TAUTAU	3.112	2.93	0.480	0.059	0.005	0.009	0.003	0.003
AFB_MUMU	0.571	0.69	0.120	0.069	0.000	0.014	0.000	0.004
AFB_TAUTAU	0.571	0.52	0.120	0.049	0.000	0.010	0.000	0.003

L3 results at 196 GeV

* Exact centre-of-mass energy: 195.5 GeV

*

XSEC_QQ	20.212	20.14	0.580	0.152	0.027	0.038	0.016	0.008
XSEC_MUMU	2.972	3.05	0.250	0.097	0.010	0.020	0.007	0.005
XSEC_TAUTAU	2.972	3.22	0.300	0.069	0.006	0.010	0.004	0.004
AFB_MUMU	0.566	0.53	0.070	0.039	0.000	0.008	0.000	0.002
AFB_TAUTAU	0.566	0.44	0.090	0.049	0.000	0.010	0.000	0.003

L3 results at 200 GeV

* Exact centre-of-mass energy: 199.6 GeV

*

XSEC_QQ	19.133	19.09	0.570	0.152	0.027	0.038	0.016	0.008
XSEC_MUMU	2.837	2.85	0.240	0.087	0.009	0.018	0.006	0.004
XSEC_TAUTAU	2.836	2.97	0.300	0.069	0.006	0.010	0.004	0.004
AFB_MUMU	0.561	0.44	0.080	0.039	0.000	0.008	0.000	0.002
AFB_TAUTAU	0.561	0.46	0.100	0.049	0.000	0.010	0.000	0.003

L3 results at 202 GeV

* Exact centre-of-mass energy: 201.8 GeV

*

XSEC_QQ	18.593	19.33	0.890	0.152	0.027	0.038	0.016	0.008
XSEC_MUMU	2.768	2.97	0.350	0.097	0.010	0.020	0.007	0.005
XSEC_TAUTAU	2.767	2.81	0.420	0.007	0.001	0.001	0.000	0.000
AFB_MUMU	0.559	0.59	0.090	0.020	0.000	0.004	0.000	0.001
AFB_TAUTAU	0.559	0.47	0.130	0.078	0.000	0.016	0.000	0.004

L3 results at 205 GeV

* Exact centre-of-mass energy: 204.9 GeV

*

XSEC_QQ	17.872	18.46	0.590	0.133	0.024	0.033	0.014	0.007
XSEC_MUMU	2.675	2.37	0.220	0.068	0.007	0.014	0.005	0.004
XSEC_TAUTAU	2.675	2.93	0.320	0.069	0.006	0.010	0.004	0.004
AFB_MUMU	0.556	0.48	0.090	0.029	0.000	0.006	0.000	0.002
AFB_TAUTAU	0.556	0.56	0.090	0.049	0.000	0.010	0.000	0.003

L3 results at 207 GeV

* Exact centre-of-mass energy: 206.5 GeV

*

XSEC_QQ	17.518	17.87	0.440	0.123	0.022	0.031	0.013	0.007
XSEC_MUMU	2.629	2.24	0.170	0.058	0.006	0.012	0.004	0.003
XSEC_TAUTAU	2.629	2.34	0.210	0.079	0.007	0.011	0.005	0.004
AFB_MUMU	0.554	0.54	0.060	0.020	0.000	0.004	0.000	0.001
AFB_TAUTAU	0.554	0.61	0.070	0.088	0.000	0.018	0.000	0.004

OPAL

OPAL results at 130 GeV

* Exact centre-of-mass energy: 130.12 GeV

*

XSEC_QQ	83.078	79.30	3.8	1.25	0.52	0.47	0.20	0.54
XSEC_MUMU	8.453	7.63	1.14	0.16	0.05	0.03	0.02	0.26
XSEC_TAUTAU	8.450	6.83	1.40	0.18	0.05	0.03	0.02	0.16
AFB_MUMU	0.705	0.40	0.15	0.02	0.0	0.004	0.0	0.0
AFB_TAUTAU	0.705	0.80	0.22	0.01	0.0	0.004	0.0	0.0

OPAL results at 136 GeV

* Exact centre-of-mass energy: 136.08 GeV

*

XSEC_QQ	66.875	66.30	3.3	1.04	0.43	0.40	0.17	0.47
XSEC_MUMU	7.298	10.37	1.31	0.16	0.07	0.03	0.03	0.23
XSEC_TAUTAU	7.295	7.32	1.39	0.19	0.05	0.02	0.02	0.15

AFB_MUMU	0.685	0.71	0.12	0.01	0.0	0.002	0.0	0.0
AFB_TAUTAU	0.684	0.86	0.20	0.01	0.0	0.003	0.0	0.0

OPAL results at 161 GeV

* Exact centre-of-mass energy: 161.34 GeV

*

XSEC_QQ	33.606	35.20	2.00	0.73	0.16	0.22	0.09	0.07
XSEC_MUMU	4.419	4.49	0.67	0.07	0.02	0.02	0.01	0.11
XSEC_TAUTAU	4.418	6.22	1.01	0.17	0.03	0.02	0.02	0.05
AFB_MUMU	0.609	0.45	0.14	0.01	0.0	0.005	0.0	0.0
AFB_TAUTAU	0.609	0.56	0.14	0.01	0.0	0.005	0.0	0.0

OPAL results at 172 GeV

* Exact centre-of-mass energy: 172.12 GeV

*

XSEC_QQ	27.566	26.80	1.80	0.57	0.13	0.16	0.07	0.05
XSEC_MUMU	3.790	3.56	0.59	0.08	0.02	0.02	0.01	0.11
XSEC_TAUTAU	3.789	3.85	0.78	0.11	0.02	0.02	0.01	0.06
AFB_MUMU	0.590	0.55	0.15	0.01	0.0	0.005	0.0	0.0
AFB_TAUTAU	0.590	0.56	0.19	0.01	0.0	0.005	0.0	0.0

OPAL results at 183 GeV

* Exact centre-of-mass energy: 182.69 GeV

*

XSEC_QQ	24.237	23.50	0.72	0.35	0.08	0.15	0.06	0.06
XSEC_MUMU	3.445	3.463	0.264	0.045	0.012	0.013	0.009	0.105
XSEC_TAUTAU	3.445	3.315	0.301	0.103	0.012	0.011	0.008	0.028
AFB_MUMU	0.576	0.543	0.071	0.011	0.0	0.004	0.0	0.0
AFB_TAUTAU	0.576	0.683	0.088	0.002	0.0	0.004	0.0	0.0

OPAL results at 189 GeV

* Exact centre-of-mass energy: 188.635 GeV

*

XSEC_QQ	22.188	21.99	0.37	0.09	0.04	0.09	0.03	0.03
XSEC_MUMU	3.206	3.142	0.145	0.033	0.005	0.005	0.004	0.007
XSEC_TAUTAU	3.206	3.445	0.211	0.085	0.006	0.002	0.004	0.020
AFB_MUMU	0.569	0.548	0.039	0.004	0.0	0.002	0.0	0.002
AFB_TAUTAU	0.569	0.591	0.054	0.008	0.0	0.001	0.0	0.010

OPAL results at 192 GeV

* Exact centre-of-mass energy: 191.590 GeV

*

XSEC_QQ	21.276	22.23	0.94	0.08	0.07	0.08	0.03	0.02
XSEC_MUMU	3.097	2.857	0.344	0.030	0.008	0.004	0.003	0.005

XSEC_TAUTAU	3.097	3.167	0.503	0.078	0.009	0.001	0.004	0.015
AFB_MUMU	0.566	0.341	0.102	0.004	0.0	0.002	0.0	0.002
AFB_TAUTAU	0.566	0.813	0.138	0.005	0.0	0.001	0.0	0.012

OPAL results at 196 GeV

* Exact centre-of-mass energy: 195.526 GeV

*

XSEC_QQ	20.154	19.78	0.55	0.08	0.04	0.07	0.02	0.02
XSEC_MUMU	2.961	2.932	0.215	0.031	0.007	0.004	0.004	0.004
XSEC_TAUTAU	2.961	2.893	0.298	0.072	0.007	0.001	0.003	0.011
AFB_MUMU	0.562	0.683	0.055	0.004	0.0	0.002	0.0	0.002
AFB_TAUTAU	0.562	0.373	0.103	0.013	0.0	0.001	0.0	0.005

OPAL results at 200 GeV

* Exact centre-of-mass energy: 199.522 GeV

*

XSEC_QQ	19.112	18.89	0.54	0.08	0.05	0.06	0.02	0.01
XSEC_MUMU	2.833	2.772	0.207	0.029	0.007	0.004	0.003	0.003
XSEC_TAUTAU	2.833	3.136	0.304	0.077	0.007	0.001	0.004	0.010
AFB_MUMU	0.558	0.637	0.059	0.004	0.0	0.002	0.0	0.001
AFB_TAUTAU	0.558	0.700	0.077	0.006	0.0	0.001	0.0	0.006

OPAL results at 202 GeV

* Exact centre-of-mass energy: 201.636 GeV

*

XSEC_QQ	18.596	18.54	0.77	0.08	0.05	0.05	0.02	0.01
XSEC_MUMU	2.768	2.363	0.280	0.025	0.006	0.004	0.003	0.003
XSEC_TAUTAU	2.768	2.954	0.430	0.072	0.008	0.001	0.004	0.009
AFB_MUMU	0.556	0.489	0.100	0.004	0.0	0.002	0.0	0.001
AFB_TAUTAU	0.556	0.440	0.130	0.010	0.0	0.001	0.0	0.004

OPAL results at 205 GeV

* Exact centre-of-mass energy: 204.881 GeV

*

XSEC_QQ	17.847	18.18	0.52	0.08	0.04	0.05	0.02	0.01
XSEC_MUMU	2.674	2.885	0.210	0.030	0.007	0.004	0.003	0.004
XSEC_TAUTAU	2.674	2.721	0.283	0.067	0.006	0.001	0.003	0.011
AFB_MUMU	0.553	0.512	0.063	0.004	0.0	0.002	0.0	0.002
AFB_TAUTAU	0.553	0.575	0.092	0.009	0.0	0.001	0.0	0.006

OPAL results at 207 GeV

* Exact centre-of-mass energy: 206.561 GeV

*

XSEC_QQ	17.479	16.81	0.39	0.08	0.04	0.04	0.02	0.02
---------	--------	-------	------	------	------	------	------	------

XSEC_MUMU	2.627	2.766	0.158	0.029	0.006	0.004	0.003	0.005
XSEC_TAUTAU	2.627	2.782	0.219	0.068	0.006	0.001	0.003	0.013
AFB_MUMU	0.552	0.508	0.050	0.004	0.0	0.002	0.0	0.002
AFB_TAUTAU	0.552	0.472	0.075	0.010	0.0	0.001	0.0	0.005

B.2 Differential Cross-Section for Muon- and Tau-Pair Final States

The following lists show for each centre-of-mass energy point (rounded in GeV) the LEP-combined differential lepton-pair cross-sections (DC) for $\mu^+\mu^-$ (MM) and $\tau^+\tau^-$ (TT) final states in 10 $\cos\theta$ -bins (1 – 10) of constant width 0.2, comparing the LEP average value and its total error with the SM prediction. Also shown is the overall χ^2/dof and the bin-by-bin χ^2/dof contribution. The overall matrix of correlation coefficients and inverse covariance matrix are available at the LEPEWWG web site: <http://www.cern.ch/LEPEWWG>.

Total chi2/NDF = 352.156/320

183_DC_MM_1	average = 0.197 +- 0.183	SM= 0.547	chi2/NDF = 0.688/1
183_DC_MM_2	average = 0.589 +- 0.163	SM= 0.534	chi2/NDF = 0.717/1
183_DC_MM_3	average = 0.807 +- 0.174	SM= 0.627	chi2/NDF = 2.204/1
183_DC_MM_4	average = 1.033 +- 0.197	SM= 0.823	chi2/NDF = 0.211/1
183_DC_MM_5	average = 1.178 +- 0.236	SM= 1.121	chi2/NDF = 0.014/1
183_DC_MM_6	average = 1.778 +- 0.276	SM= 1.521	chi2/NDF = 0.007/1
183_DC_MM_7	average = 2.143 +- 0.315	SM= 2.020	chi2/NDF = 0.777/1
183_DC_MM_8	average = 2.690 +- 0.367	SM= 2.619	chi2/NDF = 4.165/1
183_DC_MM_9	average = 2.916 +- 0.420	SM= 3.314	chi2/NDF = 1.199/1
183_DC_MM_10	average = 4.368 +- 0.529	SM= 4.096	chi2/NDF = 0.254/1
183_DC_TT_1	average = 0.302 +- 0.351	SM= 0.548	chi2/NDF = 1.439/1
183_DC_TT_2	average = 0.206 +- 0.240	SM= 0.535	chi2/NDF = 1.677/1
183_DC_TT_3	average = 0.198 +- 0.230	SM= 0.627	chi2/NDF = 1.127/1
183_DC_TT_4	average = 0.542 +- 0.254	SM= 0.823	chi2/NDF = 0.176/1
183_DC_TT_5	average = 1.364 +- 0.302	SM= 1.121	chi2/NDF = 0.206/1
183_DC_TT_6	average = 1.519 +- 0.350	SM= 1.521	chi2/NDF = 0.045/1
183_DC_TT_7	average = 1.583 +- 0.389	SM= 2.020	chi2/NDF = 0.403/1
183_DC_TT_8	average = 2.296 +- 0.450	SM= 2.619	chi2/NDF = 0.095/1
183_DC_TT_9	average = 3.954 +- 0.574	SM= 3.313	chi2/NDF = 0.321/1
183_DC_TT_10	average = 4.156 +- 0.919	SM= 4.095	chi2/NDF = 0.263/1
189_DC_MM_1	average = 0.614 +- 0.080	SM= 0.532	chi2/NDF = 4.079/3
189_DC_MM_2	average = 0.420 +- 0.065	SM= 0.514	chi2/NDF = 1.836/3
189_DC_MM_3	average = 0.530 +- 0.069	SM= 0.595	chi2/NDF = 0.702/3
189_DC_MM_4	average = 0.651 +- 0.077	SM= 0.772	chi2/NDF = 2.544/3
189_DC_MM_5	average = 1.064 +- 0.089	SM= 1.044	chi2/NDF = 10.239/3
189_DC_MM_6	average = 1.313 +- 0.111	SM= 1.411	chi2/NDF = 1.906/3
189_DC_MM_7	average = 2.038 +- 0.123	SM= 1.872	chi2/NDF = 1.168/3
189_DC_MM_8	average = 2.158 +- 0.139	SM= 2.426	chi2/NDF = 0.374/3
189_DC_MM_9	average = 2.954 +- 0.158	SM= 3.072	chi2/NDF = 2.558/3
189_DC_MM_10	average = 3.795 +- 0.216	SM= 3.799	chi2/NDF = 0.853/3
189_DC_TT_1	average = 0.389 +- 0.123	SM= 0.532	chi2/NDF = 7.662/3
189_DC_TT_2	average = 0.379 +- 0.093	SM= 0.515	chi2/NDF = 5.211/3
189_DC_TT_3	average = 0.485 +- 0.089	SM= 0.595	chi2/NDF = 10.195/3
189_DC_TT_4	average = 0.809 +- 0.100	SM= 0.772	chi2/NDF = 0.944/3
189_DC_TT_5	average = 0.848 +- 0.118	SM= 1.044	chi2/NDF = 0.139/3
189_DC_TT_6	average = 1.323 +- 0.139	SM= 1.411	chi2/NDF = 7.994/3

189_DC_TT_7	average =	1.989 +- 0.154	SM=	1.872	chi2/NDF =	2.494/3
189_DC_TT_8	average =	2.445 +- 0.179	SM=	2.426	chi2/NDF =	0.841/3
189_DC_TT_9	average =	2.467 +- 0.225	SM=	3.071	chi2/NDF =	2.313/3
189_DC_TT_10	average =	4.111 +- 0.357	SM=	3.798	chi2/NDF =	7.763/3
192_DC_MM_1	average =	0.481 +- 0.198	SM=	0.524	chi2/NDF =	6.372/2
192_DC_MM_2	average =	0.384 +- 0.173	SM=	0.504	chi2/NDF =	1.804/2
192_DC_MM_3	average =	0.788 +- 0.186	SM=	0.579	chi2/NDF =	2.816/2
192_DC_MM_4	average =	0.581 +- 0.212	SM=	0.748	chi2/NDF =	0.388/2
192_DC_MM_5	average =	1.324 +- 0.248	SM=	1.008	chi2/NDF =	2.698/2
192_DC_MM_6	average =	1.187 +- 0.292	SM=	1.360	chi2/NDF =	3.178/2
192_DC_MM_7	average =	1.932 +- 0.334	SM=	1.803	chi2/NDF =	6.530/2
192_DC_MM_8	average =	2.080 +- 0.379	SM=	2.337	chi2/NDF =	0.245/2
192_DC_MM_9	average =	3.003 +- 0.429	SM=	2.960	chi2/NDF =	2.441/2
192_DC_MM_10	average =	3.083 +- 0.552	SM=	3.662	chi2/NDF =	2.378/2
192_DC_TT_1	average =	0.014 +- 0.325	SM=	0.524	chi2/NDF =	1.103/2
192_DC_TT_2	average =	0.355 +- 0.247	SM=	0.505	chi2/NDF =	2.256/2
192_DC_TT_3	average =	0.479 +- 0.245	SM=	0.580	chi2/NDF =	1.130/2
192_DC_TT_4	average =	0.762 +- 0.278	SM=	0.748	chi2/NDF =	2.704/2
192_DC_TT_5	average =	0.816 +- 0.331	SM=	1.008	chi2/NDF =	0.540/2
192_DC_TT_6	average =	1.609 +- 0.385	SM=	1.360	chi2/NDF =	0.055/2
192_DC_TT_7	average =	1.810 +- 0.433	SM=	1.803	chi2/NDF =	0.026/2
192_DC_TT_8	average =	2.059 +- 0.491	SM=	2.337	chi2/NDF =	0.688/2
192_DC_TT_9	average =	2.643 +- 0.599	SM=	2.959	chi2/NDF =	1.439/2
192_DC_TT_10	average =	2.575 +- 0.935	SM=	3.661	chi2/NDF =	6.306/2
196_DC_MM_1	average =	0.535 +- 0.119	SM=	0.512	chi2/NDF =	3.633/2
196_DC_MM_2	average =	0.485 +- 0.103	SM=	0.491	chi2/NDF =	1.848/2
196_DC_MM_3	average =	0.668 +- 0.111	SM=	0.560	chi2/NDF =	0.766/2
196_DC_MM_4	average =	0.484 +- 0.126	SM=	0.718	chi2/NDF =	1.473/2
196_DC_MM_5	average =	0.802 +- 0.147	SM=	0.964	chi2/NDF =	1.659/2
196_DC_MM_6	average =	1.507 +- 0.172	SM=	1.298	chi2/NDF =	2.480/2
196_DC_MM_7	average =	1.657 +- 0.197	SM=	1.720	chi2/NDF =	1.467/2
196_DC_MM_8	average =	2.303 +- 0.223	SM=	2.229	chi2/NDF =	0.450/2
196_DC_MM_9	average =	2.949 +- 0.253	SM=	2.824	chi2/NDF =	0.068/2
196_DC_MM_10	average =	3.272 +- 0.325	SM=	3.495	chi2/NDF =	1.622/2
196_DC_TT_1	average =	0.810 +- 0.211	SM=	0.513	chi2/NDF =	2.172/2
196_DC_TT_2	average =	0.738 +- 0.147	SM=	0.491	chi2/NDF =	2.311/2
196_DC_TT_3	average =	0.524 +- 0.141	SM=	0.560	chi2/NDF =	9.697/2
196_DC_TT_4	average =	0.688 +- 0.162	SM=	0.718	chi2/NDF =	0.718/2
196_DC_TT_5	average =	0.976 +- 0.195	SM=	0.964	chi2/NDF =	1.445/2
196_DC_TT_6	average =	0.977 +- 0.225	SM=	1.298	chi2/NDF =	0.257/2
196_DC_TT_7	average =	1.648 +- 0.252	SM=	1.719	chi2/NDF =	3.406/2
196_DC_TT_8	average =	1.965 +- 0.289	SM=	2.228	chi2/NDF =	0.535/2
196_DC_TT_9	average =	2.269 +- 0.357	SM=	2.823	chi2/NDF =	1.278/2
196_DC_TT_10	average =	3.346 +- 0.557	SM=	3.494	chi2/NDF =	0.714/2
200_DC_MM_1	average =	0.558 +- 0.113	SM=	0.501	chi2/NDF =	1.899/2
200_DC_MM_2	average =	0.376 +- 0.098	SM=	0.478	chi2/NDF =	3.670/2
200_DC_MM_3	average =	0.799 +- 0.105	SM=	0.541	chi2/NDF =	2.306/2

200_DC_MM_4	average =	0.817 +- 0.118	SM=	0.689	chi2/NDF =	2.762/2
200_DC_MM_5	average =	1.105 +- 0.139	SM=	0.922	chi2/NDF =	1.269/2
200_DC_MM_6	average =	1.462 +- 0.162	SM=	1.239	chi2/NDF =	0.517/2
200_DC_MM_7	average =	1.849 +- 0.185	SM=	1.640	chi2/NDF =	0.217/2
200_DC_MM_8	average =	2.122 +- 0.211	SM=	2.126	chi2/NDF =	5.430/2
200_DC_MM_9	average =	2.947 +- 0.239	SM=	2.694	chi2/NDF =	0.365/2
200_DC_MM_10	average =	3.474 +- 0.306	SM=	3.336	chi2/NDF =	0.435/2
200_DC_TT_1	average =	0.489 +- 0.201	SM=	0.501	chi2/NDF =	0.340/2
200_DC_TT_2	average =	0.619 +- 0.141	SM=	0.478	chi2/NDF =	7.623/2
200_DC_TT_3	average =	0.528 +- 0.137	SM=	0.541	chi2/NDF =	0.040/2
200_DC_TT_4	average =	0.628 +- 0.155	SM=	0.689	chi2/NDF =	0.631/2
200_DC_TT_5	average =	1.067 +- 0.186	SM=	0.922	chi2/NDF =	2.966/2
200_DC_TT_6	average =	1.130 +- 0.214	SM=	1.239	chi2/NDF =	1.361/2
200_DC_TT_7	average =	1.871 +- 0.240	SM=	1.640	chi2/NDF =	0.687/2
200_DC_TT_8	average =	2.043 +- 0.274	SM=	2.125	chi2/NDF =	0.684/2
200_DC_TT_9	average =	2.777 +- 0.339	SM=	2.694	chi2/NDF =	1.916/2
200_DC_TT_10	average =	3.437 +- 0.523	SM=	3.336	chi2/NDF =	0.841/2
202_DC_MM_1	average =	1.137 +- 0.162	SM=	0.495	chi2/NDF =	3.111/2
202_DC_MM_2	average =	0.295 +- 0.139	SM=	0.471	chi2/NDF =	2.215/2
202_DC_MM_3	average =	0.506 +- 0.149	SM=	0.531	chi2/NDF =	3.903/2
202_DC_MM_4	average =	0.455 +- 0.169	SM=	0.674	chi2/NDF =	0.372/2
202_DC_MM_5	average =	0.860 +- 0.197	SM=	0.900	chi2/NDF =	1.540/2
202_DC_MM_6	average =	1.010 +- 0.230	SM=	1.208	chi2/NDF =	0.967/2
202_DC_MM_7	average =	1.749 +- 0.264	SM=	1.599	chi2/NDF =	6.636/2
202_DC_MM_8	average =	1.844 +- 0.299	SM=	2.072	chi2/NDF =	2.847/2
202_DC_MM_9	average =	2.268 +- 0.339	SM=	2.627	chi2/NDF =	0.898/2
202_DC_MM_10	average =	3.396 +- 0.435	SM=	3.254	chi2/NDF =	0.873/2
202_DC_TT_1	average =	0.968 +- 0.287	SM=	0.495	chi2/NDF =	10.336/2
202_DC_TT_2	average =	0.322 +- 0.189	SM=	0.471	chi2/NDF =	2.713/2
202_DC_TT_3	average =	0.420 +- 0.194	SM=	0.531	chi2/NDF =	0.236/2
202_DC_TT_4	average =	0.731 +- 0.220	SM=	0.674	chi2/NDF =	1.905/2
202_DC_TT_5	average =	0.922 +- 0.263	SM=	0.900	chi2/NDF =	2.804/2
202_DC_TT_6	average =	0.789 +- 0.300	SM=	1.208	chi2/NDF =	0.094/2
202_DC_TT_7	average =	1.953 +- 0.341	SM=	1.599	chi2/NDF =	2.468/2
202_DC_TT_8	average =	1.838 +- 0.386	SM=	2.072	chi2/NDF =	4.162/2
202_DC_TT_9	average =	3.129 +- 0.479	SM=	2.626	chi2/NDF =	9.918/2
202_DC_TT_10	average =	3.186 +- 0.747	SM=	3.254	chi2/NDF =	1.368/2
205_DC_MM_1	average =	0.621 +- 0.113	SM=	0.485	chi2/NDF =	2.027/2
205_DC_MM_2	average =	0.385 +- 0.098	SM=	0.461	chi2/NDF =	0.169/2
205_DC_MM_3	average =	0.382 +- 0.104	SM=	0.517	chi2/NDF =	4.554/2
205_DC_MM_4	average =	0.443 +- 0.118	SM=	0.654	chi2/NDF =	0.774/2
205_DC_MM_5	average =	0.891 +- 0.137	SM=	0.870	chi2/NDF =	1.913/2
205_DC_MM_6	average =	1.205 +- 0.160	SM=	1.166	chi2/NDF =	1.383/2
205_DC_MM_7	average =	1.614 +- 0.183	SM=	1.542	chi2/NDF =	5.186/2
205_DC_MM_8	average =	1.663 +- 0.209	SM=	1.998	chi2/NDF =	0.393/2
205_DC_MM_9	average =	2.097 +- 0.237	SM=	2.534	chi2/NDF =	0.449/2
205_DC_MM_10	average =	3.318 +- 0.306	SM=	3.140	chi2/NDF =	6.351/2

205_DC_TT_1	average =	0.363 +- 0.203	SM=	0.486	chi2/NDF =	6.520/2
205_DC_TT_2	average =	0.562 +- 0.137	SM=	0.461	chi2/NDF =	0.697/2
205_DC_TT_3	average =	0.603 +- 0.135	SM=	0.517	chi2/NDF =	4.695/2
205_DC_TT_4	average =	0.443 +- 0.154	SM=	0.654	chi2/NDF =	0.276/2
205_DC_TT_5	average =	0.397 +- 0.179	SM=	0.870	chi2/NDF =	0.237/2
205_DC_TT_6	average =	1.242 +- 0.209	SM=	1.166	chi2/NDF =	0.132/2
205_DC_TT_7	average =	1.522 +- 0.237	SM=	1.542	chi2/NDF =	0.804/2
205_DC_TT_8	average =	1.846 +- 0.268	SM=	1.998	chi2/NDF =	1.367/2
205_DC_TT_9	average =	2.045 +- 0.330	SM=	2.533	chi2/NDF =	3.717/2
205_DC_TT_10	average =	4.671 +- 0.520	SM=	3.140	chi2/NDF =	1.658/2
207_DC_MM_1	average =	0.518 +- 0.087	SM=	0.481	chi2/NDF =	0.388/2
207_DC_MM_2	average =	0.496 +- 0.075	SM=	0.456	chi2/NDF =	0.051/2
207_DC_MM_3	average =	0.473 +- 0.079	SM=	0.510	chi2/NDF =	5.634/2
207_DC_MM_4	average =	0.781 +- 0.089	SM=	0.643	chi2/NDF =	5.052/2
207_DC_MM_5	average =	0.795 +- 0.104	SM=	0.855	chi2/NDF =	2.185/2
207_DC_MM_6	average =	0.995 +- 0.121	SM=	1.145	chi2/NDF =	0.627/2
207_DC_MM_7	average =	1.630 +- 0.139	SM=	1.515	chi2/NDF =	0.808/2
207_DC_MM_8	average =	2.247 +- 0.159	SM=	1.963	chi2/NDF =	4.025/2
207_DC_MM_9	average =	2.491 +- 0.179	SM=	2.489	chi2/NDF =	4.407/2
207_DC_MM_10	average =	2.995 +- 0.231	SM=	3.086	chi2/NDF =	1.136/2
207_DC_TT_1	average =	0.272 +- 0.145	SM=	0.481	chi2/NDF =	0.134/2
207_DC_TT_2	average =	0.412 +- 0.106	SM=	0.456	chi2/NDF =	6.521/2
207_DC_TT_3	average =	0.534 +- 0.104	SM=	0.510	chi2/NDF =	0.745/2
207_DC_TT_4	average =	0.563 +- 0.118	SM=	0.644	chi2/NDF =	0.133/2
207_DC_TT_5	average =	0.683 +- 0.140	SM=	0.855	chi2/NDF =	5.976/2
207_DC_TT_6	average =	1.443 +- 0.161	SM=	1.145	chi2/NDF =	1.658/2
207_DC_TT_7	average =	1.351 +- 0.181	SM=	1.514	chi2/NDF =	1.519/2
207_DC_TT_8	average =	1.761 +- 0.207	SM=	1.962	chi2/NDF =	6.867/2
207_DC_TT_9	average =	1.655 +- 0.255	SM=	2.489	chi2/NDF =	0.561/2
207_DC_TT_10	average =	3.597 +- 0.399	SM=	3.085	chi2/NDF =	3.709/2

B.3 Differential Cross-Section for Electron-Positron Final States

The following lists show for each centre-of-mass energy point (rounded in GeV) the LEP-combined differential cross-sections (DC) for e^+e^- (EE) final states in 15 $\cos\theta$ -bins (1 – 15 with bin boundaries as defined in Tables 3.11 and 3.12), comparing the LEP average value and its total error with the SM prediction. Also shown is the overall χ^2/dof and the bin-by-bin χ^2/dof contribution. The overall matrix of correlation coefficients and inverse covariance matrix are available at the LEPEWWG web site: <http://www.cern.ch/LEPEWWG>.

Total χ^2/NDF = 199.402/189

189_DC_EE_1	average = 1.401 +- 0.161	SM= 1.590	χ^2/NDF = 1.576/1
189_DC_EE_2	average = 2.030 +- 0.160	SM= 1.816	χ^2/NDF = 6.274/2
189_DC_EE_3	average = 2.162 +- 0.170	SM= 2.162	χ^2/NDF = 1.237/2
189_DC_EE_4	average = 2.298 +- 0.186	SM= 2.681	χ^2/NDF = 0.654/2
189_DC_EE_5	average = 4.321 +- 0.230	SM= 3.906	χ^2/NDF = 4.262/2
189_DC_EE_6	average = 4.898 +- 0.348	SM= 5.372	χ^2/NDF = 2.403/2
189_DC_EE_7	average = 6.090 +- 0.404	SM= 6.892	χ^2/NDF = 6.751/2
189_DC_EE_8	average = 8.838 +- 0.476	SM= 9.610	χ^2/NDF = 2.341/2
189_DC_EE_9	average = 12.781 +- 0.576	SM= 13.345	χ^2/NDF = 3.970/2
189_DC_EE_10	average = 19.586 +- 0.707	SM= 19.445	χ^2/NDF = 0.115/2
189_DC_EE_11	average = 30.598 +- 0.895	SM= 30.476	χ^2/NDF = 2.386/2
189_DC_EE_12	average = 50.488 +- 1.135	SM= 51.012	χ^2/NDF = 2.339/2
189_DC_EE_13	average = 95.178 +- 1.520	SM= 95.563	χ^2/NDF = 0.211/2
189_DC_EE_14	average = 211.427 +- 2.900	SM= 212.390	χ^2/NDF = 2.620/1
189_DC_EE_15	average = 679.146 +- 5.773	SM= 689.989	χ^2/NDF = 1.921/1
192_DC_EE_1	average = 1.300 +- 0.364	SM= 1.539	χ^2/NDF = 0.051/1
192_DC_EE_2	average = 2.099 +- 0.419	SM= 1.754	χ^2/NDF = 0.462/2
192_DC_EE_3	average = 1.871 +- 0.385	SM= 2.091	χ^2/NDF = 1.602/2
192_DC_EE_4	average = 1.808 +- 0.422	SM= 2.604	χ^2/NDF = 1.619/2
192_DC_EE_5	average = 3.800 +- 0.519	SM= 3.778	χ^2/NDF = 3.179/2
192_DC_EE_6	average = 5.015 +- 0.891	SM= 5.205	χ^2/NDF = 1.897/2
192_DC_EE_7	average = 5.695 +- 0.976	SM= 6.692	χ^2/NDF = 9.314/2
192_DC_EE_8	average = 9.239 +- 1.175	SM= 9.242	χ^2/NDF = 0.003/2
192_DC_EE_9	average = 12.941 +- 1.414	SM= 12.800	χ^2/NDF = 0.749/2
192_DC_EE_10	average = 20.761 +- 1.807	SM= 18.776	χ^2/NDF = 0.371/2
192_DC_EE_11	average = 26.466 +- 2.074	SM= 29.471	χ^2/NDF = 4.398/2
192_DC_EE_12	average = 49.382 +- 2.671	SM= 49.338	χ^2/NDF = 1.721/2
192_DC_EE_13	average = 89.676 +- 3.615	SM= 92.079	χ^2/NDF = 2.159/2
192_DC_EE_14	average = 204.579 +- 6.760	SM= 206.087	χ^2/NDF = 0.054/1
192_DC_EE_15	average = 655.724 +- 12.588	SM= 669.173	χ^2/NDF = 0.482/1
196_DC_EE_1	average = 1.470 +- 0.261	SM= 1.483	χ^2/NDF = 1.887/1
196_DC_EE_2	average = 1.527 +- 0.221	SM= 1.695	χ^2/NDF = 0.421/2
196_DC_EE_3	average = 2.058 +- 0.250	SM= 2.000	χ^2/NDF = 0.865/2
196_DC_EE_4	average = 2.788 +- 0.284	SM= 2.498	χ^2/NDF = 0.014/2
196_DC_EE_5	average = 3.646 +- 0.318	SM= 3.610	χ^2/NDF = 0.212/2
196_DC_EE_6	average = 5.887 +- 0.521	SM= 4.999	χ^2/NDF = 1.809/2

196_DC_EE_7	average =	6.233 +- 0.591	SM=	6.406	chi2/NDF =	1.078/2
196_DC_EE_8	average =	9.016 +- 0.694	SM=	8.832	chi2/NDF =	2.379/2
196_DC_EE_9	average =	13.444 +- 0.856	SM=	12.326	chi2/NDF =	0.593/2
196_DC_EE_10	average =	18.568 +- 0.977	SM=	18.039	chi2/NDF =	11.452/2
196_DC_EE_11	average =	27.056 +- 1.223	SM=	28.300	chi2/NDF =	0.962/2
196_DC_EE_12	average =	49.391 +- 1.619	SM=	47.362	chi2/NDF =	0.784/2
196_DC_EE_13	average =	88.163 +- 2.154	SM=	88.473	chi2/NDF =	0.982/2
196_DC_EE_14	average =	197.369 +- 4.121	SM=	198.250	chi2/NDF =	0.438/1
196_DC_EE_15	average =	637.846 +- 8.003	SM=	642.688	chi2/NDF =	0.118/1
200_DC_EE_1	average =	1.483 +- 0.245	SM=	1.420	chi2/NDF =	0.002/1
200_DC_EE_2	average =	1.638 +- 0.214	SM=	1.623	chi2/NDF =	0.802/2
200_DC_EE_3	average =	2.068 +- 0.227	SM=	1.885	chi2/NDF =	3.449/2
200_DC_EE_4	average =	2.362 +- 0.250	SM=	2.409	chi2/NDF =	0.753/2
200_DC_EE_5	average =	4.251 +- 0.313	SM=	3.435	chi2/NDF =	1.068/2
200_DC_EE_6	average =	5.244 +- 0.506	SM=	4.770	chi2/NDF =	1.098/2
200_DC_EE_7	average =	5.888 +- 0.571	SM=	6.157	chi2/NDF =	0.142/2
200_DC_EE_8	average =	8.244 +- 0.667	SM=	8.471	chi2/NDF =	3.666/2
200_DC_EE_9	average =	9.506 +- 0.736	SM=	11.773	chi2/NDF =	8.162/2
200_DC_EE_10	average =	16.376 +- 0.920	SM=	17.262	chi2/NDF =	3.021/2
200_DC_EE_11	average =	27.000 +- 1.214	SM=	27.117	chi2/NDF =	2.513/2
200_DC_EE_12	average =	44.614 +- 1.537	SM=	45.607	chi2/NDF =	5.241/2
200_DC_EE_13	average =	86.454 +- 2.060	SM=	85.143	chi2/NDF =	0.582/2
200_DC_EE_14	average =	190.962 +- 3.941	SM=	190.786	chi2/NDF =	0.760/1
200_DC_EE_15	average =	604.986 +- 7.608	SM=	617.718	chi2/NDF =	0.059/1
202_DC_EE_1	average =	1.568 +- 0.368	SM=	1.401	chi2/NDF =	2.070/1
202_DC_EE_2	average =	1.344 +- 0.276	SM=	1.579	chi2/NDF =	0.070/2
202_DC_EE_3	average =	2.107 +- 0.345	SM=	1.836	chi2/NDF =	1.503/2
202_DC_EE_4	average =	3.240 +- 0.406	SM=	2.361	chi2/NDF =	1.130/2
202_DC_EE_5	average =	2.911 +- 0.394	SM=	3.356	chi2/NDF =	3.574/2
202_DC_EE_6	average =	4.603 +- 0.628	SM=	4.669	chi2/NDF =	0.358/2
202_DC_EE_7	average =	6.463 +- 0.861	SM=	6.017	chi2/NDF =	1.590/2
202_DC_EE_8	average =	7.457 +- 0.957	SM=	8.320	chi2/NDF =	3.276/2
202_DC_EE_9	average =	11.032 +- 1.113	SM=	11.554	chi2/NDF =	0.602/2
202_DC_EE_10	average =	16.428 +- 1.338	SM=	16.891	chi2/NDF =	1.489/2
202_DC_EE_11	average =	27.153 +- 1.643	SM=	26.583	chi2/NDF =	4.350/2
202_DC_EE_12	average =	46.490 +- 2.214	SM=	44.786	chi2/NDF =	0.246/2
202_DC_EE_13	average =	87.253 +- 2.887	SM=	83.473	chi2/NDF =	1.047/2
202_DC_EE_14	average =	189.026 +- 5.516	SM=	186.904	chi2/NDF =	0.626/1
202_DC_EE_15	average =	599.860 +- 10.339	SM=	605.070	chi2/NDF =	0.476/1
205_DC_EE_1	average =	1.102 +- 0.205	SM=	1.355	chi2/NDF =	3.910/1
205_DC_EE_2	average =	1.470 +- 0.195	SM=	1.539	chi2/NDF =	4.105/2
205_DC_EE_3	average =	2.050 +- 0.231	SM=	1.786	chi2/NDF =	0.679/2
205_DC_EE_4	average =	2.564 +- 0.255	SM=	2.280	chi2/NDF =	0.611/2
205_DC_EE_5	average =	3.410 +- 0.300	SM=	3.253	chi2/NDF =	1.269/2
205_DC_EE_6	average =	5.308 +- 0.472	SM=	4.479	chi2/NDF =	1.159/2
205_DC_EE_7	average =	5.836 +- 0.571	SM=	5.820	chi2/NDF =	1.925/2
205_DC_EE_8	average =	7.996 +- 0.635	SM=	8.077	chi2/NDF =	0.869/2

205_DC_EE_9	average = 10.607 +- 0.764	SM= 11.200	chi2/NDF = 0.581/2
205_DC_EE_10	average = 14.729 +- 0.874	SM= 16.322	chi2/NDF = 1.139/2
205_DC_EE_11	average = 26.189 +- 1.157	SM= 25.722	chi2/NDF = 0.829/2
205_DC_EE_12	average = 43.124 +- 1.497	SM= 43.217	chi2/NDF = 0.942/2
205_DC_EE_13	average = 79.255 +- 1.976	SM= 80.939	chi2/NDF = 0.758/2
205_DC_EE_14	average =179.842 +- 3.838	SM=180.878	chi2/NDF = 3.902/1
205_DC_EE_15	average =587.999 +- 7.527	SM=586.205	chi2/NDF = 2.437/1
207_DC_EE_1	average = 1.440 +- 0.196	SM= 1.339	chi2/NDF = 0.019/1
207_DC_EE_2	average = 1.426 +- 0.163	SM= 1.517	chi2/NDF = 1.800/2
207_DC_EE_3	average = 1.889 +- 0.177	SM= 1.745	chi2/NDF = 0.809/2
207_DC_EE_4	average = 2.156 +- 0.198	SM= 2.240	chi2/NDF = 4.511/2
207_DC_EE_5	average = 3.215 +- 0.233	SM= 3.194	chi2/NDF = 2.133/2
207_DC_EE_6	average = 4.434 +- 0.357	SM= 4.380	chi2/NDF = 4.019/2
207_DC_EE_7	average = 6.393 +- 0.463	SM= 5.729	chi2/NDF = 1.649/2
207_DC_EE_8	average = 6.951 +- 0.481	SM= 7.972	chi2/NDF = 1.727/2
207_DC_EE_9	average = 11.221 +- 0.615	SM= 11.019	chi2/NDF = 1.981/2
207_DC_EE_10	average = 15.933 +- 0.739	SM= 16.053	chi2/NDF = 1.275/2
207_DC_EE_11	average = 25.676 +- 0.923	SM= 25.254	chi2/NDF = 5.712/2
207_DC_EE_12	average = 42.075 +- 1.188	SM= 42.456	chi2/NDF = 0.527/2
207_DC_EE_13	average = 77.611 +- 1.569	SM= 79.639	chi2/NDF = 0.550/2
207_DC_EE_14	average =173.825 +- 3.002	SM=178.042	chi2/NDF = 0.026/1
207_DC_EE_15	average =573.637 +- 6.024	SM=576.688	chi2/NDF = 3.200/1

Appendix C

Determination of the LEP Centre-of-Mass Energy Using Radiative-Return Events

The LEP collaborations performed measurements of radiative Z boson production, $e^+e^- \rightarrow Z + \gamma \rightarrow \bar{f}f + \gamma$, at centre-of-mass energies well above the Z peak, $\sqrt{s} = 161 - 209$ GeV [151, 255, 256, 257]. Events with pairs of electrons, muons, taus, and hadronic jets were selected. The presence of hard ISR photons, mostly emitted at small polar angles with respect to the beam directions and recoiling against the di-fermion system, led to typical event topologies with acollinear fermions measured in the detector. Due to the photon emission, the mass of the two-fermion system, $\sqrt{s'}$, is reduced to values less than \sqrt{s} . The spectrum of $\sqrt{s'}$ exhibits a resonance peak around the Z boson mass and allows a determination of m_Z . The determination of $\sqrt{s'}$ furthermore involves the knowledge of the e^+e^- centre-of-mass mass energy, because in the kinematic reconstruction of the $Z + \gamma \rightarrow \bar{f}f + \gamma$ events, energy-momentum conservation is imposed. Thus, a measurement of the Z boson mass in radiative-return events, $m_Z^{\bar{f}f}$, is equivalent to determining the average \sqrt{s} of each analysed data set. Figure C.1 shows two examples of the two-fermion mass spectra measured by the LEP experiments.

The ISR photons are either detected as isolated energy depositions in the calorimeters compatible with an electromagnetic shower or as missing momentum pointing along the beam directions. Typically, the energy of the calorimeter shower is required to be larger than 30 – 60 GeV. For hadronic final states, a kinematic fit is applied to the event imposing energy and momentum conservation. In case the ISR photons are not observed in the detector, the sum of the photon momenta is assumed to either point along only one beam direction or along both beam axes. In the kinematic fit, usually both possibilities are tested and the one obtaining the best fit results is eventually chosen. In this way, the mass of the two-fermion system is reconstructed with optimised precision. In leptonic final states, $\sqrt{s'}$ is determined using the well-measured polar angles of the leptons, according to the following equation:

$$\sqrt{s'} = \sqrt{1 - \frac{2E_{\text{ISR}}}{\sqrt{s}}}, \text{ with} \quad (\text{C.1})$$

$$E_{\text{ISR}} = \sqrt{s} \frac{|\sin(\theta_1 + \theta_2)|}{\sin \theta_1 + \sin \theta_2 + |\sin(\theta_1 + \theta_2)|}. \quad (\text{C.2})$$

The leptonic polar angles θ_1 and θ_2 are determined either relative to the beam axis if no photon

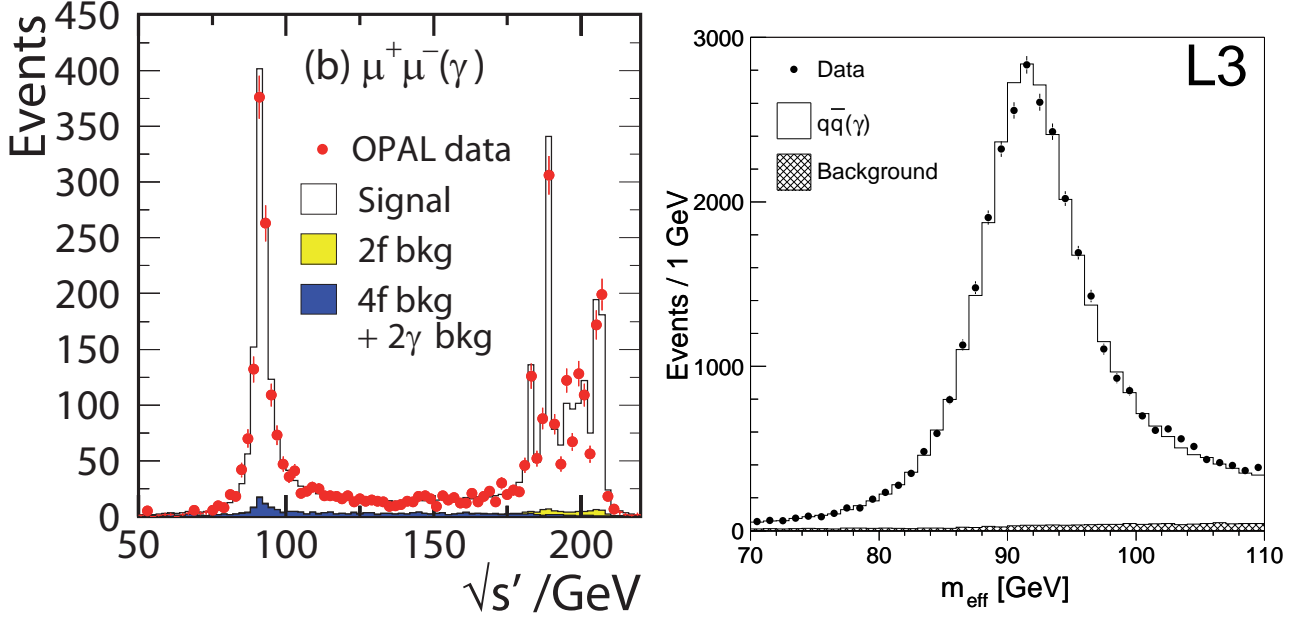


Figure C.1: Examples of reconstructed two-fermion mass spectra in the $Z + \gamma \rightarrow \mu^+ \mu^- + \gamma$ channel (left) and in the hadronic channel (right), as measured by OPAL and by L3, respectively [257]. The data collected at different centre-of-mass energies is combined and compared to Monte-Carlo predictions using the nominal Z bosons mass [4]. The Z resonance peak is clearly visible.

is measured in the detector, or relative to the direction of the measured ISR photon.

After correcting for remaining background, the mass of the Z boson is extracted either by applying a Monte-Carlo event reweighting based on the corresponding matrix element of the signal process or by fitting an analytical function describing the signal spectrum to the data. The measured Z mass, m_Z^{ff} , is then compared to the Z mass determined in precision measurements at Z-pole energies [4], $m_Z = 91.1875 \pm 0.0021$ GeV. The comparison is converted into a difference in terms of the centre-of-mass energy, $\Delta\sqrt{s}$, between \sqrt{s} derived from radiative return events and the nominal centre-of-mass energy, \sqrt{s}_{LEP} , determined by the precise LEP energy calibration [246]:

$$\Delta\sqrt{s} = \sqrt{s} - \sqrt{s}_{\text{LEP}} = \sqrt{s} \frac{m_Z^{\text{ff}} - m_Z}{m_Z}. \quad (\text{C.3})$$

This observable is eventually used to combine the results of the four LEP experiments.

Various sources of systematic uncertainties are studied and possible correlations between them are taken into account in the combination procedure. The dominant uncertainty is due to the modelling of the fragmentation process in hadronic Z decays. An uncertainty of 22 MeV on $\Delta\sqrt{s}$ is derived from a comparison of different fragmentation models implemented in the PYTHIA [140], HERWIG [258], and ARIADNE [254] software packages. The Monte-Carlo predictions of the $e^+e^- \rightarrow \text{ff} + \gamma$ process are calculated using the KK v4.02 [60] Monte-Carlo generator. Theoretical uncertainties in the description of ISR and FSR and missing higher order corrections are estimated by reweighting events applying different orders of α in the prediction and comparing it to the $\mathcal{O}(\alpha^2)$ calculations in the Coherent Exclusive Exponentiation scheme. Furthermore, the effect of neglecting the interference between ISR and FSR was studied. The

Source	Uncertainty on $\Delta\sqrt{s}$ [MeV]
Fragmentation	22
ISR/FSR Modelling	7
Four Fermion Background	6
Z Mass	1
LEP Parameters	3
Total Correlated	23
Monte-Carlo Statistics	7
Detector Bias and Resolution	28
Total Uncorrelated	29
Total Systematics	37
Total Statistical	40
Total	54

Table C.1: Systematic and statistical uncertainties on the measurement of the LEP centre-of-mass energy shift, $\Delta\sqrt{s}$.

total systematic uncertainties due to modelling of ISR and FSR amounts to 7 MeV. The uncertainty due to the prediction of the four-fermion background using measured cross-sections as input is estimated to be 6 MeV. The operational parameters of the LEP collider may also influence the reconstruction of the two-fermion mass. In particular, the effects of beam energy spread and a possible asymmetry in beam energy were studied and found to influence $\Delta\sqrt{s}$ by less than 3 MeV. The uncertainty on the nominal Z boson mass contributes with less than 1 MeV. All these sources of systematic uncertainties are assumed to be fully correlated between experiments.

Each experiment determined the influence of detector alignment, bias in angular measurements, uncertainty of energy and momentum scale and resolution in great detail. Control samples were selected in data to measure the various detector and resolution effects. These uncertainties are treated as uncorrelated between experiments. Uncertainties from limited Monte-Carlo statistics also contribute. If sources of systematic uncertainties affect data from different data taking periods or different channels similarly also the corresponding correlations are taken into account. A summary of the different sources of systematic uncertainties is listed in Table C.1. The uncertainties due to Monte-Carlo statistics and detector bias and resolution are uncorrelated between experiments. Details of the systematic effects due to detector bias and resolution combine several individual sources of uncertainty and are discussed in the publications by the experiments [151, 255, 256, 257]. The total statistical and systematic uncertainties on the LEP average for $\Delta\sqrt{s}$ are 40 MeV and 36 MeV, respectively.

When combining all available LEP data [151, 255, 256, 257] with Z decays to hadrons, and to electron, muon, and tau pairs, the difference is found to be:

$$\Delta\sqrt{s} = -54 \pm 54 \text{ MeV}, \tag{C.4}$$

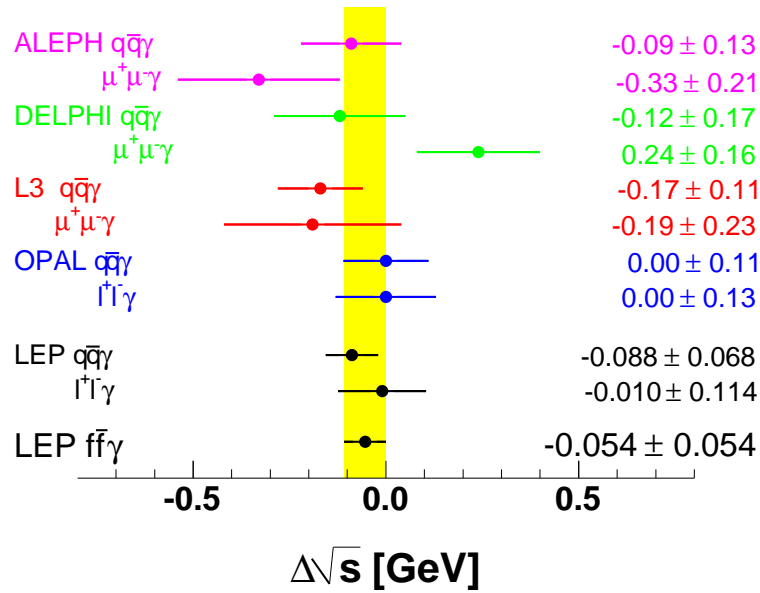
in good agreement with no shift with respect to the more precise standard LEP energy calibration. There is also no significant shift observed when analysing the leptonic and hadronic

Data set	$\Delta\sqrt{s}$ [MeV]
$e^+e^- \rightarrow \text{hadrons} + \gamma$	$-88 \pm 40 \pm 56$
$e^+e^- \rightarrow \ell^+\ell^- + \gamma$	$-10 \pm 80 \pm 26$
$\sqrt{s} = 183 \text{ GeV}$	$70 \pm 98 \pm 50$
$\sqrt{s} = 189 \text{ GeV}$	$-86 \pm 60 \pm 46$
$\sqrt{s} = 192 - 202 \text{ GeV}$	$-66 \pm 62 \pm 44$
$\sqrt{s} = 205 - 209 \text{ GeV}$	$-140 \pm 70 \pm 52$
All LEP data	$-54 \pm 40 \pm 36$

Table C.2: Combined results of ALEPH, DELPHI, L3, and OPAL on the determination of the LEP centre-of-mass energy shift, $\Delta\sqrt{s}$, with respect to the nominal value of \sqrt{s} . The results are shown for the leptonic and hadronic final states, as well as for the different data taking periods, together with the LEP combined value. Statistical and systematic uncertainties are given separately.

decay channels separately. Furthermore, there is no significant dependence on the LEP beam energy, respectively data taking periods, as illustrated in Figure C.2 and Table C.2.

LEP Z-Return Results



LEP Z-Return Results

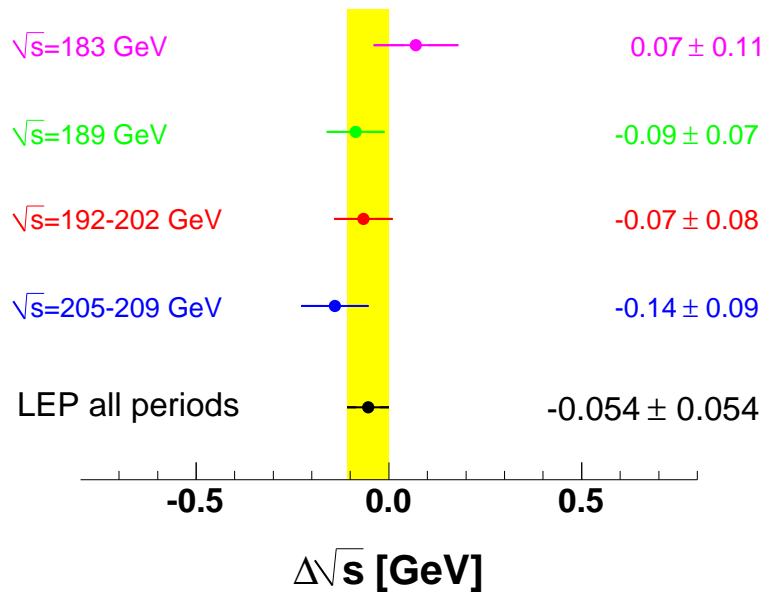


Figure C.2: Difference between the energy determined in Z-return events and the nominal LEP centre-of-mass energy, $\Delta\sqrt{s}$, for the different experiments and final states (top), and for the data taking periods with energies well above the W-pair threshold (bottom). The individual measurements as well as the LEP combined values take systematic uncertainties and their correlations into account.

Appendix D

Tests of the Colour-Reconnection Combination Procedure

Here we report on the tests of the LEP combination procedure used to combine the measurements of the LEP experiments on colour-reconnection (CR). It is shown that the LEP combination procedure is able to reproduce the combination of each experiment separately.

For each measurement, the dependence of the measured observable on the model parameter k_I is determined based on Monte-Carlo simulations. For the particle-flow based measurements, the results are reported in Table D.1. The corresponding parameter values for the phenomenological function shown in Equation 4.4 are listed in Table D.2. The parametrisations of $\delta_{\Delta m_W, i}(k_I)$ which are used to introduce systematic uncertainties for the likelihood functions of the CR measurements from Δm_W by ALEPH, DELPHI, and OPAL are given by:

$$\delta_{\Delta m_W, A}(k_I) = \begin{cases} 0.416408 + (0.624184)^2 \cdot k_I & , k_I \in [0.0, 1.3) \\ 1.227847 + (0.251441)^2 \cdot (k_I - 1.3) & , k_I \in [1.3, 2.5) \\ 1.529576 + (0.750313)^2 \cdot (k_I - 2.5) & , k_I \in [2.5, 4.5) \\ 3.030202 + (0.279341)^2 \cdot (k_I - 4.5) & , k_I \in [4.5, 6.0) \\ 3.449214 + (0.600389)^2 \cdot (k_I - 6.0) & , k_I \in [6.0, \infty) \end{cases} \quad (\text{D.1})$$

$$\delta_{\Delta m_W, D}(k_I) = 0.233054 + (0.486925)^2 \cdot k_I \quad (\text{D.2})$$

$$\delta_{\Delta m_W, O}(k_I) = 0.666308 + (0.483630)^2 \cdot k_I. \quad (\text{D.3})$$

A graphical comparison of the original input and the parametrised $\Delta\chi^2$ distributions is displayed in Figure 4.2 and shows good agreement.

The ALEPH input is available as a set of $\Delta\chi^2(k_I)$ values including systematic uncertainties, which can be evaluated directly. The result is shown in Figure D.1 and the numerical analysis yields:

$$k_I = 0.33_{-0.33}^{+1.82}. \quad (\text{D.4})$$

By construction, this agrees well with the original ALEPH result [111]. However, the ALEPH input does not include BEC systematic uncertainties. To incorporate also this effect, the correlated part of the systematic uncertainties is increased by 11%. This value is derived from

k_I	$R_N(k_I)$ for SK1 Model	
	L3	OPAL
0.10	0.8613 ± 0.0037	1.2816 ± 0.0028
0.15	0.8598 ± 0.0037	1.2792 ± 0.0028
0.20	0.8585 ± 0.0037	1.2759 ± 0.0028
0.25	0.8561 ± 0.0037	1.2738 ± 0.0028
0.35	0.8551 ± 0.0037	1.2683 ± 0.0028
0.45	0.8509 ± 0.0036	1.2643 ± 0.0028
0.60	0.8482 ± 0.0036	1.2575 ± 0.0028
0.80	0.8414 ± 0.0037	1.2495 ± 0.0028
0.90	–	1.2464 ± 0.0028
1.00	0.8381 ± 0.0036	1.2420 ± 0.0028
1.10	–	1.2389 ± 0.0028
1.20	–	1.2355 ± 0.0028
1.30	–	1.2326 ± 0.0028
1.50	0.8318 ± 0.0036	1.2265 ± 0.0028
1.75	–	1.2201 ± 0.0028
2.00	–	1.2133 ± 0.0028
2.50	–	1.2029 ± 0.0028
3.00	0.8135 ± 0.0036	1.1942 ± 0.0028
5.00	0.7989 ± 0.0035	1.1705 ± 0.0028
10.00	–	1.1413 ± 0.0028
30.00	–	1.1101 ± 0.0028
60.00	–	1.0997 ± 0.0028
100.00	–	1.0918 ± 0.0028
10000.00	0.7482 ± 0.0033	1.0780 ± 0.0028

Table D.1: Monte-Carlo predictions for the particle-flow parameter $R_N(k_I)$ provided for the SK1 model by L3 and OPAL.

Experiment	a_1	a_2	a_3	a_4	b
L3	-12.1076	2.03107	-0.23384	-10.1780	1.18954
OPAL	-0.26969	0.20543	-0.06698	0.03388	10.8576

Table D.2: Parameter sets used for the functional description of the particle-flow input provided for the SK1 model by L3 and OPAL.

a dedicated study, not included in the ALEPH publication. The final result using only ALEPH data and including BEC uncertainties is

$$k_I = 0.34_{-0.34}^{+1.86}. \quad (\text{D.5})$$

The 68% upper limit is about 3% higher compared to the original ALEPH input.

DELPHI provides $\Delta\chi^2(k_I)$ inputs from their ΔM_W and particle-flow analyses. In the DELPHI publication, both curves are simply added neglecting correlations, yielding [128]:

$$k_I = 2.2_{-1.3}^{+2.5}. \quad (\text{D.6})$$

As a cross-check, the same combination strategy is applied, i.e., assuming no correlations. When using a total $\chi^2(k_I)$ of:

$$\chi^2(k_I, c) = \Delta\chi_{\Delta m_W, D, \text{full}}^2(k_I) + \Delta\chi_{\text{p-flow}, D, \text{full}}^2(k_I), \quad (\text{D.7})$$

the following result is obtained:

$$k_I = 2.17_{-1.33}^{+2.55}, \quad (\text{D.8})$$

which is consistent with the combination performed by DELPHI. The LEP combination procedure allows a more refined treatment of correlations. Using a correlation coefficient of 0.50 between the measurements, motivated by the full covariance matrix for the particle-flow combination, the fit obtains:

$$k_I = 2.12_{-1.33}^{+2.61}. \quad (\text{D.9})$$

This corresponds to a 5% increase of the positive uncertainty and a small shift of the minimum. The result is shown in Figure D.1.

The L3 input is provided in terms of $r(k_I)$ derived from Monte-Carlo simulations and the measured r_{data} together with measurement uncertainties. The fit results in:

$$k_I = 0.76_{-1.22}^{+1.89}, \quad (\text{D.10})$$

and the corresponding $\Delta\chi^2$ curve is shown in Figure D.1. The result obtained is different from the L3 paper on CR [129], where a value of $k_I = 0.08_{-0.08}^{+1.02}$ is derived. This is due to the difference between the non-CR reference Monte-Carlo simulation used by L3 and the common LEP Monte-Carlo sample used in this combination. These Monte-Carlo samples were generated with different fragmentation and hadronisation parameters; the former was tuned to describe L3 data best. The difference in the k_I result is fully compatible with the systematic uncertainty assigned to hadronisation and fragmentation effects.

OPAL measures k_I in W -mass shift and particle-flow analyses. As for DELPHI, a correlation coefficient of 0.50 is assumed between the correlated uncertainties in both inputs. Both $\Delta\chi^2$ curves and their combination are shown in Figure D.1. The combined fit yields

$$k_I = 1.24_{-0.77}^{+1.13}. \quad (\text{D.11})$$

The 68% C.L. upper limit of 2.37 is in good agreement with the OPAL result $k_I < 2.3$ at 68% C.L. [114]. OPAL presents the results in terms of $p_{\text{reco}} = 0.43_{-0.20}^{+0.15}$ which translates into $k_I \approx 1.3_{-0.8}^{+1.1}$, using the conversion from p_{reco} to k_I based on OPAL's Monte-Carlo simulation. Using only information from ΔM_W , the fit obtains $k_I = 1.75_{-1.28}^{+1.99}$, also agreeing well with the OPAL publication: $k_I = 1.7_{-1.2}^{+2.0}$.

In summary, the LEP combination procedure reproduces well the results obtained by each collaboration, with the observed differences explained by known systematic effects.

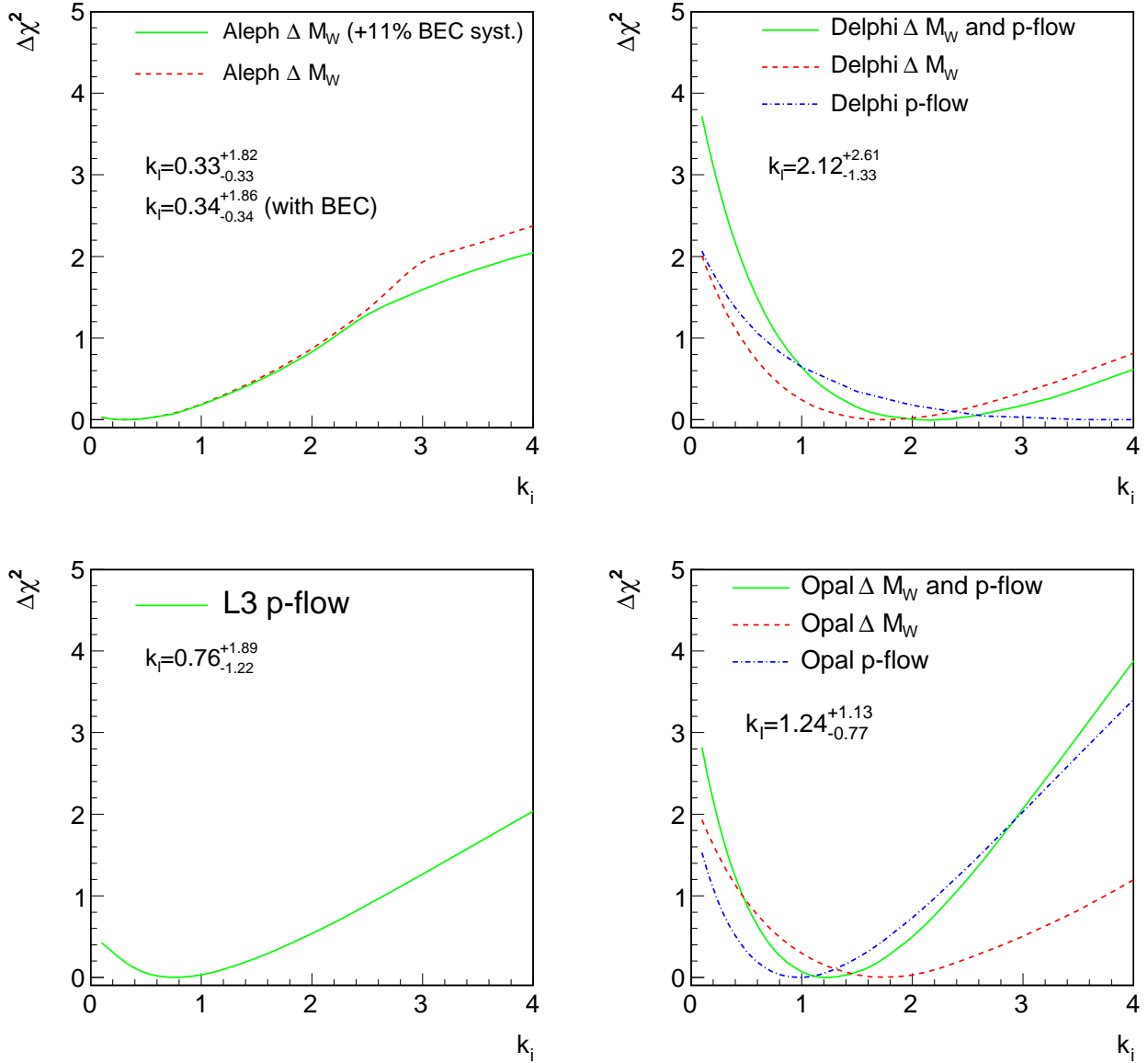


Figure D.1: LEP input to the CR measurement in terms of $\Delta\chi^2$ curves. The input data provided by the ALEPH experiment are shown as a dashed line and are compared to the data used in the LEP combination, where additional BEC systematic uncertainties are taken into account. The DELPHI and OPAL results from the analysis of the W -mass shift, Δm_W , and from the measurement of particle-flow are shown as dashed and dotted lines, respectively. The solid line represents the combined results taking correlations into account. The L3 experiment provided input from the particle-flow measurement, also shown as a solid line.

Appendix E

Detailed Inputs and Results of LEP Four-Fermion Averages

Tables E.1–E.21 give the details of the inputs and of the results for the calculation of LEP averages of the measured four-fermion cross-sections and the corresponding ratios of measured cross-sections to the theoretical predictions. For both inputs and results, whenever relevant, the breakdown of the errors into their various components is given in the tables.

For each measurement, the collaborations have privately provided unpublished information which is necessary for the combination of the LEP results, such as the expected statistical error or the split of the total systematic uncertainty into correlated and uncorrelated components. Where necessary, minor re-arrangements with respect to published results across error categories have been applied.

\sqrt{s} (GeV)	σ_{WW}	$\Delta\sigma_{\text{WW}}^{\text{stat}}$	(LCEC) $\Delta\sigma_{\text{WW}}^{\text{syst}}$	(LUEU) $\Delta\sigma_{\text{WW}}^{\text{syst}}$	(LUEC) $\Delta\sigma_{\text{WW}}^{\text{syst}}$	$\Delta\sigma_{\text{WW}}^{\text{syst}}$	$\Delta\sigma_{\text{WW}}$
ALEPH [157]							
182.7	15.86	± 0.61	± 0.08	± 0.08	± 0.09	± 0.14	± 0.63
188.6	15.78	± 0.34	± 0.07	± 0.05	± 0.09	± 0.12	± 0.36
191.6	17.10	± 0.90	± 0.07	± 0.07	± 0.09	± 0.14	± 0.90
195.5	16.60	± 0.52	± 0.07	± 0.06	± 0.09	± 0.12	± 0.54
199.5	16.93	± 0.50	± 0.07	± 0.06	± 0.09	± 0.12	± 0.52
201.6	16.63	± 0.70	± 0.07	± 0.07	± 0.09	± 0.13	± 0.71
204.9	16.84	± 0.53	± 0.07	± 0.06	± 0.09	± 0.13	± 0.54
206.6	17.42	± 0.41	± 0.07	± 0.06	± 0.09	± 0.13	± 0.43
DELPHI [158]							
182.7	16.07	± 0.68	± 0.09	± 0.09	± 0.08	± 0.15	± 0.70
188.6	16.09	± 0.39	± 0.08	± 0.09	± 0.09	± 0.15	± 0.42
191.6	16.64	± 0.99	± 0.09	± 0.10	± 0.09	± 0.16	± 1.00
195.5	17.04	± 0.58	± 0.09	± 0.10	± 0.09	± 0.16	± 0.60
199.5	17.39	± 0.55	± 0.09	± 0.10	± 0.09	± 0.16	± 0.57
201.6	17.37	± 0.80	± 0.10	± 0.10	± 0.09	± 0.17	± 0.82
204.9	17.56	± 0.57	± 0.10	± 0.10	± 0.09	± 0.17	± 0.59
206.6	16.35	± 0.44	± 0.10	± 0.10	± 0.09	± 0.17	± 0.47
L3 [159]							
182.7	16.53	± 0.67	± 0.19	± 0.13	± 0.12	± 0.26	± 0.72
188.6	16.17	± 0.37	± 0.11	± 0.06	± 0.11	± 0.17	± 0.41
191.6	16.11	± 0.90	± 0.11	± 0.07	± 0.11	± 0.17	± 0.92
195.5	16.22	± 0.54	± 0.11	± 0.06	± 0.10	± 0.16	± 0.57
199.5	16.49	± 0.56	± 0.11	± 0.07	± 0.11	± 0.17	± 0.58
201.6	16.01	± 0.82	± 0.11	± 0.06	± 0.12	± 0.17	± 0.84
204.9	17.00	± 0.58	± 0.12	± 0.06	± 0.11	± 0.17	± 0.60
206.6	17.33	± 0.44	± 0.12	± 0.04	± 0.11	± 0.17	± 0.47
OPAL [160]							
182.7	15.45	± 0.61	± 0.10	± 0.04	± 0.05	± 0.12	± 0.62
188.6	16.24	± 0.35	± 0.10	± 0.04	± 0.03	± 0.11	± 0.37
191.6	15.93	± 0.86	± 0.10	± 0.04	± 0.03	± 0.11	± 0.86
195.5	18.27	± 0.57	± 0.11	± 0.05	± 0.04	± 0.12	± 0.58
199.5	16.29	± 0.54	± 0.11	± 0.04	± 0.03	± 0.12	± 0.55
201.6	18.01	± 0.81	± 0.11	± 0.05	± 0.04	± 0.13	± 0.82
204.9	16.05	± 0.52	± 0.11	± 0.04	± 0.04	± 0.12	± 0.53
206.6	17.64	± 0.42	± 0.11	± 0.05	± 0.04	± 0.13	± 0.44

Table E.1: W-pair production cross-section (in pb) for different centre-of-mass energies from the four LEP experiments. The first column contains the centre-of-mass energy and the second the measurements. Observed statistical uncertainties are used in the fit and are listed in the third column; when asymmetric errors are quoted by the collaborations, the positive error is listed in the table and used in the fit. The fourth, fifth and sixth columns contain the components of the systematic errors, as subdivided by the collaborations into LEP-correlated energy-correlated (LCEC), LEP-uncorrelated energy-uncorrelated (LUEU), LEP-uncorrelated energy-correlated (LUEC). The total systematic error is given in the seventh column, the total error in the eighth.

LEP Averages								
\sqrt{s} (GeV)	σ_{WW}	$\Delta\sigma_{\text{WW}}^{\text{stat}}$	(LCEC) $\Delta\sigma_{\text{WW}}^{\text{syst}}$	(LUEU) $\Delta\sigma_{\text{WW}}^{\text{syst}}$	(LUEC) $\Delta\sigma_{\text{WW}}^{\text{syst}}$	$\Delta\sigma_{\text{WW}}^{\text{syst}}$	$\Delta\sigma_{\text{WW}}$	χ^2/dof
182.7	15.92	± 0.33	± 0.10	± 0.04	± 0.04	± 0.11	± 0.34	} 26.6/24
188.6	16.05	± 0.18	± 0.08	± 0.03	± 0.04	± 0.10	± 0.21	
191.6	16.42	± 0.46	± 0.08	± 0.04	± 0.04	± 0.10	± 0.47	
195.5	16.99	± 0.28	± 0.08	± 0.03	± 0.04	± 0.10	± 0.29	
199.5	16.77	± 0.27	± 0.08	± 0.03	± 0.04	± 0.10	± 0.29	
201.6	16.98	± 0.39	± 0.08	± 0.04	± 0.04	± 0.10	± 0.40	
204.9	16.81	± 0.27	± 0.08	± 0.03	± 0.04	± 0.10	± 0.29	
206.6	17.20	± 0.21	± 0.09	± 0.03	± 0.04	± 0.11	± 0.24	

Table E.2: LEP combined W-pair production cross-section (in pb) for different centre-of-mass energies. The first column contains the centre-of-mass energy and the second the measurements. Observed statistical uncertainties are used in the fit and are listed in the third column; when asymmetric errors are quoted by the collaborations, the positive error is listed in the table and used in the fit. The fourth, fifth and sixth columns contain the components of the systematic errors, as subdivided by the collaborations into LEP-correlated energy-correlated (LCEC), LEP-uncorrelated energy-uncorrelated (LUEU), LEP-uncorrelated energy-correlated (LUEC). The total systematic error is given in the seventh column, the total error in the eighth. The χ^2/dof of the fit is also given in the ninth column.

$\sqrt{s}(\text{GeV})$	182.7	188.6	191.6	195.5	199.5	201.6	204.9	206.6
182.7	1.000	0.145	0.065	0.104	0.105	0.076	0.104	0.130
188.6	0.145	1.000	0.093	0.148	0.149	0.108	0.148	0.186
191.6	0.065	0.093	1.000	0.066	0.067	0.048	0.066	0.083
195.5	0.104	0.148	0.066	1.000	0.107	0.077	0.106	0.133
199.5	0.105	0.149	0.067	0.107	1.000	0.078	0.106	0.134
201.6	0.076	0.108	0.048	0.077	0.078	1.000	0.077	0.097
204.9	0.104	0.148	0.066	0.106	0.106	0.077	1.000	0.132
206.6	0.130	0.186	0.083	0.133	0.134	0.097	0.132	1.000

Table E.3: Correlation matrix for the LEP combined W-pair cross-sections listed in Table E.2. Correlations are all positive and range from 5% to 19%.

\sqrt{s} (GeV)	WW cross-section (pb)	
	$\sigma_{\text{WW}}^{\text{YFSWW}}$	$\sigma_{\text{WW}}^{\text{RACOONWW}}$
182.7	15.361 ± 0.005	15.368 ± 0.008
188.6	16.266 ± 0.005	16.249 ± 0.011
191.6	16.568 ± 0.006	16.519 ± 0.009
195.5	16.841 ± 0.006	16.801 ± 0.009
199.5	17.017 ± 0.007	16.979 ± 0.009
201.6	17.076 ± 0.006	17.032 ± 0.009
204.9	17.128 ± 0.006	17.079 ± 0.009
206.6	17.145 ± 0.006	17.087 ± 0.009

Table E.4: W-pair cross-section predictions (in pb) for different centre-of-mass energies, according to YFSWW [161, 167] and RACOONWW [168], for $m_W = 80.35$ GeV. The errors listed in the table are only the statistical errors from the numerical integration of the cross-section.

\sqrt{s} (GeV)	\mathcal{R}_{WW}	$\Delta\mathcal{R}_{WW}^{\text{stat}}$	(LCEU) $\Delta\mathcal{R}_{WW}^{\text{syst}}$	(LCEC) $\Delta\mathcal{R}_{WW}^{\text{syst}}$	(LUEU) $\Delta\mathcal{R}_{WW}^{\text{syst}}$	(LUEC) $\Delta\mathcal{R}_{WW}^{\text{syst}}$	$\Delta\mathcal{R}_{WW}$	χ^2/dof
YFSWW [161, 167]								
182.7	1.037	± 0.021	± 0.000	± 0.006	± 0.003	± 0.003	± 0.022	} 26.6/24
188.6	0.987	± 0.011	± 0.000	± 0.005	± 0.002	± 0.003	± 0.013	
191.6	0.991	± 0.028	± 0.000	± 0.005	± 0.002	± 0.002	± 0.028	
195.5	1.009	± 0.016	± 0.000	± 0.005	± 0.002	± 0.002	± 0.018	
199.5	0.985	± 0.016	± 0.000	± 0.005	± 0.002	± 0.003	± 0.017	
201.6	0.994	± 0.023	± 0.000	± 0.005	± 0.002	± 0.003	± 0.023	
204.9	0.982	± 0.016	± 0.000	± 0.005	± 0.002	± 0.002	± 0.017	
206.6	1.003	± 0.013	± 0.000	± 0.005	± 0.002	± 0.002	± 0.014	
Average	0.995	± 0.006	± 0.000	± 0.005	± 0.001	± 0.003	± 0.008	32.2/31
RACOONWW [168]								
182.7	1.036	± 0.021	± 0.001	± 0.007	± 0.003	± 0.003	± 0.022	} 26.6/24
188.6	0.988	± 0.011	± 0.001	± 0.005	± 0.002	± 0.003	± 0.013	
191.6	0.994	± 0.028	± 0.001	± 0.005	± 0.002	± 0.002	± 0.028	
195.5	1.011	± 0.017	± 0.001	± 0.005	± 0.002	± 0.003	± 0.018	
199.5	0.987	± 0.016	± 0.001	± 0.005	± 0.002	± 0.003	± 0.017	
201.6	0.997	± 0.023	± 0.001	± 0.005	± 0.002	± 0.003	± 0.024	
204.9	0.984	± 0.016	± 0.001	± 0.005	± 0.002	± 0.002	± 0.017	
206.6	1.007	± 0.013	± 0.001	± 0.005	± 0.002	± 0.002	± 0.014	
Average	0.997	± 0.006	± 0.000	± 0.005	± 0.001	± 0.003	± 0.008	32.0/31

Table E.5: Ratios of LEP combined W-pair cross-section measurements to the expectations of the considered theoretical models, for different centre-of-mass energies and for all energies combined. The first column contains the centre-of-mass energy, the second the combined ratios, the third the statistical errors. The fourth, fifth, sixth and seventh columns contain the sources of systematic errors that are considered as LEP-correlated energy-uncorrelated (LCEU), LEP-correlated energy-correlated (LCEC), LEP-uncorrelated energy-uncorrelated (LUEU), LEP-uncorrelated energy-correlated (LUEC). The total error is given in the eighth column. The only LCEU systematic sources considered are the statistical errors on the cross-section theoretical predictions, while the LCEC, LUEU and LUEC sources are those coming from the corresponding errors on the cross-section measurements. For the LEP averages, the χ^2/dof of the fit is also given in the ninth column.

Decay channel	\mathcal{B}	$\Delta\mathcal{B}^{\text{stat}}$	(unc) $\Delta\mathcal{B}^{\text{syst}}$	(cor) $\Delta\mathcal{B}^{\text{syst}}$	$\Delta\mathcal{B}^{\text{syst}}$	$\Delta\mathcal{B}$	3×3 correlation for $\Delta\mathcal{B}$
ALEPH [157]							
$\mathcal{B}(W \rightarrow e\bar{\nu}_e)$	10.78	± 0.27	± 0.09	± 0.04	± 0.10	± 0.29	$\begin{pmatrix} 1.000 & -0.009 & -0.332 \\ -0.009 & 1.000 & -0.268 \\ -0.332 & -0.268 & 1.000 \end{pmatrix}$
$\mathcal{B}(W \rightarrow \mu\bar{\nu}_\mu)$	10.87	± 0.25	± 0.07	± 0.04	± 0.08	± 0.26	
$\mathcal{B}(W \rightarrow \tau\bar{\nu}_\tau)$	11.25	± 0.32	± 0.19	± 0.05	± 0.20	± 0.38	
DELPHI [158]							
$\mathcal{B}(W \rightarrow e\bar{\nu}_e)$	10.55	± 0.31	± 0.13	± 0.05	± 0.14	± 0.34	$\begin{pmatrix} 1.000 & 0.030 & -0.340 \\ 0.030 & 1.000 & -0.170 \\ -0.340 & -0.170 & 1.000 \end{pmatrix}$
$\mathcal{B}(W \rightarrow \mu\bar{\nu}_\mu)$	10.65	± 0.26	± 0.06	± 0.05	± 0.08	± 0.27	
$\mathcal{B}(W \rightarrow \tau\bar{\nu}_\tau)$	11.46	± 0.39	± 0.17	± 0.09	± 0.19	± 0.43	
L3 [159]							
$\mathcal{B}(W \rightarrow e\bar{\nu}_e)$	10.78	± 0.29	± 0.10	± 0.08	± 0.13	± 0.32	$\begin{pmatrix} 1.000 & -0.016 & -0.279 \\ -0.016 & 1.000 & -0.295 \\ -0.279 & -0.295 & 1.000 \end{pmatrix}$
$\mathcal{B}(W \rightarrow \mu\bar{\nu}_\mu)$	10.03	± 0.29	± 0.10	± 0.07	± 0.12	± 0.31	
$\mathcal{B}(W \rightarrow \tau\bar{\nu}_\tau)$	11.89	± 0.40	± 0.17	± 0.11	± 0.20	± 0.45	
OPAL [160]							
$\mathcal{B}(W \rightarrow e\bar{\nu}_e)$	10.71	± 0.25	± 0.09	± 0.06	± 0.11	± 0.27	$\begin{pmatrix} 1.000 & 0.135 & -0.303 \\ 0.135 & 1.000 & -0.230 \\ -0.303 & -0.230 & 1.000 \end{pmatrix}$
$\mathcal{B}(W \rightarrow \mu\bar{\nu}_\mu)$	10.78	± 0.24	± 0.07	± 0.07	± 0.10	± 0.26	
$\mathcal{B}(W \rightarrow \tau\bar{\nu}_\tau)$	11.14	± 0.31	± 0.16	± 0.06	± 0.17	± 0.35	
LEP Average (without lepton universality assumption)							
$\mathcal{B}(W \rightarrow e\bar{\nu}_e)$	10.71	± 0.14	± 0.05	± 0.05	± 0.07	± 0.16	$\begin{pmatrix} 1.000 & 0.136 & -0.201 \\ 0.136 & 1.000 & -0.122 \\ -0.201 & -0.122 & 1.000 \end{pmatrix}$
$\mathcal{B}(W \rightarrow \mu\bar{\nu}_\mu)$	10.63	± 0.13	± 0.04	± 0.05	± 0.07	± 0.15	
$\mathcal{B}(W \rightarrow \tau\bar{\nu}_\tau)$	11.38	± 0.17	± 0.09	± 0.07	± 0.11	± 0.21	
χ^2/dof	6.3/9						
LEP Average (with lepton universality assumption)							
$\mathcal{B}(W \rightarrow \ell\bar{\nu}_\ell)$	10.86	± 0.06	± 0.03	± 0.06	± 0.07	± 0.09	
$\mathcal{B}(W \rightarrow \text{had.})$	67.41	± 0.18	± 0.10	± 0.17	± 0.20	± 0.27	
χ^2/dof	15.4/11						

Table E.6: W branching fraction measurements (in %). The first column contains the decay channel, the second the measurements, the third the statistical uncertainty. The fourth and fifth column list the uncorrelated and correlated components of the systematic errors, as provided by the collaborations. The total systematic error is given in the sixth column and the total error in the seventh. Correlation matrices for the three leptonic branching fractions are given in the last column.

ALEPH [157]

\sqrt{s} interval (GeV)		Luminosity (pb ⁻¹)				Luminosity weighted \sqrt{s} (GeV)				
180-184		56.81				182.65				
$\cos\theta_{W^-}$ bin i	1	2	3	4	5	6	7	8	9	10
σ_i (pb)	0.216	0.498	0.696	1.568	1.293	1.954	2.486	2.228	4.536	6.088
$\delta\sigma_i(\text{stat})$ (pb)	0.053	0.137	0.185	0.517	0.319	0.481	0.552	0.363	0.785	0.874
$\delta\sigma_i(\text{stat,exp.})$ (pb)	0.263	0.276	0.309	0.341	0.376	0.415	0.459	0.523	0.597	0.714
$\delta\sigma_i(\text{syst,unc})$ (pb)	0.012	0.018	0.017	0.025	0.023	0.021	0.036	0.047	0.047	0.066
$\delta\sigma_i(\text{syst,cor})$ (pb)	0.004	0.003	0.003	0.003	0.003	0.004	0.004	0.003	0.004	0.006
\sqrt{s} interval (GeV)		Luminosity (pb ⁻¹)				Luminosity weighted \sqrt{s} (GeV)				
184-194		203.14				189.05				
$\cos\theta_{W^-}$ bin i	1	2	3	4	5	6	7	8	9	10
σ_i (pb)	0.665	0.743	0.919	0.990	1.156	2.133	2.795	3.070	3.851	5.772
$\delta\sigma_i(\text{stat})$ (pb)	0.148	0.140	0.158	0.142	0.144	0.287	0.337	0.297	0.300	0.366
$\delta\sigma_i(\text{stat,exp.})$ (pb)	0.132	0.147	0.157	0.175	0.196	0.223	0.246	0.282	0.332	0.408
$\delta\sigma_i(\text{syst,unc})$ (pb)	0.010	0.016	0.015	0.024	0.021	0.020	0.035	0.047	0.049	0.075
$\delta\sigma_i(\text{syst,cor})$ (pb)	0.003	0.003	0.003	0.002	0.002	0.003	0.003	0.003	0.005	0.005
\sqrt{s} interval (GeV)		Luminosity (pb ⁻¹)				Luminosity weighted \sqrt{s} (GeV)				
194-204		208.03				198.42				
$\cos\theta_{W^-}$ bin i	1	2	3	4	5	6	7	8	9	10
σ_i (pb)	0.802	0.475	0.886	0.972	1.325	1.889	2.229	3.581	4.428	6.380
$\delta\sigma_i(\text{stat})$ (pb)	0.225	0.082	0.162	0.147	0.186	0.248	0.245	0.363	0.343	0.368
$\delta\sigma_i(\text{stat,exp.})$ (pb)	0.124	0.134	0.149	0.167	0.188	0.214	0.241	0.281	0.338	0.433
$\delta\sigma_i(\text{syst,unc})$ (pb)	0.007	0.013	0.012	0.021	0.018	0.016	0.032	0.046	0.049	0.082
$\delta\sigma_i(\text{syst,cor})$ (pb)	0.003	0.002	0.002	0.002	0.002	0.002	0.002	0.003	0.003	0.004
\sqrt{s} interval (GeV)		Luminosity (pb ⁻¹)				Luminosity weighted \sqrt{s} (GeV)				
204-210		214.62				205.90				
$\cos\theta_{W^-}$ bin i	1	2	3	4	5	6	7	8	9	10
σ_i (pb)	0.334	0.637	0.800	1.229	1.229	1.789	2.810	2.740	4.192	8.005
$\delta\sigma_i(\text{stat})$ (pb)	0.072	0.136	0.148	0.224	0.176	0.237	0.351	0.246	0.306	0.474
$\delta\sigma_i(\text{stat,exp.})$ (pb)	0.114	0.126	0.143	0.155	0.180	0.206	0.234	0.273	0.338	0.443
$\delta\sigma_i(\text{syst,unc})$ (pb)	0.008	0.013	0.013	0.020	0.018	0.017	0.033	0.046	0.052	0.089
$\delta\sigma_i(\text{syst,cor})$ (pb)	0.003	0.003	0.003	0.002	0.002	0.003	0.003	0.003	0.004	0.005

Table E.7: W^- differential angular cross-section in the 10 angular bins for the four chosen energy intervals for the ALEPH experiment. For each energy range, the measured integrated luminosity and the luminosity-weighted centre-of-mass energy is reported. The results per angular bin in each energy interval are then presented: σ_i indicates the average of $d[\sigma_{WW}(\text{BR}_{e\nu} + \text{BR}_{\mu\nu})]/d\cos\theta_{W^-}$ in the i -th bin of $\cos\theta_{W^-}$ with width 0.2. The values in each bin of the measured and expected statistical error and of the systematic errors, LEP uncorrelated and correlated, are reported as well. All values are expressed in pb.

DELPHI [158]

\sqrt{s} interval (GeV)		Luminosity (pb ⁻¹)				Luminosity weighted \sqrt{s} (GeV)				
180-184		51.63				182.65				
$\cos\theta_{W^-}$ bin i	1	2	3	4	5	6	7	8	9	10
σ_i (pb)	0.715	0.795	1.175	1.365	1.350	1.745	1.995	2.150	4.750	6.040
$\delta\sigma_i(\text{stat})$ (pb)	0.320	0.315	0.380	0.400	0.400	0.450	0.485	0.510	0.775	0.895
$\delta\sigma_i(\text{stat,exp.})$ (pb)	0.320	0.315	0.350	0.370	0.405	0.450	0.505	0.580	0.695	0.850
$\delta\sigma_i(\text{syst,unc})$ (pb)	0.020	0.025	0.035	0.035	0.040	0.085	0.050	0.065	0.095	0.075
$\delta\sigma_i(\text{syst,cor})$ (pb)	0.045	0.025	0.020	0.015	0.015	0.025	0.015	0.015	0.030	0.035
\sqrt{s} interval (GeV)		Luminosity (pb ⁻¹)				Luminosity weighted \sqrt{s} (GeV)				
184-194		178.32				189.03				
$\cos\theta_{W^-}$ bin i	1	2	3	4	5	6	7	8	9	10
σ_i (pb)	0.865	0.760	0.990	0.930	1.330	1.460	1.675	2.630	4.635	5.400
$\delta\sigma_i(\text{stat})$ (pb)	0.180	0.170	0.185	0.180	0.215	0.225	0.240	0.300	0.405	0.455
$\delta\sigma_i(\text{stat,exp.})$ (pb)	0.165	0.170	0.180	0.200	0.215	0.240	0.270	0.320	0.385	0.490
$\delta\sigma_i(\text{syst,unc})$ (pb)	0.020	0.020	0.035	0.035	0.040	0.085	0.050	0.060	0.100	0.085
$\delta\sigma_i(\text{syst,cor})$ (pb)	0.040	0.020	0.020	0.015	0.015	0.020	0.015	0.015	0.025	0.035
\sqrt{s} interval (GeV)		Luminosity (pb ⁻¹)				Luminosity weighted \sqrt{s} (GeV)				
194-204		193.52				198.46				
$\cos\theta_{W^-}$ bin i	1	2	3	4	5	6	7	8	9	10
σ_i (pb)	0.600	0.675	1.510	1.150	1.055	1.635	2.115	3.175	4.470	7.140
$\delta\sigma_i(\text{stat})$ (pb)	0.155	0.160	0.215	0.190	0.185	0.225	0.255	0.320	0.385	0.500
$\delta\sigma_i(\text{stat,exp.})$ (pb)	0.150	0.160	0.170	0.180	0.200	0.230	0.260	0.310	0.380	0.505
$\delta\sigma_i(\text{syst,unc})$ (pb)	0.015	0.020	0.030	0.035	0.035	0.085	0.045	0.055	0.105	0.100
$\delta\sigma_i(\text{syst,cor})$ (pb)	0.025	0.015	0.015	0.015	0.015	0.015	0.010	0.015	0.025	0.030
\sqrt{s} interval (GeV)		Luminosity (pb ⁻¹)				Luminosity weighted \sqrt{s} (GeV)				
204-210		198.59				205.91				
$\cos\theta_{W^-}$ bin i	1	2	3	4	5	6	7	8	9	10
σ_i (pb)	0.275	0.590	0.575	0.930	1.000	1.190	2.120	2.655	4.585	7.290
$\delta\sigma_i(\text{stat})$ (pb)	0.120	0.145	0.140	0.170	0.175	0.195	0.255	0.290	0.385	0.505
$\delta\sigma_i(\text{stat,exp.})$ (pb)	0.145	0.150	0.160	0.175	0.195	0.220	0.250	0.300	0.380	0.520
$\delta\sigma_i(\text{syst,unc})$ (pb)	0.015	0.020	0.025	0.035	0.035	0.085	0.045	0.055	0.110	0.110
$\delta\sigma_i(\text{syst,cor})$ (pb)	0.020	0.015	0.010	0.010	0.015	0.010	0.010	0.010	0.020	0.030

Table E.8: W^- differential angular cross-section in the 10 angular bins for the four chosen energy intervals for the DELPHI experiment. For each energy range, the measured integrated luminosity and the luminosity-weighted centre-of-mass energy is reported. The results per angular bin in each energy interval are then presented: σ_i indicates the average of $d[\sigma_{WW}(\text{BR}_{e\nu} + \text{BR}_{\mu\nu})]/d\cos\theta_{W^-}$ in the i -th bin of $\cos\theta_{W^-}$ with width 0.2. The values in each bin of the measured and expected statistical error and of the systematic errors, LEP uncorrelated and correlated, are reported as well. All values are expressed in pb.

L3 [159]

\sqrt{s} interval (GeV)		Luminosity (pb ⁻¹)				Luminosity weighted \sqrt{s} (GeV)				
180-184		55.46				182.68				
$\cos\theta_{W^-}$ bin i	1	2	3	4	5	6	7	8	9	10
σ_i (pb)	0.691	0.646	0.508	0.919	1.477	2.587	3.541	3.167	3.879	4.467
$\delta\sigma_i(\text{stat})$ (pb)	0.270	0.265	0.243	0.322	0.407	0.539	0.640	0.619	0.708	0.801
$\delta\sigma_i(\text{stat,exp.})$ (pb)	0.269	0.290	0.329	0.364	0.404	0.453	0.508	0.591	0.704	0.877
$\delta\sigma_i(\text{syst,unc})$ (pb)	0.016	0.009	0.007	0.011	0.018	0.031	0.043	0.039	0.048	0.058
$\delta\sigma_i(\text{syst,cor})$ (pb)	0.002	0.002	0.002	0.003	0.005	0.009	0.012	0.011	0.013	0.015

\sqrt{s} interval (GeV)		Luminosity (pb ⁻¹)				Luminosity weighted \sqrt{s} (GeV)				
184-194		206.49				189.16				
$\cos\theta_{W^-}$ bin i	1	2	3	4	5	6	7	8	9	10
σ_i (pb)	0.759	0.902	1.125	1.320	1.472	1.544	2.085	2.870	4.144	6.022
$\delta\sigma_i(\text{stat})$ (pb)	0.128	0.151	0.173	0.190	0.209	0.213	0.254	0.303	0.370	0.459
$\delta\sigma_i(\text{stat,exp.})$ (pb)	0.115	0.137	0.160	0.180	0.205	0.223	0.262	0.304	0.367	0.461
$\delta\sigma_i(\text{syst,unc})$ (pb)	0.017	0.013	0.015	0.015	0.017	0.018	0.024	0.034	0.048	0.074
$\delta\sigma_i(\text{syst,cor})$ (pb)	0.003	0.003	0.004	0.005	0.005	0.005	0.007	0.010	0.014	0.021

\sqrt{s} interval (GeV)		Luminosity (pb ⁻¹)				Luminosity weighted \sqrt{s} (GeV)				
194-204		203.50				198.30				
$\cos\theta_{W^-}$ bin i	1	2	3	4	5	6	7	8	9	10
σ_i (pb)	0.652	0.709	0.880	0.859	1.140	1.295	2.114	2.334	3.395	5.773
$\delta\sigma_i(\text{stat})$ (pb)	0.105	0.123	0.146	0.155	0.179	0.192	0.255	0.264	0.333	0.442
$\delta\sigma_i(\text{stat,exp.})$ (pb)	0.092	0.117	0.140	0.164	0.184	0.209	0.245	0.288	0.354	0.459
$\delta\sigma_i(\text{syst,unc})$ (pb)	0.014	0.010	0.011	0.010	0.013	0.015	0.024	0.027	0.040	0.071
$\delta\sigma_i(\text{syst,cor})$ (pb)	0.002	0.002	0.003	0.003	0.004	0.004	0.007	0.008	0.012	0.020

\sqrt{s} interval (GeV)		Luminosity (pb ⁻¹)				Luminosity weighted \sqrt{s} (GeV)				
204-210		217.30				205.96				
$\cos\theta_{W^-}$ bin i	1	2	3	4	5	6	7	8	9	10
σ_i (pb)	0.678	0.578	0.768	1.052	1.620	1.734	1.873	2.903	4.638	7.886
$\delta\sigma_i(\text{stat})$ (pb)	0.111	0.114	0.140	0.168	0.212	0.226	0.238	0.302	0.394	0.534
$\delta\sigma_i(\text{stat,exp.})$ (pb)	0.089	0.117	0.141	0.164	0.186	0.216	0.251	0.303	0.387	0.528
$\delta\sigma_i(\text{syst,unc})$ (pb)	0.015	0.008	0.010	0.012	0.019	0.020	0.021	0.034	0.054	0.097
$\delta\sigma_i(\text{syst,cor})$ (pb)	0.002	0.002	0.003	0.004	0.006	0.006	0.006	0.010	0.016	0.027

Table E.9: W^- differential angular cross-section in the 10 angular bins for the four chosen energy intervals for the L3 experiment. For each energy range, the measured integrated luminosity and the luminosity-weighted centre-of-mass energy is reported. The results per angular bin in each energy interval are then presented: σ_i indicates the average of $d[\sigma_{WW}(\text{BR}_{e\nu} + \text{BR}_{\mu\nu})]/d\cos\theta_{W^-}$ in the i -th bin of $\cos\theta_{W^-}$ with width 0.2. The values in each bin of the measured and expected statistical error and of the systematic errors, LEP uncorrelated and correlated, are reported as well. All values are expressed in pb.

OPAL [160]

\sqrt{s} interval (GeV)		Luminosity (pb ⁻¹)				Luminosity weighted \sqrt{s} (GeV)				
180-184		57.38				182.68				
$\cos\theta_{W^-}$ bin i	1	2	3	4	5	6	7	8	9	10
σ_i (pb)	0.462	0.910	1.101	1.247	1.910	2.291	2.393	2.871	3.851	4.746
$\delta\sigma_i(\text{stat})$ (pb)	0.228	0.298	0.313	0.333	0.408	0.451	0.461	0.507	0.602	0.689
$\delta\sigma_i(\text{stat,exp.})$ (pb)	0.276	0.286	0.296	0.328	0.353	0.396	0.444	0.502	0.599	0.735
$\delta\sigma_i(\text{syst,unc})$ (pb)	0.008	0.013	0.013	0.020	0.018	0.017	0.033	0.046	0.052	0.089
$\delta\sigma_i(\text{syst,cor})$ (pb)	0.003	0.003	0.003	0.002	0.002	0.003	0.003	0.003	0.004	0.005

\sqrt{s} interval (GeV)		Luminosity (pb ⁻¹)				Luminosity weighted \sqrt{s} (GeV)				
184-194		212.37				189.04				
$\cos\theta_{W^-}$ bin i	1	2	3	4	5	6	7	8	9	10
σ_i (pb)	0.621	0.980	1.004	1.125	1.193	1.944	2.190	2.696	3.622	5.798
$\delta\sigma_i(\text{stat})$ (pb)	0.135	0.160	0.158	0.165	0.168	0.213	0.228	0.256	0.305	0.401
$\delta\sigma_i(\text{stat,exp.})$ (pb)	0.139	0.145	0.154	0.167	0.180	0.202	0.230	0.267	0.326	0.417
$\delta\sigma_i(\text{syst,unc})$ (pb)	0.008	0.013	0.013	0.020	0.018	0.017	0.033	0.046	0.052	0.089
$\delta\sigma_i(\text{syst,cor})$ (pb)	0.003	0.003	0.003	0.002	0.002	0.003	0.003	0.003	0.004	0.005

\sqrt{s} interval (GeV)		Luminosity (pb ⁻¹)				Luminosity weighted \sqrt{s} (GeV)				
194-204		190.67				198.35				
$\cos\theta_{W^-}$ bin i	1	2	3	4	5	6	7	8	9	10
σ_i (pb)	0.651	0.678	0.834	1.397	1.543	1.994	1.844	2.422	4.168	7.044
$\delta\sigma_i(\text{stat})$ (pb)	0.147	0.145	0.153	0.191	0.200	0.224	0.219	0.256	0.344	0.472
$\delta\sigma_i(\text{stat,exp.})$ (pb)	0.140	0.148	0.156	0.168	0.185	0.204	0.238	0.282	0.353	0.478
$\delta\sigma_i(\text{syst,unc})$ (pb)	0.008	0.013	0.013	0.020	0.018	0.017	0.033	0.046	0.052	0.089
$\delta\sigma_i(\text{syst,cor})$ (pb)	0.003	0.003	0.003	0.002	0.002	0.003	0.003	0.003	0.004	0.005

\sqrt{s} interval (GeV)		Luminosity (pb ⁻¹)				Luminosity weighted \sqrt{s} (GeV)				
204-210		220.45				205.94				
$\cos\theta_{W^-}$ bin i	1	2	3	4	5	6	7	8	9	10
σ_i (pb)	0.496	0.606	0.453	0.989	1.116	1.919	2.303	2.874	4.573	7.129
$\delta\sigma_i(\text{stat})$ (pb)	0.122	0.129	0.111	0.151	0.158	0.206	0.227	0.256	0.335	0.442
$\delta\sigma_i(\text{stat,exp.})$ (pb)	0.123	0.133	0.140	0.149	0.164	0.185	0.215	0.258	0.331	0.458
$\delta\sigma_i(\text{syst,unc})$ (pb)	0.008	0.013	0.013	0.020	0.018	0.017	0.033	0.046	0.052	0.089
$\delta\sigma_i(\text{syst,cor})$ (pb)	0.003	0.003	0.003	0.002	0.002	0.003	0.003	0.003	0.004	0.005

Table E.10: W^- differential angular cross-section in the 10 angular bins for the four chosen energy intervals for the OPAL experiment. For each energy range, the measured integrated luminosity and the luminosity-weighted centre-of-mass energy is reported. The results per angular bin in each energy interval are then presented: σ_i indicates the average of $d[\sigma_{WW}(\text{BR}_{e\nu} + \text{BR}_{\mu\nu})]/d\cos\theta_{W^-}$ in the i -th bin of $\cos\theta_{W^-}$ with width 0.2. The values in each bin of the measured and expected statistical error and of the systematic errors, LEP uncorrelated and correlated, are reported as well. All values are expressed in pb.

\sqrt{s} (GeV)	σ_{ZZ}	$\Delta\sigma_{ZZ}^{\text{stat}}$	(LCEC) $\Delta\sigma_{ZZ}^{\text{syst}}$	(LUEU) $\Delta\sigma_{ZZ}^{\text{syst}}$	(LUEC) $\Delta\sigma_{ZZ}^{\text{syst}}$	$\Delta\sigma_{ZZ}$	$\Delta\sigma_{ZZ}^{\text{stat (exp)}}$
ALEPH [179]							
182.7	0.11	$^{+0.16}_{-0.11}$	± 0.01	± 0.03	± 0.03	$^{+0.16}_{-0.12}$	± 0.14
188.6	0.67	$^{+0.13}_{-0.12}$	± 0.01	± 0.03	± 0.03	$^{+0.14}_{-0.13}$	± 0.13
191.6	0.62	$^{+0.40}_{-0.32}$	± 0.01	± 0.06	± 0.01	$^{+0.40}_{-0.33}$	± 0.36
195.5	0.73	$^{+0.24}_{-0.21}$	± 0.01	± 0.06	± 0.01	$^{+0.25}_{-0.22}$	± 0.23
199.5	0.91	$^{+0.24}_{-0.21}$	± 0.01	± 0.08	± 0.01	$^{+0.25}_{-0.22}$	± 0.23
201.6	0.71	$^{+0.31}_{-0.26}$	± 0.01	± 0.08	± 0.01	$^{+0.32}_{-0.27}$	± 0.29
204.9	1.20	$^{+0.27}_{-0.25}$	± 0.01	± 0.07	± 0.02	$^{+0.28}_{-0.26}$	± 0.26
206.6	1.05	$^{+0.21}_{-0.20}$	± 0.01	± 0.06	± 0.01	$^{+0.22}_{-0.21}$	± 0.21
DELPHI [180]							
182.7	0.35	$^{+0.20}_{-0.15}$	± 0.01	± 0.00	± 0.02	$^{+0.20}_{-0.15}$	± 0.16
188.6	0.52	$^{+0.12}_{-0.11}$	± 0.01	± 0.00	± 0.02	$^{+0.12}_{-0.11}$	± 0.13
191.6	0.63	$^{+0.36}_{-0.30}$	± 0.01	± 0.01	± 0.02	$^{+0.36}_{-0.30}$	± 0.35
195.5	1.05	$^{+0.25}_{-0.22}$	± 0.01	± 0.01	± 0.02	$^{+0.25}_{-0.22}$	± 0.21
199.5	0.75	$^{+0.20}_{-0.18}$	± 0.01	± 0.01	± 0.01	$^{+0.20}_{-0.18}$	± 0.21
201.6	0.85	$^{+0.33}_{-0.28}$	± 0.01	± 0.01	± 0.01	$^{+0.33}_{-0.28}$	± 0.32
204.9	1.03	$^{+0.23}_{-0.20}$	± 0.02	± 0.01	± 0.01	$^{+0.23}_{-0.20}$	± 0.23
206.6	0.96	$^{+0.16}_{-0.15}$	± 0.02	± 0.01	± 0.01	$^{+0.16}_{-0.15}$	± 0.17
L3 [181]							
182.7	0.31	± 0.16	± 0.05	± 0.00	± 0.01	± 0.17	± 0.16
188.6	0.73	± 0.15	± 0.02	± 0.02	± 0.02	± 0.15	± 0.15
191.6	0.29	± 0.22	± 0.01	± 0.01	± 0.02	± 0.22	± 0.34
195.5	1.18	± 0.24	± 0.04	± 0.05	± 0.06	± 0.26	± 0.22
199.5	1.25	± 0.25	± 0.04	± 0.05	± 0.07	± 0.27	± 0.24
201.6	0.95	± 0.38	± 0.03	± 0.04	± 0.05	± 0.39	± 0.35
204.9	0.77	$^{+0.21}_{-0.19}$	± 0.01	± 0.01	± 0.04	$^{+0.21}_{-0.19}$	± 0.22
206.6	1.09	$^{+0.17}_{-0.16}$	± 0.02	± 0.02	± 0.06	$^{+0.18}_{-0.17}$	± 0.17
OPAL [182]							
182.7	0.12	$^{+0.20}_{-0.18}$	± 0.00	± 0.03	± 0.00	$^{+0.20}_{-0.18}$	± 0.19
188.6	0.80	$^{+0.14}_{-0.13}$	± 0.01	± 0.05	± 0.03	$^{+0.15}_{-0.14}$	± 0.14
191.6	1.29	$^{+0.47}_{-0.40}$	± 0.02	± 0.09	± 0.05	$^{+0.48}_{-0.41}$	± 0.36
195.5	1.13	$^{+0.26}_{-0.24}$	± 0.02	± 0.06	± 0.05	$^{+0.27}_{-0.25}$	± 0.25
199.5	1.05	$^{+0.25}_{-0.22}$	± 0.02	± 0.05	± 0.04	$^{+0.26}_{-0.23}$	± 0.25
201.6	0.79	$^{+0.35}_{-0.29}$	± 0.02	± 0.05	± 0.03	$^{+0.36}_{-0.30}$	± 0.37
204.9	1.07	$^{+0.27}_{-0.24}$	± 0.02	± 0.06	± 0.04	$^{+0.28}_{-0.25}$	± 0.26
206.6	0.97	$^{+0.19}_{-0.18}$	± 0.02	± 0.05	± 0.04	$^{+0.20}_{-0.19}$	± 0.20

Table E.11: Z-pair production cross-section (in pb) at different energies from the four LEP experiments. The first column contains the LEP centre-of-mass energy, the second the measurements and the third the statistical uncertainty. The fourth, the fifth and the sixth columns list the different components of the systematic errors as defined in Table E.5. The total error is given in the seventh column, and the eighth column lists the symmetrised expected statistical error for each of the four experiments.

LEP							
\sqrt{s} (GeV)	σ_{ZZ}	$\Delta\sigma_{ZZ}^{\text{stat}}$	(LCEC) $\Delta\sigma_{ZZ}^{\text{syst}}$	(LUEU) $\Delta\sigma_{ZZ}^{\text{syst}}$	(LUEC) $\Delta\sigma_{ZZ}^{\text{syst}}$	$\Delta\sigma_{ZZ}$	χ^2/dof
182.7	0.22	± 0.08	± 0.02	± 0.01	± 0.01	± 0.08	} 14.5/24
188.6	0.66	± 0.07	± 0.01	± 0.01	± 0.01	± 0.07	
191.6	0.67	± 0.17	± 0.01	± 0.03	± 0.01	± 0.18	
195.5	1.00	± 0.11	± 0.02	± 0.02	± 0.02	± 0.12	
199.5	0.95	± 0.12	± 0.02	± 0.02	± 0.02	± 0.12	
201.6	0.81	± 0.17	± 0.02	± 0.02	± 0.01	± 0.18	
204.9	0.98	± 0.12	± 0.01	± 0.02	± 0.02	± 0.13	
206.6	1.00	± 0.09	± 0.02	± 0.02	± 0.02	± 0.09	

Table E.12: LEP combined Z-pair production cross-section (in pb) at different energies. The first column contains the LEP centre-of-mass energy, the second the measurements and the third the statistical uncertainty. The fourth, the fifth and the sixth columns list the different components of the systematic errors as defined in Table E.5. The total error is given in the seventh column, and the eighth column lists the χ^2/dof of the fit.

\sqrt{s} (GeV)	ZZ cross-section (pb)	
	$\sigma_{ZZ}^{\text{YFSZZ}}$	$\sigma_{ZZ}^{\text{ZZTO}}$
182.7	0.254[1]	0.25425[2]
188.6	0.655[2]	0.64823[1]
191.6	0.782[2]	0.77670[1]
195.5	0.897[3]	0.89622[1]
199.5	0.981[2]	0.97765[1]
201.6	1.015[1]	1.00937[1]
204.9	1.050[1]	1.04335[1]
206.6	1.066[1]	1.05535[1]

Table E.13: Z-pair cross-section predictions (in pb) interpolated at the data centre-of-mass energies, according to the YFSZZ [183] and ZZTO [184] predictions. The numbers in brackets are the errors on the last digit and arise from the numerical integration of the cross-section only.

\sqrt{s} (GeV)	\mathcal{R}_{ZZ}	$\Delta\mathcal{R}_{ZZ}^{\text{stat}}$	(LCEU) $\Delta\mathcal{R}_{ZZ}^{\text{syst}}$	(LCEC) $\Delta\mathcal{R}_{ZZ}^{\text{syst}}$	(LUEU) $\Delta\mathcal{R}_{ZZ}^{\text{syst}}$	(LUEC) $\Delta\mathcal{R}_{ZZ}^{\text{syst}}$	$\Delta\mathcal{R}_{ZZ}$	χ^2/dof
YFSZZ [183]								
182.7	0.857	± 0.307	± 0.018	± 0.068	± 0.041	± 0.040	± 0.320	} 14.5/24
188.6	1.007	± 0.104	± 0.020	± 0.019	± 0.022	± 0.018	± 0.111	
191.6	0.859	± 0.220	± 0.017	± 0.013	± 0.032	± 0.016	± 0.224	
195.5	1.118	± 0.127	± 0.023	± 0.021	± 0.025	± 0.019	± 0.134	
199.5	0.970	± 0.119	± 0.020	± 0.018	± 0.025	± 0.016	± 0.126	
201.6	0.800	± 0.170	± 0.016	± 0.016	± 0.023	± 0.012	± 0.174	
204.9	0.928	± 0.116	± 0.019	± 0.013	± 0.019	± 0.014	± 0.121	
206.6	0.938	± 0.085	± 0.019	± 0.014	± 0.017	± 0.016	± 0.091	
Average	0.960	± 0.045	± 0.008	± 0.017	± 0.009	± 0.015	± 0.052	17.4/31
ZZTO [184]								
182.7	0.857	± 0.307	± 0.018	± 0.068	± 0.041	± 0.040	± 0.320	} 14.5/24
188.6	1.017	± 0.105	± 0.021	± 0.019	± 0.022	± 0.019	± 0.113	
191.6	0.865	± 0.222	± 0.018	± 0.014	± 0.033	± 0.016	± 0.226	
195.5	1.118	± 0.127	± 0.023	± 0.021	± 0.025	± 0.019	± 0.134	
199.5	0.974	± 0.120	± 0.020	± 0.018	± 0.025	± 0.016	± 0.126	
201.6	0.805	± 0.171	± 0.016	± 0.016	± 0.023	± 0.012	± 0.174	
204.9	0.934	± 0.117	± 0.019	± 0.013	± 0.019	± 0.013	± 0.122	
206.6	0.948	± 0.085	± 0.019	± 0.014	± 0.017	± 0.016	± 0.092	
Average	0.966	± 0.046	± 0.008	± 0.017	± 0.009	± 0.015	± 0.052	17.4/31

Table E.14: Ratios of LEP combined Z-pair cross-section measurements to the expectations, for different centre-of-mass energies and for all energies combined. The first column contains the centre-of-mass energy, the second the combined ratios, the third the statistical errors. The fourth to seventh columns contain the sources of systematic errors as defined in Table E.5. The total error is given in the eighth column. The only LCEU systematic sources considered are the statistical errors on the cross-section theoretical predictions, while the LCEC, LUEU and LUEC sources are those coming from the corresponding errors on the cross-section measurements. For the LEP averages, the χ^2/dof of the fit is also given in the ninth column.

\sqrt{s} (GeV)	$\sigma_{W e \nu \text{ had}}$	$\Delta\sigma_{W e \nu \text{ had}}^{\text{stat}}$	(LCEC) $\Delta\sigma_{W e \nu \text{ had}}^{\text{syst}}$	(LUEU) $\Delta\sigma_{W e \nu \text{ had}}^{\text{syst}}$	(LUEC) $\Delta\sigma_{W e \nu \text{ had}}^{\text{syst}}$	$\Delta\sigma_{W e \nu \text{ had}}$	$\Delta\sigma_{W e \nu \text{ had}}^{\text{stat (exp)}}$
ALEPH [190]							
182.7	0.44	+0.29 -0.24	± 0.01	± 0.01	± 0.01	+0.29 -0.24	± 0.26
188.6	0.33	+0.16 -0.14	± 0.02	± 0.01	± 0.01	+0.16 -0.15	± 0.16
191.6	0.52	+0.52 -0.40	± 0.02	± 0.01	± 0.01	+0.52 -0.40	± 0.45
195.5	0.61	+0.28 -0.25	± 0.02	± 0.01	± 0.01	+0.28 -0.25	± 0.25
199.5	1.06	+0.30 -0.27	± 0.02	± 0.01	± 0.01	+0.30 -0.27	± 0.24
201.6	0.72	+0.39 -0.33	± 0.02	± 0.01	± 0.02	+0.39 -0.33	± 0.34
204.9	0.34	+0.24 -0.21	± 0.02	± 0.01	± 0.02	+0.24 -0.21	± 0.25
206.6	0.64	+0.21 -0.19	± 0.02	± 0.01	± 0.02	+0.21 -0.19	± 0.19
DELPHI [191]							
182.7	0.11	+0.30 -0.11	± 0.02	± 0.03	± 0.08	+0.31 -0.14	± 0.30
188.6	0.57	+0.19 -0.18	± 0.02	± 0.04	± 0.08	+0.21 -0.20	± 0.18
191.6	0.30	+0.47 -0.30	± 0.02	± 0.03	± 0.08	+0.48 -0.31	± 0.43
195.5	0.50	+0.29 -0.26	± 0.02	± 0.03	± 0.08	+0.30 -0.27	± 0.27
199.5	0.57	+0.27 -0.25	± 0.02	± 0.02	± 0.08	+0.28 -0.26	± 0.25
201.6	0.67	+0.39 -0.35	± 0.02	± 0.03	± 0.08	+0.40 -0.36	± 0.35
204.9	0.99	+0.32 -0.30	± 0.02	± 0.05	± 0.08	+0.33 -0.31	± 0.28
206.6	0.81	+0.22 -0.20	± 0.02	± 0.04	± 0.08	+0.23 -0.22	± 0.20
L3 [192, 193, 194]							
182.7	0.58	+0.23 -0.20	± 0.03	± 0.03	± 0.00	+0.23 -0.20	± 0.21
188.6	0.52	+0.14 -0.13	± 0.02	± 0.02	± 0.00	+0.14 -0.13	± 0.14
191.6	0.84	+0.44 -0.37	± 0.03	± 0.03	± 0.00	+0.44 -0.37	± 0.41
195.5	0.66	+0.24 -0.22	± 0.02	± 0.03	± 0.00	+0.25 -0.23	± 0.21
199.5	0.37	+0.22 -0.20	± 0.01	± 0.02	± 0.00	+0.22 -0.20	± 0.22
201.6	1.10	+0.40 -0.35	± 0.05	± 0.05	± 0.00	+0.40 -0.35	± 0.35
204.9	0.42	+0.25 -0.21	± 0.02	± 0.03	± 0.00	+0.25 -0.21	± 0.25
206.6	0.66	+0.19 -0.17	± 0.02	± 0.03	± 0.00	+0.20 -0.18	± 0.20
LEP							χ^2/dof
182.7	0.42	± 0.15	± 0.02	± 0.02	± 0.01	± 0.15	} 13.2/16
188.6	0.47	± 0.09	± 0.02	± 0.01	± 0.01	± 0.09	
191.6	0.56	± 0.25	± 0.02	± 0.02	± 0.02	± 0.25	
195.5	0.60	± 0.14	± 0.02	± 0.01	± 0.02	± 0.14	
199.5	0.65	± 0.14	± 0.02	± 0.01	± 0.02	± 0.14	
201.6	0.82	± 0.20	± 0.03	± 0.02	± 0.02	± 0.20	
204.9	0.54	± 0.15	± 0.02	± 0.02	± 0.02	± 0.15	
206.6	0.69	± 0.11	± 0.02	± 0.02	± 0.02	± 0.12	

Table E.15: Single-W hadronic production cross-section (in pb) at different energies. The first column contains the LEP centre-of-mass energy, and the second the measurements. The third column reports the statistical error, and the fourth to the sixth columns list the different systematic uncertainties. The labels LCEC, LUEU and LUEC are defined in Table E.5. The seventh column contains the total error and the eighth lists the symmetrised expected statistical error for the three LEP measurements, and, for the LEP combined value, the χ^2/dof of the fit.

\sqrt{s} (GeV)	$\sigma_{We\nu\text{ tot}}$	$\Delta\sigma_{We\nu\text{ tot}}^{\text{stat}}$	(LCEC) $\Delta\sigma_{We\nu\text{ tot}}^{\text{syst}}$	(LUEU) $\Delta\sigma_{We\nu\text{ tot}}^{\text{syst}}$	(LUEC) $\Delta\sigma_{We\nu\text{ tot}}^{\text{syst}}$	$\Delta\sigma_{We\nu\text{ tot}}$	$\Delta\sigma_{We\nu\text{ tot}}^{\text{stat (exp)}}$
ALEPH [190]							
182.7	0.60	+0.32 -0.26	± 0.02	± 0.01	± 0.01	+0.32 -0.26	± 0.29
188.6	0.55	+0.18 -0.16	± 0.02	± 0.01	± 0.01	+0.18 -0.16	± 0.18
191.6	0.89	+0.58 -0.44	± 0.02	± 0.01	± 0.02	+0.58 -0.44	± 0.48
195.5	0.87	+0.31 -0.27	± 0.03	± 0.01	± 0.02	+0.31 -0.27	± 0.28
199.5	1.31	+0.32 -0.29	± 0.03	± 0.01	± 0.02	+0.32 -0.29	± 0.26
201.6	0.80	+0.42 -0.35	± 0.03	± 0.01	± 0.02	+0.42 -0.35	± 0.38
204.9	0.65	+0.27 -0.23	± 0.03	± 0.02	± 0.02	+0.27 -0.23	± 0.27
206.6	0.81	+0.22 -0.20	± 0.03	± 0.02	± 0.02	+0.22 -0.20	± 0.22
DELPHI [191]							
182.7	0.69	+0.41 -0.23	± 0.02	± 0.04	± 0.08	+0.42 -0.25	± 0.33
188.6	0.75	+0.22 -0.20	± 0.02	± 0.04	± 0.08	+0.23 -0.22	± 0.20
191.6	0.40	+0.54 -0.31	± 0.02	± 0.03	± 0.08	+0.55 -0.33	± 0.48
195.5	0.68	+0.33 -0.28	± 0.02	± 0.03	± 0.08	+0.34 -0.38	± 0.30
199.5	0.95	+0.33 -0.29	± 0.02	± 0.03	± 0.08	+0.34 -0.30	± 0.29
201.6	1.24	+0.51 -0.42	± 0.02	± 0.04	± 0.08	+0.52 -0.43	± 0.41
204.9	1.06	+0.36 -0.30	± 0.02	± 0.05	± 0.08	+0.37 -0.32	± 0.33
206.6	1.14	+0.26 -0.23	± 0.02	± 0.04	± 0.08	+0.28 -0.25	± 0.23
L3 [192, 193, 194]							
182.7	0.80	+0.28 -0.25	± 0.04	± 0.04	± 0.01	+0.28 -0.25	± 0.26
188.6	0.69	+0.16 -0.14	± 0.03	± 0.03	± 0.01	+0.16 -0.15	± 0.15
191.6	1.11	+0.48 -0.41	± 0.02	± 0.04	± 0.01	+0.48 -0.41	± 0.46
195.5	0.97	+0.27 -0.25	± 0.02	± 0.02	± 0.01	+0.27 -0.25	± 0.25
199.5	0.88	+0.26 -0.24	± 0.02	± 0.03	± 0.01	+0.26 -0.24	± 0.25
201.6	1.50	+0.45 -0.40	± 0.03	± 0.04	± 0.02	+0.45 -0.40	± 0.38
204.9	0.78	+0.29 -0.25	± 0.02	± 0.03	± 0.01	+0.29 -0.25	± 0.29
206.6	1.08	+0.21 -0.20	± 0.02	± 0.03	± 0.01	+0.21 -0.20	± 0.23
LEP							χ^2/dof
182.7	0.70	± 0.17	± 0.03	± 0.02	± 0.02	± 0.17	} 8.1/16
188.6	0.66	± 0.10	± 0.02	± 0.02	± 0.01	± 0.10	
191.6	0.81	± 0.27	± 0.02	± 0.02	± 0.02	± 0.28	
195.5	0.85	± 0.16	± 0.02	± 0.01	± 0.02	± 0.16	
199.5	1.05	± 0.15	± 0.02	± 0.01	± 0.02	± 0.16	
201.6	1.17	± 0.23	± 0.03	± 0.02	± 0.02	± 0.23	
204.9	0.80	± 0.17	± 0.02	± 0.02	± 0.02	± 0.17	
206.6	1.00	± 0.13	± 0.03	± 0.02	± 0.02	± 0.14	

Table E.16: Single-W total production cross-section (in pb) at different energies. The first column contains the LEP centre-of-mass energy, and the second the measurements. The third column reports the statistical error, and the fourth to the sixth columns list the different systematic uncertainties. The labels LCEC, LUEU and LUEC are defined in Table E.5. The seventh column contains the total error and the eighth lists the symmetrised expected statistical error for the three LEP measurements, and, for the LEP combined values, the χ^2/dof of the fit.

\sqrt{s} (GeV)	We $\nu \rightarrow$ qqe ν cross-section (pb)			We ν total cross-section (pb)	
	$\sigma_{\text{We}\nu \text{ had}}^{\text{grc4f}}$	$\sigma_{\text{We}\nu \text{ had}}^{\text{WPHACT}}$	$\sigma_{\text{We}\nu \text{ had}}^{\text{WTO}}$	$\sigma_{\text{We}\nu \text{ tot}}^{\text{grc4f}}$	$\sigma_{\text{We}\nu \text{ tot}}^{\text{WPHACT}}$
182.7	0.4194[1]	0.4070[2]	0.40934[8]	0.6254[1]	0.6066[2]
188.6	0.4699[1]	0.4560[2]	0.45974[9]	0.6999[1]	0.6796[2]
191.6	0.4960[1]	0.4810[2]	0.4852[1]	0.7381[2]	0.7163[2]
195.5	0.5308[2]	0.5152[2]	0.5207[1]	0.7896[2]	0.7665[3]
199.5	0.5673[2]	0.5509[3]	0.5573[1]	0.8431[2]	0.8182[3]
201.6	0.5870[2]	0.5704[4]	0.5768[1]	0.8718[2]	0.8474[4]
204.9	0.6196[2]	0.6021[4]	0.6093[2]	0.9185[3]	0.8921[4]
206.6	0.6358[2]	0.6179[4]	0.6254[2]	0.9423[3]	0.9157[5]

Table E.17: Single-W hadronic and total cross-section predictions (in pb) interpolated at the data centre-of-mass energies, according to the `grc4f` [187], `WPHACT` [195] and `WTO` [198] predictions. The numbers in brackets are the errors on the last digit and arise from the numerical integration of the cross-section only.

\sqrt{s} (GeV)	$\mathcal{R}_{We\nu}$	$\Delta\mathcal{R}_{We\nu}^{\text{stat}}$	(LCEU) $\Delta\mathcal{R}_{We\nu}^{\text{syst}}$	(LCEC) $\Delta\mathcal{R}_{We\nu}^{\text{syst}}$	(LUEU) $\Delta\mathcal{R}_{We\nu}^{\text{syst}}$	(LUEC) $\Delta\mathcal{R}_{We\nu}^{\text{syst}}$	$\Delta\mathcal{R}_{We\nu}$	χ^2/dof
grc4f [187]								
182.7	1.122	± 0.266	± 0.001	± 0.041	± 0.029	± 0.026	± 0.272	} 8.1/16
188.6	0.936	± 0.142	± 0.001	± 0.033	± 0.022	± 0.024	± 0.149	
191.6	1.094	± 0.370	± 0.001	± 0.030	± 0.026	± 0.028	± 0.373	
195.5	1.081	± 0.199	± 0.001	± 0.028	± 0.017	± 0.023	± 0.203	
199.5	1.242	± 0.183	± 0.001	± 0.028	± 0.017	± 0.022	± 0.187	
201.6	1.340	± 0.258	± 0.001	± 0.031	± 0.021	± 0.023	± 0.261	
204.9	0.873	± 0.185	± 0.001	± 0.025	± 0.020	± 0.020	± 0.189	
206.6	1.058	± 0.138	± 0.001	± 0.026	± 0.019	± 0.021	± 0.143	
Average	1.058	± 0.068	± 0.000	± 0.029	± 0.008	± 0.022	± 0.078	12.2/24
WPHACT [195]								
182.7	1.157	± 0.274	± 0.001	± 0.043	± 0.030	± 0.027	± 0.281	} 8.1/16
188.6	0.965	± 0.146	± 0.001	± 0.034	± 0.023	± 0.024	± 0.154	
191.6	1.128	± 0.382	± 0.001	± 0.031	± 0.027	± 0.029	± 0.385	
195.5	1.115	± 0.206	± 0.001	± 0.029	± 0.017	± 0.023	± 0.210	
199.5	1.280	± 0.188	± 0.001	± 0.029	± 0.018	± 0.022	± 0.193	
201.6	1.380	± 0.265	± 0.001	± 0.032	± 0.022	± 0.024	± 0.269	
204.9	0.899	± 0.191	± 0.001	± 0.026	± 0.020	± 0.020	± 0.195	
206.6	1.089	± 0.142	± 0.001	± 0.027	± 0.020	± 0.022	± 0.148	
Average	1.090	± 0.070	± 0.000	± 0.030	± 0.008	± 0.023	± 0.080	12.2/24

Table E.18: Ratios of LEP combined total single-W cross-section measurements to the expectations, for different centre-of-mass energies and for all energies combined. The first column contains the centre-of-mass energy, the second the combined ratios, the third the statistical errors. The fourth to seventh columns contain the sources of systematic errors, as defined in Table E.5. The total error is given in the eighth column. The only LCEU systematic sources considered are the statistical errors on the cross-section theoretical predictions, while the LCEC, LUEU and LUEC sources are those arising from the corresponding errors on the cross-section measurements.

\sqrt{s} (GeV)	σ_{Zee}	$\Delta\sigma_{Zee}^{\text{stat}}$	(LCEC) $\Delta\sigma_{Zee}^{\text{syst}}$	(LUEU) $\Delta\sigma_{Zee}^{\text{syst}}$	(LUEC) $\Delta\sigma_{Zee}^{\text{syst}}$	$\Delta\sigma_{Zee}$	$\Delta\sigma_{Zee}^{\text{stat (exp)}}$
ALEPH [190]							
182.7	0.27	$^{+0.21}_{-0.16}$	± 0.01	± 0.02	± 0.01	$^{+0.21}_{-0.16}$	± 0.20
188.6	0.42	$^{+0.14}_{-0.12}$	± 0.01	± 0.03	± 0.01	$^{+0.14}_{-0.12}$	± 0.12
191.6	0.61	$^{+0.39}_{-0.29}$	± 0.01	± 0.03	± 0.01	$^{+0.39}_{-0.29}$	± 0.29
195.5	0.72	$^{+0.24}_{-0.20}$	± 0.01	± 0.03	± 0.01	$^{+0.24}_{-0.20}$	± 0.18
199.5	0.60	$^{+0.21}_{-0.18}$	± 0.01	± 0.03	± 0.01	$^{+0.21}_{-0.18}$	± 0.17
201.6	0.89	$^{+0.35}_{-0.28}$	± 0.01	± 0.03	± 0.01	$^{+0.35}_{-0.28}$	± 0.24
204.9	0.42	$^{+0.17}_{-0.14}$	± 0.01	± 0.03	± 0.01	$^{+0.17}_{-0.14}$	± 0.17
206.6	0.70	$^{+0.17}_{-0.15}$	± 0.01	± 0.03	± 0.01	$^{+0.17}_{-0.15}$	± 0.14
DELPHI [191]							
182.7	0.56	$^{+0.27}_{-0.22}$	± 0.01	± 0.06	± 0.02	$^{+0.28}_{-0.23}$	± 0.24
188.6	0.64	$^{+0.15}_{-0.14}$	± 0.01	± 0.03	± 0.02	$^{+0.16}_{-0.14}$	± 0.14
191.6	0.63	$^{+0.40}_{-0.30}$	± 0.01	± 0.03	± 0.03	$^{+0.40}_{-0.30}$	± 0.32
195.5	0.66	$^{+0.22}_{-0.18}$	± 0.01	± 0.02	± 0.03	$^{+0.22}_{-0.19}$	± 0.19
199.5	0.57	$^{+0.20}_{-0.17}$	± 0.01	± 0.02	± 0.02	$^{+0.20}_{-0.17}$	± 0.18
201.6	0.19	$^{+0.21}_{-0.16}$	± 0.01	± 0.02	± 0.01	$^{+0.21}_{-0.16}$	± 0.25
204.9	0.37	$^{+0.18}_{-0.15}$	± 0.01	± 0.02	± 0.02	$^{+0.18}_{-0.15}$	± 0.19
206.6	0.69	$^{+0.16}_{-0.14}$	± 0.01	± 0.01	± 0.03	$^{+0.16}_{-0.14}$	± 0.14
L3 [203]							
182.7	0.51	$^{+0.19}_{-0.16}$	± 0.02	± 0.01	± 0.03	$^{+0.19}_{-0.16}$	± 0.16
188.6	0.55	$^{+0.10}_{-0.09}$	± 0.02	± 0.01	± 0.03	$^{+0.11}_{-0.10}$	± 0.09
191.6	0.60	$^{+0.26}_{-0.21}$	± 0.01	± 0.01	± 0.03	$^{+0.26}_{-0.21}$	± 0.21
195.5	0.40	$^{+0.13}_{-0.11}$	± 0.01	± 0.01	± 0.03	$^{+0.13}_{-0.11}$	± 0.13
199.5	0.33	$^{+0.12}_{-0.10}$	± 0.01	± 0.01	± 0.03	$^{+0.13}_{-0.11}$	± 0.14
201.6	0.81	$^{+0.27}_{-0.23}$	± 0.02	± 0.02	± 0.03	$^{+0.27}_{-0.23}$	± 0.19
204.9	0.56	$^{+0.16}_{-0.14}$	± 0.01	± 0.01	± 0.03	$^{+0.16}_{-0.14}$	± 0.14
206.6	0.59	$^{+0.12}_{-0.10}$	± 0.01	± 0.01	± 0.03	$^{+0.12}_{-0.11}$	± 0.11
LEP							χ^2/dof
182.7	0.45	± 0.11	± 0.01	± 0.02	± 0.01	± 0.11	} 13.0/16
188.6	0.53	± 0.07	± 0.01	± 0.01	± 0.01	± 0.07	
191.6	0.61	± 0.15	± 0.01	± 0.02	± 0.01	± 0.15	
195.5	0.55	± 0.09	± 0.01	± 0.01	± 0.01	± 0.10	
199.5	0.47	± 0.09	± 0.01	± 0.02	± 0.01	± 0.10	
201.6	0.67	± 0.13	± 0.01	± 0.01	± 0.01	± 0.13	
204.9	0.47	± 0.10	± 0.01	± 0.01	± 0.01	± 0.10	
206.6	0.65	± 0.07	± 0.01	± 0.01	± 0.01	± 0.08	

Table E.19: Single-Z hadronic production cross-section (in pb) at different energies. The first column contains the LEP centre-of-mass energy, and the second the measurements. The third column reports the statistical error, and the fourth to the sixth columns list the different systematic uncertainties. The labels LCEC, LUEU and LUEC are defined in Table E.5. The seventh column contains the total error and the eighth lists the symmetrised expected statistical error for each of the three LEP experiments, and, for the LEP combined value, the χ^2/dof of the fit.

\sqrt{s} (GeV)	Zee cross-section (pb)	
	$\sigma_{Zee}^{\text{WPHACT}}$	$\sigma_{Zee}^{\text{grc4f}}$
182.7	0.51275[4]	0.51573[4]
188.6	0.53686[4]	0.54095[5]
191.6	0.54883[4]	0.55314[5]
195.5	0.56399[5]	0.56891[4]
199.5	0.57935[5]	0.58439[4]
201.6	0.58708[4]	0.59243[4]
204.9	0.59905[4]	0.60487[4]
206.6	0.61752[4]	0.60819[4]

Table E.20: Zee hadronic cross-section predictions (in pb) interpolated at the data centre-of-mass energies, according to the WPHACT [195] and grc4f [187] predictions. The numbers in brackets are the errors on the last digit and arise from the numerical integration of the cross-section only.

\sqrt{s} (GeV)	\mathcal{R}_{Zee}	$\Delta\mathcal{R}_{Zee}^{\text{stat}}$	(LCEU) $\Delta\mathcal{R}_{Zee}^{\text{syst}}$	(LCEC) $\Delta\mathcal{R}_{Zee}^{\text{syst}}$	(LUEU) $\Delta\mathcal{R}_{Zee}^{\text{syst}}$	(LUEC) $\Delta\mathcal{R}_{Zee}^{\text{syst}}$	$\Delta\mathcal{R}_{Zee}$	χ^2/dof
grc4f [187]								
182.7	0.871	± 0.214	± 0.000	± 0.020	± 0.035	± 0.025	± 0.219	} 13.0/16
188.6	0.982	± 0.120	± 0.000	± 0.022	± 0.023	± 0.024	± 0.126	
191.6	1.104	± 0.272	± 0.000	± 0.019	± 0.027	± 0.025	± 0.276	
195.5	0.964	± 0.163	± 0.000	± 0.016	± 0.024	± 0.025	± 0.167	
199.5	0.809	± 0.160	± 0.000	± 0.018	± 0.030	± 0.023	± 0.165	
201.6	1.126	± 0.219	± 0.000	± 0.023	± 0.024	± 0.021	± 0.222	
204.9	0.769	± 0.157	± 0.000	± 0.019	± 0.019	± 0.021	± 0.160	
206.6	1.062	± 0.119	± 0.000	± 0.018	± 0.018	± 0.024	± 0.124	
Average	0.955	± 0.057	± 0.000	± 0.019	± 0.009	± 0.023	± 0.065	17.1/23
WPHACT [195]								
182.7	0.876	± 0.215	± 0.000	± 0.020	± 0.035	± 0.025	± 0.220	} 13.0/16
188.6	0.990	± 0.120	± 0.000	± 0.022	± 0.023	± 0.025	± 0.127	
191.6	1.112	± 0.274	± 0.000	± 0.020	± 0.027	± 0.026	± 0.277	
195.5	0.972	± 0.164	± 0.000	± 0.016	± 0.025	± 0.025	± 0.168	
199.5	0.816	± 0.161	± 0.000	± 0.019	± 0.030	± 0.023	± 0.167	
201.6	1.135	± 0.221	± 0.000	± 0.023	± 0.024	± 0.021	± 0.224	
204.9	0.776	± 0.158	± 0.000	± 0.019	± 0.019	± 0.021	± 0.162	
206.6	1.067	± 0.120	± 0.000	± 0.018	± 0.018	± 0.024	± 0.125	
Average	0.962	± 0.057	± 0.000	± 0.020	± 0.009	± 0.024	± 0.065	17.0/23

Table E.21: Ratios of LEP combined single-Z hadronic cross-section measurements to the expectations, for different centre-of-mass energies and for all energies combined. The first column contains the centre-of-mass energy, the second the combined ratios, the third the statistical errors. The fourth to seventh columns contain the sources of systematic errors as defined in Table E.5. The total error is given in the eighth column. The only LCEU systematic sources considered are the statistical errors on the cross-section theoretical predictions, while the LCEC, LUEU and LUEC sources are those arising from the corresponding errors on the cross-section measurements. For the LEP averages, the χ^2/dof of the fit is also given in the ninth column.

Appendix F

Constraints on the Standard Model

F.1 Introduction

The experimental measurements used here to place constraints on the Standard Model (SM) consist of three groups: (i) the final Z-pole results measured in electron-positron collisions by the ALEPH, DELPHI, L3, OPAL and SLD experiments, as combined in Reference [4]; (ii) the mass and width of the W boson measured at LEP-II and described earlier in this report; and (iii) the measurements of the mass of the top quark and the mass and width of the W boson at the Tevatron collider.

The measurements allow checks of the validity of the SM and, within its framework, to infer valuable information about its fundamental parameters. The accuracy of the Z-boson and W-boson measurements makes them sensitive to the mass of the top quark m_t , and to the mass of the Higgs boson m_H through electroweak loop corrections. While the leading m_t dependence is quadratic, the leading m_H dependence is logarithmic. Therefore, the inferred constraints on m_t are much stronger than those on m_H .

In a first step, the predictions for the mass and width of the W boson based on measurements performed at lower Z-pole centre-of-mass energies (LEP-I, SLC, etc) [4] are compared to the direct measurements performed at LEP-II and the Tevatron. The comparison between prediction and direct measurement is also performed for the mass of the top quark. Finally, all measurements are used to infer constraints on the Higgs boson of the minimal SM.

This analysis updates our previous analysis [4]. Similar analyses of this type are presented in References [178, 272], obtaining equivalent results when accounting for the different sets of measurements considered.

F.2 Measurements

The measured quantities considered here are summarised in Table F.1. The predictions of these observables are also shown in this table, derived from the results of the SM fit to the combined high- Q^2 measurements described in the last column of Table F.2. The measurements obtained at the Z pole by the LEP and SLC experiments ALEPH, DELPHI, L3, OPAL and SLD and their combinations, reported in parts a), b) and c) of Table F.1, are final and published [4].

The measurements of the W-boson mass published by CDF [274, 241] and D0 [281, 242], and on the W-boson width published by CDF [289, 239] and D0 [290, 240] are combined by the Tevatron Electroweak Working Group, based on a detailed treatment of correlated systematic uncertainties, with the result: $m_W = 80.387 \pm 0.016$ GeV [291] and $\Gamma_W = 2.050 \pm 0.058$ GeV [292].

Combining these Tevatron results with the final LEP-II results presented in Chapter 7 of this report, $m_W = 80.376 \pm 0.033$ GeV and $\Gamma_W = 2.195 \pm 0.083$ GeV, the resulting world averages are:

$$m_W = 80.385 \pm 0.015 \text{ GeV} \quad (\text{F.1})$$

$$\Gamma_W = 2.085 \pm 0.042 \text{ GeV}, \quad (\text{F.2})$$

and are used in the following.

For the mass of the top quark, m_t , the published results from CDF [293] and D0 [301] are combined by the Tevatron Electroweak Working Group with the result: $m_t = 173.2 \pm 0.9$ GeV [307].

In addition to these high- Q^2 results, the following results measured in low- Q^2 interactions and reported in Table F.3 are considered: (i) the measurements of atomic parity violation in caesium[309], with the numerical result[312] based on a revised analysis of QED radiative corrections applied to the raw measurement; (ii) the result of the E-158 collaboration on the electroweak mixing angle¹ measured in Møller scattering [313]; and (iii) the final result of the NuTeV collaboration on neutrino-nucleon neutral to charged current cross-section ratios [315].

Using neutrino-nucleon data with an average $Q^2 \simeq 20$ GeV², the NuTeV collaboration has extracted the left- and right-handed couplings combinations $g_{\nu\text{Lud}}^2 = 4g_{L\nu}^2(g_{L\text{u}}^2 + g_{L\text{d}}^2) = [1/2 - \sin^2 \theta_{\text{eff}} + (5/9) \sin^4 \theta_{\text{eff}}] \rho_\nu \rho_{\text{ud}}$ and $g_{\nu\text{Rud}}^2 = 4g_{R\nu}^2(g_{R\text{u}}^2 + g_{R\text{d}}^2) = (5/9) \sin^4 \theta_{\text{eff}} \rho_\nu \rho_{\text{ud}}$, with the ρ parameters for example defined in [317]. The NuTeV results for the effective couplings are: $g_{\nu\text{Lud}}^2 = 0.30005 \pm 0.00137$ and $g_{\nu\text{Rud}}^2 = 0.03076 \pm 0.00110$, with a correlation of -0.017 . While the result on $g_{\nu\text{Rud}}$ agrees with the SM expectation, the result on $g_{\nu\text{Lud}}$, relatively measured nearly eight times more precisely than $g_{\nu\text{Rud}}$, shows a deficit with respect to the expectation at the level of 2.9 standard deviations [315]. A recent study finds that EMC-like isovector effects are able to explain this difference [318].

An important quantity in electroweak analyses is given by the running electromagnetic fine-structure constant, $\alpha(m_Z^2)$. The uncertainty in $\alpha(m_Z^2)$ arises from the contribution of light quarks to the photon vacuum polarisation, $\Delta\alpha_{\text{had}}^{(5)}(m_Z^2)$:

$$\alpha(m_Z^2) = \frac{\alpha(0)}{1 - \Delta\alpha_\ell(m_Z^2) - \Delta\alpha_{\text{had}}^{(5)}(m_Z^2) - \Delta\alpha_{\text{top}}(m_Z^2)}, \quad (\text{F.3})$$

where $\alpha(0) = 1/137.036$. The top contribution, $-0.00007(1)$, depends on the mass of the top quark. The leptonic contribution is calculated to third order [320] to be 0.03150, with negligible uncertainty. For the hadronic contribution $\Delta\alpha_{\text{had}}^{(5)}(m_Z^2)$, we use the new result 0.02750 ± 0.00033 [321] listed in the first row of Table F.1, which takes into account recent results on electron-positron annihilations into hadrons at low centre-of-mass energies measured by the BES, CMD-2, KLOE and BABAR collaborations. The reduced uncertainty of 0.00033 still causes an error of 0.00012 on the SM prediction of $\sin^2 \theta_{\text{eff}}^{\text{lept}}$ and of 0.08 on the fitted value of $\log(m_H)$, while the $\alpha_S(m_Z^2)$ values presented here are stable against a variation of $\alpha(m_Z^2)$ in the interval quoted. Several evaluations of $\Delta\alpha_{\text{had}}^{(5)}(m_Z^2)$ exist which are more theory driven [322, 335], resulting in a much reduced uncertainty. To show the effect of the $\alpha(m_Z^2)$ uncertainty on the results, we also use the most recent of these evaluations, 0.02757 ± 0.00010 [335].

¹ E-158 quotes in the $\overline{\text{MS}}$ scheme, evolved to $Q^2 = m_Z^2$. We add 0.00029 to the quoted value in order to obtain the effective electroweak mixing angle [178].

	Measurement with Total Error	Systematic Error	Standard- Model fit	Pull
$\Delta\alpha_{\text{had}}^{(5)}(m_Z^2)[321]$	0.02750 ± 0.00033		0.02759	-0.3
a) <u>LEP-I</u> line-shape and lepton asymmetries: m_Z [GeV] Γ_Z [GeV] σ_{had}^0 [nb] R_ℓ^0 $A_{\text{FB}}^{0,\ell}$ + correlation matrix [4] τ polarisation: $\mathcal{A}_\ell(\mathcal{P}_\tau)$ q \bar{q} charge asymmetry: $\sin^2\theta_{\text{eff}}^{\text{lept}}(Q_{\text{FB}}^{\text{had}})$	91.1875 ± 0.0021 2.4952 ± 0.0023 41.540 ± 0.037 20.767 ± 0.025 0.0171 ± 0.0010 0.1465 ± 0.0033 0.2324 ± 0.0012	$^{(a)}0.0017$ $^{(a)}0.0012$ $^{(b)}0.028$ $^{(b)}0.007$ $^{(b)}0.0003$ 0.0016 0.0010	91.1874 2.4959 41.478 20.742 0.0164 0.1481 0.231439	0.0 -0.3 1.7 1.0 0.7 -0.5 0.8
b) <u>SLD</u> \mathcal{A}_ℓ (SLD)	0.1513 ± 0.0021	0.0010	0.1481	1.6
c) <u>LEP-I/SLD Heavy Flavour</u> R_b^0 R_c^0 $A_{\text{FB}}^{0,b}$ $A_{\text{FB}}^{0,c}$ \mathcal{A}_b \mathcal{A}_c + correlation matrix [4]	0.21629 ± 0.00066 0.1721 ± 0.0030 0.0992 ± 0.0016 0.0707 ± 0.0035 0.923 ± 0.020 0.670 ± 0.027	0.00050 0.0019 0.0007 0.0017 0.013 0.015	0.21579 0.1723 0.1038 0.0742 0.935 0.668	0.8 -0.1 -2.9 -1.0 -0.6 0.1
d) <u>LEP-II and Tevatron</u> m_W [GeV] (LEP-II, Tevatron) Γ_W [GeV] (LEP-II, Tevatron) m_t [GeV] (Tevatron [307])	80.385 ± 0.015 2.085 ± 0.042 173.2 ± 0.9		80.377 2.092 173.3	0.5 -0.2 -0.1

Table F.1: Summary of high- Q^2 measurements included in the combined analysis of SM parameters. Section a) summarises LEP-I averages, Section b) SLD results (\mathcal{A}_ℓ includes A_{LR} and the polarised lepton asymmetries), Section c) the LEP-I and SLD heavy flavour results, and Section d) electroweak measurements from LEP-II and the Tevatron. The total errors in column 2 include the systematic errors listed in column 3; the determination of the systematic part of each error is approximate. The SM results in column 4 and the pulls (difference between measurement and fit in units of the total measurement error) in column 5 are derived from the SM fit to all high- Q^2 data, see Table F.2 column 4.

^(a)The systematic errors on m_Z and Γ_Z contain the errors arising from the uncertainties in the LEP-I beam energy only.

^(b)Only common systematic errors are indicated. 213

An additional input parameter, not shown in Table F.1, is the Fermi constant G_F , determined from the μ lifetime: $G_F = 1.16637(1) \cdot 10^{-5} \text{ GeV}^{-2}$ [337]. New measurements of G_F yield values which are in good agreement [340]. The relative error of G_F is comparable to that of m_Z ; both uncertainties have negligible effects on the fit results.

F.3 Theoretical Uncertainties

Detailed studies of the theoretical uncertainties in the SM predictions due to missing higher-order electroweak corrections and their interplay with QCD corrections had been carried out by the working group on ‘Precision calculations for the Z resonance’ [317], and later in References [343] and [344]. Theoretical uncertainties are evaluated by comparing different but, within our present knowledge, equivalent treatments of aspects such as resummation techniques, momentum transfer scales for vertex corrections and factorisation schemes. The effects of these theoretical uncertainties are reduced by the inclusion of higher-order corrections [345, 349] in the electroweak libraries TOPAZ0 [351] and ZFITTER [36].

The use of the higher-order QCD corrections [349] increases the value of $\alpha_S(m_Z^2)$ by 0.001, as expected. The effect of missing higher-order QCD corrections on $\alpha_S(m_Z^2)$ dominates missing higher-order electroweak corrections and uncertainties in the interplay of electroweak and QCD corrections. A discussion of theoretical uncertainties in the determination of α_S can be found in References [317] and [355], with a more recent analysis in Reference [358] where the theoretical uncertainty is estimated to be about 0.001 for the analyses presented in the following.

The complete (fermionic and bosonic) two-loop corrections for the calculation of m_W [359], and the complete fermionic two-loop corrections for the calculation of $\sin^2 \theta_{\text{eff}}^{\text{lept}}$ [360] have been calculated. Including three-loop top-quark contributions to the ρ parameter in the limit of large m_t [361], efficient routines for evaluating these corrections have been implemented since version 6.40 in the semi-analytical program ZFITTER. The remaining theoretical uncertainties are estimated to be 4 MeV on m_W and 0.000049 on $\sin^2 \theta_{\text{eff}}^{\text{lept}}$. The latter uncertainty dominates the theoretical uncertainty in the SM fits and the extraction of constraints on the mass of the Higgs boson presented below. For a consistent treatment, the complete two-loop calculation for the partial Z decay widths should be calculated.

The theoretical uncertainties discussed above are not included in the results presented in Tables F.2 and F.3. At present the impact of theoretical uncertainties on the determination of SM parameters from the precise electroweak measurements is small compared to the error due to the uncertainty in the value of $\alpha(m_Z^2)$, which is included in the results.

F.4 Standard-Model Analyses

Strong Coupling Constant

Of the measurements listed in Table F.1, R_ℓ^0 is the one most sensitive to QCD corrections. For $m_Z = 91.1875 \text{ GeV}$ and imposing $m_t = 173.2 \pm 0.9 \text{ GeV}$ [307] as a constraint, $\alpha_S = 0.1223 \pm 0.0038$ is obtained. Alternatively, $\sigma_{\text{lep}}^0 \equiv \sigma_{\text{had}}^0 / R_\ell^0 = 2.0003 \pm 0.0027 \text{ nb}$ [4], which has higher sensitivity to QCD corrections and less dependence on m_H , yields: $\alpha_S = 0.1179 \pm 0.0030$. The central values obtained increase by 0.0013 and 0.0010, respectively, when changing m_H from 100 GeV to 300 GeV. These results on α_S , as well as those reported in the next section, are in good agreement with both independent measurements of α_S and the world average $\alpha_S(m_Z^2) = 0.1184 \pm 0.0007$ [362].

Electroweak Analyses

In the following, several different SM analyses as reported in Table F.2 are discussed. The χ^2 minimisation is performed with the program MINUIT [155], and the predictions are calculated with ZFITTER 6.43 as a function of the five SM input parameters $\Delta\alpha_{\text{had}}^{(5)}(m_Z^2)$, $\alpha_S(m_Z^2)$, m_Z , m_t and $\log_{10}(m_H/\text{GeV})$ which are varied simultaneously in the fits; see [4] for details on the fit procedure. The somewhat large χ^2/dof for all of these fits is caused by the large dispersion in the values of the leptonic effective electroweak mixing angle measured through the various asymmetries at LEP-I and SLD [4]. Following [4] for the analyses presented here, this dispersion is interpreted as a fluctuation in one or more of the input measurements, and thus we neither modify nor exclude any of them. A further significant increase in χ^2/dof is observed when the low- Q^2 NuTeV results are included in the analysis.

To test the agreement between the Z-pole data [4] (LEP-I and SLD) and the SM, a fit to these data is performed. This fit differs from the corresponding analysis reported in Reference [4] in that the new result for $\Delta\alpha_{\text{had}}^{(5)}(m_Z^2)$ [321], reported in Table F.1, is used. The result is shown in Table F.2, column 1. The indirect constraints on m_W and m_t are shown in Figure F.1, compared with the direct measurements. Also shown are the SM predictions for Higgs masses between 114 and 1000 GeV. The indirect and direct results on m_W and m_t are in good agreement. In both cases, a low value of the Higgs-boson mass is preferred.

For the fit shown in column 2 of Table F.2, the direct measurement of m_t from the Tevatron experiments is included, in order to obtain the best indirect determination of m_W . The result is also shown in Figure F.2. The indirect determination of the W-boson mass, 80.363 ± 0.020 GeV, is in good agreement with the direct measurements at LEP-II and the Tevatron, $m_W = 80.385 \pm 0.015$ GeV. For the fit shown in column 3 of Table F.2 and Figure F.3, the direct m_W and Γ_W measurements from LEP-II and the Tevatron are included instead of the direct m_t measurement, in order to obtain the constraint $m_t = 178_{-8}^{+11}$ GeV, in good agreement with the much more precise direct measurement of $m_t = 173.2 \pm 0.9$ GeV.

The best constraints on m_H are obtained when all high- Q^2 measurements are used in the fit. The results of this fit are shown in column 4 of Table F.2. The predictions of this fit for observables measured in high- Q^2 and low- Q^2 reactions are listed in Tables F.1 and F.3, respectively. In Figure F.4 the observed value of $\Delta\chi^2 \equiv \chi^2 - \chi_{\text{min}}^2$ as a function of m_H is plotted for this fit including all high- Q^2 results. The solid curve is the result using ZFITTER, and corresponds to the last column of Table F.2. The shaded band represents the uncertainty due to uncalculated higher-order corrections, as estimated by ZFITTER. Also shown is the result (dashed curve) obtained when using $\Delta\alpha_{\text{had}}^{(5)}(m_Z^2)$ of Reference [335].

The 95% one-sided confidence level upper limit on m_H (taking the band into account) is 152 GeV. When the 95% C.L. lower limit on m_H of 114.4 GeV obtained from direct searches at LEP-II [363] is included, the upper limit increases from 152 GeV to 171 GeV.

Given the direct measurements of the other four SM input parameters, each observable is equivalent to a constraint on the mass of the SM Higgs boson. These constraints are compared in Figure F.5. For very low Higgs-masses, the constraints are qualitative only as the effects of real Higgs-strahlung, neither included in the experimental analyses nor in the SM calculations of expectations, may become sizeable [364]. Besides the measurement of the W mass, the most sensitive measurements are the asymmetries, *i.e.*, $\sin^2 \theta_{\text{eff}}^{\text{lept}}$. A reduced uncertainty for the value of $\alpha(m_Z^2)$ would therefore result in an improved constraint on $\log m_H$ and thus m_H , as already shown in Figure F.4.

Direct searches for the Higgs boson of the SM are currently performed at the Tevatron and

	- 1 - all Z-pole data	- 2 - all Z-pole data plus m_t	- 3 - all Z-pole data plus m_W, Γ_W	- 4 - all Z-pole data plus m_t, m_W, Γ_W
m_t [GeV]	173_{-10}^{+13}	$173.2_{-0.9}^{+0.9}$	$178.1_{-7.8}^{+10.9}$	$173.3_{-0.9}^{+0.9}$
m_H [GeV]	118_{-64}^{+203}	122_{-41}^{+59}	148_{-81}^{+237}	94_{-24}^{+29}
$\log_{10}(m_H/\text{GeV})$	$2.07_{-0.34}^{+0.43}$	$2.09_{-0.18}^{+0.17}$	$2.17_{-0.35}^{+0.41}$	$1.97_{-0.13}^{+0.12}$
$\alpha_S(m_Z^2)$	0.1190 ± 0.0027	0.1191 ± 0.0027	0.1190 ± 0.0028	0.1185 ± 0.0026
$\chi^2/\text{dof} (P)$	16.0/10 (9.9%)	16.0/11 (14%)	16.5/12 (17%)	16.9/13 (21%)
$\sin^2 \theta_{\text{eff}}^{\text{lept}}$	0.23149 ± 0.00016	0.23149 ± 0.00016	0.23144 ± 0.00014	0.23139 ± 0.00011
$\sin^2 \theta_W$	0.22334 ± 0.00062	0.22332 ± 0.00039	0.22298 ± 0.00026	0.22305 ± 0.00023
m_W [GeV]	80.362 ± 0.032	80.363 ± 0.020	80.381 ± 0.013	80.377 ± 0.012

Table F.2: Results of the fits to: (1) all Z-pole data (LEP-I and SLD), (2) all Z-pole data plus the direct m_t determination, (3) all Z-pole data plus the direct m_W and Γ_W determinations, (4) all Z-pole data plus the direct m_t, m_W, Γ_W determinations (i.e., all high- Q^2 results). As the sensitivity to m_H is logarithmic, both m_H as well as $\log_{10}(m_H/\text{GeV})$ are quoted. The bottom part of the table lists derived results for $\sin^2 \theta_{\text{eff}}^{\text{lept}}$, $\sin^2 \theta_W$ and m_W . See text for a discussion of theoretical errors not included in the errors above.

	Measurement with Total Error	Standard-Model High- Q^2 Fit	Pull
APV [312]			
$Q_W(\text{Cs})$	-72.74 ± 0.46	-72.909 ± 0.025	0.4
Møller [313]			
$\sin^2 \theta_{\overline{\text{MS}}}(m_Z)$	0.2330 ± 0.0015	0.23110 ± 0.00011	1.3
νN [315]			
$g_{\nu\text{Lud}}^2$	0.30005 ± 0.00137	0.30397 ± 0.00013	2.9
$g_{\nu\text{Rud}}^2$	0.03076 ± 0.00110	0.03011 ± 0.00002	0.6

Table F.3: Summary of measurements performed in low- Q^2 reactions: atomic parity violation, e^-e^- Møller scattering and neutrino-nucleon scattering. The SM results and the pulls (difference between measurement and fit in units of the total measurement error) are derived from the SM fit including all high- Q^2 data (Table F.2, column 4) with the Higgs mass treated as a free parameter.

the LHC. In summer 2012, the combined Higgs-boson analyses of the Tevatron experiments CDF and D0 excluded the mass ranges of 100 – 103 GeV and 147 – 180 GeV and reported evidence for a new particle with a combined significance of about three standard deviations [365]. At the same time, using both 2011 and some 2012 data, the LHC collaborations ATLAS and CMS excluded the mass regions of 110 – 122 GeV and 128 – 600 GeV and both reported independently the observation of a new particle in Higgs-boson searches with a significance of five or more standard deviations [260]. The electroweak precision data are well compatible with the hypothesis that the new particle, observed with a mass in the range of 125 – 126 GeV, is the Higgs boson of the SM, as is also evident from Figures F.1 to F.5. If the new particle is not the Higgs boson of the SM, the results of electroweak fits such as those presented here may be unreliable because in that case the new particle is not considered in the calculation of electroweak radiative corrections.

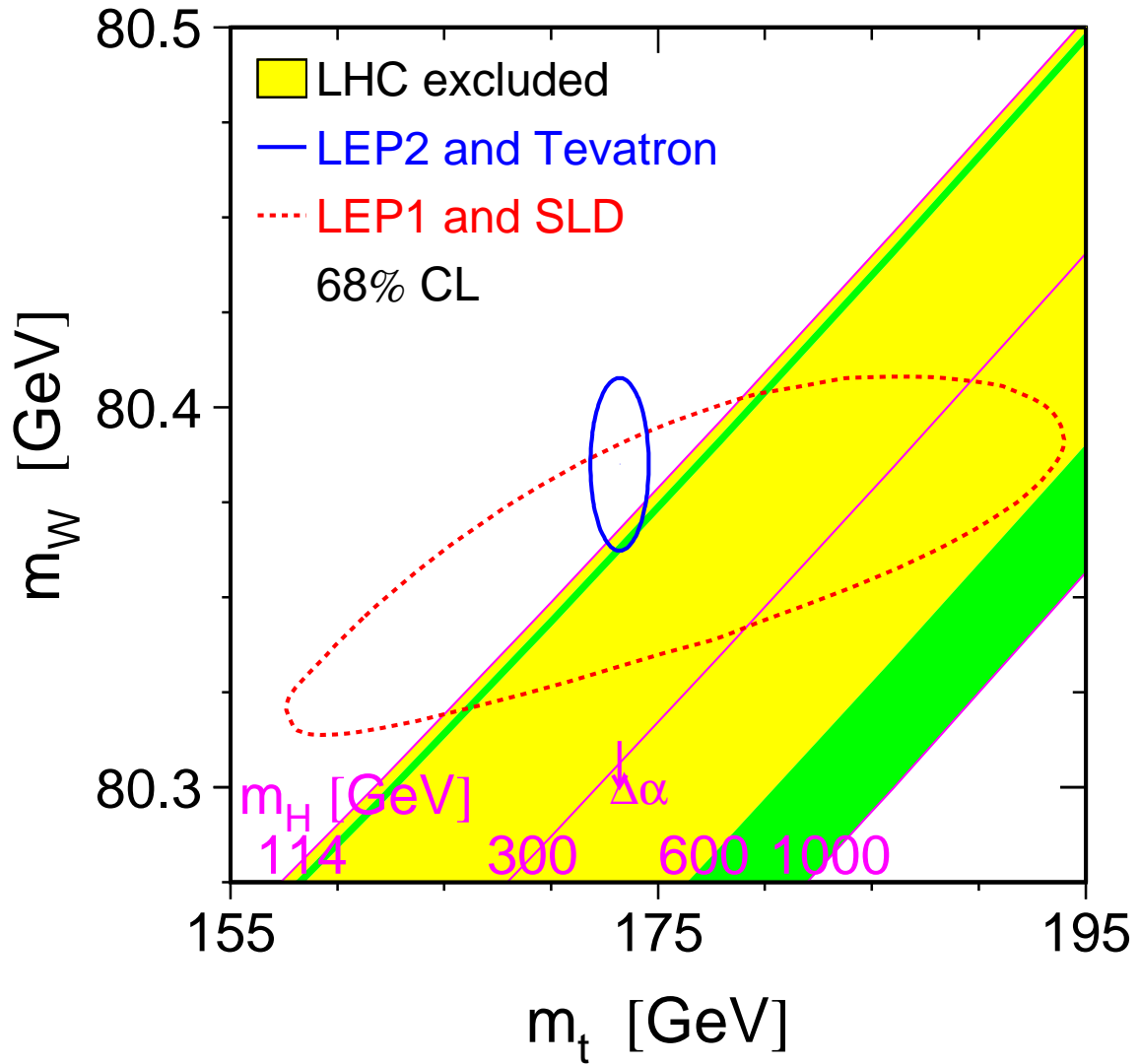


Figure F.1: The comparison of the indirect constraints on m_W and m_t based on LEP-I/SLD data (dashed contour) and the direct measurements from the LEP-II/Tevatron experiments (solid contour). In both cases the 68% CL contours are plotted. Also shown is the SM relationship for the masses as a function of the Higgs mass in the region favoured by theory (< 1000 GeV) and allowed by direct searches (dark green bands). The arrow labelled $\Delta\alpha$ shows the variation of this relation if $\alpha(m_Z^2)$ is changed by plus/minus one standard deviation. This variation gives an additional uncertainty to the SM band shown in the figure.

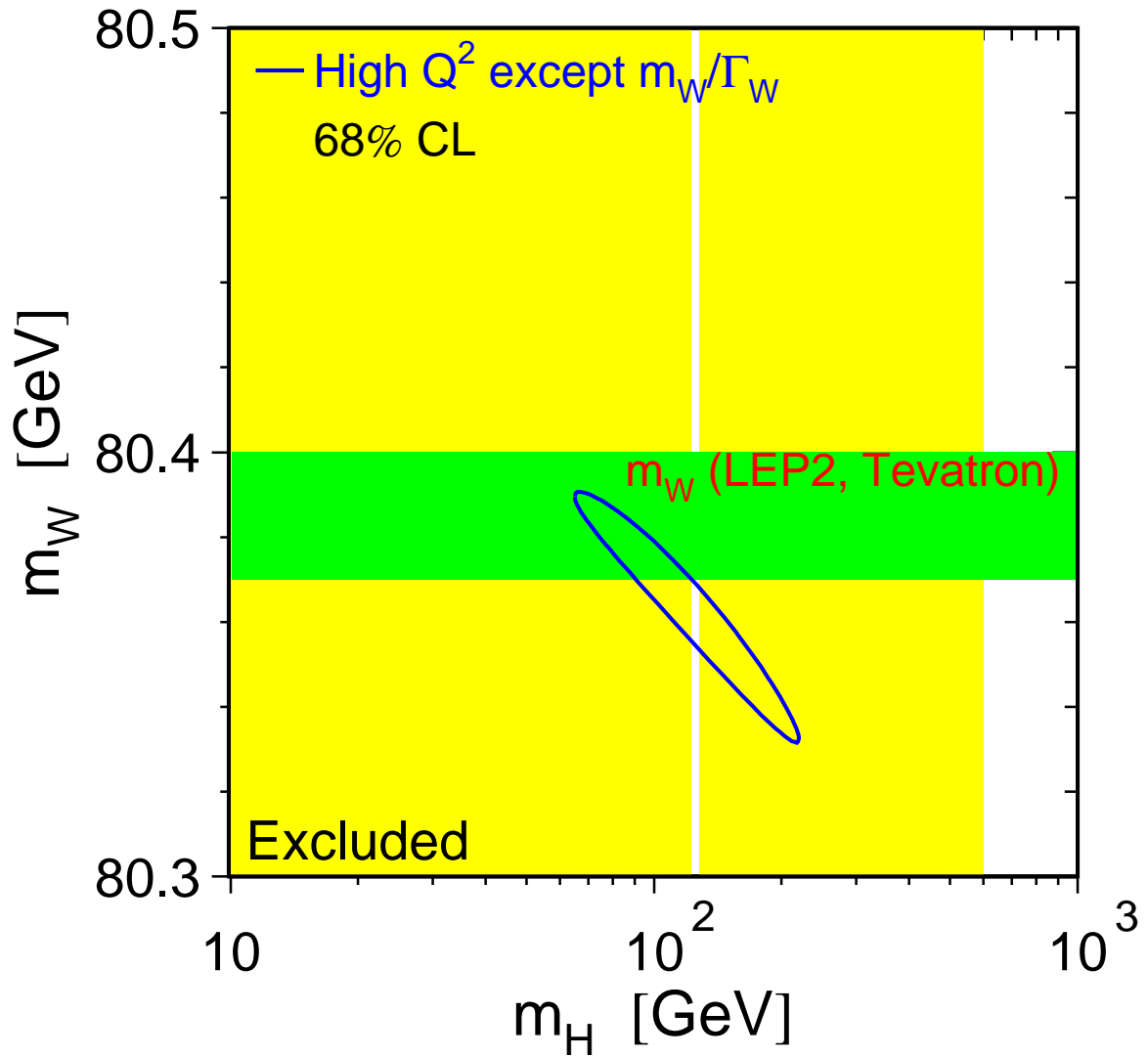


Figure F.2: The 68% confidence level contour in m_W and m_H for the fit to all data except the direct measurement of m_W , indicated by the shaded horizontal band of ± 1 sigma width. The vertical bands show the 95% CL exclusion ranges on m_H from the direct searches.

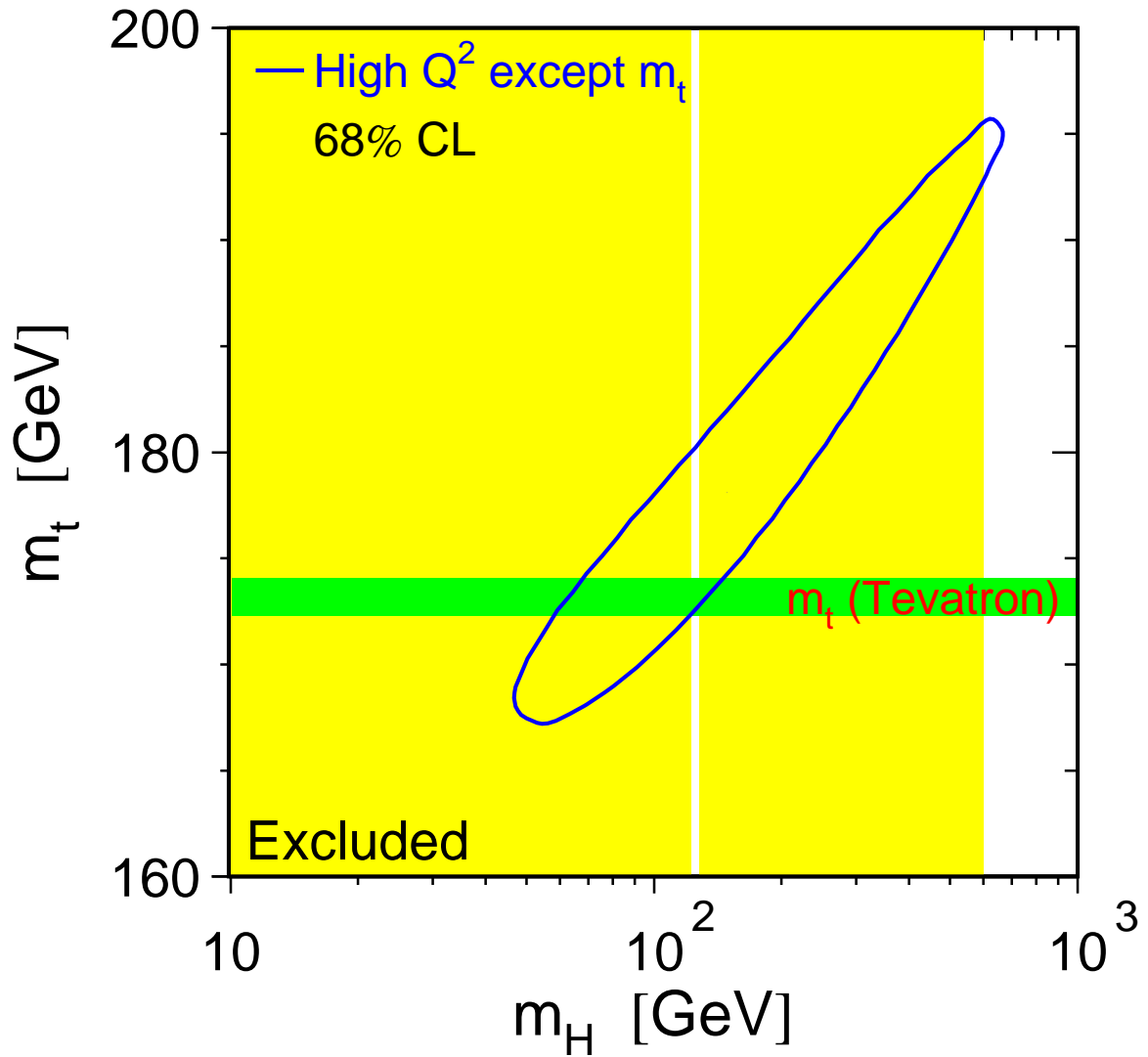


Figure F.3: The 68% confidence level contour in m_t and m_H for the fit to all data except the direct measurement of m_t , indicated by the shaded horizontal band of ± 1 sigma width. The vertical bands show the 95% CL exclusion ranges on m_H from the direct searches.

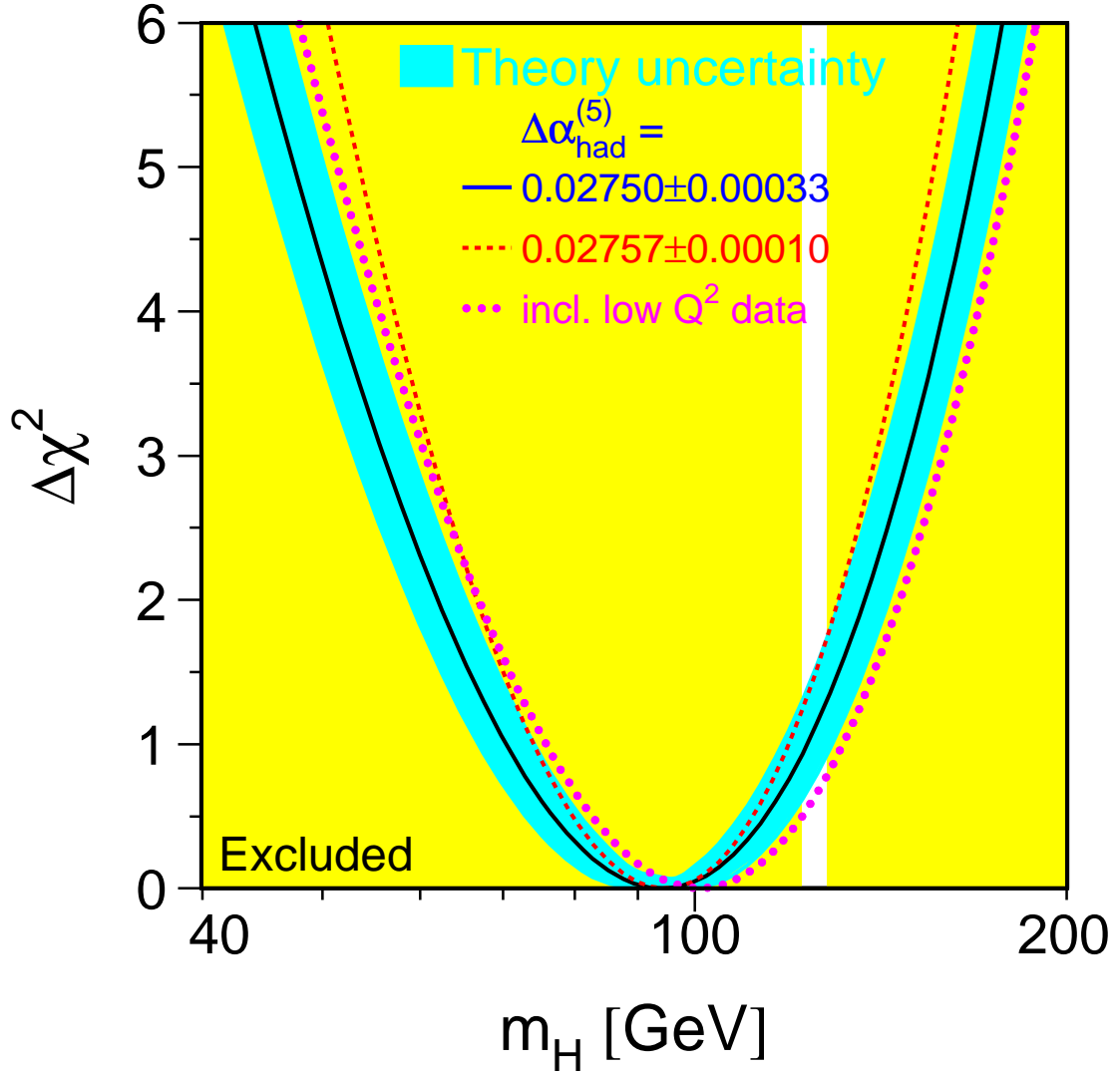


Figure F.4: $\Delta\chi^2 = \chi^2 - \chi_{\min}^2$ vs. m_H curve. The line is the result of the fit using all high- Q^2 data (last column of Table F.2); the band represents an estimate of the theoretical error due to missing higher order corrections. The vertical bands show the 95% CL exclusion ranges on m_H from the direct searches. The dashed curve is the result obtained using the evaluation of $\Delta\alpha_{\text{had}}^{(5)}(m_Z^2)$ from Reference [335]. The dotted curve corresponds to a fit including also the low- Q^2 data from Table F.3.

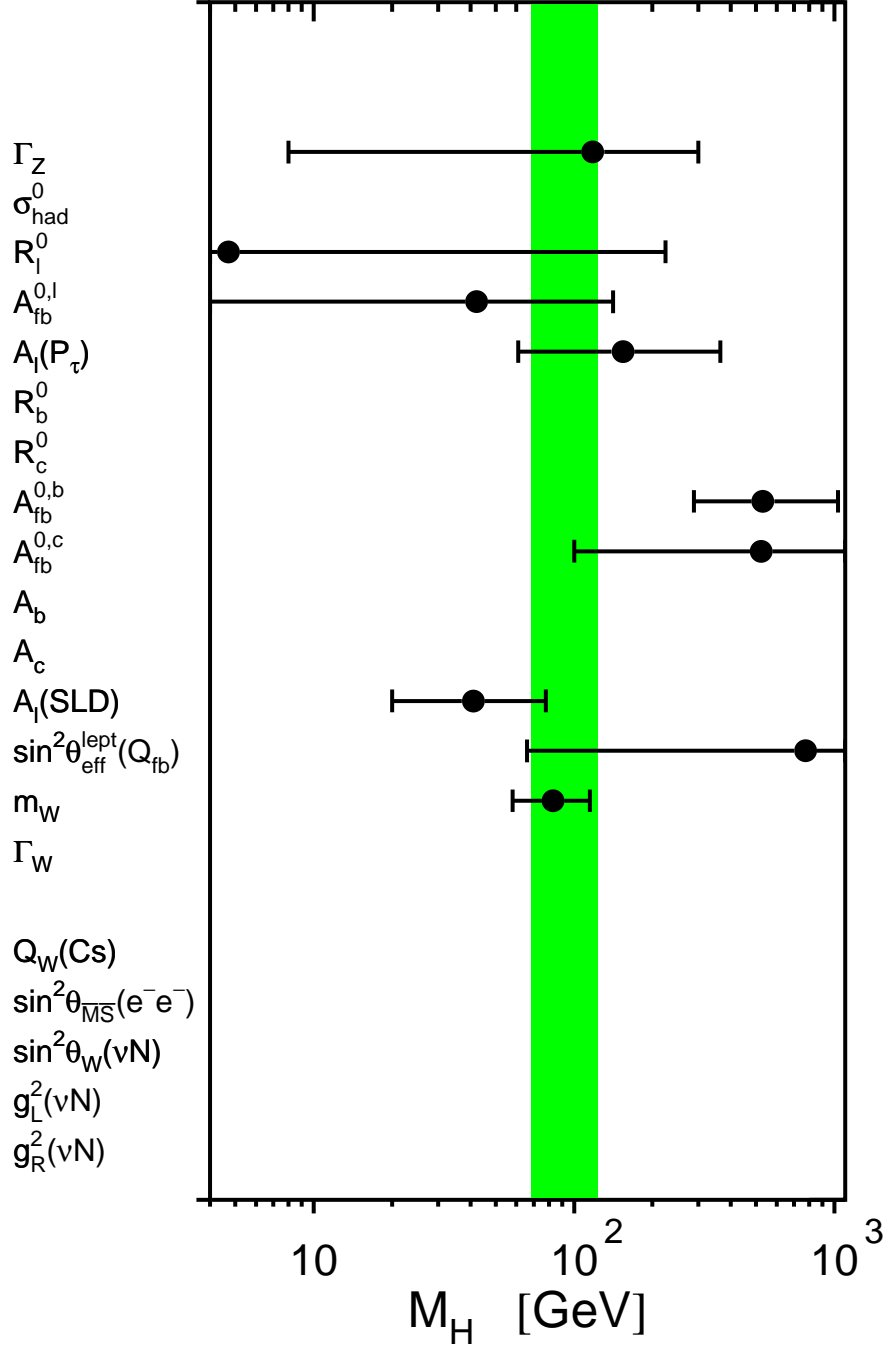


Figure F.5: Constraints on the mass of the Higgs boson from each observable. The Higgs-boson mass and its 68% CL uncertainty is obtained from a five-parameter SM fit to the observable, constraining $\Delta\alpha_{\text{had}}^{(5)}(m_Z^2) = 0.02750 \pm 0.00033$, $\alpha_S(m_Z^2) = 0.118 \pm 0.003$, $m_Z = 91.1875 \pm 0.0021$ GeV and $m_t = 173.2 \pm 0.9$ GeV. Because of these four common constraints the resulting Higgs-boson mass values are highly correlated. The shaded band denotes the overall constraint on the mass of the Higgs boson derived from all observables including the above four SM parameters as reported in the last column of Table F.2. Results are only shown for observables whose measurement accuracy allows to constrain the Higgs-boson mass on the scale of the figure.

Bibliography

- [1] S. Glashow, Nucl.Phys. **22** (1961) 579–588
- [2] S. Weinberg, Phys.Rev.Lett. **19** (1967) 1264–1266
- [3] A. Salam, Conf.Proc. **C680519** (1968) 367–377
- [4] ALEPH Collaboration, DELPHI Collaboration, L3 Collaboration, OPAL Collaboration, SLD Collaboration, LEP Electroweak Working Group, SLD Electroweak and Heavy Flavour Groups, Phys.Rept. **427** (2006) 257–454
- [5] ALEPH Collaboration, A. Heister *et al.*, Eur.Phys.J. **C28** (2003) 1–13
- [6] DELPHI Collaboration, J. Abdallah *et al.*, Eur.Phys.J. **C37** (2004) 405–419
- [7] L3 Collaboration, P. Achard *et al.*, Phys.Lett. **B531** (2002) 28–38
- [8] OPAL Collaboration, G. Abbiendi *et al.*, Eur.Phys.J. **C26** (2003) 331–344
- [9] W. Heitler, Quantum Theory of Radiation, (Oxford University Press, second edition, 1944), pages 204–207
- [10] M. Capdequi Peyranere, Y. Loubatieres, and M. Talon, Nucl.Phys. **B249** (1985) 61
- [11] J. Fujimoto, M. Igarashi, and Y. Shimizu, Prog.Theor.Phys. **77** (1987) 118
- [12] S. Drell, Annals Phys. **4** (1958) 75–80
- [13] F. Low, Phys.Rev.Lett. **14** (1965) 238–239
- [14] O. J. Eboli, A. Natale, and S. Novaes, Phys.Lett. **B271** (1991) 274–276
- [15] I. Antoniadis *et al.*, Phys.Lett. **B436** (1998) 257–263
- [16] K. Agashe and N. Deshpande, Phys.Lett. **B456** (1999) 60–67
- [17] P. Mery, M. Perrottet, and F. Renard, Z.Phys. **C38** (1988) 579
- [18] S. J. Brodsky and S. Drell, Phys.Rev. **D22** (1980) 2236
- [19] F. Renard, Phys.Lett. **B116** (1982) 264
- [20] B. Vachon, Search for excited charged leptons in electron positron collisions, Ph.D. thesis, Victoria University, 2002, UMI-NQ-74948

- [21] B. Vachon, *Excited electron contribution to the $e^+e^- \rightarrow \gamma\gamma$ cross-section*, Eprint hep-ph/0103132v2, 2004
- [22] F. A. Berends and R. Kleiss, Nucl.Phys. **B186** (1981) 22
- [23] VENUS Collaboration, K. Abe *et al.*, Z.Phys. **C45** (1989) 175–191
- [24] ALEPH Collaboration, D. Buskulic *et al.*, Z.Phys. **C59** (1993) 215–230
- [25] DELPHI Collaboration, P. Abreu *et al.*, Phys.Lett. **B327** (1994) 386–396
- [26] L3 Collaboration, B. Adeva *et al.*, Phys.Lett. **B250** (1990) 199–204
- [27] L3 Collaboration, O. Adriani *et al.*, Phys.Lett. **B288** (1992) 404–411
- [28] L3 Collaboration, M. Acciarri *et al.*, Phys.Lett. **B353** (1995) 136–144
- [29] OPAL Collaboration, M. Akrawy *et al.*, Phys.Lett. **B241** (1990) 133
- [30] OPAL Collaboration, M. Akrawy *et al.*, Phys.Lett. **B257** (1991) 531–540
- [31] O. J. Eboli, A. Natale, and S. Novaes, Phys.Lett. **B271** (1991) 274–276
- [32] ALEPH Collaboration, S. Schael *et al.*, Eur.Phys.J. **C49** (2007) 411–437
- [33] DELPHI Collaboration, J. Abdallah *et al.*, Eur.Phys.J. **C45** (2006) 589–632
- [34] L3 Collaboration, P. Achard *et al.*, Eur.Phys.J. **C47** (2006) 1–19
- [35] OPAL Collaboration, G. Abbiendi *et al.*, Eur.Phys.J. **C33** (2004) 173–212
- [36] D. Y. Bardin *et al.*, Z.Phys. **C44** (1989) 493
- [37] D. Y. Bardin *et al.*, Comput.Phys.Commun. **59** (1990) 303–312
- [38] D. Y. Bardin *et al.*, Nucl.Phys. **B351** (1991) 1–48
- [39] D. Y. Bardin *et al.*, Phys.Lett. **B255** (1991) 290–296
- [40] D. Y. Bardin *et al.*, *ZFITTER: An Analytical program for fermion pair production in e^+e^- annihilation*, Eprint hep-ph/9412201, 1992
- [41] D. Y. Bardin *et al.*, Comput.Phys.Commun. **133** (2001) 229–395
- [42] A. Arbuzov, *Light pair corrections to electron positron annihilation at LEP / SLC*, Eprint hep-ph/9907500, 1999
- [43] A. Arbuzov, JHEP **0107** (2001) 043
- [44] A. Arbuzov *et al.*, Comput.Phys.Commun. **174** (2006) 728–758
- [45] ZFITTER support group, ZFITTER 6.43, June 2008, <http://zfitter.desy.de>
- [46] ALEPH Collaboration, R. Barate *et al.*, Eur.Phys.J. **C12** (2000) 183–207
- [47] ALEPH Collaboration, S. Schael *et al.*, Eur.Phys.J. **C49** (2007) 411–437

- [48] DELPHI Collaboration, P. Abreu *et al.*, Eur.Phys.J. **C11** (1999) 383–407
- [49] DELPHI Collaboration, P. Abreu *et al.*, Phys.Lett. **B485** (2000) 45–61
- [50] DELPHI Collaboration, J. Abdallah *et al.*, Eur.Phys.J. **C45** (2006) 589–632
- [51] L3 Collaboration, M. Acciarri *et al.*, Phys.Lett. **B407** (1997) 361–376
- [52] L3 Collaboration, M. Acciarri *et al.*, Phys.Lett. **B479** (2000) 101–117
- [53] L3 Collaboration, P. Achard *et al.*, Eur.Phys.J. **C47** (2006) 1–19
- [54] OPAL Collaboration, K. Ackerstaff *et al.*, Phys.Lett. **B391** (1997) 221–234
- [55] OPAL Collaboration, K. Ackerstaff *et al.*, Eur.Phys.J. **C2** (1998) 441–472
- [56] OPAL Collaboration, G. Abbiendi *et al.*, Eur.Phys.J. **C6** (1999) 1–18
- [57] OPAL Collaboration, G. Abbiendi *et al.*, Eur.Phys.J. **C13** (2000) 553–572
- [58] OPAL Collaboration, G. Abbiendi *et al.*, Eur.Phys.J. **C33** (2004) 173–212
- [59] Two Fermion Working Group, M. Kobel *et al.*, *Reports of the Working Groups on Precision Calculations for LEP2 Physics: Proceedings. Two fermion production in electron positron collisions*, Eprint hep-ph/0007180, 2000
- [60] S. Jadach, B. Ward, and Z. Was, Comput.Phys.Commun. **130** (2000) 260–325
- [61] S. Jadach, B. Ward, and Z. Was, Phys.Rev. **D63** (2001) 113009
- [62] L. Lyons, D. Gibaut, and P. Clifford, Nucl.Instrum.Meth. **A270** (1988) 110
- [63] A. Valassi, Nucl.Instrum.Meth. **A500** (2003) 391–405
- [64] S. Jadach, W. Placzek, and B. Ward, Phys.Lett. **B390** (1997) 298–308
- [65] P. Langacker, AIP Conf.Proc. **1200** (2010) 55–63
- [66] P. Langacker, Rev.Mod.Phys. **81** (2009) 1199–1228
- [67] A. Leike, Phys.Rept. **317** (1999) 143–250
- [68] J. L. Hewett and T. G. Rizzo, Phys.Rept. **183** (1989) 193
- [69] P. Langacker, R. W. Robinett, and J. L. Rosner, Phys.Rev. **D30** (1984) 1470
- [70] D. London and J. L. Rosner, Phys.Rev. **D34** (1986) 1530
- [71] J. C. Pati and A. Salam, Phys.Rev. **D10** (1974) 275–289
- [72] J. C. Pati and A. Salam, Phys.Rev. **D11** (1974) 703–703
- [73] R. N. Mohapatra and J. C. Pati, Phys.Rev. **D11** (1975) 566–571
- [74] G. Altarelli, B. Mele, and M. Ruiz-Altaba, Z.Phys. **C45** (1989) 109

- [75] G. Altarelli, B. Mele, and M. Ruiz-Altaba, *Z.Phys.* **C47** (1990) 676
- [76] DELPHI Collaboration, P. Abreu *et al.*, *Z.Phys.* **C65** (1995) 603–618
- [77] A. Leike, S. Riemann, and T. Riemann, *Z Z-prime mixing in presence of standard weak loop corrections*, Eprint hep-ph/9808374, 1991
- [78] A. Leike, S. Riemann, and T. Riemann, *Phys.Lett.* **B291** (1992) 187–194
- [79] E. Eichten, K. D. Lane, and M. E. Peskin, *Phys.Rev.Lett.* **50** (1983) 811–814
- [80] H. Kroha, *Phys.Rev.* **D46** (1992) 58–69
- [81] D. Bourilkov, *JHEP* **9908** (1999) 006
- [82] D. Bourilkov, *Phys.Rev.* **D62** (2000) 076005
- [83] D. Bourilkov, *Phys.Rev.* **D64** (2001) 071701
- [84] N. Arkani-Hamed, S. Dimopoulos, and G. Dvali, *Phys.Lett.* **B429** (1998) 263–272
- [85] I. Antoniadis *et al.*, *Phys.Lett.* **B436** (1998) 257–263
- [86] N. Arkani-Hamed, S. Dimopoulos, and G. Dvali, *Phys.Rev.* **D59** (1999) 086004
- [87] J. L. Hewett, *Phys.Rev.Lett.* **82** (1999) 4765–4768
- [88] T. G. Rizzo, *Phys.Rev.* **D59** (1999) 115010
- [89] G. F. Giudice, R. Rattazzi, and J. D. Wells, *Nucl.Phys.* **B544** (1999) 3–38
- [90] T. Han, J. D. Lykken, and R.-J. Zhang, *Phys.Rev.* **D59** (1999) 105006
- [91] S. Nussinov and R. Shrock, *Phys.Rev.* **D59** (1999) 105002
- [92] W. Buchmuller, R. Ruckl, and D. Wyler, *Phys.Lett.* **B191** (1987) 442–448
- [93] W. Buchmuller, R. Ruckl, and D. Wyler, *Phys.Lett.* **B448** (1999) 320
- [94] J. Kalinowski *et al.*, *Z.Phys.* **C74** (1997) 595–603
- [95] R. Hanbury Brown and R. Twiss, *Nature* **178** (1956) 1046–1048
- [96] G. Goldhaber *et al.*, *Phys.Rev.Lett.* **3** (1959) 181–183
- [97] D. Boal, C. Gelbke, and B. Jennings, *Rev.Mod.Phys.* **62** (1990) 553–602
- [98] G. Baym, *Acta Phys.Polon.* **B29** (1998) 1839–1884
- [99] ARGUS Collaboration, H. Albrecht *et al.*, *Phys.Lett.* **B162** (1985) 395
- [100] CLEO Collaboration, P. Haas *et al.*, *Phys.Rev.Lett.* **55** (1985) 1248
- [101] G. Gustafson, U. Pettersson, and P. Zerwas, *Phys.Lett.* **B209** (1988) 90
- [102] T. Sjöstrand and V. A. Khoze, *Z.Phys.* **C62** (1994) 281–310

- [103] L. Lomblad, Z.Phys. **C70** (1996) 107–114
- [104] G. Corcella *et al.*, JHEP **0101** (2001) 010
- [105] G. Gustafson and J. Hakkinen, Z.Phys. **C64** (1994) 659–664
- [106] J. R. Ellis and K. Geiger, Phys.Rev. **D54** (1996) 1967–1990
- [107] J. Rathsman, Phys.Lett. **B452** (1999) 364–371
- [108] ALEPH Collaboration, S. Schael *et al.*, Eur.Phys.J. **C48** (2006) 685–698
- [109] L3 Collaboration, P. Achard *et al.*, Phys.Lett. **B581** (2004) 19–30
- [110] OPAL Collaboration, G. Abbiendi *et al.*, Eur.Phys.J. **C35** (2004) 293–312
- [111] ALEPH Collaboration, S. Schael *et al.*, Eur.Phys.J. **C47** (2006) 309–335
- [112] DELPHI Collaboration, J. Abdallah *et al.*, Eur.Phys.J. **C55** (2008) 1–38
- [113] L3 Collaboration, P. Achard *et al.*, Eur.Phys.J. **C45** (2006) 569–587
- [114] OPAL Collaboration, G. Abbiendi *et al.*, Eur.Phys.J. **C45** (2006) 307–335
- [115] OPAL Collaboration, G. Abbiendi *et al.*, Eur.Phys.J. **C45** (2006) 291–305
- [116] DELPHI Collaboration, P. Abreu *et al.*, Eur.Phys.J. **C18** (2000) 203–228
- [117] V. A. Khoze and T. Sjöstrand, Eur.Phys.J. **C6** (1999) 271–284
- [118] D. Duchesneau, *New method based on energy and particle flow in $e^+e^- \rightarrow W^+W^- \rightarrow$ hadrons events for color reconnection studies*, LAPP-EXP-2000-02, 2000
- [119] D. Duchesneau, Nucl.Phys.Proc.Suppl. **96** (2001) 13–22
- [120] A. Ballestrero *et al.*, J.Phys.G **G24** (1998) 365–403
- [121] JADE Collaboration, W. Bartel *et al.*, Phys.Lett. **B101** (1981) 129
- [122] JADE Collaboration, W. Bartel *et al.*, Z.Phys. **C21** (1983) 37
- [123] JADE Collaboration, W. Bartel *et al.*, Phys.Lett. **B134** (1984) 275
- [124] JADE Collaboration, W. Bartel *et al.*, Phys.Lett. **B157** (1985) 340
- [125] TPC/Two Gamma Collaboration, H. Aihara *et al.*, Z.Phys. **C28** (1985) 31
- [126] TPC/Two Gamma Collaboration, H. Aihara *et al.*, Phys.Rev.Lett. **57** (1986) 945
- [127] TASSO Collaboration, M. Althoff *et al.*, Z.Phys. **C29** (1985) 29
- [128] DELPHI Collaboration, J. Abdallah *et al.*, Eur.Phys.J. **C51** (2007) 249–269
- [129] L3 Collaboration, P. Achard *et al.*, Phys.Lett. **B561** (2003) 202–212
- [130] S. Catani *et al.*, Phys.Lett. **B269** (1991) 432–438

- [131] Y. L. Dokshitzer, V. A. Khoze, and S. Troian, *J.Phys.G* **G17** (1991) 1481–1492
- [132] S. Bethke *et al.*, *Nucl.Phys.* **B370** (1992) 310–334
- [133] S. Bethke *et al.*, *Nucl.Phys.* **B523** (1998) 681
- [134] T. Sjöstrand, *Comput.Phys.Commun.* **27** (1982) 243
- [135] T. Sjöstrand, *Comput.Phys.Commun.* **28** (1983) 229
- [136] T. Sjöstrand, *Comput.Phys.Commun.* **39** (1986) 347–407
- [137] T. Sjöstrand and M. Bengtsson, *Comput.Phys.Commun.* **43** (1987) 367
- [138] M. Bengtsson and T. Sjöstrand, *Nucl.Phys.* **B289** (1987) 810
- [139] S. Jadach *et al.*, *Comput.Phys.Commun.* **140** (2001) 475–512
- [140] T. Sjöstrand, *Comput.Phys.Commun.* **82** (1994) 74–90
- [141] W. A. Rolke, A. M. Lopez, and J. Conrad, *Nucl.Instrum.Meth.* **A551** (2005) 493–503
- [142] S. Chekanov, E. De Wolf, and W. Kittel, *Eur.Phys.J.* **C6** (1999) 403–411
- [143] DELPHI Collaboration, P. Abreu *et al.*, *Phys.Lett.* **B401** (1997) 181–191
- [144] E. De Wolf, *Correlations in $e^+e^- \rightarrow W^+W^-$ hadronic decays*, Eprint hep-ph/0101243, 2001
- [145] ALEPH Collaboration, R. Barate *et al.*, *Phys.Lett.* **B478** (2000) 50–64
- [146] ALEPH Collaboration, S. Schael *et al.*, *Phys.Lett.* **B606** (2005) 265–275
- [147] DELPHI Collaboration, J. Abdallah *et al.*, *Eur.Phys.J.* **C44** (2005) 161–174
- [148] L3 Collaboration, P. Achard *et al.*, *Phys.Lett.* **B547** (2002) 139–150
- [149] OPAL Collaboration, G. Abbiendi *et al.*, *Eur.Phys.J.* **C36** (2004) 297–308
- [150] L. Lonnblad and T. Sjöstrand, *Eur.Phys.J.* **C2** (1998) 165–180
- [151] ALEPH Collaboration, S. Schael *et al.*, *Eur.Phys.J.* **C47** (2006) 309–335
- [152] DELPHI Collaboration, J. Abdallah *et al.*, *Eur.Phys.J.* **C55** (2008) 1–38
- [153] L3 Collaboration, P. Achard *et al.*, *Eur.Phys.J.* **C45** (2006) 569–587
- [154] OPAL Collaboration, G. Abbiendi *et al.*, *Eur.Phys.J.* **C45** (2006) 307–335
- [155] F. James and M. Roos, *Comput.Phys.Commun.* **10** (1975) 343–367
- [156] M. W. Grünewald *et al.*, *Reports of the Working Groups on Precision Calculations for LEP2 Physics: Proceedings. Four fermion production in electron positron collisions*, Eprint hep-ph/0005309, 2000
- [157] ALEPH Collaboration, A. Heister *et al.*, *Eur.Phys.J.* **C38** (2004) 147–160

- [158] DELPHI Collaboration, J. Abdallah *et al.*, Eur.Phys.J. **C34** (2004) 127–144
- [159] L3 Collaboration, P. Achard *et al.*, Phys.Lett. **B600** (2004) 22–40
- [160] OPAL Collaboration, G. Abbiendi *et al.*, Eur.Phys.J. **C52** (2007) 767–785
- [161] S. Jadach *et al.*, Phys.Rev. **D54** (1996) 5434–5442
- [162] S. Jadach *et al.*, Phys.Lett. **B417** (1998) 326–336
- [163] S. Jadach *et al.*, Phys.Rev. **D61** (2000) 113010
- [164] S. Jadach *et al.*, Phys.Rev. **D65** (2002) 093010
- [165] S. Jadach *et al.*, Comput.Phys.Comm. **140** (2001) 432–474
- [166] The YFSWW cross-sections at 155–215 GeV have been kindly provided by the authors
- [167] S. Jadach *et al.*, Comput.Phys.Comm. **140** (2001) 475–512
- [168] A. Denner *et al.*, Nucl.Phys. **B560** (1999) 33–65
- [169] A. Denner *et al.*, Phys.Lett. **B475** (2000) 127–134
- [170] A. Denner *et al.*, Nucl.Phys. **B587** (2000) 67–117
- [171] A. Denner *et al.*, *Off-shell W pair production: Universal versus nonuniversal corrections*, Eprint hep-ph/0101257, 2001
- [172] The RACOONWW cross-sections at 155–215 GeV have been kindly provided by the authors
- [173] D. Y. Bardin *et al.*, Comput.Phys.Comm. **104** (1997) 161–187
- [174] M. Skrzypek *et al.*, Phys.Lett. **B372** (1996) 289–298
- [175] M. Skrzypek *et al.*, Comput.Phys.Comm. **94** (1996) 216–248
- [176] S. Jadach *et al.*, Comput.Phys.Comm. **119** (1999) 272–311
- [177] The KORALW cross-sections at 155–215 GeV have been kindly provided by the authors. They have actually been computed using YFSWW [161, 167], switching off non-leading $\mathcal{O}(\alpha)$ radiative corrections and the screening of the Coulomb correction, to reproduce the calculation from KORALW
- [178] Particle Data Group, K. Nakamura *et al.*, J.Phys.G **G37** (2010) 075021
- [179] ALEPH Collaboration, S. Schael *et al.*, JHEP **0904** (2009) 124
- [180] DELPHI Collaboration, J. Abdallah *et al.*, Eur.Phys.J. **C30** (2003) 447–466
- [181] L3 Collaboration, P. Achard *et al.*, Phys.Lett. **B572** (2003) 133–144
- [182] OPAL Collaboration, G. Abbiendi *et al.*, Eur.Phys.J. **C32** (2003) 303–322
- [183] S. Jadach, W. Placzek, and B. Ward, Phys.Rev. **D56** (1997) 6939–6941

- [184] G. Passarino, ZZTO, in [156], pages 134–140
- [185] DELPHI Collaboration, J. Abdallah *et al.*, Eur.Phys.J. **C51** (2007) 503–523
- [186] L3 Collaboration, P. Achard *et al.*, Phys.Lett. **B616** (2005) 159–173
- [187] J. Fujimoto *et al.*, *grc4f v1.0: A Four fermion event generator for e^+e^- collisions*, Eprint hep-ph/9603394, 1996
- [188] J. Fujimoto *et al.*, Comput.Phys.Comm. **100** (1997) 128–156
- [189] Y. Kurihara *et al.*, Prog.Theor.Phys. **103** (2000) 1199–1211
- [190] ALEPH Collaboration, S. Schael *et al.*, Phys.Lett. **B605** (2005) 49–62
- [191] DELPHI Collaboration, J. Abdallah *et al.*, Eur.Phys.J. **C45** (2006) 273–289
- [192] L3 Collaboration, M. Acciarri *et al.*, Phys.Lett. **B436** (1998) 417–427
- [193] L3 Collaboration, M. Acciarri *et al.*, Phys.Lett. **B487** (2000) 229–240
- [194] L3 Collaboration, P. Achard *et al.*, Phys.Lett. **B547** (2002) 151–163
- [195] E. Accomando and A. Ballestrero, Comput.Phys.Comm. **99** (1997) 270–296
- [196] E. Accomando, A. Ballestrero, and E. Maina, Comput.Phys.Comm. **150** (2003) 166–196
- [197] The WPHACT cross-sections at 160–210 GeV have been kindly provided by A. Ballestrero
- [198] G. Passarino, Comput.Phys.Comm. **97** (1996) 261–303
- [199] G. Passarino, Nucl.Phys. **B574** (2000) 451–494
- [200] G. Passarino, Nucl.Phys. **B578** (2000) 3–26
- [201] The WTO cross-sections at 160–210 GeV have been kindly provided by the author
- [202] G. Montagna *et al.*, Eur.Phys.J. **C20** (2001) 217–225
- [203] L3 Collaboration, P. Achard *et al.*, Phys.Lett. **B561** (2003) 202–212
- [204] OPAL Collaboration, G. Abbiendi *et al.*, Phys.Lett. **B438** (1998) 391–404
- [205] OPAL Collaboration, G. Abbiendi *et al.*, Eur.Phys.J. **C24** (2002) 1–15
- [206] DELPHI Collaboration, J. Abdallah *et al.*, Eur.Phys.J. **C31** (2003) 139–147
- [207] L3 Collaboration, P. Achard *et al.*, Phys.Lett. **B527** (2002) 29–38
- [208] OPAL Collaboration, G. Abbiendi *et al.*, Phys.Lett. **B580** (2004) 17–36
- [209] W. J. Stirling and A. Werthenbach, Eur.Phys.J. **C14** (2000) 103–110
- [210] G. Altarelli *et al.*, *Physics at LEP2: Vol. 1*, Eprint CERN Yellow Report CERN-96-01-V-1, 1996

- [211] ALEPH Collaboration, S. Schael *et al.*, Phys.Lett. **B614** (2005) 7–26
- [212] DELPHI Collaboration, J. Abdallah *et al.*, Eur.Phys.J. **C66** (2010) 35–56
- [213] L3 Collaboration, P. Achard *et al.*, Phys.Lett. **B586** (2004) 151–166
- [214] OPAL Collaboration, G. Abbiendi *et al.*, Eur.Phys.J. **C33** (2004) 463–476
- [215] K. Gaemers and G. Gounaris, Z.Phys. **C1** (1979) 259
- [216] K. Hagiwara *et al.*, Nucl.Phys. **B282** (1987) 253
- [217] K. Hagiwara *et al.*, Phys.Lett. **B283** (1992) 353–359
- [218] K. Hagiwara *et al.*, Phys.Rev. **D48** (1993) 2182–2203
- [219] K. Hagiwara *et al.*, Nucl.Phys. **B496** (1997) 66–102
- [220] M. S. Bilenky *et al.*, Nucl.Phys. **B409** (1993) 22–68
- [221] M. S. Bilenky *et al.*, Nucl.Phys. **B419** (1994) 240–253
- [222] I. Kuss and D. Schildknecht, Phys.Lett. **B383** (1996) 470–474
- [223] G. Gounaris and C. G. Papadopoulos, Eur.Phys.J. **C2** (1998) 365–372
- [224] G. Gounaris, J. Layssac, and F. Renard, Phys.Rev. **D62** (2000) 073013
- [225] R. Brunelière *et al.*, Phys.Lett. **B533** (2002) 75–84
- [226] J. Alcaraz, *A proposal for the combination of TGC measurements*, L3 Note 2718
- [227] R. Brunelière, *Tests on the LEP TGC combination procedures*, ALEPH 2002-008 PHYS-2002-007 (2002)
- [228] L3 Collaboration, M. Acciarri *et al.*, Phys.Lett. **B467** (1999) 171–184
- [229] L3 Collaboration, P. Achard *et al.*, Phys.Lett. **B586** (2004) 151–166
- [230] L3 Collaboration, P. Achard *et al.*, Phys.Lett. **B547** (2002) 151–163
- [231] ALEPH Collaboration, S. Schael *et al.*, JHEP **0904** (2009) 124
- [232] DELPHI Collaboration, J. Abdallah *et al.*, Eur.Phys.J. **C51** (2007) 525–542
- [233] L3 Collaboration, P. Achard *et al.*, Phys.Lett. **B597** (2004) 119–130
- [234] OPAL Collaboration, G. Abbiendi *et al.*, Eur.Phys.J. **C17** (2000) 553–566
- [235] L3 Collaboration, P. Achard *et al.*, Phys.Lett. **B572** (2003) 133–144
- [236] OPAL Collaboration, G. Abbiendi *et al.*, Eur.Phys.J. **C32** (2003) 303–322
- [237] O. Klein, Surveys High Energ.Phys. **5** (1986) 269–285

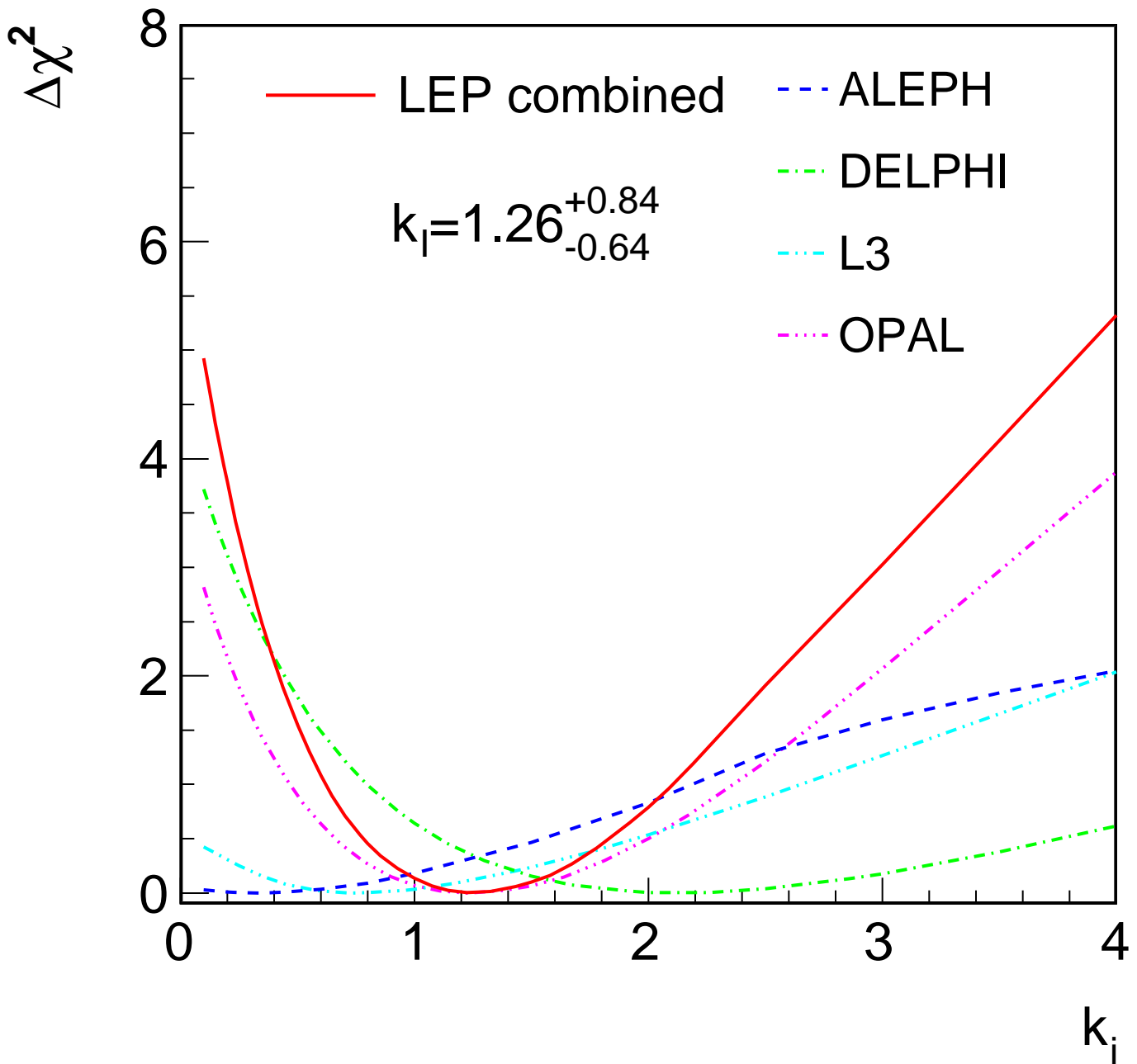
- [238] L.Maiani and P.M.Zerwas, *W Static ELM Parameters*, Memorandum to the TGC Combination Group (1998)
- [239] CDF Collaboration, T. Aaltonen *et al.*, Phys.Rev.Lett. **100** (2008) 071801
- [240] D0 Collaboration, V. Abazov *et al.*, Phys.Rev.Lett. **103** (2009) 231802
- [241] CDF Collaboration, T. Aaltonen *et al.*, Phys.Rev.Lett. **108** (2012) 151803
- [242] D0 Collaboration, V. M. Abazov *et al.*, Phys.Rev.Lett. **108** (2012) 151804
- [243] ALEPH Collaboration, R. Barate *et al.*, Phys.Lett. **B415** (1997) 435–444
- [244] L3 Collaboration, M. Acciarri *et al.*, Phys.Lett. **B407** (1997) 419–431
- [245] OPAL Collaboration, K. Ackerstaff *et al.*, Phys.Lett. **B389** (1996) 416–428
- [246] LEP Energy Working Group, R. Assmann *et al.*, Eur.Phys.J. **C6** (1999) 187–223
- [247] LEP Energy Working Group, R. Assmann *et al.*, Eur.Phys.J. **C39** (2005) 253–292
- [248] OPAL Collaboration, G. Abbiendi *et al.*, Eur.Phys.J. **C26** (2003) 321–330
- [249] L. Lonnblad, Z.Phys. **C58** (1993) 471–478
- [250] Y. L. Dokshitzer *et al.*, JHEP **9708** (1997) 001
- [251] S. Bentvelsen and I. Meyer, Eur.Phys.J. **C4** (1998) 623–629
- [252] S. Jadach, J. H. Kuhn, and Z. Was, Comput.Phys.Commun. **64** (1990) 275–299
- [253] S. Jadach *et al.*, Comput.Phys.Commun. **76** (1993) 361–380
- [254] L. Lonnblad, Comput.Phys.Commun. **71** (1992) 15–31
- [255] DELPHI Collaboration, J. Abdallah *et al.*, Eur.Phys.J. **C46** (2006) 295–305
- [256] L3 Collaboration, P. Achard *et al.*, Phys.Lett. **B585** (2004) 42–52
- [257] OPAL Collaboration, G. Abbiendi *et al.*, Phys.Lett. **B604** (2004) 31–47
- [258] G. Marchesini *et al.*, Comput.Phys.Commun. **67** (1992) 465–508
- [259] F. Cossutti, Eur.Phys.J. **C44** (2005) 383–393
- [260] ATLAS Collaboration, G. Aad *et al.*, Phys.Lett.B **716** (2012) 1–29
- [261] CMS Collaboration, S. Chatrchyan *et al.*, Phys.Lett.B **716** (2012) 30–61
- [262] The LEP Collaborations ALEPH, DELPHI, L3, OPAL, and the LEP Electroweak Working Group, *A Combination of Preliminary Electroweak Measurements and Constraints on the Standard Model*, Eprint hep-ex/0612034, CERN, 2006
- [263] A. Borrelli *et al.*, Nucl.Phys. **B333** (1990) 357
- [264] R. G. Stuart, Phys.Lett. **B272** (1991) 353–358

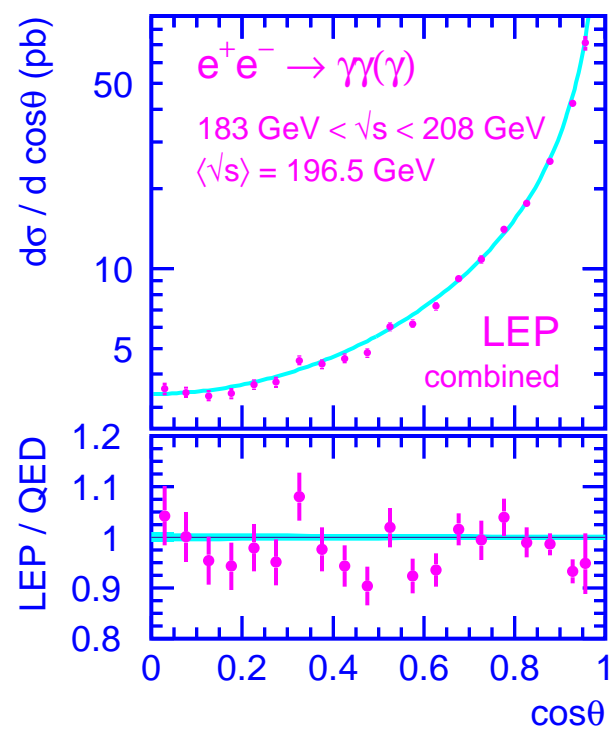
- [265] A. Leike, T. Riemann, and J. Rose, Phys.Lett. **B273** (1991) 513–518
- [266] T. Riemann, Phys.Lett. **B293** (1992) 451–456
- [267] S. Kirsch and T. Riemann, Comput.Phys.Commun. **88** (1995) 89–108
- [268] The ALEPH Collaboration, *S-Matrix fits to cross-section and forward-backward asymmetry measurements at LEP 1 and 2*, ALEPH 2000-042 PHYSICS 2000-015 (2002)
- [269] DELPHI Collaboration, J. Abdallah *et al.*, Eur.Phys.J. **C45** (2006) 589–632
- [270] L3 Collaboration, M. Acciarri *et al.*, Eur.Phys.J. **C16** (2000) 1–40
- [271] OPAL Collaboration, G. Abbiendi *et al.*, Eur.Phys.J. **C19** (2001) 587–651
- [272] H. Flacher *et al.*, Eur.Phys.J. **C60** (2009) 543–583
- [273] M. Baak *et al.*, Eur.Phys.J. **C72** (2012) 2003
- [274] CDF Collaboration, F. Abe *et al.*, Phys.Rev.Lett. **65** (1990) 2243–2246
- [275] CDF Collaboration, F. Abe *et al.*, Phys.Rev. **D43** (1991) 2070–2093
- [276] CDF Collaboration, F. Abe *et al.*, Phys.Rev.Lett. **75** (1995) 11–16
- [277] CDF Collaboration, F. Abe *et al.*, Phys.Rev. **D52** (1995) 4784–4827
- [278] CDF Collaboration, T. Affolder *et al.*, Phys.Rev. **D64** (2001) 052001
- [279] CDF Collaboration, T. Aaltonen *et al.*, Phys.Rev.Lett. **99** (2007) 151801
- [280] CDF Collaboration, T. Aaltonen *et al.*, Phys.Rev. **D77** (2008) 112001
- [281] D0 Collaboration, S. Abachi *et al.*, Phys.Rev.Lett. **77** (1996) 3309–3314
- [282] D0 Collaboration, B. Abbott *et al.*, Phys.Rev. **D58** (1998) 012002
- [283] D0 Collaboration, B. Abbott *et al.*, Phys.Rev.Lett. **80** (1998) 3008
- [284] D0 Collaboration, B. Abbott *et al.*, Phys.Rev. **D58** (1998) 092003
- [285] D0 Collaboration, B. Abbott *et al.*, Phys.Rev. **D62** (2000) 092006
- [286] D0 Collaboration, B. Abbott *et al.*, Phys.Rev.Lett. **84** (2000) 222–227
- [287] D0 Collaboration, V. Abazov *et al.*, Phys.Rev. **D66** (2002) 012001
- [288] D0 Collaboration, V. M. Abazov *et al.*, Phys.Rev.Lett. **103** (2009) 141801
- [289] CDF Collaboration, T. Affolder *et al.*, Phys.Rev.Lett. **85** (2000) 3347–3352
- [290] D0 Collaboration, V. Abazov *et al.*, Phys.Rev. **D66** (2002) 032008
- [291] The Tevatron Electroweak Working Group for the CDF and D0 Collaborations, *2012 Update of the Combination of CDF and D0 Results for the Mass of the W Boson*, Eprint 1204.0042, FERMILAB, 2012

- [292] The Tevatron Electroweak Working Group for the CDF and D0 Collaborations, *Combina-
tion of CDF and D0 Results on the Width of the W boson*, Eprint 1003.2826, FERMILAB,
2010
- [293] CDF Collaboration, T. Aaltonen *et al.*, Phys.Rev.Lett. **105** (2010) 252001
- [294] CDF Collaboration, T. Affolder *et al.*, Phys.Rev. **D63** (2001) 032003
- [295] CDF Collaboration, T. Aaltonen *et al.*, Phys.Lett. **B714** (2012) 24–31
- [296] CDF Collaboration, T. Aaltonen *et al.*, Phys.Rev. **D83** (2011) 111101
- [297] CDF Collaboration, F. Abe *et al.*, Phys.Rev.Lett. **82** (1999) 271–276
- [298] CDF Collaboration, F. Abe *et al.*, Phys.Rev.Lett. **82** (1999) 2808–2809
- [299] CDF Collaboration, T. Aaltonen *et al.*, Phys.Rev.Lett. **107** (2011) 232002
- [300] CDF Collaboration, T. Aaltonen *et al.*, Phys.Rev. **D81** (2010) 032002
- [301] D0 Collaboration, V. M. Abazov *et al.*, Phys.Rev. **D84** (2011) 032004
- [302] D0 Collaboration, V. Abazov *et al.*, Nature **429** (2004) 638–642
- [303] D0 Collaboration, S. Abachi *et al.*, Phys.Rev.Lett. **79** (1997) 1197–1202
- [304] D0 Collaboration, V. M. Abazov *et al.*, Phys.Rev. **D86** (2012) (R)
- [305] D0 Collaboration, B. Abbott *et al.*, Phys.Rev.Lett. **80** (1998) 2063–2068
- [306] D0 Collaboration, B. Abbott *et al.*, Phys.Rev. **D60** (1999) 052001
- [307] The Tevatron Electroweak Working Group, for the CDF and D0 Collaborations, *Combi-
nation of CDF and D0 results on the mass of the top quark using up to 5.8/fb of data*,
Eprint 1107.5255, 2011
- [308] CDF Collaboration, D0 Collaboration, T. Aaltonen *et al.*, Phys.Rev. **D86** (2012) 092003
- [309] C. Wood *et al.*, Science **275** (1997) 1759–1763
- [310] S. Bennett and C. E. Wieman, Phys.Rev.Lett. **82** (1999) 2484–2487
- [311] S. Bennett and C. Wieman, Phys.Rev.Lett. **82** (1999) 4153–4153
- [312] J. Ginges and V. Flambaum, Phys.Rept. **397** (2004) 63–154
- [313] SLAC E158 Collaboration, P. Anthony *et al.*, Phys.Rev.Lett. **92** (2004) 181602
- [314] SLAC E158 Collaboration, P. Anthony *et al.*, Phys.Rev.Lett. **95** (2005) 081601
- [315] NuTeV Collaboration, G. Zeller *et al.*, Phys.Rev.Lett. **88** (2002) 091802
- [316] NuTeV Collaboration, G. Zeller *et al.*, Phys.Rev.Lett. **90** (2003) 239902(E)
- [317] D. Y. Bardin *et al.*, *Electroweak working group report*, Eprint hep-ph/9709229, 1997

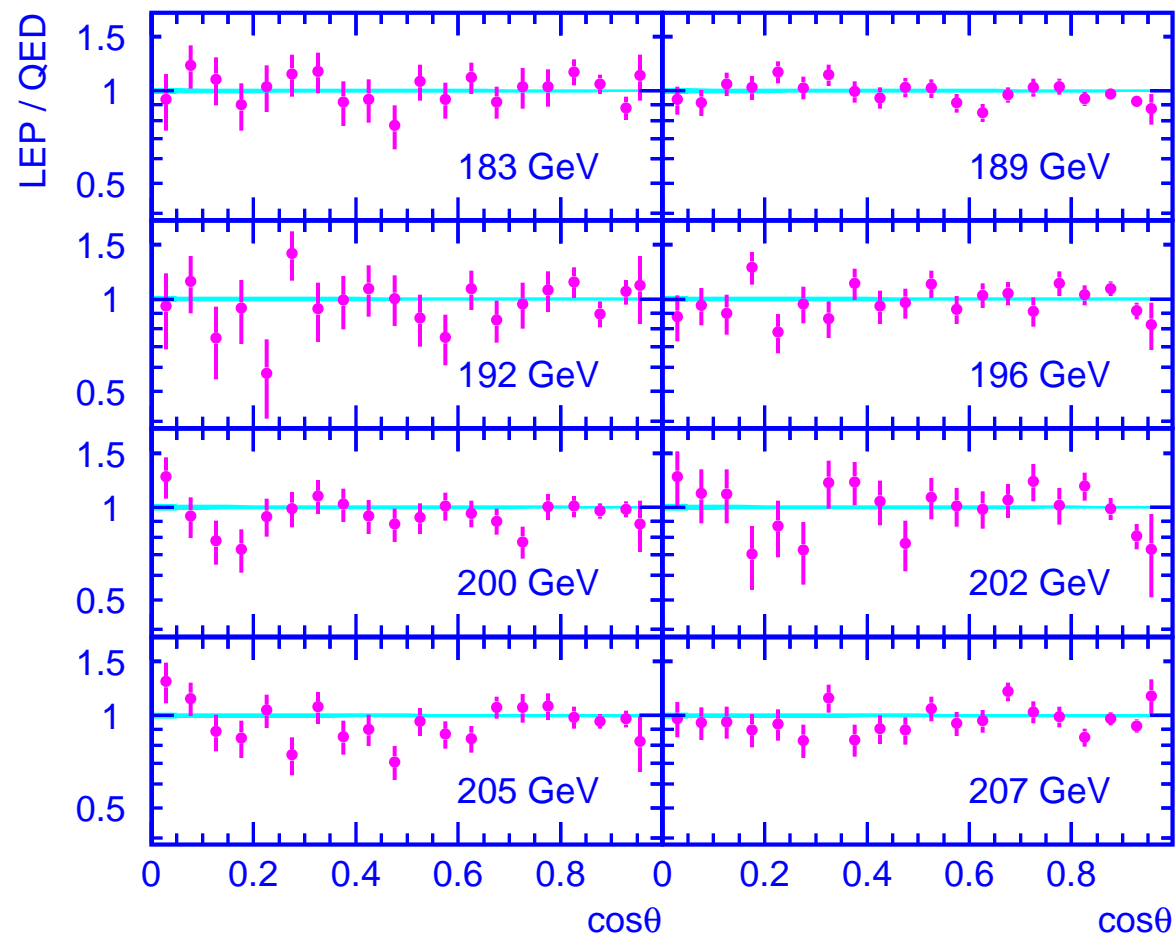
- [318] I. Cloet, W. Bentz, and A. Thomas, Phys.Rev.Lett. **102** (2009) 252301
- [319] W. Bentz *et al.*, Phys.Lett. **B693** (2010) 462–466
- [320] M. Steinhauser, Phys.Lett. **B429** (1998) 158–161
- [321] H. Burkhardt and B. Pietrzyk, Phys.Rev. **D84** (2011) 037502
- [322] M. L. Swartz, Phys.Rev. **D53** (1996) 5268–5282
- [323] A. D. Martin and D. Zeppenfeld, Phys.Lett. **B345** (1995) 558–563
- [324] R. Alemany, M. Davier, and A. Hocker, Eur.Phys.J. **C2** (1998) 123–135
- [325] M. Davier and A. Hocker, Phys.Lett. **B419** (1998) 419–431
- [326] J. H. Kuhn and M. Steinhauser, Phys.Lett. **B437** (1998) 425–431
- [327] F. Jegerlehner, *Hadronic effects in $(g - 2)(\mu)$ and $\alpha(QED)(M(Z))$: Status and perspectives*, Eprint hep-ph/9901386, 1999
- [328] J. Erler, Phys.Rev. **D59** (1999) 054008
- [329] A. D. Martin, J. Outhwaite, and M. Ryskin, Phys.Lett. **B492** (2000) 69–73
- [330] J. de Troconiz and F. Yndurain, Phys.Rev. **D65** (2002) 093002
- [331] K. Hagiwara *et al.*, Phys.Rev. **D69** (2004) 093003
- [332] J. de Troconiz and F. Yndurain, Phys.Rev. **D71** (2005) 073008
- [333] T. Teubner *et al.*, *Update of $g-2$ of the Muon and Delta Alpha*, Eprint 1001.5401, 2010
- [334] K. Hagiwara *et al.*, J.Phys.G **G38** (2011) 085003
- [335] M. Davier *et al.*, Eur.Phys.J. **C71** (2011) 1515
- [336] M. Davier *et al.*, Eur.Phys.J. **C72** (2012) 1874
- [337] T. van Ritbergen and R. G. Stuart, Phys.Rev.Lett. **82** (1999) 488–491
- [338] T. van Ritbergen and R. G. Stuart, Nucl.Phys. **B564** (2000) 343–390
- [339] M. Steinhauser and T. Seidensticker, Phys.Lett. **B467** (1999) 271–278
- [340] MuLan Collaboration, D. Chitwood *et al.*, Phys.Rev.Lett. **99** (2007) 032001
- [341] FAST Collaboration, A. Barczyk *et al.*, Phys.Lett. **B663** (2008) 172–180
- [342] MuLan Collaboration, D. Webber *et al.*, Phys.Rev.Lett. **106** (2011) 041803
- [343] D. Y. Bardin and G. Passarino, *Upgrading of precision calculations for electroweak observables*, Eprint hep-ph/9803425, 1998
- [344] D. Y. Bardin, M. W. Gr unewald, and G. Passarino, *Precision calculation project report*, Eprint hep-ph/9902452, 1999

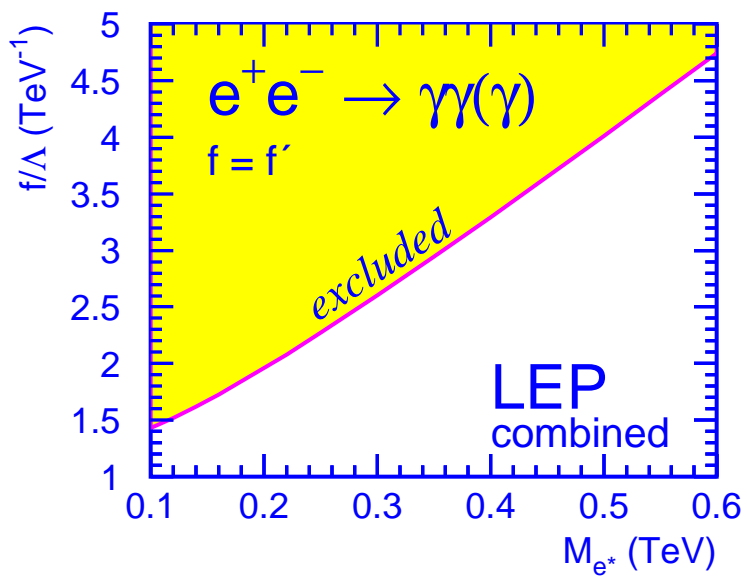
- [345] G. Degrossi, S. Fanchiotti, and A. Sirlin, Nucl.Phys. **B351** (1991) 49–69
- [346] G. Degrossi and A. Sirlin, Nucl.Phys. **B352** (1991) 342–366
- [347] G. Degrossi, P. Gambino, and A. Vicini, Phys.Lett. **B383** (1996) 219–226
- [348] G. Degrossi, P. Gambino, and A. Sirlin, Phys.Lett. **B394** (1997) 188–194
- [349] A. Czarnecki and J. H. Kuhn, Phys.Rev.Lett. **77** (1996) 3955–3958
- [350] R. Harlander, T. Seidensticker, and M. Steinhauser, Phys.Lett. **B426** (1998) 125–132
- [351] G. Montagna *et al.*, Nucl.Phys. **B401** (1993) 3–66
- [352] G. Montagna *et al.*, Comput.Phys.Comm. **76** (1993) 328–360
- [353] G. Montagna *et al.*, Comput.Phys.Comm. **93** (1996) 120–126
- [354] G. Montagna *et al.*, Comput.Phys.Comm. **117** (1999) 278–289, updated to include initial state pair radiation (G. Passarino, priv. comm.)
- [355] T. Hebbeker *et al.*, Phys.Lett. **B331** (1994) 165–170
- [356] P. A. Raczka and A. Szymacha, Phys.Rev. **D54** (1996) 3073–3084
- [357] D. E. Soper and L. R. Surguladze, Phys.Rev. **D54** (1996) 4566–4577
- [358] H. Stenzel, JHEP **0507** (2005) 0132
- [359] M. Awramik *et al.*, Phys.Rev. **D69** (2004) 053006
- [360] M. Awramik *et al.*, Phys.Rev.Lett. **93** (2004) 201805
- [361] M. Faisst *et al.*, Nucl.Phys. **B665** (2003) 649–662
- [362] S. Bethke, Eur.Phys.J. **C64** (2009) 689–703
- [363] ALEPH, DELPHI, L3, and OPAL Collaborations, The LEP Working Group for Higgs Boson Searches, Phys.Lett. **B565** (2003) 61–75
- [364] T. Kawamoto and R. Kellogg, Phys.Rev. **D69** (2004) 113008
- [365] Tevatron New Physics Higgs Working Group, CDF Collaboration, D0 Collaboration, *Updated Combination of CDF and D0 Searches for Standard Model Higgs Boson Production with up to 10.0 fb⁻¹ of Data*, Eprint 1207.0449, 2012
- [366] CDF Collaboration, D0 Collaboration, T. Aaltonen *et al.*, Phys.Rev.Lett. **109** (2012) 071804.

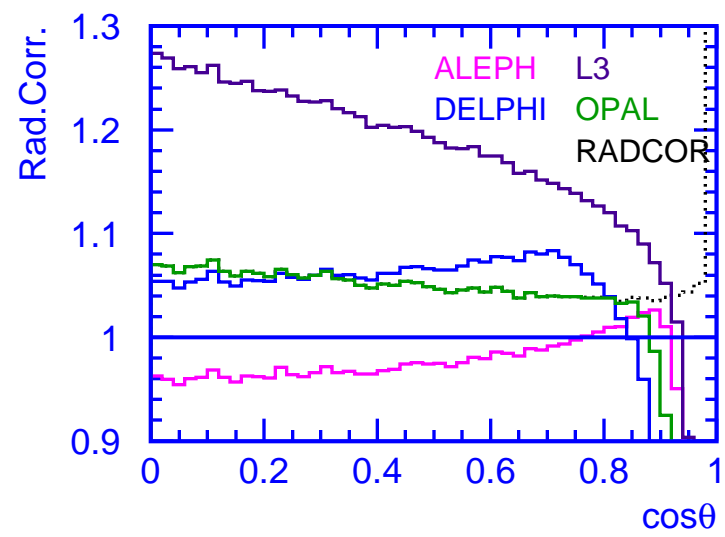


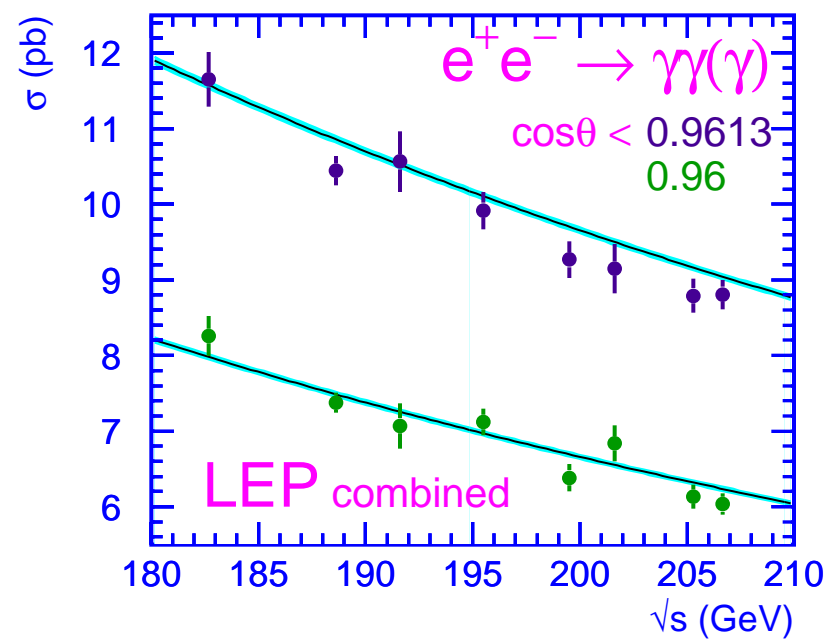


$e^+e^- \rightarrow \gamma\gamma(\gamma)$ LEP combined
 $d\sigma_{\text{LEP}}/d\cos\theta / d\sigma_{\text{QED}}/d\cos\theta$









Identification of b-quark jets with the CMS experiment

This content has been downloaded from IOPscience. Please scroll down to see the full text.

2013 JINST 8 P04013

(<http://iopscience.iop.org/1748-0221/8/04/P04013>)

View [the table of contents for this issue](#), or go to the [journal homepage](#) for more

Download details:

IP Address: 84.195.56.240

This content was downloaded on 31/10/2016 at 23:04

Please note that [terms and conditions apply](#).

You may also be interested in:

[Performance of \$\tau\$ -lepton reconstruction and identification in CMS](#)

CMS Collaboration

[Determination of jet energy calibration and transverse momentum resolution in CMS](#)

The CMS collaboration

[Missing transverse energy performance of the CMS detector](#)

The CMS collaboration

[Description and performance of track and primary-vertex reconstruction with the CMS tracker](#)

The CMS Collaboration

[CMS Physics Technical Design Report, Volume II: Physics Performance](#)

The CMS Collaboration

[Status of Higgs boson searches at the beginning of the LHC era](#)

A Sopczak

LHC REFERENCE VOLUME

Identification of b-quark jets with the CMS experiment



The CMS collaboration

E-mail: cms-publication-committee-chair@cern.ch

ABSTRACT: At the Large Hadron Collider, the identification of jets originating from b quarks is important for searches for new physics and for measurements of standard model processes. A variety of algorithms has been developed by CMS to select b-quark jets based on variables such as the impact parameters of charged-particle tracks, the properties of reconstructed decay vertices, and the presence or absence of a lepton, or combinations thereof. The performance of these algorithms has been measured using data from proton-proton collisions at the LHC and compared with expectations based on simulation. The data used in this study were recorded in 2011 at $\sqrt{s} = 7$ TeV for a total integrated luminosity of 5.0 fb^{-1} . The efficiency for tagging b-quark jets has been measured in events from multijet and t-quark pair production. CMS has achieved a b-jet tagging efficiency of 85% for a light-parton misidentification probability of 10% in multijet events. For analyses requiring higher purity, a misidentification probability of only 1.5% has been achieved, for a 70% b-jet tagging efficiency.

KEYWORDS: Large detector-systems performance; Pattern recognition, cluster finding, calibration and fitting methods; Performance of High Energy Physics Detectors

ARXIV EPRINT: [1211.4462](https://arxiv.org/abs/1211.4462)



Contents

1	Introduction	2
2	The CMS detector	2
3	Data samples and simulation	3
4	Algorithms for b-jet identification	5
4.1	Reconstructed objects used in b-jet identification	5
4.2	Identification using track impact parameters	6
4.3	Identification using secondary vertices	9
4.4	Performance of the algorithms in simulation	10
4.5	Impact of running conditions on b-jet identification	12
5	Efficiency measurement with multijet events	14
5.1	Efficiency measurement with kinematic properties of muon jets	15
5.2	Efficiency measurement with the System8 method	16
5.3	Efficiency measurement using a reference lifetime algorithm	18
5.4	Systematic uncertainties on efficiency measurements	20
6	Efficiency measurement with $t\bar{t}$ events	23
6.1	Event selection	23
6.2	Systematic uncertainties	25
6.3	Profile likelihood ratio method	27
6.4	Flavour tag consistency method	29
6.5	Flavour tag matching method	31
6.6	Efficiency measurement from a b-enriched jet sample	33
7	Efficiency measurement results	35
7.1	Results from multijet events	35
7.2	Results from $t\bar{t}$ events	38
7.3	Comparison of results	40
8	Misidentification probability measurement	40
9	Conclusions	46
	The CMS collaboration	52

1 Introduction

Jets that arise from bottom-quark hadronization (b jets) are present in many physics processes, such as the decay of top quarks, the Higgs boson, and various new particles predicted by supersymmetric models. The ability to accurately identify b jets is crucial in reducing the otherwise overwhelming background to these channels from processes involving jets from gluons (g) and light-flavour quarks (u, d, s), and from c-quark fragmentation.

The properties of the bottom and, to a lesser extent, the charm hadrons can be used to identify the hadronic jets into which the b and c quarks fragment. These hadrons have relatively large masses, long lifetimes and daughter particles with hard momentum spectra. Their semileptonic decays can be exploited as well. The Compact Muon Solenoid (CMS) detector, with its precise charged-particle tracking and robust lepton identification systems, is well matched to the task of b-jet identification (b-jet tagging). The first physics results using b-jet tagging have been published [1–3] from the first data samples collected at the Large Hadron Collider (LHC).

This paper describes the b-jet tagging algorithms used by the CMS experiment and measurements of their performance. A description of the apparatus is given in section 2. The event samples and simulation are discussed in section 3. The algorithms for b-jet tagging are defined in section 4. The distributions of the relevant observables are compared between simulation and proton-proton collision data collected in 2011 at a centre-of-mass energy of 7 TeV. The robustness of the algorithms with respect to running conditions, such as the alignment of the detector elements and the presence of additional collisions in the same bunch crossing (pileup), is also discussed.

Physics analyses using b-jet identification require the values of the efficiency and misidentification probability of the chosen algorithm, and, in general, these are a function of the transverse momentum (p_T) and pseudorapidity (η) of a jet. They can also depend on parameters such as the efficiency of the track reconstruction, the resolution of the reconstructed track parameters, or the track density in a jet. While the CMS simulation reproduces the performance of the detector to a high degree of precision, it is difficult to model all the parameters relevant for b-jet tagging. Therefore it is essential to measure the performance of the algorithms directly from data. These measurements are performed with jet samples that are enriched in b jets, either chosen by applying a discriminating variable on jets in multijet events or by selecting jets from top-quark decays. The methods that are used to measure the performance are described in sections 5 and 6. The measurements are complementary: multijet events cover a wider range in p_T , while the results obtained from $t\bar{t}$ events are best suited for some studies of top-quark physics. The efficiency measurements are summarized and compared in section 7. The measurement of the misidentification probability of light-parton (u, d, s, g) jets as b jets in the data is presented in section 8.

2 The CMS detector

The central feature of the CMS apparatus is a superconducting solenoid, of 6 m internal diameter, which provides a magnetic field of 3.8 T. Within the field volume are the silicon tracker, the crystal electromagnetic calorimeter, and the brass/scintillator hadron calorimeter. Muons are measured in gas-ionization detectors embedded in the steel return yoke.

CMS uses a right-handed coordinate system, with the origin at the nominal interaction point, the x axis pointing to the centre of the LHC ring and the z axis along the counterclockwise-beam direction. The polar angle, θ , is measured from the positive z axis and the azimuthal angle, ϕ , is measured in the x - y plane. The pseudorapidity is defined as $\eta \equiv -\ln[\tan(\theta/2)]$. A more detailed description of the CMS detector can be found elsewhere [4].

The most relevant detector elements for the identification of b jets and the measurement of algorithm performance are the tracking system and the muon detectors. The inner tracker consists of 1440 silicon pixel and 15 148 silicon strip detector modules. It measures charged particles up to a pseudorapidity of $|\eta| < 2.5$. The pixel modules are arranged in three cylindrical layers in the central part of CMS and two endcap disks on each side of the interaction point. The silicon strip detector comprises two cylindrical barrel detectors with a total of 10 layers and two endcap systems with a total of 12 layers at each end of CMS. The tracking system provides an impact parameter (IP) resolution of about 15 (30) μm at a p_T of 100 (5) GeV/c . In comparison typical IP values for tracks from b-hadron decays are at the level of a few 100 μm . Muons are measured and identified in detection layers that use three technologies: drift tubes, cathode-strip chambers, and resistive-plate chambers. The muon system covers the pseudorapidity range $|\eta| < 2.4$. The combination of the muon and tracking systems yields muon candidates of high purity with a p_T resolution of about 1 to 3%, for p_T values from 5 to 100 GeV/c .

3 Data samples and simulation

Samples of inclusive multijet events for the measurement of efficiencies and misidentification probabilities were collected using jet triggers with p_T thresholds of 30 to 300 GeV/c . For efficiency measurements, dedicated triggers were used to enrich the data sample with jets from semimuonic b-hadron decays. These triggers required the presence of at least two jets with p_T thresholds ranging from 20 to 110 GeV/c . One of these jets was required to include a muon with $p_T > 5 \text{ GeV}/c$ within a cone of $\Delta R = 0.4$ around the jet axis, where ΔR is defined as $\sqrt{(\Delta\phi)^2 + (\Delta\eta)^2}$. Triggers with low- p_T thresholds were prescaled in order to limit the overall trigger rates. Depending on the prescale applied to the trigger, the multijet analyses used datasets with integrated luminosities of up to 5.0 fb^{-1} .

Data for the analysis of $t\bar{t}$ events were collected with single- (e or μ) and double-lepton (ee or $e\mu$ or $\mu\mu$) triggers. The samples were collected in the first part of the 2011 data taking with an integrated luminosity of 2.3 fb^{-1} . The precision on the b-jet tagging efficiency from $t\bar{t}$ events is limited by systematic uncertainties. Using the full dataset collected in 2011 would not significantly reduce the overall uncertainty.

Monte Carlo (MC) simulated samples of multijet events were generated with PYTHIA 6.424 [5] using the Z2 tune [6]. For b-jet tagging efficiency studies, dedicated multijet samples have been produced with the explicit requirement of a muon in the final state.

In the simulation, a reconstructed jet is matched with a generated parton if the direction of the parton is within a cone of radius $\Delta R = 0.3$ around the jet axis. The jet is then assigned the flavour of the parton. Should more than one parton be matched to a given jet, the flavour assigned is that of the heaviest parton. The b flavour is given priority over the c flavour, which in turn is given priority

over light partons. According to this definition jets originating from gluon splitting to $b\bar{b}$, which constitute an irreducible background for all tagging algorithms, are classified as b jets.

Events involving $t\bar{t}$ production were simulated using the MADGRAPH [7] event generator (v. 5.1.1.0), where the top quark pairs were generated with up to four additional partons in the final state. A top quark mass of $m_t = 172.5 \text{ GeV}/c^2$ was assumed. The parton configurations generated by MADGRAPH were processed with PYTHIA to provide showering of the generated particles. The soft radiation was matched with the contributions from the matrix element computation using the k_T -MLM prescription [8]. The tau-lepton decays were handled with TAUOLA (v. 27.121.5) [9].

The electroweak production of single top quarks is considered as a background process for analyses using $t\bar{t}$ events, and was simulated using POWHEG 301 [10]. The production of $W/Z + \text{jets}$ events, where the vector boson decays leptonically, has a signature similar to $t\bar{t}$ and constitutes the main background. These events were simulated using MADGRAPH +PYTHIA, with up to four additional partons in the final state. The bottom and charm components are separated from the light-parton components in the analysis by matching reconstructed jets to partons in the simulation.

Signal and background processes used in the analysis of $t\bar{t}$ events were normalized to next-to-leading-order (NLO) and next-to-next-to-leading-order (NNLO) cross sections, with the exception of the QCD background.

The top-quark pair production NLO cross section was calculated to be $\sigma_{t\bar{t}} = 157_{-24}^{+23} \text{ pb}$, using MCFM [11]. The uncertainty in this cross section includes the scale uncertainties, estimated by varying simultaneously the factorization and renormalization scales by factors of 0.5 or 2 with respect to the nominal scale of $(2m_t)^2 + (\sum p_T^{\text{parton}})^2$, where p_T^{parton} are the transverse momenta of the partons in the event. The uncertainties from the parton distribution functions (PDF) and the value of the strong coupling constant α_s were estimated following the procedures from the MSTW2008 [12], CTEQ6.6 [13], and NNPDF2.0 [14] sets. The uncertainties were then combined according to the PDF4LHC prescriptions [15].

The t -channel single top NLO cross section was calculated to be $\sigma_t = 64.6_{-3.2}^{+3.4} \text{ pb}$ using MCFM [11, 16–18]. The uncertainty was evaluated in the same way as for top-quark pair production. The single top-quark associated production (tW) cross section was set to $\sigma_{tW} = 15.7 \pm 1.2 \text{ pb}$ [19]. The s -channel single top-quark next-to-next-to-leading-log (NNLL) cross section was determined to be $\sigma_s = 4.6 \pm 0.1 \text{ pb}$ [20].

The NNLO cross section of the inclusive production of W bosons multiplied by its branching fraction to leptons was determined to be $\sigma_{W \rightarrow \ell\nu} = 31.3 \pm 1.6 \text{ nb}$ using FEWZ [21], setting the renormalization and factorization scales to $(m_W)^2 + (\sum p_T^{\text{jet}})^2$ with $m_W = 80.398 \text{ GeV}/c^2$. The uncertainty was determined in the same way as in top-quark pair production. The normalizations of the $W+b$ jets and $W+c$ jets components were determined in a measurement of the top pair production cross section in the lepton+jet channel [1], where a simultaneous fit of the $t\bar{t}$ cross section and the normalization of the main backgrounds was performed.

The Drell–Yan production cross section at NNLO was calculated using FEWZ as $\sigma_{Z/\gamma^* \rightarrow \ell\ell}(m_{\ell\ell} > 20 \text{ GeV}) = 5.00 \pm 0.27 \text{ nb}$, where $m_{\ell\ell}$ is the invariant mass of the two leptons and the scales were set using the Z boson mass $m_Z = 91.1876 \text{ GeV}/c^2$ [22].

All generated events were passed through the full simulation of the CMS detector based on GEANT4 [23]. The samples were generated with a different pileup distribution than that observed in the data. The simulated events were therefore reweighted to match the observed pileup distribution.

4 Algorithms for b-jet identification

A variety of reconstructed objects — tracks, vertices and identified leptons — can be used to build observables that discriminate between b and light-parton jets. Several simple and robust algorithms use just a single observable, while others combine several of these objects to achieve a higher discrimination power. Each of these algorithms yields a single discriminator value for each jet. The minimum thresholds on these discriminators define loose (“L”), medium (“M”), and tight (“T”) operating points with a misidentification probability for light-parton jets of close to 10%, 1%, and 0.1%, respectively, at an average jet p_T of about 80 GeV/c. Throughout this paper, the tagging criteria will be labelled with the letter characterizing the operating point appended to the acronym of one of the algorithms described in sections 4.2 and 4.3. The application of such a tagging criterion will be called a “tagger”.

After a short description of the reconstructed objects used as inputs, details on the tagging algorithms are given in the following subsections, proceeding in order of increasing complexity. Muon-based b-jet identification is mainly used as a reference method for performance measurements. It is described in more detail in section 5.

4.1 Reconstructed objects used in b-jet identification

Jets are clustered from objects reconstructed by the particle-flow algorithm [24, 25]. This algorithm combines information from all subdetectors to create a consistent set of reconstructed particles for each event. The particles are then clustered into jets using the anti- k_T clustering algorithm [26] with a distance parameter of 0.5. The raw jet energies are corrected to obtain a uniform response in η and an absolute calibration in p_T [27]. Although particle-flow jets are used as the default, the b-jet tagging algorithms can be applied to jets clustered from other reconstructed objects.

Each algorithm described in the next section uses the measured kinematic properties of charged particles, including identified leptons, in a jet. The trajectories of these particles are reconstructed in the CMS tracking system in an iterative procedure using a standard Kalman filter-based method. Details on the pattern recognition, the track-parameter estimation, and the tracking performance in proton-proton collisions can be found in refs. [4, 28].

A “global” muon reconstruction, using information from multiple detector systems, is achieved by first reconstructing a muon track in the muon chambers. This is then matched to a track measured in the silicon tracker [29]. A refit is then performed using the measurements on both tracks.

Primary vertex candidates are selected by clustering reconstructed tracks based on the z coordinate of their closest approach to the beam line. An adaptive vertex fit [30] is then used to estimate the vertex position using a sample of tracks compatible with originating from the interaction region. Among the primary vertices found in this way, the one with the highest $\sum (p_T^{\text{track}})^2$ is selected as a candidate for the origin of the hard interaction, where the p_T^{track} are the transverse momenta of the tracks associated to the vertex.

The b-jet tagging algorithms require a sample of well-reconstructed tracks of high purity. Specific requirements are imposed in addition to the selection applied in the tracking step. The fraction of misreconstructed or poorly reconstructed tracks is reduced by requiring a transverse momentum of at least 1 GeV/c. At least eight hits must be associated with the track. To ensure a good fit, $\chi^2/\text{n.d.o.f.} < 5$ is required, where n.d.o.f. stands for the number of degrees of freedom in

the fit. At least two hits are required in the pixel system since track measurements in the innermost layers provide most of the discriminating power. A loose selection on the track impact parameters is used to further increase the fraction of well-reconstructed tracks and to reduce the contamination by decay products of long-lived particles, e.g. neutral kaons. The impact parameters d_{xy} and d_z are defined as the transverse and longitudinal distance to the primary vertex at the point of closest approach in the transverse plane. Their absolute values must be smaller than 0.2 cm and 17 cm, respectively. Tracks are associated to jets in a cone $\Delta R < 0.5$ around the jet axis, where the jet axis is defined by the primary vertex and the direction of the jet momentum. The distance of a track to the jet axis is defined as the distance of closest approach of the track to the axis. In order to reject tracks from pileup this quantity is required to be less than $700 \mu\text{m}$. The point of closest approach must be within 5 cm of the primary vertex. This sample of associated tracks is the basis for all algorithms that use impact parameters for discrimination.

Properties of the tracks and the average multiplicity after the selection (except for the variable plotted) are shown in figure 1. The uncertainties shown in this and all following figures are statistical unless otherwise stated. The data were recorded with a prescaled jet trigger in the second part of 2011 when the number of pileup events was highest. The jet p_T threshold was $60 \text{ GeV}/c$. The distributions show satisfactory agreement with the expectations from simulation. The track multiplicity and the lower part of the momentum spectrum are particularly sensitive to the modelling of the particle multiplicity and kinematics by the Monte Carlo generator, as are other distributions such as the number of hits in the innermost pixel layers. Detector effects that are not modelled by the simulation, such as the dynamic readout inefficiency in the pixel system, can also contribute to the remaining discrepancies. In figure 1 and the following figures, simulated events with gluon splitting to $b\bar{b}$ are shown as a special category. The b jets in these events tend to be close in space and can be inadvertently merged by the clustering algorithm, resulting in a higher average track multiplicity per jet.

The combinatorial complexity of the reconstruction of the decay points (secondary vertices) of b or c hadrons is more challenging in the presence of multiple proton-proton interactions. In order to minimize this complexity a different track selection is applied. Tracks must be within a cone of $\Delta R = 0.3$ around the jet axis with a maximal distance to this axis of 0.2 cm and pass a “high-purity” criterion [28]. The “high-purity” criterion uses the normalized χ^2 of the track fit, the track length, and impact parameter information to optimize the purity for each of the iterations in track reconstruction. The vertex finding procedure begins with tracks defined by this selection and proceeds iteratively. A vertex candidate is identified by applying an adaptive vertex fit [30], which is robust in the presence of outliers. The fit estimates the vertex position and assigns a weight between 0 and 1 to each track based on its compatibility with the vertex. All tracks with weights > 0.5 are then removed from the sample. The fit procedure is repeated until no new vertex candidate can be found. In the first iteration the interaction region is used as a constraint in order to identify the prompt tracks in the jet. The subsequent iterations produce decay vertex candidates.

4.2 Identification using track impact parameters

The impact parameter of a track with respect to the primary vertex can be used to distinguish the decay products of a b hadron from prompt tracks. The IP is calculated in three dimensions by taking advantage of the excellent resolution of the pixel detector along the z axis. The impact parameter has the same sign as the scalar product of the vector pointing from the primary vertex to the point

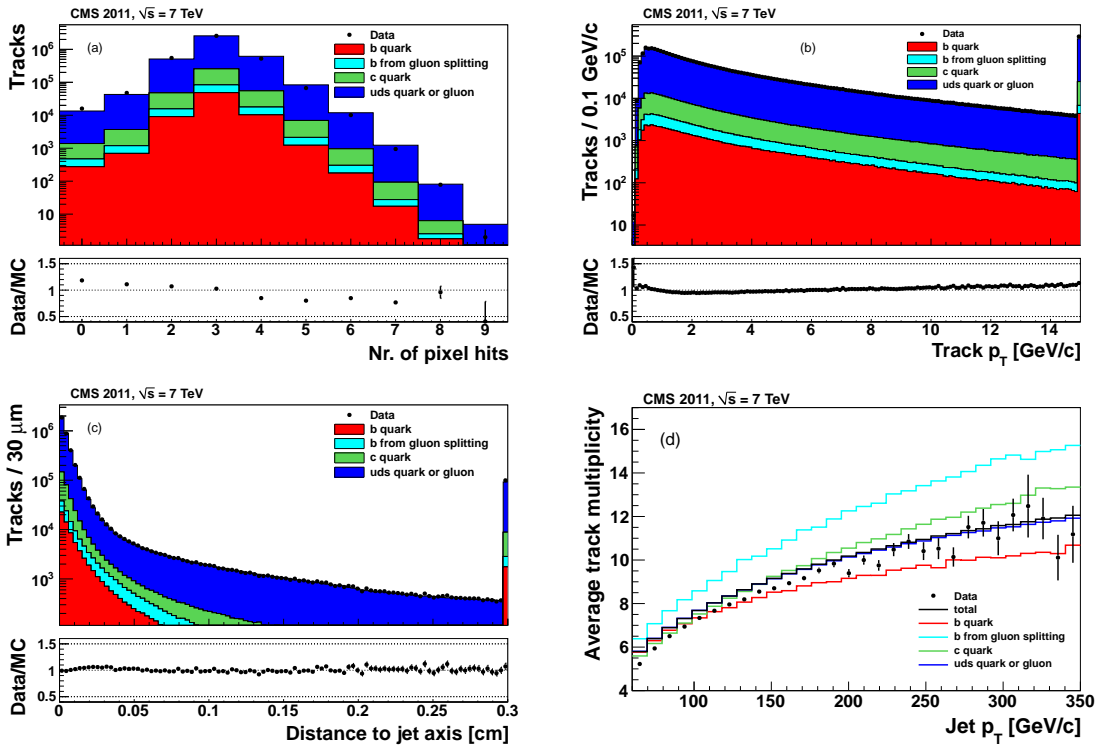


Figure 1. Track properties after basic selection (except for the variable plotted): (a) number of hits in the pixel system, (b) transverse momentum, (c) distance to the jet axis. The average number of tracks passing the basic selection is shown in (d) as a function of the transverse momentum of the jet. In (a)–(c) the distributions from simulation have been normalized to match the counts in data. The filled circles correspond to data. The stacked, coloured histograms indicate the contributions of different components from simulated multijet (“QCD”) samples. Simulated events involving gluon splitting to b quarks (“b from gluon splitting”) are indicated separately from the other b production processes (“b quark”). In each histogram, the rightmost bin includes all events from the overflow. The sample corresponds to a trigger selection with jet $p_T > 60 \text{ GeV}/c$.

of closest approach with the jet direction. Tracks originating from the decay of particles travelling along the jet axis will tend to have positive IP values. In contrast, the impact parameters of prompt tracks can have positive or negative IP values. The resolution of the impact parameter depends strongly on the p_T and η of a track. The impact parameter significance S_{IP} , defined as the ratio of the IP to its estimated uncertainty, is used as an observable. The distributions of IP values and their significance are shown in figure 2. In general, good agreement with simulation is observed with the exception of a small difference in the width of the core of the IP significance distribution.

By itself the impact parameter significance has discriminating power between the decay products of b and non-b jets. The *Track Counting* (TC) algorithm sorts tracks in a jet by decreasing values of the IP significance. Although the ranking tends to bias the values for the first track to high positive IP significances, the probability to have several tracks with high positive values is low for light-parton jets. Therefore the two different versions of the algorithm use the IP significance of the second and third ranked track as the discriminator value. These two versions of the algorithm are called *Track Counting High Efficiency* (TCHE) and *Track Counting High Purity* (TCHP), respectively. The distribution of the TCHE discriminator is shown in figure 3 (a).

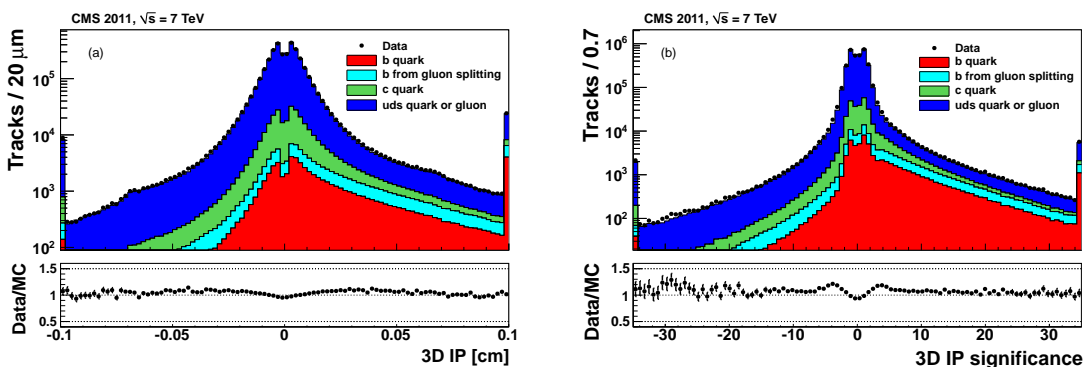


Figure 2. Distributions of (a) the 3D impact parameter and (b) the significance of the 3D impact parameter for all selected tracks. Selection and symbols are the same as in figure 1. Underflow and overflow are added to the first and last bins, respectively.

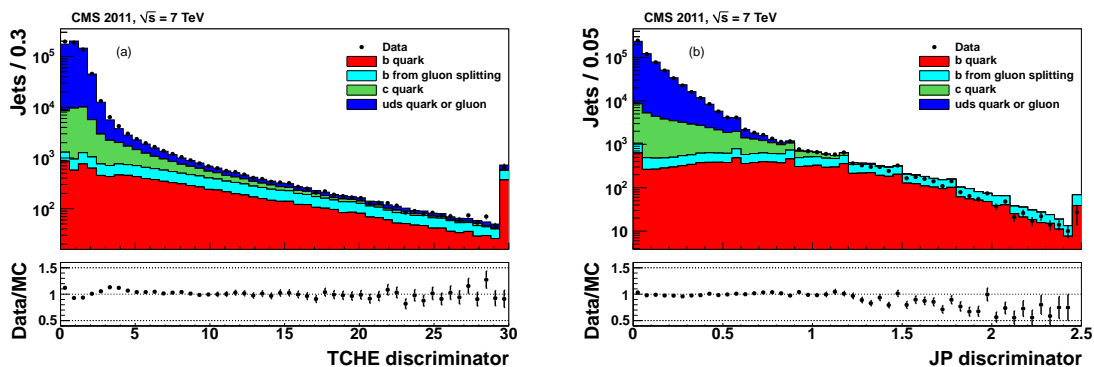


Figure 3. Discriminator values for (a) the TCHE and (b) the JP algorithms. Selection and symbols are the same as in figure 1. The small discontinuities in the JP distributions are due to the single track probabilities which are required to be greater than 0.5%.

A natural extension of the TC algorithms is the combination of the IP information of several tracks in a jet. Two discriminators are computed from additional algorithms. The *Jet Probability* (JP) algorithm uses an estimate of the likelihood that all tracks associated to the jet come from the primary vertex. The *Jet B Probability* (JBP) algorithm gives more weight to the tracks with the highest IP significance, up to a maximum of four such tracks, which matches the average number of reconstructed charged particles from b-hadron decays. The estimate for the likelihood, P_{jet} , is defined as

$$P_{\text{jet}} = \Pi \cdot \sum_{i=0}^{N-1} \frac{(-\ln \Pi)^i}{i!} \quad \text{with} \quad \Pi = \prod_{i=1}^N \max(P_i, 0.005), \quad (4.1)$$

where N is the number of tracks under consideration and P_i is the estimated probability for track i to come from the primary vertex [31, 32]. The P_i are based on the probability density functions for the IP significance of prompt tracks. These functions are extracted from data for different track quality classes, using the shape of the negative part of the S_{IP} distribution. Eight quality classes are defined for tracks with $\chi^2/\text{n.d.o.f} < 2.5$, depending on the momentum (< 8 or $> 8 \text{ GeV}/c$) and

pseudorapidity ($|\eta|$ within 0-0.8, 0.-1.6, 1.6-2.4 if there are at least three pixel hits or $|\eta| < 2.4$ if there are only two pixel hits). A ninth quality class is defined for tracks with $\chi^2/\text{n.d.o.f} > 2.5$. The cut-off parameter for P_i at 0.5% limits the effect of single, poorly reconstructed tracks on the global estimate. The discriminators for the jet probability algorithms have been constructed to be proportional to $-\ln P_{\text{jet}}$. The distribution of the JP discriminator in data and simulation is shown in figure 3 (b).

4.3 Identification using secondary vertices

The presence of a secondary vertex and the kinematic variables associated with this vertex can be used to discriminate between b and non-b jets. Two of these variables are the flight distance and direction, using the vector between primary and secondary vertices. The other variables are related to various properties of the system of associated secondary tracks such as the multiplicity, the mass (assuming the pion mass for all secondary tracks), or the energy. Secondary-vertex candidates must meet the following requirements to enhance the b purity:

- secondary vertices must share less than 65% of their associated tracks with the primary vertex and the significance of the radial distance between the two vertices has to exceed 3σ ;
- secondary vertex candidates with a radial distance of more than 2.5 cm with respect to the primary vertex, with masses compatible with the mass of K^0 or exceeding $6.5 \text{ GeV}/c^2$ are rejected, reducing the contamination by vertices corresponding to the interactions of particles with the detector material and by decays of long-lived mesons;
- the flight direction of each candidate has to be within a cone of $\Delta R < 0.5$ around the jet direction.

The *Simple Secondary Vertex* (SSV) algorithms use the significance of the flight distance (the ratio of the flight distance to its estimated uncertainty) as the discriminating variable. The algorithms' efficiencies are limited by the secondary vertex reconstruction efficiency to about 65%. Similar to the *Track Counting* algorithms, there exist two versions optimized for different purity: the *High Efficiency* (SSVHE) version uses vertices with at least two associated tracks, while for the *High Purity* (SSVHP) version at least three tracks are required. In figure 4 the flight distance significance and the mass associated with the secondary vertex are shown.

A more complex approach involves the use of secondary vertices, together with track-based lifetime information. By using these additional variables, the *Combined Secondary Vertex* (CSV) algorithm provides discrimination also in cases when no secondary vertices are found, increasing the maximum efficiency with respect to the SSV algorithms. In many cases, tracks with an $S_{\text{IP}} > 2$ can be combined in a “pseudo vertex”, allowing for the computation of a subset of secondary-vertex-based quantities even without an actual vertex fit. When even this is not possible, a “no vertex” category reverts to track-based variables that are combined in a way similar to that of the JP algorithm.

The following set of variables with high discriminating power and low correlations is used (in the “no vertex” category only the last two variables are available):

- the vertex category (real, “pseudo,” or “no vertex”);

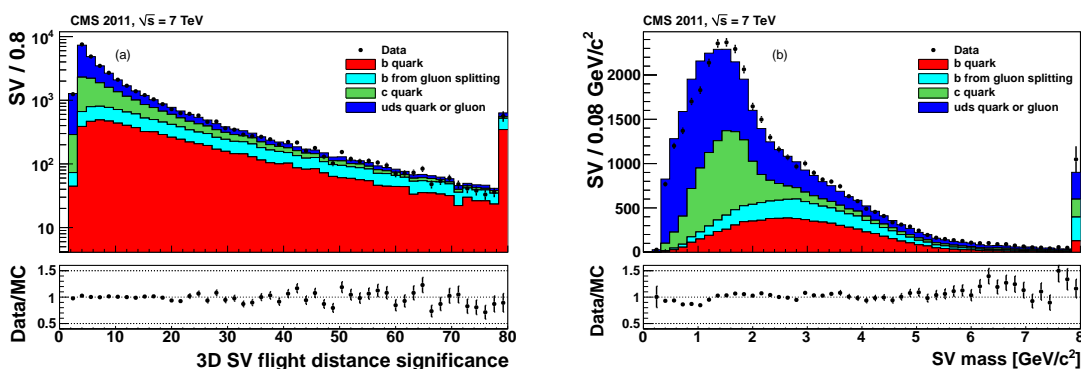


Figure 4. Properties of reconstructed decay vertices: (a) the significance of the 3D secondary vertex (3D SV) flight distance and (b) the mass associated with the secondary vertex. Selection and symbols are the same as in figure 1.

- the flight distance significance in the transverse plane (“2D”);
- the vertex mass;
- the number of tracks at the vertex;
- the ratio of the energy carried by tracks at the vertex with respect to all tracks in the jet;
- the pseudorapidities of the tracks at the vertex with respect to the jet axis;
- the 2D IP significance of the first track that raises the invariant mass above the charm threshold of $1.5 \text{ GeV}/c^2$ (tracks are ordered by decreasing IP significance and the mass of the system is recalculated after adding each track);
- the number of tracks in the jet;
- the 3D IP significances for each track in the jet.

Two likelihood ratios are built from these variables. They are used to discriminate between b and c jets and between b and light-parton jets. They are combined with prior weights of 0.25 and 0.75, respectively. The distributions of the vertex multiplicity and of the CSV discriminator are presented in figure 5.

4.4 Performance of the algorithms in simulation

The performance of the algorithms described above is summarized in figure 6 where the predictions of the simulation for the misidentification probabilities (the efficiencies to tag non-b jets) are shown as a function of the b-jet efficiencies. Jets with $p_T > 60 \text{ GeV}/c$ in a sample of simulated multijet events are used to obtain the efficiencies and misidentification probabilities. For loose selections with 10% misidentification probability for light-parton jets a b-jet tagging efficiency of $\sim 80\text{--}85\%$ is achieved. In this region the JBP has the highest b-jet tagging efficiency. For tight selections with misidentification probabilities of 0.1%, the typical b-jet tagging efficiency values are $\sim 45\text{--}55\%$. For medium and tight selections the CSV algorithm shows the best performance. As can be seen in

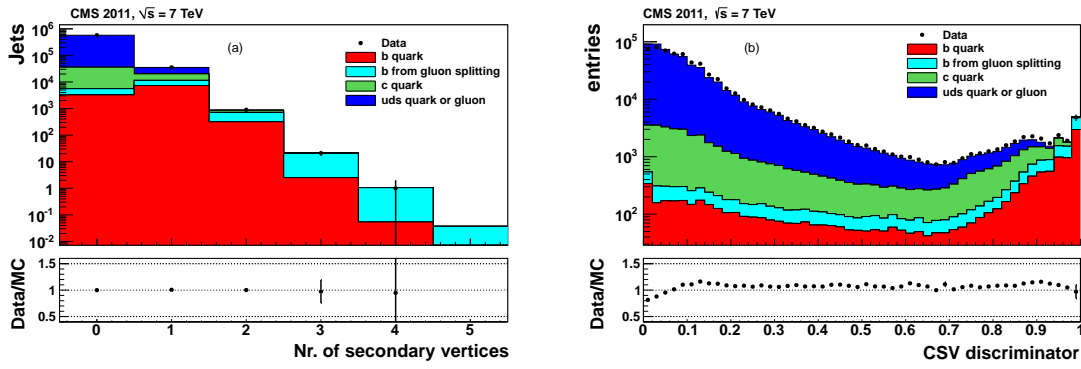


Figure 5. Distributions of (a) the secondary vertex multiplicity and (b) the CSV discriminator. Selection and symbols are the same as in figure 1.

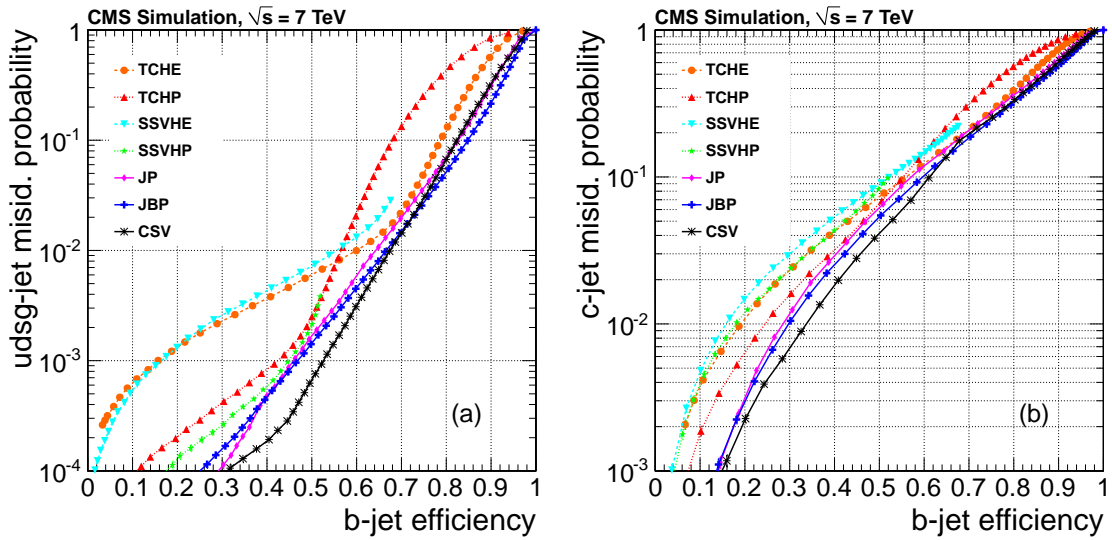


Figure 6. Performance curves obtained from simulation for the algorithms described in the text. (a) light-parton- and (b) c-jet misidentification probabilities as a function of the b-jet efficiency. Jets with $p_T > 60 \text{ GeV}/c$ in a sample of simulated multijet events are used to obtain the efficiency and misidentification probability values.

figure 6, the TC and SSV algorithms cannot be tuned to provide good performance for the whole range of operating points. Therefore two versions of these algorithms are provided, with the “high efficiency” version to be used for loose to medium operating points and the “high purity” version for tighter selections. Because of the non-negligible lifetime of c hadrons the separation of c from b jets is naturally more challenging. Due to the explicit tuning of the CSV algorithm for light-parton- and c-jet rejection it provides the best c-jet rejection values in the high-purity region.

Figure 7 presents the efficiencies and misidentification probabilities as a function of jet p_T and pseudorapidity for the JPL and CSVM taggers. Two simulated samples are used: a QCD multijet sample with a jet p_T trigger threshold of $60 \text{ GeV}/c$ applied to the leading jet, and a $t\bar{t}$ sample. Jets with $p_T > 30 \text{ GeV}/c$ and $|\eta| < 2.4$ are considered in both cases. The b-jet identification efficiency

is slightly larger in $t\bar{t}$ events at small jet p_T ($< 100\text{ GeV}/c$) due to the presence of more central jets. At large jet p_T ($> 200\text{ GeV}/c$), the presence of b and c jets from gluon splitting explains the apparent higher identification efficiency in the QCD multijet sample. The b-jet efficiency and the c-jet misidentification probability rise with jet p_T for values below $100\text{ GeV}/c$ and decrease above $200\text{ GeV}/c$. This dependence is due to a convolution of the track impact parameter resolution (which is larger at low p_T), of the heavy-hadron decay lengths (which scale with jet p_T) and of the track-selection criteria. The misidentification probability for light-parton jets rises continuously with jet p_T due to the logarithmic increase of the number of particles in jets and the higher fraction of merged hits in the innermost layers of the tracking system. However, both the identification efficiencies and misidentification probabilities stay roughly constant over most of the pixel detector acceptance.

4.5 Impact of running conditions on b-jet identification

All tagging algorithms rely on a high track identification efficiency and a reliable estimation of the track parameters and their uncertainties. These are both potentially sensitive to changes in the running conditions of the experiment. The robustness of the algorithms with respect to the misalignment of the tracking system and an increase in the density of tracks due to pile up, which are the most important of the changes in conditions, has been studied.

The alignment of the CMS tracker is performed using a mixture of tracks from cosmic rays and minimum bias collisions [33, 34], and is regularly monitored. During the 2011 data taking, the most significant movements were between the two halves of the pixel barrel detector, where discrete changes in the relative z position of up to $30\mu\text{m}$ were observed. The sensitivity of b-jet identification to misalignment was studied on simulated $t\bar{t}$ samples. With the current estimated accuracy of the positions of the active elements, no significant deterioration is observed with respect to a perfectly aligned detector. The effect of displacements between the two parts of the pixel barrel detector was studied by introducing artificial separations of 40, 80, 120, and $160\mu\text{m}$ in the detector simulation. The movements observed in 2011 were not found to cause any significant degradation of the performance.

Because of the luminosity profile of the 2011 data, the number of proton collisions taking place simultaneously in one bunch crossing was of the order of 5 to 20 depending on the time period. Although these additional collisions increase the total number of tracks in the event, the track selection is able to reject tracks from nearby primary vertices. The multiplicity distribution of selected tracks is almost independent of the number of primary vertices, as shown in figure 8 (a). There is an indication of a slightly lower tracking efficiency in events with high pileup. The rejection of the additional tracks is mainly due to the requirement on the distance of the tracks with respect to the jet axis. This selection criterion is very efficient for the rejection of tracks from pileup. The reconstruction of track parameters is hardly affected. The distribution of the second-highest IP significance is stable, as shown in figure 8 (b). The impact of high pileup on the b-jet tagging performance is illustrated in figure 9. This shows the light-parton misidentification probability versus the b-jet tagging efficiency for the TCHP and SSVHP algorithms. In order to focus on the changes due to the b-jet tagging algorithms, the performance curves have been compared using a jet p_T threshold of $60\text{ GeV}/c$ at the generator level. The changes are small and concentrated in the regions of very high purity.

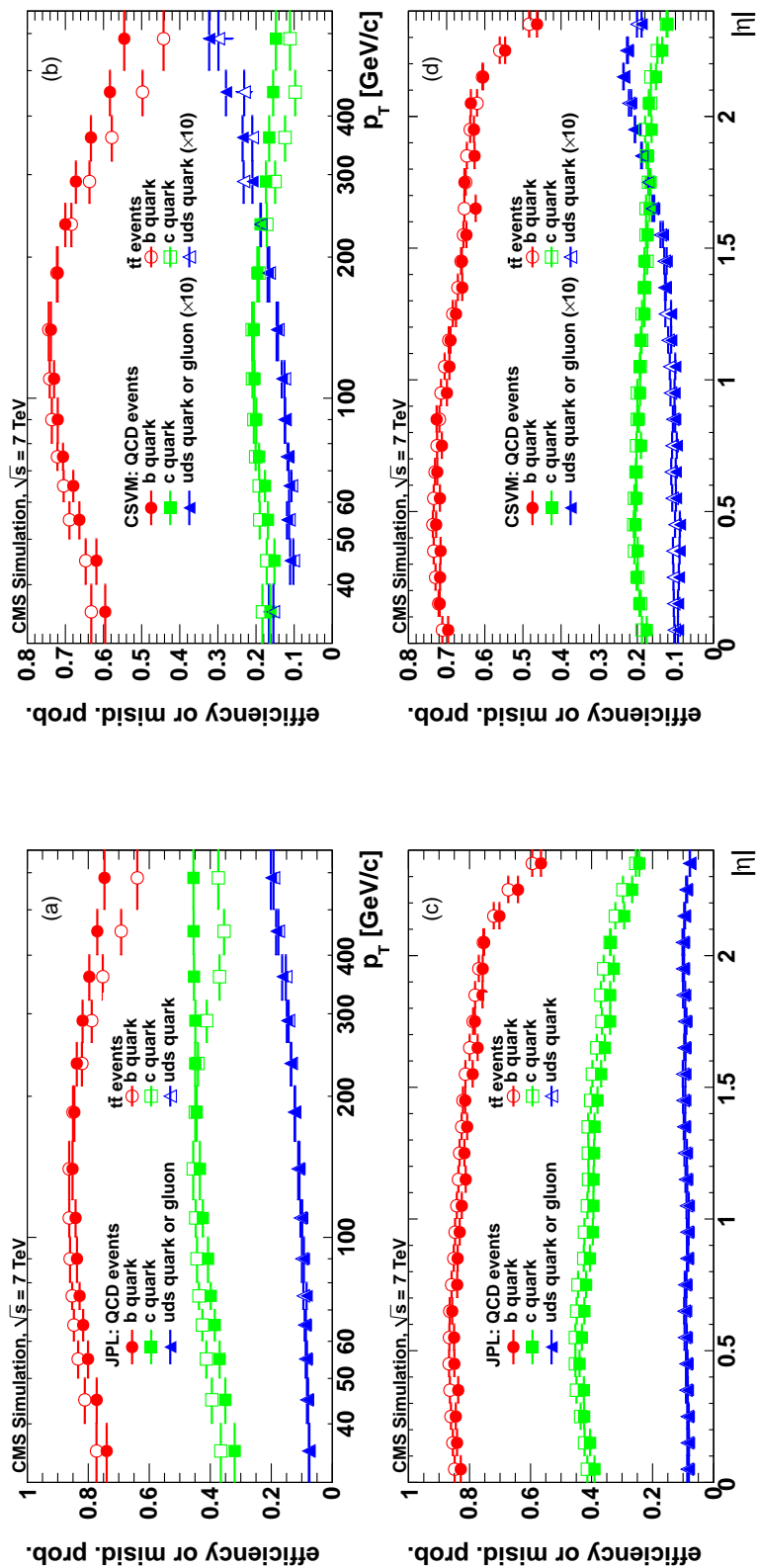


Figure 7. Efficiency for b-jets and misidentification probabilities for c and light-parton jets of the (a, c) JPL and (b, d) CSVM taggers as a function of (a, b) jet p_T and (c, d) jet pseudorapidity in QCD multijet events (filled symbols) and $t\bar{t}$ events (open symbols). A trigger threshold of $p_T > 60 \text{ GeV}/c$ is applied to the leading jet in the QCD events. Jets with $p_T > 30 \text{ GeV}/c$ and $|\eta| < 2.4$ are used in both samples. In (a) and (b), the rightmost bins includes all jets with $p_T > 500 \text{ GeV}/c$. For the CSVM tagger, the misidentification probability for light partons is scaled up by a factor of ten.

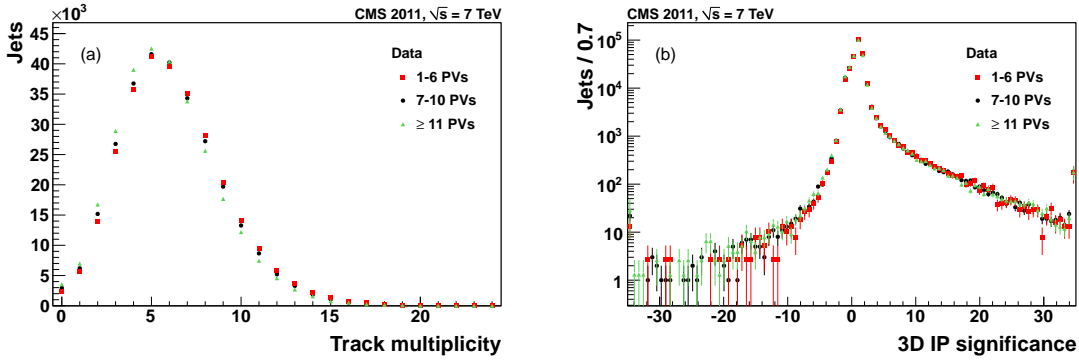


Figure 8. (a) the number of tracks associated with the selected jets for three ranges of primary vertex (PV) multiplicity. (b) the IP significance of the second-most significant track, for the three ranges of primary vertex multiplicity. The selection is the same as in figure 1. The distributions are normalized to the event count for 1–6 PV range. Underflow and overflow entries are added to the first and last bins, respectively.

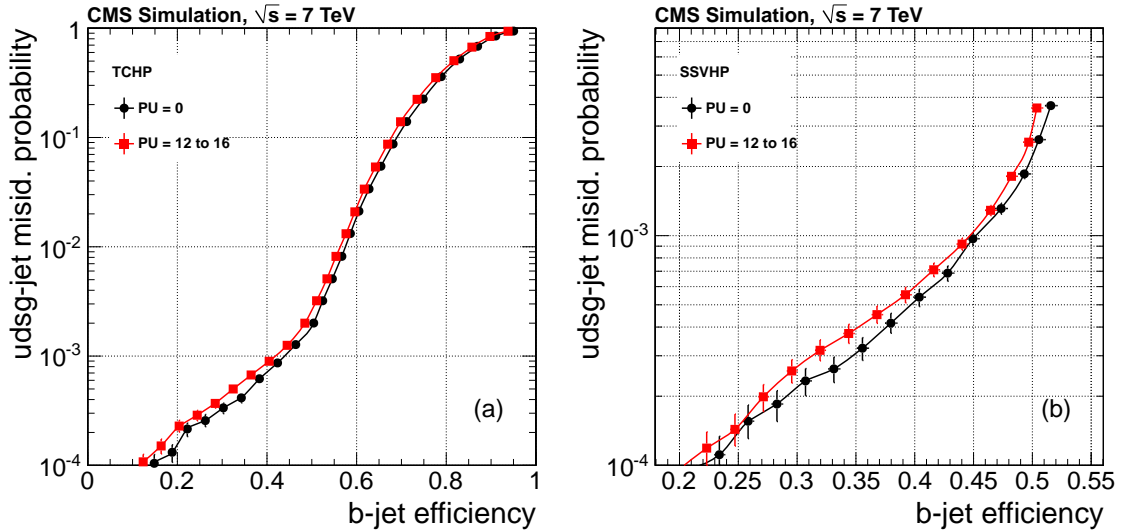


Figure 9. Light-parton misidentification probability versus b-jet tagging efficiency for jets with $p_T > 60 \text{ GeV}/c$ at generator level for the (a) TCHP and (b) SSVHP algorithms for different pileup (PU) scenarios.

5 Efficiency measurement with multijet events

For the b-jet tagging algorithms to be used in physics analyses, it is crucial to know the efficiency for each algorithm to select genuine b jets. There are a number of techniques that can be applied to CMS data to measure the efficiencies *in situ*, and thus reduce the reliance on simulations. If event distributions from MC simulation match those observed in data reasonably well, then the simulation can be used for a wide range of topologies after applying corrections determined from specific data samples. Corrections can be applied to simulated events using a scale factor SF_b , defined as the ratio of the efficiency measured with collision data to the efficiency found in the equivalent simulated samples, using MC generator-level information to identify the jet flavour.

Furthermore, the measurement techniques used for data are also applied to the simulation in order to validate the different algorithms.

Some efficiency measurements are performed using samples that include a jet with a muon within $\Delta R = 0.4$ from the jet axis (a “muon jet”). Because the semileptonic branching fraction of b hadrons is significantly larger than that for other hadrons (about 11%, or 20% when $b \rightarrow c \rightarrow \ell$ cascade decays are included), these jets are more likely to arise from b quarks than from another flavour. Muons are identified very efficiently in the CMS detector, making it straightforward to collect samples of jets with at least one muon. These muons can be used to measure the performance of the lifetime-based tagging algorithms, since the efficiencies of the muon- and lifetime-based b-jet identification techniques are largely uncorrelated. Sections 5.1 and 5.2 describe efficiency measurements that use muon jets, while the technique of section 5.3 makes use of a more generic dijet sample. The results are given in section 7.

5.1 Efficiency measurement with kinematic properties of muon jets

Due to the large b-quark mass, the momentum component of the muon transverse to the jet axis, p_T^{rel} , is larger for muons from b-hadron decays than for muons in light-parton jets or from charm hadrons. This component is used as the discriminant for the “PtRel” method. In addition, the impact parameter of the muon track, calculated in three dimensions, is also larger for b hadrons than for other hadrons. This parameter is used as the discriminant for the “IP3D” method. Both of these variables can thus be used as a discriminant in the b-jet tagging efficiency determination. In both cases, the discriminating power of the variable depends on the muon jet p_T . The muon p_T^{rel} (IP) distributions provide better separation for jets with p_T smaller (greater) than about $120 \text{ GeV}/c$. The PtRel and IP3D methods rely on fits to the p_T^{rel} [35] and muon IP distributions in the data with respect to simulated spectra for the b signal and charm+light-parton background.

In the two methods, the p_T^{rel} and IP spectra for muon jets are modelled using simulated distributions that represent the spectra expected for different jet flavours to obtain the b-jet content of the sample. The efficiency for a particular tagger is obtained by measuring the fraction of muon jets that satisfy the requirements of the tagger. To make the treatment of the statistical uncertainty more straightforward, the muon jet sample is separated into those jets that satisfy and those that fail the requirements of the tagger. These jets are referred to as “tagged” and “untagged.”

A dijet sample with high b-jet purity is obtained by requiring that events have exactly two reconstructed jets: the muon jet as defined above and another jet fulfilling the TCHPM b-jet tagging criterion (the “medium” operating point for the TCHP algorithm). Simulated MC events are used to establish p_T^{rel} and IP spectra for muon jets resulting from the fragmentation of b, c, and light partons. Muons in light-parton jets mostly arise from the decay of charged pions or kaons and from misidentified muons or hadronic punch-through in the calorimeters, effects that might not be modelled well in the simulation. The spectra for light-parton jets from simulation can be validated against control samples of collision data. In figure 10 the distributions of p_T^{rel} and $\ln(|\text{IP}|[\text{cm}])$ derived from the simulation are compared to the ones obtained for tracks in inclusive jet data by applying the same kinematic selection and track reconstruction quality requirements as for the muon candidates. In order to measure the ability of the simulation to model the investigated spectra, we apply the same procedure to a sample of simulated inclusive jet events. The spectra derived for

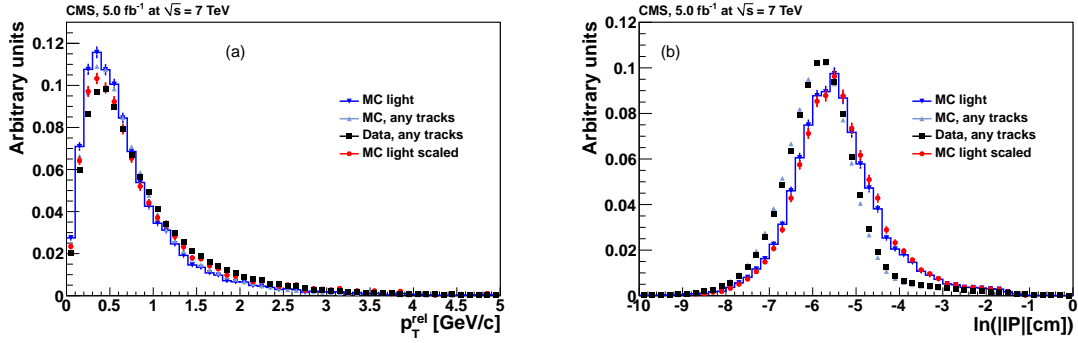


Figure 10. Comparison of distributions of (a) muon p_T^{rel} for jets with p_T between 80 and 120 GeV/c and (b) $\ln(|\text{IP}|[\text{cm}])$ for jets with p_T between 160 and 320 GeV/c for muons in simulated light-parton jets (“MC light”), tracks from simulated inclusive jet events (“any tracks”), tracks from data, and muons in simulated light-parton jets after corrections based on data (“MC light scaled”).

low- p_T muons from light-parton jets in simulation are corrected by multiplying them with the ratio of shapes of the inclusive distributions obtained in data and simulation on a bin-by-bin basis.

The fractions of each jet flavour in the dijet sample are extracted with a binned maximum likelihood fit using p_T^{rel} and IP templates for b, c and light-parton jets derived from simulation or inclusive jet data. The fits are performed independently in the tagged and untagged subsamples of the muon jets. Results of representative fits are shown in figures 11 and 12.

From each fit the fractions of b jets (f_b^{tag} , f_b^{untag}) are extracted from the data. With these fractions and the total yields of tagged and untagged muon jets ($N_{\text{data}}^{\text{tag}}$, $N_{\text{data}}^{\text{untag}}$), the number of b jets in these samples are calculated, and the efficiency ϵ_b^{tag} for tagging b jets in the data is inferred:

$$\epsilon_b^{\text{tag}} = \frac{f_b^{\text{tag}} \cdot N_{\text{data}}^{\text{tag}}}{f_b^{\text{tag}} \cdot N_{\text{data}}^{\text{tag}} + f_b^{\text{untag}} \cdot N_{\text{data}}^{\text{untag}}} \quad (5.1)$$

To obtain SF_b , the efficiency for tagging b jets in the simulation is obtained from jets that have been identified as b jets with MC generator-level matching.

5.2 Efficiency measurement with the System8 method

The “System8” method [36, 37] is applied to events with a muon jet and at least one other, “away-tag”, jet. The muon jet is used as a probe. The reference lifetime tagger and a supplementary p_T^{rel} -based selection are tested on this jet. The away-tag jet is tested with a separate lifetime tagger. There are eight quantities that can be counted from the full data sample. The quantities depend on the number of passing or failing tags. A set of equations correlates these eight quantities with the tagging efficiencies.

A muon jet can be tagged as a b jet using either a lifetime tagger, or by requiring that the muon has large p_T^{rel} . In this analysis, the requirement is $p_T^{\text{rel}} > 0.8 \text{ GeV}/c$. These two tagging criteria have efficiencies ϵ_b^{tag} and $\epsilon_b^{\text{PtRel}}$, respectively, for b jets. The third tagging criterion is the requirement that another jet in the event passes also a lifetime-based tagger. This last requirement defines the “away-tag sample”. It enriches the b content of the events, and thus makes it more likely that the muon jet is a b jet. Correlations between the efficiencies of the two tagging criteria are estimated

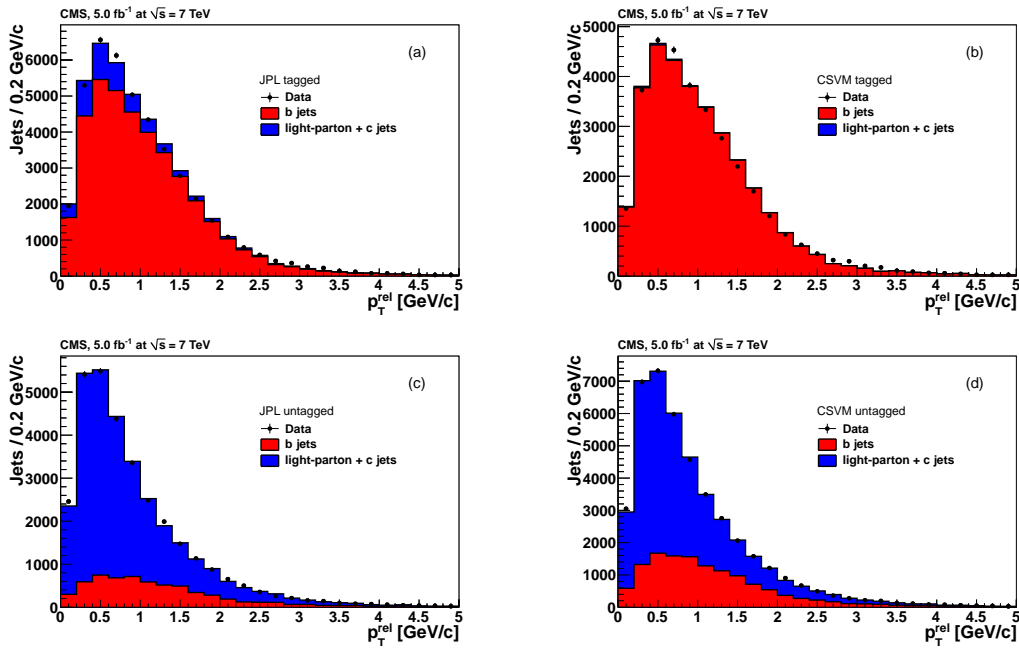


Figure 11. Fits of the summed b and non-b templates, for simulated muon jets, to the muon p_T^{rel} distributions from data. (a) and (c) show the results for muon jets that pass (tagged) or fail (untagged) the b-jet tagging criteria of the JPL method, respectively. (b) and (d) are the equivalent plots for the CSVM method. The muon jet p_T is between 80 and 120 GeV/c.

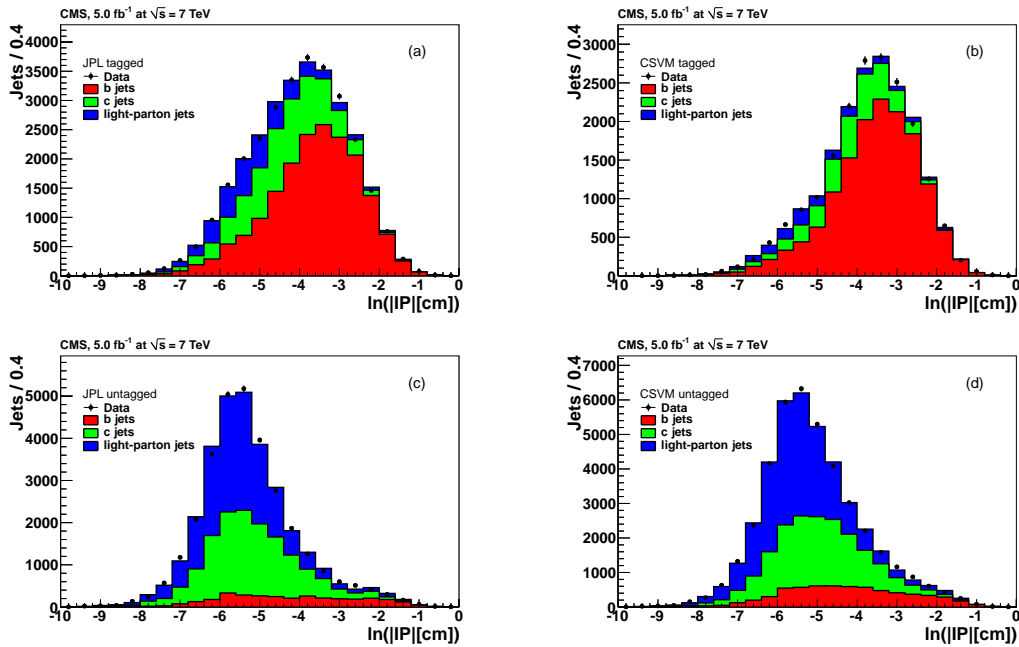


Figure 12. Same as figure 11 using the $\ln(|\text{IP}|[\text{cm}])$ distributions. The muon jet p_T is between 160 and 320 GeV/c.

from simulation. As p_T^{rel} provides less discrimination between jet flavours at higher jet energies, the System8 method loses sensitivity for jet $p_T > 120 \text{ GeV}/c$.

With these criteria eight quantities are measured. The four quantities for the muon jets are: the total number of muon jets in the sample n , the number of muon jets that pass the lifetime-tagging criterion n^{tag} , the number of muon jets that pass the p_T^{rel} requirement n^{PtRel} , and the number of muon jets that pass both criteria $n^{\text{tag,PtRel}}$. Likewise, the four quantities for the away-tag sample are labelled p , p^{tag} , p^{PtRel} , $p^{\text{tag,PtRel}}$. The away-tag jets are tagged with the TCHPL criterion.

The full muon jet sample, n , and the away-tag sample, p , are each composed of an unknown mix of b and non-b jets. The non-b jets are labelled “cℓ”. The muon sample thus comprises n_b and $n_{c\ell}$, and the away-tag sample, p_b and $p_{c\ell}$. The efficiencies of the two tagging criteria on b jets (ϵ_b^{tag} , $\epsilon_b^{\text{PtRel}}$) and on non-b jets ($\epsilon_{c\ell}^{\text{tag}}$, $\epsilon_{c\ell}^{\text{PtRel}}$) are also unknown, for a total of eight unknown quantities. Thus, a system of eight equations can be written that relates the measurable quantities to the unknowns:

$$\begin{aligned}
 n &= n_b + n_{c\ell} , \\
 p &= p_b + p_{c\ell} , \\
 n^{\text{tag}} &= \epsilon_b^{\text{tag}} n_b + \epsilon_{c\ell}^{\text{tag}} n_{c\ell} , \\
 p^{\text{tag}} &= \beta^{\text{tag}} \epsilon_b^{\text{tag}} p_b + \alpha^{\text{tag}} \epsilon_{c\ell}^{\text{tag}} p_{c\ell} , \\
 n^{\text{PtRel}} &= \epsilon_b^{\text{PtRel}} n_b + \epsilon_{c\ell}^{\text{PtRel}} n_{c\ell} , \\
 p^{\text{PtRel}} &= \beta^{\text{PtRel}} \epsilon_b^{\text{PtRel}} p_b + \alpha^{\text{PtRel}} \epsilon_{c\ell}^{\text{PtRel}} p_{c\ell} , \\
 n^{\text{tag,PtRel}} &= \beta^n \epsilon_b^{\text{tag}} \epsilon_b^{\text{PtRel}} n_b + \alpha^n \epsilon_{c\ell}^{\text{tag}} \epsilon_{c\ell}^{\text{PtRel}} n_{c\ell} , \\
 p^{\text{tag,PtRel}} &= \beta^p \epsilon_b^{\text{tag}} \epsilon_b^{\text{PtRel}} p_b + \alpha^p \epsilon_{c\ell}^{\text{tag}} \epsilon_{c\ell}^{\text{PtRel}} p_{c\ell} .
 \end{aligned} \tag{5.2}$$

The method assumes that the efficiencies for a combination of tagging criteria are factorizable. Thus eight correlation factors are introduced to solve the system of equations: α^{tag} , β^{tag} , α^{PtRel} , β^{PtRel} , α^n , β^n , α^p , and β^p . These factors are obtained from the simulation as a function of the muon jet p_T and $|\eta|$. The factors α and β are determined for non-b and b jets, respectively. The superscripts “tag” and “PtRel” of α and β indicate the efficiency ratio of the p to the n samples for the lifetime and p_T^{rel} criteria. The superscripts “n” and “p” refer to the correlation between the two tagging efficiencies, “tag” and “PtRel”, in the n and p samples.

The simulation predicts that the correlation coefficients typically range between 0.95 and 1.05 for those associated with the b-jet tagging efficiencies, and between 0.7 and 1.2 for those associated with the c+ℓ-tagging efficiencies. A numerical computation is applied to solve the system of eight equations in the data to determine the eight unknowns, thus simultaneously determining the tagging efficiencies and flavour contents of both the full and away-tag samples.

5.3 Efficiency measurement using a reference lifetime algorithm

While muon p_T^{rel} provides less discrimination power between jet flavours at large jet p_T , the lifetime-based algorithms described in sections 4.2 and 4.3 (TCHE, TCHP, JP, JBP, SSVHE, SSVHP and CSV) retain their sensitivity to distinguish different jet flavours. In particular, the discriminant for the jet probability algorithm has different distributions for different jet flavours for jet momenta in the range $30 < p_T < 700 \text{ GeV}/c$. The JP algorithm can be calibrated directly with data. Tracks

with negative impact parameter are used to compute the probability that those tracks come from the primary vertex. The same calibration is performed separately in simulated samples. As a result, the JP algorithm serves as a reference for estimating the fraction of b jets in a data sample, and also for estimating the fraction of b jets in a subsample that has been selected by an independent tagging algorithm. In this manner the efficiency of the independent algorithm can be measured. This method is called the lifetime tagging method (“LT”). It can be performed on both inclusive and muon jet samples. The resulting scale factors are compared to obtain an estimate of the systematic uncertainty.

The efficiency measurement is performed in inclusive jet events in which at least one jet must be above a given p_T threshold, and separately in dijet events in which at least one jet is a muon jet. To increase the fraction of b jets in the inclusive sample, an additional jet tagged by the JPM algorithm is also required. The sample with muon jets is already sufficiently enriched in b jets by the muon requirement. The same set of samples can be established with simulated events, so that the true tagging efficiency can be measured there and a scale factor computed.

Because a value of the JP discriminant can be defined for jets that have as few as one track with a positive impact parameter significance, the discriminant can be calculated for most b jets, regardless of their p_T . The fraction of b jets that have JP information, C_b , rises from about 0.91 at $p_T = 20 \text{ GeV}/c$ to more than 0.98 for $p_T > 50 \text{ GeV}/c$.

Figure 13 shows the JP discriminant distributions in the muon jet sample and the inclusive sample, before and after tagging the jets with an independent tagger, in this case the CSVM tagger. Also shown is a fit to the distributions using JP-discriminant templates derived from simulations of b, c, and light-parton jets. The normalization of the relative flavour fractions f_b , f_c and f_{light} is left free, with the constraint that $f_b + f_c + f_{\text{light}} = 1$. The b-jet tagging efficiency is the ratio of the number of b jets that are tagged by the independent tagger to the number of b jets before the tagging. The numbers are calculated using the fit. The b-jet tagging efficiency is corrected for the fraction of jets that have JP information,

$$\epsilon_b^{\text{tag}} = \frac{C_b \cdot f_b^{\text{tag}} \cdot N_{\text{data}}^{\text{tag}}}{f_b^{\text{before tag}} \cdot N_{\text{data}}^{\text{before tag}}}, \quad (5.3)$$

where the superscripts “before tag” and “tag” refer to the samples before and after application of the tagging criterion.

Examples of the efficiencies measured for the JPL and CSVM taggers are shown in figure 14. In both cases the results from simulation are close to those obtained from data.

This technique cannot be used to measure the efficiency of the JP algorithm itself, as the JP discriminant is used in the fit to determine the b-jet content of the sample. However, the CSV discriminant, which is mostly based on information from secondary vertices, can be used in its place to determine the flavour content. More than 90% of jets have CSV information, as is the case with the JP discriminant. But unlike the JP discriminant, the CSV discriminant cannot be calibrated solely with the data. To remedy this, the CSV discriminant is used to estimate the tagging efficiency of the TC algorithms. By comparing these results to those using the JP discriminant, the bias due to using the CSV discriminant is determined to be (0–2%, 4–6%, 6–9%) for the (loose, medium, tight) operating points. The efficiencies and scale factors for the JP algorithm are corrected for these biases.

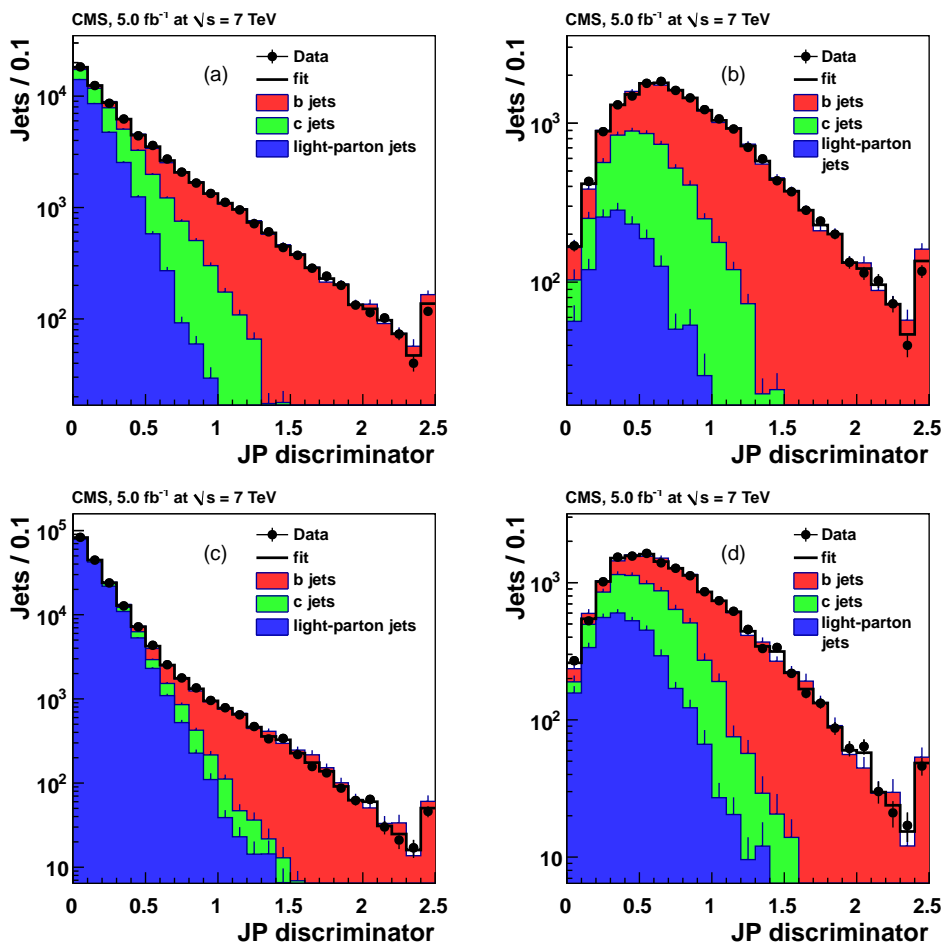


Figure 13. Fits of the summed b, c and light-parton templates, for simulated jets, to the JP-discriminant distributions from data. (a) and (b) show the results for muon jets before and after identification with the CSVM tagger, respectively. (c) and (d), the equivalent plots for inclusive jets. The black line is the sum of the contributions from the templates. The jet p_T is in the range $260 < p_T < 320 \text{ GeV}/c$. Overflows are displayed in the rightmost bins.

5.4 Systematic uncertainties on efficiency measurements

Several systematic uncertainties affect the measurement of the b-jet tagging efficiency. Some are common to all four methods (PtRel, IP3D, System8, LT), some are common to a subset of them, and some are unique to a particular method.

Common systematic uncertainties for all methods:

- **Pileup:** the measured b-jet tagging efficiency depends on the number of pp collisions superimposed on the primary interaction of interest. The systematic uncertainty is computed by varying the average value of the pileup in data by 10% and calculating the difference in the values of SF_b after reweighting the simulation with the modified distribution.
- **Gluon splitting:** studies of angular correlation between b jets at the LHC [38] indicate that QCD events may have a larger fraction of gluon splitting into $b\bar{b}$ pairs than is assumed in the

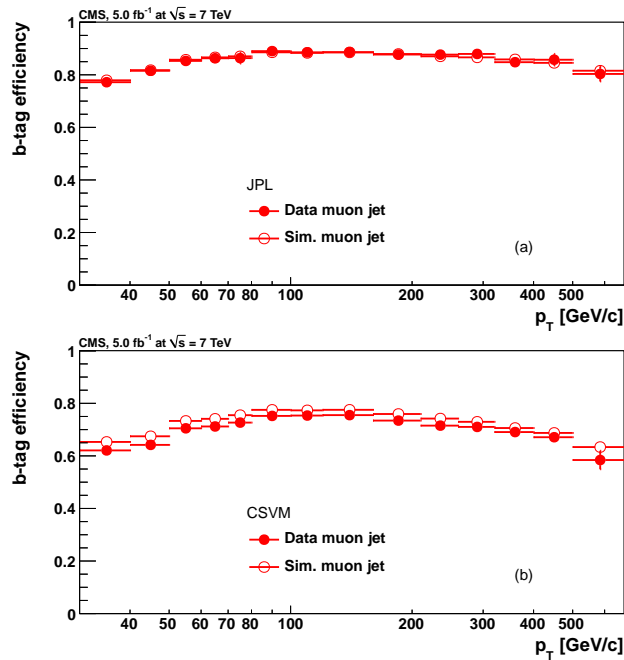


Figure 14. Efficiencies for the identification of b-jets measured for (a) the JPL and (b) the CSVM tagger with the LT method in the muon jet sample. Filled and open circles correspond to data and simulation, respectively.

generation of the simulation. A study was carried out with the MC sample where the number of events with gluon splitting was artificially changed by 50%. Results obtained with this modified gluon splitting MC sample are then compared to those with the original sample. The observed deviation is quoted as a systematic uncertainty.

- **Muon p_T^μ :** the central value of the b-jet tagging efficiency is extracted from data with muon $p_T^\mu > 5 \text{ GeV}/c$. The choice of the selection affects the shape of the template distributions used in fits, and also the number of events used to measure the tagging efficiencies. The p_T^μ threshold is varied up to $9 \text{ GeV}/c$ to test the sensitivity to this choice.

Common uncertainty for the PtRel, IP3D and System8 methods:

- **Away-jet tagger:** the dependency of the calculated b-jet tagging efficiency on the away-jet tagger is studied by comparing the results obtained by tagging the away jets with different variants of the TC algorithm (TCHEL, TCHEM, TCHPM). The measured SF_b tends to increase when the away tag is tighter. The maximum deviation from the default away-jet tagger is taken as a systematic uncertainty.

Uncertainty unique to the PtRel method:

- **Ratio of light-parton to charm jets in simulation:** the shapes of the p_T^{rel} and IP spectra for light-parton jets have been obtained from control samples in data, which minimizes the bias due to a mismodelling of the muon kinematics in the simulation. However, since the p_T^{rel} distribution in data is fitted with a sum of templates for b jets and for c+udsg jets, uncertainties

on the ratio between light-parton and charmed jets in the simulation must be considered. To do so, the predicted ratio is varied by $\pm 20\%$, and the fit is repeated, taking the variation in the results as a systematic uncertainty. This uncertainty does not apply to the IP method, where a three-component fit is performed that determines the light-parton and charm contributions independently.

Uncertainties unique to the System8 method:

- **Selection on p_T^{rel} :** one of the System8 criteria is a selection on the muon $p_T^{\text{rel}} > 0.8 \text{ GeV}/c$. In order to test the sensitivity to the b purity in the muon jet sample and the relative charm/light-parton fraction in the non-b background, this selection was changed from 0.5 to 1.2 GeV/c in the data. The correlation factors were recomputed accordingly in the simulation and the System8 method was applied again to the data in order to compute the b-jet tagging efficiency. The largest deviation observed from the central value is quoted as a systematic uncertainty.
- **MC closure test:** the b-jet tagging efficiency can be directly calculated from the simulated QCD muon-enriched sample, as the flavour of the jets at generator level is known. In this case, the efficiency can be measured by taking the number of identified true b jets over all true b jets. The resulting value is denoted as the MC truth b-jet tagging efficiency. The System8 method is also applied to this MC sample. The resulting b-jet tagging efficiencies are in good agreement with the MC truth, giving a negligible systematic uncertainty. (This systematic uncertainty does not appear for the other methods as they rely on template fits, making such a test trivial.)

Uncertainties unique to the LT method:

- **Fraction of b jets with JP information:** the fraction of inclusive jets with JP information is well described by the simulation. As explained above, the number of b jets before tagging is measured by a fit to the JP distribution and corrected by the fraction C_b of b jets with JP information. A systematic uncertainty of half the residual correction, $(1 - C_b)/(2C_b)$, is estimated from the simulation as a function of the b-jet p_T . A corresponding factor with a similar uncertainty is needed for measuring the efficiency of the JP and JBP taggers with the CSV discriminator spectrum.
- **Difference between muon jets and inclusive jets:** in the fits to the Jet Probability discriminator, the shape for the light-parton contribution is mostly calibrated from the data. However, as the LT method relies on a lifetime discriminator, a systematic effect may arise from some mismodelling of correlations for b jets between the JP discriminator and the other tagging criterion under study. This effect is specific to the LT method. In order to estimate the uncertainty due to this effect, two independent samples with different b-jet fractions are considered: the muon-jet sample and an inclusive jet sample (where another jet is tagged by the JPM criterion). The difference between the measured SF_b in muon jets and in inclusive b jets is taken as a systematic uncertainty. This is the largest contribution to the systematic uncertainty on SF_b with the LT method. Due to the large statistical uncertainty on SF_b for inclusive jets with $p_T < 80 \text{ GeV}/c$, the same systematic uncertainty is used for $p_T < 80 \text{ GeV}/c$

and for the range 80–210 GeV/c. If the difference on SF_b between muon jets and inclusive jets is smaller than the statistical error on SF_b for inclusive jets, this uncertainty is used for the systematic uncertainty estimate.

- **Bias for the JP and JBP taggers:** the uncertainty on the measurement of the bias, when using the CSV discriminant to measure the efficiency of the JP and JBP taggers as estimated for the TC taggers, is propagated into the uncertainty on the scale factors for these taggers.

The systematic uncertainties on the data/MC scale factors for different tagging criteria are detailed in tables 1–4 for the PtRel and System8 methods at low jet p_T ($80 < p_T < 120$ GeV/c) and for the IP3D and LT methods at higher jet p_T ($160 < p_T < 320$ GeV/c). In these momentum ranges the average uncertainty is about 3% for the PtRel method, 6–10% for the System8 method, 3–4% for the IP3D method, and 2–7% for the LT method.

6 Efficiency measurement with $t\bar{t}$ events

In the framework of the standard model, the top quark is expected to decay to a W boson and a b quark about 99.8% of the time [22]. Experimentally, the measurement of the heavy-flavour content of $t\bar{t}$ events can provide either a direct measurement of the branching fraction of the decay of the top quark to a W boson and a b quark, $B(t \rightarrow Wb)$, or, assuming $B(t \rightarrow Wb) = 1$, the b-jet tagging efficiency. The b jets in $t\bar{t}$ events have an average p_T of about 80 GeV/c and cover a p_T range relevant for many processes both within the standard model and for many models beyond the standard model.

In this section, we present several methods to study the heavy-flavour content of $t\bar{t}$ events. The profile likelihood ratio (PLR) method, described in section 6.3, and the flavour tag matching (FTM) method, described in section 6.5, use $t\bar{t}$ events in the dilepton channel in which both W bosons decay into leptons. The flavour tag consistency (FTC) method, described in section 6.4, and the bSample method (section 6.6) use $t\bar{t}$ events in the lepton+jets channel, in which one W boson decays into quarks and the other into a charged lepton and a neutrino. These methods are used to measure the efficiency of tagging b jets in the data and the simulation over the average p_T and η range of jets in the top-quark events. The differences in efficiencies observed between the data and MC simulation are provided as a data/MC scale factor SF_b similar to the techniques described in section 5.

6.1 Event selection

The event reconstruction used herein follows closely the event selection performed for the $t\bar{t}$ production cross section measurements [1, 39], with the exception of the b-jet tagging requirements. All objects are reconstructed using a particle-flow algorithm.

In the lepton+jets channel, the final state is composed of four jets, one energetic isolated muon and missing transverse energy. Events are required to pass a single-muon trigger. After offline reconstruction, events are selected requiring exactly one isolated muon with $p_T > 30$ GeV/c and $|\eta| < 2.1$ and at least four jets with $p_T > 30$ GeV/c and $|\eta| < 2.4$. The FTC method further requires

Table 1. Relative systematic uncertainties on SF_b for the PtRel method in the muon jet p_T range 80–120 GeV/c, using the medium operating point of the b-jet tagging algorithms.

b tagger	pileup	$g \rightarrow b\bar{b}$	p_T^μ	away jet	light / charm	total
JPM	1.6%	1.6%	1.1%	1.9%	0.4%	3.2%
JBPM	0.9%	0.5%	1.8%	1.2%	0.5%	2.5%
TCHEM	1.5%	0.5%	1.4%	1.6%	0.4%	2.7%
TCHPM	1.1%	0.1%	2.3%	1.1%	0.6%	2.8%
SSVHEM	0.7%	1.3%	2.0%	0.4%	0.4%	2.5%
CSVM	1.4%	1.3%	1.3%	1.2%	0.5%	2.6%

Table 2. Relative systematic uncertainties on SF_b for the System8 method in the muon jet p_T range 80–120 GeV/c, using the medium operating point of the b-jet tagging algorithms.

b tagger	pileup	$g \rightarrow b\bar{b}$	p_T^μ	away jet	p_T^{rel}	MC closure	total
JPM	1.4%	0.6%	4.2%	3.9%	1.6%	0.1%	6.1%
JBPM	1.5%	1.9%	6.5%	1.5%	4.0%	<0.1%	8.2%
TCHEM	1.3%	1.3%	6.6%	2.1%	2.4%	<0.1%	7.5%
TCHPM	1.3%	2.7%	8.2%	1.9%	4.0%	0.1%	9.7%
SSVHEM	1.3%	0.1%	3.7%	2.8%	3.0%	<0.1%	5.6%
CSVM	1.5%	0.4%	4.3%	1.3%	4.5%	0.1%	6.5%

Table 3. Relative systematic uncertainties on SF_b for the IP3D method in the muon jet p_T range 160–320 GeV/c, using the medium operating point of the b-jet tagging algorithms.

b tagger	pileup	$g \rightarrow b\bar{b}$	p_T^μ	away jet	total
JPM	0.1%	0.7%	0.1%	3.2%	3.2%
JBPM	0.2%	1.7%	0.4%	2.8%	3.3%
TCHEM	0.1%	1.2%	0.4%	2.4%	2.7%
TCHPM	0.2%	2.3%	0.7%	2.2%	3.3%
SSVHEM	0.6%	2.2%	0.3%	2.9%	3.6%
CSVM	0.6%	2.3%	0.1%	3.2%	4.0%

Table 4. Relative systematic uncertainty on SF_b with the LT method in the muon jet p_T range 160–320 GeV/c, using the medium operating point of the b-jet tagging algorithms.

b tagger	pileup	$g \rightarrow b\bar{b}$	p_T^μ	C_b	inc. jets	bias	total
JPM	0.1%	0.8%	0.5%	0.1%	4.4%	4.0%	6.0%
JBPM	0.1%	0.4%	0.8%	0.1%	4.3%	4.0%	5.9%
TCHEM	0.1%	1.6%	0.3%	0.2%	2.8%	—	3.2%
TCHPM	0.2%	0.5%	0.5%	0.2%	1.7%	—	1.9%
SSVHEM	0.1%	2.3%	0.8%	0.2%	6.6%	—	7.0%
CSVM	0.2%	2.3%	0.7%	0.2%	5.2%	—	5.7%

that the two leading jets have transverse momenta greater than $70\text{ GeV}/c$ and $50\text{ GeV}/c$ respectively, and that the transverse momentum of the muon is greater than $35\text{ GeV}/c$. The reconstructed missing transverse energy (\cancel{E}_T) is required to be above 20 GeV .

In the dilepton channel, the final state is composed of two jets, two energetic isolated leptons (electron or muon) and missing transverse energy. Events are required to pass dilepton triggers in which two muons, two electrons, or one electron and one muon are required to be present. After offline reconstruction, events are selected with two isolated, oppositely charged leptons with $p_T > 20\text{ GeV}/c$ and $|\eta| < 2.5$ (2.4) for electrons (muons), at least two jets with $p_T > 30\text{ GeV}/c$ and $|\eta| < 2.4$, and $\cancel{E}_T > 30\text{ GeV}$ for $ee/\mu\mu$ events. The selected leptons and jets are required to originate from the same primary interaction vertex. Events with same-flavour lepton pairs in the dilepton mass window ($76 < m_{\ell\ell} < 106\text{ GeV}/c^2$) are removed to suppress the dominant Z+jet background. Dilepton pairs from heavy-flavour resonances and low-mass Drell–Yan production are also removed by requiring a minimum dilepton invariant mass of $12\text{ GeV}/c^2$.

The numbers of observed and predicted events in the lepton+jets channel and the dilepton channel are given in tables 5 and 6, respectively. The uncertainties include the uncertainties on the luminosity measurement and the cross sections. For all MC predictions, events are reweighted to take into account differences in trigger and lepton selection efficiencies between data and simulation [1, 39]. The lepton selection efficiency scale factors are estimated from data using Z events. For dilepton events, the trigger efficiencies are estimated on a data sample using a trigger that is weakly correlated to the dilepton triggers. The dilepton trigger selection efficiency is estimated on events which contain two leptons that fulfil the complete dilepton event selection.

The Drell–Yan background is measured using data. Two different methods are used, and the two estimates are compatible. In the PLR method, for the ee and $\mu\mu$ channels, the ratio of Drell–Yan events outside and inside the dilepton invariant mass window, $R_{\text{out/in}}$, is estimated from the simulation. This is used to estimate the Drell–Yan background using the number of data events inside the dilepton invariant mass window [39]. A contamination from other backgrounds can still be present in the Z-mass window, and this contribution is subtracted using the $e\mu$ channel scaled according to the event yields in the ee and $\mu\mu$ channels. For the $e\mu$ channel, the DY background yield is estimated after performing a binned maximum-likelihood fit to the dilepton invariant mass distribution. In the FTM method, the number of Drell–Yan events in the ee and $\mu\mu$ channels is estimated from the shape of the distribution of the angle between the momentum vectors of the two leptons. For the $e\mu$ channel, the predictions are taken from simulation.

6.2 Systematic uncertainties

Most of the sources of systematic uncertainties are common to all methods, and several methods have specific additional contributions. A description of the common systematic uncertainties is given in this section. The description of the procedure to estimate the systematic uncertainties in each analysis and the influence of the different sources will be given separately for each analysis in its relevant section.

There are different sources of uncertainties originating from the detector knowledge or related to the theory and the simulation. These uncertainties can affect the normalization factor for each process or they can distort the distributions themselves.

Table 5. Number of observed and predicted events in the lepton+jets sample after applying all selection requirements of the FTC method. All MC samples have been scaled to an integrated luminosity of 2.3 fb^{-1} . The uncertainties include the uncertainties on the luminosity and the cross sections. The CSVM operating point has been used for the b-jet tagging requirement.

	no tagging	≥ 1 b-tagged jets	≥ 2 b-tagged jets
$t\bar{t}$	8504 ± 1275	7425 ± 1113	3744 ± 561
Single top	477 ± 82	394 ± 118	162 ± 49
W+jets	6170 ± 1851	1367 ± 410	214 ± 64
Z+jets	459 ± 138	83 ± 25	15 ± 5
QCD	23 ± 7	3 ± 1	0.20 ± 0.06
Total prediction	15633 ± 2253	9272 ± 1921	4134 ± 566
Data	14391	8781	3897

Table 6. Number of observed and predicted events in the dilepton sample after applying all selection requirements of the PLR method. All MC samples have been scaled to a luminosity of 2.3 fb^{-1} . The uncertainties include the uncertainties on the luminosity and the cross sections. The TCHEL operating point has been used for the b-jet tagging requirement. The component “ $t\bar{t}$ signal” stands for the dilepton events. The component “ $t\bar{t}$ other” contains the events in all other decay channels.

Processes	Channel ee	Channel $\mu\mu$	Channel $e\mu$
Without b-jet tagging requirement			
$t\bar{t}$ signal	971 ± 147	1275 ± 182	3453 ± 521
$t\bar{t}$ other	11.5 ± 5.7	3.3 ± 1.7	23.6 ± 11.8
Single top	48.7 ± 14.6	62.7 ± 18.9	163.7 ± 49.0
Di-bosons	22.3 ± 6.7	29.2 ± 8.8	49.4 ± 14.8
Z+jets	409 ± 204	545 ± 273	200 ± 100
W+jets	12.0 ± 6.0	< 0.5	11.4 ± 5.7
Total prediction	1475 ± 259	1915 ± 343	3902 ± 512
Data	1442	1773	3898
With ≥ 1 b-tagged jets			
Total prediction	1088 ± 170	1429 ± 218	3390 ± 475
Data	1080	1364	3375
With ≥ 2 b-tagged jets			
Total prediction	529 ± 73	697 ± 97	1827 ± 263
Data	554	686	1854

The dominant sources of uncertainty arise from the MC simulation. The uncertainty due to the modelling of the underlying event is estimated by comparing results between the main sample generated with the Z2 tune to that with the D6T tune [40]. The effect due to the scale used to match clustered jets to partons (i.e., jet-parton matching) is estimated with dedicated samples generated by varying the nominal matching p_T thresholds by factors of 2 and 1/2. Effects due to the definition of the renormalization and factorization scales used in the simulation of the signal are studied with dedicated MC samples with the scales varied simultaneously by factors of 2 and 1/2. The

uncertainties related to the parton distribution function (PDF) used to model the hard scattering of the proton-proton collisions are estimated by varying the parameters of the PDF by $\pm 1\sigma$ with respect to their nominal values and using the PDF4LHC prescription [13, 15]. Variations in the relative composition of the simulated samples are studied by varying the contributions of each background with respect to the signal and each other.

Several systematic uncertainties pertain to the modelling of the CMS detector in the MC simulations. Important uncertainties are the energy scales of the jets and, to a lesser extent, of the leptons, as they shift the momenta of the reconstructed objects. Similarly, the uncertainty in jet energy resolution has also been considered. The effects of the jet energy scale are taken into account by varying the energy scale of the jets according to its uncertainty [27]. A further source comes from the uncertainties associated with the measurement of the trigger and lepton selection efficiencies. The uncertainty due to pileup is evaluated by varying the mean value of the measured pileup distribution by $\pm 10\%$.

6.3 Profile likelihood ratio method

In this method, the data/MC scale factor of the b-jet tagging efficiency is measured with the PLR method using the 2-dimensional distribution of the jet multiplicity versus the b-tagged jet multiplicity in dilepton events. The uncertainties in the event yield and in the shape of the distribution are considered as nuisance parameters in the likelihood function and are then fitted during the minimization procedure. This leads to combined statistical and systematic uncertainties associated with the measurement of the scale factor.

The likelihood function for a given dilepton channel j (ee , $e\mu$ or $\mu\mu$) and a given bin i of the 2-dimensional distribution (corresponding to n jets and m b-tagged jets) is written as [41]:

$$\mathcal{L}_{i,j}(SF_b, N_{i,j}^{\text{obs}}, \{U_k\}) = \text{Poisson}(N_{i,j}^{\text{obs}}, \mu_{i,j}(SF_b, \{U_k\})) \times \prod_k \text{Gauss}(U_k, 0, 1), \quad (6.1)$$

where $N_{i,j}^{\text{obs}}$ is the number of observed events, $\mu_{i,j}$ the number of expected events, and U_k the nuisance parameters. The distribution of the number of b-tagged jets observed in data and predicted in the simulation for the TCHEL operating point for $t\bar{t}$ and background events is shown in figure 15. The likelihood function for a given channel j is then the product of the likelihood functions over all the bins of the distribution:

$$\mathcal{L}_j(SF_b, \{N_{i,j}^{\text{obs}}\}, \{U_k\}) = \prod_i \mathcal{L}_{i,j}(SF_b, N_{i,j}^{\text{obs}}, \{U_k\}). \quad (6.2)$$

Since the decay channels are statistically independent, the overall likelihood function is then simply the product of the individual channel likelihoods:

$$\mathcal{L}(SF_b, \{N_{i,j}^{\text{obs}}\}, \{U_k\}) = \prod_j \mathcal{L}_j. \quad (6.3)$$

The expression of the profile likelihood ratio LR is then

$$LR(SF_b) = \frac{\mathcal{L}(SF_b, \{\hat{U}_i\})}{\mathcal{L}(\hat{SF}_b, \{\hat{U}_i\})}, \quad (6.4)$$

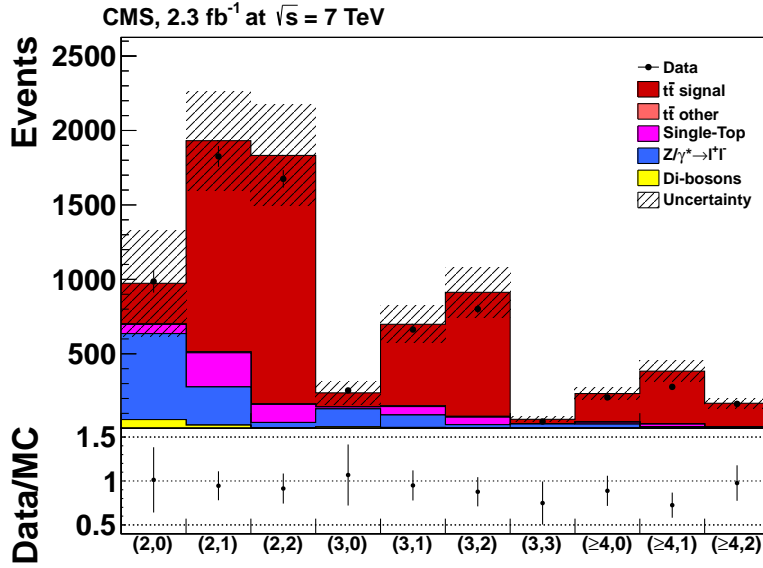


Figure 15. Number of b-tagged jets per event in the dilepton channel for the TCHEL operating point, in the data (filled circles) and the simulation (solid histograms), before the fit. The simulated distribution is normalized to an integrated luminosity of 2.3 fb^{-1} . The bin labels (m, n) refer to the number of events with m jets in the event of which n are tagged. The component “ $t\bar{t}$ signal” are the dilepton events, and the component “ $t\bar{t}$ other” contains the events in all other decay channels. The hatched area corresponds to the combined statistical and systematic uncertainty.

where \hat{U}_i represents the conditional maximum likelihood estimates of U_i obtained with the scale factor SF_b fixed while $\hat{S}F_b$ and \hat{U}_i are the estimates obtained with SF_b free.

The distribution of $-2 \ln(LR(SF_b))$ is asymptotically distributed as a χ^2 distribution with one degree of freedom (Wilk’s theorem [42]). An LR curve is obtained by scanning the values of SF_b in a given range and used to determine a 68% confidence level interval. These uncertainties are the combination of the statistical uncertainty and the systematic uncertainties considered as nuisance parameters. All the nuisance parameters are common to the three channels except the estimation of the backgrounds from data for W+jets and Z+jets. The Z+jets background is estimated from data as described in section 6.1. The small W+jets background is estimated from data using the matrix method [39].

The expected number of b-tagged jets in events with n jets of a given dilepton final state, $\mu_{i,j}$ in eq. (6.1), is derived from pre-tagged simulated events with n jets. This is carried out by applying per-jet b-jet tagging efficiencies, considering all jet tagging combinations. These efficiencies are derived as a function of p_T and η , using simulated $t\bar{t}$ events for b jets and using data samples dominated by light-parton jets. A constant scale factor SF_b is applied to the b- and c-jet efficiencies to model the b-jet tagging efficiency in data. The value of SF_b is then extracted by minimizing the LR as described above. A closure test is performed on simulated signal events to check that, for a unit scale factor, the b-tagged jet multiplicity distribution obtained with the reweighting procedure is the same as the one obtained directly from MC simulation using a requirement on the b-jet tagging discriminant.

Several uncertainties are considered as nuisance parameters in the likelihood function and are then fitted during the minimization procedure. These are the uncertainties on the energy scale of the jets and the leptons, the expected number of events of the different contributions, and the uncertainty on the light-parton jet scale factor.

Further contributions to the systematic uncertainties are estimated outside the PLR procedure. The expected input distributions to the PLR method are re-derived, using MC samples with varied parameters, and the b-jet tagging scale factors are re-measured. The relative differences of SF_b with respect to the nominal values are taken as systematic uncertainties, and added in quadrature to the total uncertainty from the fit. These uncertainties include the uncertainties on the jet-parton matching scale, the parton-shower/matrix-element threshold, and the top mass.

The factorization scale is the dominant systematic uncertainty, as it affects the jet multiplicity distribution, with a relative uncertainty of approximately 1.7% on the scale factor of the CSVL operating point. The second-largest contribution is from the uncertainty on the $t\bar{t}$ event yield, which is estimated to be 20%. It includes the uncertainties on the $t\bar{t}$ cross section, the trigger and lepton selection efficiencies, and the branching fraction of the decays of the W bosons. This results in an uncertainty of 1.4% on the scale factor of the CSVL operating point. Further, the statistical uncertainty on the b-jet tagging efficiency in the simulation was found to range between 0.4% and 1.6% depending on the operating point considered. A 1.6% systematic uncertainty on the scale factor was therefore chosen for all the operating points.

Finally, to account for a possible uncertainty coming from the fitting algorithm itself, an additional uncertainty is estimated using different choices of the likelihood minimization. This is taken as a 1% relative uncertainty.

6.4 Flavour tag consistency method

The FTC method requires consistency between the observed and expected number of tags in the lepton+jets events to study the performance of the heavy-flavour algorithms.

In a sample of $t\bar{t}$ pair candidates in the lepton+jets channel, the expected number of events with n b-tagged jets $\langle N_n \rangle$ can be written as

$$\langle N_n \rangle = L \cdot \sigma_{t\bar{t}} \cdot \varepsilon \cdot \sum_{i,j,k} F_{ijk} \sum_{\substack{i' \leq i, j' \leq j, k' \leq k \\ i'+j'+k'=n}} [C_i^{i'} \varepsilon_b^{i'} (1 - \varepsilon_b)^{(i-i')} C_j^{j'} \varepsilon_c^{j'} (1 - \varepsilon_c)^{(j-j')} C_k^{k'} \varepsilon_l^{k'} (1 - \varepsilon_l)^{(k-k')}], \quad (6.5)$$

where L is the integrated luminosity, $\sigma_{t\bar{t}}$ is the $t\bar{t}$ cross section, ε is the pre-tagging selection efficiency, C_a^b is the binomial coefficient, and $\varepsilon_b, \varepsilon_c,$ and ε_l are the b-, c-, and light-parton jet tagging efficiencies. The factors F_{ijk} are the fractions of events with i b jets, j c jets, and k light-parton jets. They are derived from the $t\bar{t}$ simulation in which the true flavour of the jets is known.

As an example, the F_{112} term contributes to the expected number of events with 1 b-tagged jet $\langle N_1 \rangle$ in the following way:

$$\langle N_1 \rangle \propto F_{112} \times \left(\underbrace{1 \cdot \varepsilon_b (1 - \varepsilon_c) (1 - \varepsilon_l)^2}_{\text{the b jet}} + \underbrace{1 \cdot (1 - \varepsilon_b) \varepsilon_c (1 - \varepsilon_l)^2}_{\text{the c jet}} + \underbrace{2 \cdot (1 - \varepsilon_b) (1 - \varepsilon_c) \varepsilon_l (1 - \varepsilon_l)}_{\text{the light-parton jet}} \right). \quad (6.6)$$

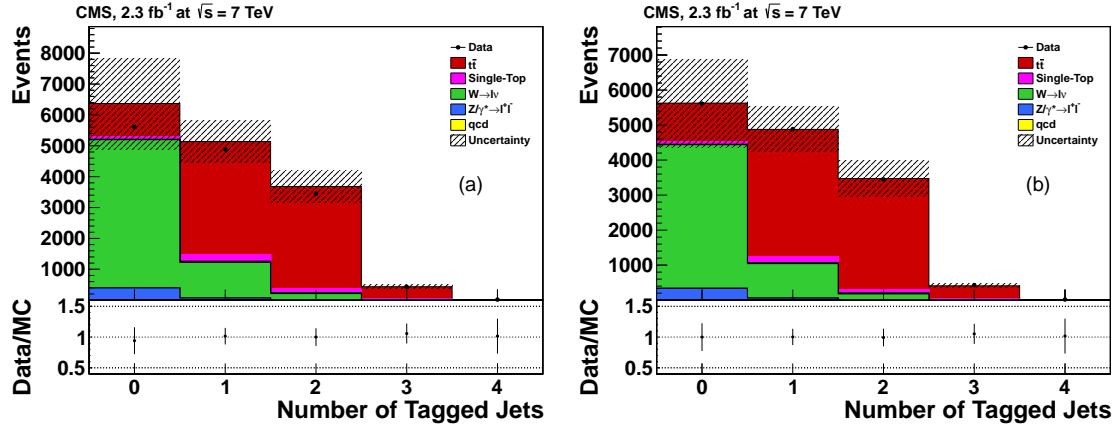


Figure 16. Number of tagged jets per event in the lepton+jet channel with the FTC method with the CSVM operating point, in the data (filled circles) and the simulation (solid histograms), (a) before and (b) after the fit. The simulated distribution is normalized to an integrated luminosity of 2.3fb^{-1} . The hatched area corresponds to the combined statistical and systematic uncertainty.

To account for the non-negligible amount of background, eq. (6.5) is modified to include each background sample:

$$\begin{aligned}
 \langle N_n \rangle &= \langle N_n^{\bar{t}\bar{t}} \rangle + \langle N_n^{\text{background}} \rangle \\
 &= L \cdot \sigma_{\bar{t}\bar{t}} \cdot \epsilon_{\bar{t}\bar{t}} \cdot \left[\sum_{i,j,k} F_{ijk}^{\bar{t}\bar{t}} \sum_{\substack{i' \leq i, j' \leq j, k' \leq k \\ i'+j'+k'=n}} (\dots) \right. \\
 &\quad \left. + \frac{\sigma_{\text{background}}}{\sigma_{\bar{t}\bar{t}}} \cdot \frac{\epsilon_{\text{background}}}{\epsilon_{\bar{t}\bar{t}}} \cdot \sum_{i,j,k} F_{ijk}^{\text{background}} \sum_{\substack{i' \leq i, j' \leq j, k' \leq k \\ i'+j'+k'=n}} (\dots) \right], \quad (6.7)
 \end{aligned}$$

where (\dots) stands for the expression in square brackets from eq. (6.5).

The tagging efficiencies and the $\bar{t}\bar{t}$ production cross section are then measured by minimizing the log-likelihood function:

$$\mathcal{L} = -2 \log \prod_n \text{Poisson}(N_n, \langle N_n \rangle), \quad (6.8)$$

where N_n is the number of observed events with n b-tagged jets. The distribution of the number of b-tagged jets observed in data and predicted in the simulation before and after the fit for $\bar{t}\bar{t}$ and background events is shown in figure 16.

In the current implementation the likelihood only uses the b-tagged jet multiplicity in $\bar{t}\bar{t}$ lepton+jets events with between four to seven reconstructed jets, as it emphasizes the measurement of the heavy-flavour b-jet tagging efficiency. The b-jet tagging efficiencies and $\bar{t}\bar{t}$ cross section are treated as free parameters in the fit. The $\bar{t}\bar{t}$ cross section determined in the fits are consistent with the published values. The c- and light-parton-jet tagging efficiencies are taken from the simulation corrected for the data/MC scale factors.

The systematic uncertainties are determined from ensembles of pseudo-experiments. In each of these pseudo-experiments, the number of signal and background events are generated using

Poisson statistics, using as mean values the number of expected events in each channel. Events are then randomly chosen in the simulated samples and the b-tagged jet multiplicity distributions are populated according to the simulated jet multiplicity in each event. The measurement is then performed as described above using the factors F_{ijk} from the nominal simulation. The average b-jet tagging efficiency is compared to the average b-jet tagging efficiency value measured in ensemble tests with the nominal samples. The difference is taken as a systematic uncertainty.

The dominant contribution is the uncertainty on the jet energy scale, with a relative uncertainty of 2.2% on the scale factor of the CSVL operating point. The second-largest uncertainty arises from the uncertainty on the production cross section of the W+heavy flavour jets, with a relative uncertainty of 0.97%. The uncertainties due to the factorization scale and the jet-parton matching are 0.41% and 0.35%, respectively, for the CSVL operating point.

6.5 Flavour tag matching method

The FTM method requires consistency between the observed and expected number of tags in dilepton events. The expected number of events with n b-tagged jets $\langle N_n \rangle$ is written as

$$\langle N_n \rangle = \sum_{k \text{ jets}=2}^{\text{all jets}} n_k \cdot P_{n,k}, \quad (6.9)$$

where n_k is the observed number of events with k jets, and $P_{n,k}$ is the probability to count n b-tagged jets in a k -jet event. These probability functions are written in terms of the tagging efficiencies and the expected jet composition.

In order to illustrate explicitly the construction of the probability functions, the exclusive two-jet multiplicity bin is used and the following expression is obtained:

$$P_{n,2} = \sum_{\substack{i \text{ jets}=0 \\ \text{from top decay}}}^2 \alpha_i \cdot P_{n,2,i}, \quad (6.10)$$

where $P_{n,2,i}$ is the probability that n b tags are observed in an event with two jets of which i jets come from $t\bar{t}$ decays.

The misassignment probabilities α_i denote the probability in the sample that i jets from the decay of the $t\bar{t}$ pair have been reconstructed and selected. These are normalized such that $\sum_i \alpha_i = 1$. For example, α_2 is the probability that both b jets from the $t\bar{t}$ decay have been selected. They take into account both the contribution from the background, which is small in the dilepton channel, and jet misassignment. Either or both of the jets from the decays of the two top quarks may not be selected, and jets from initial- and final- state radiation, or jets from the proton recoil may enter the selection, further diluting the sample.

As an example, for the case where two tagged jets are found in a two-jet event, the probabilities can be explicitly written as:

$$\begin{aligned} P_{2,2,0} &= \varepsilon_q^2 && \text{if no jets are from } t\bar{t} \text{ decays;} \\ P_{2,2,1} &= 2\varepsilon_b \varepsilon_q && \text{if 1 jet is from } t\bar{t} \text{ decays;} \\ P_{2,2,2} &= \varepsilon_b^2 && \text{if 2 jets are from } t\bar{t} \text{ decays.} \end{aligned} \quad (6.11)$$

The misidentification probability ε_q is an effective measurement of the probability of tagging gluon, light and charm quark jets in the dilepton sample. Similar expressions can easily be derived for the other jet multiplicity bins.

The misassignment probabilities are determined from data, and used in the subsequent likelihood of the b-tagged jet multiplicity distribution. In order to estimate the actual fraction of b jets from top-quark decays in the selected sample, kinematic properties of the top decay topology are used. The invariant mass of the lepton-jet pairs from a $t \rightarrow Wb$ decay have a kinematic end-point at $M_{\ell,b}^{\max} \equiv \sqrt{m_t^2 - m_W^2} \approx 156 \text{ GeV}/c^2$. The invariant mass of misassigned lepton-jet pairs exhibits a longer tail towards high mass values. The shape of the misassigned pairs can be modelled by mixing lepton-jet pairs from different events or randomly changing the lepton momentum direction. The fraction of jets from $t \rightarrow Wb$ decays can thus be measured normalizing the spectrum obtained from the combinatorial model to the number of pairs observed in the tail (i.e. $M_{\ell,b} > 180 \text{ GeV}/c^2$). This is estimated independently for each dilepton channel and for each jet-multiplicity bin. The procedure is checked and found to be unbiased from MC pseudo-experiments. Taking into account the expected contribution of $t\bar{t}$ and single-top events to the final sample, the sample composition in terms of events with 2, 1, or 0 correctly reconstructed and selected b jets is estimated.

The b-jet tagging efficiency ε_b can then be measured by maximizing the likelihood function:

$$\mathcal{L}(\varepsilon_b, \varepsilon_q, \alpha_i) = \prod_{n=0}^{\text{all jets}} \text{Poisson}(N_n, \langle N_n \rangle), \quad (6.12)$$

where N_n is the observed number of events with n b-tagged jets.

The likelihood only uses the b tagged jet multiplicity in $t\bar{t}$ dilepton events with two and three reconstructed jets. Gaussian constraints are added for the effective c- and light-parton jet tagging efficiency ε_q and the misassignment probabilities:

$$\mathcal{L} = \prod_{n=0}^{\text{all jets}} \text{Poisson}(N_n, \langle N_n \rangle) \cdot \prod_i \text{Gauss}(\alpha_i, \hat{\alpha}_i, \sigma_{\alpha_i}) \cdot \text{Gauss}(\varepsilon_q, \hat{\varepsilon}_q, \sigma_{\varepsilon_q}). \quad (6.13)$$

The central value $\hat{\varepsilon}_q$ and width σ_{ε_q} of ε_q are determined from the simulation. For the misassignment probabilities α_i , the central values $\hat{\alpha}_i$ are taken from the measurement described above, and the width σ_{α_i} derived from the uncertainty of the expected contribution of $t\bar{t}$ and single-top events to the final sample.

The systematic uncertainties affect the measurement of the b-jet tagging probability through their effect on the parameters of the fit, namely the measured misassignment probabilities and the misidentification probability for non-b jets. The effect on the measured misassignment probabilities is determined from ensembles of pseudo-experiments, where, for each source of uncertainty, the bias on the probabilities is determined. Most sources of uncertainties such as jet energy scale and resolution, and pileup have little effect. This is because the method used to derive the misassignment probabilities is based on templates for the lepton-jet invariant mass obtained from control samples in data. Other sources, which might affect the contribution from top-quark decays and from initial- and final-state radiation jets to the final sample, are evaluated using samples where the QCD factorisation and renormalisation scales and the jet-parton matching scales are varied. In the pseudo-experiments the standard $t\bar{t}$ sample is substituted by each of these samples and the process is repeated.

This bias is then used to shift the measured misassignment probabilities. The likelihood fit of the data is repeated with the modified values. The difference with respect to the nominal result is taken as the systematic uncertainty. The same procedure is applied to evaluate the uncertainty on the misidentification probability for non-b jets.

The final uncertainty is dominated by factors which tend to increase the contamination of background or alter the jet environment. The main uncertainties are the factorization scale, and to a smaller extent, the jet-parton matching with relative uncertainties on the scale factor of 2.3% and 1.4% respectively, for the CSVL operating point. The second-largest uncertainty arises from the 1.5% uncertainty on the light-parton jet tagging efficiency.

6.6 Efficiency measurement from a b-enriched jet sample

In this method, the b-jet tagging efficiency is measured from a sample enriched with b jets (bSample) in lepton+jets events. The contamination of this sample due to light-parton jets is estimated from data and subtracted.

In order to select the correct jets originating from the decay of the top quarks, a χ^2 is calculated for each jet-parton combination based on the masses of the reconstructed W boson m_{qq} and the hadronically decaying top quark m_{bqq} :

$$\chi^2 = \left(\frac{m_{bqq} - m_t}{\sigma_t} \right)^2 + \left(\frac{m_{qq} - m_W}{\sigma_W} \right)^2. \quad (6.14)$$

The mean masses and widths are obtained from the $t\bar{t}$ simulation using a Gaussian fit to the mass distributions of the combination with the correct jet-to-quark assignment. The mean and width of the reconstructed top-quark mass distribution are $172.5 \text{ GeV}/c^2$ and $16.3 \text{ GeV}/c^2$, respectively. The mean and width of the reconstructed W-boson distribution are $82.9 \text{ GeV}/c^2$ and $9.5 \text{ GeV}/c^2$, respectively. Using the four leading jets, with transverse momenta above $30 \text{ GeV}/c$, there are 12 combinations to pair the four reconstructed jets with the quarks from $t\bar{t}$ decay. The combination with the lowest χ^2 is selected to represent the event topology. The event is rejected if the lowest χ^2 is above 90.

A generic b-candidate sample is constructed by taking the jet assigned to the lepton. This sample is further subdivided into b-enriched and b-depleted subsamples by using the invariant mass of that jet and the muon (called the jet-muon mass, $m_{\mu j}$). The distribution of this variable is shown in figure 17. For the b-enriched subsample, the jet-muon mass is required to be in the range $80 < m_{\mu j} < 150 \text{ GeV}/c^2$. For the b-depleted subsample the jet-muon mass is required to be in the range $150 < m_{\mu j} < 250 \text{ GeV}/c^2$. Based on the simulation, the purities of the two subsamples are 45% and 16%, respectively.

The distribution of the discriminators of the taggers for true b jets, $\hat{\Delta}_b^{\text{enr}}$, is obtained by subtracting the discriminator distribution of the b-depleted subsample, Δ_b^{depl} from the discriminator distribution of the b-enriched subsample, Δ_b^{enr} :

$$\hat{\Delta}_b^{\text{enr}} = \Delta_b^{\text{enr}} - F \times \Delta_b^{\text{depl}}. \quad (6.15)$$

The factor F represents the ratio of the number of non-b jets in the b-enriched and b-depleted subsamples. It is measured from a background dominated sample composed mainly of light-flavour

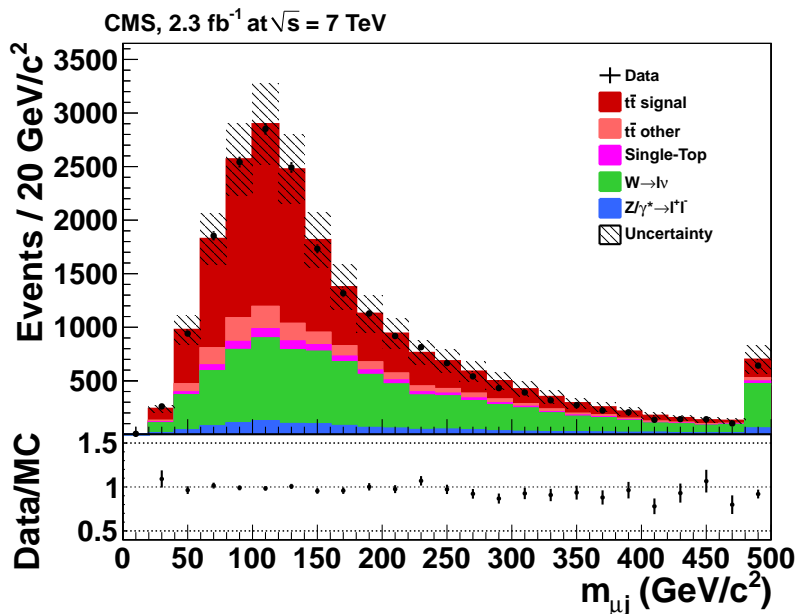


Figure 17. Distribution of the jet-muon mass in the data (filled circles) and the simulation (solid histograms). The simulated distribution is normalized to an integrated luminosity of 2.3 fb^{-1} . The component “ $t\bar{t}$ signal” stands for the lepton+jet events. The component “ $t\bar{t}$ other” contains the events in all other decay channels. The hatched area corresponds to the combined statistical and systematic uncertainty. Overflow entries are added to the last bin.

quark jets. This sample is obtained by using the jets attributed to the decay of the W boson and ensuring that they both fail the b-jet tagging requirements of the TCHEM operating point. Both jets are used to construct a jet-muon mass distribution, and the same subsamples are defined as for the signal sample. The purity of light-flavour quark jets is 92% in the region $80 < m_{\mu j} < 150 \text{ GeV}/c^2$ and 95% in the region $150 < m_{\mu j} < 250 \text{ GeV}/c^2$. To match the shape of the jet-muon mass distribution of this background sample to that of the signal sample, the jets in the background sample are reweighted according to the (p_T, η) of the signal sample. After this reweighting, the two samples have similar jet-muon mass distribution. The factor F is taken as the ratio of the number of events in the $80 < m_{\mu j} < 150 \text{ GeV}/c^2$ and the $150 < m_{\mu j} < 250 \text{ GeV}/c^2$ regions in the background sample, and is found to be 1.16 ± 0.02 .

A small correlation between the jet-muon mass and the discriminators has to be corrected for. This correlation is attributed to the correlation between the transverse momentum of the jet and the jet-muon mass. This correlation distorts the distribution of the discriminants of the b-jet tagging algorithms in the b-depleted subsample with respect to the distribution of the non-b jets in the b-enhanced subsample. This effect is corrected by reweighting the jets in the b-depleted subsample according to the transverse momentum distribution of the jets in the b-enhanced subsample.

The systematic uncertainties for the b-jet tagging efficiency and the scale factors are the absolute differences between the nominal simulation sample and the sample with modified parameters. Additionally, a systematic uncertainty is assigned based on tests of the method in simulation. The tests show no bias in the method with an uncertainty driven by statistical uncertainties on available

Table 7. Data/MC scale factors SF_b as measured using the PtRel, System8, and LT methods and their combination. Results are given for jet p_T between 80 and 120 GeV/c. The first uncertainty on SF_b is statistical and the second is systematic. For the combination the total uncertainty is quoted.

b tagger	SF_b (PtRel)	SF_b (System8)	SF_b (LT)	SF_b (comb.)
JPL	$0.98 \pm 0.01 \pm 0.03$	$1.00 \pm 0.02 \pm 0.07$	$1.00 \pm 0.01 \pm 0.04$	0.99 ± 0.03
JBPL	$0.99 \pm 0.01 \pm 0.02$	$0.98 \pm 0.02 \pm 0.04$	$1.01 \pm 0.01 \pm 0.04$	0.99 ± 0.02
TCHL	$0.99 \pm 0.01 \pm 0.02$	$0.97 \pm 0.02 \pm 0.05$	$1.00 \pm 0.01 \pm 0.01$	1.00 ± 0.01
CSVL	$1.00 \pm 0.01 \pm 0.02$	$1.01 \pm 0.02 \pm 0.06$	$0.98 \pm 0.01 \pm 0.02$	0.99 ± 0.02
JPM	$0.90 \pm 0.01 \pm 0.03$	$0.93 \pm 0.03 \pm 0.06$	$0.99 \pm 0.01 \pm 0.05$	0.92 ± 0.03
JBPM	$0.92 \pm 0.01 \pm 0.02$	$0.96 \pm 0.03 \pm 0.08$	$0.99 \pm 0.01 \pm 0.05$	0.91 ± 0.03
TCHEM	$0.94 \pm 0.01 \pm 0.03$	$0.99 \pm 0.03 \pm 0.07$	$0.98 \pm 0.01 \pm 0.03$	0.95 ± 0.02
TCHPM	$0.95 \pm 0.01 \pm 0.03$	$0.94 \pm 0.02 \pm 0.09$	$0.97 \pm 0.01 \pm 0.02$	0.96 ± 0.02
SSVHEM	$0.92 \pm 0.01 \pm 0.02$	$0.92 \pm 0.03 \pm 0.05$	$0.97 \pm 0.01 \pm 0.02$	0.95 ± 0.02
CSVM	$0.93 \pm 0.01 \pm 0.02$	$0.97 \pm 0.03 \pm 0.06$	$0.97 \pm 0.01 \pm 0.03$	0.95 ± 0.02
JPT	$0.82 \pm 0.01 \pm 0.05$	$0.85 \pm 0.03 \pm 0.07$	$0.96 \pm 0.01 \pm 0.07$	0.87 ± 0.05
JBPT	$0.83 \pm 0.01 \pm 0.06$	$0.89 \pm 0.03 \pm 0.11$	$0.96 \pm 0.01 \pm 0.08$	0.87 ± 0.06
TCHPT	$0.87 \pm 0.01 \pm 0.05$	$0.91 \pm 0.03 \pm 0.10$	$0.94 \pm 0.01 \pm 0.04$	0.91 ± 0.04
SSVHPT	$0.87 \pm 0.01 \pm 0.03$	$0.84 \pm 0.03 \pm 0.10$	$0.96 \pm 0.01 \pm 0.03$	0.92 ± 0.03
CSVT	$0.86 \pm 0.01 \pm 0.04$	$0.92 \pm 0.03 \pm 0.07$	$0.94 \pm 0.01 \pm 0.04$	0.90 ± 0.03

samples. For the CSVL operating point, the relative uncertainty is 3.1%. The jet energy scale and resolution have a small contribution from the change in the mean masses and widths used for the χ^2 . For the CSVL operating point, the relative uncertainties on the scale factor are 1.4% and 2.2%, respectively. A small uncertainty of 0.5% is due to the choice of the boundaries of the b-depleted region. The high tail of the jet-muon mass distribution is composed mainly of background events and wrongly combined jets that do not reflect the kinematics of the signal events. The effect of imposing an upper limit on the region is assessed by varying the boundary between 200 and 300 GeV/c².

7 Efficiency measurement results

7.1 Results from multijet events

The methods described in section 5 cover a large range of jet transverse momenta. The PtRel and the System8 methods provide precise measurements for the lower part of the spectrum. The IP3D and the LT methods have been designed for high jet p_T . The measured data/MC scale factors are given in table 7 for jets with low p_T from 80 to 120 GeV/c, and in table 8 for jets with high p_T , from 160 to 320 GeV/c. In these ranges the methods give compatible results within the quoted uncertainties. While some of the methods measure the efficiencies and scale factors only for muon jets, and not inclusive b jets, simulation studies have shown that the difference in tagging efficiencies between the two are only a few percent. We assume that these small differences have no significant effect on the scale factors, which are relative data/MC measurements.

Table 8. Data/MC scale factors SF_b as measured using the IP3D and LT methods and their combination. Results are given for jet p_T between 160 and 320 GeV/c. The first uncertainty on SF_b is statistical and the second is systematic. For the combination the total uncertainty is quoted.

b tagger	SF_b (IP3D)	SF_b (LT)	SF_b (comb.)
JPL	$0.99 \pm 0.01 \pm 0.01$	$1.00 \pm 0.01 \pm 0.06$	0.99 ± 0.02
JBPL	$1.00 \pm 0.01 \pm 0.01$	$1.00 \pm 0.01 \pm 0.05$	1.00 ± 0.02
TCHL	$1.00 \pm 0.01 \pm 0.02$	$1.00 \pm 0.01 \pm 0.02$	1.00 ± 0.02
CSVL	$0.98 \pm 0.02 \pm 0.01$	$0.96 \pm 0.01 \pm 0.04$	0.97 ± 0.03
JPM	$0.93 \pm 0.02 \pm 0.03$	$0.99 \pm 0.01 \pm 0.06$	0.95 ± 0.04
JBPM	$0.97 \pm 0.02 \pm 0.03$	$0.99 \pm 0.01 \pm 0.06$	0.97 ± 0.04
TCHEM	$0.96 \pm 0.02 \pm 0.03$	$0.97 \pm 0.01 \pm 0.03$	0.96 ± 0.03
TCHPM	$0.97 \pm 0.02 \pm 0.03$	$0.97 \pm 0.01 \pm 0.02$	0.97 ± 0.02
SSVHEM	$0.98 \pm 0.02 \pm 0.04$	$0.98 \pm 0.01 \pm 0.07$	0.98 ± 0.04
CSVM	$0.95 \pm 0.02 \pm 0.04$	$0.97 \pm 0.01 \pm 0.06$	0.96 ± 0.04
JPT	$0.89 \pm 0.02 \pm 0.04$	$0.95 \pm 0.01 \pm 0.10$	0.91 ± 0.05
JBPT	$0.91 \pm 0.02 \pm 0.03$	$0.96 \pm 0.01 \pm 0.11$	0.92 ± 0.05
TCHPT	$0.89 \pm 0.02 \pm 0.03$	$0.94 \pm 0.01 \pm 0.04$	0.92 ± 0.04
SSVHPT	$0.92 \pm 0.02 \pm 0.04$	$0.96 \pm 0.01 \pm 0.05$	0.94 ± 0.04
CSVT	$0.90 \pm 0.02 \pm 0.07$	$0.94 \pm 0.01 \pm 0.09$	0.92 ± 0.07

The results have been combined to provide the best measurements of the data/MC scale factors for $30 < p_T < 670$ GeV/c. For each jet p_T range the most precise results have been used: the PtRel and System8 methods for $p_T < 120$ GeV/c, the IP3D method for $p_T > 120$ GeV/c and the LT method for the full momentum range.

The combination is based on a weighted mean of the scale factors in each jet p_T bin [43]. However, there are a significant number of jets from QCD dijet and multijet events (with at least one muon associated to a jet) which are shared between the methods. The shared fraction of jets varies with jet p_T . Typical values are 10–25% between the LT and PtRel/IP3D methods, 40–50% between the PtRel and System8 methods, and 20–50% between the System8 and LT methods. This overlap has been taken into account in the combination.

Several sources of systematic uncertainties are common for all methods: the effects due to pileup, gluon splitting, and the selection criteria for muons. The muon PtRel and IP3D methods have the same sensitivity to the choice of the away-jet tagger. The corresponding uncertainties were assumed to be fully correlated or anticorrelated according to the sign of the variations observed for the different methods. All other systematic effects are specific to individual methods and have been treated as uncorrelated. A conservative value for the uncertainty is used if the χ^2 from the fit exceeds the number of degrees of freedom, in which case the uncertainty is scaled by the square root of the normalised χ^2 . Summaries for the individual and combined scale factor measurements for the JPL and the CSVM taggers are shown in figure 18. Also shown are the parameterizations of the combined scale factor of the form $SF_b(p_T) = \alpha(1 + \beta p_T)/(1 + \gamma p_T)$. Combined values for a low and a high jet p_T range are shown in the right hand columns of tables 7 and 8, respectively. The same studies have been performed separately for muon jets with $|\eta| < 1.2$ and $1.2 < |\eta| < 2.4$. Compatible scale factor values are obtained in both regions.

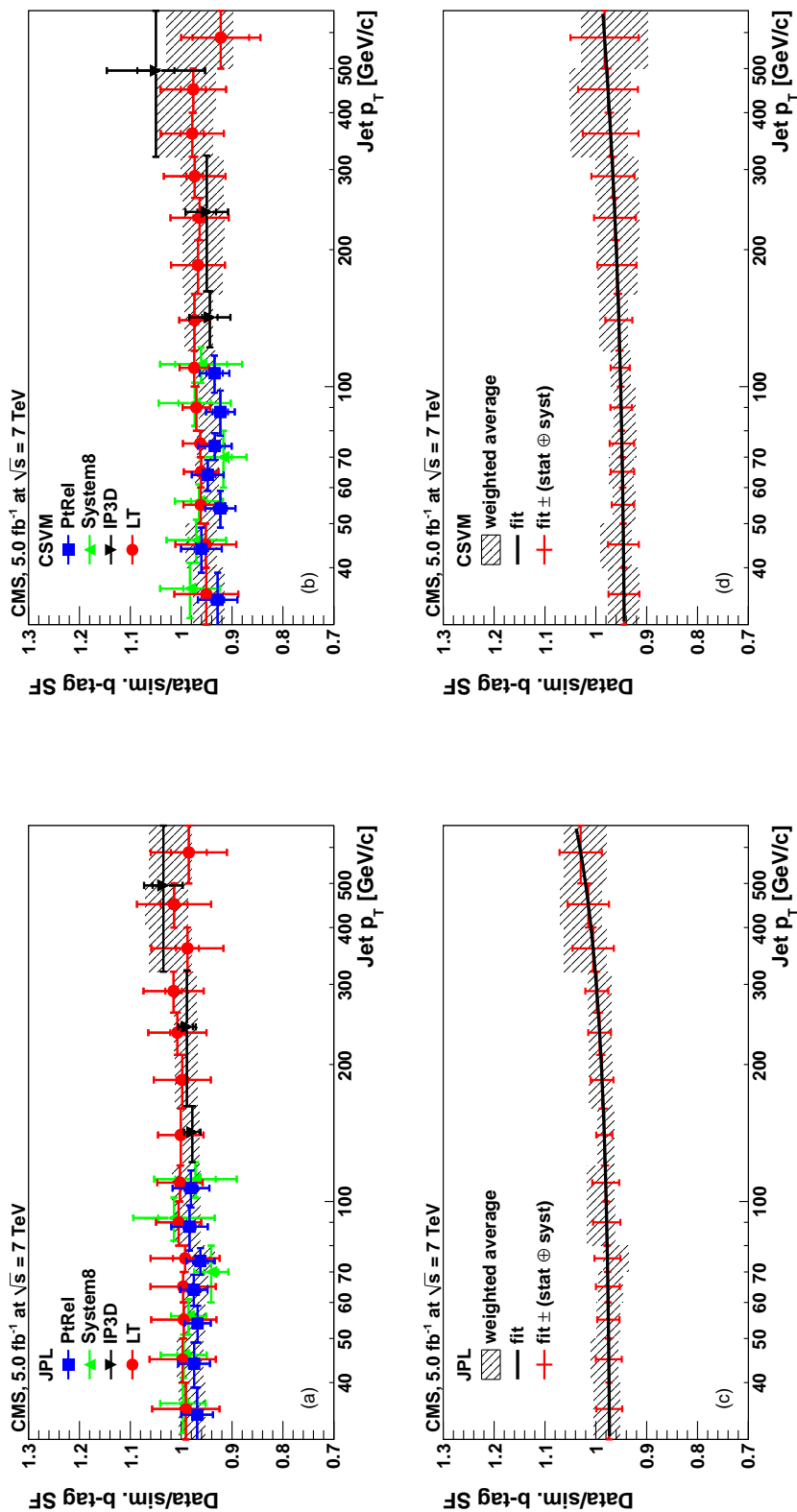


Figure 18. Individual and combined measurements of the ratio of the b-jet tagging efficiencies of the data to that in simulation for the (a, c) JPL and (b, d) CSVM taggers. Figures (a) and (b) show the individual measurements from the muon p_T^{rel} (“PtRel”), System8 (“System8”), muon IP (“IP3D”), and lifetime tagger (“LT”) methods. The inner and outer error bars indicate the statistical and the combined uncertainties, respectively. The hatched areas represent the combined measurements. In figures (c) and (d) the combined measurements have been parameterized by functions of the form $SF_b(p_T) = \alpha(1 + \beta p_T)/(1 + \gamma p_T)$. The error bars attached to the function have the same size as the uncertainties from the combined measurement in each bin.

Table 9. The scale factors SF_b as measured using the PLR, FTC, FTM and bSample methods, and the weighted mean (WM). The uncertainties are the combined statistical and systematic uncertainty.

b tagger	PLR	FTC	FTM	bSample	WM
JPL	0.96 ± 0.03	0.99 ± 0.03	0.96 ± 0.03	0.96 ± 0.05	0.97 ± 0.03
JBPL	0.97 ± 0.03	1.00 ± 0.05	0.96 ± 0.03	0.97 ± 0.05	0.98 ± 0.03
TCHL	0.96 ± 0.03	0.94 ± 0.04	0.95 ± 0.03	0.92 ± 0.05	0.95 ± 0.03
CSVL	1.00 ± 0.03	1.03 ± 0.03	0.99 ± 0.04	0.97 ± 0.05	1.01 ± 0.03
JPM	0.95 ± 0.03	0.95 ± 0.04	0.93 ± 0.03	0.94 ± 0.06	0.95 ± 0.03
JBPM	0.93 ± 0.03	0.95 ± 0.04	0.91 ± 0.03	0.93 ± 0.06	0.94 ± 0.03
TCHM	0.96 ± 0.03	0.97 ± 0.04	0.96 ± 0.03	0.93 ± 0.06	0.96 ± 0.03
TCHPM	0.94 ± 0.03	0.93 ± 0.04	0.95 ± 0.04	0.92 ± 0.06	0.93 ± 0.03
SSVHEM	0.95 ± 0.03	0.98 ± 0.04	0.98 ± 0.04	0.95 ± 0.07	0.96 ± 0.03
CSVM	0.97 ± 0.03	0.98 ± 0.04	0.97 ± 0.04	0.95 ± 0.06	0.97 ± 0.03
JPT	0.90 ± 0.03	0.89 ± 0.05	0.90 ± 0.03	0.95 ± 0.07	0.90 ± 0.03
JBPT	0.90 ± 0.03	0.88 ± 0.05	0.90 ± 0.03	0.90 ± 0.07	0.89 ± 0.03
TCHPT	0.93 ± 0.03	0.92 ± 0.05	0.94 ± 0.04	0.91 ± 0.07	0.93 ± 0.03
SSVHPT	0.95 ± 0.03	0.95 ± 0.04	0.96 ± 0.04	0.89 ± 0.07	0.95 ± 0.03
CSVT	0.95 ± 0.03	0.97 ± 0.05	0.96 ± 0.03	0.95 ± 0.06	0.96 ± 0.03

7.2 Results from $t\bar{t}$ events

The statistical properties of the four methods presented in sections 6.3 to 6.6 have been studied using ensembles of pseudo-experiments based on the expected numbers of signal and background events. The distributions of the estimated values and their uncertainties show that the methods are unbiased. This is shown by the pull distributions, which have mean values close to zero and standard deviations close to one.

The scale factors $SF_b = \varepsilon_b^{\text{meas}} / \varepsilon_b^{\text{MC}}$ measured with the different algorithms are shown in table 9 using data with an integrated luminosity of 2.3 fb^{-1} . The scale factors were stable over the whole data-taking period and can be applied to the full dataset. The measured b-jet tagging efficiencies and scale factors for the CSV algorithm are shown in figure 19.

The PLR and FTC methods are used to calculate a combined scale factor for use in analyses, by taking the weighted mean of the scale factors from each method. The two methods are chosen because each has the smallest uncertainty among the analyses in its respective decay channel. By choosing one analysis in the dilepton channel and one in the lepton+jets channel, there is no statistical correlation between the two measurements as the samples are mutually exclusive. Based on the statistical and systematic uncertainties of the PLR and FTC methods, the uncertainty of the resulting scale factor is ± 0.03 for all operating points.

A continuous function for the scale factors is required in physics analyses that use b-jet tagging discriminators with multivariate methods. The function is obtained from a linear fit to the distribution of the scale factors measured with the FTC method. This is offset vertically to match the weighted mean of the medium operating point, as illustrated in figure 20.

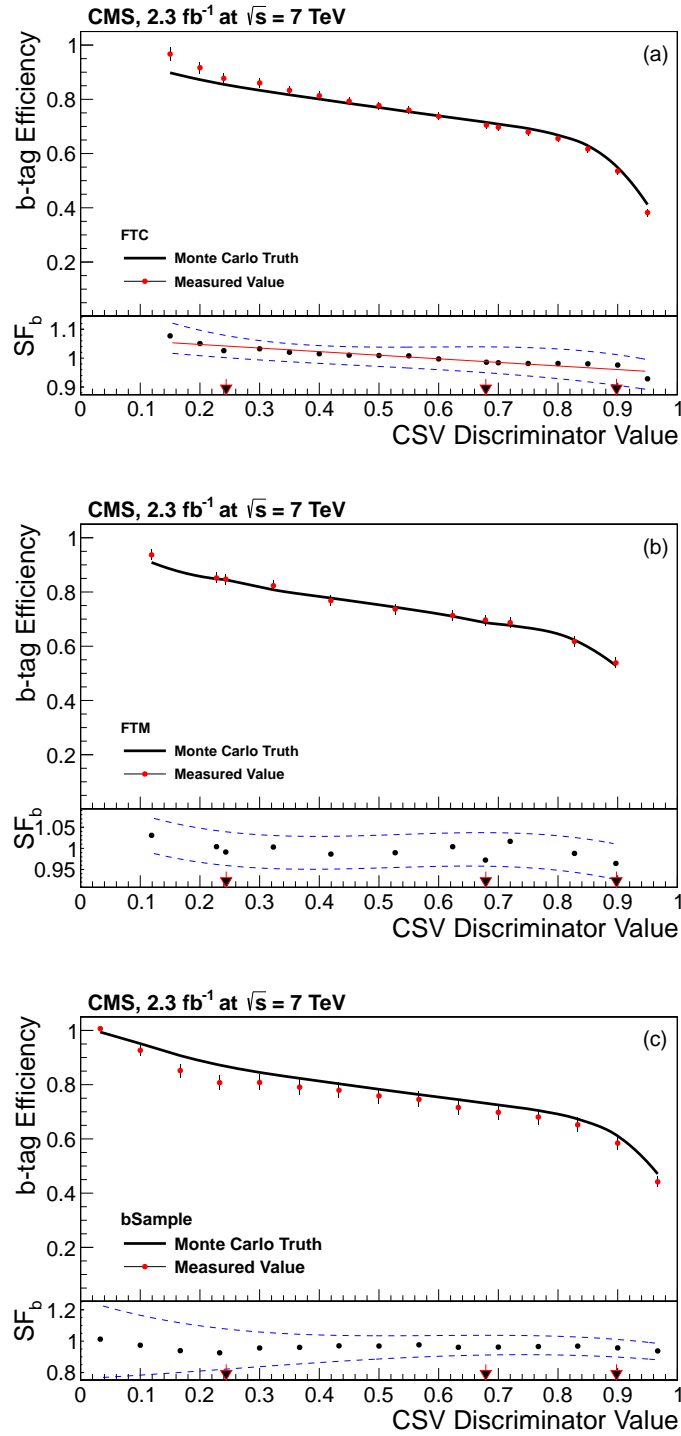


Figure 19. Measured b-jet tagging efficiency as a function of the flavour discriminator threshold for the CSV algorithm, measured with the (a) FTC method, (b) FTM method and (c) bSample method. The absolute b-jet tagging efficiencies measured from data and predicted from simulation are shown in the upper histograms of each panel. The scale factors SF_b are shown in the lower histogram, where the blue dashed lines represent the combined statistical and systematic uncertainty. The arrows indicate the standard operating points. For the FTC method, the red line represents a linear function fitted on the distribution of the scale factors.

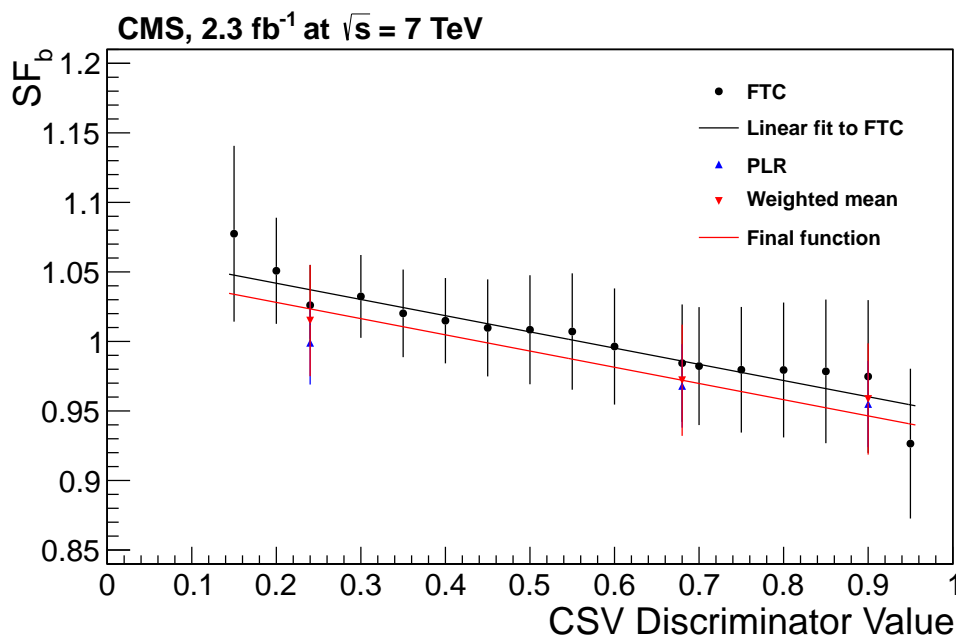


Figure 20. Scale factors measured with the PLR and FTC methods and weighted mean as a function of the discriminator threshold for the CSV algorithm. The black function is derived from a fit to the values measured with the FTC method. The red function labelled “Final function” corresponds to the same function offset vertically to match the weighted mean of the medium operating point. The uncertainties are the combined statistical and systematic uncertainty.

7.3 Comparison of results

The p_T -dependent scale factors measured in dijet and multijet events have been compared by reweighted them to match the jet p_T spectrum observed in $t\bar{t}$ events. The results are shown in table 10 and are in good agreement with each other. This justifies the assumption that the scale factors for the muon jets and inclusive jets are compatible.

8 Misidentification probability measurement

The measurement of the misidentification probability for light-parton jets relies on the definition of inverted tagging algorithms, selecting non- b jets using the same variables and techniques as the standard versions. These “negative taggers” can be used in the same way as the regular b -jet tagging algorithms both in data and in the simulation. As the negative-tagged jets are enriched in light flavours, the misidentification probability can be measured from data, with the simulation used to extract a correction factor.

The misidentification probability is evaluated from tracks with a negative impact parameter or from secondary vertices with a negative decay length (see section 4). When a negative tagger is applied to jets of any flavour, the corresponding tagging efficiency is denoted “negative tag rate”. The negative and positive b -jet tagging discriminator distributions in data are compared with the simulation in figure 21. The events are selected by requiring jet triggers with a p_T threshold of

Table 10. The efficiency scale factors SF_b , and their uncertainties, obtained in multijet and $t\bar{t}$ events for b jets in the expected p_T range of $t\bar{t}$ events.

b tagger	SF_b in multijet events	SF_b in $t\bar{t}$ events
JPL	0.98 ± 0.02	0.97 ± 0.03
JBPL	0.98 ± 0.02	0.98 ± 0.03
TCHEL	0.98 ± 0.02	0.95 ± 0.03
CSVL	0.99 ± 0.02	1.01 ± 0.03
JPM	0.92 ± 0.03	0.95 ± 0.03
JBPM	0.92 ± 0.03	0.94 ± 0.03
TCHEM	0.95 ± 0.03	0.96 ± 0.03
TCHPM	0.94 ± 0.03	0.93 ± 0.03
SSVHEM	0.95 ± 0.03	0.96 ± 0.03
CSVM	0.95 ± 0.03	0.97 ± 0.03
JPT	0.87 ± 0.04	0.90 ± 0.03
JBPT	0.87 ± 0.05	0.89 ± 0.03
TCHPT	0.91 ± 0.04	0.93 ± 0.03
SSVHPT	0.92 ± 0.03	0.95 ± 0.03
CSVT	0.91 ± 0.03	0.96 ± 0.03

30 GeV/c, corresponding to an average p_T over all jets in the events of 44 GeV/c. For all b-jet tagging algorithms, the data and simulation are found to be in agreement to within about $\pm 20\%$. Similar results are found for a sample of events selected by requiring jet triggers with a p_T threshold of 300 GeV/c, in which the average p_T is 213 GeV/c. Depending on the prescales applied, the data correspond to an integrated luminosity of up to 5.0 fb^{-1} .

The misidentification probability is evaluated as:

$$\epsilon_{\text{data}}^{\text{misid}} = \epsilon_{\text{data}}^- \cdot R_{\text{light}}, \quad (8.1)$$

where ϵ_{data}^- is the negative tag rate as measured in jet data, defined as the fraction of jets that are negatively tagged. $R_{\text{light}} = \epsilon_{\text{MC}}^{\text{misid}} / \epsilon_{\text{MC}}^-$, a correction factor taken from simulation, is the ratio of the misidentification probability for light-parton jets to the negative tag rate for jets of all flavours in the simulation.

The rate ϵ_{data}^- depends on the numbers of c and b quarks in the negative-tagged jets (which tend to decrease R_{light}), on the residual differences between light-flavour quark and gluon jets, the number of tracks from other displaced processes (such as K_S^0 and Λ decays, and interactions in the detector material), and mismeasured tracks (which tend to increase R_{light}). Due to these contributions the simulation predicts ranges of R_{light} , for the different algorithms and jet p_T values, of about 1.1 to 1.4, 1 to 2, and 1 to 4, for the loose, medium, and tight operating points, respectively.

To compare the measured misidentification probability to that predicted by the simulation, a scale factor SF_{light} is defined:

$$SF_{\text{light}} = \epsilon_{\text{data}}^{\text{misid}} / \epsilon_{\text{MC}}^{\text{misid}}. \quad (8.2)$$

The following systematic effects on the misidentification probability based on negative tags are considered:

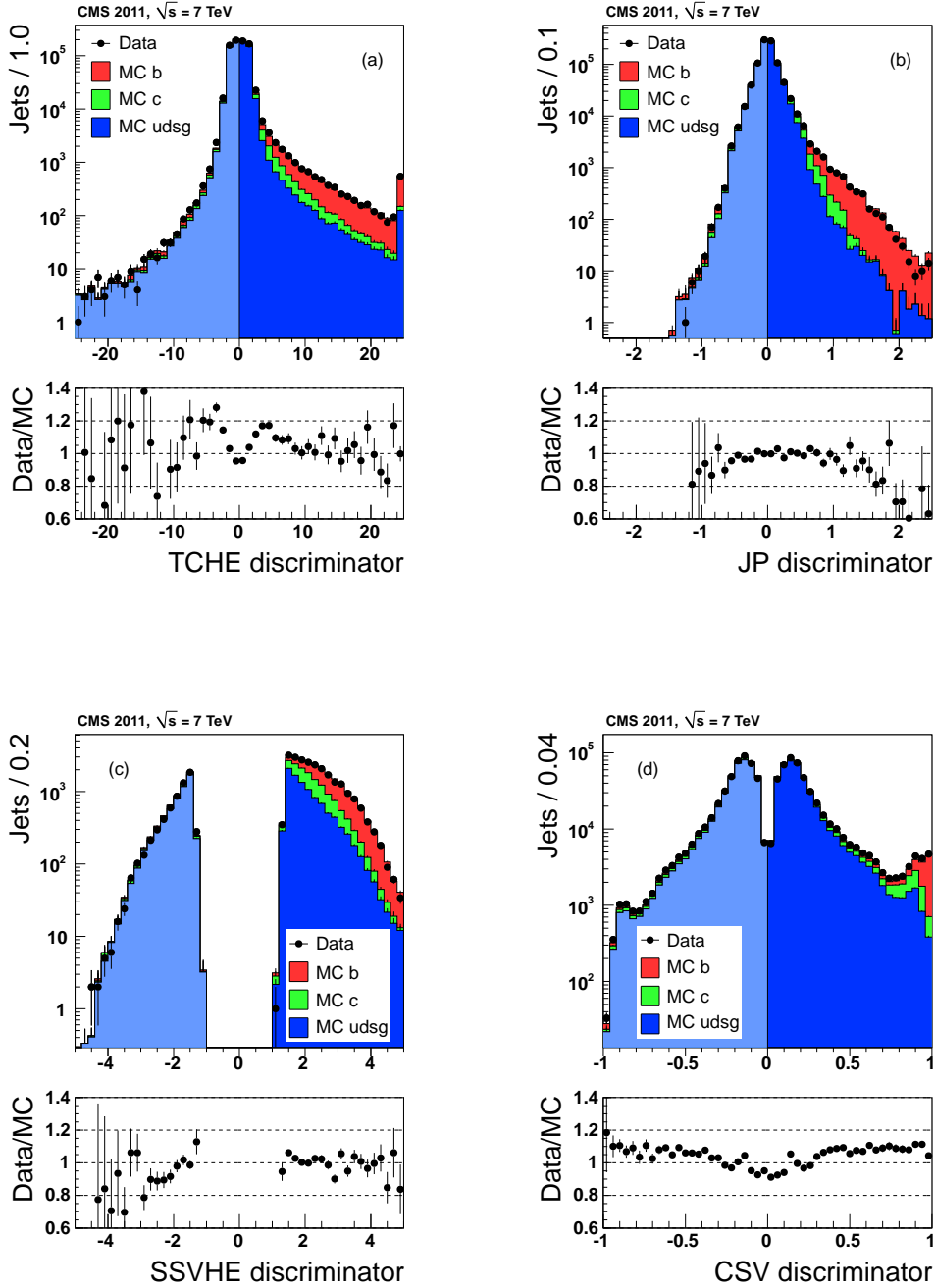


Figure 21. Signed b-jet tagging discriminators in data (dots) and simulation for light-parton jets (blue histogram, with a lighter colour for the negative discriminators), c jets (green histogram), and b jets (red histogram) for the (a) TCHE, (b) JP, (c) SSVHE, and (d) CSV algorithms. A jet-trigger p_T threshold of $30\text{ GeV}/c$ is required for both data and simulation. The simulation is normalized to the number of entries in the data. Underflow and overflow entries are added to the first and last bins, respectively.

- **b and c fractions:** the fraction of b-flavour jets has been measured in CMS to agree with the simulation within a $\pm 20\%$ uncertainty [44]. A $\pm 20\%$ uncertainty is conservatively estimated for the overall fraction of b and c jets. The b- and c-flavour fraction is varied in the QCD multijet simulation, from which a systematic uncertainty on R_{light} is inferred.
- **Gluon fraction:** this affects both the misidentification probability in simulation and the overall negative tag rates. The average fraction of gluon jets depends on the details of the parton density and hadronization functions used in the simulation. An uncertainty of $\pm 20\%$ is extracted from the comparison of simulation with data [45].
- **Long-lived K_S^0 and Λ decays:** the amount of reconstructed K_S^0 and Λ are found to be larger in the data than in the simulation [46]. To estimate the uncertainty on R_{light} due to the K_S^0 and Λ contribution, the simulated jets are reweighted by factors of 1.3 ± 0.3 and 1.5 ± 0.5 , respectively, in order to match the observed yield of K_S^0 and Λ in the data. The quoted uncertainties on the factors account for the p_T dependence. The yield is varied accordingly and the inferred variation on R_{light} is taken as a systematic uncertainty.
- **Photon conversion and nuclear interactions:** the rate of secondary interactions in the pixel detector layers has been measured with $\pm 5\%$ precision [28, 47]. The corresponding variation implies a systematic uncertainty on R_{light} .
- **Mismeasured tracks:** according to the simulation, jets with a reconstructed track not associated with a genuine charged particle also present an excess of positive over negative tags. To correct for residual mismeasurement effects, a $\pm 50\%$ variation on this contribution is taken into account in the systematic uncertainty on R_{light} .
- **Sign flip:** small differences in the angle between a track and the jet axis can lead to a change of the sign of the impact parameter (“sign flip”) and modify the negative tag rate. In order to quantify this effect the ratio of the number of negative to positive tagged jets is computed in a muon jet sample similar to the one described in section 5, with a larger than 80% b purity. Data and simulation are found to be in good agreement. From the statistical uncertainty on the comparison, the absolute uncertainty on this ratio is estimated as 2%, 1%, and 0.5% for loose, medium, and tight operating points, respectively. This sign flip uncertainty can be translated into a systematic uncertainty on R_{light} .
- **Pileup:** the misidentification probability depends on the pileup model used in the simulation. The simulated events are reweighted in order to match the pileup rate in the data. Differences between R_{light} values obtained for different running periods are used to estimate the systematic uncertainty, which is about $\pm 1\%$ for all taggers.
- **Event sample:** physics analyses use jets from different event topologies. For a given jet p_T , the misidentification probability is different for the leading jet or if there are other jets with higher p_T values in the same event. Measured misidentification scale factors for leading and subleading jets have a dispersion of about 7%. In addition, misidentification scale factors vary by 2–7%, depending on the tagger, for different running periods. These two uncertainties are added in quadrature to account for an uncertainty due to sample dependence. This is the dominant contribution to the overall systematic uncertainty on the misidentification probability.

Table 11. Relative systematic uncertainties on SF_{light} for jet p_T in the range 80–120 GeV/c. The columns correspond to the different sources of systematics in the order described in the text.

b tagger	b and c jets	gluon	V^0 and 2^{nd} int.	mismeas.	sign flip	MC stat	pileup and evt. sample	total
JPM	8.6%	0.8%	7.9%	1.0%	6.4%	0.9%	9.4%	16.5%
JBPM	6.2%	1.2%	6.9%	0.5%	1.6%	0.9%	9.0%	13.2%
TCHEM	4.5%	0.8%	6.2%	1.2%	5.1%	0.7%	8.0%	12.4%
TCHPM	1.6%	1.0%	3.0%	0.6%	2.5%	0.6%	9.2%	10.3%
SSVHEM	1.0%	0.9%	3.2%	1.9%	2.9%	0.7%	7.3%	9.0%
CSVM	3.2%	1.8%	4.4%	0.7%	4.6%	0.7%	7.4%	10.6%

Table 12. Misidentification probabilities and the corresponding data/MC scale factors SF_{light} for different algorithms and operating points for jet p_T in the range 80–120 GeV/c. The statistical uncertainties are quoted for the misidentification probabilities, while both the statistical and the systematic uncertainties are given for the scale factors.

b tagger	misidentification probability	SF_{light}
JPL	0.1000 ± 0.0004	$0.99 \pm 0.01 \pm 0.10$
JBPL	0.1019 ± 0.0004	$0.96 \pm 0.01 \pm 0.09$
TCHEL	0.1989 ± 0.0005	$1.10 \pm 0.01 \pm 0.09$
CSVL	0.1020 ± 0.0004	$1.10 \pm 0.01 \pm 0.09$
JPM	0.0107 ± 0.0001	$1.03 \pm 0.01 \pm 0.17$
JBPM	0.0110 ± 0.0001	$0.95 \pm 0.01 \pm 0.13$
TCHEM	0.0282 ± 0.0003	$1.21 \pm 0.01 \pm 0.15$
TCHPM	0.0304 ± 0.0003	$1.24 \pm 0.01 \pm 0.13$
SSVHEM	0.0208 ± 0.0002	$0.94 \pm 0.01 \pm 0.08$
CSVM	0.0151 ± 0.0002	$1.11 \pm 0.01 \pm 0.12$
JPT	0.00116 ± 0.00005	$1.03 \pm 0.04 \pm 0.25$
JBPT	0.00117 ± 0.00004	$0.95 \pm 0.04 \pm 0.19$
TCHPT	0.00284 ± 0.00009	$1.26 \pm 0.04 \pm 0.21$
SSVHPT	0.00207 ± 0.00009	$1.02 \pm 0.04 \pm 0.17$
CSVT	0.00120 ± 0.00005	$1.17 \pm 0.05 \pm 0.21$

The systematic uncertainties are detailed in table 11 for the various algorithms and for the example of the medium operating points in the jet p_T range between 80 and 120 GeV/c.

The measured misidentification probabilities and data/MC scale factors are presented in figures 22 and 23 as a function of the jet p_T for the JPL and CSVM taggers. For a jet p_T of about 80 GeV/c the misidentification probabilities are close to 10% and 1% for the loose (JPL) and medium (CSVM) selections, respectively. Both algorithms show an increase of the misidentification probability with jet p_T that can be explained by the higher track densities in collimated jets. The simulation reproduces this dependence to a large extent. The observed scale factors are close to one with a decrease of $\sim 10\%$ toward the highest jet p_T . The misidentification probabilities measured with data and the data/MC scale factors are given in table 12 for jets with p_T between

80 and 120 GeV/c. The scale factors for the misidentification probability have also been measured as a function of the jet p_T for jets in several pseudorapidity intervals: $|\eta| < 0.5$, $0.5 \leq |\eta| < 1.0$, $1.0 \leq |\eta| < 1.5$ and $1.5 \leq |\eta| < 2.4$ for the loose operating points and $|\eta| < 0.8$, $0.8 \leq |\eta| < 1.6$ and $1.6 \leq |\eta| < 2.4$ for the medium operating points. For each b-tagging algorithm, the scale factors are compatible within about 10%. These pseudorapidity-dependent scale factors for the misidentification probabilities are used in physics analyses.

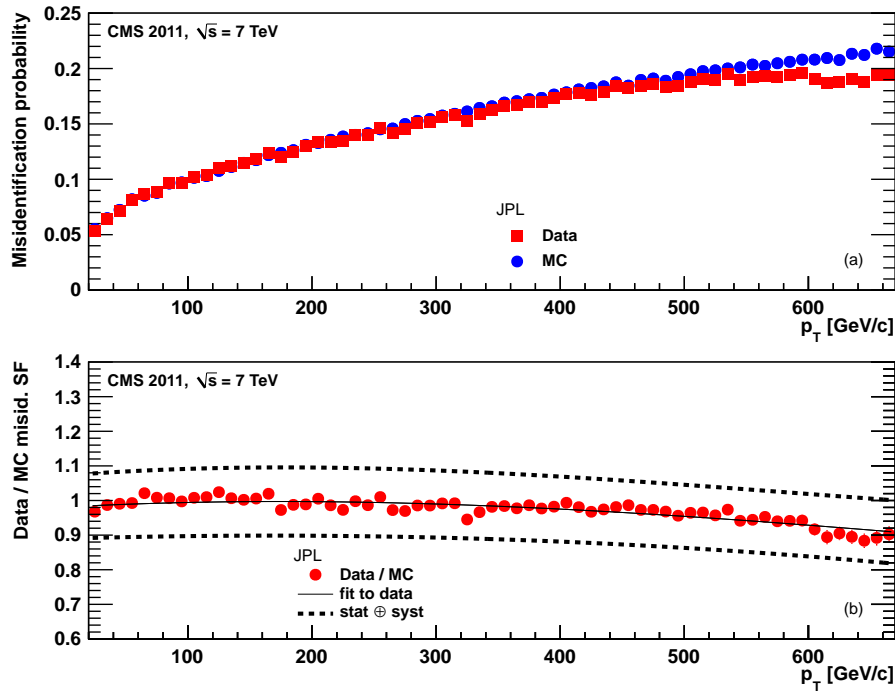


Figure 22. For the JPL tagger: (a) misidentification probability in data (red squares) and simulation (blue dots); (b) scale factor for the misidentification probability. The last p_T bin in each plot includes all jets with $p_T > 670$ GeV/c. The solid curve is the result of a polynomial fit to the data points. The dashed curves represent the overall statistical and systematic uncertainties on the measurements.

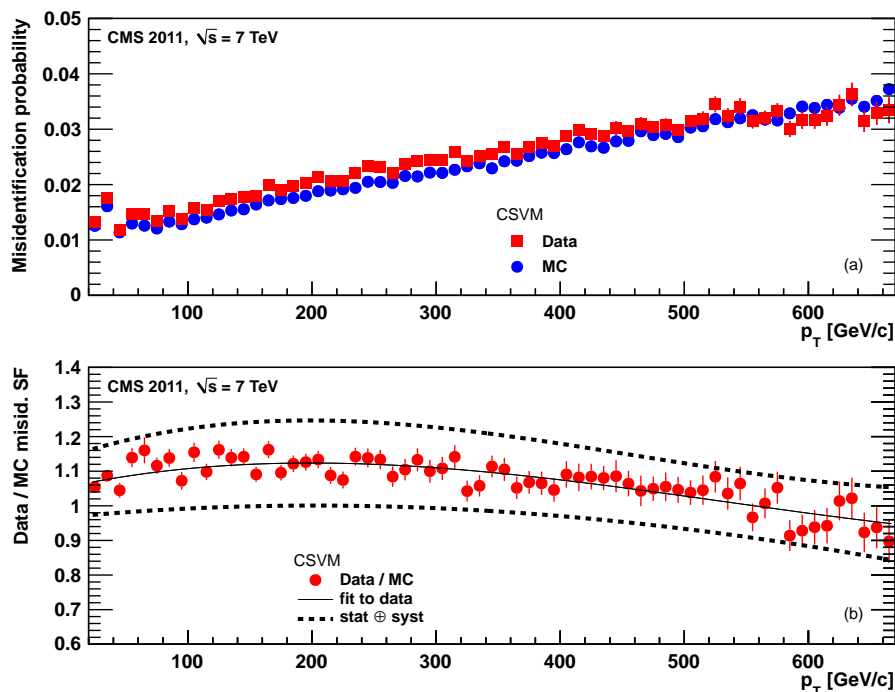


Figure 23. Same as figure 22 but for the CSV M tagger.

9 Conclusions

The CMS collaboration has developed a variety of algorithms that are used to identify jets that arise from the hadronization of bottom quarks. Early analyses relied on simple and robust techniques, based on the second or third highest impact parameter significance of the tracks associated to a jet, or the flight distance measured using a reconstructed secondary vertex. More recent analyses use algorithms with better performance that define a powerful discriminant from the combination of several variables. The use of these more advanced algorithms is made possible by the high degree of agreement achieved between data and simulation, and by the robustness of the algorithms against variations in the running conditions.

The algorithms provide selections at several operating points. The efficiencies of the algorithms at these operating points have been measured with a number of methods using multijet and $t\bar{t}$ events. A differential measurement of the efficiency as a function of jet p_T , from 30 to 670 GeV/c, has been carried out with the multijet sample. This information is used in analyses that require knowledge of the performance of b-jet tagging over a wide range of transverse momenta. The information is also helpful for analyses such as the measurement of the $t\bar{t}$ cross section in order to avoid the strong correlations that can occur if the efficiencies are inferred from the $t\bar{t}$ event sample itself.

The $t\bar{t}$ sample provides inclusive results, which are suitable for measurements of top-quark properties and for the analysis of standard model processes with similar jet momentum spectra and multiplicities. The misidentification probability, that a light-parton jet is mistaken as a b-quark jet, has been measured by applying inverted tagging algorithms to the multijet events.

The most effective algorithm is the Combined Secondary Vertex tagger. Using a loose selection, CMS achieves b-jet tagging efficiencies of about 85%, for a light-parton misidentification probability of 10%. This selection is suited for $t\bar{t}$ analyses. In analyses requiring higher b-jet purity, such as searches for supersymmetric particles, approximately 70% b-jet tagging efficiency is achieved, for a light-parton misidentification probability of only 1.5%. These values apply for jet transverse momenta typically observed in $t\bar{t}$ events.

The measured b-jet tagging performance is quantified and implemented in CMS analyses by using scale factor corrections to the MC simulation. These scale factors have been used extensively to enable studies over a wide range of event topologies that would otherwise not be possible due to limited statistics. The scale factors for the b-jet tagging efficiencies are measured with uncertainties of 2–4%, and 3–8%, in the jet p_T range 30–320 GeV/c and 320–670 GeV/c respectively. The maximum deviation of these scale factors from unity is approximately 10%. The scale factors for light-parton jet misidentification probabilities are measured to a precision of 8–17% over the full p_T range, and differ from unity by at most 25%. The scale factors for c-jet tagging efficiency are assumed to be the same as for b jets, with the corresponding uncertainty conservatively doubled.

The b-jet identification techniques discussed in this paper have been used in more than 40 analyses published by CMS, including measurements of top-quark properties, the Higgs boson, and searches for signals of physics beyond the standard model. The reduction of the uncertainties on the b-jet tagging scale factors has enabled the CMS experiment to decrease the light-parton background to unprecedented levels while maintaining high b-jet tagging efficiency for a wide range of processes containing heavy-flavour jets.

Acknowledgments

We congratulate our colleagues in the CERN accelerator departments for the excellent performance of the LHC machine. We thank the technical and administrative staff at CERN and other CMS institutes. This work was supported by the Austrian Federal Ministry of Science and Research; the Belgium Fonds de la Recherche Scientifique, and Fonds voor Wetenschappelijk Onderzoek; the Brazilian Funding Agencies (CNPq, CAPES, FAPERJ, and FAPESP); the Bulgarian Ministry of Education and Science; CERN; the Chinese Academy of Sciences, Ministry of Science and Technology, and National Natural Science Foundation of China; the Colombian Funding Agency (COLCIENCIAS); the Croatian Ministry of Science, Education and Sport; the Research Promotion Foundation, Cyprus; the Ministry of Education and Research, Recurrent financing contract SF0690030s09 and European Regional Development Fund, Estonia; the Academy of Finland, Finnish Ministry of Education and Culture, and Helsinki Institute of Physics; the Institut National de Physique Nucléaire et de Physique des Particules / CNRS, and Commissariat à l'Énergie Atomique et aux Énergies Alternatives / CEA, France; the Bundesministerium für Bildung und Forschung, Deutsche Forschungsgemeinschaft, and Helmholtz-Gemeinschaft Deutscher Forschungszentren, Germany; the General Secretariat for Research and Technology, Greece; the National Scientific Research Foundation, and National Office for Research and Technology, Hungary; the Department of Atomic Energy and the Department of Science and Technology, India; the Institute for Studies in Theoretical Physics and Mathematics, Iran; the Science Foundation, Ireland; the Istituto Nazionale di Fisica Nucleare, Italy; the Korean Ministry of Education, Science and

Technology and the World Class University program of NRF, Korea; the Lithuanian Academy of Sciences; the Mexican Funding Agencies (CINVESTAV, CONACYT, SEP, and UASLP-FAI); the Ministry of Science and Innovation, New Zealand; the Pakistan Atomic Energy Commission; the Ministry of Science and Higher Education and the National Science Centre, Poland; the Fundação para a Ciência e a Tecnologia, Portugal; JINR (Armenia, Belarus, Georgia, Ukraine, Uzbekistan); the Ministry of Education and Science of the Russian Federation, the Federal Agency of Atomic Energy of the Russian Federation, Russian Academy of Sciences, and the Russian Foundation for Basic Research; the Ministry of Science and Technological Development of Serbia; the Secretaría de Estado de Investigación, Desarrollo e Innovación and Programa Consolider-Ingenio 2010, Spain; the Swiss Funding Agencies (ETH Board, ETH Zurich, PSI, SNF, UniZH, Canton Zurich, and SER); the National Science Council, Taipei; the Scientific and Technical Research Council of Turkey, and Turkish Atomic Energy Authority; the Science and Technology Facilities Council, UK; the US Department of Energy, and the US National Science Foundation.

Individuals have received support from the Marie-Curie programme and the European Research Council (European Union); the Leventis Foundation; the A. P. Sloan Foundation; the Alexander von Humboldt Foundation; the Austrian Science Fund (FWF); the Belgian Federal Science Policy Office; the Fonds pour la Formation à la Recherche dans l'Industrie et dans l'Agriculture (FRIA-Belgium); the Agentschap voor Innovatie door Wetenschap en Technologie (IWT-Belgium); the Council of Science and Industrial Research, India; the Compagnia di San Paolo (Torino); and the HOMING PLUS programme of Foundation for Polish Science, cofinanced from European Union, Regional Development Fund.

References

- [1] CMS collaboration, *Measurement of the $t\bar{t}$ production cross section in pp collisions at 7 TeV in lepton + jets events using b quark jet identification*, *Phys. Rev. D* **84** (2011) 092004 [[arXiv:1108.3773](#)].
- [2] CMS collaboration, *Search for supersymmetry in events with b Jets and missing transverse momentum at the LHC*, *JHEP* **07** (2011) 113 [[arXiv:1106.3272](#)].
- [3] CMS collaboration, *Measurement of the t -channel single top quark production cross section in pp collisions at $\sqrt{s} = 7$ TeV*, *Phys. Rev. Lett.* **107** (2011) 091802 [[arXiv:1106.3052](#)].
- [4] CMS collaboration, *The CMS experiment at the CERN LHC*, *2008 JINST* **3** S08004.
- [5] T. Sjöstrand, S. Mrenna and P.Z. Skands, *PYTHIA 6.4 physics and manual*, *JHEP* **05** (2006) 026 [[hep-ph/0603175](#)].
- [6] R. Field, *Early LHC Underlying Event Data - Findings and Surprises*, [arXiv:1010.3558](#).
- [7] J. Alwall, M. Herquet, F. Maltoni, O. Mattelaer and T. Stelzer, *MadGraph 5: going beyond*, *JHEP* **06** (2011) 128 [[arXiv:1106.0522](#)].
- [8] M.L. Mangano, M. Moretti, F. Piccinini and M. Treccani, *Matching matrix elements and shower evolution for top-quark production in hadronic collisions*, *JHEP* **01** (2007) 013 [[hep-ph/0611129](#)].
- [9] N. Davidson, G. Nanava, T. Przedziński, E. Richter-Wąs and Z. Wąs, *Universal Interface of TAUOLA Technical and Physics Documentation*, *Comput. Phys. Commun.* **183** (2012) 821 [[arXiv:1002.0543](#)].

- [10] S. Frixione, P. Nason and C. Oleari, *Matching NLO QCD computations with parton shower simulations: the POWHEG method*, *JHEP* **11** (2007) 070 [[arXiv:0709.2092](#)].
- [11] J.M. Campbell and R.K. Ellis, *MCFM for the Tevatron and the LHC*, *Nucl. Phys. Proc. Suppl.* **205-206** (2010) 10 [[arXiv:1007.3492](#)].
- [12] A.D. Martin, W. Stirling, R. Thorne and G. Watt, *Uncertainties on α_s in global parton distribution functions analyses and implications for predicted hadronic cross sections*, *Eur. Phys. J. C* **64** (2009) 653 [[arXiv:0905.3531](#)].
- [13] H.-L. Lai, J. Huston, Z. Li, P. Nadolsky, J. Pumplin, et al., *Uncertainty induced by QCD coupling in the CTEQ global analysis of parton distributions*, *Phys. Rev. D* **82** (2010) 054021 [[arXiv:1004.4624](#)].
- [14] F. Demartin, S. Forte, E. Mariani, J. Rojo and A. Vicini, *The impact of PDF and α_s uncertainties on Higgs Production in gluon fusion at hadron colliders*, *Phys. Rev. D* **82** (2010) 014002 [[arXiv:1004.0962](#)].
- [15] M. Botje et al., *The PDF4LHC Working Group Interim Recommendations*, [arXiv:1101.0538](#).
- [16] J.M. Campbell, R. Frederix, F. Maltoni and F. Tramontano, *Next-to-Leading-Order Predictions for t -Channel Single-Top Production at Hadron Colliders*, *Phys. Rev. Lett.* **102** (2009) 182003 [[arXiv:0903.0005](#)].
- [17] J.M. Campbell and F. Tramontano, *Next-to-leading order corrections to Wt production and decay*, *Nucl. Phys. B* **726** (2005) 109 [[hep-ph/0506289](#)].
- [18] J.M. Campbell, R.K. Ellis and F. Tramontano, *Single top production and decay at next-to-leading order*, *Phys. Rev. D* **70** (2004) 094012 [[hep-ph/0408158](#)].
- [19] N. Kidonakis, *Two-loop soft anomalous dimensions for single top quark associated production with a W^- or H^-* , *Phys. Rev. D* **82** (2010) 054018 [[arXiv:1005.4451](#)].
- [20] N. Kidonakis, *Next-to-next-to-leading logarithm resummation for s -channel single top quark production*, *Phys. Rev. D* **81** (2010) 054028 [[arXiv:1001.5034](#)].
- [21] K. Melnikov and F. Petriello, *Electroweak gauge boson production at hadron colliders through $O(\alpha_s^2)$* , *Phys. Rev. D* **74** (2006) 114017 [[hep-ph/0609070](#)].
- [22] PARTICLE DATA GROUP, J. Beringer et al., *Review of Particle Physics (RPP)*, *Phys. Rev. D* **86** (2012) 010001.
- [23] GEANT4 collaboration, S. Agostinelli et al., *GEANT4 — a simulation toolkit*, *Nucl. Instrum. Meth. A* **506** (2003) 250.
- [24] CMS collaboration, *Particle-Flow Event Reconstruction in CMS and Performance for Jets, Taus and MET*, CMS Physics Analysis Summary [CMS-PAS-PFT-09-001](#).
- [25] CMS collaboration, *Commissioning of the Particle-Flow reconstruction in Minimum-Bias and Jet Events from pp Collisions at 7 TeV*, CMS Physics Analysis Summary [CMS-PAS-PFT-10-002](#).
- [26] M. Cacciari, G.P. Salam and G. Soyez, *The Anti- k_r jet clustering algorithm*, *JHEP* **04** (2008) 063 [[arXiv:0802.1189](#)].
- [27] CMS collaboration, *Determination of jet energy calibration and transverse momentum resolution in CMS*, *2011 JINST* **6** P11002 [[arXiv:1107.4277](#)].
- [28] CMS collaboration, *CMS Tracking performance results from early LHC Operation*, *Eur. Phys. J. C* **70** (2010) 1165 [[arXiv:1007.1988](#)].

- [29] CMS collaboration, *Performance of CMS muon reconstruction in pp collision events at $\sqrt{s} = 7$ TeV*, *2012 JINST* **7** P10002 [[arXiv:1206.4071](#)].
- [30] R. Frühwirth, W. Waltenberger and P. Vanlaer, *Adaptive vertex fitting*, *J. Phys.* **G 34** (2007) N343.
- [31] ALEPH collaboration, D. Buskulic et al., *A precise measurement of $\Gamma_{Z \rightarrow b\bar{b}} / \Gamma_{Z \rightarrow \text{hadrons}}$* , *Phys. Lett. B* **313** (1993) 535.
- [32] G. Borisov and C. Mariotti, *Fine tuning of track impact parameter resolution of the DELPHI detector*, *Nucl. Instrum. Meth. A* **372** (1996) 181.
- [33] V. Blobel, *Software alignment for tracking detectors*, *Nucl. Instrum. Meth. A* **566** (2006) 5.
- [34] G. Flucke, P. Schleper, G. Steinbrück and M. Stoye, *CMS silicon tracker alignment strategy with the Millepede II algorithm*, *2008 JINST* **3** P09002.
- [35] UA1 collaboration, C. Albajar et al., *Study of heavy flavor production in events with a muon accompanied by jet(s) at the CERN proton-antiproton collider*, *Z. Phys. C* **37** (1988) 489.
- [36] B. Clément, *Electroweak production of the top quark in the Run II of the D0 experiment*, Ph.D. thesis, IPHC, Université de Strasbourg, France, 2006, <http://scd-theses.u-strasbg.fr/1103/>.
- [37] D0 collaboration, V. Abazov et al., *b-Jet Identification in the D0 Experiment*, *Nucl. Instrum. Meth. A* **620** (2010) 490 [[arXiv:1002.4224](#)].
- [38] CMS collaboration, *Measurement of $B\bar{B}$ angular correlations based on secondary vertex reconstruction at $\sqrt{s} = 7$ TeV*, *JHEP* **03** (2011) 136 [[arXiv:1102.3194](#)].
- [39] CMS collaboration, *Measurement of the $t\bar{t}$ production cross section in the dilepton channel in pp collisions at $\sqrt{s} = 7$ TeV*, *JHEP* **11** (2012) 067 [[arXiv:1208.2671](#)].
- [40] R. Field, *Studying the underlying event at CDF and the LHC*, proceedings of the *First International Workshop, Multiple Partonic Interactions at the LHC (MPI'08)*, Perugia, Italy, October 27-31, 2008 [[arXiv:1003.4220](#) 12].
- [41] F. James, *Statistical Methods in Experimental Physics*, World Scientific, 2nd edition, 2006.
- [42] S.S. Wilks, *The Large-Sample Distribution of the Likelihood Ratio for Testing Composite Hypotheses*, *Ann. Math. Statist.* **9** (1938) 60.
- [43] L. Lyons, D. Gibaut and P. Clifford, *How to combine correlated estimates of a single physical quantity*, *Nucl. Instrum. Meth. A* **270** (1988) 110.
- [44] CMS collaboration, *Inclusive b-jet production in pp collisions at $\sqrt{s} = 7$ TeV*, *JHEP* **04** (2012) 084 [[arXiv:1202.4617](#)].
- [45] CMS collaboration, *Measurement of the Inclusive Jet Cross Section in pp Collisions at $\sqrt{s} = 7$ TeV*, *Phys. Rev. Lett.* **107** (2011) 132001 [[arXiv:1106.0208](#)].
- [46] CMS collaboration, *Strange particle production in pp collisions at $\sqrt{s} = 0.9$ and 7 TeV*, *JHEP* **05** (2011) 064 [[arXiv:1102.4282](#)].
- [47] CMS collaboration, *Studies of Tracker Material*, CMS Physics Analysis Summary [CMS-PAS-TRK-10-003](#).

Glossary

- bSample** Method to measure the b-jet tagging efficiency in $t\bar{t}$ events from a b-enriched sample
- CSVL** Combined Secondary Vertex algorithm at the loose operating point
- CSVM** Combined Secondary Vertex algorithm at the medium operating point
- CSVT** Combined Secondary Vertex algorithm at the tight operating point
- FTC** Flavour Tag Consistency method for the measurement of the b-jet tagging efficiency in $t\bar{t}$ events
- FTM** Flavour Tag Matching method for the measurement of the b-jet tagging efficiency in $t\bar{t}$ events
- IP3D (method)** Method for the measurement of the b-jet tagging efficiency in multijet events based on the impact parameters of muons
- IP** Impact parameter of a track
- JBPL** Jet B Probability algorithm at the loose operating point
- JBPM** Jet B Probability algorithm at the medium operating point
- JBPT** Jet B Probability algorithm at the tight operating point
- JPL** Jet Probability algorithm at the loose operating point
- JPM** Jet Probability algorithm at the medium operating point
- JPT** Jet Probability algorithm at the tight operating point
- LT (method)** Lifetime Tagging method for the measurement of the b-jet tagging efficiency in multijet events
- PLR** Profile Likelihood Ratio method for the measurement of the b-jet tagging efficiency in $t\bar{t}$ events
- PtRel (method)** Method for the measurement of the b-jet tagging efficiency in multijet events based on the transverse momenta of muons w.r.t. the jet axis
- PV** Primary Vertex (proton-proton interaction point)
- SIP** Significance of the impact parameter of a track
- SSVHEM** Simple Secondary Vertex High Efficiency algorithm at the medium operating point
- SSVHPT** Simple Secondary Vertex High Purity algorithm at the tight operating point
- SV** Secondary Vertex (decay vertex of a long-lived particle)
- TC** Track Counting (TCHE and TCHP) algorithms
- TCHEL** Track Counting High Efficiency algorithm at the loose operating point
- TCHEM** Track Counting High Efficiency algorithm at the medium operating point
- TCHPM** Track Counting High Purity algorithm at the medium operating point
- TCHPT** Track Counting High Purity algorithm at the tight operating point

The CMS collaboration

Yerevan Physics Institute, Yerevan, Armenia

S. Chatrchyan, V. Khachatryan, A.M. Sirunyan, A. Tumasyan

Institut für Hochenergiephysik der OeAW, Wien, Austria

W. Adam, E. Aguilo, T. Bergauer, M. Dragicevic, J. Erö, C. Fabjan¹, M. Friedl, R. Frühwirth¹, V.M. Ghete, J. Hammer, N. Hörmann, J. Hrubec, M. Jeitler¹, W. Kiesenhofer, V. Knünz, M. Krammer¹, I. Krätschmer, D. Liko, I. Mikulec, M. Pernicka[†], B. Rahbaran, C. Rohringer, H. Rohringer, R. Schöfbeck, J. Strauss, A. Taurok, W. Waltenberger, G. Walzel, E. Widl, C.-E. Wulz¹

National Centre for Particle and High Energy Physics, Minsk, Belarus

V. Mossolov, N. Shumeiko, J. Suarez Gonzalez

Universiteit Antwerpen, Antwerpen, Belgium

M. Bansal, S. Bansal, T. Cornelis, E.A. De Wolf, X. Janssen, S. Luyckx, L. Mucibello, S. Ochesanu, B. Roland, R. Rougny, M. Selvaggi, Z. Staykova, H. Van Haevermaet, P. Van Mechelen, N. Van Remortel, A. Van Spilbeeck

Vrije Universiteit Brussel, Brussel, Belgium

F. Blekman, S. Blyweert, J. D'Hondt, R. Gonzalez Suarez, A. Kalogeropoulos, M. Maes, A. Olbrechts, W. Van Doninck, P. Van Mulders, G.P. Van Onsem, I. Villella

Université Libre de Bruxelles, Bruxelles, Belgium

B. Clerbaux, G. De Lentdecker, V. Dero, A.P.R. Gay, T. Hreus, A. Léonard, P.E. Marage, A. Mohammadi, T. Reis, L. Thomas, G. Vander Marcken, C. Vander Velde, P. Vanlaer, J. Wang

Ghent University, Ghent, Belgium

V. Adler, K. Beernaert, A. Cimmino, S. Costantini, G. Garcia, M. Grunewald, B. Klein, J. Lellouch, A. Marinov, J. McCartin, A.A. Ocampo Rios, D. Ryckbosch, N. Strobbe, F. Thyssen, M. Tytgat, P. Verwilligen, S. Walsh, E. Yazgan, N. Zaganidis

Université Catholique de Louvain, Louvain-la-Neuve, Belgium

S. Basegmez, G. Bruno, R. Castello, L. Ceard, C. Delaere, T. du Pree, D. Favart, L. Forthomme, A. Giammanco², J. Hollar, V. Lemaitre, J. Liao, O. Militaru, C. Nuttens, D. Pagano, A. Pin, K. Piotrkowski, N. Schul, J.M. Vizan Garcia

Université de Mons, Mons, Belgium

N. Bely, T. Caebergs, E. Daubie, G.H. Hammad

Centro Brasileiro de Pesquisas Fisicas, Rio de Janeiro, Brazil

G.A. Alves, M. Correa Martins Junior, D. De Jesus Damiao, T. Martins, M.E. Pol, M.H.G. Souza

Universidade do Estado do Rio de Janeiro, Rio de Janeiro, Brazil

W.L. Aldá Júnior, W. Carvalho, A. Custódio, E.M. Da Costa, C. De Oliveira Martins, S. Fonseca De Souza, D. Matos Figueiredo, L. Mundim, H. Nogima, V. Oguri, W.L. Prado Da Silva, A. Santoro, L. Soares Jorge, A. Sznajder

Instituto de Fisica Teorica ^a, Universidade Estadual Paulista ^b, Sao Paulo, Brazil

T.S. Anjos^{b,3}, C.A. Bernardes^{b,3}, F.A. Dias^{a,4}, T.R. Fernandez Perez Tomei^a, E.M. Gregores^{b,3}, C. Lagana^a, F. Marinho^a, P.G. Mercadante^{b,3}, S.F. Novaes^a, Sandra S. Padula^a

Institute for Nuclear Research and Nuclear Energy, Sofia, Bulgaria

V. Genchev⁵, P. Iaydjiev⁵, S. Piperov, M. Rodozov, S. Stoykova, G. Sultanov, V. Tcholakov, R. Trayanov, M. Vutova

University of Sofia, Sofia, Bulgaria

A. Dimitrov, R. Hadjiiska, V. Kozhuharov, L. Litov, B. Pavlov, P. Petkov

Institute of High Energy Physics, Beijing, China

J.G. Bian, G.M. Chen, H.S. Chen, C.H. Jiang, D. Liang, S. Liang, X. Meng, J. Tao, J. Wang, X. Wang, Z. Wang, H. Xiao, M. Xu, J. Zang, Z. Zhang

State Key Lab. of Nucl. Phys. and Tech., Peking University, Beijing, China

C. Asawatangtrakuldee, Y. Ban, S. Guo, Y. Guo, W. Li, S. Liu, Y. Mao, S.J. Qian, H. Teng, D. Wang, L. Zhang, B. Zhu, W. Zou

Universidad de Los Andes, Bogota, Colombia

C. Avila, J.P. Gomez, B. Gomez Moreno, A.F. Osorio Oliveros, J.C. Sanabria

Technical University of Split, Split, Croatia

N. Godinovic, D. Lelas, R. Plestina⁶, D. Polic, I. Puljak⁵

University of Split, Split, Croatia

Z. Antunovic, M. Kovac

Institute Rudjer Boskovic, Zagreb, Croatia

V. Brigljevic, S. Duric, K. Kadija, J. Luetic, S. Morovic

University of Cyprus, Nicosia, Cyprus

A. Attikis, M. Galanti, G. Mavromanolakis, J. Mousa, C. Nicolaou, F. Ptochos, P.A. Razis

Charles University, Prague, Czech Republic

M. Finger, M. Finger Jr.

Academy of Scientific Research and Technology of the Arab Republic of Egypt, Egyptian Network of High Energy Physics, Cairo, Egypt

Y. Assran⁷, S. Elgammal⁸, A. Ellithi Kamel⁹, M.A. Mahmoud¹⁰, A. Radi^{11,12}

National Institute of Chemical Physics and Biophysics, Tallinn, Estonia

M. Kadastik, M. Müntel, M. Raidal, L. Rebane, A. Tiko

Department of Physics, University of Helsinki, Helsinki, Finland

P. Eerola, G. Fedi, M. Voutilainen

Helsinki Institute of Physics, Helsinki, Finland

J. Härkönen, A. Heikkinen, V. Karimäki, R. Kinnunen, M.J. Kortelainen, T. Lampén, K. Lassila-Perini, S. Lehti, T. Lindén, P. Luukka, T. Mäenpää, T. Peltola, E. Tuominen, J. Tuominiemi, E. Tuovinen, D. Ungaro, L. Wendland

Lappeenranta University of Technology, Lappeenranta, Finland

K. Banzuzi, A. Karjalainen, A. Korpela, T. Tuuva

DSM/IRFU, CEA/Saclay, Gif-sur-Yvette, France

M. Besancon, S. Choudhury, M. Dejardin, D. Denegri, B. Fabbro, J.L. Faure, F. Ferri, S. Ganjour, A. Givernaud, P. Gras, G. Hamel de Monchenault, P. Jarry, E. Locci, J. Malcles, L. Millischer, A. Nayak, J. Rander, A. Rosowsky, I. Shreyber, M. Titov

Laboratoire Leprince-Ringuet, Ecole Polytechnique, IN2P3-CNRS, Palaiseau, France

S. Baffioni, F. Beaudette, L. Benhabib, L. Bianchini, M. Bluj¹³, C. Broutin, P. Busson, C. Charlot, N. Daci, T. Dahms, L. Dobrzynski, R. Granier de Cassagnac, M. Haguenaer, P. Miné, C. Mironov, I.N. Naranjo, M. Nguyen, C. Ochando, P. Paganini, D. Sabes, R. Salerno, Y. Sirois, C. Veelken, A. Zabi

Institut Pluridisciplinaire Hubert Curien, Université de Strasbourg, Université de Haute Alsace Mulhouse, CNRS/IN2P3, Strasbourg, France

J.-L. Agram¹⁴, J. Andrea, D. Bloch, D. Bodin, J.-M. Brom, M. Cardaci, E.C. Chabert, C. Collard, E. Conte¹⁴, F. Drouhin¹⁴, C. Ferro, J.-C. Fontaine¹⁴, D. Gelé, U. Goerlach, P. Juillot, A.-C. Le Bihan, P. Van Hove

Centre de Calcul de l'Institut National de Physique Nucleaire et de Physique des Particules, CNRS/IN2P3, Villeurbanne, France, Villeurbanne, France

F. Fassi, D. Mercier

Université de Lyon, Université Claude Bernard Lyon 1, CNRS-IN2P3, Institut de Physique Nucléaire de Lyon, Villeurbanne, France

S. Beauceron, N. Beaupere, O. Bondu, G. Boudoul, J. Chasserat, R. Chierici⁵, D. Contardo, P. Depasse, H. El Mamouni, J. Fay, S. Gascon, M. Gouzevitch, B. Ille, T. Kurca, M. Lethuillier, L. Mirabito, S. Perries, V. Sordini, Y. Tschudi, P. Verdier, S. Viret

Institute of High Energy Physics and Informatization, Tbilisi State University, Tbilisi, Georgia

Z. Tsamalaidze¹⁵

RWTH Aachen University, I. Physikalisches Institut, Aachen, Germany

G. Anagnostou, S. Beranek, M. Edelhoff, L. Feld, N. Heracleous, O. Hindrichs, R. Jussen, K. Klein, J. Merz, A. Ostapchuk, A. Perieanu, F. Raupach, J. Sammet, S. Schael, D. Sprenger, H. Weber, B. Wittmer, V. Zhukov¹⁶

RWTH Aachen University, III. Physikalisches Institut A, Aachen, Germany

M. Ata, J. Caudron, E. Dietz-Laursonn, D. Duchardt, M. Erdmann, R. Fischer, A. Güth, T. Hebbeker, C. Heidemann, K. Hoepfner, D. Klingebiel, P. Kreuzer, C. Magass, M. Merschmeyer, A. Meyer, M. Olschewski, P. Papacz, H. Pieta, H. Reithler, S.A. Schmitz, L. Sonnenschein, J. Steggemann, D. Teyssier, M. Weber

RWTH Aachen University, III. Physikalisches Institut B, Aachen, Germany

M. Bontenackels, V. Cherepanov, Y. Erdogan, G. Flügge, H. Geenen, M. Geisler, W. Haj Ahmad, F. Hoehle, B. Kargoll, T. Kress, Y. Kuessel, A. Nowack, L. Perchalla, O. Pooth, P. Sauerland, A. Stahl

Deutsches Elektronen-Synchrotron, Hamburg, Germany

M. Aldaya Martin, J. Behr, W. Behrenhoff, U. Behrens, M. Bergholz¹⁷, A. Bethani, K. Borras, A. Burgmeier, A. Cakir, L. Calligaris, A. Campbell, E. Castro, F. Costanza, D. Dammann, C. Diez Pardos, G. Eckertlin, D. Eckstein, G. Flucke, A. Geiser, I. Glushkov, P. Gunnellini, S. Habib, J. Hauk, G. Hellwig, H. Jung, M. Kasemann, P. Katsas, C. Kleinwort, H. Kluge, A. Knutsson, M. Krämer, D. Krücker, E. Kuznetsova, W. Lange, W. Lohmann¹⁷, B. Lutz, R. Mankel, I. Marfin, M. Marienfeld, I.-A. Melzer-Pellmann, A.B. Meyer, J. Mnich, A. Mussgiller, S. Naumann-Emme, J. Olzem, H. Perrey, A. Petrukhin, D. Pitzl, A. Raspereza, P.M. Ribeiro Cipriano, C. Riedl, E. Ron, M. Rosin, J. Salfeld-Nebgen, R. Schmidt¹⁷, T. Schoerner-Sadenius, N. Sen, A. Spiridonov, M. Stein, R. Walsh, C. Wissing

University of Hamburg, Hamburg, Germany

C. Autermann, V. Blobel, J. Draeger, H. Enderle, J. Erfle, U. Gebbert, M. Görner, T. Hermanns, R.S. Höing, K. Kaschube, G. Kaussen, H. Kirschenmann, R. Klanner, J. Lange, B. Mura, F. Nowak, T. Peiffer, N. Pietsch,

D. Rathjens, C. Sander, H. Schettler, P. Schleper, E. Schlieckau, A. Schmidt, M. Schröder, T. Schum, M. Seidel, V. Sola, H. Stadie, G. Steinbrück, J. Thomsen, L. Vanelderren

Institut für Experimentelle Kernphysik, Karlsruhe, Germany

C. Barth, J. Berger, C. Böser, T. Chwalek, W. De Boer, A. Descroix, A. Dierlamm, M. Feindt, M. Guthoff⁵, C. Hackstein, F. Hartmann, T. Hauth⁵, M. Heinrich, H. Held, K.H. Hoffmann, S. Honc, I. Katkov¹⁶, J.R. Komaragiri, P. Lobelle Pardo, D. Martschei, S. Mueller, Th. Müller, M. Niegel, A. Nürnberg, O. Oberst, A. Oehler, J. Ott, G. Quast, K. Rabbertz, F. Ratnikov, N. Ratnikova, S. Röcker, A. Scheurer, F.-P. Schilling, G. Schott, H.J. Simonis, F.M. Stober, D. Troendle, R. Ulrich, J. Wagner-Kuhr, S. Wayand, T. Weiler, M. Zeise

Institute of Nuclear Physics "Demokritos", Aghia Paraskevi, Greece

G. Daskalakis, T. Gerasis, S. Kesisoglou, A. Kyriakis, D. Loukas, I. Manolagos, A. Markou, C. Markou, C. Mavrommatis, E. Ntomari

University of Athens, Athens, Greece

L. Gouskos, T.J. Mertzimekis, A. Panagiotou, N. Saoulidou

University of Ioánnina, Ioánnina, Greece

I. Evangelou, C. Foudas, P. Kokkas, N. Manthos, I. Papadopoulos, V. Patras

KFKI Research Institute for Particle and Nuclear Physics, Budapest, Hungary

G. Bencze, C. Hajdu, P. Hidas, D. Horvath¹⁸, F. Sikler, V. Veszpremi, G. Vesztergombi¹⁹

Institute of Nuclear Research ATOMKI, Debrecen, Hungary

N. Beni, S. Czellar, J. Molnar, J. Palinkas, Z. Szillasi

University of Debrecen, Debrecen, Hungary

J. Karancsi, P. Raics, Z.L. Trocsanyi, B. Ujvari

Panjab University, Chandigarh, India

S.B. Beri, V. Bhatnagar, N. Dhingra, R. Gupta, M. Kaur, M.Z. Mehta, N. Nishu, L.K. Saini, A. Sharma, J.B. Singh

University of Delhi, Delhi, India

Ashok Kumar, Arun Kumar, S. Ahuja, A. Bhardwaj, B.C. Choudhary, S. Malhotra, M. Naimuddin, K. Ranjan, V. Sharma, R.K. Shivpuri

Saha Institute of Nuclear Physics, Kolkata, India

S. Banerjee, S. Bhattacharya, S. Dutta, B. Gomber, Sa. Jain, Sh. Jain, R. Khurana, S. Sarkar, M. Sharan

Bhabha Atomic Research Centre, Mumbai, India

A. Abdulsalam, R.K. Choudhury, D. Dutta, S. Kailas, V. Kumar, P. Mehta, A.K. Mohanty⁵, L.M. Pant, P. Shukla

Tata Institute of Fundamental Research - EHEP, Mumbai, India

T. Aziz, S. Ganguly, M. Guchait²⁰, M. Maity²¹, G. Majumder, K. Mazumdar, G.B. Mohanty, B. Parida, K. Sudhakar, N. Wickramage

Tata Institute of Fundamental Research - HECR, Mumbai, India

S. Banerjee, S. Dugad

Institute for Research in Fundamental Sciences (IPM), Tehran, Iran

H. Arfaei, H. Bakhshiansohi²², S.M. Etesami²³, A. Fahim²², M. Hashemi, H. Hesari, A. Jafari²², M. Khakzad, M. Mohammadi Najafabadi, S. Paktinat Mehdiabadi, B. Safarzadeh²⁴, M. Zeinali²³

INFN Sezione di Bari ^a, Università di Bari ^b, Politecnico di Bari ^c, Bari, Italy

M. Abbrescia^{a,b}, L. Barbone^{a,b}, C. Calabria^{a,b,5}, S.S. Chhibra^{a,b}, A. Colaleo^a, D. Creanza^{a,c}, N. De Filippis^{a,c,5}, M. De Palma^{a,b}, L. Fiore^a, G. Iaselli^{a,c}, L. Lusito^{a,b}, G. Maggi^{a,c}, M. Maggi^a, B. Marangelli^{a,b}, S. My^{a,c}, S. Nuzzo^{a,b}, N. Pacifico^{a,b}, A. Pompili^{a,b}, G. Pugliese^{a,c}, G. Selvaggi^{a,b}, L. Silvestris^a, G. Singh^{a,b}, R. Venditti^{a,b}, G. Zito^a

INFN Sezione di Bologna ^a, Università di Bologna ^b, Bologna, Italy

G. Abbiendi^a, A.C. Benvenuti^a, D. Bonacorsi^{a,b}, S. Braibant-Giacomelli^{a,b}, L. Brigliadori^{a,b}, P. Capiluppi^{a,b}, A. Castro^{a,b}, F.R. Cavallo^a, M. Cuffiani^{a,b}, G.M. Dallavalle^a, F. Fabbri^a, A. Fanfani^{a,b}, D. Fasanella^{a,b,5}, P. Giacomelli^a, C. Grandi^a, L. Guiducci^{a,b}, S. Marcellini^a, G. Masetti^a, M. Meneghelli^{a,b,5}, A. Montanari^a, F.L. Navarria^{a,b}, F. Odorici^a, A. Perrotta^a, F. Primavera^{a,b}, A.M. Rossi^{a,b}, T. Rovelli^{a,b}, G.P. Siroli^{a,b}, R. Travaglini^{a,b}

INFN Sezione di Catania ^a, Università di Catania ^b, Catania, Italy

S. Albergo^{a,b}, G. Cappello^{a,b}, M. Chiorboli^{a,b}, S. Costa^{a,b}, R. Potenza^{a,b}, A. Tricomi^{a,b}, C. Tuve^{a,b}

INFN Sezione di Firenze ^a, Università di Firenze ^b, Firenze, Italy

G. Barbagli^a, V. Ciulli^{a,b}, C. Civinini^a, R. D'Alessandro^{a,b}, E. Focardi^{a,b}, S. Frosali^{a,b}, E. Gallo^a, S. Gonzi^{a,b}, M. Meschini^a, S. Paoletti^a, G. Sguazzoni^a, A. Tropiano^a

INFN Laboratori Nazionali di Frascati, Frascati, Italy

L. Benussi, S. Bianco, S. Colafranceschi²⁵, F. Fabbri, D. Piccolo

INFN Sezione di Genova ^a, Università di Genova ^b, Genova, Italy

P. Fabbri^a, R. Musenich^a, S. Tosi^{a,b}

INFN Sezione di Milano-Bicocca ^a, Università di Milano-Bicocca ^b, Milano, Italy

A. Benaglia^{a,b,5}, F. De Guio^{a,b}, L. Di Matteo^{a,b,5}, S. Fiorendi^{a,b}, S. Gennai^{a,5}, A. Ghezzi^{a,b}, S. Malvezzi^a, R.A. Manzoni^{a,b}, A. Martelli^{a,b}, A. Massironi^{a,b,5}, D. Menasce^a, L. Moroni^a, M. Paganoni^{a,b}, D. Pedrini^a, S. Ragazzi^{a,b}, N. Redaelli^a, S. Sala^a, T. Tabarelli de Fatis^{a,b}

INFN Sezione di Napoli ^a, Università di Napoli "Federico II" ^b, Napoli, Italy

S. Buontempo^a, C.A. Carrillo Montoya^a, N. Cavallo^{a,26}, A. De Cosa^{a,b,5}, O. Dogangun^{a,b}, F. Fabozzi^{a,26}, A.O.M. Iorio^a, L. Lista^a, S. Meola^{a,27}, M. Merola^{a,b}, P. Paolucci^{a,5}

INFN Sezione di Padova ^a, Università di Padova ^b, Università di Trento (Trento) ^c, Padova, Italy

P. Azzi^a, N. Bacchetta^{a,5}, D. Bisello^{a,b}, A. Branca^{a,b,5}, R. Carlin^{a,b}, P. Checchia^a, T. Dorigo^a, U. Dosselli^a, F. Gasparini^{a,b}, U. Gasparini^{a,b}, A. Gozzelino^a, K. Kanishchev^{a,c}, S. Lacaprara^a, I. Lazzizzera^{a,c}, M. Margoni^{a,b}, A.T. Meneguzzo^{a,b}, J. Pazzini^{a,b}, N. Pozzobon^{a,b}, P. Ronchese^{a,b}, F. Simonetto^{a,b}, E. Torassa^a, M. Tosi^{a,b,5}, S. Vanini^{a,b}, P. Zotto^{a,b}, G. Zumerle^{a,b}

INFN Sezione di Pavia ^a, Università di Pavia ^b, Pavia, Italy

M. Gabusi^{a,b}, S.P. Ratti^{a,b}, C. Riccardi^{a,b}, P. Torre^{a,b}, P. Vitulo^{a,b}

INFN Sezione di Perugia ^a, Università di Perugia ^b, Perugia, Italy

M. Biasini^{a,b}, G.M. Bilei^a, L. Fanò^{a,b}, P. Lariccia^{a,b}, A. Lucaroni^{a,b,5}, G. Mantovani^{a,b}, M. Menichelli^a, A. Nappi^{a,b,†}, F. Romeo^{a,b}, A. Saha^a, A. Santocchia^{a,b}, A. Spiezia^{a,b}, S. Taroni^{a,b}

INFN Sezione di Pisa ^a, Università di Pisa ^b, Scuola Normale Superiore di Pisa ^c, Pisa, Italy

P. Azzurri^{a,c}, G. Bagliesi^a, J. Bernardini^a, T. Boccali^a, G. Broccolo^{a,c}, R. Castaldi^a, R.T. D'Agnolo^{a,c}, R. Dell'Orso^a, F. Fiori^{a,b,5}, L. Foà^{a,c}, A. Giassi^a, A. Kraan^a, F. Ligabue^{a,c}, T. Lomtadze^a, L. Martini^{a,28},

A. Messineo^{a,b}, F. Palla^a, A. Rizzi^{a,b}, A.T. Serban^{a,29}, P. Spagnolo^a, P. Squillacioti^{a,5}, R. Tenchini^a, G. Tonelli^{a,b,5}, A. Venturi^a, P.G. Verdini^a

INFN Sezione di Roma ^a, Università di Roma ^b, Roma, Italy

L. Barone^{a,b}, F. Cavallari^a, D. Del Re^{a,b}, M. Diemoz^a, C. Fanelli^{a,b}, M. Grassi^{a,b,5}, E. Longo^{a,b}, P. Meridiani^{a,5}, F. Micheli^{a,b}, S. Nourbakhsh^{a,b}, G. Organtini^{a,b}, R. Paramatti^a, S. Rahatlou^{a,b}, M. Sigamani^a, L. Soffi^{a,b}

INFN Sezione di Torino ^a, Università di Torino ^b, Università del Piemonte Orientale (Novara) ^c, Torino, Italy

N. Amapane^{a,b}, R. Arcidiacono^{a,c}, S. Argiro^{a,b}, M. Arneodo^{a,c}, C. Biino^a, N. Cartiglia^a, M. Costa^{a,b}, N. Demaria^a, C. Mariotti^{a,5}, S. Maselli^a, G. Mazza^a, E. Migliore^{a,b}, V. Monaco^{a,b}, M. Musich^{a,5}, M.M. Obertino^{a,c}, N. Pastrone^a, M. Pelliccioni^a, A. Potenza^{a,b}, A. Romero^{a,b}, R. Sacchi^{a,b}, A. Solano^{a,b}, A. Staiano^a, A. Vilela Pereira^a

INFN Sezione di Trieste ^a, Università di Trieste ^b, Trieste, Italy

S. Belforte^a, V. Candelise^{a,b}, F. Cossutti^a, G. Della Ricca^{a,b}, B. Gobbo^a, M. Marone^{a,b,5}, D. Montanino^{a,b,5}, A. Penzo^a, A. Schizzi^{a,b}

Kangwon National University, Chunchon, Korea

S.G. Heo, T.Y. Kim, S.K. Nam

Kyungpook National University, Daegu, Korea

S. Chang, D.H. Kim, G.N. Kim, D.J. Kong, H. Park, S.R. Ro, D.C. Son, T. Son

Chonnam National University, Institute for Universe and Elementary Particles, Kwangju, Korea

J.Y. Kim, Zero J. Kim, S. Song

Korea University, Seoul, Korea

S. Choi, D. Gyun, B. Hong, M. Jo, H. Kim, T.J. Kim, K.S. Lee, D.H. Moon, S.K. Park

University of Seoul, Seoul, Korea

M. Choi, J.H. Kim, C. Park, I.C. Park, S. Park, G. Ryu

Sungkyunkwan University, Suwon, Korea

Y. Cho, Y. Choi, Y.K. Choi, J. Goh, M.S. Kim, E. Kwon, B. Lee, J. Lee, S. Lee, H. Seo, I. Yu

Vilnius University, Vilnius, Lithuania

M.J. Bilinskas, I. Grigelionis, M. Janulis, A. Juodagalvis

Centro de Investigacion y de Estudios Avanzados del IPN, Mexico City, Mexico

H. Castilla-Valdez, E. De La Cruz-Burelo, I. Heredia-de La Cruz, R. Lopez-Fernandez, R. Magaña Villalba, J. Martínez-Ortega, A. Sánchez-Hernández, L.M. Villaseñor-Cendejas

Universidad Iberoamericana, Mexico City, Mexico

S. Carrillo Moreno, F. Vazquez Valencia

Benemerita Universidad Autonoma de Puebla, Puebla, Mexico

H.A. Salazar Ibarquen

Universidad Autónoma de San Luis Potosí, San Luis Potosí, Mexico

E. Casimiro Linares, A. Morelos Pineda, M.A. Reyes-Santos

University of Auckland, Auckland, New Zealand

D. Krofcheck

University of Canterbury, Christchurch, New Zealand

A.J. Bell, P.H. Butler, R. Doesburg, S. Reucroft, H. Silverwood

National Centre for Physics, Quaid-I-Azam University, Islamabad, Pakistan

M. Ahmad, M.H. Ansari, M.I. Asghar, H.R. Hoorani, S. Khalid, W.A. Khan, T. Khurshid, S. Qazi, M.A. Shah, M. Shoaib

National Centre for Nuclear Research, Swierk, Poland

H. Bialkowska, B. Boimska, T. Frueboes, R. Gokieli, M. Górski, M. Kazana, K. Nawrocki, K. Romanowska-Rybinska, M. Szleper, G. Wrochna, P. Zalewski

Institute of Experimental Physics, Faculty of Physics, University of Warsaw, Warsaw, Poland

G. Brona, K. Bunkowski, M. Cwiok, W. Dominik, K. Doroba, A. Kalinowski, M. Konecki, J. Krolikowski

Laboratório de Instrumentação e Física Experimental de Partículas, Lisboa, Portugal

N. Almeida, P. Bargassa, A. David, P. Faccioli, P.G. Ferreira Parracho, M. Gallinaro, J. Seixas, J. Varela, P. Vischia

Joint Institute for Nuclear Research, Dubna, Russia

I. Belotelov, P. Bunin, M. Gavrilenko, I. Golutvin, I. Gorbunov, A. Kamenev, V. Karjavin, G. Kozlov, A. Lanev, A. Malakhov, P. Moisenz, V. Palichik, V. Perelygin, S. Shmatov, V. Smirnov, A. Volodko, A. Zarubin

Petersburg Nuclear Physics Institute, Gatchina (St. Petersburg), Russia

S. Evstyukhin, V. Golovtsov, Y. Ivanov, V. Kim, P. Levchenko, V. Murzin, V. Oreshkin, I. Smirnov, V. Sulimov, L. Uvarov, S. Vavilov, A. Vorobyev, An. Vorobyev

Institute for Nuclear Research, Moscow, Russia

Yu. Andreev, A. Dermenev, S. Gninenko, N. Golubev, M. Kirsanov, N. Krasnikov, V. Matveev, A. Pashenkov, D. Tlisov, A. Toropin

Institute for Theoretical and Experimental Physics, Moscow, Russia

V. Epshteyn, M. Erofeeva, V. Gavrilov, M. Kossov, N. Lychkovskaya, V. Popov, G. Safronov, S. Semenov, V. Stolin, E. Vlasov, A. Zhokin

Moscow State University, Moscow, RussiaA. Belyaev, E. Boos, M. Dubinin⁴, L. Dudko, A. Ershov, A. Gribushin, A. Kaminskiy³⁰, V. Klyukhin, O. Kodolova, I. Lokhtin, A. Markina, S. Obraztsov, M. Perfilov, S. Petrushanko, A. Popov, L. Sarycheva[†], V. Savrin**P.N. Lebedev Physical Institute, Moscow, Russia**

V. Andreev, M. Azarkin, I. Dremin, M. Kirakosyan, A. Leonidov, G. Mesyats, S.V. Rusakov, A. Vinogradov

State Research Center of Russian Federation, Institute for High Energy Physics, Protvino, RussiaI. Azhgirey, I. Bayshev, S. Bitioukov, V. Grishin⁵, V. Kachanov, D. Konstantinov, A. Korablev, V. Krychkine, V. Petrov, R. Ryutin, A. Sobol, L. Tourtchanovitch, S. Troshin, N. Tyurin, A. Uzunian, A. Volkov**University of Belgrade, Faculty of Physics and Vinca Institute of Nuclear Sciences, Belgrade, Serbia**P. Adzic³¹, M. Djordjevic, M. Ekmedzic, D. Krpic³¹, J. Milosevic

Centro de Investigaciones Energéticas Medioambientales y Tecnológicas (CIEMAT), Madrid, Spain

M. Aguilar-Benitez, J. Alcaraz Maestre, P. Arce, C. Battilana, E. Calvo, M. Cerrada, M. Chamizo Llatas, N. Colino, B. De La Cruz, A. Delgado Peris, D. Domínguez Vázquez, C. Fernandez Bedoya, J.P. Fernández Ramos, A. Ferrando, J. Flix, M.C. Fouz, P. Garcia-Abia, O. Gonzalez Lopez, S. Goy Lopez, J.M. Hernandez, M.I. Josa, G. Merino, J. Puerta Pelayo, A. Quintario Olmeda, I. Redondo, L. Romero, J. Santaolalla, M.S. Soares, C. Willmott

Universidad Autónoma de Madrid, Madrid, Spain

C. Albajar, G. Codispoti, J.F. de Trocóniz

Universidad de Oviedo, Oviedo, Spain

H. Brun, J. Cuevas, J. Fernandez Menendez, S. Folgueras, I. Gonzalez Caballero, L. Lloret Iglesias, J. Piedra Gomez

Instituto de Física de Cantabria (IFCA), CSIC-Universidad de Cantabria, Santander, Spain

J.A. Brochero Cifuentes, I.J. Cabrillo, A. Calderon, S.H. Chuang, J. Duarte Campderros, M. Felcini³², M. Fernandez, G. Gomez, J. Gonzalez Sanchez, A. Graziano, C. Jorda, A. Lopez Virto, J. Marco, R. Marco, C. Martinez Rivero, F. Matorras, F.J. Munoz Sanchez, T. Rodrigo, A.Y. Rodríguez-Marrero, A. Ruiz-Jimeno, L. Scodellaro, M. Sobron Sanudo, I. Vila, R. Vilar Cortabitarte

CERN, European Organization for Nuclear Research, Geneva, Switzerland

D. Abbaneo, E. Auffray, G. Auzinger, P. Baillon, A.H. Ball, D. Barney, J.F. Benitez, C. Bernet⁶, G. Bianchi, P. Bloch, A. Bocci, A. Bonato, C. Botta, H. Breuker, T. Camporesi, G. Cerminara, T. Christiansen, J.A. Coarasa Perez, D. D'Enterria, A. Dabrowski, A. De Roeck, S. Di Guida, M. Dobson, N. Dupont-Sagorin, A. Elliott-Peisert, B. Frisch, W. Funk, G. Georgiou, M. Giffels, D. Gigi, K. Gill, D. Giordano, M. Giunta, F. Glege, R. Gomez-Reino Garrido, P. Govoni, S. Gowdy, R. Guida, M. Hansen, P. Harris, C. Hartl, J. Harvey, B. Hegner, A. Hinzmann, V. Innocente, P. Janot, K. Kaadze, E. Karavakis, K. Kousouris, P. Lecoq, Y.-J. Lee, P. Lenzi, C. Lourenço, T. Mäki, M. Malberti, L. Malgeri, M. Mannelli, L. Masetti, F. Meijers, S. Mersi, E. Meschi, R. Moser, M.U. Mozer, M. Mulders, P. Musella, E. Nesvold, T. Orimoto, L. Orsini, E. Palencia Cortezon, E. Perez, L. Perrozzi, A. Petrilli, A. Pfeiffer, M. Pierini, M. Pimiä, D. Piparo, G. Polese, L. Quertenmont, A. Racz, W. Reece, J. Rodrigues Antunes, G. Rolandi³³, C. Rovelli³⁴, M. Rovere, H. Sakulin, F. Santanastasio, C. Schäfer, C. Schwick, I. Segoni, S. Sekmen, A. Sharma, P. Siegrist, P. Silva, M. Simon, P. Sphicas³⁵, D. Spiga, A. Tsirou, G.I. Veres¹⁹, J.R. Vlimant, H.K. Wöhri, S.D. Worm³⁶, W.D. Zeuner

Paul Scherrer Institut, Villigen, Switzerland

W. Bertl, K. Deiters, W. Erdmann, K. Gabathuler, R. Horisberger, Q. Ingram, H.C. Kaestli, S. König, D. Kotlinski, U. Langenegger, F. Meier, D. Renker, T. Rohe, J. Sibille³⁷

Institute for Particle Physics, ETH Zurich, Zurich, Switzerland

L. Bäni, P. Bortignon, M.A. Buchmann, B. Casal, N. Chanon, A. Deisher, G. Dissertori, M. Dittmar, M. Donegà, M. Dünser, J. Eugster, K. Freudenreich, C. Grab, D. Hits, P. Lecomte, W. Lustermann, A.C. Marini, P. Martinez Ruiz del Arbol, N. Mohr, F. Moortgat, C. Nägeli³⁸, P. Nef, F. Nessi-Tedaldi, F. Pandolfi, L. Pape, F. Pauss, M. Peruzzi, F.J. Ronga, M. Rossini, L. Sala, A.K. Sanchez, A. Starodumov³⁹, B. Stieger, M. Takahashi, L. Tauscher[†], A. Thea, K. Theofilatos, D. Treille, C. Urscheler, R. Wallny, H.A. Weber, L. Wehrli

Universität Zürich, Zurich, Switzerland

C. AMSLER, V. Chiochia, S. De Visscher, C. Favaro, M. Ivova Rikova, B. Millan Mejias, P. Otiougova, P. Robmann, H. Snoek, S. Tuppeuti, M. Verzetti

National Central University, Chung-Li, Taiwan

Y.H. Chang, K.H. Chen, C.M. Kuo, S.W. Li, W. Lin, Z.K. Liu, Y.J. Lu, D. Mekterovic, A.P. Singh, R. Volpe, S.S. Yu

National Taiwan University (NTU), Taipei, Taiwan

P. Bartalini, P. Chang, Y.H. Chang, Y.W. Chang, Y. Chao, K.F. Chen, C. Dietz, U. Grundler, W.-S. Hou, Y. Hsiung, K.Y. Kao, Y.J. Lei, R.-S. Lu, D. Majumder, E. Petrakou, X. Shi, J.G. Shiu, Y.M. Tzeng, X. Wan, M. Wang

Cukurova University, Adana, Turkey

A. Adiguzel, M.N. Bakirci⁴⁰, S. Cerci⁴¹, C. Dozen, I. Dumanoglu, E. Eskut, S. Girgis, G. Gokbulut, E. Gurpinar, I. Hos, E.E. Kangal, T. Karaman, G. Karapinar⁴², A. Kayis Topaksu, G. Onengut, K. Ozdemir, S. Ozturk⁴³, A. Polatoz, K. Sogut⁴⁴, D. Sunar Cerci⁴¹, B. Tali⁴¹, H. Topakli⁴⁰, L.N. Vergili, M. Vergili

Middle East Technical University, Physics Department, Ankara, Turkey

I.V. Akin, T. Aliev, B. Bilin, S. Bilmis, M. Deniz, H. Gamsizkan, A.M. Guler, K. Ocalan, A. Ozpineci, M. Serin, R. Sever, U.E. Surat, M. Yalvac, E. Yildirim, M. Zeyrek

Bogazici University, Istanbul, Turkey

E. Gülmez, B. Isildak⁴⁵, M. Kaya⁴⁶, O. Kaya⁴⁶, S. Ozkorucuklu⁴⁷, N. Sonmez⁴⁸

Istanbul Technical University, Istanbul, Turkey

K. Cankocak

National Scientific Center, Kharkov Institute of Physics and Technology, Kharkov, Ukraine

L. Levchuk

University of Bristol, Bristol, United Kingdom

F. Bostock, J.J. Brooke, E. Clement, D. Cussans, H. Flacher, R. Frazier, J. Goldstein, M. Grimes, G.P. Heath, H.F. Heath, L. Kreczko, S. Metson, D.M. Newbold³⁶, K. Nirunpong, A. Poll, S. Senkin, V.J. Smith, T. Williams

Rutherford Appleton Laboratory, Didcot, United Kingdom

L. Basso⁴⁹, K.W. Bell, A. Belyaev⁴⁹, C. Brew, R.M. Brown, D.J.A. Cockerill, J.A. Coughlan, K. Harder, S. Harper, J. Jackson, B.W. Kennedy, E. Olaiya, D. Petyt, B.C. Radburn-Smith, C.H. Shepherd-Themistocleous, I.R. Tomalin, W.J. Womersley

Imperial College, London, United Kingdom

R. Bainbridge, G. Ball, R. Beuselinck, O. Buchmuller, D. Colling, N. Cripps, M. Cutajar, P. Dauncey, G. Davies, M. Della Negra, W. Ferguson, J. Fulcher, D. Futyan, A. Gilbert, A. Guneratne Bryer, G. Hall, Z. Hatherell, J. Hays, G. Iles, M. Jarvis, G. Karapostoli, L. Lyons, A.-M. Magnan, J. Marrouche, B. Mathias, R. Nandi, J. Nash, A. Nikitenko³⁹, A. Papageorgiou, J. Pela, M. Pesaresi, K. Petridis, M. Pioppi⁵⁰, D.M. Raymond, S. Rogerson, A. Rose, M.J. Ryan, C. Seez, P. Sharp[†], A. Sparrow, M. Stoye, A. Tapper, M. Vazquez Acosta, T. Virdee, S. Wakefield, N. Wardle, T. Whyntie

Brunel University, Uxbridge, United Kingdom

M. Chadwick, J.E. Cole, P.R. Hobson, A. Khan, P. Kyberd, D. Leggat, D. Leslie, W. Martin, I.D. Reid, P. Symonds, L. Teodorescu, M. Turner

Baylor University, Waco, USA

K. Hatakeyama, H. Liu, T. Scarborough

The University of Alabama, Tuscaloosa, USA

O. Charaf, C. Henderson, P. Rumerio

Boston University, Boston, USA

A. Avetisyan, T. Bose, C. Fantasia, A. Heister, J. St. John, P. Lawson, D. Lazic, J. Rohlf, D. Sperka, L. Sulak

Brown University, Providence, USA

J. Alimena, S. Bhattacharya, D. Cutts, A. Ferapontov, U. Heintz, S. Jabeen, G. Kukartsev, E. Laird, G. Landsberg, M. Luk, M. Narain, D. Nguyen, M. Segala, T. Sinthuprasith, T. Speer, K.V. Tsang

University of California, Davis, Davis, USA

R. Breedon, G. Breto, M. Calderon De La Barca Sanchez, S. Chauhan, M. Chertok, J. Conway, R. Conway, P.T. Cox, J. Dolen, R. Erbacher, M. Gardner, R. Houtz, W. Ko, A. Kopecky, R. Lander, T. Miceli, D. Pellett, F. Ricci-Tam, B. Rutherford, M. Searle, J. Smith, M. Squires, M. Tripathi, R. Vasquez Sierra

University of California, Los Angeles, Los Angeles, USA

V. Andreev, D. Cline, R. Cousins, J. Duris, S. Erhan, P. Everaerts, C. Farrell, J. Hauser, M. Ignatenko, C. Jarvis, C. Plager, G. Rakness, P. Schlein[†], P. Traczyk, V. Valuev, M. Weber

University of California, Riverside, Riverside, USA

J. Babb, R. Clare, M.E. Dinardo, J. Ellison, J.W. Gary, F. Giordano, G. Hanson, G.Y. Jeng⁵¹, H. Liu, O.R. Long, A. Luthra, H. Nguyen, S. Paramesvaran, J. Sturdy, S. Sumowidagdo, R. Wilken, S. Wimpenny

University of California, San Diego, La Jolla, USA

W. Andrews, J.G. Branson, G.B. Cerati, S. Cittolin, D. Evans, F. Golf, A. Holzner, R. Kelley, M. Lebourgeois, J. Letts, I. Macneill, B. Mangano, S. Padhi, C. Palmer, G. Petrucciani, M. Pieri, M. Sani, V. Sharma, S. Simon, E. Sudano, M. Tadel, Y. Tu, A. Vartak, S. Wasserbaech⁵², F. Würthwein, A. Yagil, J. Yoo

University of California, Santa Barbara, Santa Barbara, USA

D. Barge, R. Bellan, C. Campagnari, M. D'Alfonso, T. Danielson, K. Flowers, P. Geffert, J. Incandela, C. Justus, P. Kalavase, S.A. Koay, D. Kovalskyi, V. Krutelyov, S. Lowette, N. Mccoll, V. Pavlunin, F. Rebassoo, J. Ribnik, J. Richman, R. Rossin, D. Stuart, W. To, C. West

California Institute of Technology, Pasadena, USA

A. Apresyan, A. Bornheim, Y. Chen, E. Di Marco, J. Duarte, M. Gataullin, Y. Ma, A. Mott, H.B. Newman, C. Rogan, M. Spiropulu, V. Timciuc, J. Veverka, R. Wilkinson, S. Xie, Y. Yang, R.Y. Zhu

Carnegie Mellon University, Pittsburgh, USA

B. Akgun, V. Azzolini, A. Calamba, R. Carroll, T. Ferguson, Y. Iiyama, D.W. Jang, Y.F. Liu, M. Paulini, H. Vogel, I. Vorobiev

University of Colorado at Boulder, Boulder, USA

J.P. Cumalat, B.R. Drell, C.J. Edelmaier, W.T. Ford, A. Gaz, B. Heyburn, E. Luigi Lopez, J.G. Smith, K. Stenson, K.A. Ulmer, S.R. Wagner

Cornell University, Ithaca, USA

J. Alexander, A. Chatterjee, N. Eggert, L.K. Gibbons, B. Heltsley, A. Khukhunaishvili, B. Kreis, N. Mirman, G. Nicolas Kaufman, J.R. Patterson, A. Ryd, E. Salvati, W. Sun, W.D. Teo, J. Thom, J. Thompson, J. Tucker, J. Vaughan, Y. Weng, L. Winstrom, P. Wittich

Fairfield University, Fairfield, USA

D. Winn

Fermi National Accelerator Laboratory, Batavia, USA

S. Abdullin, M. Albrow, J. Anderson, L.A.T. Bauerdick, A. Beretvas, J. Berryhill, P.C. Bhat, I. Bloch, K. Burkett, J.N. Butler, V. Chetluru, H.W.K. Cheung, F. Chlebana, V.D. Elvira, I. Fisk, J. Freeman, Y. Gao, D. Green, O. Gutsche, J. Hanlon, R.M. Harris, J. Hirschauer, B. Hooberman, S. Jindariani, M. Johnson, U. Joshi, B. Kilminster, B. Klima, S. Kunori, S. Kwan, C. Leonidopoulos, J. Linacre, D. Lincoln, R. Lipton, J. Lykken, K. Maeshima, J.M. Marraffino, S. Maruyama, D. Mason, P. McBride, K. Mishra, S. Mrenna, Y. Musienko⁵³, C. Newman-Holmes, V. O'Dell, O. Prokofyev, E. Sexton-Kennedy, S. Sharma, W.J. Spalding, L. Spiegel, P. Tan, L. Taylor, S. Tkaczyk, N.V. Tran, L. Uplegger, E.W. Vaandering, R. Vidal, J. Whitmore, W. Wu, F. Yang, F. Yumiceva, J.C. Yun

University of Florida, Gainesville, USA

D. Acosta, P. Avery, D. Bourilkov, M. Chen, T. Cheng, S. Das, M. De Gruttola, G.P. Di Giovanni, D. Dobur, A. Drozdetskiy, R.D. Field, M. Fisher, Y. Fu, I.K. Furic, J. Gartner, J. Hugon, B. Kim, J. Konigsberg, A. Korytov, A. Kropivnitskaya, T. Kypreos, J.F. Low, K. Matchev, P. Milenovic⁵⁴, G. Mitselmakher, L. Muniz, R. Remington, A. Rinkevicius, P. Sellers, N. Skhirtladze, M. Snowball, J. Yelton, M. Zakaria

Florida International University, Miami, USA

V. Gaultney, S. Hewamanage, L.M. Lebolo, S. Linn, P. Markowitz, G. Martinez, J.L. Rodriguez

Florida State University, Tallahassee, USA

T. Adams, A. Askew, J. Bochenek, J. Chen, B. Diamond, S.V. Gleyzer, J. Haas, S. Hagopian, V. Hagopian, M. Jenkins, K.F. Johnson, H. Prosper, V. Veeraraghavan, M. Weinberg

Florida Institute of Technology, Melbourne, USA

M.M. Baarmand, B. Dorney, M. Hohlmann, H. Kalakhety, I. Vodopiyanov

University of Illinois at Chicago (UIC), Chicago, USA

M.R. Adams, I.M. Anghel, L. Apanasevich, Y. Bai, V.E. Bazterra, R.R. Betts, I. Bucinskaite, J. Callner, R. Cavanaugh, C. Dragoiu, O. Evdokimov, L. Gauthier, C.E. Gerber, D.J. Hofman, S. Khalatyan, F. Lacroix, M. Malek, C. O'Brien, C. Silkworth, D. Strom, N. Varelas

The University of Iowa, Iowa City, USA

U. Akgun, E.A. Albayrak, B. Bilki⁵⁵, W. Clarida, F. Duru, S. Griffiths, J.-P. Merlo, H. Mermerkaya⁵⁶, A. Mestvirishvili, A. Moeller, J. Nachtman, C.R. Newsom, E. Norbeck, Y. Onel, F. Ozok, S. Sen, E. Tiras, J. Wetzel, T. Yetkin, K. Yi

Johns Hopkins University, Baltimore, USA

B.A. Barnett, B. Blumenfeld, S. Bolognesi, D. Fehling, G. Giurgiu, A.V. Gritsan, Z.J. Guo, G. Hu, P. Maksimovic, S. Rappoccio, M. Swartz, A. Whitbeck

The University of Kansas, Lawrence, USA

P. Baringer, A. Bean, G. Benelli, O. Grachov, R.P. Kenny Iii, M. Murray, D. Noonan, S. Sanders, R. Stringer, G. Tinti, J.S. Wood, V. Zhukova

Kansas State University, Manhattan, USA

A.F. Barfuss, T. Bolton, I. Chakaberia, A. Ivanov, S. Khalil, M. Makouski, Y. Maravin, S. Shrestha, I. Svintradze

Lawrence Livermore National Laboratory, Livermore, USA

J. Gronberg, D. Lange, D. Wright

University of Maryland, College Park, USA

A. Baden, M. Boutemour, B. Calvert, S.C. Eno, J.A. Gomez, N.J. Hadley, R.G. Kellogg, M. Kirn, T. Kolberg, Y. Lu, M. Marionneau, A.C. Mignerey, K. Pedro, A. Peterman, A. Skuja, J. Temple, M.B. Tonjes, S.C. Tonwar, E. Twedt

Massachusetts Institute of Technology, Cambridge, USA

A. Apyan, G. Bauer, J. Bendavid, W. Busza, E. Butz, I.A. Cali, M. Chan, V. Dutta, G. Gomez Ceballos, M. Goncharov, K.A. Hahn, Y. Kim, M. Klute, K. Krajczar⁵⁷, W. Li, P.D. Luckey, T. Ma, S. Nahn, C. Paus, D. Ralph, C. Roland, G. Roland, M. Rudolph, G.S.F. Stephans, F. Stöckli, K. Sumorok, K. Sung, D. Velicanu, E.A. Wenger, R. Wolf, B. Wyslouch, M. Yang, Y. Yilmaz, A.S. Yoon, M. Zanetti

University of Minnesota, Minneapolis, USA

S.I. Cooper, B. Dahmes, A. De Benedetti, G. Franzoni, A. Gude, S.C. Kao, K. Klapoetke, Y. Kubota, J. Mans, N. Pastika, R. Rusack, M. Sasseville, A. Singovsky, N. Tambe, J. Turkewitz

University of Mississippi, Oxford, USA

L.M. Cremaldi, R. Kroeger, L. Perera, R. Rahmat, D.A. Sanders

University of Nebraska-Lincoln, Lincoln, USA

E. Avdeeva, K. Bloom, S. Bose, J. Butt, D.R. Claes, A. Dominguez, M. Eads, J. Keller, I. Kravchenko, J. Lazo-Flores, H. Malbouisson, S. Malik, G.R. Snow

State University of New York at Buffalo, Buffalo, USA

U. Baur, A. Godshalk, I. Iashvili, S. Jain, A. Kharchilava, A. Kumar, S.P. Shipkowski, K. Smith

Northeastern University, Boston, USA

G. Alverson, E. Barberis, D. Baumgartel, M. Chasco, J. Haley, D. Nash, D. Trocino, D. Wood, J. Zhang

Northwestern University, Evanston, USA

A. Anastassov, A. Kubik, N. Mucia, N. Odell, R.A. Ofierzynski, B. Pollack, A. Pozdnyakov, M. Schmitt, S. Stoynev, M. Velasco, S. Won

University of Notre Dame, Notre Dame, USA

L. Antonelli, D. Berry, A. Brinkerhoff, M. Hildreth, C. Jessop, D.J. Karmgard, J. Kolb, K. Lannon, W. Luo, S. Lynch, N. Marinelli, D.M. Morse, T. Pearson, M. Planer, R. Ruchti, J. Slaunwhite, N. Valls, M. Wayne, M. Wolf

The Ohio State University, Columbus, USA

B. Bylsma, L.S. Durkin, C. Hill, R. Hughes, R. Hughes, K. Kotov, T.Y. Ling, D. Puigh, M. Rodenburg, C. Vuosalo, G. Williams, B.L. Winer

Princeton University, Princeton, USA

N. Adam, E. Berry, P. Elmer, D. Gerbaudo, V. Halyo, P. Hebda, J. Hegeman, A. Hunt, P. Jindal, D. Lopes Pegna, P. Lujan, D. Marlow, T. Medvedeva, M. Mooney, J. Olsen, P. Piroué, X. Quan, A. Raval, B. Safdi, H. Saka, D. Stickland, C. Tully, J.S. Werner, A. Zuranski

University of Puerto Rico, Mayaguez, USA

J.G. Acosta, E. Brownson, X.T. Huang, A. Lopez, H. Mendez, S. Oliveros, J.E. Ramirez Vargas, A. Zatserklyaniy

Purdue University, West Lafayette, USA

E. Alagoz, V.E. Barnes, D. Benedetti, G. Bolla, D. Bortoletto, M. De Mattia, A. Everett, Z. Hu, M. Jones, O. Koybasi, M. Kress, A.T. Laasanen, N. Leonardo, V. Maroussov, P. Merkel, D.H. Miller, N. Neumeister, I. Shipsey, D. Silvers, A. Svyatkovskiy, M. Vidal Marono, H.D. Yoo, J. Zablocki, Y. Zheng

Purdue University Calumet, Hammond, USA

S. Guragain, N. Parashar

Rice University, Houston, USA

A. Adair, C. Boulahouache, K.M. Ecklund, F.J.M. Geurts, B.P. Padley, R. Redjimi, J. Roberts, J. Zabel

University of Rochester, Rochester, USA

B. Betchart, A. Bodek, Y.S. Chung, R. Covarelli, P. de Barbaro, R. Demina, Y. Eshaq, A. Garcia-Bellido, P. Goldenzweig, J. Han, A. Harel, D.C. Miner, D. Vishnevskiy, M. Zielinski

The Rockefeller University, New York, USA

A. Bhatti, R. Ciesielski, L. Demortier, K. Goulianos, G. Lungu, S. Malik, C. Mesropian

Rutgers, the State University of New Jersey, Piscataway, USA

S. Arora, A. Barker, J.P. Chou, C. Contreras-Campana, E. Contreras-Campana, D. Duggan, D. Ferencek, Y. Gershtein, R. Gray, E. Halkiadakis, D. Hidas, A. Lath, S. Panwalkar, M. Park, R. Patel, V. Rekovic, J. Robles, K. Rose, S. Salur, S. Schnetzer, C. Seitz, S. Somalwar, R. Stone, S. Thomas

University of Tennessee, Knoxville, USA

G. Cerizza, M. Hollingsworth, S. Spanier, Z.C. Yang, A. York

Texas A&M University, College Station, USA

R. Eusebi, W. Flanagan, J. Gilmore, T. Kamon⁵⁸, V. Khotilovich, R. Montalvo, I. Osipenkov, Y. Pakhotin, A. Perloff, J. Roe, A. Safonov, T. Sakuma, S. Sengupta, I. Suarez, A. Tatarinov, D. Toback

Texas Tech University, Lubbock, USA

N. Akchurin, J. Damgov, P.R. Duderov, C. Jeong, K. Kovitanggoon, S.W. Lee, T. Libeiro, Y. Roh, I. Volobouev

Vanderbilt University, Nashville, USA

E. Appelt, A.G. Delannoy, C. Florez, S. Greene, A. Gurrola, W. Johns, C. Johnston, P. Kurt, C. Maguire, A. Melo, M. Sharma, P. Sheldon, B. Snook, S. Tuo, J. Velkovska

University of Virginia, Charlottesville, USA

M.W. Arenton, M. Balazs, S. Boutle, B. Cox, B. Francis, J. Goodell, R. Hirosky, A. Ledovskoy, C. Lin, C. Neu, J. Wood, R. Yohay

Wayne State University, Detroit, USA

S. Gollapinni, R. Harr, P.E. Karchin, C. Kottachchi Kankanamge Don, P. Lamichhane, A. Sakharov

University of Wisconsin, Madison, USA

M. Anderson, M. Bachtis, D. Belknap, L. Borrello, D. Carlsmith, M. Cepeda, S. Dasu, E. Friis, L. Gray, K.S. Grogg, M. Grothe, R. Hall-Wilton, M. Herndon, A. Hervé, P. Klabbers, J. Klukas, A. Lanaro, C. Lazaridis, J. Leonard, R. Loveless, A. Mohapatra, I. Ojalvo, F. Palmonari, G.A. Pierro, I. Ross, A. Savin, W.H. Smith, J. Swanson

†: Deceased

1: Also at Vienna University of Technology, Vienna, Austria

2: Also at National Institute of Chemical Physics and Biophysics, Tallinn, Estonia

3: Also at Universidade Federal do ABC, Santo Andre, Brazil

4: Also at California Institute of Technology, Pasadena, USA

5: Also at CERN, European Organization for Nuclear Research, Geneva, Switzerland

- 6: Also at Laboratoire Leprince-Ringuet, Ecole Polytechnique, IN2P3-CNRS, Palaiseau, France
- 7: Also at Suez Canal University, Suez, Egypt
- 8: Also at Zewail City of Science and Technology, Zewail, Egypt
- 9: Also at Cairo University, Cairo, Egypt
- 10: Also at Fayoum University, El-Fayoum, Egypt
- 11: Also at British University in Egypt, Cairo, Egypt
- 12: Now at Ain Shams University, Cairo, Egypt
- 13: Also at National Centre for Nuclear Research, Swierk, Poland
- 14: Also at Université de Haute-Alsace, Mulhouse, France
- 15: Now at Joint Institute for Nuclear Research, Dubna, Russia
- 16: Also at Moscow State University, Moscow, Russia
- 17: Also at Brandenburg University of Technology, Cottbus, Germany
- 18: Also at Institute of Nuclear Research ATOMKI, Debrecen, Hungary
- 19: Also at Eötvös Loránd University, Budapest, Hungary
- 20: Also at Tata Institute of Fundamental Research - HECR, Mumbai, India
- 21: Also at University of Visva-Bharati, Santiniketan, India
- 22: Also at Sharif University of Technology, Tehran, Iran
- 23: Also at Isfahan University of Technology, Isfahan, Iran
- 24: Also at Plasma Physics Research Center, Science and Research Branch, Islamic Azad University, Tehran, Iran
- 25: Also at Facoltà Ingegneria, Università di Roma, Roma, Italy
- 26: Also at Università della Basilicata, Potenza, Italy
- 27: Also at Università degli Studi Guglielmo Marconi, Roma, Italy
- 28: Also at Università degli Studi di Siena, Siena, Italy
- 29: Also at University of Bucharest, Faculty of Physics, Bucuresti-Magurele, Romania
- 30: Also at INFN Sezione di Padova; Università di Padova; Università di Trento (Trento), Padova, Italy
- 31: Also at Faculty of Physics of University of Belgrade, Belgrade, Serbia
- 32: Also at University of California, Los Angeles, Los Angeles, USA
- 33: Also at Scuola Normale e Sezione dell'INFN, Pisa, Italy
- 34: Also at INFN Sezione di Roma; Università di Roma, Roma, Italy
- 35: Also at University of Athens, Athens, Greece
- 36: Also at Rutherford Appleton Laboratory, Didcot, United Kingdom
- 37: Also at The University of Kansas, Lawrence, USA
- 38: Also at Paul Scherrer Institut, Villigen, Switzerland
- 39: Also at Institute for Theoretical and Experimental Physics, Moscow, Russia
- 40: Also at Gaziosmanpasa University, Tokat, Turkey
- 41: Also at Adiyaman University, Adiyaman, Turkey
- 42: Also at Izmir Institute of Technology, Izmir, Turkey
- 43: Also at The University of Iowa, Iowa City, USA
- 44: Also at Mersin University, Mersin, Turkey
- 45: Also at Ozyegin University, Istanbul, Turkey
- 46: Also at Kafkas University, Kars, Turkey
- 47: Also at Suleyman Demirel University, Isparta, Turkey
- 48: Also at Ege University, Izmir, Turkey
- 49: Also at School of Physics and Astronomy, University of Southampton, Southampton, United Kingdom
- 50: Also at INFN Sezione di Perugia; Università di Perugia, Perugia, Italy
- 51: Also at University of Sydney, Sydney, Australia
- 52: Also at Utah Valley University, Orem, USA
- 53: Also at Institute for Nuclear Research, Moscow, Russia
- 54: Also at University of Belgrade, Faculty of Physics and Vinca Institute of Nuclear Sciences, Belgrade, Serbia
- 55: Also at Argonne National Laboratory, Argonne, USA
- 56: Also at Erzincan University, Erzincan, Turkey
- 57: Also at KFKI Research Institute for Particle and Nuclear Physics, Budapest, Hungary
- 58: Also at Kyungpook National University, Daegu, Korea



Observation of a new boson at a mass of 125 GeV with the CMS experiment at the LHC [☆]

CMS Collaboration ^{*}

CERN, Switzerland

This paper is dedicated to the memory of our colleagues who worked on CMS but have since passed away. In recognition of their many contributions to the achievement of this observation.

ARTICLE INFO

Article history:

Received 31 July 2012

Received in revised form 9 August 2012

Accepted 11 August 2012

Available online 18 August 2012

Editor: W.-D. Schlatter

Keywords:

CMS

Physics

Higgs

ABSTRACT

Results are presented from searches for the standard model Higgs boson in proton–proton collisions at $\sqrt{s} = 7$ and 8 TeV in the Compact Muon Solenoid experiment at the LHC, using data samples corresponding to integrated luminosities of up to 5.1 fb^{-1} at 7 TeV and 5.3 fb^{-1} at 8 TeV. The search is performed in five decay modes: $\gamma\gamma$, ZZ, W^+W^- , $\tau^+\tau^-$, and $b\bar{b}$. An excess of events is observed above the expected background, with a local significance of 5.0 standard deviations, at a mass near 125 GeV, signalling the production of a new particle. The expected significance for a standard model Higgs boson of that mass is 5.8 standard deviations. The excess is most significant in the two decay modes with the best mass resolution, $\gamma\gamma$ and ZZ; a fit to these signals gives a mass of $125.3 \pm 0.4(\text{stat.}) \pm 0.5(\text{syst.}) \text{ GeV}$. The decay to two photons indicates that the new particle is a boson with spin different from one.

© 2012 CERN. Published by Elsevier B.V. Open access under [CC BY-NC-ND license](#).

1. Introduction

The standard model (SM) of elementary particles provides a remarkably accurate description of results from many accelerator and non-accelerator based experiments. The SM comprises quarks and leptons as the building blocks of matter, and describes their interactions through the exchange of force carriers: the photon for electromagnetic interactions, the W and Z bosons for weak interactions, and the gluons for strong interactions. The electromagnetic and weak interactions are unified in the electroweak theory. Although the predictions of the SM have been extensively confirmed, the question of how the W and Z gauge bosons acquire mass whilst the photon remains massless is still open.

Nearly fifty years ago it was proposed [1–6] that spontaneous symmetry breaking in gauge theories could be achieved through the introduction of a scalar field. Applying this mechanism to the electroweak theory [7–9] through a complex scalar doublet field leads to the generation of the W and Z masses, and to the prediction of the existence of the SM Higgs boson (H). The scalar field also gives mass to the fundamental fermions through the Yukawa interaction. The mass m_H of the SM Higgs boson is not predicted by theory. However, general considerations [10–13] suggest that

m_H should be smaller than ~ 1 TeV, while precision electroweak measurements imply that $m_H < 152$ GeV at 95% confidence level (CL) [14]. Over the past twenty years, direct searches for the Higgs boson have been carried out at the LEP collider, leading to a lower bound of $m_H > 114.4$ GeV at 95% CL [15], and at the Tevatron proton–antiproton collider, excluding the mass range 162–166 GeV at 95% CL [16] and detecting an excess of events, recently reported in [17–19], in the range 120–135 GeV.

The discovery or exclusion of the SM Higgs boson is one of the primary scientific goals of the Large Hadron Collider (LHC) [20]. Previous direct searches at the LHC were based on data from proton–proton collisions corresponding to an integrated luminosity of 5 fb^{-1} collected at a centre-of-mass energy $\sqrt{s} = 7$ TeV. The CMS experiment excluded at 95% CL a range of masses from 127 to 600 GeV [21]. The ATLAS experiment excluded at 95% CL the ranges 111.4–116.6, 119.4–122.1 and 129.2–541 GeV [22]. Within the remaining allowed mass region, an excess of events near 125 GeV was reported by both experiments. In 2012 the proton–proton centre-of-mass energy was increased to 8 TeV and by the end of June an additional integrated luminosity of more than 5 fb^{-1} had been recorded by each of these experiments, thereby enhancing significantly the sensitivity of the search for the Higgs boson.

This Letter reports the results of a search for the SM Higgs boson using samples collected by the CMS experiment, comprising data recorded at $\sqrt{s} = 7$ and 8 TeV. The search is performed in

[☆] © CERN for the benefit of the CMS Collaboration.

^{*} E-mail address: cms-publication-committee-chair@cern.ch.

five decay modes, $H \rightarrow \gamma\gamma$, ZZ , W^+W^- , $\tau^+\tau^-$, and $b\bar{b}$, in the low-mass range from 110 up to 160 GeV. In this mass range the Higgs boson production cross section is predicted to have values between 23 (29) and 10 (14) pb at $\sqrt{s} = 7$ (8) TeV [23]. The natural width of the SM Higgs boson over the same range is less than 100 MeV and the width of any observed peak would be entirely dominated by instrumental mass resolution. In what follows, ℓ stands for electrons or muons, $H \rightarrow W^+W^-$ is denoted as $H \rightarrow WW$, $H \rightarrow \tau^+\tau^-$ as $H \rightarrow \tau\tau$, and $H \rightarrow b\bar{b}$ as $H \rightarrow bb$. For the final states ZZ and WW in the low-mass region, one or more of the Z or W bosons is off mass shell.

With respect to the published analyses [24–28], most analyses have been re-optimized, incorporating improvements in reconstruction performance and event selection, and mitigating the more challenging conditions due to the higher LHC intensities in 2012. The new analyses presented herein, of 8 TeV samples, and of 7 TeV samples featuring modified event selection criteria, were performed in a “blind” way: the algorithms and selection procedures were formally approved and fixed before the results from data in the signal region were examined. In the previously published analyses similar but less formal procedures were followed.

Within the context of this search for the SM Higgs boson, we report the observation of an excess of events above the expected background, consistent with the production of a new particle with mass near 125 GeV. The observed local significance is 5.0 standard deviations (σ), compared with an expected significance of 5.8σ . The evidence is strongest in the two final states with the best mass resolution, namely $H \rightarrow \gamma\gamma$ with a significance of 4.1σ and $H \rightarrow ZZ$ (with the Z bosons decaying to electrons or muons) with a significance of 3.2σ . The decay to two photons indicates that the new particle is a boson with spin different from one.

2. The CMS experiment

The possibility of detection of the SM Higgs boson played a crucial role in the conceptual design of the CMS experiment as a benchmark to test the performance of the detector [29–31]. Since the SM Higgs boson mass is not predicted by theory and its production cross section and natural width vary widely over the allowed mass range, a search was envisaged over a large range of masses and in diverse decay modes: pairs of photons, Z bosons, W bosons, τ leptons, and b quarks. Planning in view of the analysis of all these channels ensured a detector capable of observing a Higgs boson over a broad mass range and able to detect most potential signals of new physics.

The central feature of the CMS apparatus [32] is a superconducting solenoid of 6 m internal diameter, which provides a magnetic field of 3.8 T. Within the field volume are a silicon pixel and strip tracker, a lead tungstate crystal electromagnetic calorimeter (ECAL), and a brass/scintillator hadron calorimeter (HCAL). Muons are measured in gas-ionization detectors embedded in the steel flux-return yoke. Extensive forward calorimeters complement the coverage provided by the barrel and endcap detectors.

Charged particles are tracked within the pseudorapidity range $|\eta| < 2.5$, where $\eta = -\ln[\tan(\theta/2)]$, and θ is the polar angle measured from the positive z axis (along the anticlockwise beam direction). The silicon pixel tracker comprises 66 million $100 \times 150 \mu\text{m}^2$ pixels, arranged in three barrel layers and two disks at each end. The silicon strip tracker, organized in ten barrel layers and twelve disks at each end, comprises 9.3 million strips with pitch between 80 and $180 \mu\text{m}$, with a total silicon surface area of 198 m^2 . The tracker has a track-finding efficiency larger than 99% for muons with transverse momentum p_T greater than 1 GeV and a transverse momentum resolution between 1.5 and 2.5% for charged

tracks of $p_T \sim 100$ GeV in the central region ($|\eta| < 1.5$). Measurements of the impact parameters of charged tracks and secondary vertices are used to identify jets that are likely to contain the hadronisation and decay products of b quarks (“ b jets”). A b -jet tagging efficiency of more than 50% is achieved with a rejection factor for light-quark jets of ~ 200 , as measured in $t\bar{t}$ events in data [33]. The dimuon mass resolution at the Υ mass, dominated by instrumental effects, is measured to be 0.6% in the barrel region [34], consistent with the design goal.

The ECAL is a fine-grained hermetic calorimeter consisting of 75 848 lead tungstate crystals, arranged in a quasi-projective geometry and distributed in a barrel region ($|\eta| < 1.48$) and two endcaps that extend up to $|\eta| = 3.0$. The front-face cross section of the crystals is $22 \times 22 \text{ mm}^2$ in the barrel region and $28.6 \times 28.6 \text{ mm}^2$ in the endcaps. Preshower detectors consisting of two planes of silicon sensors interleaved with a total of three radiation lengths of lead absorber are located in front of the endcaps. Electromagnetic showers are very narrow in lead tungstate (Molière radius of 21 mm), helping in particle identification and in the implementation of isolation criteria. In the central barrel region the energy resolution of electrons that do not radiate substantially in the tracker material indicates that the resolution of unconverted photons is consistent with design goals. For such photons the diphoton mass resolution is 1.1 GeV at a mass of 125 GeV.

The HCAL barrel and endcaps are sampling calorimeters consisting of brass and scintillator plates, covering $|\eta| < 3.0$. Their thickness varies from 7 to 11 interaction lengths, depending on η ; a scintillator “tail catcher” placed outside the coil of the solenoid, just in front of the innermost muon detector, extends the instrumented thickness to more than 10 interaction lengths everywhere. Iron forward calorimeters with quartz fibers, read out by photomultipliers, extend the calorimeter coverage up to $|\eta| = 5.0$.

Muons are measured in the range $|\eta| < 2.4$, with detection planes based on three technologies: drift tubes ($|\eta| < 1.2$), cathode strip chambers ($0.9 < |\eta| < 2.4$), and resistive plate chambers ($|\eta| < 1.6$). The first two technologies provide a precise position measurement and trigger whilst the third provides precise timing information as well as a second and independent trigger. The muon system consists of four stations in the barrel and endcaps, designed to ensure robust triggering and detection of muons over a large angular range. In the barrel region each muon station consists of twelve drift-tube layers, except for the outermost station, which has eight layers. In the endcaps, each muon station consists of six detection planes. The precision of the r - ϕ measurement is $100 \mu\text{m}$ in the drift tubes and varies from 60 to $140 \mu\text{m}$ in the cathode strip chambers.

The CMS trigger and data acquisition systems ensure that potentially interesting events are recorded with high efficiency. The first level (L1) trigger, comprising the calorimeter, muon, and global trigger processors, uses coarse-granularity information to select the most interesting events in less than $4 \mu\text{s}$. The detector data are pipelined to ensure negligible deadtime up to a L1 rate of 100 kHz. After L1 triggering, data are transferred from the readout electronics of all subdetectors, through the readout network, to the high-level-trigger processor farm, which operates offline-quality reconstruction algorithms to decrease the event rate to around 0.5 kHz, before data storage.

The CMS experiment employs a highly distributed computing infrastructure, with a primary Tier-0 centre at CERN, supplemented by seven Tier-1, more than 50 Tier-2, and many Tier-3 centres at national laboratories and universities throughout the world. The CMS software running on this high-performance computing system executes numerous tasks, including the reconstruction and analysis of the collected data, as well as the generation and detailed detector simulation of Monte Carlo (MC) event samples.

3. Event reconstruction

The CMS “particle-flow” event description algorithm [35,36] is used to reconstruct and identify each single particle with an optimized combination of all subdetector information. In this process, the identification of the particle (photon, electron, muon, charged hadron, neutral hadron) plays an important role in the determination of the particle momentum. The reconstructed particles are henceforth referred to as objects.

Jets are reconstructed by clustering the particle-flow objects with the anti- k_T algorithm [37] using a distance parameter of 0.5. Additional selection criteria are applied to each event to remove spurious features originating from isolated noise patterns in certain HCAL regions, and from anomalous signals caused by particles depositing energy in the silicon avalanche photodiodes used in the ECAL barrel region. The average number of pp interactions per LHC bunch crossing is estimated to be about 9 and 19 in the 7 TeV (2011) and 8 TeV (2012) data sets, respectively. Energy from overlapping pp interactions (“pileup”), and from the underlying event, is subtracted using the FASTJET technique [38–40], which is based on the calculation of the η -dependent transverse momentum density, evaluated on an event-by-event basis.

The jet momentum is determined as the vector sum of all particle momenta in the jet. Jet energy corrections are derived from simulation studies and from in situ measurements using the energy balance of dijet and Z/γ + jet events [41]. These corrections are between 5% and 10% of the true momentum over the entire p_T spectrum and detector acceptance. The jet momentum resolution achieved is $\sigma(p_T)/p_T = 85\%/\sqrt{p_T/\text{GeV}} \oplus 4\%$ for central jets. A selection is applied to separate jets originating in the primary interaction from those due to energy deposits associated with pileup. The discrimination is based on the differences in the jet shapes, in the relative multiplicity of charged and neutral components, and in the fraction of transverse momentum carried by the hardest components. Within the tracker acceptance the jet tracks are also required to be consistent with originating at the primary vertex.

The missing transverse energy vector is taken as the negative vector sum of all particle transverse momenta, and its magnitude is referred to as E_T^{miss} . The typical missing transverse energy resolution is around $0.5\sqrt{\sum E_T}$ GeV [42], where $\sum E_T$ is the scalar sum of all particle transverse momenta in GeV.

The energy deposited in the ECAL is clustered both with general clustering algorithms [43] and with algorithms that constrain the clusters in η and ϕ to the shapes expected from electrons and photons with high p_T [44]. These specialised algorithms are used to cluster electromagnetic showers without any hypothesis regarding whether the particle originating from the interaction point was a photon or an electron; doing this for electrons from $Z \rightarrow ee$ events provides a measurement of the photon trigger, reconstruction, and identification efficiencies, as well as of the photon energy scale and resolution. The width of the reconstructed Z resonance is used to quantify the performance of the ECAL, using decays to two electrons whose energies are measured using the ECAL alone, with only their directions being determined from the tracks. In the 7 TeV data set, the dielectron mass resolution at the Z boson mass is 1.56 GeV in the barrel and 2.57 GeV in the endcaps, while in the 8 TeV sample, reconstructed with preliminary calibration constants, the corresponding values are 1.61 and 3.75 GeV. For electrons, the reconstruction combines the clusters in the ECAL and the trajectory in the silicon tracker [45]. Trajectories in the tracker volume are reconstructed using a model of electron energy loss and fitted with a Gaussian sum filter [46]. The electron momentum is determined from the combination of ECAL and tracker measurements.

Table 1

Summary of the subchannels, or categories, used in the analysis of each decay mode.

Decay mode	Production tagging	No. of subchannels	m_H range (GeV)	Int. Lum. (fb^{-1})	
				7 TeV	8 TeV
$\gamma\gamma$	untagged	4	110–150	5.1	5.3
	dijet (VBF)	1 or 2			
ZZ	untagged	3	110–160	5.1	5.3
	WW	4			
$\tau\tau$	untagged	16	110–145	4.9	5.1
	dijet (VBF)	4			
bb	lepton, E_T^{miss} (VH)	10	110–135	5.0	5.1

Muon candidates are reconstructed with two algorithms, one in which the tracks in the silicon detector are matched to segments in the muon chambers, and another in which a combined fit is performed to the signals found in both the silicon tracker and muon systems [43]. The efficiency to reconstruct a muon of $p_T > 5$ GeV is larger than 95%, while the probability to misidentify a hadron as a muon is below 0.1%. For $p_T > 200$ GeV the precision of the momentum measurement improves when the silicon tracker signals are complemented with the information from the muon chambers.

Selection based on isolation of lepton and photon objects is used extensively. A requirement is placed on the scalar sum of the transverse momenta of the particles reconstructed within a distance ΔR_{max} of the object, sometimes normalised to the p_T of the object. The distance ΔR is defined as $\Delta R = \sqrt{(\Delta\eta)^2 + (\Delta\phi)^2}$, where $\Delta\eta$ and $\Delta\phi$ are the pseudorapidity and azimuthal angle differences between the particle direction and the object direction. Typically ΔR_{max} is chosen to be 0.3 or 0.4.

The measurement of the integrated luminosity in CMS is based on a pixel cluster counting method, which exploits the large number of silicon pixels, and hence their low occupancy in a pp collision [47]. The cross section normalisation is derived from van der Meer scans [48]. The uncertainties in the luminosity measurements are 2.2% and 4.4% for the 7 TeV and 8 TeV data sets, respectively.

4. Searches for the standard model Higgs boson

Initial phenomenological discussions of Higgs boson production and decay can be found in Refs. [49–56]. Four main mechanisms are predicted for Higgs boson production in pp collisions: the gluon–gluon fusion mechanism, which has the largest cross section, followed in turn by vector-boson fusion (VBF), associated WH and ZH production (VH), and production in association with top quarks ($t\bar{t}H$). The cross sections for the individual production mechanisms and the decay branching fractions, together with their uncertainties, have been computed following Refs. [57–101] and are compiled in Refs. [23,102].

The particular set of sensitive decay modes of the SM Higgs boson depends strongly on m_H . The results presented in this Letter are based on the five most sensitive decay modes in the low-mass region: $H \rightarrow \gamma\gamma$; $H \rightarrow ZZ$ followed by ZZ decays to 4ℓ ; $H \rightarrow WW$ followed by decays to $2\ell 2\nu$; $H \rightarrow \tau\tau$ followed by at least one leptonic τ decay; and $H \rightarrow bb$ followed by b-quark fragmentation into jets. This list is presented in Table 1 and comprises the full set of decay modes and subchannels, or categories, for which both the 7 and 8 TeV data sets have been analysed. Other lower sensitivity subchannels ($t\bar{t}H$, $H \rightarrow bb$; W/ZH, $H \rightarrow \tau\tau$; W/ZH, $H \rightarrow WW \rightarrow 2\ell 2\nu$; $H \rightarrow ZZ \rightarrow 2\ell 2q$) have also been studied, so far only in the 7 TeV data, and are not included here. Adding these analyses in the combination results in an improvement of 0.1σ in the overall expected local significance at $m_H = 125$ GeV.

For a given value of m_H , the search sensitivity depends on the production cross section, the decay branching fraction into the chosen final state, the signal selection efficiency, the mass resolution, and the level of background from identical or similar final-state topologies.

Samples of MC events used to represent signal and background are fully simulated using `GEANT4` [103]. The simulations include pileup interactions matching the distribution of the number of such interactions observed in data. The description of the Higgs boson signal is obtained from MC simulation using, for most of the decay modes and production processes, the next-to-leading-order (NLO) matrix-element generator `POWHEG` [104,105], interfaced with `PYTHIA 6.4` [106]. For the dominant gluon–gluon fusion process, the transverse momentum spectrum of the Higgs boson in the 7 TeV MC samples is reweighted to the next-to-next-to-leading-logarithmic (NNLL) + NLO distribution computed with `HqT` [71,72,107] and `FEHiPro` [108,109], except in the $H \rightarrow ZZ$ analysis, where the effect is marginal. The agreement of the p_T spectrum in the simulation at 8 TeV with the NNLL + NLO distribution makes reweighting unnecessary. The improved agreement is due to a modification in the `POWHEG` setup recommended in Ref. [102]. The simulation of associated-production signal samples uses `PYTHIA` and all signal samples for $H \rightarrow bb$ are made using `POWHEG` interfaced to `HERWIG++` [110]. Samples used for background studies are generated with `PYTHIA`, `POWHEG`, and `MADGRAPH` [111], and the normalisations are obtained from the best available NNLO or NLO calculations. The uncertainty in the signal cross section related to the choice of parton distribution functions is determined with the `PDF4LHC` prescription [96–100].

The overall statistical methodology [112] used in this Letter was developed by the CMS and ATLAS Collaborations in the context of the LHC Higgs Combination Group. A more concise summary of CMS usage in the search for a Higgs boson is given in Ref. [21]. The modified frequentist criterion CL_s [113,114] is used for the calculation of exclusion limits. Systematic uncertainties are incorporated as nuisance parameters and are treated according to the frequentist paradigm. The combination of searches requires simultaneous analysis of the data selected by all individual analyses, accounting for all statistical and systematic uncertainties and their correlations. The probability for a background fluctuation to be at least as large as the observed maximum excess is termed the local p -value, and that for an excess *anywhere* in a specified mass range the global p -value. This probability can be evaluated by generating sets of simulated data incorporating all correlations between analyses optimized for different Higgs boson masses. The global p -value (for the specified region) is greater than the local p -value, and this fact is often referred to as the look-elsewhere effect (LEE) [115]. Both the local and global p -values can be expressed as a corresponding number of standard deviations using the one-sided Gaussian tail convention. The magnitude of a possible Higgs boson signal is characterised by the production cross section times the relevant branching fractions, relative to the SM expectation, denoted σ/σ_{SM} and referred to as the signal strength. The results presented in this Letter are obtained using asymptotic formulae [116], including updates recently introduced in the `ROOTSTATS` package [117].

Fig. 1 shows the expected local p -values in the mass range 110–145 GeV for the five decay modes reported here. The expected significance of a SM Higgs boson signal at $m_H = 125$ GeV when the five decay modes are combined is 5.6σ . The highest sensitivity in this mass range is achieved in the ZZ , $\gamma\gamma$, and WW channels. Because of the excellent mass resolution (1–2 GeV) achieved in the $\gamma\gamma$ and ZZ channels, they play a special role in the low-mass region, where the natural width of the SM Higgs boson is predicted to be less than 100 MeV. The expected signature in these channels

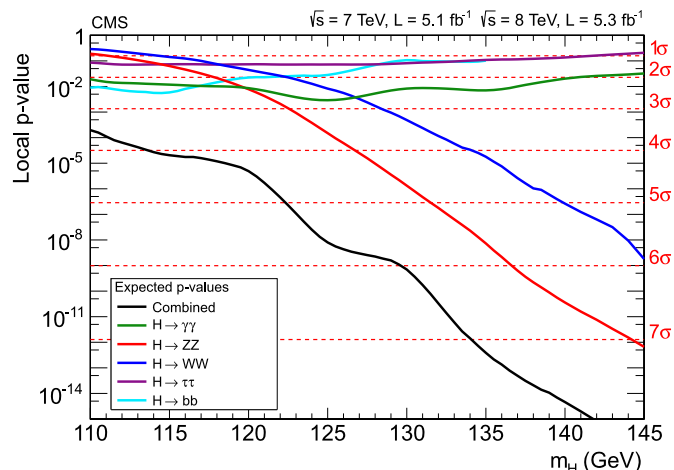


Fig. 1. Expected local p -values for a SM Higgs boson as a function of m_H , for the decay modes $\gamma\gamma$, ZZ , WW , $\tau\tau$, and bb and their combination.

is therefore a narrow resonance above background, with a width consistent with the detector resolution.

5. Decay modes with high mass resolution

5.1. $H \rightarrow \gamma\gamma$

In the $H \rightarrow \gamma\gamma$ analysis a search is made for a narrow peak in the diphoton invariant mass distribution in the range 110–150 GeV, on a large irreducible background from QCD production of two photons. There is also a reducible background where one or more of the reconstructed photon candidates originate from misidentification of jet fragments. Early detailed studies indicated this to be one of the most promising channels in the search for a SM Higgs boson in the low-mass range [118].

To enhance the sensitivity of the analysis, candidate diphoton events are separated into mutually exclusive categories of different expected signal-to-background ratios, based on the properties of the reconstructed photons and on the presence of two jets satisfying criteria aimed at selecting events in which a Higgs boson is produced through the VBF process. The analysis uses multivariate techniques for the selection and classification of the events. As an independent cross-check, an analysis is also performed that is almost identical to the one described in Ref. [24], using simpler criteria based on the properties of the reconstructed photons to select and classify events. The multivariate analysis achieves 15% higher sensitivity than the cross-check analysis.

The reconstructed primary vertex that most probably corresponds to the interaction vertex of the diphoton candidate is identified using the kinematic properties of the tracks associated with that vertex and their correlation with the diphoton kinematics. In addition, if either of the photons converts and the tracks from the conversion are reconstructed and identified, the direction of the converted photon contributes to the identification of the hard-scattering vertex. More details can be found in Ref. [24].

The event selection requires two photon candidates satisfying p_T requirements and “loose” photon identification criteria. These photons must be reconstructed within the fiducial region, $|\eta| < 2.5$, excluding the barrel–endcap transition region, $1.44 < |\eta| < 1.57$. A p_T threshold of $m_{\gamma\gamma}/3$ ($m_{\gamma\gamma}/4$) is applied to the photon leading (subleading) in p_T , where $m_{\gamma\gamma}$ is the diphoton invariant mass. Scaling the p_T thresholds in this way avoids distortion of the shape of the $m_{\gamma\gamma}$ distribution. In the case of events passing the dijet selection, the requirement on the leading photon

Table 2
Expected numbers of SM Higgs boson events ($m_H = 125$ GeV) and estimated background (at $m_{\gamma\gamma} = 125$ GeV) for all event categories of the 7 and 8 TeV data sets. There are two dijet-tagged categories for the 8 TeV data as described in the text, and for both data sets the remaining untagged events are separated into four categories labelled here BDT 0–3, BDT 0 having the largest expected signal-to-background ratio. The composition of the SM Higgs boson signal in terms of the production processes, and its mass resolution, are also given.

Event categories		SM Higgs boson expected signal ($m_H = 125$ GeV)						Background $m_{\gamma\gamma} = 125$ GeV (events/GeV)	
		Events	ggH	VBF	VH	ttH	σ_{eff} (GeV)		FWHM/2.35 (GeV)
7 TeV, 5.1 fb ⁻¹	BDT 0	3.2	61%	17%	19%	3%	1.21	1.14	3.3 ± 0.4
	BDT 1	16.3	88%	6%	6%	–	1.26	1.08	37.5 ± 1.3
	BDT 2	21.5	92%	4%	4%	–	1.59	1.32	74.8 ± 1.9
	BDT 3	32.8	92%	4%	4%	–	2.47	2.07	193.6 ± 3.0
	Dijet tag	2.9	27%	72%	1%	–	1.73	1.37	1.7 ± 0.2
8 TeV, 5.3 fb ⁻¹	BDT 0	6.1	68%	12%	16%	4%	1.38	1.23	7.4 ± 0.6
	BDT 1	21.0	87%	6%	6%	1%	1.53	1.31	54.7 ± 1.5
	BDT 2	30.2	92%	4%	4%	–	1.94	1.55	115.2 ± 2.3
	BDT 3	40.0	92%	4%	4%	–	2.86	2.35	256.5 ± 3.4
	Dijet tight	2.6	23%	77%	–	–	2.06	1.57	1.3 ± 0.2
	Dijet loose	3.0	53%	45%	2%	–	1.95	1.48	3.7 ± 0.4

is increased to $m_{\gamma\gamma}/2$, further reducing background with negligible loss of signal.

Jet selection criteria are applied to the two jets of largest p_T in the event within $|\eta| < 4.7$. The jet selection requirements are optimized using simulated VBF signal and diphoton background events. The p_T thresholds for the two jets are 30 and 20 GeV, and their η separation is required to be greater than 3.5. The dijet invariant mass is required to be greater than 350 and 250 GeV for the 7 and 8 TeV data sets, respectively. The lower dijet invariant mass requirement for the 8 TeV data set reflects the fact that for the analysis of that data set, the dijet event category is divided into two to increase the search sensitivity. This division creates a second “tight” dijet-tagged category in which the dijet invariant mass must be greater than 500 GeV and both jets must have $p_T > 30$ GeV. Two additional selection criteria, relating the dijet to the diphoton system, are applied: the difference between the average pseudorapidity of the two jets and the pseudorapidity of the diphoton system is required to be less than 2.5, and the difference in azimuthal angle between the diphoton system and the dijet system is required to be greater than 2.6 radians.

A multivariate regression is used to extract the photon energy and a photon-by-photon estimate of the uncertainty in that measurement. The calibration of the photon energy scale uses the Z boson mass as a reference; ECAL showers coming from electrons in $Z \rightarrow ee$ events are clustered and reconstructed in exactly the same way as photon showers. The photon selection efficiency, energy resolution, and associated systematic uncertainties are estimated from data, using $Z \rightarrow ee$ events to derive data/simulation correction factors. The jet reconstruction efficiency, the efficiency to correctly locate the vertex position, and the trigger efficiency, together with the corresponding systematic uncertainties, are also evaluated from data.

For the multivariate analysis, a boosted decision tree (BDT) [119,120] is trained to give a high output value (score) for signal-like events and for events with good diphoton invariant mass resolution, based on the following observables: (i) the photon quality determined from electromagnetic shower shape and isolation variables; (ii) the expected mass resolution; (iii) the per-event estimate of the probability of locating the diphoton vertex within 10 mm of its true location along the beam direction; and (iv) kinematic characteristics of the photons and the diphoton system. The kinematic variables are constructed so as to contain no information about the invariant mass of the diphoton system. The diphoton events not satisfying the dijet selection are classified into five categories based on the output of the BDT, with category boundaries optimized for sensitivity to a SM Higgs boson. Events in the category with small-

est expected signal-to-background ratio are rejected, leaving four categories of events. Dijet-tagged events with BDT scores smaller than the threshold for the fourth category are also rejected. Simulation studies indicate that the background in the selected event categories is dominated by the irreducible background from QCD production of two photons and that fewer than 30% of the diphoton events used in the analysis contain one or more misidentified photons (predominantly from $\gamma + \text{jet}$ production).

Table 2 shows the expected number of signal events in each event category for a SM Higgs boson (of $m_H = 125$ GeV), and the background at $m_{\gamma\gamma} = 125$ GeV, estimated from the fit described below. The estimated mass resolution is also shown, measured both by σ_{eff} , half the minimum width containing 68% of the signal events, and by the full width at half maximum (FWHM). A large variation in the expected signal-to-background ratio between the categories can be seen, although as a consequence of the optimization of the category boundaries the expected signal significances in each category are rather similar. The differences in the relative signal-to-background ratio between the categories are almost independent of m_H .

The background is estimated from data, without the use of MC simulation, by fitting the diphoton invariant mass distribution in each of the categories in a range ($100 < m_{\gamma\gamma} < 180$ GeV) extending slightly above and below that in which the search is performed. The choices of the function used to model the background and of the fit range are made based on a study of the possible bias in the measured signal strength. Polynomial functions are used. The degree is chosen by requiring that the potential bias be at least a factor of 5 smaller than the statistical accuracy of the fit prediction. The required polynomial degree ranges from 3 to 5.

A further independent analysis (referred to as the sideband background model) is performed using a different approach to the background modelling. Its sensitivity is very similar to that of the standard analysis. It employs a fit to the output of an additional BDT that takes as input the diphoton invariant mass and the diphoton BDT output, and uses a background model derived from the sidebands of the invariant mass distribution. A fit to the diphoton invariant mass distribution is used to obtain the background normalisation. This fit is of a power law and excludes a window of width $\pm 2\% \times m_H$ around the mass hypothesis. The methodology allows a systematic uncertainty to be assigned to the fit shape.

The expected 95% CL upper limit on the signal strength $\sigma/\sigma_{\text{SM}}$, in the background-only hypothesis, for the combined 7 and 8 TeV data, is less than 1.0 in the range $110 < m_H < 140$ GeV, with a value of 0.76 at $m_H = 125$ GeV. The observed limit indicates the

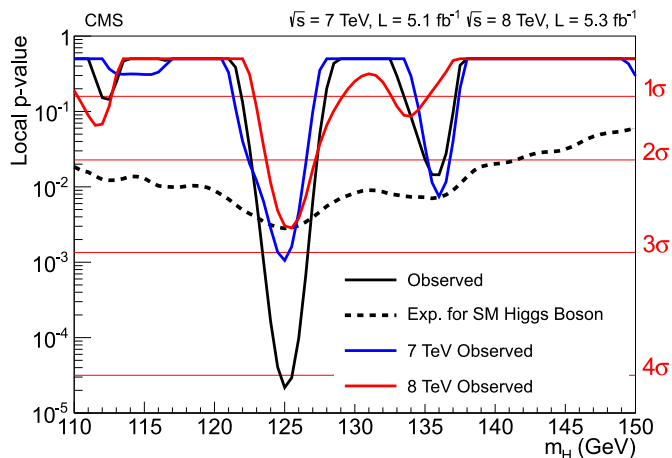


Fig. 2. The local p -value as a function of m_H in the $\gamma\gamma$ decay mode for the combined 7 and 8 TeV data sets. The additional lines show the values for the two data sets taken individually. The dashed line shows the expected local p -value for the combined data sets, should a SM Higgs boson exist with mass m_H .

presence of a significant excess at $m_H = 125$ GeV in both the 7 and 8 TeV data. The features of the observed limit are confirmed by the independent sideband-background-model and cross-check analyses. The local p -value is shown as a function of m_H in Fig. 2 for the 7 and 8 TeV data, and for their combination. The expected (observed) local p -value for a SM Higgs boson of mass 125 GeV corresponds to $2.8(4.1)\sigma$. In the sideband-background-model and cross-check analyses, the observed local p -values for $m_H = 125$ GeV correspond to 4.6 and 3.7σ , respectively. The best-fit signal strength for a SM Higgs boson mass hypothesis of 125 GeV is $\sigma/\sigma_{\text{SM}} = 1.6 \pm 0.4$.

In order to illustrate, in the $m_{\gamma\gamma}$ distribution, the significance given by the statistical methods, it is necessary to take into account the large differences in the expected signal-to-background ratios of the event categories shown in Table 2. The events are weighted according to the category in which they fall. A weight proportional to $S/(S+B)$ is used, as suggested in Ref. [121], where S and B are the number of signal and background events, respectively, calculated from the simultaneous signal-plus-background fit to all categories (with varying overall signal strength) and integrating over a $2\sigma_{\text{eff}}$ wide window, in each category, centred on 125 GeV. Fig. 3 shows the data, the signal model, and the background model, all weighted. The weights are normalised such that the integral of the weighted signal model matches the number of signal events given by the best fit. The unweighted distribution, using the same binning but in a more restricted mass range, is shown as an inset. The excess at 125 GeV is evident in both the weighted and unweighted distributions.

5.2. $H \rightarrow ZZ$

In the $H \rightarrow ZZ \rightarrow 4\ell$ decay mode a search is made for a narrow four-lepton mass peak in the presence of a small continuum background. Early detailed studies outlined the promise of this mode over a wide range of Higgs boson masses [122]. Only the search in the range 110–160 GeV is reported here. Since there are differences in the reducible background rates and mass resolutions between the subchannels $4e$, 4μ , and $2e2\mu$, they are analysed separately. The background sources include an irreducible four-lepton contribution from direct ZZ production via $q\bar{q}$ and gluon-gluon processes. Reducible contributions arise from $Z + b\bar{b}$ and $t\bar{t}$ production where the final states contain two isolated leptons and two b -quark jets producing secondary leptons. Additional background

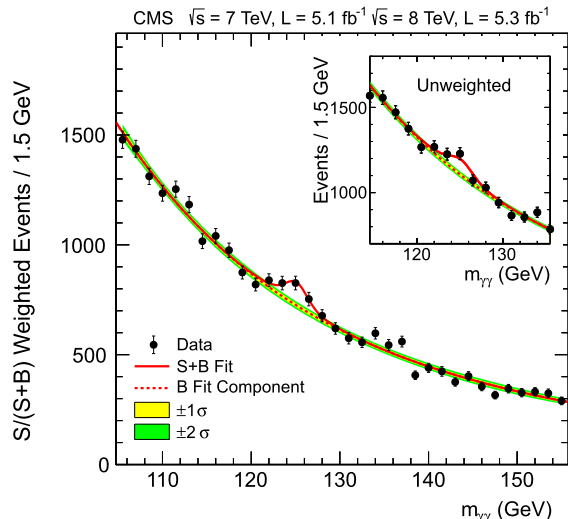


Fig. 3. The diphoton invariant mass distribution with each event weighted by the $S/(S+B)$ value of its category. The lines represent the fitted background and signal, and the coloured bands represent the ± 1 and ± 2 standard deviation uncertainties in the background estimate. The inset shows the central part of the unweighted invariant mass distribution. (For interpretation of the references to colour in this figure legend, the reader is referred to the web version of this Letter.)

arises from $Z + \text{jets}$ and $WZ + \text{jets}$ events where jets are misidentified as leptons. Compared to the analysis reported in Ref. [25], the present analysis employs improved muon reconstruction, improved lepton identification and isolation, and a kinematic discriminant exploiting the decay kinematics expected for the signal events. An algorithm to recover final-state radiation (FSR) photons has also been deployed.

Electrons are required to have $p_T > 7$ GeV and $|\eta| < 2.5$. The corresponding requirements for muons are $p_T > 5$ GeV and $|\eta| < 2.4$. Electrons are selected using a multivariate identifier trained using a sample of $W + \text{jets}$ events, and the working point is optimized using $Z + \text{jets}$ events. Both muons and electrons are required to be isolated. The combined reconstruction and selection efficiency is measured using electrons and muons in Z boson decays. Muon reconstruction and identification efficiency for muons with $p_T < 15$ GeV is measured using J/ψ decays.

The electron or muon pairs from Z boson decays are required to originate from the same primary vertex. This is ensured by requiring that the significance of the impact parameter with respect to the event vertex satisfy $|S_{\text{IP}}| < 4$ for each lepton, where $S_{\text{IP}} = l/\sigma_l$, l is the three-dimensional lepton impact parameter at the point of closest approach to the vertex, and σ_l its uncertainty.

Final-state radiation from the leptons is recovered and included in the computation of the lepton-pair invariant mass. The FSR recovery is tuned using simulated samples of $ZZ \rightarrow 4\ell$ and tested on data samples of Z boson decays to electrons and muons. Photons reconstructed within $|\eta| < 2.4$ are considered as possibly due to FSR. The photons must satisfy the following requirements. They must be within $\Delta R < 0.07$ of a muon and have $p_T^\gamma > 2$ GeV (most photon showers within this distance of an electron having already been automatically clustered with the electron shower); or if their distance from a lepton is in the range $0.07 < \Delta R < 0.5$, they must satisfy $p_T^\gamma > 4$ GeV, and be isolated within $\Delta R = 0.3$. Such photon candidates are combined with the lepton if the resulting three-body invariant mass is less than 100 GeV and closer to the Z boson mass than the mass before the addition of the photon.

The event selection requires two pairs of same-flavour, oppositely charged leptons. The pair with invariant mass closest to the Z boson mass is required to have a mass in the range 40–120 GeV

Table 3

The number of selected events, compared to the expected background yields and expected number of signal events ($m_H = 125$ GeV) for each final state in the $H \rightarrow ZZ$ analysis. The estimates of the $Z + X$ background are based on data. These results are given for the mass range from 110 to 160 GeV. The total background and the observed numbers of events are also shown for the three bins (“signal region”) of Fig. 4 where an excess is seen ($121.5 < m_{4\ell} < 130.5$ GeV).

Channel	4e	4 μ	2e2 μ	4 ℓ
ZZ background	2.7 ± 0.3	5.7 ± 0.6	7.2 ± 0.8	15.6 ± 1.4
Z + X	$1.2^{+1.1}_{-0.8}$	$0.9^{+0.7}_{-0.6}$	$2.3^{+1.8}_{-1.4}$	$4.4^{+2.2}_{-1.7}$
All backgrounds (110 < $m_{4\ell}$ < 160 GeV)	4.0 ± 1.0	6.6 ± 0.9	9.7 ± 1.8	20 ± 3
Observed (110 < $m_{4\ell}$ < 160 GeV)	6	6	9	21
Signal ($m_H = 125$ GeV)	1.36 ± 0.22	2.74 ± 0.32	3.44 ± 0.44	7.54 ± 0.78
All backgrounds (signal region)	0.7 ± 0.2	1.3 ± 0.1	1.9 ± 0.3	3.8 ± 0.5
Observed (signal region)	1	3	5	9

and the other pair is required to have a mass in the range 12–120 GeV. The ZZ background is evaluated from MC simulation studies. Two different approaches are employed to estimate the reducible and instrumental backgrounds from data. Both start by selecting events in a background control region, well separated from the signal region, by relaxing the isolation and identification criteria for two same-flavour reconstructed leptons. In the first approach, the additional pair of leptons is required to have the same charge (to avoid signal contamination) while in the second, two opposite-charge leptons failing the isolation and identification criteria are required. In addition, a control region with three passing leptons and one failing lepton is used to estimate contributions from backgrounds with three prompt leptons and one misidentified lepton. The event rates measured in the background control region are extrapolated to the signal region using the measured probability for a reconstructed lepton to pass the isolation and identification requirements. This probability is measured in an independent sample. Within uncertainties, comparable background counts in the signal region are estimated by both methods.

The number of selected ZZ \rightarrow 4 ℓ candidate events in the mass range $110 < m_{4\ell} < 160$ GeV, in each of the three final states, is given in Table 3, where $m_{4\ell}$ is the four-lepton invariant mass. The number of predicted background events, in each of the three final states, and their uncertainties are also given, together with the number of signal events expected from a SM Higgs boson of $m_H = 125$ GeV. The $m_{4\ell}$ distribution is shown in Fig. 4. There is a clear peak at the Z boson mass where the decay $Z \rightarrow 4\ell$ is reconstructed. This feature of the data is well reproduced by the background estimation. The figure also shows an excess of events above the expected background around 125 GeV. The total background and the numbers of events observed in the three bins where an excess is seen are also shown in Table 3. The combined signal reconstruction and selection efficiency, with respect to the $m_H = 125$ GeV generated signal with $m_{\ell\ell} > 1$ GeV as the only cut, is 18% for the 4e channel, 40% for the 4 μ channel, and 27% for the 2e2 μ channel.

The kinematics of the $H \rightarrow ZZ \rightarrow 4\ell$ process in its centre-of-mass frame, for a given invariant mass of the four-lepton system, is fully described by five angles and the invariant masses of the two lepton pairs [123–125]. These seven variables provide significant discriminating power between signal and background. The momentum of the ZZ system may further differentiate signal from background, but would introduce dependence on the production mechanism, and on the modelling of the QCD effects, and is therefore not considered here. A kinematic discriminant is constructed based on the probability ratio of the signal and background hypotheses, $K_D = \mathcal{P}_{\text{sig}} / (\mathcal{P}_{\text{sig}} + \mathcal{P}_{\text{bkg}})$, as described in Ref. [126]. The likelihood ratio is defined for each value of $m_{4\ell}$. For the signal, the phase-space and Z propagator terms [127] are included in a fully analytic parameterization [124], while the background probability

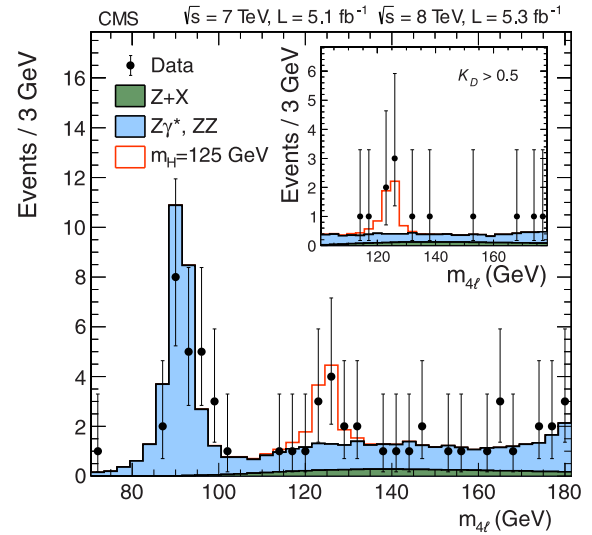


Fig. 4. Distribution of the four-lepton invariant mass for the $ZZ \rightarrow 4\ell$ analysis. The points represent the data, the filled histograms represent the background, and the open histogram shows the signal expectation for a Higgs boson of mass $m_H = 125$ GeV, added to the background expectation. The inset shows the $m_{4\ell}$ distribution after selection of events with $K_D > 0.5$, as described in the text.

is tabulated using a simulation of the $q\bar{q} \rightarrow ZZ/Z\gamma$ process. The statistical analysis only includes events with $m_{4\ell} > 100$ GeV.

Fig. 5 (upper) shows the distribution of K_D versus $m_{4\ell}$ for events selected in the 4 ℓ subchannels. The colour-coded regions show the expected background. Fig. 5 (lower) shows the same two-dimensional distribution of events, but this time superimposed on the expected event density from a SM Higgs boson ($m_H = 125$ GeV). A clustering of events is observed around 125 GeV with a large value of K_D , where the background expectation is low and the signal expectation is high, corresponding to the excess seen in the one-dimensional mass distribution. The $m_{4\ell}$ distribution of events satisfying $K_D > 0.5$ is shown in the inset in Fig. 4.

There are three final states and two data sets (7 and 8 TeV), and thus the statistical treatment requires six simultaneous two-dimensional maximum-likelihood fits for each value of m_H , in the variables $m_{4\ell}$ and K_D . Systematic uncertainties are evaluated from data for the trigger efficiency and for the combined lepton reconstruction, identification, and isolation efficiencies, as described in [128]. Systematic uncertainties in the energy/momentum calibration and in the energy resolution are estimated from data. Additional systematic uncertainties arise from limited statistical precision in the reducible background control regions.

The expected 95% CL upper limit on the signal strength $\sigma/\sigma_{\text{SM}}$, in the background-only hypothesis, for the combined 7 and 8 TeV

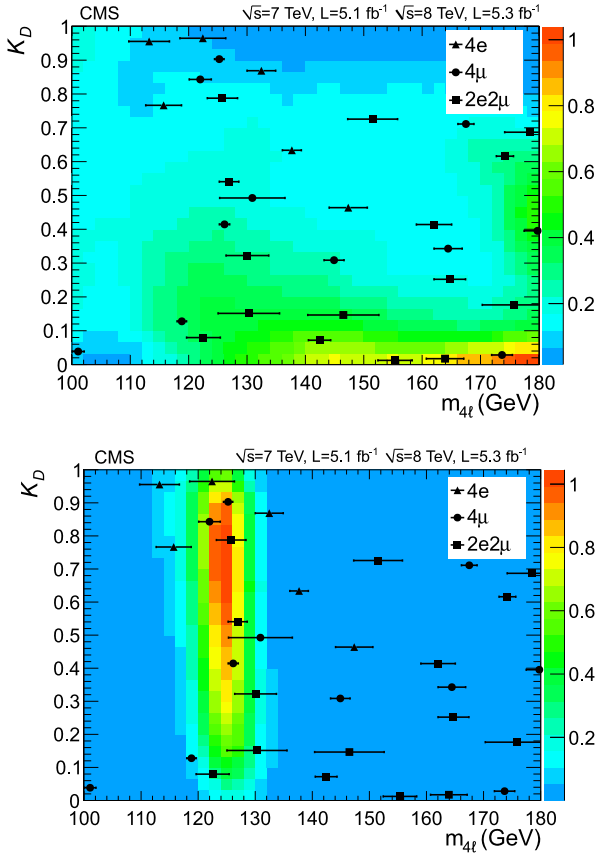


Fig. 5. The distribution of events selected in the 4ℓ subchannels for the kinematic discriminant K_D versus $m_{4\ell}$. Events in the three final states are marked by filled symbols (defined in the legend). The horizontal error bars indicate the estimated mass resolution. In the upper plot the colour-coded regions show the background expectation; in the lower plot the colour-coded regions show the event density expected from a SM Higgs boson ($m_H = 125$ GeV) (both in arbitrary units). (For interpretation of the references to colour in this figure legend, the reader is referred to the web version of this Letter.)

data, falls steeply between 110 and 140 GeV, and has a value of 0.6 at $m_H = 125$ GeV. The observed upper limit indicates the presence of a significant excess in the range $120 < m_H < 130$ GeV. The local p -value is shown as a function of m_H in Fig. 6 for the 7 and 8 TeV data, and for their combination. The minimum local p -value in the data occurs at $m_H = 125.6$ GeV and has a significance of 3.2σ (expected 3.8σ). The combined best-fit signal strength for a SM Higgs boson mass hypothesis of 125.6 GeV is $\sigma/\sigma_{SM} = 0.7^{+0.4}_{-0.3}$.

6. Decay modes with low mass resolution

6.1. $H \rightarrow WW$

The decay mode $H \rightarrow WW$ is highly sensitive to a SM Higgs boson in the mass range around the WW threshold of 160 GeV. With the development of tools for lepton identification and E_T^{miss} reconstruction optimized for LHC pileup conditions, it is possible to extend the sensitivity down to 120 GeV. This decay mode is analysed by selecting events in which both W bosons decay leptonically, resulting in a signature with two isolated, oppositely charged leptons (electrons or muons) and large E_T^{miss} due to the undetected neutrinos [129,130]. A p_T threshold of 20 (10) GeV is applied to the lepton leading (subleading) in p_T . The analysis of the 7 TeV data is described in Ref. [26] and remains unchanged, while the 8 TeV analysis was modified to cope with more difficult conditions induced by the higher pileup of the 2012 data taking.

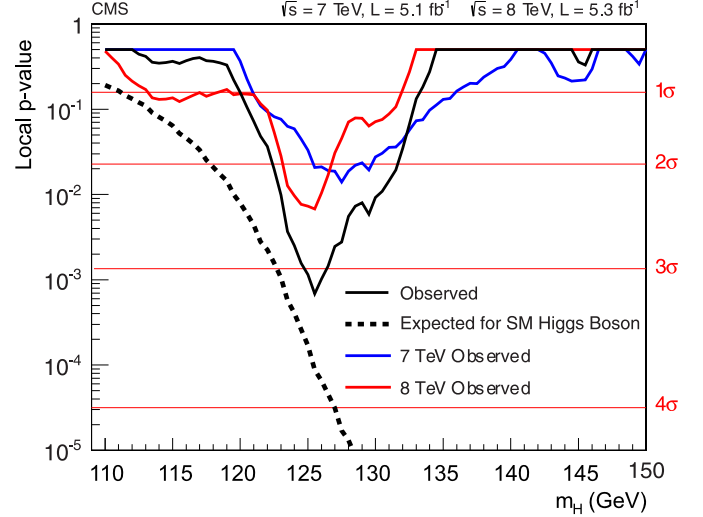


Fig. 6. The observed local p -value for the ZZ decay mode as a function of the SM Higgs boson mass. The dashed line shows the expected local p -values for a SM Higgs boson with a mass m_H .

Events are classified according to the number of jets (0, 1, or 2) with $p_T > 30$ GeV and within $|\eta| < 4.7$ ($|\eta| < 5.0$ for the 7 TeV data set), and further separated into same-flavour (ee and $\mu\mu$) or different-flavour ($e\mu$) categories. Events with more than two jets are rejected. To improve the sensitivity of the analysis, the selection criteria are optimized separately for the different event categories since they are characterised by different dominating backgrounds. The zero-jet $e\mu$ category has the best signal sensitivity. Its main backgrounds are irreducible nonresonant WW production and reducible $W + \text{jets}$ processes, where a jet is misidentified as a lepton. The one-jet $e\mu$ and zero-jet same-flavour categories only contribute to the signal sensitivity at the 10% level because of larger backgrounds, from top-quark decays and Drell-Yan production, respectively. Event selection in the two-jet category is optimized for the VBF production mechanism. This category has the highest expected signal-to-background ratio, but its contribution to the overall sensitivity is small owing to the lower cross section relative to inclusive production.

The projected E_T^{miss} variable [26] is used to reduce the Drell-Yan background arising from events where the E_T^{miss} vector is aligned with the lepton p_T , as well as events with mismeasured E_T^{miss} associated with poorly reconstructed leptons and jets. The projected E_T^{miss} is defined as the transverse component of the E_T^{miss} vector with respect to the closest lepton direction, if it is closer than $\pi/2$ in azimuthal angle, or the full E_T^{miss} otherwise. Since pileup degrades the projected E_T^{miss} resolution, the minimum of two different projected E_T^{miss} definitions is used: the first includes all particle candidates in the event, while the second uses only the charged particle candidates associated with the primary vertex. In the 8 TeV analysis, the minimum projected E_T^{miss} defined in this way is then required to be above a threshold that varies by category. For $m_H > 140$ GeV, projected E_T^{miss} is required to be greater than 20 GeV in the $e\mu$ channel, and greater than 45 GeV in the same-flavour channels. For $m_H \leq 140$ GeV in the same-flavour channels, where it is more difficult to separate the signal from the Drell-Yan background, a multivariate selection is used, combining kinematic and topological variables. In the two-jet category, a simple selection of $E_T^{\text{miss}} > 45$ GeV is applied. To further reduce the Drell-Yan background in the same-flavour final states, events with a dilepton mass within 15 GeV of the Z boson mass are rejected.

Table 4

Observed number of events, background estimates, and signal predictions for $m_H = 125$ GeV in each category of the WW analysis of the 8 TeV data set. All the selection requirements have been applied. The combined experimental and theoretical, systematic and statistical uncertainties are shown. The $Z\gamma$ process includes the dimuon, dielectron, and $\tau\tau \rightarrow \ell\ell$ final states.

Category:	0-jet $e\mu$	0-jet $\ell\ell$	1-jet $e\mu$	1-jet $\ell\ell$	2-jet $e\mu$	2-jet $\ell\ell$
WW	87.6 ± 9.5	60.4 ± 6.7	19.5 ± 3.7	9.7 ± 1.9	0.4 ± 0.1	0.3 ± 0.1
WZ + ZZ + $Z\gamma$	2.2 ± 0.2	37.7 ± 12.5	2.4 ± 0.3	8.7 ± 4.9	0.1 ± 0.0	3.1 ± 1.8
Top	9.3 ± 2.7	1.9 ± 0.5	22.3 ± 2.0	9.5 ± 1.1	3.4 ± 1.9	2.0 ± 1.2
W + jets	19.1 ± 7.2	10.8 ± 4.3	11.7 ± 4.6	3.9 ± 1.7	0.3 ± 0.3	0.0 ± 0.0
$W\gamma^{(*)}$	6.0 ± 2.3	4.6 ± 2.5	5.9 ± 3.2	1.3 ± 1.2	0.0 ± 0.0	0.0 ± 0.0
All backgrounds	124.2 ± 12.4	115.5 ± 15.0	61.7 ± 7.0	33.1 ± 5.7	4.1 ± 1.9	5.4 ± 2.2
Signal ($m_H = 125$ GeV)	23.9 ± 5.2	14.9 ± 3.3	10.3 ± 3.0	4.4 ± 1.3	1.5 ± 0.2	0.8 ± 0.1
Data	158	123	54	43	6	7

The background from low-mass resonances is rejected by requiring a dilepton invariant mass greater than 12 GeV.

To suppress the top-quark background, a “top tagging” technique based on soft-muon and b-jet tagging is applied. The first method is designed to veto events containing muons in b jets coming from decays of top quarks. The second method uses a b-jet tagging algorithm, which looks within jets for tracks with large impact parameters. The algorithm is applied also in the case of zero-jet events, which may contain low- p_T jets below the selection threshold. To reduce the background from WZ production, events with a third lepton passing the identification and isolation requirements are rejected.

Yields for the dominant backgrounds are estimated using control regions in the data. The W + jets contribution is derived from data using a “tight-loose” sample in which one lepton passes the standard criteria and the other does not, but instead satisfies a “loose” set of requirements. The efficiency ϵ_{loose} for a jet that satisfies the loose selection to pass the tight selection is determined using data from an independent loose lepton-trigger sample dominated by jets. The background contamination is then estimated using the events of the “tight-loose” sample weighted by $\epsilon_{\text{loose}}/(1 - \epsilon_{\text{loose}})$. The normalisation of the top-quark background is estimated by counting the number of top-tagged events and applying the corresponding top-tagging efficiency. The nonresonant WW contribution is normalised by using events with a dilepton mass larger than 100 GeV, where the Higgs boson signal contamination is negligible, extrapolated to the signal region using simulated samples. The same-flavour Drell-Yan background is normalised using the number of events observed with a dilepton mass within 7.5 GeV of the Z boson mass, after subtracting the non-Drell-Yan contribution. Other minor backgrounds from WZ, ZZ, and $W\gamma$ are estimated from simulation.

The 7 TeV data are analysed by training a BDT for each Higgs boson mass hypothesis in the zero-jet and one-jet event categories, while a simple selection strategy is employed in the VBF category [26]. In the BDT analysis, the Higgs boson signal is separated from the background by using a binned maximum-likelihood fit to the classifier distribution. The 8 TeV analysis is based on a simple selection strategy optimized for each mass hypothesis, where additional kinematic and topological requirements are applied to improve the signal-to-background ratio. One of the most sensitive variables to discriminate between $H \rightarrow WW$ decays and nonresonant WW production is the dilepton invariant mass $m_{\ell\ell}$. This quantity is shown in Fig. 7 for the zero-jet $e\mu$ category after the full selection for $m_H = 125$ GeV, except for the selection on $m_{\ell\ell}$ itself. Table 4 shows for the 8 TeV analysis the number of events selected in data, background estimates, and signal predictions for $m_H = 125$ GeV in each analysis category after applying all the selection requirements. About 97% of the signal events selected

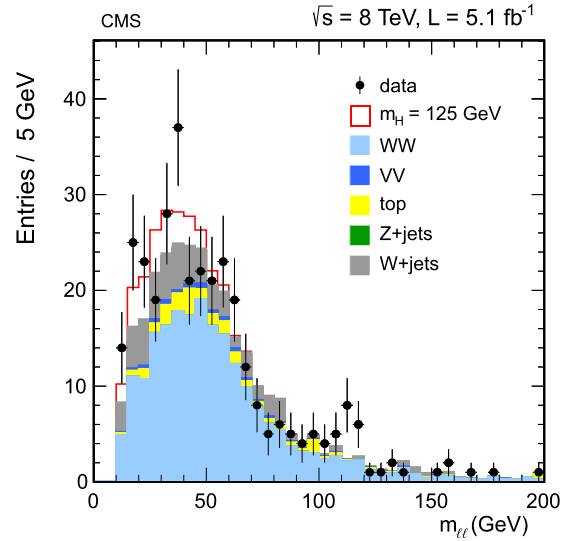


Fig. 7. Distribution of $m_{\ell\ell}$ for the zero-jet $e\mu$ category in the $H \rightarrow WW$ search at 8 TeV. The signal expected from a Higgs boson with a mass $m_H = 125$ GeV is shown added to the background.

in the zero-jet $e\mu$ category are expected to be produced by the gluon-gluon fusion process, whereas 83% of the signal in the two-jet $e\mu$ category is expected to be produced by the VBF process. The 95% CL expected and observed limits for the combination of the 7 and 8 TeV analyses are shown in Fig. 8. A broad excess is observed that is consistent with a SM Higgs boson of mass 125 GeV. This is illustrated by the dotted curve in Fig. 8 showing the median expected limit in the presence of a SM Higgs boson with $m_H = 125$ GeV. The expected significance for a SM Higgs of mass 125 GeV is 2.4σ and the observed significance is 1.6σ .

6.2. $H \rightarrow \tau\tau$

The decay mode $H \rightarrow \tau\tau$ is searched for in four exclusive sub-channels, corresponding to different decays of the τ pair: $e\mu$, $\mu\mu$, $e\tau_h$, and $\mu\tau_h$, where electrons and muons arise from leptonic τ decays, and τ_h denotes hadronic τ decays. The latter are reconstructed by selecting τ decays consistent with the hypothesis of three charged pions, or one charged pion and up to two neutral pions [131]. The search is made in the mass range 110–145 GeV, and a signal should appear as a broad excess in the distribution of the τ -pair invariant mass $m_{\tau\tau}$.

The sensitivity of the search is improved by classifying the events according to jet multiplicity and the transverse momentum of the reconstructed τ . The multiplicity of jets with $p_T > 30$ GeV

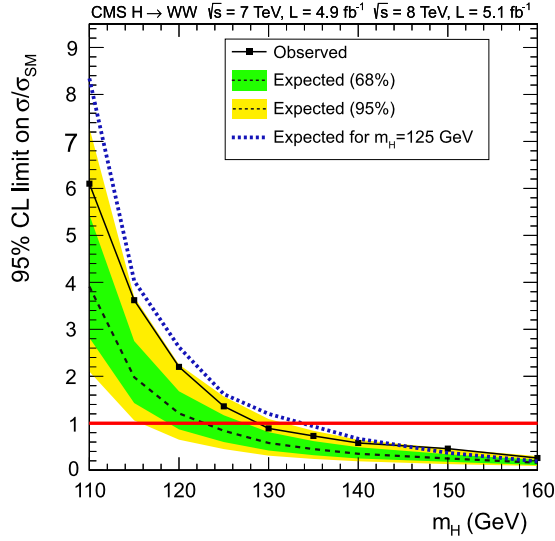


Fig. 8. The 95% CL limit on $\sigma/\sigma_{\text{SM}}$ for a Higgs boson decaying, via a W boson pair, to two leptons and two neutrinos, for the combined 7 and 8 TeV data sets. The symbol $\sigma/\sigma_{\text{SM}}$ denotes the production cross section times the relevant branching fractions, relative to the SM expectation. The background-only expectations are represented by their median (dashed line) and by the 68% and 95% CL bands. The dotted curve shows the median expected limit for a SM Higgs boson with $m_H = 125$ GeV.

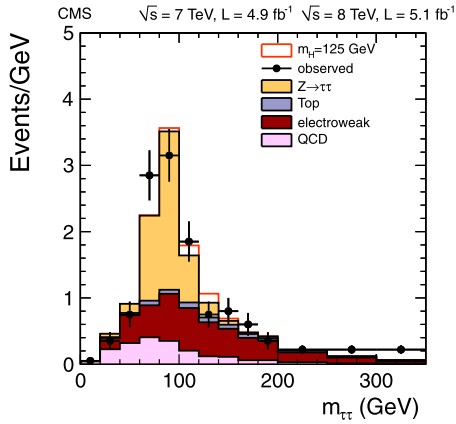


Fig. 9. Distribution of $m_{\tau\tau}$ in the combined 7 and 8 TeV data sets for the $\mu\tau_h$ VBF category of the $H \rightarrow \tau\tau$ search. The signal expected from a SM Higgs boson ($m_H = 125$ GeV) is added to the background.

reflects the production mechanism: events with zero or one jet are likely to come from the gluon–gluon fusion process, while events with two jets are candidates for VBF production. Events including b jets with $p_T > 20$ GeV are removed from zero- and one-jet categories. The signal purities in the zero- and one-jet categories are increased, and the $m_{\tau\tau}$ resolution is improved, by separating events into low- and high- p_T subchannels. The high- p_T subchannels are defined by $p_T^{\tau_h} > 40$ GeV in channels with a hadronic τ decay, and $p_T^\mu > 35$ (30) GeV in the $e\mu$ ($\mu\mu$) channel. The mass $m_{\tau\tau}$ is reconstructed with an algorithm [132] combining the visible τ decay products and the missing transverse energy, achieving a resolution of about 20% on $m_{\tau\tau}$. Fig. 9 shows as an example the reconstructed $m_{\tau\tau}$ distribution in the $\mu\tau_h$ VBF category for the combined 7 and 8 TeV data samples.

Backgrounds in the $e\mu$ and $\mu\mu$ channels arise from $t\bar{t}$ and Drell–Yan production, while W and Z production with a misidentified τ_h candidate from an electron, muon, or jet dominates in the hadronic channels. Backgrounds from $Z \rightarrow \tau\tau$ decays are modelled with $Z \rightarrow \mu\mu$ events in data where each muon is replaced

Table 5

Numbers of expected and observed events in the most sensitive event categories (VBF) in the $H \rightarrow \tau\tau$ analysis for the 7 and 8 TeV data sets. The expected signal yields for a SM Higgs boson with $m_H = 125$ GeV are also shown. Combined statistical and systematic uncertainties in each estimate are reported.

Subchannel	$e\tau_h$	$\mu\tau_h$	$e\mu$	$\mu\mu$
$Z \rightarrow \tau\tau$	53 ± 5	100 ± 9	56 ± 12	5.3 ± 0.4
QCD	35 ± 7	41 ± 9	7.4 ± 1.4	–
W + jets	46 ± 10	72 ± 15	–	–
Z + jets	13 ± 2	2.5 ± 0.6	–	–
$Z \rightarrow \mu\mu$	–	–	–	70 ± 8
$t\bar{t}$	7.0 ± 1.7	14 ± 3	24 ± 2	6.7 ± 1.5
Dibosons	1.2 ± 0.9	2.9 ± 2.1	11 ± 2	2.4 ± 0.9
All backgrounds	156 ± 13	233 ± 20	99 ± 13	85 ± 9
Signal ($m_H = 125$ GeV)	4.3 ± 0.6	7.7 ± 1.1	3.5 ± 0.4	0.8 ± 0.1
Data	142	263	110	83

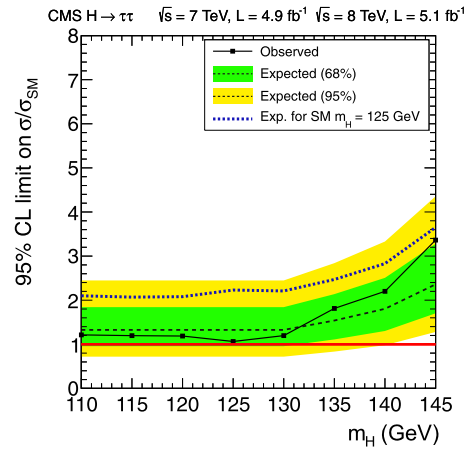


Fig. 10. The 95% CL limit on the signal strength $\sigma/\sigma_{\text{SM}}$ for a Higgs boson decaying to τ pairs, for the combined 7 and 8 TeV data sets. The symbol $\sigma/\sigma_{\text{SM}}$ denotes the production cross section times the relevant branching fractions, relative to the SM expectation. The background-only expectations are represented by their median (dashed line) and by the 68% and 95% CL bands. The dotted curve shows the median expected limit for a SM Higgs boson with $m_H = 125$ GeV.

with particles from simulated decays of a τ with the same momentum as the muon. Reducible backgrounds, comprising W + jets, QCD multijet production, and residual $Z \rightarrow ee$ events, are estimated from the data [27]. An improved signal-to-background ratio is achieved by including explicitly in the event selection for the VBF production mechanism the pseudorapidity separation between forward jets and the large invariant mass of the dijet system. Table 5 shows the numbers of expected and observed events in the most sensitive event categories (VBF) for the 7 and 8 TeV data sets. The expected signal yields for a SM Higgs boson with $m_H = 125$ GeV are also shown.

To search for the presence of a Higgs boson signal in the selected events, a binned maximum-likelihood fit to $m_{\tau\tau}$ is performed jointly across the four final states, each with five event categories. Systematic uncertainties are represented by nuisance parameters in the fitting process. The expected and observed 95% CL limits on the signal strength for the combination of all categories are shown in Fig. 10. The expected and observed limits are 1.3 and 1.1 times the SM Higgs boson cross section at mass 125 GeV, respectively. The expected significance for a SM Higgs boson of mass 125 GeV is 1.4σ , and the observed value is zero.

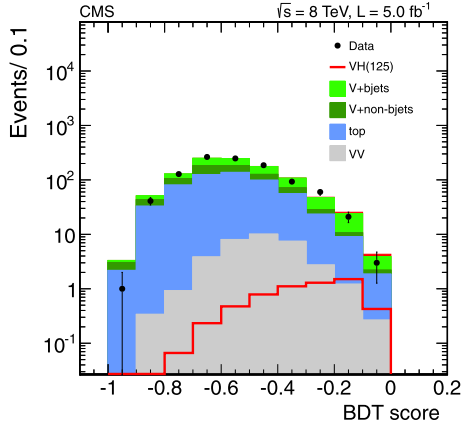


Fig. 11. Distribution of BDT scores for the high- p_T subchannel of the $Z(\nu\nu)H(bb)$ search in the 8 TeV data set after all selection criteria have been applied. The signal expected from a Higgs boson ($m_H = 125$ GeV), including $W(\ell\nu)H$ events where the charged lepton is not reconstructed, is shown added to the background and also overlaid for comparison with the diboson background.

6.3. $H \rightarrow bb$

For $m_H \leq 135$ GeV, the decay $H \rightarrow bb$ has the largest branching fraction of the five search modes, but the inclusive signal is overwhelmed by QCD production of bottom quarks. The analysis is therefore designed to search for the associated production of the Higgs boson in events where a dijet resonance is produced at high p_T in association with a W or Z boson; this largely suppresses the QCD background. Five independent search channels are explored corresponding to different decays of the vector boson: $Z(\ell\ell)H$, $Z(\nu\nu)H$, and $W(\ell\nu)H$. Events are further separated into two categories based on the p_T of the vector boson, ranging from 50–100 GeV for the lowest bin in the $Z(\ell\ell)$ search, to greater than 170 GeV for the highest bin in the $W(\ell\nu)$ search. For the $Z(\nu\nu)$ search, two subchannels are defined as $120 < E_T^{\text{miss}} < 160$ GeV and $E_T^{\text{miss}} > 160$ GeV. The two jets comprising the candidate Higgs boson decay are required to be identified as b jets, and the dijet system must satisfy a p_T threshold that is optimized within each channel: greater than 120 GeV for WH , 160 GeV for $Z(\nu\nu)H$, and no explicit threshold for $Z(\ell\ell)H$.

Dominant backgrounds arise from production of vector bosons in association with jets, pair- or single-production of top quarks, and diboson production (WW , WZ , ZZ) with one of the bosons decaying hadronically. Significant background rejection is achieved in general by requiring large p_T for the dijet, while also requiring that there be minimal additional jet activity and that the vector boson and dijet be back to back in azimuth. The effect on the signal efficiency of this selection due to higher-order electroweak [133] and QCD [91] corrections is accounted for in the systematic uncertainties. Further signal discrimination is obtained from the dijet invariant mass, which is expected to peak near m_H . A multivariate regression algorithm to better estimate b -jet p_T is trained on jets in simulated signal events and achieves a final dijet mass resolution of 8–9% for $m_H = 125$ GeV. The performance of the regression algorithm is checked in data using W/Z + jets and $t\bar{t}$ events.

A search for the signal is made in the distribution of scores of a BDT trained at discrete mass points. Input variables to the BDT algorithm exploit kinematic and topological information about the vector boson and dijet systems, and the colour-singlet nature of the Higgs boson [134]. The distribution of scores in simulated background events is checked using control regions in the data designed to enrich individual background contributions. Fig. 11 shows as an example the BDT scores for the high- p_T subchannel

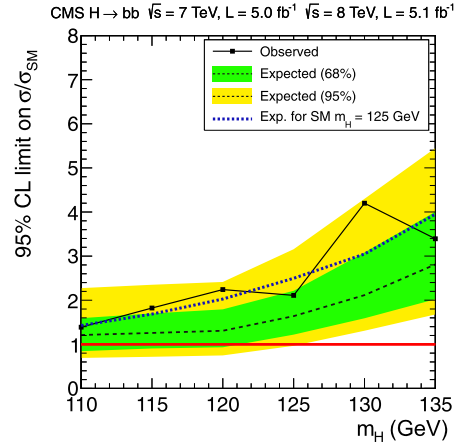


Fig. 12. The 95% CL limit on the signal strength $\sigma/\sigma_{\text{SM}}$ for a Higgs boson decaying to two b quarks, for the combined 7 and 8 TeV data sets. The symbol $\sigma/\sigma_{\text{SM}}$ denotes the production cross section times the relevant branching fractions, relative to the SM expectation. The background-only expectations are represented by their median (dashed line) and by the 68% and 95% CL bands. The dotted curve shows the median expected limit for a SM Higgs boson with $m_H = 125$ GeV.

of the $Z(\nu\nu)H$ channel in the 8 TeV data set, after all selection criteria have been applied.

The rates for the dominant backgrounds arising from production of W/Z + jets and top-quark pairs are estimated in data [28], while contributions from single-top and diboson production are estimated from simulation studies. The signal is then searched for as an excess in the BDT score distribution using the predicted shapes for signal and background events, for Higgs boson masses in the range 110–135 GeV.

Combined results for expected and observed 95% CL limits obtained from the 7 and 8 TeV data sets are displayed in Fig. 12. The expected and observed limits are 1.6 and 2.1 times the SM Higgs boson cross section at mass 125 GeV. The expected local p -value for a SM Higgs of mass 125 GeV corresponds to 1.9σ , while the observed value corresponds to 0.7σ .

7. Combined results

The individual results for the channels analysed for the five decay modes, summarised in Table 1, are combined using the methods outlined in Section 4. The combination assumes the relative branching fractions predicted by the SM and takes into account the experimental statistical and systematic uncertainties as well as the theoretical uncertainties, which are dominated by the imperfect knowledge of the QCD scale and parton distribution functions. The CL_s is shown in Fig. 13 as a function of the Higgs boson mass hypothesis. The observed values are shown by the solid points. The dashed line indicates the median of the expected results for the background-only hypothesis, with the green (dark) and yellow (light) bands indicating the ranges in which the CL_s values are expected to lie in 68% and 95% of the experiments under the background-only hypothesis. The probabilities for an observation, in the absence of a signal, to lie above or below the 68% (95%) band are 16% (2.5%) each. The thick horizontal lines indicate CL_s values of 0.05, 0.01, and 0.001. The mass regions where the observed CL_s values are below these lines are excluded with the corresponding $(1 - CL_s)$ confidence levels. Our previously published results exclude the SM Higgs boson from 127 to 600 GeV [21]. In the search described here, the SM Higgs boson is excluded at 95% CL in the range $110 < m_H < 121.5$ GeV. In the range $121.5 < m_H < 128$ GeV a significant excess is seen and the SM Higgs boson cannot be excluded at 95% CL.

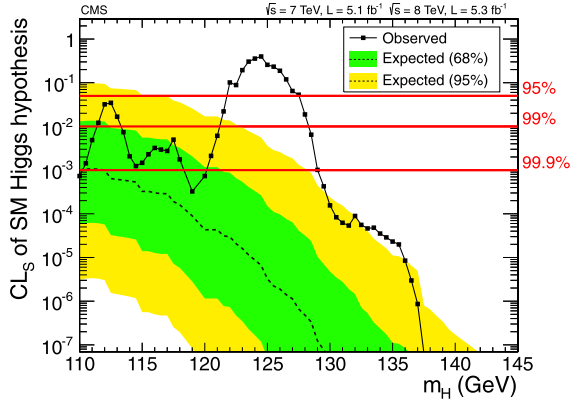


Fig. 13. The CL_s values for the SM Higgs boson hypothesis as a function of the Higgs boson mass in the range 110–145 GeV. The background-only expectations are represented by their median (dashed line) and by the 68% and 95% CL bands. (For interpretation of the references to colour, the reader is referred to the web version of this Letter.)

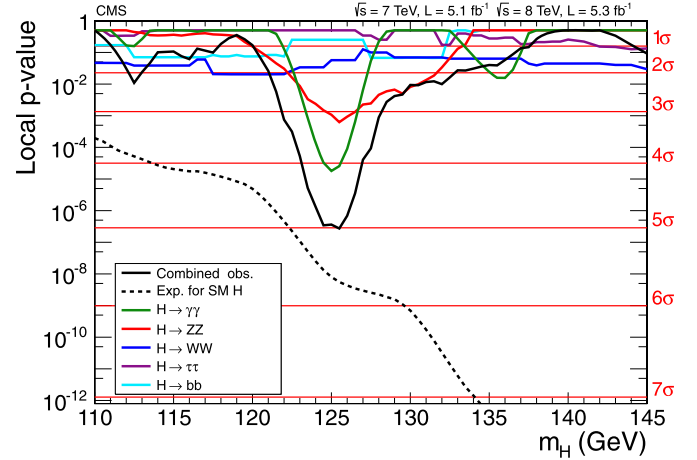


Fig. 15. The observed local p -value for the five decay modes and the overall combination as a function of the SM Higgs boson mass. The dashed line shows the expected local p -values for a SM Higgs boson with a mass m_H .

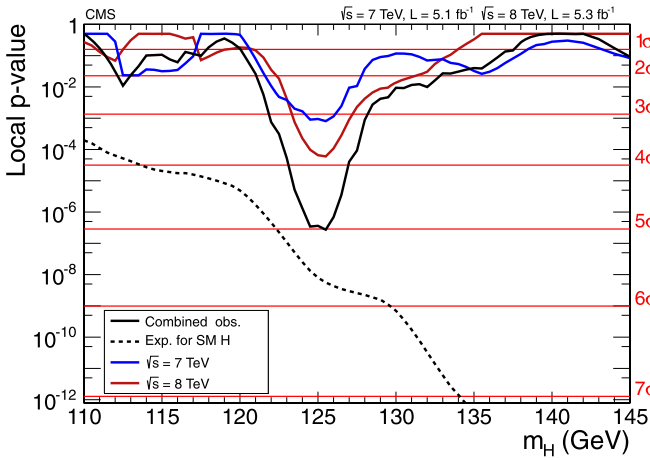


Fig. 14. The observed local p -value for 7 TeV and 8 TeV data, and their combination as a function of the SM Higgs boson mass. The dashed line shows the expected local p -values for a SM Higgs boson with a mass m_H .

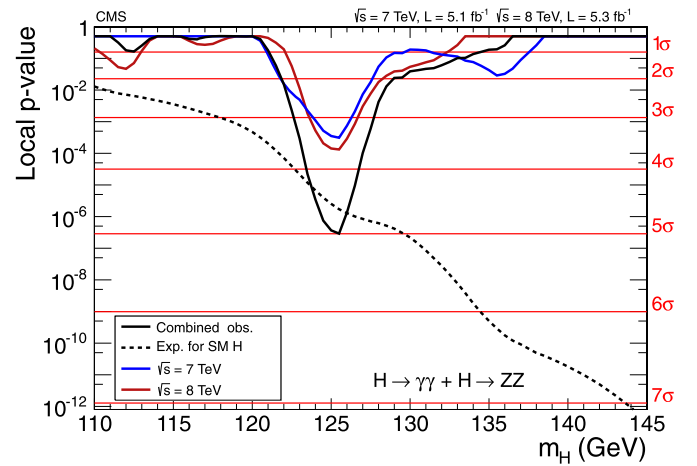


Fig. 16. The observed local p -value for decay modes with high mass-resolution channels, $\gamma\gamma$ and ZZ , as a function of the SM Higgs boson mass. The dashed line shows the expected local p -values for a SM Higgs boson with a mass m_H .

7.1. Significance of the observed excess

The consistency of the observed excess with the background-only hypothesis may be judged from Fig. 14, which shows a scan of the local p -value for the 7 and 8 TeV data sets and their combination. The 7 and 8 TeV data sets exhibit an excess of 3.2σ and 3.8σ significance, respectively, for a Higgs boson mass of approximately 125 GeV. In the overall combination the significance is 5.0σ for $m_H = 125.5$ GeV. Fig. 15 gives the local p -value for the five decay modes individually and displays the expected overall p -value.

The largest contributors to the overall excess in the combination are the $\gamma\gamma$ and ZZ decay modes. They both have very good mass resolution, allowing good localization of the invariant mass of a putative resonance responsible for the excess. Their combined significance reaches 5.0σ (Fig. 16). The WW decay mode has an exclusion sensitivity comparable to the $\gamma\gamma$ and ZZ decay modes but does not have a good mass resolution. It has an excess with local significance 1.6σ for $m_H \sim 125$ GeV. When added to the $\gamma\gamma$ and ZZ decay modes, the combined significance becomes 5.1σ . Adding the $\tau\tau$ and bb channels in the combination, the final significance becomes 5.0σ . Table 6 summarises the expected and observed local p -values for a SM Higgs boson mass hypothesis of 125.5 GeV for the various combinations of channels.

Table 6

The expected and observed local p -values, expressed as the corresponding number of standard deviations of the observed excess from the background-only hypothesis, for $m_H = 125.5$ GeV, for various combinations of decay modes.

Decay mode/combination	Expected (σ)	Observed (σ)
$\gamma\gamma$	2.8	4.1
ZZ	3.8	3.2
$\tau\tau + bb$	2.4	0.5
$\gamma\gamma + ZZ$	4.7	5.0
$\gamma\gamma + ZZ + WW$	5.2	5.1
$\gamma\gamma + ZZ + WW + \tau\tau + bb$	5.8	5.0

The global p -value for the search range 115–130 (110–145) GeV is calculated using the method suggested in Ref. [115], and corresponds to 4.6σ (4.5σ). These results confirm the very low probability for an excess as large as or larger than that observed to arise from a statistical fluctuation of the background. The excess constitutes the observation of a new particle with a mass near 125 GeV, manifesting itself in decays to two photons or to ZZ . These two decay modes indicate that the new particle is a boson; the two-photon decay implies that its spin is different from one [135,136].

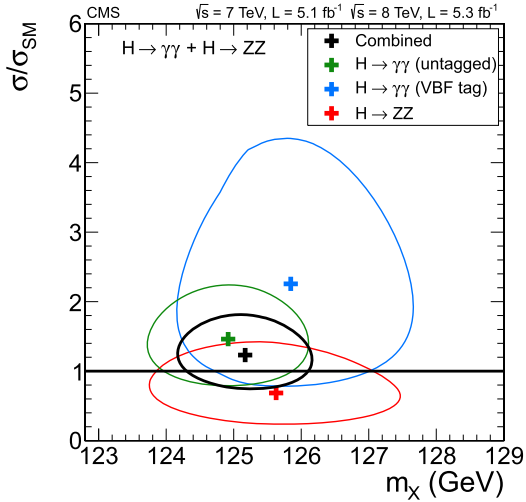


Fig. 17. The 68% CL contours for the signal strength $\sigma/\sigma_{\text{SM}}$ versus the boson mass m_χ for the untagged $\gamma\gamma$, $\gamma\gamma$ with VBF-like dijet, 4ℓ , and their combination. The symbol $\sigma/\sigma_{\text{SM}}$ denotes the production cross section times the relevant branching fractions, relative to the SM expectation. In this combination, the relative signal strengths for the three decay modes are constrained by the expectations for the SM Higgs boson.

7.2. Mass of the observed boson

The mass m_χ of the observed boson is determined using the $\gamma\gamma$ and ZZ decay modes, with the former dominating the precision of the measurement. The calibration of the energy scale in the $\gamma\gamma$ decay mode is achieved with reference to the known Z boson mass, as described in Section 5.1. There are two main sources of systematic uncertainty: (i) imperfect simulation of the differences between electrons and photons and (ii) the need to extrapolate from m_Z to $m_\chi \approx 125$ GeV. The systematic uncertainties are evaluated by making comparisons between data and simulated samples of $Z \rightarrow ee$ and $H \rightarrow \gamma\gamma$ ($m_H = 90$ GeV). The two uncertainties, which together amount to 0.5%, are assumed to be fully correlated between all the $\gamma\gamma$ event categories in the 7 and 8 TeV data. For the $ZZ \rightarrow 4\ell$ decay mode the energy scale (for electrons) and momentum scale (for muons) are calibrated using the leptonic decays of the Z boson, with an assigned uncertainty of 0.4%.

Fig. 17 shows the two-dimensional 68% CL regions for the signal strength $\sigma/\sigma_{\text{SM}}$ versus m_χ for the three channels (untagged $\gamma\gamma$, dijet-tagged $\gamma\gamma$, and $ZZ \rightarrow 4\ell$). The combined 68% CL contour shown in Fig. 17 assumes that the relative event yields among the three channels are those expected from the standard model, while the overall signal strength is a free parameter.

To extract the value of m_χ in a model-independent way, the signal yields of the three channels are allowed to vary independently. Thus the expected event yields in these channels are scaled by independent factors, while the signal is assumed to be due to a particle with a unique mass m_χ . The combined best-fit mass is $m_\chi = 125.3 \pm 0.4(\text{stat.}) \pm 0.5(\text{syst.})$ GeV.

7.3. Compatibility with the SM Higgs boson hypothesis

A first test of the compatibility of the observed boson with the SM Higgs boson is provided by examination of the best-fit value for the common signal strength $\sigma/\sigma_{\text{SM}}$, obtained in a combination of all search channels. Fig. 18 shows a scan of the overall $\sigma/\sigma_{\text{SM}}$ obtained in the combination of all channels versus a hypothesised Higgs boson mass m_H . The band corresponds to the $\pm 1\sigma$ uncertainty (statistical and systematic). The excesses seen in the 7 TeV and 8 TeV data, and in their combination, around 125 GeV are

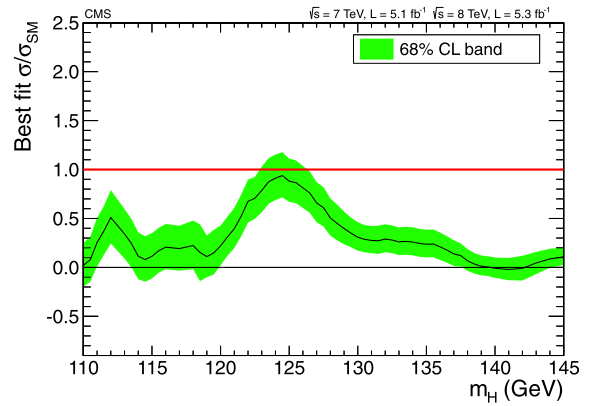


Fig. 18. The observed best-fit signal strength $\sigma/\sigma_{\text{SM}}$ as a function of the SM Higgs boson mass in the range 110–145 GeV for the combined 7 and 8 TeV data sets. The symbol $\sigma/\sigma_{\text{SM}}$ denotes the production cross section times the relevant branching fractions, relative to the SM expectation. The band corresponds to the ± 1 standard deviation uncertainty in $\sigma/\sigma_{\text{SM}}$.

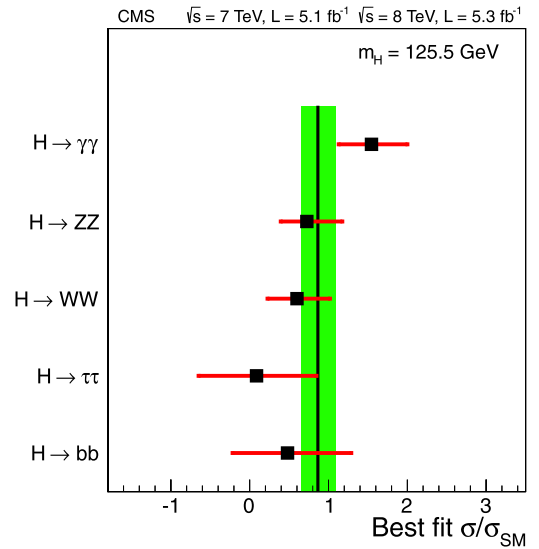


Fig. 19. Values of $\sigma/\sigma_{\text{SM}}$ for the combination (solid vertical line) and for individual decay modes (points). The vertical band shows the overall $\sigma/\sigma_{\text{SM}}$ value 0.87 ± 0.23 . The symbol $\sigma/\sigma_{\text{SM}}$ denotes the production cross section times the relevant branching fractions, relative to the SM expectation. The horizontal bars indicate the ± 1 standard deviation uncertainties in the $\sigma/\sigma_{\text{SM}}$ values for individual modes; they include both statistical and systematic uncertainties.

consistent with unity within the $\pm 1\sigma$ uncertainties. The observed $\sigma/\sigma_{\text{SM}}$ value for an excess at 125.5 GeV in a combination of all data is 0.87 ± 0.23 . The different decay channels and data sets have been examined for self-consistency. Fig. 19 shows the measured values of $\sigma/\sigma_{\text{SM}}$ results obtained for the different decay modes. These results are consistent, within uncertainties, with the expectations for the SM Higgs boson.

8. Conclusions

Results are presented from searches for the standard model Higgs boson in proton–proton collisions at $\sqrt{s} = 7$ and 8 TeV in the CMS experiment at the LHC, using data samples corresponding to integrated luminosities of up to 5.1 fb^{-1} at 7 TeV and 5.3 fb^{-1} at 8 TeV. The search is performed in five decay modes: $\gamma\gamma$, ZZ , W^+W^- , $\tau^+\tau^-$, and $b\bar{b}$. An excess of events is observed above the expected background, with a local significance of 5.0σ , at a mass near 125 GeV, signalling the production of a new par-

ticle. The expected local significance for a standard model Higgs boson of that mass is 5.8σ . The global p -value in the search range of 115–130 (110–145) GeV corresponds to 4.6σ (4.5σ). The excess is most significant in the two decay modes with the best mass resolution, $\gamma\gamma$ and ZZ , and a fit to these signals gives a mass of $125.3 \pm 0.4(\text{stat.}) \pm 0.5(\text{syst.})$ GeV. The decay to two photons indicates that the new particle is a boson with spin different from one. The results presented here are consistent, within uncertainties, with expectations for the standard model Higgs boson. The collection of further data will enable a more rigorous test of this conclusion and an investigation of whether the properties of the new particle imply physics beyond the standard model.

Acknowledgements

We congratulate our colleagues in the CERN accelerator departments for the excellent performance of the LHC machine. We thank the computing centres in the Worldwide LHC computing Grid for the provisioning and excellent performance of computing infrastructure essential to our analyses. We gratefully acknowledge the contributions of the technical staff at CERN and other CMS institutes. We also thank the administrative staff at CERN and the other CMS institutes and acknowledge support from BMWF and FWF (Austria); FNRS and FWO (Belgium); CNPq, CAPES, FAPERJ, and FAPESP (Brazil); MES (Bulgaria); CERN; CAS, MoST, and NSFC (China); COLCIENCIAS (Colombia); MSES (Croatia); RPF (Cyprus); MEYS (Czech Republic); MoER, SF0690030s09 and ERDF (Estonia); Academy of Finland, MEC, and HIP (Finland); CEA and CNRS/IN2P3 (France); BMBF, DFG, and HGF (Germany); GSRT (Greece); OTKA and NKTH (Hungary); DAE and DST (India); IPM (Iran); SFI (Ireland); INFN (Italy); NRF and WCU (Republic of Korea); LAS (Lithuania); CINVESTAV, CONACYT, SEP, and UASLP-FAI (Mexico); MSI (New Zealand); PAEC (Pakistan); MSHE and NSC (Poland); FCT (Portugal); JINR (Armenia, Belarus, Georgia, Ukraine, Uzbekistan); MON, RosAtom, RAS and RFBR (Russia); MSTD (Serbia); SEIDI and CPAN (Spain); Swiss Funding Agencies (Switzerland); NSC (Taipei); TUBITAK and TAEK (Turkey); NASU (Ukraine); STFC (United Kingdom); DOE and NSF (USA). Individuals have received support from the Marie-Curie programme and the European Research Council (European Union); the Leventis Foundation; the A.P. Sloan Foundation; the Alexander von Humboldt Foundation; the Austrian Science Fund (FWF); the Belgian Federal Science Policy Office; the Fonds pour la Formation à la Recherche dans l'Industrie et dans l'Agriculture (FRIA-Belgium); the Agentschap voor Innovatie door Wetenschap en Technologie (IWT-Belgium); the Council of Science and Industrial Research, India; the Compagnia di San Paolo (Torino); and the HOMING PLUS programme of Foundation for Polish Science, cofinanced from European Union, Regional Development Fund.

Open access

This article is published Open Access at sciencedirect.com. It is distributed under the terms of the Creative Commons Attribution License 3.0, which permits unrestricted use, distribution, and reproduction in any medium, provided the original authors and source are credited.

References

- [1] F. Englert, R. Brout, Phys. Rev. Lett. 13 (1964) 321, <http://dx.doi.org/10.1103/PhysRevLett.13.321>.
- [2] P.W. Higgs, Phys. Lett. 12 (1964) 132, [http://dx.doi.org/10.1016/0031-9163\(64\)91136-9](http://dx.doi.org/10.1016/0031-9163(64)91136-9).
- [3] P.W. Higgs, Phys. Rev. Lett. 13 (1964) 508, <http://dx.doi.org/10.1103/PhysRevLett.13.508>.
- [4] G.S. Guralnik, C.R. Hagen, T.W.B. Kibble, Phys. Rev. Lett. 13 (1964) 585, <http://dx.doi.org/10.1103/PhysRevLett.13.585>.
- [5] P.W. Higgs, Phys. Rev. 145 (1966) 1156, <http://dx.doi.org/10.1103/PhysRev.145.1156>.
- [6] T.W.B. Kibble, Phys. Rev. 155 (1967) 1554, <http://dx.doi.org/10.1103/PhysRev.155.1554>.
- [7] S.L. Glashow, Nucl. Phys. 22 (1961) 579, [http://dx.doi.org/10.1016/0029-5582\(61\)90469-2](http://dx.doi.org/10.1016/0029-5582(61)90469-2).
- [8] S. Weinberg, Phys. Rev. Lett. 19 (1967) 1264, <http://dx.doi.org/10.1103/PhysRevLett.19.1264>.
- [9] A. Salam, in: N. Svartholm (Ed.), Elementary Particle Physics: Relativistic Groups and Analyticity, Almqvist & Wiskell, 1968, p. 367, proceedings of the eighth Nobel symposium.
- [10] J.M. Cornwall, D.N. Levin, G. Tiktopoulos, Phys. Rev. Lett. 30 (1973) 1268, <http://dx.doi.org/10.1103/PhysRevLett.30.1268>.
- [11] J.M. Cornwall, D.N. Levin, G. Tiktopoulos, Phys. Rev. D 10 (1974) 1145, <http://dx.doi.org/10.1103/PhysRevD.10.1145>, also Erratum, <http://dx.doi.org/10.1103/PhysRevD.11.972>.
- [12] C.H. Llewellyn Smith, Phys. Lett. B 46 (1973) 233, [http://dx.doi.org/10.1016/0370-2693\(73\)90692-8](http://dx.doi.org/10.1016/0370-2693(73)90692-8).
- [13] B.W. Lee, C. Quigg, H.B. Thacker, Phys. Rev. D 16 (1977) 1519, <http://dx.doi.org/10.1103/PhysRevD.16.1519>.
- [14] ALEPH, CDF, D0, DELPHI, L3, OPAL, SLD Collaborations, the LEP Electroweak Working Group, the Tevatron Electroweak Working Group, and the SLD Electroweak and Heavy Flavour Groups, Precision electroweak measurements and constraints on the standard model, CERN PH-EP-2010-095, at this time, the most up-to-date Higgs boson mass constraints come from <http://lepewwg.web.cern.ch/LEPEWWG/plots/winter2012/>, arXiv:1012.2367, 2010, <http://cdsweb.cern.ch/record/1313716>.
- [15] ALEPH, DELPHI, L3, OPAL Collaborations, and LEP Working Group for Higgs Boson Searches, Phys. Lett. B 565 (2003) 61, arXiv:hep-ex/0306033, [http://dx.doi.org/10.1016/S0370-2693\(03\)00614-2](http://dx.doi.org/10.1016/S0370-2693(03)00614-2).
- [16] CDF and D0 Collaborations, Phys. Rev. Lett. 104 (2010) 061802, <http://dx.doi.org/10.1103/PhysRevLett.104.061802>.
- [17] CDF Collaboration, Phys. Rev. Lett. (2012), submitted for publication, arXiv:1207.1707.
- [18] CDF and D0 Collaborations, Phys. Rev. Lett. 109 (2012) 071804, <http://dx.doi.org/10.1103/PhysRevLett.109.071804>.
- [19] D0 Collaboration, Phys. Rev. Lett. (2012), submitted for publication, arXiv:1207.6631.
- [20] L. Evans, P. Bryant (Eds.), LHC Machine, JINST 3 (2008) S08001, <http://dx.doi.org/10.1088/1748-0221/3/08/S08001>.
- [21] S. Chatrchyan, et al., Phys. Lett. B 710 (2012) 26, arXiv:1202.1488, <http://dx.doi.org/10.1016/j.physletb.2012.02.064>.
- [22] G. Aad, et al., Phys. Rev. D 86 (2012) 032003, arXiv:1207.0319, <http://dx.doi.org/10.1103/PhysRevD.86.032003>.
- [23] LHC Higgs Cross Section Working Group, in: S. Dittmaier, C. Mariotti, G. Passarino, R. Tanaka (Eds.), Handbook of LHC Higgs Cross Sections: 1. Inclusive Observables, CERN, Geneva, 2011, arXiv:1101.0593, <http://cdsweb.cern.ch/record/1318996>.
- [24] S. Chatrchyan, et al., Phys. Lett. B 710 (2012) 403, arXiv:1202.1487, <http://dx.doi.org/10.1016/j.physletb.2012.03.003>.
- [25] S. Chatrchyan, et al., Phys. Rev. Lett. 108 (2012) 111804, arXiv:1202.1997, <http://dx.doi.org/10.1103/PhysRevLett.108.111804>.
- [26] S. Chatrchyan, et al., Phys. Lett. B 710 (2012) 91, arXiv:1202.1489, <http://dx.doi.org/10.1016/j.physletb.2012.02.076>.
- [27] S. Chatrchyan, et al., Phys. Lett. B 713 (2012) 68, arXiv:1202.4083, <http://dx.doi.org/10.1016/j.physletb.2012.05.028>.
- [28] S. Chatrchyan, et al., Phys. Lett. B 710 (2012) 284, arXiv:1202.4195, <http://dx.doi.org/10.1016/j.physletb.2012.02.085>.
- [29] M. Della Negra, et al., in: G. Jarlskog, D. Rein (Eds.), Proceedings of the Large Hadron Collider Workshop, Aachen, Germany, 1990, p. 467, CERN 90-10-V-3/ECFA 90-133-V-3, <http://cdsweb.cern.ch/record/215299/files/CERN-90-10-V-3.pdf>.
- [30] M. Della Negra, et al., Letter of intent by the CMS Collaboration for a general purpose detector at the LHC, Tech. Rep. CERN-LHCC-92-03, CERN-LHCC-I-1, CERN, 1992, <https://cdsweb.cern.ch/record/290808>.
- [31] N. Ellis, T.S. Virdee, Ann. Rev. Nucl. Part. Sci. 44 (1994) 609, <http://dx.doi.org/10.1146/annurev.ns.44.120194.003141>.
- [32] S. Chatrchyan, et al., The CMS experiment at the CERN LHC, JINST 3 (2008) S08004, <http://dx.doi.org/10.1088/1748-0221/3/08/S08004>.
- [33] CMS Collaboration, b-jet identification in the CMS experiment, CMS Physics Analysis Summary CMS-PAS-BTV-11-004, 2012, <https://cdsweb.cern.ch/record/1427247>.
- [34] V. Khachatryan, et al., Phys. Rev. D 83 (2011) 112004, arXiv:1012.5545, <http://dx.doi.org/10.1103/PhysRevD.83.112004>.
- [35] CMS Collaboration, Particle-flow event reconstruction in CMS and performance for jets, taus, and E_{miss} , CMS Physics Analysis Summary CMS-PAS-PFT-09-001, 2009, <http://cdsweb.cern.ch/record/1194487>.

- [36] CMS Collaboration, Commissioning of the particle-flow event reconstruction with the first LHC collisions recorded in the CMS detector, CMS Physics Analysis Summary CMS-PAS-PFT-10-001, 2010, <http://cdsweb.cern.ch/record/1247373>.
- [37] M. Cacciari, G.P. Salam, G. Soyez, JHEP 0804 (2008) 063, <http://dx.doi.org/10.1088/1126-6708/2008/04/063>.
- [38] M. Cacciari, G.P. Salam, Phys. Lett. B 659 (2008) 119, <http://dx.doi.org/10.1016/j.physletb.2007.09.077>.
- [39] M. Cacciari, G.P. Salam, G. Soyez, JHEP 0804 (2008) 005, <http://dx.doi.org/10.1088/1126-6708/2008/04/005>.
- [40] M. Cacciari, G.P. Salam, G. Soyez, Eur. Phys. J. C 72 (2012) 1896, arXiv:1111.6097, <http://dx.doi.org/10.1140/epjc/s10052-012-1896-2>.
- [41] S. Chatrchyan, et al., JINST 6 (2011) 11002, arXiv:1107.4277, <http://dx.doi.org/10.1088/1748-0221/6/11/P11002>.
- [42] S. Chatrchyan, et al., JINST 6 (2011) 9001, arXiv:1106.5048, <http://dx.doi.org/10.1088/1748-0221/6/09/P09001>.
- [43] CMS Collaboration, Commissioning of the particle-flow event reconstruction with leptons from J/ψ and W decays at 7 TeV, CMS Physics Analysis Summary CMS-PAS-PFT-10-003, 2010, <http://cdsweb.cern.ch/record/1279347>.
- [44] CMS Collaboration, Electron reconstruction and identification at $\sqrt{s} = 7$ TeV, CMS Physics Analysis Summary CMS-PAS-EGM-10-004, 2010, <http://cdsweb.cern.ch/record/1299116>.
- [45] S. Baffioni, C. Charlot, F. Ferri, D. Futyan, P. Meridiani, et al., Eur. Phys. J. C 49 (2007) 1099, <http://dx.doi.org/10.1140/epjc/s10052-006-0175-5>.
- [46] W. Adam, R. Fruhwirth, A. Strandlie, T. Todorov, J. Phys. G 31 (2005) N9, <http://dx.doi.org/10.1088/0954-3889/31/9/N01>.
- [47] CMS Collaboration, Absolute calibration of the luminosity measurement at CMS: Winter 2012 update, CMS Physics Analysis Summary CMS-PAS-SMP-12-008, 2012, <https://cdsweb.cern.ch/record/1434360>.
- [48] S. van der Meer, Calibration of the effective beam height in the ISR, Tech. Rep. CERN-ISR-PO-68-31, CERN, Geneva, 1968, <https://cdsweb.cern.ch/record/296752>.
- [49] J.R. Ellis, M.K. Gaillard, D.V. Nanopoulos, Nucl. Phys. B 106 (1976) 292, [http://dx.doi.org/10.1016/0550-3213\(76\)90382-5](http://dx.doi.org/10.1016/0550-3213(76)90382-5).
- [50] H.M. Georgi, S.L. Glashow, M.E. Machacek, D.V. Nanopoulos, Phys. Rev. Lett. 40 (1978) 692, <http://dx.doi.org/10.1103/PhysRevLett.40.692>.
- [51] S.L. Glashow, D.V. Nanopoulos, A. Yildiz, Phys. Rev. D 18 (1978) 1724, <http://dx.doi.org/10.1103/PhysRevD.18.1724>.
- [52] R.N. Cahn, S.D. Ellis, R. Kleiss, W.J. Stirling, Phys. Rev. D 35 (1987) 1626, <http://dx.doi.org/10.1103/PhysRevD.35.1626>.
- [53] J.F. Gunion, G.L. Kane, J. Wudka, Nucl. Phys. B 299 (1988) 231, [http://dx.doi.org/10.1016/0550-3213\(88\)90284-2](http://dx.doi.org/10.1016/0550-3213(88)90284-2).
- [54] D.L. Rainwater, D. Zeppenfeld, JHEP 9712 (1997) 005, arXiv:hep-ph/9712271, <http://dx.doi.org/10.1088/1126-6708/1997/12/005>.
- [55] D.L. Rainwater, D. Zeppenfeld, K. Hagiwara, Phys. Rev. D 59 (1998) 014037, arXiv:hep-ph/9808468, <http://dx.doi.org/10.1103/PhysRevD.59.014037>.
- [56] D.L. Rainwater, D. Zeppenfeld, Phys. Rev. D 60 (1999) 113004, arXiv:hep-ph/9906218, <http://dx.doi.org/10.1103/PhysRevD.60.113004>, also Erratum, <http://dx.doi.org/10.1103/PhysRevD.61.099901>.
- [57] A. Djouadi, M. Spira, P.M. Zerwas, Phys. Lett. B 264 (1991) 440, [http://dx.doi.org/10.1016/0370-2693\(91\)90375-Z](http://dx.doi.org/10.1016/0370-2693(91)90375-Z).
- [58] S. Dawson, Nucl. Phys. B 359 (1991) 283, [http://dx.doi.org/10.1016/0550-3213\(91\)90061-2](http://dx.doi.org/10.1016/0550-3213(91)90061-2).
- [59] M. Spira, A. Djouadi, D. Graudenz, P.M. Zerwas, Nucl. Phys. B 453 (1995) 17, arXiv:hep-ph/9504378, [http://dx.doi.org/10.1016/0550-3213\(95\)00379-7](http://dx.doi.org/10.1016/0550-3213(95)00379-7).
- [60] R.V. Harlander, W.B. Kilgore, Phys. Rev. Lett. 88 (2002) 201801, arXiv:hep-ph/0201206, <http://dx.doi.org/10.1103/PhysRevLett.88.201801>.
- [61] C. Anastasiou, K. Melnikov, Nucl. Phys. B 646 (2002) 220, arXiv:hep-ph/0207004, [http://dx.doi.org/10.1016/S0550-3213\(02\)00837-4](http://dx.doi.org/10.1016/S0550-3213(02)00837-4).
- [62] V. Ravindran, J. Smith, W.L. van Neerven, Nucl. Phys. B 665 (2003) 325, arXiv:hep-ph/0302135, [http://dx.doi.org/10.1016/S0550-3213\(03\)00457-7](http://dx.doi.org/10.1016/S0550-3213(03)00457-7).
- [63] S. Catani, D. de Florian, M. Grazzini, P. Nason, JHEP 0307 (2003) 028, <http://dx.doi.org/10.1088/1126-6708/2003/07/028>.
- [64] U. Aglietti, R. Bonciani, G. Degrassi, A. Vicini, Phys. Lett. B 595 (2004) 432, arXiv:hep-ph/0404071, <http://dx.doi.org/10.1016/j.physletb.2004.06.063>.
- [65] G. Degrassi, F. Maltoni, Phys. Lett. B 600 (2004) 255, arXiv:hep-ph/0407249, <http://dx.doi.org/10.1016/j.physletb.2004.09.008>.
- [66] S. Actis, G. Passarino, C. Sturm, S. Uccirati, Phys. Lett. B 670 (2008) 12, arXiv:0809.1301, <http://dx.doi.org/10.1016/j.physletb.2008.10.018>.
- [67] C. Anastasiou, R. Boughezal, F. Petriello, JHEP 0904 (2009) 003, arXiv:0811.3458, <http://dx.doi.org/10.1088/1126-6708/2009/04/003>.
- [68] D. de Florian, M. Grazzini, Phys. Lett. B 674 (2009) 291, arXiv:0901.2427, <http://dx.doi.org/10.1016/j.physletb.2009.03.033>.
- [69] J. Baglio, A. Djouadi, JHEP 1103 (2011) 055, arXiv:1012.0530, [http://dx.doi.org/10.1007/JHEP03\(2011\)055](http://dx.doi.org/10.1007/JHEP03(2011)055).
- [70] D. de Florian, M. Grazzini, Higgs production at the LHC: updated cross sections at $\sqrt{s} = 8$ TeV, arXiv:1206.4133, 2012.
- [71] G. Bozzi, S. Catani, D. de Florian, M. Grazzini, Nucl. Phys. B 737 (2006) 73, arXiv:hep-ph/0508068, <http://dx.doi.org/10.1016/j.nuclphysb.2005.12.022>.
- [72] D. de Florian, G. Ferrera, M. Grazzini, D. Tommasini, JHEP 1111 (2011) 064, [http://dx.doi.org/10.1007/JHEP11\(2011\)064](http://dx.doi.org/10.1007/JHEP11(2011)064).
- [73] G. Passarino, C. Sturm, S. Uccirati, Nucl. Phys. B 834 (2010) 77, arXiv:1001.3360, <http://dx.doi.org/10.1016/j.nuclphysb.2010.03.013>.
- [74] I.W. Stewart, F.J. Tackmann, Phys. Rev. D 85 (2012) 034011, arXiv:1107.2117, <http://dx.doi.org/10.1103/PhysRevD.85.034011>.
- [75] A. Djouadi, J. Kalinowski, M. Spira, Comput. Phys. Commun. 108 (1998) 56, arXiv:hep-ph/9704448, [http://dx.doi.org/10.1016/S0010-4655\(97\)00123-9](http://dx.doi.org/10.1016/S0010-4655(97)00123-9).
- [76] A. Djouadi, J. Kalinowski, M. Muhlleitner, M. Spira, in: The Les Houches 2009 workshop on TeV colliders: The tools and Monte Carlo working group summary report, arXiv:1003.1643, 2010.
- [77] A. Bredenstein, A. Denner, S. Dittmaier, M.M. Weber, Phys. Rev. D 74 (2006) 013004, arXiv:hep-ph/0604011, <http://dx.doi.org/10.1103/PhysRevD.74.013004>.
- [78] A. Bredenstein, A. Denner, S. Dittmaier, M.M. Weber, JHEP 0702 (2007) 080, arXiv:hep-ph/0611234, <http://dx.doi.org/10.1088/1126-6708/2007/02/080>.
- [79] S. Actis, G. Passarino, C. Sturm, S. Uccirati, Nucl. Phys. B 811 (2009) 182, arXiv:0809.3667, <http://dx.doi.org/10.1016/j.nuclphysb.2008.11.024>.
- [80] A. Denner, S. Heinemeyer, I. Puljak, D. Rebuszi, M. Spira, Eur. Phys. J. C 71 (2011) 1753, arXiv:1107.5909, <http://dx.doi.org/10.1140/epjc/s10052-011-1753-8>.
- [81] M. Ciccolini, A. Denner, S. Dittmaier, Phys. Rev. Lett. 99 (2007) 161803, arXiv:0707.0381, <http://dx.doi.org/10.1103/PhysRevLett.99.161803>.
- [82] M. Ciccolini, A. Denner, S. Dittmaier, Phys. Rev. D 77 (2008) 013002, arXiv:0710.4749, <http://dx.doi.org/10.1103/PhysRevD.77.013002>.
- [83] T. Figg, C. Oleari, D. Zeppenfeld, Phys. Rev. D 68 (2003) 073005, arXiv:hep-ph/0306109, <http://dx.doi.org/10.1103/PhysRevD.68.073005>.
- [84] K. Arnold, M. Bahr, G. Bozzi, F. Campanario, C. Englert, et al., Comput. Phys. Commun. 180 (2009) 1661, arXiv:0811.4559, <http://dx.doi.org/10.1016/j.cpc.2009.03.006>.
- [85] P. Bolzoni, F. Maltoni, S.-O. Moch, M. Zaro, Phys. Rev. Lett. 105 (2010) 011801, arXiv:1003.4451, <http://dx.doi.org/10.1103/PhysRevLett.105.011801>.
- [86] T. Han, S. Willenbrock, Phys. Lett. B 273 (1991) 167, [http://dx.doi.org/10.1016/0370-2693\(91\)90572-8](http://dx.doi.org/10.1016/0370-2693(91)90572-8).
- [87] O. Brein, A. Djouadi, R. Harlander, Phys. Lett. B 579 (2004) 149, arXiv:hep-ph/0307206, <http://dx.doi.org/10.1016/j.physletb.2003.10.112>.
- [88] M.L. Ciccolini, S. Dittmaier, M. Krämer, Phys. Rev. D 68 (2003) 073003, arXiv:hep-ph/0306234, <http://dx.doi.org/10.1103/PhysRevD.68.073003>.
- [89] R. Hamberg, W.L. van Neerven, T. Matsuura, Nucl. Phys. B 359 (1991) 343, [http://dx.doi.org/10.1016/0550-3213\(91\)90064-5](http://dx.doi.org/10.1016/0550-3213(91)90064-5).
- [90] A. Denner, S. Dittmaier, S. Kallweit, A. Muck, EW corrections to Higgs strahlung at the Tevatron and the LHC with HAWK, arXiv:1112.5258, 2011.
- [91] G. Ferrera, M. Grazzini, F. Tramontano, Phys. Rev. Lett. 107 (2011) 152003, arXiv:1107.1164, <http://dx.doi.org/10.1103/PhysRevLett.107.152003>.
- [92] W. Beenakker, S. Dittmaier, M. Kramer, B. Plumper, M. Spira, et al., Phys. Rev. Lett. 87 (2001) 201805, arXiv:hep-ph/0107081, <http://dx.doi.org/10.1103/PhysRevLett.87.201805>.
- [93] W. Beenakker, S. Dittmaier, M. Kramer, B. Plumper, M. Spira, et al., Nucl. Phys. B 653 (2003) 151, arXiv:hep-ph/0211352, [http://dx.doi.org/10.1016/S0550-3213\(03\)00044-0](http://dx.doi.org/10.1016/S0550-3213(03)00044-0).
- [94] S. Dawson, L.H. Orr, L. Reina, D. Wackerth, Phys. Rev. D 67 (2003) 071503, arXiv:hep-ph/0211438, <http://dx.doi.org/10.1103/PhysRevD.67.071503>.
- [95] S. Dawson, C. Jackson, L.H. Orr, L. Reina, D. Wackerth, Phys. Rev. D 68 (2003) 034022, arXiv:hep-ph/0305087, <http://dx.doi.org/10.1103/PhysRevD.68.034022>.
- [96] M. Botje, J. Butterworth, A. Cooper-Sarkar, A. de Roeck, J. Feltesse, et al., The PDF4LHC Working Group interim recommendations, arXiv:1101.0538, 2011.
- [97] S. Alekhin, S. Alioli, R.D. Ball, V. Bertone, J. Blumlein, et al., The PDF4LHC Working Group interim report, arXiv:1101.0536, 2011.
- [98] H.-L. Lai, M. Guzzi, J. Huston, Z. Li, P.M. Nadolsky, et al., Phys. Rev. D 82 (2010) 074024, arXiv:1007.2241, <http://dx.doi.org/10.1103/PhysRevD.82.074024>.
- [99] A.D. Martin, W.J. Stirling, R.S. Thorne, G. Watt, Eur. Phys. J. C 63 (2009) 189, arXiv:0901.0002, <http://dx.doi.org/10.1140/epjc/s10052-009-1072-5>.
- [100] R.D. Ball, et al., Nucl. Phys. B 849 (2011) 296, arXiv:1101.1300, <http://dx.doi.org/10.1016/j.nuclphysb.2011.03.021>.
- [101] C. Anastasiou, S. Buehler, F. Herzog, A. Lazopoulos, JHEP 1204 (2012) 004, arXiv:1202.3638, [http://dx.doi.org/10.1007/JHEP04\(2012\)004](http://dx.doi.org/10.1007/JHEP04(2012)004).
- [102] LHC Higgs Cross Section Working Group, in: S. Dittmaier, C. Mariotti, G. Passarino, R. Tanaka (Eds.), Handbook of LHC Higgs Cross Sections: 2. Differential Distributions, CERN, Geneva, 2012, arXiv:1201.3084.
- [103] S. Agostinelli, et al., Nucl. Instrum. Meth. A 506 (2003) 250, [http://dx.doi.org/10.1016/S0168-9002\(03\)01368-8](http://dx.doi.org/10.1016/S0168-9002(03)01368-8).
- [104] S. Alioli, P. Nason, C. Oleari, E. Re, JHEP 0904 (2009) 002, <http://dx.doi.org/10.1088/1126-6708/2009/04/002>.
- [105] P. Nason, C. Oleari, JHEP 1002 (2010) 037, [http://dx.doi.org/10.1007/JHEP02\(2010\)037](http://dx.doi.org/10.1007/JHEP02(2010)037).
- [106] T. Sjöstrand, S. Mrenna, P.Z. Skands, JHEP 0605 (2006) 026, <http://dx.doi.org/10.1088/1126-6708/2006/05/026>.
- [107] G. Bozzi, S. Catani, D. de Florian, M. Grazzini, Phys. Lett. B 564 (2003) 65, [http://dx.doi.org/10.1016/S0370-2693\(03\)00656-7](http://dx.doi.org/10.1016/S0370-2693(03)00656-7).

- [108] C. Anastasiou, K. Melnikov, F. Petriello, Nucl. Phys. B 724 (2005) 197, <http://dx.doi.org/10.1016/j.nuclphysb.2005.06.036>.
- [109] C. Anastasiou, S. Bucherer, Z. Kunszt, JHEP 0910 (2009) 068, <http://dx.doi.org/10.1088/1126-6708/2009/10/068>.
- [110] S. Gieseke, D. Grellscheid, K. Hamilton, A. Ribon, P. Richardson, et al., Herwig++ 2.0 Release Note, arXiv:hep-ph/0609306, 2006.
- [111] J. Alwall, P. Demin, S. de Visscher, R. Frederix, M. Herquet, et al., JHEP 0709 (2007) 028, arXiv:0706.2334, <http://dx.doi.org/10.1088/1126-6708/2007/09/028>.
- [112] ATLAS and CMS Collaborations, LHC Higgs Combination Group, Procedure for the LHC Higgs boson search combination in Summer 2011, Tech. Rep. ATL-PHYS-PUB 2011-11, CMS NOTE 2011/005, 2011, <http://cdsweb.cern.ch/record/1379837>.
- [113] T. Junk, Nucl. Instrum. Meth. A 434 (1999) 435, [http://dx.doi.org/10.1016/S0168-9002\(99\)00498-2](http://dx.doi.org/10.1016/S0168-9002(99)00498-2).
- [114] A.L. Read, J. Phys. G 28 (2002) 2693, <http://dx.doi.org/10.1088/0954-3899/28/10/313>.
- [115] E. Gross, O. Vitells, Eur. Phys. J. C 70 (2010) 525, arXiv:1005.1891, <http://dx.doi.org/10.1140/epjc/s10052-010-1470-8>.
- [116] G. Cowan, K. Cranmer, E. Gross, O. Vitells, Eur. Phys. J. C 71 (2011) 1554, arXiv:1007.1727, <http://dx.doi.org/10.1140/epjc/s10052-011-1554-0>.
- [117] L. Moneta, K. Belasco, K. Cranmer, S. Kreiss, et al., in: 13th Int. Workshop on Advanced Computing and Analysis Techniques in Physics Research (ACAT2010), 2010, PoS ACAT:057, arXiv:1009.1003, http://pos.sissa.it/archive/conferences/093/057/ACAT2010_057.pdf.
- [118] C.J. Seez, T.S. Virdee, L. Di Lella, R.H. Kleiss, Z. Kunszt, W.J. Stirling, in: G. Jarlskog, D. Rein (Eds.), Proceedings of the Large Hadron Collider Workshop, Aachen, Germany, 1990, p. 474, CERN 90-10-V-2/ECFA 90-133-V-2, <http://cdsweb.cern.ch/record/220524>.
- [119] B.P. Roe, H.-J. Yang, J. Zhu, Y. Liu, I. Stancu, et al., Nucl. Instrum. Meth. A 543 (2005) 577, <http://dx.doi.org/10.1016/j.nima.2004.12.018>.
- [120] H. Voss, A. Höcker, J. Stelzer, F. Tegenfeldt, in: XI Int. Workshop on Advanced Computing and Analysis Techniques in Physics Research, 2007, PoS ACAT:040, arXiv:physics/0703039, http://pos.sissa.it/archive/conferences/050/040/ACAT_040.pdf.
- [121] R.J. Barlow, J. Comp. Phys. 72 (1987) 202, [http://dx.doi.org/10.1016/0021-9991\(87\)90078-7](http://dx.doi.org/10.1016/0021-9991(87)90078-7).
- [122] M. Della Negra, D. Froidevaux, K. Jakobs, R. Kinnunen, R. Kleiss, A. Nisati, T. Sjöstrand, in: G. Jarlskog, D. Rein (Eds.), Proceedings of the Large Hadron Collider Workshop, Aachen, Germany, 1990, p. 509, CERN 90-10-V-2/ECFA 90-133-V-2, <http://cdsweb.cern.ch/record/215298>.
- [123] N. Cabibbo, A. Maksymowicz, Phys. Rev. B 137 (1965) 438, <http://dx.doi.org/10.1103/PhysRev.137.B438>, also Erratum, <http://dx.doi.org/10.1103/PhysRev.168.1926>.
- [124] Y. Gao, A.V. Gritsan, Z. Guo, K. Melnikov, M. Schulze, et al., Phys. Rev. D 81 (2010) 075022, arXiv:1001.3396, <http://dx.doi.org/10.1103/PhysRevD.81.075022>.
- [125] A. De Rijula, J. Lykken, M. Pierini, C. Rogan, M. Spiropulu, Phys. Rev. D 82 (2010) 013003, arXiv:1001.5300, <http://dx.doi.org/10.1103/PhysRevD.82.013003>.
- [126] S. Chatrchyan, et al., JHEP 1204 (2012) 036, arXiv:1202.1416, [http://dx.doi.org/10.1007/JHEP04\(2012\)036](http://dx.doi.org/10.1007/JHEP04(2012)036).
- [127] S.Y. Choi, D.J. Miller, M.M. Muhlleitner, P.M. Zerwas, Phys. Lett. B 553 (2003) 61, arXiv:hep-ph/0210077, [http://dx.doi.org/10.1016/S0370-2693\(02\)03191-X](http://dx.doi.org/10.1016/S0370-2693(02)03191-X).
- [128] S. Chatrchyan, et al., JHEP 1110 (2011) 132, [http://dx.doi.org/10.1007/JHEP10\(2011\)132](http://dx.doi.org/10.1007/JHEP10(2011)132).
- [129] V.D. Barger, G. Bhattacharya, T. Han, B.A. Kniehl, Phys. Rev. D 43 (1991) 779, <http://dx.doi.org/10.1103/PhysRevD.43.779>.
- [130] M. Dittmar, H.K. Dreiner, Phys. Rev. D 55 (1997) 167, arXiv:hep-ph/9608317, <http://dx.doi.org/10.1103/PhysRevD.55.167>.
- [131] S. Chatrchyan, et al., JINST 7 (2011) P01001, <http://dx.doi.org/10.1088/1748-0221/7/01/P01001>.
- [132] S. Chatrchyan, et al., Phys. Rev. Lett. 106 (2011) 231801, arXiv:1104.1619, <http://dx.doi.org/10.1103/PhysRevLett.106.231801>.
- [133] A. Denner, S. Dittmaier, S. Kallweit, A. Muck, JHEP 1203 (2012) 075, arXiv:1112.5142, [http://dx.doi.org/10.1007/JHEP03\(2012\)075](http://dx.doi.org/10.1007/JHEP03(2012)075).
- [134] J. Gallicchio, M.D. Schwartz, Phys. Rev. Lett. 105 (2010) 022001, arXiv:1001.5027, <http://dx.doi.org/10.1103/PhysRevLett.105.022001>.
- [135] L.D. Landau, Dokl. Akad. Nauk 60 (1948) 207.
- [136] C.N. Yang, Phys. Rev. 77 (1950) 242, <http://dx.doi.org/10.1103/PhysRev.77.242>.

CMS Collaboration

S. Chatrchyan, V. Khachatryan, A.M. Sirunyan, A. Tumasyan

Yerevan Physics Institute, Yerevan, Armenia

W. Adam, E. Aguilo, T. Bergauer, M. Dragicevic, J. Erö, C. Fabjan¹, M. Friedl, R. Frühwirth¹, V.M. Ghete, J. Hammer, M. Hoch, N. Hörmann, J. Hrubec, M. Jeitler¹, W. Kiesenhofer, V. Knünz, M. Krammer¹, I. Krätschmer, D. Liko, W. Majerotto, I. Mikulec, M. Pernicka[†], B. Rahbaran, C. Rohringer, H. Rohringer, R. Schöfbeck, J. Strauss, F. Szoncsó, A. Taurok, W. Waltenberger, G. Walzel, E. Widl, C.-E. Wulz¹

Institut für Hochenergiephysik der OeAW, Wien, Austria

V. Chekhovsky, I. Emeliantchik, A. Litomin, V. Makarenko, V. Mossolov, N. Shumeiko, A. Solin, R. Stefanovitch, J. Suarez Gonzalez

National Centre for Particle and High Energy Physics, Minsk, Belarus

A. Fedorov, M. Korzhik, O. Missevitch, R. Zuyewski

Research Institute for Nuclear Problems, Minsk, Belarus

M. Bansal, S. Bansal, W. Beaumont, T. Cornelis, E.A. De Wolf, D. Druzhkin, X. Janssen, S. Luyckx, L. Mucibello, S. Ochesanu, B. Roland, R. Rougny, M. Selvaggi, Z. Staykova, H. Van Haevermaet, P. Van Mechelen, N. Van Remortel, A. Van Spilbeeck

Universiteit Antwerpen, Antwerpen, Belgium

F. Blekman, S. Blyweert, J. D'Hondt, O. Devroede, R. Gonzalez Suarez, R. Goorens, A. Kalogeropoulos, M. Maes, A. Olbrechts, S. Tavernier, W. Van Doninck, L. Van Lancker, P. Van Mulders, G.P. Van Onsem, I. Villella

Vrije Universiteit Brussel, Brussel, Belgium

B. Clerbaux, G. De Lentdecker, V. Dero, J.P. Dewulf, A.P.R. Gay, T. Hreus, A. Léonard, P.E. Marage, A. Mohammadi, T. Reis, S. Rugovac, L. Thomas, C. Vander Velde, P. Vanlaer, J. Wang, J. Wickens

Université Libre de Bruxelles, Bruxelles, Belgium

V. Adler, K. Beernaert, A. Cimmino, S. Costantini, G. Garcia, M. Grunewald, B. Klein, J. Lellouch, A. Marinov, J. McCartin, A.A. Ocampo Rios, D. Ryckbosch, N. Strobbe, F. Thyssen, M. Tytgat, S. Walsh, E. Yazgan, N. Zaganidis

Ghent University, Ghent, Belgium

S. Basegmez, G. Bruno, R. Castello, L. Ceard, J. De Favereau De Jeneret, C. Delaere, P. Demin, T. du Pree, D. Favart, L. Forthomme, A. Giammanco², G. Grégoire, J. Hollar, V. Lemaitre, J. Liao, O. Militaru, C. Nuttens, D. Pagano, A. Pin, K. Piotrkowski, N. Schul, J.M. Vizan Garcia

Université Catholique de Louvain, Louvain-la-Neuve, Belgium

N. Belyi, T. Caebegs, E. Daubie, G.H. Hammad

Université de Mons, Mons, Belgium

G.A. Alves, L. Brito, M. Correa Martin Junior, T. Martins, M.E. Pol, M.H.G. Souza

Centro Brasileiro de Pesquisas Fisicas, Rio de Janeiro, Brazil

W.L. Aldá Júnior, W. Carvalho, A. Custódio, E.M. Da Costa, D. De Jesus Damiao, C. De Oliveira Martins, S. Fonseca De Souza, D. Matos Figueiredo, L. Mundim, H. Nogima, V. Oguri, W.L. Prado Da Silva, A. Santoro, A. Sznajder, A. Vilela Pereira

Universidade do Estado do Rio de Janeiro, Rio de Janeiro, Brazil

T.S. Anjos³, C.A. Bernardes³, F.A. Dias⁴, T.R. Fernandez Perez Tomei, E.M. Gregores³, R.L. Iope, C. Lagana, S.M. Lietti, F. Marinho, P.G. Mercadante³, S.F. Novaes, Sandra S. Padula

Instituto de Fisica Teorica, Universidade Estadual Paulista, Sao Paulo, Brazil

L. Dimitrov, V. Genchev⁵, P. Iaydjiev⁵, S. Piperov, M. Rodozov, S. Stoykova, G. Sultanov, V. Tcholakov, R. Trayanov, I. Vankov, M. Vutova

Institute for Nuclear Research and Nuclear Energy, Sofia, Bulgaria

C. Roumenin, D. Uzunova, R. Zahariev

Institute of System Engineering and Robotics, Sofia, Bulgaria

A. Dimitrov, R. Hadjiiska, V. Kozhuharov, L. Litov, B. Pavlov, P. Petkov

University of Sofia, Sofia, Bulgaria

J.G. Bian, G.M. Chen, H.S. Chen, K.L. He, C.H. Jiang, W.G. Li, D. Liang, S. Liang, X. Meng, G. Sun, H.S. Sun, J. Tao, J. Wang, X. Wang, Z. Wang, H. Xiao, M. Xu, M. Yang, J. Zang, X. Zhang, Z. Zhang, Z. Zhang, W.R. Zhao, Z. Zhu

Institute of High Energy Physics, Beijing, China

C. Asawatangtrakuldee, Y. Ban, J. Cai, S. Guo, Y. Guo, W. Li, H.T. Liu, S. Liu, Y. Mao, S.J. Qian, H. Teng, D. Wang, Y.L. Ye, L. Zhang, B. Zhu, W. Zou

State Key Lab. of Nucl. Phys. and Tech., Peking University, Beijing, China

C. Avila, J.P. Gomez, B. Gomez Moreno, A.F. Osorio Oliveros, J.C. Sanabria

Universidad de Los Andes, Bogota, Colombia

N. Godinovic, D. Lelas, R. Plestina⁶, D. Polic, I. Puljak⁵

Technical University of Split, Split, Croatia

Z. Antunovic, M. Kovac

University of Split, Split, Croatia

V. Brigljevic, S. Duric, K. Kadija, J. Luetic, S. Morovic

Institute Rudjer Boskovic, Zagreb, Croatia

A. Attikis, M. Galanti, G. Mavromanolakis, J. Mousa, C. Nicolaou, F. Ptochos, P.A. Razis

University of Cyprus, Nicosia, Cyprus

M. Finger, M. Finger Jr.

Charles University, Prague, Czech Republic

A. Aly, Y. Assran⁷, A. Awad, S. Elgammal⁸, A. Ellithi Kamel⁹, S. Khalil⁸, M.A. Mahmoud¹⁰, A. Mahrous, A. Radi^{11,12}

Academy of Scientific Research and Technology of the Arab Republic of Egypt, Egyptian Network of High Energy Physics, Cairo, Egypt

A. Hektor, M. Kadastik, K. Kannike, M. Müntel, M. Raidal, L. Rebane, A. Strumia, A. Tiko

National Institute of Chemical Physics and Biophysics, Tallinn, Estonia

P. Eerola, G. Fedi, M. Voutilainen

Department of Physics, University of Helsinki, Helsinki, Finland

E. Anttila, J. Härkönen, A. Heikkinen, V. Karimäki, H.M. Katajisto, R. Kinnunen, M.J. Kortelainen, M. Kotamäki, T. Lampén, K. Lassila-Perini, S. Lehti, T. Lindén, P. Luukka, T. Mäenpää, T. Peltola, E. Tuominen, J. Tuominiemi, E. Tuovinen, D. Ungaro, T.P. Vanhala, L. Wendland

Helsinki Institute of Physics, Helsinki, Finland

K. Banzuzi, A. Karjalainen, A. Korpela, T. Tuuva

Lappeenranta University of Technology, Lappeenranta, Finland

M. Anfreville, M. Besancon, S. Choudhury, M. Dejardin, D. Denegri, B. Fabbro, J.L. Faure, F. Ferri, S. Ganjour, F.X. Gentit, A. Givernaud, P. Gras, G. Hamel de Monchenault, P. Jarry, F. Kircher, M.C. Lemaire, E. Locci, J. Malcles, I. Mandjavidze, A. Nayak, J.P. Pansart, J. Rander, J.M. Reymond, A. Rosowsky, I. Shreyber, M. Titov, P. Verrecchia

DSM/IRFU, CEA/Saclay, Gif-sur-Yvette, France

J. Badier, S. Baffioni, F. Beaudette, E. Becheva, L. Benhabib, L. Bianchini, M. Bluj¹³, C. Broutin, P. Busson, M. Cerutti, D. Chamont, C. Charlot, N. Daci, T. Dahms, M. Dalchenko, L. Dobrzynski, Y. Geerebaert, R. Granier de Cassagnac, M. Haguenaue, P. Hennion, G. Milleret, P. Miné, C. Mironov, I.N. Naranjo, M. Nguyen, C. Ochando, P. Paganini, T. Romanteau, D. Sabes, R. Salerno, A. Sartirana, Y. Sirois, C. Thiebaut, C. Veelken, A. Zabi

Laboratoire Leprince-Ringuet, Ecole Polytechnique, IN2P3–CNRS, Palaiseau, France

J.-L. Agram¹⁴, J. Andrea, A. Besson, D. Bloch, D. Bodin, J.-M. Brom, M. Cardaci, E.C. Chabert, C. Collard, E. Conte¹⁴, F. Drouhin¹⁴, C. Ferro, J.-C. Fontaine¹⁴, D. Gelé, U. Goerlach, C. Goetzmann, L. Gross, D. Huss, P. Juillot, E. Kieffer, A.-C. Le Bihan, J. Pansanel, Y. Patois, P. Van Hove

Institut Pluridisciplinaire Hubert Curien, Université de Strasbourg, Université de Haute Alsace Mulhouse, CNRS/IN2P3, Strasbourg, France

D. Boutigny, D. Mercier

Centre de Calcul de l'Institut National de Physique Nucleaire et de Physique des Particules, CNRS/IN2P3, Villeurbanne, France, Villeurbanne, France

G. Baulieu, S. Beauceron, N. Beaupere, M. Bedjidian, O. Bondu, G. Boudoul, S. Brochet, J. Chasserat, R. Chierici⁵, C. Combaret, D. Contardo, P. Depasse, H. El Mamouni, J. Fay, S. Gascon, N. Giraud, M. Gouzevitch, R. Haroutunian, B. Ille, T. Kurca, M. Lethuillier, N. Lumb, H. Mathez, L. Mirabito, S. Perries, L. Sgandurra, V. Sordini, Y. Tschudi, M. Vander Donckt, P. Verdier, S. Viret

Université de Lyon, Université Claude Bernard Lyon 1, CNRS-IN2P3, Institut de Physique Nucléaire de Lyon, Villeurbanne, France

V. Roinishvili, L. Rurua

E. Andronikashvili Institute of Physics, Academy of Science, Tbilisi, Georgia

N. Amaglobeli, I. Bagaturia, B. Chiladze, R. Kvatadze, D. Lomidze, R. Shanidze, Z. Tsamalaidze¹⁵

Institute of High Energy Physics and Informatization, Tbilisi State University, Tbilisi, Georgia

R. Adolphi, G. Anagnostou, C. Autermann, S. Beranek, R. Brauer, W. Braunschweig, B. Calpas, M. Edelhoff, L. Feld, N. Heracleous, O. Hindrichs, R. Jussen, W. Karpinski, K. Klein, K. Lübelmeyer, J. Merz, A. Ostapchuk, D. Pandoulas, A. Perieanu, F. Raupach, J. Sammet, S. Schael, D. Schmitz, A. Schultz von Dratzig, R. Siedling, D. Sprenger, H. Weber, B. Wittmer, M. Wlochal, V. Zhukov¹⁶

RWTH Aachen University, I. Physikalisches Institut, Aachen, Germany

M. Ata, P. Biallass, J. Caudron, E. Dietz-Laursonn, D. Duchardt, M. Erdmann, R. Fischer, A. Güth, T. Hebbeker, C. Heidemann, G. Hilgers, K. Hoepfner, C. Hof, T. Klimkovich, D. Klingebiel, P. Kreuzer, C. Magass, M. Merschmeyer, A. Meyer, M. Olschewski, P. Papacz, B. Philipps, H. Pieta, H. Reithler, S.A. Schmitz, L. Sonnenschein, M. Sowa, J. Steggemann, D. Teyssier, M. Weber

RWTH Aachen University, III. Physikalisches Institut A, Aachen, Germany

M. Bontenackels, V. Cherepanov, Y. Erdogan, G. Flügge, H. Geenen, M. Geisler, W. Haj Ahmad, F. Hoehle, B. Kargoll, T. Kress, Y. Kuessel, J. Lingemann⁵, A. Nowack, L. Perchalla, O. Pooth, P. Sauerland, A. Stahl, M.H. Zoeller

RWTH Aachen University, III. Physikalisches Institut B, Aachen, Germany

M. Aldaya Martin, J. Behr, W. Behrenhoff, U. Behrens, M. Bergholz¹⁷, A. Bethani, K. Borras, A. Burgmeier, A. Cakir, L. Calligaris, A. Campbell, E. Castro, F. Costanza, D. Dammann, C. Diez Pardos, G. Eckerlin, D. Eckstein, A. Flossdorf, G. Flucke, A. Geiser, I. Glushkov, P. Goettlicher, A. Grebenyuk, P. Gunnellini, S. Habib, J. Hauk, G. Hellwig, H. Jung, M. Kasemann, P. Katsas, C. Kleinwort, H. Kluge, A. Knutsson, M. Krämer, D. Krücker, E. Kuznetsova, W. Lange, B. Lewendel, W. Lohmann¹⁷, B. Lutz, R. Mankel, I. Marfin, M. Marienfeld, I.-A. Melzer-Pellmann, A.B. Meyer, J. Mnich, C. Muhl, A. Mussgiller, S. Naumann-Emme, O. Novgorodova, J. Olzem, A. Parenti, H. Perrey, A. Petrukhin, D. Pitzl, A. Raspereza, P.M. Ribeiro Cipriano, C. Riedl, E. Ron, C. Rosemann, M. Rosin, J. Salfeld-Nebgen, R. Schmidt¹⁷, T. Schoerner-Sadenius, N. Sen, A. Spiridonov, M. Stein, J. Tomaszewska, D. Volyanskyy, R. Walsh, C. Wissing, C. Youngman

Deutsches Elektronen-Synchrotron, Hamburg, Germany

V. Blobel, J. Draeger, H. Enderle, J. Erfle, U. Gebbert, M. Görner, T. Hermanns, R.S. Höing, K. Kaschube, G. Kaussen, H. Kirschenmann, R. Klanner, J. Lange, B. Mura, F. Nowak, T. Peiffer, N. Pietsch, D. Rathjens, C. Sander, H. Schettler, P. Schleper, E. Schlieckau, A. Schmidt, M. Schröder, T. Schum, M. Seidel, J. Sibille¹⁸, V. Sola, H. Stadie, G. Steinbrück, J. Thomsen, L. Vanelderden

University of Hamburg, Hamburg, Germany

C. Barth, J. Bauer, J. Berger, P. Blüm, C. Böser, V. Buege, Z.Y. Chen, S. Chowdhury, T. Chwalek, D. Daeuwel, W. De Boer, A. Descroix, A. Dierlamm, G. Dirkes, M. Fahrner, M. Feindt, U. Felzmann, M. Frey, A. Furgeri,

I. Gebauer, A. Gessler, J. Gruschke, M. Guthoff⁵, C. Hackstein, F. Hartmann, F. Hauler, T. Hauth⁵, S. Heier, S.M. Heindl, M. Heinrich, A. Heiss, H. Held, K.H. Hoffmann, S. Honc, U. Husemann, M. Imhof, C. Jung, S. Junghans, I. Katkov¹⁶, U. Kerzel, D. Knoblauch, J.R. Komaragiri, M. Kräber, T. Kuhr, T. Liamsuwan, P. Lobelle Pardo, D. Martschei, A. Menchikov, X. Mol, D. Mörmann, S. Mueller, Th. Müller, D. Neuberger, M.B. Neuland, M. Niegel, A. Nürnberg, O. Oberst, A. Oehler, T. Ortega Gomez, J. Ott, C. Piasecki, A. Poschlad, G. Quast, K. Rabbertz, F. Ratnikov, N. Ratnikova, M. Renz, S. Röcker, F. Roederer, A. Sabellek, C. Saout, A. Scheurer, D. Schieferdecker, P. Schieferdecker, F.-P. Schilling, M. Schmanau, G. Schott, W. Schwerdtfeger, H.J. Simonis, A. Skiba, F.M. Stober, A. Theel, W.H. Thümmel, D. Troendle, A. Trunov, R. Ulrich, J. Wagner-Kuhr, S. Wayand, M. Weber, T. Weiler, M. Zeise, E.B. Ziebarth, M. Zvada

Institut für Experimentelle Kernphysik, Karlsruhe, Germany

G. Daskalakis, T. Gerasis, S. Kesisoglou, A. Kyriakis, D. Loukas, I. Manolakos, A. Markou, C. Markou, C. Mavrommatis, E. Ntomari

Institute of Nuclear Physics "Demokritos", Aghia Paraskevi, Greece

L. Gouskos, A. Panagiotou, N. Saoulidou

University of Athens, Athens, Greece

I. Evangelou, C. Foudas, P. Kokkas, N. Manthos, I. Papadopoulos, V. Patras, F.A. Triantis

University of Ioánnina, Ioánnina, Greece

G. Bencze, C. Hajdu, P. Hidas, D. Horvath¹⁹, F. Sikler, V. Veszpremi, G. Vesztergombi²⁰, P. Zalan

KFKI Research Institute for Particle and Nuclear Physics, Budapest, Hungary

N. Beni, S. Czellar, A. Fenyvesi, J. Molnar, J. Palinkas, Z. Szillasi

Institute of Nuclear Research ATOMKI, Debrecen, Hungary

J. Karancsi, P. Raics, Z.L. Trocsanyi, B. Ujvari, G. Zilizi

University of Debrecen, Debrecen, Hungary

S.B. Beri, V. Bhandari, V. Bhatnagar, N. Dhingra, R. Gupta, M. Kaur, J.M. Kohli, M.Z. Mehta, N. Nishu, L.K. Saini, A. Sharma, J.B. Singh

Panjab University, Chandigarh, India

Ashok Kumar, Arun Kumar, S. Ahuja, A. Bhardwaj, S. Chatterji, B.C. Choudhary, P. Gupta, S. Malhotra, M. Naimuddin, K. Ranjan, V. Sharma, R.K. Shivpuri

University of Delhi, Delhi, India

S. Banerjee, S. Bhattacharya, S. Dutta, B. Gomber, Sa. Jain, Sh. Jain, R. Khurana, S. Sarkar, M. Sharan

Saha Institute of Nuclear Physics, Kolkata, India

A. Abdulsalam, R.K. Choudhury, D. Dutta, M. Ghodgaonkar, S. Kailas, S.K. Kataria, V. Kumar, P. Mehta, A.K. Mohanty⁵, L.M. Pant, P. Shukla, A. Topkar

Bhabha Atomic Research Centre, Mumbai, India

T. Aziz, S. Chendvankar, P.V. Deshpande, S.N. Ganguli, S. Ganguly, M. Guchait²¹, A. Gurtu²², M. Maity²³, K. Mazumdar, G.B. Mohanty, B. Parida, M.R. Patil, R. Raghavan, K. Sudhakar, N. Wickramage

Tata Institute of Fundamental Research – EHEP, Mumbai, India

B.S. Acharya, S. Banerjee, S. Bheesette, S. Dugad, S.D. Kalmani, M.R. Krishnaswamy, V.R. Lakkireddi, N.K. Mondal, V.S. Narasimham, N. Panyam, P. Verma

Tata Institute of Fundamental Research – HECR, Mumbai, India

F. Ardalan, H. Arfaei²⁴, H. Bakhshiansohi, S.M. Etesami²⁵, A. Fahim²⁴, M. Hashemi, A. Jafari, M. Khakzad, M. Mohammadi Najafabadi, S. Paktinat Mehdiabadi, B. Safarzadeh²⁶, M. Zeinali

Institute for Research in Fundamental Sciences (IPM), Tehran, Iran

M. Abbrescia^{a,b}, L. Barbone^{a,b}, C. Calabria^{a,b,5}, S.S. Chhibra^{a,b}, A. Colaleo^a, D. Creanza^{a,c}, N. De Filippis^{a,c,5}, M. De Palma^{a,b}, G. De Robertis^a, G. Donvito^a, L. Fiore^a, G. Iaselli^{a,c}, F. Loddo^a, G. Maggi^{a,c}, M. Maggi^a, N. Manna^{a,b}, B. Marangelli^{a,b}, S. My^{a,c}, S. Natali^{a,b}, S. Nuzzo^{a,b}, N. Pacifico^a, A. Pompili^{a,b}, G. Pugliese^{a,c}, A. Ranieri^a, F. Romano^{a,c}, G. Selvaggi^{a,b}, L. Silvestris^a, G. Singh^{a,b}, V. Spinoso^a, R. Venditti^{a,b}, P. Verwilligen, G. Zito^a

^a INFN Sezione di Bari, Bari, Italy

^b Università di Bari, Bari, Italy

^c Politecnico di Bari, Bari, Italy

G. Abbiendi^a, A.C. Benvenuti^a, D. Bonacorsi^{a,b}, S. Braibant-Giacomelli^{a,b}, L. Brigliadori^{a,b}, P. Capiluppi^{a,b}, A. Castro^{a,b}, F.R. Cavallo^a, M. Cuffiani^{a,b}, G.M. Dallavalle^a, F. Fabbri^a, A. Fanfani^{a,b}, D. Fasanella^{a,b}, P. Giacomelli^a, C. Grandi^a, L. Guiducci^{a,b}, S. Marcellini^a, G. Masetti^a, M. Meneghelli^{a,b,5}, A. Montanari^a, F.L. Navarria^{a,b}, F. Odorici^a, A. Perrotta^a, F. Primavera^{a,b}, A.M. Rossi^{a,b}, T. Rovelli^{a,b}, G.P. Siroli^{a,b}, R. Travaglini^{a,b}

^a INFN Sezione di Bologna, Bologna, Italy

^b Università di Bologna, Bologna, Italy

S. Albergo^{a,b}, G. Cappello^{a,b}, M. Chiorboli^{a,b}, S. Costa^{a,b}, F. Noto^a, R. Potenza^{a,b}, M.A. Saizu^{a,27}, A. Tricomi^{a,b}, C. Tuve^{a,b}

^a INFN Sezione di Catania, Catania, Italy

^b Università di Catania, Catania, Italy

G. Barbagli^a, V. Ciulli^{a,b}, C. Civinini^a, R. D'Alessandro^{a,b}, E. Focardi^{a,b}, S. Frosali^{a,b}, E. Gallo^a, C. Genta^a, S. Gozzi^{a,b}, M. Meschini^a, S. Paoletti^a, G. Parrini^a, R. Ranieri^a, G. Sguazzoni^a, A. Tropiano^{a,b}

^a INFN Sezione di Firenze, Firenze, Italy

^b Università di Firenze, Firenze, Italy

L. Benussi, S. Bianco, S. Colafranceschi²⁸, F. Fabbri, D. Piccolo

INFN Laboratori Nazionali di Frascati, Frascati, Italy

P. Fabbriatore, S. Farinon, M. Greco, R. Musenich, S. Tosi

INFN Sezione di Genova, Genova, Italy

A. Benaglia^{a,b}, L. Carbone^a, P. D'Angelo^a, F. De Guio^{a,b}, L. Di Matteo^{a,b,5}, P. Dini^a, F.M. Farina^{a,b}, S. Fiorendi^{a,b}, S. Gennai^{a,5}, A. Ghezzi^{a,b}, S. Malvezzi^a, R.A. Manzoni^{a,b}, A. Martelli^{a,b}, A. Massironi^{a,b}, D. Menasce^a, L. Moroni^a, P. Negri^{a,b,†}, M. Paganoni^{a,b}, D. Pedrini^a, A. Pullia^{a,b}, S. Ragazzi^{a,b}, N. Redaelli^a, S. Sala^a, T. Tabarelli de Fatis^{a,b}

^a INFN Sezione di Milano-Bicocca, Milano, Italy

^b Università di Milano-Bicocca, Milano, Italy

S. Buontempo^a, C.A. Carrillo Montoya^a, N. Cavallo^{a,29}, A. De Cosa^{a,b,5}, O. Dogangun^{a,b}, F. Fabozzi^{a,29}, A.O.M. Iorio^{a,b}, L. Lista^a, S. Meola^{a,30}, M. Merola^a, P. Paolucci^{a,5}

^a INFN Sezione di Napoli, Napoli, Italy

^b Università di Napoli "Federico II", Napoli, Italy

P. Azzi ^a, N. Bacchetta ^{a,5}, M. Bellato ^a, M. Benettoni ^a, M. Biasotto ^{a,31}, D. Bisello ^{a,b},
 A. Branca ^{a,5}, R. Carlin ^{a,b}, P. Checchia ^a, T. Dorigo ^a, U. Dosselli ^a, F. Fanzago ^a, F. Gasparini ^{a,b},
 U. Gasparini ^{a,b}, P. Giubilato ^{a,b}, F. Gonella ^a, A. Gozzelino ^a, M. Gulmini ^{a,31}, K. Kanishchev ^{a,c},
 S. Lacaprara ^a, I. Lazzizzera ^{a,c}, M. Loretì ^a, M. Margoni ^{a,b}, G. Maron ^{a,31}, M. Mazzucato ^a,
 A.T. Meneguzzo ^{a,b}, F. Montecassiano ^a, M. Passaseo ^a, J. Pazzini ^{a,b}, M. Pegoraro ^a, N. Pozzobon ^{a,b},
 P. Ronchese ^{a,b}, F. Simonetto ^{a,b}, E. Torassa ^a, M. Tosi ^{a,b}, S. Vanini ^{a,b}, S. Ventura ^a, P. Zotto ^{a,b},
 G. Zumerle ^{a,b}

^a INFN Sezione di Padova, Padova, Italy

^b Università di Padova, Padova, Italy

^c Università di Trento (Trento), Padova, Italy

U. Berzano ^a, M. Gabusi ^{a,b}, S.P. Ratti ^{a,b}, C. Riccardi ^{a,b}, P. Torre ^{a,b}, P. Vitulo ^{a,b}

^a INFN Sezione di Pavia, Pavia, Italy

^b Università di Pavia, Pavia, Italy

M. Biasini ^{a,b}, G.M. Bilei ^a, L. Fanò ^{a,b}, P. Lariccia ^{a,b}, A. Lucaroni ^{a,b,5}, G. Mantovani ^{a,b}, M. Menichelli ^a,
 A. Nappi ^{a,b,†}, D. Passeri ^{a,b}, P. Placidi ^{a,b}, F. Romeo ^{a,b}, A. Saha ^a, A. Santocchia ^{a,b}, L. Servoli ^a,
 A. Spiezia ^{a,b}, S. Taroni ^{a,b}, M. Valdata ^{a,b}

^a INFN Sezione di Perugia, Perugia, Italy

^b Università di Perugia, Perugia, Italy

F. Angelini ^a, S. Arezzini ^a, P. Azzurri ^{a,c}, G. Bagliesi ^a, A. Basti ^a, R. Bellazzini ^a, J. Bernardini ^a, T. Boccali ^a,
 F. Bosi ^a, A. Brez ^a, G. Broccolo ^{a,c}, F. Calzolari ^a, A. Carboni ^a, R. Castaldi ^a, C. Cerri ^a, A. Ciampa ^a,
 R.T. D’Agnolo ^{a,c,5}, R. Dell’Orso ^a, F. Fiori ^{a,b,5}, L. Foà ^{a,c}, A. Giassi ^a, S. Giusti ^a, A. Kraan ^a, L. Latronico ^a,
 F. Ligabue ^{a,c}, S. Linari ^a, T. Lomtadze ^a, L. Martini ^{a,32}, M. Massa ^a, M.M. Massai ^a, E. Mazzone ^a,
 A. Messineo ^{a,b}, A. Moggi ^a, F. Palla ^a, F. Raffaelli ^a, A. Rizzi ^{a,b}, G. Sanguinetti ^a, G. Segneri ^a,
 A.T. Serban ^{a,33}, P. Spagnolo ^a, G. Spandre ^a, P. Squillacioti ^{a,5}, R. Tenchini ^a, G. Tonelli ^{a,b}, A. Venturi ^a,
 P.G. Verdini ^a

^a INFN Sezione di Pisa, Pisa, Italy

^b Università di Pisa, Pisa, Italy

^c Scuola Normale Superiore di Pisa, Pisa, Italy

S. Baccaro ^{a,34}, L. Barone ^{a,b}, A. Bartoloni ^a, F. Cavallari ^a, I. Dafinei ^a, D. Del Re ^{a,b}, M. Diemoz ^a, C. Fanelli,
 M. Grassi ^{a,b,5}, E. Longo ^{a,b}, P. Meridiani ^{a,5}, F. Micheli ^{a,b}, S. Nourbakhsh ^{a,b}, G. Organtini ^{a,b},
 R. Paramatti ^a, S. Rahatlou ^{a,b}, M. Sigamani ^a, L. Soffi ^{a,b}, I.G. Talamo ^a

^a INFN Sezione di Roma, Roma, Italy

^b Università di Roma “La Sapienza”, Roma, Italy

N. Amapane ^{a,b}, R. Arcidiacono ^{a,c}, S. Argiro ^{a,b}, M. Arneodo ^{a,c}, C. Biino ^a, N. Cartiglia ^a, M. Costa ^{a,b},
 N. Demaria ^a, C. Mariotti ^{a,5}, S. Maselli ^a, E. Migliore ^{a,b}, V. Monaco ^{a,b}, M. Musich ^{a,5}, M.M. Obertino ^{a,c},
 N. Pastrone ^a, M. Pelliccioni ^a, C. Peroni ^{a,b}, A. Potenza ^{a,b}, A. Romero ^{a,b}, M. Ruspà ^{a,c}, R. Sacchi ^{a,b},
 A. Solano ^{a,b}, A. Staiano ^a

^a INFN Sezione di Torino, Torino, Italy

^b Università di Torino, Torino, Italy

^c Università del Piemonte Orientale (Novara), Torino, Italy

F. Ambroglini ^{a,b}, S. Belforte ^a, V. Candelise ^{a,b}, M. Casarsa ^a, F. Cossutti ^a, G. Della Ricca ^{a,b}, B. Gobbo ^a,
 C. Kavka ^a, M. Marone ^{a,b,5}, D. Montanino ^{a,b,5}, A. Penzo ^a, A. Schizzi ^{a,b}

^a INFN Sezione di Trieste, Trieste, Italy

^b Università di Trieste, Trieste, Italy

T.Y. Kim, S.K. Nam

Kangwon National University, Chunchon, Republic of Korea

S. Chang, J. Chung, S.W. Ham, D. Han, J. Kang, D.H. Kim, G.N. Kim, J.E. Kim, K.S. Kim, D.J. Kong, M.W. Lee, Y.D. Oh, H. Park, S.R. Ro, D. Son, D.C. Son, J.S. Suh

Kyungpook National University, Daegu, Republic of Korea

J.Y. Kim, Zero J. Kim, S. Song

Chonnam National University, Institute for Universe and Elementary Particles, Kwangju, Republic of Korea

S. Choi, D. Gyun, B. Hong, M. Jo, Y. Jo, M. Kang, H. Kim, T.J. Kim, K.S. Lee, D.H. Moon, S.K. Park, K.S. Sim

Korea University, Seoul, Republic of Korea

M. Choi, G. Hahn, S. Kang, H. Kim, J.H. Kim, C. Park, I.C. Park, S. Park, G. Ryu

University of Seoul, Seoul, Republic of Korea

Y. Choi, Y.K. Choi, J. Goh, M.S. Kim, E. Kwon, B. Lee, J. Lee, S. Lee, H. Seo, I. Yu

Sungkyunkwan University, Suwon, Republic of Korea

M. Janulis, A. Juodagalvis, R. Naujikas

Vilnius University, Vilnius, Lithuania

H. Castilla-Valdez, E. De La Cruz-Burelo, I. Heredia-de La Cruz, R. Lopez-Fernandez, R. Magaña Villalba, J. Martínez-Ortega, A. Sánchez-Hernández, L.M. Villaseñor-Cendejas

Centro de Investigacion y de Estudios Avanzados del IPN, Mexico City, Mexico

S. Carrillo Moreno, F. Vazquez Valencia

Universidad Iberoamericana, Mexico City, Mexico

H.A. Salazar Ibarguen

Benemerita Universidad Autonoma de Puebla, Puebla, Mexico

E. Casimiro Linares, A. Morelos Pineda, M.A. Reyes-Santos

Universidad Autónoma de San Luis Potosí, San Luis Potosí, Mexico

P. Allfrey, D. Krofcheck

University of Auckland, Auckland, New Zealand

A.J. Bell, N. Bernardino Rodrigues, A.P.H. Butler, P.H. Butler, R. Doesburg, D. Pfeiffer, S. Reucroft, H. Silverwood, J.C. Williams

University of Canterbury, Christchurch, New Zealand

M. Ahmad, M.H. Ansari, M.I. Asghar, J. Butt, H.R. Hoorani, S. Khalid, W.A. Khan, T. Khurshid, S. Qazi, M.A. Shah, M. Shoaib

National Centre for Physics, Quaid-I-Azam University, Islamabad, Pakistan

H. Bialkowska, B. Boimska, T. Frueboes, R. Gokieli, L. Gosciolo, M. Górski, M. Kazana, I.M. Kudla, K. Nawrocki, K. Romanowska-Rybinska, M. Szleper, G. Wrochna, P. Zalewski

National Centre for Nuclear Research, Swierk, Poland

G. Brona, K. Bunkowski, M. Cwiok, H. Czyrkowski, R. Dabrowski, W. Dominik, K. Doroba, A. Kalinowski, M. Konecki, J. Krolikowski, W. Oklinski, K. Pozniak³⁵, W. Zabolotny³⁵, P. Zych

Institute of Experimental Physics, Faculty of Physics, University of Warsaw, Warsaw, Poland

G. Kasprowicz, R. Romaniuk

Warsaw University of Technology, Institute of Electronic Systems, Warsaw, Poland

R. Alemany-Fernandez, N. Almeida, P. Bargassa, A. David, P. Faccioli, P.G. Ferreira Parracho, M. Gallinaro, P.Q. Ribeiro, J. Seixas, J. Silva, J. Varela, P. Vischia

Laboratório de Instrumentação e Física Experimental de Partículas, Lisboa, Portugal

S. Afanasiev, I. Belotelov, P. Bunin, Y. Ershov, M. Gavrilenko, A. Golunov, I. Golutvin, N. Gorbounov, I. Gorbunov, I. Gramenitski, V. Kalagin, A. Kamenev, V. Karjavin, V. Konoplyanikov, V. Korenkov, G. Kozlov, A. Kurenkov, A. Lanev, A. Makankin, A. Malakhov, I. Melnitchenko, V.V. Mitsyn, P. Moisenz, D. Oleynik, A. Orlov, V. Palichik, V. Perelygin, A. Petrosyan, M. Savina, R. Semenov, S. Shmatov, S. Shulha, A. Skachkova, N. Skatchkov, V. Smetannikov, V. Smirnov, D. Smolin, E. Tikhonenko, S. Vasil'ev, A. Volodko, A. Zarubin, V. Zhiltsov

Joint Institute for Nuclear Research, Dubna, Russia

S. Evstyukhin, V. Golovtsov, Y. Ivanov, V. Kim, P. Levchenko, V. Murzin, V. Oreshkin, I. Smirnov, V. Sulimov, L. Uvarov, S. Vavilov, A. Vorobyev, An. Vorobyev

Petersburg Nuclear Physics Institute, Gatchina (St. Petersburg), Russia

Yu. Andreev, A. Anisimov, A. Dermenev, S. Gninenko, N. Golubev, D. Gorbunov, A. Karneyeu, M. Kirsanov, N. Krasnikov, V. Matveev, A. Pashenkov, G. Pivovarov, V.E. Postoev, V. Rubakov, V. Shirinyants, A. Solovev, D. Tlisov, A. Toropin, S. Troitsky

Institute for Nuclear Research, Moscow, Russia

V. Epshteyn, M. Erofeeva, V. Gavrillov, V. Kaftanov[†], I. Kiselevich, V. Kolosov, A. Konoplyannikov, M. Kossov, Y. Kozlov, A. Krokhotin, D. Litvintsev, N. Lychkovskaya, A. Oulianov, V. Popov, G. Safronov, S. Semenov, N. Stepanov, V. Stolin, E. Vlasov, V. Zaytsev, A. Zhokin

Institute for Theoretical and Experimental Physics, Moscow, Russia

A. Belyaev, E. Boos, V. Bunichev, A. Demiyarov, M. Dubinin⁴, L. Dudko, A. Ershov, A. Gribushin, V. Ilyin, A. Kaminskiy³⁶, V. Klyukhin, O. Kodolova, V. Korotkikh, A. Kryukov, I. Lokhtin, A. Markina, S. Obraztsov, M. Perfilov, S. Petrushanko, A. Popov, A. Proskuryakov, L. Sarycheva[†], V. Savrin, A. Snigirev, I. Vardanyan

Moscow State University, Moscow, Russia

V. Andreev, M. Azarkin, I. Dremin, M. Kirakosyan, A. Leonidov, G. Mesyats, S.V. Rusakov, A. Vinogradov

P.N. Lebedev Physical Institute, Moscow, Russia

I. Azhgirey, I. Bayshev, S. Bitiukov, V. Grishin⁵, V. Kachanov, A. Kalinin, D. Konstantinov, A. Korablev, V. Krychkine, A. Levine, V. Petrov, A. Ryabov, R. Ryutin, A. Sobol, V. Talov, L. Tourtchanovitch, S. Troshin, N. Tyurin, A. Uzunian, A. Volkov

State Research Center of Russian Federation, Institute for High Energy Physics, Protvino, Russia

P. Adzic³⁷, M. Djordjevic, M. Ekmedzic, D. Krpic³⁷, J. Milosevic, N. Smiljkovic, M. Zupan

University of Belgrade, Faculty of Physics and Vinca Institute of Nuclear Sciences, Belgrade, Serbia

M. Aguilar-Benitez, J. Alcaraz Maestre, P. Arce, C. Battilana, E. Calvo, M. Cerrada, M. Chamizo Llatas, N. Colino, B. De La Cruz, A. Delgado Peris, D. Domínguez Vázquez, C. Fernandez Bedoya, J.P. Fernández Ramos, A. Ferrando, J. Flix, M.C. Fouz, P. Garcia-Abia, O. Gonzalez Lopez, S. Goy Lopez, J.M. Hernandez, M.I. Josa, G. Merino, J. Puerta Pelayo, A. Quintario Olmeda, I. Redondo, L. Romero, J. Santaolalla, M.S. Soares, C. Willmott

Centro de Investigaciones Energéticas Medioambientales y Tecnológicas (CIEMAT), Madrid, Spain

C. Albajar, G. Codispoti, J.F. de Trocóniz

Universidad Autónoma de Madrid, Madrid, Spain

H. Brun, J. Cuevas, J. Fernandez Menendez, S. Folgueras, I. Gonzalez Caballero, L. Lloret Iglesias, J. Piedra Gomez

Universidad de Oviedo, Oviedo, Spain

J.A. Brochero Cifuentes, I.J. Cabrillo, A. Calderon, S.H. Chuang, J. Duarte Campderros, M. Felcini³⁸, M. Fernandez, G. Gomez, J. Gonzalez Sanchez, A. Graziano, C. Jorda, A. Lopez Virto, J. Marco, R. Marco, C. Martinez Rivero, F. Matorras, F.J. Munoz Sanchez, T. Rodrigo, A.Y. Rodríguez-Marrero, A. Ruiz-Jimeno, L. Scodellaro, M. Sobron Sanudo, I. Vila, R. Vilar Cortabitarte

Instituto de Física de Cantabria (IFCA), CSIC-Universidad de Cantabria, Santander, Spain

D. Abbaneo, P. Aspell, E. Auffray, G. Auzinger, M. Bachtis, J. Baechler, P. Baillon, A.H. Ball, D. Barney, J.F. Benitez, C. Bernet⁶, W. Bialas, G. Bianchi, P. Bloch, A. Bocci, A. Bonato, C. Botta, H. Breuker, D. Campi, T. Camporesi, E. Cano, G. Cerminara, A. Charkiewicz, T. Christiansen, J.A. Coarasa Perez, B. Curé, D. D'Enterria, A. Dabrowski, J. Daguin, A. De Roeck, S. Di Guida, M. Dobson, N. Dupont-Sagorin, A. Elliott-Peisert, M. Eppard, B. Frisch, W. Funk, A. Gaddi, M. Gastal, G. Georgiou, H. Gerwig, M. Giffels, D. Gigi, K. Gill, D. Giordano, M. Girone, M. Giunta, F. Glege, R. Gomez-Reino Garrido, P. Govoni, S. Gowdy, R. Guida, J. Gutleber, M. Hansen, P. Harris, C. Hartl, J. Harvey, B. Hegner, A. Hinzmann, A. Honma, V. Innocente, P. Janot, K. Kaadze, E. Karavakis, K. Kloukinas, K. Kousouris, P. Lecoq, Y.-J. Lee, P. Lenzi, R. Loos, C. Lourenço, N. Magini, T. Mäki, M. Malberti, L. Malgeri, M. Mannelli, A. Marchioro, J. Marques Pinho Noite, L. Masetti, F. Meijers, S. Mersi, E. Meschi, L. Moneta, M.U. Mozer, M. Mulders, P. Musella, A. Onnela, T. Orimoto, L. Orsini, J.A. Osborne, E. Palencia Cortezon, E. Perez, L. Perrozzi, P. Petagna, A. Petrilli, A. Petrucci, A. Pfeiffer, M. Pierini, M. Pimiä, D. Piparo, G. Polese, H. Postema, L. Quertenmont, A. Racz, W. Reece, D. Ricci, J. Rodrigues Antunes, G. Rolandi³⁹, C. Rovelli⁴⁰, M. Rovere, V. Ryjov, H. Sakulin, D. Samyn, F. Santanastasio, C. Schäfer, C. Schwick, A. Sciaba, I. Segoni, S. Sekmen, A. Sharma, P. Siegrist, P. Silva, M. Simon, P. Sphicas^{*,41}, D. Spiga, B.G. Taylor, P. Tropea, J. Troska, A. Tsirou, F. Vasey, L. Veillet, G.I. Veres²⁰, P. Vichoudis, J.R. Vlimant, P. Wertelaers, H.K. Wöhri, S.D. Worm⁴², W.D. Zeuner

CERN, European Organization for Nuclear Research, Geneva, Switzerland

W. Bertl, K. Deiters, W. Erdmann, D. Feichtinger, K. Gabathuler, R. Horisberger, Q. Ingram, H.C. Kaestli, S. König, D. Kotlinski, U. Langenegger, B. Meier, F. Meier, D. Renker, T. Rohe, T. Sakhelashvili⁴³

Paul Scherrer Institut, Villigen, Switzerland

L. Bäni, F. Behner, B. Betev, B. Blau, P. Bortignon, M.A. Buchmann, B. Casal, N. Chanon, Z. Chen, D.R. Da Silva Di Calafiori, S. Dambach⁴⁴, G. Davatz, A. Deisher, G. Dissertori, M. Dittmar, L. Djambazov, M. Donegà, M. Dünser, C. Eggel⁴⁴, J. Eugster, G. Faber, K. Freudenreich, C. Grab, W. Hintz, D. Hits, H. Hofer, O. Holme, I. Horvath, P. Lecomte, W. Lustermann, C. Marchica⁴⁴, A.C. Marini, P. Martinez Ruiz del Arbol, N. Mohr, F. Moortgat, C. Nägeli⁴⁴, P. Nef, F. Nessi-Tedaldi, F. Pandolfi, L. Pape, F. Pauss, M. Peruzzi, T. Punz, F.J. Ronga, U. Röser, M. Rossini, L. Sala, A.K. Sanchez, M.-C. Sawley, D. Schinzel, A. Starodumov⁴⁵, B. Stieger, H. Suter, M. Takahashi, L. Tauscher[†], A. Thea, K. Theofilatos, D. Treille, P. Trüb⁴⁴, S. Udriot, C. Urscheler, G. Viertel, H.P. von Gunten, R. Wallny, H.A. Weber, L. Wehrli, J. Weng, S. Zelepoukine⁴⁶

Institute for Particle Physics, ETH Zurich, Zurich, Switzerland

C. Amsler⁴⁷, V. Chiochia, S. De Visscher, C. Favaro, M. Ivova Rikova, B. Millan Mejias, P. Otiougova, P. Robmann, H. Snoek, S. Tupputi, M. Verzetti

Universität Zürich, Zurich, Switzerland

Y.H. Chang, K.H. Chen, W.T. Chen, A. Go, C.M. Kuo, S.W. Li, W. Lin, M.H. Liu, Z.K. Liu, Y.J. Lu, D. Mekterovic, A.P. Singh, R. Volpe, J.H. Wu, S.S. Yu

National Central University, Chung-Li, Taiwan

P. Bartalini, P. Chang, Y.H. Chang, Y.W. Chang, Y. Chao, K.F. Chen, C. Dietz, Z. Gao⁵, U. Grundler, W.-S. Hou, Y. Hsiung, K.Y. Kao, Y.J. Lei, J.J. Liao, S.W. Lin, R.-S. Lu, D. Majumder, E. Petrakou, X. Shi, J.G. Shiu, Y.M. Tzeng, K. Ueno, Y. Velikzhanin, X. Wan, C.C. Wang, M. Wang, J.T. Wei, P. Yeh

National Taiwan University (NTU), Taipei, Taiwan

B. Asavapibhop, N. Srimanobhas

Chulalongkorn University, Bangkok, Thailand

A. Adiguzel, M.N. Bakirci⁴⁸, S. Cerci⁴⁹, C. Dozen, I. Dumanoglu, E. Eskut, S. Girgis, G. Gokbulut, E. Garpinar, I. Hos, E.E. Kangal, T. Karaman, G. Karapinar⁵⁰, A. Kayis Topaksu, G. Onengut, K. Ozdemir, S. Ozturk⁵¹, A. Polatoz, K. Sogut⁵², D. Sunar Cerci⁴⁹, B. Tali⁴⁹, H. Topakli⁴⁸, L.N. Vergili, M. Vergili

Cukurova University, Adana, Turkey

I.V. Akin, T. Aliev, B. Bilin, M. Deniz, H. Gamsizkan, A.M. Guler, K. Ocalan, A. Ozpineci, M. Serin, R. Sever, U.E. Surat, M. Zeyrek

Middle East Technical University, Physics Department, Ankara, Turkey

M. Deliomeroğlu, E. Gülmez, B. Isildak⁵³, M. Kaya⁵⁴, O. Kaya⁵⁴, S. Ozkorucuklu⁵⁵, N. Sonmez⁵⁶

Bogazici University, Istanbul, Turkey

K. Cankocak

Istanbul Technical University, Istanbul, Turkey

B. Grynyov

Institute of Single Crystals of National Academy of Science, Kharkov, Ukraine

L. Levchuk, S. Lukyanenko, D. Soroka, P. Sorokin

National Scientific Center, Kharkov Institute of Physics and Technology, Kharkov, Ukraine

M.K.H. Ahmad, A. Branson, R. McClatchey, M. Odeh, J. Shamdasani, K. Soomro

Centre for Complex Cooperative Systems, University of the West of England, Bristol, United Kingdom

T. Barrass, F. Bostock, J.J. Brooke, E. Clement, D. Cussans, H. Flacher, R. Frazier, J. Goldstein, M. Grimes, G.P. Heath, H.F. Heath, L. Kreczko, W. Laceso, S. Metson, D.M. Newbold⁴², K. Nirunpong, A. Poll, S. Senkin, V.J. Smith, T. Williams

University of Bristol, Bristol, United Kingdom

L. Basso⁵⁷, E. Bateman, K.W. Bell, A. Belyaev⁵⁷, C. Brew, R.M. Brown, B. Camanzi, D.J.A. Cockerill, J.F. Connolly[†], J.A. Coughlan, L.G. Denton, P.S. Flower, M.J. French, R.J.S. Greenhalgh, R.N.J. Halsall, K. Harder, S. Harper, J.A. Hill, J. Jackson, B.W. Kennedy, A.L. Lintern, A.B. Lodge, E. Olaiya, M.R. Pearson, D. Petyt, B.C. Radburn-Smith, C.H. Shepherd-Themistocleous, B.J. Smith, M. Sproston, R. Stephenson, I.R. Tomalin, M.J. Torbet, J.H. Williams[†], W.J. Womersley

Rutherford Appleton Laboratory, Didcot, United Kingdom

R. Bainbridge, G. Ball, J. Ballin, D. Bauer, R. Beuselinck, O. Buchmuller, D. Colling, N. Cripps, M. Cutajar, P. Dauncey, G. Davies, M. Della Negra, W. Ferguson, J. Fulcher, D. Futyan, A. Gilbert, A. Guneratne Bryer, G. Hall, Z. Hatherell, J. Hays, G. Iles, M. Jarvis, J. Jones, G. Karapostoli, M. Kenzie, J. Leaver, L. Lyons,

A.-M. Magnan, J. Marrouche, B. Mathias, D.G. Miller, R. Nandi, J. Nash, A. Nikitenko⁴⁵, M. Noy, A. Papageorgiou, J. Pela, M. Pesaresi, K. Petridis, M. Pioppi⁵⁸, D. Rand, D.M. Raymond, S. Rogerson, A. Rose, M.J. Ryan, C. Seez, P. Sharp[†], A. Sparrow, M. Stoye, A. Tapper, C. Timlin, S. Tourneur, M. Vazquez Acosta, T. Virdee, S. Wakefield, N. Wardle, T. Whyntie, M. Wingham, O. Zorba

Imperial College, London, United Kingdom

M. Chadwick, J.E. Cole, P.R. Hobson, A. Khan, P. Kyberd, D. Leggat, D. Leslie, W. Martin, I.D. Reid, P. Symonds, L. Teodorescu, M. Turner

Brunel University, Uxbridge, United Kingdom

J. Dittmann, K. Hatakeyama, H. Liu, T. Scarborough

Baylor University, Waco, USA

O. Charaf, C. Henderson, P. Rumerio

The University of Alabama, Tuscaloosa, USA

A. Avetisyan, T. Bose, E. Carrera Jarrin, C. Fantasia, E. Hazen, A. Heister, J.St. John, P. Lawson, D. Lazic, J. Rohlf, D. Sperka, L. Sulak, F. Varela Rodriguez, S. Wu

Boston University, Boston, USA

J. Alimena, S. Bhattacharya, D. Cutts, Z. Demiragli, A. Ferapontov, A. Garabedian, U. Heintz, R. Hooper, S. Jabeen, G. Kukartsev, E. Laird, G. Landsberg, M. Luk, M. Narain, D. Nguyen, M. Segala, T. Sinthuprasith, T. Speer, K.V. Tsang, Z. Unalan

Brown University, Providence, USA

R. Breedon, G. Breto, M. Calderon De La Barca Sanchez, M. Case, S. Chauhan, M. Chertok, J. Conway, R. Conway, P.T. Cox, J. Dolen, R. Erbacher, M. Gardner, G. Grim, J. Gunion, B. Holbrook, W. Ko, A. Kopecky, R. Lander, F.C. Lin, T. Miceli, P. Murray, M. Nikolic, D. Pellett, F. Ricci-tam, J. Rowe, B. Rutherford, M. Searle, J. Smith, M. Squires, M. Tripathi, R. Vasquez Sierra, R. Yohay

University of California, Davis, Davis, USA

V. Andreev, K. Arisaka, D. Cline, R. Cousins, J. Duris, S. Erhan, P. Everaerts, C. Farrell, J. Hauser, M. Ignatenko, C. Jarvis, J. Kubic, S. Otwinowski, C. Plager, G. Rakness, P. Schlein[†], P. Traczyk, V. Valuev, M. Weber, X. Yang, Y. Zheng

University of California, Los Angeles, Los Angeles, USA

J. Babb, R. Clare, M.E. Dinardo, J. Ellison, J.W. Gary, F. Giordano, G. Hanson, G.Y. Jeng⁵⁹, J.G. Layter, H. Liu, O.R. Long, A. Luthra, H. Nguyen, S. Paramesvaran, B.C. Shen[†], J. Sturdy, S. Sumowidagdo, R. Wilken, S. Wimpenny

University of California, Riverside, Riverside, USA

W. Andrews, J.G. Branson, G.B. Cerati, M. Cinquilli, S. Cittolin, D. Evans, F. Golf, A. Holzner, R. Kelley, M. Lebourgeois, J. Letts, I. Macneill, B. Mangano, T. Martin, A. Mrak-Tadel, S. Padhi, C. Palmer, G. Petrucciani, M. Pieri, M. Sani, I. Sfiligoi, V. Sharma, S. Simon, E. Sudano, M. Tadel, Y. Tu, A. Vartak, S. Wasserbaech⁶⁰, F. Würthwein, A. Yagil, J. Yoo

University of California, San Diego, La Jolla, USA

D. Barge, R. Bellan, C. Campagnari, M. D'Alfonso, T. Danielson, K. Flowers, P. Geffert, J. Incandela, C. Justus, P. Kalavase, S.A. Koay, D. Kovalskyi, V. Krutelyov, S. Kyre, S. Lowette, G. Magazzu, N. Mccoll, V. Pavlunin, F. Rebassoo, J. Ribnik, J. Richman, R. Rossin, D. Stuart, W. To, C. West, D. White

University of California, Santa Barbara, Santa Barbara, USA

D. Adamczyk, A. Apresyan, A. Barczyk, A. Bornheim, J. Bunn, Y. Chen, G. Denis, E. Di Marco, J. Duarte, P. Galvez, M. Gataullin, D. Kcira, I. Legrand, V. Litvine, Y. Ma, Z. Maxa, A. Mott, A. Mughal, D. Nae, H.B. Newman, S. Ravot, C. Rogan, S.G. Rozsa, S. Shevchenko, K. Shin, M. Spiropulu, C. Steenberg, M. Thomas, V. Timciuc, F. van Lingen, J. Veverka, B.R. Voicu, R. Wilkinson, S. Xie, Y. Yang, L. Zhang, K. Zhu, R.Y. Zhu

California Institute of Technology, Pasadena, USA

B. Akgun, V. Azzolini, A. Calamba, R. Carroll, T. Ferguson, Y. Iiyama, D.W. Jang, S.Y. Jun, Y.F. Liu, M. Paulini, J. Russ, N. Terentyev, H. Vogel, I. Vorobiev

Carnegie Mellon University, Pittsburgh, USA

J.P. Cumalat, B.R. Drell, W.T. Ford, A. Gaz, B. Heyburn, D. Johnson, E. Luiggi Lopez, U. Nauenberg, J.G. Smith, K. Stenson, K.A. Ulmer, S.R. Wagner, S.L. Zang

University of Colorado at Boulder, Boulder, USA

L. Agostino, J. Alexander, A. Chatterjee, N. Eggert, L.K. Gibbons, B. Heltsley, A. Khukhunaishvili, B. Kreis, V. Kuznetsov, N. Mirman, G. Nicolas Kaufman, J.R. Patterson, D. Riley, A. Ryd, E. Salvati, S. Stroiney, W. Sun, W.D. Teo, J. Thom, J. Thompson, J. Tucker, J. Vaughan, Y. Weng, L. Winstrom, P. Wittich

Cornell University, Ithaca, USA

D. Winn

Fairfield University, Fairfield, USA

S. Abdullin, M. Albert, M. Albrow, J. Anderson, G. Apollinari, M. Atac[†], W. Badgett, J.A. Bakken, B. Baldin, K. Banicz, L.A.T. Bauerdick, A. Beretvas, J. Berryhill, P.C. Bhat, M. Binkley[†], F. Borchering, K. Burkett, J.N. Butler, V. Chetluru, H.W.K. Cheung, F. Chlebana, S. Cihangir, W. Dagenhart, G. Derylo, C. Dumitrescu, D. Dykstra, D.P. Eartly, J.E. Elias[†], V.D. Elvira, G. Eulisse, D. Evans, D. Fagan, I. Fisk, S. Foulkes, J. Freeman, I. Gaines, Y. Gao, P. Garton, L. Giacchetti, E. Gottschalk, D. Green, Y. Guo, O. Gutsche, A. Hahn, J. Hanlon, R.M. Harris, J. Hirschauer, B. Holzman, B. Hooberman, J. Howell, C.h. Huang, D. Hufnagel, S. Jindariani, M. Johnson, C.D. Jones, U. Joshi, E. Juska, B. Kilminster, B. Klima, S. Kunori, S. Kwan, K. Larson, C. Leonidopoulos, J. Linacre, D. Lincoln, R. Lipton, J.A. Lopez Perez, S. Los, J. Lykken, K. Maeshima, J.M. Marraffino, S. Maruyama, D. Mason, P. McBride, T. McCauley, K. Mishra, S. Moccia, R.K. Mommsen, S. Mrenna, Y. Musienko⁶¹, S. Muzaffar, C. Newman-Holmes, V. O'Dell, I. Osborne, J. Pivarski, S. Popescu²⁷, R. Pordes, O. Prokofyev, V. Rapsevicius, A. Ronzhin, P. Rossman, S. Ryu, E. Sexton-Kennedy, S. Sharma, T.M. Shaw, R.P. Smith[†], A. Soha, W.J. Spalding, L. Spiegel, W. Tanenbaum, L. Taylor, R. Thompson, A. Tiradani, S. Tkaczyk, N.V. Tran, L. Tuura, L. Uplegger, E.W. Vaandering, R. Vidal, J. Whitmore, W. Wu, F. Yang, J. Yarba, J.C. Yun, T. Zimmerman

Fermi National Accelerator Laboratory, Batavia, USA

D. Acosta, P. Avery, V. Barashko, D. Bourilkov, M. Chen, T. Cheng, S. Das, M. De Gruttola, G.P. Di Giovanni, D. Dobur, S. Dolinsky, A. Drozdetskiy, R.D. Field, M. Fisher, Y. Fu, I.K. Furic, J. Gartner, L. Gorn, D. Holmes, J. Hugon, B. Kim, J. Konigsberg, A. Korytov, A. Kropivnitskaya, T. Kypreos, J.F. Low, A. Madorsky, K. Matchev, P. Milenovic⁶², G. Mitselmakher, L. Muniz, M. Park, R. Remington, A. Rinkevicius, B. Scurlock, N. Skhirtladze, M. Snowball, J. Stasko, J. Yelton, M. Zakaria

University of Florida, Gainesville, USA

V. Gaultney, S. Hewamanage, L.M. Lebolo, S. Linn, P. Markowitz, G. Martinez, J.L. Rodriguez

Florida International University, Miami, USA

T. Adams, A. Askew, M. Bertoldi, J. Bochenek, J. Chen, W.G.D. Dharmaratna, B. Diamond, S.V. Gleyzer, J. Haas, S. Hagopian, V. Hagopian, M. Jenkins, K.F. Johnson, H. Prosper, S. Tentindo, V. Veeraraghavan, M. Weinberg

Florida State University, Tallahassee, USA

M.M. Baarmand, B. Dorney, M. Hohlmann, H. Kalakhety, R. Ralich, I. Vodopiyanov, F. Yumiceva

Florida Institute of Technology, Melbourne, USA

M.R. Adams, I.M. Anghel, L. Apanasevich, Y. Bai, V.E. Bazterra, R.R. Betts, I. Bucinskaite, J. Callner, R. Cavanaugh, M.H. Chung, O. Evdokimov, E.J. Garcia-Solis, L. Gauthier, C.E. Gerber, D.J. Hofman, R. Hollis, A. Iordanova, S. Khalatyan, G.J. Kunde⁶³, F. Lacroix, M. Malek, C. O'Brien, C. Silkworth, C. Silvestre, A. Smoron, D. Strom, P. Turner, N. Varelas

University of Illinois at Chicago (UIC), Chicago, USA

U. Akgun, E.A. Albayrak, A.S. Ayan, B. Bilki⁶⁴, W. Clarida, P. Debbins, F. Duru, F.D. Ingram, E. McCliment, J.-P. Merlo, H. Mermerkaya⁶⁵, A. Mestvirishvili, M.J. Miller, A. Moeller, J. Nachtman, C.R. Newsom, E. Norbeck, J. Olson, Y. Onel, F. Ozok⁶⁶, I. Schmidt, S. Sen, P. Tan, E. Tiras, J. Wetzel, T. Yetkin, K. Yi

The University of Iowa, Iowa City, USA

B.A. Barnett, B. Blumenfeld, S. Bolognesi, D. Fehling, G. Giurgiu, A.V. Gritsan, Z.J. Guo, G. Hu, P. Maksimovic, S. Rappoccio, M. Swartz, A. Whitbeck

Johns Hopkins University, Baltimore, USA

P. Baringer, A. Bean, G. Benelli, D. Coppage, O. Grachov, R.P. Kenny Iii, M. Murray, D. Noonan, V. Radicci, S. Sanders, R. Stringer, G. Tinti, J.S. Wood, V. Zhukova

The University of Kansas, Lawrence, USA

A.F. Barfuss, T. Bolton, I. Chakaberia, A. Ivanov, S. Khalil, M. Makouski, Y. Maravin, S. Shrestha, I. Svintradze

Kansas State University, Manhattan, USA

J. Gronberg, D. Lange, D. Wright

Lawrence Livermore National Laboratory, Livermore, USA

A. Baden, R. Bard, M. Boutemur, B. Calvert, S.C. Eno, J.A. Gomez, T. Grassi, N.J. Hadley, R.G. Kellogg, M. Kirn, T. Kolberg, Y. Lu, M. Marionneau, A.C. Mignerey, K. Pedro, A. Peterman, K. Rossato, A. Skuja, J. Temple, M.B. Tonjes, S.C. Tonwar, T. Toole, E. Twedt

University of Maryland, College Park, USA

A. Apyan, G. Bauer, J. Bendavid, W. Busza, E. Butz, I.A. Cali, M. Chan, V. Dutta, G. Gomez Ceballos, M. Goncharov, K.A. Hahn, Y. Kim, M. Klute, K. Krajczar⁶⁷, A. Levin, P.D. Luckey, T. Ma, S. Nahn, C. Paus, D. Ralph, C. Roland, G. Roland, M. Rudolph, G.S.F. Stephans, F. Stöckli, K. Sumorok, K. Sung, D. Velicanu, E.A. Wenger, R. Wolf, B. Wyslouch, M. Yang, Y. Yilmaz, A.S. Yoon, M. Zanetti

Massachusetts Institute of Technology, Cambridge, USA

D. Bailleux, S.I. Cooper, P. Cushman, B. Dahmes, A. De Benedetti, R. Egeland, G. Franzoni, A. Gude, J. Haupt, A. Inyakin, S.C. Kao, K. Klapoetke, Y. Kubota, J. Mans, N. Pastika, R. Rusack, A. Singovsky, N. Tambe, J. Turkewitz

University of Minnesota, Minneapolis, USA

L.M. Cremaldi, R. Kroeger, L. Perera, R. Rahmat, J. Reidy, D.A. Sanders, D. Summers

University of Mississippi, University, USA

G. Attebury, E. Avdeeva, K. Bloom, B. Bockelman, S. Bose, D.R. Claes, A. Dominguez, M. Eads, J. Keller, I. Kravchenko, J. Lazo-Flores, C. Lundstedt, H. Malbouisson, S. Malik, R. Snihur, G.R. Snow, D. Swanson

University of Nebraska-Lincoln, Lincoln, USA

U. Baur, A. Godshalk, I. Iashvili, S. Jain, A. Kharchilava, A. Kumar, S.P. Shipkowski, K. Smith

State University of New York at Buffalo, Buffalo, USA

G. Alverson, E. Barberis, D. Baumgartel, M. Chasco, J. Haley, J. Moromisato, D. Nash, J. Swain, D. Trocino, E. Von Goeler, D. Wood, J. Zhang

Northeastern University, Boston, USA

A. Anastassov, B. Gobbi, A. Kubik, L. Lusito, N. Odell, R.A. Ofierzynski, B. Pollack, A. Pozdnyakov, M. Schmitt, S. Stoynev, M. Velasco, S. Won

Northwestern University, Evanston, USA

L. Antonelli, B. Baumbaugh, D. Berry, A. Brinkerhoff, K.M. Chan, A.H. Heering, M. Hildreth, C. Jessop, D.J. Karmgard, N. Kellams, J. Kolb, K. Lannon, W. Luo, S. Lynch, N. Marinelli, D.M. Morse, T. Pearson, M. Planer, R. Ruchti, J. Slaunwhite, N. Valls, M. Wayne, M. Wolf, A. Woodard

University of Notre Dame, Notre Dame, USA

B. Bylsma, L.S. Durkin, C. Hill, R. Hughes, K. Kotov, T.Y. Ling, D. Puigh, M. Rodenburg, C.J. Rush, V. Sehgal, C. Vuosalo, G. Williams, B.L. Winer

The Ohio State University, Columbus, USA

N. Adam, E. Berry, P. Elmer, D. Gerbaudo, V. Halyo, P. Hebda, J. Hegeman, A. Hunt, P. Jindal, D. Lopes Pegna, P. Lujan, D. Marlow, T. Medvedeva, M. Mooney, J. Olsen, P. Piroué, X. Quan, A. Raval, H. Saka, D. Stickland, C. Tully, J.S. Werner, T. Wildish, Z. Xie, S.C. Zenz, A. Zuranski

Princeton University, Princeton, USA

J.G. Acosta, M. Bonnett Del Alamo, E. Brownson, X.T. Huang, A. Lopez, H. Mendez, S. Oliveros, J.E. Ramirez Vargas, A. Zatserklyaniy

University of Puerto Rico, Mayaguez, USA

E. Alagoz, K. Arndt, V.E. Barnes, D. Benedetti, G. Bolla, D. Bortoletto, A. Bujak, M. De Mattia, A. Everett, L. Gutay, Z. Hu, M. Jones, O. Koybasi, M. Kress, A.T. Laasanen, J. Lee, N. Leonardo, C. Liu, V. Maroussov, P. Merkel, D.H. Miller, J. Miyamoto, N. Neumeister, C. Rott, A. Roy, I. Shipsey, D. Silvers, A. Svyatkovskiy, M. Vidal Marono, H.D. Yoo, J. Zablocki, Y. Zheng

Purdue University, West Lafayette, USA

S. Guragain, N. Parashar

Purdue University Calumet, Hammond, USA

A. Adair, C. Boulahouache, V. Cuplov, K.M. Ecklund, F.J.M. Geurts, S.J. Lee, W. Li, J.H. Liu, M. Matveev, B.P. Padley, R. Redjimi, J. Roberts, A. Tumanov, P. Yepes, J. Zabel

Rice University, Houston, USA

B. Betchart, A. Bodek, H. Budd, Y.S. Chung, R. Covarelli, P. de Barbaro, R. Demina, Y. Eshaq, T. Ferbel, A. Garcia-Bellido, G. Ginther, P. Goldenzweig, Y. Gotra, J. Han, A. Harel, S. Korjenevski, D.C. Miner, D. Orbaker, W. Sakumoto, P. Slattery, D. Vishnevskiy, M. Zielinski

University of Rochester, Rochester, USA

A. Bhatti, R. Ciesielski, L. Demortier, K. Goulios, G. Lungu, S. Malik, C. Mesropian

The Rockefeller University, New York, USA

S. Arora, A. Barker, J.P. Chou, C. Contreras-Campana, E. Contreras-Campana, D. Duggan, D. Ferencek, Y. Gershtein, R. Gray, E. Halkiadakis, D. Hidas, A. Lath, S. Panwalkar, M. Park, R. Patel, V. Rekovic, J. Robles, K. Rose, S. Salur, S. Schnetzer, C. Seitz, S. Somalwar, R. Stone, S. Thomas

Rutgers, the State University of New Jersey, Piscataway, USA

G. Cerizza, M. Hollingsworth, G. Raghianti, S. Spanier, Z.C. Yang, A. York

University of Tennessee, Knoxville, USA

O. Bouhali, R. Eusebi, W. Flanagan, J. Gilmore, T. Kamon⁶⁸, V. Khotilovich, R. Montalvo, C.N. Nguyen, I. Osipenkov, Y. Pakhotin, A. Perloff, J. Roe, A. Safonov, T. Sakuma, S. Sengupta, I. Suarez, A. Tatarinov, D. Toback

Texas A&M University, College Station, USA

N. Akchurin, J. Damgov, C. Dragoiu, P.R. Duder, C. Jeong, K. Kovitanggoon, S.W. Lee, T. Libeiro, Y. Roh, A. Sill, I. Volobouev, R. Wigmans

Texas Tech University, Lubbock, USA

E. Appelt, A.G. Delannoy, D. Engh, C. Florez, W. Gabella, S. Greene, A. Gurrola, W. Johns, P. Kurt, C. Maguire, A. Melo, M. Sharma, P. Sheldon, B. Snook, S. Tuo, J. Velkovska

Vanderbilt University, Nashville, USA

D. Andelin, M.W. Arenton, M. Balazs, S. Boutle, S. Conetti, B. Cox, B. Francis, J. Goodell, R. Hirosky, A. Ledovskoy, C. Lin, C. Neu, D. Phillips II, J. Wood

University of Virginia, Charlottesville, USA

S. Gollapinni, R. Harr, P.E. Karchin, C. Kottachchi Kankanamge Don, P. Lamichhane, M. Mattson, C. Milstène, A. Sakharov

Wayne State University, Detroit, USA

M. Anderson, D. Belknap, J.N. Bellinger, L. Borrello, D. Bradley, D. Carlsmith, M. Cepeda, I. Crotty⁵, S. Dasu, F. Feyzi, E. Friis, T. Gorski, L. Gray, K.S. Grogg, M. Grothe, R. Hall-Wilton, M. Herndon, A. Hervé, P. Klabbers, J. Klukas, J. Lackey, A. Lanaro, C. Lazaridis, J. Leonard, R. Loveless, S. Lusin⁵, M. Magrans de Abril, W. Maier, A. Mohapatra, I. Ojalvo, F. Palmonari, G.A. Pierro, D. Reeder, I. Ross, A. Savin, W.H. Smith, J. Swanson, D. Wenman

University of Wisconsin, Madison, USA

* Corresponding author.

† Deceased.

¹ Also at Vienna University of Technology, Vienna, Austria.

² Also at National Institute of Chemical Physics and Biophysics, Tallinn, Estonia.

³ Also at Universidade Federal do ABC, Santo Andre, Brazil.

⁴ Also at California Institute of Technology, Pasadena, USA.

⁵ Also at CERN, European Organization for Nuclear Research, Geneva, Switzerland.

⁶ Also at Laboratoire Leprince-Ringuet, Ecole Polytechnique, IN2P3–CNRS, Palaiseau, France.

⁷ Also at Suez Canal University, Suez, Egypt.

⁸ Also at Zewail City of Science and Technology, Zewail, Egypt.

- ⁹ Also at Cairo University, Cairo, Egypt.
- ¹⁰ Also at Fayoum University, El-Fayoum, Egypt.
- ¹¹ Also at British University, Cairo, Egypt.
- ¹² Now at Ain Shams University, Cairo, Egypt.
- ¹³ Also at National Centre for Nuclear Research, Swierk, Poland.
- ¹⁴ Also at Université de Haute-Alsace, Mulhouse, France.
- ¹⁵ Also at Joint Institute for Nuclear Research, Dubna, Russia.
- ¹⁶ Also at Moscow State University, Moscow, Russia.
- ¹⁷ Also at Brandenburg University of Technology, Cottbus, Germany.
- ¹⁸ Also at The University of Kansas, Lawrence, USA.
- ¹⁹ Also at Institute of Nuclear Research ATOMKI, Debrecen, Hungary.
- ²⁰ Also at Eötvös Loránd University, Budapest, Hungary.
- ²¹ Also at Tata Institute of Fundamental Research – HECR, Mumbai, India.
- ²² Now at King Abdulaziz University, Jeddah, Saudi Arabia.
- ²³ Also at University of Visva-Bharati, Santiniketan, India.
- ²⁴ Also at Sharif University of Technology, Tehran, Iran.
- ²⁵ Also at Isfahan University of Technology, Isfahan, Iran.
- ²⁶ Also at Plasma Physics Research Center, Science and Research Branch, Islamic Azad University, Teheran, Iran.
- ²⁷ Also at Horia Hulubei National Institute of Physics and Nuclear Engineering (IFIN-HH), Bucharest, Romania.
- ²⁸ Also at Facoltà Ingegneria Università di Roma, Roma, Italy.
- ²⁹ Also at Università della Basilicata, Potenza, Italy.
- ³⁰ Also at Università degli Studi Guglielmo Marconi, Roma, Italy.
- ³¹ Also at Laboratori Nazionali di Legnaro dell' INFN, Legnaro, Italy.
- ³² Also at Università degli Studi di Siena, Siena, Italy.
- ³³ Also at University of Bucharest, Faculty of Physics, Bucuresti-Magurele, Romania.
- ³⁴ Also at ENEA – Casaccia Research Center, S. Maria di Galeria, Italy.
- ³⁵ Also at Warsaw University of Technology, Institute of Electronic Systems, Warsaw, Poland.
- ³⁶ Also at INFN Sezione di Padova; Università di Padova; Università di Trento (Trento), Padova, Italy.
- ³⁷ Also at Faculty of Physics of University of Belgrade, Belgrade, Serbia.
- ³⁸ Also at University of California, Los Angeles, Los Angeles, USA.
- ³⁹ Also at Scuola Normale e Sezione dell'INFN, Pisa, Italy.
- ⁴⁰ Also at INFN Sezione di Roma; Università di Roma “La Sapienza”, Roma, Italy.
- ⁴¹ Also at University of Athens, Athens, Greece.
- ⁴² Also at Rutherford Appleton Laboratory, Didcot, United Kingdom.
- ⁴³ Also at Institute of High Energy Physics and Informatization, Tbilisi State University, Tbilisi, Georgia.
- ⁴⁴ Also at Paul Scherrer Institut, Villigen, Switzerland.
- ⁴⁵ Also at Institute for Theoretical and Experimental Physics, Moscow, Russia.
- ⁴⁶ Also at University of Wisconsin, Madison, USA.
- ⁴⁷ Also at Albert Einstein Center for Fundamental Physics, Bern, Switzerland, BERN, SWITZERLAND.
- ⁴⁸ Also at Gaziosmanpasa University, Tokat, Turkey.
- ⁴⁹ Also at Adiyaman University, Adiyaman, Turkey.
- ⁵⁰ Also at Izmir Institute of Technology, Izmir, Turkey.
- ⁵¹ Also at The University of Iowa, Iowa City, USA.
- ⁵² Also at Mersin University, Mersin, Turkey.
- ⁵³ Also at Ozyegin University, Istanbul, Turkey.
- ⁵⁴ Also at Kafkas University, Kars, Turkey.
- ⁵⁵ Also at Suleyman Demirel University, Isparta, Turkey.
- ⁵⁶ Also at Ege University, Izmir, Turkey.
- ⁵⁷ Also at School of Physics and Astronomy, University of Southampton, Southampton, United Kingdom.
- ⁵⁸ Also at INFN Sezione di Perugia; Università di Perugia, Perugia, Italy.
- ⁵⁹ Also at University of Sydney, Sydney, Australia.
- ⁶⁰ Also at Utah Valley University, Orem, USA.
- ⁶¹ Also at Institute for Nuclear Research, Moscow, Russia.
- ⁶² Also at University of Belgrade, Faculty of Physics and Vinca Institute of Nuclear Sciences, Belgrade, Serbia.
- ⁶³ Also at Los Alamos National Laboratory, Los Alamos, USA.
- ⁶⁴ Also at Argonne National Laboratory, Argonne, USA.
- ⁶⁵ Also at Erzincan University, Erzincan, Turkey.
- ⁶⁶ Also at Mimar Sinan University, Istanbul, Istanbul, Turkey.
- ⁶⁷ Also at KFKI Research Institute for Particle and Nuclear Physics, Budapest, Hungary.
- ⁶⁸ Also at Kyungpook National University, Daegu, Republic of Korea.



First measurement of the cross section for top-quark pair production in proton–proton collisions at $\sqrt{s} = 7$ TeV [☆]

CMS Collaboration

CERN, Switzerland

ARTICLE INFO

Article history:

Received 30 October 2010
 Received in revised form 18 November 2010
 Accepted 26 November 2010
 Available online 1 December 2010
 Editor: M. Doser

Keywords:

CMS
 LHC
 Physics
 Top quark
 Cross section

ABSTRACT

The first measurement of the cross section for top-quark pair production in pp collisions at the Large Hadron Collider at center-of-mass energy $\sqrt{s} = 7$ TeV has been performed using a data sample corresponding to an integrated luminosity of $3.1 \pm 0.3 \text{ pb}^{-1}$ recorded by the CMS detector. This result utilizes the final state with two isolated, highly energetic charged leptons, large missing transverse energy, and two or more jets. Backgrounds from Drell–Yan and non-W/Z boson production are estimated from data. Eleven events are observed in the data with 2.1 ± 1.0 events expected from background. The measured cross section is $194 \pm 72(\text{stat.}) \pm 24(\text{syst.}) \pm 21(\text{lumi.}) \text{ pb}$, consistent with next-to-leading order predictions.

© 2010 CERN. Published by Elsevier B.V. All rights reserved.

Since its discovery [1,2], the properties of the top quark have been subject to numerous detailed studies [3], which until recently have only been possible at the Tevatron proton–antiproton collider. With the advent of the Large Hadron Collider (LHC) era [4], top-quark processes can be studied for the first time in multi-TeV proton–proton collisions. In both $p\bar{p}$ and pp collisions, top quarks are expected to be produced primarily via the strong interaction in top–antitop ($t\bar{t}$) pairs. At the LHC, the $t\bar{t}$ production mechanism is expected to be dominated by a gluon fusion process, whereas at the Tevatron, top-quark pairs are predominantly produced through quark–antiquark annihilation. Measurements of top-quark production at the LHC are therefore important new tests of our understanding of the $t\bar{t}$ production mechanism. This is a crucial component of the early LHC physics program, since many signatures of new physics models accessible at the LHC either suffer from top-quark production as a significant background or contain top quarks themselves.

In this Letter we present the first measurement of the cross section for $t\bar{t}$ production in proton–proton collisions at the LHC at center-of-mass energy $\sqrt{s} = 7$ TeV. The results are based on a data sample corresponding to an integrated luminosity of $3.1 \pm 0.3 \text{ pb}^{-1}$ [5] recorded by the CMS experiment [6] between March and August 2010. This measurement is an important milestone for

CMS, demonstrating the experiment’s capabilities in extracting an intricate signature.

Within the standard model, the top quark decays via the weak process $t \rightarrow Wb$ almost exclusively. Experimentally, top-quark pair events are categorized according to the decay of the two W bosons: the all-hadronic channel, in which both W bosons decay into quarks; the lepton + jets channel, in which one W boson decays leptonically, the other into quarks; and the dilepton channel, in which both W bosons decay into leptons. The measurement described herein is performed using the e^+e^- , $\mu^+\mu^-$, and $e^\pm\mu^\mp$ dilepton $t\bar{t}$ modes. These modes comprise $(6.45 \pm 0.11)\%$ [7] of the total branching fraction for $t\bar{t}$ when including contributions from tau leptons that subsequently decay to electrons and muons, as is done here. Therefore, the final state studied in this analysis contains two oppositely charged leptons (electrons or muons), two neutrinos from the W boson decays, and at least two jets of particles resulting from the hadronization of the b quarks. Similar measurements have been performed recently at the Tevatron [8,9].

The central feature of the CMS apparatus is a superconducting solenoid, 13 m in length and 6 m in diameter, which provides an axial magnetic field of 3.8 T. The bore of the solenoid is outfitted with various particle detection systems. Charged particle trajectories are measured by the silicon pixel and strip tracker, covering $0 < \phi < 2\pi$ in azimuth and $|\eta| < 2.5$, where the pseudorapidity η is defined as $\eta = -\ln[\tan\theta/2]$, with θ being the polar angle of the trajectory of the particle with respect to the beam direction. A crystal electromagnetic calorimeter (ECAL)

[☆] © CERN, for the benefit of the CMS Collaboration.

E-mail address: cms-publication-committee-chair@cern.ch.

and a brass/scintillator hadronic calorimeter (HCAL) surround the tracking volume; in this analysis the calorimetry provides high-resolution energy and direction measurements of electrons and hadronic jets. Muons are measured in gas detectors embedded in the steel return yoke outside the solenoid. The detector is nearly hermetic, allowing for energy balance measurements in the plane transverse to the beam directions. A two-tier trigger system selects the most interesting pp collision events for use in physics analysis. A more detailed description of the CMS detector can be found elsewhere [6].

The trigger providing the data sample used in this analysis is based on the presence of at least one charged lepton, either an electron or a muon, with a minimum transverse momentum p_T of 9 (15) GeV/c for the muon (electron). This data sample is used both for the selection of the signal and for signal-depleted control regions used for studies related to background processes. Simulated signal events that pass the event selection, as described below, satisfy the trigger requirements with an efficiency above 97% in the $\mu^+\mu^-$ decay mode and above 99% in the other two modes, in agreement with estimates from Z boson events in the data.

Before further consideration, events are required to have at least one good reconstructed pp interaction vertex [10]. Among these events, selection criteria are applied to reconstructed objects to identify candidates consistent with dilepton $t\bar{t}$ processes.

Muon candidates are reconstructed [11] using two algorithms that require consistent hits in the tracker and muon systems: one is an algorithm based on the matching of extrapolated trajectories from the silicon tracker to hits in the muon system (tracker-based muons); the second is an algorithm based on performing a global fit of consistent hits in the tracker and the muon system (globally-fitted muons). Candidates are required to have $p_T > 20$ GeV/c and $|\eta| < 2.5$. Additionally, the track associated with the muon candidate is required to have a minimum number of hits in the silicon tracker, to be consistent with originating from the beam spot, and to have a high-quality global fit including a minimum number of hits in the muon detector.

Electron candidates are reconstructed [12] starting from a cluster of energy deposits in the crystals of the ECAL, which is then matched to hits in the silicon tracker, used to initiate a special track reconstruction algorithm. The electron reconstruction algorithm takes into account the possibility of significant energy loss of the electron through bremsstrahlung as it traverses the material of the tracker. Electron candidates are required to have $p_T > 20$ GeV/c and pseudorapidity $|\eta| < 2.5$. The electron candidate track is required to be consistent with originating from the beam spot. Requirements on the values of electron identification variables based on shower shape and track-cluster matching are applied to the reconstructed candidates; the criteria are optimized for inclusive $W \rightarrow e\nu$ selection and are designed to maximize the rejection of electron candidates from QCD multijet production while maintaining 90% efficiency for electrons from the decay of W/Z bosons. Electron candidates within $\Delta R = \sqrt{\Delta\phi^2 + \Delta\eta^2} < 0.1$ of a tracker-based or globally-fitted muon are rejected to remove fake electron candidates due to muon bremsstrahlung. In addition, electrons consistent with anomalous depositions in the ECAL or with photon conversions are rejected.

Charged leptons from the decay of W bosons are expected to be isolated from other activity in the event. For selected muon and electron candidates, a cone of $\Delta R < 0.3$ is constructed around the track direction at the origin and the scalar sum of the track transverse momenta and calorimeter energy deposits, projected onto a plane transverse to the beam, is calculated. The contribution from the candidate itself is excluded. If the value of this scalar sum is more than 15% of the candidate's transverse momentum, the candidate is considered to be non-isolated and is rejected.

Lepton trigger, identification, and isolation efficiencies are measured using inclusive Z events from data and are compared with simulation. All comparisons show good agreement, generally within 2%. The residual differences between the efficiencies estimated in data and simulation are treated as systematic uncertainties.

Events are required to have at least one pair of oppositely charged leptons. Both charged leptons are required to originate from within 1 cm along the beam line of the reconstructed pp interaction location. To veto contributions from Z production, the invariant mass of the dilepton system, $M_{\ell\ell}$, is required to be outside a ± 15 GeV/ c^2 window centered at the mass of the Z boson for the e^+e^- and $\mu^+\mu^-$ modes. Additionally, dilepton candidate events with $M_{\ell\ell} < 10$ GeV/ c^2 are removed, at essentially no penalty for the collected signal.

The neutrinos from the W boson decays do not interact with the detector and escape without depositing any of their energy. The presence of a neutrino manifests itself as an imbalance in the measured energy depositions; the imbalance in the projection perpendicular to the beam line (missing transverse energy, \cancel{E}_T) is an important distinguishing feature of $t\bar{t}$ events in this channel. At CMS there are several techniques for calculating \cancel{E}_T [13]; here, the raw \cancel{E}_T , calculated from calorimeter signals, is made more accurate through a series of corrections taking into account the contribution from the minimally interacting muons and, most importantly, a per-track correction for the expected imperfect response of the calorimeter, derived from simulation. This track correction results in an improved energy resolution, especially for low-energy charged particles. Neither the dominant background processes, Drell–Yan $Z/\gamma^* \rightarrow e^+e^-$ and $\mu^+\mu^-$, nor the difficult-to-model background from isolated lepton candidates produced in QCD multijet events, contain a natural source of large \cancel{E}_T . Hence, in the e^+e^- and $\mu^+\mu^-$ modes, $\cancel{E}_T > 30$ GeV is required; in the $e^\pm\mu^\mp$ mode a looser requirement of $\cancel{E}_T > 20$ GeV is used due to the significantly smaller contribution of Drell–Yan background.

Dilepton $t\bar{t}$ events will have at least two hadronic jets from the hadronization of the two b quarks. The anti- k_T clustering algorithm [14] with $R = 0.5$ is used for jet clustering. Jets are reconstructed using calorimeter information and corrected using reconstructed tracks [15]. Further corrections are applied to the raw jet momenta to establish a relative uniform response of the calorimeter in jet η and an absolute uniform response in jet p_T . The jet energy scale uncertainty for these track-corrected jets is 5%. Jet candidates are required to have $p_T > 30$ GeV/c, $|\eta| < 2.5$, and must not overlap with any electron or muon candidate within $\Delta R < 0.4$. Events with fewer than two jets are not used in the measurement.

The selection efficiency of signal events is evaluated in a simulated $t\bar{t}$ event sample modeled with the MADGRAPH event generator version 4.4.12 [16] with up to three additional hadronic jets. The events are subsequently processed with PYTHIA (v. 6.420) [17] to provide showering of generated particles, and then processed with a full CMS detector simulation based on GEANT4 (v. 9.2 Rev01) [18]. The total next-to-leading order (NLO) cross section for top-quark pair production used here to scale simulated signal distributions is $\sigma_{t\bar{t}} = 158_{-24}^{+23}$ pb, as obtained with MCFM [19–22] for a top-quark mass of 172.5 GeV/ c^2 . Approximate next-to-next-to-leading order (NNLO) calculations for the $t\bar{t}$ cross section have been completed (see for example [23–29]) but are not used here. The theoretical uncertainty on the cross section includes the scale uncertainties, determined by varying the factorization and renormalization scales by factors of 2 and 0.5 around the central scale, corresponding to the assumed top-quark mass, and the uncertainties from the parton distribution functions (PDFs) and the value of α_s ,

Table 1

The expected number of dilepton $t\bar{t}$ signal and background events passing the full selection criteria, compared to the number of observed events. The procedures for estimating the expected numbers of events and their uncertainties are described in the text. For the backgrounds estimated from data, the statistical and systematic uncertainties are quoted separately. The expected signal yield assumes a $t\bar{t}$ cross section of $\sigma_{t\bar{t}} = 158^{+23}_{-24}$ pb.

Source	Number of events
Expected $t\bar{t}$	7.7 ± 1.5
Dibosons (VV)	0.13 ± 0.07
Single top (tW)	0.25 ± 0.13
Drell–Yan $Z/\gamma^* \rightarrow \tau^+\tau^-$	0.18 ± 0.09
Drell–Yan $Z/\gamma^* \rightarrow e^+e^-, \mu^+\mu^-$	$1.4 \pm 0.5 \pm 0.5$
Events with non-W/Z leptons	$0.1 \pm 0.5 \pm 0.3$
Total backgrounds	2.1 ± 1.0
Expected total, including $t\bar{t}$	9.8 ± 1.8
Data	11

following the procedures from the MSTW2008 [30], CTEQ6.6 [31], and NNPDF2.0 [32] sets. From the simulated $t\bar{t}$ sample, the total signal acceptance, including geometric acceptance and event reconstruction and selection efficiencies, is found to be $(23.0 \pm 1.4)\%$ for events contributing to the e^+e^- , $\mu^+\mu^-$, and $e^\pm\mu^\mp$ modes combined, where the systematic uncertainty on the acceptance is described later in the text. The expected yield of events passing the selection criteria, assuming the NLO production cross section, is 1.5 ± 0.3 , 1.7 ± 0.3 , and 4.5 ± 0.9 for the e^+e^- , $\mu^+\mu^-$, and $e^\pm\mu^\mp$ decay modes, respectively. The uncertainties on these predicted event yields combine the systematic uncertainties on the event selection, the theoretical production cross section, and the integrated luminosity of the sample, where the contribution from the last two sources dominates the total. Note that the simulated $t\bar{t}$ signal sample used for the estimate of the expected signal events was generated with the $W \rightarrow \ell\nu$ branching fraction set to 1/9, which is different from the standard value (0.1080 ± 0.0009) [7] used in the cross section measurement.

The selected sample is not 100% pure in dilepton $t\bar{t}$ events. There are two types of background estimation techniques used in this analysis. One strategy utilizes simulated pp collision events to model background processes. There are, however, some pathological backgrounds that are harder to model accurately. In such cases, it is preferred to estimate the yields of these events from the data.

Contributions from diboson production (VV, where $V = W$ or Z/γ^*), based on a leading-order production cross section of $\sigma_{VV} = 4.8$ pb [16], and electroweak single-top production in the tW channel ($\sigma_{tW} = 10.6$ pb [33]) are modeled with the MADGRAPH event generator and are processed in an equivalent fashion as the simulated $t\bar{t}$ sample used to assess the signal yield. The Drell–Yan $Z/\gamma^* \rightarrow \tau\tau$ process ($\sigma_{Z/\gamma^* \rightarrow \tau\tau} = 1666$ pb [34]) is modeled with PYTHIA and MADGRAPH. The uncertainties on these production cross sections are well within the total systematic uncertainty of 50% used for each of these backgrounds. Table 1 gives the simulation-based predictions for the event yields from these processes.

The contributions from two important background sources are estimated from the data: exceptional Drell–Yan events that evade the Z veto and are accompanied by significant missing transverse energy; and dilepton candidate events from multijet and W + jets production. Difficult-to-simulate instrumental effects influence both topologies and hence it is preferable to use calibration samples from the data in these estimations.

The events rejected by the Z veto are used to estimate the residual contributions from Drell–Yan $Z/\gamma^* \rightarrow e^+e^-$ and $\mu^+\mu^-$ in the surviving selected sample. In the $\mu^+\mu^-$ final state the rate of events surviving the Z veto is equal to an estimate of the Drell–

Yan contribution near the $M_{\ell\ell}$ peak, scaled by the expected ratio of off-peak to near-peak events derived from simulation. The near-peak Drell–Yan Z/γ^* contribution is estimated from the number of all events failing the Z veto, after subtraction of the non-Drell–Yan contribution estimated from $e^\pm\mu^\mp$ events passing the same selection and corrected for the differences between the electron and muon identification efficiencies. The estimate in the e^+e^- mode is done in a similar fashion; the summed contribution is shown in Table 1. The systematic uncertainty of this method, evaluated in each mode separately, is estimated to be 50%. This is dominated by detector calibration effects and changes of the fraction of Z-vetoed Drell–Yan Z/γ^* events with increasingly stringent requirements (additional jets and missing transverse energy) as estimated from simulation.

Dilepton candidate events from multijet and W + jets production mostly arise from jets that are able to satisfy the tight lepton identification criteria. These contributions to the selected sample from isolated lepton candidates from non-W/Z decays are also derived from data. A superset of dilepton candidate events is chosen by loosening the lepton identification criteria in the data samples used for the measurement. The number of these candidates passing the loosened selection criteria from non-W/Z leptons can be weighted by the ratio of yields of tight-to-loose lepton candidates (R_{TL}) to produce an estimate of non-W/Z leptons passing the tight selections. The ratio R_{TL} is measured as a function of candidate transverse momentum and pseudorapidity in a multijet-dominated data sample containing events with one lepton candidate passing loose selection criteria. Additional selection criteria, based on the missing transverse energy and on the transverse mass of the system defined by the \cancel{E}_T and charged lepton candidate p_T , are applied to suppress the residual contribution to the loose lepton sample from electroweak processes. We assume this R_{TL} is appropriate for use in the dilepton signal sample, and we also consider R_{TL} to be independent from the other lepton in events with two leptons. In this measurement, the value of R_{TL} changes slightly as a function of candidate p_T and $|\eta|$; for both muon and electron candidates, R_{TL} is in the interval between 0.2 and 0.4.

Estimates for the contributions from lepton candidates in pure multijet QCD, with two such non-W/Z candidates, and in W + jets, with one such candidate beyond that from the decay of the W, are derived separately. A sample of loose dilepton events both failing the tight selections is used to estimate the multijet QCD contribution. Loose dilepton events with only one lepton failing the tight requirements include contributions from W + jets events, but are contaminated by multijets and leptons from W/Z decays. The multijet QCD contamination is subtracted using the previous estimate, while the contamination from W/Z leptons is measured from a sample of Z events fulfilling loose selection requirements.

The prediction for these non-W/Z leptons is shown in Table 1. The systematic uncertainty on the non-W/Z lepton estimate is primarily from differences in the jet momentum spectrum and flavor composition between the QCD-dominated sample in which R_{TL} is measured and the sample where it is applied. Other subdominant contributions to the systematic uncertainties include the R_{TL} measurement biases due to electroweak signal contribution, the dissimilarity in the trigger between the R_{TL} calibration sample and the signal sample to which it is applied, and from the statistical limitations on the R_{TL} calibration sample. The systematic uncertainty on the electron R_{TL} is 50%, which corresponds to a 50% (100%) uncertainty on a raw estimate of the W + jets (QCD multijets) non-W/Z isolated lepton contribution, prior to accounting for the signal contribution to the estimate. Similarly, the systematic uncertainty on the muon R_{TL} is $^{+50}_{-100}\%$, which corresponds to a $^{+50}_{-100}\%$ ($^{+100}_{-100}\%$) uncertainty on the estimate of the W + jets (QCD multijets) non-W/Z isolated lepton contribution.

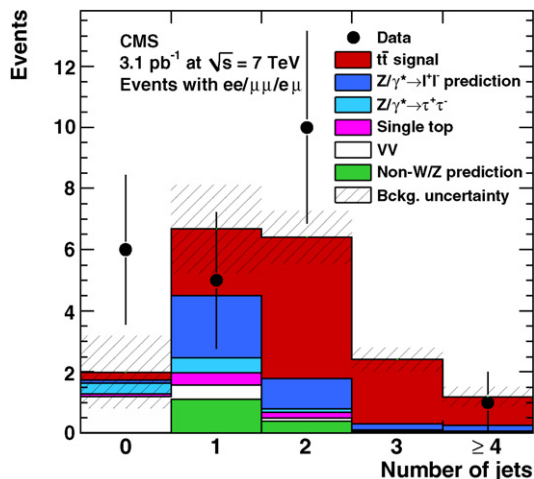


Fig. 1. Number of jets in events passing all dilepton selection criteria before the ≥ 2 -jet requirement for all three dilepton modes combined, compared to signal and background predictions. The hatched bands reflect the uncertainties on the background predictions.

Expected yields from simulated signal and background processes, normalized to estimates from data where appropriate, are shown in Fig. 1 as a function of jet multiplicity for events satisfying the complete dilepton event selection criteria except the ≥ 2 -jet requirement; the $t\bar{t}$ signal dominates the bins with at least two jets.

Eleven dilepton events ($3 e^+e^-$, $3 \mu^+\mu^-$, $5 e^\pm\mu^\mp$) are observed in the data after applying the event selection criteria, with a total of 2.1 ± 1.0 background events expected. We attribute the excess of events above the background expectation to top-quark pair production.

The top-quark mass reconstruction methods of [35] (KIN, i.e., KINematic, method) and [36] (MWT, i.e., Matrix Weighting Technique) are applied to the selected events. In both methods, numerical solutions to the kinematic equations appropriate for a $t\bar{t}$ decay with two charged leptons in the final state are found for each event. The solutions are based on an ensemble of values of jet momenta and missing energy, generated corresponding to their expected resolution around the measured values. In the KIN method the underconstrained system is solved by introducing an additional constraint on the longitudinal momentum of the $t\bar{t}$ system, whose probability distribution is expected to have a negligible dependence on the top-quark mass and is therefore assumed from simulation. The top-quark mass value corresponding to the largest number of solutions is the reconstructed mass for each event. In the MWT method the system is solved for a range of top-quark mass values, and weights, dependent on the momentum of the initial partons and the lepton energies in the top-quark rest frame, are assigned based on the likelihood of each solution. The mass for which the sum of the weights of all solutions is maximized is used as the mass estimator. Fig. 2 shows that the kinematics of the selected events are statistically compatible with predictions based on a top-quark mass of $172.5 \text{ GeV}/c^2$, demonstrating the consistency of the selected sample with top-quark pair production.

Further, beyond the complete event selection described above, the property that the two jets expected in dilepton $t\bar{t}$ events both originate from b quarks is exploited to further confirm the top-quark signal. A b-quark jet identification algorithm that relies on the presence of charged particle tracks displaced from the primary pp interaction location, as expected from the decay products of long-lived b hadrons [37], is used. A jet is identified to be from

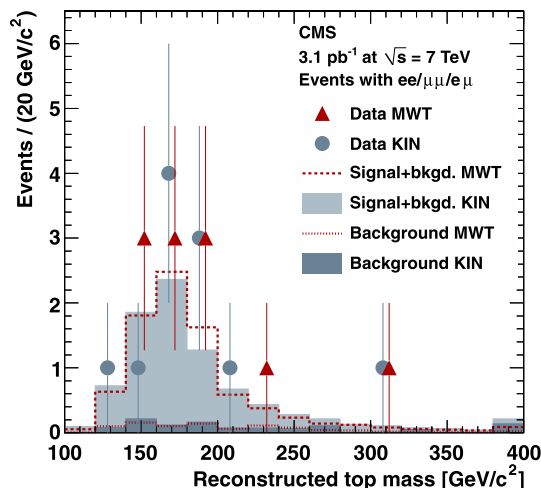


Fig. 2. Distribution of the top-quark mass using two different reconstruction methods [35,36], compared with the expected yields from simulated signal-plus-background and background-only hypotheses. The points in each bin for the two methods are slightly offset in reconstructed mass to allow coincident points to be visible. The last bin contains the overflow.

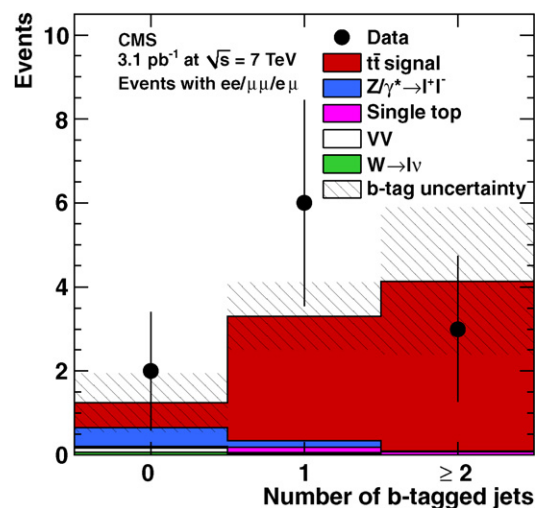


Fig. 3. Number of b-tagged jets in events passing all dilepton selection criteria for all three dilepton modes combined, compared to signal and background directly from simulations. The hatched bands reflect the expected uncertainties on the b-tag efficiency for signal events.

a b quark if there are at least two tracks satisfying a minimum impact parameter significance requirement. The efficiency of this algorithm for a b-quark jet in dilepton $t\bar{t}$ signal events is about 80% with a 10% false positive rate, as estimated in simulated QCD multi-jet events with no b quarks. This algorithm is applied to events passing all the selection criteria. The multiplicity of jets satisfying these b-tagging criteria in events passing the full dilepton event selection is shown in Fig. 3. Although not used directly in the cross section extraction, the b-tag multiplicity provides additional support for the hypothesis that the selected data are consistent with dilepton $t\bar{t}$ production.

The top-quark pair production cross section is determined from the ratio of the number of observed events in the data after background subtraction with the product of the total signal acceptance, the branching fractions, and the integrated luminosity. The impact of systematic uncertainty is included on each piece, as described below.

Various sources of systematic uncertainty related to the event selection have been evaluated. The systematic uncertainty assigned to the dilepton selection efficiency is 4.4%, obtained from a comparison of Z events in data and simulation, together with half of the difference between the efficiencies obtained in simulated Z and $t\bar{t}$ events. The effect of multiple pp interactions in a single beam crossing – an effect that is present in the data but not in these simulated samples – is included in this uncertainty. The systematic uncertainty due to the reconstruction of jets and missing transverse energy is estimated by varying the jet energy scale by $\pm 5\%$, simultaneously with a $\pm 5\%$ variation in the hadronic part of the missing transverse energy, resulting in a value of 3.7%. Uncertainties on the simulation of the signal selection efficiency include the amount of QCD radiation, hadron and tau decay modeling, and the W leptonic branching fraction; these sources combined give a systematic uncertainty of 2.8%. Other sources of systematic uncertainty pertaining to the signal, including uncertainties in the parton distribution functions inside the colliding protons, the effect of uncertainty on the world-average top-quark mass measurement [38], and the effect of additional minimum bias interactions in the signal selection, are neglected because they were found to have a relatively small impact. The overall systematic uncertainty on the total $t\bar{t}$ cross section from the above sources is 6.4%.

The background contributions from single-top, diboson, and Drell–Yan $Z/\gamma^* \rightarrow \tau^+\tau^-$ processes shown in Table 1 are obtained from simulation and found to be small compared to the total event yield. Each of these backgrounds is assigned a 50% systematic uncertainty. The contributions from Drell–Yan e^+e^- and $\mu^+\mu^-$ processes and events with non-W/Z isolated leptons are estimated from data with absolute systematic uncertainties of 0.5 and 0.3 events, respectively. The contribution to the systematic uncertainty on the cross section from the uncertainties on the background estimates is 11%.

The total systematic uncertainty on the measured cross section, dominated by the uncertainty on the estimated background yield, is 24 pb. An additional systematic effect of 21 pb, due to a 11% relative uncertainty on the integrated luminosity measurement [5], is quoted separately.

Taking into account the data yield, the background estimation, the branching fraction, the signal acceptance, the integrated luminosity, and all associated statistical and systematic uncertainties, the top-quark pair production cross section is measured to be

$$\sigma(pp \rightarrow t\bar{t} + X) = 194 \pm 72(\text{stat.}) \pm 24(\text{syst.}) \pm 21(\text{lumi.}) \text{ pb.}$$

An alternative analysis, exploiting jets constructed only from silicon tracker information [39] and without missing transverse energy requirements in the event selection, yields a similar cross section. The quoted measurement can be compared with the calculated NLO theoretical cross section of 158_{-24}^{+23} pb for a top-quark mass of $172.5 \text{ GeV}/c^2$ [19,20].

In conclusion, the first measurement at the LHC of the cross section for $t\bar{t}$ production has been completed. This measurement, made with an integrated luminosity of $3.1 \pm 0.3 \text{ pb}^{-1}$, is only the beginning of a rich top-quark physics program to be conducted at the CMS experiment.

Acknowledgements

We wish to congratulate our colleagues in the CERN accelerator departments for the excellent performance of the LHC machine. We thank the technical and administrative staff at CERN and other CMS institutes, and acknowledge support from: FMSR (Austria); FNRS and FWO (Belgium); CNPq, CAPES, FAPERJ, and FAPESP

(Brazil); MES (Bulgaria); CERN; CAS, MoST, and NSFC (China); COLCIENCIAS (Colombia); MSES (Croatia); RPF (Cyprus); Academy of Sciences and NICPB (Estonia); Academy of Finland, ME, and HIP (Finland); CEA and CNRS/IN2P3 (France); BMBF, DFG, and HGF (Germany); GSRT (Greece); OTKA and NKTH (Hungary); DAE and DST (India); IPM (Iran); SFI (Ireland); INFN (Italy); NRF and WCU (Korea); LAS (Lithuania); CINVESTAV, CONACYT, SEP, and UASLP-FAI (Mexico); PAEC (Pakistan); SCSR (Poland); FCT (Portugal); JINR (Armenia, Belarus, Georgia, Ukraine, Uzbekistan); MST and MAE (Russia); MSTD (Serbia); MICINN and CPAN (Spain); Swiss Funding Agencies (Switzerland); NSC (Taipei); TUBITAK and TAEC (Turkey); STFC (United Kingdom); DOE and NSF (USA).

Open access

This article is published Open Access at sciencedirect.com. It is distributed under the terms of the Creative Commons Attribution License 3.0, which permits unrestricted use, distribution, and reproduction in any medium, provided the original authors and source are credited.

References

- [1] F. Abe, et al., Phys. Rev. Lett. 74 (1995) 2626, doi:10.1103/PhysRevLett.74.2626, arXiv:hep-ex/9503002.
- [2] S. Abachi, et al., Phys. Rev. Lett. 74 (1995) 2632, doi:10.1103/PhysRevLett.74.2632, arXiv:hep-ex/9503003.
- [3] J.R. Incandela, A. Quadt, W. Wagner, D. Wicke, Prog. Part. Nucl. Phys. 63 (2009) 239, doi:10.1016/j.pnpnp.2009.08.001, arXiv:0904.2499.
- [4] L. Evans, P. Bryant (Eds.), LHC Machine, JINST 3 (2008) S08001, doi:10.1088/1748-0221/3/08/S08001.
- [5] CMS Collaboration, Measurement of CMS luminosity, CMS Physics Analysis Summary CMS-PAS-EWK-10-004, <http://cdsweb.cern.ch/record/1279145>.
- [6] R. Adolph, et al., JINST 0803 (2008) S08004, doi:10.1088/1748-0221/3/08/S08004.
- [7] K. Nakamura, J. Phys. G 37 (2010) 075021, doi:10.1088/0954-3899/37/7A/075021.
- [8] T. Aaltonen, et al., Phys. Rev. D 82 (2010) 052002, doi:10.1103/PhysRevD.82.052002, arXiv:1002.2919.
- [9] V.M. Abazov, et al., Phys. Lett. B 679 (2009) 177, doi:10.1016/j.physletb.2009.07.032, arXiv:0901.2137.
- [10] CMS Collaboration, CMS tracking performance results from early LHC operation, CMS Physics Analysis Summary CMS-PAS-TRK-10-001, arXiv:1007.1988, <http://cdsweb.cern.ch/record/1277738>.
- [11] CMS Collaboration, Performance of muon identification in pp collisions at $\sqrt{s} = 7 \text{ TeV}$, CMS Physics Analysis Summary CMS-PAS-MUO-10-002, <http://cdsweb.cern.ch/record/1279140>.
- [12] CMS Collaboration, Electron reconstruction and identification at $\sqrt{s} = 7 \text{ TeV}$, CMS Physics Analysis Summary CMS-PAS-EGM-10-004, <http://cdsweb.cern.ch/record/1299116>.
- [13] CMS Collaboration, CMS MET performance in events containing electroweak bosons from pp collisions at $\sqrt{s} = 7 \text{ TeV}$, CMS Physics Analysis Summary CMS-PAS-JME-10-005, <http://cdsweb.cern.ch/record/1294501>.
- [14] M. Cacciari, G.P. Salam, G. Soyez, JHEP 0804 (2008) 063, doi:10.1088/1126-6708/2008/04/063, arXiv:0802.1189.
- [15] CMS Collaboration, Jet performance in pp collisions at $\sqrt{s} = 7 \text{ TeV}$, CMS Physics Analysis Summary CMS-PAS-JME-10-003, <http://cdsweb.cern.ch/record/1279362>.
- [16] F. Maltoni, T. Stelzer, JHEP 0302 (2003) 027, arXiv:hep-ph/0208156.
- [17] T. Sjöstrand, S. Mrenna, P. Skands, JHEP 0605 (2006) 026, arXiv:hep-ph/0603175.
- [18] J. Allison, et al., IEEE Trans. Nucl. Sci. 53 (2006) 270, doi:10.1109/TNS.2006.869826.
- [19] J.M. Campbell, R.K. Ellis, MCFM for the Tevatron and the LHC, arXiv:1007.3492, 2010.
- [20] R. Kleiss, W.J. Stirling, Z. Phys. C 40 (1988) 419, doi:10.1007/BF01548856.
- [21] P. Nason, S. Dawson, R.K. Ellis, Nucl. Phys. B 303 (1988) 607, doi:10.1016/0550-3213(88)90422-1.
- [22] W. Beenakker, H. Kuijf, W.L. van Neerven, J. Smith, Phys. Rev. D 40 (1989) 54, doi:10.1103/PhysRevD.40.54.
- [23] N. Kidonakis, Next-to-next-to-leading soft-gluon corrections for the top quark cross section and transverse momentum distribution, arXiv:1009.4935, 2010.
- [24] N. Kidonakis, R. Vogt, Phys. Rev. D 78 (2008) 074005, doi:10.1103/PhysRevD.78.074005, arXiv:0805.3844.

- [25] M. Cacciari, S. Frixione, M.L. Mangano, P. Nason, G. Ridolfi, JHEP 0809 (2008) 127, doi:10.1088/1126-6708/2008/09/127, arXiv:0804.2800.
- [26] S. Moch, P. Uwer, Phys. Rev. D 78 (2008) 034003, doi:10.1103/PhysRevD.78.034003, arXiv:0804.1476.
- [27] U. Langenfeld, S. Moch, P. Uwer, New results for $t\bar{t}$ production at hadron colliders, arXiv:0907.2527, 2009.
- [28] U. Langenfeld, S. Moch, P. Uwer, Phys. Rev. D 80 (2009) 054009, doi:10.1103/PhysRevD.80.054009, arXiv:0906.5273.
- [29] V. Ahrens, A. Ferroglia, M. Neubert, B.D. Pecjak, L.L. Yang, JHEP 1009 (2010) 097, doi:10.1007/JHEP09(2010)097, arXiv:1003.5827.
- [30] A.D. Martin, W.J. Stirling, R.S. Thorne, G. Watt, Eur. Phys. J. C 64 (2009) 653, doi:10.1140/epjc/s10052-009-1164-2, arXiv:0905.3531.
- [31] H.-L. Lai, et al., Uncertainty induced by QCD coupling in the CTEQ-TEA global analysis of parton distributions, arXiv:1004.4624, 2010.
- [32] F. Demartin, S. Forte, E. Mariani, J. Rojo, A. Vicini, Phys. Rev. D 82 (2010) 014002, doi:10.1103/PhysRevD.82.014002, arXiv:1004.0962.
- [33] J.M. Campbell, F. Tramontano, Nucl. Phys. B 726 (2005) 109, doi:10.1016/j.nuclphysb.2005.08.015, arXiv:hep-ph/0506289.
- [34] K. Melnikov, F. Petriello, Phys. Rev. D 74 (2006) 114017, doi:10.1103/PhysRevD.74.114017, arXiv:hep-ph/0609070.
- [35] A. Abulencia, et al., Phys. Rev. D 73 (2006) 112006, doi:10.1103/PhysRevD.73.112006, arXiv:hep-ex/0602008.
- [36] V.M. Abazov, et al., Phys. Rev. D 80 (2009) 092006, doi:10.1103/PhysRevD.80.092006, arXiv:0904.3195.
- [37] CMS Collaboration, Commissioning of b-jet identification with pp collisions at $\sqrt{s} = 7$ TeV, CMS Physics Analysis Summary CMS-PAS-BTV-10-001, <http://cdsweb.cern.ch/record/1279144>.
- [38] Tevatron Electroweak Working Group, Combination of CDF and D0 results on the mass of the top quark, arXiv:1007.3178, 2010.
- [39] CMS Collaboration, Commissioning of Trackjets in pp collisions at $\sqrt{s} = 7$ TeV, CMS Physics Analysis Summary CMS-PAS-JME-10-006, <http://cdsweb.cern.ch/record/1275133>.

CMS Collaboration

V. Khachatryan, A.M. Sirunyan, A. Tumasyan

Yerevan Physics Institute, Yerevan, Armenia

W. Adam, T. Bergauer, M. Dragicevic, J. Erö, C. Fabjan, M. Friedl, R. Frühwirth, V.M. Ghete, J. Hammer¹, S. Häsnel, C. Hartl, M. Hoch, N. Hörmann, J. Hrubec, M. Jeitler, G. Kasieczka, W. Kiesenhofer, M. Krammer, D. Liko, I. Mikulec, M. Pernicka, H. Rohringer, R. Schöfbeck, J. Strauss, A. Taurok, F. Teischinger, W. Waltenberger, G. Walzel, E. Widl, C.-E. Wulz

Institut für Hochenergiephysik der OeAW, Wien, Austria

V. Mossolov, N. Shumeiko, J. Suarez Gonzalez

National Centre for Particle and High Energy Physics, Minsk, Belarus

L. Benucci, L. Ceard, E.A. De Wolf, X. Janssen, T. Maes, L. Mucibello, S. Ochesanu, B. Roland, R. Rougny, M. Selvaggi, H. Van Haevermaet, P. Van Mechelen, N. Van Remortel

Universiteit Antwerpen, Antwerpen, Belgium

V. Adler, S. Beauceron, S. Blyweert, J. D'Hondt, O. Devroede, A. Kalogeropoulos, J. Maes, M. Maes, S. Tavernier, W. Van Doninck, P. Van Mulders, G.P. Van Onsem, I. Villella

Vrije Universiteit Brussel, Brussel, Belgium

O. Charaf, B. Clerbaux, G. De Lentdecker, V. Dero, A.P.R. Gay, G.H. Hammad, T. Hreus, P.E. Marage, L. Thomas, C. Vander Velde, P. Vanlaer, J. Wickens

Université Libre de Bruxelles, Bruxelles, Belgium

S. Costantini, M. Grunewald, B. Klein, A. Marinov, D. Ryckbosch, F. Thyssen, M. Tytgat, L. Vanelderren, P. Verwilligen, S. Walsh, N. Zaganidis

Ghent University, Ghent, Belgium

S. Basegmez, G. Bruno, J. Caudron, J. De Favereau De Jeneret, C. Delaere, P. Demin, D. Favart, A. Giammanco, G. Grégoire, J. Hollar, V. Lemaitre, J. Liao, O. Militaru, S. Oryn, D. Pagano, A. Pin, K. Piotrkowski, L. Quertenmont, N. Schul

Université Catholique de Louvain, Louvain-la-Neuve, Belgium

N. Bely, T. Caebegs, E. Daubie

Université de Mons, Mons, Belgium

G.A. Alves, D. De Jesus Damiao, M.E. Pol, M.H.G. Souza

Centro Brasileiro de Pesquisas Fisicas, Rio de Janeiro, Brazil

W. Carvalho, E.M. Da Costa, C. De Oliveira Martins, S. Fonseca De Souza, L. Mundim, H. Nogima, V. Oguri, J.M. Otalora Goicochea, W.L. Prado Da Silva, A. Santoro, S.M. Silva Do Amaral, A. Sznajder, F. Torres Da Silva De Araujo

Universidade do Estado do Rio de Janeiro, Rio de Janeiro, Brazil

F.A. Dias, M.A.F. Dias, T.R. Fernandez Perez Tomei, E.M. Gregores², F. Marinho, S.F. Novaes, Sandra S. Padula

Instituto de Fisica Teorica, Universidade Estadual Paulista, Sao Paulo, Brazil

N. Dardanov¹, L. Dimitrov, V. Genchev¹, P. Iaydjiev¹, S. Piperov, M. Rodozov, S. Stoykova, G. Sultanov, V. Tcholakov, R. Trayanov, I. Vankov

Institute for Nuclear Research and Nuclear Energy, Sofia, Bulgaria

M. Dyulendarova, R. Hadjiiska, V. Kozhuharov, L. Litov, E. Marinova, M. Mateev, B. Pavlov, P. Petkov

University of Sofia, Sofia, Bulgaria

J.G. Bian, G.M. Chen, H.S. Chen, C.H. Jiang, D. Liang, S. Liang, J. Wang, J. Wang, X. Wang, Z. Wang, M. Yang, J. Zang, Z. Zhang

Institute of High Energy Physics, Beijing, China

Y. Ban, S. Guo, Z. Hu, W. Li, Y. Mao, S.J. Qian, H. Teng, B. Zhu

State Key Lab. of Nucl. Phys. and Tech., Peking University, Beijing, China

A. Cabrera, B. Gomez Moreno, A.A. Ocampo Rios, A.F. Osorio Oliveros, J.C. Sanabria

Universidad de Los Andes, Bogota, Colombia

N. Godinovic, D. Lelas, K. Lelas, R. Plestina³, D. Polic, I. Puljak

Technical University of Split, Split, Croatia

Z. Antunovic, M. Dzelalija

University of Split, Split, Croatia

V. Brigljevic, S. Duric, K. Kadija, S. Morovic

Institute Rudjer Boskovic, Zagreb, Croatia

A. Attikis, R. Fereos, M. Galanti, J. Mousa, C. Nicolaou, F. Ptochos, P.A. Razis, H. Rykaczewski

University of Cyprus, Nicosia, Cyprus

A. Abdel-basit⁴, Y. Assran⁵, M.A. Mahmoud⁶

Academy of Scientific Research and Technology of the Arab Republic of Egypt, Egyptian Network of High Energy Physics, Cairo, Egypt

A. Hektor, M. Kadastik, K. Kannike, M. Müntel, M. Raidal, L. Rebane

National Institute of Chemical Physics and Biophysics, Tallinn, Estonia

V. Azzolini, P. Eerola

Department of Physics, University of Helsinki, Helsinki, Finland

S. Czellar, J. Härkönen, A. Heikkinen, V. Karimäki, R. Kinnunen, J. Klem, M.J. Kortelainen, T. Lampén, K. Lassila-Perini, S. Lehti, T. Lindén, P. Luukka, T. Mäenpää, E. Tuominen, J. Tuominiemi, E. Tuovinen, D. Ungaro, L. Wendland

Helsinki Institute of Physics, Helsinki, Finland

K. Banzuzi, A. Korpela, T. Tuuva

Lappeenranta University of Technology, Lappeenranta, Finland

D. Sillou

Laboratoire d'Annecy-le-Vieux de Physique des Particules, IN2P3–CNRS, Annecy-le-Vieux, France

M. Besancon, M. Dejardin, D. Denegri, B. Fabbro, J.L. Faure, F. Ferri, S. Ganjour, F.X. Gentit, A. Givernaud, P. Gras, G. Hamel de Monchenault, P. Jarry, E. Locci, J. Malcles, M. Marionneau, L. Millischer, J. Rander, A. Rosowsky, M. Titov, P. Verrecchia

DSM/IRFU, CEA/Saclay, Gif-sur-Yvette, France

S. Baffioni, L. Bianchini, M. Bluj⁷, C. Broutin, P. Busson, C. Charlot, L. Dobrzynski, R. Granier de Cassagnac, M. Haguenaer, P. Miné, C. Mironov, C. Ochando, P. Paganini, D. Sabes, R. Salerno, Y. Sirois, C. Thiebaux, B. Wyslouch⁸, A. Zabi

Laboratoire Leprince-Ringuet, Ecole Polytechnique, IN2P3–CNRS, Palaiseau, France

J.-L. Agram⁹, J. Andrea, A. Besson, D. Bloch, D. Bodin, J.-M. Brom, M. Cardaci, E.C. Chabert, C. Collard, E. Conte⁹, F. Drouhin⁹, C. Ferro, J.-C. Fontaine⁹, D. Gelé, U. Goerlach, S. Greder, P. Juillot, M. Karim⁹, A.-C. Le Bihan, Y. Mikami, P. Van Hove

Institut Pluridisciplinaire Hubert Curien, Université de Strasbourg, Université de Haute Alsace Mulhouse, CNRS/IN2P3, Strasbourg, France

F. Fassi, D. Mercier

Centre de Calcul de l'Institut National de Physique Nucléaire et de Physique des Particules (IN2P3), Villeurbanne, France

C. Baty, N. Beaupere, M. Bedjidian, O. Bondu, G. Boudoul, D. Boumediene, H. Brun, N. Chanon, R. Chierici, D. Contardo, P. Depasse, H. El Mamouni, A. Falkiewicz, J. Fay, S. Gascon, B. Ille, T. Kurca, T. Le Grand, M. Lethuillier, L. Mirabito, S. Perries, V. Sordini, S. Tosi, Y. Tschudi, P. Verdier, H. Xiao

Université de Lyon, Université Claude Bernard Lyon 1, CNRS–IN2P3, Institut de Physique Nucléaire de Lyon, Villeurbanne, France

V. Roinishvili

E. Andronikashvili Institute of Physics, Academy of Science, Tbilisi, Georgia

G. Anagnostou, M. Edelhoff, L. Feld, N. Heracleous, O. Hindrichs, R. Jussen, K. Klein, J. Merz, N. Mohr, A. Ostapchuk, A. Perieanu, F. Raupach, J. Sammet, S. Schael, D. Sprenger, H. Weber, M. Weber, B. Wittmer

RWTH Aachen University, I. Physikalisches Institut, Aachen, Germany

M. Ata, W. Bender, M. Erdmann, J. Frangenheim, T. Hebbeker, A. Hinzmann, K. Hoepfner, C. Hof, T. Klimkovich, D. Klingebiel, P. Kreuzer¹, D. Lanske[†], C. Magass, G. Masetti, M. Merschmeyer, A. Meyer, P. Papacz, H. Pieta, H. Reithler, S.A. Schmitz, L. Sonnenschein, J. Steggemann, D. Teysier

RWTH Aachen University, III. Physikalisches Institut A, Aachen, Germany

M. Bontenackels, M. Davids, M. Duda, G. Flügge, H. Geenen, M. Giffels, W. Haj Ahmad, D. Heydhausen, T. Kress, Y. Kuessel, A. Linn, A. Nowack, L. Perchalla, O. Pooth, J. Rennefeld, P. Sauerland, A. Stahl, M. Thomas, D. Tornier, M.H. Zoeller

RWTH Aachen University, III. Physikalisches Institut B, Aachen, Germany

M. Aldaya Martin, W. Behrenhoff, U. Behrens, M. Bergholz¹⁰, K. Borras, A. Cakir, A. Campbell, E. Castro, D. Dammann, G. Eckerlin, D. Eckstein, A. Flossdorf, G. Flucke, A. Geiser, I. Glushkov, J. Hauk, H. Jung, M. Kasemann, I. Katkov, P. Katsas, C. Kleinwort, H. Kluge, A. Knutsson, D. Krücker, E. Kuznetsova, W. Lange, W. Lohmann¹⁰, R. Mankel, M. Marienfeld, I.-A. Melzer-Pellmann, A.B. Meyer, J. Mnich, A. Mussgiller, J. Olzem, A. Parenti, A. Raspereza, A. Raval, R. Schmidt¹⁰, T. Schoerner-Sadenius, N. Sen, M. Stein, J. Tomaszewska, D. Volyanskyy, R. Walsh, C. Wissing

Deutsches Elektronen-Synchrotron, Hamburg, Germany

C. Autermann, S. Bobrovskiy, J. Draeger, H. Enderle, U. Gebbert, K. Kaschube, G. Kaussen, R. Klanner, B. Mura, S. Naumann-Emme, F. Nowak, N. Pietsch, C. Sander, H. Schettler, P. Schleper, M. Schröder, T. Schum, J. Schwandt, A.K. Srivastava, H. Stadie, G. Steinbrück, J. Thomsen, R. Wolf

University of Hamburg, Hamburg, Germany

J. Bauer, V. Buege, T. Chwalek, D. Daeuwel, W. De Boer, A. Dierlamm, G. Dirkes, M. Feindt, J. Gruschke, C. Hackstein, F. Hartmann, S.M. Heindl, M. Heinrich, H. Held, K.H. Hoffmann, S. Honc, T. Kuhr, D. Martschei, S. Mueller, Th. Müller, M.B. Neuland, M. Niegel, O. Oberst, A. Oehler, J. Ott, T. Peiffer, D. Piparo, G. Quast, K. Rabbertz, F. Ratnikov, M. Renz, A. Sabellek, C. Saout, A. Scheurer, P. Schieferdecker, F.-P. Schilling, G. Schott, H.J. Simonis, F.M. Stober, D. Troendle, J. Wagner-Kuhr, M. Zeise, V. Zhukov¹¹, E.B. Ziebarth

Institut für Experimentelle Kernphysik, Karlsruhe, Germany

G. Daskalakis, T. Gerasis, S. Kesisoglou, A. Kyriakis, D. Loukas, I. Manolakos, A. Markou, C. Markou, C. Mavrommatis, E. Petrakou

Institute of Nuclear Physics "Demokritos", Aghia Paraskevi, Greece

L. Gouskos, T. Mertzimekis, A. Panagiotou¹

University of Athens, Athens, Greece

I. Evangelou, C. Foudas, P. Kokkas, N. Manthos, I. Papadopoulos, V. Patras, F.A. Triantis

University of Ioánnina, Ioánnina, Greece

A. Aranyi, G. Bencze, L. Boldizsar, G. Debreczeni, C. Hajdu¹, D. Horvath¹², A. Kapusi, K. Krajczar¹³, A. Laszlo, F. Sikler, G. Vesztergombi¹³

KFKI Research Institute for Particle and Nuclear Physics, Budapest, Hungary

N. Beni, J. Molnar, J. Palinkas, Z. Szillasi, V. Veszpremi

Institute of Nuclear Research ATOMKI, Debrecen, Hungary

P. Raics, Z.L. Trocsanyi, B. Ujvari

University of Debrecen, Debrecen, Hungary

S. Bansal, S.B. Beri, V. Bhatnagar, M. Jindal, M. Kaur, J.M. Kohli, M.Z. Mehta, N. Nishu, L.K. Saini, A. Sharma, R. Sharma, A.P. Singh, J.B. Singh, S.P. Singh

Panjab University, Chandigarh, India

S. Ahuja, S. Bhattacharya, S. Chauhan, B.C. Choudhary, P. Gupta, S. Jain, S. Jain, A. Kumar, R.K. Shivpuri

University of Delhi, Delhi, India

R.K. Choudhury, D. Dutta, S. Kailas, S.K. Kataria, A.K. Mohanty¹, L.M. Pant, P. Shukla, P. Suggisetti

Bhabha Atomic Research Centre, Mumbai, India

T. Aziz, M. Guchait¹⁴, A. Gurtu, M. Maity¹⁵, D. Majumder, G. Majumder, K. Mazumdar, G.B. Mohanty, A. Saha, K. Sudhakar, N. Wickramage

Tata Institute of Fundamental Research – EHEP, Mumbai, India

S. Banerjee, S. Dugad, N.K. Mondal

Tata Institute of Fundamental Research – HEER, Mumbai, India

H. Arfaei, H. Bakhshiansohi, S.M. Etesami, A. Fahim, M. Hashemi, A. Jafari, M. Khakzad, A. Mohammadi, M. Mohammadi Najafabadi, S. Paktinat Mehdiabadi, B. Safarzadeh, M. Zeinali

Institute for Studies in Theoretical Physics & Mathematics (IPM), Tehran, Iran

M. Abbrescia^{a,b}, L. Barbone^{a,b}, C. Calabria^{a,b}, A. Colaleo^a, D. Creanza^{a,c}, N. De Filippis^{a,c}, M. De Palma^{a,b}, A. Dimitrov^a, F. Fedele^a, L. Fiore^a, G. Iaselli^{a,c}, L. Lusito^{a,b,1}, G. Maggi^{a,c}, M. Maggi^a, N. Manna^{a,b}, B. Marangelli^{a,b}, S. My^{a,c}, S. Nuzzo^{a,b}, N. Pacifico^{a,b}, G.A. Pierro^a, A. Pompili^{a,b}, G. Pugliese^{a,c}, F. Romano^{a,c}, G. Roselli^{a,b}, G. Selvaggi^{a,b}, L. Silvestris^a, R. Trentadue^a, S. Tuppiti^{a,b}, G. Zito^a

^a INFN Sezione di Bari, Bari, Italy

^b Università di Bari, Bari, Italy

^c Politecnico di Bari, Bari, Italy

G. Abbiendi^a, A.C. Benvenuti^a, D. Bonacorsi^a, S. Braibant-Giacomelli^{a,b}, P. Capiluppi^{a,b}, A. Castro^{a,b}, F.R. Cavallo^a, M. Cuffiani^{a,b}, G.M. Dallavalle^a, F. Fabbri^a, A. Fanfani^{a,b}, D. Fasanella^a, P. Giacomelli^a, M. Giunta^a, C. Grandi^a, S. Marcellini^a, M. Meneghelli^{a,b}, A. Montanari^a, F.L. Navarria^{a,b}, F. Odorici^a, A. Perrotta^a, A.M. Rossi^{a,b}, T. Rovelli^{a,b}, G. Siroli^{a,b}, R. Travaglini^{a,b}

^a INFN Sezione di Bologna, Bologna, Italy

^b Università di Bologna, Bologna, Italy

S. Albergo^{a,b}, G. Cappello^{a,b}, M. Chiorboli^{a,b,1}, S. Costa^{a,b}, A. Tricomi^{a,b}, C. Tuve^a

^a INFN Sezione di Catania, Catania, Italy

^b Università di Catania, Catania, Italy

G. Barbagli^a, V. Ciulli^{a,b}, C. Civinini^a, R. D'Alessandro^{a,b}, E. Focardi^{a,b}, S. Frosali^{a,b}, E. Gallo^a, C. Genta^a, P. Lenzi^{a,b}, M. Meschini^a, S. Paoletti^a, G. Sguazzoni^a, A. Tropiano^{a,1}

^a INFN Sezione di Firenze, Firenze, Italy

^b Università di Firenze, Firenze, Italy

L. Benussi, S. Bianco, S. Colafranceschi¹⁶, F. Fabbri, D. Piccolo

INFN Laboratori Nazionali di Frascati, Frascati, Italy

P. Fabbriatore, R. Musenich

INFN Sezione di Genova, Genova, Italy

A. Benaglia^{a,b}, G.B. Cerati^{a,b}, F. De Guio^{a,b,1}, L. Di Matteo^{a,b}, A. Ghezzi^{a,b,1}, P. Govoni^{a,b}, M. Malberti^{a,b}, S. Malvezzi^a, A. Martelli^{a,b}, A. Massironi^{a,b}, D. Menasce^a, L. Moroni^a, M. Paganoni^{a,b}, D. Pedrini^a, S. Ragazzi^{a,b}, N. Redaelli^a, S. Sala^a, T. Tabarelli de Fatis^{a,b}, V. Tancini^{a,b}

^a INFN Sezione di Milano-Bicocca, Milano, Italy

^b Università di Milano-Bicocca, Milano, Italy

S. Buontempo^a, C.A. Carrillo Montoya^a, A. Cimmino^{a,b}, A. De Cosa^{a,b,1}, M. De Gruttola^{a,b}, F. Fabozzi^{a,17}, A.O.M. Iorio^a, L. Lista^a, M. Merola^{a,b}, P. Noli^{a,b}, P. Paolucci^a

^a INFN Sezione di Napoli, Napoli, Italy

^b Università di Napoli "Federico II", Napoli, Italy

P. Azzi^a, N. Bacchetta^a, P. Bellan^{a,b}, D. Bisello^{a,b}, A. Branca^a, R. Carlin^{a,b}, P. Checchia^a, M. De Mattia^{a,b}, T. Dorigo^a, U. Dosselli^a, F. Gasparini^{a,b}, U. Gasparini^{a,b}, P. Giubilato^{a,b}, A. Gresele^{a,c}, S. Lacaprara^{a,18}, I. Lazzizzera^{a,c}, M. Margoni^{a,b}, M. Mazzucato^a, A.T. Meneguzzo^{a,b}, M. Nespolo^a, L. Perrozzi^{a,1}, N. Pozzobon^{a,b}, P. Ronchese^{a,b}, F. Simonetto^{a,b}, E. Torassa^a, M. Tosi^{a,b}, A. Triossi^a, S. Vanini^{a,b}, P. Zotto^{a,b}, G. Zumerle^{a,b}

^a INFN Sezione di Padova, Padova, Italy

^b Università di Padova, Padova, Italy

^c Università di Trento (Trento), Padova, Italy

P. Baesso^{a,b}, U. Berzano^a, C. Riccardi^{a,b}, P. Torre^{a,b}, P. Vitulo^{a,b}, C. Viviani^{a,b}

^a INFN Sezione di Pavia, Pavia, Italy

^b Università di Pavia, Pavia, Italy

M. Biasini^{a,b}, G.M. Bilei^a, B. Caponeri^{a,b}, L. Fanò^{a,b}, P. Lariccia^{a,b}, A. Lucaroni^{a,b,1}, G. Mantovani^{a,b}, M. Menichelli^a, A. Nappi^{a,b}, A. Santocchia^{a,b}, L. Servoli^a, S. Taroni^{a,b}, M. Valdata^{a,b}, R. Volpe^{a,b,1}

^a INFN Sezione di Perugia, Perugia, Italy

^b Università di Perugia, Perugia, Italy

P. Azzurri^{a,c}, G. Bagliesi^a, J. Bernardini^{a,b}, T. Boccali^{a,1}, G. Broccolo^{a,c}, R. Castaldi^a, R.T. D'Agnolo^{a,c}, R. Dell'Orso^a, F. Fiori^{a,b}, L. Foà^{a,c}, A. Giassi^a, A. Kraan^a, F. Ligabue^{a,c}, T. Lomtadze^a, L. Martini^a, A. Messineo^{a,b}, F. Palla^a, F. Palmonari^a, S. Sarkar^{a,c}, G. Segneri^a, A.T. Serban^a, P. Spagnolo^a, R. Tenchini^{a,*}, G. Tonelli^{a,b,1}, A. Venturi^{a,1}, P.G. Verdini^a

^a INFN Sezione di Pisa, Pisa, Italy

^b Università di Pisa, Pisa, Italy

^c Scuola Normale Superiore di Pisa, Pisa, Italy

L. Barone^{a,b}, F. Cavallari^a, D. Del Re^{a,b}, E. Di Marco^{a,b}, M. Diemoz^a, D. Franci^{a,b}, M. Grassi^a, E. Longo^{a,b}, G. Organtini^{a,b}, A. Palma^{a,b}, F. Pandolfi^{a,b,1}, R. Paramatti^a, S. Rahatlou^{a,b,1}

^a INFN Sezione di Roma, Roma, Italy

^b Università di Roma "La Sapienza", Roma, Italy

N. Amapane^{a,b}, R. Arcidiacono^{a,c}, S. Argiro^{a,b}, M. Arneodo^{a,c}, C. Biino^a, C. Botta^{a,b,1}, N. Cartiglia^a, R. Castello^{a,b}, M. Costa^{a,b}, N. Demaria^a, A. Graziano^{a,b,1}, C. Mariotti^a, M. Marone^{a,b}, S. Maselli^a, E. Migliore^{a,b}, G. Mila^{a,b}, V. Monaco^{a,b}, M. Musich^{a,b}, M.M. Obertino^{a,c}, N. Pastrone^a, M. Pelliccioni^{a,b,1}, A. Romero^{a,b}, M. Ruspa^{a,c}, R. Sacchi^{a,b}, V. Sola^{a,b}, A. Solano^{a,b}, A. Staiano^a, D. Trocino^{a,b}, A. Vilela Pereira^{a,b,1}

^a INFN Sezione di Torino, Torino, Italy

^b Università di Torino, Torino, Italy

^c Università del Piemonte Orientale (Novara), Torino, Italy

F. Ambroglini^{a,b}, S. Belforte^a, F. Cossutti^a, G. Della Ricca^{a,b}, B. Gobbo^a, D. Montanino^{a,b}, A. Penzo^a

^a INFN Sezione di Trieste, Trieste, Italy

^b Università di Trieste, Trieste, Italy

S.G. Heo

Kangwon National University, Chunchon, Republic of Korea

S. Chang, J. Chung, D.H. Kim, G.N. Kim, J.E. Kim, D.J. Kong, H. Park, D. Son, D.C. Son

Kyungpook National University, Daegu, Republic of Korea

Zero Kim, J.Y. Kim, S. Song

Chonnam National University, Institute for Universe and Elementary Particles, Kwangju, Republic of Korea

S. Choi, B. Hong, M. Jo, H. Kim, J.H. Kim, T.J. Kim, K.S. Lee, D.H. Moon, S.K. Park, H.B. Rhee, E. Seo, S. Shin, K.S. Sim

Korea University, Seoul, Republic of Korea

M. Choi, S. Kang, H. Kim, C. Park, I.C. Park, S. Park, G. Ryu

University of Seoul, Seoul, Republic of Korea

Y. Choi, Y.K. Choi, J. Goh, J. Lee, S. Lee, H. Seo, I. Yu

Sungkyunkwan University, Suwon, Republic of Korea

M.J. Bilinskas, I. Grigelionis, M. Janulis, D. Martisiute, P. Petrov, T. Sabonis

Vilnius University, Vilnius, Lithuania

H. Castilla Valdez, E. De La Cruz Burelo, R. Lopez-Fernandez, A. Sánchez Hernández, L.M. Villasenor-Cendejas

Centro de Investigacion y de Estudios Avanzados del IPN, Mexico City, Mexico

S. Carrillo Moreno, F. Vazquez Valencia

Universidad Iberoamericana, Mexico City, Mexico

H.A. Salazar Ibarquen

Benemerita Universidad Autonoma de Puebla, Puebla, Mexico

E. Casimiro Linares, A. Morelos Pineda, M.A. Reyes-Santos

Universidad Autónoma de San Luis Potosí, San Luis Potosí, Mexico

P. Allfrey, D. Krofcheck, J. Tam

University of Auckland, Auckland, New Zealand

P.H. Butler, R. Doesburg, H. Silverwood

University of Canterbury, Christchurch, New Zealand

M. Ahmad, I. Ahmed, M.I. Asghar, H.R. Hoorani, W.A. Khan, T. Khurshid, S. Qazi

National Centre for Physics, Quaid-I-Azam University, Islamabad, Pakistan

M. Cwiok, W. Dominik, K. Doroba, A. Kalinowski, M. Konecki, J. Krolikowski

Institute of Experimental Physics, Warsaw, Poland

T. Frueboes, R. Gokieli, M. Górski, M. Kazana, K. Nawrocki, M. Szleper, G. Wrochna, P. Zalewski

Soltan Institute for Nuclear Studies, Warsaw, Poland

N. Almeida, A. David, P. Faccioli, P.G. Ferreira Parracho, M. Gallinaro, P. Martins, G. Mini, P. Musella, A. Nayak, L. Raposo, P.Q. Ribeiro, J. Seixas, P. Silva, D. Soares, J. Varela¹, H.K. Wöhri

Laboratório de Instrumentação e Física Experimental de Partículas, Lisboa, Portugal

I. Belotelov, P. Bunin, M. Finger, M. Finger Jr., I. Golutvin, A. Kamenev, V. Karjavin, G. Kozlov, A. Lanev, P. Moisenz, V. Palichik, V. Perelygin, S. Shmatov, V. Smirnov, A. Volodko, A. Zarubin

Joint Institute for Nuclear Research, Dubna, Russia

N. Bondar, V. Golovtsov, Y. Ivanov, V. Kim, P. Levchenko, V. Murzin, V. Oreshkin, I. Smirnov, V. Sulimov, L. Uvarov, S. Vavilov, A. Vorobyev

Petersburg Nuclear Physics Institute, Gatchina (St Petersburg), Russia

Yu. Andreev, S. Gninenko, N. Golubev, M. Kirsanov, N. Krasnikov, V. Matveev, A. Pashenkov, A. Toropin, S. Troitsky

Institute for Nuclear Research, Moscow, Russia

V. Epshteyn, V. Gavrillov, V. Kaftanov[†], M. Kossov¹, A. Krokhotin, N. Lychkovskaya, G. Safronov, S. Semenov, I. Shreyber, V. Stolin, E. Vlasov, A. Zhokin

Institute for Theoretical and Experimental Physics, Moscow, Russia

E. Boos, M. Dubinin¹⁹, L. Dudko, A. Ershov, A. Gribushin, O. Kodolova, I. Lokhtin, S. Obraztsov, S. Petrushanko, L. Sarycheva, V. Savrin, A. Snigirev

Moscow State University, Moscow, Russia

V. Andreev, M. Azarkin, I. Dremin, M. Kirakosyan, S.V. Rusakov, A. Vinogradov

P.N. Lebedev Physical Institute, Moscow, Russia

I. Azhgirey, S. Bitioukov, V. Grishin¹, V. Kachanov, D. Konstantinov, A. Korablev, V. Krychkine, V. Petrov, R. Ryutin, S. Slabospitsky, A. Sobol, L. Tourtchanovitch, S. Troshin, N. Tyurin, A. Uzunian, A. Volkov

State Research Center of Russian Federation, Institute for High Energy Physics, Protvino, Russia

P. Adzic²⁰, M. Djordjevic, D. Krpic²⁰, J. Milosevic

University of Belgrade, Faculty of Physics and Vinca Institute of Nuclear Sciences, Belgrade, Serbia

M. Aguilar-Benitez, J. Alcaraz Maestre, P. Arce, C. Battilana, E. Calvo, M. Cepeda, M. Cerrada, N. Colino, B. De La Cruz, C. Diez Pardos, C. Fernandez Bedoya, J.P. Fernández Ramos, A. Ferrando, J. Flix, M.C. Fouz, P. Garcia-Abia, O. Gonzalez Lopez, S. Goy Lopez, J.M. Hernandez, M.I. Josa, G. Merino, J. Puerta Pelayo, I. Redondo, L. Romero, J. Santaolalla, C. Willmott

Centro de Investigaciones Energéticas Medioambientales y Tecnológicas (CIEMAT), Madrid, Spain

C. Albajar, G. Codispoti, J.F. de Trocóniz

Universidad Autónoma de Madrid, Madrid, Spain

J. Cuevas, J. Fernandez Menendez, S. Folgueras, I. Gonzalez Caballero, L. Lloret Iglesias, J.M. Vizan Garcia

Universidad de Oviedo, Oviedo, Spain

I.J. Cabrillo, A. Calderon, M. Chamizo Llatas, S.H. Chuang, J. Duarte Campderros, M. Felcini²¹, M. Fernandez, G. Gomez, J. Gonzalez Sanchez, R. Gonzalez Suarez, C. Jorda, P. Lobelle Pardo, A. Lopez Virto, J. Marco, R. Marco, C. Martinez Rivero, F. Matorras, J. Piedra Gomez²², T. Rodrigo, A. Ruiz Jimeno, L. Scodellaro, M. Sobron Sanudo, I. Vila, R. Vilar Cortabitarte

Instituto de Física de Cantabria (IFCA), CSIC – Universidad de Cantabria, Santander, Spain

D. Abbaneo, E. Auffray, P. Baillon, A.H. Ball, D. Barney, F. Beaudette³, A.J. Bell²³, D. Benedetti, C. Bernet³, W. Bialas, P. Bloch, A. Bocci, S. Bolognesi, H. Breuker, G. Brona, K. Bunkowski, T. Camporesi, E. Cano, G. Cerminara, T. Christiansen, J.A. Coarasa Perez, R. Covarelli, B. Curé, D. D'Enterria, T. Dahms, A. De Roeck, A. Elliott-Peisert, W. Funk, A. Gaddi, S. Gennai, G. Georgiou, H. Gerwig, D. Gigi, K. Gill, D. Giordano, F. Glege, R. Gomez-Reino Garrido, M. Gouzevitch, S. Gowdy, L. Guiducci, M. Hansen, J. Harvey, J. Hegeman, B. Hegner, C. Henderson, H.F. Hoffmann, A. Honma, V. Innocente, P. Janot,

E. Karavakis, P. Lecoq, C. Leonidopoulos, C. Lourenço, A. Macpherson, T. Mäki, L. Malgeri, M. Mannelli, L. Masetti, F. Meijers, S. Mersi, E. Meschi, R. Moser, M.U. Mozer, M. Mulders, E. Nesvold¹, T. Orimoto, L. Orsini, E. Perez, A. Petrilli, A. Pfeiffer, M. Pierini, M. Pimiä, G. Polese, A. Racz, G. Rolandi²⁴, T. Rommerskirchen, C. Rovelli²⁵, M. Rovere, H. Sakulin, C. Schäfer, C. Schwick, I. Segoni, A. Sharma, P. Siegrist, M. Simon, P. Sphicas²⁶, D. Spiga, M. Spiropulu¹⁹, F. Stöckli, M. Stoye, P. Tropea, A. Tsirou, A. Tsyganov, G.I. Veres¹³, P. Vichoudis, M. Voutilainen, W.D. Zeuner

CERN, European Organization for Nuclear Research, Geneva, Switzerland

W. Bertl, K. Deiters, W. Erdmann, K. Gabathuler, R. Horisberger, Q. Ingram, H.C. Kaestli, S. König, D. Kotlinski, U. Langenegger, F. Meier, D. Renker, T. Rohe, J. Sibille²⁷, A. Starodumov²⁸

Paul Scherrer Institut, Villigen, Switzerland

P. Bortignon, L. Caminada²⁹, Z. Chen, S. Cittolin, G. Dissertori, M. Dittmar, J. Eugster, K. Freudenreich, C. Grab, A. Hervé, W. Hintz, P. Lecomte, W. Lustermann, C. Marchica²⁹, P. Martinez Ruiz del Arbol, P. Meridiani, P. Milenovic³⁰, F. Moortgat, A. Nardulli, P. Nef, F. Nessi-Tedaldi, L. Pape, F. Pauss, T. Punz, A. Rizzi, F.J. Ronga, L. Sala, A.K. Sanchez, M.-C. Sawley, B. Stieger, L. Tauscher[†], A. Thea, K. Theofilatos, D. Treille, C. Urscheler, R. Wallny²¹, M. Weber, L. Wehrli, J. Weng

Institute for Particle Physics, ETH Zurich, Zurich, Switzerland

E. Aguiló, C. AMSler, V. Chiochia, S. De Visscher, C. Favaro, M. Ivova Rikova, A. Jaeger, B. Millan Mejias, C. Regenfus, P. Robmann, A. Schmidt, H. Snoek, L. Wilke

Universität Zürich, Zurich, Switzerland

Y.H. Chang, K.H. Chen, W.T. Chen, S. Dutta, A. Go, C.M. Kuo, S.W. Li, W. Lin, M.H. Liu, Z.k. Liu, Y.J. Lu, J.H. Wu, S.S. Yu

National Central University, Chung-Li, Taiwan

P. Bartalini, P. Chang, Y.H. Chang, Y.W. Chang, Y. Chao, K.F. Chen, W.-S. Hou, Y. Hsiung, K.Y. Kao, Y.J. Lei, R.-S. Lu, J.G. Shiu, Y.M. Tzeng, M. Wang, J.T. Wei

National Taiwan University (NTU), Taipei, Taiwan

A. Adiguzel, M.N. Bakirci, S. Cerci³¹, Z. Demir, C. Dozen, I. Dumanoglu, E. Eskut, S. Girgis, G. Gökbulut, Y. Güler, E. Gurpinar, I. Hos, E.E. Kangal, T. Karaman, A. Kayis Topaksu, A. Nart, G. Öngüt, K. Ozdemir, S. Ozturk, A. Polatöz, K. Sogut³², B. Tali, H. Topakli, D. Uzun, L.N. Vergili, M. Vergili, C. Zorbilmez

Cukurova University, Adana, Turkey

I.V. Akin, T. Aliev, S. Bilmis, M. Deniz, H. Gamsizkan, A.M. Guler, K. Ocalan, A. Ozpineci, M. Serin, R. Sever, U.E. Surat, E. Yildirim, M. Zeyrek

Middle East Technical University, Physics Department, Ankara, Turkey

M. Deliomeroğlu, D. Demir³³, E. Gülmez, A. Halu, B. Isildak, M. Kaya³⁴, O. Kaya³⁴, M. Özbek, S. Ozkorucuklu³⁵, N. Sonmez³⁶

Bogazici University, Istanbul, Turkey

L. Levchuk

National Scientific Center, Kharkov Institute of Physics and Technology, Kharkov, Ukraine

P. Bell, F. Bostock, J.J. Brooke, T.L. Cheng, D. Cussans, R. Frazier, J. Goldstein, M. Grimes, M. Hansen, G.P. Heath, H.F. Heath, B. Huckvale, J. Jackson, L. Kreczko, S. Metson, D.M. Newbold³⁷, K. Nirunpong, A. Poll, V.J. Smith, S. Ward

University of Bristol, Bristol, United Kingdom

L. Basso, K.W. Bell, A. Belyaev, C. Brew, R.M. Brown, B. Camanzi, D.J.A. Cockerill, J.A. Coughlan, K. Harder, S. Harper, B.W. Kennedy, E. Olaiya, D. Petyt, B.C. Radburn-Smith, C.H. Shepherd-Themistocleous, I.R. Tomalin, W.J. Womersley, S.D. Worm

Rutherford Appleton Laboratory, Didcot, United Kingdom

R. Bainbridge, G. Ball, J. Ballin, R. Beuselinck, O. Buchmuller, D. Colling, N. Cripps, M. Cutajar, G. Davies, M. Della Negra, J. Fulcher, D. Futyan, A. Guneratne Bryer, G. Hall, Z. Hatherell, J. Hays, G. Iles, G. Karapostoli, L. Lyons, A.-M. Magnan, J. Marrouche, R. Nandi, J. Nash, A. Nikitenko²⁸, A. Papageorgiou, M. Pesaresi, K. Petridis, M. Pioppi³⁸, D.M. Raymond, N. Rompotis, A. Rose, M.J. Ryan, C. Seez, P. Sharp, A. Sparrow, A. Tapper, S. Tourneur, M. Vazquez Acosta, T. Virdee¹, S. Wakefield, D. Wardrope, T. Whyntie

Imperial College, London, United Kingdom

M. Barrett, M. Chadwick, J.E. Cole, P.R. Hobson, A. Khan, P. Kyberd, D. Leslie, W. Martin, I.D. Reid, L. Teodorescu

Brunel University, Uxbridge, United Kingdom

K. Hatakeyama

Baylor University, Waco, USA

T. Bose, E. Carrera Jarrin, A. Clough, C. Fantasia, A. Heister, J.St. John, P. Lawson, D. Lazic, J. Rohlf, D. Sperka, L. Sulak

Boston University, Boston, USA

A. Avetisyan, S. Bhattacharya, J.P. Chou, D. Cutts, S. Esen, A. Ferapontov, U. Heintz, S. Jabeen, G. Kukartsev, G. Landsberg, M. Narain, D. Nguyen, M. Segala, T. Speer, K.V. Tsang

Brown University, Providence, USA

M.A. Borgia, R. Breedon, M. Calderon De La Barca Sanchez, D. Cebra, M. Chertok, J. Conway, P.T. Cox, J. Dolen, R. Erbacher, E. Friis, W. Ko, A. Kopecky, R. Lander, H. Liu, S. Maruyama, T. Miceli, M. Nikolic, D. Pellett, J. Robles, T. Schwarz, M. Searle, J. Smith, M. Squires, M. Tripathi, R. Vasquez Sierra, C. Veelken

University of California, Davis, USA

V. Andreev, K. Arisaka, D. Cline, R. Cousins, A. Deisher, J. Duris, S. Erhan, C. Farrell, J. Hauser, M. Ignatenko, C. Jarvis, C. Plager, G. Rakness, P. Schlein[†], J. Tucker, V. Valuev

University of California, Los Angeles, USA

J. Babb, R. Clare, J. Ellison, J.W. Gary, F. Giordano, G. Hanson, G.Y. Jeng, S.C. Kao, F. Liu, H. Liu, A. Luthra, H. Nguyen, G. Pasztor³⁹, A. Satpathy, B.C. Shen[†], R. Stringer, J. Sturdy, S. Sumowidagdo, R. Wilken, S. Wimpenny

University of California, Riverside, USA

W. Andrews, J.G. Branson, E. Dusinger, D. Evans, F. Golf, A. Holzner, R. Kelley, M. Lebourgeois, J. Letts, B. Mangano, J. Muelmenstaedt, S. Padhi, C. Palmer, G. Petrucciani, H. Pi, M. Pieri, R. Ranieri, M. Sani, V. Sharma¹, S. Simon, Y. Tu, A. Vartak, F. Würthwein, A. Yagil

University of California, San Diego, La Jolla, USA

D. Barge, R. Bellan, C. Campagnari, M. D'Alfonso, T. Danielson, P. Geffert, J. Incandela, C. Justus, P. Kalavase, S.A. Koay, D. Kovalskyi, V. Krutelyov, S. Lowette, N. Mccoll, V. Pavlunin, F. Rebassoo, J. Ribnik, J. Richman, R. Rossin, D. Stuart, W. To, J.R. Vlimant, M. Witherell

University of California, Santa Barbara, USA

A. Bornheim, J. Bunn, Y. Chen, M. Gataullin, D. Kcira, V. Litvine, Y. Ma, A. Mott, H.B. Newman, C. Rogan, K. Shin, V. Timciuc, P. Traczyk, J. Veverka, R. Wilkinson, Y. Yang, R.Y. Zhu

California Institute of Technology, Pasadena, USA

B. Akgun, A. Calamba, R. Carroll, T. Ferguson, Y. Iiyama, D.W. Jang, S.Y. Jun, Y.F. Liu, M. Paulini, J. Russ, N. Terentyev, H. Vogel, I. Vorobiev

Carnegie Mellon University, Pittsburgh, USA

J.P. Cumalat, M.E. Dinardo, B.R. Drell, C.J. Edelmaier, W.T. Ford, B. Heyburn, E. Luiggi Lopez, U. Nauenberg, J.G. Smith, K. Stenson, K.A. Ulmer, S.R. Wagner, S.L. Zang

University of Colorado at Boulder, Boulder, USA

L. Agostino, J. Alexander, F. Blekman, A. Chatterjee, S. Das, N. Eggert, L.J. Fields, L.K. Gibbons, B. Heltsley, K. Henriksson, W. Hopkins, A. Khukhunaishvili, B. Kreis, V. Kuznetsov, Y. Liu, G. Nicolas Kaufman, J.R. Patterson, D. Puigh, D. Riley, A. Ryd, M. Saelim, X. Shi, W. Sun, W.D. Teo, J. Thom, J. Thompson, J. Vaughan, Y. Weng, L. Winstrom, P. Wittich

Cornell University, Ithaca, USA

A. Biselli, G. Cirino, D. Winn

Fairfield University, Fairfield, USA

S. Abdullin, M. Albrow, J. Anderson, G. Apollinari, M. Atac, J.A. Bakken, S. Banerjee, L.A.T. Bauerdick, A. Beretvas, J. Berryhill, P.C. Bhat, I. Bloch, F. Borcherding, K. Burkett, J.N. Butler, V. Chetluru, H.W.K. Cheung, F. Chlebana, S. Cihangir, M. Demarteau, D.P. Eartly, V.D. Elvira, I. Fisk, J. Freeman, Y. Gao, E. Gottschalk, D. Green, K. Gunthoti, O. Gutsche, A. Hahn, J. Hanlon, R.M. Harris, J. Hirschauer, B. Hooberman, E. James, H. Jensen, M. Johnson, U. Joshi, R. Khatiwada, B. Kilminster, B. Klima, K. Kousouris, S. Kunori, S. Kwan, P. Limon, R. Lipton, J. Lykken, K. Maeshima, J.M. Marraffino, D. Mason, P. McBride, T. McCauley, T. Miao, K. Mishra, S. Mrenna, Y. Musienko⁴⁰, C. Newman-Holmes, V. O'Dell, S. Popescu, R. Pordes, O. Prokofyev, N. Saoulidou, E. Sexton-Kennedy, S. Sharma, A. Soha, W.J. Spalding, L. Spiegel, P. Tan, L. Taylor, S. Tkaczyk, L. Uplegger, E.W. Vaandering, R. Vidal, J. Whitmore, W. Wu, F. Yang, F. Yumiceva, J.C. Yun

Fermi National Accelerator Laboratory, Batavia, USA

D. Acosta, P. Avery, D. Bourilkov, M. Chen, G.P. Di Giovanni, D. Dobur, A. Drozdetskiy, R.D. Field, M. Fisher, Y. Fu, I.K. Furic, J. Gartner, S. Goldberg, B. Kim, S. Klimentko, J. Konigsberg, A. Korytov, K. Kotov, A. Kropivnitskaya, T. Kypreos, K. Matchev, G. Mitselmakher, L. Muniz, Y. Pakhotin, M. Petterson, C. Prescott, R. Remington, M. Schmitt, B. Scurlock, P. Sellers, N. Skhirtladze, M. Snowball, D. Wang, J. Yelton, M. Zakaria

University of Florida, Gainesville, USA

C. Ceron, V. Gaultney, L. Kramer, L.M. Lebolo, S. Linn, P. Markowitz, G. Martinez, D. Mesa, J.L. Rodriguez

Florida International University, Miami, USA

T. Adams, A. Askew, J. Bochenek, J. Chen, B. Diamond, S.V. Gleyzer, J. Haas, S. Hagopian, V. Hagopian, M. Jenkins, K.F. Johnson, H. Prosper, S. Sekmen, V. Veeraraghavan

Florida State University, Tallahassee, USA

M.M. Baarmand, B. Dorney, S. Guragain, M. Hohlmann, H. Kalakhety, R. Ralich, I. Vodopiyanov

Florida Institute of Technology, Melbourne, USA

M.R. Adams, I.M. Anghel, L. Apanasevich, Y. Bai, V.E. Bazterra, R.R. Betts, J. Callner, R. Cavanaugh, C. Dragoiu, E.J. Garcia-Solis, C.E. Gerber, D.J. Hofman, S. Khalatyan, F. Lacroix, C. O'Brien, C. Silvestre, A. Smoron, D. Strom, N. Varelas

University of Illinois at Chicago (UIC), Chicago, USA

U. Akgun, E.A. Albayrak, B. Bilki, K. Cankocak⁴¹, W. Clarida, F. Duru, C.K. Lae, E. McCliment, J.-P. Merlo, H. Mermerkaya, A. Mestvirishvili, A. Moeller, J. Nachtman, C.R. Newsom, E. Norbeck, J. Olson, Y. Onel, F. Ozok, S. Sen, J. Wetzel, T. Yetkin, K. Yi

The University of Iowa, Iowa City, USA

B.A. Barnett, B. Blumenfeld, A. Bonato, C. Eskew, D. Fehling, G. Giurgiu, A.V. Gritsan, Z.J. Guo, G. Hu, P. Maksimovic, S. Rappoccio, M. Swartz, N.V. Tran, A. Whitbeck

Johns Hopkins University, Baltimore, USA

P. Baringer, A. Bean, G. Benelli, O. Grachov, M. Murray, D. Noonan, V. Radicci, S. Sanders, J.S. Wood, V. Zhukova

The University of Kansas, Lawrence, USA

D. Bandurin, T. Bolton, I. Chakaberia, A. Ivanov, M. Makouski, Y. Maravin, S. Shrestha, I. Svintradze, Z. Wan

Kansas State University, Manhattan, USA

J. Gronberg, D. Lange, D. Wright

Lawrence Livermore National Laboratory, Livermore, USA

A. Baden, M. Boutemour, S.C. Eno, D. Ferencek, J.A. Gomez, N.J. Hadley, R.G. Kellogg, M. Kirn, Y. Lu, A.C. Mignerey, K. Rossato, P. Rumerio, F. Santanastasio, A. Skuja, J. Temple, M.B. Tonjes, S.C. Tonwar, E. Twedt

University of Maryland, College Park, USA

B. Alver, G. Bauer, J. Bendavid, W. Busza, E. Butz, I.A. Cali, M. Chan, V. Dutta, P. Everaerts, G. Gomez Ceballos, M. Goncharov, K.A. Hahn, P. Harris, Y. Kim, M. Klute, Y.-J. Lee, W. Li, C. Loizides, J. Lopez, P.D. Luckey, T. Ma, S. Nahn, C. Paus, C. Roland, G. Roland, M. Rudolph, G.S.F. Stephans, K. Sumorok, K. Sung, E.A. Wenger, S. Xie, M. Yang, Y. Yilmaz, A.S. Yoon, M. Zanetti

Massachusetts Institute of Technology, Cambridge, USA

P. Cole, S.I. Cooper, P. Cushman, B. Dahmes, A. De Benedetti, P.R. Duderu, G. Franzoni, J. Haupt, K. Klapoetke, Y. Kubota, J. Mans, V. Rekovic, R. Rusack, M. Sasseville, A. Singovsky

University of Minnesota, Minneapolis, USA

L.M. Cremaldi, R. Godang, R. Kroeger, L. Perera, R. Rahmat, D.A. Sanders, D. Summers

University of Mississippi, University, USA

K. Bloom, S. Bose, J. Butt, D.R. Claes, A. Dominguez, M. Eads, J. Keller, T. Kelly, I. Kravchenko, J. Lazo-Flores, C. Lundstedt, H. Malbouisson, S. Malik, G.R. Snow

University of Nebraska-Lincoln, Lincoln, USA

U. Baur, A. Godshalk, I. Iashvili, A. Kharchilava, A. Kumar, K. Smith, J. Zennamo

State University of New York at Buffalo, Buffalo, USA

G. Alverson, E. Barberis, D. Baumgartel, O. Boeriu, M. Chasco, K. Kaadze, S. Reucroft, J. Swain, D. Wood, J. Zhang

Northeastern University, Boston, USA

A. Anastassov, A. Kubik, N. Odell, R.A. Ofierzynski, B. Pollack, A. Pozdnyakov, M. Schmitt, S. Stoynev, M. Velasco, S. Won

Northwestern University, Evanston, USA

L. Antonelli, D. Berry, M. Hildreth, C. Jessop, D.J. Karmgard, J. Kolb, T. Kolberg, K. Lannon, W. Luo, S. Lynch, N. Marinelli, D.M. Morse, T. Pearson, R. Ruchti, J. Slaunwhite, N. Valls, J. Warchol, M. Wayne, J. Ziegler

University of Notre Dame, Notre Dame, USA

B. Bylsma, L.S. Durkin, J. Gu, C. Hill, P. Killewald, T.Y. Ling, M. Rodenburg, G. Williams

The Ohio State University, Columbus, USA

N. Adam, E. Berry, P. Elmer, D. Gerbaudo, V. Halyo, P. Hebda, A. Hunt, J. Jones, E. Laird, D. Lopes Pegna, D. Marlow, T. Medvedeva, M. Mooney, J. Olsen, P. Piroué, X. Quan, H. Saka, D. Stickland, C. Tully, J.S. Werner, A. Zuranski

Princeton University, Princeton, USA

J.G. Acosta, X.T. Huang, A. Lopez, H. Mendez, S. Oliveros, J.E. Ramirez Vargas, A. Zatserklyaniy

University of Puerto Rico, Mayaguez, USA

E. Alagoz, V.E. Barnes, G. Bolla, L. Borrello, D. Bortoletto, A. Everett, A.F. Garfinkel, Z. Gecse, L. Gutay, M. Jones, O. Koybasi, A.T. Laasanen, N. Leonardo, C. Liu, V. Maroussov, M. Meier, P. Merkel, D.H. Miller, N. Neumeister, K. Potamianos, I. Shipsey, D. Silvers, H. Sun, A. Svyatkovskiy, H.D. Yoo, J. Zablocki, Y. Zheng

Purdue University, West Lafayette, USA

P. Jindal, N. Parashar

Purdue University Calumet, Hammond, USA

C. Boulahouache, V. Cuplov, K.M. Ecklund, F.J.M. Geurts, J.H. Liu, J. Morales, B.P. Padley, R. Redjimi, J. Roberts, J. Zabel

Rice University, Houston, USA

B. Betchart, A. Bodek, Y.S. Chung, P. de Barbaro, R. Demina, Y. Eshaq, H. Flacher, A. Garcia-Bellido, P. Goldenzweig, Y. Gotra, J. Han, A. Harel, D.C. Miner, D. Orbaker, G. Petrillo, D. Vishnevskiy, M. Zielinski

University of Rochester, Rochester, USA

A. Bhatti, L. Demortier, K. Goulianos, G. Lungu, C. Mesropian, M. Yan

The Rockefeller University, New York, USA

O. Atramentov, A. Barker, D. Duggan, Y. Gershtein, R. Gray, E. Halkiadakis, D. Hidas, D. Hits, A. Lath, S. Panwalkar, R. Patel, A. Richards, K. Rose, S. Schnetzer, S. Somalwar, R. Stone, S. Thomas

Rutgers, the State University of New Jersey, Piscataway, USA

G. Cerizza, M. Hollingsworth, S. Spanier, Z.C. Yang, A. York

University of Tennessee, Knoxville, USA

J. Asaadi, R. Eusebi, J. Gilmore, A. Gurrola, T. Kamon, V. Khotilovich, R. Montalvo, C.N. Nguyen, J. Pivarski, A. Safonov, S. Sengupta, A. Tatarinov, D. Toback, M. Weinberger

Texas A&M University, College Station, USA

N. Akchurin, C. Bardak, J. Damgov, C. Jeong, K. Kovitanggoon, S.W. Lee, P. Mane, Y. Roh, A. Sill, I. Volobouev, R. Wigmans, E. Yazgan

Texas Tech University, Lubbock, USA

E. Appelt, E. Brownson, D. Engh, C. Florez, W. Gabella, W. Johns, P. Kurt, C. Maguire, A. Melo, P. Sheldon, J. Velkovska

Vanderbilt University, Nashville, USA

M.W. Arenton, M. Balazs, S. Boutle, M. Buehler, S. Conetti, B. Cox, B. Francis, R. Hirosky, A. Ledovskoy, C. Lin, C. Neu, T. Patel, R. Yohay

University of Virginia, Charlottesville, USA

S. Gollapinni, R. Harr, P.E. Karchin, V. Loggins, M. Mattson, C. Milstène, A. Sakharov

Wayne State University, Detroit, USA

M. Anderson, M. Bachtis, J.N. Bellinger, D. Carlsmith, S. Dasu, J. Efron, L. Gray, A. Gregerson, K.S. Grogg, M. Grothe, R. Hall-Wilton¹, M. Herndon, P. Klabbers, J. Klukas, A. Lanaro, C. Lazaridis, J. Leonard, J. Liu, D. Lomidze, R. Loveless, A. Mohapatra, W. Parker, D. Reeder, I. Ross, A. Savin, W.H. Smith, J. Swanson, M. Weinberg

University of Wisconsin, Madison, USA

* Corresponding author.

E-mail address: Roberto.Tenchini@cern.ch (R. Tenchini).

† Deceased.

¹ Also at CERN, European Organization for Nuclear Research, Geneva, Switzerland.

² Also at Universidade Federal do ABC, Santo Andre, Brazil.

³ Also at Laboratoire Leprince-Ringuet, Ecole Polytechnique, IN2P3–CNRS, Palaiseau, France.

⁴ Also at Cairo University, Cairo, Egypt.

⁵ Also at Suez Canal University, Suez, Egypt.

⁶ Also at Fayoum University, El-Fayoum, Egypt.

⁷ Also at Sołtan Institute for Nuclear Studies, Warsaw, Poland.

⁸ Also at Massachusetts Institute of Technology, Cambridge, USA.

⁹ Also at Université de Haute-Alsace, Mulhouse, France.

¹⁰ Also at Brandenburg University of Technology, Cottbus, Germany.

¹¹ Also at Moscow State University, Moscow, Russia.

¹² Also at Institute of Nuclear Research ATOMKI, Debrecen, Hungary.

¹³ Also at Eötvös Loránd University, Budapest, Hungary.

¹⁴ Also at Tata Institute of Fundamental Research – HECR, Mumbai, India.

¹⁵ Also at University of Visva-Bharati, Santiniketan, India.

¹⁶ Also at Facoltà Ingegneria, Università di Roma “La Sapienza”, Roma, Italy.

¹⁷ Also at Università della Basilicata, Potenza, Italy.

¹⁸ Also at Laboratori Nazionali di Legnaro dell’INFN, Legnaro, Italy.

¹⁹ Also at California Institute of Technology, Pasadena, USA.

²⁰ Also at Faculty of Physics of University of Belgrade, Belgrade, Serbia.

²¹ Also at University of California, Los Angeles, Los Angeles, USA.

²² Also at University of Florida, Gainesville, USA.

²³ Also at Université de Genève, Geneva, Switzerland.

²⁴ Also at Scuola Normale e Sezione dell’INFN, Pisa, Italy.

²⁵ Also at INFN Sezione di Roma; Università di Roma “La Sapienza”, Roma, Italy.

²⁶ Also at University of Athens, Athens, Greece.

²⁷ Also at The University of Kansas, Lawrence, USA.

²⁸ Also at Institute for Theoretical and Experimental Physics, Moscow, Russia.

²⁹ Also at Paul Scherrer Institut, Villigen, Switzerland.

³⁰ Also at University of Belgrade, Faculty of Physics and Vinca Institute of Nuclear Sciences, Belgrade, Serbia.

³¹ Also at Adiyaman University, Adiyaman, Turkey.

³² Also at Mersin University, Mersin, Turkey.

³³ Also at Izmir Institute of Technology, Izmir, Turkey.

³⁴ Also at Kafkas University, Kars, Turkey.

³⁵ Also at Suleyman Demirel University, Isparta, Turkey.

³⁶ Also at Ege University, Izmir, Turkey.

³⁷ Also at Rutherford Appleton Laboratory, Didcot, United Kingdom.

³⁸ Also at INFN Sezione di Perugia; Università di Perugia, Perugia, Italy.

³⁹ Also at KFKI Research Institute for Particle and Nuclear Physics, Budapest, Hungary.

⁴⁰ Also at Institute for Nuclear Research, Moscow, Russia.

⁴¹ Also at Istanbul Technical University, Istanbul, Turkey.

Short CV of Prof. Dr. Ben Craps

(30/10/2016)



PERSONAL INFORMATION

Family name, First name: Craps, Ben

Researcher unique identifier(s): <http://inspirehep.net/author/profile/B.Craps.1>

<http://orcid.org/0000-0002-0805-0403>

<http://www.researcherid.com/rid/J-8429-2016>

Date of birth: 28/04/1974

Nationality: Belgian

EDUCATION

2000 PhD Physics, KU Leuven / FWO, Belgium

1996 Master Physics, KU Leuven, Belgium

CURRENT POSITION(S)

2014 – Professor, Theoretical Physics, Vrije Universiteit Brussel (VUB), Belgium

2012 – Group Leader Theoretical High-Energy Physics of HEP@VUB Strategic Research Program

2007 – Assistant to the Director, International Solvay Institutes, Belgium

PREVIOUS POSITIONS

May 2014 Visiting Professor, École Normale Supérieure, Paris, France

2006 – 2013 Assistant/Associate Professor, Vrije Universiteit Brussel, Belgium

2003 – 2005 Postdoc, Universiteit van Amsterdam / Stichting FOM, Netherlands

2000 – 2003 Postdoc, Enrico Fermi Institute, University of Chicago, USA

FELLOWSHIPS AND AWARDS

2009 Frans Van Cauwelaert prize, Royal Flemish Academy of Belgium for Sciences and Arts

SUPERVISION OF GRADUATE STUDENTS AND POSTDOCTORAL FELLOWS

2006 – Supervised 8 postdocs, 12 PhD students (incl. 5 ongoing), 10 Master students at VUB

Oleg Evnin is now a long-term research scholar at Chulalongkorn University, Bangkok

Alexey Koshelev has a long-term position at University of Beira Interior, Portugal

Alberto Mariotti is now a full-time faculty member at VUB

Piotr Surówka went on to *Harvard University* and *MPI Munich*

Hongbao Zhang is moving to a faculty position at Beijing Normal University

Alice Bernamonti went on to *Leuven U.* and a 3+2 year position at *Perimeter Institute*

Nele Callebaut went on to *Princeton University* and *Columbia University*

Frederik De Roo went on to *Karlsruhe Institute of Technology*

Federico Galli went on to *Leuven U.* and a 3+2 year position at *Perimeter Institute*

Wieland Staessens went on to *Mainz University* and *UAM Madrid*

SCIENTIFIC TRACK RECORD

Author of 67 papers, 48 of which published in major journals (PRL, JHEP, PRD, JCAP, PLB, NPB, CMP, CQG, Optics Express); 2115 citations, $h=25$. Source: Inspire (30/10/2016) + WoS for optics papers. In addition, postdocs and PhD students working under my direct supervision have written more than 75 papers not signed by me. Lecture series at 8 international PhD schools. About 40 invited talks at international conferences, and about 70 invited seminars and colloquia.

RESEARCH FUNDING

2006 – More than €2,000,000 plus 24 PhD years as PI + similar amount as (de facto) co-PI.

ORGANISATION OF SCIENTIFIC MEETINGS

2009 – 2015 Organizer of 7 editions of APC/PI/Solvay workshop on Cosmological Frontiers in Fundamental Physics, Belgium/Canada/France
2008 – 2016 Organizer of 9 editions of the three-month Amsterdam-Brussels-Geneva-Paris doctoral school on Quantum Field Theory, Strings and Gravity
2010 – 2016 Organizer of 7 editions of two-day meeting of mathematical and theoretical physicists of Flanders, Oostduinkerke/Oostende, Belgium
2015 Organizer of The String Theory Universe; 21st European string workshop, Leuven, Belgium
2013 Organizer of workshop on Holographic Thermalization, Regensburg, Germany
2013 Organizer of conference on the occasion of A. Van Proeyen's 60th birthday, Leuven, Belgium
2012 Organizer of Lorentz Center workshop on Holographic Thermalization, Leiden, Netherlands
2012 Organizer of General Scientific Meeting of Belgian Physical Society, Brussels, Belgium
2011 Organizer of Solvay workshop on Gauge Theories, Strings and Geometry, Brussels, Belgium
2010 Organizer of Crete workshop on the Frontiers of Cosmology, Heraklion, Greece
2007 Organizer of Solvay workshop on Gauge Theories, Strings and Geometry, Brussels, Belgium

INSTITUTIONAL RESPONSIBILITIES

2009 – 2012 Chairman of Physics Department, VUB
2009 – 2012 Member of Faculty Board, VUB
2007 – Assistant to the Director, International Solvay Institutes, Brussels, Belgium
2007 – Member of Local Scientific Committee, International Solvay Institutes, Brussels, Belgium
2014 – Chairman of exam committee, Bachelor's Physics and Astrophysics, VUB
2014 – Substitute chairman of university level Review Committee for Teaching Professionalization of Professors, VUB
2007 – Representative of the Physics Department in the Research Committee of the Faculty of Science and Bio-Engineering Sciences, VUB
2015 – Representative of the Physics Department in the Committee for Student Affairs of the Faculty of Science and Bio-Engineering Sciences, VUB

COMMISSIONS OF TRUST

2012 – Member of faculty hiring/search committees at KU Leuven, UGent and VUB, Belgium
2010 – Frequent evaluator for hiring permanent and temporary researchers, FNRS, Belgium
2015 Evaluator for renewal of Associate Faculty member, Perimeter Institute, Canada
2011 – Project evaluator for Swiss National Science Foundation, FNRS (Belgium), National Science Foundation (USA), Israel Science Foundation
2016 Expert/Rapporteur: Marie Skłodowska-Curie Individual Fellowships
2016 Evaluator for Aarhus Institute of Advanced Studies-Cofund (Marie Curie) fellowship
2006 – Chairman or Member of 29 PhD committees in Belgium, France and the Netherlands

MEMBERSHIPS OF SCIENTIFIC SOCIETIES

2016 – Board Member, Belgian Physical Society
2009 – Member, General Assembly of the International Solvay Institutes

Information from Prof. Dr. Ben Craps (section 11) (2011-2016)

Most important scientific publications (*: 5 most important publications):

(Authors are ordered alphabetically; *team members are indicated in italics.*)

- *B. Craps, E. J. Lindgren and A. Taliotis*, “Holographic thermalization in a top-down confining model,” JHEP 1512 (2015) 116.
- (*) *B. Craps, O. Evnin and J. Vanhoof*, “Renormalization, averaging, conservation laws and AdS (in)stability,” JHEP 1501 (2015) 108.
- (*) *B. Craps, O. Evnin and J. Vanhoof*, “Renormalization group, secular term resummation and AdS (in)stability,” JHEP 1410 (2014) 048.
- *B. Craps, E. Kiritsis, C. Rosen, A. Taliotis, J. Vanhoof and H. b. Zhang*, “Gravitational collapse and thermalization in the hard wall model,” JHEP 1402 (2014) 120.
- *V. Balasubramanian, A. Bernamonti, J. de Boer, B. Craps, L. Franti, F. Galli, E. Keski-Vakkuri, B. Müller and A. Schäfer*, “Inhomogeneous Thermalization in Strongly Coupled Field Theories,” Phys. Rev. Lett. 111 (2013) 231602.
- *V. Balasubramanian, A. Bernamonti, B. Craps, V. Keränen, E. Keski-Vakkuri, B. Müller, L. Thorlacius and J. Vanhoof*, “Thermalization of the spectral function in strongly coupled two dimensional conformal field theories”, JHEP 1304 (2013) 069.
- *B. Craps, T. Hertog, N. Turok*, “Quantum resolution of cosmological singularities using AdS/CFT correspondence”, Phys. Rev. D 86 (2012) 043513.
- (*) *V. Balasubramanian, A. Bernamonti, N. Copland, B. Craps and F. Galli*, “Thermalization of mutual and tripartite information in strongly coupled two dimensional conformal field theories,” Phys. Rev. D 84 (2011) 105017.
- (*) *V. Balasubramanian, A. Bernamonti, J. de Boer, N. Copland, B. Craps, E. Keski-Vakkuri, B. Müller, A. Schäfer, M. Shigemori and W. Staessens*, “Holographic Thermalization,” Phys. Rev. D 84 (2011) 026010.
- (*) *V. Balasubramanian, A. Bernamonti, J. de Boer, N. Copland, B. Craps, E. Keski-Vakkuri, B. Müller, A. Schäfer, M. Shigemori and W. Staessens*, “Thermalization of Strongly Coupled Field Theories,” Phys. Rev. Lett. 106 (2011) 191601.

Most important scientific reviews:

- *B. Craps, O. Evnin*, “AdS (in)stability: an analytic approach”, Fortsch. Phys. 64 (2016) 336-344.

Applications for international research funding, and VUB-promotorships of applications for Odysseus funding:

- Applied for ERC Advanced grant (2016); result not known yet.
- Promotor for Jelle Hartong, Odysseus-II (2015); selected by FWO jury, but not funded by VUB due to budget constraints.

Promotorships of awarded PhD's:

- *Wieland Staessens*, Aspects of Type II Superstring Theory: Supersymmetric D-Branes, T-duality and Holographic Thermalization, 27/6/2011.
- *Alice Bernamonti*, Applications of the AdS/CFT correspondence to strongly coupled dynamics, 22/5/2012.
- *Federico Galli*, Applications of the AdS/CFT correspondence to non-equilibrium physics at strong coupling, 15/5/2013.
- *Bettina Oexl*, Gravitino production at colliders, 1/7/2014.
- *Nele Callebaut*, Background field and time dependence effects in holographic models, 28/8/2014.
- *Joris Vanhoof*, Holographic models of out-of-equilibrium systems, 2/7/2015.

Realisations of added value outside the academic community, and of technology transfer:

- Involved as Assistant to the Director in the activities of the International Solvay Institutes (which include major outreach events such as yearly public lectures).
- Board Member of Belgian Physical Society (since 2016).
- Contributed to the movie “Kwantumrevolutie” (general advice and feedback; suggested two of the young scientists interviewed in the movie) (2015).
- Contributions in popular science magazines (Heelal, Kijk).
- Popularizing lectures for high schools, student organizations, adult education.

Renormalization, averaging, conservation laws and AdS (in)stability

Ben Craps,^a Oleg Evnin^{b,a} and Joris Vanhoof^a

^a*Theoretische Natuurkunde, Vrije Universiteit Brussel and The International Solvay Institutes, Pleinlaan 2, B-1050 Brussels, Belgium*

^b*Department of Physics, Faculty of Science, Chulalongkorn University, Thanon Phayathai, Pathumwan, Bangkok 10330, Thailand*

E-mail: Ben.Craps@vub.ac.be, oleg.evnin@gmail.com,
Joris.Vanhoof@vub.ac.be

ABSTRACT: We continue our analytic investigations of non-linear spherically symmetric perturbations around the anti-de Sitter background in gravity-scalar field systems, and focus on conservation laws restricting the (perturbatively) slow drift of energy between the different normal modes due to non-linearities. We discover two conservation laws in addition to the energy conservation previously discussed in relation to AdS instability. A similar set of three conservation laws was previously noted for a self-interacting scalar field in a non-dynamical AdS background, and we highlight the similarities of this system to the fully dynamical case of gravitational instability. The nature of these conservation laws is best understood through an appeal to averaging methods which allow one to derive an effective Lagrangian or Hamiltonian description of the slow energy transfer between the normal modes. The conservation laws in question then follow from explicit symmetries of this averaged effective theory.

KEYWORDS: Classical Theories of Gravity, AdS-CFT Correspondence, Black Holes, Holography and quark-gluon plasmas

ARXIV EPRINT: [1412.3249](https://arxiv.org/abs/1412.3249)

Contents

1	Introduction	1
2	Non-linear perturbation theory around the AdS background	4
2.1	Setup of the system	4
2.2	Weakly non-linear perturbation theory	5
2.3	Renormalization flow equations	6
3	Conservation laws	8
4	Lagrangian form of the conservation laws	9
4.1	Renormalization flow equations in boundary time gauge	9
4.2	Relation between the renormalization flows in different gauges	10
4.3	Computation of the renormalization flow equations in the boundary time gauge	11
5	Averaging methods	12
5.1	Averaging over fast oscillations and the periodic normal form	13
5.2	Equivalence of averaging and multiscale methods	15
5.3	Lagrangian and Hamiltonian averaging	16
6	AdS averaging	18
6.1	Effective action for the scalar field	18
6.2	Averaged Hamiltonian system	20
A	Coefficients of the renormalization flow equations	21
B	Symmetry of R_{ij} coefficients in AdS₃	22
C	Effective action for the scalar field	23
D	Relating the coefficients in the renormalization and averaging procedures	25

1 Introduction

Non-linear instability of anti-de Sitter (AdS) space has attracted a considerable amount of attention since the pioneering observations of [1]. Reasons include the inherent mathematical depth of the problem and its dual interpretation in terms of thermalization processes in quantum gauge theories (in the context of the AdS/CFT correspondence). AdS space is known to be linearly stable, but all frequencies of normal modes are integer in appropriate units, in which case non-linearities are known to induce significant (perturbatively)

slow resonant transfer of energy between different normal modes, no matter how small the perturbation amplitudes are.

The ultimate fate of the energy flow between the different normal modes induced by non-linearities is a subtle matter [1–13], and most of the available considerations are numerical. At first, a series of numerical examples of smooth initial data that develop a turbulent cascade leading to energy transfer to very short wave length modes and black hole formation was presented in [1]. It was later observed, however, that other initial profiles do not lead to collapse [5, 6] and that some explicit finite deformations of AdS make it stable [3]. This seems to imply a complicated interplay of stable and unstable behavior described by a rich topography in the phase space. It was further suggested in [12] that the instability domain might even shrink to a set of measure zero as the perturbation amplitude is decreased, but more analysis will be required to either confirm or rule out this possibility.

The subtleties of the AdS stability phenomena make it necessary to go beyond the inherent uncertainty of numerical methods and attempt to develop some analytic understanding. The evolution of small deviations from the AdS background is governed by non-linear perturbation theory. Possibilities of significant transfer of energy between the modes (at small amplitude values) manifest themselves as secular terms (terms exhibiting unbounded growth in time) in naïve asymptotic expansions of the solutions to the equations of motion in powers of the perturbation amplitude, as noted already in [1]. These terms by themselves, however, do not provide any reliable information on the ultimate fate of the system and simply signify a break-down of the naïve perturbation theory at late times. Various techniques can be employed to re-structure (resum) the naïve perturbation theory and produce modified asymptotic expansions valid at late times. Since the instability cascade takes a very long time to develop, it can only be analytically discussed in the context of such improved asymptotic expansions.

In [11], we described a perturbative resummation technique, based on the idea of the renormalization group, that produces effective equations describing the slow energy flow between the normal modes, and at the same time eliminates the secular terms at lowest non-trivial order, making the perturbation theory valid on long time intervals. A closely related technique, called the ‘Two-Time Framework’, had been previously employed for the same system in [10], though in a way geared towards numerical modelling rather than analytic study, and restricted to a finite set of low-lying modes. We have observed that only a subset of secular terms that could have appeared based on the normal mode frequency spectrum actually appear in the AdS case we study. This feature is further reflected in the effective energy flow equations we have derived, since a number of terms in those equations that could be present in fact vanish, restricting the availability of energy flow channels.

In light of the complex interplay of stability and instability that has been revealed in AdS space through numerical simulations, it is important to study precisely the constraints on the energy flow of the type we mentioned. Since the instability is generated by resonant transfer of energy to short wave-length, high-frequency modes, any limitation on the energy transfer channels available will hinder the instability onset. Such constraints are particularly apparent if formulated explicitly as conservation laws in our effective equations describing the energy transfer. This approach will form the main subject of our present

study. We shall extract the three conservation laws present in the equations of [10, 11], analyze their origin and note that one of the three laws is explicitly related to the absence of certain types of secular terms proved in [11].

The three conservation laws we find form a direct parallel to the considerations of [14], where an identical mathematical structure was described for the case of a self-interacting probe scalar field in a non-dynamical AdS space. In that paper, averaging over fast oscillations was used to produce an effective Lagrangian governing the slow energy transfer. The three conservation laws follow naturally from the symmetries of this effective Lagrangian. Since we find such perception very appealing, we shall extend this picture to the case involving fully dynamical gravity, which is algebraically much more elaborate. In addition, we shall comment on different possible implementations of the averaging over fast oscillations and the relation of this approach to the resummation schemes of [10, 11]. This will also strengthen the theoretical foundations of the results of [14].

It may appear surprising that the cases of self-interacting scalar field in a fixed background and full gravitational non-linearity appear so similar in terms of the constraints on slow energy transfer between the modes. The structure of secular terms in non-linear perturbation theory, and hence the restrictions on energy transfer channels depend crucially on the type of non-linearities involved. It happens nonetheless that scalar field self-interactions and gravitational forces produce similar energy transfer patterns in our setting.

Our observations suggest that a self-interacting scalar field in a fixed AdS background is likely to be an efficient toy model to the full gravitational weak turbulence, which is a much more complicated process. Of course, one would not be able to discuss black hole formation in this toy model setting, since the geometric background does not evolve. In general, one has to maintain a clear understanding that weak turbulence and black hole formation are distinct, even if often related, manifestations of AdS instability. Black hole formation occurs through focusing of the scalar field wave profile, for which transfer of energy to short wavelength modes is necessary. There are settings, however, when such energy transfer occurs but a black hole does not form. A self-interacting scalar field in a fixed geometry is a completely obvious example. In a more subtle way, collapse in AdS₃ cannot occur in the weak field regime, since there is a finite minimal mass for black holes in that space. Yet, the flow of energy renders the dynamics just as turbulent as in higher dimensions [7]. Turbulence is conveniently analyzed by estimating the growth of Sobolev norms (weighted sums of mode energies preferentially representing the ultraviolet modes). A classic treatment of this sort (for the weak turbulence of the non-linear Schrödinger equation on a torus) can be found in [15]. At the same time, as emphasized in [12], mode energies by themselves are insufficient for making statements about horizon formation, since focusing in position space is sensitive to phases as well as amplitudes of individual normal modes.

The paper is organized as follows. In section 2, we review the non-linear perturbation theory in the AdS background along the lines of [11]. In section 3, we demonstrate by a brute force verification that these equations admit three conservation laws. In section 4, we demonstrate that a (field-dependent) time reparametrization allows one to give the effective dynamics a Lagrangian form and relate the three conservation laws to explicit symmetries of the Lagrangian. (The reasons why this Lagrangian structure of the effective

energy transfer equations only becomes apparent in certain variables are somewhat subtle and will become apparent from our subsequent systematic discussion.) We then turn to averaging methods in section 5 in hope of being able to derive a Lagrangian or Hamiltonian effective theory directly. We review the relation between averaging and the multi-scale resummation methods employed to describe the energy transfer in [10, 11], and we show in general how averaging can be performed directly at the level of the Hamiltonian. Finally, in section 6 we give a technical implementation of the averaging approach for the case of non-linear AdS perturbations.

Sections 3 and 4 are rather technical in nature and are meant to give a matter-of-fact statement of the conservation laws in the context of the renormalization flow formalism developed in [11]. A more systematic picture based on averaging methods is given in sections 5 and 6, which may be read semi-independently from sections 3 and 4.

2 Non-linear perturbation theory around the AdS background

2.1 Setup of the system

We briefly recapitulate the setup of [1, 11, 16] in which we will study the stability of AdS_{d+1} space-time, with d standing for the number of spatial dimensions. Einstein gravity with negative cosmological constant $\Lambda = -d(d-1)/(2L^2)$ is coupled to a free massless scalar field, leading to the equations of motion

$$R_{\mu\nu} - \frac{1}{2}g_{\mu\nu}R + \Lambda g_{\mu\nu} - 8\pi G \left(\partial_\mu \phi \partial_\nu \phi - \frac{1}{2}g_{\mu\nu}(\partial\phi)^2 \right) = 0 \tag{2.1}$$

and

$$\frac{1}{\sqrt{-g}} \partial_\mu (\sqrt{-g} g^{\mu\nu} \partial_\nu \phi) = 0. \tag{2.2}$$

Restricting to spherically symmetric configurations, we consider the metric ansatz

$$ds^2 = \frac{L^2}{\cos^2 x} \left(\frac{dx^2}{A} - Ae^{-2\delta} dt^2 + \sin^2 x d\Omega_{d-1}^2 \right), \tag{2.3}$$

where the metric functions $A(x, t)$ and $\delta(x, t)$, as well as the scalar field $\phi(x, t)$, only depend on the time coordinate t , which takes values in \mathbb{R} , and the radial coordinate x , which takes values in $[0, \pi/2)$. The metric (2.3) is not completely gauge fixed: one still has the freedom to transform $\delta(x, t) \mapsto \delta(x, t) + q(t)$ together with a redefinition of the time variable t . Two possible gauge fixing conditions have appeared in the literature: $\delta(0, t) = 0$ [1, 10, 11] and $\delta(\pi/2, t) = 0$ [13]. The first choice corresponds to t being the proper time measured in the interior at $x = 0$, while the second choice means that t is the proper time measured at the boundary.

We introduce the notation $\Phi \equiv \phi'$ and $\Pi \equiv A^{-1}e^\delta \dot{\phi}$ (where dots and primes denote the t - and x -derivatives, respectively) together with the convention $8\pi G = d-1$. Furthermore, it is convenient to define

$$\mu(x) \equiv (\tan x)^{d-1} \quad \text{and} \quad \nu(x) \equiv \frac{(d-1)}{\mu'(x)} = \frac{\sin x \cos x}{(\tan x)^{d-1}}. \tag{2.4}$$

The equations of motion then reduce to

$$\dot{\Phi} = \left(A e^{-\delta} \Pi \right)', \quad \dot{\Pi} = \frac{1}{\mu} \left(\mu A e^{-\delta} \Phi \right)', \quad (2.5a)$$

$$A' = \frac{\nu'}{\nu} (A - 1) - \mu\nu (\Phi^2 + \Pi^2) A, \quad \delta' = -\mu\nu (\Phi^2 + \Pi^2), \quad (2.5b)$$

$$\dot{A} = -2\mu\nu A^2 e^{-\delta} \Phi \Pi. \quad (2.5c)$$

A static solution of these equations is the AdS-Schwarzschild black hole $A(x, t) = 1 - M\nu(x)$, $\delta(x, t) = 0$ and $\phi(x, t) = 0$. Unperturbed AdS space itself corresponds to $A = 1$, $\delta = \phi = 0$.

2.2 Weakly non-linear perturbation theory

We will search for an approximate solution of the equations of motion (2.5), subject to initial conditions $(\phi(x, t)|_{t=0}, \dot{\phi}(x, t)|_{t=0}) = (\epsilon\phi_0(x), \epsilon\psi_0(x))$. Therefore, we expand the unknown functions in the amplitude of the initial conditions:

$$\phi(x, t) = \sum_{k=0}^{\infty} \epsilon^{2k+1} \phi_{2k+1}(x, t), \quad A(x, t) = 1 + \sum_{k=1}^{\infty} \epsilon^{2k} A_{2k}(x, t), \quad \delta(x, t) = \sum_{k=1}^{\infty} \epsilon^{2k} \delta_{2k}(x, t). \quad (2.6)$$

At first order in the ϵ -expansion, the equations of motion (2.5) are linearized and result in the homogeneous partial differential equation

$$\ddot{\phi}_1 + \hat{L}\phi_1 = 0 \quad \text{with} \quad \hat{L} \equiv -\frac{1}{\mu(x)} \partial_x (\mu(x) \partial_x). \quad (2.7)$$

The operator \hat{L} is self-adjoint on the subspace of functions $\psi(x)$ that vanish at the boundary $\psi(\pi/2) = 0$. The inner product on this Hilbert space is

$$\langle \psi, \chi \rangle \equiv \int_0^{\pi/2} \bar{\psi}(x) \chi(x) \mu(x) dx. \quad (2.8)$$

The eigenvalues and eigenfunctions for \hat{L} are ω_n^2 , with

$$\omega_n = d + 2n, \quad n = 0, 1, \dots, \quad (2.9)$$

and

$$e_n(x) = k_n (\cos x)^d P_n^{(\frac{d}{2}-1, \frac{d}{2})}(\cos(2x)) \quad \text{with} \quad k_n = \frac{2\sqrt{n!(n+d-1)!}}{\Gamma(n + \frac{d}{2})}. \quad (2.10)$$

The function $P_n^{(a,b)}(x)$ is a Jacobi polynomial of order n . These eigenfunctions are normalized such that $\hat{L}e_j = \omega_j^2 e_j$ and $\langle e_i, e_j \rangle = \delta_{ij}$. Note that all the mode frequencies ω_n are integer and therefore the spectrum is fully resonant. We can expand the unknown functions in the basis $\{e_n(x)\}$ of eigenmodes:

$$\phi_{2k+1}(x, t) = \sum_{n=0}^{\infty} c_n^{(2k+1)}(t) e_n(x) \quad \text{with} \quad c_n^{(2k+1)}(t) = \langle \phi_{2k+1}(x, t), e_n(x) \rangle. \quad (2.11)$$

Equation (2.7) then translates to $\ddot{c}_n^{(1)} + \omega_n^2 c_n^{(1)} = 0$ and yields the general solution of the linearized equation for ϕ_1 ,

$$\phi_1(x, t) = \sum_{n=0}^{\infty} A_n \cos(\omega_n t + B_n) e_n(x). \quad (2.12)$$

The backreaction on the metric appears at second order. It is given by

$$A_2(x, t) = -\nu(x) \int_0^x \left(\dot{\phi}_1(y, t)^2 + \phi_1'(y, t)^2 \right) \mu(y) dy, \quad (2.13)$$

$$\delta_2(x, t) = \begin{cases} -\int_0^x \left(\dot{\phi}_1(y, t)^2 + \phi_1'(y, t)^2 \right) \mu(y) \nu(y) dy & \text{in the gauge } \delta(0, t) = 0 \\ \int_x^{\pi/2} \left(\dot{\phi}_1(y, t)^2 + \phi_1'(y, t)^2 \right) \mu(y) \nu(y) dy & \text{in the gauge } \delta(\pi/2, t) = 0. \end{cases} \quad (2.14)$$

At third order in the ϵ -expansion, the equations of motion (2.5) lead to the inhomogeneous equation

$$\ddot{\phi}_3 + \hat{L}\phi_3 = S \equiv 2(A_2 - \delta_2) \ddot{\phi}_1 + (\dot{A}_2 - \dot{\delta}_2) \dot{\phi}_1 + (A_2' - \delta_2') \phi_1'. \quad (2.15)$$

We can project this equation onto the eigenbasis $\{e_n\}$, such that

$$\ddot{c}_n^{(3)} + \omega_n^2 c_n^{(3)} = S_n \quad \text{with} \quad S_n = \langle S, e_n \rangle. \quad (2.16)$$

After a tedious but straightforward calculation [11], one finds an explicit expression for the source term $S_n(t)$ in terms of the $c_n^{(1)}(t)$. Because the spectrum (2.9) of linear perturbations is resonant, this source contains resonant terms that will induce secular growth of $c_n^{(3)}(t)$.

2.3 Renormalization flow equations

The secular behavior of the solutions at order $\mathcal{O}(\epsilon^3)$ can be resummed by absorbing it in the renormalized amplitudes A_l and phases B_l . The renormalization group resummation of these secular terms conducted in [11] (using the gauge fixing condition $\delta(0) = 0$) leads to the general renormalization flow equations,

$$\frac{2\omega_l}{\epsilon^2} \frac{dA_l}{d\tau} = - \underbrace{\sum_i \sum_j \sum_k}_{\omega_i + \omega_j = \omega_k + \omega_l}^{\{i,j\} \neq \{k,l\}} S_{ijkl} A_i A_j A_k \sin(B_l + B_k - B_i - B_j) \quad (2.17)$$

and

$$\frac{2\omega_l A_l}{\epsilon^2} \frac{dB_l}{d\tau} = -T_l A_l^3 - \sum_i^{i \neq l} R_{il} A_i^2 A_l - \underbrace{\sum_i \sum_j \sum_k}_{\omega_i + \omega_j = \omega_k + \omega_l}^{\{i,j\} \neq \{k,l\}} S_{ijkl} A_i A_j A_k \cos(B_l + B_k - B_i - B_j). \quad (2.18)$$

The coefficients that appear in these equations are written explicitly in appendix A. $\{i, j\} \neq \{k, l\}$ means that neither i nor j coincides with either k or l . Potentially, there could have been extra contributions in these equations: terms proportional to $A_i A_j A_k \sin(B_l - B_i - B_j - B_k)$ in (2.17) and to $A_i A_j A_k \cos(B_l - B_i - B_j - B_k)$ in (2.18), from the resonant frequency

addition pattern $\omega_l = \omega_i + \omega_j + \omega_k$, and terms proportional to $A_i A_j A_k \sin(B_l + B_j + B_k - B_i)$ in (2.17) and to $A_i A_j A_k \cos(B_l + B_j + B_k - B_i)$ in (2.18), from the resonant frequency addition pattern $\omega_l = \omega_i - \omega_j - \omega_k$. We have proved in [11], however, that all such terms vanish for the AdS case. This property is not generic for all systems¹ that have equations of motion of the form (2.5), but depends on the particular dynamics of AdS_{d+1} .

For our purposes, the symmetry properties of the non-vanishing coefficients T_i , R_{ij} and S_{ijkl} will be more important than their precise values. Whenever the resonance condition $\omega_i + \omega_j = \omega_k + \omega_l$ is satisfied, one has $S_{ijkl} = S_{jikl}$, $S_{ijkl} = S_{ijlk}$ and $S_{ijkl} = S_{klij}$. Another useful observation is that

$$R_{ij} - R_{ji} = \omega_i^2(A_{jj} + \omega_j^2 V_{jj}) - \omega_j^2(A_{ii} + \omega_i^2 V_{ii}), \quad (2.19)$$

where the coefficients A_{ij} and V_{ij} are defined in appendix A. We can thus conclude that the R_{ij} coefficients are generically non-symmetric. A noteworthy exception to this is AdS_3 , as proven in appendix B.

The equations can be simplified by adopting the complex notation $\alpha_k = \frac{A_k}{2} e^{-iB_k}$ (used, for instance, in [10]), such that the first order scalar field solution is written as

$$\phi_1(x, t) = \sum_{k=0}^{\infty} A_k \cos(\omega_k t + B_k) e_k(x) = \sum_{k=0}^{\infty} (\alpha_k e^{-i\omega_k t} + \bar{\alpha}_k e^{i\omega_k t}) e_k(x). \quad (2.20)$$

The two renormalization flow equations (2.17), (2.18) can then be combined into

$$\frac{\omega_l}{(2i\epsilon^2)} \frac{d\alpha_l}{d\tau} = T_l |\alpha_l|^2 \alpha_l + \sum_{i \neq l} R_{il} |\alpha_i|^2 \alpha_l + \underbrace{\sum_i \sum_j \sum_k}_{\omega_i + \omega_j = \omega_k + \omega_l} S_{ijkl} \alpha_i \alpha_j \bar{\alpha}_k. \quad (2.21)$$

Note that the extra terms we have described under (2.18), which are absent due to special properties of the AdS space, would have resulted in contributions of the form $\alpha_i \alpha_j \alpha_k$, etc. in the above equation. This would have had an impact on the conservation laws we shall derive in section 3.

It is instructive to define the quantity

$$V = \sum_i T_i |\alpha_i|^4 + \sum_{i,j}^{i \neq j} R_{ij}^S |\alpha_i|^2 |\alpha_j|^2 + \underbrace{\sum_i \sum_j \sum_k \sum_l}_{\omega_i + \omega_j = \omega_k + \omega_l} S_{ijkl} \alpha_i \alpha_j \bar{\alpha}_k \bar{\alpha}_l, \quad (2.22)$$

in terms of which the renormalization flow equation (2.21) can be simplified to

$$\frac{\omega_j}{(2i\epsilon^2)} \frac{d\alpha_j}{d\tau} = \frac{1}{2} \frac{\partial V}{\partial \bar{\alpha}_j} + \sum_i R_{ij}^A |\alpha_i|^2 \alpha_j. \quad (2.23)$$

In the previous two formulas, $R_{ij}^S = (R_{ij} + R_{ji})/2$ and $R_{ij}^A = (R_{ij} - R_{ji})/2$. Note that in (2.23) we were allowed to drop the $i \neq j$ requirement from the sum over i because $R_{ii}^A = 0$.

¹For example a spherical cavity in 4-dimensional Minkowski spacetime with Dirichlet boundary conditions [17] and a holographic hard wall model in AdS_4 with Neumann boundary conditions [18, 19] are described by equations of motion of the same form as (2.5) and display a resonant spectrum of linearized modes. The extra terms in the renormalization flow equations vanishing in our case are present for those systems.

3 Conservation laws

We now proceed to prove the existence of three conserved quantities of the renormalization flow. First note that by equation (2.21) and its complex conjugate, we have

$$\omega_l \frac{d|\alpha_l|^2}{d\tau} = \omega_l \bar{\alpha}_l \frac{d\alpha_l}{d\tau} + \omega_l \alpha_l \frac{d\bar{\alpha}_l}{d\tau} = (2i\epsilon^2) \underbrace{\sum_i \sum_j \sum_k}_{\omega_i + \omega_j = \omega_k + \omega_l}^{\{i,j\} \neq \{k,l\}} S_{ijkl} (\alpha_i \alpha_j \bar{\alpha}_k \bar{\alpha}_l - \bar{\alpha}_i \bar{\alpha}_j \alpha_k \alpha_l), \quad (3.1)$$

and therefore

$$\frac{d}{d\tau} \left(\sum_l \omega_l |\alpha_l|^2 \right) = (2i\epsilon^2) \underbrace{\sum_i \sum_j \sum_k \sum_l}_{\omega_i + \omega_j = \omega_k + \omega_l}^{\{i,j\} \neq \{k,l\}} S_{ijkl} (\alpha_i \alpha_j \bar{\alpha}_k \bar{\alpha}_l - \bar{\alpha}_i \bar{\alpha}_j \alpha_k \alpha_l). \quad (3.2)$$

Since under interchange of $(i, j) \leftrightarrow (k, l)$ the coefficients S_{ijkl} are symmetric, while the tensor $(\alpha_i \alpha_j \bar{\alpha}_k \bar{\alpha}_l - \bar{\alpha}_i \bar{\alpha}_j \alpha_k \alpha_l)$ is antisymmetric, we find that

$$J = \sum_l \omega_l |\alpha_l|^2 \quad (3.3)$$

is a conserved quantity of the renormalization flow equations (2.21).

Similarly, from (3.1) we obtain

$$\begin{aligned} \frac{d}{d\tau} \left(\sum_l \omega_l^2 |\alpha_l|^2 \right) &= (2i\epsilon^2) \underbrace{\sum_i \sum_j \sum_k \sum_l}_{\omega_i + \omega_j = \omega_k + \omega_l}^{\{i,j\} \neq \{k,l\}} S_{ijkl} (\alpha_i \alpha_j \bar{\alpha}_k \bar{\alpha}_l - \bar{\alpha}_i \bar{\alpha}_j \alpha_k \alpha_l) \omega_l \\ &= \frac{1}{2} (2i\epsilon^2) \underbrace{\sum_i \sum_j \sum_k \sum_l}_{\omega_i + \omega_j = \omega_k + \omega_l}^{\{i,j\} \neq \{k,l\}} S_{ijkl} (\alpha_i \alpha_j \bar{\alpha}_k \bar{\alpha}_l - \bar{\alpha}_i \bar{\alpha}_j \alpha_k \alpha_l) (\omega_l + \omega_k). \end{aligned} \quad (3.4)$$

In the last step, we interchanged the summation indices k and l and used the fact that $S_{ijkl} = S_{ijlk}$. Now note that whenever the resonance condition $\omega_i + \omega_j = \omega_k + \omega_l$ is satisfied, the tensor $S_{ijkl}(\omega_l + \omega_k)$ is symmetric under interchange of $(i, j) \leftrightarrow (k, l)$. Since the tensor $(\alpha_i \alpha_j \bar{\alpha}_k \bar{\alpha}_l - \bar{\alpha}_i \bar{\alpha}_j \alpha_k \alpha_l)$ is antisymmetric, we find that

$$E = \sum_l \omega_l^2 |\alpha_l|^2 \quad (3.5)$$

is a conserved quantity of the renormalization flow equations (2.21).

Finally, using the renormalization flow equations (2.23), one can check that

$$\begin{aligned} \frac{dV}{d\tau} &= \sum_j \left(\frac{\partial V}{\partial \alpha_j} \frac{d\alpha_j}{d\tau} + \frac{\partial V}{\partial \bar{\alpha}_j} \frac{d\bar{\alpha}_j}{d\tau} \right) = - \sum_{i,j} R_{ij}^A |\alpha_i|^2 \left(\frac{2i\epsilon^2}{\omega_j} \right) \left(\bar{\alpha}_j \frac{\partial V}{\partial \bar{\alpha}_j} - \alpha_j \frac{\partial V}{\partial \alpha_j} \right) \\ &= -2 \sum_{i,j} R_{ij}^A |\alpha_i|^2 \left(\bar{\alpha}_j \frac{d\alpha_j}{d\tau} + \alpha_j \frac{d\bar{\alpha}_j}{d\tau} \right) = -2 \sum_{i,j} R_{ij}^A |\alpha_i|^2 \frac{d|\alpha_j|^2}{d\tau}. \end{aligned} \quad (3.6)$$

Using (2.19) this becomes

$$\begin{aligned} \frac{dV}{d\tau} &= - \sum_{i,j} (\omega_i^2 (A_{jj} + \omega_j^2 V_{jj}) - \omega_j^2 (A_{ii} + \omega_i^2 V_{ii})) |\alpha_i|^2 \frac{d|\alpha_j|^2}{d\tau} \\ &= -E \frac{d}{d\tau} \sum_j (A_{jj} + \omega_j^2 V_{jj}) |\alpha_j|^2 + \sum_i (A_{ii} + \omega_i^2 V_{ii}) |\alpha_i|^2 \frac{dE}{d\tau}. \end{aligned} \quad (3.7)$$

Since we already know that E is conserved, $dE/d\tau = 0$, we conclude that

$$W = V + E \sum_j (A_{jj} + \omega_j^2 V_{jj}) |\alpha_j|^2 \quad (3.8)$$

is a conserved quantity of the renormalization flow equations (2.21). For $d = 2$, this expression reduces to $W = V + E^2$.

We have thus found three integrals of motion (J , E and W) of the renormalization flow equations. E and W can be understood as the ‘free motion’ and ‘interaction’ energies of the oscillators comprising the scalar field. They are conserved separately under renormalization flow. J is akin to a classical version of the number operator in quantum field theory (note that our normalization of α_k differs from the canonical normalization of creation-annihilation operators in field theory). The conservation of J depends crucially on the absence of extra terms mentioned under (2.18) and (2.21) in the renormalization flow equations, and is specific to the AdS case we are considering.

4 Lagrangian form of the conservation laws

In order to relate the conserved quantities in section 3 to symmetries using a Noether procedure, one might be tempted to try and find a Lagrangian $L(\alpha, \bar{\alpha})$ that gives rise to the renormalization flow equations (2.23). However, since for $d \geq 3$ the R_{ij} coefficients are non-symmetric, the right hand side of (2.23) violates an integrability condition (the curl of the force is not zero) and therefore the equations of motion cannot be derived in a usual way from a Lagrangian. In this section, we will show that this problem can be overcome by working in a different gauge for δ .

4.1 Renormalization flow equations in boundary time gauge

The renormalization flow equations (2.17) and (2.18) were computed in [11] using the interior time gauge fixing condition $\delta(0, t) = 0$. In section 4.3, we shall repeat that calculation in the boundary time gauge $\delta(\pi/2, t) = 0$ and find the renormalization flow equations

$$\frac{\omega_j}{(2i\epsilon^2)} \frac{d\alpha_j}{d\tau} = \frac{1}{2} \frac{\partial W}{\partial \bar{\alpha}_j}, \quad (4.1)$$

where W is the quantity defined in equation (3.8). In contrast to the renormalization flow equations in interior time gauge (2.23), these equations are the Euler-Lagrange equations associated to a Lagrangian,

$$L = \sum_k i\omega_k \left(\bar{\alpha}_k \frac{d\alpha_k}{d\tau} - \alpha_k \frac{d\bar{\alpha}_k}{d\tau} \right) + 2\epsilon^2 W. \quad (4.2)$$

As was done in section 3.1 of [14] for a simpler system, we can identify three symmetries:

- A U(1) symmetry for which all α_n have the same charge: $\alpha_n \mapsto e^{i\theta} \alpha_n$. The conserved quantity associated to this symmetry is $J = \sum_n \omega_n |\alpha_n|^2$. The absence of the possible extra terms mentioned under (2.18) and (2.21) is crucial for this symmetry to occur.
- A U(1) symmetry for which α_n has charge ω_n : $\alpha_n \mapsto e^{i\omega_n \theta} \alpha_n$. The conserved quantity associated to this symmetry is $E = \sum_n \omega_n^2 |\alpha_n|^2$.
- A time translation symmetry $\tau \mapsto \tau - \tau_0$. The conserved quantity associated to this symmetry is W .

These conserved quantities are exactly the same as the ones that we determined in section 3 for the renormalization flow (2.23) in the interior time gauge.

4.2 Relation between the renormalization flows in different gauges

One may wonder why the renormalization flow equations are derivable from a Lagrangian in one gauge but not in another. Furthermore, one may ask why the flow equations in both gauges have exactly the same conserved quantities.

In order to gain insight in these questions, we compare the result (4.1) to the renormalization flow equations (2.23) that appear in the interior time gauge,

$$\frac{\omega_j}{(2i\epsilon^2)} \frac{d\beta_j}{d\tau} = \frac{1}{2} \frac{\partial V}{\partial \beta_j} + \sum_i R_{ij}^A |\beta_i|^2 \beta_j, \quad (4.3)$$

where we have replaced α by β to highlight the difference with equation (4.1). From the metric ansatz (2.3), we observe that the interior proper time t_I and the boundary proper time t_B are related by

$$\begin{aligned} dt_B &= e^{-\delta(\frac{\pi}{2}, t_I)} dt_I = \left(1 + \epsilon^2 \int_0^{\pi/2} dx ((\varphi')^2 + (\dot{\varphi})^2) \mu\nu + \mathcal{O}(\epsilon^4) \right) dt_I, \\ &= \left(1 + \epsilon^2 \sum_{ij} (A_{ij} c_i c_j + V_{ij} \dot{c}_i \dot{c}_j) + \mathcal{O}(\epsilon^4) \right) dt_I, \end{aligned} \quad (4.4)$$

where, again, the coefficients A_{ij} and V_{ij} are defined in appendix A. If one expresses c_j through the complex amplitudes β_j as $c_j = \beta_j e^{-i\omega_j t_I} + \bar{\beta}_j e^{i\omega_j t_I}$ and substitutes into the above equation, there are two types of terms: the ones rapidly oscillating (with periods of order 1) and the ones that depend on time only through slow modulations of β_j (on time scales of order $1/\epsilon^2$). The former terms will only produce minuscule contributions to t_B upon integration, whereas the latter can become appreciable at late times, despite being formally of order ϵ^2 . This structure is quite similar to how secular terms generally appear in perturbatively expanded solutions to the equations of motion. Retaining only the slowly varying terms, in a manner closely related to the averaging methods we shall describe in the next section, one obtains

$$t_B \approx t_I + 2\epsilon^2 \int^{t_I} dt \left(\sum_i (A_{ii} + \omega_i^2 V_{ii}) |\beta_i|^2 \right). \quad (4.5)$$

Comparing (2.20) in boundary and interior gauges then suggests $\alpha_j e^{-i\omega_j t_B} = \beta_j e^{-i\omega_j t_I}$, or

$$\alpha_j(\tau) = e^{2i\epsilon^2 \omega_j \theta(\tau)} \beta_j(\tau), \quad (4.6)$$

with the phase

$$\theta(\tau) = \int_{\tau_0}^{\tau} dt \left(\sum_i (A_{ii} + \omega_i^2 V_{ii}) |\beta_i|^2 \right). \quad (4.7)$$

Indeed, using the fact that this transformation satisfies $|\alpha_i|^2 = |\beta_i|^2$, $W(\alpha, \bar{\alpha}) = W(\beta, \bar{\beta})$ and

$$\frac{\omega_j}{(2i\epsilon^2)} \frac{d\alpha_j}{d\tau} = e^{2i\epsilon^2 \omega_j \theta} \left(\frac{\omega_j}{(2i\epsilon^2)} \frac{d\beta_j}{d\tau} + \omega_j^2 \beta_j \sum_i (A_{ii} + \omega_i^2 V_{ii}) |\beta_i|^2 \right), \quad (4.8)$$

one can show that the transformation (4.6) relates the renormalization flow equations (4.1) and (4.3) in the different gauges. This also illuminates the fact that both renormalization flow equations share the same conserved quantities.

One can check that substituting (4.6) in the effective Lagrangian (4.2) leads to a local Lagrangian $L(\beta, \bar{\beta})$ despite the transformation itself being non-local. We know, however, that the renormalization flow equations in interior time gauge do not straightforwardly arise from varying a Lagrangian, so one may wonder what happens if we simply vary $L(\beta, \bar{\beta})$. First of all, if one extremizes this Lagrangian under variations that satisfy $\delta\beta|_{\tau=\tau_i} = \delta\beta|_{\tau=\tau_f} = 0$ at the initial and final time, one indeed does not reproduce the renormalization flow equations. So what went wrong? In the boundary time gauge, we extremized the Lagrangian under variations that satisfied $\delta\alpha|_{\tau=\tau_i} = \delta\alpha|_{\tau=\tau_f} = 0$. The point is that, because of the non-local relation (4.6), $\delta\alpha|_{\tau=\tau_i} = \delta\alpha|_{\tau=\tau_f} = 0$ is not equivalent to $\delta\beta|_{\tau=\tau_i} = \delta\beta|_{\tau=\tau_f} = 0$, but rather to a much more complicated condition that involves the values of $\delta\beta$ for all times. To summarize, in the boundary time gauge, the renormalization flow equations can be straightforwardly obtained from extremizing a Lagrangian under variations that vanish at the initial and final time. If one translates this procedure to interior time gauge, one would have to extremize the Lagrangian under variations that satisfy very unusual, awkward boundary conditions.

4.3 Computation of the renormalization flow equations in the boundary time gauge

We elaborate here on the computation of the renormalization flow equations in the boundary time gauge $\delta(\pi/2) = 0$. Readers who are not interested in the particular details of this calculation may skip this section without loss of continuity. When repeating the calculation of [11] in this new gauge, one has to replace everywhere the solution

$$\delta_2 = - \int_0^x dy \left((\dot{\phi}_1)^2 + (\phi_1')^2 \right) \mu\nu, \quad (4.9)$$

by the expression

$$\delta_2 = \int_x^{\pi/2} dy \left((\dot{\phi}_1)^2 + (\phi_1')^2 \right) \mu\nu. \quad (4.10)$$

In particular, this replacement has to be done in the computation of the source term S_l (see appendix A of [11]) that appears in the equation at order $\mathcal{O}(\epsilon^3)$. The only two terms that will change are $\langle \delta_2 \ddot{\phi}_1, e_l \rangle$ and $\langle \delta_2 \dot{\phi}_1, e_l \rangle$. In the end, the source term in the boundary time gauge will be related to the source term in the interior time gauge by

$$S_l^{\delta(\pi/2)=0} = S_l^{\delta(0)=0} + 2 \sum_{i=0}^{\infty} \sum_{j=0}^{\infty} \omega_l^2 c_l(t) \{ \dot{c}_i(t) \dot{c}_j(t) V_{ij} + c_i(t) c_j(t) A_{ij} \} - \sum_{i=0}^{\infty} \sum_{j=0}^{\infty} \dot{c}_l(t) \frac{\partial}{\partial t} \{ \dot{c}_i(t) \dot{c}_j(t) V_{ij} + c_i(t) c_j(t) A_{ij} \}. \quad (4.11)$$

The rest of the computation is analogous to that in [11] and leads to the renormalization flow equations²

$$\frac{\omega_l}{(2i\epsilon^2)} \frac{d\alpha_l}{d\tau} = (T_l + \omega_l^2 (A_{ll} + \omega_l^2 V_{ll})) |\alpha_l|^2 \alpha_l + \sum_{i \neq l} (R_{il} + \omega_l^2 (A_{ii} + \omega_i^2 V_{ii})) |\alpha_i|^2 \alpha_i + \underbrace{\sum_i \sum_j \sum_k}_{\omega_i + \omega_j = \omega_k + \omega_l} S_{ijkl} \alpha_i \alpha_j \bar{\alpha}_k. \quad (4.12)$$

Using (3.8), these equations can be written as (4.1).

5 Averaging methods

In the previous section, the renormalization group equation governing the slow energy transfer between the modes due to resonant non-linear interactions were rewritten in a Lagrangian form. Thereupon, the three conservation laws restricting the energy flow became an obvious consequence of the symmetries of this effective Lagrangian. A very attractive picture for a similar set of conservation laws was obtained in [14] for a simpler closely related system, namely, a probe scalar field with ϕ^4 self-interactions.

In [14], an ansatz involving (linearized) fast oscillations of the scalar field with slowly drifting amplitudes and phases was substituted directly into the ϕ^4 Lagrangian in the AdS background, and an averaging was performed over the fast oscillation, leaving an effective Lagrangian for the slow drift. This Lagrangian had a structure very similar to our (4.2), with the same set of symmetries and the same conservation laws,³ though of course, the

²Effectively, we need to replace everywhere the coefficients $P_{ijl} \mapsto P_{ijl} - V_{ij}$ and $B_{ijl} \mapsto B_{ijl} - A_{ij}$.

³As we explained in sections 3 and 4, one of the three conservation laws we find, and the corresponding Lagrangian symmetry, depend crucially on the absence of +++ and +- - secular terms established for a free scalar field in a fully dynamical geometry in [11]. It is not obvious, but true, that a similar property holds for a probe self-interacting scalar field. This can in fact be demonstrated with considerably greater ease than for the gravitational case. In short, the coefficients of the ϕ^4 secular terms are proportional to $\int dx \mu e_i e_j e_k e_l \sec^2 x$, as can be deduced from (2.4) of [14]. This can be re-written as an integral of a product of the corresponding Jacobi polynomials $P_i P_j P_k P_l$ times another fixed polynomial of degree $d - 1$, with the standard Jacobi polynomial measure. If $\omega_l = \omega_i + \omega_j + \omega_k$, then $l = d + i + j + k$ and the degree of P_l is higher than the sum of the degrees of all the remaining polynomials. This structure vanishes by the Jacobi polynomial orthogonality. A similar argument, with l and i interchanged, holds for the case $\omega_l = \omega_i - \omega_j - \omega_k$.

exact coefficients in the potential term are different, since they depend on the exact form of the non-linearities.

It could be desirable to derive a similar elegant picture of the conservation laws for the fully dynamical gravitational instability, and we shall do that in the next section. It is worthwhile, however, to review the systematics of fast oscillation averaging and its relation to the perturbative resummation methods we have previously employed. Averaging at the level of the equation of motion is standard material in non-linear perturbation theory; a lucid and elementary detailed exposition can be found in [20], and will be briefly summarized here. In addition, given our interest in deriving the flow equations directly from a Lagrangian or Hamiltonian, we will develop a systematic Hamiltonian averaging method, which in the next section will be applied to our system of interest.

5.1 Averaging over fast oscillations and the periodic normal form

It is a natural idea that if the dynamics of a system involves rapid oscillations superimposed on slow drift behavior, there should be some sort of simplified effective description of the slow motion, in which the fast oscillations have been ‘integrated out’. The Born-Oppenheimer approximation in quantum mechanics is a familiar example of that.

The ideas of fast oscillation averaging in classical differential equations are well-developed and stand in close relation to methods of non-linear perturbation theory. It is not generally true that one can simply discard rapidly oscillating terms in a consistent fashion, and there are known counterexamples. However, there is a class of systems of what is known as the ‘periodic normal form’ for which discarding rapidly oscillating terms has been proved to be accurate in a well-defined sense:

$$\frac{d\vec{x}}{dt} = \varepsilon \vec{f}(\vec{x}, t), \tag{5.1}$$

where \vec{f} is periodic in t with period 2π . Here, \vec{x} evolves on a timescale of order $1/\varepsilon$, whereas \vec{f} oscillates on timescales of order 1, which is fast compared to the variation of \vec{x} . One can then introduce a time-averaged version of \vec{f} ,

$$\vec{f}_{\text{avr}} = \frac{1}{2\pi} \int_0^{2\pi} dt \vec{f}(\vec{x}, t), \tag{5.2}$$

and the corresponding averaged equation,

$$\frac{d\vec{x}_{\text{avr}}}{dt} = \varepsilon \vec{f}_{\text{avr}}(\vec{x}_{\text{avr}}). \tag{5.3}$$

Importantly, there is an explicit accuracy theorem for this procedure, bounding the deviations of \vec{x}_{avr} from \vec{x} uniformly on long time intervals. Namely, for any T , there exist constants c and ε_1 such that

$$|\vec{x}(t) - \vec{x}_{\text{avr}}(t)| < c\varepsilon \quad \text{for} \quad 0 < t < \frac{T}{\varepsilon}, \quad 0 < \varepsilon < \varepsilon_1. \tag{5.4}$$

(For a more accurate version, see theorem 6.2.2 of [20].)

It is straightforward to put the oscillatory systems of the sort we study,

$$\ddot{c}_j + \omega_j^2 c_j = S_j(c), \tag{5.5}$$

with a cubic⁴ source S_j in the periodic normal form. To this end, one first introduces the conjugate momenta $\pi_j = \dot{c}_j$ to obtain

$$\dot{c}_j = \pi_j, \quad \dot{\pi}_j = -\omega_j^2 c_j + S_j(c). \tag{5.6}$$

Note that this is just the Hamiltonian form of the equations, and we shall return to this fact in section 5.3 in the context of the Hamiltonian averaging. One then introduces complex variables $\alpha_j(t)$ such that⁵

$$c_j = \varepsilon (\alpha_j e^{-i\omega_j t} + \bar{\alpha}_j e^{i\omega_j t}), \quad \pi_j = -i\varepsilon\omega_j (\alpha_j e^{-i\omega_j t} - \bar{\alpha}_j e^{i\omega_j t}). \tag{5.7}$$

The equations for $\alpha_j(t)$ are in the periodic normal form (we are using the fact that the source S_j is a cubic polynomial in c):

$$\dot{\alpha}_j = \varepsilon^2 S_j(\alpha, \bar{\alpha}, t), \tag{5.8}$$

where the source has acquired an explicit periodic time dependence on t through the explicit time dependences in (5.7). Note that the fully resonant spectrum of AdS perturbations that generates the complexity of AdS stability phenomena here works in our favor, as it makes S_j in (5.8) exactly periodic with a period of at most 2π in the units of AdS time we are using, since all the frequencies are integer. One can then average (5.8), and the standard accuracy theorems will hold without any need for modifications. These averaged equations are in fact exactly the same as the ones describing the slow renormalization running of complex amplitudes in the context of secular term resummation, as we shall show in section 5.2.

Note that the time-scales of order $1/\varepsilon^2$, on which the uniform accuracy of averaging is guaranteed in (5.8), are exactly the same as the time-scales for black hole formation and turbulence suggested by numerical studies. Of course, in a collapse situation, large values of fields develop in small spatial regions, invalidating our neglect of higher-order terms in the polynomial expansion of the source S_j that preceded our application of the averaging method. Nevertheless, the standard accuracy theorems give considerable strength to the averaged equations at early stages of collapse and for non-collapsing solutions. They should provide a reliable tool for probing the characteristic AdS phenomena that have been

⁴In the context of AdS, the source is a complicated non-linear function, and one works with the cubic part of its polynomial expansion at lowest order in perturbation amplitudes. We shall not discuss accurately the systematics of neglecting the higher-order terms, and simply observe that they are suppressed by higher powers of the expansion parameter.

⁵For those familiar with multiscale methods, the expressions for c_j and π_j we write may look like resummed perturbative expansions including slow modulations of the complex amplitudes α_j , truncated to the lowest order. This picture is indeed valid, and we comment on the equivalence of averaging and multiscale methods in section 5.2. Note, however, that from the onset, the averaging procedure is not formulated in the context of asymptotic expansions, but rather as a qualitatively motivated simplification in the equations of motion, which is explicitly proved to be accurate in the small ε limit. (5.7) is just a change of variables, treated as exact in our context.

observed numerically. Note also that, in a collapse situation, there is a different form of weak field expansion that reliably describes horizon formation [21]. This latter possibility is outside our present investigation, though.

5.2 Equivalence of averaging and multiscale methods

The averaging procedure we have described is formulated rather differently from the perturbative resummation methods we were dealing with in [11] and in sections 3–4 of this paper. In the context of perturbative resummation methods, one was starting with a naïve expansion of the solutions in powers of the perturbation amplitude, discovering that these expansions contained growing (secular) terms that invalidated perturbation theory at late times, and then finding a way to reorganize perturbative expansions in a way that eliminates the secular terms. This modified expansion included slow time dependences of the integration constants of the linearized (zeroth order) solutions described by renormalization flow equations very similar to the ones resulting from the averaging procedure. We would now like to see more explicitly how this happens.

One can start with the non-linear oscillator equations written in the periodic normal form (5.8), construct the corresponding naïve perturbation theory, examine secular terms and see how they should be eliminated with a renormalization flow. This renormalization flow will coincide with an averaged version of (5.8). (This is slightly different from the construction we employed in [11], since there, we were working in the oscillating variables of (5.5). However, those variables and the complex amplitudes α are related by linear transformations (5.7), which act straightforwardly on perturbative expansions and transform secular terms to secular terms.)

The naïve perturbative expansion for (5.8) is extremely simple. The zeroth order is just $\alpha_j(t) = \alpha_{j,0} = \text{const}$. One then looks for perturbative solutions of the form

$$\alpha_j(t) = \alpha_{j,0} + \varepsilon^2 \alpha_j^{(1)} + \dots \tag{5.9}$$

$\alpha_j^{(1)}$ satisfies

$$\dot{\alpha}_j^{(1)} = S_j(\alpha_{j,0}, \bar{\alpha}_{j,0}, t), \tag{5.10}$$

which is trivially solved by

$$\alpha_j^{(1)}(t) = \int_0^t dt S_j(\alpha_{j,0}, \bar{\alpha}_{j,0}, t). \tag{5.11}$$

Since S is a periodic function of t with a period 2π , the latter expression can be written as

$$\alpha_j^{(1)}(t) = \frac{t}{2\pi} \int_0^{2\pi} dt S_j(\alpha_{j,0}, \bar{\alpha}_{j,0}, t) + \alpha_j^{(1, \text{non-secular})}(t), \tag{5.12}$$

where $\alpha_j^{(1, \text{non-secular})}(t)$ remains bounded at large times and does not compromise the validity of perturbation theory.

The renormalization method (like other related multi-scale methods) gives a prescription for eliminating the first (secular) term on the right-hand side of (5.12) that grows with time and invalidates naïve perturbation theory at times of order $1/\varepsilon^2$. (We only give a brief practical sketch here; further details and explanations can be found in [11].) Given a secular term proportional to t , one introduces an arbitrary time τ , writes $t = (t - \tau) + \tau$ and absorbs the contribution proportional to τ in ‘renormalized’ integration constants of the zeroth order solution. In our case, the integration constants $\alpha_{j,0}$ are related to their renormalized versions by

$$\alpha_{j,0} = \alpha_{j,R}(\tau) - \frac{\varepsilon^2 \tau}{2\pi} \int_0^{2\pi} dt S_j(\alpha_{j,R}(\tau), \bar{\alpha}_{j,R}(\tau), t). \quad (5.13)$$

If this is substituted into (5.9), the secular term in (5.12) is indeed exactly cancelled at the moment $t = \tau$. One then demands that the expansions with different ‘renormalization scale’ τ represent the same solution,

$$\frac{d}{d\tau} \left[\alpha_{j,R}(\tau) + \frac{\varepsilon^2(t - \tau)}{2\pi} \int_0^{2\pi} dt S_j(\alpha_{j,R}(\tau), \bar{\alpha}_{j,R}(\tau), t) \right] = 0. \quad (5.14)$$

To leading nontrivial order in ε , this results in

$$\frac{d\alpha_{j,R}}{d\tau} = \frac{\varepsilon^2}{2\pi} \int_0^{2\pi} dt S_j(\alpha_{j,R}(\tau), \bar{\alpha}_{j,R}(\tau), t), \quad (5.15)$$

exactly identical to the averaged form of (5.8). Finally, one sets $\tau = t$. By the standard lore of renormalization, perturbation theory expressed through $\alpha_{j,R}(\tau)$ at a gliding scale $\tau = t$ is free of (lowest order) secular terms at all times and valid on long time intervals. Since we have established equivalence of the lowest order renormalization resummation and lowest order averaging, the standard accuracy theorems for averaging also apply.

5.3 Lagrangian and Hamiltonian averaging

One of the primary motivations for our appeal to averaging methods has been the picture of conservation laws for a probe self-interacting scalar field developed in [14]. By performing averaging directly in the Lagrangian, the authors derive a Lagrangian form of the effective theory as a descendant of the Lagrangian form of the fundamental theory. The conservation laws are manifest in this procedure. By contrast, in multi-scale resummation approaches, the effective equations for slow energy transfer are derived by specific techniques having nothing to do with the Lagrangian formalism, and the Lagrangian nature of the resulting flow equations has to be guessed, together with the conservation laws.

Even though the qualitative picture developed in [14] is very attractive, the practical implementation of averaging can be considerably improved in terms of consistency and rigor. The authors consider a Lagrangian for oscillators with weak non-linear couplings (the same structure that we are dealing with, only the values of the couplings are different

for their system) and make the following substitution (more similar in spirit to the ‘Two-Time Framework’ than to rigorous implementations of averaging):

$$c_j = \alpha_j(\tau)e^{i\omega_j t} + \bar{\alpha}_j(\tau)e^{-i\omega_j t}. \tag{5.16}$$

They then average the Lagrangian over time to be left with a theory for τ -evolution. It is difficult to implement this procedure accurately however, since one sometimes pretends that τ -dependent (but t -independent) terms are constants, but while differentiating c_j , one uses $\tau = \varepsilon^2 t$, as in the ‘Two-Time Framework’ of [10] (remember that the expansion parameter is ε^2 for the AdS case). At the same time, terms containing two τ -derivatives are discarded on the basis of being ‘small’, whereas discarding highest derivative terms is, in general, a subtle operation. The results of [14] are essentially correct and must be derivable by more accurate methods. We shall now explain how to bring them in accord with the standard lore of fast oscillation averaging.

Since most rigorous results on averaging are formulated in the context of the first order periodic normal form equations (5.1), it is natural to work in the Hamiltonian, rather than Lagrangian formalism, since the Hamiltonian equations are naturally first order. Of course, if one obtains an effective Hamiltonian theory for the slow energy transfer at the end, it is straightforward to convert it to a Lagrangian theory. Furthermore, conservation laws can be deduced from symmetries of the Hamiltonian directly.

One can easily bring the equations for a system with a Hamiltonian $H_0 + \varepsilon H_1$ to the periodic normal form (5.1) while maintaining their Hamiltonian character. This can be accomplished in a number of ways, for example by the following method, which is the classical analog of the familiar quantum-mechanical ‘interaction picture’. Let q and p be the canonical coordinates and momenta of the original system. One can then define new (‘interaction picture’) canonical variables \tilde{q} and \tilde{p} by the following (time-dependent) canonical transformation: for given q and p at moment t , we define \tilde{q} and \tilde{p} to be the initial conditions at moment 0 that, under the evolution induced by H_0 , evolve to q and p at moment t . Such transformations induced by a Hamiltonian evolution are known to be canonical, with a generating function equal to the action S_0 of the classical solution of H_0 connecting \tilde{q} at $t = 0$ with q at t . The new Hamiltonian for \tilde{q}, \tilde{p} is

$$\tilde{H} = H_0 + \varepsilon H_1 + \frac{\partial S_0}{\partial t} = \varepsilon H_1, \tag{5.17}$$

where we have used the Hamilton-Jacobi equation for H_0 , and the equations of motion are explicitly of the periodic normal form:

$$\frac{d\tilde{p}}{dt} = -\varepsilon \frac{\partial H_1}{\partial \tilde{q}}, \quad \frac{d\tilde{q}}{dt} = \varepsilon \frac{\partial H_1}{\partial \tilde{p}}. \tag{5.18}$$

Since the canonical transformation we have employed depends on time, H_1 expressed in terms of the new variables also has an explicit dependence on time. Averaging over that dependence commutes with differentiation with respect to \tilde{q} and \tilde{p} , hence the result of applying the standard averaging procedure would still be in the Hamiltonian form,

$$\frac{d\tilde{p}}{dt} = -\varepsilon \frac{\partial \bar{H}}{\partial \tilde{q}}, \quad \frac{d\tilde{q}}{dt} = \varepsilon \frac{\partial \bar{H}}{\partial \tilde{p}}, \tag{5.19}$$

where \bar{H} is the time average of H_1 (after it has been expressed in the ‘interaction picture’, and only averaging over explicit time dependences is understood, as in all the rigorous implementations of averaging we have described). Thus, the standard averaging of the equations of motion in the ‘periodic normal form’ can be simply implemented by averaging (explicit time dependence of) the Hamiltonian expressed in the ‘interaction picture’.

In application to systems of non-linear oscillators of the form (5.5), we shall simply employ the transformation (5.7), closely related to the canonical transformation described above (5.17). The only difference is that in addition to cancelling the part of the evolution corresponding to the free part of the Hamiltonian, one changes to the complex amplitude representation. The resulting equations of motion are in the periodic normal form, being the Hamiltonian version of (5.8). Similarly to what we described above, one can apply the averaging procedure to these equations by simply applying it to the Hamiltonian. This is a straightforward reformulation of the standard averaging and the validity of the accuracy theorems is maintained.

6 AdS averaging

6.1 Effective action for the scalar field

Since our aim is to obtain an effective averaged Hamiltonian theory for the slow energy transfer between the scalar field modes, we must start by revealing the Lagrangian/Hamiltonian structures in the underlying fundamental theory. The field equations (2.1) and (2.2) can be reproduced by extremizing the action

$$\mathcal{S} = \int_{\mathcal{M}} d^{d+1}\mathbf{x}\sqrt{-g} \left(\frac{1}{16\pi G}(R - 2\Lambda) - \frac{1}{2}(\partial\phi)^2 \right) + \frac{1}{8\pi G} \int_{\partial\mathcal{M}} d^d\mathbf{x}\sqrt{-\gamma}K + \mathcal{S}_C, \quad (6.1)$$

where the boundary term consists of the Gibbons-Hawking term and a holographic counterterm

$$\mathcal{S}_C = -\frac{1}{8\pi G} \int_{\partial\mathcal{M}} d^d\mathbf{x}\sqrt{-\gamma} \left(\frac{d-1}{L} \right). \quad (6.2)$$

We can write the variation of this action as

$$\begin{aligned} \delta\mathcal{S} = & \int_{\mathcal{M}} d^{d+1}\mathbf{x}\sqrt{-g} \left(\frac{1}{16\pi G}E_{\mu\nu}\delta g^{\mu\nu} + \square\phi\delta\phi \right) \\ & + \int_{\partial\mathcal{M}} d^d\mathbf{x}\sqrt{-\gamma} \left(\frac{1}{16\pi G} \left(K_{ij} - K\gamma_{ij} + \left(\frac{d-1}{L} \right) \gamma_{ij} \right) \delta\gamma^{ij} - n^\mu\partial_\mu\phi\delta\phi \right), \end{aligned} \quad (6.3)$$

where $E_{\mu\nu}$ and $\square\phi$ are the left-hand sides of (2.1) and (2.2). Demanding that this should vanish under variations which at the boundary satisfy $\delta\gamma^{ij} = 0$ and $\delta\phi = 0$, indeed leads to (2.1) and (2.2).

Using the constraint equations (2.5b), one can integrate out the metric dependence in the action (6.1) and expand to lowest non-trivial order in powers of the scalar field. The constraint equations (2.5b) can be rewritten as

$$1 - A = e^\delta \nu \int_0^x dy (\Phi^2 + \Pi^2) e^{-\delta} \mu \quad (6.4)$$

and

$$\delta = \int_x^{\pi/2} dy (\Phi^2 + \Pi^2) \mu\nu, \tag{6.5}$$

and can be solved perturbatively in powers of the scalar field ϕ . Substituting the resulting expressions for the metric functions in the action, one obtains an effective action for the scalar field. For the boundary time gauge $\delta(\pi/2, t) = 0$, the computation described in appendix C results in the effective action

$$\tilde{S} = -\frac{L^{d-1}V_{d-1}}{2} \int dx \int dt \left(((\phi')^2 - (\dot{\phi})^2) \mu - ((\phi')^2 + (\dot{\phi})^2) \mu\nu \int_0^x dy ((\phi')^2 + (\dot{\phi})^2) \mu \right), \tag{6.6}$$

where V_{d-1} represents the volume of the sphere S^{d-1} . This gives an effective action for ϕ up to first non-trivial order in the interactions.

We briefly pause to discuss why we computed the effective action in boundary time gauge rather than interior time gauge. One can anticipate as follows that this is the correct choice. After solving for the metric functions using the constraints, it is clear that the variations in (6.3) are no longer independent, since, in any given gauge, the metric functions are specific functionals of the scalar field. If we consider variations of the scalar field that vanish at the boundary, then in boundary time gauge the metric variations vanish automatically at the boundary (e.g., the metric function δ vanishes at the boundary by the gauge condition, and so will its variation) and the variational principle straightforwardly reproduces the correct equations of motion. In interior time gauge, however, variations of the scalar field that vanish at the boundary will generically lead to variations of the metric function δ that do not vanish at the boundary (because the boundary value of δ also depends on the scalar field in the bulk), so a naive implementation of the variational principle would not reproduce the correct equations of motion. This difference between the two gauges is similar and related to the difference discussed at the end of section 4.2 for renormalization flows, where a useful Lagrangian description could only be found in the boundary time gauge. We will therefore limit our attention to the boundary time gauge.

Expanding in modes $\phi(x, t) = \epsilon \sum_k c_k(t) e_k(x)$ and defining the coefficients

$$W_{ijkl}^{(a,b)} = \int_0^{\pi/2} dx e_i^{(a)}(x) e_j^{(a)}(x) \mu(x) \nu(x) \int_0^x e_k^{(b)}(y) e_l^{(b)}(y) \mu(y), \tag{6.7}$$

where $e_i^{(a)}$ denotes the a th derivative of e_i , etc, we can write this effective action as $\tilde{S} = L^{d-1}V_{d-1}\epsilon^2 \int dt \mathcal{L}$, with Lagrangian

$$\begin{aligned} \mathcal{L} = & \frac{1}{2} \sum_k (\dot{c}_k^2 - \omega_k^2 c_k^2) \\ & + \frac{\epsilon^2}{2} \sum_{ijkl} \left(c_i c_j c_k c_l W_{ijkl}^{(1,1)} + \dot{c}_i \dot{c}_j c_k c_l W_{ijkl}^{(0,1)} + c_i c_j \dot{c}_k \dot{c}_l W_{ijkl}^{(1,0)} + \dot{c}_i \dot{c}_j \dot{c}_k \dot{c}_l W_{ijkl}^{(0,0)} \right) + \mathcal{O}(\epsilon^4). \end{aligned} \tag{6.8}$$

Because of the interchange symmetry of the arguments, we really need the symmetric part

$$W_{(ijkl)}^{(a,a)} = \frac{1}{6} \left(W_{ijkl}^{(a,a)} + W_{klij}^{(a,a)} + W_{ikjl}^{(a,a)} + W_{jlik}^{(a,a)} + W_{iljk}^{(a,a)} + W_{jkil}^{(a,a)} \right). \tag{6.9}$$

6.2 Averaged Hamiltonian system

For the effective Lagrangian (6.8), the canonical momenta are given by

$$\pi_k = \frac{\partial \mathcal{L}}{\partial \dot{c}_k} = \dot{c}_k + \epsilon^2 \sum_{ijl} \left(\dot{c}_l c_i c_j W_{kl ij}^{(0,1)} + c_i c_j \dot{c}_l W_{ij kl}^{(1,0)} + 2 \dot{c}_i \dot{c}_j \dot{c}_l W_{(ij kl)}^{(0,0)} \right) + \mathcal{O}(\epsilon^4), \quad (6.10)$$

such that the Hamiltonian $\mathcal{H} = \sum_k \pi_k \dot{c}_k - \mathcal{L}$ becomes

$$\begin{aligned} \mathcal{H} = & \frac{1}{2} \sum_k \left(\pi_k^2 + \omega_k^2 c_k^2 \right) \\ & - \frac{\epsilon^2}{2} \sum_{ijkl} \left(c_i c_j c_k c_l W_{(ij kl)}^{(1,1)} + \pi_i \pi_j c_k c_l W_{ij kl}^{(0,1)} + c_i c_j \pi_k \pi_l W_{ij kl}^{(1,0)} + \pi_i \pi_j \pi_k \pi_l W_{(ij kl)}^{(0,0)} \right) + \mathcal{O}(\epsilon^4). \end{aligned} \quad (6.11)$$

Next, one performs a (time dependent) canonical transformation of the sort we described above (5.17):

$$c_k = \tilde{c}_k \cos \omega_k t + \frac{\tilde{\pi}_k}{\omega_k} \sin \omega_k t, \quad \pi_k = \tilde{\pi}_k \cos \omega_k t - \omega_k \tilde{c}_k \sin \omega_k t. \quad (6.12)$$

The time dependences are chosen precisely in a way that puts the system in the ‘interaction picture’, i.e., cancels the free evolution given by the first line of (6.11). The new equations of motion are

$$\dot{\tilde{c}}_k = \frac{\partial \tilde{\mathcal{H}}}{\partial \tilde{\pi}_k}, \quad \dot{\tilde{\pi}}_k = -\frac{\partial \tilde{\mathcal{H}}}{\partial \tilde{c}_k}. \quad (6.13)$$

where $\tilde{\mathcal{H}}$ is the second line of (6.11), expressed through \tilde{c}_k and $\tilde{\pi}_k$.

Equations (6.13) are of the periodic normal form. As per our general discussion in section 5, the standard averaging procedure can be implemented by simply averaging the explicit time dependence in $\tilde{\mathcal{H}}$ (acquired due to the explicit time dependence of the canonical transformation we have employed):

$$\overline{\mathcal{H}}(\tilde{c}_k, \tilde{\pi}_k) = \frac{1}{2\pi} \int_0^{2\pi} dt \tilde{\mathcal{H}}(\tilde{c}_k, \tilde{\pi}_k, t). \quad (6.14)$$

It is convenient to re-express the averaged Hamiltonian through the complex amplitudes α_k that we have been using in the preceding sections of this paper:

$$\tilde{c}_k = \alpha_k + \bar{\alpha}_k, \quad \tilde{\pi}_k = -i\omega_k(\alpha_k - \bar{\alpha}_k). \quad (6.15)$$

Since this transformation is time-independent, it does not interfere with the averaging in (6.14):

$$\overline{\mathcal{H}}(\alpha_k, \bar{\alpha}_k) = \frac{1}{2\pi} \int_0^{2\pi} dt \tilde{\mathcal{H}}(\alpha_k, \bar{\alpha}_k, t). \quad (6.16)$$

The relation of the original c_k, π_k and the complex amplitudes α_k is given by the standard formulas,

$$c_k = e^{-i\omega_k t} \alpha_k + e^{i\omega_k t} \bar{\alpha}_k, \quad \pi_k = -i\omega_k \left(e^{-i\omega_k t} \alpha_k - e^{i\omega_k t} \bar{\alpha}_k \right). \quad (6.17)$$

The averaged form of (6.13) is simply

$$\dot{\tilde{c}}_k = \frac{\partial \overline{\mathcal{H}}}{\partial \tilde{\pi}_k}, \quad \dot{\tilde{\pi}}_k = -\frac{\partial \overline{\mathcal{H}}}{\partial \tilde{c}_k}, \quad (6.18)$$

or in terms of the complex amplitudes

$$\dot{\alpha}_k = \frac{1}{2i\omega_k} \frac{\partial \overline{\mathcal{H}}}{\partial \bar{\alpha}_k}. \quad (6.19)$$

After some algebra, described in detail in appendix D, one finds that computing (6.16) gives

$$\overline{\mathcal{H}} = -2\epsilon^2 W, \quad (6.20)$$

where W is the quantity defined in (3.8). Equation (6.19) then becomes

$$-i\omega_k \dot{\alpha}_k = \epsilon^2 \frac{\partial W}{\partial \bar{\alpha}_k}, \quad (6.21)$$

which is exactly the renormalization flow equations (4.1). The averaged Lagrangian $\overline{\mathcal{L}}$ corresponding to the averaged Hamiltonian $\overline{\mathcal{H}}$ is exactly the Lagrangian (4.2) that appeared in section 4. The conservation laws, which have been the main subject-matter of our treatment, are straightforward consequences of the symmetries of these averaged Lagrangian and Hamiltonian, as described under (4.2).

Acknowledgments

We would like to thank Pallab Basu, Alex Buchel, Chethan Krishnan, Gautam Mandal and Shiraz Minwalla for useful discussions. The work of B.C. and J.V. has been supported by the Belgian Federal Science Policy Office through the Interuniversity Attraction Pole P7/37, by FWO-Vlaanderen through project G020714N, and by the Vrije Universiteit Brussel through the Strategic Research Program “High-Energy Physics.” The research of O.E. has been supported by Ratchadaphisek Sompote Endowment Fund. J.V. is supported by a PhD Fellowship of the Research Foundation Flanders (FWO).

A Coefficients of the renormalization flow equations

Here, we shall summarize (simplified versions of) the expressions of [11] for the coefficients that appear in the renormalization flow equations in terms of integrals of the mode functions,⁶

$$\begin{aligned} T_l &= \frac{1}{2}\omega_l^2 X_{lll} + \frac{3}{2}Y_{lll} + 2\omega_l^4 W_{lll} + 2\omega_l^2 W_{lll}^* - \omega_l^2(A_{ll} + \omega_l^2 V_{ll}), \\ R_{il} &= \frac{1}{2} \left(\frac{\omega_i^2 + \omega_l^2}{\omega_l^2 - \omega_i^2} \right) (\omega_l^2 X_{illi} - \omega_i^2 X_{liil}) + 2 \left(\frac{\omega_l^2 Y_{ilil} - \omega_i^2 Y_{lili}}{\omega_l^2 - \omega_i^2} \right) + \left(\frac{\omega_i^2 \omega_l^2}{\omega_l^2 - \omega_i^2} \right) (X_{illi} - X_{lili}) \end{aligned} \quad (A.1)$$

⁶Compared to the corresponding results in [11], we used that $H_{ijkl} = \omega_k^2 X_{ijkl} - Y_{ijkl} + \omega_i^2 X_{klij} - Y_{klij}$ and $M_{ijk} = \omega_i^2 W_{ijk} + B_{ijk} - A_{ij} - X_{ijkk}$, which can be shown using integration by parts, along with the relations $W_{ijk} = W_{ijkk}$, $P_{ijk} = V_{ij} - W_{ijkk}$ and $B_{ijk} = A_{ij} - W_{ijkk}^*$, which follow directly from the definitions.

$$+ \frac{1}{2}(Y_{iill} + Y_{liii}) + \omega_i^2 \omega_l^2 (W_{llii} + W_{iill}) + \omega_i^2 W_{llii}^* + \omega_l^2 W_{iill}^* - \omega_l^2 (A_{ii} + \omega_i^2 V_{ii}), \quad (\text{A.2})$$

$$\begin{aligned} S_{ijkl} = & -\frac{1}{4} \left(\frac{1}{\omega_i + \omega_j} + \frac{1}{\omega_i - \omega_k} + \frac{1}{\omega_j - \omega_k} \right) (\omega_i \omega_j \omega_k X_{lijk} - \omega_l Y_{iljk}) \\ & -\frac{1}{4} \left(\frac{1}{\omega_i + \omega_j} + \frac{1}{\omega_i - \omega_k} - \frac{1}{\omega_j - \omega_k} \right) (\omega_j \omega_k \omega_l X_{ijkl} - \omega_i Y_{jikl}) \\ & -\frac{1}{4} \left(\frac{1}{\omega_i + \omega_j} - \frac{1}{\omega_i - \omega_k} + \frac{1}{\omega_j - \omega_k} \right) (\omega_i \omega_k \omega_l X_{jikl} - \omega_j Y_{ijkl}) \\ & -\frac{1}{4} \left(\frac{1}{\omega_i + \omega_j} - \frac{1}{\omega_i - \omega_k} - \frac{1}{\omega_j - \omega_k} \right) (\omega_i \omega_j \omega_l X_{kijl} - \omega_k Y_{ikjl}), \end{aligned} \quad (\text{A.3})$$

$$\begin{aligned} Q_{ijkl} = & \frac{1}{12} \left(\frac{1}{\omega_i + \omega_j} + \frac{1}{\omega_i + \omega_k} + \frac{1}{\omega_j + \omega_k} \right) (\omega_i \omega_j \omega_k X_{lijk} + \omega_l Y_{iljk}) \\ & + \frac{1}{12} \left(\frac{1}{\omega_i + \omega_j} + \frac{1}{\omega_i + \omega_k} - \frac{1}{\omega_j + \omega_k} \right) (\omega_j \omega_k \omega_l X_{ijkl} + \omega_i Y_{jikl}) \\ & + \frac{1}{12} \left(\frac{1}{\omega_i + \omega_j} - \frac{1}{\omega_i + \omega_k} + \frac{1}{\omega_j + \omega_k} \right) (\omega_i \omega_k \omega_l X_{jikl} + \omega_j Y_{ijkl}) \\ & + \frac{1}{12} \left(-\frac{1}{\omega_i + \omega_j} + \frac{1}{\omega_i + \omega_k} + \frac{1}{\omega_j + \omega_k} \right) (\omega_i \omega_j \omega_l X_{kijl} + \omega_k Y_{ikjl}), \end{aligned} \quad (\text{A.4})$$

where Q_{ijkl} is the would-be coefficient of the +++ secular terms, proved to vanish in [11]. The expressions for the S and Q coefficients given above are substantial simplifications of what has been published previously. The integrals that appear in these expressions are defined by

$$X_{ijkl} = \int_0^{\pi/2} dx e'_i(x) e_j(x) e_k(x) e_l(x) (\mu(x))^2 \nu(x), \quad (\text{A.5a})$$

$$Y_{ijkl} = \int_0^{\pi/2} dx e'_i(x) e_j(x) e'_k(x) e'_l(x) (\mu(x))^2 \nu(x), \quad (\text{A.5b})$$

$$W_{ijkl} = \int_0^{\pi/2} dx e_i(x) e_j(x) \mu(x) \nu(x) \int_0^x dy e_k(y) e_l(y) \mu(y), \quad (\text{A.5c})$$

$$W_{ijkl}^* = \int_0^{\pi/2} dx e'_i(x) e'_j(x) \mu(x) \nu(x) \int_0^x dy e_k(y) e_l(y) \mu(y), \quad (\text{A.5d})$$

$$V_{ij} = \int_0^{\pi/2} dx e_i(x) e_j(x) \mu(x) \nu(x), \quad (\text{A.5e})$$

$$A_{ij} = \int_0^{\pi/2} dx e'_i(x) e'_j(x) \mu(x) \nu(x). \quad (\text{A.5f})$$

B Symmetry of R_{ij} coefficients in AdS₃

Renormalization coefficients possess some special properties for $d = 2$. We shall now show that $R_{ij} = R_{ji}$ in AdS₃. First, we introduce

$$V_{ij} = \int_0^{\pi/2} dx e_i e_j \mu \nu \quad , \quad N_{ij} = \int_0^{\pi/2} dx e'_i e_j \mu \nu' \quad . \quad \text{and} \quad A_{ij} = \int_0^{\pi/2} dx e'_i e'_j \mu \nu. \quad (\text{B.1})$$

Using integration by parts and the fact that $(\mu e_i')' = -\omega_i^2 \mu e_i$ and $(\mu \nu')' = -4\mu \nu$, we find that

$$N_{ij} + A_{ij} = \omega_i^2 V_{ij} \tag{B.2}$$

and

$$N_{ij} + N_{ji} = C_i C_j + 4V_{ij} \quad \text{with} \quad C_i \equiv \frac{2\sqrt{d-2}}{\Gamma(d/2)} \sqrt{\frac{(i+d-1)!}{i!}}. \tag{B.3}$$

For this last result, we have also used that $\lim_{x \rightarrow 0} (e_i(x)e_j(x)\mu(x)\nu'(x)) = -C_i C_j$. Combining these two equations, we find that

$$R_{ij} - R_{ji} = \omega_i^2 (A_{jj} + \omega_j^2 V_{jj}) - \omega_j^2 (A_{ii} + \omega_i^2 V_{ii}) = 2\omega_i^2 (\omega_j^2 - 1) V_{jj} - 2\omega_j^2 (\omega_i^2 - 1) V_{ii} - \frac{\omega_i^2}{2} C_j^2 + \frac{\omega_j^2}{2} C_i^2. \tag{B.4}$$

We can use the identity

$$(2n + a + b + 2)(1 + x)P_n^{(a,b+1)}(x) = (2n + 2b + 2)P_n^{(a,b)}(x) + (2n + 2)P_{n+1}^{(a,b)}(x), \tag{B.5}$$

to rewrite the eigenfunctions for $d = 2$ as

$$e_n(x) = k_n (\cos x)^2 P_n^{(0,1)}(\cos(2x)) = \frac{1}{2} k_n \left(P_n^{(0,0)}(\cos(2x)) + P_{n+1}^{(0,0)}(\cos(2x)) \right). \tag{B.6}$$

We can relate this to associated Legendre polynomials $p_l^m(x)$ as

$$P_n^{(a,a)}(x) = (-1)^a \frac{2^a (a+n)!}{(2a+n)!} (1-x^2)^{-\frac{a}{2}} p_{a+n}^a(x), \tag{B.7}$$

such that

$$e_n(x) = \sqrt{n+1} (p_n(\cos(2x)) + p_{n+1}(\cos(2x))), \tag{B.8}$$

In this expression, the functions $p_n(x) = p_n^0(x)$ are the ordinary Legendre polynomials. These are defined by

$$p_n(x) = \frac{1}{2^n n!} \frac{d^n}{dx^n} [(x^2 - 1)^n], \tag{B.9}$$

and satisfy the following useful identity,

$$\int_0^{\pi/2} p_n(\cos(2x)) p_m(\cos(2x)) \sin x \cos x \, dx = \frac{1}{2(2n+1)} \delta_{nm}. \tag{B.10}$$

It follows from this expression that for $d = 2$, we have that $V_{ii} = \frac{1}{2} \left(\frac{\omega_i^2}{\omega_i^2 - 1} \right)$. Notice that also $C_i = 0$ for $d = 2$. This completes the proof that $R_{ij} = R_{ji}$ for $d = 2$.

C Effective action for the scalar field

An effective action for the scalar field can be obtained by integrating out the metric components from the action (6.1) using the constraint equations (2.5b). If we formally extract the amplitude of the scalar field as $\phi = \xi \varphi$, we get

$$\delta = \xi^2 \Delta_2 + \xi^4 \Delta_4 + \mathcal{O}(\xi^6) \quad \text{and} \quad A = 1 + \xi^2 \Lambda_2 + \xi^4 \Lambda_4 + \mathcal{O}(\xi^6), \tag{C.1}$$

with

$$\Delta_2 = \int_x^{\pi/2} dy ((\varphi')^2 + (\dot{\varphi})^2) \mu\nu \quad \text{and} \quad \Lambda_2 = -\nu \int_0^x dy ((\varphi')^2 + (\dot{\varphi})^2) \mu. \quad (\text{C.2})$$

Using the metric ansatz (2.3), we find that

$$L^2 R + d(d-1) = \frac{(\cos x)^2 e^\delta}{(\tan x)^{d-1}} \left(\frac{\partial C_x}{\partial x} - \frac{\partial C_t}{\partial t} - \mu'(x) e^{-\delta} (A-1) \delta' \right), \quad (\text{C.3})$$

with

$$C_x = e^{-\delta} \left(\mu(x) (2A\delta' - A') - \mu'(x) (A-1) - 2(\tan x)^d A \right) \quad \text{and} \quad C_t = \mu(x) \frac{e^\delta \dot{A}}{A^2}. \quad (\text{C.4})$$

For the measure, one has

$$\int d^{d+1} \mathbf{x} \sqrt{-g}(\dots) = L^{d+1} V_{d-1} \int dx \int dt e^{-\delta} \frac{(\tan x)^{d-1}}{(\cos x)^2}(\dots). \quad (\text{C.5})$$

The volume of the angular part \mathcal{S}^{d-1} is given by $V_{d-1} = \int_{\mathcal{S}^{d-1}} d\Omega_{d-1} = \frac{2\pi^{d/2}}{\Gamma(d/2)}$. If we expand the metric part of the action (6.1) in powers of ξ , we find that

$$\begin{aligned} \mathcal{S}_g &= \frac{1}{16\pi G} \int d^{d+1} \mathbf{x} \sqrt{-g} \left(R + \frac{d(d-1)}{L^2} \right) \\ &= \frac{L^{d-1} V_{d-1}}{2(d-1)} \int dx \int dt \left(\frac{\partial C_x}{\partial x} - \frac{\partial C_t}{\partial t} - \mu'(x) (\Lambda_2 \Delta'_2) \xi^4 + \mathcal{O}(\xi^6) \right). \end{aligned} \quad (\text{C.6})$$

The Gibbons-Hawking boundary term can be written as

$$\mathcal{S}_{GH} = \frac{1}{8\pi G} \int_{\partial\mathcal{M}} d^d \mathbf{x} \sqrt{-\gamma} K = -\frac{L^{d-1} V_{d-1}}{2(d-1)} \int dt \left(C_x - \mu'(x) (1+A) e^{-\delta} \right) \Big|_{x=\frac{\pi}{2}}. \quad (\text{C.7})$$

The total derivative of C_x in the bulk action will cancel with the C_x in the boundary action. The second (divergent) term in the boundary action is removed by the counterterm

$$\mathcal{S}_C = -\frac{1}{8\pi G} \int_{\partial\mathcal{M}} d^d \mathbf{x} \sqrt{-\gamma} \left(\frac{d-1}{L} \right) = -\frac{L^{d-1} V_{d-1}}{(d-1)} \int dt \left((d-1) \frac{(\tan x)^{d-1}}{\cos x} e^{-\delta} \sqrt{A} \right) \Big|_{x=\frac{\pi}{2}}. \quad (\text{C.8})$$

One needs to use the fact that $A \rightarrow 1$ when $x \rightarrow \pi/2$. In the end, we have

$$\begin{aligned} \mathcal{S}_{g+GH+C} &= -\frac{L^{d-1} V_{d-1}}{2} \int dx \int dt \left(\frac{\Lambda_2 \Delta'_2}{\nu} \right) \xi^4 + \mathcal{O}(\xi^6) \\ &= -\frac{L^{d-1} V_{d-1}}{2} \int dx \int dt \left(((\varphi')^2 + (\dot{\varphi})^2) \mu\nu \int_0^x dy ((\varphi')^2 + (\dot{\varphi})^2) \mu \right) \xi^4 + \mathcal{O}(\xi^6). \end{aligned} \quad (\text{C.9})$$

On the other hand,

$$L^2 (\partial\phi)^2 = (\cos x)^2 A (\phi')^2 - \frac{(\cos x)^2}{A} e^{2\delta} (\dot{\phi})^2 = (\cos x)^2 A (\Phi^2 - \Pi^2), \quad (\text{C.10})$$

and thus

$$\begin{aligned}
 S_\phi &= \int d^{d+1}\mathbf{x}\sqrt{-g} \left(-\frac{1}{2}(\partial\phi)^2 \right) = -\frac{L^{d-1}V_{d-1}}{2} \int dx \int dt A e^{-\delta} (\Phi^2 - \Pi^2) \mu \\
 &= -\frac{L^{d-1}V_{d-1}}{2} \int dx \int dt \left(((\phi')^2 - (\dot{\phi})^2) \mu \xi^2 + (\Lambda_2 - \Delta_2) ((\phi')^2 + (\dot{\phi})^2) \mu \xi^4 \right) + \mathcal{O}(\xi^6) \\
 &= -\frac{L^{d-1}V_{d-1}}{2} \int dx \int dt \left(((\phi')^2 - (\dot{\phi})^2) \mu \right) \xi^2 \\
 &\quad - \frac{L^{d-1}V_{d-1}}{2} \int dx \int dt \left(\Lambda_2 ((\phi')^2 + (\dot{\phi})^2) \mu + \Delta'_2 \int_0^x dy ((\phi')^2 + (\dot{\phi})^2) \mu \right) \xi^4 + \mathcal{O}(\xi^6) \\
 &= -\frac{L^{d-1}V_{d-1}}{2} \int dx \int dt \left(((\phi')^2 - (\dot{\phi})^2) \mu \right) \xi^2 \\
 &\quad - \frac{L^{d-1}V_{d-1}}{2} \int dx \int dt \left(-2 ((\phi')^2 + (\dot{\phi})^2) \mu \nu \int_0^x dy ((\phi')^2 + (\dot{\phi})^2) \mu \right) \xi^4 + \mathcal{O}(\xi^6) \quad (\text{C.11})
 \end{aligned}$$

All in all, up to fourth order in the scalar field, we find the action

$$\tilde{S} = -\frac{L^{d-1}V_{d-1}}{2} \int dx \int dt \left(((\phi')^2 - (\dot{\phi})^2) \mu - ((\phi')^2 + (\dot{\phi})^2) \mu \nu \int_0^x dy ((\phi')^2 + (\dot{\phi})^2) \mu \right). \quad (\text{C.12})$$

D Relating the coefficients in the renormalization and averaging procedures

Here, we present the details of the calculations that led to the result (6.20) for the averaged Hamiltonian $\bar{\mathcal{H}}$. Following the procedure outlined in section 6.2, we find after some straightforward algebra that

$$\bar{\mathcal{H}} = -\frac{\epsilon^2}{2} \sum_{ijkl} \Omega_{ijkl} \alpha_i \alpha_j \bar{\alpha}_k \bar{\alpha}_l - \frac{\epsilon^2}{2} \sum_{ijkl} \Gamma_{ijkl} (\bar{\alpha}_i \bar{\alpha}_j \bar{\alpha}_k \alpha_l + \alpha_i \alpha_j \alpha_k \bar{\alpha}_l), \quad (\text{D.1})$$

where the coefficients Ω_{ijkl} and Γ_{ijkl} are given explicitly in terms of the $W_{ijkl}^{(a,b)}$ coefficients (6.7) as

$$\begin{aligned}
 \Omega_{ijkl} &= 6W_{(ijkl)}^{(1,1)} - \omega_i \omega_j W_{ijkl}^{(0,1)} - \omega_k \omega_l W_{kl ij}^{(0,1)} + \omega_i \omega_k W_{ik j l}^{(0,1)} + \omega_i \omega_l W_{il k j}^{(0,1)} \\
 &\quad + \omega_j \omega_k W_{kj il}^{(0,1)} + \omega_j \omega_l W_{lj ki}^{(0,1)} - \omega_i \omega_j W_{kl ij}^{(1,0)} - \omega_k \omega_l W_{ij kl}^{(1,0)} + \omega_i \omega_k W_{jl ik}^{(1,0)} + \omega_i \omega_l W_{kj il}^{(1,0)} \\
 &\quad + \omega_j \omega_k W_{ilk j}^{(1,0)} + \omega_j \omega_l W_{kil j}^{(1,0)} + 6\omega_i \omega_j \omega_k \omega_l W_{(ijkl)}^{(0,0)} \quad (\text{D.2})
 \end{aligned}$$

and

$$\begin{aligned}
 3\Gamma_{ijkl} &= 12W_{(ijkl)}^{(1,1)} - 2\omega_i \omega_j W_{ijkl}^{(0,1)} - 2\omega_i \omega_k W_{ik j l}^{(0,1)} - 2\omega_j \omega_k W_{j k il}^{(0,1)} + 2\omega_k \omega_l W_{kl ij}^{(0,1)} \\
 &\quad + 2\omega_j \omega_l W_{jl ik}^{(0,1)} + 2\omega_i \omega_l W_{il j k}^{(0,1)} - 2\omega_i \omega_j W_{kl ij}^{(1,0)} - 2\omega_i \omega_k W_{jl ik}^{(1,0)} - 2\omega_k \omega_j W_{il j k}^{(1,0)} \\
 &\quad + 2\omega_k \omega_l W_{ij kl}^{(1,0)} + 2\omega_j \omega_l W_{ik j l}^{(1,0)} + 2\omega_i \omega_l W_{j k il}^{(1,0)} - 12\omega_i \omega_j \omega_k \omega_l W_{(ijkl)}^{(0,0)}. \quad (\text{D.3})
 \end{aligned}$$

The Ω_{ijkl} coefficients satisfy the symmetry relations $\Omega_{ijkl} = \Omega_{jikl}$, $\Omega_{ijkl} = \Omega_{ijlk}$ and $\Omega_{ijkl} = \Omega_{klij}$ and the Γ_{ijkl} coefficients are totally symmetric in the first three indices. Using integration by parts, one can establish the relations

$$W_{ijkl}^{(0,1)} - \omega_k^2 W_{ijkl}^{(0,0)} = X_{kijl}, \quad W_{ijkl}^{(1,1)} - \omega_k^2 W_{ijkl}^{(1,0)} = Y_{iljk}, \quad (\text{D.4a})$$

$$(\omega_k^2 - \omega_l^2) W_{ijkl}^{(0,0)} = X_{lijk} - X_{kijl}, \quad (\omega_k^2 - \omega_l^2) W_{ijkl}^{(1,0)} = Y_{ikjl} - Y_{iljk}, \quad (\text{D.4b})$$

$$(\omega_k^2 - \omega_l^2) W_{ijkl}^{(0,1)} = \omega_k^2 X_{lijk} - \omega_l^2 X_{kijl}, \quad (\omega_k^2 - \omega_l^2) W_{ijkl}^{(1,1)} = \omega_k^2 Y_{ikjl} - \omega_l^2 Y_{iljk}. \quad (\text{D.4c})$$

The coefficients X_{ijkl} and Y_{ijkl} that appear here are defined in appendix A. These identities can be used to show that

$$\Omega_{lll} = 4T_l + 4\omega_l^2 (A_{ll} + \omega_l^2 V_{ll}), \quad (\text{D.5a})$$

$$\Omega_{iil} = 2R_{il} + 2\omega_l^2 (A_{ii} + \omega_i^2 V_{ii}) \quad \text{if } i \neq l, \quad (\text{D.5b})$$

$$\Omega_{ijkl} = 4S_{ijkl} \quad \text{if } \{i, j\} \neq \{k, l\} \quad \text{and} \quad \omega_i + \omega_j = \omega_k + \omega_l, \quad (\text{D.5c})$$

$$\Gamma_{ijkl} = 8Q_{ijkl} = 0 \quad \text{if } \omega_i + \omega_j + \omega_k = \omega_l. \quad (\text{D.5d})$$

In the end, after comparing with the expression (3.8) for W , we deduce (6.20).

Open Access. This article is distributed under the terms of the Creative Commons Attribution License ([CC-BY 4.0](https://creativecommons.org/licenses/by/4.0/)), which permits any use, distribution and reproduction in any medium, provided the original author(s) and source are credited.

References

- [1] P. Bizon and A. Rostworowski, *On weakly turbulent instability of anti-de Sitter space*, *Phys. Rev. Lett.* **107** (2011) 031102 [[arXiv:1104.3702](https://arxiv.org/abs/1104.3702)] [[INSPIRE](#)].
- [2] O.J.C. Dias, G.T. Horowitz and J.E. Santos, *Gravitational turbulent instability of anti-de Sitter space*, *Class. Quant. Grav.* **29** (2012) 194002 [[arXiv:1109.1825](https://arxiv.org/abs/1109.1825)] [[INSPIRE](#)].
- [3] O.J.C. Dias, G.T. Horowitz, D. Marolf and J.E. Santos, *On the nonlinear stability of asymptotically anti-de Sitter solutions*, *Class. Quant. Grav.* **29** (2012) 235019 [[arXiv:1208.5772](https://arxiv.org/abs/1208.5772)] [[INSPIRE](#)].
- [4] H.P. de Oliveira, L.A. Pando Zayas and E.L. Rodrigues, *A Kolmogorov-Zakharov spectrum in AdS gravitational collapse*, *Phys. Rev. Lett.* **111** (2013) 051101 [[arXiv:1209.2369](https://arxiv.org/abs/1209.2369)] [[INSPIRE](#)].
- [5] M. Maliborski and A. Rostworowski, *Time-periodic solutions in an Einstein AdS-massless-scalar-field system*, *Phys. Rev. Lett.* **111** (2013) 051102 [[arXiv:1303.3186](https://arxiv.org/abs/1303.3186)] [[INSPIRE](#)].
- [6] A. Buchel, S.L. Liebling and L. Lehner, *Boson stars in AdS spacetime*, *Phys. Rev. D* **87** (2013) 123006 [[arXiv:1304.4166](https://arxiv.org/abs/1304.4166)] [[INSPIRE](#)].
- [7] P. Bizoń and J. Jahnmużna, *Globally regular instability of AdS₃*, *Phys. Rev. Lett.* **111** (2013) 041102 [[arXiv:1306.0317](https://arxiv.org/abs/1306.0317)] [[INSPIRE](#)].
- [8] J. Abajo-Arrostia, E. da Silva, E. Lopez, J. Mas and A. Serantes, *Holographic relaxation of finite size isolated quantum systems*, *JHEP* **05** (2014) 126 [[arXiv:1403.2632](https://arxiv.org/abs/1403.2632)] [[INSPIRE](#)].

- [9] M. Maliborski and A. Rostworowski, *What drives AdS spacetime unstable?*, *Phys. Rev. D* **89** (2014) 124006 [[arXiv:1403.5434](#)] [[INSPIRE](#)].
- [10] V. Balasubramanian, A. Buchel, S.R. Green, L. Lehner and S.L. Liebling, *Holographic thermalization, stability of anti-de Sitter space and the Fermi-Pasta-Ulam paradox*, *Phys. Rev. Lett.* **113** (2014) 071601 [[arXiv:1403.6471](#)] [[INSPIRE](#)].
- [11] B. Craps, O. Evnin and J. Vanhoof, *Renormalization group, secular term resummation and AdS (in)stability*, *JHEP* **10** (2014) 048 [[arXiv:1407.6273](#)] [[INSPIRE](#)].
- [12] F.V. Dimitrakopoulos, B. Freivogel, M. Lippert and I.-S. Yang, *Instability corners in AdS space*, [arXiv:1410.1880](#) [[INSPIRE](#)].
- [13] A. Buchel, S.R. Green, L. Lehner and S.L. Liebling, *Universality of non-equilibrium dynamics of CFTs from holography*, [arXiv:1410.5381](#) [[INSPIRE](#)].
- [14] P. Basu, C. Krishnan and A. Saurabh, *A stochasticity threshold in holography and the instability of AdS*, [arXiv:1408.0624](#) [[INSPIRE](#)].
- [15] J. Colliander, M. Keel, G. Staffilani, H. Takaoka and T. Tao, *Transfer of energy to high frequencies in the cubic defocusing nonlinear Schrödinger equation*, *Invent. Math.* **181** (2010) 39 [[arXiv:0808.1742](#)].
- [16] M. Maliborski and A. Rostworowski, *Lecture notes on turbulent instability of anti-de Sitter spacetime*, *Int. J. Mod. Phys. A* **28** (2013) 1340020 [[arXiv:1308.1235](#)] [[INSPIRE](#)].
- [17] M. Maliborski, *Instability of flat space enclosed in a cavity*, *Phys. Rev. Lett.* **109** (2012) 221101 [[arXiv:1208.2934](#)] [[INSPIRE](#)].
- [18] B. Craps et al., *Gravitational collapse and thermalization in the hard wall model*, *JHEP* **02** (2014) 120 [[arXiv:1311.7560](#)] [[INSPIRE](#)].
- [19] B. Craps, E.J. Lindgren, A. Taliotis, J. Vanhoof and H.-B. Zhang, *Holographic gravitational infall in the hard wall model*, *Phys. Rev. D* **90** (2014) 086004 [[arXiv:1406.1454](#)] [[INSPIRE](#)].
- [20] J.A. Murdock, *Perturbations: theory and methods*, SIAM, U.S.A. (1987).
- [21] S. Bhattacharyya and S. Minwalla, *Weak field black hole formation in asymptotically AdS spacetimes*, *JHEP* **09** (2009) 034 [[arXiv:0904.0464](#)] [[INSPIRE](#)].

Renormalization group, secular term resummation and AdS (in)stability

Ben Craps,^{a,b} Oleg Evnin^c and Joris Vanhoof^a

^a*Theoretische Natuurkunde, Vrije Universiteit Brussel and The International Solvay Institutes, Pleinlaan 2, B-1050 Brussels, Belgium*

^b*Laboratoire de Physique Théorique, Ecole Normale Supérieure, 24 rue Lhomond, F-75231 Paris Cedex 05, France*

^c*Department of Physics, Faculty of Science, Chulalongkorn University, Thanon Phayathai, Pathumwan, Bangkok 10330, Thailand*

E-mail: Ben.Craps@vub.ac.be, oleg.evnin@gmail.com, Joris.Vanhoof@vub.ac.be

ABSTRACT: We revisit the issues of non-linear AdS stability, its relation to growing (secular) terms in naïve perturbation theory around the AdS background, and the need and possible strategies for resumming such terms. To this end, we review a powerful and elegant resummation method, which is mathematically identical to the standard renormalization group treatment of ultraviolet divergences in perturbative quantum field theory. We apply this method to non-linear gravitational perturbation theory in the AdS background at first non-trivial order and display the detailed structure of the emerging renormalization flow equations. We prove, in particular, that a majority of secular terms (and the corresponding terms in the renormalization flow equations) that could be present on general grounds given the spectrum of frequencies of linear AdS perturbations, do not in fact arise.

KEYWORDS: Classical Theories of Gravity, AdS-CFT Correspondence, Holography and quark-gluon plasmas

ARXIV EPRINT: [1407.6273](https://arxiv.org/abs/1407.6273)

Contents

1	Introduction	1
2	Renormalization group resummation	3
2.1	Ubiquity of secular terms	3
2.2	Frequency adjustment and multi-scale resummation	5
2.3	Renormalization group method	9
3	AdS (in)stability	13
3.1	Setup of the system	13
3.2	Weakly non-linear perturbation theory	14
3.3	Vanishing secular terms	16
3.4	Non-vanishing secular terms and renormalization flow	20
3.5	Renormalization flow and quasi-periodic solutions	21
A	Calculation of S_l	23
B	FORM-based analysis of secular term coefficients	26

1 Introduction

Time-dependent perturbation theory is often plagued by secular terms. While suppressed by the expansion parameter, secular terms grow with time. They invalidate the naïve perturbation theory at time scales that are typically proportional to some inverse power of the expansion parameter. In order to extend the validity of perturbation theory to larger times, secular terms need to be resummed.

To set the stage, consider the anharmonic oscillator [1, 2]

$$\ddot{x} + x + \epsilon x^3 = 0 \tag{1.1}$$

with small positive ϵ , and construct a perturbative solution $x(t) = x_0(t) + \epsilon x_1(t) + \dots$. For initial conditions $x(0) = 1$, $\dot{x}(0) = 0$, the zeroth order solution is $x_0(t) = \cos t$. At first order, we find

$$\ddot{x}_1 + x_1 = -\frac{1}{4} \cos 3t - \frac{3}{4} \cos t. \tag{1.2}$$

The last term is a resonant source term, giving rise to a secular term proportional to $t \sin t$:

$$x(t) = \cos(t) + \epsilon \left[\frac{1}{32} (\cos 3t - \cos t) - \frac{3}{8} t \sin t \right] + \dots \tag{1.3}$$

According to the Poincaré-Lindstedt method, the secular term can be absorbed in a small frequency shift, leading to a generalized asymptotic expansion that provides more accurate approximations for longer time intervals,

$$x(t) = \cos \left[\left(1 + \frac{3\epsilon}{8} + \dots \right) t \right] + \frac{\epsilon}{32} \cos \left[3 \left(1 + \frac{3\epsilon}{8} + \dots \right) t \right] + \dots \quad (1.4)$$

For a single oscillator described by a Hamiltonian, this is all that is needed. When dealing with dissipative systems, or with multiple oscillators exhibiting resonances, one needs more elaborate resummation techniques, known as multiple scale methods. A particularly elegant such method was proposed by Chen, Goldenfeld and Oono [3], and is based on the renormalization group (RG). We will review it in section 2 and rely on it in the remainder of this paper.

Our focus will be on Hamiltonian systems. Historically, the study of perturbation theory was driven by celestial mechanics, in particular the question whether the solar system is stable on very long time scales (given that interactions between planets perturb the Keplerian orbits). These studies culminated in the Kolmogorov-Arnol'd-Moser (KAM) theory [4], which showed with mathematical rigor that both stable and unstable orbits exist, depending on whether unperturbed frequencies are resonant. The stable orbits occur for non-resonant frequencies, and correspond to small perturbations of the unperturbed orbits.

In recent years, secular terms have appeared quite prominently in studies of non-linear stability of anti-de Sitter (AdS) space and closely related spacetimes. In [7], Bizoń and Rostworowski provided numerical evidence that arbitrarily weak spherically symmetric perturbations can cause global AdS to collapse into a black hole (possibly after multiple scatterings from the AdS boundary). In addition, they showed that in weakly nonlinear perturbation theory secular terms appear that cannot be removed by frequency shifts, and suggested that these secular terms signal a turbulent flow of energy to higher and higher frequencies. These additional secular terms (beyond those that can be removed via the Poincaré-Lindstedt method) arise from resonances in the spectrum of a scalar field in global AdS, as we will review in section 3. Many papers have further investigated this and related systems, mostly using numerical general relativity supplemented with weakly nonlinear perturbation theory (see, for instance, [8–14]). After quite a few surprises, a rich phenomenology has been uncovered, with the space of initial conditions exhibiting islands of stability within a sea of instability.

These results raise several conceptual questions: can the additional terms be removed by multiple scale/RG techniques? What is the precise relation between AdS instability and secular terms? Does the weakly nonlinear perturbation theory exhibit additional structure that can be uncovered by analytical means?

Some of these questions were also addressed in the recent paper [14], in which a multiple scale method (referred to as “Two Time Framework” and valid to first non-trivial order in the perturbation) was applied to the system of [7] truncated to a finite set of modes. The resulting equations were studied numerically, and the output was compared with results from numerical general relativity. One point that was emphasized in [14] is that secular terms that cannot be absorbed in frequency shifts do not necessarily imply AdS instability.

Due to the finite time range of numerical simulations and/or the required resolution, it is not always straightforward, however, to reach firm conclusions on the long-time behavior of given initial conditions; for instance, the fate of certain “two-mode” initial data discussed in [7] and [14] is still being debated.¹ This illustrates the fact that a more systematic understanding would be very welcome.

The purpose of the present work is to resum systematically the secular terms of [7] using the RG method of [3].² Our RG setup agrees to lowest non-trivial order with the Two Time Framework of [14], but the focus is different. Our work will be analytic rather than numerical, leading to explicit results at first order that are valid for all modes. In particular, we will show analytically that a majority of secular terms that could be present on the basis of frequency relations among the linearized AdS perturbations are in fact absent, and will provide explicit analytic expressions for all nonvanishing secular terms. Note that deriving all-mode expressions for the secular term coefficients is not a matter of pure pedantry. In a system prone to turbulence, one expects that high frequency modes typically get involved in the evolution. Having all-mode expressions for the secular term coefficients (and the corresponding energy drift), and in particular their ultraviolet asymptotics, is likely to be crucial for any analytic considerations of the turbulent behavior.

It is interesting that weakly nonlinear perturbation theory in global AdS exhibits a fully resonant spectrum (which drives instability), but at the same time a majority of secular terms allowed for such a spectrum are in fact absent (which weakens the instability). This interplay of conflicting factors may underlie the apparent complexity of the AdS stability domain that has been observed numerically [7–14]. We provide some comments on relations between the absence of some classes of secular terms and the abundance of quasi-periodic solutions in section 3.5.

The general structure of the paper is as follows: section 2 contains a systematic discussion of the RG method introduced in [3]. In section 3 this method is applied to weakly nonlinear perturbation theory in AdS. Two appendices contain technical details on our computations.

2 Renormalization group resummation

2.1 Ubiquity of secular terms

When dealing with a system subject to a small perturbation, it is natural to describe its evolution by an asymptotic series in the perturbation magnitude, an approach familiar under the name of perturbation theory. This strategy is equally applicable when one perturbs the initial conditions rather than the definition of the system proper. Solutions are then presented as an asymptotic series in the magnitude of the deviation from the specific chosen initial conditions, for which an exact solution is known.

The nature and accuracy of such an asymptotic series approximation is necessarily subtle, except for the rare cases when the asymptotic series happens to converge. Nonetheless, the usual practical wisdom tells us that, as long as the subsequent terms in the series

¹We thank P. Bizoń, A. Buchel and L. Lehner for correspondence on this issue.

²In the context of the AdS/CFT correspondence, the RG method of [3] has recently also appeared in [5, 6].

are smaller than the preceding ones, the expansion is usable and sound. In fact, some of the most precise predictions in physics have been made using such truncated asymptotic expansions (a very slippery step from a purely mathematical perspective).

If one fixes the time interval whereupon the evolution is considered, and diminishes the magnitude of the perturbation, the higher-order terms in the asymptotic expansion diminish relatively to the lower-order terms (being weighted by higher powers of the perturbation magnitude). One is then in a regime when the asymptotic series is expected to approximate the exact evolution on the said fixed time interval more and more accurately.

Unfortunately, evolution due to a small perturbation on a fixed time interval is usually not what a physicist wants to consider. A problem of much greater phenomenological significance is to be able to trace the effect of a small perturbation over large times, when its impact on the evolution becomes appreciable despite its smallness. This is precisely the regime when the so-called secular terms in perturbation theory come into play.

Prototype examples of this sort come from celestial mechanics. The solar system is, to a high degree of accuracy, an integrable system described by the planets moving in the central potential of the Sun, whose position is fixed at the origin. Yet, interplanetary interactions and other physical processes (including processes of non-gravitational nature), introduce small perturbations to the idealized integrable picture. Jupiter, in particular, exerts a relatively strong influence on the motion of the Earth. The physical question is not in the minuscule corrections such perturbations induce over, say, one revolution of the Earth around the Sun, but rather how such minuscule corrections accumulate over a large time to produce substantial effects. This is precisely the question that naïve perturbation theory fails to answer.

Indeed, as described above, the magnitude of higher-order terms in naïve perturbation theory is guaranteed to decrease on a fixed time interval when the magnitude of the perturbation is decreased, but nothing prevents a growth of the coefficients of higher orders in naïve perturbation theory. This growth, if present, will make the asymptotic series unusable at large times, as higher-order terms will be comparable in magnitude to lower-order terms. In fact, the growing terms at higher orders in the naïve perturbation theory typically appear in realistic situations, and they have become known as ‘secular’ terms (from the Latin word for ‘century’, referring to terms that become significant when considering planetary perturbations over the course of centuries). Such terms need to be restructured by means of resummation, if one is aiming at a perturbative description of the large-time dynamics at all.

Perhaps the easiest way to appreciate the ubiquity of secular terms is to examine them in a quantum-mechanical setting. The linearity of the Schrödinger equation allows one to write an explicit result for all orders of the perturbative expansion. Since each classical system is a limit of the corresponding quantum system, the presence of secular terms in the quantum formalism sheds some light on classical Hamiltonian systems as well.

Consider for a moment a general perturbed quantum system described by the Hamiltonian, $H = H_0(t) + \lambda V(t)$ and the corresponding evolution operator $U(t)$ satisfying

$$i\frac{dU}{dt} = HU, \quad U(0) = 1. \quad (2.1)$$

Converting to the interaction picture, we introduce $u(t) = U_0^\dagger(t)U(t)$, where $U_0(t)$ satisfies

$$i\frac{dU_0}{dt} = H_0U_0, \quad U_0(0) = 1. \quad (2.2)$$

Then,

$$i\frac{du}{dt} = \lambda v(t)u, \quad u(0) = 1, \quad (2.3)$$

with $v(t) = U_0^\dagger(t)V(t)U_0(t)$. For (2.3), one obtains the standard naïve perturbative expansion

$$u(t) = 1 - i\lambda \int_0^t dt_1 v(t_1) + (-i\lambda)^2 \int_0^t dt_1 \int_0^{t_1} dt_2 v(t_1)v(t_2) + \dots \quad (2.4)$$

This expansion is generically plagued by secular terms at large t , except for special situations like scattering, when (perhaps for a subset of matrix elements) $v(t)$ effectively vanishes outside a finite time interval. Indeed, unless the interactions are effectively cut off in this fashion, the natural scale of the n th order term in (2.4) is $\lambda^n t^n$ rather than simply λ^n , which means that the naïve perturbative expansion becomes completely useless at $t \sim 1/\lambda$. (The details, of course, depend on the particular time dependences involved.)

For the familiar case of time-independent H_0 and V , it is well-known from textbooks that (2.4) is not the right way to expand. Indeed, in the standard approach (which occasionally goes under the name of Rayleigh-Schrödinger perturbation theory) one expands the eigenstates and their energies in a power series in λ , rather than expanding the evolution operator. Since the energies enter the evolution operator through $\exp(-iE_n t)$, correcting the unperturbed energies by a power series in λ is analogous to shifting the oscillator frequencies in (1.4). In fact, the Rayleigh-Schrödinger perturbation theory can be derived from (2.4) by a resummation analogous to the one leading from (1.3) to (1.4).

Our purpose for the rest of this section will be to review some approaches to secular term resummation in a general setting, before returning to the case of non-linear gravitational perturbation theory in the AdS background in section 3.

2.2 Frequency adjustment and multi-scale resummation

We shall now examine the question of what kind of secular terms may arise when a particular perturbation is applied in the context of classical Hamiltonian systems. It will be sufficient for us to focus on linear unperturbed systems with perturbations polynomial in the canonical variables. For one thing, our main goal in this paper is to shed some light on the dynamics of weakly non-linear gravitational perturbations in the AdS background. In this context, the unperturbed system is linearized gravity in the AdS background. Similar set-ups will be produced by other weakly non-linear perturbative expansions. (More generally, when dealing with the effect of an explicit dynamical perturbation on a given solution of a non-linear system, one can always treat non-linearities, expanded in the vicinity of that given solution, as merely an additional contribution to the perturbation.) As to the restriction to polynomial perturbations, it is also natural in the context of studying small

deviations from a given exact solution, since, at any given order of the perturbation theory, a non-polynomial perturbation can be identically replaced by its truncated polynomial expansion up to this order.

If the unperturbed system is linear, one can always switch to the normal coordinates c_i , for which the unperturbed solutions are simply

$$c_i^{(0)}(t) = a_i \cos \theta_i(t), \quad \theta_i(t) = \omega_i t + b_i. \quad (2.5)$$

The exact solutions satisfy

$$\ddot{c}_i + \omega_i^2 c_i = S_i, \quad c_i(t) = c_i^{(0)}(t) + \epsilon c_i^{(1)}(t) + \epsilon^2 c_i^{(2)}(t) + \dots, \quad (2.6)$$

where S_i collectively represents all the non-linear terms contributing to the equation for c_i .

We can now solve (2.6) iteratively, determining each $c_i^{(n)}$ in terms of lower order corrections,

$$\ddot{c}_i^{(n)} + \omega_i^2 c_i^{(n)} = S_i^{(n)}(c^{(0)}, c^{(1)}, \dots, c^{(n-1)}). \quad (2.7)$$

What kind of terms can emerge on the right-hand side of (2.7)? We may examine this question starting from the lowest order and working all the way up. $c^{(0)}$ is a pure cosine. Multiplication of $c^{(0)}$ is governed by the formula

$$\cos \theta_i \cos \theta_j = \frac{1}{2} [\cos(\theta_i + \theta_j) + \cos(\theta_i - \theta_j)]. \quad (2.8)$$

Then, in a general polynomial expression made of $c^{(0)}$, all the terms will be of the form

$$\cos(\theta_{i_1} \pm \theta_{i_2} \pm \theta_{i_3} \pm \dots) = \cos((\omega_{i_1} \pm \omega_{i_2} \pm \omega_{i_3} \pm \dots)t + b_{i_1} \pm b_{i_2} \pm b_{i_3} \pm \dots), \quad (2.9)$$

where (i_1, i_2, i_3, \dots) can be any set of mode numbers, and all the choices of plus and minus signs on the left hand side of (2.9) are independent of each other. The right-hand side of (2.7) is a sum of such terms. What does one get for $c^{(1)}$?

If there is a contribution to $S_i^{(1)}$ of the form (2.9) with a particular set of (i_1, i_2, i_3, \dots) , a particular assignment for each \pm , and $\pm\omega_i \neq \omega_{i_1} \pm \omega_{i_2} \pm \omega_{i_3} \pm \dots$, then this term will simply give a contribution to $c^{(1)}$ that is itself proportional to (2.9). One can then safely proceed to the next order, multiplying the different contributions to $c^{(0)}$ and $c^{(1)}$ using (2.8) to obtain the different terms in $S^{(2)}$, all of which will again be of the form (2.9), and so on ad infinitum.

The only point where this picture fails is that there may be terms with $\pm\omega_i = \omega_{i_1} \pm \omega_{i_2} \pm \omega_{i_3} \pm \dots$. For those, substituting them to the right-hand side of (2.7) does not produce a contribution to $c^{(n)}$ of the form (2.9), but rather of the form

$$t \sin(\theta_{i_1} \pm \theta_{i_2} \pm \theta_{i_3} \pm \dots). \quad (2.10)$$

This is a secular term that grows with time and invalidates perturbation theory at sufficiently large t . Such terms must be eliminated by restructuring the perturbative expansion along the lines of the frequency shift we employed in going from (1.3) to (1.4).

The kind of secular terms that may arise as we develop the ϵ -expansion iteratively depends crucially on whether the spectrum of mode frequencies is *resonant*. ‘Resonant’ in

this context means that there exist sets of integers m_i such that $\sum_i m_i \omega_i = 0$. If no such relations with non-zero m_i exist, then the spectrum is called non-resonant.

For a non-resonant spectrum, there is only one way $\pm\omega_i = \omega_{i_1} \pm \omega_{i_2} \pm \omega_{i_3} \pm \dots$ can be satisfied. Namely, the number of times ω_i is present in the sum on the right-hand side with a plus sign should be one greater (or one smaller) than the number of times it is present with a minus sign, whereas for all other modes ($i_k \neq i$), the number of times they are present with a plus sign should be exactly the same as with a minus sign. Any other combination of ω_{i_k} cannot equal ω_i since that would have implied a resonant relation between the frequencies. Hence, if $\pm\omega_i = \omega_{i_1} \pm \omega_{i_2} \pm \omega_{i_3} \pm \dots$, then (2.9) becomes simply

$$\cos(\omega_i t + b_i), \tag{2.11}$$

and the corresponding secular term, i.e., the contribution to $c_i^{(n)}$ resulting from a term of the form (2.11) in $S_i^{(n)}$ of (2.7), becomes

$$\varepsilon^n \mathcal{A}_i^{(n)}(a) t \sin(\omega_i t + b_i), \tag{2.12}$$

where $\mathcal{A}_i^{(n)}(a)$ is a certain polynomial made of the amplitudes a_k of (2.5), which depends on the precise form of the non-linearities in S .

A key observation regarding the case of a fully non-resonant frequency spectrum is that any contribution to $c_i^{(n)}$ of the form (2.12) can be absorbed into an (amplitude-dependent) shift of the frequency ω_i since

$$\cos((\omega_i + \alpha)t + b_i) = \cos(\omega_i t + b_i) - \alpha t \sin(\omega_i t + b_i) + \dots \tag{2.13}$$

After the secular terms of the form (2.12) have been absorbed in this fashion, all the remaining terms in $c_i^{(n)}$ are of the form (2.9), and one can proceed to order ε^{n+1} , where the entire argument can be repeated verbatim.

We hence conclude that, for a fully non-resonant case, all secular terms can be iteratively removed from perturbation theory by perturbatively adjusting the frequencies ω_i . This procedure is known as the Poincaré-Lindstedt method. After the frequencies have been corrected, the perturbed motion is described by small corrections to the unperturbed one for longer and longer time intervals depending on the order of accuracy in the perturbative frequency shift. (Note that the picture we have outlined is something of a pedestrian pre-requisite for the KAM theory [4], which takes the argument much further and develops stability arguments for the non-resonant case at finite small ε , rather than in an unreliable framework of asymptotic expansions.)

The situation becomes more complicated when resonant relations between unperturbed frequencies are present. In that case, there may be many different addition-subtraction patterns that satisfy $\pm\omega_i = \omega_{i_1} \pm \omega_{i_2} \pm \omega_{i_3} \pm \dots$. One then cannot specify the form of (2.9) for the resonant terms beyond

$$\cos(\omega_i t \pm b_{i_1} \pm b_{i_2} \pm b_{i_3} \pm \dots) \tag{2.14}$$

with a (generally complicated) combination of phases. The corresponding secular term resulting from the contribution of (2.14) to $S_i^{(n)}$ of (2.7) is

$$\varepsilon^n \mathcal{A}_i^{(n)}(a) t \sin(\omega_i t \pm b_{i_1} \pm b_{i_2} \pm b_{i_3} \pm \dots), \tag{2.15}$$

where $\mathcal{A}_i^{(n)}(a)$ is a certain polynomial made of the amplitudes a_k of (2.5), which depends on the precise form of the non-linearities in S .

Since the phase of the sine in (2.15) does not have to equal b_i , it cannot be in general absorbed into a shift of ω_i by means of (2.13). Of course, this term could always be absorbed into a shift of *both* ω_i and a_i . However, the shift of a_i would have to grow linearly with time, so that one generates $t \sin(\omega_i t + b_i)$ from the shift of ω_i and $t \cos(\omega_i t + b_i)$ from the shift of a_i , and a combination of such terms can always match (2.15). By itself, a linearly growing a_i is no better and no worse than the original secular term, and more powerful resummation methods are needed. We shall turn to such methods shortly.

Physically, the fact that a frequency adjustment is not sufficient for the resonant case, but one also obtains terms that look like amplitude drifts, simply means that, over large times, significant energy transfer occurs between different modes, even when the perturbation is small. This is in contrast to the non-resonant case, where a small perturbation can only induce small amplitude oscillations of the energy back and forth between different modes, without significant energy transfer occurring even over large time scales.

The long-term fate of a resonant system under the impact of a dynamical perturbation can only be determined after a resummation of secular terms has been performed. The failure of the Poincaré-Lindstedt frequency shift by itself should by no means be interpreted as a sign of instability. A complete resummation can produce long-period oscillations of energy between the modes, or perhaps transfer of energy to high-frequency modes (turbulence), etc. Many scenarios are possible.

There is a number of resummation methods described in the literature (see, e.g., [15]). One encounters descriptions of the multi-scale method particularly often. We shall very quickly review this method here, only stating the general idea and referring the reader to [15] for further details. The lowest-order multi-scale method (under the name of ‘Two-Time Framework’) has been applied to the problem of AdS stability in [14].

We have already alluded above that a general secular term can be absorbed into perturbatively small frequency adjustments and a slow drift of the amplitudes. Note that the frequency adjustment can be thought of as a slow drift of the phases. One thus arrives at the concept of absorbing secular terms into a slow variation of the integration constants in the zeroth order solution $c_i^{(0)}$. This general idea is shared by both the multiscale method and the renormalization group method we shall describe further below. Note that the Poincaré-Lindstedt method is a special case of this set-up, for which the phases acquire a slow linear drift, whereas the amplitudes do not evolve.

The ‘slow variation of the integration constants’ we mentioned above is a rather vague concept and one needs to decide in practice how this dependence is distributed between different orders of perturbation theory. In the multiscale method, one introduces dependences with explicit powers of ϵ in the form

$$a_i = a_i(\epsilon t, \epsilon^2 t, \epsilon^3 t, \dots), \quad b_i = b_i(\epsilon t, \epsilon^2 t, \epsilon^3 t, \dots). \quad (2.16)$$

When the functions are specified in this form, one knows, for example, that a term quadratic in ϵ can arise from differentiating two times with respect to the first argument or one time

with respect to the second argument, etc. The term ‘multiscale’ comes precisely from the multiple scales (ϵt , $\epsilon^2 t$, $\epsilon^3 t$, etc) involved in this construction. (At first non-trivial order, only t and ϵt are involved, hence the ‘Two-Time Framework’ of [14].)

One then substitutes (2.16) to (2.5) and then to the equations of motion (2.7), and demands that the terms resulting from differentiating (2.16) conspire in precisely such a way as to remove the resonant terms in S_i (the terms whose frequency is ω_i). At n th order, this results in a differential equation that fixes the dependence of a_i and b_i on $\epsilon^n t$, which is then fed to the next order. To address the issue of non-linear stability, one should examine the behavior of the amplitudes after the resummation has been performed.

The multiscale method is a powerful resummation scheme applicable in a general setting and including the Poincaré-Lindstedt method as a simple special case. (Whether the result of the resummation is free from pathological growth depends, of course, on the particular system at hand.) However, the need to explicitly prescribe how the slow dependence of the (unperturbed) integration constants on time is distributed between different orders of perturbation theory, as in (2.16), may create complications in more subtle cases. For example, the case of stability analysis for Mathieu equation is mentioned in [3], where an unusual scale $\epsilon^{3/2} t$ appears through resummations, and that would have to be guessed in the initial ansatz (2.16) for the multiscale method. Even if that does not happen, the method becomes rather convoluted at higher orders, since new ‘slow’ secular terms dependent on the slow time variables develop in (2.16) and those ‘slow’ secular terms have to be removed by adjusting the dependence of (2.16) on even slower time scales. Detailed explanations can be found in [15]. As one aspect of this highly convoluted procedure, it may turn out inconvenient, depending on the circumstances, that the multiscale method does not take as its input the naïve perturbative expansion, but rather requires re-deriving an alternative expansion order-by-order from scratch. The renormalization group method we shall present below is an alternative formulation with many appealing features.

2.3 Renormalization group method

In the preceding exposition, we have reviewed the general problem of secular terms in non-linear perturbation theory, the types of secular terms arising when the unperturbed system is linear (or, more generally, integrable) and Hamiltonian, and a general multiscale method for resumming such secular terms.

One could in principle rest content with this state of affairs and proceed applying the resummation techniques to our particular problem (AdS instability). However, we believe it is useful to review another resummation strategy [3], modelled on the renormalization group treatment of ultraviolet divergences in quantum field theory. This method is as powerful as multiscale resummation we have briefly reviewed above, but has the advantage in that its sole input is the naïve perturbative expansion (without the need to re-solve the perturbation theory equations). The method also has the appeal of being intuitive, especially for people with high energy theory backgrounds.

The renormalization method (just like the multiscale method we reviewed above) aims at constructing slow time dependences of the integration constants of unperturbed solutions in a way that eliminates secular terms from perturbative expansions. We shall start by

a simple matter-of-fact statement of the method and applying it to secular terms of the form (2.14), and then give some qualifying explanatory remarks. The recipe [3] is as follows:

- 1) Choose a moment of time τ and introduce a perturbative ϵ -dependence to the integration constants of the unperturbed problem in such a way that the secular terms³ are exactly cancelled at the moment τ . In the language of (2.5), one writes:

$$\begin{aligned} a &= a(\tau, \epsilon) = a_R(\tau) + \epsilon a^{(1)}(a_R, b_R; \tau) + \epsilon^2 a^{(2)}(a_R, b_R; \tau) + \dots, \\ b &= b(\tau, \epsilon) = b_R(\tau) + \epsilon b^{(1)}(a_R, b_R; \tau) + \epsilon^2 b^{(2)}(a_R, b_R; \tau) + \dots, \end{aligned} \tag{2.17}$$

where $a_R(\tau)$ and $b_R(\tau)$ denote ‘renormalized integration constants’ and we have omitted the mode number index. Note that the cancellation of secular terms at a given moment τ can always be arranged, simply because adjusting the initial conditions permits one to give the unperturbed trajectory absolutely any value at τ . (2.17) have to be substituted to the naïve perturbative expansion and everything should be expressed through a_R and b_R .

- 2) One demands that the resulting perturbative expansion in terms of a_R and b_R should be independent of τ . Note that, once we introduce an ϵ -dependence in the unperturbed solution in (2.17), we are no longer dealing with a single solution to the underlying problem, but with a family of asymptotic expansions. Demanding that the entire expansion is independent of τ simply amounts to forcing this family of asymptotic expansion to represent a single solution to the underlying problem (merely expanded in different ways), which is what we ultimately want to construct, rather than a family of solutions. Requiring the τ -derivative of the expansion to vanish generates a first order differential equation for the renormalized integration constants, $a_R(\tau)$ and $b_R(\tau)$ for (2.17). This equation defines their renormalization flow.
- 3) After solving the renormalization flow equation obtained in 2), one substitutes the result in the expansion in terms of $a_R(\tau)$ and $b_R(\tau)$, and finally sets τ to t (this corresponds to working with a running coupling in perturbative quantum field theory). The result is free from secular terms by construction.

In application to secular terms of the form (2.14) at first non-trivial order it is easy to see how the renormalization group method works. One may write the expansion as

$$a_i \cos(\omega_i t + b_i) + \dots + \epsilon^n \mathcal{A}_i^{(n)}(a) t \sin(\omega_i t + \sum_k m_k b_k) + \dots \tag{2.18}$$

where we focus on the contribution of just one such term and the dots represent other terms, and m_k is a certain set of integers. One first represents the secular term as

$$\epsilon^n \mathcal{A}_i^{(n)}(a) t \cos(\sum_k m_k b_k - b_i) \sin(\omega_i t + b_i) + \epsilon^n \mathcal{A}_i^{(n)}(a) t \sin(\sum_k m_k b_k - b_i) \cos(\omega_i t + b_i). \tag{2.19}$$

³There is some ambiguity in identifying secular terms. Indeed, one can always add some regular terms to what one calls a secular term. This will result in a somewhat different renormalization flow equation. It may be important to make use of this freedom advantageously.

Then one can absorb the secular term at moment τ by introducing

$$\begin{aligned} a_i &= a_{R,i} - \varepsilon^n \mathcal{A}_i^{(n)}(a_R) \tau \sin(\sum_k m_k b_{R,k} - b_{R,i}), \\ b_i &= b_{R,i} + \frac{\varepsilon^n}{a_i} \mathcal{A}_i^{(n)}(a_R) \tau \cos(\sum_k m_k b_{R,k} - b_{R,i}). \end{aligned} \tag{2.20}$$

As a result of re-expressing the expansion (2.18) in terms of a_R and b_R , one gets

$$\begin{aligned} a_{R,i} \cos(\omega_i t + b_{R,i}) + \dots + \varepsilon^n \mathcal{A}_i^{(n)}(a_R) (t - \tau) \cos(\sum_k m_k b_{R,k} - b_{R,i}) \sin(\omega_i t + b_{R,i}) \\ + \varepsilon^n \mathcal{A}_i^{(n)}(a_R) (t - \tau) \sin(\sum_k m_k b_{R,k} - b_{R,i}) \cos(\omega_i t + b_{R,i}) + \dots \end{aligned} \tag{2.21}$$

Equating to zero the τ -derivative of this expression, one obtains the following renormalization flow equations:

$$\begin{aligned} \frac{da_{R,i}}{d\tau} &= -\varepsilon^n \mathcal{A}_i^{(n)}(a_R) \sin(b_{R,i} - \sum_k m_k b_{R,k}) + \dots, \\ a_{R,i} \frac{db_{R,i}}{d\tau} &= -\varepsilon^n \mathcal{A}_i^{(n)}(a_R) \cos(b_{R,i} - \sum_k m_k b_{R,k}) + \dots, \end{aligned} \tag{2.22}$$

where the dots represent contributions from other secular terms. Note that the same equations would have resulted from formally differentiating (2.20) with respect to τ . In this way, one formally bypasses some of the steps in our above description of the method following [3]. (This is analogous to deriving the running of the renormalized coupling by differentiating the bare coupling with respect to the renormalization scale.)

For N degrees of freedom, (2.22) are $2N$ first order differential equations, a system of the same type⁴ as our starting point (2.6). Of course, (2.22) contains less information than (2.6) as it is entirely derived from a truncated perturbative expansion, whereas (2.6) is exact. Nonetheless, one should generally not expect miraculous analytic solutions coming out of perturbative resummation under general circumstances. Equations (2.22) are advantageous in that they explicitly describe very slow long-time energy flow between the different modes. They can thus be useful for analytic considerations of qualitative issues.

Having given a practical statement of the renormalization method in application to secular terms, we would like to zoom out for a moment and re-examine why and how the method works. When constructing naïve perturbation theory, one encounters growing terms at higher orders, which invalidate the perturbative expansion at large times. Nonetheless, one expects that the perturbative expansion is accurate for evolution over short times, before secular terms develop significant values. Logically, there is an obvious

⁴Note, however, that if a particular mode does not enter any frequency resonance relations $\sum_i m_i \omega_i = 0$, then this particular mode effectively decouples in (2.22). The rank of the system is thereby reduced. The decoupling happens in the following way: for a completely non-resonant mode, the only secular terms allowed are (2.12). Such terms, according to (2.22), induce an amplitude-dependent phase drift, but no amplitude drift. Similarly, the way a non-resonant mode enters the secular terms for the other modes is only through its (constant) amplitude, but not through its phase. Therefore, one can solve the equations for the entire set of resonant modes first, and then the result will simply contribute a slow phase drift to non-resonant modes. The Poincaré-Lindstedt method relies on an extreme version of this picture, when all the modes are non-resonant. Our main interest in this article is in non-linear AdS perturbations, a fully resonant system where none of such simplifications occur.

strategy here: to take the initial data at t , evolve them to $t+\Delta t$ using the naïve perturbation theory, build a new unperturbed solution starting from the values at $t+\Delta t$, develop a naïve perturbative expansion using this new solution, use it to evolve from $t+2\Delta t$, and so on, until one reaches the desired final time, which can be large. In this approach, one never uses the naïve perturbation theory outside its range of validity, and secular terms do not arise.

There is, in fact, more freedom than we have displayed in the construction from the previous passage. Indeed, when reaching $t+\Delta t$, we did not have to take the exact value of our variables as the initial value for the unperturbed solution on the interval $[t+\Delta t, t+2\Delta t]$. Rather, we could distribute this value in a convenient way between the initial value for the new unperturbed solution and the initial value for the perturbation. For example, we could only absorb the would-be secular terms into the new unperturbed solution on the interval $[t+\Delta t, t+2\Delta t]$, continuing the regular perturbative terms on the interval $[t, t+\Delta t]$ to the perturbation on the interval $[t+\Delta t, t+2\Delta t]$. We could also take Δt to zero and implement these rearrangements in the perturbation series continuously on-the-go. This is precisely the picture underlying the renormalization group method. (Note that a slow running of the integration constants of the unperturbed solution emerges automatically in this perspective.)

The situation is directly analogous to what one encounters while dealing with ultraviolet divergences in perturbative field theory, with dependence on energy logarithm replacing the dependence on time. The naïve perturbative expansion for a quantity involving momenta of order k regularized with a cut-off scale Λ , involves terms of the type $\ln(\Lambda^2/k^2)$. These terms become huge when the cut-off is sent to infinity and invalidate the perturbation theory (despite being suppressed by positive powers of the coupling). They are thus analogous to secular terms. One can formally introduce renormalized couplings at momentum scale μ related to the bare couplings by ill-behaved asymptotic series involving coefficients of the sort $\ln(\Lambda^2/\mu^2)$, so that the giant logarithms of the original perturbative expansion are replaced by $\ln(\mu^2/k^2)$ when physical quantities are re-expressed through renormalized couplings. The new perturbation series is well-behaved for k^2 close to μ^2 , but ill-behaved elsewhere, when $\ln(\mu^2/k^2)$ (which is roughly analogous to Δt of the previous passages) becomes large. Finally, one can demand that the whole construction should be independent of μ , derive the corresponding renormalization group equation for the renormalized coupling dependence on μ , solve them, and thereafter do all expansions at $\mu^2 = k^2$ using the value of the renormalized coupling at k^2 , thereby eliminating the (‘secular’) logarithms.

In fact, the renormalization method in application to secular term resummation operates in a mathematically much better defined setting than what quantum field theory may offer. One may hope to develop more transparent and tightly controlled derivations. We believe that starting from the time-stepping procedure described above, one should be able to derive the prescriptions of [3] in a way that never involves ill-behaved asymptotic expansions with large coefficients at the intermediate steps. We shall nonetheless not pursue this program here.

3 AdS (in)stability

Having reviewed some possible strategies to deal with the problem of secular terms in naïve perturbation theory, we shall now turn to the issue of non-linear stability of the AdS space-time, in which such secular terms play a central role.

We shall work with the renormalization-based resummation of [3] at lowest non-trivial order. In principle, this approach is identical to the multiscale treatment of the same problem (at the same order) in [14]. Our perspective is quite different from [14], however. There, the main focus was on numerical studies of the ‘energy flow’ equations of the type (2.22), truncated to a finite set of low-lying modes. Our main goal is to develop a neat analytic representation of these equations for all modes, with a view of future analytic studies of qualitative properties of this system. The main practical result we shall present here is the vanishing of an infinite number of terms of a particular type in the flow equations, which are allowed on general grounds by the spectrum of frequencies of linear AdS perturbations.

3.1 Setup of the system

The equations of motion that we consider are Einstein’s equations with a negative cosmological constant which are minimally coupled to a scalar field:

$$G_{\mu\nu} - \frac{d(d-1)}{2L^2}g_{\mu\nu} = 8\pi G \left(\partial_\mu\phi\partial_\nu\phi - \frac{1}{2}g_{\mu\nu}(\partial\phi)^2 \right) \quad \text{and} \quad \square\phi = 0. \quad (3.1)$$

Following the conventions of [10], we will parameterize the geometry by two functions $A(x, t)$ and $\delta(x, t)$ as

$$ds^2 = \frac{L^2}{\cos^2 x} \left(\frac{dx^2}{A} - Ae^{-2\delta} dt^2 + \sin^2 x d\Omega_{d-1}^2 \right). \quad (3.2)$$

The coordinates take values in $t \in]-\infty, \infty[$ and $x \in [0, \pi/2[$. The scalar field is also considered to be isotropic, $\phi = \phi(x, t)$. We introduce the notation $\Phi \equiv \phi'$ and $\Pi \equiv A^{-1}e^\delta\dot{\phi}$ (where overdots and primes denote derivatives with respect to t and x , respectively) together with the convention $8\pi G = d-1$. Furthermore, it is convenient to define

$$\mu(x) \equiv (\tan x)^{d-1} \quad \text{and} \quad \nu(x) \equiv \frac{(d-1)}{\mu'(x)} = \frac{\sin x \cos x}{(\tan x)^{d-1}}. \quad (3.3)$$

The equations of motion then reduce to

$$\dot{\Phi} = \left(Ae^{-\delta}\Pi \right)', \quad \dot{\Pi} = \frac{1}{\mu} \left(\mu Ae^{-\delta}\Phi \right)', \quad (3.4a)$$

$$A' = \frac{\nu'}{\nu} (A-1) - \mu\nu (\Phi^2 + \Pi^2) A, \quad \delta' = -\mu\nu (\Phi^2 + \Pi^2), \quad (3.4b)$$

$$\dot{A} = -2\mu\nu A^2 e^{-\delta} \Phi \Pi. \quad (3.4c)$$

A static solution of these equations is the AdS-Schwarzschild black hole $A(x, t) = 1 - M\nu(x)$, $\delta(x, t) = 0$ and $\phi(x, t) = 0$. The unperturbed AdS space itself corresponds to $A = 1$, $\delta = \phi = 0$.

3.2 Weakly non-linear perturbation theory

We will look for an approximate solution of the equations of motion (3.4) with initial conditions $\phi(0, x) = \epsilon f(x)$ and $\dot{\phi}(0, x) = \epsilon g(x)$. Therefore, we expand the unknown functions in the amplitude of the initial conditions:

$$\phi(x, t) = \sum_{k=0}^{\infty} \epsilon^{2k+1} \phi_{2k+1}(x, t), \quad A(x, t) = 1 + \sum_{k=1}^{\infty} \epsilon^{2k} A_{2k}(x, t), \quad \delta(x, t) = \sum_{k=1}^{\infty} \epsilon^{2k} \delta_{2k}(x, t). \quad (3.5)$$

At first order in the ϵ -expansion, the equations of motion (3.4) are linearized and result in the homogeneous partial differential equation

$$\ddot{\phi}_1 + \hat{L}\phi_1 = 0 \quad \text{with} \quad \hat{L} \equiv -\frac{1}{\mu(x)} \partial_x (\mu(x) \partial_x). \quad (3.6)$$

The operator \hat{L} is self-adjoint with respect to the inner product

$$\langle \psi, \chi \rangle \equiv \int_0^{\pi/2} \bar{\psi}(x) \chi(x) \mu(x) dx. \quad (3.7)$$

The eigenvalues and eigenfunctions for \hat{L} are $\omega_j^2 = (d + 2j)^2$ (with indices $j = 0, 1, 2, \dots$) and

$$e_j(x) = k_j (\cos x)^d P_j^{(\frac{d}{2}-1, \frac{d}{2})}(\cos(2x)) \quad \text{with} \quad k_j = \frac{2\sqrt{j!(j+d-1)!}}{\Gamma(j + \frac{d}{2})}. \quad (3.8)$$

The function $P_n^{(a,b)}(x)$ is a Jacobi polynomial⁵ of order n . These eigenfunctions are defined such that $\hat{L}e_j = \omega_j^2 e_j$ and $\langle e_i, e_j \rangle = \delta_{ij}$. Note that all the mode frequencies ω_j are integer and the spectrum is *fully resonant*, suggesting a large number of secular terms in non-linear perturbation theory.

We expand the unknown functions in the basis (3.8):

$$\phi_{2k+1}(x, t) = \sum_{j=0}^{\infty} c_j^{(2k+1)}(t) e_j(x) \quad \text{with} \quad c_j^{(2k+1)}(t) = \langle \phi_{2k+1}(x, t), e_j(x) \rangle. \quad (3.9)$$

The solution of the linearized equation for ϕ_1 is then given by

$$\phi_1(x, t) = \sum_{k=0}^{\infty} c_j(t) e_j(x). \quad (3.10)$$

The coefficients $c_j \equiv c_j^{(1)}$ satisfy $\ddot{c}_j + \omega_j^2 c_j = 0$ and are thus given by

$$c_j(t) = a_j \cos(\omega_j t + b_j), \quad (3.11)$$

where the amplitudes a_j and phases b_j are determined by the initial profiles $f(x)$ and $g(x)$. The backreaction on the metric appears at second order. It is determined by the equations

$$A'_2 = \frac{\nu'}{\nu} A_2 - \mu \nu \left((\dot{\phi}_1)^2 + (\phi'_1)^2 \right), \quad (3.12a)$$

⁵Jacobi polynomials $P_n^{(a,b)}(x)$ are a system of orthogonal polynomials with respect to the measure $(1-x)^a(1+x)^b$ on the interval $(-1, 1)$. A good summary of their properties with derivations is given in [16].

$$\delta'_2 = -\mu\nu \left((\dot{\phi}_1)^2 + (\phi'_1)^2 \right), \quad (3.12b)$$

$$\dot{A}_2 = -2\mu\nu \dot{\phi}_1 \phi'_1. \quad (3.12c)$$

These equations can be directly integrated to give

$$A_2(x, t) = -\nu(x) \int_0^x \left(\dot{\phi}_1(y, t)^2 + \phi'_1(y, t)^2 \right) \mu(y) dy, \quad (3.13)$$

$$\delta_2(x, t) = - \int_0^x \left(\dot{\phi}_1(y, t)^2 + \phi'_1(y, t)^2 \right) \mu(y) \nu(y) dy. \quad (3.14)$$

At third order in the ϵ -expansion, the equations of motion (3.4) lead to the inhomogeneous equation

$$\ddot{\phi}_3 + L\phi_3 = S \equiv 2(A_2 - \delta_2) \ddot{\phi}_1 + (\dot{A}_2 - \dot{\delta}_2) \dot{\phi}_1 + (A'_2 - \delta'_2) \phi'_1. \quad (3.15)$$

We can project this equation on to the eigenbasis $\{e_j\}$, such that

$$\ddot{c}_j^{(3)} + \omega_j^2 c_j^{(3)} = S_j \quad \text{with} \quad S_j = \langle S, e_j \rangle. \quad (3.16)$$

After a tedious but straightforward calculation (more details are explained in appendix A), one finds the source term

$$\begin{aligned} S_l = & \langle (A'_2 - \delta'_2) \phi'_1, e_l \rangle + 2\langle A_2 \ddot{\phi}_1, e_l \rangle + \langle \dot{A}_2 \dot{\phi}_1, e_l \rangle - 2\langle \delta_2 \ddot{\phi}_1, e_l \rangle - \langle \dot{\delta}_2 \dot{\phi}_1, e_l \rangle \\ = & \frac{1}{2} \sum_{i=0}^{\infty} \sum_{\substack{j=0 \\ j \neq i}}^{\infty} \sum_{k=0}^{\infty} a_i a_j a_k \omega_j (H_{ijkl} - 2X_{ijkl} \omega_k^2) \left[\frac{1}{\omega_i - \omega_j} (\cos(\theta_i - \theta_j - \theta_k) + \cos(\theta_i - \theta_j + \theta_k)) \right. \\ & \left. - \frac{1}{\omega_j + \omega_i} (\cos(\theta_i + \theta_j - \theta_k) + \cos(\theta_i + \theta_j + \theta_k)) \right] \\ - & \frac{1}{4} \sum_{i=0}^{\infty} \sum_{k=0}^{\infty} a_k a_i^2 (H_{iikl} - 2\omega_k^2 X_{iikl}) (\cos(2\theta_i - \theta_k) + \cos(2\theta_i + \theta_k)) \\ - & \frac{1}{2} \sum_{i=0}^{\infty} \sum_{k=0}^{\infty} a_k a_i^2 (H_{iikl} + 2\omega_i^2 M_{kli} - 2\omega_k^2 X_{iikl} - 4\omega_k^2 \omega_i^2 W_{kli}) \cos(\theta_k) \\ - & \frac{1}{2} \sum_{i=0}^{\infty} \sum_{j=0}^{\infty} \sum_{k=0}^{\infty} X_{ijkl} a_i a_j a_k \omega_j \omega_k [\cos(\theta_k - \theta_j - \theta_i) + \cos(\theta_k - \theta_j + \theta_i) \\ & - \cos(\theta_k + \theta_j - \theta_i) - \cos(\theta_k + \theta_j + \theta_i)] \\ + & \frac{1}{4} \sum_{k=0}^{\infty} \sum_{i=0}^{\infty} \sum_{\substack{j=0 \\ k \neq l}}^{\infty} \frac{a_i a_j a_k \omega_k}{(\omega_l^2 - \omega_k^2)} \left\{ Z_{ijkl}^+ (2\omega_k + \omega_j - \omega_i) \cos(\theta_i - \theta_j - \theta_k) \right. \\ & + Z_{ijkl}^+ (2\omega_k - \omega_j + \omega_i) \cos(\theta_i - \theta_j + \theta_k) \\ & + Z_{ijkl}^- (\omega_i + \omega_j - 2\omega_k) \cos(\theta_i + \theta_j - \theta_k) \\ & \left. - Z_{ijkl}^- (2\omega_k + \omega_j + \omega_i) \cos(\theta_i + \theta_j + \theta_k) \right\} \\ - & \frac{1}{4} \sum_{i=0}^{\infty} \sum_{j=0}^{\infty} a_i a_j a_l \omega_l \{ [\omega_i \omega_j P_{ijl} + B_{ijl}] (2\omega_l + \omega_j - \omega_i) \cos(\theta_i - \theta_j - \theta_l) \} \end{aligned}$$

$$\begin{aligned}
& +[\omega_i\omega_j P_{ijl} + B_{ijl}](2\omega_l - \omega_j - \omega_i) \cos(\theta_i - \theta_j + \theta_l) \\
& +[\omega_i\omega_j P_{ijl} - B_{ijl}](\omega_j + \omega_i - 2\omega_l) \cos(\theta_i + \theta_j - \theta_l) \\
& -[\omega_i\omega_j P_{ijl} - B_{ijl}](2\omega_l + \omega_j + \omega_i) \cos(\theta_i + \theta_j + \theta_l) \}, \tag{3.17}
\end{aligned}$$

where we used the shorthand notation $\theta_i(t) = \omega_i t + b_i$. The coefficients that appear in these expressions are certain integrals of products of eigenfunctions:

$$H_{ijkl} = \int_0^{\frac{\pi}{2}} dx e'_i(x) e_j(x) e'_k(x) e_l(x) (\mu(x))^2 \nu'(x), \tag{3.18a}$$

$$X_{ijkl} = \int_0^{\frac{\pi}{2}} dx e'_i(x) e_j(x) e_k(x) e_l(x) (\mu(x))^2 \nu(x), \tag{3.18b}$$

$$Y_{ijkl} = \int_0^{\frac{\pi}{2}} dx e'_i(x) e_j(x) e'_k(x) e'_l(x) (\mu(x))^2 \nu(x), \tag{3.18c}$$

$$Z_{ijkl}^{\pm} = \omega_i \omega_j (X_{klij} - X_{lkij}) \pm (Y_{klij} - Y_{lkij}), \tag{3.18d}$$

$$M_{ijk} = \int_0^{\frac{\pi}{2}} dx e'_i(x) e_j(x) \mu(x) \nu'(x) \int_0^x dy (e_k(y))^2 \mu(y), \tag{3.18e}$$

$$W_{ijk} = \int_0^{\frac{\pi}{2}} dx e_i(x) e_j(x) \mu(x) \nu(x) \int_0^x dy (e_k(y))^2 \mu(y), \tag{3.18f}$$

$$P_{ijk} = \int_0^{\frac{\pi}{2}} dx e_i(x) e_j(x) \mu(x) \nu(x) \left(1 - \int_0^x dy (e_k(y))^2 \mu(y) \right), \tag{3.18g}$$

$$B_{ijk} = \int_0^{\frac{\pi}{2}} dx e'_i(x) e'_j(x) \mu(x) \nu(x) \left(1 - \int_0^x dy (e_k(y))^2 \mu(y) \right). \tag{3.18h}$$

3.3 Vanishing secular terms

As already discussed above (2.10), secular terms appear when the set of frequencies $\{\omega_i, \omega_j, \omega_k\}$ satisfies the resonance condition $\omega_i \pm \omega_j \pm \omega_k = \pm\omega_l$. In this case, a resonant term should (generally) arise in the source S_l of the mode $c_l^{(3)}$. Equation (3.16) will then have a solution that involves a secular term,

$$\ddot{c}_l^{(3)}(t) + \omega_l^2 c_l^{(3)}(t) = \mathcal{A} \cos(\omega_l t + \mathcal{B}) + (\dots) \quad \Rightarrow \quad c_l^{(3)}(t) = \frac{\mathcal{A}}{2\omega_l} t \sin(\omega_l t + \mathcal{B}) + (\dots). \tag{3.19}$$

There are eight choices of the signs in $\omega_i \pm \omega_j \pm \omega_k = \pm\omega_l$. First, one can have $\omega_i + \omega_j + \omega_k = \omega_l$. We shall call the corresponding terms ‘+++ terms’. $\omega_i + \omega_j + \omega_k = -\omega_l$ cannot be satisfied due to frequency positivity. Of the remaining six choices, three can be brought to the form $\omega_i + \omega_j - \omega_k = \omega_l$ by permuting i, j and k . We shall call these ‘++- terms’. After that, the three remaining choices can be brought to the form $\omega_i - \omega_j - \omega_k = \omega_l$ by permuting i, j and k . We shall call these ‘+-- terms’.

Our goal in this section is to prove that the +++ and +-- terms vanish due to properties of the AdS mode functions, despite being allowed by the frequency spectrum. We shall give explicit expressions for the ++- terms in section 3.4.

We shall first focus on the +++ terms in (3.17), for which $\omega_i + \omega_j + \omega_k = \omega_l$. One finds that

$$S_l = (\dots) + \sum_{\substack{i \\ j \\ k \\ i+j+k+d=l}} Q_{ijkl} a_i a_j a_k \cos(\theta_i + \theta_j + \theta_k), \quad (3.20)$$

where (...) represents the non-resonant terms as well as resonant terms of other types. The coefficients Q_{ijkl} are given by

$$\begin{aligned} Q_{ijkl} = & -\frac{1}{12} H_{ijkl} \frac{\omega_j(2\omega_j + \omega_i + \omega_k)}{(\omega_j + \omega_i)(\omega_j + \omega_k)} - \frac{1}{12} H_{jkil} \frac{\omega_k(2\omega_k + \omega_i + \omega_j)}{(\omega_k + \omega_i)(\omega_k + \omega_j)} \\ & - \frac{1}{12} H_{kijl} \frac{\omega_i(2\omega_i + \omega_j + \omega_k)}{(\omega_i + \omega_j)(\omega_i + \omega_k)} + \frac{1}{6} X_{ijkl} \omega_j \omega_k \left(1 + \frac{\omega_k}{(\omega_j + \omega_i)} + \frac{\omega_j}{(\omega_k + \omega_i)} \right) \\ & + \frac{1}{6} X_{jkil} \omega_i \omega_k \left(1 + \frac{\omega_k}{(\omega_i + \omega_j)} + \frac{\omega_i}{(\omega_k + \omega_j)} \right) + \frac{1}{6} X_{kijl} \omega_i \omega_j \left(1 + \frac{\omega_i}{(\omega_j + \omega_k)} + \frac{\omega_j}{(\omega_i + \omega_k)} \right) \\ & - \frac{1}{12} Z_{ijkl}^- \frac{\omega_k}{(\omega_i + \omega_j)} - \frac{1}{12} Z_{jkil}^- \frac{\omega_i}{(\omega_j + \omega_k)} - \frac{1}{12} Z_{kijl}^- \frac{\omega_j}{(\omega_i + \omega_k)}. \end{aligned} \quad (3.21)$$

We will now show that all coefficients Q_{ijkl} vanish whenever $i + j + k + d = l$, i.e., when the resonance condition is satisfied. This is a non-trivial statement (though it may well have a more straightforward and elegant proof based on the symmetries of AdS), since the structure of the linearized frequency spectrum allows such terms.

To analyze (3.21) we employ the following transformations:

1) We notice that

$$H_{ijkl} = \omega_k^2 X_{ijkl} - Y_{ijkl} + \omega_i^2 X_{klij} - Y_{klij}. \quad (3.22)$$

This identity is proved by integration by parts removing the derivative from ν in (3.18a). Antisymmetrizing (3.22) with respect to i and j , one gets:

$$Y_{ijkl} - Y_{jikl} = (\omega_i^2 - \omega_j^2) X_{klij} + \omega_k^2 (X_{ijkl} - X_{jikl}) - (H_{ijkl} - H_{jikl}). \quad (3.23)$$

This relation is used to eliminate Y from Z^+ of (3.18d), and hence from (3.21).

2) After the above manipulation, (3.21) only contains H and X of (3.18). H and X are integrals of products of mode functions e_i, e_j, e_k, e_l and their derivatives. An important distinction among the different terms is whether e_l (in the integrand of H or X) is differentiated. (e_l is the mode function of the mode receiving the secular term contribution.) If it is, we remove the derivative from it using integration by parts:

$$\begin{aligned} H_{lijk} &= -(H_{ikjl} + H_{kijl}) + \omega_j^2 D_{ijkl} + 4X_{jikl}, \\ X_{lijk} &= -(X_{ijkl} + X_{jikl} + X_{kijl}) - E_{ijkl}, \end{aligned} \quad (3.24)$$

with

$$\begin{aligned} D_{ijkl} &= \int_0^{\frac{\pi}{2}} dx e_i e_j e_k e_l \mu^2 \nu', \\ E_{ijkl} &= \int_0^{\frac{\pi}{2}} dx e_i e_j e_k e_l (\mu^2 \nu)'. \end{aligned} \quad (3.25)$$

(We have used the identity $(\mu\nu')' = -4\mu\nu$.) At this point,⁶ (3.21) takes the form

$$Q_{ijkl} \sim \int_0^{\frac{\pi}{2}} dx e_l(x) q_{ijk}(x), \tag{3.26}$$

where $q_{ijk}(x)$ can only receive the following contributions: from H -terms, a product of e_i, e_j, e_k , two of which are differentiated, times $\mu^2\nu'$; from X -terms, a product of e_i, e_j, e_k , one of which is differentiated, times $\mu^2\nu$; from D -terms, $e_i e_j e_k e_l \mu^2\nu'$; from E -terms, $e_i e_j e_k e_l (\mu^2\nu)'$.

- 3) From (3.26) and the expression for mode functions in terms of Jacobi polynomials (3.8), one can bring (3.21) to the form⁷

$$Q_{ijkl} \sim \int_{-1}^1 P_l^{(\frac{d}{2}-1, \frac{d}{2})}(\xi) \mathcal{Q}_{ijk}(\xi) (1-\xi)^{\frac{d}{2}-1} (1+\xi)^{\frac{d}{2}} d\xi \tag{3.27}$$

with $\xi = \cos 2x$. Here, $\mathcal{Q}_{ijk}(\xi)$ is a polynomial of degree $i+j+k+d+1 = l+1$ made of $P_i^{(\frac{d}{2}-1, \frac{d}{2})}, P_j^{(\frac{d}{2}-1, \frac{d}{2})}, P_k^{(\frac{d}{2}-1, \frac{d}{2})}$, their first derivatives and various trigonometric functions appearing in (3.26), re-expressed through $\cos 2x$. Note that the integration measure appearing in (3.27) is precisely the same as the one used for defining the Jacobi polynomials.

- 4) Finally, to prove that (3.27) vanishes, it suffices to show that the expansion of $\mathcal{Q}_{ijk}(\xi)$ in terms of Jacobi polynomials $P_n^{(\frac{d}{2}-1, \frac{d}{2})}$ does not contain $P_l^{(\frac{d}{2}-1, \frac{d}{2})}$. Since $\mathcal{Q}_{ijk}(\xi)$ is a polynomial of degree $l+1$, whether that happens or not can be decided on the basis of considering the coefficients of its two highest powers. More specifically, the coefficients of the two highest powers in Jacobi polynomials (which we need only up to the overall normalization) can be extracted from known formulas (see, e.g., [16]) as

$$P_n^{(d/2-1, d/2)}(\xi) \sim (1+\xi)^n - \frac{n(d+2n)}{d+2n-1} (1+\xi)^{n-1} + \dots \tag{3.28}$$

If one uses this representation for $P_i^{(\frac{d}{2}-1, \frac{d}{2})}, P_j^{(\frac{d}{2}-1, \frac{d}{2})}, P_k^{(\frac{d}{2}-1, \frac{d}{2})}$ to recover the coefficients of the two highest powers in \mathcal{Q}_{ijk} , one finds

$$\mathcal{Q}_{ijk} \sim (1+\xi)^{i+j+k+d+1} - \frac{(d+i+j+k+1)(3d+2i+2j+2k+2)}{3d+2i+2j+2k+1} (1+\xi)^{i+j+k+d} + \dots, \tag{3.29}$$

which exactly matches (3.28) with $n = l+1 = i+j+k+d+1$. Therefore, if one subtracts from \mathcal{Q}_{ijk} its projection on $P_{l+1}^{(d/2-1, d/2)}$, the remaining polynomial is of degree $l-1$ and cannot have a non-zero projection on $P_l^{(d/2-1, d/2)}$. Then, from (3.27),

$$Q_{ijkl} = 0. \tag{3.30}$$

⁶One could have skipped directly from (3.21) to (3.26), though the integrands would have involved more derivatives than what we get after having performed the integrations by parts and are less convenient to handle. For the case of $+ -$ terms we consider below, the integrations by parts we have described are necessary to establish the analog of (3.26).

⁷Each of the types of terms listed under (3.26) is individually of this form.

We have thus proved that all secular terms resulting from addition of three mode frequencies vanish for non-linear perturbation theory in the AdS background, even if the said combination of frequencies resonates with another perturbation mode. In relation to our proof sketched above, it remains only to comment on how one in practice computes the polynomial $\mathcal{Q}_{ijk}(\xi)$ in (3.27), and thus establishes (3.29).

The computation reconstructing $\mathcal{Q}_{ijk}(\xi)$ in (3.27) is, in principle, a completely straightforward polynomial manipulation, but it is the forbiddingly large size of the polynomial expressions that makes the manipulations demanding. For the special case $i = j = k$, we have been able to do the entire computation by hand and derive (3.29). However, for arbitrary i, j and k one has to either invent powerful analytic tricks, perform pages upon pages of completely mechanical polynomial manipulations, or resort to (fully analytic) computer algebra. For the purposes of this article, we have chosen the latter and employed FORM, a powerful script-based symbolic manipulation system particularly suited for working with long polynomial expressions [17]. Our FORM script, essentially retracing the steps presented above in this section, is given in appendix B. (3.29) can be read off from the output of that script, thereby completing our proof.

We now turn to the $+-$ terms with $\omega_i - \omega_j - \omega_k = \omega_l$. These terms vanish in a way very similar to what we have just observed for the $+++$ terms. The corresponding contribution to the source S_l is given by

$$S_l = (\dots) + \sum_j \sum_k U_{(j+k+l+d)jkl} a_{j+k+l+d} a_j a_k \cos(\theta_{j+k+l+d} - \theta_j - \theta_k) \quad (3.31)$$

with the following coefficients:

$$\begin{aligned} U_{ijkl} = & \frac{1}{4} H_{ijkl} \frac{\omega_j(2\omega_j - \omega_i + \omega_k)}{(\omega_i - \omega_j)(\omega_j + \omega_k)} + \frac{1}{4} H_{jkil} \frac{\omega_k(2\omega_k - \omega_i + \omega_j)}{(\omega_i - \omega_k)(\omega_k + \omega_j)} + \frac{1}{4} H_{kijl} \frac{\omega_i(\omega_j + \omega_k - 2\omega_i)}{(\omega_i - \omega_j)(\omega_i - \omega_k)} \\ & - \frac{1}{2} X_{ijkl} \omega_j \omega_k \left(\frac{\omega_k}{(\omega_i - \omega_j)} + \frac{\omega_j}{(\omega_i - \omega_k)} - 1 \right) + \frac{1}{2} X_{jkil} \omega_i \omega_k \left(\frac{\omega_k}{(\omega_i - \omega_j)} + \frac{\omega_i}{(\omega_k + \omega_j)} - 1 \right) \\ & + \frac{1}{2} X_{kijl} \omega_i \omega_j \left(\frac{\omega_i}{(\omega_j + \omega_k)} + \frac{\omega_j}{(\omega_i - \omega_k)} - 1 \right) \\ & - \frac{1}{4} Z_{ijkl}^+ \frac{\omega_k}{(\omega_i - \omega_j)} + \frac{1}{4} Z_{jkil}^- \frac{\omega_i}{(\omega_j + \omega_k)} - \frac{1}{4} Z_{kijl}^+ \frac{\omega_j}{(\omega_i - \omega_k)}. \end{aligned} \quad (3.32)$$

One can show that $U_{ijkl} = 0$ whenever the resonance condition is satisfied, i.e., $i = j + k + l + d$, in other words, the $+-$ terms do not arise.

One can construct a proof that $U_{ijkl} = 0$ essentially repeating the procedure we employed above for the $+++$ terms, except that the roles of i and l become interchanged. Performing appropriate integrations by parts using (3.23)–(3.24), one arrives at the following representation:

$$U_{ijkl} \sim \int_{-1}^1 P_i^{\left(\frac{d}{2}-1, \frac{d}{2}\right)}(\xi) \mathcal{U}_{jkl}(\xi) (1-\xi)^{\frac{d}{2}-1} (1+\xi)^{\frac{d}{2}} d\xi, \quad (3.33)$$

where $\mathcal{U}_{jkl}(\xi)$ is a polynomial of degree $j + l + k + d + 1 = i + 1$. Substituting explicit expressions for the mode functions, one finds that the coefficients of the two highest powers

in $\mathcal{U}_{jkl}(\xi)$ are in the same ratio as in $P_{i+1}^{(\frac{d}{2}-1, \frac{d}{2})}$ (in practice, we have used a FORM script to perform this polynomial evaluation, and the output of the script is given at the end of appendix B). $\mathcal{U}_{jkl}(\xi)$ is then orthogonal to $P_i^{(\frac{d}{2}-1, \frac{d}{2})}(\xi)$ and (3.33) vanishes, which completes our proof of the absence of the $+-$ secular terms.

It would be desirable to develop a more elegant and less computationally intensive proof of the vanishing of the $+++$ and $+-$ terms, and indeed understand the qualitative reason for these terms to vanish. In section 3.5 we make some preliminary comments on the relation between the absence of these classes of secular terms and abundance of quasiperiodic solutions to the full non-linear system.

3.4 Non-vanishing secular terms and renormalization flow

The non-vanishing ($++-$) resonant terms in the source S_l arise from resonances that have the form $\omega_i + \omega_j - \omega_k = \omega_l$ and are given by

$$\begin{aligned}
 S_l = (\dots) &+ T_l a_l^3 \cos(\theta_l + \theta_l - \theta_l) + \sum_{i, (i \neq l)} R_{il} a_i^2 a_l \cos(\theta_i + \theta_l - \theta_i) \\
 &+ \underbrace{\sum_{i, (i \neq l)} \sum_{j, (j \neq l)} S_{ij(i+j-l)} a_i a_j a_{i+j-l}}_{l \leq i+j} \cos(\theta_i + \theta_j - \theta_{i+j-l}), \quad (3.34)
 \end{aligned}$$

where (\dots) represents the non-resonant terms. The coefficients S_{ijkl} , R_{il} and T_l are given by

$$\begin{aligned}
 S_{ijkl} = &-\frac{1}{4} H_{ijkl} \omega_j \left(\frac{1}{\omega_j + \omega_i} + \frac{1}{\omega_j - \omega_k} \right) - \frac{1}{4} H_{jkil} \omega_k \left(\frac{1}{\omega_k - \omega_i} + \frac{1}{\omega_k - \omega_j} \right) \\
 &-\frac{1}{4} H_{kijl} \omega_i \left(\frac{1}{\omega_i + \omega_j} + \frac{1}{\omega_i - \omega_k} \right) + \frac{1}{2} X_{kijl} \omega_i \omega_j \left(\frac{\omega_j}{\omega_i - \omega_k} + \frac{\omega_i}{\omega_j - \omega_k} + 1 \right) \\
 &+ \frac{1}{2} X_{ijkl} \omega_j \omega_k \left(\frac{\omega_k}{\omega_j + \omega_i} + \frac{\omega_j}{\omega_k - \omega_i} - 1 \right) + \frac{1}{2} X_{jkil} \omega_k \omega_i \left(\frac{\omega_k}{\omega_i + \omega_j} + \frac{\omega_i}{\omega_k - \omega_j} - 1 \right) \\
 &+ \frac{1}{4} \left(\frac{\omega_k}{\omega_i + \omega_j} \right) Z_{ijkl}^- + \frac{1}{4} \left(\frac{\omega_i}{\omega_j - \omega_k} \right) Z_{jkil}^+ + \frac{1}{4} \left(\frac{\omega_j}{\omega_i - \omega_k} \right) Z_{kijl}^+, \quad (3.35)
 \end{aligned}$$

$$\begin{aligned}
 R_{il} = &\left(\frac{\omega_i^2}{\omega_l^2 - \omega_i^2} \right) (H_{liil} - 2\omega_i^2 X_{liil}) - \left(\frac{\omega_l^2}{\omega_l^2 - \omega_i^2} \right) (H_{ilil} - 2\omega_i^2 X_{ilil}) - \omega_i^2 X_{liil} \\
 &-\frac{1}{2} (H_{iill} + 2\omega_i^2 M_{lli}) + \omega_l^2 (X_{iill} + 2\omega_i^2 W_{lli}) - \omega_l^2 (\omega_i^2 P_{iil} + B_{iil}) \\
 &+ \left(\frac{\omega_i^2}{\omega_l^2 - \omega_i^2} \right) (Y_{illi} - Y_{lili} + \omega_l^2 (X_{illi} - X_{lili})), \quad (3.36)
 \end{aligned}$$

$$T_l = -\frac{3}{4} H_{lll} + \omega_l^2 X_{lll} - \omega_l^2 M_{lll} - \omega_l^2 B_{lll} + 2\omega_l^4 W_{lll} - \omega_l^4 P_{lll}. \quad (3.37)$$

As per (3.19), to convert these source terms to secular terms in the solution for $c_l^{(3)}$, one simply needs to replace all cosines by sines, and multiply by $t/(2\omega_l)$. From such an expression for the secular terms, retracing the steps between (2.18) and (2.22), one obtains the following renormalization flow equations for non-linear perturbation theory in the AdS

background at first non-trivial order:

$$\frac{2\omega_l}{\epsilon^2} \frac{dA_l}{dt} = - \sum_{\substack{i, (i \neq l) \\ l \leq i+j}} \sum_{j, (j \neq l)} S_{ij(i+j-l)l} A_i A_j A_{i+j-l} \sin(B_l + B_{i+j-l} - B_i - B_j), \quad (3.38)$$

$$\begin{aligned} \frac{2\omega_l A_l}{\epsilon^2} \frac{dB_l}{dt} = & -T_l A_l^3 - \sum_{i, (i \neq l)} R_{il} A_i^2 A_l \\ & - \sum_{\substack{i, (i \neq l) \\ l \leq i+j}} \sum_{j, (j \neq l)} S_{ij(i+j-l)l} A_i A_j A_{i+j-l} \cos(B_l + B_{i+j-l} - B_i - B_j), \end{aligned} \quad (3.39)$$

where A_l and B_l are the (slowly) running renormalized amplitudes and phases, and the numerical coefficients T , R and S can be read off (3.3), (3.8), (3.18), (3.35)–(3.37).

3.5 Renormalization flow and quasi-periodic solutions

Numerical investigations of [7–14] have revealed a complex interplay between stability and instability depending on the shape of the initial AdS perturbation. We feel that this feature finds a reflection in the weakly non-linear perturbation theory, since, despite the fact that the frequency spectrum is fully resonant (and thus, for example, no orbits at all are protected from instability by the KAM theorem), only a subset of possible secular terms (an correspondingly, energy transfer channels in the renormalization flow equations) actually appear.

To make this more precise, we revisit the perturbative analysis of quasiperiodic solutions in [14]. In that article, ‘Two-Time Framework’ equations identical to our (3.38)–(3.39) were derived. The coefficients were not given analytic expressions, but rather evaluated explicitly using a computer for a system truncated to low-lying modes. The vanishing of the +++ and +-- secular term, for which we have given an analytic proof in section 3.3, was of course observed (for a particular set of low-lying modes) in the results of those direct evaluations. The authors then asked whether their ‘Two-Time Framework’ equation predict solutions that remain quasi-periodic for times of order $1/\epsilon^2$ (which is the validity range of the resummed perturbation theory).

We can ask the same quasi-periodicity question in the context of our system (3.38)–(3.39), and also contemplate how the presence of more general terms in (3.38)–(3.39) would have affected the abundance of quasi-periodic solutions. More general terms in (3.38)–(3.39) could be there given the frequency spectrum of AdS perturbation but are in fact absent due to the vanishing of some classes of secular terms specific to the AdS background, which we have analyzed in section 3.3.

Quasiperiodicity in the language of (3.38)–(3.39) simply means that the renormalized amplitudes A_l are constant. In that case, there is no significant energy transfer between the modes (small energy oscillations are produced by non-secular terms in perturbation theory), and the only significant effect of non-linearities on the evolution is the linear drift of the renormalized phases B_l due to (3.39) which is nothing but a Poincaré-Lindstedt frequency shift. (This picture of quasi-periodic motion in a non-linear non-integrable system

is familiar from the KAM theory, though the fully resonant frequency spectrum we are dealing with is exactly the opposite of the KAM theory assumptions.)

A_l in (3.38) will vanish if

$$B_l + B_{i+j-l} - B_i - B_j = 0 \quad (3.40)$$

for all l, i, j . As observed already in [14], this is solved by

$$B_j = B_0 + j(B_1 - B_0), \quad (3.41)$$

where B_0 and B_1 can be arbitrary. One then substitutes this relation into (3.39) and obtains a system of algebraic equations for B_0, B_1 and A_l . As pointed out in [14], if one truncates this system to a finite subset of low-lying modes up to $j = j_{\max}$, one obtains $j_{\max} + 1$ equations for $j_{\max} + 3$ equations, giving a 2-parameter family of solutions, which actually becomes a 1-parameter family of essentially different quasi-periodic solutions after the obvious scaling symmetry $A_l(t) \rightarrow \xi A_l(t/\xi^2)$, $B_l(t) \rightarrow B_l(t/\xi^2)$ present in (3.38)–(3.39) is taken into account. (Removing the mode cut-off is subtle and we shall not attempt to do it carefully at present.)

What we would like to emphasize in the context of our study is that the situation would have changed if more general terms (that vanish specifically for the AdS case) were present on the right-hand side of (3.38). Such terms would have different dependences on phases. For example, the +++ terms of section 3.3 would have produced $\sin(B_l - B_i - B_j - B_{l-d-i-j})$ and the +- - terms would have produced $\sin(B_l + B_i + B_j - B_{l+i+j+d})$. Demanding these terms to vanish would produce more equations, in addition to (3.40), which can in general only be solved by

$$B_j = \frac{\omega_j}{\omega_0} B_0 = \left(1 + \frac{2j}{d}\right) B_0. \quad (3.42)$$

This equation contains only one free parameter, B_0 , whereas (3.41) contains two, B_0 and B_1 . Consequently, based on this simple counting we observe that the number of free parameters labelling different quasiperiodic solutions diminishes by one when general secular terms are present, compared to the AdS case, where the +++ and +- - term vanish. This observation gives some non-perturbative meaning to the restrictions on the type of secular terms appearing in the AdS perturbation theory. It would be good to make these ideas more precise.

Acknowledgments

We would like to thank Piotr Bizoń, Alex Buchel, Luis Lehner and Andrzej Rostworowski for useful discussions. The work of B.C. and J.V. has been supported by the Belgian Federal Science Policy Office through the Interuniversity Attraction Pole P7/37, by FWO-Vlaanderen through project G020714N, and by the Vrije Universiteit Brussel through the Strategic Research Program “High-Energy Physics.” The research of O.E. has been supported by Ratchadaphisek Sompote Endowment Fund. J.V. is supported by a PhD Fellowship of the Research Foundation Flanders (FWO).

A Calculation of S_l

In this section, we give details on the computation of $S_l = \langle S, e_l \rangle$. Before we start, we list some useful identities and definitions. From the equation $\ddot{c}_j + \omega_j^2 c_j = 0$ for the modes $c_j(t)$ it follows that $\frac{d}{dt}(\omega_j^2 c_j^2 + \dot{c}_j^2) = 0$. Therefore, we can define the constants

$$C_i = \omega_i^2 c_i^2 + \dot{c}_i^2. \quad (\text{A.1})$$

The equation for the modes also implies the identity

$$\frac{d}{dt}(\omega_j^2 c_i c_j + \dot{c}_i \dot{c}_j) = (\omega_j^2 - \omega_i^2) \dot{c}_j c_i. \quad (\text{A.2})$$

From the eigenfunction equation $\hat{L}e_j = \omega_j^2 e_j$, we have that $-(\mu e_j)' = \omega_j^2 \mu e_j$ such that

$$(\mu e_i e_j)' = (\mu e_i)' e_j + \mu e_i' e_j' = \mu(-\omega_i^2 e_i e_j + e_i' e_j'). \quad (\text{A.3})$$

We can take the permutation $i \leftrightarrow j$ of this expression and take proper linear combinations of these two expressions to obtain the identities

$$(\omega_j^2 - \omega_i^2) \mu e_j e_i = (\mu(e_i' e_j - e_j' e_i))' \quad (\text{A.4})$$

and

$$(\omega_j^2 - \omega_i^2) \mu e_j' e_i' = (\mu(\omega_j^2 e_i' e_j - \omega_i^2 e_j' e_i))'. \quad (\text{A.5})$$

Subtracting (3.12a) and (3.12b), we find that

$$A_2'(x, t) - \delta_2'(x, t) = \frac{\nu'(x)}{\nu(x)} A_2(x, t) = -\nu'(x) \int_0^x (\dot{\phi}_1(y, t)^2 + \phi_1'(y, t)^2) \mu(y) dy. \quad (\text{A.6})$$

Therefore

$$\begin{aligned} \langle (A_2' - \delta_2') \phi_1', e_l \rangle &= - \int_0^{\frac{\pi}{2}} dx \phi_1'(x, t) e_l(x) \mu(x) \nu'(x) \int_0^x dy (\dot{\phi}_1(y, t)^2 + \phi_1'(y, t)^2) \mu(y) \\ &= - \sum_{i=0}^{\infty} \sum_{j=0}^{\infty} \sum_{k=0}^{\infty} c_k(t) \int_0^{\frac{\pi}{2}} dx e_k'(x) e_l(x) \mu(x) \nu'(x) \\ &\quad \int_0^x dy \{ \dot{c}_i(t) \dot{c}_j(t) e_i(y) e_j(y) + c_i(t) c_j(t) e_i'(y) e_j'(y) \} \mu(y) \\ &= - \sum_{i=0}^{\infty} \sum_{\substack{j=0 \\ j \neq i}}^{\infty} \sum_{k=0}^{\infty} \frac{c_k(t)}{(\omega_j^2 - \omega_i^2)} \int_0^{\frac{\pi}{2}} dx e_k'(x) e_l(x) (\mu(x))^2 \nu'(x) \\ &\quad \{ (\dot{c}_i(t) \dot{c}_j(t) + \omega_j^2 c_i(t) c_j(t)) e_i'(x) e_j(x) - (\dot{c}_i(t) \dot{c}_j(t) + \omega_i^2 c_i(t) c_j(t)) e_j'(x) e_i(x) \} \\ &\quad - \sum_{i=0}^{\infty} \sum_{k=0}^{\infty} c_k(t) \int_0^{\frac{\pi}{2}} dx e_k'(x) e_l(x) \mu(x) \nu'(x) \left\{ c_i^2(t) e_i'(x) e_i(x) \mu(x) + C_i \int_0^x dy (e_i(y))^2 \mu(y) \right\} \\ &= -2 \sum_{i=0}^{\infty} \sum_{\substack{j=0 \\ j \neq i}}^{\infty} \sum_{k=0}^{\infty} \frac{c_k(t) H_{ijkl}}{(\omega_j^2 - \omega_i^2)} (\dot{c}_i(t) \dot{c}_j(t) + \omega_j^2 c_i(t) c_j(t)) - \sum_{i=0}^{\infty} \sum_{k=0}^{\infty} c_k(t) \{ c_i^2(t) H_{iikl} + C_i M_{kli} \}. \end{aligned}$$

The integrals of the form $\int_0^x dy$ have been performed using the identities (A.3), (A.4), (A.5). Using (3.13), we can proceed in a similar fashion to obtain

$$\begin{aligned}
 \langle A_2 \ddot{\phi}_1, e_l \rangle &= - \int_0^{\frac{\pi}{2}} dx \ddot{\phi}_1(x, t) e_l(x) \mu(x) \nu(x) \int_0^x dy \left(\dot{\phi}_1(y, t)^2 + \phi_1'(y, t)^2 \right) \mu(y) \\
 &= - \sum_{i=0}^{\infty} \sum_{j=0}^{\infty} \sum_{k=0}^{\infty} \ddot{c}_k(t) \int_0^{\frac{\pi}{2}} dx e_k(x) e_l(x) \mu(x) \nu(x) \\
 &\quad \int_0^x dy \left\{ \dot{c}_i(t) \dot{c}_j(t) e_i(y) e_j(y) + c_i(t) c_j(t) e_i'(y) e_j'(y) \right\} \mu(y) \\
 &= - \sum_{i=0}^{\infty} \sum_{\substack{j=0 \\ j \neq i}}^{\infty} \sum_{k=0}^{\infty} \frac{\ddot{c}_k(t)}{(\omega_j^2 - \omega_i^2)} \int_0^{\frac{\pi}{2}} dx e_k(x) e_l(x) (\mu(x))^2 \nu(x) \\
 &\quad \left\{ (\dot{c}_i(t) \dot{c}_j(t) + \omega_j^2 c_i(t) c_j(t)) e_i'(x) e_j(x) - (\dot{c}_i(t) \dot{c}_j(t) + \omega_i^2 c_i(t) c_j(t)) e_j'(x) e_i(x) \right\} \\
 &\quad - \sum_{i=0}^{\infty} \sum_{k=0}^{\infty} \ddot{c}_k(t) \int_0^{\frac{\pi}{2}} dx e_k(x) e_l(x) \mu(x) \nu(x) \left\{ c_i^2(t) e_i'(x) e_i(x) \mu(x) + C_i \int_0^x dy (e_i(y))^2 \mu(y) \right\} \\
 &= 2 \sum_{i=0}^{\infty} \sum_{\substack{j=0 \\ j \neq i}}^{\infty} \sum_{k=0}^{\infty} \frac{\omega_k^2 c_k(t) X_{ijkl}}{(\omega_j^2 - \omega_i^2)} (\dot{c}_i(t) \dot{c}_j(t) + \omega_j^2 c_i(t) c_j(t)) + \sum_{i=0}^{\infty} \sum_{k=0}^{\infty} \omega_k^2 c_k(t) \left\{ c_i^2(t) X_{iikl} + C_i W_{kli} \right\}.
 \end{aligned}$$

and

$$\begin{aligned}
 \langle \dot{A}_2 \dot{\phi}_1, e_l \rangle &= - \int_0^{\frac{\pi}{2}} dx \dot{\phi}_1(x, t) e_l(x) \mu(x) \nu(x) \int_0^x dy \frac{\partial}{\partial t} \left(\dot{\phi}_1(y, t)^2 + \phi_1'(y, t)^2 \right) \mu(y) \\
 &= - \sum_{i=0}^{\infty} \sum_{j=0}^{\infty} \sum_{k=0}^{\infty} \dot{c}_k(t) \int_0^{\frac{\pi}{2}} dx e_k(x) e_l(x) \mu(x) \nu(x) \\
 &\quad \int_0^x dy \frac{\partial}{\partial t} \left\{ \dot{c}_i(t) \dot{c}_j(t) e_i(y) e_j(y) + c_i(t) c_j(t) e_i'(y) e_j'(y) \right\} \mu(y) \\
 &= - \sum_{i=0}^{\infty} \sum_{\substack{j=0 \\ j \neq i}}^{\infty} \sum_{k=0}^{\infty} \frac{\dot{c}_k(t)}{(\omega_j^2 - \omega_i^2)} \int_0^{\frac{\pi}{2}} dx e_k(x) e_l(x) (\mu(x))^2 \nu(x) \\
 &\quad \frac{\partial}{\partial t} \left\{ (\dot{c}_i(t) \dot{c}_j(t) + \omega_j^2 c_i(t) c_j(t)) e_i'(x) e_j(x) - (\dot{c}_i(t) \dot{c}_j(t) + \omega_i^2 c_i(t) c_j(t)) e_j'(x) e_i(x) \right\} \\
 &\quad - \sum_{i=0}^{\infty} \sum_{k=0}^{\infty} \dot{c}_k(t) \int_0^{\frac{\pi}{2}} dx e_k(x) e_l(x) \mu(x) \nu(x) \frac{\partial}{\partial t} \left\{ c_i^2(t) e_i'(x) e_i(x) \mu(x) + C_i \int_0^x dy (e_i(y))^2 \mu(y) \right\} \\
 &= -2 \sum_{i=0}^{\infty} \sum_{j=0}^{\infty} \sum_{k=0}^{\infty} \dot{c}_k(t) c_i(t) \dot{c}_j(t) X_{ijkl}.
 \end{aligned}$$

In the last step, we have used the identity (A.2).

From (3.14), we can deduce that

$$\langle \delta_2 \ddot{\phi}_1, e_l \rangle = - \int_0^{\frac{\pi}{2}} dx \ddot{\phi}_1(x, t) e_l(x) \mu(x) \int_0^x dy \left(\dot{\phi}_1(y, t)^2 + \phi_1'(y, t)^2 \right) \mu(y) \nu(y)$$

$$\begin{aligned}
 &= - \int_0^{\frac{\pi}{2}} dy \left(\dot{\phi}_1(y, t)^2 + \phi_1'(y, t)^2 \right) \mu(y) \nu(y) \int_y^{\frac{\pi}{2}} dx \ddot{\phi}_1(x, t) e_l(x) \mu(x) \\
 &= - \sum_{k=0}^{\infty} \ddot{c}_k(t) \int_0^{\frac{\pi}{2}} dy \left(\dot{\phi}_1(y, t)^2 + \phi_1'(y, t)^2 \right) \mu(y) \nu(y) \left(\delta_{kl} - \int_0^y dx e_k(x) e_l(x) \mu(x) \right) \\
 &= \sum_{\substack{k=0 \\ k \neq l}}^{\infty} \frac{\ddot{c}_k(t)}{(\omega_l^2 - \omega_k^2)} \int_0^{\frac{\pi}{2}} dy \left(\dot{\phi}_1(y, t)^2 + \phi_1'(y, t)^2 \right) (\mu(y))^2 \nu(y) (e_k'(y) e_l(y) - e_l'(y) e_k(y)) \\
 &\quad - \ddot{c}_l(t) \int_0^{\frac{\pi}{2}} dy \left(\dot{\phi}_1(y, t)^2 + \phi_1'(y, t)^2 \right) \mu(y) \nu(y) \left(1 - \int_0^y dx (e_l(x))^2 \mu(x) \right) \\
 &= \sum_{\substack{k=0 \\ k \neq l}}^{\infty} \sum_{i=0}^{\infty} \sum_{j=0}^{\infty} \frac{\ddot{c}_k(t)}{(\omega_l^2 - \omega_k^2)} \int_0^{\frac{\pi}{2}} dy \{ \dot{c}_i(t) \dot{c}_j(t) e_i(y) e_j(y) + c_i(t) c_j(t) e_i'(y) e_j'(y) \} \\
 &\quad (\mu(y))^2 \nu(y) (e_k'(y) e_l(y) - e_l'(y) e_k(y)) \\
 &\quad - \sum_{i=0}^{\infty} \sum_{j=0}^{\infty} \ddot{c}_l(t) \int_0^{\frac{\pi}{2}} dy \{ \dot{c}_i(t) \dot{c}_j(t) e_i(y) e_j(y) + c_i(t) c_j(t) e_i'(y) e_j'(y) \} \\
 &\quad \mu(y) \nu(y) \left(1 - \int_0^y dx (e_l(x))^2 \mu(x) \right) \\
 &= - \sum_{\substack{k=0 \\ k \neq l}}^{\infty} \sum_{i=0}^{\infty} \sum_{j=0}^{\infty} \frac{\omega_k^2 c_k(t)}{(\omega_l^2 - \omega_k^2)} \{ \dot{c}_i(t) \dot{c}_j(t) (X_{kl ij} - X_{lk ij}) + c_i(t) c_j(t) (Y_{kl ij} - Y_{lk ij}) \} \\
 &\quad + \sum_{i=0}^{\infty} \sum_{j=0}^{\infty} \omega_l^2 c_l(t) \{ \dot{c}_i(t) \dot{c}_j(t) P_{ijl} + c_i(t) c_j(t) B_{ijl} \}.
 \end{aligned}$$

We have interchanged the integration $\int dx \int dy \rightarrow \int dy \int dx$ and then separated the integral $\int_y^{\frac{\pi}{2}} dx = \int_0^{\frac{\pi}{2}} dx - \int_0^y dx$.

In a similar way, we finally obtain

$$\begin{aligned}
 \langle \delta_2 \dot{\phi}_1, e_l \rangle &= - \int_0^{\frac{\pi}{2}} dx \dot{\phi}_1(x, t) e_l(x) \mu(x) \int_0^x dy \frac{\partial}{\partial t} \left(\dot{\phi}_1(y, t)^2 + \phi_1'(y, t)^2 \right) \mu(y) \nu(y) \\
 &= - \int_0^{\frac{\pi}{2}} dy \frac{\partial}{\partial t} \left(\dot{\phi}_1(y, t)^2 + \phi_1'(y, t)^2 \right) \mu(y) \nu(y) \int_y^{\frac{\pi}{2}} dx \dot{\phi}_1(x, t) e_l(x) \mu(x) \\
 &= - \sum_{k=0}^{\infty} \dot{c}_k(t) \int_0^{\frac{\pi}{2}} dy \frac{\partial}{\partial t} \frac{\partial}{\partial t} \left(\dot{\phi}_1(y, t)^2 + \phi_1'(y, t)^2 \right) \mu(y) \nu(y) \left(\delta_{kl} - \int_0^y dx e_k(x) e_l(x) \mu(x) \right) \\
 &= \sum_{\substack{k=0 \\ k \neq l}}^{\infty} \frac{\dot{c}_k(t)}{(\omega_l^2 - \omega_k^2)} \int_0^{\frac{\pi}{2}} dy \frac{\partial}{\partial t} \left(\dot{\phi}_1(y, t)^2 + \phi_1'(y, t)^2 \right) (\mu(y))^2 \nu(y) (e_k'(y) e_l(y) - e_l'(y) e_k(y)) \\
 &\quad - \dot{c}_l(t) \int_0^{\frac{\pi}{2}} dy \frac{\partial}{\partial t} \left(\dot{\phi}_1(y, t)^2 + \phi_1'(y, t)^2 \right) \mu(y) \nu(y) \left(1 - \int_0^y dx (e_l(x))^2 \mu(x) \right)
 \end{aligned}$$

$$\begin{aligned}
&= \sum_{\substack{k=0 \\ k \neq l}}^{\infty} \sum_{i=0}^{\infty} \sum_{j=0}^{\infty} \frac{\dot{c}_k(t)}{(\omega_l^2 - \omega_k^2)} \int_0^{\frac{\pi}{2}} dy \frac{\partial}{\partial t} \{ \dot{c}_i(t) \dot{c}_j(t) e_i(y) e_j(y) + c_i(t) c_j(t) e'_i(y) e'_j(y) \} \\
&\quad (\mu(y))^2 \nu(y) (e'_k(y) e_l(y) - e'_l(y) e_k(y)) \\
&\quad - \sum_{i=0}^{\infty} \sum_{j=0}^{\infty} \dot{c}_l(t) \int_0^{\frac{\pi}{2}} dy \frac{\partial}{\partial t} \{ \dot{c}_i(t) \dot{c}_j(t) e_i(y) e_j(y) + c_i(t) c_j(t) e'_i(y) e'_j(y) \} \\
&\quad \mu(y) \nu(y) \left(1 - \int_0^y dx (e_l(x))^2 \mu(x) \right) \\
&= \sum_{\substack{k=0 \\ k \neq l}}^{\infty} \sum_{i=0}^{\infty} \sum_{j=0}^{\infty} \frac{\dot{c}_k(t)}{(\omega_l^2 - \omega_k^2)} \frac{\partial}{\partial t} \{ \dot{c}_i(t) \dot{c}_j(t) (X_{klij} - X_{lkij}) + c_i(t) c_j(t) (Y_{klij} - Y_{lkij}) \} \\
&\quad - \sum_{i=0}^{\infty} \sum_{j=0}^{\infty} \dot{c}_l(t) \frac{\partial}{\partial t} \{ \dot{c}_i(t) \dot{c}_j(t) P_{ijl} + c_i(t) c_j(t) B_{ijl} \}.
\end{aligned}$$

Using all these expressions, we deduce from (3.15) the equation (3.17).

B FORM-based analysis of secular term coefficients

In this section we present our FORM script dealing with the +++ secular terms, which retraces the derivation steps given in section 3.3 and produces the following output, which should be matched to (3.29):

```

Secular =
+ P1*[3d+2i+2j+2k]*[(d+2i)(d+2j)(d+2k)]*[(3d+2i+2j+2k+1)eta^7-(d+i+j+k+
1)(3d+2i+2j+2k+2)eta^6] * ( 1 + [d+2i]^-1*[d+2j] + [d+2j]^-1*[d+2k] +
[d+2i]*[d+2k]^-1 );

```

The script, given below, is extremely straightforward, and should be reasonably easy to interpret even for readers completely unfamiliar with FORM programming. It starts with declaring an expression matching (3.21) up to normalization, and then applying a sequence of symbolic substitutions that implement integration by parts, re-expression through Jacobi polynomials, substituting the two highest order terms from each Jacobi polynomial, extracting the two highest-order terms of the entire (polynomial) expression, and finally, simplifying and factorizing the result. The lines starting with * are comments that do not affect the execution of the script.

```

Symbols d, P1, eta, [eta^7], [eta^6];
Symbols i, j, k, l, any1, any2, any3;
Symbols [d+2i], [d+2j], [d+2k], [3d+2i+2j+2k], [3d+2i+2j+2k+1], [3d+2i+2j+2k+2],
[d+2i-1], [d+2j-1], [d+2k-1], [d+i+j+k+1], [(d+2i)(d+2j)(d+2k)];
Symbols [eta^7(3d+2i+2j+2k+1)], [eta^6(d+i+j+k+1)(3d+2i+2j+2k+2)],
[(3d+2i+2j+2k+1)eta^7-(d+i+j+k+1)(3d+2i+2j+2k+2)eta^6];

```

```

CFunctions om, H, X, Ydiff, Z, E, D, e, epr, munu, tanx, P, Ppr;

* Secular = Qijkl multiplied with (omi+omj)(omj+omk)(omi+omk)

Local Secular=
-1/2*H(i,j,k,l)*om(j)*(om(i)+om(k))*(2*om(j)+om(i)+om(k))
-1/2*H(j,k,i,l)*om(k)*(om(i)+om(j))*(2*om(k)+om(i)+om(j))
-1/2*H(k,i,j,l)*om(i)*(om(j)+om(k))*(2*om(i)+om(j)+om(k))
+X(i,j,k,l)*om(j)*om(k)*(om(j)+om(k))*
  ((om(i)+om(j))*(om(i)+om(k))+om(k)*(om(i)+om(k))+om(j)*(om(i)+om(j)))
+X(j,k,i,l)*om(i)*om(k)*(om(i)+om(k))*
  ((om(i)+om(j))*(om(j)+om(k))+om(k)*(om(j)+om(k))+om(i)*(om(i)+om(j)))
+X(k,i,j,l)*om(i)*om(j)*(om(i)+om(j))*
  ((om(i)+om(k))*(om(j)+om(k))+om(i)*(om(i)+om(k))+om(j)*(om(j)+om(k)))
-1/2*Z(i,j,k,l)*om(k)*(om(i)+om(k))*(om(j)+om(k))
-1/2*Z(j,k,i,l)*om(i)*(om(i)+om(j))*(om(i)+om(k))
-1/2*Z(k,i,j,l)*om(j)*(om(i)+om(j))*(om(j)+om(k));

id Z(i?,j?,k?,l?)=om(i)*om(j)*(X(k,l,i,j)-X(l,k,i,j))-Ydiff(k,l,i,j);

* eliminating Y

id Ydiff(i?,j?,k?,l?)=(om(i)^2-om(j)^2)*X(k,l,i,j)+om(k)^2*(X(i,j,k,l)-X(j,i,k,l))
  -(H(i,j,k,l)-H(j,i,k,l));

id om(l)=om(i)+om(j)+om(k);
.sort

* integrating by parts to remove the derivatives from e_l

id X(l,i?,j?,k?)=-(X(i,j,k,l)+X(j,i,k,l)+X(k,i,j,l))-E(i,j,k,l);
id H(l,i?,j?,k?)=-(H(i,k,j,l)+H(k,i,j,l))+om(j)^2*D(i,j,k,l)+4*X(j,i,k,l);

* eta=1+cos2x

id H(i?,j?,k?,l?)=epr(i)*e(j)*epr(k)*e(l)*(-d+eta);
id X(i?,j?,k?,l?)=epr(i)*e(j)*e(k)*e(l)*munu(eta);
id E(i?,j?,k?,l?)=e(i)*e(j)*e(k)*e(l)*(d-2+eta);
id D(i?,j?,k?,l?)=e(i)*e(j)*e(k)*e(l)*(-d+eta);
.sort

* substituting the mode functions with the overall normalization stripped
* and divided by (cos x)^d

id e(i?)=P(i);
id epr(i?)=-d*tanx(eta)*P(i)-4*munu(eta)*Ppr(i);

id P(l)=Pl;

```

```

id munu(eta)^2= eta*(2-eta)/4;
id tanx(eta)^2 = (2-eta)/eta;
id tanx(eta)*munu(eta)=1-(eta/2);

* 2 leading terms for each Jacobi polynomial, divided by
* eta^(i-2), eta^(j-2), eta^(k-2), respectively
* overall normalization stripped

id P(i)=eta^2-i*([d+2i-1]+1)*[d+2i-1]^(-1)*eta;
id P(j)=eta^2-j*([d+2j-1]+1)*[d+2j-1]^(-1)*eta;
id P(k)=eta^2-k*([d+2k-1]+1)*[d+2k-1]^(-1)*eta;

id Ppr(i)=i*eta-i*(i-1)*([d+2i-1]+1)*[d+2i-1]^(-1);
id Ppr(j)=j*eta-j*(j-1)*([d+2j-1]+1)*[d+2j-1]^(-1);
id Ppr(k)=k*eta-k*(k-1)*([d+2k-1]+1)*[d+2k-1]^(-1);

* remove low powers

id eta^i?{<6}=0;
id eta^7=[eta^7];
id eta^6=[eta^6];
.sort

id om(i)=[d+2i-1]+1;
id om(j)=[d+2j-1]+1;
id om(k)=[d+2k-1]+1;

id i=([d+2i-1]+1-d)/2;
id j=([d+2j-1]+1-d)/2;
id k=([d+2k-1]+1-d)/2;
.sort

* inverse powers of [d+2i-1], [d+2j-1], [d+2k-1] have cancelled out

id [d+2i-1]=[d+2i]-1;
id [d+2j-1]=[d+2j]-1;
id [d+2k-1]=[d+2k]-1;
.sort

* proceed with factorizations

id [eta^7]*[d+2i]^any1?=[eta^7]*([3d+2i+2j+2k+1]-1-[d+2j]-[d+2k])^any1;
id [3d+2i+2j+2k+1]^any1?{>1}=[3d+2i+2j+2k+1]*([d+2i]+[d+2j]+[d+2k]+1)^(any1-1);
.sort

id [eta^6]*[d+2i]^any1?=[eta^6]*([3d+2i+2j+2k+2]-2-[d+2j]-[d+2k])^any1;
id [3d+2i+2j+2k+2]^any1?{>1}=[3d+2i+2j+2k+2]*([d+2i]+[d+2j]+[d+2k]+2)^(any1-1);
.sort

```

```

id [eta^6]*[d+2i]^any1?=[eta^6]*(2*[d+i+j+k+1]-2+d-[d+2j]-[d+2k])^any1;
id [d+i+j+k+1]^any1?{>1}=[d+i+j+k+1]*(( [d+2i]+[d+2j]+[d+2k]+2-d)/2)^(any1-1);
.sort

id [eta^6]*[d+i+j+k+1]*[3d+2i+2j+2k+2]=[eta^6(d+i+j+k+1)(3d+2i+2j+2k+2)];
id [eta^7]*[3d+2i+2j+2k+1]=[eta^7(3d+2i+2j+2k+1)];
.sort

id [eta^7(3d+2i+2j+2k+1)]=[ (3d+2i+2j+2k+1)eta^7-(d+i+j+k+1)(3d+2i+2j+2k+2)eta^6]
                               +[eta^6(d+i+j+k+1)(3d+2i+2j+2k+2)];
.sort

id [d+2k]=[3d+2i+2j+2k]-[d+2i]-[d+2j];
id [3d+2i+2j+2k]^any1?{>1}=[3d+2i+2j+2k]*([d+2i]+[d+2j]+[d+2k])^(any1-1);
.sort

id P1=P1*[(d+2i)(d+2j)(d+2k)]*[d+2i]^(-1)*[d+2j]^(-1)*[d+2k]^(-1);

Bracket P1, [(3d+2i+2j+2k+1)eta^7-(d+i+j+k+1)(3d+2i+2j+2k+2)eta^6],
            [3d+2i+2j+2k], [(d+2i)(d+2j)(d+2k)];

Print;
.end

```

(It may appear surprising that the output of our script is not manifestly symmetric under all permutations of i , j and k , even if the starting expression is. There is no contradiction here, however, since the integration by parts (3.23) we employ only preserves the permutation symmetry of the total integral expressions, but upsets some of the permutation symmetries of the integrands. In our case, since the end result of the integration is 0, it is trivially fully permutation-symmetric, even if an explicit formula for the integrand we give is not.)

We have also employed a very similar script, with the roles played by i and l interchanged and starting with (3.32) rather than (3.21), to analyze the $+-$ secular terms and derive the coefficients of the two highest powers in $\mathcal{U}_{jkl}(\xi)$ of (3.33), which can be read off from the following output (what matters for us is the ratio of the two coefficients, hence only the expression in the square brackets of the first line of the output is relevant):

```

Secular =
+ Pi*[(3d+2l+2j+2k+1)eta^7-(d+l+j+k+1)(3d+2l+2j+2k+2)eta^6] * ( 2*
  [d+2j]*[d+2k]^3 + 2*[d+2j]^2*[d+2k]^2 + 2*[d+2j]^3*[d+2k] + [d+2l]*
  [d+2k]^3 + [d+2l]*[d+2j]*[d+2k]^2 + 2*[d+2l]*[d+2j]^2*[d+2k] + [d+2l]
  *[d+2j]^3 - [d+2l]^2*[d+2k]^2 - [d+2l]^2*[d+2j]*[d+2k] + 2*[d+2l]^2*
  [d+2j]^2 + [d+2l]^3*[d+2j] );

```

Open Access. This article is distributed under the terms of the Creative Commons Attribution License ([CC-BY 4.0](https://creativecommons.org/licenses/by/4.0/)), which permits any use, distribution and reproduction in any medium, provided the original author(s) and source are credited.

References

- [1] L.D. Landau and E.M. Lifshitz, *Mechanics*, 3rd edition, Reed Publishing, (1981), pg. 86.
- [2] J.D. Logan, *Applied mathematics*, 3rd edition, John Wiley & Sons, (2006), pg. 93.
- [3] L.-Y. Chen, N. Goldenfeld and Y. Oono, *The renormalization group and singular perturbations: multiple scales, boundary layers and reductive perturbation theory*, *Phys. Rev. E* **54** (1996) 376 [[hep-th/9506161](#)] [[INSPIRE](#)].
- [4] V.I. Arnol'd, V.V. Kozlov and A.I. Neistadt, *Mathematical aspects of classical and celestial mechanics*, Springer, (1997).
- [5] Y. Nakayama, *Holographic interpretation of renormalization group approach to singular perturbations in nonlinear differential equations*, *Phys. Rev. D* **88** (2013) 105006 [[arXiv:1305.4117](#)] [[INSPIRE](#)].
- [6] S. Kuperstein and A. Mukhopadhyay, *Spacetime emergence via holographic RG flow from incompressible Navier-Stokes at the horizon*, *JHEP* **11** (2013) 086 [[arXiv:1307.1367](#)] [[INSPIRE](#)].
- [7] P. Bizon and A. Rostworowski, *On weakly turbulent instability of anti-de Sitter space*, *Phys. Rev. Lett.* **107** (2011) 031102 [[arXiv:1104.3702](#)] [[INSPIRE](#)].
- [8] O.J.C. Dias, G.T. Horowitz and J.E. Santos, *Gravitational turbulent instability of anti-de Sitter space*, *Class. Quant. Grav.* **29** (2012) 194002 [[arXiv:1109.1825](#)] [[INSPIRE](#)].
- [9] O.J.C. Dias, G.T. Horowitz, D. Marolf and J.E. Santos, *On the nonlinear stability of asymptotically anti-de Sitter solutions*, *Class. Quant. Grav.* **29** (2012) 235019 [[arXiv:1208.5772](#)] [[INSPIRE](#)].
- [10] M. Maliborski and A. Rostworowski, *Time-periodic solutions in an Einstein AdS-massless-scalar-field system*, *Phys. Rev. Lett.* **111** (2013) 051102 [[arXiv:1303.3186](#)] [[INSPIRE](#)].
- [11] A. Buchel, S.L. Liebling and L. Lehner, *Boson stars in AdS spacetime*, *Phys. Rev. D* **87** (2013) 123006 [[arXiv:1304.4166](#)] [[INSPIRE](#)].
- [12] J. Abajo-Arrastia, E. da Silva, E. Lopez, J. Mas and A. Serantes, *Holographic relaxation of finite size isolated quantum systems*, *JHEP* **05** (2014) 126 [[arXiv:1403.2632](#)] [[INSPIRE](#)].
- [13] M. Maliborski and A. Rostworowski, *What drives AdS unstable?*, *Phys. Rev. D* **89** (2014) 124006 [[arXiv:1403.5434](#)] [[INSPIRE](#)].
- [14] V. Balasubramanian, A. Buchel, S.R. Green, L. Lehner and S.L. Liebling, *Holographic thermalization, stability of AdS and the Fermi-Pasta-Ulam-Tsingou paradox*, *Phys. Rev. Lett.* **113** (2014) 071601 [[arXiv:1403.6471](#)] [[INSPIRE](#)].
- [15] J.A. Murdock, *Perturbations: theory and methods*, *SIAM*, (1987).
- [16] J. Shen, T. Tang and L.-L. Wang, *Spectral methods: algorithms, analysis and applications*, Springer, (2011).
- [17] J. Kuipers, T. Ueda, J.A.M. Vermaseren and J. Vollinga, *FORM version 4.0*, *Comput. Phys. Commun.* **184** (2013) 1453 [[arXiv:1203.6543](#)] [[INSPIRE](#)].

Holographic thermalization

V. Balasubramanian,¹ A. Bernamonti,² J. de Boer,³ N. Copland,² B. Craps,² E. Keski-Vakkuri,^{4,5}
 B. Müller,⁶ A. Schäfer,⁷ M. Shigemori,⁸ and W. Staessens²

¹*David Rittenhouse Laboratory, University of Pennsylvania, Philadelphia, Pennsylvania 19104, USA*

²*Theoretische Natuurkunde, Vrije Universiteit Brussel, and International Solvay Institutes, Pleinlaan 2, B-1050 Brussels, Belgium*

³*Institute for Theoretical Physics, University of Amsterdam, Science Park 904, Postbus 94485, 1090 GL Amsterdam, The Netherlands*

⁴*Helsinki Institute of Physics & Department of Physics, P. O. Box 64, FIN-00014 University of Helsinki, Finland,*

⁵*Department of Physics and Astronomy, Uppsala University, SE-751 08 Uppsala, Sweden*

⁶*Department of Physics & CTMS, Duke University, Durham, North Carolina 27708, USA*

⁷*Institut für Theoretische Physik, Universität Regensburg, D-93040 Regensburg, Germany*

⁸*Kobayashi-Maskawa Institute for the Origin of Particles and the Universe, Nagoya University, Nagoya 464-8602, Japan*

(Received 7 April 2011; published 25 July 2011)

Using the AdS/CFT correspondence, we probe the scale dependence of thermalization in strongly coupled field theories following a sudden injection of energy via calculations of two-point functions, Wilson loops, and entanglement entropy in $d = 2, 3, 4$. In the saddle-point approximation these probes are computed in AdS space in terms of invariant geometric objects—geodesics, minimal surfaces, and minimal volumes. Our calculations for two-dimensional field theories are analytical. In our strongly coupled setting, all probes in all dimensions share certain universal features in their thermalization: (1) a slight delay in the onset of thermalization, (2) an apparent nonanalyticity at the endpoint of thermalization, (3) top-down thermalization where the UV thermalizes first. For homogeneous initial conditions the entanglement entropy thermalizes slowest and sets a timescale for equilibration that saturates a causality bound over the range of scales studied. The growth rate of entanglement entropy density is nearly volume-independent for small volumes, but slows for larger volumes.

DOI: 10.1103/PhysRevD.84.026010

PACS numbers: 11.25.Tq, 12.38.Mh

I. INTRODUCTION**A. Motivation**

The observed nearly inviscid hydrodynamic expansion of the hot QCD matter produced in nuclear collisions at the Relativistic Heavy Ion Collider (RHIC) indicates that matter produced in these nuclear reactions is strongly coupled [1–3]. The inability of perturbation theory to account for this phenomenon has motivated studies of nonequilibrium dynamics in analytically tractable, strongly coupled gauge theories. The prototype of such theories is the maximally supersymmetric Yang-Mills theory in the large- N_c , large 't Hooft coupling limit, which is holographically dual to the classical limit of a superstring theory on the anti-de Sitter space $\text{AdS}_5 \times S^5$ background [4]. Hydrodynamical evolution with a minimal shear viscosity emerges naturally as late-time behavior in the longitudinal expansion of a thermal gauge plasma in this model [5,6]. In the dual supergravity theory, the thermal state of the gauge theory is represented by a black brane in the asymptotic AdS_5 space, and the near-equilibrium dynamics of the gauge theory giving rise to hydrodynamic behavior is mapped onto the dynamics of perturbations of the AdS_5 -black brane metric. A nice recent review on the holographic study of hot QCD matter, focused on equilibrium and near-equilibrium aspects, is [7].

While the near-equilibrium dynamics of the strongly coupled super-Yang-Mills (SYM) theory is well studied,

the process of thermalization itself is still poorly understood. The RHIC data demand that the time scale for equilibration of matter is considerably shorter than expected in the framework of perturbative approaches to thermalization [8,9]. The dearth of other nonperturbative tools for the description of the short prehydrodynamic stage of the nuclear collision motivates the use of the AdS/CFT correspondence to study thermalization of strongly coupled plasmas. Phenomenologically, the central rapidity region of a high energy collision turns out to be boost-invariant to a good approximation, so it is natural to consider boost-invariant configurations [6,10–12]. One interesting question is how thermal equilibrium is reached in such systems. This is the question we will address in the present paper, albeit in the case of translationally invariant plasmas.

We investigate the thermalization process not only in the strongly coupled $(3 + 1) = 4$ -dimensional super-Yang-Mills theory, but also in the analogous lower (2 and 3) dimensional field theories. This has several motivations. The first reason is that the 2-dimensional version, which is dual to classical (super-)gravity on AdS_3 space, admits analytical solutions and thus allows us to explore thermalization over a wide range of parameters. A second motivation is that some version of the 2-dimensional dual theory, $(1 + 1)$ dimensional super-Yang-Mills theory, can be formulated on a lattice and solved nonperturbatively [13,14]. Finally, the comparison of theories in different

dimensions makes it easier to distinguish generic aspects of thermalization of strongly coupled quantum field theories from aspects that are special features of 4-dimensional field theories.

B. Holographic models of thermalization

1. Thermalization scenarios

What is appropriately called the thermalization time may not only depend on the probe of the state of the field but also on the initial field configuration that evolves toward thermal equilibrium. Here one can distinguish between two broad classes of scenarios. The first class considers small perturbations around thermal equilibrium and asks how equilibrium is reached. For a gauge theory with a holographic dual, this approach amounts to studying the decay of small perturbations of an AdS-black brane geometry. This is conveniently studied in terms of the quasinormal modes of fields propagating in the black brane background [15]. The imaginary parts of the eigenvalues of these modes describe the thermal relaxation rates of various excitations, such as anisotropic perturbations of the stress-energy tensor. In the context of relativistic heavy-ion collisions, this approach is relevant for the study of viscous corrections to hydrodynamics and other transport processes in the presence of a thermal gauge theory plasma (see, e.g., [16] for a review).

The second class of scenarios considers the thermalization of an initial field configuration, which is generally far from equilibrium. Through the AdS/CFT correspondence, the approach to thermal equilibrium in the boundary gauge theory is related to the process of black hole formation in the bulk. In early work, before the motivation from RHIC experiments, the goal was to understand how black hole formation from a gravitational collapse of a shell of matter would be encoded in the field theory in the boundary [17–20]. Also, in more recent work, the initial conditions have usually been defined directly in the dual gravity theory—in most, if not all, of these cases the precise form of the initial condition is not known in terms of gauge theory excitations. Examples of such configurations are colliding gravitational shock waves [21], sheets of fundamental strings that may provide an AdS model of densely packed flux tubes [22], and sudden perturbations of the metric near the boundary that propagate into the bulk [11,23]. Motivated by the properties of the initial state of a relativistic heavy-ion collision, which contains two highly energetic nuclei, these scenarios have injecting energy into the AdS geometry at high momentum or short distance scales in common.

Some of these recent studies of gravitational collapse in AdS₅ started from translation invariant, but locally anisotropic perturbations of the metric near the boundary and followed their propagation into the bulk, ultimately resulting in the formation of an event horizon [11]. The initial anisotropy of the metric is dissipated by the black brane,

asymptotically resulting in viscous, boost-invariant scaling hydrodynamics on the boundary [12,24]. Gravitational collapse in AdS_{*d*+1} induced by a scalar field perturbation was studied in [23], most explicitly for the case of AdS₄, where the bulk equations of motion for gravity coupled to a massless scalar field were solved perturbatively for a small-amplitude scalar perturbation that propagates in from the AdS boundary. The perturbation was taken to be translationally invariant along the spatial directions of the boundary and to vanish outside of a short time interval. An interesting technical result is that for this translationally invariant collapse in AdS₄, the metric outside the infalling shell of matter coincides with a black brane metric to first nontrivial order in the perturbation [23]. This has the consequence that expectation values of local observables thermalize essentially instantaneously in the field theory dual to the infalling shell background.

Similarly to the approach of [23], in [25] the equilibrating field configuration was modeled by a homogeneous, infalling thin mass shell. The motivation for choosing such a configuration was that it naturally arises in the AdS dual description of the asymptotic limit of a transversely extended ensemble of flux tubes. Hence, in distinction to the matter shells in early work, the shell has tension which in part contributes to the collapse dynamics. The flux tubes represent the energy density deposited by the colliding leading gauge charges (i.e. the valence quarks of the colliding nuclei), and the AdS description involves a sufficiently simple geometry to admit analytic or semianalytic solutions. Our model does not allow us to study the approach to local isotropy and hydrodynamical behavior, but it enables us to investigate the approach of the field to a thermal configuration in momentum space and to measure the growth of its entanglement entropy, as discussed in Secs. II C and III C. In this sense, our present study is complementary to those mentioned above which focus on the approach to the hydrodynamical limit. Note that the work [25] considered a quasistatic approximation with metrics that correspond to stationary “snapshots” of the dynamic geometry containing the infalling mass shell. Here we study both the dynamic and the quasistationary geometries and show that there are some significant differences in the pictures that they yield of thermalization. Various aspects of the dynamic case of a thin infalling shell have been investigated in [26–28]. The effect of a dynamical boundary condition has also been studied in the background of a moving mirror [29]. New techniques for the evaluation of various Green functions in nonequilibrium backgrounds have been developed in [30], in addition to the complex contour approach by [31]. The counterpart to the Chandrasekhar limit for a gravitational collapse of a degenerate star to a black hole in AdS/CFT has been investigated in [32]. Finally, thermalization after a quantum quench (a sudden change in the parameters of the Hamiltonian) in gauge theory has also been modeled by

a sudden change in couplings or other background fields than the bulk metric [33,34]. In the probe brane approach such a change then can manifest as time dependence in the induced metric on the brane.

Concretely, we focus on the $(d + 1)$ -dimensional infalling shell geometry described in Poincaré coordinates by the Vaidya metric

$$ds^2 = \frac{1}{z^2} [-(1 - m(v)z^d)dv^2 - 2dzdv + d\mathbf{x}^2], \quad (1)$$

where v labels ingoing null trajectories and we have set the AdS radius equal to 1. The boundary spacetime is located at $z = 0$ and $\mathbf{x} = (x_1, \dots, x_{d-1})$ correspond to the spatial coordinates on the boundary. For constant $m(v) = M$, the coordinate transformation

$$dv = dt - \frac{dz}{1 - Mz^d} \quad (2)$$

brings the metric (1) in the form

$$ds^2 = \frac{1}{z^2} \left[-(1 - Mz^d)dt^2 + \frac{dz^2}{1 - Mz^d} + d\mathbf{x}^2 \right]. \quad (3)$$

On the boundary, the coordinates v and t coincide. We take the mass function of the infalling shell to be

$$m(v) = \frac{M}{2} \left(1 + \tanh \frac{v}{v_0} \right), \quad (4)$$

where v_0 parametrizes the thickness of the shell falling along $v = 0$. We will often be interested in the zero thickness limit $v_0 \rightarrow 0$. The Vaidya metric describes a shell composed of tensionless null dust, which represents an analytical simplification of the tensionful shell models studied in [25] and of the model of [23].

The geometry outside the infalling shell (which corresponds to $v > 0$ in the zero thickness limit) is identical to that of an AdS-black brane geometry with Hawking

temperature $T = dM^{1/d}/4\pi$, while the geometry inside the shell ($v < 0$ when $v_0 \rightarrow 0$) is the same as that of pure AdS geometry. The causal structure of the Vaidya spacetime is shown in Fig. 1.

2. Probes of thermalization

In order to probe the dynamics of the thermalization process, one can study a variety of observables of the boundary gauge theory. Expectation values of local gauge-invariant operators, such as the energy-momentum tensor and its derivatives provide valuable information about the applicability of viscous hydrodynamics, but they cannot be used to explore deviations from thermal equilibrium in detail. Nonlocal observables such as pair correlation functions, Wilson loop expectation values, and entanglement entropy provide much more information about progress towards thermalization. (They are also relevant to the physics probed in relativistic heavy-ion collisions, e.g., through the jet quenching parameter \hat{q} [35,36] and the color screening length.)

To illustrate, consider spatially homogeneous states of a weakly interacting massless scalar field. The energy-momentum tensor can be expressed as

$$T^{\mu\nu} = \int \frac{d\mathbf{k}}{k^0} k^\mu k^\nu n(\mathbf{k}), \quad (5)$$

where $n(\mathbf{k}) = \langle a_{\mathbf{k}}^\dagger a_{\mathbf{k}} \rangle$ denotes the occupation number of a momentum mode of the scalar field. (There is no spatial dependence of the stress tensor because the field configuration is homogeneous here.) It is obvious from (5) that this observable contains only limited information about the particle distribution. In particular, $T^{\mu\nu}$ cannot inform us whether thermal equilibrium has been reached; it only tells us whether the pressure is locally isotropic. This is not even a sufficient condition for the matching of the field theory to hydrodynamics, because the equation of state relies on the assumption of thermal occupation numbers for the various modes. It is also insufficient to answer many other questions, e.g., about the expected spectrum of radiation emitted by collisions among the scalar particles. The equal-time two-point function, on the other hand, is given by

$$G(\mathbf{x}) = \int \frac{d\mathbf{k}}{k^0} [n(\mathbf{k}) + 1] \exp(i\mathbf{k} \cdot \mathbf{x}), \quad (6)$$

which allows us to extract detailed information about the particle distribution and thus probe its closeness to a thermal distribution in detail. Note that even the two-point function is insufficient to probe for the phase relationship between the occupation amplitudes of different field modes. This information can, however, be obtained by an analysis of the four-point function of the field.

In an interacting quantum field theory, the two-point function is determined not only by the mode occupation numbers $n(\mathbf{k})$ but also by the spectral density function $\sigma(k^0, \mathbf{k})$. For the free field, $\sigma(k) = 2\pi\delta(k^2 - m^2)$, but

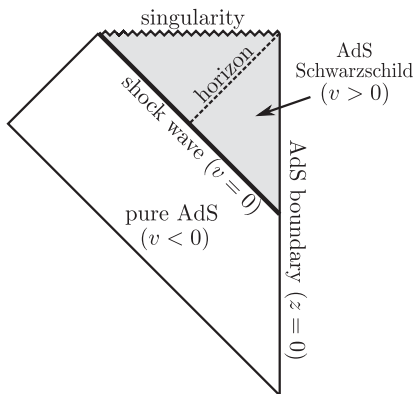


FIG. 1. The causal structure of the Vaidya spacetime (in the $v_0 \rightarrow 0$ limit) shown in the Poincaré patch of AdS space. In this presentation, the asymptotic boundary (vertical line on the right hand side) is planar and the null lines on the left hand side of the diagram represent the Poincaré horizon.

more generally the spectral function is determined by the exact self-energy $\Pi(k^0, \mathbf{k})$ as follows:

$$\sigma(k^0, \mathbf{k}) = \frac{2\text{Im}\Pi(k^0, \mathbf{k})}{[(k^0)^2 - \mathbf{k}^2 - m^2 - \text{Re}\Pi(k^0, \mathbf{k})]^2 + \text{Im}\Pi(k^0, \mathbf{k})^2}. \quad (7)$$

Since the self-energy is a function of the temperature, so is the spectral density function. For a weakly coupled field, the medium dependence is reflected, e.g., in medium modifications of particle masses and widths. In the strongly coupled gauge theory, the vacuum spectral function has the generic form [37]

$$\sigma(k^0, \mathbf{k}) \sim ((k^0)^2 - \mathbf{k}^2)^\nu \theta((k^0)^2 - \mathbf{k}^2), \quad (8)$$

where the exponent ν depends on the dimension of the considered field. This becomes a sigmoidal function at finite temperature. The mode occupation number $n(\mathbf{k})$ and the spectral function $\sigma(k^0, \mathbf{k})$ combine multiplicatively to yield the true, physical excitation probability of a momentum mode \mathbf{k} . The time evolution of the equal-time two-point function probes the approach of this excitation probability to thermal equilibrium.

In the AdS/CFT correspondence there is a geometric intuition for why expectation values of local gauge-invariant operators are insensitive to details of the progress towards thermalization—they are only sensitive to phenomena near the AdS boundary. Thus, they do not probe the details of phenomena occurring near the thermal scale. By contrast, nonlocal objects, such as two-point correlators of gauge-invariant operators and expectation values of Wilson loops, are dual to AdS quantities that probe deeper into the spacetime and further away from the boundary. For example, at strong 't Hooft coupling, it is possible to approximate the path integral for the connected two-point correlator as a sum over all possible AdS geodesics connecting the two endpoints, which are placed on the AdS boundary [38]. (For certain subtleties regarding this statement, see [39–41].) The geodesics probe the interior of AdS space, which is dual to the statement that they are sensitive to a wide range of energy scales in the boundary field theory. As we will see, Wilson loop expectation values [42] and entanglement entropy [26,43,44] are also related to minimal lengths, surfaces, and volumes of various kinds in AdS. These also extend into the bulk of AdS and hence probe a range of energy scales.

C. Overview of this work

We consider two-, three-, and four-dimensional field theories dual to gravity in asymptotically AdS₃, AdS₄, and AdS₅ spacetimes, respectively. The motivation for studying all these cases (rather than only the case of four-dimensional field theories potentially relevant for heavy-ion collisions) is that we are interested in generic conclusions on strongly coupled field theories with gravity duals. Lower dimensional theories are technically much

simpler: analytic computations are possible in AdS₃. Furthermore, our basic methods are similar in all dimensions—we calculate field theory observable that can be related to invariant geometric objects—minimal lengths, surfaces, and volumes—in AdS spacetimes of different dimensions. Our results show that many conclusions are not sensitive to the dimension.

Section II discusses three measures of thermalization—two-point functions, Wilson loop expectation values, and entanglement entropy. We compute these observables at thermal equilibrium, and, in Sec. III we use deviations from these results as probes of incomplete thermalization by examining the duals to these observables in gravity backgrounds with infalling shells of matter in AdS₃, AdS₄, and AdS₅. The infalling shells of matter collapse to form black branes, representing the process of equilibration and thermalization in the dual field theory after a sudden injection of energy. In these dynamical backgrounds we compute nonlocal observables as a function of time and track the rate at which thermalization progresses for each observable at different spatial scales in the field theory. Section IV concludes the paper by summarizing our findings. An Appendix describes how the results would differ in a quasistatic approximation. A brief account of this work has appeared in [45].

One broad finding is that these models exhibit a “top-down” thermalization mechanism, see also [25]. We would like to stress that this is very much in contrast with the standard “bottom-up” paradigm [8] based on perturbative gauge theory. In the “bottom-up” scenario, hard quanta of the gauge field do not equilibrate directly by randomizing their momenta in two-body collisions, but they do so by radiating softer quanta, which gradually fill up the thermal phase space and equilibrate by collisions among themselves. In other words, infrared modes are the first to thermalize, and the thermalization proceeds gradually (“from the bottom-up”) to more energetic modes of the gauge field. The bottom-up scenario is closely linked to the infrared divergence of the splitting functions of gauge bosons and fermions in the perturbative gauge theory. This contrasts with the “democratic” splitting properties of excitations in the strongly coupled SYM theory, which favor an approximately equal sharing of energy and momentum [46,47]. We should therefore expect that the thermalization process proceeds quite differently in the strongly coupled gauge theory. The phase space for radiation and, at strong coupling, also the spectral weight (8) is largest for the most energetic quanta. They then divide their energy and momentum approximately equally among their siblings, leading to a rapid cascading down to a thermal distribution. This consideration suggests that the thermalization process more closely resembles a “top-down” scenario in which energetic gauge field modes equilibrate first and soft modes last. Further broad conclusions appear in Sec. IV.

It is appropriate here to comment on the differences and overlap between the current work and the recent related work in the literature. In [26,27], geodesics (or equivalently, entanglement entropy) in AdS₃ Vaidya were studied numerically for a thin but finite shell. In contrast, we also study geodesics in AdS₃ Vaidya analytically for an infinitesimally thin shell. In [28], Wilson loops (or equivalently, entanglement entropy) were studied in AdS₄ Vaidya, for the case of circular and rectangular loops. We do not only confirm their results but also study geodesics in AdS₄ Vaidya, which have not been closely investigated in the context of holographic thermalization as far as we know. Moreover, we study AdS₅ Vaidya geometries for the first time by computing geodesics, circular and rectangular Wilson lines, and entanglement entropy for spherical volumes on the boundary.

II. PROBES OF THERMALITY

We are interested in processes where energy is injected into a strongly coupled field theory and equilibrates over time. Thus we need probes that take *instantaneous* snapshots of the state of the system which can be compared to the thermally equilibrated state. As discussed above, expectation values of *local* gauge-invariant operators are insufficient. Thus, in this section we describe three non-local probes—two-point functions, Wilson loop expectation values, and entanglement entropy—which can be elegantly computed using geometric techniques in the AdS/CFT correspondence. We will show how these quantities computed in strongly coupled theory at thermal equilibrium differ from the corresponding quantities in the vacuum. In Sec. III we will use the same quantities as probes of thermalization following a sudden injection of energy, by comparing the instantaneous values of the probes with the values at thermal equilibrium.

A. Equal-time two-point functions

We begin our exploration with the equal-time two-point functions, which can be analytically calculated in two-dimensional conformal field theories at thermal equilibrium. We first remind the reader how the thermal occupation probabilities of momentum modes enter into the two-point function and how they are related to the spatial form of the equal-time Wightman function. We then explain how we generalize this approach to higher dimensional theories, where we can easily calculate the Wightman function in the saddle-point approximation.

1. Two-dimensional free scalar field in thermal equilibrium

We would like to understand how we can extract information about the thermalization process from the time dependence of the Wightman function

$$G_{\mathcal{O}}^{\gt}(t, \mathbf{x}; t', \mathbf{x}') = \langle \mathcal{O}(t, \mathbf{x}) \mathcal{O}(t', \mathbf{x}') \rangle, \quad (9)$$

where \mathcal{O} is a local operator of dimension Δ . As a warm-up exercise we consider the free massless scalar field in two dimensions with mode expansion

$$\begin{aligned} \phi(t, x) &= \phi(x^-, x^+) \\ &= \int_{k^+ \geq 0} \frac{dk^+}{2\pi} \left[\frac{1}{k^+} e^{-ik^+ x^-} a_{k^+}^\dagger + cc \right] \\ &\quad + \int_{k^- \geq 0} \frac{dk^-}{2\pi} \left[\frac{1}{k^-} e^{-ik^- x^+} \tilde{a}_{k^-}^\dagger + cc \right]. \end{aligned} \quad (10)$$

We defined the operators a_k^\dagger as dimensionless, which implies the commutation relation $[a_{k^+}, a_{k'^+}^\dagger] = k^+ \delta(k^+ - k'^+)$, etc. Employing the free spectral function $\sigma_0(k) = 2\pi \delta(k^2) = 2\pi \delta(k^+ k^-)$, this can be written as

$$\phi(x^-, x^+) = \int \frac{d^2 k}{(2\pi)^2} \sigma_0(k) e^{ik^+ x^- + ik^- x^+} b_{k^+, k^-}, \quad (11)$$

where for $k^+, k^- \geq 0$: $b_{k^+, 0} = a_{k^+}$, $b_{-k^+, 0} = a_{k^+}^\dagger$, $b_{0, k^-} = \tilde{a}_{k^-}$, $b_{0, -k^-} = \tilde{a}_{k^-}^\dagger$. Consider the dimension one operators $\partial^+ \phi$ or $\partial^- \phi$. The vacuum two-point function of $\partial^\pm \phi$ is time and space translation invariant, so we consider

$$\begin{aligned} G_{\pm}^{\gt}(x^\pm) &= \langle \partial^\pm \phi(0) \partial^\pm \phi(x^\pm) \rangle \\ &= \int_{k^\pm \geq 0} \frac{d^2 k}{(2\pi)^2} (k^\pm)^2 \sigma_0(k) e^{-ik^+ x^- - ik^- x^+} \\ &= \int_{k^\pm \geq 0} \frac{dk^\pm}{2\pi} k^\pm e^{-ik^\pm x^\pm} \sim \frac{1}{(x^\pm)^2}. \end{aligned} \quad (12)$$

For nonzero temperature, the spectral function of the free field remains unchanged, and we find

$$\begin{aligned} G_+^{\gt}(x^\pm; T) &= \int_{k^+ > 0} dk^+ k^+ (e^{-ik^+ x^-} (n(k^+) + 1) \\ &\quad + e^{ik^+ x^-} n(k^+)), \end{aligned} \quad (13)$$

where $n(k) = (e^{\beta k} - 1)^{-1}$ is the standard (Bose) thermal occupation number. This can be rewritten as

$$\int_{k^+} dk^+ e^{-ik^+ x^+} \frac{e^{\beta k^+}}{e^{\beta k^+} - 1} k^+ \sim \frac{1}{\beta^2 \sinh^2(\frac{\pi x^+}{\beta})}. \quad (14)$$

This is exactly the result expected from conformal invariance. The finite temperature computation is a computation on a Euclidean cylinder, which can be mapped to the complex plane using the exponential map, and we already know the answer on the plane. Undoing the coordinate transformation leads to the above two-point function.

2. Strongly interacting scalar field theory in equilibrium from AdS/CFT

For an interacting field theory the spectral function changes with temperature. As a preparatory example of an interacting two-dimensional thermal field theory defined by a gauge-gravity duality we consider the AdS₃ case, i.e., the Banados-Teitelboim-Zanelli (BTZ) black

hole, and make use of the results presented in [48]. Writing $\omega = (k^+ + k^-)/\sqrt{2}$ and $k = (k^+ - k^-)/\sqrt{2}$, the thermal Wightman function for a scalar field in such a theory is [48]

$$G^>(k) = i\left(1 - \coth\frac{\omega}{2T}\right)\text{Im}G_{\text{R}}(k) = \frac{-2i}{e^{\omega/T} - 1}\text{Im}G_{\text{R}}(k), \quad (15)$$

where G_{R} is the retarded Green's function and $-2\text{Im}G_{\text{R}}$ yields the spectral function. The precise form of the thermal retarded Green function depends on the dimension Δ of the field in the operator. For $\Delta = 1$, we have [48]

$$G_{\text{R}}(\omega, k) = \frac{1}{2\pi}\left[\psi\left(\frac{1}{2} - i\frac{\omega - k}{4\pi T}\right) + \psi\left(\frac{1}{2} - i\frac{\omega + k}{4\pi T}\right)\right]. \quad (16)$$

Using $\text{Im}\psi\left(\frac{1}{2} + iy\right) = \frac{\pi}{2}\tanh\pi y$ gives the spectral density of states as

$$\sigma(\omega, k) = -2\text{Im}G_{\text{R}}(\omega, k) = \frac{\sinh\frac{\omega}{2T}}{\cosh\frac{\omega}{2T} + \cosh\frac{k}{2T}}. \quad (17)$$

What can we learn from the equal-time Wightman function? One strategy is to use the vacuum subtracted Wightman function which at thermal equilibrium depends only on $\Delta t = t' - t$

$$\begin{aligned} G_{\text{sub}}^>(\Delta t, k; T) &= G^>(\Delta t, k; T) - G^>(\Delta t, k; T = 0) \\ &= \int \frac{d\omega}{2\pi} e^{-i\omega\Delta t} [G^>(\omega, k; T) - G^>(\omega, k; T = 0)]. \end{aligned} \quad (18)$$

Using the Bose occupation number density $n_B(\omega) = (e^{\omega/T} - 1)^{-1}$, the equal-time Wightman function ($\Delta t = 0$) is then

$$\begin{aligned} G_{\text{sub}}^>(0, k; T) &= i \int_{-\infty}^{\infty} \frac{d\omega}{2\pi} n_B(\omega) \sigma(\omega, k; T) \\ &\quad + i \int_{-\infty}^{\infty} \frac{d\omega}{2\pi} \theta(-\omega) \sigma(\omega, k; 0) \\ &= 2i \int_0^{\infty} \frac{d\omega}{2\pi} n_B(\omega) \sigma(\omega, k; T) \\ &\quad + i \int_0^{\infty} \frac{d\omega}{2\pi} [\sigma(\omega, k; T) - \sigma(\omega, k; 0)]. \end{aligned} \quad (19)$$

Inserting the explicit expressions, we obtain after some manipulations

$$\begin{aligned} G_{\text{sub}}^>(0, k; T) &= i \int_0^{\infty} \frac{d\omega}{2\pi} \left[\left(\frac{2}{e^{\omega/T} - 1} + 1 \right) \right. \\ &\quad \left. \times \frac{\sinh\frac{\omega}{2T}}{\cosh\frac{\omega}{2T} + \cosh\frac{k}{2T}} - 1 \right] + i \int_0^k \frac{d\omega}{2\pi} \\ &= -i \int_0^{\infty} \frac{d\omega}{2\pi} \frac{\cosh\frac{k}{2T}}{\cosh\frac{\omega}{2T} + \cosh\frac{k}{2T}} + i \frac{k}{2\pi}. \end{aligned} \quad (20)$$

Introducing the notation $\text{cosh}a = \coth(k/2T)$, and using the integral identity

$$\begin{aligned} \int_0^{\infty} \frac{d\omega}{2T} \left[\sinh a \cosh\frac{\omega}{2T} + \text{cosh}a \right]^{-1} \\ = \frac{1}{2} \ln \left| \frac{1 + \text{cosh}a}{1 - \text{cosh}a} \right| = \frac{k}{2T}, \end{aligned} \quad (21)$$

the final result reads

$$\begin{aligned} G_{\text{sub}}^>(k, T) &= G^>(0, k; T) - G^>(0, k; T = 0) \\ &= -\frac{i}{2\pi} \frac{k}{e^{k/T} - 1}. \end{aligned} \quad (22)$$

Having derived the functional form of the equal-time Wightman function for a thermally equilibrated state in AdS_3 , we ask what we could learn from the same function at nonequilibrium background. In that case time translation invariance is lost. As in the above, we could define a vacuum subtracted Wightman function $G_{\text{sub}}^>(t, k)$ now depending on the equal time $t = t'$ and expect that thermalization implies $G_{\text{sub}}^>(t, k) \rightarrow G_{\text{sub}}^>(k; T)$. This gives us a way to estimate equilibration times for different momentum scales k by analyzing how this limiting behavior is approached. The result (22), that the thermal contribution to the equal-time Wightman function of the two-dimensional field theory is proportional to the Bose distribution justifies a more complete investigation of the equilibration properties of the Wightman function in two and more dimensions. For this purpose, we now turn to the methods made available by the holographic duality between strongly coupled supersymmetric gauge theories and gravity theories. We will also analyze thermalization times at different scales, in the spirit of the above motivation, but the details will differ somewhat.

3. The geodesic approximation

While the approach described above would give detailed information regarding scale-dependent thermalization, there is a technical challenge for strongly coupled field theories, even if they have a dual description in terms of gravity in an AdS space. The easiest case is the two-dimensional field theory with a three-dimensional gravity dual. In this case, the thermal Wightman function in momentum space is known in closed form for operators of general conformal dimension Δ ($\Delta = 1$ was analyzed above) [48]. However, the integral with respect to ω that is needed to compute the equal-time Green function is sensitive to the ultraviolet completion of the theory and thus requires careful regulation. Thus, it would-be more convenient to directly compute the equal-time thermal Wightman function from the AdS_3 theory. The next simplest case involves three-dimensional field theories with an AdS_4 dual. In this case there is not even a closed form expression for the thermal Wightman function. Thus, we cannot pursue the approach discussed above analytically.

Furthermore, we are really interested in computing the equal-time Wightman function in a nonequilibrium setting in which matter collapsing in AdS to form a black hole models the thermalization of energy injected into the strongly interacting field theory. In this situation, there are no known analytic solutions for the Green functions in any dimension, and we have to resort to approximation schemes and/or numerical analysis.

An insightful approach is to probe the nonequilibrium state of the strongly coupled field theory with a very heavy operator whose Wightman function can be approximated in terms of AdS geodesics as described below. According to the AdS/CFT dictionary, a massive scalar field $\varphi(z, t, \mathbf{x})$ with mass m in $(d + 1)$ dimensions is dual to an operator $\mathcal{O}(t, \mathbf{x})$ of conformal dimension $\Delta(m, d) = \frac{1}{2}(d + \sqrt{d^2 + 4m^2})$ [4]. In coordinates where the boundary of AdS is at $z = 0$, the scalar field φ behaves like

$$\varphi(z, t, \mathbf{x}) = z^{d-\Delta} \phi_{(0)}(t, \mathbf{x}) + \dots + z^\Delta \phi_{(1)}(t, \mathbf{x}) + \dots, \quad (23)$$

where the ellipsis corresponds to subleading terms in the z expansion. In conformal field theory (CFT) language we interpret the non-normalizable mode $\phi_{(0)}(t, \mathbf{x})$ as the source to which $\mathcal{O}(t, \mathbf{x})$ couples and the normalizable mode $\phi_{(1)}(t, \mathbf{x})$ as the vacuum expectation value of the renormalized operator $\mathcal{O}^{\text{ren}}(t, \mathbf{x})$ [49],

$$\phi_{(1)}(t, \mathbf{x}) \sim \langle \mathcal{O}^{\text{ren}}(t, \mathbf{x}) \rangle. \quad (24)$$

The bare operator $\mathcal{O}(t, \mathbf{x})$ and the renormalized operator $\mathcal{O}^{\text{ren}}(t, \mathbf{x})$ are related to each other by

$$\mathcal{O}(t, \mathbf{x}) = z_0^\Delta \mathcal{O}^{\text{ren}}(t, \mathbf{x}), \quad (25)$$

where z_0 represents an IR bulk cutoff. Working with renormalized operators, instead of bare operators, ensures finite expressions when the cutoff z_0 is removed, since renormalized operators do not depend on the cutoff z_0 . A useful heuristic treatment can be found in, e.g., [50]. The two-point function $\langle \mathcal{O}(t', \mathbf{x}') \mathcal{O}(t, \mathbf{x}) \rangle$ is often computed using the on-shell (supergravity) action for φ , when the action is explicitly given and solutions to the wave equation can be readily computed.

However, for our purposes it is more convenient to follow [38] and to observe that the equal-time Green function can be computed via a path integral as

$$\langle \mathcal{O}(t, \mathbf{x}) \mathcal{O}(t, \mathbf{x}') \rangle = \int \mathcal{D}\mathcal{P} e^{i\Delta L(\mathcal{P})} \approx \sum_{\text{geodesics}} e^{-\Delta \mathcal{L}}. \quad (26)$$

The first expression sums over all paths that begin and end at the boundary points (t, \mathbf{x}) and (t, \mathbf{x}') , with $L(\mathcal{P})$ being the proper length of the path [$L(\mathcal{P})$ is imaginary for spacelike trajectories]. The second expression is a saddle-point approximation to the path sum as a sum over geodesics [38] (here \mathcal{L} is the real length of the geodesic between the boundary points). The latter approximation is effective when the probe operator is heavy so that $\Delta \gg 1$. It is

easy, to check, for example, that in the zero temperature theory modeled by empty AdS space, this formula gives the correct conformally invariant equal-time two-point function of the renormalized operator [38]

$$\langle \mathcal{O}^{\text{ren}}(t, 0) \mathcal{O}^{\text{ren}}(t, x_0) \rangle = \frac{1}{x_0^{2\Delta}}. \quad (27)$$

Some care is necessary in evaluating Lorentzian correlators using the geodesic approximation, because careful consideration of steepest descent contours of integration is generally necessary [39–41].

The geodesic length \mathcal{L} diverges due to contributions near the AdS boundary. Therefore, we define a renormalized length $\delta \mathcal{L} \equiv \mathcal{L} + 2 \ln(z_0/2)$, in terms of the cutoff z_0 , by removing the divergent part of the geodesic length in pure AdS [see Eq. (51) below]. The renormalized equal-time two-point function is

$$\langle \mathcal{O}(t, \mathbf{x}) \mathcal{O}(t, \mathbf{x}') \rangle_{\text{ren}} \sim e^{-\Delta \delta \mathcal{L}}. \quad (28)$$

The geodesic approach to computing equal-time correlators gives a clear indication for how thermalization proceeds in a strongly coupled theory with an AdS dual (Fig. 2). Consider injecting energy homogeneously into the field theory—we model this in the AdS theory by dropping in a shell of matter from infinity. As the shell progresses inward into AdS space, the spacetime outside the shell will be well described by the AdS-black brane metric (except within the shell itself), while the metric inside the shell will be well described by the empty AdS metric. Now consider the two-point function calculation using geodesics. If the two points are close together on the boundary, the associated geodesic will not penetrate very much into the bulk space, and thus will not cross the matter shell. Thus, at these separations the correlation function should look thermal, because a thermal field theory is modeled by a black brane background in AdS. At larger boundary separations, the associated geodesic will penetrate the shell and be “refracted” by it (Fig. 2) leading to deviations from thermality. As time passes, the shell will penetrate deeper into the bulk and thus an ever larger range of spatial scales in the field theory will have associated geodesics that do not penetrate the shell and hence have thermal correlators. Thus, we can come to a qualitative conclusion that thermalization proceeds top-down in this setup—ultraviolet, i.e., short distance, degrees of freedom thermalize first. In subsequent sections we will calculate the rates at which different spatial scales thermalize.

4. Two-point function for two-dimensional field theories in equilibrium: Analytic computation

In order to gain intuition for the two-point function in the geodesic approximation, we return to the case of two-dimensional boundary field theories. In order to obtain the thermal boundary-to-boundary Wightman function, we need to study spacelike geodesics in the thermal black

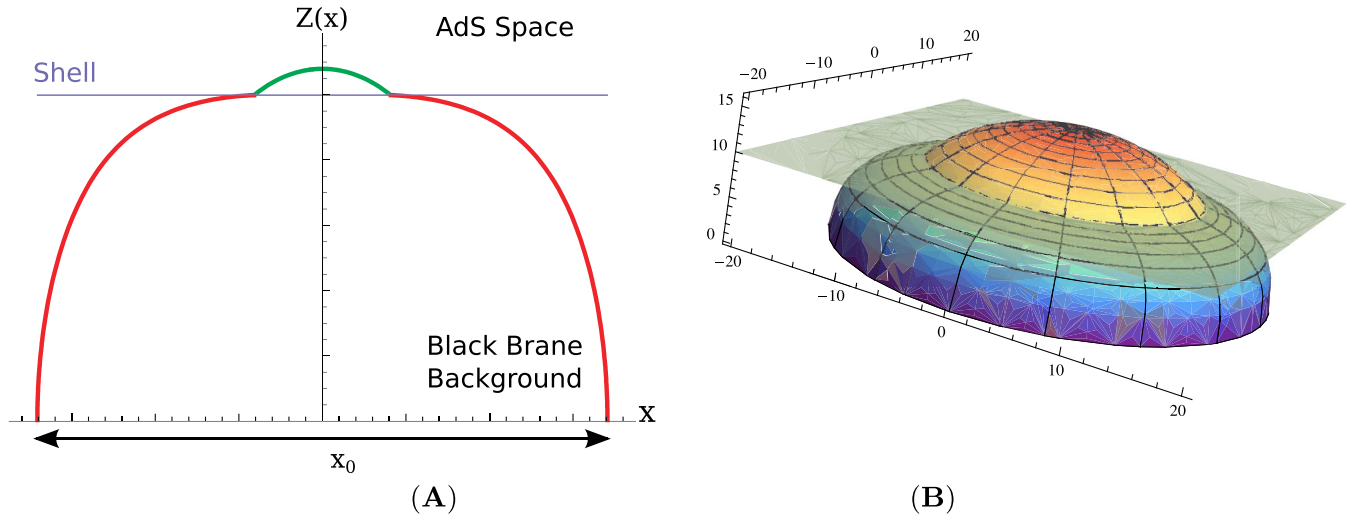


FIG. 2 (color online). (A) An example spacelike geodesic that starts and ends on the boundary of AdS ($z = 0$) with a separation x_0 . Outside the shell, the geodesic propagates in a black brane geometry, while inside it propagates in an empty AdS geometry. The shell refracts the geodesic. The Wightman function at scales associated to geodesics that do not penetrate the shell of matter will be thermalized. (B) The minimal surface in AdS space associated to a circular Wilson loop. The shell of matter (indicated in light green) refracts the surface. Loops with associated surfaces that never penetrate the shell of matter will be thermalized. Both figures illustrate a quasistatic situation where the geodesic or minimal surface lies entirely at a fixed time. When the shell is dynamically falling into AdS, the geodesic or minimal surface, while remaining spacelike, may not lie entirely within an equal-time surface. In both figures we are at late-time when the shell is close to where the event horizon would be, so that the “refraction” at the shell is clearly visible.

brane geometry in three dimensions. The metric is obtained by setting $m(v) = M$ in (1), and is given by

$$ds^2 = -(r^2 - r_H^2)dt^2 + \frac{dr^2}{r^2 - r_H^2} + r^2 dx^2, \quad \text{with} \quad (29)$$

$$t = v - \frac{1}{2r_H} \ln \frac{|r - r_H|}{r + r_H}, \quad r \equiv \frac{1}{z}. \quad (29)$$

This is a black brane geometry with a horizon at $r_H \equiv \sqrt{M}$ [51]. The Vaidya geometry in three dimensions with a constant $m(v) = M$ can be put in this form.

Parametrizing the geodesic by the geodesic length λ , the geodesic equations in the geometry (29) are

$$-r_H E = -(r^2 - r_H^2)\dot{t}, \quad (30)$$

$$r_H J = r^2 \dot{x}, \quad (31)$$

$$1 = -(r^2 - r_H^2)\dot{t}^2 + \frac{\dot{r}^2}{r^2 - r_H^2} + r^2 \dot{x}^2, \quad (32)$$

where E, J are constants and $\dot{} \equiv d/d\lambda$. Plugging (30) and (31) into (32) and solving for \dot{r} ,

$$\dot{r} = \pm \frac{1}{r} \sqrt{r^4 + (-1 + E^2 - J^2)r_H^2 r^2 + J^2 r_H^4}. \quad (33)$$

Integrating this, we obtain

$$r(\lambda)^2 = \frac{r_H^2}{4} [e^{\lambda - \lambda_0} + B_+ e^{-(\lambda - \lambda_0)}] [e^{\lambda - \lambda_0} + B_- e^{-(\lambda - \lambda_0)}] \quad (34)$$

or, equivalently,

$$r(\lambda)^2 - r_H^2 = \frac{r_H^2}{4} [e^{\lambda - \lambda_0} + A_+ e^{-(\lambda - \lambda_0)}] \times [e^{\lambda - \lambda_0} + A_- e^{-(\lambda - \lambda_0)}]. \quad (35)$$

Here, λ_0 is an integration constant which we will henceforth set to zero, $\lambda_0 = 0$, by absorbing it into the definition of the parameter λ . Also, we defined the combinations

$$A_{\pm} \equiv J^2 - (1 \pm E)^2, \quad B_{\pm} \equiv (J \pm 1)^2 - E^2. \quad (36)$$

The geodesic reaches the boundary $r = \infty$ (or $z = 0$) as $\lambda \rightarrow +\infty$.

As we can see from (34) and (35), the signs of A_{\pm}, B_{\pm} determine the behavior of the geodesic. The relation between the values of the parameters E, J and the signs of A_{\pm}, B_{\pm} is shown in Fig. 3. Note that not all possible combinations of signs occur. We discuss different cases (A)–(D) shown in Fig. 4 in turn below.

(i) If $A_{\pm}, B_{\pm} > 0$, the geodesic is entirely outside the horizon. $r(\lambda)$ takes its minimum value $r = r_H [1 + (A_+^{1/2} + A_-^{1/2})^2/4]^{1/2} > r_H$ at $\lambda_{\min} = (1/4) \ln(A_+ A_-)$ while $r(\lambda) \rightarrow \infty$ as $\lambda \rightarrow \pm\infty$. One sample profile of this case is shown in Fig. 4(a).

(ii) If $A_+ A_- < 0$ and $B_+ B_- < 0$, the geodesic crosses the horizon $r = r_H$ and reaches the singularity $r = 0$. Since in this case

$$\dot{r}(\lambda) = \frac{r_H}{2} \frac{e^{2\lambda} - A_+ A_- e^{-2\lambda}}{\sqrt{(e^{\lambda} + B_+ e^{-\lambda})(e^{\lambda} + B_- e^{-\lambda})}} > 0 \quad (37)$$

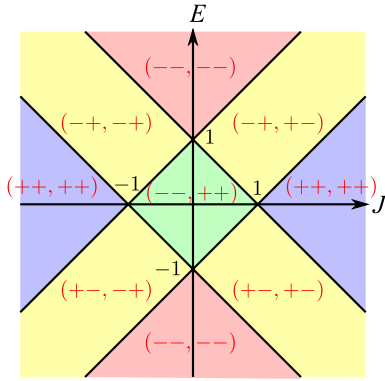


FIG. 3 (color online). The values of E , J and the signs of A_{\pm} , B_{\pm} . The signs of A_{\pm}, B_{\pm} are written in the form (A_+A_-, B_+B_-) . See text for the behavior of geodesics in each regime of parameters.

(recall that we have set $\lambda_0 = 0$), $r(\lambda)$ is a monotonically increasing function of λ and the geodesic crosses the horizon only once. One sample plot of this behavior is presented in Fig. 4(b).

- (iii) If $A_{\pm} < 0$ and $B_{\pm} > 0$, the geodesic crosses the horizon twice at

$$\lambda_{H\pm} = \frac{1}{2} \ln(-A_{\pm}) \quad (38)$$

but does not reach the singularity. One sample plot of this behavior is presented in Fig. 4(c).

- (iv) If $A_{\pm}, B_{\pm} < 0$, the geodesic crosses the horizon twice at (38) and furthermore hits the singularity twice at

$$\lambda_{O\pm} = \frac{1}{2} \ln(-B_{\pm}). \quad (39)$$

r is pure imaginary between λ_{O+} and λ_{O-} . One sample plot of this behavior is presented in Fig. 4(d).

If one is interested in geodesics that start and end on the boundary of the BTZ black brane geometry (29), the only relevant cases are (i) and (iii). However, if one is interested in geodesics in the Vaidya geometry (1) for which the BTZ geometry (29) is only a part of the entire spacetime, then one should also consider cases (ii) and (iv) since they can appear as a part of geodesics in the full spacetime.

Substituting (34) into (30) and (31) and integrating the two equations, we find the expressions for t and x :

$$t(\lambda) = t_0 + \frac{1}{2r_H} \ln \left| \frac{e^{\lambda} + A_+ e^{-\lambda}}{e^{\lambda} + A_- e^{-\lambda}} \right|, \quad (40)$$

$$x(\lambda) = x_0 + \frac{1}{2r_H} \ln \left(\frac{e^{\lambda} + B_- e^{-\lambda}}{e^{\lambda} + B_+ e^{-\lambda}} \right), \quad (41)$$

where t_0, x_0 are constants of integration corresponding the values of t, x at $\lambda = +\infty$. Comparing (40) with (35), it can be seen that the quantity inside the absolute value of (40) vanishes or diverges at the horizon $r = r_H$ and thus $t(\lambda)$ diverges there. This is due to the well-known fact that the Schwarzschild time t is not well-defined at the horizon. Note that $t(\lambda) \rightarrow \mp\infty$ as $\lambda \rightarrow \lambda_{H\pm}$ and therefore λ_{H+} (λ_{H-}) corresponds to the past (future) horizon.

On the other hand, the Eddington-Finkelstein coordinate v defined by

$$v(\lambda) = t(\lambda) + \frac{1}{2r_H} \ln \frac{|r(\lambda) - r_H|}{r(\lambda) + r_H} \quad (42)$$

[see (29)] is well-defined across the future horizon $\lambda = \lambda_{H-}$, because the log divergence in $t(\lambda)$ gets canceled by the second term of (42) and $v(\lambda)$ is finite across the future horizon. On the other hand, the divergence at the past horizon $\lambda = \lambda_{H+}$ is not canceled and $v(\lambda)$ diverges across the past horizon. The argument of the logarithm in (41), on the other hand, is always positive for $r > 0$; see (34).

The above parametric expression of r, t, x, v in terms of λ is useful for understanding the behavior of the geodesic, but for computational purposes it is useful to eliminate λ and write t, x, v as functions of r . Inverting the relation (34), we obtain the following two branches for $\lambda(r)$:

$$\lambda_{\pm}(r) = \frac{1}{2} \ln \left[-1 + E^2 - J^2 + \frac{2r^2}{r_H^2} \pm \frac{2}{r_H^2} \sqrt{D(r)} \right], \quad (43)$$

$$D(r) \equiv r^4 + (-1 + E^2 - J^2)r_H^2 r^2 + J^2 r_H^4.$$

Note that we have been setting $\lambda_0 = 0$. Substituting (43) into (40)–(42) and setting $x_0 = 0$, we get

$$t(r)_{\pm} = t_0 + \frac{1}{2r_H} \ln \left| \frac{r^2 - (E+1)r_H^2 \pm \sqrt{D(r)}}{r^2 + (E-1)r_H^2 \pm \sqrt{D(r)}} \right|, \quad (44)$$

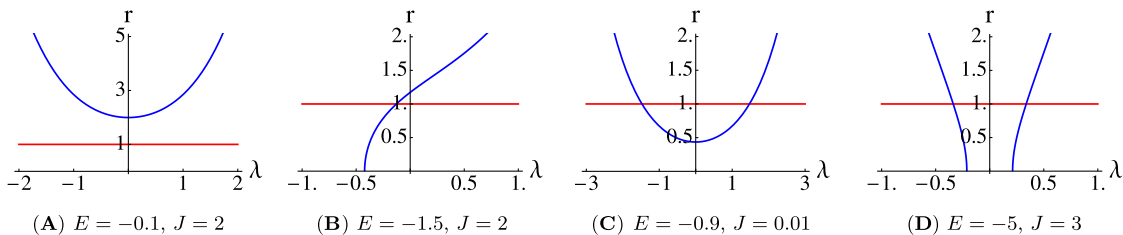


FIG. 4 (color online). Sample profiles of $r(\lambda)$ (in blue) in the AdS_3 black brane background. The event horizon $r_H = 1$ is shown as a red horizontal line in all four plots. The integration constant λ_0 appearing in (34) has been set to $\lambda_0 = -1/4 \ln(|A_+|/|A_-|)$.

$$x(r)_\pm = \frac{1}{2r_H} \ln \left[\frac{r^2 - Jr_H^2 \pm \sqrt{D(r)}}{r^2 + Jr_H^2 \pm \sqrt{D(r)}} \right], \quad (45)$$

$$v(r)_\pm = t_0 + \frac{1}{2r_H} \ln \left[\frac{r - r_H}{r + r_H} \frac{r^2 - (E+1)r_H^2 \pm \sqrt{D(r)}}{r^2 + (E-1)r_H^2 \pm \sqrt{D(r)}} \right]. \quad (46)$$

We will refer to the branch given by $(t(r)_+, x(r)_+, v(r)_+)$ as branch 1 and the one given by $(t(r)_-, x(r)_-, v(r)_-)$ as branch 2. Only by combining both branches can we recover the full geodesic described by (34), (40), and (41).

From (40) and (41), we can compute the coordinate difference between the two boundary points on which the geodesics end:

$$\begin{aligned} \Delta t &\equiv t(\lambda = -\infty) - t(\lambda = \infty) = \frac{1}{2r_H} \log \frac{A_+}{A_-} \\ &= \frac{1}{2r_H} \log \frac{J^2 - (1+E)^2}{J^2 - (1-E)^2}, \end{aligned} \quad (47)$$

$$\begin{aligned} \ell &\equiv x(\lambda = -\infty) - x(\lambda = \infty) = \frac{1}{2r_H} \log \frac{B_+}{B_-} \\ &= \frac{1}{2r_H} \log \frac{(J+1)^2 - E^2}{(J-1)^2 - E^2}. \end{aligned} \quad (48)$$

We see that geodesics connecting endpoints at the same time ($\Delta t = 0$) correspond to taking $E = 0$. If one is interested in such geodesics in the pure BTZ geometry, then we have only to consider the $E = 0$ case. However, in Sec. III, we will be interested in geodesics in the Vaidya geometry, which are composed of two pieces stretching, respectively, in AdS and BTZ, and glued together at the shell location. In this case, one should also consider $E \neq 0$ geodesics since they can appear as part of geodesics between equal-time endpoints in the full spacetime.

Now let us focus on the equal-time geodesics with $E = 0$ and compute the relation between the spatial boundary separation ℓ and the geodesic length $\mathcal{L}_{\text{thermal}}$ in the black brane background. By setting $E = 0$ in (48), ℓ is computed as

$$\ell = \frac{1}{r_H} \ln \frac{J+1}{J-1}, \quad \text{or} \quad J = \coth \frac{r_H \ell}{2}. \quad (49)$$

On the other hand, the geodesic length $\mathcal{L}_{\text{thermal}}$ is computed from (43) as

$$\begin{aligned} \mathcal{L}_{\text{thermal}} &= \lambda_+(r = r_0) - \lambda_-(r = r_0) \\ &= 2 \ln \frac{2r_0}{r_H \sqrt{|J^2 - 1|}} = 2 \ln \frac{2r_0 \sinh \frac{r_H \ell}{2}}{r_H}, \end{aligned} \quad (50)$$

where $r_0 = 1/z_0$ is the bulk IR cutoff and we dropped the $\mathcal{O}(1/r_0)$ quantity that vanishes as $r_0 \rightarrow \infty$. In the last equality, we used (49).

As discussed in Sec. II A 3, the geodesic length (50) is divergent in the $r_0 \rightarrow \infty$ limit and should be regularized by subtracting the corresponding divergent part of the quantity in pure AdS geometry. Because the pure AdS geometry can be obtained by setting $M \rightarrow 0$ or $r_H \rightarrow 0$ in the BTZ geometry (29), we can simply send $r_H \rightarrow 0$ in various quantities to obtain the corresponding quantities for pure AdS. By sending $r_H \rightarrow 0$ in (50), we obtain the geodesic length in pure AdS:

$$\mathcal{L}_{\text{pure AdS}} = 2 \ln(2r_0) + (\text{finite}). \quad (51)$$

Subtracting the divergent part of this from (50), we obtain

$$\delta \mathcal{L}_{\text{thermal}}(\ell) \equiv \mathcal{L}_{\text{thermal}} - 2 \ln(2r_0) = 2 \ln \frac{\sinh \frac{r_H \ell}{2}}{r_H}, \quad (52)$$

which allows us to compute the thermal renormalized two-point function defined in (28). Observe that the two-point function result computed in the geodesic approximation coincides with the weak coupling result (14) for $\Delta = 1$. Actually this is a consequence of conformal invariance, because the boundary CFT lives in noncompact space (namely, the x direction is not compactified in our setting).

We can also obtain the expression for the equal-time geodesic in pure AdS geometry by sending $r_H \rightarrow 0$ in (45). In doing this, we should send $J \rightarrow \infty$ at the same time because (49) becomes $J = 2/(r_H \ell)$. In this limit, (43) and (45) give

$$\lambda(r)_\pm = \pm \cosh^{-1} \frac{\ell r}{2}, \quad (53)$$

$$x(r)_\pm = \pm \frac{\ell}{2} \sqrt{1 - \left(\frac{2}{\ell r}\right)^2} = \pm \frac{\ell}{2} \sqrt{1 - \left(\frac{2z}{\ell}\right)^2}, \quad (54)$$

where we dropped constants. The second equation (54) says that the equal-time geodesic is a semicircle on the z - x plane,

$$z^2 + x^2 = \left(\frac{\ell}{2}\right)^2. \quad (55)$$

Note that the pure AdS results (51) and (53)–(55) are correct not only for $d = 2$ but for general dimensions, because it is only the z - x plane that is relevant for such geodesics.

5. Two-point function for $d \geq 2$ -dimensional field theories in equilibrium: numerical computation

In any dimension we can consider a Vaidya-type background (1) with constant mass function $m(v) = M$. This is a $(d+1)$ -dimensional black brane geometry, and in the special case of three dimensions it can be put in the form (29). We consider spacelike geodesics connecting the boundary points $(t, x_1) = (t_0, -\ell/2)$ and $(t', x'_1) = (t_0, \ell/2)$ of such black brane geometries [for $d = 3$, we also have $x_2 = x'_2$ and for $d = 4$, $(x_2, x_3) = (x'_2, x'_3)$]. If we

parametrize the geodesic in terms of the coordinate x_1 , which we will simply denote x in the rest of the section, the solution will be given by the profiles $v = v(x)$ and $z = z(x)$. Inserting the IR bulk cutoff z_0 , the boundary conditions read

$$z(-\ell/2) = z_0 = z(\ell/2), \quad v(-\ell/2) = t_0 = v(\ell/2), \quad (56)$$

and are symmetric with respect to the z and v axes. The geodesic length reads

$$\mathcal{L}_{\text{thermal}} = \int_{-\ell/2}^{\ell/2} dx \frac{\sqrt{1 - 2z'(x)v'(x) - (1 - Mz(x)^d)v'(x)^2}}{z(x)}, \quad (57)$$

with $l \equiv d/dx$. The action is not explicitly dependent on x , which implies the existence of a conserved quantity. The conservation equation reads

$$1 - 2z'v' - (1 - Mz^d)v'^2 = \left(\frac{z_*}{z}\right)^2, \quad (58)$$

where z_* is the value of $z(x)$ at the midpoint. Notice also that v is a cyclic coordinate, implying a conserved momentum. From Eq. (2), it follows

$$v = t_0 - \int_{z_0}^z \frac{d\tilde{z}}{1 - M\tilde{z}^d}. \quad (59)$$

Inserting the relation between v and z of Eq. (59) into the conservation equation (58) yields a first-order differential equation in terms of $z(x)$ only. We take the derivative of this equation with respect to x and solve the resulting second-order differential equation

$$z'' = -\frac{z^2}{z^3} + \frac{2-d}{2} Mz^{d-3} z_*^2 + \frac{d}{2} Mz^{d-1}, \quad (60)$$

starting from the midpoint, where $z(0) = z_*$ and $z'(0) = 0$. We can then read off the boundary separation ℓ corresponding to a specific midpoint value z_* via $z(\ell/2) = z_0$. By substituting the conservation equation into the expression for the geodesic length, we can simplify the expression to

$$\mathcal{L}_{\text{thermal}} = 2 \int_{z_0}^{z_*} \frac{dz}{z} \frac{1}{\sqrt{(1 - Mz^d)(1 - \frac{z^2}{z_*^2})}}. \quad (61)$$

The renormalized length $\delta \mathcal{L}_{\text{thermal}}$ is

$$\delta \mathcal{L}_{\text{thermal}}(\ell) \equiv \mathcal{L}_{\text{thermal}} + 2 \ln\left(\frac{z_0}{2}\right), \quad (62)$$

from which one obtains the renormalized equal-time two-point function through (28). We plot the renormalized length $\delta \mathcal{L}_{\text{thermal}}$ as a function of the spatial scale ℓ in Fig. 5.

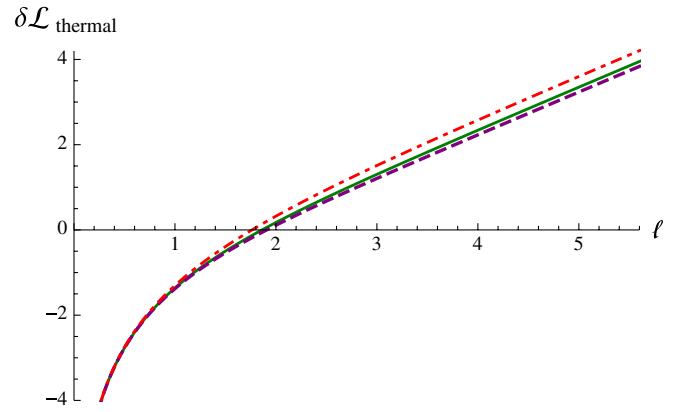


FIG. 5 (color online). $\delta \mathcal{L}_{\text{thermal}}$ as a function of spatial scale ℓ for $d = 2$ (red, dot-dashed line), $d = 3$ (green line), and $d = 4$ (purple, dashed line) for a black brane geometry with $M = 1$. The results for $d = 2$ agree with the analytical results of Sec. II A 4 in the limit of a shell of zero thickness.

B. Space-like Wilson loops

Above we examined the Wightman functions for field theories at finite temperature in order to get a sense of what thermal equilibrium looks like according to this measure. A second nonlocal probe that can be used to discuss the thermality of field theories is the (expectation value of the) Wilson loop. The Wilson loop is a gauge-invariant observable, constructed as the path-ordered contour integral over a closed loop C of the gauge field

$$W(C) = \frac{1}{N} \text{Tr}(\mathcal{P}e^{\oint_C A}). \quad (63)$$

Wilson loops contain useful information about the non-perturbative behavior of (nonabelian) gauge theories, but are, in general, hard to calculate. In the AdS/CFT correspondence, the expectation value for the Wilson loop is related to the string partition function with a string world sheet Σ extending in the bulk and ending on the loop C at the boundary

$$\langle W(C) \rangle = \int \mathcal{D}\Sigma e^{-A(\Sigma)}, \quad (64)$$

where we integrate over all inequivalent string surfaces Σ such that $\partial\Sigma = C$ at the AdS boundary and where $A(\Sigma)$ corresponds to the string action. In the strongly coupled limit, we can consider a saddle-point approximation for the string partition function and reduce the calculation of the Wilson loop expectation value to determining the minimal area surface of the (classical) string world sheet whose endpoints trace out the desired Wilson loop C on the AdS boundary

$$\langle W(C) \rangle \sim e^{-(1/\alpha')\mathcal{A}(\Sigma_0)}. \quad (65)$$

$\mathcal{A}(\Sigma_0)$ represents the area of the minimal area surface Σ_0 with boundary C . The surface Σ_0 is a solution to the equations of motion arising from the bosonic action of

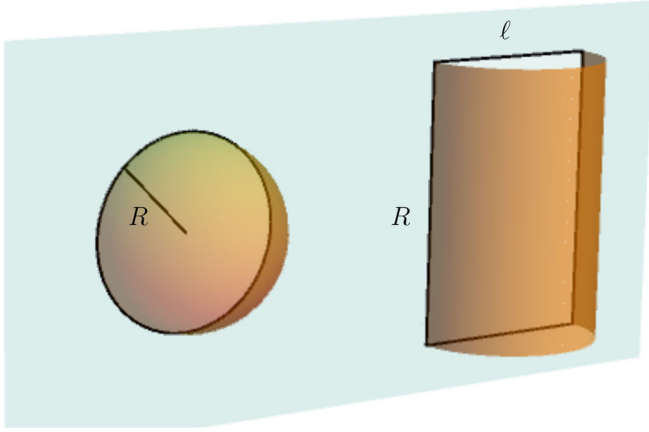


FIG. 6 (color online). Two Wilson loop shapes with their minimal string surface: the circular Wilson loop (left) and the rectangular Wilson loop (right).

the string. Thus, the expectation value of a Wilson loop in the AdS/CFT correspondence is given by the area of a minimal surface in AdS space which is bounded by the loop C [42].

In this section, we will compute spacelike Wilson loop expectation values in the vacuum and in the thermally equilibrated theory (the black brane background) for $d \geq 3$ -dimensional field theories. In Sec. III, we will compute Wilson loops in a strongly coupled theory following a sudden injection of energy and compare them to the thermal results to assess progress towards thermalization. We will study two loop shapes—circles and strips as sketched in Fig. 6—to test how and whether the shape of the loop affects the rate of thermalization.

1. Circular Wilson loops

We first examine the circular spacelike Wilson loop in a strongly coupled $d \geq 3$ -dimensional field theory at finite temperature. At zero temperature the dual geometry is pure AdS_{d+1} , and the associated minimal surface in AdS is simply a hemisphere [52]. This surprisingly simple solution to a complicated second-order nonlinear equation of motion was obtained by taking an infinite straight Wilson line on the boundary, and applying a special conformal transformation to map this straight line to a circle. Since the conformal group of the boundary corresponds to reparametrizations of AdS we can apply the appropriate reparametrization to the AdS space, and it maps the original world sheet—which was flat and extended straight into the AdS—to the hemisphere. This trick only works in pure AdS space where conformal invariance is preserved, so we are obliged to use numerical methods of solving the equations of motion when we want to calculate the Wilson loop for thermal or out-of-equilibrium states.

For now, we want to study the minimal hemisphere surface in a thermal black brane background, with the metric given by (1) with $m(v) = M$, where M is the

constant tension of the black brane. On the boundary we choose a two-dimensional plane (x_1, x_2) in which the circular Wilson loop is set. To parametrize the Wilson loop we introduce polar coordinates (ρ, φ) . The minimal space-like surface with the circular Wilson loop as its basis also has an azimuthal symmetry. The tip of the surface occurs at $(v, z, \mathbf{x}) = (v_*, z_*, \mathbf{0})$. The cross section at fixed z and v is a circle, and thus the surface is conveniently parametrized in terms of the radii ρ of these circles. The Nambu-Goto action for the string with circular symmetry in the $(d + 1)$ -dimensional AdS-black brane background is

$$A_{\text{NG}} = \frac{1}{\alpha'} \int_0^R d\rho \frac{\rho}{z(\rho)^2} \times \sqrt{1 - (1 - Mz(\rho)^d)v'(\rho)^2 - 2z'(\rho)v'(\rho)}, \quad (66)$$

where we integrated out the φ factor as both z and v are independent of φ due to the circular symmetry. This action has an explicit ρ dependence, implying that the second-order differential equation in $z(\rho)$ cannot be integrated to a first-order differential equation. The coordinate v is still a cyclic coordinate, which implies that the associated momentum is conserved. To solve for an equal-time Wilson loop, we set the conserved energy to zero, which implies a relation between v and z as given in Eq. (59). Inserting this relation in the action,

$$A_{\text{NG}}(R) = \frac{1}{\alpha'} \int_0^R d\rho \frac{\rho}{z^2} \sqrt{1 + \frac{z'^2}{1 - Mz^d}}, \quad (67)$$

the resulting equation of motion reduces to a second-order differential equation in $z(\rho)$

$$z'' = -\left(\frac{2}{z} + \frac{z'}{\rho} \frac{1}{1 - Mz^d}\right)(1 - Mz^d + z'^2) - \frac{d}{2} \frac{Mz^{d-1}z'^2}{1 - Mz^d}. \quad (68)$$

One can easily check that the hemisphere is an analytic solution in pure AdS (obtained by setting $M = 0$ in the above). It is given by

$$z(\rho) = \sqrt{z_*^2 - \rho^2}. \quad (69)$$

In case of a black brane background ($M \neq 0$) we have to resort to numerical means. We impose boundary conditions at the midpoint assuming reflection symmetry along the z axis

$$z(0) = z_*, \quad z'(0) = 0, \quad (70)$$

and read off the boundary radius $z(R) = z_0$. Note that because the second term in the first bracket of (68) causes numerical issues at $\rho = 0$ (the numerator and denominator both go to zero, but the ratio should take a fixed value), we cannot construct the solutions starting from the midpoint. Therefore we choose to solve (68) in the neighborhood of the midpoint by expanding around $\rho = 0$ to quadratic order (odd powers vanish by the symmetry)

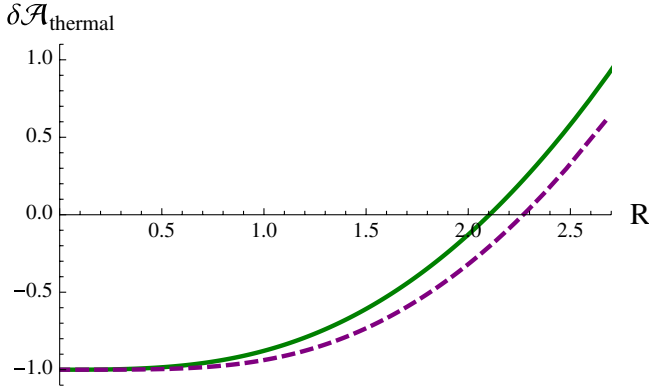


FIG. 7 (color online). $\delta \mathcal{A}_{\text{thermal}}$ against the boundary radius R . The curves represent the string surface areas in a black brane background with unit mass for $d = 3$ (green line) and $d = 4$ (purple, dashed line).

$$z_p(\rho) = z_* - \frac{1 - Mz_*^d}{2z_*} \rho^2. \quad (71)$$

The boundary conditions for the numerical solution are obtained by matching at a point ρ_p close to the midpoint; $z(\rho_p) = z_p(\rho_p)$ and $z'(\rho_p) = z'_p(\rho_p)$.

The logarithm of the expectation value of Wilson loop operators is approximated by the area ($\mathcal{A}_{\text{thermal}} = \alpha' A_{\text{NG}}$) of the minimal surface. The largest contributions to the area are coming from the near-boundary region, because of the diverging AdS volume there. We subtract the divergent piece, which is proportional to the UV-cutoff $1/z_0$. This procedure is interpreted in the dual CFT as removing the UV divergence of the Coulomb self-energy of a point charge. Subtraction of R/z_0 gives the regularized area

$$\delta \mathcal{A}_{\text{thermal}}(R) = \mathcal{A}_{\text{thermal}}(R) - \frac{R}{z_0}. \quad (72)$$

The regularized area is depicted for AdS₄ and AdS₅ in Fig. 7.

2. Infinite rectangular strips

A less symmetric Wilson loop is the rectangular strip parametrized by the boundary coordinates (x_1, x_2) . Assume that the strip is translationally invariant along the x_2 axis, such that the profile of the associated minimal surface in AdS _{$d+1$} is described by $z(x_1)$ and $v(x_1)$. In the following, we again denote $x \equiv x_1$. We impose the boundary conditions

$$z(-\ell/2) = z_0 = z(\ell/2), \quad v(-\ell/2) = t_0 = v(\ell/2). \quad (73)$$

As for the circular Wilson loop, the equation of motion for the minimal surface is obtained by minimizing the Nambu-Goto action. In this case, because of the symmetries, the analysis closely resembles that of geodesics with some small differences in the action and the equations of motion. The Nambu-Goto action for a segment stretching between

$x_2 \in (0, R)$ in Eddington-Finkelstein coordinates is given by

$$A_{\text{NG}} = \frac{R}{2\pi\alpha'} \int_{\ell/2}^{\ell/2} dx \frac{\sqrt{1 - (1 - Mz(x)^d)v'(x)^2 - 2z'(x)v'(x)}}{z(x)^2}. \quad (74)$$

The action does not exhibit an explicit x or v dependence, hence we can use the existence of two conserved quantities to simplify: these can be taken to be the midpoint of $z(x)$, z_* , and the momentum conjugate to $v(x)$. The z_* conservation equation reads

$$1 - (1 - Mz^d)v'^2 - 2z'v' = \left(\frac{z_*}{z}\right)^4, \quad (75)$$

while the conservation of the momentum conjugate to $v(x)$ implies the same relation as in Eq. (59). Inserting this relation in the conservation equation gives a first-order differential equation in $z(x)$. We then take the derivative with respect to x to obtain a second-order differential equation in $z(x)$

$$z'' = -2\frac{z_*^4}{z^5} + \frac{4-d}{2}Mz^{d-5}z_*^4 + \frac{d}{2}Mz^{d-1}. \quad (76)$$

We impose the boundary conditions $z'(0) = 0$, $z(0) = z_*$ at the midpoint, and read off the boundary separation ℓ via $z(\ell/2) = z_0$. Inserting the conservation equation in the Nambu-Goto action we get the following formula for the area ($\mathcal{A}_{\text{thermal}} = \alpha' A_{\text{NG}}$) of the minimal surface

$$\mathcal{A}_{\text{thermal}} = \frac{R}{\pi} \int_{z_0}^{z_*} \frac{dz}{z^2} \frac{1}{\sqrt{(1 - \frac{z_*^4}{z^4})(1 - Mz^d)}}. \quad (77)$$

The regularized area reads

$$\delta \mathcal{A}_{\text{thermal}}(\ell, R) = \mathcal{A}_{\text{thermal}} - \frac{1}{z_0} \frac{R}{\pi}, \quad (78)$$

and is plotted in Fig. 8 for a four- and five-dimensional background. We have chosen to plot the results after dividing out R/π as we are concerned purely with the dependence of the area on the boundary separation ℓ .

C. Entanglement entropy

It is still an open question whether a suitable notion of “local entropy” density exists which is valid out-of-equilibrium and which satisfies some basic physical properties; in particular, it must be a nondecreasing function of time. To define a local entropy density using gauge/gravity duality, one typically employs horizons since their area increases in time, and it has been suggested in [11,53] that apparent horizons provide more compelling notions of local entropy density than global horizons do. In our case, the entropy associated to the apparent horizon instantaneously thermalizes, in the limit of a zero thickness shell, and does not provide a useful probe of thermalization.

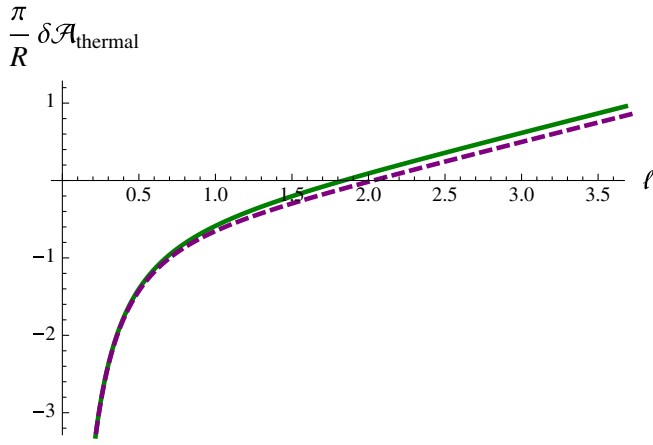


FIG. 8 (color online). $\delta\mathcal{A}_{\text{thermal}}/(R/\pi)$ as function of the spatial scale ℓ . The curves represent the string surface areas in a black brane background with unit mass. The base of the surface is a rectangular strip at the AdS boundary. The green curve corresponds to $d = 3$ and the purple, dashed curve to $d = 4$.

Skepticism against the identification of entropy with apparent horizon area in full generality has also been raised in a number of other papers, including [27,53,54].

Another way of assessing thermalization at different spatial scales in an out-of-equilibrium theory is by measuring the entanglement entropy associated with volumes of different sizes and shapes. To review, consider dividing a quantum mechanical system in a state $|\Phi\rangle$ into two spatially disjoint parts A and B . The density matrix of the system restricted to A and its entropy are computed by taking the traces

$$\rho_A = \text{tr}_B |\Phi\rangle\langle\Phi|; \quad S(A) = -\text{tr}_A(\rho_A \ln \rho_A). \quad (79)$$

In a $(1+1)$ -dimensional conformal field theory, where A is an interval of length ℓ , the entanglement entropy can be calculated analytically, yielding the universal result [55,56]:

$$\begin{aligned} \text{vacuum: } S_0(\ell) &= \frac{c}{3} \ln\left(\frac{\ell}{a}\right); \\ \text{thermal equilibrium: } S_T(\ell) &= \frac{c}{3} \ln\left(\frac{\beta}{\pi a} \sinh\frac{\pi\ell}{\beta}\right). \end{aligned} \quad (80)$$

Here a is the UV cutoff of the field theory, c is the central charge, and $\beta = T^{-1}$ denotes the inverse temperature.

The entanglement entropy $S(A)$ describes the amount of information loss associated with the restriction of an observer to the volume A . In the vacuum state for $d > 2$ dimensions, $S_0(A)$ is proportional to the surface area of A [57,58]; in $d = 2$ dimensions, as Eq. (80) shows, S_0 depends logarithmically on the length of the interval ℓ . At nonzero temperature, $S(A)$ receives an additional contribution, which can be interpreted as thermal entropy [43,44]. In the limit $T \rightarrow \infty$, the thermal contribution is proportional to the volume of the region A , just like the statistically defined thermal equilibrium entropy. Computing the

time-dependent entanglement entropy as a function of spatial scale and studying its approach to $S_T(\ell)$ thus will provide a probe of scale-dependent thermalization.

There is a precise proposal for computing entanglement entropy in strongly coupled field theories with AdS duals [26,43,44], where we think of the field theory as living on the boundary of an AdS space. Specifically, consider the boundary ∂A of a connected region in the field theory whose entanglement entropy we wish to compute. For a two-dimensional field theory, ∂A is a pair of points, for a three-dimensional field theory ∂A is a closed curve, and for a four-dimensional theory a surface. Now construct the minimal surface σ_A in AdS space that meets ∂A on the AdS boundary. For a two-dimensional field theory, σ_A is a geodesic in AdS₃ that approaches the boundary points ∂A , while for a three-dimensional field theory, σ_A is a minimal surface in AdS₄ with boundary ∂A . For a four-dimensional field theory, σ_A is a minimal volume in AdS₅ which ends on the surface ∂A on the AdS boundary. The entanglement entropy of the region A of the field theory is then given by

$$S_A = \frac{\text{Area}(\sigma_A)}{4G_N}, \quad (81)$$

where G_N denotes Newton's gravitational constant (and "Area" stands for the length of geodesics, the area of 2-surfaces, and the volume of 3-surfaces). The authors of [26,43,44] showed that this formula precisely reproduces the universal entropy formula of two-dimensional conformal field theories in thermal equilibrium [55,56]. The restriction of the entanglement entropy to a finite spatial volume can be understood as a kind of coarse graining by the discretization of the available momentum space modes of the information contained in the quantum state [59].

Thus, to measure entanglement entropy in two-dimensional field theories, we need to calculate spacelike geodesics in the dual asymptotically AdS₃ background. This means there is an intimate relation between two-dimensional entanglement entropy and the equal-time Wightman functions computed in the geodesic approximation. Indeed, the two quantities can be interpreted in terms of each other, as was also observed in [27]. For three-dimensional field theories, we need to compute spacelike, two-dimensional minimal surfaces in a dynamical, asymptotically AdS₄ background. These coincide precisely with classical spacelike worldsheets of fundamental strings with a fixed boundary, as previously studied in [28]. As we discussed above, the exponential of the action of such objects (essentially the area) is known to give the expectation value of Wilson loops in the field theory [42]. Thus, in these three-dimensional field theories, there is an intimate relation between entanglement entropy and Wilson loop expectation values, as we explore in this article.

For four-dimensional field theories, the proposed measure of entanglement entropy for spherical regions involves minimal volume hypersurfaces whose cross sections with

respect to the AdS radial coordinate are spheres. In particular, in AdS₅ we can look for a 3-dimensional volume with 2-sphere cross section which terminates on the AdS boundary. This allows us to examine the thermalization of the entanglement entropy in the 4-dimensional field theory. The methods used to compute these volumes are very similar to those for the circular Wilson loop described in Sec. II B 1, with only some powers changing with the dimension. Briefly, the action for the general spherically symmetric p volume in AdS _{d} ($p \leq d - 1$) black brane background is

$$\mathcal{V}_{\text{thermal}} = \mathcal{A}_{S^{p-1}} \int_0^R d\rho \frac{\rho^{p-1}}{z(\rho)^p} \times \sqrt{1 - (1 - Mz(\rho)^d)v'(\rho)^2 - 2z'(\rho)v'(\rho)}, \quad (82)$$

where $\mathcal{A}_{S^{p-1}}$ is surface area of a unit S^{p-1} . Things continue to proceed as for the Wilson loops: the solution in the pure AdS ($M = 0$) background is now a hemi-hypersphere and still obeys (69). What changes is the volume evaluated on the solution, which we evaluate with a cutoff near the boundary and subtract to renormalize as before. The result in the vacuum ($M = 0$) is

$$\begin{aligned} \mathcal{V}_{\text{AdS}} &= 4\pi R \int_0^{\rho(z_0)} d\rho \frac{\rho^2}{(R^2 - \rho^2)^2} \\ &= 2\pi \left(\frac{R^2}{z_0^2} + \log \frac{z_0}{\sqrt{2}R} \right) + (\text{finite}). \end{aligned} \quad (83)$$

The regularized volume is calculated analogously to previous cases by subtracting the divergent part of the volume of a pure AdS 3-surface with terminates on the same sphere on the boundary,

$$\delta \mathcal{V}_{\text{thermal}}(R) = \mathcal{V}_{\text{thermal}} - 2\pi \left(\frac{R^2}{z_0^2} + \log \frac{z_0}{\sqrt{2}R} \right). \quad (84)$$

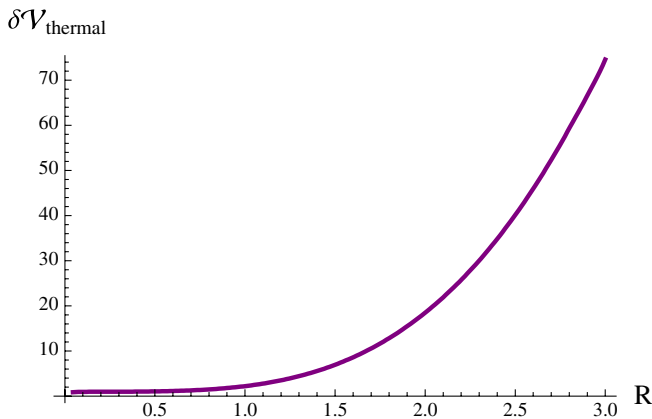


FIG. 9 (color online). Regularized volume $\delta \mathcal{V}_{\text{thermal}}$ as a function of the spatial scale R for $d = 4$.

We plot the regularized volume $\delta \mathcal{V}_{\text{thermal}}$ as a function of the radius R of the sphere on the boundary in Fig. 9.

III. SCALE-DEPENDENT THERMALIZATION FROM ADS/CFT

In the previous section we discussed how the equal-time Wightman function (related to geodesics in AdS space) and Wilson loops (related to minimal surfaces in AdS space) and entanglement entropy (related to minimal lengths, surfaces and volumes in different dimensions) can probe thermal equilibrium. In this section we will use the same probes to study the dynamics of equilibration in strongly coupled field theories. The basic setup is to drop a shell of matter with vanishing rest mass (“null dust”) into AdS space to form a black hole. This is dual to the homogeneous injection of energy into the dual field theory and its subsequent thermalization. We want to probe the rates at which thermalization occurs on different spatial scales. To this end we consider dynamical Vaidya-type backgrounds, again given by Eq. (1), but this time using the continuous mass-function of Eq. (4). This dynamical background continuously interpolates between pure AdS and AdS with a Schwarzschild black brane. Recall that the parameter v_0 in the mass-function (4) dictates how “thick” the shell is. $v_0 \rightarrow 0$ is the step-function limit corresponding to an infinitely thin shell. In this limit, the infalling shell represents a shock wave.

A. Equilibration of the two-point function

1. Two-dimensional field theories: Analytic treatment

We first consider the $d = 2$ case where analytic computations are possible. In this case, the Vaidya metric (1) becomes

$$ds^2 = -[r^2 - m(v)]dv^2 + 2drdv + r^2dx^2, \quad r \equiv \frac{1}{z}. \quad (85)$$

In order to have analytic control over the solution, let us consider the thin-shell limit $v_0 \rightarrow 0$ of the mass profile (4), which gives

$$m(v) = r_H^2 \theta(v), \quad r_H \equiv \sqrt{M}, \quad (86)$$

where $\theta(v)$ is the step function.

Outside the shock wave, $v > 0$, the metric is the standard planar black brane metric (29)

$$\begin{aligned} ds_{\text{out}}^2 &= -(r^2 - r_H^2)dt^2 + \frac{dr^2}{r^2 - r_H^2} + r^2dx^2, \\ t &= v - \frac{1}{2r_H} \ln \frac{|r - r_H|}{r + r_H}, \end{aligned} \quad (87)$$

which we studied in detail in the previous section. Inside the shock wave, $v < 0$, the metric is the Poincaré AdS₃:

$$ds_{\text{in}}^2 = -r^2 dt^2 + \frac{dr^2}{r^2} + r^2 dx^2, \quad t = v + \frac{1}{r}. \quad (88)$$

We would like to study geodesics in the AdS₃ Vaidya geometry which is (87) and (88) glued together across the infalling shell at $v = 0$. In particular, we focus on the equal-time geodesic which starts and ends at the same time $t = t_0$ on the boundary $r = \infty$. There are two possible cases: (i) the geodesic does not reach the shell and is entirely outside of it, and (ii) the geodesic crosses the shell. Because case (ii) is more involved than case (i), let us first discuss case (i) briefly and then turn to the discussion of case (ii).

In case (i), the geodesic is given by the equal-time geodesic in the pure black brane geometry, namely, by (44)–(46) with $E = 0$. Therefore, the relation between the (renormalized) geodesic length $\delta\mathcal{L}_{\text{thermal}}$ and the boundary separation ℓ is given by (52).

Now let us turn to case (ii). In this case, the part of the geodesic that is inside the shell is given by the equal-time geodesic in the pure AdS geometry, namely, by (54), which we write in the following form:

$$x(r) = \frac{\sqrt{r^2 - r_*^2}}{r_* r}, \quad (89)$$

where we set $r_* \equiv 2/\ell$. On the other hand, the part of the geodesic that is outside the shell is given by the geodesic in the pure black brane geometry, namely, by (44)–(46). In the present case, we should not set the parameter E to zero, because the geodesic gets refracted at the shell and it does not have to be in a constant t slice.

The two parts of the geodesics, the inside part and the outside part, should be connected so that the total geodesic length is minimized. Just like Snell's law, this can be stated as a refraction law for the angles entering and exiting the shell, as follows. Let us write the metric (87) and (88) as

$$ds^2 = -f(r)^2 dv^2 + 2drdv + r^2 dx^2, \quad (90)$$

where

$$f(r)^2 = \begin{cases} f_{\text{in}}(r)^2 = r^2 & v < 0 \\ f_{\text{out}}(r)^2 = r^2 - r_H^2 & v > 0 \end{cases} \quad (91)$$

and focus on the region very close to the shell at $v = 0$. Consider a point P_{in} (P_{out}) just inside (outside) the shell and let the coordinate difference between P_{in} and P_{out} be $\Delta X = (\Delta v, \Delta r, \Delta x)$. Take another point M on the shell $v = 0$, and let the coordinate difference between P_{in} (P_{out}) and M be $\Delta X_{\text{in}} = (\Delta v_{\text{in}}, \Delta r_{\text{in}}, \Delta x_{\text{in}})$ [$\Delta X_{\text{out}} = (\Delta v_{\text{out}}, \Delta r_{\text{out}}, \Delta x_{\text{out}})$], so that $\Delta X_{\text{in}} + \Delta X_{\text{out}} = \Delta X$. Then the distance from P_{in} to P_{out} via M is

$$\begin{aligned} \Delta s = & \sqrt{-f_{\text{in}}^2 \Delta v_{\text{in}}^2 + 2\Delta r_{\text{in}} \Delta v_{\text{in}} + r^2 \Delta x_{\text{in}}^2} \\ & + \sqrt{-f_{\text{out}}^2 \Delta v_{\text{out}}^2 + 2(\Delta r - \Delta r_{\text{in}}) \Delta v_{\text{out}} + r^2 (\Delta x - \Delta x_{\text{in}})^2}. \end{aligned} \quad (92)$$

We want to find the point M that minimizes Δs . Extremizing this with respect to Δr_{in} , Δx_{in} , we find

$$\frac{\Delta r_{\text{in}}}{\Delta v_{\text{in}}} = \frac{\Delta r + \frac{1}{2}(f_{\text{in}}^2 - f_{\text{out}}^2) \Delta v_{\text{out}}}{\Delta v}, \quad \frac{\Delta x_{\text{in}}}{\Delta v_{\text{in}}} = \frac{\Delta x}{\Delta v}, \quad (93)$$

and therefore

$$\frac{\Delta r_{\text{out}}}{\Delta v_{\text{out}}} = \frac{\Delta r + \frac{1}{2}(f_{\text{out}}^2 - f_{\text{in}}^2) \Delta v_{\text{in}}}{\Delta v}, \quad \frac{\Delta x_{\text{out}}}{\Delta v_{\text{out}}} = \frac{\Delta x}{\Delta v}. \quad (94)$$

From these we obtain the following refraction law as required:

$$\left. \frac{dr}{dv} \right|_{\text{in}} - \left. \frac{dr}{dv} \right|_{\text{out}} = \frac{r_H^2}{2}, \quad \left. \frac{dx}{dv} \right|_{\text{in}} = \left. \frac{dx}{dv} \right|_{\text{out}}. \quad (95)$$

By plugging the inside solution, (89), and the outside solution, (44)–(46), into the refraction condition (95), we obtain the relation between the parameters of the geodesic:

$$E = \pm \frac{r_H \sqrt{r_{\text{sw}}^2 - r_*^2}}{2r_{\text{sw}}^2} \quad \text{and} \quad J = \mp \frac{r_*}{r_H}, \quad (96)$$

where r_{sw} is the value of r at which the geodesic intersects the shell, and how to determine it will be explained below. The first sign combination applies to branch 1 for $r_{\text{sw}} \leq r_H/\sqrt{2}$ and branch 2 for $r_{\text{sw}} \geq r_H/\sqrt{2}$, while the second sign applies to branch 1 for $r_{\text{sw}} \geq r_H/\sqrt{2}$ and branch 2 for $r_{\text{sw}} \leq r_H/\sqrt{2}$. Recall that branches 1 and 2 were defined in Sec. II A 4, below Eq. (46).

It is possible that the geodesic crosses the horizon ($r = r_H$) before reaching the shell ($v = 0$). When this happens, let us require that the geodesic goes to the boundary $r = \infty$ at $\lambda = \infty$ and, as we decrease λ , it enters the horizon with v staying finite. In the previous section, we saw that the geodesic crosses the horizon at $\lambda = \lambda_{H\pm}$ and, below (42), we observed that v is finite across $\lambda = \lambda_{H-}$ but not across $\lambda = \lambda_{H+}$. Therefore, we need that $\lambda_{H+} < \lambda_{H-}$ which means that $E < 0$. So, we choose the second sign combination in (96):

$$E = - \frac{r_H \sqrt{r_{\text{sw}}^2 - r_*^2}}{2r_{\text{sw}}^2} \quad \text{and} \quad J = \frac{r_*}{r_H}. \quad (97)$$

This leaves branch 1 for $r_{\text{sw}} \geq r_H/\sqrt{2}$ and branch 2 for $r_{\text{sw}} \leq r_H/\sqrt{2}$.

Equation (97) depends on r_{sw} which is where the geodesic hits the shell. Because the shell is at $v = 0$, the value of r_{sw} is determined by

$$0 = v(r_{\text{sw}}) = \frac{1}{2r_H} \log \left[\frac{r_{\text{sw}} - r_H}{r_{\text{sw}} + r_H} \frac{r_{\text{sw}}^2 - (1+E)r_H^2 \pm \sqrt{r_{\text{sw}}^4 - (1+J^2-E^2)r_H^2 r_{\text{sw}}^2 + J^2 r_H^4}}{r_{\text{sw}}^2 - (1-E)r_H^2 \pm \sqrt{r_{\text{sw}}^4 - (1+J^2-E^2)r_H^2 r_{\text{sw}}^2 + J^2 r_H^4}} \right] + t_0, \quad (98)$$

where in the second equality we used (46) and the \pm signs correspond to branch 1 and 2, respectively. If we rewrite E, J in favor of r_{sw}, r_* using the relation (97), this becomes

$$0 = \frac{1}{2r_H} \log \left[\frac{2r_{\text{sw}}^2(r_{\text{sw}} - r_H) + \sqrt{r_{\text{sw}}^2 - r_*^2}(2r_{\text{sw}}^2 - 2r_{\text{sw}}r_H + r_H^2)}{2r_{\text{sw}}^2(r_{\text{sw}} + r_H) + \sqrt{r_{\text{sw}}^2 - r_*^2}(2r_{\text{sw}}^2 + 2r_{\text{sw}}r_H + r_H^2)} \right] + t_0. \quad (99)$$

Note that the two possible signs in (98) lead to the same condition (99). To solve this, let us make the convenient definitions

$$\rho \equiv \frac{r_{\text{sw}}}{r_H}, \quad \rho \sin \theta \equiv \frac{r_*}{r_H}, \quad a \equiv e^{2r_H t_0}. \quad (100)$$

The range of the parameters is $\theta \in [0, \frac{\pi}{2}]$, $\rho \geq 0$, and $a \geq 1$. In terms of these, the relation (99) becomes

$$\frac{4\rho(1+c)}{c+2\rho(1+\rho)(1+c)} = 1 - \frac{1}{a}, \quad (101)$$

with $c \equiv \cos \theta$. This can be solved for ρ , giving two branches of solutions:

$$\rho(a, c)_{\pm} = \frac{a+1}{2(a-1)} \pm \frac{1}{2} \sqrt{\left(\frac{a+1}{a-1}\right)^2 - \frac{2c}{c+1}}. \quad (102)$$

We can see that only ρ_+ is allowed, as follows. First, we can show that, for fixed c , the derivative of $\rho(a, c)_{\pm}$ with respect to a is always negative (positive) in the range $a \in (1, \infty)$, $c \in (0, 1]$ [60], so that $\rho(a, c)_{\pm}$ monotonically decreases (increases) as we increase a . Furthermore,

$$\rho(a, c)_{\pm} \rightarrow \frac{1}{2} \left(1 \pm \sqrt{\frac{1-c}{1+c}} \right) \text{ as } a \rightarrow \infty \quad (\text{or } t_0 \rightarrow \infty). \quad (103)$$

Therefore, for any finite values of t_0 ,

$$\begin{aligned} \rho(a, c)_- &< \frac{1}{2} \left(1 - \sqrt{\frac{1-c}{1+c}} \right) \\ &\leq \frac{1}{2} \leq \frac{1}{2} \left(1 + \sqrt{\frac{1-c}{1+c}} \right) < \rho(a, c)_+. \end{aligned} \quad (104)$$

For $r_{\text{sw}} \geq r_H/\sqrt{2}$ (i.e. $\rho > 1/\sqrt{2}$), this means that we should take the ρ_+ branch. The case with $r_{\text{sw}} < r_H/\sqrt{2}$ (i.e. $\rho < 1/\sqrt{2}$) needs some more work. We only need to consider geodesics that do not reach $r = 0$, since otherwise we cannot glue branch 1 to branch 2 at λ_{min} before the geodesic reaches the singularity. Thus, when $r_{\text{sw}} < r_H/\sqrt{2}$, we need $A_{\pm} < 0$ and $B_{\pm} > 0$, that is $J < 1 + E$, for $E < 0$ and $0 < J < 1$. Using (97), the last condition translates into the following condition for ρ :

$$\begin{cases} \frac{1}{2} \left(1 - \sqrt{\frac{1+c}{1-c}} \right) < -\frac{1}{2} \left(1 - \sqrt{\frac{1+c}{1-c}} \right) < \rho < \frac{1}{\sqrt{2}} & \text{for } c \in \left[0, \frac{1}{\sqrt{2}} \right] \\ \frac{1}{2} \left(1 + \sqrt{\frac{1-c}{1+c}} \right) < \rho < \frac{1}{\sqrt{2}} & \text{for } c \in \left(\frac{1}{\sqrt{2}}, 1 \right] \end{cases} \quad (105)$$

This means that we should take ρ_+ in (102) for all $c \in [0, 1]$.

In Figs. 10 and 11, geodesics in the (v, r) plane are plotted for different values of t_0 and ℓ . The geodesics start from the boundary at $(r, v) = (\infty, t_0)$, plunge in the bulk in the planar BTZ geometry, eventually refract at the shell

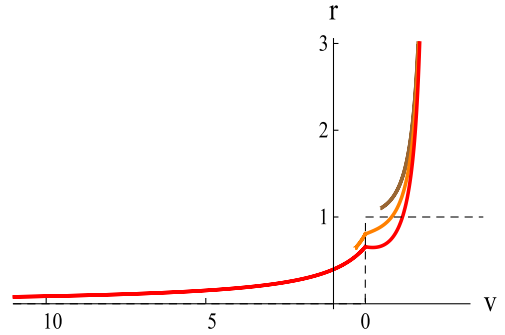


FIG. 10 (color online). Geodesics in the (v, r) plane for fixed $t_0 = 2$ and $\ell \approx 3.0$ (brown, top), $\ell \approx 4.6$ (orange, middle), $\ell \approx 68.2$ (red, bottom). In black dashed, the apparent horizon.

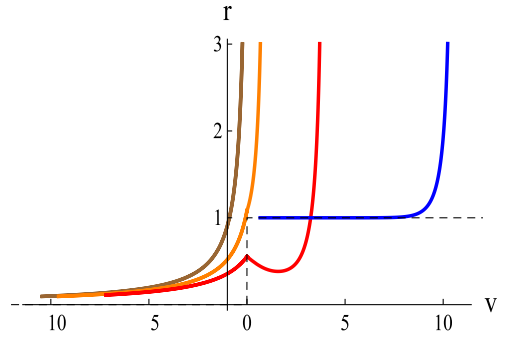


FIG. 11 (color online). Geodesics in the (v, r) plane for fixed $\ell \approx 21.3$ and, from left to right, $t_0 = 0.1$ (brown), $t_0 = 1$ (orange), $t_0 = 4$ (red), $t_0 \approx 10.6$ (blue). In black dashed, the apparent horizon.

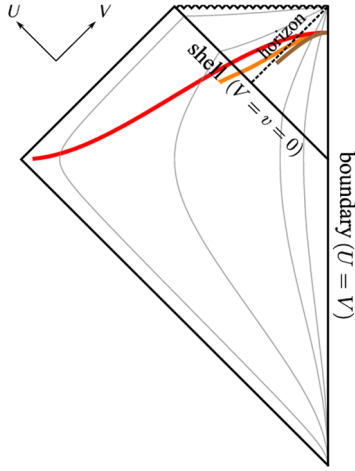


FIG. 12 (color online). Geodesics in the spacetime Carter-Penrose diagram for fixed $t_0 = 2$ and $\ell \approx 3.0$ (brown, bottom), $\ell \approx 4.6$ (orange, middle), $\ell \approx 68.2$ (red, top). Surfaces of constant r are plotted in gray.

$v = 0$, and propagate in pure AdS. All profiles are symmetric under $x \rightarrow -x$. The curve in black dashed is the apparent horizon.

In Figs. 12 and 13, we display the boundary time and spatial separation dependence of the geodesics in the Carter-Penrose diagram of Vaidya spacetime. The transformations to the (U, V) coordinates are given by

$$U \equiv \frac{2}{\pi} \tan^{-1} \left[\frac{r_H}{2} \left(t + \frac{1}{r} \right) \right], \quad V \equiv \frac{2}{\pi} \tan^{-1} \left[\frac{r_H}{2} \left(t - \frac{1}{r} \right) \right], \quad (106)$$

for $v < 0$,

$$U \equiv \frac{2}{\pi} \tan^{-1} \left[\tanh \left(\frac{r_H}{2} \left(t + \frac{1}{r_H} \coth^{-1} \frac{r}{r_H} \right) \right) \right], \\ V \equiv \frac{2}{\pi} \tan^{-1} \left[\tanh \left(\frac{r_H}{2} \left(t - \frac{1}{r_H} \coth^{-1} \frac{r}{r_H} \right) \right) \right], \quad (107)$$

for $v > 0$ and $r > r_H$, and

$$\delta \mathcal{L} = 2 \ln \frac{r_{\text{sw}} + \sqrt{r_{\text{sw}}^2 - r_*^2}}{r_*} - \ln \left[\frac{4r_{\text{sw}}^4 (2r_{\text{sw}}^2 - r_*^2 - r_H^2) + r_H^4 (r_{\text{sw}}^2 - r_*^2) + 4r_{\text{sw}}^3 (2r_{\text{sw}}^2 - r_H^2) \sqrt{r_{\text{sw}}^2 - r_*^2}}{4r_{\text{sw}}^4} \right]. \quad (109)$$

Here, just as in (52), $\delta \mathcal{L}$ has been renormalized by subtracting an IR divergent quantity $2 \ln(2r_0)$. The spatial boundary separation can also be computed by summing the contribution from the inside part (89) and the outside part (45), the result being

$$\ell = 2 \frac{\sqrt{r_{\text{sw}}^2 - r_*^2}}{r_* r_{\text{sw}}} + \frac{1}{r_H} \ln \left[\frac{2r_{\text{sw}} (r_{\text{sw}}^2 + r_* r_H) + (2r_{\text{sw}}^2 - r_H^2) \sqrt{r_{\text{sw}}^2 - r_*^2}}{2r_{\text{sw}} (r_{\text{sw}}^2 - r_* r_H) + (2r_{\text{sw}}^2 - r_H^2) \sqrt{r_{\text{sw}}^2 - r_*^2}} \right]. \quad (110)$$

Although $\delta \mathcal{L}$ and ℓ are written in terms of r_{sw} and r_* in the above expressions, we can write them in terms of t_0 and $s \equiv \sqrt{1 - c^2}$ using the definitions (100) and plugging in the solution $\rho = \rho(a, c)_+$ of Eq. (102)

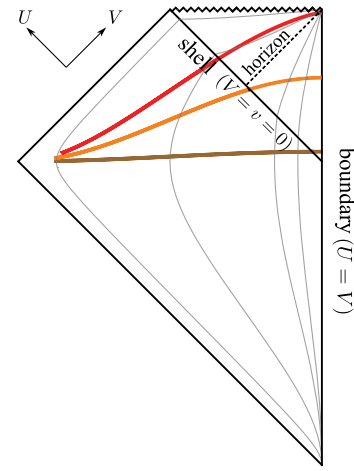


FIG. 13 (color online). Geodesics in the spacetime Carter-Penrose diagram for fixed $\ell \approx 21.3$ and $t_0 = 0.1$ (brown, bottom), $t_0 = 1$ (orange, middle), $t_0 = 4$ (red, top). Surfaces of constant r are plotted in gray. We do not display in the diagram the geodesic with $t_0 \approx 10.6$ (in blue in Fig. 11) because it would cover the horizon.

$$U \equiv \frac{2}{\pi} \tan^{-1} \left[\coth \left(\frac{r_H}{2} \left(t + \frac{1}{r_H} \tanh^{-1} \frac{r}{r_H} \right) \right) \right], \\ V \equiv \frac{2}{\pi} \tan^{-1} \left[\tanh \left(\frac{r_H}{2} \left(t - \frac{1}{r_H} \tanh^{-1} \frac{r}{r_H} \right) \right) \right], \quad (108)$$

for $v > 0$ and $r < r_H$. In these coordinates, the singularity is located at $U + V = 1$ and is depicted by a wavy line in Fig. 12 and 13, the shell is at $V = 0$ and the horizon is at $U = 1/2$ (dashed line).

With all the relations above in hand, we can compute the geodesic length and spatial boundary separation in terms of the parameters of the geodesic. The geodesic length is the sum of the geodesic length for the inside part, which can be computed from (53), and the one for the outside part, which can be computed from (43). The result is

$$2\rho = \coth(r_H t_0) + \sqrt{\coth^2(r_H t_0) - \frac{2c}{c+1}}. \quad (111)$$

Explicitly,

$$\delta \mathcal{L}(t_0, \ell) = 2 \ln \left[\frac{\sinh(r_H t_0)}{r_H s(\ell, t_0)} \right], \quad (112)$$

where $s(\ell, t_0) \in [0, 1]$ is parametrically defined by

$$\ell = \frac{1}{r_H} \left[\frac{2c}{s\rho} + \ln \left(\frac{2(1+c)\rho^2 + 2s\rho - c}{2(1+c)\rho^2 - 2s\rho - c} \right) \right]. \quad (113)$$

2. $d \geq 2$ dimensional field theories: Numerical analysis

As in the AdS₃ case, we consider a four- or five-dimensional dynamical metric which interpolates between pure planar AdS at early times and a Schwarzschild black brane at late times. The transition is induced by an infalling shell of null dust. The metric in $(d+1)$ dimensions was given in Eq. (1). We again consider the mass function (4), where the profile parameter is set to $v_0 = 0.01$ in the remainder. We consider geodesics with a boundary separation along x_1 , denoted x in the following, while the $(d-2)$ coordinates (x_2, \dots, x_{d-2}) of both endpoints are the same. This implies that z and v only depend on x , i.e., $z = z(x)$ and $v = v(x)$. We assume that x runs between $-\ell/2$ and $+\ell/2$. Then the length of the geodesic is given by

$$\mathcal{L} = \int_{-\ell/2}^{\ell/2} dx \frac{\sqrt{1 - (1 - m(v)z^d)v'^2 - 2z'v'}}{z(x)}, \quad (114)$$

where $l \equiv d/dx$. We notice that the integrand has no explicit x dependence, implying the existence of a conserved quantity, similar to the black brane case. The conservation equation reads

$$1 - (1 - m(v)z^d)v'^2 - 2z'v' = \left(\frac{z_*}{z} \right)^2. \quad (115)$$

The two equations of motion following from (114) are

$$zv'' + 2z'v' - 1 + v'^2 + \frac{d-2}{2}m(v)z^d v'^2 = 0, \quad (116)$$

$$z'' + (1 - m(v)z^d)v'' - \frac{\dot{m}(v)}{2}z^d v'^2 - dm(v)z^{d-1}z'v' = 0, \quad (117)$$

where $\dot{m}(v) = dm(v)/dv$. It is possible to show that (115) and (116) imply (117) after taking the derivative of (115) with respect to x . Therefore, we restrict ourselves to solving (115) and (116). We construct solutions $z(x)$ and $v(x)$ with the $x \rightarrow -x$ symmetry which is already present in the equations of motion, and which satisfy the boundary conditions

$$z(0) = z_*, \quad v(0) = v_*, \quad v'(0) = 0 = z'(0). \quad (118)$$

After constructing a geodesic for a specific choice of values (z_*, v_*) , information about the boundary separation and boundary time at which the geodesic is inserted follows from

$$z(\ell/2) = z_0, \quad v(\ell/2) = t_0. \quad (119)$$

The on-shell length is obtained from Eq. (114), upon use of the conservation equation (115),

$$\mathcal{L}(\ell, t_0) = 2 \int_0^{\ell/2} dx \frac{z_*}{z(x)^2}. \quad (120)$$

This length should be regularized by subtracting the cut-off dependent part $2 \ln(2/z_0)$, yielding $\delta \mathcal{L}(\ell, t_0)$.

3. Thermalization

Having collected the geodesic lengths in the infalling shell backgrounds in AdS_{3,4,5}, we can use these to describe the process of thermalization following a sudden injection of energy. To this end, we measure the approach to thermal equilibrium by comparing $\delta \mathcal{L}$ at any given time with the late-time result $\delta \mathcal{L}_{\text{thermal}}$. In any dimension, this compares the logarithm of the two-point correlator at different spatial scales with the logarithm of the thermal correlator. However, we find it more revealing to consider $\tilde{\mathcal{L}} \equiv \delta \mathcal{L}/\ell$, where we divide by the spatial separation on the boundary (we will discuss the significance of this later in Sec. III C where we deal with entanglement and Kolmogorov-Sinai entropies). In Fig. 14 we plot this measure for two-, three-, and four-dimensional field theories. In all three cases we observe a delay in the onset of thermalization. The reason for this delay is simply that the effect of the medium only becomes fully apparent at distances of the order of the thermal screening length $\ell_D \sim (\pi T)^{-1}$. Although a very small volume of linear dimension $\ell \ll \ell_D$ would appear fully thermalized after a time $t_0 = \ell/2$, its contribution to the entropy of a large volume would be disproportionately small because it does not support the momentum modes that constitute the thermal medium at large. As a consequence, the rapid linear increase of the logarithm of the two-point function seen in Fig. 14 thus

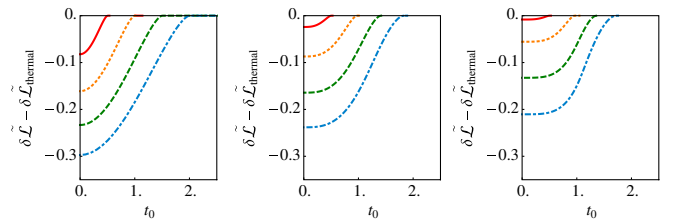


FIG. 14 (color online). $\delta \tilde{\mathcal{L}} - \delta \tilde{\mathcal{L}}_{\text{thermal}}$ ($\tilde{\mathcal{L}} \equiv \mathcal{L}/\ell$) as a function of boundary time t_0 for $d = 2$ (left), $d = 3$ (middle), and $d = 4$ (right) for a thin-shell ($v_0 = 0.01$). The boundary separations were taken to be $\ell = 1, 2, 3, 4$ (from top to bottom curve). All quantities are given in units of M . These numerical results coincide with our analytical expressions in AdS₃ ($d = 2$) in the limit $v_0 \rightarrow 0$.

only sets in after some delay. Obviously, this effect is more pronounced in higher dimensions.

From the curves in Fig. 14 we can extract different thermalization times for any spatial scale:

- (1) The critical time τ_{crit} at which the tip of the geodesic grazes the middle of the shell at $v = 0$. This can be computed by asking when a geodesic with a given boundary separation in the black brane geometry outside the infalling shell just grazes the latter: $\tau_{\text{crit}}(\ell) = \int_{z_0}^{z_*} \frac{dz}{1-Mz^d}$, where z_* is determined by the boundary separation ℓ .
- (2) The half-thermalization time $\tau_{1/2}$: time that measures the duration for the curves to reach half of their equilibrium value.
- (3) The time τ_{max} : time at which thermalization proceeds most rapidly, thus for which the curves in Fig. 14 are steepest.

For two-, three-, and four-dimensional field theories all these times are plotted in Fig. 15. In $d = 2$ we can analytically derive the linear relation $\tau_{\text{crit}} \equiv \ell/2$, as also observed in [27].

The linearity of $\tau_{\text{crit}}(\ell)$ in two dimensions is expected from general arguments in conformal field theory [56], and the coefficient is as small as possible under the constraints of causality following a quantum quench. The thermalization time scales $\tau_{1/2}$ and τ_{max} for three- and four-dimensional field theories (Fig. 15, middle and right) are sublinear in the spatial scale. In the range we study, the complete thermalization time τ_{crit} deviates slightly from linearity, and is somewhat shorter than $\ell/2$. These observations pose the question whether a rigorous causality bound for thermalization processes exists or not. We will come back to this question below, after examining other probes than two-point functions. One of the issues here is that the initial conditions are homogeneous—thus different domains will be independently coming to equilibrium at the same temperature possibly leading to apparent violations of causality.

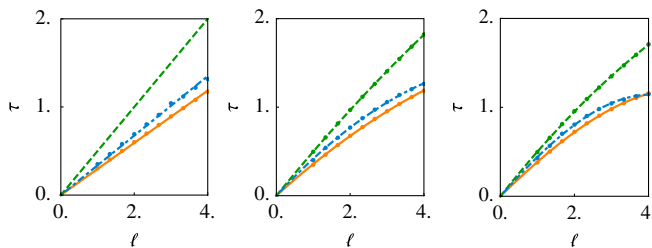


FIG. 15 (color online). Thermalization times (τ_{crit} , top line; τ_{max} , middle line; $\tau_{1/2}$, bottom line) as a function of spatial scale for $d = 2$ (left), $d = 3$ (middle), and $d = 4$ (right) for a thin shell ($v_0 = 0.01$). All thermalization time scales are linear in ℓ in two dimensions, and deviate from linearity in ℓ in three and four dimensions.

General arguments for a sharp quench in a 2-dimensional field theory [27,56] predict a nonanalytic feature where thermalization at a spatial scale ℓ is completed abruptly at $\tau_{\text{crit}}(\ell)$. This is evident in Fig. 14 (left) as a sudden change in the slope at τ_{crit} , smoothed out only by the small nonzero thickness of the shell, or equivalently, by the intrinsic duration of the quench. We find a similar (higher-order) nonanalyticity for $d = 3, 4$ (Fig. 14, middle and right) and expect this to be a general feature for quantum quenches in all dimensions.

Figure 15 shows that complete thermalization of the equal-time correlator is first observed at short length scales, or large momentum scales (see also [25]), in contrast with the behavior of weakly coupled gauge theories. In the “bottom-up” scenario [8] applicable to that case, hard quanta of the gauge field do not equilibrate directly by randomizing their momenta, but gradually degrade their energy by radiating soft quanta, which fill up the thermal phase space and equilibrate by collisions among themselves. This bottom-up scenario is linked to the infrared divergence of the splitting functions of gauge bosons and fermions in perturbative gauge theory. It contrasts with the democratic splitting properties of excitations in strongly coupled SYM theory that favor an approximately equal sharing of energy and momentum [46]. One might, therefore, have expected that thermalization proceeds fundamentally differently (“top-down”) in strongly coupled gauge theories, and this is evident within the AdS/CFT paradigm with the natural initial conditions used here.

B. Equilibration of Wilson loops

Another nonlocal probe of thermalization is the Wilson loop expectation value. As we discussed in Sec. II B, this quantity is related in the AdS/CFT correspondence to the area of a minimal surface in AdS space that bounds the desired loop on the AdS boundary. In this section we compute such minimal areas in the infalling shell background.

1. Circular Wilson loops

We first consider minimal surfaces corresponding to circular Wilson loops in the Vaidya background. The corresponding minimal surfaces were analyzed for the vacuum (pure AdS) and finite temperature equilibrium (AdS-black brane) situations in Sec. II B 1. This setup was also analyzed in [28] in the context of studying entanglement entropy. The parameterization of the surface and boundary conditions are as given in Sec. II B 1, the only difference being that the mass function $m(v)$ is now given by (4). The area functional is a slight modification of (66) ($\mathcal{A} = \alpha' A_{\text{NG}}$) given by

$$\mathcal{A}(t_0, R) = \int_0^R d\rho \frac{\rho}{z^2} \sqrt{1 - (1 - m(v)z^d)v'^2 - 2z'v'}, \quad (121)$$

where $l \equiv d/\rho$. The explicit ρ dependence again means there is no conservation equation. The equations of motion become quite involved and we omit them here.

We solve the equations of motion numerically and although we want our output as a function of the boundary radius R , for practical purposes we have to input boundary conditions at the tip of the surface at $\rho = 0$ where $z = z_*$ and $v = v_*$. For each value of v_* we consider, we find numerical solutions for the functions $z(\rho)$ and $v(\rho)$ for various values of z_* , each of which reaches the boundary (which is cut off at z_0) at $\rho_0(z_*)$. We then make an interpolation of $\rho_0(z_*)$, which allows us to find the exact value of z_* such that $\rho_0(z_*) = R$. For each value of v_* , we now know the value of z_* giving the surface with boundary radius R , and we calculate the area (using the functional above) and the boundary time $t_0 = v(R)$. These are the quantities we finally plot. There are further numerical challenges with a divergence as $\rho \rightarrow 0$ and with integrating our solutions near the AdS boundary, where contributions to the area are weighted much higher. Thus, we used an expansion around $\rho = 0$, and different techniques to deal with a separate integral near the boundary, as necessary.

As in (72) we regulate the boundary by subtracting the cut-off dependent piece of the AdS area,

$$\delta\mathcal{A}(t_0, R) = \mathcal{A}(t_0, R) - \frac{R}{z_0}. \quad (122)$$

We define $\delta\tilde{\mathcal{A}} \equiv \delta\mathcal{A}/(\pi R^2)$ dividing by the area of the region on the boundary bounded by the loop. We then plot $\delta\tilde{\mathcal{A}} - \delta\tilde{\mathcal{A}}_{\text{thermal}}$ as a function of the boundary time, subtracting the black brane value to show the approach to thermalization. This is shown in Fig. 16 for AdS₄ and AdS₅ for a series of values of R .

Repeating the analysis performed for Wightman functions, we calculate the three thermalization times defined earlier (see Sec. III A 3) as a function of the loop diameter (Fig. 17). We use the diameter rather than the radius here as it is the analogue of the separation ℓ that we plotted for the geodesics. The complete thermalization time $\tau_{\text{crit}}(D)$ is close to being a straight line of slope 1/2 for three-dimensional theories over the range of scales that we study (also see [28]) (it would be unit slope as a function of the

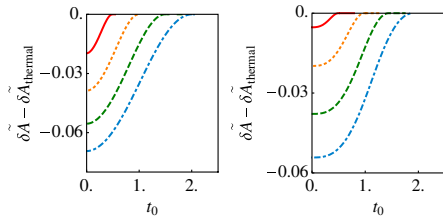


FIG. 16 (color online). $\delta\tilde{\mathcal{A}} - \delta\tilde{\mathcal{A}}_{\text{thermal}}$ ($\tilde{\mathcal{A}} \equiv \mathcal{A}/(\pi R^2)$) as a function of t_0 for circular Wilson loop radii $R = 0.5, 1, 1.5, 2$ (top curve to bottom curve) and mass shell parameters $v_0 = 0.01$, $M = 1$, in three-dimensional (left panel) and four-dimensional (right panel) field theories.

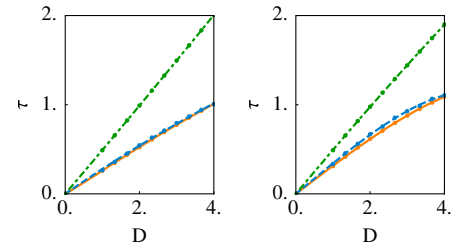


FIG. 17 (color online). Wilson loop thermalization times (τ_{crit} , top line; τ_{max} , middle line; $\tau_{1/2}$, bottom line) as a function of the diameter for circular Wilson loop operators in three-dimensional (left) and four-dimensional (right) field theories.

radius). But in four dimensions $\tau_{\text{crit}}(D)$ deviates somewhat from linearity and is shorter than $D/2$. Overall, our thermalization times for Wilson loop averages are remarkably similar to those for two-point correlators. This suggests that higher-order correlators thermalize similarly to the basic Green function in these strongly coupled theories, so that any of these nonlocal probes fairly assesses progress towards thermalization.

2. Infinite rectangular strips

As a second example we consider an infinite strip, similarly to [28]. A key difference between the strip and the Wilson circle is that the size of the latter is set by a single scale, the radius. The strip could be regarded as a limit of a ellipsoidal loop with a highly elongated semi-major axis. Thus, there are, in effect, two scales involved in the Wilson strip—the width and the (infinite) length. As before, at early times the background is AdS₄, but evolves to a black brane at late times due to an infalling shell of null dust. The metric is at all times given by (1) with $d = 3$ or 4. Again, the mass function $m(v)$ determining the evolution of the metric as a function of the bulk light-cone time v is modeled by the expression (4). We set the parameter $v_0 = 0.01$. At the AdS₄ boundary we consider a rectangular strip parametrized by the coordinates x_1 and x_2 , such that

$$x_1 \in (-\ell/2, \ell/2), \quad x_2 \in (0, R), \quad (123)$$

where R will be taken to infinity. The coordinate x_1 is denoted x in the rest of the section. The area of the string surface with this rectangular base is given by

$$\mathcal{A}(t_0, \ell, R) = \frac{R}{2\pi} \int_{-\ell/2}^{\ell/2} dx \frac{\sqrt{1 - (1 - m(v)z^d)v'^2 - 2z'v'}}{z^2}, \quad (124)$$

when we consider the following embedding profile for the string:

$$v \equiv v(x), \quad z \equiv z(x), \quad z(\pm\ell/2) = z_0, \quad v(\pm\ell/2) = t_0. \quad (125)$$

We notice that z and v only depend on x and that x itself does not appear in the action, similarly to the geodesic

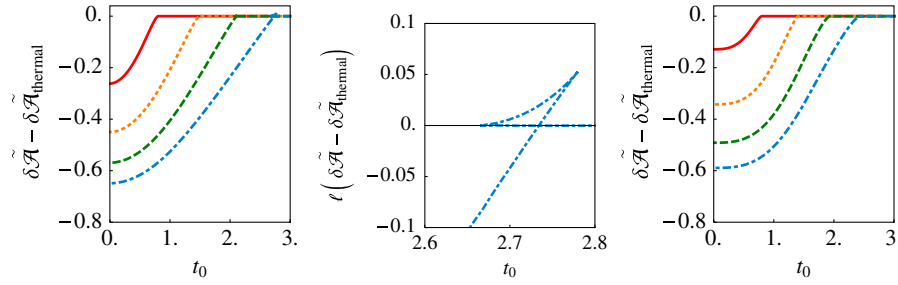


FIG. 18 (color online). $\delta\tilde{\mathcal{A}} - \delta\tilde{\mathcal{A}}_{\text{thermal}}$ ($\tilde{\mathcal{A}} \equiv \mathcal{A}/(R\ell/\pi)$) as a function of boundary time t_0 for $d = 3$ (left) and $d = 4$ (right) for a thin shell ($v_0 = 0.01$). The boundary separations were taken to be $\ell = 1, 2, 3, 4$ (from the top to the bottom curve). All quantities are given in units of M . The middle panel shows a zoomed-in version of the swallow tail for $\ell = 4$, where we plot $\ell(\delta\tilde{\mathcal{A}} - \delta\tilde{\mathcal{A}}_{\text{thermal}})$ to amplify the effect.

length in a dynamical Vaidya background. There exists a conserved quantity corresponding to the maximum value of z denoted as z_* . The conservation equation then reads

$$1 - (1 - m(v)z^d)v'^2 - 2z'v' = \left(\frac{z_*}{z}\right)^4. \quad (126)$$

From the action (124) we obtain the following two equations of motion:

$$zv'' + 4z'v' - 2 + 2v'^2 + \frac{d-4}{2}m(v)z^d v'^2 = 0, \quad (127)$$

$$z'' + (1 - m(v)z^d)v'' - \frac{\dot{m}(v)}{2}z^d v'^2 - dm(v)z^{d-1}z'v' = 0. \quad (128)$$

One can show that taking the derivative of (126) with respect to x and combining with (127) leads to (128). This is sufficient to solve (126) and (127). In order to do this numerically we use the symmetry of the string surface, i.e., we construct one half of the solution $z(x)$ and $v(x)$ and then use the reflection symmetry to construct the other half. Our boundary conditions are $z(0) = z_*$, $v(0) = v_*$, $v'(0) = 0 = z'(0)$. After constructing a string surface satisfying these boundary conditions, we read off the boundary separation and the boundary time using $z(\ell/2) = z_0$, $v(\ell/2) = t_0$.

Using the symmetries of the embedded string surface and the conservation equation (126), we obtain the on-shell area as

$$\mathcal{A}(t_0, \ell, R) = \frac{R}{\pi} \int_0^{\ell/2} dx \frac{z_*^2}{z^4}. \quad (129)$$

We regulate the area by subtracting the cut-off dependent part

$$\delta\mathcal{A}(t_0, \ell, R) = \mathcal{A}(t_0, \ell, R) - \frac{1}{z_0} \frac{R}{\pi}. \quad (130)$$

We then compare the area in the shell background with the area in a thermalized background at different times for fixed scales in Fig. 18, where we defined

$\delta\tilde{\mathcal{A}} \equiv \delta\mathcal{A}/(R\ell/\pi)$. In four dimensions ($d = 3$) it turns out that there is a range of times t_0 and Wilson strip widths ℓ for which there are three different minimal surfaces in AdS_4 . Thus, in this case, we observe a ‘‘swallow tail’’ in the Wilson loop thermalization curve for large enough boundary separations, as was also noted in [28]. However, in five dimensions ($d = 4$) the thermalization curves do not exhibit the swallow tail.

In Fig. 19 we plot the three different thermalization times τ_{crit} , $\tau_{1/2}$ and τ_{max} for $d = 3$ and $d = 4$ dimensional field theories. In three and four dimensions, the time for complete thermalization, τ_{crit} (dashed green curve), exceeds the linear relation $\ell/2$. The half-time $\tau_{1/2}$ (orange curve) is sublinear. The time τ_{max} (dot-dashed blue curve) exhibits a different behavior in three and four dimensions. The time for complete thermalization for a strip of width ℓ is slower than the thermalization time of a circular loop of radius R . This may be because the long direction of the strip provides a second, larger scale.

C. Equilibration of the entanglement entropy

Finally, we consider how the entanglement entropy equilibrates following a sudden injection of energy. Because it measures all contributions to the information loss caused by the restriction of the field theory to a finite volume, this quantity provides for a more comprehensive

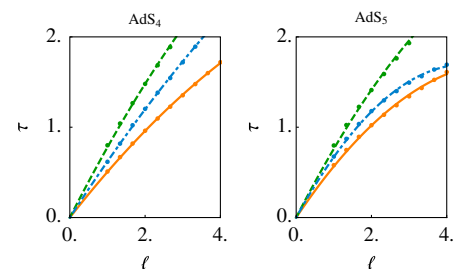


FIG. 19 (color online). Wilson strip thermalization times (τ_{crit} , top line; τ_{max} , middle line; $\tau_{1/2}$, bottom line) as a function of the spatial scale for $d = 3$ (left) and $d = 4$ (right) for a thin shell ($v_0 = 0.01$). All thermalization times deviate from linearity in the spatial scale.

measure of equilibration than either the two-point function or the Wilson loop expectation value. The entanglement entropy can be considered as a special case of the standard coarse grained entropy of equilibrating quantum systems [59]. As discussed in Sec. II C, the entanglement entropy in a two-dimensional field theory is related to geodesic lengths in AdS₃, while in three-dimensional field theory entanglement is related to minimal surface areas in AdS₄. Both of these quantities have been computed above in the infalling shell background in the process of studying two-point functions and Wilson loops. It is interesting that the Wightman function in 2 dimensions and the Wilson loop in 3 dimensions are so closely related to entanglement.

For 4-dimensional theories, to study the entanglement entropy in spherical regions, we need to compute the volume of minimal three-surfaces with the S^2 cross section in the asymptotically AdS₅ infalling shell geometry. As with the pure AdS and black brane cases we discussed in Sec. II C, the method is a straightforward generalization of the circular Wilson loop case, so we do not repeat the details of Sec. III B 1. We replace the black brane tension M in Eq. (82) with the dynamical mass function [Eq. (4)]. We can regulate the resulting volumes by subtracting the divergent part of the 3-volume of the 3-surface of the same boundary radius in pure AdS, which is given analytically in (83). We call this regulated volume $\delta\tilde{\mathcal{V}}$. However, as in previous cases, to illustrate the thermalization process we find it more instructive to subtract the renormalized

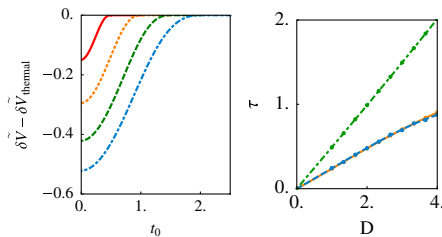


FIG. 20 (color online). The left panel shows $\delta\tilde{\mathcal{V}} - \delta\tilde{\mathcal{V}}_{\text{thermal}}$ [$\tilde{\mathcal{V}} \equiv \mathcal{V}/(4\pi R^3/3)$] as a function of boundary time t_0 for a 3-surface in $d = 4$ for a thin-shell ($v_0 = 0.01$) and 4 equally spaced boundary radii $R = 0.5, 1, 1.5, 2$. The right figure shows the thermalization times (τ_{crit} , top line; τ_{max} , middle line; $\tau_{1/2}$, bottom line) as a function of spatial scale for the same 3-surface.

3-volume of the solution of the same radius in the black brane background, $\delta\tilde{\mathcal{V}}_{\text{thermal}}$. We ultimately plot $\delta\tilde{\mathcal{V}} - \delta\tilde{\mathcal{V}}_{\text{thermal}}$ against the boundary time in the left panel of Fig. 20. $\tilde{\mathcal{V}}$ is defined as \mathcal{V} divided by the volume of the region that it bounds on the boundary. As in previous cases we can also calculate the three thermalization times we defined earlier for the 3-volume, at different values of the diameter $D = 2R$. These are shown in the right panel of Fig. 20.

Our thermalization times for Wilson loop averages and entanglement entropy seem remarkably similar to those for two-point correlators. Slightly “faster-than-causal” thermalization, possibly due to the homogeneity of the initial configuration, seems to occur for the probes that do not correspond to entanglement entropy in each dimension. For the latter, the thermalization time is linear in the spatial scale and saturates the causality bound. As the actual thermalization rate of a system is set by the slowest observable, our results suggest that in strongly coupled theories with a gravity dual, thermalization occurs “as fast as possible” at each scale, subject to the constraint of causality.

The average growth rate of the *coarse grained* entropy in nonlinear dynamical systems is measured by the Kolmogorov-Sinai (KS) entropy rate h_{KS} [61], which is given by the sum of all positive Lyapunov exponents. For a classical SU(2) lattice gauge theory in 4 dimensions, h_{KS} has been shown to be proportional to the volume [62]. For a system starting far from equilibrium, the KS entropy rate generally describes the rate of growth of the coarse grained entropy during a period of linear growth after an initial dephasing period and before the close approach to equilibrium [63]. Here we observe similar linear growth of *entanglement* entropy density in $d = 2, 3, 4$ (leftmost panels Figs. 14, 16, and 20). For small boundary volumes, the growth rate of entropy *density* is nearly independent of the boundary volume (almost parallel slopes in the leftmost panels of Figs. 14, 16, and 20 and nearly constant maximal growth rate in Fig. 21, left). Equivalently, the growth rate of the entropy is proportional to the volume—suggesting that entropy growth is a local phenomenon. However, in $d = 2$ where our analytic results enable study of large

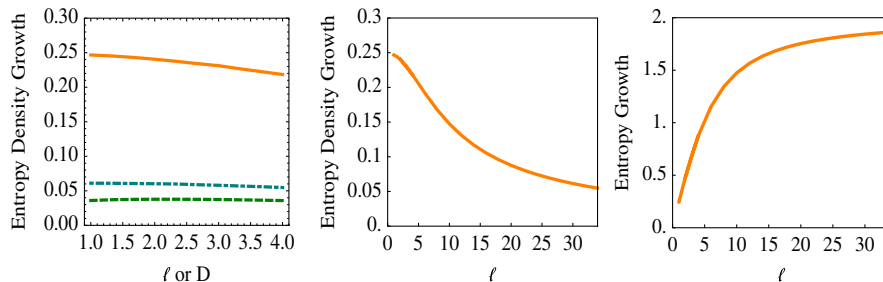


FIG. 21 (color online). (Left) Maximal growth rate of entanglement entropy *density* vs diameter of entangled region for $d = 2, 3, 4$ (top to bottom). (Middle) Same plot for $d = 2$, larger range of ℓ . (Right) Maximal entropy growth rate for $d = 2$.

boundary volumes ℓ , we find that the growth rate of the entanglement entropy density changes for large ℓ , falling asymptotically as $1/\ell$ (Fig. 21 middle panel). Equivalently, the entropy has a growth rate that approaches a constant limiting value for large ℓ (Fig. 21 right panel) and thus cannot arise from a local phenomenon. This behavior suggests that entanglement entropy and coarse grained entropy have different dynamical properties.

In summary, we have investigated the scale dependence of thermalization following a sudden injection of energy in 2-, 3-, and 4-dimensional strongly coupled field theories with gravity duals. We found that the entanglement entropy sets a time scale for equilibration that saturates a causality bound. Our results raise interesting questions about the relationship between the entanglement entropy growth rate and the KS entropy growth rate defined by coarse graining of the phase space distribution.

IV. DISCUSSION

In this work, we explored the approach to thermal equilibrium of simple nonlocal observables in strongly coupled conformal field theories with a gravity dual. In particular, we investigated the behavior during the thermalization of equal-time two-point functions, Wilson loops and entanglement entropy in boundary field theories holographically represented by asymptotically AdS geometries. The thermalization process was modeled in the bulk by the collapse of a spatially homogeneous thin shell of null dust that eventually forms a black hole. The thickness v_0 of the shell is related to the duration of the process of energy deposition in the boundary field theory. In the limit $v_0 \ll z_0$, where z_0 parametrizes the effective UV cut off of the field theory, the energy deposition can be considered as instantaneous.

As null dust does not obviously appear in supergravity theories, one may ask what is the relevance of our Vaidya model to honest AdS/CFT models. One answer to this question was given in [23], where it was shown that Vaidya geometries appear at leading nontrivial order in a small-amplitude expansion in models that can be embedded in AdS/CFT. More generally, our main qualitative conclusion (namely that thermalization is not instantaneous but proceeds top-down) only depends on the metric approaching that of a black brane outside the shell and not inside, which seems more general than our specific model.

Our observables were calculated in a semiclassical approximation appropriate for high-dimension operators, in which they correspond to geodesics or minimal surfaces in the bulk. For the AdS₃ case, where the thermal limit is represented by the planar BTZ black hole, we were able to solve the problem analytically. Not only did this provide a check on our numerical approach, which is required for higher dimensional cases, it also allowed us to obtain results in regimes beyond reach of our numerical analysis.

In all cases we found that the thermal limit is reached after a finite time τ_{crit} , which is a function of the geometric size of the probe in the boundary field theory, e.g., the separation ℓ of the two points of the equal-time Wightman function or the radius R of the circular Wilson loop. For those cases where the logarithm of the correlation function is proportional to the entanglement entropy of the enclosed area on the boundary, i.e., for geodesics in AdS₃, minimal surfaces bounded by a circle in AdS₄, and minimal codimension two surfaces bounded by a spherical shell in AdS₅, we found that $\tau_{\text{crit}} = \ell/2$ (AdS₃) and $\tau_{\text{crit}} = D/2$ (AdS_{4,5}), in the regimes we were able to study. Our result confirms a general rule for two-dimensional conformal field theories implied by causality (as also observed in [27]) and generalizes it to higher dimensions (as also done in [28] for AdS₄).

The conclusion we can draw from these results is that the decoherence and equilibration of instantaneously deposited energy generally propagates at the speed of light in the conformal field theory. This makes sense, because the process can be qualitatively understood as a cascade of gauge boson splittings, which transfers energy from all momentum scales into the infrared until all energy is distributed thermally. The speed by which this process evolves is determined by the speed of propagation of the gauge quanta, i.e., the speed of light. Alternatively, if the initial energy deposition were spatially inhomogeneous, one would expect the dissipation of the local inhomogeneities in the initial energy density to be constrained by the speed of sound, which is equal to $c/\sqrt{3}$ in a conformal field theory. This argument invites the conjecture that local equilibration of energy, in the sense of hydrodynamics, is controlled by the speed of light in conformal field theories, whereas global equilibration requiring hydrodynamic transport of energy is governed by the speed of sound. On the other hand, we found that the naive causality argument does not hold for the two-point function in 3d and 4d field theories and for Wilson loops in 4d field theories, which do not have an interpretation as entanglement entropy. In this case we obtained $\tau_{\text{crit}} < \ell/2$. This is not as surprising as it might sound: we already know of other observables that thermalize faster than the entanglement entropy, for instance one-point functions.

We also found that the transition to full thermal equilibrium is abrupt and nonanalytic, as expected from the causality argument. This nonanalyticity will presumably disappear once we go to finite g_s and N , since we do not expect infinitely thin shells to exist at finite g_s and N . One might have objected that the nonanalyticity of the transition to full thermal equilibrium is probably due to the geodesic approximation and will be smoothed out once we consider the exact Wightman function. Corrections to the geodesic approximation can be worked out by considering the exact first-quantized path integral representation of the propagator, whose saddle points are given by

geodesics. Possible corrections are then due to fluctuations around the saddle point. However, if the geodesic saddle point lies entirely within the AdS Schwarzschild geometry and does not graze the shell, such higher-order corrections will not be sensitive to the presence of the shell, since the shell is invisible in perturbation theory around the geodesic. This remains valid when we couple the heavy bulk scalar field to other bulk degrees of freedom. At best, there could possibly be nonperturbative corrections due to other complex saddle points which are sensitive to the existence of the shell, but it is unclear how to detect those in time-dependent situations. For finite-dimension operators, there could therefore be corrections that are invisible in an expansion in the inverse dimension. Their computation would be interesting but is beyond the scope of the present paper.

The nonanalyticity is probably a consequence of our treatment of the endpoints of the Wightman function, which are both located at the same bulk variable z_0 . The origin of a similar problem has been studied in the theory of boundary critical phenomena, where one typically introduces an extrapolation length τ_0 to tame the sharp UV cutoff of the conformal field theory [64,65]. This corresponds to the introduction of a smooth UV cutoff of the form $\exp(-E\tau_0)$, where E is the energy. The sharp cusp in the asymptotic result is then rounded over a region $|t - \ell/2| \sim \tau_0$. In our holographic setting, a similar approach would smear the two endpoints of the correlation function independently over some range of values z_0 . We have not studied the consequences of such a prescription.

One may wonder whether our results are in tension with those of [66], where instantaneous thermalization was found for two-point functions related to Brownian motion of a “quark” represented by a string stretching from the boundary to the horizon of an AdS₃-Vaidya spacetime. While the two-point functions studied in [66] did not involve high-dimension operators, so that there is no reason to expect a geodesic approximation to be valid, one can get some intuition by computing geodesics in the induced geometry on the string world sheet. We have done so, and find that geodesics connecting two points on the string outside the shell never cross the shell. So within a geodesic approximation, this would explain why the observable considered in [66] thermalizes instantaneously, in contrast to the observables studied in the present paper.

The fact that correlation functions of a small geometric size thermalize earlier than those of a large size implies that high momentum modes in the boundary field theory approach thermal equilibrium faster than long wavelength modes. In other words, the boundary field theory thermalizes first in its ultraviolet domain and later in the infrared or, as one might say, thermalization proceeds from the top-down. In part, this is a consequence of the fact that the specific energy injection mechanism considered here has support in the UV: the energy shell is injected into the

geometry near the boundary and then falls into the deeper regions of the AdS space, which represent IR modes of the boundary field theory. While this appears natural when viewed from the gravity side, it represents a radical deviation of the thermalization behavior of the dual field theory from that known in weakly coupled non-Abelian gauge theories, where thermalization occurs from the bottom-up, independent of how the energy is injected into the field theory. For the reader unfamiliar with heavy-ion collision phenomenology, we point out that the scale at which energy is deposited in the collision—the parton saturation scale Q_s of the colliding nuclei—is higher by an inverse power of the coupling constant α_s than the thermal scale T after thermalization. Thus, while the energy is not injected in the *extreme* UV in a nuclear collision, it is certainly not injected in the infrared. We also note that the difference in thermalization behavior is closely related to the observation that highly localized excitations in the strongly coupled gauge theory do not evolve into jets as is commonly found in weakly coupled, asymptotically free gauge theories that permit a perturbative treatment.

It is tempting to speculate to which extent our results may apply to the thermalization of QCD matter that is produced in relativistic heavy-ion collisions. Phenomenologically, it is known that the thermalization has to occur fast, allowing the matter to expand according to the laws of nearly ideal hydrodynamics. If the relevant length scale for thermalization is given by the thermal scale $\ell \sim \hbar/T$, our results suggest that $\tau_{\text{crit}} \sim 0.5\hbar/T$ if the matter is strongly coupled. For initial temperature value $T \approx 300\text{--}400$ MeV at heavy-ion collider energies, we obtain the estimate $\tau_{\text{crit}} \sim 0.3$ fm/c, comfortably short enough to account for the experimental observations. We know that such a short thermalization time applies to all momentum scales, because jets are created in the nuclear collisions, albeit at suppressed levels. However, as already mentioned, the relevant momentum scale for energy deposition is the parton saturation scale Q_s of the colliding nuclei, i.e., the transverse momentum below which most partons in the colliding nuclei are found. For achievable energies and large nuclei, $Q_s \leq 3$ GeV; in this range of momenta QCD may well be considered as a strongly coupled gauge theory.

Though this was not the emphasis in this paper, the rapid thermalization studied in this paper may also be of relevance for black hole physics. It has been suggested that black hole creation is the fastest possible form of thermalization that exists in nature [67] and it would therefore be of particular interest to more directly link the causality bound to this conjecture.

We also encountered phenomena that do not appear to have a simple explanation. For example, for long rectangular Wilson loops in the boundary gauge theory of AdS₄, the area of the minimal surface exhibits a swallow tail behavior: the transition to the thermal limit proceeds via

a discontinuous succession of shapes of the minimal surface. It is unclear why this phenomenon occurs for the rectangular Wilson loop but not for the two-point function, as the differential equation for the stationary surface is quite similar to that for the geodesic curve.

Finally, we briefly comment on the difference between dynamically collapsing shells and quasistatic shells that adiabatically approach the event horizon. As we show in the Appendix, the swallow tail behavior is ubiquitous for quasistatic shells close to the horizon, leading to significant differences between dynamical and quasistatic shells for large boundary separations.

ACKNOWLEDGMENTS

We thank V. Hubeny, M. Rangamani, and S. Ross for helpful discussions. This research is supported by the Belgian Federal Science Policy Office through the Interuniversity Attraction Pole IAP VI/11, by FWO-Vlaanderen through project G011410N, by the Foundation of Fundamental Research on Matter (FOM), by DOE Grant No. DE-FG02-05ER-41367, by the BMBF, and by Academy of Finland Grant No. 1127482. A. B. and W. S. are supported by FWO-Vlaanderen.

APPENDIX: A THE QUASI-STATIC APPROXIMATION

In the main text we considered a dynamical shell of matter falling into AdS space as a model of thermalization. An adiabatic approximation to the process of thermalization can be constructed by treating the computation of correlation functions and Wilson loops in a quasistatic manner. To do this we observe that the dynamical shell is falling into AdS space on a null trajectory. Then, at any given time, we imagine a shell located statically at the corresponding location on the null trajectory and compute Wightman functions, Wilson loops, and entanglement entropy via the geodesic and minimal surface methods described in the previous section. In this quasistatic approximation the geodesics and minimal surfaces with endpoints at a given boundary time remain localized on the equal-time surface in the bulk of AdS space (Fig. 2).

As we will see, in the quasistatic approximation, there are generically multiple geodesics connecting a pair of endpoints on the AdS boundary. We demonstrate this explicitly for AdS₃ and have found similar results for AdS₄ (not shown). There can also be multiple minimal surfaces that trace out a given loop on the AdS₄ boundary. This “swallow tail phenomenon” was also described in the full dynamical setting for the strip Wilson loop (see [28] and above). When multiple geodesics or minimal surfaces are present in a dynamical setting, it will generally be necessary to analyze which of these saddlepoints lie within steepest descent integration contours in the path integral. Here, for completeness, we document the situations we

TABLE I. Overview: swallow tail (\surd); no swallow tail (\times).

Holographic probe	Quasistatic	Dynamical
Geodesics in AdS ₃	\surd	\times
Geodesics in AdS ₄	\surd	\times
strip in AdS ₄	\surd	\surd
Circular loop in AdS ₄	\surd	\times

have found where multiple saddlepoints exist (see below and Table I). Note that in a quasistatic setting the saddle point of minimal action will dominate.

1. Geodesics in the quasistatic approximation

We study the equal-time geodesic in the shell background in the quasistatic approximation for $d = 2$. In the quasistatic approximation, the AdS₃ geometry with a shell at a fixed radial coordinate $r = r_s$ can be written as

$$ds^2 = -f(r)^2 dt^2 + \frac{dr^2}{f(r)^2} + r^2 dX^2;$$

$$f(r)^2 = \begin{cases} f_{\text{in}}(r)^2 = r^2 & r < r_s \\ f_{\text{out}}(r)^2 = r^2 - r_H^2 & r > r_s \end{cases}, \quad (\text{A1})$$

where r_H ($< r_s$) is the position of the would-be horizon. Outside the shell, $r > r_s$, the metric (A1) is the planar black brane metric that we studied in the text in II A 4, while inside the shell, $r < r_s$, it is the empty AdS₃ we discussed around (53)–(55). Therefore, for studying the equal-time geodesic in the shell spacetime (A1), we can use our previous results. Outside the shell, the relevant expressions are found in (34), (35), (41), and (45). The outside geodesics are parametrized by two parameters E and J which correspond to the energy and angular momentum, respectively. We take $E = 0$ so that they describe equal-time geodesics [see below (48)]. Also, we can take $J \geq 0$ without loss of generality, because flipping the sign of J just corresponds to the reverse parametrization of the same geodesic. Inside the shell, the expressions for geodesics are found in (53), (54), and (89). The inside geodesics are parametrized by $r_* \equiv 2/\ell$. As is clear from (89), r_* is the minimum value of r on the geodesic.

The geodesic in the entire shell background spacetime (A1) is obtained by gluing outside and inside geodesics across the shell using a refraction law so that the geodesic length is extremized. In the current situation the refraction law can be derived in very much the same way as it was in the shockwave background around (95), and the result is

$$f_{\text{in}} \frac{dX}{dr} \Big|_{r=r_s} = f_{\text{out}} \frac{dX}{dr} \Big|_{r=r_s}. \quad (\text{A2})$$

By substituting the expression for the outside geodesic (45) and the inside one (89) into (A2), we see that the parameters in the inner and outer regions are related by

$$r_* = r_H J. \quad (\text{A3})$$

Just as we did in the main text for the shockwave geometry, we can compute the renormalized geodesic length $\delta\mathcal{L}$ and spatial boundary separation ℓ in terms of the parameters J , r_* of the geodesic. The geodesic length is the sum of the geodesic length for the inside part, which can be computed from (53), and the length for the outside part, which can be computed from (43) with $E = 0$. The result is

$$\ell = \frac{2\sqrt{r_s^2 - r_H^2 J^2}}{r_H r_s J} + \frac{2}{r_H} \ln \left[\frac{r_s (J+1)}{J\sqrt{r_s^2 - r_H^2} + \sqrt{r_s^2 - r_H^2 J^2}} \right],$$

$$\delta\mathcal{L} = 2 \ln \left[\frac{r_s + \sqrt{r_s^2 - r_H^2 J^2}}{r_H J (\sqrt{r_s^2 - r_H^2} + \sqrt{r_s^2 - r_H^2 J^2})} \right]. \quad (\text{A4})$$

Here, we regularized \mathcal{L} by subtracting the divergent quantity $2 \ln(2r_0)$ just as we did in the main text. Note that (A4) is valid if the geodesic is partly inside the shell, which is the case if $J \leq r_s/r_H$. In this case, (A4) gives implicitly the relation between ℓ and $\delta\mathcal{L}$ through the parameter J [note that J and r_* are related by (A3)].

If $J \geq r_s/r_H$, instead, the entire geodesic is outside the shell and the relation between ℓ and $\delta\mathcal{L}$ is given by (52).

In Fig. 22, we plotted $\delta\mathcal{L}$ versus ℓ for different values of r_s/r_H . We see that the curve has more nontrivial structure for $r_s/r_H \approx 1$. So, let us focus on this case. If $r_s/r_H \approx 1$, then from (A4) one can derive that, depending on the value of J , the relation between ℓ and $\delta\mathcal{L}$ has the following regimes:

$$\begin{aligned} \text{(i)} \quad J \gg 1: \quad \ell \ll \frac{1}{r_H}, \quad \delta\mathcal{L} \approx 2 \ln \frac{\ell}{2}, \\ \text{(ii)} \quad J \geq \frac{r_s}{r_H} \quad \text{and} \quad J \sim 1: \quad \frac{1}{r_H} \ll \ell \leq \frac{1}{r_H} \ln \frac{r_s + r_H}{r_s - r_H}, \\ \delta\mathcal{L} \approx r_H \ell - 2 \ln(2r_H), \\ \text{(iii)} \quad J \leq \frac{r_s}{r_H} \quad \text{and} \quad J \sim 1: \quad \frac{1}{r_H} \ll \ell \leq \frac{1}{r_H} \ln \frac{r_s + r_H}{r_s - r_H}, \\ \delta\mathcal{L} \approx r_H \ell - 2 \ln(2r_H), \\ \text{(iv)} \quad \frac{1}{r_H} \gg J > 0: \quad \ell \gg \frac{\sqrt{r_s^2 - r_H^2}}{r_H}, \\ \delta\mathcal{L} \approx 2 \ln \frac{\ell}{2} + 2 \ln \frac{2r_s}{r_s + \sqrt{r_s^2 - r_H^2}}. \end{aligned} \quad (\text{A5})$$

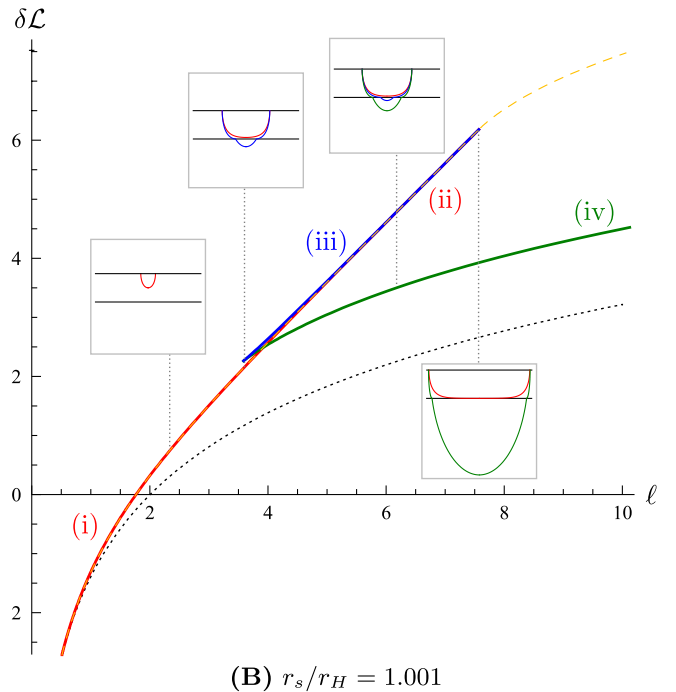
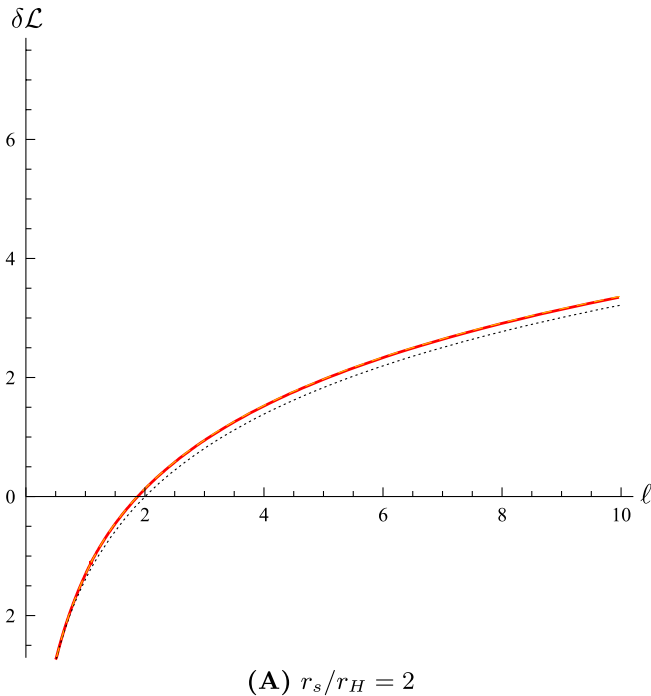


FIG. 22 (color online). The $\delta\mathcal{L}$ versus ℓ curves (solid lines) for the values of r_s/r_H (A) sufficiently larger than 1 and (B) sufficiently close to 1. We set $r_H = 1$. For comparison, we plotted $\delta\mathcal{L}(\ell)$ for pure AdS₃ in dotted black lines and for AdS₃ Vaidya in dashed yellow lines. Note that most of the Vaidya curves (dashed yellow) are overlapping with quasistatic curves (solid, in various colors). For the values of t_0 used for the Vaidya curves, see text [Eq. (A6)]. In (B), we used (partly) different colors for the different regimes (i)–(iv) explained in the text in Eq. (A5). In the insets are the actual shapes of the geodesics for some selected values of ℓ , in different colors corresponding to different branches, in the $(X, z = 1/r)$ coordinates (actual values of the coordinates not shown). The two horizontal lines in each inset represent the boundary ($z = 0$) and the shell ($z_s = 1/r_s$).

The geodesic does not cross the shell in regimes (i) and (ii) while it crosses the shell in regimes (iii) and (iv). In regime (i), the ℓ - $\delta\mathcal{L}$ relation is the same as the one for empty AdS₃, because the geodesic is near the boundary of the AdS space where the background metric is same as the empty AdS metric. In regime (ii) the geodesic length $\delta\mathcal{L}$ grows linearly with the boundary separation ℓ because the geodesic extends almost parallel to the shell just above it. This happens because the shell at $r = r_s$ is very close to the would-be horizon at $r = r_H$. Regime (iii) is similar to regime (ii) except that a small middle part of the geodesic dips into the inside geometry. In regime (iv), the ℓ - $\delta\mathcal{L}$ relation is the same as the one for empty AdS, up to a constant shift. This is because most of the geodesic is inside the shell where the metric is equal to the empty AdS metric. However, the part of geodesic outside the shell still sees the BTZ metric and leads to the constant shift that survives even for $\ell \rightarrow \infty$.

So, if $r_s/r_H \approx 1$, within a certain range of the spatial separation ℓ , there are three possible geodesics and three corresponding values of $\delta\mathcal{L}(\ell)$; see Fig. 22. The upper bound of the range is $\ell_{\max} = (1/r_H) \ln[(r_s + r_H)/(r_s - r_H)]$ while the lower bound can be computed from the condition $\partial\ell/\partial J = 0$ and is given in the $r_s \rightarrow r_H$ limit by $\ell_{\min} \approx 3.7/r_H$. As $r_s \rightarrow r_H$, we can make the upper bound ℓ_{\max} arbitrarily large and the ‘‘spike’’ in Fig. 22 arbitrarily long.

In general, in the presence of multiple geodesics in Lorentzian signature, which geodesic makes the dominant contribution to the correlation function is a subtle issue [39–41]. However, in the present approximation where the spacetime is static, it is simply the shortest geodesic that contributes most to the correlation function. Therefore, in spite of the existence of the peculiar ‘‘linear’’ regimes (ii) and (iii), it is (i) and (iv) that determine the correlation function.

For comparison, in Fig. 22, we also plotted $\delta\mathcal{L}(\ell)$ for the Vaidya geometry we studied in III A 1. The relevant expressions are found in (102) and (112). The Vaidya geodesics are parametrized by t_0 , the time at which the boundary operators are inserted. In the plot, we determined the value of t_0 in terms of r_s so that the shock wave in the Vaidya geometry is at $r = r_s$ at time t_0 just as in the quasistatic metric (A1). Namely, because the shock wave is at $v = 0$, by setting $v = 0$ in (29), we obtain the relation between t_0 and r_s :

$$t_0 = \frac{1}{2r_H} \ln \frac{r_s + r_H}{r_s - r_H}. \quad (\text{A6})$$

Note that, in the large ℓ limit with r_s fixed, the quasistatic computation (A4) gives the asymptotic behavior:

$$\delta\mathcal{L} \approx 2\ln\frac{\ell}{2} + 2\ln\frac{2r_s}{r_s + \sqrt{r_s^2 - r_H^2}} = 2\ln\frac{\ell}{2} + 2\ln\left[\frac{\cosh(r_H t_0)}{\cosh^2\left(\frac{r_H t_0}{2}\right)}\right] \quad (\text{quasi-static}), \quad (\text{A7})$$

where in the second expression we used (A6). In the same limit [which corresponds in (112) to $c \rightarrow 1$, $r_*/r_H \rightarrow 0$ with fixed t_0], the Vaidya result (112) gives the following asymptotic behavior:

$$\delta\mathcal{L} \approx 2\ln\frac{\ell}{2} - \ln\frac{16a}{(\sqrt{a} + 1)^4} = 2\ln\frac{\ell}{2} + 4\ln\left(\cosh\frac{r_H t_0}{2}\right) \quad (\text{Vaidya}), \quad (\text{A8})$$

where we used $a = e^{2r_H t_0}$. These lead to the difference in the $\ell \rightarrow \infty$ behavior of the quasistatic and Vaidya curves that we can observe in Fig. 22.

2. Wilson loops in the quasistatic approximation

In four dimensions the entanglement entropy is related to the area of the spacelike string surface whose base is a Wilson loop at the AdS boundary. In [28] it was noticed that there can exist three different string surfaces for the same boundary time and the same boundary separation in a dynamical background with a thermal quench (see also III B 2). In this subsection we will investigate whether the quasistatic approximation for Wilson loops and Wilson strips exhibits multiple string surfaces for the same boundary.

a. Circular loops

Similar to the geodesic analysis, the four-dimensional background can be divided into a black brane part (outside the shell) and a pure AdS part (inside the shell). However, we cannot solve the differential equations analytically and instead we rely on numerical methods. Outside the shell the solution satisfies the differential equation (68) in the black brane background (with $d = 3$), while inside the shell we must find a minimal surface in pure AdS (i.e. we set the mass M to zero in Eq. (68)). The minimal surface in pure AdS consists of a hemisphere. In the thin-shell limit, at the position of the shell $z = z_s$, the minimal surface should satisfy the refraction condition

$$\left.\frac{dz_{\text{out}}}{d\rho}\right|_{z_s} = \sqrt{1 - Mz_s^3} \left.\frac{dz_{\text{in}}}{d\rho}\right|_{z_s}. \quad (\text{A9})$$

This is derived analogously to the geodesic case (A2) in which case it agrees with numerical results obtained by minimizing the path of the geodesic. Note that in the dynamical case we do not use such a condition and solve the equations of motion in the whole space with mass function (4). However, here, taking advantage of this simple relation allows to use much less computationally intensive numerics in the limit of a thin shell (where the mass function is a step-function). We start by constructing a hemispherical string surface whose tip is given by $z(0) = z_* > z_s$ and $z'(0) = 0$, thus lying inside the shell. For this solution we can determine the intersection point ρ_1 with the shell and the gradient at that point analytically. We can then use the refraction condition to generate the rest of the

solution in the black brane background, using the boundary condition $z(\rho_1) = z_s$ and $z'(\rho_1) = z'_{\text{out}}$. Where this part of the solution intersects the boundary (cut off at z_0) gives us the boundary radius R of the Wilson loop. We can also construct surfaces wholly outside the shell, which are just the thermal Wilson loops from Sec. II B 1. Thus we get $R(z_*)$ for any shell position z_s .

As with the geodesics case we can get multiple surfaces with the same boundary radius and shell position (such as in Fig. 22). An easy way to check whether these multiple solutions exist before calculating any areas (see also [28]) is to invert our numerical data appropriately so that we can plot it on a graph of z_* against boundary time t_0 , the boundary time being obtained as a function of the shell position z_s :

$$t_0 = \int_{z_0}^{z_s} \frac{dz}{1 - Mz^3}. \quad (\text{A10})$$

The multiple solutions will show up as multiple possible values of z_* for the same t_0 . We see this in Fig. 23(a) where we have plotted for three different boundary radii.

The area of the minimal surface consists of three parts: we add the areas of the piece in empty AdS (inside the shell) and of the piece in the black brane background (outside the shell) and subtract the area of the solution in empty AdS with the same boundary radius,

$$\begin{aligned} \delta \mathcal{A}(R, t_0) = & \int_0^{\rho_1(t_0)} d\rho \frac{\rho}{z^2} \sqrt{1 + z'^2} \\ & + \int_{\rho_1(t_0)}^R d\rho \frac{\rho}{z^2} \sqrt{1 + \frac{z'^2}{1 - Mz^3}} - \left(\frac{R}{z_0} - 1 \right). \end{aligned} \quad (\text{A11})$$

In Fig. 23(b), we plot $\delta \mathcal{A}(R, t_0)$ as a function of R for a fixed shell position. The three branches appear in a very similar fashion to those for geodesics in AdS₃ shown in Fig. 22. Figure 23(c) then shows $\delta \mathcal{A}(R, t_0)$ as a function of the boundary time t_0 for three different boundary radii. The

appearance of the three branches gives a swallow tail as found in [28] in the dynamical case for the infinite rectangular strip, and as we also find in Sec. III B 2. However, there are no such multiple solutions in the dynamical Wilson loop case as shown in [28] and Sec. III B 1. This can be taken as an indication of the limits of the quasistatic approximation in accurately capturing the behavior as the shell gets closer to the horizon (recall that to get the three branches in Fig. 23(b) we have to wait till the shell approaches the would-be horizon, here $M^{1/3}z_s = 1/1.001$). The appearance of three branches does not, however, signify that something is unphysical. As mentioned, they also appear in the dynamical case for the infinite strip. What it does mean is that since we are using a saddle-point approximation to calculate field theory quantities and our spacetime is Lorentzian, when there are multiple geodesics we should carefully follow a steepest descent procedure.

The numerics are hard to pursue around the earliest time where the three branches occur in Fig. 23(c) and we see some noise around one corner of the swallow tail. Here the tip of the sphere at z_* , which is our initial condition, is very close to the shell, and very small variations in z_* give rise to large variations in R and hence $\delta \mathcal{A}$.

b. Strip

We can perform a similar analysis for the Wilson strip in a quasistatic background. Eq. (76) is now the differential equation we solve numerically in the black brane background (with $d = 3$). Considering a similar boundary setup for the strip as in section II B 2, we follow a similar procedure to construct solutions as for the quasistatic Wilson loops. Also the refraction condition through the shell (in the thin-shell approximation) is the same as for circular Wilson loops. Hence, we will not work this case out explicitly will immediately give the results. The string surface area consists of three different pieces: the part of the solution inside the shell (empty AdS) \mathcal{A}_{AdS} , the part of the solution outside the shell (black brane background) \mathcal{A}_{BB} , and a subtracting part corresponding to the full solution in

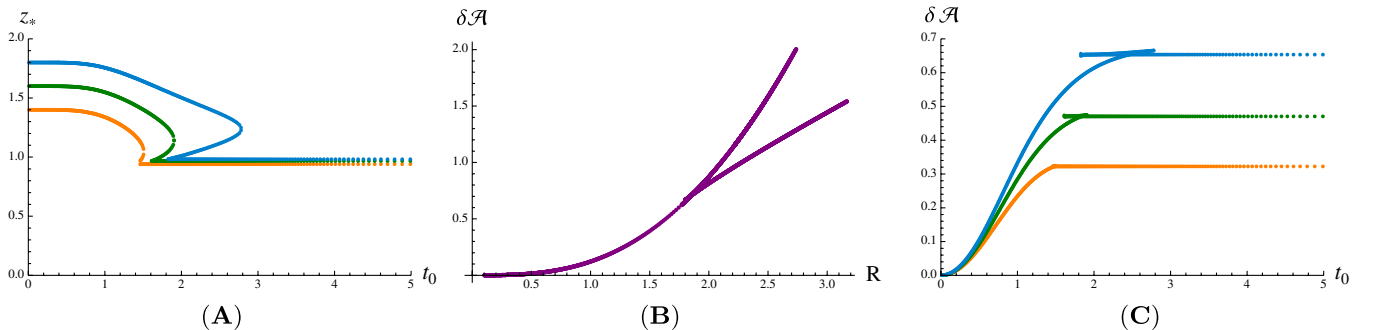


FIG. 23 (color online). (A) z_* against t_0 for $R = 1.4, 1.6, 1.8$ (from bottom curve to top curve). Three z_* values for a certain range of t_0 make it clear we have multiple branches. (B) $\delta \mathcal{A}$ against R for $M^{1/3}z_s = 1/1.001$. We have multiple solutions for the same radius in the region with the spike. (C) $\delta \mathcal{A}$ against t_0 for $R = 1.4, 1.6, 1.8$, (from bottom curve to top curve) we have three branches and the behavior of the curve there is complicated.

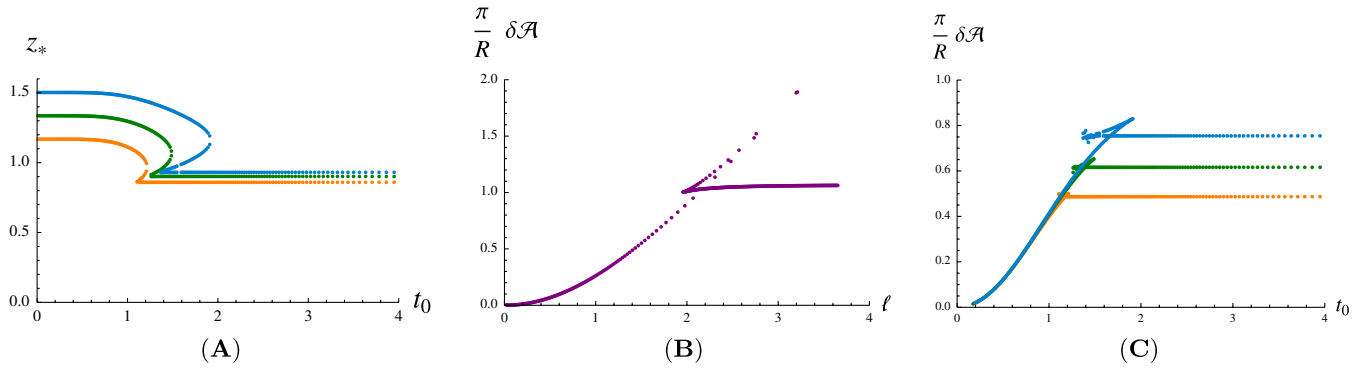


FIG. 24 (color online). (A) z_* against t_0 for $\ell = 1.4, 1.6, 1.8$ (from bottom curve to top curve). We see indeed the existence of three different solutions for the same boundary time t_0 . (B) $\delta\mathcal{A}/(R/\pi)$ against ℓ for a fixed position of the shell: $M^{1/3}z_s = 1/1.001$. (C) $\delta\mathcal{A}/(R/\pi)$ against t_0 for $\ell = 1.4, 1.6, 1.8$ (from bottom curve to top curve).

empty AdS with the same boundary separation ℓ . The full area in the shell background is given by

$$\delta\mathcal{A}(\ell, t_0) = \mathcal{A}_{\text{AdS}}(z_s(t_0), \tilde{x}) + \mathcal{A}_{\text{BB}}(\tilde{x}, \ell) - \mathcal{A}_{\text{AdS}}(z_0, \ell), \quad (\text{A12})$$

where \tilde{x} represents the spacelike separation of the part inside the shell. The area formula in empty AdS is given by the relation

$$\mathcal{A}_{\text{AdS}}(z, y) \equiv \frac{R}{\pi} \left(\frac{1}{z} + \frac{1}{2y} \frac{\pi\Gamma(-1/4)\Gamma(3/4)}{\Gamma(1/4)^2} \right), \quad (\text{A13})$$

where R corresponds to the height of the Wilson strip at the boundary (see II B 2) and the black brane area is given by

$$\mathcal{A}_{\text{BB}}(y_1, y_2) \equiv \frac{R}{\pi} \int_{y_1}^{y_2} dx \frac{1}{z(x)^2} \sqrt{1 + \frac{z'(x)^2}{1 - Mz^3}}. \quad (\text{A14})$$

In Fig. 24(a), we plot the midpoint of $z(x)$, namely z_* , as a function of the boundary time t_0 . In the middle panel of Fig. 24, we plot the area $\delta\mathcal{A}(\ell, t_0)$ (with R/π divided out) as a function of the boundary separation ℓ for a fixed shell position z_s (thus for a fixed boundary time t_0). On the right panel of Fig. 24 we plot the area $\delta\mathcal{A}(\ell, t_0)$ (with R/π divided out) as a function of the boundary time t_0 for three fixed boundary separations. As in the dynamical case, we have three branches of solutions appearing, but here they show up already for smaller values of the radius.

-
- [1] I. Arsene *et al.* (BRAHMS Collaboration), *Nucl. Phys.* **A757**, 1 (2005); K. Adcox *et al.* (PHENIX Collaboration), *Nucl. Phys.* **A757**, 184 (2005); B. B. Back *et al.* (PHOBOS Collaboration), *Nucl. Phys.* **A757**, 28 (2005); J. Adams *et al.* (STAR Collaboration), *Nucl. Phys.* **A757**, 102 (2005).
- [2] M. Gyulassy and L. McLerran, *Nucl. Phys.* **A750**, 30 (2005).
- [3] J. W. Harris and B. Müller, *Annu. Rev. Nucl. Part. Sci.* **46**, 71 (1996).
- [4] J. M. Maldacena, *Adv. Theor. Math. Phys.* **2**, 231 (1998); *Int. J. Theor. Phys.* **38**, 1113 (1999); S. S. Gubser, I. R. Klebanov, and A. M. Polyakov, *Phys. Lett. B* **428**, 105 (1998); E. Witten, *Adv. Theor. Math. Phys.* **2**, 253 (1998).
- [5] G. Policastro, D. T. Son, and A. O. Starinets, *Phys. Rev. Lett.* **87**, 081601 (2001).
- [6] R. A. Janik and R. B. Peshanski, *Phys. Rev. D* **73**, 045013 (2006).
- [7] J. Casalderrey-Solana, H. Liu, D. Mateos, K. Rajagopal, and U. A. Wiedemann, *arXiv:1101.0618*.
- [8] R. Baier, A. H. Mueller, D. Schiff, and D. T. Son, *Phys. Lett. B* **502**, 51 (2001).
- [9] A. H. Mueller, A. I. Shoshi, and S. M. H. Wong, *Phys. Lett. B* **632**, 257 (2006).
- [10] Y. V. Kovchegov and A. Taliotis, *Phys. Rev. C* **76**, 014905 (2007).
- [11] P. M. Chesler and L. G. Yaffe, *Phys. Rev. Lett.* **102**, 211601 (2009); *Phys. Rev. D* **82**, 026006 (2010).
- [12] G. Beuf, M. P. Heller, R. A. Janik, and R. Peshanski, *J. High Energy Phys.* **10** (2009) 043.
- [13] S. Catterall, A. Joseph, and T. Wiseman, *J. High Energy Phys.* **12** (2010) 022.
- [14] M. Hanada, *J. High Energy Phys.* **11** (2010) 112.
- [15] S. Chandrasekhar and S. L. Detweiler, *Proc. R. Soc. A* **344**, 441 (1975); G. T. Horowitz and V. E. Hubeny, *Phys. Rev. D* **62**, 024027 (2000); A. O. Starinets, *Phys. Rev. D* **66**, 124013 (2002); P. K. Kovtun and A. O. Starinets, *Phys. Rev. D* **72**, 086009 (2005); R. A. Janik and R. B. Peshanski, *Phys. Rev. D* **74**, 046007 (2006); J. J. Friess, S. S. Gubser, G. Michalogiorgakis, and S. S. Pufu, *J. High Energy Phys.* **04** (2007) 080; N. Iqbal and H. Liu, *Phys. Rev. D* **79**, 025023 (2009).
- [16] V. E. Hubeny and M. Rangamani, *Adv. High Energy Phys.* **2010**, 297916 (2010).

- [17] U. H. Danielsson, E. Keski-Vakkuri, and M. Kruczenski, *Nucl. Phys.* **B563**, 279 (1999).
- [18] S. B. Giddings and S. F. Ross, *Phys. Rev. D* **61**, 024036 (1999).
- [19] U. H. Danielsson, E. Keski-Vakkuri, and M. Kruczenski, *J. High Energy Phys.* **02** (2000) 039.
- [20] S. B. Giddings and A. Nudelman, *J. High Energy Phys.* **02** (2002) 003.
- [21] K. Kang and H. Nastase, *Phys. Rev. D* **72**, 106003 (2005); S. S. Gubser, S. S. Pufu, and A. Yarom, *J. High Energy Phys.* **07** (2008) 108; D. Grumiller and P. Romatschke, *J. High Energy Phys.* **08** (2008) 027; S. S. Gubser, S. S. Pufu, and A. Yarom, *Phys. Rev. D* **78**, 066014 (2008); J. L. Albacete, Y. V. Kovchegov, and A. Taliotis, *J. High Energy Phys.* **07** (2008) 100; L. Alvarez-Gaume, C. Gomez, A. Sabio Vera, A. Tavanfar, and M. A. Vazquez-Mozo, *J. High Energy Phys.* **02** (2009) 009; J. L. Albacete, Y. V. Kovchegov, and A. Taliotis, *J. High Energy Phys.* **05** (2009) 060; S. Lin and E. Shuryak, *Phys. Rev. D* **79**, 124015 (2009); S. S. Gubser, S. S. Pufu, and A. Yarom, *J. High Energy Phys.* **11** (2009) 050; Y. V. Kovchegov and S. Lin, *J. High Energy Phys.* **03** (2010) 057; Y. V. Kovchegov, *Prog. Theor. Phys. Suppl.* **187**, 96 (2011); P. M. Chesler and L. G. Yaffe, *Phys. Rev. Lett.* **106**, 021601 (2011).
- [22] S. Lin and E. Shuryak, *Phys. Rev. D* **77**, 085013 (2008); **77**, 085014 (2008).
- [23] S. Bhattacharyya and S. Minwalla, *J. High Energy Phys.* **09** (2009) 034.
- [24] R. A. Janik, *Phys. Rev. Lett.* **98**, 022302 (2007).
- [25] S. Lin and E. Shuryak, *Phys. Rev. D* **78**, 125018 (2008).
- [26] V. E. Hubeny, M. Rangamani, and T. Takayanagi, *J. High Energy Phys.* **07** (2007) 062.
- [27] J. Abajo-Arrestia, J. Aparicio, and E. Lopez, *J. High Energy Phys.* **11** (2010) 149.
- [28] T. Albash and C. V. Johnson, *New J. Phys.* **13**, 045017 (2011).
- [29] J. Erdmenger, S. Lin, and T. H. Ngo, *J. High Energy Phys.* **04** (2011) 035.
- [30] S. Caron-Huot, P. M. Chesler, and D. Teaney, [arXiv:1102.1073](https://arxiv.org/abs/1102.1073) [*Phys. Rev. D* (to be published)].
- [31] K. Skenderis and B. C. van Rees, *Phys. Rev. Lett.* **101**, 081601 (2008); *J. High Energy Phys.* **05** (2009) 085.
- [32] X. Arsiwalla, J. de Boer, K. Papadodimas, and E. Verlinde, *J. High Energy Phys.* **01** (2011) 144.
- [33] S. R. Das, T. Nishioka, and T. Takayanagi, *J. High Energy Phys.* **07** (2010) 071.
- [34] K. Hashimoto, N. Iizuka, and T. Oka, [arXiv:1012.4463](https://arxiv.org/abs/1012.4463).
- [35] A. Kovner and U. A. Wiedemann, *Phys. Rev. D* **64**, 114002 (2001).
- [36] H. Liu, K. Rajagopal, and U. A. Wiedemann, *J. High Energy Phys.* **03** (2007) 066.
- [37] P. Kovtun and A. Starinets, *Phys. Rev. Lett.* **96**, 131601 (2006).
- [38] V. Balasubramanian and S. F. Ross, *Phys. Rev. D* **61**, 044007 (2000).
- [39] J. Louko, D. Marolf, and S. F. Ross, *Phys. Rev. D* **62**, 044041 (2000).
- [40] L. Fidkowski, V. Hubeny, M. Kleban, and S. Shenker, *J. High Energy Phys.* **02** (2004) 014.
- [41] G. Festuccia and H. Liu, *J. High Energy Phys.* **04** (2006) 044.
- [42] J. M. Maldacena, *Phys. Rev. Lett.* **80**, 4859 (1998); S. J. Rey and J. T. Yee, *Eur. Phys. J. C* **22**, 379 (2001).
- [43] S. Ryu and T. Takayanagi, *Phys. Rev. Lett.* **96**, 181602 (2006).
- [44] T. Nishioka, S. Ryu, and T. Takayanagi, *J. Phys. A* **42**, 504008 (2009).
- [45] V. Balasubramanian, A. Bernamonti, J. de Boer, N. Copland, B. Craps, E. Keski-Vakkuri, B. Müller, A. Schäfer, M. Shigemori, and W. Staessens, *Phys. Rev. Lett.* **106**, 191601 (2011).
- [46] Y. Hatta, E. Iancu, and A. H. Mueller, *J. High Energy Phys.* **05** (2008) 037.
- [47] E. Iancu, *Acta Phys. Pol. B* **39**, 3213 (2008).
- [48] D. T. Son and A. O. Starinets, *J. High Energy Phys.* **09** (2002) 042.
- [49] V. Balasubramanian, P. Kraus, and A. E. Lawrence, *Phys. Rev. D* **59**, 046003 (1999).
- [50] J. McGreevy, *Adv. High Energy Phys.* **2010**, 723105 (2010).
- [51] Since we are taking the coordinate x to be noncompact, in terms of the metric the spacetime (29) is identical to empty AdS_3 . Furthermore, $r = 0$, which is a Milne-type singularity for compact x , is not a singularity. However, we still refer to $r = 0$ as the singularity. As the geodesics we consider in the current paper never reach $r = 0$, this does not matter to us.
- [52] D. E. Berenstein, R. Corrado, W. Fischler, and J. M. Maldacena, *Phys. Rev. D* **59**, 105023 (1999).
- [53] P. Figueras, V. E. Hubeny, M. Rangamani, and S. F. Ross, *J. High Energy Phys.* **04** (2009) 137.
- [54] V. E. Hubeny, [arXiv:1103.1999](https://arxiv.org/abs/1103.1999).
- [55] P. Calabrese and J. L. Cardy, *J. Stat. Mech.* **06** (2004) P002.
- [56] P. Calabrese and J. Cardy, *J. Phys. A* **42**, 504005 (2009).
- [57] M. Srednicki, *Phys. Rev. Lett.* **71**, 666 (1993).
- [58] L. Bombelli, R. K. Koul, J. Lee, and R. D. Sorkin, *Phys. Rev. D* **34**, 373 (1986).
- [59] T. Takayanagi and T. Ugajin, *J. High Energy Phys.* **11** (2010) 054.
- [60] $\partial\rho(a, c)_-/\partial a$ actually vanishes when $c = 0$, while $\partial\rho(a, c)_+/\partial a < 0$ also for $c = 0$.
- [61] A. N. Kolmogorov, *Dokl. Akad. Nauk SSSR* **119**, 861 (1958); **124**, 754 (1959); Ya. G. Sinai, *Dokl. Akad. Nauk SSSR* **124**, 768 (1959).
- [62] J. Bolte, B. Müller, and A. Schäfer, *Phys. Rev. D* **61**, 054506 (2000); T. Kunihiko *et al.*, *Phys. Rev. D* **82**, 114015 (2010).
- [63] V. Latora and M. Baranger, *Phys. Rev. Lett.* **82**, 520 (1999).
- [64] P. Calabrese and J. Cardy, *Phys. Rev. Lett.* **96**, 136801 (2006).
- [65] P. Calabrese and J. Cardy, *J. Stat. Mech.* **06** (2007) P06008.
- [66] H. Ebrahim and M. Headrick, [arXiv:1010.5443](https://arxiv.org/abs/1010.5443).
- [67] Y. Sekino and L. Susskind, *J. High Energy Phys.* **10** (2008) 065.

Thermalization of mutual and tripartite information in strongly coupled two dimensional conformal field theories

V. Balasubramanian,^{1,*} A. Bernamonti,^{2,†} N. Copland,^{2,3,‡} B. Craps,^{2,§} and F. Galli^{2,||}

¹David Rittenhouse Laboratory, University of Pennsylvania, Philadelphia, Pennsylvania 19104, USA

²Theoretische Natuurkunde, Vrije Universiteit Brussel, and International Solvay Institutes, Pleinlaan 2, B-1050 Brussels, Belgium

³Centre for Quantum Spacetime, Sogang University, Seoul 121-742, Korea

(Received 10 October 2011; published 14 November 2011)

The mutual and tripartite information between pairs and triples of disjoint regions in a quantum field theory are sensitive probes of the spread of correlations in an equilibrating system. We compute these quantities in strongly coupled two-dimensional conformal field theories with a gravity dual following the homogenous deposition of energy. The injected energy is modeled in anti-de Sitter space as an infalling shell, and the information shared by disjoint intervals is computed in terms of geodesic lengths in this background. For given widths and separation of the intervals, the mutual information typically starts at its vacuum value, then increases in time to reach a maximum, and then declines to the value at thermal equilibrium. A simple causality argument qualitatively explains this behavior. The tripartite information is generically nonzero and time-dependent throughout the process. This contrasts with (but does not contradict) the time-independent tripartite information one finds after a two-dimensional quantum quench in the limit of large time and distance scales compared to the initial inverse mass gap.

DOI: 10.1103/PhysRevD.84.105017

PACS numbers: 03.65.Ud, 11.25.Tq

I. INTRODUCTION

Consider a quantum field theory whose state is described by the density matrix ρ . Measurements made within a spatial region A (with complement \bar{A}) can all be described in terms of the reduced density matrix $\rho_A = \text{tr}_{\bar{A}}\rho$. The entanglement entropy of A is defined as $S(A) = -\text{tr}[\rho_A \log \rho_A]$. If the full system is in a pure state, S_A equals $S_{\bar{A}}$ and measures the amount of entanglement between A and \bar{A} . Now consider two disjoint regions A and B . The amount of correlation between these regions (both classical and quantum) is measured by the *mutual information*

$$I(A, B) = S(A) + S(B) - S(A \cup B). \quad (1.1)$$

While the entanglement entropy of a spatial region A has a UV divergence proportional to the area of the boundary of A , the mutual information is finite, making it an especially convenient quantity to study. The mutual information appears in bounds that limit how well an observer of A can predict events in B . Indeed $I(A, B) \geq 0$ with equality if and only if A and B are uncorrelated, i.e. $\rho_{A \cup B} = \rho_A \otimes \rho_B$. Mutual information can potentially provide a powerful description of how correlations evolve and spread in an out-of-equilibrium system.

Progress in computing mutual information has been made for certain two-dimensional conformal field theories in special limits [1]. In particular, Calabrese and Cardy

have studied the evolution of entanglement entropy following a quantum quench [2]. They studied quenches in which a two-dimensional field theory with a gap suddenly becomes conformal (e.g., because a parameter in the Hamiltonian such as an external field is changed). The evolution of mutual information in this system can be computed in limits where the time, the interval sizes, and the interval separations are all large compared to the initial inverse mass gap. It was found that the entanglement entropy of an arbitrary number of intervals (and hence the mutual information defined above) exhibits a piecewise linear behavior in time. This behavior is consistent with a simple model based on causal propagation with the speed of light from an initial state with short-range correlations.

Another interesting quantity to consider in this context is the *tripartite information*, which measures the degree of extensivity of the mutual information. This quantity is defined for three spatial regions A , B and C as

$$\begin{aligned} I_3(A, B, C) &= S(A) + S(B) + S(C) - S(A \cup B) \\ &\quad - S(A \cup C) - S(B \cup C) + S(A \cup B \cup C) \\ &= I(A, B) + I(A, C) - I(A, B \cup C). \end{aligned} \quad (1.2)$$

By definition, it is symmetric under permutations of its arguments. In a generic field theory, depending on the choice of the regions, it can be positive, negative or zero, meaning that the mutual information is subextensive, superextensive or extensive, respectively. It does not have the UV divergences present in the entanglement entropy. This is true even when the three regions share boundaries (in contrast to the mutual information which is cutoff dependent in this case and needs to be renormalized).

*vijay@physics.upenn.edu

†Alice.Bernamonti@vub.ac.be

‡ncopland@sogang.ac.kr

§Ben.Craps@vub.ac.be

||Federico.Galli@vub.ac.be

For equilibrium states of field theories that have a gravity dual, the AdS/CFT correspondence gives us a simple recipe for computing entanglement entropy in terms of the areas of minimal surfaces in a dual spacetime [3]. The mutual and the tripartite information between regions can then be computed through (1.1) and (1.2). Applying this method, an interesting phase transition was observed, where the mutual information between a pair of disjoint intervals in two-dimensional field theory is of $O(1)$ for large separations, but of order the central charge for small separations [3,4]. A recent work [5] has also proven that for quantum field theories at equilibrium with a holographic dual, the mutual information is always extensive or super-extensive, meaning that $I_3(A, B, C) \leq 0$.

The purpose of our paper is to understand how these results extend to a dynamical setting where energy is injected at $t = 0$ and then proceeds to equilibrate. We model the injection of energy as a shell of null dust falling into anti-de Sitter (AdS) space. We then apply a proposal of [6] for computing entanglement entropy in a time-dependent AdS/CFT setting in terms of the areas of extremal surface in the dual spacetime. A key difference between our setting and that of [2] is that our theory is always conformal and hence starts with long-range correlations, whereas their model is gapped at early times so that the correlations are essentially local [7].

We find that the mutual information between intervals in our setting starts at the vacuum value and ends at the thermal value, but usually passes through an intermediate phase where it is higher than either. The rise and fall are nearly linear in time. A causality argument (slightly modified from [2,7]) explains qualitative features of our results. We find that the tripartite information is nonpositive in all the cases that we study, matching the expectation based on the results of [5] who studied static configurations. In our dynamical setting the tripartite information changes with time during the process of thermalization in many parameter regimes. In contrast, the Calabrese and Cardy results for

two-dimensional quantum quenches, where a mass gap is suddenly taken to zero, imply that I_3 is constant in their setting [2]. If the AdS/CFT entanglement entropy proposal of [6] is correct, the difference is probably due to the fact that our initial state has long distance correlations. In other words, the ‘‘mass gap’’ in our setup would be zero, so that we are studying the system on time and distance scales small compared to the would be inverse initial mass gap.

II. MUTUAL INFORMATION

Consider the three-dimensional infalling shell geometry described by the Vaidya metric

$$ds^2 = -(r^2 - r_H^2 \Theta(v))dv^2 + 2drdv + r^2 dx^2, \quad (2.1)$$

where v labels ingoing null trajectories, Θ is the step function and we have set the AdS radius equal to 1. In this form, the Vaidya metric describes a zero thickness shell composed of tensionless null dust (Fig. 1(a)). Outside the infalling shell ($v > 0$), the geometry is identical to that of an AdS black brane with Hawking temperature $T = r_H/2\pi$, while inside the shell ($v < 0$) it is the same as that of pure AdS. The change of coordinates

$$v = \begin{cases} t + \frac{1}{2r_H} \ln \frac{|r-r_H|}{r+r_H} & v > 0 \\ t - \frac{1}{r} & v < 0 \end{cases} \quad (2.2)$$

brings the two metrics to the standard form

$$ds^2 = \begin{cases} -(r^2 - r_H^2)dt^2 + \frac{dr^2}{r^2 - r_H^2} + r^2 dx^2 & v > 0 \\ -r^2 dt^2 + \frac{dr^2}{r^2} + r^2 dx^2 & v < 0 \end{cases}. \quad (2.3)$$

On the boundary, at $r = \infty$, the coordinates v and t coincide.

We consider the time evolution of the mutual information between disjoint intervals of length ℓ separated by a distance d on the boundary of the Vaidya spacetime (2.1). In three bulk dimensions the entanglement entropy of a connected region A on the spacetime boundary is proposed

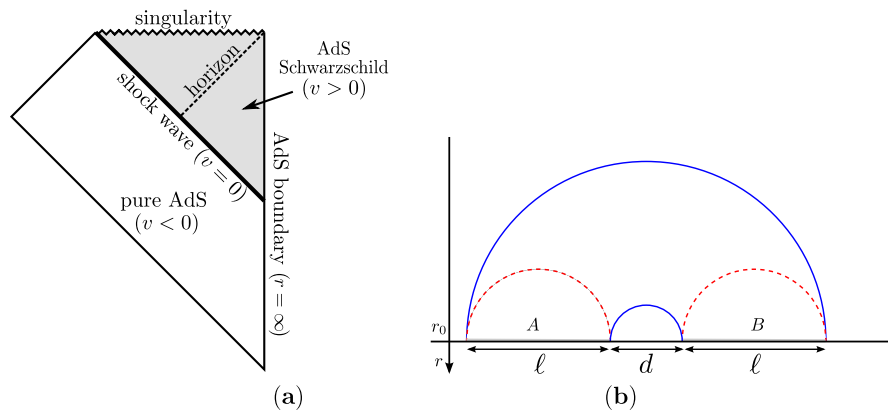


FIG. 1 (color online). (a) The causal structure of the Vaidya spacetime shown in the Poincaré patch of AdS space. The asymptotic boundary (vertical line on the right hand side) is planar, and the null lines on the left hand side of the diagram represent the Poincaré horizon. (b) Connected (in blue) and disconnected (in red dashed) locally minimal surfaces for the boundary region $A \cup B$ in AdS_3 .

to be computed holographically by the length of the bulk geodesic that connects the end points of A [6]. For disjoint intervals A and B there are multiple candidates for the geodesics that contribute to $S(A \cup B)$. In [4], it was shown that for equilibrium configurations, $S(A \cup B)$ is given by the minimum of the lengths of two sets of geodesics (shown as solid and dashed lines in Fig. 1(b)). We will assume that this prescription extends to the dynamical Vaidya background as a rule saying that $S(A \cup B)$ is determined by the length of the shortest collection of geodesics connecting the end points of A and B .¹

The geodesics connecting two equal-time boundary end points $(t_0, 0)$ and (t_0, ℓ) have been studied in [7,8]. These results have been extended to non-equal-time spacelike geodesics in [9]. Since the geodesic length \mathcal{L} diverges due to contributions near the AdS boundary, it is more convenient to work with a regularized length computed by introducing a large radius cutoff in AdS at $r = r_0$ and defining $\delta\mathcal{L} \equiv \mathcal{L} - 2 \ln(2r_0)$. This removes the divergent part of the length in the vacuum state (pure AdS). For $t_0 \leq 0$ (before the shell falls in) the geodesics lie entirely in AdS at fixed time $t = t_0$. Their renormalized length is

$$\delta\mathcal{L}_{\text{vacuum}}(\ell) = 2 \ln \frac{\ell}{2}. \quad (2.4)$$

For $0 < t_0 < \ell/2$, the geodesics cross the infalling shell and their renormalized length is

$$\delta\mathcal{L}_{\text{shell}}(\ell, t_0) = 2 \ln \left[\frac{\sinh(r_H t_0)}{r_H s(\ell, t_0)} \right], \quad (2.5)$$

where $s(\ell, t_0) \in [0, 1]$ is parametrically defined by

$$\ell = \frac{1}{r_H} \left[\frac{2c}{s\rho} + \ln \left(\frac{2(1+c)\rho^2 + 2s\rho - c}{2(1+c)\rho^2 - 2s\rho - c} \right) \right], \quad (2.6)$$

with $c = \sqrt{1 - s^2}$ and

$$2\rho = \coth(r_H t_0) + \sqrt{\coth^2(r_H t_0) - \frac{2c}{c+1}}. \quad (2.7)$$

For $t_0 \geq \ell/2$, the geodesics lie on the $t = t_0$ surface in the black brane geometry and

$$\delta\mathcal{L}_{\text{thermal}}(\ell) = 2 \ln \frac{\sinh \frac{r_H \ell}{2}}{r_H}. \quad (2.8)$$

In terms of these geodesic lengths our formula for the mutual information between the intervals A and B is

$$I(A, B) = \frac{1}{4G_N} \{ 2\delta\mathcal{L}(\ell) - \text{Min}[2\delta\mathcal{L}(\ell), \delta\mathcal{L}(2\ell + d) + \delta\mathcal{L}(d)] \}. \quad (2.9)$$

¹There is also a topological condition [4] that the geodesics should be continuously deformable to the AdS boundary. This condition will not come into play for us.

Observe that in principle we should also consider geodesics of spatial separation $\ell + d$, which connect the two left (right) end points of the two intervals A and B . We should thus evaluate in (2.9)

$$\text{Min}[2\delta\mathcal{L}(\ell), \delta\mathcal{L}(2\ell + d) + \delta\mathcal{L}(d), 2\delta\mathcal{L}(\ell + d)]. \quad (2.10)$$

However, for any fixed boundary time t_0 :

$$\begin{aligned} \delta\mathcal{L}_{\text{vacuum}}(\ell + d) &\geq \delta\mathcal{L}_{\text{vacuum}}(\ell), \\ \delta\mathcal{L}_{\text{thermal}}(\ell + d) &\geq \delta\mathcal{L}_{\text{thermal}}(\ell), \\ \delta\mathcal{L}_{\text{shell}}(\ell + d, t_0) &\geq \delta\mathcal{L}_{\text{shell}}(\ell, t_0), \end{aligned} \quad (2.11)$$

since, in each case, $\delta\mathcal{L}$ is monotonically increasing as a function of the spatial boundary separation, as is seen from (2.4) and (2.8) and numerically from (2.5). Therefore, when all the possible competing geodesics are of the same type (in terms of crossing the shell or not), it is enough to consider (2.9). There are however time intervals in which the property (2.11) is not enough to exclude the case of intersecting geodesics of length $\delta\mathcal{L}(\ell + d)$ from (2.10). For example, when $\ell > d$ and $t_0 \in [\ell/2, (\ell + d)/2)$, one has $\delta\mathcal{L}(\ell + d) = \delta\mathcal{L}_{\text{shell}}(\ell + d, t_0)$ while $\delta\mathcal{L}(\ell) = \delta\mathcal{L}_{\text{thermal}}(\ell)$. In these cases, however, it follows from (2.5) and (2.8) that

$$\delta\mathcal{L}_{\text{shell}}(\ell + d, t_0) \geq \delta\mathcal{L}_{\text{thermal}}(\ell) \quad (2.12)$$

in the relevant time interval, and it is therefore always enough to consider (2.9).

In the Vaidya spacetime (2.1), for $t_0 \leq 0$, the mutual information of A and B coincides with the vacuum AdS result of [4]:

$$I(A, B)_{\text{vacuum}} = \begin{cases} 0, & d \geq d_{\text{vacuum}} \\ \frac{c}{3} \ln \left[\frac{\ell^2}{d(2\ell + d)} \right], & d \leq d_{\text{vacuum}} \end{cases} \quad (2.13)$$

where we have used (2.4), the central charge $c = 3/(2G_N)$ and $d_{\text{vacuum}}(\ell) \equiv (\sqrt{2} - 1)\ell$. For $t_0 \geq (2\ell + d)/2$, all the geodesics lie entirely in a black brane background and the mutual information is given by [10]:

$$\begin{aligned} I(A, B)_{\text{thermal}} &= \frac{1}{4G_N} \{ 2\delta\mathcal{L}_{\text{thermal}}(\ell) \\ &\quad - \text{Min}[2\delta\mathcal{L}_{\text{thermal}}(\ell), \delta\mathcal{L}_{\text{thermal}}(2\ell + d) + \delta\mathcal{L}_{\text{thermal}}(d)] \} \\ &= \begin{cases} 0, & d \geq d_{\text{thermal}} \\ \frac{c}{3} \ln \left[\frac{\sinh^2(r_H \ell/2)}{\sinh(r_H(2\ell + d)/2) \sinh(r_H d/2)} \right], & d \leq d_{\text{thermal}} \end{cases} \end{aligned} \quad (2.14)$$

using (2.8), where

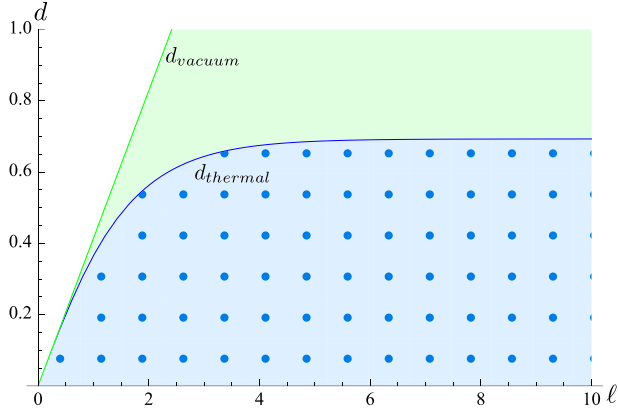


FIG. 2 (color online). d_{thermal} and d_{vacuum} as a function of ℓ for $r_H = 1$. The mutual information surely vanishes for $t_0 \leq 0$ and $t_0 \geq (2\ell + d)/2$ for d and ℓ in the white region, for $t_0 \geq (2\ell + d)/2$ in the green shaded region, while it is generically everywhere nonzero in the blue dotted region.

$$d_{\text{thermal}}(\ell) \equiv \frac{1}{r_H} \ln[1 - e^{r_H \ell} + e^{2r_H \ell} + \sqrt{(1 - e^{r_H \ell} + e^{2r_H \ell})^2 - e^{2r_H \ell}}] - 2\ell. \quad (2.15)$$

As the intervals size $\ell \rightarrow \infty$, $d_{\text{thermal}}(\ell) \rightarrow d_\infty = \frac{\ln 2}{r_H}$.

From these results, we see that for a fixed interval size ℓ when $d_{\text{thermal}} \leq d < d_{\text{vacuum}}$ the mutual information must vanish for $t_0 \geq (2\ell + d)/2$. The reason is that at these late times, all the geodesics that can potentially contribute to the mutual information (see Fig. 1(b)) will lie in the black brane background. When $d \geq d_{\text{vacuum}}$ it is zero also for $t_0 \leq 0$ because at early times all the relevant geodesics lie in the empty AdS background. When $d < d_{\text{thermal}}$ the mutual information can be nonzero for all times (Fig. 2).

In the Vaidya background the mutual information should interpolate between the vacuum and thermal results. The interpolation occurs in the period $0 < t_0 < (2\ell + d)/2$, when one or more geodesics intersect the shell. Crossing the shell has the effect of lowering (raising) the geodesic length for a fixed boundary separation, with respect to the black brane (AdS) background. When $\text{Max}(\ell/2, d/2) \leq t_0 < (2\ell + d)/2$ only the outermost geodesic with boundary separation $2\ell + d$ crosses the shell. When $\text{Min}(\ell/2, d/2) \leq t_0 < \text{Max}(\ell/2, d/2)$ geodesics with boundary separation $2\ell + d$ and $\text{Max}(\ell, d)$ cross it, and so on. The mutual information in this range of times can be computed using the appropriate geodesic lengths $\delta \mathcal{L}_{\text{shell}}$ in (2.5) and $\delta \mathcal{L}_{\text{thermal}}$ in (2.8). The mutual information computed in this way starts at the vacuum value at early times and ends at the thermal value at late times. Remarkably, it increases sharply to a peak at intermediate times (Fig. 3). These results are easily extended to a situation where the

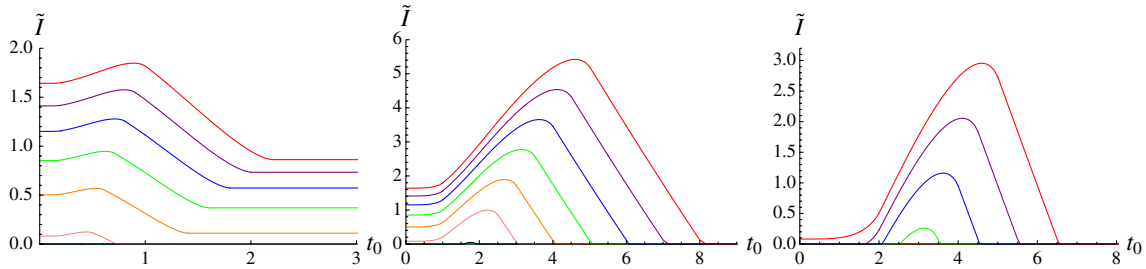


FIG. 3 (color online). Rescaled mutual information $\tilde{I} \equiv 4G_N I$ as a function of boundary time t_0 for $d = 0.4$ (left), $d = 2$ (center) and $d = 4$ (right), and $r_H = 1$. The various curves correspond to different values of ℓ which increases from the bottom up. The left panel shows $\ell = 0.2, 0.4, \dots, 2.0$, while the center panel and the right one show $\ell = 1, 2, \dots, 10$ (some of the curves in the three panels are not visible because everywhere vanishing).

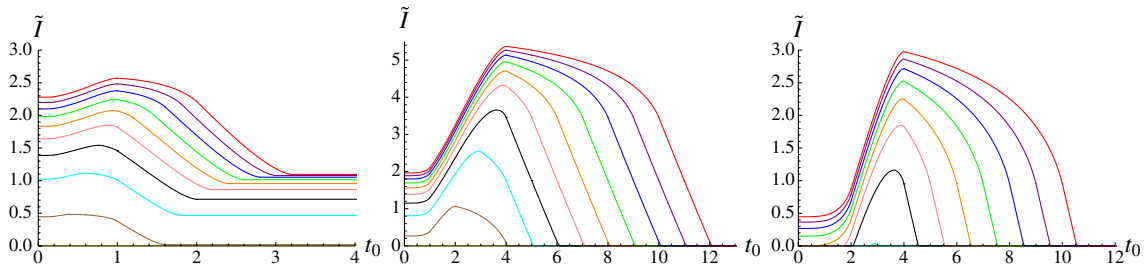


FIG. 4 (color online). Rescaled mutual information $\tilde{I} \equiv 4G_N I$ as a function of boundary time t_0 for $d = 0.4$, $\ell_1 = 2$ (left), $d = 2$, $\ell_1 = 8$ (center) and $d = 4$, $\ell_1 = 8$ (right), and $r_H = 1$. The various curves correspond to different values of ℓ_2 which increases from the bottom up. The left panel shows $\ell_2 = 0.4, 0.8, \dots, 4.0$ while the center and the right panels have $\ell_2 = 2, 4, \dots, 20$.

two intervals have different lengths ℓ_1 and ℓ_2 . The logic is identical, so we merely plot the results in Fig. 4.

III. A QUALITATIVE EXPLANATION FOR THE MUTUAL INFORMATION?

Why does the mutual information increase and then decrease again in our setup? For understanding the entanglement entropy of a single interval in the same setting it was useful to compare the AdS results with exact computations for quantum quenches [2,7]. The entanglement entropy for multiple intervals after a quench was also computed by Calabrese and Cardy [2] for times and spatial scales large compared to the inverse mass gap of the early time state. From their results we can compute the mutual information following (1.1). Since the Calabrese-Cardy theory starts, unlike ours, with a gapped initial state and a type of energy deposition with short-range correlations, their results need not agree with ours [7]. However, the explicit result nevertheless has a sharp feature in the middle.

A simple toy model developed by [2] gives a physical interpretation for this principal feature of the mutual information in the quantum quench. The idea was that before the quench there is a mass gap and a finite correlation length. Thus, after the quench only excitations originating at almost the same point will be entangled. At later times, such a pair of correlated particles will only contribute to the mutual information between two intervals, if each interval contains one of the two particles. As shown in Fig. 5 this naive model would lead to a linear rise and subsequent decline in the mutual information. An extension of this toy model to the Vaidya setup reproduced the entanglement entropy of a single interval by including power law long-range correlations in the initial state [7].

To try to reproduce our results more accurately, further modifications of the toy model would be needed. Consider, for example, the nonzero final state mutual information that is present in some cases. This can occur in a naive particle picture if the initial energy deposition had a finite

spatial correlation length, and we consider particle pairs that travel in the *same* direction as well as in opposite directions. In this setup, two intervals separated by a distance d will always be populated at late times with particle pairs that move in the same direction and were produced at a separation slightly larger than d . If the initial correlation length was bigger than d a final state mutual information can result.

IV. TRIPARTITE INFORMATION

Now consider the time evolution of the tripartite information (1.2) for three intervals on the boundary of the dynamical Vaidya background (2.1). From (1.2), in addition to the computations that we have already done, we need to compute $S(A \cup B \cup C)$. Following the previous sections, we will assume that this is determined by the length of the shortest collection of geodesics connecting the end points of A , B and C .

We first consider the case of three adjacent intervals A , B and C , of length ℓ , d and ℓ respectively, on the boundary of the Vaidya spacetime. This corresponds to the setting considered in Sec. II for the mutual information, now promoting the region of length d , which separates the two intervals of length ℓ , to a third interval.

We plot in Fig. 6 the results for the tripartite information (1.2) for different values of ℓ and d as a function of the boundary time t_0 . For large values of d (center and right panels of Fig. 6) the tripartite information starts at the vacuum value and ends at the (larger) thermal value passing through an intermediate phase where it is more negative than either. For small d (left panel of Fig. 6) and large enough ℓ , the behavior is different. In this case, the vacuum value is less negative than the thermal one and the tripartite information just decreases nonlinearly. Incidentally, in this parameter range the thermal mutual information is non-vanishing (see Fig. 3, and values of ℓ and d in the blue dotted region of Fig. 2).

For the value of d in the center panel of Fig. 6, for some values of ℓ , the tripartite information goes through an

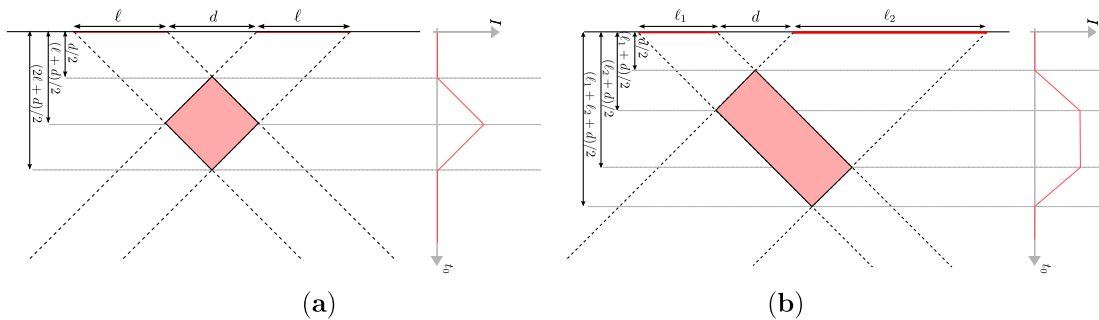


FIG. 5 (color online). (a) A simple causality derived picture for two intervals after a quench. After the quench at $t = 0$ signals propagate outwards at the speed of light in both directions. These will give correlations which contribute to the mutual information at $t = t_0$ if one signal is in each interval, which occurs only for signals originating in the shaded pink diamond. (b) The analogous picture for two intervals of different length.

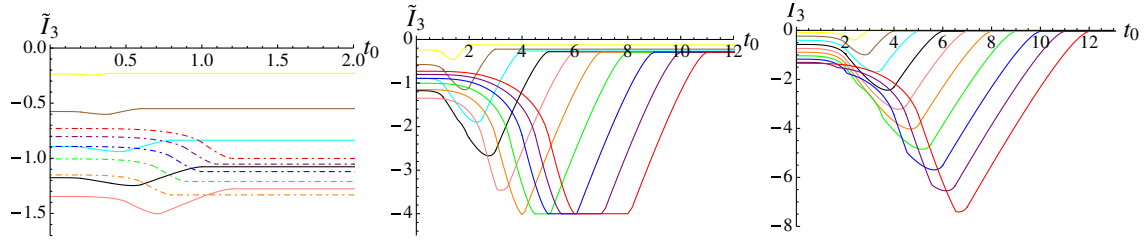


FIG. 6 (color online). Rescaled tripartite information $\tilde{I}_3 \equiv 4G_N I_3$ for three adjacent intervals of length ℓ , d and ℓ as a function of boundary time t_0 , for $d = 0.4$ (left), $d = 2$ (center) and $d = 4$ (right), and $r_H = 1$. The various curves correspond to different values of ℓ . The left panel shows $\ell = 0.2, \dots, 1, 0$ in continuous lines with ℓ decreasing from the bottom up, while the curves in dot-dashed have $\ell = 1.2, \dots, 2.0$ increasing from the bottom up. The center and right panels have $\ell = 1, 2, \dots, 10$ decreasing from right to left.

intermediate phase where it is constant. This can be understood looking at the first line of (1.2). In this phase, all the contributions are constant except for $S(A \cup C)$ and $S(A \cup B \cup C)$, whose time-dependent contributions cancel each other in (1.2). To see this, first note that $S(A)$, $S(B)$, $S(C)$, $S(A \cup B)$ and $S(B \cup C)$ all correspond to geodesics extending in the thermal background and have a constant value. Meanwhile $S(A \cup B \cup C)$ is given by the geodesic that ends on the two end points of $A \cup B \cup C$, which

crosses the shell. Finally, $S(A \cup C)$ is determined by the two geodesics enclosing a connected region in the bulk – the outer geodesic of this pair is the same one that appears in $S(A \cup B \cup C)$. Therefore the two contributions that cross the shell and are time-dependent cancel each other between $S(A \cup B \cup C)$ and $S(A \cup C)$, leading to a constant result for the tripartite information. For large enough ℓ/d , this constant value is approximately ℓ -independent, as can be seen from (2.8). The same type of argument applies to late

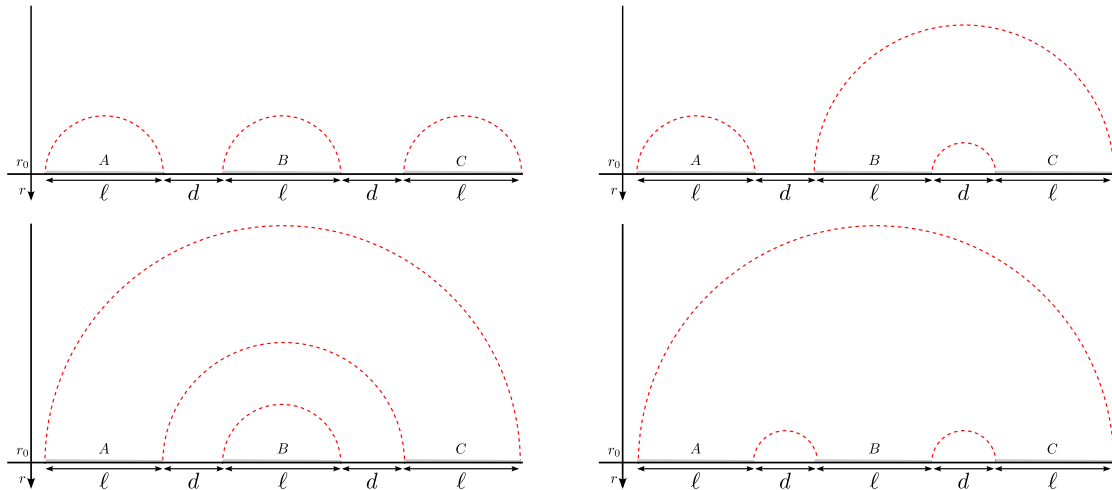


FIG. 7 (color online). A schematic representation of locally minimal surfaces for the boundary region $A \cup B \cup C$ in AdS_3 . The top right figure with A and C interchanged also contributes.

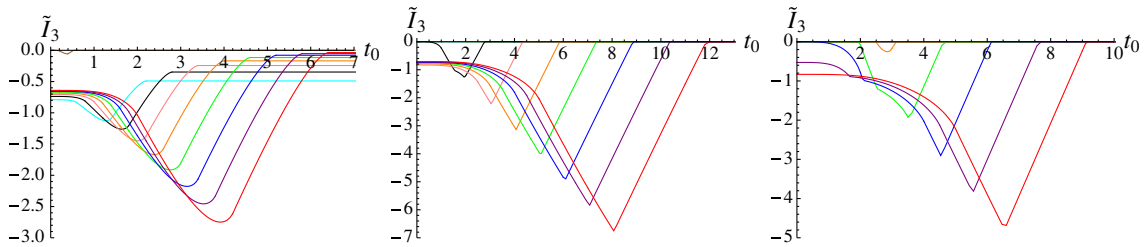


FIG. 8 (color online). Rescaled tripartite information $\tilde{I}_3 \equiv 4G_N I_3$ as a function of boundary time t_0 for $d = 0.4$ (left), $d = 2$ (center) and $d = 4$ (right), and $r_H = 1$. The various curves correspond to different values of ℓ which decreases from right to left. The left panel shows $\ell = 0.4, 0.8, \dots, 4.0$, the center and right panels have $\ell = 1, 2, \dots, 10$ (although only $\ell = 3, \dots, 10$ and $\ell = 6, \dots, 10$ are not everywhere vanishing in the center and right panel, respectively).

times, when all the geodesics extend in the thermal background.

As shown in Fig. 6, we find a nonpositive tripartite information at all times. Even though we are dealing with a dynamical setup, this behavior matches [5], where it has been shown that in holographic theories at equilibrium the mutual information is extensive or superextensive.

While the case of adjacent intervals is a direct extension of the computation of the mutual information (Sec. II), the tripartite information for three disjoint intervals is more subtle. However, using the fact that only nonintersecting geodesics are local minimal surfaces for two disjoint intervals, as was the case in (2.9), the collection of geodesics that potentially contribute to the tripartite information of $A \cup B \cup C$ in the Vaidya background reduces to those shown in Fig. 7.

The time evolution of the tripartite information for three disjoint intervals of length ℓ , each separated by a distance d from adjacent ones, is plotted in Fig. 8 for various values of d and ℓ . It mainly shows the same features as the tripartite information of adjacent intervals.

We have found that the tripartite information computed in the Vaidya geometry is generically nonzero. Now recall that Calabrese and Cardy found that the entanglement entropy of N disjoint intervals (u_{2j-1}, u_{2j}) , with $1 \leq j \leq N$ and $u_k < u_{k+1}$, after a quantum quench [2] evolves in time according to the formula

$$S \sim S_\infty + \frac{\pi c}{12\tau_0} \sum_{k,l=1}^{2N} (-1)^{k-l-1} \text{Max}[u_k - t, u_l + t]. \quad (4.1)$$

Here c is the central charge and τ_0 is a parameter of the same order as the inverse mass gap (refer to [2] for more details). This formula holds only in the limit where the time t and all separations $|u_k - u_l|$ are much larger than the

initial inverse mass gap. Using (4.1), it follows that the time-dependent part of the tripartite information vanishes in this regime because each contribution associated to an extremum u_j appears an equal number of times with a minus and a plus sign in (1.2). In contrast, the tripartite information for the Vaidya background (Fig. 8) is generally time-dependent and is only constant (and vanishing) if $I(A, B)$, $I(A, C)$ and $I(A, B \cup C)$ in (1.2) are all identically zero.

The results of Calabrese and Cardy need not agree with ours since they start with a gapped initial state which lacks long-range correlations. Nevertheless it is interesting that important qualitative features of the time evolution of the mutual information matched between their model and ours, while the behavior of the tripartite information is sharply different. In any case, the disagreement shows clearly that the simple causality argument of Sec. III, where interactions were not taken into account, is not enough to capture the qualitative features of our strongly coupled two-dimensional dynamics.

ACKNOWLEDGMENTS

This research is supported by the DOE under Grant No. DE-FG02-95ER40893, the Belgian Federal Science Policy Office through the Interuniversity Attraction Pole IAP VI/11, by FWO-Vlaanderen through Project No. G011410N and the National Research Foundation of Korea (NRF) grant funded by the Korea government (MEST) through the Center for Quantum Spacetime (CQUeST) of Sogang University under Grant No. 2005-0049409. A. B. and F. G. are Aspirant FWO. V. B. and B. C. thank the ICTP, Trieste for hospitality while this paper was being completed.

-
- [1] P. Calabrese, J. Cardy, and E. Tonni, *J. Stat. Mech.* **01** (2011) P01021.
 - [2] P. Calabrese and J.L. Cardy, *J. Stat. Mech.* **04** (2005) P04010; P. Calabrese and J. Cardy, *J. Phys. A* **42**, 504005 (2009).
 - [3] S. Ryu and T. Takayanagi, *Phys. Rev. Lett.* **96**, 181602 (2006); *J. High Energy Phys.* **08** (2006) 045.
 - [4] M. Headrick, *Phys. Rev. D* **82**, 126010 (2010).
 - [5] P. Hayden, M. Headrick, and A. Maloney, arXiv:1107.2940.
 - [6] V.E. Hubeny, M. Rangamani, and T. Takayanagi, *J. High Energy Phys.* **07** (2007) 062.
 - [7] J. Abajo-Arastia, J. Aparicio, and E. Lopez, *J. High Energy Phys.* **11** (2010) 149.
 - [8] V. Balasubramanian *et al.*, *Phys. Rev. Lett.* **106**, 191601 (2011); V. Balasubramanian *et al.*, *Phys. Rev. D* **84**, 026010 (2011).
 - [9] J. Aparicio and E. Lopez, arXiv:1109.3571.
 - [10] E. Tonni, *J. High Energy Phys.* **05** (2011) 004.

Thermalization of Strongly Coupled Field Theories

V. Balasubramanian,¹ A. Bernamonti,² J. de Boer,³ N. Copland,² B. Craps,² E. Keski-Vakkuri,⁴ B. Müller,⁵
A. Schäfer,⁶ M. Shigemori,⁷ and W. Staessens²

¹*David Rittenhouse Laboratory, University of Pennsylvania, Philadelphia, Pennsylvania 19104, USA*

²*Theoretische Natuurkunde, Vrije Universiteit Brussel, and International Solvay Institutes, B-1050 Brussels, Belgium*

³*Institute for Theoretical Physics, University of Amsterdam, 1090 GL Amsterdam, The Netherlands*

⁴*Helsinki Institute of Physics and Department of Physics, FIN-00014 University of Helsinki, Finland*

⁵*Department of Physics and CTMS, Duke University, Durham, North Carolina 27708, USA*

⁶*Institut für Theoretische Physik, Universität Regensburg, D-93040 Regensburg, Germany*

⁷*Kobayashi-Maskawa Institute for the Origin of Particles and the Universe, Nagoya University, Nagoya 464-8602, Japan*

(Received 28 January 2011; published 9 May 2011)

Using the holographic mapping to a gravity dual, we calculate 2-point functions, Wilson loops, and entanglement entropy in strongly coupled field theories in $d = 2, 3$, and 4 to probe the scale dependence of thermalization following a sudden injection of energy. For homogeneous initial conditions, the entanglement entropy thermalizes slowest and sets a time scale for equilibration that saturates a causality bound. The growth rate of entanglement entropy density is nearly volume-independent for small volumes but slows for larger volumes. In this setting, the UV thermalizes first.

DOI: 10.1103/PhysRevLett.106.191601

PACS numbers: 11.25.Tq, 11.25.-w, 52.27.Gr

It is widely believed that the observed nearly inviscid hydrodynamics of relativistic heavy ion collisions at collider energies is an indication that the matter produced in these nuclear reactions is strongly coupled [1]. Some such strongly coupled field theories can be studied by using the holographic duality between gravitational theories in asymptotically anti-de Sitter (AdS) space-times and quantum field theories on the boundary of AdS. The thermal state of the field theory is represented by a black brane in AdS, and near-equilibrium dynamics is studied in terms of perturbations of the black hole metric. A key remaining challenge is to understand the far from equilibrium process of thermalization. The AdS/CFT correspondence relates the approach to thermal equilibrium in the boundary theory to black hole formation in the bulk.

Recent works studied the gravitational collapse of energy injected into AdS₅ and the formation of an event horizon [2]. These works started from locally anisotropic metric perturbations near the AdS boundary and studied the rate at which isotropic pressure was established by examining the evolution of the stress tensor. By studying gravitational collapse induced by a small scalar perturbation, the authors of Ref. [3] concluded that local observables behaved as if the system thermalized almost instantaneously. Here we model the equilibrating field configuration in AdS by an infalling homogeneous thin mass shell [4,5] and study how the rate of thermalization varies with spatial scale and dimension. We consider $2d$, $3d$, and $4d$ field theories dual to gravity in asymptotically AdS₃, AdS₄, and AdS₅ space-times, respectively. Our treatment of $2d$ field theories is analytic.

Expectation values of local gauge-invariant operators, including the energy-momentum tensor and its derivatives,

provide valuable information about the applicability of viscous hydrodynamics but cannot be used to explore the scale dependence of deviations from thermal equilibrium. Equivalently, in the dual gravitational description these quantities are sensitive only to the metric close to the AdS boundary. Nonlocal operators, such as Wilson loops and 2-point correlators of gauge-invariant operators, probe the thermal nature of the quantum state on extended spatial scales. In the AdS language, these probes reach deeper into the bulk space-time, which corresponds to probing further into the infrared of the field theory. They are also relevant to the physics probed in relativistic heavy ion collisions, e.g., through the jet quenching parameter \hat{q} [6] and the color screening length.

A global probe of thermalization is the entanglement entropy S_A [7,8] of a domain A , measured after subtraction of its vacuum value. In the strong coupling limit, it has been proposed that S_A for a region A with boundary ∂A in the field theory is proportional to the area of the minimal surface γ in AdS whose boundary coincides with ∂A : $S_A = \text{Area}(\gamma)/4G_N$, where G_N is Newton's constant [8]. Thus, for a $(d = 2)$ -dimensional field theory, S_A is the length of a geodesic curve in AdS₃ (studied in Ref. [9]); for $d = 3$, S_A is the area of a $2d$ sheet in AdS₄ (studied in Ref. [10]); and for $d = 4$, S_A is the volume of a $3d$ region in AdS₅. In $d = 3$ the exponential of the area of the minimal surface that measures S_A also computes the expectation value of the Wilson loop that bounds the minimal surface. Wilson loops in $d = 4$ correspond to $2d$ minimal surfaces as well.

First, we consider equal-time 2-point correlators of gauge-invariant operators \mathcal{O} of large conformal dimension Δ . In the dual supergravity theory this correlator can be expressed, in the semiclassical limit, in terms of the length

$\mathcal{L}(\mathbf{x}, t)$ of the bulk geodesic curve that connects the end points on the boundary: $\langle \mathcal{O}(\mathbf{x}, t) \mathcal{O}(0, t) \rangle \sim \exp[-\Delta \mathcal{L}(\mathbf{x}, t)]$ [11]. When multiple such geodesics exist, one has to consider steepest descent contours to determine the contribution from each geodesic.

We consider a $(d+1)$ -dimensional infalling shell geometry described in Poincaré coordinates by the Vaidya metric

$$ds^2 = \frac{1}{z^2} \{-[1 - m(v)z^d]dv^2 - 2dzdv + dx^2\}, \quad (1)$$

where v labels ingoing null trajectories, and we set the AdS radius to 1. The boundary is at $z = 0$, where v coincides with the observer time t . The mass function of the infalling shell is

$$m(v) = (M/2)[1 + \tanh(v/v_0)], \quad (2)$$

where v_0 determines the thickness of a shell falling along $v = 0$. The metric interpolates between vacuum AdS inside the shell and an AdS black brane geometry with Hawking temperature $T = dM^{1/d}/4\pi$ outside the shell. 2-point functions agree with those of a boundary field theory at thermal equilibrium only if they are dominated by geodesics that stay outside the shell.

The geodesic length \mathcal{L} diverges due to contributions near the AdS boundary. We introduce an ultraviolet cutoff z_0 and define a renormalized correlator $\delta \mathcal{L} = \mathcal{L} + 2 \ln(z_0/2)$ by removing the divergent part of the correlator in the vacuum state (pure AdS). The renormalized equal-time 2-point function is $\langle \mathcal{O}(\mathbf{x}, t) \mathcal{O}(0, t) \rangle_{\text{ren}} \sim \exp[-\Delta \delta \mathcal{L}(\mathbf{x}, t)]$. We compute the renormalized correlator as a function of \mathbf{x} and t in a state evolving towards thermal equilibrium and compare it to the corresponding thermal correlator. In the bulk, this amounts to computing geodesic lengths in a collapsing shell geometry and comparing them to geodesic lengths in the black brane geometry ($\delta \mathcal{L}_{\text{thermal}}$) resulting from the collapse.

We study geodesics with boundary separation ℓ in the x direction in AdS₃, AdS₄, and AdS₅ modified by the infalling shell. The end point locations are denoted as $(v, z, x) = (t_0, z_0, \pm \ell/2)$, where z_0 is the UV cutoff. The lowest point of the geodesic in the bulk is the midpoint located at $(v, z, x) = (v_*, z_*, 0)$. Geodesics are obtained by solving differential equations for the functions $v(x)$ and $z(x)$ with these boundary conditions and are unique in the infalling shell background. The length of the geodesics is $\mathcal{L}(\ell, t_0) = 2 \int_0^{\ell/2} dx z_*(x)^{-2}$. In empty AdS, this gives the renormalized geodesic length $\delta \mathcal{L}_{\text{AdS}} = 2 \ln(\ell/2)$.

A numerical solution for the length of geodesics crossing the shell in the $d = 2$ (AdS₃) case was obtained in Ref. [9]. We checked that physical results do not depend significantly on the shell thickness when v_0 is small and then derived an analytical solution in the $v_0 \rightarrow 0$ limit:

$$\delta \mathcal{L}(\ell, t_0) = 2 \ln \left[\frac{\sinh(\sqrt{M}t_0)}{\sqrt{M}s(\ell, t_0)} \right], \quad (3)$$

where $s(\ell, t_0) \in [0, 1]$ is parametrically defined by

$$\ell = \frac{1}{\sqrt{M}} \left[\frac{2c}{s\rho} + \ln \left(\frac{2(1+c)\rho^2 + 2s\rho - c}{2(1+c)\rho^2 - 2s\rho - c} \right) \right], \quad (4)$$

$$2\rho = \coth(\sqrt{M}t_0) + \sqrt{\coth^2(\sqrt{M}t_0) - \frac{2c}{c+1}},$$

with $c = \sqrt{1-s^2}$ and $\rho = (\sqrt{M}z_c)^{-1}$. Here z_c is the radial location of the intersection between the geodesic and the shell. For any given ℓ , at sufficiently late times, the geodesic lies entirely in the black brane background outside the shell. In this case the length is

$$\delta \mathcal{L}_{\text{thermal}}(\ell) = 2 \ln[(1/\sqrt{M}) \sinh(\sqrt{M}\ell/2)], \quad (5)$$

representing the result for thermal equilibrium.

We use these analytic relations in $d = 2$ and find $\delta \mathcal{L}(\ell, t_0)$ in $d = 3, 4$ by numerical integration. We measure the approach to thermal equilibrium by comparing $\delta \mathcal{L}$ at any given time with the late time thermal result (see Fig. 1). In any dimension, this compares the logarithm of the 2-point correlator at different spatial scales with the logarithm of the thermal correlator. For $d = 2$, the same quantity measures by how much the entanglement entropy at a given spatial scale differs from the entropy at thermal equilibrium.

Various thermalization times can be extracted from Fig. 1. For any spatial scale we can ask for (a) the time τ_{dur} until full thermalization (measured as the time when the geodesic between two boundary points just grazes the infalling shell), (b) the half-thermalization time $\tau_{1/2}$, which measures the duration for the curves to reach half of their equilibrium value, and (c) the time τ_{max} at which thermalization proceeds most rapidly, namely, the time for which the curves in Fig. 1 are steepest. These are plotted in Fig. 2. In $d = 2$ we can analytically derive the linear relation $\tau_{\text{dur}} \equiv \ell/2$, as also observed in Ref. [9].

The linearity of $\tau_{\text{dur}}(\ell)$ in $2d$ is expected from general arguments in conformal field theory [7], and the coefficient is as small as possible under the constraints of causality. The thermalization time scales $\tau_{1/2}$ and τ_{max} for $3d$ and $4d$ field theories (Fig. 2, middle and right) are sublinear in the

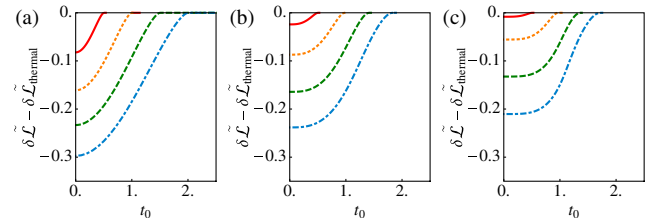


FIG. 1 (color online). $\delta \tilde{\mathcal{L}} - \delta \tilde{\mathcal{L}}_{\text{thermal}}$ ($\tilde{\mathcal{L}} \equiv \mathcal{L}/\ell$) as a function of boundary time t_0 for $d = 2, 3, 4$ (left, right, middle) for a thin shell ($v_0 = 0.01$). The boundary separations are $\ell = 1, 2, 3, 4$ (top to bottom curve). All quantities are given in units of M . These numerical results match analytical results for $d = 2$ as $v_0 \rightarrow 0$.

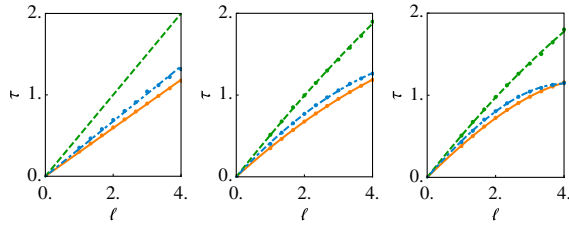


FIG. 2 (color online). Thermalization times (τ_{dur} , top line; τ_{max} , middle line; $\tau_{1/2}$, bottom line) as a function of spatial scale for $d = 2$ (left), $d = 3$ (middle), and $d = 4$ (right) for a thin shell ($v_0 = 0.01$). All thermalization time scales are linear in ℓ for $d = 2$ and deviate from linearity for $d = 3, 4$.

spatial scale. In the range we study, the complete thermalization time τ_{dur} deviates slightly from linearity and is somewhat shorter than $\ell/2$. We will later discuss whether a rigorous causality bound for thermalization processes exists or not.

In $2d$ “quantum quenches” where a pure state prepared as the ground state of a Hamiltonian with a mass gap is followed as it evolves according to a different, critical Hamiltonian, a nonanalytic feature was found where thermalization at a spatial scale ℓ is completed abruptly at $\tau_{\text{dur}}(\ell)$ [7,9]. An analogous feature is evident in Fig. 1 (left) as a sudden change in the slope at τ_{dur} , smoothed out only by the small nonzero thickness of the shell or, equivalently, by the intrinsic duration of the injection of energy. We find a similar (higher-order) nonanalyticity for $d = 3, 4$ (Fig. 1, middle and right) and expect this to be a general consequence of abrupt injection of energy in any dimension.

Figure 2 shows that complete thermalization of the equal-time correlator is first observed at short length scales or large momentum scales (see also [5]). While this behavior follows directly in our setup with a shell falling in from the (“UV”) boundary of AdS, this “top-down” thermalization contrasts with the behavior of weakly coupled gauge theories even with energy injected in the UV. In the “bottom-up” scenario [12] applicable to that case, hard quanta of the gauge field do not equilibrate directly by randomizing their momenta but gradually degrade their energy by radiating soft quanta, which fill up the thermal phase space and equilibrate by collisions among themselves. This bottom-up scenario is linked to the infrared divergence of the splitting functions of gauge bosons and fermions in perturbative gauge theory. It contrasts with the “democratic” splitting properties of excitations in strongly coupled super Yang-Mills theory that favor an approximately equal sharing of energy and momentum [13].

The thermal limit of the Wightman function that we studied above is a necessary but not a sufficient condition for complete thermalization. To examine whether thermalization proceeds similarly for other probes, we also studied entanglement entropy and spacelike Wilson loop expectation values in $3d$ (following [10]) and $4d$ field theories. Entanglement entropy in $3d$ field theories is holographically related to minimal surfaces in AdS_4 and hence

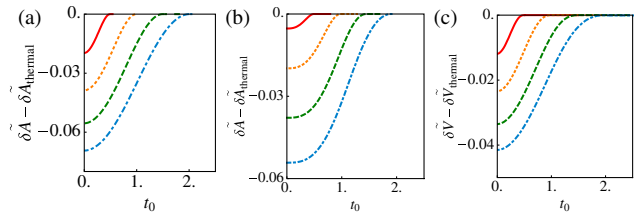


FIG. 3 (color online). $\delta\tilde{\mathcal{A}} - \delta\tilde{\mathcal{A}}_{\text{thermal}}$ ($\tilde{\mathcal{A}} \equiv \mathcal{A}/\pi R^2$; left and middle panels) and $\delta\tilde{V} - \delta\tilde{V}_{\text{thermal}}$ [$\tilde{V} \equiv V/(4\pi R^3/3)$; right panel] as a function of t_0 for radii $R = 0.5, 1, 1.5, 2$ (top curve to bottom curve) and mass shell parameters $v_0 = 0.01$, $M = 1$, in $d = 3$ (left panel) and $d = 4$ (middle and right panel) field theories.

to the logarithm of the expectation value of Wilson loops. We considered circular loops of radius R in $d = 3, 4$. The minimal spacelike surface in AdS_{d+1} whose boundary is this circular loop extends into the bulk space radially and into the past. The tip occurs at $(v_*, z_*, \mathbf{x} = \mathbf{0})$. The cross section at fixed z and v is a circle, and thus the surface is parameterized in terms of the radii ρ of these circles. The overall shape minimizes the action for the two functions $z(\rho)$ and $v(\rho)$:

$$\mathcal{A}[R] = 2\pi \int_0^R d\rho \frac{\rho}{z^2} \sqrt{1 - [1 - m(v)z^d]v'^2 - 2z'v'}, \quad (6)$$

where $z'(\rho) = dz/d\rho$, etc. The resulting Euler-Lagrange equations can be numerically integrated. We regularize the area by subtracting the divergent piece of the area in “empty” AdS: $\delta\mathcal{A}[R] = \mathcal{A}[R] - (R/z_0)$. Entanglement entropy of spherical volumes in $d = 4$ is similarly computed in terms of minimal volumes in AdS_5 by minimizing an equation similar to (6) and defining $\delta V[R]$ by subtracting the divergent volume in empty AdS.

The deficit area $\delta\mathcal{A} - \delta\mathcal{A}_{\text{thermal}}$ for Wilson loops in $d = 3, 4$ and the deficit volume $\delta V - \delta V_{\text{thermal}}$ are plotted in Fig. 3 for several boundary radii R as a function of the boundary time t_0 . By subtracting the thermal values, we can observe the deviation from equilibrium for each spatial scale at a time t_0 . Comparing the three thermalization times defined earlier as a function of the loop diameter (Fig. 4), we find that for the entanglement entropy in $d = 3, 4$, the complete thermalization time $\tau_{\text{dur}}(R)$ is close to being a straight line with unit slope over the range of scales that we

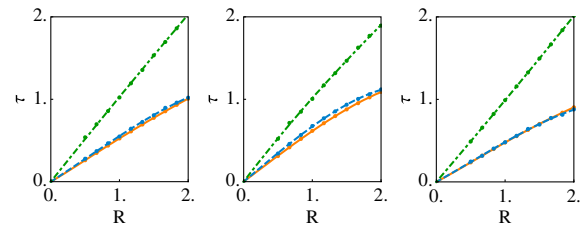


FIG. 4 (color online). Thermalization times (τ_{dur} , top line; τ_{max} , middle line; $\tau_{1/2}$, bottom line) as a function of the diameter for circular Wilson loops in $d = 3, 4$ (left, middle) and for entanglement entropy of spherical regions in $d = 4$ (right).

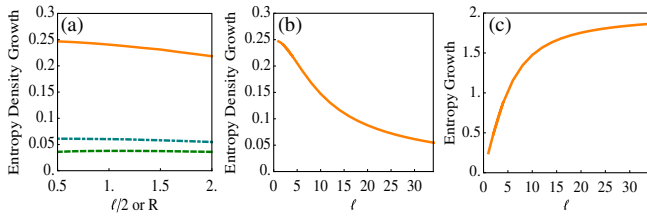


FIG. 5 (color online). (Left) Maximal growth rate of entanglement entropy *density* vs radius of entangled region for $d = 2, 3, 4$ (top to bottom). (Middle) The same plot for $d = 2$, larger range of ℓ . (Right) Maximal entropy growth rate for $d = 2$.

study (as observed in [10] for $d = 3$). On the other hand, for Wilson loops in $d = 4$, $\tau_{\text{dur}}(R)$ deviates somewhat from linearity and is shorter than R .

Our thermalization times for Wilson loop averages and entanglement entropy seem remarkably similar to those for 2-point correlators (after noting that R here is the radius of the thermalizing region and ℓ in Fig. 2 is the diameter). Slightly “faster-than-causal” thermalization, possibly due to the homogeneity of the initial configuration, seems to occur for the probes that do not correspond to entanglement entropy in each dimension. For the latter, the thermalization time is linear in the spatial scale and saturates the causality bound. As the actual thermalization rate of a system is set by the slowest observable, our results suggest that in strongly coupled theories with a gravity dual, thermalization occurs “as fast as possible” at each scale, subject to the constraint of causality. Taking the thermal scale $\ell \sim \hbar/T$ as the length scale, this suggests that for strongly coupled matter $\tau_{\text{dur}} \sim 0.5\hbar/T$, in particular, $\tau_{\text{dur}} \sim 0.3 \text{ fm}/c$ at heavy ion collider energies ($T \approx 300\text{--}400 \text{ MeV}$), comfortably short enough to account for the experimental observations.

The average growth rate of the *coarse grained* entropy in nonlinear dynamical systems is measured by the Kolmogorov-Sinai (KS) entropy rate h_{KS} [14], which is given by the sum of all positive Lyapunov exponents. For a classical $\text{SU}(2)$ lattice gauge theory in $4d$, h_{KS} has been shown to be proportional to the volume [15]. For a system starting far from equilibrium, the KS entropy rate generally describes the rate of growth of the coarse grained entropy during a period of linear growth after an initial dephasing period and before the close approach to equilibrium [16]. Here we observe similar linear growth of *entanglement* entropy density in $d = 2, 3, 4$ [Figs. 1(a), 3(a), and 3(c)]. For small boundary volumes, the growth rate of entropy *density* is nearly independent of the boundary volume [almost parallel slopes in Figs. 1(a), 3(a), and 3(c) and nearly constant maximal growth rate in Fig. 5(a)]. Equivalently, the growth rate of the entropy is proportional to the volume—suggesting that entropy growth is a local phenomenon. However, in $d = 2$ where our analytic results enable study of large boundary volumes ℓ , we find that the growth rate of the entanglement entropy density changes for large ℓ , falling asymptotically as $1/\ell$ [Fig. 5(b)]. Equivalently, the entropy has a growth rate that approaches

a constant limiting value for large ℓ [Fig. 5(c)] and thus cannot arise from a local phenomenon. This behavior suggests that entanglement entropy and coarse grained entropy have different dynamical properties.

We have investigated the scale dependence of thermalization following a sudden injection of energy in $2d$, $3d$, and $4d$ strongly coupled field theories with gravity duals. The entanglement entropy sets a time scale for equilibration that saturates a causality bound. The relationship between the entanglement entropy growth rate and the KS entropy growth rate defined by coarse graining of the phase space distribution raises interesting questions.

We thank V. Hubeny for helpful discussions and E. Lopez for comments on an earlier version of the manuscript. This research is supported by the Belgian Federal Science Policy Office, by FWO-Vlaanderen, by the Foundation of Fundamental Research on Matter (FOM), by the DOE, by the BMBF, and by the Academy of Finland.

-
- [1] M. Gyulassy and L. McLerran, *Nucl. Phys.* **A750**, 30 (2005); J.W. Harris and B. Müller, *Annu. Rev. Nucl. Part. Sci.* **46**, 71 (1996).
 - [2] R. A. Janik and R. B. Peshanski, *Phys. Rev. D* **73**, 045013 (2006); P.M. Chesler and L.G. Yaffe, *Phys. Rev. Lett.* **102**, 211601 (2009).
 - [3] S. Bhattacharyya and S. Minwalla, *J. High Energy Phys.* **09** (2009) 034.
 - [4] U.H. Danielsson, E. Keski-Vakkuri, and M. Kruczenski, *Nucl. Phys.* **B563**, 279 (1999).
 - [5] S. Lin and E. Shuryak, *Phys. Rev. D* **78**, 125018 (2008).
 - [6] A. Kovner and U.A. Wiedemann, *Phys. Rev. D* **64**, 114002 (2001); H. Liu, K. Rajagopal, and U.A. Wiedemann, *J. High Energy Phys.* **03** (2007) 066.
 - [7] P. Calabrese and J. Cardy, *J. Phys. A* **42**, 504005 (2009).
 - [8] T. Nishioka, S. Ryu, and T. Takayanagi, *J. Phys. A* **42**, 504008 (2009).
 - [9] V.E. Hubeny, M. Rangamani, and T. Takayanagi, *J. High Energy Phys.* **07** (2007) 062; J. Abajo-Arastia, J. Aparicio, and E. Lopez, *J. High Energy Phys.* **11** (2010) 149.
 - [10] T. Albash and C.V. Johnson, *arXiv:1008.3027*.
 - [11] V. Balasubramanian and S.F. Ross, *Phys. Rev. D* **61**, 044007 (2000).
 - [12] R. Baier, A.H. Mueller, D. Schiff, and D.T. Son, *Phys. Lett. B* **502**, 51 (2001).
 - [13] Y. Hatta, E. Iancu, and A.H. Mueller, *J. High Energy Phys.* **05** (2008) 037; E. Iancu, *Acta Phys. Pol. B* **39**, 3213 (2008).
 - [14] A.N. Kolmogorov, *Dokl. Akad. Nauk SSSR* **119**, 861 (1958); **124**, 754 (1959); Ya. G. Sinai, *Dokl. Akad. Nauk SSSR* **124**, 768 (1959).
 - [15] J. Bolte, B. Müller, and A. Schäfer, *Phys. Rev. D* **61**, 054506 (2000); T. Kunihiro *et al.*, *Phys. Rev. D* **82**, 114015 (2010).
 - [16] V. Latora and M. Baranger, *Phys. Rev. Lett.* **82**, 520 (1999).

Short CV of Prof. Dr. Nick van Eijndhoven

(November 2016)



After finalising his PhD thesis on a neutrino scattering experiment at the CERN-SPS accelerator complex in Geneva, Switzerland, prof. van Eijndhoven became a CERN staff fellow to work on the LEP e^+e^- collider experiment Delphi. Within this large international collaboration he performed a leading role in the preparation studies to determine the sensitivity for various physics processes. In addition he was coordinating the development of physics criteria to detect the decay of a light Higgs particle, as expected from the standard model of particle physics. With the start of the first data taking, prof. van Eijndhoven was given the management of the offline analysis.

When he joined the Utrecht University in The Netherlands, prof. van Eijndhoven introduced a new research line in the field of ultra-relativistic heavy-ion collisions with the CERN accelerator facilities, which placed Utrecht on the map with respect to activities at CERN. Within various large international collaborations concerning the heavy-ion research he has played a role as coordinator of both the design of detection systems and the development of analysis methods. Within the CERN-LHC Alice collaboration prof. van Eijndhoven was one of the founding fathers by leading the simulation efforts for the detector design. He also became the projectleader of the "Event generators and physics performance" group. In view of this he was a member of the Alice Physics Board and as Utrecht representative he was also a member of the Alice Collaboration Board, the policy making body of the Alice collaboration.

In 2002 prof. van Eijndhoven took the initiative to start an activity in the interdisciplinary field between astrophysics and particle physics, called astroparticle physics. In collaboration with colleagues from the Utrecht astrophysics department and the Netherlands Institute for Space Research (SRON) this resulted in 2003 in a participation within the international IceCube project; the world's largest neutrino telescope at the South Pole. Within IceCube he acted as the projectleader for the Dutch group and also as member of the IceCube Collaboration Board, being the panel that coordinates the construction, physics research and policy of the experiment.

In 2009 prof. van Eijndhoven became a laureate of the prestigious Odysseus senior award of the Belgian FWO for his innovative work in neutrino astronomy with the IceCube observatory. This event made him to move his scientific activities to the Vrije Universiteit Brussel (VUB) in Belgium. At the VUB he is currently leading a group of scientists in the field of astroparticle physics within the Inter-university Institute for High Energies (IIHE). The research of his group comprises, among others, searches for the sources of the recently discovered flux of high-energy cosmic neutrinos with the IceCube neutrino observatory.

Over the years prof. van Eijndhoven had the supervision of numerous postdocs, PhD and undergraduate students and performed university teaching at all levels, comprising (astro)physics, cosmology, statistics, computer simulations and data analysis. In addition to this he gave many invited talks at conferences and workshops, provided various masterclasses and participated in many outreach projects.

EDUCATION AND TRAINING :

- Basic and senior qualification university teaching, Utrecht University, The Netherlands.
- PhD (exp. high-energy physics), University of Amsterdam, The Netherlands, 1987.
- Drs. (MSc.) in exp. physics, University of Nijmegen, The Netherlands, 1983.

PROFESSIONAL EXPERIENCE :

- Astroparticle Physics programme leader, Vrije Universiteit Brussel (VUB), Belgium, since 2011.
- IceCube project leader at the IIHE(ULB-VUB), Brussels, Belgium, since 2009.
- Full professor, Vrije Universiteit Brussel (VUB), Belgium, since 2009.
- Dutch group leader within the IceCube neutrino observatory 2003-2009.
- Staff member c.q. associate professor, Utrecht University, The Netherlands, 1992-2009
- CERN associate scientist, Geneva, Switzerland, 1991-1992.
- CERN staff-fellow, Geneva, Switzerland, 1987-1991.

INSTITUTIONAL AND RESEARCH RESPONSIBILITIES, among others :

- President or member of various (international) PhD committees.
- Chair of the educational board, Dept. of Physics, VUB Brussels, Belgium, since 2016.
- Responsible for plagiarism control, Dept. of Physics, VUB Brussels, Belgium, since 2013.
- Faculty coordinator of the educational audit, VUB Brussels, Belgium, 2012-2013.
- Member of the education council, Faculty of Science, VUB Brussels, Belgium, since 2012.
- Chair of the curriculum board, Dept. of Physics, VUB Brussels, Belgium, since 2011.
- Belgian representative in the HEP board of the European Physical Society, since 2016.
- Scientific Programme Committee member International Cosmic Ray Conference, since 2012.
- Member of the "Dutch Astronomers Association" since 2003.
- Collaboration board member of IceCube since 2003.
- Adviser for the National Research Foundation (NRF), South Africa, since 2000.
- Member of the "Alice Physics Board", 1995-2002.
- Board member of the "Dutch Physics Society (NNV)", 1993-1997.
- Referee for various international scientific journals, since 1992.
- Collaboration board member of Alice, 1992-1996.

FELLOWSHIPS AND AWARDS :

- FWO Odysseus senior award and VUB research professorship, Brussels, Belgium, 2009.
- Visiting professor, University of Cape Town, South Africa, 2000 and 2002.
- Visiting professor, University of Lund, Sweden, 1994.
- CERN associate, funded by the Dutch Institute for Fundamental Research (FOM), 1991-1992.
- CERN staff fellow, Geneva, Switzerland, 1987-1991.

COLLECTIVE AWARDS :

- Discovery of high-energy cosmic neutrinos : "Breakthrough of the year 2013" by Physics World.

OBTAINED RESEARCH FUNDING :

Funding was obtained for 5 PhD positions and the corresponding infrastructure from the Dutch FOM and the Utrecht University for high-energy heavy-ion research. Furthermore, a grant of about 1 M€ was obtained from FOM for the design and construction of the silicon strip inner tracker system of the Alice LHC experiment. Concerning the neutrino astronomy efforts with IceCube, funding was obtained for 1 postdoc and 1 PhD position from the Utrecht University, in addition to the usual research infrastructure.

The Odysseus senior grant of 2 M€ from the Belgian FWO allowed building up the necessary IceCube research infrastructure at the Vrije Universiteit Brussel (VUB), including the hiring of 9 postdocs and 6 PhD students. In addition to this a Big Science grant of about 570 k€ to support the IceCube experiment was obtained from FWO as well as several PhD and postdoc scholarships.

ORGANISATION OF SCIENTIFIC EVENTS, among others :

- Co-organiser of the Gravitational Wave Symposium, Brussel, Belgium, 2016.
- Co-organiser of the International IceCube Collaboration meeting, Brussel, Belgium, 2010.
- Organiser of the International IceCube Collaboration meeting, Utrecht, The Netherlands, 2008.
- Organiser of the General Physics Colloquium, Utrecht University, 2004-2009.

SCIENCE COMMUNICATION AND OUTREACH, among others :

- Various articles c.q. interviews appeared in newspapers, magazines and radio broadcasts.
- Numerous masterclasses, workshops and lectures for the broad public have been provided.

Information from Prof. Dr. Nick van Eijndhoven (section 11) (2011-2016)

Most important scientific publications (*: 5 most important publications) :

- Obscured flat spectrum radio AGN as sources of high-energy neutrinos.
G. Maggi *et al.*, Physical Review **D** (2016), *in press* (arXiv:1608.00028).
- The cosmic-ray air-shower signal in Askaryan radio detectors.
K.D. de Vries *et al.*, Astroparticle Physics **74** (2016) 96 (arXiv:1503.02808)
- Search for Correlations Between the Arrival Directions of IceCube Neutrino Events and Ultrahigh-Energy Cosmic Rays Detected by the Pierre Auger Observatory and the Telescope Array.
IceCube, Pierre Auger and Telescope Array collaborations, Journal of Cosmology and Astroparticle Physics **JCAP01** (2016) 037 (arXiv:1511.09408).
- Evidence for Astrophysical Muon Neutrinos from the Northern Sky with IceCube.
IceCube collaboration, Physical Review Letters **115** (2015) 081102 (arXiv:1507.04005).
- (*) Observation of High-Energy Astrophysical Neutrinos in Three Years of IceCube Data.
IceCube collaboration, Physical Review Letters **113** (2014) 101101 (arXiv:1405.5303).
- (*) Searches for Extended and Point-like Neutrino Sources with Four Years of IceCube Data.
IceCube collaboration, The Astrophysical Journal **796** (2014) 109 (arXiv:1406.6757).
- (*) Evidence for High-Energy Extraterrestrial Neutrinos at the IceCube Detector.
IceCube collaboration, Science **342** (2013) 1242856 (arXiv:1311.5238).
- (*) First Observation of PeV-energy Neutrinos with IceCube.
IceCube collaboration, Physical Review Letters **111** (2013) 021103 (arXiv:1304.5356).
- (*) An absence of neutrinos associated with cosmic-ray acceleration in gamma-ray bursts.
IceCube collaboration, Nature **484** (2012) 351 (arXiv:1204.4219).
- Measurement of the Atmospheric Neutrino Energy Spectrum from 100 GeV to 400 TeV with IceCube.
IceCube collaboration, Physical Review **D83** (2011) 012001 (arXiv:1010.3980).

Applications for international research funding :

In our field of research it is custom that the various partners of large international collaborations apply in their home country for national c.q. regional funding in order to establish the required budgets to support large international research facilities, like for instance the IceCube Neutrino Observatory at the South Pole. In order to steer this process, dedicated international committees and boards have been formed. Consequently, most of the funding of the Astroparticle Physics programme comes from national/regional funding agencies and not from international programmes. After having obtained the Odysseus senior grant of 2 M€ in 2009 and having moved to Brussels, I got access to Belgian c.q. Flemish funding programmes. Applications have been submitted for FWO research projects, the Methusalem grant and the Big Science research grant. In the period 2011-2016 this resulted in a total amount of about 750 k€, excluding running budgets from the university and individual grants for postdoc and PhD scholarships. Applications for the latter are indicated below.

VUB promotorships of applications for Odysseus c.q. external funding :

- Promotor for Simona Toscano, Odysseus-II, not funded.
- Promotor for Paolo Desiati, Odysseus-II, not funded.
- Promotor for Martin Casier, FWO PhD scholarship, not funded.
- Promotor for Krijn de Vries, FWO postdoc mandate, granted.
- Promotor for Gwenhael de Wasseige, IUAP PhD scholarship, granted.
- Promotor for Jan Lünemann, IUAP postdoc scholarship, granted.
- Promotor for Simona Toscano, Marie Curie fellowship, not funded.

Promotorships of awarded PhD's :

- Martin Casier, Search for High-Energy Neutrino Production in Short Gamma Ray Bursts with the IceCube Neutrino Observatory, 12-nov-2015.
- Jan Kunnen, A search for Dark Matter in the Center of the Earth with the IceCube Neutrino Detector, 11-dec-2015.
- Lionel Brayeur, Search for High-Energy Neutrinos Associated with Long Gamma Ray Bursts using the IceCube Detector, 19-jan-2016.

Realisations of added value outside the academic community :

- Providing various IceCube workshops per year for high school students. (e.g. VUB Campus visits and so called "Autumn camps").
- Ijsklont klaar voor de kosmos. (Ice block ready for the cosmos)
Interview Dutch newspaper *De Volkskrant* (<http://www.volkskrant.nl>), 08-jan-2011.
- Het heelal in het ijs. (The Universe in the ice)
Interview *Akados* (<http://www.vub.ac.be/downloads/Akadosfebruari2011.pdf>).
- IceCube : Catching Neutrinos at Antarctica.
Fall lecture for Belgian highschools, Brussels, Belgium, 04-nov-2011.
- IceCube : Ghost particles at the South Pole.
Public lecture, *Beta Excellent*, Rotterdam, The Netherlands, 29-mar-2012.
- Oorsprong kosmische straling blijft voorlopig mysterie.
(Origin of cosmic rays stays still a mystery)
Interview *Knack magazine* (<http://www.knack.be>), 18-apr-2012.
- Toonaangevende theorie over afkomst kosmische straling weerlegd.
(Leading theory about origin of cosmic rays disproven)
Interview *Belga News Agency* (<http://www.belga.be>), 18-apr-2012.
- Grootste neutrino telescoop ter wereld staat op de Zuidpool.
(The world's largest neutrino telescope at the South Pole).
Interview *I-mag magazine* (<http://www.vik.be>), april 2012.
- Le mystère des rayons cosmiques. (The mystery of cosmic rays)
Interview Belgian newspaper *Le Soir* (<http://www.lesoir.be>), 19-apr-2012.
- De kosmos vangen in een blok ijs. (Catching the cosmos in a block of ice)
Interview Dutch newspaper *NRC handelsblad* (<http://www.nrc.nl>), 19-apr-2012.

- Pooltelescoop ziet nog geen flits. (Polar telescope does not observe a flash)
Interview Dutch newspaper *De Volkskrant* (<http://www.volkskrant.nl>), 21-apr-2012.
- Gammastralen mogelijk niet de bron van kosmische straling.
(Gamma rays possibly not the source of cosmic rays)
Interview *Knack magazine* (<http://www.knack.be>), 23-may-2012.
- IceCube en de oorsprong van kosmische straling. (IceCube and the origin of cosmic rays)
Interview *Akados* (<http://www.vub.ac.be/downloads/Akadosmeijuni2012.pdf>).
- Neutrinos on Ice !
Interview *Athena magazine* (<http://difst.wallonie.be>), 01-jun-2012.
- IceCube : Neutrinos on the rocks.
Public lecture Flemish Science Week, Brussels, Belgium, 22-nov-2012.
- The hunt for the Higgs and cosmic ghost particles.
Public lecture, *Bois le Duc*, Den Dungen, The Netherlands, 24-jun-2013.
- Cosmic neutrinos provide a new window on the Universe.
Interview on the Belgian Radio1, 22-nov-2013.
(www.radio1.be/programmas/joos/bert-en-ernie-bieden-een-nieuwe-kijk-op-het-heelal)
- IceCube exhibition at the "Printemps des Sciences", Brussels, 18-24 march 2014.
- IceCube : A Neutrino Telescope at the South Pole.
IceCube Masterclass, Brussels, Belgium, 21-may-2014.
- Presentation of a 3D IceCube movie in the Brussels Planetarium, oct.-dec. 2014.
(www.planetarium.be)
- Production of a short movie explaining our GRB research, 2014.
(https://drive.google.com/file/d/0B8g69KtNJ35tOHd4X083S1huMXc/view?usp=doclist_api)
- IceCube : A new window on the Universe.
IceCube masterclass, Brussels, Belgium, 18-mar-2015.
- IceCube : Extreme Science at the South Pole.
Public discussion forum at "Kijk Live!", Leiden, The Netherlands, 25-sep-2015.
- IceCube : The Universe observed through a block of ice.
IceCube masterclass, Brussels, Belgium, 02-mar-2016.
- Exploring the Cosmos with High-Energy Neutrinos.
Public lecture Flemish Science Week, Brussels, Belgium, 24-oct-2016.

SEARCHES FOR EXTENDED AND POINT-LIKE NEUTRINO SOURCES WITH FOUR YEARS OF ICECUBE DATA

M. G. AARTSEN¹, M. ACKERMANN², J. ADAMS³, J. A. AGUILAR⁴, M. AHLERS⁵, M. AHRENS⁶, D. ALTMANN⁷, T. ANDERSON⁸, C. ARGUELLES⁵, T. C. ARLEN⁸, J. AUFFENBERG⁹, X. BAI¹⁰, S. W. BARWICK¹¹, V. BAUM¹², J. J. BEATTY^{13,14}, J. BECKER TJUS¹⁵, K.-H. BECKER¹⁶, S. BENZVI⁵, P. BERGHAUS², D. BERLEY¹⁷, E. BERNARDINI², A. BERNHARD¹⁸, D. Z. BESSON¹⁹, G. BINDER^{20,21}, D. BINDIG¹⁶, M. BISSOK⁹, E. BLAUFUSS¹⁷, J. BLUMENTHAL⁹, D. J. BOERSMA²², C. BOHM⁶, F. BOS¹⁵, D. BOSE²³, S. BÖSER²⁴, O. BOTNER²², L. BRAYEUR²⁵, H.-P. BRETZ², A. M. BROWN³, J. CASEY²⁶, M. CASIER²⁵, E. CHEUNG¹⁷, D. CHIRKIN⁵, A. CHRISTOV⁴, B. CHRISTY¹⁷, K. CLARK²⁷, L. CLASSEN⁷, F. CLEVERMANN²⁸, S. COENDERS¹⁸, D. F. COWEN^{8,29}, A. H. CRUZ SILVA², M. DANNINGER⁶, J. DAUGHHETEE²⁶, J. C. DAVIS¹³, M. DAY⁵, J. P. A. M. DE ANDRÉ⁸, C. DE CLERCQ²⁵, S. DE RIDDER³⁰, P. DESIATI⁵, K. D. DE VRIES²⁵, M. DE WITH³¹, T. DEYOUNG⁸, J. C. DÍAZ-VÉLEZ⁵, M. DUNKMAN⁸, R. EAGAN⁸, B. EBERHARDT¹², B. EICHMANN¹⁵, J. EISCH⁵, S. EULER²², P. A. EVENSON³², O. FADIRAN⁵, A. R. FAZELY³³, A. FEDYNITCH¹⁵, J. FEINTZEIG⁵, J. FELDE¹⁷, T. FEUSELS³⁰, K. FILIMONOV²¹, C. FINLEY⁶, T. FISCHER-WASELS¹⁶, S. FLIS⁶, A. FRANCKOWIAK²⁴, K. FRANTZEN²⁸, T. FUCHS²⁸, T. K. GAISSER³², J. GALLAGHER³⁴, L. GERHARDT^{20,21}, D. GIER⁹, L. GLADSTONE⁵, T. GLÜSENKAMP², A. GOLDSCHMIDT²⁰, G. GOLUP²⁵, J. G. GONZALEZ³², J. A. GOODMAN¹⁷, D. GÓRA², D. T. GRANDMONT³⁵, D. GRANT³⁵, P. GRETSKOV⁹, J. C. GROH⁸, A. GROß¹⁸, C. HA^{20,21}, C. HAACK⁹, A. HAJ ISMAIL³⁰, P. HALLEN⁹, A. HALLGREN²², F. HALZEN⁵, K. HANSON³⁶, D. HEBECKER²⁴, D. HEEREMAN³⁶, D. HEINEN⁹, K. HELBING¹⁶, R. HELLAUER¹⁷, D. HELLWIG⁹, S. HICKFORD³, G. C. HILL¹, K. D. HOFFMAN¹⁷, R. HOFFMANN¹⁶, A. HOMEIER²⁴, K. HOSHINA^{5,37}, F. HUANG⁸, W. HUELSNIITZ¹⁷, P. O. HULTH⁶, K. HULTQVIST⁶, S. HUSSAIN³², A. ISHIHARA³⁸, E. JACOBI², J. JACOBSEN⁵, K. JAGIELSKI⁹, G. S. JAPARIDZE³⁹, K. JERO⁵, O. JLELATI³⁰, M. JURKOVIC¹⁸, B. KAMINSKY², A. KAPPES⁷, T. KARG², A. KARLE⁵, M. KAUER⁵, J. L. KELLEY⁵, A. KHEIRANDISH⁵, J. KIRYLUK⁴⁰, J. KLÄS¹⁶, S. R. KLEIN^{20,21}, J.-H. KÖHNE²⁸, G. KOHNEN⁴¹, H. KOLANOSKI³¹, A. KOOB⁹, L. KÖPKE¹², C. KOPPER⁵, S. KOPPER¹⁶, D. J. KOSKINEN⁴², M. KOWALSKI²⁴, A. KRIESTEN⁹, K. KRINGS⁹, G. KROLL¹², M. KROLL¹⁵, J. KUNNEN²⁵, N. KURAHASHI⁵, T. KUWABARA³², M. LABARE³⁰, D. T. LARSEN⁵, M. J. LARSON⁴², M. LESIAK-BZDAK⁴⁰, M. LEUERMANN⁹, J. LEUTE¹⁸, J. LÜNEMANN¹², O. MACÍAS³, J. MADSEN⁴³, G. MAGGI²⁵, R. MARUYAMA⁵, K. MASE³⁸, H. S. MATIS²⁰, R. MAUNU¹⁷, F. McNALLY⁵, K. MEAGHER¹⁷, M. MEDICI⁴², A. MELI³⁰, T. MEURES³⁶, S. MIARECKI^{20,21}, E. MIDDELL², E. MIDDLEMAS⁵, N. MILKE²⁸, J. MILLER²⁵, L. MOHRMANN², T. MONTARULI⁴, R. MORSE⁵, R. NAHNHAUER², U. NAUMANN¹⁶, H. NIEDERHAUSEN⁴⁰, S. C. NOWICKI³⁵, D. R. NYGREN²⁰, A. OBERTACKE¹⁶, S. ODROWSKI³⁵, A. OLIVAS¹⁷, A. OMAIRAT¹⁶, A. O'MURCHADHA³⁶, T. PALCZEWSKI⁴⁴, L. PAUL⁹, Ö. PENEK⁹, J. A. PEPPER⁴⁴, C. PÉREZ DE LOS HEROS²², C. PFENDNER¹³, D. PIELOTH²⁸, E. PINAT³⁶, J. POSSELT¹⁶, P. B. PRICE²¹, G. T. PRZYBYLSKI²⁰, J. PÜTZ⁹, M. QUINNAN⁸, L. RÄDEL⁹, M. RAMEEZ⁴, K. RAWLINS⁴⁵, P. REDL¹⁷, I. REES⁵, R. REIMANN⁹, E. RESCONI¹⁸, W. RHODE²⁸, M. RICHMAN¹⁷, B. RIEDEL⁵, S. ROBERTSON¹, J. P. RODRIGUES⁵, M. RONGEN⁹, C. ROTT²³, T. RUHE²⁸, B. RUZYBAYEV³², D. RYCKBOSCH³⁰, S. M. SABA¹⁵, H.-G. SANDER¹², J. SANDROOS⁴², M. SANTANDER⁵, S. SARKAR^{42,46}, K. SCHATTO¹², F. SCHERIAU²⁸, T. SCHMIDT¹⁷, M. SCHMITZ²⁸, S. SCHOENEN⁹, S. SCHÖNEBERG¹⁵, A. SCHÖNWALD², A. SCHUKRAFT⁹, L. SCHULTE²⁴, O. SCHULZ¹⁸, D. SECKEL³², Y. SESTAYO¹⁸, S. SEUNARINE⁴³, R. SHANIDZE², C. SHEREMATA³⁵, M. W. E. SMITH⁸, D. SOLDIN¹⁶, G. M. SPICZAK⁴³, C. SPIERING², M. STAMATIKOS^{13,47}, T. STANEV³², N. A. STANISHA⁸, A. STASKI²⁴, T. STEZELBERGER²⁰, R. G. STOKSTAD²⁰, A. STÖBL², E. A. STRAHLER²⁵, R. STRÖM²², N. L. STROTJOHANN²⁴, G. W. SULLIVAN¹⁷, H. TAAVOLA²², I. TABOADA²⁶, A. TAMBURRO³², A. TEPE¹⁶, S. TER-ANTONYAN³³, A. TERLIUK², G. TEŠIĆ⁸, S. TILAV³², P. A. TOALE⁴⁴, M. N. TOBIN⁵, D. TOSI⁵, M. TSELENGIDOU⁷, E. UNGER¹⁵, M. USNER²⁴, S. VALLECORSÀ⁴, N. VAN EIJNDHOVEN²⁵, J. VANDENBROUCKE⁵, J. VAN SANTEN⁵, M. VEHRING⁹, M. VOGEL²⁴, M. VRAEGHE³⁰, C. WALCK⁶, M. WALLRAFF⁹, CH. WEAVER⁵, M. WELLONS⁵, C. WENDT⁵, S. WESTERHOFF⁵, B. J. WHELAN¹, N. WHITEHORN⁵, C. WICHARY⁹, K. WIEBE¹², C. H. WIEBUSCH⁹, D. R. WILLIAMS⁴⁴, H. WISSING¹⁷, M. WOLF⁶, T. R. WOOD³⁵, K. WOSCHNAGG²¹, D. L. XU⁴⁴, X. W. XU³³, J. P. YANEZ², G. YODH¹¹, S. YOSHIDA³⁸, P. ZARZHITSKY⁴⁴, J. ZIEMANN²⁸, S. ZIERKE⁹, AND M. ZOLL⁶

(ICECUBE COLLABORATION)

¹ School of Chemistry and Physics, University of Adelaide, Adelaide SA, 5005 Australia

² DESY, D-15735 Zeuthen, Germany

³ Department of Physics and Astronomy, University of Canterbury, Private Bag 4800, Christchurch, New Zealand

⁴ Département de physique Nucléaire et Corpusculaire, Université de Genève, CH-1211 Genève, Switzerland

⁵ Department of Physics and Wisconsin IceCube Particle Astrophysics Center, University of Wisconsin, Madison, WI 53706, USA

⁶ Oskar Klein Centre and Department of Physics, Stockholm University, SE-10691 Stockholm, Sweden

⁷ Erlangen Centre for Astroparticle Physics, Friedrich-Alexander-Universität Erlangen-Nürnberg, D-91058 Erlangen, Germany

⁸ Department of Physics, Pennsylvania State University, University Park, PA 16802, USA

⁹ III. Physikalisches Institut, RWTH Aachen University, D-52056 Aachen, Germany

¹⁰ Physics Department, South Dakota School of Mines and Technology, Rapid City, SD 57701, USA

¹¹ Department of Physics and Astronomy, University of California, Irvine, CA 92697, USA

¹² Institute of Physics, University of Mainz, Staudinger Weg 7, D-55099 Mainz, Germany

¹³ Department of Physics and Center for Cosmology and Astro-Particle Physics, Ohio State University, Columbus, OH 43210, USA

¹⁴ Department of Astronomy, Ohio State University, Columbus, OH 43210, USA

¹⁵ Fakultät für Physik und Astronomie, Ruhr-Universität Bochum, D-44780 Bochum, Germany

¹⁶ Department of Physics, University of Wuppertal, D-42119 Wuppertal, Germany

¹⁷ Department of Physics, University of Maryland, College Park, MD 20742, USA

¹⁸ Technische Universität München, D-85748 Garching, Germany

¹⁹ Department of Physics and Astronomy, University of Kansas, Lawrence, KS 66045, USA

- ²⁰ Lawrence Berkeley National Laboratory, Berkeley, CA 94720, USA
²¹ Department of Physics, University of California, Berkeley, CA 94720, USA
²² Department of Physics and Astronomy, Uppsala University, P.O. Box 516, S-75120 Uppsala, Sweden
²³ Department of Physics, Sungkyunkwan University, Suwon 440-746, Korea
²⁴ Physikalisches Institut, Universität Bonn, Nussallee 12, D-53115 Bonn, Germany
²⁵ Vrije Universiteit Brussel, Dienst ELEM, B-1050 Brussels, Belgium
²⁶ School of Physics and Center for Relativistic Astrophysics, Georgia Institute of Technology, Atlanta, GA 30332, USA
²⁷ Department of Physics, University of Toronto, Toronto, Ontario M5S 1A7, Canada
²⁸ Department of Physics, TU Dortmund University, D-44221 Dortmund, Germany
²⁹ Department of Astronomy and Astrophysics, Pennsylvania State University, University Park, PA 16802, USA
³⁰ Department of Physics and Astronomy, University of Gent, B-9000 Gent, Belgium
³¹ Institut für Physik, Humboldt-Universität zu Berlin, D-12489 Berlin, Germany
³² Bartol Research Institute and Department of Physics and Astronomy, University of Delaware, Newark, DE 19716, USA
³³ Department of Physics, Southern University, Baton Rouge, LA 70813, USA
³⁴ Department of Astronomy, University of Wisconsin, Madison, WI 53706, USA
³⁵ Department of Physics, University of Alberta, Edmonton, Alberta T6G 2E1, Canada
³⁶ Université Libre de Bruxelles, Science Faculty CP230, B-1050 Brussels, Belgium
³⁷ Earthquake Research Institute, University of Tokyo, Bunkyo, Tokyo 113-0032, Japan
³⁸ Department of Physics, Chiba University, Chiba 263-8522, Japan
³⁹ CTSPS, Clark-Atlanta University, Atlanta, GA 30314, USA
⁴⁰ Department of Physics and Astronomy, Stony Brook University, Stony Brook, NY 11794-3800, USA
⁴¹ Université de Mons, B-7000 Mons, Belgium
⁴² Niels Bohr Institute, University of Copenhagen, DK-2100 Copenhagen, Denmark
⁴³ Department of Physics, University of Wisconsin, River Falls, WI 54022, USA
⁴⁴ Department of Physics and Astronomy, University of Alabama, Tuscaloosa, AL 35487, USA
⁴⁵ Department of Physics and Astronomy, University of Alaska Anchorage, 3211 Providence Drive, Anchorage, AK 99508, USA
⁴⁶ Department of Physics, University of Oxford, 1 Keble Road, Oxford OX1 3NP, UK
⁴⁷ NASA Goddard Space Flight Center, Greenbelt, MD 20771, USA

Received 2014 June 25; accepted 2014 September 28; published 2014 November 12

ABSTRACT

We present results on searches for point-like sources of neutrinos using four years of IceCube data, including the first year of data from the completed 86 string detector. The total livetime of the combined data set is 1373 days. For an E^{-2} spectrum, the observed 90% C.L. flux upper limits are $\sim 10^{-12}$ $\text{TeV}^{-1} \text{cm}^{-2} \text{s}^{-1}$ for energies between 1 TeV and 1 PeV in the northern sky and $\sim 10^{-11}$ $\text{TeV}^{-1} \text{cm}^{-2} \text{s}^{-1}$ for energies between 100 TeV and 100 PeV in the southern sky. This represents a 40% improvement compared to previous publications, resulting from both the additional year of data and the introduction of improved reconstructions. In addition, we present the first results from an all-sky search for extended sources of neutrinos. We update the results of searches for neutrino emission from stacked catalogs of sources and test five new catalogs; two of Galactic supernova remnants and three of active galactic nuclei. In all cases, the data are compatible with the background-only hypothesis, and upper limits on the flux of muon neutrinos are reported for the sources considered.

Key words: astroparticle physics – galaxies: active – galaxies: clusters: general – galaxies: starburst – ISM: supernova remnants – neutrinos

Online-only material: color figures

1. INTRODUCTION

Neutrinos have unique properties that can be used to probe diverse astrophysical processes. Produced in interactions of protons and nuclei with ambient radiation and matter, their low cross section allows them to travel astronomical distances without experiencing significant absorption. Unlike charged cosmic rays (CRs) which change direction as they pass through galactic and intergalactic magnetic fields, neutrinos preserve their directional information as they travel straight from the source to Earth. Astrophysical neutrinos are also tracers of hadronic interactions, and the identification of these neutrino sources may help to clarify CR acceleration processes (Anchordoqui & Montaruli 2010; Anchordoqui et al. 2014; Becker 2008; Halzen & Hooper 2002; Learned & Mannheim 2000). Candidate sources for CR acceleration (and therefore neutrino emission) include supernova remnant (SNR) shocks (Alvarez-Muñiz & Halzen 2002; Cavasinni et al. 2006; Gonzalez-Garcia et al. 2014; De Marco et al. 2006; Vissani et al. 2011), active galactic nuclei (AGNs) jets (Essey et al. 2010; Kalashev et al. 2013; Murase et al. 2014; Sironi & Spitkovsky 2011; Stecker et al. 1991; Waxman

& Bahcall 1999), starburst galaxies (Lacki et al. 2011; Loeb & Waxman 2006; Murase et al. 2013; Romero & Torres 2003), and gamma-ray bursts (Guetta et al. 2004; Mészáros 2006; Waxman & Bahcall 1997).

IceCube recently found evidence for a diffuse flux of high-energy astrophysical neutrinos (Aartsen et al. 2013e, 2014b), observing a 5.7σ excess of events between ~ 50 TeV and 2 PeV deposited within the detector. The 37 observed events are consistent with an $E^{-2.3}$ neutrino flux at the level of 1.5×10^{-11} $\text{TeV}^{-1} \text{cm}^{-2} \text{s}^{-1} \text{sr}^{-1}$ (normalized at 100 TeV), with a neutrino flavor ratio of 1:1:1. While these events have established unequivocally that astrophysical neutrinos exist, their sources have not yet been identified. One challenge is that only $\sim 20\%$ of the events in that sample are associated with a high-energy muon which leaves a visible track in the detector. The remaining events without a track have a poor angular resolution of $\sim 15^\circ$.

This paper presents the latest results of searches for point sources of astrophysical neutrinos with a sample of track-like events associated with ν_μ (and some ν_τ) charged current interactions observed by the IceCube Neutrino Observatory.

These events have an excellent angular resolution of $\leq 1^\circ$ and hence allow us to point back toward the source. As the main signature we focus on is the resultant muon, the interaction vertex is not required to lie inside the detector as in Aartsen et al. (2013e, 2014b) and the effective volume is hence effectively enhanced. The results of an all-sky search, a search among a catalog of candidate neutrino emitters and stacked source catalog searches with a similar sample of events from the data collected between 2008 and 2011, are published in Aartsen et al. (2013c). Here we update these analyses by adding the first year of data from the complete 86 string detector configuration, collected between 2011 May and 2012 May. Five new stacking analyses based on newly available catalogs are also presented here.

In this paper, we describe the results of the first all-sky survey by IceCube looking for extended regions of neutrino emission. H.E.S.S. has surveyed the Galactic plane looking for gamma-ray emissions above 200 GeV, revealing previously unknown extended regions emitting to TeV energies (Carrigan et al. 2013). The *Fermi*/Large Area Telescope (LAT) survey above 100 GeV also shows the same bright extended sources. These extended regions may be unidentified SNRs associated with molecular clouds, which are also expected to be spatially extended sources of neutrinos (Gonzalez-Garcia et al. 2014; Mandelartz & Tjus 2013). Outside the Galaxy, large clusters of galaxies such as Virgo are promising neutrino emitters expected to have spatial extensions (De Marco et al. 2006; Murase et al. 2008; Murase & Beacom 2012; Wolfe et al. 2008). It is therefore important not to limit the search for sources of neutrinos uniquely to point-like sources, but also to extended regions as shown in Tchernin et al. (2013).

Section 2 describes the IceCube detector and the event selection for data from the first year of the completed detector. Event selections for data from the previous years of operation of the detector have been extensively described in Aartsen et al. (2013c) and Abbasi et al. (2011). The methodology used to optimize the searches for various source signal hypotheses is described in Section 3. Section 4 presents the results of the analyses, which are discussed within the context of recent models of astrophysical neutrino emission. Conclusions are drawn in Section 5.

2. DETECTOR AND EVENT SELECTION

The IceCube Observatory is a cubic-kilometer-sized Cherenkov detector embedded in the ice at the geographic south pole (Achterberg et al. 2006). Optimized to detect neutrinos above TeV energies, it consists of 5160 photomultiplier tubes (PMTs) instrumented along 86 cables (called strings) at depths of 1450–2450 m beneath the surface of the ice sheet. Each PMT is housed in a digital optical module (DOM), consisting of a pressure-resistant sphere with on board digitization and calibration LEDs (light-emitting diodes; Abbasi et al. 2010). The DOMs detect Cherenkov photons emitted by charged leptons that traverse the detector (Abbasi et al. 2009). This analysis uses data taken between 2008 April and 2012 May. During this period, IceCube ran in four different configurations. Three years of data are from the partial detector composed of 40, 59, and 79 strings, respectively, and are fully described in Aartsen et al. (2013c). The following year of data was taken with the completed 86 string array. The used selection procedure and event reconstructions are similar to those applied to the previous data.

2.1. Data Reduction and Reconstruction for the IC86-1 Data Sample

Data acquisition is triggered by requiring four pairs of neighboring or next-to-neighboring DOMs to observe photoelectrons within a $5 \mu\text{s}$ time window. 2.5 kHz of data satisfy this criterion. A combination of real-time filtering at the south pole and subsequent offline CPU-intensive processing reduces the data rate to 2 Hz by rejecting misreconstructed events. At this stage, the data are dominated by atmospheric muons from CRs; both well-reconstructed down-going muons in the southern sky and down-going muons misreconstructed as up-going muons in the northern sky. The data is further reduced via quality cuts using simple reconstructions and event quality parameters followed by advanced likelihood-based muon reconstructions. The simple reconstruction removes scattered photon hits before estimating the muon position and direction via a linear fit with reduced weights for outliers (Aartsen et al. 2013b). This fit serves as a seed for more advanced likelihood reconstructions, including the multi-photoelectron (MPE) likelihood. This algorithm includes a probabilistic distribution function (PDF), which describes the scattering of photons in the ice, and is fully described in Ahrens et al. (2004).

In the processing of data from the first year of the full detector, two new muon reconstructions were used to determine event directions and reject background. The first reconstructs the muon direction by applying the MPE likelihood four times. Each iteration uses a bootstrapped pulse series, extracted randomly from the measured pulses. This is done using a multinomial distribution weighted by charge, so that high-charge pulses are more likely to be selected than low ones. The results of these four reconstructions are averaged together to seed one reconstruction using the complete pulses. Of these five fit results, the one with the best likelihood value is selected and saved. Compared to the single-iteration MPE fit, this process reduces the rate of down-going atmospheric muons misreconstructed as up-going muons by 30%, while improving the neutrino median angular resolution from $0^\circ.7$ to $0^\circ.6$ at 30 TeV.

This iterative fit also serves as a seed for the second reconstruction algorithm, which provides a more accurate result by modeling the optical properties of the Antarctic ice sheet. While previous reconstructions use analytic approximations to describe the timing distribution of Cherenkov photons arriving at a given PMT (Ahrens et al. 2004), here we use a parameterization of a Monte Carlo simulation. Photon transport is simulated using a depth-dependent model of scattering and absorption in the ice (Aartsen et al. 2013a). The arrival time of a photon is a function of the orientation and depth of the muon source and the displacement vector between the muon and the receiving PMT. Photons are simulated for different muon-receiver configurations, and a multi-dimensional spline surface is fit to the resulting arrival time distributions (Whitehorn et al. 2013). These splines are used as PDFs in the MPE likelihood. Compared to previous IceCube point source analyses (Aartsen et al. 2013c), this reconstruction algorithm leads to a 26% improvement in neutrino median angular resolution at 30 TeV (see Figure 1). As carried out in previous years, the uncertainty in the angular reconstruction for each event is estimated by fitting a paraboloid to the likelihood space around the reconstructed direction, following the method described in Abbasi et al. (2011) and Neunhoffer (2006).

After reconstructing the direction of each event, a separate algorithm fits for the muon energy loss along its track. In the fourth year of data, the energy reconstruction uses an analytic

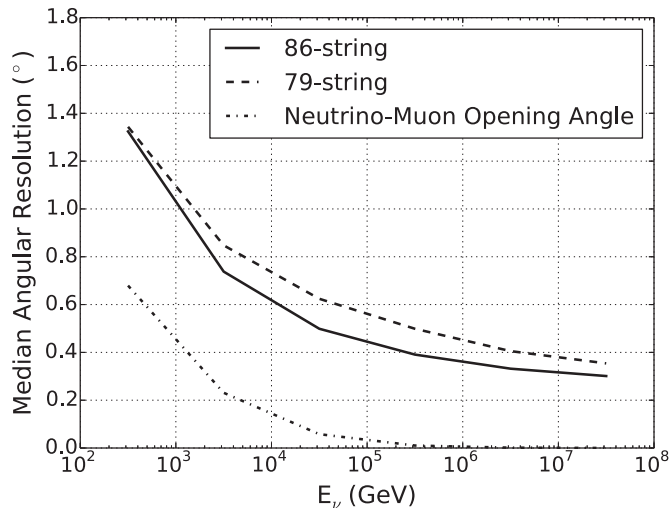


Figure 1. Median angular resolution (angle between reconstructed muon track and neutrino direction) as a function of neutrino energy for simulated northern hemisphere event samples from the 86 string (solid) and 79 string (dashed) detector configurations. The improvement is due to the new reconstruction algorithm. At 30 TeV, the 40 and 59 string event selections (not shown) give angular resolutions of ~ 0.8 and ~ 0.75 , respectively (Aartsen et al. 2013c). The dash-dotted line shows the median kinematic opening angle between the neutrino and muon.

approximation to model the muon light yield at the receiving DOMs as a function of the orientation and depth of the muon (Aartsen et al. 2014a).

2.2. Selection of the Final Sample

From the 2 Hz of remaining data (still dominated by the atmospheric muon background), 4.8 mHz of events are selected for the final analysis sample. In the northern sky, the misreconstructed muon background can be mostly eradicated to isolate a nearly pure sample of up-going atmospheric neutrinos. This is done using a classification algorithm called boosted decision trees (BDTs). Similar to previous IceCube point source analyses (Aartsen et al. 2013c), we trained four BDTs in two zenith bands to separate astrophysical neutrino signal from the atmospheric muon background. Cuts on the BDT output scores are optimized to achieve the best discovery potential for both E^{-2} and $E^{-2.7}$ signal spectra. This event selection covers the entire northern hemisphere and extends 5° above the horizon, where the Earth and glacial ice still provide a shield from the CR background.

At an angle of more than 5° above the horizon, a pure neutrino sample cannot be isolated from the high-energy atmospheric muon bundles, which are multiple muons from the same air shower that mimic neutrinos. The background can be reduced by introducing quality cuts and using parameters that select neutrinos and reject muon bundles. One BDT is trained for the entire region using data to describe the background and an E^{-2} neutrino simulation for signal. Of the 11 variables used in training the BDT, 3 exploit differences between single muons and bundles. These parameters rely on event topology and energy loss information. Large muon bundles consist of many low-energy muons that typically lose energy at a constant rate as they traverse the detector. Photons from these muon bundles are detected within a wider time range. High-energy, neutrino-induced muons instead have relatively stochastic energy loss profiles and narrower photon timing distributions. Likelihood ratios are constructed to judge whether a given data event has timing and energy loss properties more consistent with the

Table 1

Summary for Four Different IceCube Configurations for Point Source Analyses: the Expected Atmospheric Neutrino Rate from MC Simulation Weighted for the Model in Honda et al. (2007) and Numbers of Up- and Down-going Events at Final Selection Level

No. of Strings	Livetime (days)	Atm. vs (day ⁻¹)	No. of Up-going	No. of Down-going
40	376	40	14121	22779
59	348	120	43339	64230
79	316	180	50857	59009
86	333	210	69227	69095

Note. The up-going data are dominated by atmospheric neutrinos, while data in the down-going region are dominated by atmospheric muons.

simulated signal or the estimated background and are included in the BDT. To obtain the final sample, a cut on the BDT score is varied with zenith to account for the zenith-dependent properties of the background.

The final data sample for the first year of operation of the 86 string detector has 138,322 events, of which approximately half are in the northern hemisphere. The livetime and rates for all four years of detector data are summarized in Table 1. The neutrino effective area for this selection and the central 90% energy region for three signal spectra are shown in Figure 2. The effective area reaches its maximum near the horizon. Far below the horizon, high-energy neutrinos suffer from absorption in the Earth. Above the horizon, the cuts necessary to remove the background remove a significant portion of the lower-energy signal. As a result, the analysis is sensitive to the widest neutrino energy range near the horizon, while in the southern hemisphere the sensitivity rapidly deteriorates at lower energies. The discovery potential as a function of energy and declination (decl.) is shown in Figure 3. The discovery potential is defined as the flux required to observe a 5σ upward fluctuation before trials, while the analysis sensitivity is defined as the median upper limit observed in the absence of a signal. Compared to the three year point source analysis (Aartsen et al. 2013c), the addition of the first year of data from the completed detector including improved reconstruction and background rejection techniques leads to a 40%–50% improvement in both the sensitivity and discovery potential, with larger gains at energies below 1 PeV in the southern hemisphere.

3. THE LIKELIHOOD SEARCH METHOD

Point-like sources of neutrinos in the sky can be identified by searching for clusters of events significantly incompatible with the atmospheric muon and neutrino background. The significance is estimated by using an unbinned maximum likelihood ratio test as described in Braun et al. (2010). The method is expanded to allow for the combination of data from different detector geometries as described in Aartsen et al. (2013c). In addition to spatial clustering, this method also uses the energies of the events to identify signal events that are expected to have a harder spectrum than that of atmospheric neutrinos and muons. The energy response expected from a neutrino signal from a point source in the sky is modeled using simulation. Since the final event selections are still background-dominated, the background estimate is done using real data.

In time-integrated searches for a point-like source, the signal PDF S_i^j for event i observed in detector geometry j is given by

$$S_i^j = S_i^j(|\mathbf{x}_i - \mathbf{x}_s|, \sigma_i) \mathcal{E}_i^j(E_i, \delta_i, \gamma). \quad (1)$$

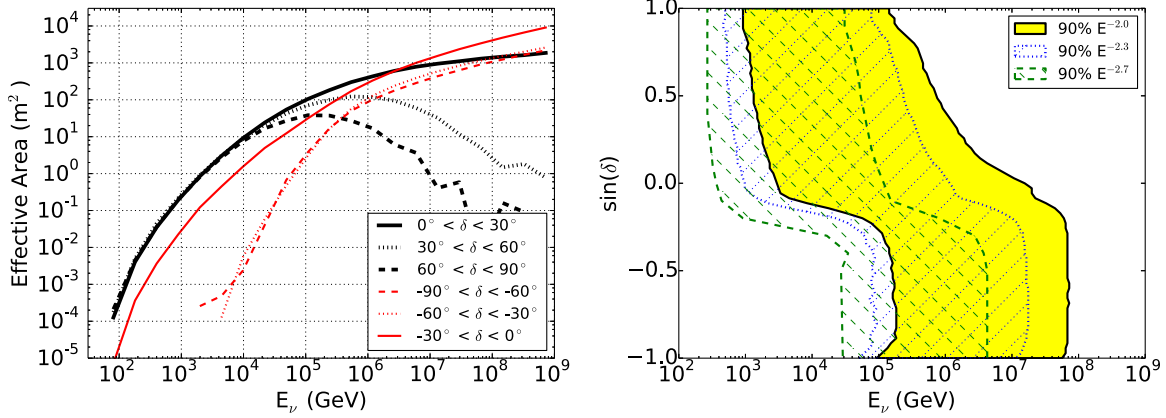


Figure 2. Left: neutrino effective area for the 86 string detector as a function of primary neutrino energy for 6 declination bands. The effective area is the average of the area for ν_μ and $\bar{\nu}_\mu$. Right: central 90% energy region for simulated neutrino events as a function of declination. This defines the region where the upper limits for E^{-2} , $E^{-2.3}$, and $E^{-2.7}$ source spectra are valid.

(A color version of this figure is available in the online journal.)

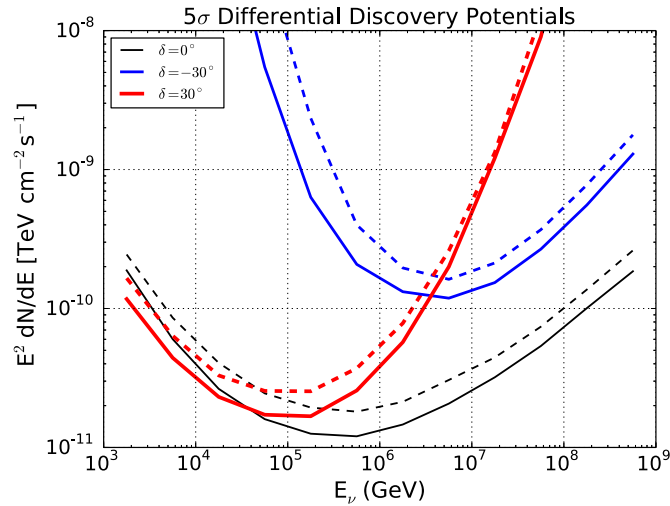


Figure 3. Discovery flux as a function of the neutrino energy at a 5σ confidence level for three different declinations (solid lines). Point sources with an E^{-2} spectrum are simulated over a half decade in energy, and the flux in each bin required for discovery forms the curve above. Results from the previous analysis with three years of the data are shown with dashed lines.

(A color version of this figure is available in the online journal.)

Here, the spatial contribution to the PDF is given by S_i^j , which depends on the angular uncertainty of the event σ_i , and the angular difference between the reconstructed direction of the event and the direction of the source. This probability is modeled as a two-dimensional Gaussian:

$$S_i^j = \frac{1}{2\pi\sigma_i^2} e^{-\frac{|x_i - x_s|^2}{2\sigma_i^2}}. \quad (2)$$

The contribution from energy $\mathcal{E}_i^j(E_i, \delta_i, \gamma)$ is described in Braun et al. (2010).

When searching for spatially extended sources, the value of σ_i is replaced with $\sigma_i^{\text{eff}} = \sqrt{\sigma_i^2 + \sigma_{\text{src}}^2}$, where σ_{src} is the width of the source. Figure 4 shows the flux needed for a 5σ discovery for a source located at a given declination as a function of the source extension. The results for two different signal hypotheses are shown; in one, the source is always assumed to have no extension, while in the other the correct source extension is included in the likelihood description. Naturally, for

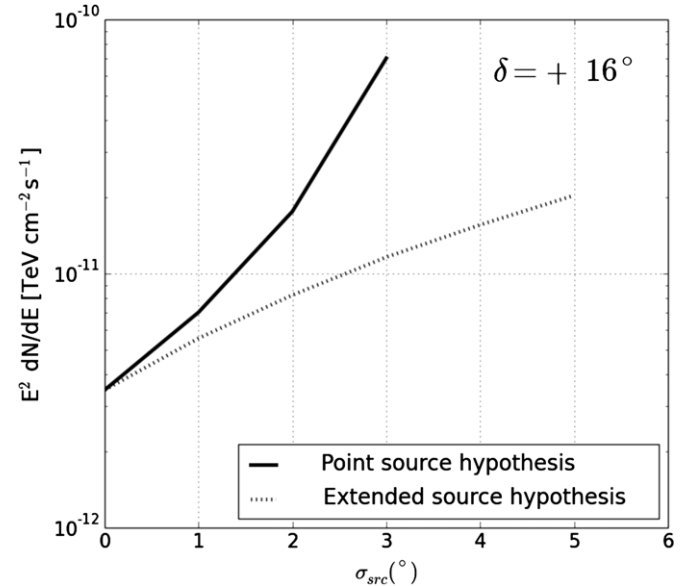


Figure 4. Flux needed for a 5σ discovery from a hypothetical source at $\delta = +16^\circ$ as a function of the true source extension for the point source signal hypothesis (solid line) and the extended signal hypothesis with the correct extension (dotted line). For a source extended by 3° , a search using the simple point source signal PDF of Equation (2) requires a flux \sim six times larger than a search incorporating the true extension of the source within the signal PDF to produce a 5σ discovery. A point source search can be viewed as a special case of an extended source search with $\sigma_{\text{src}} = 0$. When the true extension of a source varies from one of the five extensions assumed in the search hypotheses by up to 0.5° , the flux required for discovery is expected to vary by $\sim 10\%$.

sources that are truly extended, the extended hypothesis is more powerful than the point source assumption. As the real extension of the source increases, the analysis method which assumes that the source is point-like performs worse than the one that takes the extension of the source into account.

To further enhance discovery potentials and sensitivity, stacked searches can be carried out for specific catalogs of similar candidate neutrino sources.

The following is a description of all the searches performed with the four years of IceCube data (similar to those performed in Aartsen et al. 2013c).

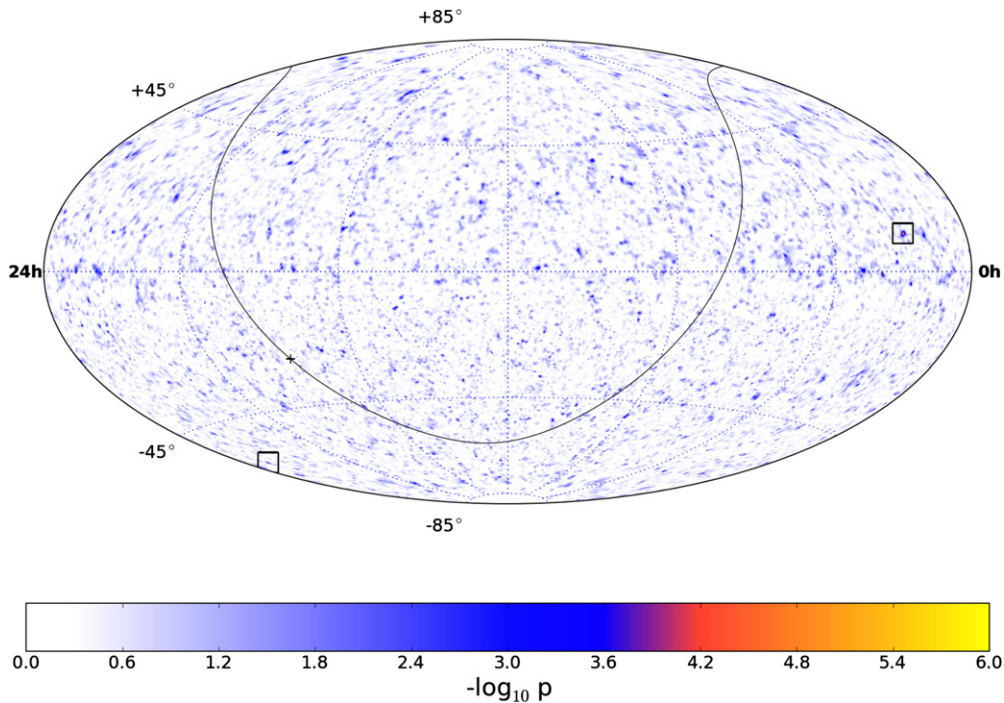


Figure 5. Pre-trial significance skymap in equatorial coordinates (J2000) of the all-sky point source scan for the combined four year data sample. The black line indicates the Galactic plane, and the black plus sign indicates the Galactic center. The most significant fluctuation in each hemisphere is indicated with a square marker. (A color version of this figure is available in the online journal.)

Table 2
Summary of the Results from the Extended All-sky Survey

Extension ($^{\circ}$)	R.A. ($^{\circ}$)	Decl. ($^{\circ}$)	\hat{n}_S	$\hat{\gamma}$	p -value (Pre-trial)	p -value (Post-trial)
1 $^{\circ}$	286.25	-43.25	49.6	2.65	6.75×10^{-5}	0.58
2 $^{\circ}$	248.75	62.75	58.2	2.38	5.52×10^{-4}	0.87
3 $^{\circ}$	30.75	-30.25	93.6	3.10	1.22×10^{-3}	0.81
4 $^{\circ}$	30.75	-30.25	99	3.10	3.29×10^{-3}	0.81
5 $^{\circ}$	251.75	61.25	102	2.54	1.06×10^{-2}	0.91

Note. The coordinates of the most significant spots located for each source extension hypothesis are given together with the respective p -values.

3.1. All-sky Searches

These searches are carried out to look for evidence of a source anywhere in the sky and are not motivated by any prior information regarding the position of the sources. The likelihood is evaluated in each direction in the sky. In these searches, the number of effective trials is very high and is related to the angular resolution of the telescope and the source extension hypotheses. In order to correct for the trial factor, the same experiment is repeated on an ensemble of scrambled data and the probability of observing a more significant spot than the one observed is obtained.

All-sky point source scan. The all-sky scan for point sources of neutrinos that has previously been carried out on data from the incomplete detector configurations is updated to include the first year of data from the complete 86 string detector. In this search, the likelihood is evaluated in steps of $0^{\circ}.1 \times 0^{\circ}.1$ within the declination range -85° to $+85^{\circ}$. We do not search for point sources at declinations $|\delta| > 85^{\circ}$ because there is not sufficient phase space in right ascension (R.A.) to estimate significances with the scrambling technique.

All-sky extended source scans. The search for extended sources is performed in a similar fashion to the all-sky point source searches. In this case, the sky is divided into a grid of $0^{\circ}.5 \times 0^{\circ}.5$ in a similar declination range. For this search, a source extension needs to be assumed for the signal. We carry out five different all-sky scans assuming extensions in step of 1° , from 1° to 5° . An additional trial factor needs to be considered from the additional number of sky scans; however, this factor can be conservatively assumed to be five.

3.2. Searches Among List of 44 Candidate Sources

In order to reduce the large number of effective trials associated with scanning the entire sky, we also performed a search for the most significant of 44 a priori selected source candidates. The sources in this list have been selected according to observations in gamma-rays or astrophysical models predicting neutrino emission.

3.3. Stacking Searches

Several sources of the same type may emit fluxes that are individually below the discovery potential but detectable

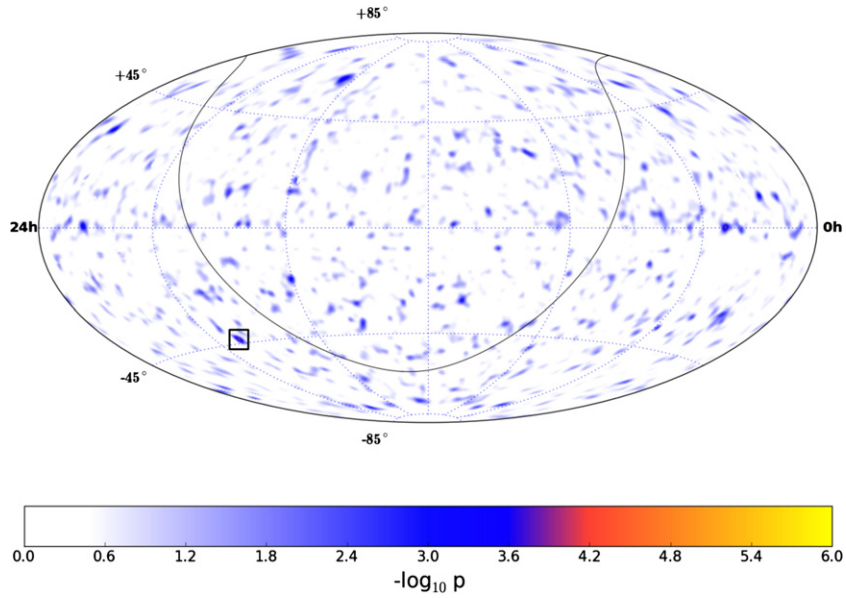


Figure 6. Pre-trial significance skymap from the all-sky scan for sources of 1° extension in equatorial coordinates. The black line indicates the Galactic plane. The most significant fluctuation is indicated with a square marker.

(A color version of this figure is available in the online journal.)

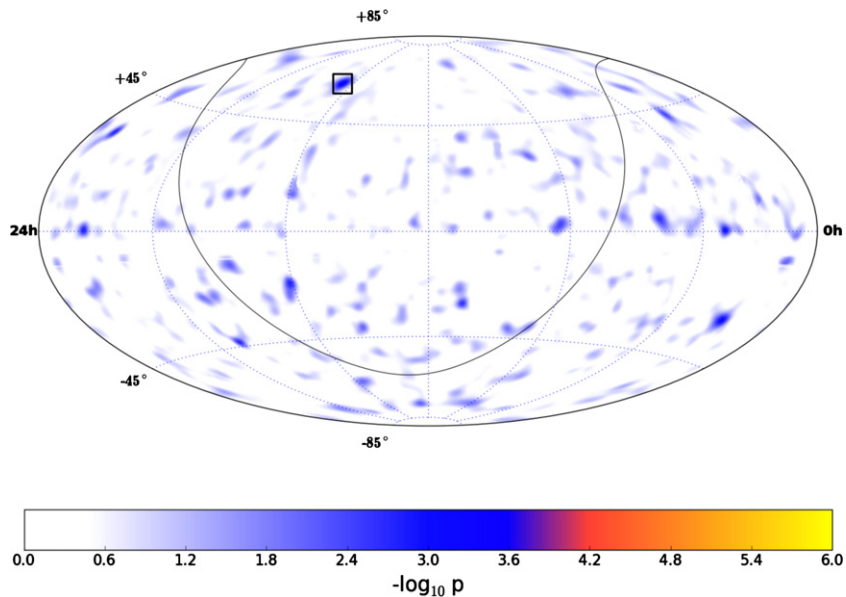


Figure 7. Same as Figure 6, but for sources of 2° extension.

(A color version of this figure is available in the online journal.)

as a class when summed up using the stacking technique. Here we report on the different catalogs of sources that have similar spectral behavior based on gamma-ray observations or astrophysical models predicting neutrino emission. For these searches, the signal PDF \mathcal{S}_i^j of Equation (1) is modified to accommodate multiple sources (see Abbasi et al. 2011). A prior knowledge of the expected luminosities of these sources can be utilized to weight the contribution of each source in the total signal PDF to make the search optimal for that signal hypothesis. Alternatively, an equal-weighting can be applied if there is no preferred model. In the following section, we summarize all the stacking searches performed with four years of data. Most of these searches are updates from the previous results using three years of data (Aartsen et al. 2013c).

Updated searches. These searches have been previously carried out on three years of data (Aartsen et al. 2013c) and are now updated to include data from the first year of operation of the completed 86 string detector.

Six Milagro TeV gamma-ray sources. The authors of the model that motivated the original analysis have hence updated the models to reflect the newer gamma-ray observations (Gonzalez-Garcia et al. 2014). For this reason, in this search an equal weight is used for each source in the likelihood with the intention of keeping our sensitivity optimal for all possible signal hypothesis.

One hundred and twenty-seven local starburst galaxies. Sources are compiled in Table A.1 in Becker et al. (2009).

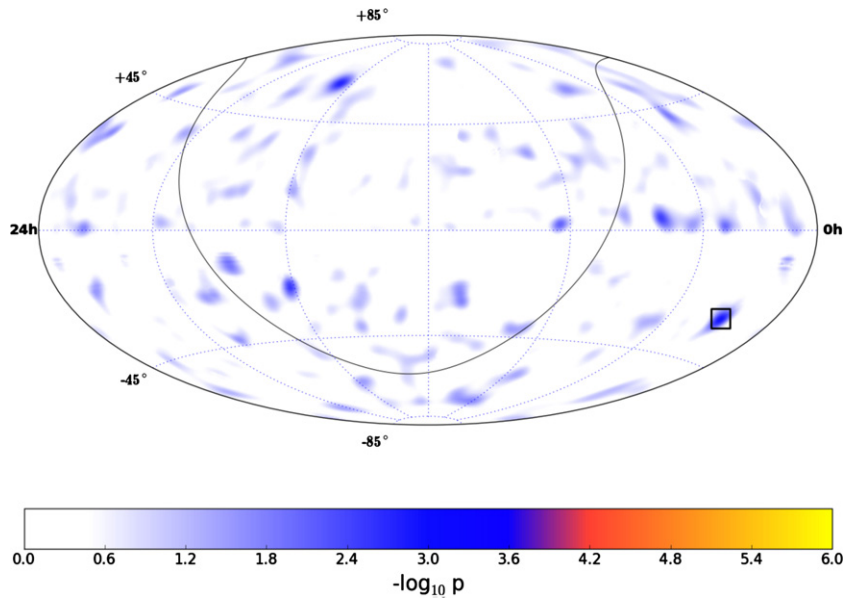


Figure 8. Same as Figure 6, but for sources of 3° extension.
(A color version of this figure is available in the online journal.)

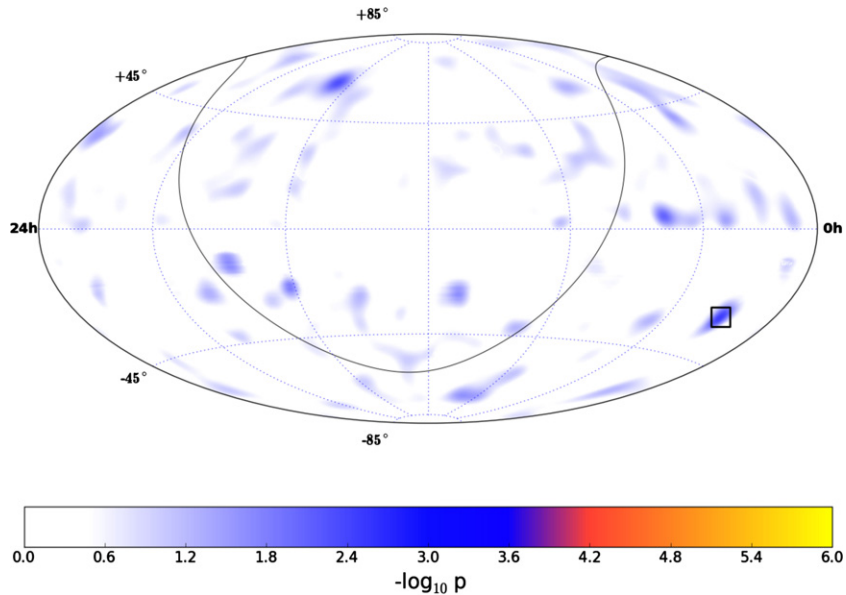


Figure 9. Same as Figure 6, but for sources of 4° extension.
(A color version of this figure is available in the online journal.)

Five nearby clusters of galaxies. This search tests four models assuming different CR spatial distribution within the source (Murase et al. 2008).

Ten SNRs associated with molecular clouds. This search is now updated to include more sources in the southern sky owing to our increased sensitivity in the southern sky due to new background rejection techniques. From the exhaustive online catalog SNRCat (Ferrand & Safi-Harb 2012), we select sources with confirmed molecular clouds associations. In order to keep the most promising neutrino emitters within the catalog, only sources that have been observed in the TeV or are younger than 10,000 yr (potentially in the Sedov blast wave phase (Sedov 1946) of expansion) are considered. The catalog contains four SNRs associated with molecular clouds in the northern sky (Abdo et al. 2007, 2009a, 2009b, 2010; Ackermann et al.

2013; Fiasson et al. 2009) that were previously considered in Aartsen et al. (2013c), and six newly introduced sources from SNRCat in the southern sky. These six sources are Sgr A East, Kes 75, 3C391, RX J1713.7–3946, CTB 37A, and 1FGL J1717.9–3729.

Two hundred and thirty-three galaxies with super-massive black holes. A sample of AGNs within the GZK (Greisen–Zatsespin–Kuzmin; Greisen 1966) radius as cataloged by Caramete & Biermann (2010) keeping only sources more massive than 5×10^8 solar masses.

New searches. These are new searches introduced with the inclusion of the first year of data from the completed 86 string detector.

Ten Galactic pulsar wind nebulae. Pulsar wind nebulae (PWNs) are potential emitters of neutrinos (Bednarek

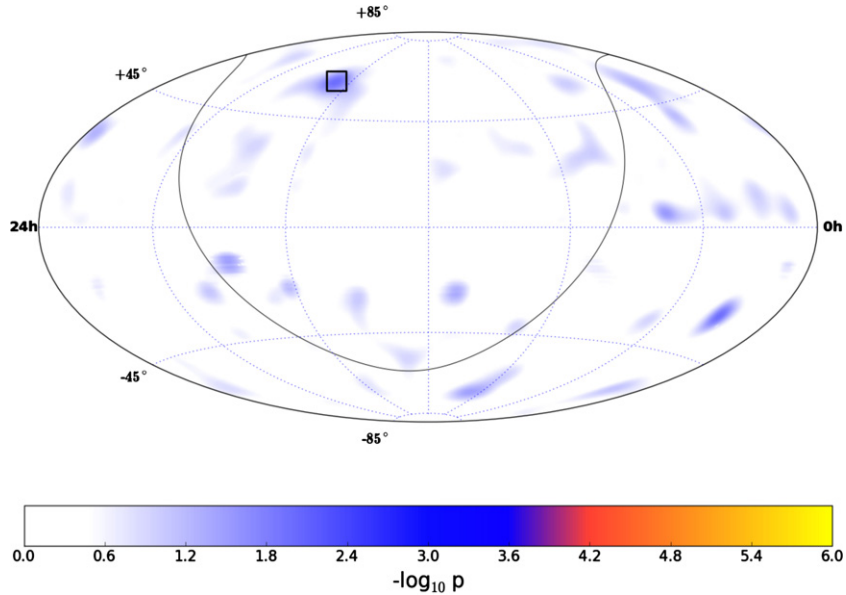


Figure 10. Same as Figure 6, but for sources of 5° extension.
(A color version of this figure is available in the online journal.)

2003). We carry out a stacked search for neutrinos coming from known PWNs within the Galaxy. From the confirmed PWNs in SNRCat (Ferrand & Safi-Harb 2012), we look at sources that are younger than 10,000 yr as only younger PWNs are efficient accelerators (Bednarek 2003). We leave out sources that are already considered by the search for SNRs associated with molecular clouds. These criteria are fulfilled by three sources in the northern sky, namely, the Crab Nebula, DA 530, and G054.1+00.3, and seven sources in the southern sky including the Pencil Nebula, W33, and MSH 11–54. These sources are weighted in likelihood by the inverse of their median age as provided by SNRCat (Ferrand & Safi-Harb 2012) to account for the higher fluxes expected from the youngest PWNs (Bednarek 2003).

Thirty Galactic SNRs. Galactic SNRs (Ferrand & Safi-Harb 2012) that neither have confirmed molecular cloud associations nor are PWNs are considered in this stacking search. As in the searches for PWNs and SNRs with molecular cloud associations, a cut on the SNR age is applied and only those younger than 10,000 yr are selected (Castro et al. 2011). This requirement is met by 30 sources in total, where 20 are located in the southern sky and 10 in the north. The inverse of the median age as provided by SNRCat (Ferrand & Safi-Harb 2012) is used as the weight for each source in likelihood in order to account for the fact that we expect the highest fluxes to come from the youngest SNRs. Remnants of recent prominent supernovae such as Cassiopeia A and *Tycho* are considered within this search.

Blazars catalogs. Three blazar catalogs were composed from the *Fermi* LAT Second AGN catalog (Ackermann et al. 2011) to allow for optimized analyses of the corresponding object classes. The first catalog contains flat spectrum radio quasars (FSRQs), which, as suggested by their broad line regions, are thought to provide efficient photomeson production (Atoyan & Dermer 2001) in dense soft photon targets. The second set is formed by low-frequency peaked (LSP) BL Lac objects that are predicted to show a significant contribution from pion decays to the overall gamma-emission in the synchrotron proton blazar model

(Mücke et al. 2003). Finally, p - p interaction models are covered by a catalog of the BL Lac objects with particularly hard gamma spectra and correspondingly large effective areas for neutrinos in IceCube (Neronov & Ribordy 2009).

The source selection and weighting for the FSRQ and LSP BL Lac catalogs, assuming prevalence of photo-hadronic neutrino production, is based on the *Fermi* LAT gamma-flux. This motivates a weighting that is based on the measured gamma-fluxes but assumes the same spectral index for all sources (hereby denoted by W1).

In proton-proton interaction models, the energy spectrum of the produced neutral secondaries follows the initial CR spectrum down to a threshold below 1 GeV. The observation of the gamma spectrum thus allows for a direct prediction of the proton spectrum behavior in the TeV range, which can be extrapolated to PeV energies to estimate the neutrino spectrum. Such an approach is not as easily possible for proton-gamma interaction models, as these typically have a lower-energy threshold above TeV energies so that the photon (and neutrino) spectrum below the threshold does not allow for the derivation of the proton spectrum (Neronov & Ribordy 2009). Hence, the third catalog of hard gamma-spectrum BL Lac objects motivates a selection and weighting based on the number of detectable neutrinos derived from the spectral shape measured by *Fermi* LAT (hereby denoted by W2).

Due to the variety of blazar models and the large model uncertainties, both weighting schemes are applied to all three catalogs. Sources with negligible weights in both weighting schemes are discarded, resulting in 33 FSRQs, 27 LSP BL Lac objects, and 37 hard gamma-spectrum BL Lac objects.

This stacked search for blazars uses a reprocessed data set of the 79 string configuration that incorporates the new reconstruction methods presented in this work for IC-86, which were not yet available at the time of the previous analyses.

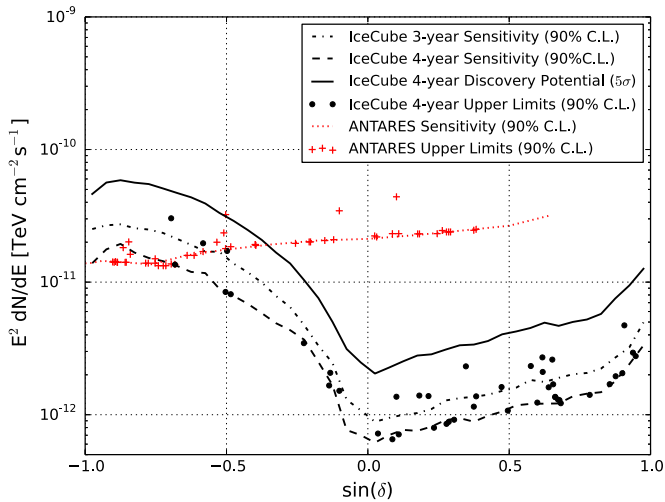


Figure 11. Muon neutrino upper limits with 90% C.L. evaluated for the 44 sources (dots) for the combined four years of data (40, 59, 79, and 86 string detector configurations). The solid black line is the flux required for 5σ discovery of a point source emitting an E^{-2} flux at different declinations, while the dashed line is the median upper limit or sensitivity also for a 90% C.L. The sensitivity of this search represents a 40%–50% improvement compared to previous IceCube results (dash-dotted line; Aartsen et al. 2013c). The ANTARES sensitivities and upper limits are also shown (Adrián-Martínez et al. 2014). For sources in the southern hemisphere, ANTARES constrains neutrino fluxes at lower energies than this work.

(A color version of this figure is available in the online journal.)

4. RESULTS AND IMPLICATIONS

In this section, we summarize all the results from the different searches and their implication on astrophysical models of neutrino emission. While no significant excess has been found in any of the searches and all results are consistent with the background-only hypothesis, this has allowed us to set upper limits that exclude some of the models.

4.1. All-sky Searches

4.1.1. All-sky Point Source Scan

Figure 5 shows the result of the all-sky scan for point sources in terms of significance at each location in the sky given in equatorial coordinates. The most significant deviation in the northern sky has a pre-trial p -value of 4.81×10^{-6} and is located at $29^{\circ}25$ R.A. and $10^{\circ}55$ decl. At this location, the best-fit values of the number of source events, \hat{n}_s , and signal spectral index, $\hat{\gamma}$, are 43.0 and 2.88, respectively. In the southern sky, the most significant deviation has a pre-trial p -value of 6.81×10^{-6} and is located at $347^{\circ}95$ R.A. and $-57^{\circ}75$ decl. Here, the best-fit values of \hat{n}_s and $\hat{\gamma}$ are 13.0 and 3.95, respectively. After accounting for the trial factor associated with scanning the sky for the most significant spots, the post-trial p -values are 0.23 for the spot located in the northern sky and 0.44 for the spot located in the southern sky.

4.1.2. All-sky Scans for Extended Sources

Table 2 summarizes the most significant hotspots in the sky from the scans for sources of various extensions. All observations were compatible with the background hypothesis. Figures 6–10 show the corresponding skymaps for 1° , 2° , 3° , 4° , and 5° extension, respectively.

Since filtering streams, reconstructions, and detector configurations evolved with time, we also examined each of the four years of data independently as an a posteriori cross-check. The

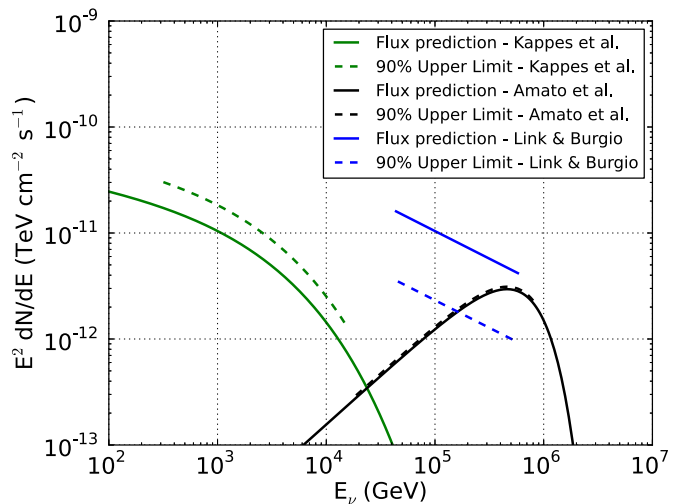


Figure 12. Flux predictions (solid) for three models of neutrino emission from the Crab Nebula, with their associated 90% C.L. upper limits (dashed) for an energy range containing 90% of the signal. Both the model from Amato et al. (2003) and the most optimistic model from Link & Burgio (2005, 2006) are now excluded at 90% C.L. For the gamma-ray-based model from Kappes et al. (2007), the upper limit is still a factor of 1.75 above the prediction.

(A color version of this figure is available in the online journal.)

largest fluctuation was observed for the 1° extension hypothesis in data from the 79 string configuration at 266.75 R.A. and 13.25 decl., where 0.35% of scrambled maps in that year resulted in a fluctuation more significant than the one observed. Since we scanned over five different extensions for every year, the corresponding trial-corrected p -value is 7.2%, well compatible with a background fluctuation. The hot-spot seems to be driven by a single well-reconstructed very high-energy event which, when folded with the wider source template, overlaps with some nearby lower-energy ones. From calibration using the shadow of the Moon (Aartsen et al. 2013d), there is no evidence for a systematic error in IceCube’s point-spread function that could lead to the observed spread for events originating from a point-like source. The region is not significant in any of the other years of data.

4.2. List of 44 Candidate Sources

The search for neutrino emission from an a priori list of 44 candidate sources produced the results shown in Tables 3 and 4. In the northern sky, 1ES 0229+200 has the strongest upward fluctuation. The pre-trial p -value of such a fluctuation is 0.053, but after considering the random chance of observing a fluctuation as strong or stronger than this in any of the sources, the post-trial p -value is 0.61. In the southern sky, PKS 0537–441 has the strongest upward fluctuation, with a pre-trials p -value of 0.083 and a post-trials p -value of 0.33. Upper limits on the E^{-2} muon neutrino flux for 90% confidence level (C.L.) from each source are listed in the table, and are shown along with the analysis sensitivity in Figure 11.

While many baseline models for CR acceleration and high-energy neutrino production predict E^{-2} neutrino spectra, individual sources with unique conditions can produce significantly different spectra. Models for any source in the sky can be tested with the analysis method used in this work, and a number of individual sources were previously considered in Aartsen et al. (2013c). Here, we update the 90% C.L. upper limits on three models of neutrino emission from the Crab Nebula (Figure 12) as well as three Galactic SNRs (Figure 13).

Table 3
Results for Galactic Objects on the A Priori Search List

Category	Source	R.A. (°)	Decl. (°)	p -value	\hat{n}_S	$\hat{\gamma}$	B_{1°	$\Phi_{\nu_\mu + \bar{\nu}_\mu}^{90\%}$
SNR	<i>Tycho</i>	6.36	64.18	...	0.0	...	17.8	2.06
	Cas A	350.85	58.81	...	0.0	...	17.8	1.70
	IC443	94.18	22.53	0.35	4.6	3.9	27.8	1.38
HMXB /mqso	LSI +63 303	40.13	61.23	...	0.0	...	17.8	1.95
	Cyg X-3	308.11	40.96	0.42	3.7	3.9	21.5	1.70
	Cyg X-1	299.59	35.20	0.18	8.9	3.9	23.4	2.33
	HESS J0632+057	98.25	5.80	0.14	13.4	3.4	37.0	1.37
	SS433	287.96	4.98	...	0.0	...	37.6	0.65
Star formation region	Cyg OB2	308.08	41.51	...	0.0	...	21.0	1.36
Pulsar/ PWN	MGRO J2019+37	305.22	36.83	...	0.0	...	23.1	1.23
	Crab Nebula	83.63	22.01	0.44	4.4	3.9	27.8	1.15
	Geminga	98.48	17.77	...	0.0	...	30.7	0.92
Galactic center	Sgr A*	266.42	-29.01	...	0.0	...	36.6	8.11
Not identified	MGRO J1908+06	286.98	6.27	...	0.0	...	36.4	0.71

Notes. Sources are grouped according to their classification as high-mass X-ray binaries or micro-quasars (HMXB/mqso), SNRs, pulsar wind nebulae (PWNs), star formation regions, and unidentified sources. The p -value is the pre-trial probability of compatibility with the background-only hypothesis. The \hat{n}_S and $\hat{\gamma}$ columns give the best-fit number of signal events and spectral index of a power-law spectrum. When $\hat{n}_S = 0$, no p -value or $\hat{\gamma}$ are reported. The eighth column gives the number of background events in a circle of 1° around the search coordinates. The last column shows the upper limits based on the classical approach (Neyman 1937) for an E^{-2} flux normalization of $\nu_\mu + \bar{\nu}_\mu$ flux in units of $10^{-12} \text{ TeV}^{-1} \text{ cm}^{-2} \text{ s}^{-1}$.

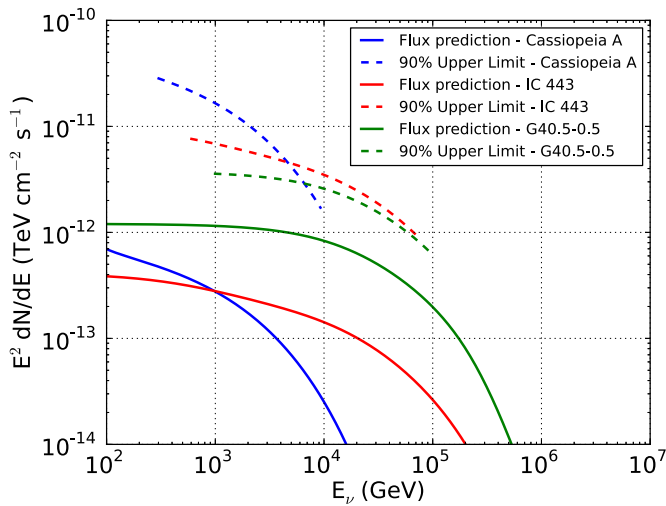


Figure 13. Flux predictions (solid) and upper limits (dashed) for three Galactic supernova remnants. The neutrino models, based on fitted gamma-ray observations, are from (Mandelartz & Tjus 2013). For the source with the highest predicted flux, G40.5–0.5, the upper limit is a factor of three above the model. (A color version of this figure is available in the online journal.)

4.3. Stacking Searches

The results of all stacking searches are compatible with the background-only hypothesis and are summarized in Table 5. The most significant deviation from the background-only hypothesis was observed in the stacked search for neutrino emission from the six Milagro TeV gamma-ray sources, with a p -value of 0.02. The fitted spectral index of 3.95, however, suggests that only low-energy events contribute toward the observation and the observed significance is from spatial clustering only. While Halzen et al. (2008) predicts a flux of much higher energy neutrinos from these sources, the assumptions made about the gamma-ray spectra of the sources in Halzen et al. (2008)

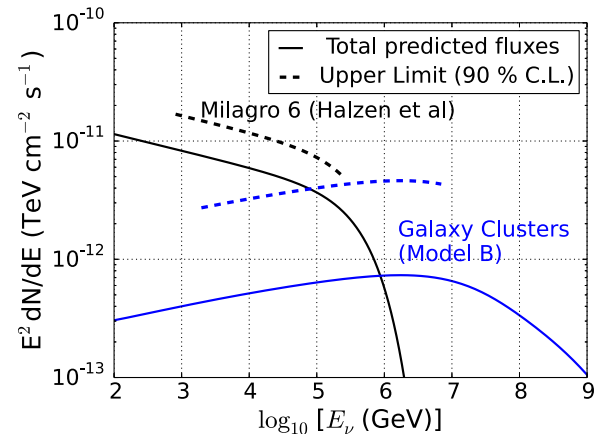


Figure 14. IceCube 90% C.L. upper limits to the models of Halzen et al. (2008) and Murase et al. (2008).

(A color version of this figure is available in the online journal.)

have later proved to be too optimistic (Abdo et al. 2012). Subsequently, the authors have updated the models (Gonzalez-Garcia et al. 2014). Figure 14 shows the IceCube upper limits to the model of Halzen et al. (2008). In Figure 14, we also compare limits on neutrino fluxes from galaxy clusters to the model from Murase et al. (2008).

4.4. Systematic Uncertainties

In all analyses described here, the background is estimated by scrambling the detector data in right ascension and is independent of theoretical uncertainties on fluxes of atmospheric neutrino and muons as well as uncertainties in the simulation of the detector. The p -values are therefore robust against most sources of systematic error. Upper limits and analysis sensitivities, however, are calculated by simulating the detector response to neutrinos. Detector uncertainties including the optical properties of the ice and the absolute efficiency of the

Table 4
Results for Extragalactic Objects on the A Priori Search List

Category	Source	R.A. (°)	Decl. (°)	p -value	\hat{n}_S	$\hat{\gamma}$	B_{1°	$\Phi_{\nu_\mu + \bar{\nu}_\mu}^{90\%}$
BL Lac object	S5 0716+71	110.47	71.34	...	0.0	...	16.5	2.77
	1ES 1959+650	300.00	65.15	0.083	9.8	3.2	17.7	4.72
	1ES 2344+514	356.77	51.70	...	0.0	...	19.1	1.41
	3C66A	35.67	43.04	...	0.0	...	20.5	1.220
	H 1426+428	217.14	42.67	...	0.0	...	20.8	1.29
	BL Lac	330.68	42.28	...	0.0	...	20.8	1.30
	Mrk 501	253.47	39.76	0.45	3.2	3.7	22.1	1.61
	Mrk 421	166.11	38.21	0.26	3.8	1.9	22.4	2.10
	W Comae	185.38	28.23	0.34	1.4	1.6	25.9	1.62
	1ES 0229+200	38.20	20.29	0.053 ^a	16.0	3.7	28.6	2.32
	PKS 0235+164	39.66	16.62	...	0.0	...	31.4	0.88
	PKS 2155–304	329.72	–30.23	...	0.0	...	37.0	8.43
	PKS 0537–441	84.71	–44.09	0.083 ^b	6.3	3.9	35.2	30.03
FSRQ	4C 38.41	248.81	38.13	0.12	10.6	2.8	22.4	2.71
	3C 454.3	343.49	16.15	...	0.0	...	31.4	0.85
	PKS 0528+134	82.73	13.53	...	0.0	...	32.3	0.80
	PKS 1502+106	226.10	10.49	0.21	6.1	2.3	33.2	1.39
	3C 273	187.28	2.05	0.45	3.2	2.6	38.9	0.72
	3C279	194.05	–5.79	...	0.0	...	33.5	1.51
	QSO 2022–077	306.42	–7.64	0.45	1.3	2.0	34.1	2.07
	PKS 1406–076	212.24	–7.87	...	0.0	...	34.1	1.66
	QSO 1730–130	263.26	–13.08	...	0.0	...	37.1	3.46
	PKS 1622–297	246.53	–29.86	0.13	6.2	2.7	36.6	17.17
	PKS 1454–354	224.36	–35.65	0.2	5.4	3.9	35.6	19.64
Starburst radio galaxies	M82	148.97	69.68	...	0.0	...	16.3	2.94
	NGC 1275	49.95	41.51	...	0.0	...	21.0	1.36
	Cyg A	299.87	40.73	0.18	1.8	1.5	21.5	2.60
	3C 123.0	69.27	29.67	...	0.0	...	25.7	1.07
	M87	187.71	12.39	0.26	8.8	3.9	32.4	1.38
	Cen A	201.37	–43.02	...	0.0	...	35.5	13.57

Notes. Sources are grouped according to their classification as BL Lac objects, radio galaxies, FSRQs, and starburst galaxies. The p -value is the pre-trial probability of compatibility with the background-only hypothesis. The \hat{n}_S and $\hat{\gamma}$ columns give the best-fit number of signal events and spectral index of a power-law spectrum. When $\hat{n}_S = 0$, no p -value or $\hat{\gamma}$ are reported. The eighth column gives the number of background events in a circle of 1° around the search coordinates. The last column shows the upper limits based on the classical approach (Neyman 1937) for an E^{-2} flux normalization of $\nu_\mu + \bar{\nu}_\mu$ flux in units of $10^{-12} \text{ TeV}^{-1} \text{ cm}^{-2} \text{ s}^{-1}$.

^a Most significant p -value in the northern sky among all Galactic and extragalactic objects on the a priori search list.

^b Most significant p -value in the southern sky among all Galactic and extragalactic objects on the a priori search list.

Table 5
Results of the Stacked Searches for Emission from Source Catalogs

Catalog	\hat{n}_S	$\hat{\gamma}$	p -value	$\Phi_{\nu_\mu + \bar{\nu}_\mu}^{90\%}$
Milagro 6	51.4	3.95	0.02	$1.98 \times \text{M.F.}$ (Halzen et al. 2008)
Galaxy clusters	Model A	1.4	4.07	$3.89 \times \text{M.F.}$ (Murase et al. 2008)
	Model B	12.6	3.95	$6.30 \times \text{M.F.}$ (Murase et al. 2008)
	Central AGN	0.0	...	$1.59 \times \text{M.F.}$ (Murase et al. 2008)
	Isobaric	0.0	...	$4.79 \times \text{M.F.}$ (Murase et al. 2008)
Starburst galaxies	0.0	$7.93 \times 10^{-12} \times E^{2.0}$
MC associated SNRs	0.0	$1.60 \times 10^{-9} \times E^{2.7}$
Supermassive black holes	17.1	3.95	0.43	$6.88 \times 10^{-12} \times E^{2.0}$
Young SNRs	0.0	$4.83 \times 10^{-12} \times E^{2.0}$
Young PWNs	0.0	$3.12 \times 10^{-12} \times E^{2.0}$
FSRQs	W1	9.8	2.45	$3.46 \times 10^{-12} \times E^{2.0}$
	W2	15.4	2.75	$34.3 \times \text{M.F.}$
	LSP BL Lac objects	W1	11.9	0.38
	W2	21.8	0.10	$13.5 \times \text{M.F.}$
Hard BL Lac objects	W1	0	...	$3.73 \times 10^{-12} \times E^{2.0}$
	W2	17.5	3.95	$0.284 \times \text{M.F.}$

Notes. M.F. stands for the model flux as described in the references motivating the analyses. $\Phi_{\nu_\mu + \bar{\nu}_\mu}^{90\%}$ is the 90% confidence level upper limit on the combined flux of ν_μ and $\bar{\nu}_\mu$ from the catalogs. The $E^{2.0}$ limits are in units of $\text{TeV}^1 \text{ cm}^{-2} \text{ s}^{-1}$.

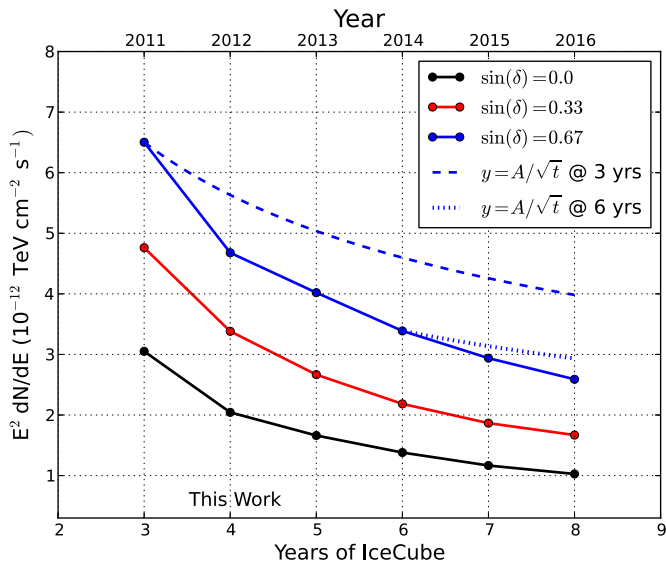


Figure 15. Predicted E^{-2} discovery potential as a function of years of running time of the IceCube Observatory for three different declinations (solid lines). Due to the relatively low background rate in this analysis, the discovery potential will continue to improve faster than the square-root of time limit (dashed and dotted lines).

(A color version of this figure is available in the online journal.)

optical modules can affect the reported sensitivities and upper limits.

After a detailed discussion of all relevant systematic uncertainties, Aartsen et al. (2013c) concludes that the level of uncertainty in the analysis using three years of data is about 18%. Since 65% of the data used here is the same as in Aartsen et al. (2013c) and the techniques for the new event selection and analyses are similar, the systematic uncertainty on the four year sample is about the same. However, the added year of data utilizes a new muon track reconstruction, which is more sensitive to uncertainties in the optical properties of the ice. We re-evaluate the effect of the ice properties on the analysis for the 2011–2012 data, finding a corresponding systematic uncertainty of +16%/–8%. This is incorporated into the overall systematic uncertainty by averaging it with the ice model effect from the previous years. The resulting overall systematic uncertainty on the quoted sensitivities and upper limits is 21%.

5. CONCLUSIONS

No evidence of neutrino emission from point-like or extended sources was found in four years of IceCube data. Searches for emissions from point-like and extended sources anywhere in the sky, from a pre-defined candidate source list, and from stacked source catalogs all returned results consistent with the background-only hypothesis. Ninety percent C.L. upper limits on the muon neutrino fluxes for models from a variety of sources were calculated and compared to predictions. The most optimistic models considered here can be excluded at 90% C.L. and in other cases limits are a factor of two to four above the predictions. This analysis includes data from the completed IceCube array, taken between 2011 May and 2012 May. IceCube will continue to run in this configuration for the foreseeable future. Future analyses will benefit from this improved integration time and the evolution of the analysis sensitivity as a function of years of data taking is shown in Figure 15. Within a few years, the analyses will surpass the sensitivity necessary to test a wider variety of neutrino point source models. Future developments in

background rejection techniques and reconstruction algorithms may lead to improvements faster than predicted in Figure 15.

We acknowledge the support from the following agencies: U.S. National Science Foundation-Office of Polar Programs, U.S. National Science Foundation-Physics Division, University of Wisconsin Alumni Research Foundation, the Grid Laboratory Of Wisconsin (GLOW) grid infrastructure at the University of Wisconsin–Madison, the Open Science Grid (OSG) grid infrastructure; U.S. Department of Energy, and National Energy Research Scientific Computing Center, the Louisiana Optical Network Initiative (LONI) grid computing resources; Natural Sciences and Engineering Research Council of Canada, West-Grid and Compute/Calcul Canada; Swedish Research Council, Swedish Polar Research Secretariat, Swedish National Infrastructure for Computing (SNIC), and Knut and Alice Wallenberg Foundation, Sweden; German Ministry for Education and Research (BMBF), Deutsche Forschungsgemeinschaft (DFG), Helmholtz Alliance for Astroparticle Physics (HAP), Research Department of Plasmas with Complex Interactions (Bochum), Germany; Fund for Scientific Research (FNRS-FWO), FWO Odysseus programme, Flanders Institute to encourage scientific and technological research in industry (IWT), Belgian Federal Science Policy Office (Belspo); University of Oxford, United Kingdom; Marsden Fund, New Zealand; Australian Research Council; Japan Society for Promotion of Science (JSPS); the Swiss National Science Foundation (SNSF), Switzerland; National Research Foundation of Korea (NRF); Danish National Research Foundation, Denmark (DNRF).

REFERENCES

- Aartsen, M. G., Abbasi, R., Abdou, Y., et al. (IceCube Coll.) 2013a, *NIMPA*, 711, 73
- Aartsen, M. G., Abbasi, R., Abdou, Y., et al. (IceCube Coll.) 2013b, *NIMPA*, 736, 143
- Aartsen, M. G., Abbasi, R., Abdou, Y., et al. (IceCube Coll.) 2013c, *ApJ*, 779, 132
- Aartsen, M. G., Abbasi, R., Ackermann, M., et al. (IceCube Coll.) 2014a, *JINST*, 9, P03009
- Aartsen, M. G., Abdou, Y., Ackermann, M., et al. (IceCube Coll.) 2013d, arXiv:1305.6811
- Aartsen, M. G., Ackermann, M., Adams, J., et al. (IceCube Coll.) 2014b, *PhRvL*, 113, 101101
- Aartsen, M. G., et al. (IceCube Coll.) 2013e, *Sci*, 342, 1242856
- Abbasi, R., Abdou, Y., Abu-Zayyad, T., et al. (IceCube Coll.) 2010, *NIMPA*, 618, 139
- Abbasi, R., Abdou, Y., Abu-Zayyad, T., et al. (IceCube Coll.) 2011, *ApJ*, 732, 18
- Abbasi, R., Ackermann, M., Adams, J., et al. (IceCube Coll.) 2009, *NIMPA*, 601, 294
- Abdo, A. A., Abeysekera, U., Allen, B. T., et al. 2012, *ApJ*, 753, 159
- Abdo, A. A., Ackermann, M., Ajello, M., et al. (Fermi Coll.) 2009a, *ApJL*, 706, L1
- Abdo, A. A., Ackermann, M., Ajello, M., et al. (Fermi Coll.) 2010, *Sci*, 327, 1103
- Abdo, A. A., Allen, B., Berley, D., et al. 2007, *ApJL*, 664, L91
- Abdo, A. A., Allen, B. T., Aune, T., et al. (Milagro Coll.) 2009b, *ApJL*, 700, L127
- Achterberg, A., Ackermann, M., Adams, J., et al. (IceCube Coll.) 2006, *Aph*, 26, 155
- Ackermann, M., Ajello, M., Allafort, A., et al. 2011, *ApJ*, 743, 171
- Ackermann, M., Ajello, M., Allafort, A., et al. (Fermi Coll.) 2013, *Sci*, 339, 807
- Adrián-Martínez, S., Albert, A., André, M., et al. (Antares Coll.) 2014, *ApJL*, 786, L5
- Ahrens, J., Bai, X., Bay, R., et al. 2004, *NIMPA*, 524, 169
- Alvarez-Muñiz, J., & Halzen, F. 2002, *ApJL*, 576, L33
- Amato, E., Guetta, D., & Blasi, P. 2003, *A&A*, 402, 827
- Anchordoqui, L. A., Barger, V., Cholis, I., et al. 2014, *JHEAp*, 1, 1

- Anchordoqui, L. A., & Montaruli, T. 2010, *ARNPS*, **60**, 129
- Atoyan, A., & Dermer, C. D. 2001, *PhRvL*, **87**, 221102
- Becker, J. 2008, *PhR*, **458**, 173
- Becker, J. K., Biermann, P. L., Dreyer, J., & Kneiske, T. M. 2009, arXiv:0901.1775
- Bednarek, W. 2003, *A&A*, **407**, 1
- Braun, J., Baker, M., Dumm, J., et al. 2010, *Aph*, **33**, 175
- Caramete, L., & Biermann, P. L. 2010, *A&A*, **521**, A55
- Carrigan, S., Brun, F., Chaves, R. C. G., et al. (HESS Coll.) 2013, in Proc. of the 48th Rencontres de Moriond, La Thuile, Italy, ed. E. Auge & J. Dumarchez (available online at http://moriond.in2p3.fr/Proceedings/2013/Moriond_QCD_2013.pdf)
- Castro, D., Slane, P., Patnaude, D. J., & Ellison, D. C. 2011, *ApJ*, **734**, 85
- Cavasinni, V., Grasso, D., & Maccione, L. 2006, *Aph*, **26**, 41
- De Marco, D., Blasi, P., Hansen, P., & Stanev, T. 2006, *PhRvD*, **73**, 043004
- Essey, W., Kalashev, O. E., Kusenko, A., & Beacom, J. F. 2010, *PhRvL*, **104**, 141102
- Ferrand, G., & Safi-Harb, S. 2012, *AdSpR*, **49**, 1313
- Fiasson, A., Marandon, V., Chaves, R. C. G., & Tibolla, O. (HESS Coll.) 2009, in Proceedings of the 31st Int. Cosmic Ray Conf., Lodz, Poland, Discovery of a VHE Gamma-Ray Source in the W51 Region, ed. J. Szabelski & M. Giller (Lodz: Univ. of Lodz)
- Gonzalez-Garcia, M. C., Halzen, F., & Niro, V. 2014, *Aph*, **57**, 39
- Greisen, K. 1966, *PhRvL*, **16**, 748
- Guetta, D., Hooper, D., Alvarez-Muñiz, J., Halzen, F., & Reuveni, E. 2004, *Aph*, **20**, 429
- Halzen, F., & Hooper, D. 2002, *RPPH*, **65**, 1025
- Halzen, F., Kappes, A., & O'Murchadha, A. 2008, *PhRvD*, **78**, 063004
- Honda, M., Kajita, T., Kasahara, K., Midorikawa, S., & Sanuki, T. 2007, *PhRvD*, **75**, 043006
- Kalashev, O. E., Kusenko, A., & Essey, W. 2013, *PhRvL*, **111**, 041103
- Kappes, A., Hinton, J., Stegmann, C., & Aharonian, F. A. 2007, *ApJ*, **656**, 870
- Lacki, B. C., Thompson, T. A., Quataert, E., Loeb, A., & Waxman, E. 2011, *ApJ*, **734**, 107
- Learned, J. G., & Mannheim, K. 2000, *ARNPS*, **50**, 679
- Link, B., & Burgio, F. 2005, *PhRvL*, **94**, 181101
- Link, B., & Burgio, F. 2006, *MNRAS*, **371**, 375
- Loeb, A., & Waxman, E. 2006, *JCAP*, **05**, 003
- Mandelartz, M., & Tjus, J. B. 2013, arXiv:1301.2437
- Mészáros, P. 2006, *RPPH*, **69**, 2259
- Mücke, A., Protheroe, R. J., Engel, R., Rachen, J. P., & Stanev, T. 2003, *Aph*, **18**, 593
- Murase, K., Ahlers, M., & Lacki, B. C. 2013, *PhRvD*, **88**, 121301
- Murase, K., & Beacom, J. F. 2012, *JCAP*, **02**, 028
- Murase, K., Inoue, Y., & Dermer, C. D. 2014, *PhRvD*, **90**, 023007
- Murase, K., Inoue, S., & Nagataki, S. 2008, *ApJL*, **689**, L105
- Neronov, A., & Ribordy, M. 2009, *PhRvD*, **80**, 083008
- Neunhoffer, T. 2006, *Aph*, **25**, 220
- Neyman, J. 1937, *RSPTA*, **236**, 333
- Romero, G. E., & Torres, D. F. 2003, *ApJL*, **586**, L33
- Sedov, L. I. 1946, *JApMM*, **10**, 241
- Sironi, L., & Spitkovsky, A. 2011, *ApJ*, **726**, 75
- Stecker, F. W., Done, C., Salamon, M. H., & Sommers, P. 1991, *PhRvL*, **66**, 2697
- Tchernin, C., Aguilar, J. A., Neronov, A., & Montaruli, T. 2013, *A&A*, **560**, A67
- Vissani, F., Aharonian, F., & Sahakyan, N. 2011, *Aph*, **34**, 778
- Waxman, E., & Bahcall, J. 1997, *PhRvL*, **78**, 2292
- Waxman, E., & Bahcall, J. 1999, *PhRvD*, **59**, 023002
- Whitehorn, N., van Santen, J., & Lafébre, S. 2013, *CoPhC*, **184**, 2214
- Wolfe, B., Melia, F., Crocker, R. M., & Volkas, R. R. 2008, *ApJ*, **687**, 193

First observation of PeV-energy neutrinos with IceCube

M. G. Aartsen,² R. Abbasi,²⁷ Y. Abdou,²² M. Ackermann,⁴¹ J. Adams,¹⁵ J. A. Aguilar,²¹ M. Ahlers,²⁷ D. Altmann,⁹ J. Auffenberg,²⁷ X. Bai,^{31,*} M. Baker,²⁷ S. W. Barwick,²³ V. Baum,²⁸ R. Bay,⁷ J. J. Beatty,^{17,18} S. Bechet,¹² J. Becker Tjus,¹⁰ K.-H. Becker,⁴⁰ M. Bell,³⁸ M. L. Benabderrahmane,⁴¹ S. BenZvi,²⁷ J. Berdermann,⁴¹ P. Berghaus,⁴¹ D. Berley,¹⁶ E. Bernardini,⁴¹ A. Bernhard,³⁰ D. Bertrand,¹² D. Z. Besson,²⁵ G. Binder,^{8,7} D. Bindig,⁴⁰ M. Bissok,¹ E. Blaufuss,¹⁶ J. Blumenthal,¹ D. J. Boersma,³⁹ S. Bohachuk,²⁰ C. Boehm,³⁴ D. Bose,¹³ S. Böser,¹¹ O. Botner,³⁹ L. Brayeur,¹³ H.-P. Bretz,⁴¹ A. M. Brown,¹⁵ R. Bruijn,²⁴ J. Brunner,⁴¹ M. Carson,²² J. Casey,⁵ M. Casier,¹³ D. Chirkin,²⁷ A. Christov,²¹ B. Christy,¹⁶ K. Clark,³⁸ F. Clevermann,¹⁹ S. Coenders,¹ S. Cohen,²⁴ D. F. Cowen,^{38,37} A. H. Cruz Silva,⁴¹ M. Danninger,³⁴ J. Daughhetee,⁵ J. C. Davis,¹⁷ C. De Clercq,¹³ S. De Ridder,²² P. Desiati,²⁷ M. de With,⁹ T. DeYoung,³⁸ J. C. Díaz-Vélez,²⁷ M. Dunkman,³⁸ R. Eagan,³⁸ B. Eberhardt,²⁸ J. Eisch,²⁷ R. W. Ellsworth,¹⁶ S. Euler,¹ P. A. Evenson,³¹ O. Fadiran,²⁷ A. R. Fazely,⁶ A. Fedynitch,¹⁰ J. Feintzeig,²⁷ T. Feusels,²² K. Filimonov,⁷ C. Finley,³⁴ T. Fischer-Wasels,⁴⁰ S. Flis,³⁴ A. Franckowiak,¹¹ R. Franke,⁴¹ K. Frantzen,¹⁹ T. Fuchs,¹⁹ T. K. Gaisser,³¹ J. Gallagher,²⁶ L. Gerhardt,^{8,7} L. Gladstone,²⁷ T. Glüsenkamp,⁴¹ A. Goldschmidt,⁸ G. Golup,¹³ J. G. Gonzalez,³¹ J. A. Goodman,¹⁶ D. Góra,⁴¹ D. Grant,²⁰ A. Groß,³⁰ M. Gurtner,⁴⁰ C. Ha,^{8,7} A. Haj Ismail,²² P. Hallen,¹ A. Hallgren,³⁹ F. Halzen,²⁷ K. Hanson,¹² D. Heereman,¹² D. Heinen,¹ K. Helbing,⁴⁰ R. Hellauer,¹⁶ S. Hickford,¹⁵ G. C. Hill,² K. D. Hoffman,¹⁶ R. Hoffmann,⁴⁰ A. Homeier,¹¹ K. Hoshina,²⁷ W. Huelsnitz,^{16,†} P. O. Hulth,³⁴ K. Hultqvist,³⁴ S. Hussain,³¹ A. Ishihara,^{14,‡} E. Jacobi,⁴¹ J. Jacobsen,²⁷ K. Jagielski,¹ G. S. Japaridze,⁴ K. Jero,²⁷ O. Jlelati,²² B. Kaminsky,⁴¹ A. Kappes,⁹ T. Karg,⁴¹ A. Karle,²⁷ J. L. Kelley,²⁷ J. Kiryluk,³⁵ F. Kislat,⁴¹ J. Kläs,⁴⁰ S. R. Klein,^{8,7} J.-H. Köhne,¹⁹ G. Kohnen,²⁹ H. Kolanoski,⁹ L. Köpke,²⁸ C. Kopper,²⁷ S. Kopper,⁴⁰ D. J. Koskinen,³⁸ M. Kowalski,¹¹ M. Krasberg,²⁷ K. Krings,¹ G. Kroll,²⁸ J. Kunnen,¹³ N. Kurahashi,²⁷ T. Kuwabara,³¹ M. Labare,¹³ H. Landsman,²⁷ M. J. Larson,³⁶ M. Lesiak-Bzdak,³⁵ M. Leuermann,¹ J. Leute,³⁰ J. Lünemann,²⁸ J. Madsen,³³ R. Maruyama,²⁷ K. Mase,¹⁴ H. S. Matis,⁸ F. McNally,²⁷ K. Meagher,¹⁶ M. Merck,²⁷ P. Mészáros,^{37,38} T. Meures,¹² S. Miarecki,^{8,7} E. Middell,⁴¹ N. Milke,¹⁹ J. Miller,¹³ L. Mohrmann,⁴¹ T. Montaruli,^{21,§} R. Morse,²⁷ R. Nahnauer,⁴¹ U. Naumann,⁴⁰ H. Niederhausen,³⁵ S. C. Nowicki,²⁰ D. R. Nygren,⁸ A. Obertacke,⁴⁰ S. Odrowski,³⁰ A. Olivas,¹⁶ M. Olivo,¹⁰ A. O'Murchadha,¹² L. Paul,¹ J. A. Pepper,³⁶ C. Pérez de los Heros,³⁹ C. Pfenndner,¹⁷ D. Pieloth,¹⁹ E. Pinat,¹² N. Pirk,⁴¹ J. Posselt,⁴⁰ P. B. Price,⁷ G. T. Przybylski,⁸ L. Rädcl,¹ M. Rameez,²¹ K. Rawlins,³ P. Redl,¹⁶ R. Reimann,¹ E. Resconi,³⁰ W. Rhode,¹⁹ M. Ribordy,²⁴ M. Richman,¹⁶ B. Riedel,²⁷ J. P. Rodrigues,²⁷ C. Rott,^{17,¶} T. Ruhe,¹⁹ B. Ruzybayev,³¹ D. Ryckbosch,²² S. M. Saba,¹⁰ T. Salameh,³⁸ H.-G. Sander,²⁸ M. Santander,²⁷ S. Sarkar,³² K. Schatto,²⁸ M. Scheel,¹ F. Scheriau,¹⁹ T. Schmidt,¹⁶ M. Schmitz,¹⁹ S. Schoenen,¹ S. Schöneberg,¹⁰ A. Schönwald,⁴¹ A. Schukraft,¹ L. Schulte,¹¹ O. Schulz,³⁰ D. Seckel,³¹ Y. Sestayo,³⁰ S. Seunarine,³³ C. Sheremata,²⁰ M. W. E. Smith,³⁸ M. Soiron,¹ D. Soldin,⁴⁰ G. M. Spiczak,³³ C. Spiering,⁴¹ M. Stamatikos,^{17,**} T. Stanev,³¹ A. Stasik,¹¹ T. Stezelberger,⁸ R. G. Stokstad,⁸ A. Stöbl,⁴¹ E. A. Strahler,¹³ R. Ström,³⁹ G. W. Sullivan,¹⁶ H. Taavola,³⁹ I. Taboada,⁵ A. Tamburro,³¹ S. Ter-Antonyan,⁶ G. Tešić,³⁸ S. Tilav,³¹ P. A. Toale,³⁶ S. Toscano,²⁷ M. Usner,¹¹ D. van der Drift,^{8,7} N. van Eijndhoven,¹³ A. Van Overloop,²² J. van Santen,²⁷ M. Vehring,¹ M. Voge,¹¹ M. Vraeghe,²² C. Walck,³⁴ T. Waldenmaier,⁹ M. Wallraff,¹ R. Wasserman,³⁸ Ch. Weaver,²⁷ M. Wellons,²⁷ C. Wendt,²⁷ S. Westerhoff,²⁷ N. Whitehorn,²⁷ K. Wiebe,²⁸ C. H. Wiebusch,¹ D. R. Williams,³⁶ H. Wissing,¹⁶ M. Wolf,³⁴ T. R. Wood,²⁰ K. Woschnagg,⁷ C. Xu,³¹ D. L. Xu,³⁶ X. W. Xu,⁶ J. P. Yanez,⁴¹ G. Yodh,²³ S. Yoshida,¹⁴ P. Zarzhitsky,³⁶ J. Ziemann,¹⁹ S. Zierke,¹ A. Zilles,¹ and M. Zoll³⁴

(IceCube Collaboration)

¹*III. Physikalisches Institut, RWTH Aachen University, D-52056 Aachen, Germany*

²*School of Chemistry & Physics, University of Adelaide, Adelaide SA, 5005 Australia*

³*Dept. of Physics and Astronomy, University of Alaska Anchorage, 3211 Providence Dr., Anchorage, AK 99508, USA*

⁴*CTSPS, Clark-Atlanta University, Atlanta, GA 30314, USA*

⁵*School of Physics and Center for Relativistic Astrophysics, Georgia Institute of Technology, Atlanta, GA 30332, USA*

⁶*Dept. of Physics, Southern University, Baton Rouge, LA 70813, USA*

⁷*Dept. of Physics, University of California, Berkeley, CA 94720, USA*

⁸*Lawrence Berkeley National Laboratory, Berkeley, CA 94720, USA*

⁹*Institut für Physik, Humboldt-Universität zu Berlin, D-12489 Berlin, Germany*

¹⁰*Fakultät für Physik & Astronomie, Ruhr-Universität Bochum, D-44780 Bochum, Germany*

¹¹*Physikalisches Institut, Universität Bonn, Nussallee 12, D-53115 Bonn, Germany*

- ¹² *Université Libre de Bruxelles, Science Faculty CP230, B-1050 Brussels, Belgium*
¹³ *Vrije Universiteit Brussel, Dienst ELEM, B-1050 Brussels, Belgium*
¹⁴ *Dept. of Physics, Chiba University, Chiba 263-8522, Japan*
¹⁵ *Dept. of Physics and Astronomy, University of Canterbury, Private Bag 4800, Christchurch, New Zealand*
¹⁶ *Dept. of Physics, University of Maryland, College Park, MD 20742, USA*
¹⁷ *Dept. of Physics and Center for Cosmology and Astro-Particle Physics, Ohio State University, Columbus, OH 43210, USA*
¹⁸ *Dept. of Astronomy, Ohio State University, Columbus, OH 43210, USA*
¹⁹ *Dept. of Physics, TU Dortmund University, D-44221 Dortmund, Germany*
²⁰ *Dept. of Physics, University of Alberta, Edmonton, Alberta, Canada T6G 2E1*
²¹ *Département de physique nucléaire et corpusculaire, Université de Genève, CH-1211 Genève, Switzerland*
²² *Dept. of Physics and Astronomy, University of Gent, B-9000 Gent, Belgium*
²³ *Dept. of Physics and Astronomy, University of California, Irvine, CA 92697, USA*
²⁴ *Laboratory for High Energy Physics, École Polytechnique Fédérale, CH-1015 Lausanne, Switzerland*
²⁵ *Dept. of Physics and Astronomy, University of Kansas, Lawrence, KS 66045, USA*
²⁶ *Dept. of Astronomy, University of Wisconsin, Madison, WI 53706, USA*
²⁷ *Dept. of Physics and Wisconsin IceCube Particle Astrophysics Center, University of Wisconsin, Madison, WI 53706, USA*
²⁸ *Institute of Physics, University of Mainz, Staudinger Weg 7, D-55099 Mainz, Germany*
²⁹ *Université de Mons, 7000 Mons, Belgium*
³⁰ *T.U. Munich, D-85748 Garching, Germany*
³¹ *Bartol Research Institute and Department of Physics and Astronomy, University of Delaware, Newark, DE 19716, USA*
³² *Dept. of Physics, University of Oxford, 1 Keble Road, Oxford OX1 3NP, UK*
³³ *Dept. of Physics, University of Wisconsin, River Falls, WI 54022, USA*
³⁴ *Oskar Klein Centre and Dept. of Physics, Stockholm University, SE-10691 Stockholm, Sweden*
³⁵ *Department of Physics and Astronomy, Stony Brook University, Stony Brook, NY 11794-3800, USA*
³⁶ *Dept. of Physics and Astronomy, University of Alabama, Tuscaloosa, AL 35487, USA*
³⁷ *Dept. of Astronomy and Astrophysics, Pennsylvania State University, University Park, PA 16802, USA*
³⁸ *Dept. of Physics, Pennsylvania State University, University Park, PA 16802, USA*
³⁹ *Dept. of Physics and Astronomy, Uppsala University, Box 516, S-75120 Uppsala, Sweden*
⁴⁰ *Dept. of Physics, University of Wuppertal, D-42119 Wuppertal, Germany*
⁴¹ *DESY, D-15735 Zeuthen, Germany*

(Dated: June 13, 2013)

We report on the observation of two neutrino-induced events which have an estimated deposited energy in the IceCube detector of 1.04 ± 0.16 and 1.14 ± 0.17 PeV, respectively, the highest neutrino energies observed so far. These events are consistent with fully contained particle showers induced by neutral-current $\nu_{e,\mu,\tau}$ ($\bar{\nu}_{e,\mu,\tau}$) or charged-current ν_e ($\bar{\nu}_e$) interactions within the IceCube detector. The events were discovered in a search for ultra-high energy neutrinos using data corresponding to 615.9 days effective livetime. The expected number of atmospheric background is $0.082 \pm 0.004(\text{stat})_{-0.057}^{+0.041}(\text{syst})$. The probability to observe two or more candidate events under the atmospheric background-only hypothesis is 2.9×10^{-3} (2.8σ) taking into account the uncertainty on the expected number of background events. These two events could be a first indication of an astrophysical neutrino flux, the moderate significance, however, does not permit a definitive conclusion at this time.

PACS numbers: 98.70.Sa, 95.55.Vj

Astrophysical neutrinos are key probes of the high-energy universe. Because of their unique properties, neutrinos escape even dense regions, are undeflected in galactic or extra-galactic magnetic fields and traverse the photon-filled universe unhindered. Thus, neutrinos provide direct information about the dynamics and interiors of cosmological objects of the high red-shift Universe like gamma-ray bursts and active galactic nuclei. Neutrinos at energies above several 100 TeV are particularly interesting as the atmospheric background in this region is very low and a few astrophysical neutrinos can be significant. This letter reports on the observation of two

high-energy particle shower events discovered in a search for ultra-high energy neutrinos above about 1 PeV using the IceCube detector.

IceCube [1] detects and reconstructs neutrinos by recording Cherenkov photons emitted from secondary charged particles produced in neutral-current (NC) or charged-current (CC) interactions of the neutrinos in the 2,800 m thick glacial ice at the geographic South Pole. IceCube was built between 2005 and 2010. It consists of an array of 5,160 optical sensors (digital optical modules, DOMs) on 86 strings at depths between 1,450 m and 2,450 m that instrument a volume of 1 km^3 of ice. Eight

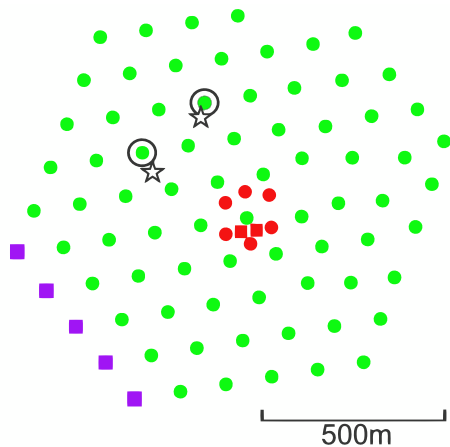


FIG. 1. Surface view of the full IceCube detector layout. Filled marks represent the positions of the IceCube strings. Red marks are the DeepCore strings. Squares represent the strings that did not exist in the IC79 configuration. Open circles are the positions of the closest strings to the observed two cascade events. Stars are their reconstructed vertex positions.

of the 86 strings belong to the DeepCore sub-array [2], a more densely instrumented volume in the bottom center of the detector. Each DOM consists of a 10" photomultiplier tube (PMT) [3] in a spherical glass pressure vessel. Events are recorded as a series of pulses (waveform) in each DOM [4] where two basic neutrino event signatures are distinguished: a track-like light pattern originating from neutrino-induced muons (tracks) and a spherical light pattern produced by hadronic or electromagnetic particle showers (cascades).

The analysis selects neutrino candidates calorimetrically using the total number of observed photo-electrons in each event (NPE) [4] as a proxy of the deposited energy [5], thus retaining both bright tracks and cascades. Backgrounds come from muons and neutrinos generated in interactions of cosmic rays in the atmosphere. Because of their steeply falling energy spectra, little background is expected in the signal region above 1 PeV. The zenith angle distribution of atmospheric muons peaks in the downward-going direction and sharply decreases towards the horizon with a cut-off at a zenith angle θ of $\cos \theta \approx 0.15$ due to absorption in the Earth. The atmospheric neutrino distributions have a weaker zenith-angle dependence. The analysis rejects downward-going atmospheric muons by employing event reconstructions based on a track hypothesis in combination with a higher NPE selection criterion in the downward-going region. All remaining events above the combined NPE threshold are considered to be signal candidates independent of their topological properties.

Data were collected between May 2010 and May 2012, an effective livetime of 615.9 days excluding 54.2 days used for the optimization of the analysis. From May 2010 to May 2011, DOMs on 79 strings (IC79) were op-

erational (285.8 days livetime with 33.4 days excluded). This period was immediately followed by the first year data taking with the full 86-string (IC86) detector that lasted until May 2012 (330.1 days livetime with 20.8 days excluded). The IC86 configuration is shown in Fig. 1. Events are triggered when eight or more DOMs record signals in local coincidences which occur when a nearest or next-to-nearest DOM on the same string triggers within $\pm 1 \mu\text{s}$ [4].

The data are filtered at the South Pole with a condition $\text{NPE} \geq 1000$, and then sent to a northern computer farm via satellite. In order to avoid biases, we performed a blind analysis and only $\sim 10\%$ of the data were used to develop the analysis. Photon arrival times are extracted from each waveform and stored as "hits". To remove hits from coincident noise, a two-staged cleaning based on the spatial separation and the time interval between hits is applied. Data from the DeepCore strings are discarded to maintain uniformity across the detector volume. To reject downward-going atmospheric muon background, only events with at least 300 hits and $\text{NPE} \geq 3200$ are retained. To further reduce this background, the directions of the remaining events are reconstructed with a track hypothesis and a stricter NPE criterion for downward-going tracks is applied (see Fig. 2 and Eq. 1): for IC79, a log-likelihood (LLH) fit is performed [7] and an event selection based on a fit quality parameter is applied to remove events which contain muons from independent air showers. For IC86, a robust regression technique [8, 9] is utilized to remove hits that have a timing significantly different from what is expected from the bulk of the photons from a muon track. Afterwards, the direction of the particle is reconstructed with a basic algorithm that assumes a plane-wave of photons traveling along the direction of the muon, "LineFit" [5]. Both algorithms reconstruct muon tracks with a zenith angle resolution of 1° or better.

Cascade events which pass the initial hit and NPE selection criteria are considered signal events and therefore should be affected as little as possible by the event rejections just described. As they resemble point-like light sources, the reconstruction behavior of the two algorithms is indeed quite different finding nearly arbitrary zenith angles, albeit with a tendency toward upward-going and horizontal directions for the LLH fit and LineFit, respectively. Since for these directions the NPE threshold value is lower than for downward-going events (see Fig. 2 and Eq. 1), such events are retained in the final sample even if they would be rejected on account of their true direction.

The NPE threshold values for the two samples were separately optimized based on the simulations to maximize the signal [10, 11] from the cosmogenic neutrino model [6]. Figure 2 shows the event distributions for the simulations and the experimental IC79 test sample (a livetime of 33.4 days). The solid lines in Fig. 2 represent

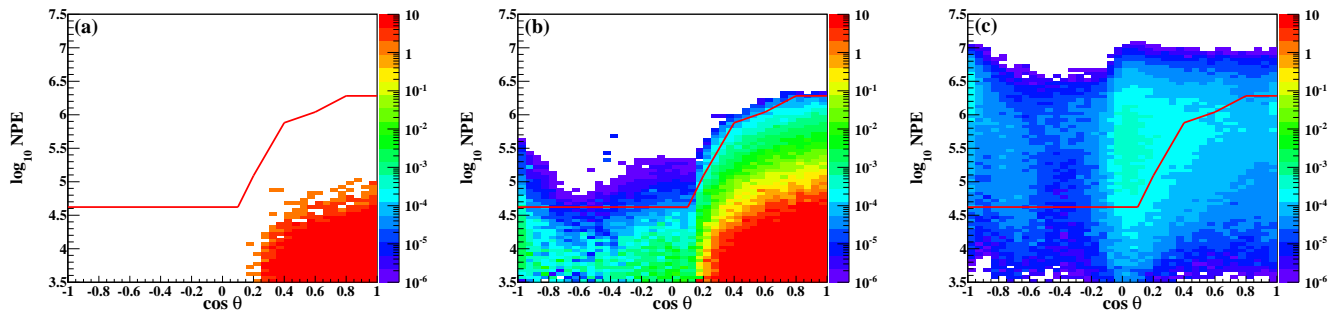


FIG. 2. Distribution of NPE and reconstructed zenith angle for (a) the IC79 experimental test sample, (b) the total background, and (c) cosmogenic signal neutrino [6]. The colors show event numbers per livetime of 33.4 days. The solid lines represent the final selection criteria for IC79.

the final selection criteria for IC79 where events above the lines constitute the final sample. The final selection criteria for the IC86 sample are:

$$\log_{10} \text{NPE} \geq \begin{cases} 4.8 & \cos \theta < 0.075 \\ 4.8 + 1.6 \sqrt{1 - \left(\frac{1.0 - \cos \theta}{0.925}\right)^2} & \cos \theta \geq 0.075. \end{cases} \quad (1)$$

The resulting neutrino effective areas, the equivalent area at the Earth's surface in which neutrinos are detected with 100% efficiency, averaged over the two-year period from May 2010 to May 2012 taking into account the different detector configurations, is shown in Fig. 3. The analysis starts to be sensitive in the energy region around 1 PeV with its sensitivity rapidly increasing with energy. The effective area is larger for ν_e than ν_μ or ν_τ below 10 PeV showing the sensitivity of the present analysis to cascade events in this energy region.

The expected numbers of background events in the final sample for the 615.9 day livetime from atmospheric muons and neutrinos from decays of pions and kaons are 0.038 ± 0.004 (stat) $^{+0.021}_{-0.038}$ (syst) and 0.012 ± 0.001 (stat) $^{+0.010}_{-0.007}$ (syst), respectively. Compared to previous analyses, the utilized atmospheric neutrino flux models [13] accommodate an improved parametrization of the primary cosmic ray spectrum and composition which accounts now for the “knee” in the cosmic ray spectrum. Adding prompt atmospheric neutrinos from decays of charmed mesons assuming the model in [14] with the improved cosmic ray spectrum modeling, the total number of background events increases to 0.082 ± 0.004 (stat) $^{+0.041}_{-0.057}$ (syst). Theoretical uncertainties in our baseline charmed-meson model [14] which uses perturbative-QCD calculations are included in the background estimation. Potential non-perturbative contributions, such as intrinsic charm in nuclei [15] or from the gluon density at small x , could lead to significantly larger cross sections and hence higher prompt neutrino fluxes. Preliminary IceCube limits on the prompt flux at 90% C.L. are a factor of 3.8 higher than the baseline model [16].

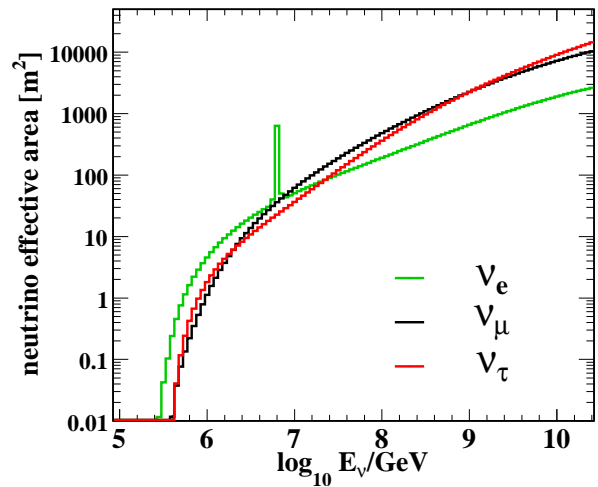


FIG. 3. The average neutrino effective area for a 4π isotropic flux, 615.9 days livetime, and the IC79 and IC86 string configurations. Exposure of the sample used in this analysis is obtained by multiplying the effective area with the livetime and 4π solid angle. The sharp-peak for $\bar{\nu}_e$ is the Glashow resonance [12].

The main systematic uncertainties on the backgrounds are from the measurement of NPE and from uncertainties in the cosmic ray flux. They are estimated by varying the associated parameters in the simulation. The two dominant sources of experimental uncertainties are the absolute DOM sensitivity and the optical properties of the ice which contribute with (+43%, -26%) and (+0%, -42%), respectively. Uncertainties in the cosmic ray flux models are dominated by the primary composition (+0%, -37%) and the flux normalization (+19%, -26%). The theoretical uncertainty in the neutrino production from charm decay [14] relative to the total background is (+13%, -16%). The systematic uncertainties are assumed to be evenly distributed in the estimated allowed range and are summed in quadrature.

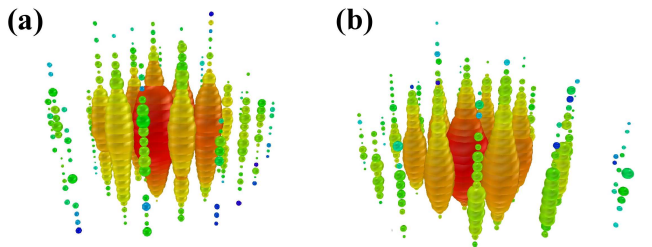


FIG. 4. The two observed events from (a) August 2011 and (b) January 2012. Each sphere represents a DOM. Colors represent the arrival times of the photons where red indicates early and blue late times. The size of the spheres is a measure for the recorded number of photo-electrons.

The atmospheric muon and neutrino background events are simulated independently. However, at higher energies, events induced by downward-going atmospheric neutrinos should also contain a significant amount of atmospheric muons produced in the same air shower as the neutrino [17]. Since these events are reconstructed as downward-going, they are more likely to be rejected with the higher NPE threshold in this region. Thus, the number of simulated atmospheric neutrino background events is likely overestimated here.

After unblinding 615.9 days of data, we observe two events that pass all the selection criteria. The hypothesis that the two events are fully explained by atmospheric background including the baseline prompt atmospheric neutrino flux [14] has a p-value of 2.9×10^{-3} (2.8σ). This value includes the uncertainties on the expected number of background events by marginalizing over a flat error distribution. While the prompt component has large theoretical uncertainties, obtaining two or more events with a probability of 10% would require a prompt flux that is about 15 times higher than the central value of our perturbative-QCD model. This contradicts our preliminary upper limit on the prompt flux [16]. Using an extreme prompt flux at the level of this upper limit which covers a potential unknown contribution from intrinsic charm [18] yields a significance of 2.3σ .

The two events are shown in Fig. 4. They are from the IC86 sample, but would have also passed the selection criteria of the IC79 sample. Their spherical photon distributions are consistent with the pattern of Cherenkov photons from particle cascades induced by neutrino interactions within the IceCube detector. There are no indications for photons from in-coming or out-going muon or tau tracks. Hence, these events are most likely induced by either CC interactions of ν_e or NC interactions of ν_e , ν_μ or ν_τ . CC interactions of ν_τ induce tau leptons with mean decay lengths of about 50 m at these energies [21]. The primary neutrino interaction and the secondary tau decay initiate separate cascades which in a fraction of

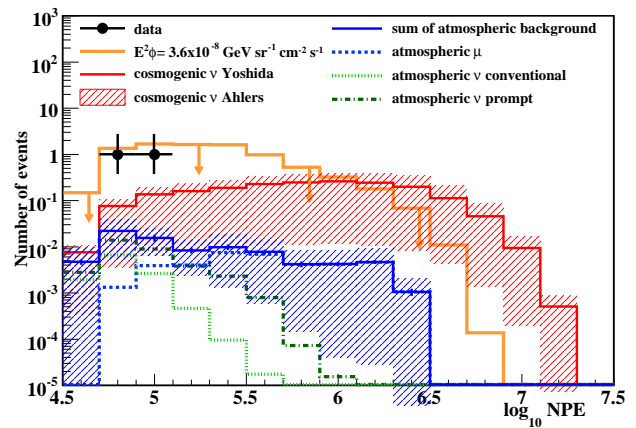


FIG. 5. NPE distributions for 615.9 days of livetime at final selection level. The black points are the experimental data. The error bars on the data show the Feldman-Cousins 68% confidence interval [19]. The solid blue line marks the sum of the atmospheric muon (dashed blue), conventional atmospheric neutrino (dotted light green) and the baseline prompt atmospheric neutrino (dot-dashed green) background. The error bars on the line and the shaded blue region are the statistical and systematic uncertainties, respectively. The red line represents the cosmogenic neutrino model [6]. The shaded region is the allowed level of the cosmogenic ν flux by Ahlers *et al.* [20]. The orange line represents an E^{-2} power-law flux up to an energy of 10^9 GeV with an all-flavor normalization of $E^2 \phi_{\nu_e + \nu_\mu + \nu_\tau} = 3.6 \times 10^{-8} \text{ GeV sr}^{-1} \text{ s}^{-1} \text{ cm}^{-2}$, which is the integral upper limit obtained in a previous search in a similar energy range [10]. The signal fluxes are summed over all neutrino flavors, assuming a flavor ratio of $\nu_e : \nu_\mu : \nu_\tau = 1 : 1 : 1$.

such events lead to an observable double-peak structure in the recorded waveforms. The two events do not show a significant indication of such a signature. Figure 5 shows the final-selection NPE distributions for the experimental data, signal models and background simulations. The two events are near the NPE threshold of the analysis and are consistent with a previous upper limit by IceCube [10] on an unbroken E^{-2} flux, while a flux corresponding to this upper limit predicts about 10 events above the NPE cut. The cosmogenic neutrino model [6] predicts an event rate of about 2 events in the corresponding livetime but at significantly higher energies.

Maximum-likelihood methods are used to reconstruct the two events. The likelihood is the product of the Poisson probabilities to observe the recorded number of photo-electrons in a given time interval and DOM for a cascade hypothesis which depends on the interaction vertex, deposited energy and direction. Here, the time of the first hit mainly determines the vertex position and the recorded NPE plays a dominant role in estimating the deposited energy. The hit information used in the reconstruction is extracted from an unfolding procedure of the waveforms. The open circles in Fig. 1 indicate the strings closest to the reconstructed vertex positions.

date (GMT)	Aug. 8, 2011	Jan. 3, 2012
NPE	7.0×10^4	9.6×10^4
number of recorded DOMs	354	312
reconstructed deposited energy (PeV)	1.04 ± 0.16	1.14 ± 0.17
reconstructed z vertex (m)	122 ± 5	25 ± 5

TABLE I. Characteristics of the two observed events. The depths of the reconstructed vertex positions “ z ” are with respect to the center of the IceCube detector at a depth of 1948 m.

The reconstructed deposited energies of the two cascades are 1.04 PeV and 1.14 PeV, respectively, with combined statistical and systematic uncertainties of $\pm 15\%$ each. The errors on the deposited energies are obtained by simulating cascade events in the vicinity of the reconstructed energies and vertices. The study is specifically performed on each event and the larger of the two event uncertainties is cited for both events. Thus, the error associated with the two events differs from that of other cascade events observed in IceCube [22]. Since there is no absolute energy standard with adequate precision at these energies, the energy scale is derived from simulations based on measured ice properties and PMT efficiencies which are assured by measurements of atmospheric muons. The main sources of systematic uncertainty on the reconstructed deposited energies are the absolute DOM sensitivity and the optical properties of the ice [23]. The effect of the latter is estimated to be $+9\%$ and -5% and is obtained by varying the scattering and absorption coefficients for the photon propagation by 10% . The reconstruction algorithm includes variations of the scattering and absorption coefficients with depth (ice layers) [24]. The effect of a possible azimuthal anisotropy of the ice parameters and a tilt of the ice layers on the reconstructed energies is estimated to be $\pm 5\%$. The reconstructed energy depends linearly on the DOM efficiency, which has a 10% systematic uncertainty. The suppression of bremsstrahlung and pair production due to the LPM effect [25] is negligible in this energy range. The properties of the two observed events are summarized in Tab. I.

The reconstructed deposited energy is the energy of the incoming neutrino if the observed cascade is the result of a CC interaction of ν_e neutrino, as in this case the total neutrino energy is deposited near the interaction vertex [26]. On the other hand, NC interactions of neutrinos of any flavor or interactions of $\bar{\nu}_e$ via the Glashow resonance at 6.3 PeV [12] with outgoing leptons induce cascades which carry only a fraction of the neutrino energy. The observed cascades are unlikely to originate from the Glashow resonance as only about 10% of these interactions will deposit 1.2 PeV or less in the detector in cascade-like signatures.

The two PeV neutrino events observed in two years of data taken with the IceCube neutrino telescope may be a first hint of an astrophysical high-energy neutrino flux. Given the yet rather moderate significance of 2.8σ with respect to the expected atmospheric background and the large uncertainties on its prompt component, a firm astrophysical interpretation requires more data in combination with analyses in other detection channels and energy ranges.

We acknowledge the support from the following agencies: U.S. National Science Foundation-Office of Polar Programs, U.S. National Science Foundation-Physics Division, University of Wisconsin Alumni Research Foundation, the Grid Laboratory Of Wisconsin (GLOW) grid infrastructure at the University of Wisconsin - Madison, the Open Science Grid (OSG) grid infrastructure; U.S. Department of Energy, and National Energy Research Scientific Computing Center, the Louisiana Optical Network Initiative (LONI) grid computing resources; Natural Sciences and Engineering Research Council of Canada, Compute Canada and Compute West High Performance Computing; Swedish Research Council, Swedish Polar Research Secretariat, Swedish National Infrastructure for Computing (SNIC), and Knut and Alice Wallenberg Foundation, Sweden; German Ministry for Education and Research (BMBF), Deutsche Forschungsgemeinschaft (DFG), Helmholtz Alliance for Astroparticle Physics (HAP), Research Department of Plasmas with Complex Interactions (Bochum), Germany; Fund for Scientific Research (FNRS-FWO), FWO Odysseus programme, Flanders Institute to encourage scientific and technological research in industry (IWT), Belgian Federal Science Policy Office (Belspo); University of Oxford, United Kingdom; Marsden Fund, New Zealand; Australian Research Council; Japan Society for Promotion of Science (JSPS); the Swiss National Science Foundation (SNSF), Switzerland.

* Physics Department, South Dakota School of Mines and Technology, Rapid City, SD 57701, USA

† Los Alamos National Laboratory, Los Alamos, NM 87545, USA

‡ Corresponding author: aya@hepburn.s.chiba-u.ac.jp (A. Ishihara)

§ also Sezione INFN, Dipartimento di Fisica, I-70126, Bari, Italy

¶ Department of Physics, Sungkyunkwan University, Suwon 440-746, Korea

** NASA Goddard Space Flight Center, Greenbelt, MD 20771, USA

- [1] A. Achterberg *et al.* (IceCube Collaboration), *Astropart.Phys.* **26**, 155 (2006).
- [2] R. Abbasi *et al.* (IceCube Collaboration), *Astropart.Phys.* **35**, 615 (2012).
- [3] R. Abbasi *et al.* (IceCube collaboration), *Nucl. Instrum.*

- Meth. **A618**, 139 (2010).
- [4] R. Abbasi *et al.* (IceCube collaboration), Nucl. Instrum. Meth. **A601**, 294 (2009).
- [5] R. Abbasi *et al.* (IceCube Collaboration), Phys. Rev. **D82**, 072003 (2010).
- [6] S. Yoshida and M. Teshima, Prog.Theor.Phys. **89**, 833 (1993), the model with the source evolution $(z_{max} + 1)^m$ with $m = 4$ extending to $z_{max} = 4.0$.
- [7] J. Ahrens *et al.*, Nucl. Instrum. Meth. **524**, 169 (2004).
- [8] P. Huber, *Robust Statistics* (Wiley, New York, 1981).
- [9] M. Wellons *et al.*, “Robust statistics in muon reconstruction,” (2013), proceedings of the 33rd International Cosmic Ray Conference (ICRC2013), to be published.
- [10] R. Abbasi *et al.* (IceCube Collaboration), Phys.Rev. **D83**, 092003 (2011).
- [11] G. Hill and K. Rawlins, Astropart. Phys. **19**, 393 (2003).
- [12] S. L. Glashow, Physical Review **118**, 316 (1960).
- [13] T. K. Gaisser, Astropart.Phys. **35**, 801 (2012).
- [14] R. Enberg, M. H. Reno, and I. Sarcevic, Phys.Rev. **D78**, 043005 (2008).
- [15] S. Brodsky *et al.*, Phys. Lett. B **93**, 451 (1980).
- [16] A. Schukraft (IceCube Collaboration), “A view of prompt atmospheric neutrinos with IceCube,” (2013), arXiv:1302.0127.
- [17] S. Schönert, T. K. Gaisser, E. Resconi, and O. Schulz, Phys. Rev. D **79**, 043009 (2009).
- [18] M. Thunman, G. Ingelman, and P. Gondolo, Astroparticle Physics **5**, 309 (1996).
- [19] G. J. Feldman and R. D. Cousins, Phys. Rev. D **57**, 3873 (1998).
- [20] M. Ahlers, L. A. Anchordoqui, M. Gonzalez-Garcia, F. Halzen, and S. Sarkar, Astropart.Phys. **34**, 106 (2010).
- [21] D. Cowen (IceCube Collaboration), J.Phys.Conf.Ser. **60**, 227 (2007).
- [22] R. Abbasi *et al.* (IceCube Collaboration), Phys. Rev. D **84**, 072001 (2011).
- [23] M. Aartsen *et al.*, Nucl. Instrum. Meth. **711**, 73 (2013).
- [24] J. Lundberg *et al.*, Nucl. Instrum. Meth. **A581**, 619 (2007).
- [25] L. Gerhardt and S. R. Klein, Phys. Rev. D **82**, 074017 (2010).
- [26] The energy reconstruction assumes that all light emission originates from an electromagnetic shower. A hadronic cascade with the same light yield as the observed events would on average have an about 10% higher energy.

Observation of High-Energy Astrophysical Neutrinos in Three Years of IceCube Data

M. G. Aartsen,² M. Ackermann,⁴⁵ J. Adams,¹⁵ J. A. Aguilar,²³ M. Ahlers,²⁸ M. Ahrens,³⁶ D. Altmann,²² T. Anderson,⁴² C. Argüelles,²⁸ T. C. Arlen,⁴² J. Auffenberg,¹ X. Bai,³⁴ S. W. Barwick,²⁵ V. Baum,²⁹ J. J. Beatty,^{17,18} J. Becker Tjus,¹⁰ K.-H. Becker,⁴⁴ S. BenZvi,²⁸ P. Berghaus,⁴⁵ D. Berley,¹⁶ E. Bernardini,⁴⁵ A. Bernhard,³¹ D. Z. Besson,²⁶ G. Binder,^{8,7} D. Bindig,⁴⁴ M. Bissok,¹ E. Blaufuss,¹⁶ J. Blumenthal,¹ D. J. Boersma,⁴³ C. Boehm,³⁶ D. Bose,³⁸ S. Böser,¹¹ O. Botner,⁴³ L. Brayer,¹³ H.-P. Bretz,⁴⁵ A. M. Brown,¹⁵ J. Casey,⁵ M. Casier,¹³ D. Chirkin,²⁸ A. Christov,²³ B. Christy,¹⁶ K. Clark,³⁹ L. Classen,²² F. Clevermann,²⁰ S. Coenders,³¹ D. F. Cowen,^{42,41} A. H. Cruz Silva,⁴⁵ M. Danninger,³⁶ J. Daughhetee,⁵ J. C. Davis,¹⁷ M. Day,²⁸ J. P. A. M. de André,⁴² C. De Clercq,¹³ S. De Ridder,²⁴ P. Desiati,²⁸ K. D. de Vries,¹³ M. de With,⁹ T. DeYoung,⁴² J. C. Díaz-Vélez,²⁸ M. Dunkman,⁴² R. Eagan,⁴² B. Eberhardt,²⁹ B. Eichmann,¹⁰ J. Eisch,²⁸ S. Euler,⁴³ P. A. Evenson,³² O. Fadiran,²⁸ A. R. Fazely,⁶ A. Fedynitch,¹⁰ J. Feintzeig,^{28,*} J. Felde,¹⁶ T. Feusels,²⁴ K. Filimonov,⁷ C. Finley,³⁶ T. Fischer-Wasels,⁴⁴ S. Flis,³⁶ A. Franckowiak,¹¹ K. Frantzen,²⁰ T. Fuchs,²⁰ T. K. Gaisser,³² J. Gallagher,²⁷ L. Gerhardt,^{8,7} D. Gier,¹ L. Gladstone,²⁸ T. Glüsenkamp,⁴⁵ A. Goldschmidt,⁸ G. Golup,¹³ J. G. Gonzalez,³² J. A. Goodman,¹⁶ D. Góra,⁴⁵ D. T. Grandmont,²¹ D. Grant,²¹ P. Gresskov,¹ J. C. Groh,⁴² A. Groß,³¹ C. Ha,^{8,7} C. Haack,¹ A. Haj Ismail,²⁴ P. Hallen,¹ A. Hallgren,⁴³ F. Halzen,²⁸ K. Hanson,¹² D. Hebecker,¹¹ D. Heereman,¹² D. Heinen,¹ K. Helbing,⁴⁴ R. Hellauer,¹⁶ D. Hellwig,¹ S. Hickford,¹⁵ G. C. Hill,² K. D. Hoffman,¹⁶ R. Hoffmann,⁴⁴ A. Homeier,¹¹ K. Hoshina,^{28,†} F. Huang,⁴² W. Huelsnitz,¹⁶ P. O. Hulth,³⁶ K. Hultqvist,³⁶ S. Hussain,³² A. Ishihara,¹⁴ E. Jacobi,⁴⁵ J. Jacobsen,²⁸ K. Jagielski,¹ G. S. Japaridze,⁴ K. Jero,²⁸ O. Jlelati,²⁴ M. Jurkovic,³¹ B. Kaminsky,⁴⁵ A. Kappes,²² T. Karg,⁴⁵ A. Karle,²⁸ M. Kauer,²⁸ J. L. Kelley,²⁸ A. Kheirandish,²⁸ J. Kiryluk,³⁷ J. Kläs,⁴⁴ S. R. Klein,^{8,7} J.-H. Köhne,²⁰ G. Kohlen,³⁰ H. Kolanoski,⁹ A. Koob,¹ L. Köpke,²⁹ C. Kopper,^{28,*} S. Kopper,⁴⁴ D. J. Koskinen,¹⁹ M. Kowalski,¹¹ A. Kriesten,¹ K. Krings,¹ G. Kroll,²⁹ J. Kunnen,¹³ N. Kurahashi,²⁸ T. Kuwabara,³² M. Labare,²⁴ D. T. Larsen,²⁸ M. J. Larson,¹⁹ M. Lesiak-Bzdak,³⁷ M. Leuermann,¹ J. Leute,³¹ J. Lünemann,²⁹ O. Macías,¹⁵ J. Madsen,³⁵ G. Maggi,¹³ R. Maruyama,²⁸ K. Mase,¹⁴ H. S. Matis,⁸ F. McNally,²⁸ K. Meagher,¹⁶ A. Meli,²⁴ T. Meures,¹² S. Miarecki,^{8,7} E. Middell,⁴⁵ E. Middlemas,²⁸ N. Milke,²⁰ J. Miller,¹³ L. Mohrmann,⁴⁵ T. Montaruli,²³ R. Morse,²⁸ R. Nahnauer,⁴⁵ U. Naumann,⁴⁴ H. Niederhausen,³⁷ S. C. Nowicki,²¹ D. R. Nygren,⁸ A. Obertacke,⁴⁴ S. Odrowski,²¹ A. Olivas,¹⁶ A. Omairat,⁴⁴ A. O'Murchadha,¹² T. Palczewski,⁴⁰ L. Paul,¹ Ö. Penek,¹ J. A. Pepper,⁴⁰ C. Pérez de los Heros,⁴³ C. Pfendner,¹⁷ D. Pieloth,²⁰ E. Pinat,¹² J. Posselt,⁴⁴ P. B. Price,⁷ G. T. Przybylski,⁸ J. Pütz,¹ M. Quinlan,⁴² L. Rädcl,¹ M. Rameez,²³ K. Rawlins,³ P. Redl,¹⁶ I. Rees,²⁸ R. Reimann,¹ E. Resconi,³¹ W. Rhode,²⁰ M. Richman,¹⁶ B. Riedel,²⁸ S. Robertson,² J. P. Rodrigues,²⁸ M. Rongen,¹ C. Rott,³⁸ T. Ruhe,²⁰ B. Ruzybayev,³² D. Ryckbosch,²⁴ S. M. Saba,¹⁰ H.-G. Sander,²⁹ M. Santander,²⁸ S. Sarkar,^{19,33} K. Schatto,²⁹ F. Scheriau,²⁰ T. Schmidt,¹⁶ M. Schmitz,²⁰ S. Schoenen,¹ S. Schöneberg,¹⁰ A. Schönwald,⁴⁵ A. Schukraft,¹ L. Schulte,¹¹ O. Schulz,³¹ D. Seckel,³² Y. Sestayo,³¹ S. Seunarine,³⁵ R. Shanidze,⁴⁵ C. Sheremata,²¹ M. W. E. Smith,⁴² D. Soldin,⁴⁴ G. M. Spiczak,³⁵ C. Spiering,⁴⁵ M. Stamatikos,^{17,‡} T. Stanev,³² N. A. Stanisha,⁴² A. Stasik,¹¹ T. Stezelberger,⁸ R. G. Stokstad,⁸ A. Stöbl,⁴⁵ E. A. Strahler,¹³ R. Ström,⁴³ N. L. Strotjohann,¹¹ G. W. Sullivan,¹⁶ H. Taavola,⁴³ I. Taboada,⁵ A. Tamburro,³² A. Tepe,⁴⁴ S. Ter-Antonyan,⁶ A. Terliuk,⁴⁵ G. Tešić,⁴² S. Tilav,³² P. A. Toale,⁴⁰ M. N. Tobin,²⁸ D. Tosi,²⁸ M. Tselengidou,²² E. Unger,¹⁰ M. Usner,¹¹ S. Vallocorsa,²³ N. van Eijndhoven,¹³ J. Vandenbroucke,²⁸ J. van Santen,²⁸ M. Vehring,¹ M. Voge,¹¹ M. Vraeghe,²⁴ C. Walck,³⁶ M. Wallraff,¹ Ch. Weaver,²⁸ M. Wellons,²⁸ C. Wendt,²⁸ S. Westerhoff,²⁸ B. J. Whelan,² N. Whitehorn,^{28,7,*} C. Wichary,¹ K. Wiebe,²⁹ C. H. Wiebusch,¹ D. R. Williams,⁴⁰ H. Wissing,¹⁶ M. Wolf,³⁶ T. R. Wood,²¹ K. Woschnagg,⁷ D. L. Xu,⁴⁰ X. W. Xu,⁶ J. P. Yanez,⁴⁵ G. Yodh,²⁵ S. Yoshida,¹⁴ P. Zarzhitsky,⁴⁰ J. Ziemann,²⁰ S. Zierke,¹ and M. Zoll³⁶

(IceCube Collaboration)

¹*III. Physikalisches Institut, RWTH Aachen University, D-52056 Aachen, Germany*

²*School of Chemistry & Physics, University of Adelaide, Adelaide SA, 5005 Australia*

³*Dept. of Physics and Astronomy, University of Alaska Anchorage, 3211 Providence Dr., Anchorage, AK 99508, USA*

⁴*CTSPS, Clark-Atlanta University, Atlanta, GA 30314, USA*

⁵*School of Physics and Center for Relativistic Astrophysics, Georgia Institute of Technology, Atlanta, GA 30332, USA*

⁶*Dept. of Physics, Southern University, Baton Rouge, LA 70813, USA*

⁷*Dept. of Physics, University of California, Berkeley, CA 94720, USA*

⁸*Lawrence Berkeley National Laboratory, Berkeley, CA 94720, USA*

- ⁹*Institut für Physik, Humboldt-Universität zu Berlin, D-12489 Berlin, Germany*
- ¹⁰*Fakultät für Physik & Astronomie, Ruhr-Universität Bochum, D-44780 Bochum, Germany*
- ¹¹*Physikalisches Institut, Universität Bonn, Nussallee 12, D-53115 Bonn, Germany*
- ¹²*Université Libre de Bruxelles, Science Faculty CP230, B-1050 Brussels, Belgium*
- ¹³*Vrije Universiteit Brussel, Dienst ELEM, B-1050 Brussels, Belgium*
- ¹⁴*Dept. of Physics, Chiba University, Chiba 263-8522, Japan*
- ¹⁵*Dept. of Physics and Astronomy, University of Canterbury, Private Bag 4800, Christchurch, New Zealand*
- ¹⁶*Dept. of Physics, University of Maryland, College Park, MD 20742, USA*
- ¹⁷*Dept. of Physics and Center for Cosmology and Astro-Particle Physics, Ohio State University, Columbus, OH 43210, USA*
- ¹⁸*Dept. of Astronomy, Ohio State University, Columbus, OH 43210, USA*
- ¹⁹*Niels Bohr Institute, University of Copenhagen, DK-2100 Copenhagen, Denmark*
- ²⁰*Dept. of Physics, TU Dortmund University, D-44221 Dortmund, Germany*
- ²¹*Dept. of Physics, University of Alberta, Edmonton, Alberta, Canada T6G 2E1*
- ²²*Erlangen Centre for Astroparticle Physics, Friedrich-Alexander-Universität Erlangen-Nürnberg, D-91058 Erlangen, Germany*
- ²³*Département de physique nucléaire et corpusculaire, Université de Genève, CH-1211 Genève, Switzerland*
- ²⁴*Dept. of Physics and Astronomy, University of Gent, B-9000 Gent, Belgium*
- ²⁵*Dept. of Physics and Astronomy, University of California, Irvine, CA 92697, USA*
- ²⁶*Dept. of Physics and Astronomy, University of Kansas, Lawrence, KS 66045, USA*
- ²⁷*Dept. of Astronomy, University of Wisconsin, Madison, WI 53706, USA*
- ²⁸*Dept. of Physics and Wisconsin IceCube Particle Astrophysics Center, University of Wisconsin, Madison, WI 53706, USA*
- ²⁹*Institute of Physics, University of Mainz, Staudinger Weg 7, D-55099 Mainz, Germany*
- ³⁰*Université de Mons, 7000 Mons, Belgium*
- ³¹*T.U. Munich, D-85748 Garching, Germany*
- ³²*Bartol Research Institute and Dept. of Physics and Astronomy, University of Delaware, Newark, DE 19716, USA*
- ³³*Dept. of Physics, University of Oxford, 1 Keble Road, Oxford OX1 3NP, UK*
- ³⁴*Dept. of Physics, South Dakota School of Mines and Technology, Rapid City, SD 57701, USA*
- ³⁵*Dept. of Physics, University of Wisconsin, River Falls, WI 54022, USA*
- ³⁶*Oskar Klein Centre and Dept. of Physics, Stockholm University, SE-10691 Stockholm, Sweden*
- ³⁷*Dept. of Physics and Astronomy, Stony Brook University, Stony Brook, NY 11794-3800, USA*
- ³⁸*Dept. of Physics, Sungkyunkwan University, Suwon 440-746, Korea*
- ³⁹*Dept. of Physics, University of Toronto, Toronto, Ontario, Canada, M5S 1A7*
- ⁴⁰*Dept. of Physics and Astronomy, University of Alabama, Tuscaloosa, AL 35487, USA*
- ⁴¹*Dept. of Astronomy and Astrophysics, Pennsylvania State University, University Park, PA 16802, USA*
- ⁴²*Dept. of Physics, Pennsylvania State University, University Park, PA 16802, USA*
- ⁴³*Dept. of Physics and Astronomy, Uppsala University, Box 516, S-75120 Uppsala, Sweden*
- ⁴⁴*Dept. of Physics, University of Wuppertal, D-42119 Wuppertal, Germany*
- ⁴⁵*DESY, D-15735 Zeuthen, Germany*

A search for high-energy neutrinos interacting within the IceCube detector between 2010 and 2012 provided the first evidence for a high-energy neutrino flux of extraterrestrial origin. Results from an analysis using the same methods with a third year (2012-2013) of data from the complete IceCube detector are consistent with the previously reported astrophysical flux in the 100 TeV - PeV range at the level of 10^{-8} GeV cm⁻² s⁻¹ sr⁻¹ per flavor and reject a purely atmospheric explanation for the combined 3-year data at 5.7σ . The data are consistent with expectations for equal fluxes of all three neutrino flavors and with isotropic arrival directions, suggesting either numerous or spatially extended sources. The three-year data set, with a livetime of 988 days, contains a total of 37 neutrino candidate events with deposited energies ranging from 30 to 2000 TeV. The 2000 TeV event is the highest-energy neutrino interaction ever observed.

High energy neutrinos are expected to be produced in astrophysical objects by the decays of charged pions made in cosmic ray interactions with radiation or gas [1–4]. As these pions decay, they produce neutrinos with typical energies of 5% those of the cosmic ray nucleons [5, 6]. These neutrinos can travel long distances undisturbed by either the absorption experienced by high-energy photons or the magnetic deflection experienced by charged particles, making them a unique tracer of cosmic

ray acceleration.

Observations since 2008 using the Antarctic gigaton IceCube detector [7] while it was under construction provided several indications of such neutrinos in a variety of channels [8–10]. Two years of data from the full detector, from May 2010 - May 2012, then provided the first strong evidence for the detection of these astrophysical neutrinos [11] using an all-flavor all-direction sample of neutrinos interacting within the detector volume. This

analysis focused on neutrinos above 100 TeV, at which the expected atmospheric neutrino background falls to the level of one event per year, allowing any harder astrophysical flux to be seen clearly. Here, following the same techniques, we add a third year of data supporting this result and begin to probe the properties of the observed astrophysical neutrino flux.

Neutrinos are detected in IceCube by observing the Cherenkov light produced in ice by charged particles created when neutrinos interact. These particles generally travel distances too small to be resolved individually and the particle shower is observed only in aggregate. In ν_μ charged-current (CC) interactions, however, as well as a minority of ν_τ CC, a high-energy muon is produced that leaves a visible track (unless produced on the detector boundary heading outward). Although deposited energy resolution is similar for all events, angular resolution for events containing visible muon tracks is much better ($\lesssim 1^\circ$, 50% CL) than for those that do not ($\sim 15^\circ$, 50% CL) [12]. For equal neutrino fluxes of all flavors (1:1:1), ν_μ CC events make up only 20% of interactions [13].

Backgrounds to astrophysical neutrino detection arise entirely from cosmic ray air showers. Muons produced by π and K decays above IceCube enter the detector at 2.8 kHz. Neutrinos produced in the same interactions [14–17] enter IceCube from above and below, and are seen at a much lower rate due to the low neutrino interaction cross-section. Because π and K mesons decay overwhelmingly to muons rather than electrons, these neutrinos are predominantly ν_μ and usually have track-type topologies in the detector [13]. As the parent meson’s energy rises, its lifetime increases, making it increasingly likely to interact before decaying. Both the atmospheric muon and neutrino fluxes thus become suppressed at high energy, with a spectrum one power steeper than the primary cosmic rays that produced them [18]. At energies above ~ 100 TeV, an analogous flux of muons and neutrinos from the decay of charmed mesons is expected to dominate, as the shorter lifetime of these particles allows this flux to avoid suppression from interaction before decay [19–25]. This flux has not yet been observed, however, and both its overall rate and cross-over energy with the π/K flux are at present poorly constrained [26]. As before [11], we estimate all atmospheric neutrino background rates using measurements of the northern-hemisphere ν_μ spectrum [9].

Event selection identifies neutrino interactions in IceCube by rejecting those events with Cherenkov-radiating particles, principally cosmic ray muons, entering from outside the detector. As before, we used a simple anti-coincidence muon veto in the outer layers of the detector [11], requiring that fewer than 3 of the first 250 detected photoelectrons (PE) be on the detector boundary. To ensure sufficient numbers of photons to reliably trigger this veto, we additionally required at least 6000 PE overall, corresponding to deposited energies of approximately 30

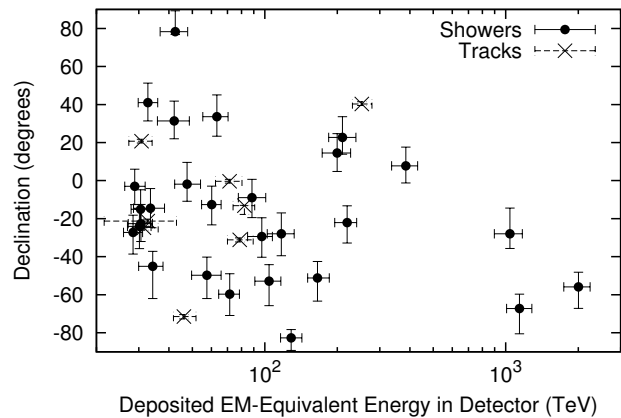


FIG. 1. Arrival angles and deposited energies of the events. Cosmic ray muon background would appear as low-energy track events in the southern sky (bottom). Atmospheric neutrino backgrounds would appear primarily in the northern sky (top), also at low energies and predominantly as tracks. The attenuation of high energy neutrinos in the Earth is visible in the top right of the figure. One event, a pair of coincident unrelated cosmic ray muons, is excluded from this plot. A tabular version of these data, including additional information such as event times, can be found in the online supplement [29].

TeV. This rejects all but one part in 10^5 of the cosmic ray muon background above 6000 PE while providing a direction and topology-neutral neutrino sample [11]. We use a data-driven method to estimate this background by using one region of IceCube to tag muons and then measuring their detection rate in a separate layer of PMTs equivalent to our veto; this predicts a total muon background in three years of 8.4 ± 4.2 events. Rejection of events containing entering muons also significantly reduces downgoing atmospheric neutrinos (the southern hemisphere) by detecting and vetoing muons produced in the neutrinos’ parent air showers [27, 28]. This southern-hemisphere suppression is a distinctive and generic feature of any neutrinos originating in cosmic ray interactions in the atmosphere.

In the full 988-day sample, we detected 37 events (Fig. 1) with these characteristics relative to an expected background of 8.4 ± 4.2 cosmic ray muon events and $6.6^{+5.9}_{-1.6}$ atmospheric neutrinos. Nine were observed in the third year. One of these (event 32) was produced by a coincident pair of background muons from unrelated air showers. This event cannot be reconstructed with a single direction and energy and is excluded from the remainder of this article where these quantities are required. This event, like event 28, had sub-threshold early hits in the IceTop surface array and our veto region, and is likely part of the expected muon background. Three additional downgoing track events are ambiguous; the remainder are uniformly distributed through the detector and appear to be neutrino interactions.

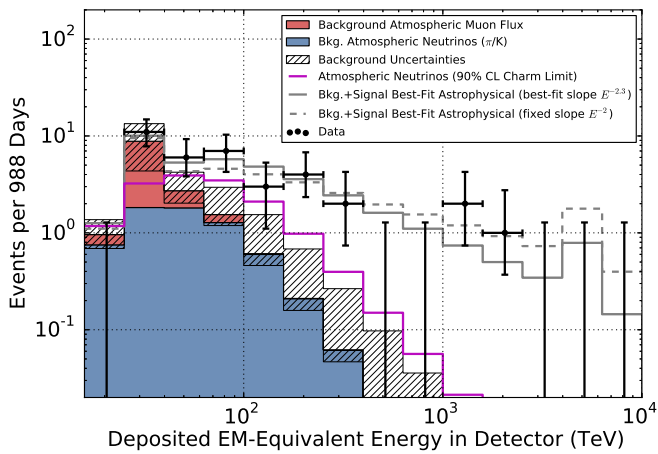


FIG. 2. Deposited energies of observed events with predictions. The hashed region shows uncertainties on the sum of all backgrounds. Muons (red) are computed from simulation to overcome statistical limitations in our background measurement and scaled to match the total measured background rate. Atmospheric neutrinos and uncertainties thereon are derived from previous measurements of both the π/K and charm components of the atmospheric ν_μ spectrum [9]. A gap larger than the one between 400 and 1000 TeV appears in 43% of realizations of the best-fit continuous spectrum.

A purely atmospheric explanation for these events is strongly disfavored by their properties. The observed deposited energy distribution extends to much higher energies (above 2 PeV, Fig. 2) than expected from the π/K atmospheric neutrino background, which has been measured up to 100 TeV [9]. While a harder spectrum is expected from atmospheric neutrinos produced in charmed meson decay, this possibility is constrained by the observed angular distribution. Although such neutrinos are produced isotropically, approximately half [27, 28] of those in the southern hemisphere are produced with muons of high enough energy to reach IceCube and trigger our muon veto. This results in a southern hemisphere charm rate $\sim 50\%$ smaller than the northern hemisphere rate, with larger ratios near the poles. Our data show no evidence of such a suppression, which is expected at some level from any atmospheric source of neutrinos (Fig. 3).

As in [11], we quantify these arguments using a likelihood fit in arrival angle and deposited energy to a combination of background muons, atmospheric neutrinos from π/K decay, atmospheric neutrinos from charmed meson decay, and an isotropic 1:1:1 astrophysical E^{-2} test flux, as expected from charged pion decays in cosmic ray accelerators [30–33]. The fit included all events with $60 \text{ TeV} < E_{dep} < 3 \text{ PeV}$. The expected muon background in this range is below 1 event in the 3-year sample, minimizing imprecisions in modeling the muon background and threshold region. The normalizations of all background and signal neutrino fluxes were left free in the fit, without reference to uncertainties from [9],

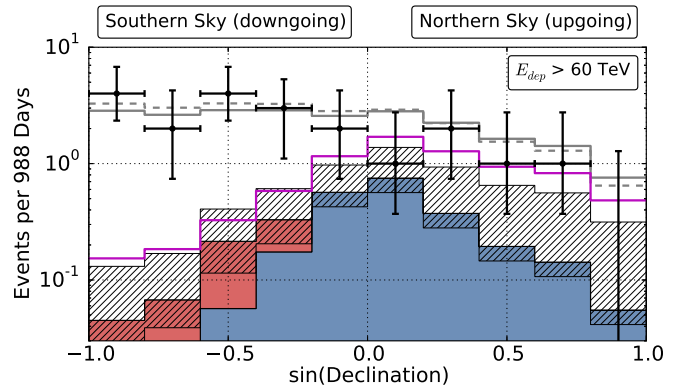


FIG. 3. Arrival angles of events with $E_{dep} > 60 \text{ TeV}$, as used in our fit and above the majority of the cosmic ray muon background. The increasing opacity of the Earth to high energy neutrinos is visible at the right of the plot. Vetoing atmospheric neutrinos by muons from their parent air showers depresses the atmospheric neutrino background on the left. The data are described well by the expected backgrounds and a hard astrophysical isotropic neutrino flux (gray lines). Colors as in Fig. 2. Variations of this figure with other energy thresholds are in the online supplement [29].

for maximal robustness. The penetrating muon background was constrained with a Gaussian prior reflecting our veto efficiency measurement. We obtain a best-fit per-flavor astrophysical flux ($\nu + \bar{\nu}$) in this energy range of $E^2 \phi(E) = 0.95 \pm 0.3 \times 10^{-8} \text{ GeV cm}^{-2} \text{ s}^{-1} \text{ sr}^{-1}$ and background normalizations within the expected ranges. Quoted errors are 1σ uncertainties from a profile likelihood scan. This model describes the data well, with both the energy spectrum (Fig. 2) and arrival directions (Fig. 3) of the events consistent with expectations for an origin in a hard isotropic 1:1:1 neutrino flux. The best-fit atmospheric-only alternative model, however, would require a charm normalization 3.6 times higher than our current 90% CL upper limit from the northern hemisphere ν_μ spectrum [9]. Even this extreme scenario is disfavored by the energy and angular distributions of the events at 5.7σ using a likelihood ratio test.

Fig. 4 shows a fit using a more general model in which the astrophysical flux is parametrized as a piecewise function of energy rather than a continuous unbroken E^{-2} power law. As before, we assume a 1:1:1 flavor ratio and isotropy. While the reconstructed spectrum is compatible with our earlier E^{-2} ansatz, an unbroken E^{-2} flux at our best-fit level predicts 3.1 additional events above 2 PeV (a higher energy search [10] also saw none). This may indicate, along with the slight excess in lower energy bins, either a softer spectrum or a cutoff at high energies. Correlated systematic uncertainties in the first few points in the reconstructed spectrum (Fig. 4) arise from the poorly constrained level of the charm atmospheric neutrino background. The presence of this softer ($E^{-2.7}$) component would decrease the non-atmospheric

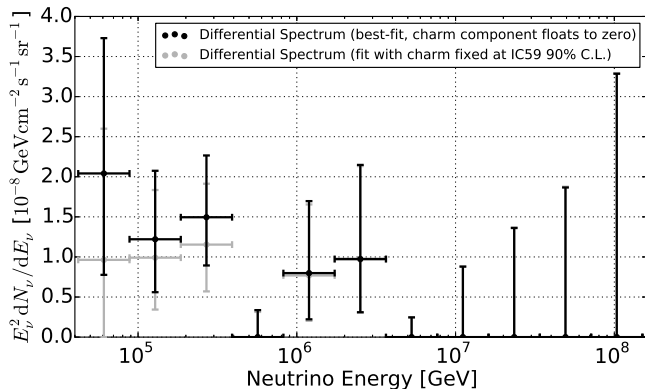


FIG. 4. Extraterrestrial neutrino flux ($\nu + \bar{\nu}$) as a function of energy. Vertical error bars indicate the $2\Delta\mathcal{L} = \pm 1$ contours of the flux in each energy bin, holding all other values, including background normalizations, fixed. These provide approximate 68% confidence ranges. An increase in the charm atmospheric background to the level of the 90% CL limit from the northern hemisphere ν_μ spectrum [9] would reduce the inferred astrophysical flux at low energies to the level shown for comparison in light gray. The best-fit power law is $E^2\phi(E) = 1.5 \times 10^{-8} (E/100\text{TeV})^{-0.3} \text{GeVcm}^{-2}\text{s}^{-1}\text{sr}^{-1}$.

excess at low energies, hardening the spectrum of the remaining data. The corresponding range of best fit astrophysical slopes within our current 90% confidence band on the charm flux [9] is -2.0 to -2.3 . As the best-fit charm flux is zero, the best-fit astrophysical spectrum is on the lower boundary of this interval at -2.3 (solid line, Figs. 2, 3) with a total statistical and systematic uncertainty of ± 0.3 .

To identify any bright neutrino sources in the data, we employed the same maximum-likelihood clustering search as before [11], as well as searched for directional correlations with TeV gamma-ray sources. For all tests, the test statistic (TS) is defined as the logarithm of the ratio between the best-fit likelihood including a point source component and the likelihood for the null hypothesis, an isotropic distribution [34]. We determined the significance of any excess by comparing to maps scrambled in right ascension, in which our polar detector has uniform exposure.

As in [11], the clustering analysis was run twice, first with the entire event sample, after removing the two events (28 and 32) with strong evidence of a cosmic-ray origin, and second with only the 28 shower events. This controls for bias in the likelihood fit toward the positions of single well-resolved muon tracks. We also conducted an additional test in which we marginalize the likelihood over a uniform prior on the position of the hypothetical point source. This reduces the bias introduced by muons, allowing track and shower events to be used together, and improves sensitivity to multiple sources by considering the entire sky rather than the single best point.

Three tests were performed to search for neutrinos cor-

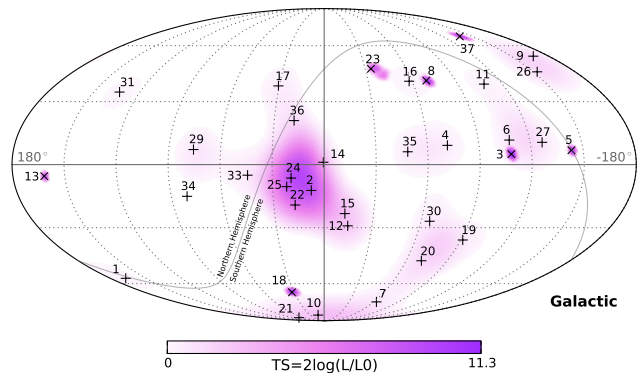


FIG. 5. Arrival directions of the events in galactic coordinates. Shower-like events (median angular resolution $\sim 15^\circ$) are marked with + and those containing muon tracks ($\lesssim 1^\circ$) with x. Approximately 40% of the events (mostly tracks [13]) are expected to originate from atmospheric backgrounds. Event IDs match those in the catalog in the online supplement [29] and are time ordered. The grey line denotes the equatorial plane. Colors show the test statistic (TS) for the point source clustering test at each location. No significant clustering was observed.

related with known gamma-ray sources, also using track and shower events together. The first two searched for clustering along the galactic plane, with a fixed width of $\pm 2.5^\circ$, based on TeV gamma-ray measurements [35], and with a free width of between $\pm 2.5^\circ$ and $\pm 30^\circ$. The last searched for correlation between neutrino events and a pre-defined catalog of potential point sources (a combination of the usual IceCube [36] and ANTARES [37] lists; see online supplement [29]). For the catalog search, the TS value was evaluated at each source location, and the post-trials significance calculated by comparing the highest observed value in each hemisphere to results from performing the analysis on scrambled datasets.

No hypothesis test yielded statistically significant evidence of clustering or correlations. For the all-sky clustering test (Fig. 5), scrambled datasets produced locations with equal or greater TS 84% and 7.2% of the time for all events and for shower-like events only. As in the two-year data set, the strongest clustering was near the galactic center. Other neutrino observations of this location give no evidence for a source [38], however, and no new events were strongly correlated with this region. When using the marginalized likelihood, a test statistic greater than or equal to the observed value was found in 28% of scrambled datasets. The source list yielded p-values for the northern and southern hemispheres of 28% and 8%, respectively. Correlation with the galactic plane was also not significant: when letting the width float freely, the best fit was $\pm 7.5^\circ$ with a post-trials chance probability of 2.8%, while a fixed width of $\pm 2.5^\circ$ returned a p-value of 24%. A repeat of the time clustering search from [11]

also found no evidence for structure.

With or without a possible galactic contribution [39, 40], the high galactic latitudes of many of the highest-energy events (Fig. 5) suggest at least some extragalactic component. Exception may be made for local large diffuse sources (e.g. the Fermi bubbles [41] or the galactic halo [42, 43]), but these models typically can explain at most a fraction of the data. If our data arise from an extragalactic flux produced by many isotropically distributed point sources, we can compare our all-sky flux with existing point-source limits. By exploiting the additional effective volume provided by use of uncontained ν_μ events, previous point-source studies would have been sensitive to a northern sky point source producing more than 1-10% of our best-fit flux, depending on declination and energy spectrum [44]. The lack of any evidence for such sources from these studies, as well as the wide distribution of our events, thus lends support to an interpretation in terms of many individually dim sources. Some contribution from a few comparatively bright sources cannot be ruled out, however, especially in the southern hemisphere, where the sensitivity of Ice-Cube to point sources in uncontained ν_μ is reduced by the large muon background and small target mass above the detector.

The neutrino spectrum (Fig. 4) can also be used to constrain source properties. In almost all candidate sources [45–69], neutrinos would be produced by the interaction of cosmic rays with either radiation or gas. Interactions with radiation ($p\gamma$) typically produce a peaked spectrum, reflecting the energy spectrum of the photons; those with gas (pp) produce a smooth power law [5, 6]. While $p\gamma$ models satisfactorily explain some aspects of the data such as the possible drop-off at high energies, many involve a central plateau smaller than our observed energy range, placing them in weak tension with the data. As an example, the $p\gamma$ AGN spectrum in [45] peaks at several PeV with much lower predictions at 100 TeV; thus, while able to explain the highest energy events, it fits poorly at lower energies and is disfavored as the sole source at the 2σ level with respect to our simple E^{-2} test flux. Gamma-ray burst $p\gamma$ models such as [58, 59] have energy ranges better aligned with our data, with central plateaus from around 100 TeV to a few PeV, although existing limits from searches for correlations with observed GRBs are more than an order of magnitude below the observed flux [70]. Cosmic ray interactions with gas, such as predicted around supernova remnants in our and other galaxies, particularly those with high star-forming rates, produce smooth spectra with slopes reflecting post-diffusion cosmic rays (e.g. $E^{-2.2}$ in [66]) and seem to describe the data well. Large uncertainties on both the measured neutrino spectrum and all models prevent any conclusions, however.

The best-fit flux level in our central energy range (10^{-8} GeV cm $^{-2}$ s $^{-1}$ sr $^{-1}$ per flavor) is similar to the

Waxman-Bahcall bound [71], the aggregate neutrino flux from charged pion decay in all extragalactic cosmic ray accelerators if they are optically thin. This bound is derived from the cosmic ray spectrum above 10^{18} eV (1000 PeV). Our neutrinos, however, are likely associated with protons at much lower energies, on the order of 1 to 10 PeV [5, 6], at which the bound may be quite different [72]. Along with large uncertainties in the neutrino spectrum (Fig. 4), this makes correspondence with the Waxman-Bahcall bound, or 10^{18} eV cosmic ray sources, unclear.

Further observations with the present or upgraded Ice-Cube detector and the planned KM3NeT [73] telescope are required to answer many questions about the sources of this astrophysical flux [74]. Gamma-ray, optical, and X-ray observations of the directions of individual high-energy neutrinos, which point directly to their origins, may also be able to identify these sources even for those with neutrino luminosities too low for identification from neutrino measurements alone.

We acknowledge support from the following agencies: U.S. National Science Foundation-Office of Polar Programs, U.S. National Science Foundation-Physics Division, University of Wisconsin Alumni Research Foundation, the Grid Laboratory Of Wisconsin (GLOW) grid infrastructure at the University of Wisconsin - Madison, the Open Science Grid (OSG) grid infrastructure; U.S. Department of Energy, and National Energy Research Scientific Computing Center, the Louisiana Optical Network Initiative (LONI) grid computing resources; Natural Sciences and Engineering Research Council of Canada, WestGrid and Compute/Calcul Canada; Swedish Research Council, Swedish Polar Research Secretariat, Swedish National Infrastructure for Computing (SNIC), and Knut and Alice Wallenberg Foundation, Sweden; German Ministry for Education and Research (BMBF), Deutsche Forschungsgemeinschaft (DFG), Helmholtz Alliance for Astroparticle Physics (HAP), Research Department of Plasmas with Complex Interactions (Bochum), Germany; Fund for Scientific Research (FNRS-FWO), FWO Odysseus programme, Flanders Institute to encourage scientific and technological research in industry (IWT), Belgian Federal Science Policy Office (Belspo); University of Oxford, United Kingdom; Marsden Fund, New Zealand; Australian Research Council; Japan Society for Promotion of Science (JSPS); the Swiss National Science Foundation (SNSF), Switzerland; National Research Foundation of Korea (NRF); Danish National Research Foundation, Denmark (DNRF). Some of the results in this paper have been derived using the HEALPix [75] package. Thanks to R. Laha, J. Beacom, K. Murase, S. Razzaque, and N. Harrington for helpful discussions.

-
- * Authors (Feintzeig, Kopper, Whitehorn) to whom correspondence should be addressed
- † Earthquake Research Institute, University of Tokyo, Bunkyo, Tokyo 113-0032, Japan
- ‡ NASA Goddard Space Flight Center, Greenbelt, MD 20771, USA
- [1] S. H. Margolis, D. N. Schramm, and R. Silberberg, *Astrophys. J.* **221**, 990 (1978).
- [2] F. W. Stecker, *Astrophys. J.* **228**, 919 (1979).
- [3] P. L. Biermann, in *Cosmic Gamma Rays and Cosmic Neutrinos*, edited by M. M. Shapiro and J. P. Wefel (1989) pp. 21–37.
- [4] W. Michalak, J. Wdowczyk, and A. W. Wolfendale, *Journal of Physics G Nuclear Physics* **16**, 1917 (1990).
- [5] A. Mücke, R. Engel, J. P. Rachen, R. J. Protheroe, and T. Stanev, *Computer Physics Communications* **124**, 290 (2000), astro-ph/9903478.
- [6] S. Kelner, F. Aharonian, and V. Bugayov, *Phys. Rev. D* **74**, 034018 (2006), arXiv:astro-ph/0606058.
- [7] R. Abbasi *et al.* (IceCube Collaboration), *Nuclear Instruments and Methods in Physics Research A* **601**, 294 (2009), arXiv:0810.4930.
- [8] M. G. Aartsen *et al.* (IceCube Collaboration), *Phys. Rev. D* **89**, 102001 (2014), arXiv:1312.0104 [astro-ph.HE].
- [9] M. G. Aartsen *et al.* (IceCube Collaboration), *Phys. Rev. D* **89**, 062007 (2014), arXiv:1311.7048 [astro-ph.HE].
- [10] M. G. Aartsen *et al.* (IceCube Collaboration), *Phys. Rev. Lett.* **111**, 021103 (2013), arXiv:1304.5356 [astro-ph.HE].
- [11] M. G. Aartsen *et al.* (IceCube Collaboration), *Science* **342**, 1242856 (2013), arXiv:1311.5238.
- [12] M. G. Aartsen *et al.* (IceCube Collaboration), *JINST* **9**, P03009 (2014), 1311.4767.
- [13] J. F. Beacom and J. Candia, *JCAP* **11**, 009 (2004), hep-ph/0409046.
- [14] T. K. Gaisser, S. A. Bludman, H. Lee, and T. Stanev, *Phys. Rev. Lett.* **51**, 223 (1983).
- [15] C. Gonzalez-Garcia, M. Maltoni, and J. Rojo, *Journal of High Energy Physics* **10**, 075 (2006), hep-ph/0607324.
- [16] P. Lipari, M. Lusignoli, and D. Meloni, *Phys. Rev. D* **75**, 123005 (2007), arXiv:0704.0718.
- [17] A. Fedynitch, J. Becker Tjus, and P. Desiati, *Phys. Rev. D* **86**, 114024 (2012), arXiv:1206.6710 [astro-ph.HE].
- [18] M. Honda, T. Kajita, K. Kasahara, S. Midorikawa, and T. Sanuki, *Phys. Rev. D* **75**, 043006 (2007), arXiv:astro-ph/0611418.
- [19] V. S. Berezhinsky, D. Cline, and D. N. Schramm, *Physics Letters B* **78**, 635 (1978).
- [20] L. V. Volkova, *International Cosmic Ray Conference* **7**, 22 (1983).
- [21] L. V. Volkova, *Physics Letters B* **462**, 211 (1999).
- [22] G. Gelmini, P. Gondolo, and G. Varieschi, *Phys. Rev. D* **61**, 056011 (2000), hep-ph/9905377.
- [23] A. D. Martin, M. G. Ryskin, and A. M. Stasto, *Acta Physica Polonica B* **34**, 3273 (2003), hep-ph/0302140.
- [24] R. Enberg, M. H. Reno, and I. Sarcevic, *Phys. Rev. D* **78**, 043005 (2008), arXiv:0806.0418 [hep-ph].
- [25] M. H. Reno, in *American Institute of Physics Conference Series*, American Institute of Physics Conference Series, Vol. 1560, edited by B. Fleming (2013) pp. 350–354.
- [26] T. K. Gaisser, in *European Physical Journal Web of Conferences*, European Physical Journal Web of Conferences, Vol. 52 (2013) p. 9004, arXiv:1303.1431 [hep-ph].
- [27] S. Schönert, T. K. Gaisser, E. Resconi, and O. Schulz, *Phys. Rev. D* **79**, 043009 (2009), arXiv:0812.4308.
- [28] T. K. Gaisser, K. Jero, A. Karle, and J. van Santen, *ArXiv e-prints* (2014), arXiv:1405.0525 [astro-ph.HE].
- [29] See Supplemental Material at [URL will be inserted by publisher] for data tables and event views.
- [30] T. K. Gaisser, F. Halzen, and T. Stanev, *Physics Reports* **258**, 173 (1995), hep-ph/9410384.
- [31] J. G. Learned and K. Mannheim, *Annual Review of Nuclear and Particle Science* **50**, 679 (2000).
- [32] F. Halzen and D. Hooper, *Reports on Progress in Physics* **65**, 1025 (2002), astro-ph/0204527.
- [33] J. K. Becker, *Physics Reports* **458**, 173 (2008), arXiv:0710.1557.
- [34] J. Braun, J. Dumm, F. de Palma, C. Finley, A. Karle, and T. Montaruli, *Astroparticle Physics* **29**, 299 (2008), arXiv:0801.1604.
- [35] A. A. Abdo *et al.* (Milagro Collaboration), *Astrophys. J.* **688**, 1078 (2008), arXiv:0805.0417.
- [36] M. G. Aartsen *et al.*, *Astrophys. J.* **779**, 132 (2013).
- [37] S. Adrián-Martínez *et al.*, *Astrophys. J.* **760**, 53 (2012), arXiv:1207.3105 [hep-ex].
- [38] S. Adrián-Martínez *et al.*, *The Astrophysical Journal Letters* **786**, L5 (2014).
- [39] A. D. Supanitsky, *Phys. Rev. D* **89**, 023501 (2014), arXiv:1312.7304 [astro-ph.HE].
- [40] M. Ahlers and K. Murase, (2013), arXiv:1309.4077 [astro-ph.HE].
- [41] C. Lunardini, S. Razzaque, K. T. Theodosiou, and L. Yang, (2013), arXiv:1311.7188 [astro-ph.HE].
- [42] Y. Bai, R. Lu, and J. Salvado, (2013), arXiv:1311.5864 [hep-ph].
- [43] A. M. Taylor, S. Gabici, and F. Aharonian, *Phys. Rev. D* **89**, 103003 (2014), arXiv:1403.3206 [astro-ph.HE].
- [44] M. Aartsen *et al.* (IceCube Collaboration), in *Proc. of the 33rd ICRC, Rio de Janeiro, Brazil* (2013) arXiv:1309.6979 [astro-ph.HE].
- [45] F. W. Stecker, C. Done, M. H. Salamon, and P. Sommers, *Phys. Rev. Lett.* **66**, 2697 (1991).
- [46] O. E. Kalashev, A. Kusenko, and W. Essey, *Phys. Rev. Lett.* **111**, 041103 (2013), arXiv:1303.0300 [astro-ph.HE].
- [47] A. M. Atoyan and C. D. Dermer, *New Astronomy Reviews* **48**, 381 (2004), astro-ph/0402646.
- [48] J. Alvarez-Muñiz and P. Mészáros, *Phys. Rev. D* **70**, 123001 (2004), astro-ph/0409034.
- [49] L. Nellen, K. Mannheim, and P. L. Biermann, *Phys. Rev. D* **47**, 5270 (1993), hep-ph/9211257.
- [50] K. Mannheim, *Astroparticle Physics* **3**, 295 (1995).
- [51] F. W. Stecker and M. H. Salamon, *Space Science Reviews* **75**, 341 (1996), astro-ph/9501064.
- [52] J. P. Rachen and P. Mészáros, *Phys. Rev. D* **58**, 123005 (1998), astro-ph/9802280.
- [53] P. Mészáros and E. Waxman, *Phys. Rev. Lett.* **87**, 171102 (2001), astro-ph/0103275.
- [54] A. Mücke, R. J. Protheroe, R. Engel, J. P. Rachen, and T. Stanev, *Astroparticle Physics* **18**, 593 (2003), astro-ph/0206164.
- [55] J. K. Becker, P. L. Biermann, and W. Rhode, *Astroparticle Physics* **23**, 355 (2005), astro-ph/0502089.
- [56] F. W. Stecker, *Phys. Rev. D* **72**, 107301 (2005), astro-ph/0510537.
- [57] B. Eichmann, R. Schlickeiser, and W. Rhode, *Astrophys. J.* **749**, 155 (2012).

- [58] E. Waxman and J. Bahcall, Phys. Rev. Lett. **78**, 2292 (1997).
- [59] D. Guetta, D. Hooper, J. Alvarez-Muñiz, F. Halzen, and E. Reuveni, Astroparticle Physics **20**, 429 (2004).
- [60] P. Baerwald, M. Bustamante, and W. Winter, ArXiv e-prints (2014), arXiv:1401.1820 [astro-ph.HE].
- [61] W. Winter, J. Becker Tjus, and S. R. Klein, ArXiv e-prints (2014), arXiv:1403.0574 [astro-ph.HE].
- [62] E. Waxman and J. N. Bahcall, Astrophys. J. **541**, 707 (2000), hep-ph/9909286.
- [63] S. Razzaque, P. Mészáros, and E. Waxman, Phys. Rev. D **68**, 083001 (2003), astro-ph/0303505.
- [64] J. K. Becker, M. Stamatikos, F. Halzen, and W. Rhode, Astroparticle Physics **25**, 118 (2006), astro-ph/0511785.
- [65] K. Murase and S. Nagataki, Phys. Rev. Lett. **97**, 051101 (2006), astro-ph/0604437.
- [66] A. Loeb and E. Waxman, JCAP **5**, 003 (2006), astro-ph/0601695.
- [67] K. Murase, M. Ahlers, and B. C. Lacki, Phys. Rev. D **88**, 121301 (2013), arXiv:1306.3417 [astro-ph.HE].
- [68] T. M. Yoast-Hull, J. S. Gallagher, III, E. G. Zweibel, and J. E. Everett, Astrophys. J. **780**, 137 (2014), arXiv:1311.5586 [astro-ph.HE].
- [69] T. A. Thompson, E. Quataert, E. Waxman, and A. Loeb, Astrophys. J. **654**, 219 (2007), astro-ph/0608699.
- [70] R. Abbasi *et al.* (IceCube Collaboration), Nature **484**, 351 (2012), arXiv:1204.4219 [astro-ph.HE].
- [71] E. Waxman and J. Bahcall, Phys. Rev. D **59**, 023002 (1999), hep-ph/9807282.
- [72] K. Mannheim, R. J. Protheroe, and J. P. Rachen, Phys. Rev. D **63**, 023003 (2001), astro-ph/9812398.
- [73] P. Bagley *et al.*, *KM3NeT Technical Design Report for a Deep-Sea Research Infrastructure Incorporating a Very Large Volume Neutrino Telescope* (KM3NeT Consortium, 2011) <http://km3net.org/TDR/TDRKM3NeT.pdf>.
- [74] R. Laha, J. F. Beacom, B. Dasgupta, S. Horiuchi, and K. Murase, Phys. Rev. D **88**, 043009 (2013), arXiv:1306.2309 [astro-ph.HE].
- [75] K. M. Górski, E. Hivon, A. J. Banday, B. D. Wandelt, F. K. Hansen, M. Reinecke, and M. Bartelmann, Astrophys. J. **622**, 759 (2005), astro-ph/0409513.

This section gives additional technical information about the result in the main article, including tabular forms of the results, alternative presentations of several figures, reviews of referenced methods, and event displays of the neutrino candidates. Some content is repeated from the main text or from our earlier publication covering the first two years of data [11] for context. Methods and performance information not provided here (e.g. effective areas) are identical to those in [11]. Event displays here include only the events first shown in this paper; displays for events 1-28 can be found in the online supplement to [11]. Further IceCube data releases can be found at <http://www.icecube.wisc.edu/science/data>.

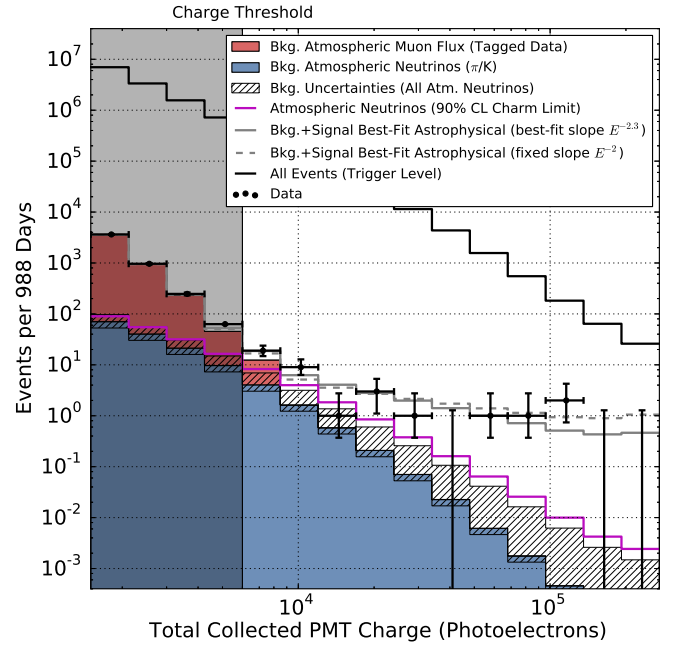
Event Information

Properties of the 37 neutrino candidate events are shown in Suppl. Tab. I. Five of these (3, 8, 18, 28, 32) contain downgoing muons and have an apparent first interaction near the detector boundary and are therefore consistent with the expected 8.4 ± 4.2 background muon events. Two of these (28 and 32) have subthreshold early hits in the veto region, as well as coincident detections in the IceTop surface air shower array, and are almost certainly penetrating cosmic ray muon background. The remaining events are uniformly distributed throughout the detector volume and are consistent with neutrino interactions. Their distribution in total PMT charge, used for event selection, is shown in Suppl. Fig. 1.

Reconstruction uncertainties given in Suppl. Tab. I include both statistical and systematic uncertainties and were determined from average reconstruction errors on a population of simulated events of the same topology in the same part of the detector with similar energies to those observed. The reconstructions used were maximum likelihood fits of the observed photon timing distributions to template events using the cascade and muon loss unfolding techniques described in [12]. Cascade angular resolution operates by observing forward/backward asymmetries in photon timing: in front of the neutrino interaction, most light is unscattered and arrives over a short period of time, whereas behind the interaction, the light has scattered at least once, producing a broader profile. Resolution as a function of energy for this analysis is shown in Fig. 14 of [12]. Event 32 is made of two coincident cosmic ray muons (see supplemental event views) and so no single energy and direction can be given for the event.

Point Source Methods

The point source searches used the unbinned maximum likelihood method from [34]:



SUPPL. FIG. 1. Distribution of deposited PMT charges (Q_{tot}). Muons at higher total charges are less likely to pass the veto layer undetected, causing the muon background (red, estimated from data) to fall faster than the overall trigger rate (uppermost line). The data events in the unshaded region, at $Q_{tot} > 6000$, are the events reported in this work. The hatched region shows current 1σ experimental uncertainties on both the π/K and prompt components of the atmospheric neutrino background [9]. For scale, the experimental 90% CL upper bound on prompt atmospheric neutrinos [9] is also shown (magenta line).

$$\mathcal{L}(n_s, \vec{x}_s) = \prod_{i=1}^N \left[\frac{n_s}{N} \mathcal{S}_i(\vec{x}_s) + \left(1 - \frac{n_s}{N}\right) \mathcal{B}_i \right]. \quad (\text{A.1})$$

Here, $\mathcal{B}_i = \frac{1}{4\pi}$ represents the isotropic background probability distribution function (PDF), and the signal PDF \mathcal{S}_i is the reconstructed directional uncertainty map for each event. N is the total number of events in the data sample and n_s is the number of signal events, which is a free parameter. For the all-sky clustering and source catalog searches, the likelihood is maximized at each location, resulting in a best-fit # of signal events. Suppl. Fig. 2 shows the arrival directions of the events and the result of the point source clustering test in equatorial coordinates (J2000), while Suppl. Tab. II and III list the results for the 78 sources in the pre-defined catalog. This catalog was chosen based on gamma-ray observations or predicted astrophysical neutrino fluxes, and is comprised of sources previously tested by IceCube [36] and ANTARES [37].

To reduce the bias in the likelihood fit towards positions of single well-resolved muon tracks, a marginalized form of the likelihood was also used for the all-sky test:

ID	Dep. Energy (TeV)	Observation Time (MJD)	Decl. (deg.)	R.A. (deg.)	Med. Angular Error (deg.)	Event Topology
1	47.6 ^{+6.5} _{-5.4}	55351.3222143	-1.8	35.2	16.3	Shower
2	117 ⁺¹⁵ ₋₁₅	55351.4659661	-28.0	282.6	25.4	Shower
3	78.7 ^{+10.8} _{-8.7}	55451.0707482	-31.2	127.9	≲ 1.4	Track
4	165 ⁺²⁰ ₋₁₅	55477.3930984	-51.2	169.5	7.1	Shower
5	71.4 ^{+9.0} _{-9.0}	55512.5516311	-0.4	110.6	≲ 1.2	Track
6	28.4 ^{+2.7} _{-2.5}	55567.6388127	-27.2	133.9	9.8	Shower
7	34.3 ^{+3.5} _{-4.3}	55571.2585362	-45.1	15.6	24.1	Shower
8	32.6 ^{+10.3} _{-11.1}	55608.8201315	-21.2	182.4	≲ 1.3	Track
9	63.2 ^{+7.1} _{-8.0}	55685.6629713	33.6	151.3	16.5	Shower
10	97.2 ^{+10.4} _{-12.4}	55695.2730461	-29.4	5.0	8.1	Shower
11	88.4 ^{+12.5} _{-10.7}	55714.5909345	-8.9	155.3	16.7	Shower
12	104 ⁺¹³ ₋₁₃	55739.4411232	-52.8	296.1	9.8	Shower
13	253 ⁺²⁶ ₋₂₂	55756.1129844	40.3	67.9	≲ 1.2	Track
14	1041 ⁺¹³² ₋₁₄₄	55782.5161911	-27.9	265.6	13.2	Shower
15	57.5 ^{+8.3} _{-7.8}	55783.1854223	-49.7	287.3	19.7	Shower
16	30.6 ^{+3.6} _{-3.5}	55798.6271285	-22.6	192.1	19.4	Shower
17	200 ⁺²⁷ ₋₂₇	55800.3755483	14.5	247.4	11.6	Shower
18	31.5 ^{+4.6} _{-3.3}	55923.5318204	-24.8	345.6	≲ 1.3	Track
19	71.5 ^{+7.0} _{-7.2}	55925.7958619	-59.7	76.9	9.7	Shower
20	1141 ⁺¹⁴³ ₋₁₃₃	55929.3986279	-67.2	38.3	10.7	Shower
21	30.2 ^{+3.5} _{-3.3}	55936.5416484	-24.0	9.0	20.9	Shower
22	220 ⁺²¹ ₋₂₄	55941.9757813	-22.1	293.7	12.1	Shower
23	82.2 ^{+8.6} _{-8.4}	55949.5693228	-13.2	208.7	≲ 1.9	Track
24	30.5 ^{+3.2} _{-2.6}	55950.8474912	-15.1	282.2	15.5	Shower
25	33.5 ^{+4.9} _{-5.0}	55966.7422488	-14.5	286.0	46.3	Shower
26	210 ⁺²⁹ ₋₂₆	55979.2551750	22.7	143.4	11.8	Shower
27	60.2 ^{+5.6} _{-5.6}	56008.6845644	-12.6	121.7	6.6	Shower
28	46.1 ^{+5.7} _{-4.4}	56048.5704209	-71.5	164.8	≲ 1.3	Track
29	32.7 ^{+3.2} _{-2.9}	56108.2572046	41.0	298.1	7.4	Shower
30	129 ⁺¹⁴ ₋₁₂	56115.7283574	-82.7	103.2	8.0	Shower
31	42.5 ^{+5.4} _{-5.7}	56176.3914143	78.3	146.1	26.0	Shower
32	—	56211.7401231	—	—	—	Coincident
33	385 ⁺⁴⁶ ₋₄₉	56221.3424023	7.8	292.5	13.5	Shower
34	42.1 ^{+6.5} _{-6.3}	56228.6055226	31.3	323.4	42.7	Shower
35	2004 ⁺²³⁶ ₋₂₆₂	56265.1338677	-55.8	208.4	15.9	Shower
36	28.9 ^{+3.0} _{-2.6}	56308.1642740	-3.0	257.7	11.7	Shower
37	30.8 ^{+3.3} _{-3.5}	56390.1887627	20.7	167.3	≲ 1.2	Track

SUPPL. TABLE I. Properties of the events. Tabular form of Fig. 1. Events 1-28 were previously published in [11] and are included here, with no changes, for completeness. Events 28 and 32 have coincident hits in the IceTop surface array, implying that they are almost certainly produced in cosmic ray air showers.

$$\mathcal{L}_M(n_s) = \int_{\vec{x}_s} \mathcal{L}(n_s, \vec{x}_s) P(\vec{x}_s) d\vec{x}_s, \quad (\text{A.2})$$

where $\mathcal{L}(n_s, \vec{x}_s)$ is equation A.1 and $P(\vec{x}_s) = \frac{1}{4\pi}$ is a uniform prior for the position of a single point source. In this procedure, there is only one free parameter (n_s) that is fit across the entire sky, instead of being varied independently at every position.

For the galactic plane search, equation A.1 is modified so the signal PDF only includes regions which overlap with the galactic plane:

$$\mathcal{S}_i(\vec{x}_j) \rightarrow \sum_j^{n_{bins}} \frac{W(\vec{x}_j) \mathcal{S}_i(\vec{x}_j)}{n_{bins}}. \quad (\text{A.3})$$

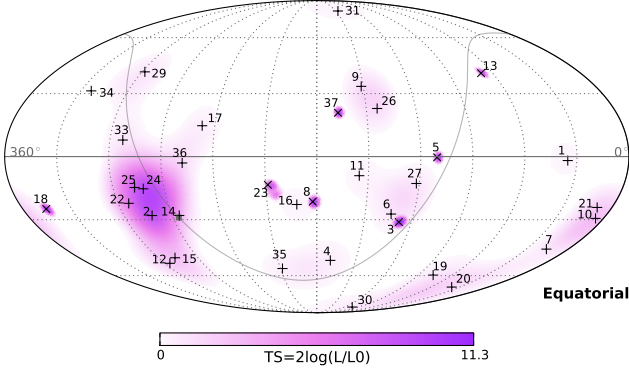
The weight $W(\vec{x}_j)$ is set to 1 for any region overlapping a galactic plane with a specific angular extent, and is set to 0 otherwise. Suppl. Fig. 3 shows the degree of

Category	Source	RA (°)	Dec (°)	\hat{n}_s	p-value
SNR	TYCHO	6.36	64.18	0.0	–
	Cas A	350.85	58.82	0.0	–
	IC443	94.18	22.53	0.0	–
	W51C	290.75	14.19	0.7	0.05
	W44	284.04	1.38	2.5	0.01
	W28	270.43	-23.34	4.3	0.01
	RX J1713.7-3946	258.25	-39.75	0.0	–
	RX J0852.0-4622	133.0	-46.37	0.0	–
	RCW 86	220.68	-62.48	0.3	0.41
XB/mqso	LSI 303	40.13	61.23	0.0	–
	Cyg X-3	308.10	41.23	0.8	0.05
	Cyg X-1	299.59	35.20	1.0	0.03
	HESS J0632+057	98.24	5.81	0.0	–
	SS433	287.96	4.98	1.5	0.02
	LS 5039	276.56	-14.83	4.9	0.002
	GX 339-4	255.7	-48.79	0.0	–
	Cir X-1	230.17	-57.17	0.0	–
Star Formation Region	Cyg OB2	308.10	41.23	0.8	0.05
Pulsar/PWN	MGRO J2019+37	305.22	36.83	0.9	0.04
	Crab Nebula	83.63	22.01	0.0	–
	Geminga	98.48	17.77	0.0	–
	HESS J1912+101	288.21	10.15	0.8	0.04
	Vela X	128.75	-45.6	0.0	–
	HESS J1632-478	248.04	-47.82	0.0	–
	HESS J1616-508	243.78	-51.40	0.0	–
	HESS J1023-575	155.83	-57.76	0.2	0.44
	MSH 15-52	228.53	-59.16	0.06	0.48
	HESS J1303-631	195.74	-63.52	0.8	0.28
	PSR B1259-63	195.74	-63.52	0.8	0.28
HESS J1356-645	209.0	-64.5	0.5	0.35	
Galactic Center	Sgr A*	266.42	-29.01	3.1	0.04
Not Identified	MGRO J1908+06	286.99	6.27	1.3	0.03
	HESS J1834-087	278.69	-8.76	4.7	0.01
	HESS J1741-302	265.25	-30.2	2.5	0.07
	HESS J1503-582	226.46	-58.74	0.2	0.45
	HESS J1507-622	226.72	-62.34	0.1	0.47

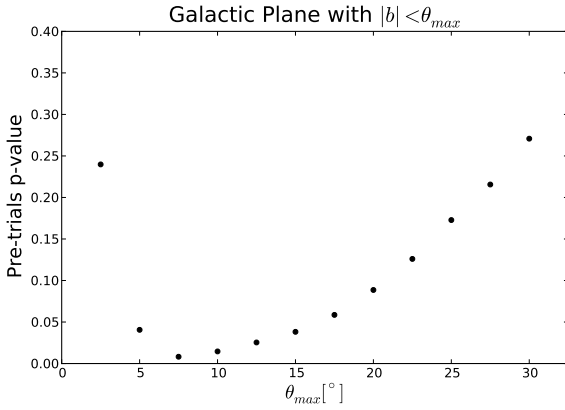
SUPPL. TABLE II. Catalog of 36 galactic sources, grouped according to their classification as supernova remnants (SNR), X-ray binaries or microquasars (XB/mqso), pulsar wind nebulae (PWN), star formation regions, and unidentified sources. The post-trials p-values for the entire catalog in the northern and southern hemispheres were 28% and 8%, respectively. For each source, the pre-trials p-value was estimated by repeating the source catalog search with the data randomized in right ascension. The fraction of test statistic (TS) values from all individual sources that were greater than or equal to the observed TS determined the pre-trials p-value. The best-fit # of signal events (\hat{n}_s) is the result of the likelihood fit at each individual source. When $\hat{n}_s = 0$, no p-value is reported. Since many sources are spatially close together relative to the angular resolution, adjacent sources often receive similar fit results. For sources separated by less than 1° , their positions are averaged and they are treated as one source.

Category	Source	RA (°)	Dec (°)	\hat{n}_s	p-value
BL Lac	S5 0716+71	110.47	71.34	0.0	–
	1ES 1959+650	300.00	65.15	0.0	–
	1ES 2344+514	356.77	51.70	0.0	–
	3C66A	35.67	43.04	0.0	–
	H 1426+428	217.14	42.67	0.0	–
	BL Lac	330.68	42.28	0.0	–
	Mrk 501	253.47	39.76	0.0	–
	Mrk 421	166.11	38.21	0.0	–
	W Comae	185.38	28.23	0.0	–
	1ES 0229+200	38.20	20.29	0.0	–
	PKS 0235+164	39.66	16.62	0.0	–
	VER J0648+152	102.2	15.27	0.0	–
	RGB J0152+017	28.17	1.79	0.1	0.15
	1ES 0347-121	57.35	-11.99	0.0	–
	1ES 1101-232	165.91	-23.49	0.0	–
	PKS 2155-304	329.72	-30.22	0.0	–
	H 2356-309	359.78	-30.63	1.8	0.08
	PKS 0548-322	87.67	-32.27	0.0	–
	PKS 0426-380	67.17	-37.93	0.0	–
PKS 0537-441	84.71	-44.08	0.0	–	
PKS 2005-489	302.37	-48.82	1.5	0.11	
FSRQ	4C 38.41	248.82	38.14	0.0	–
	3C 454.3	343.50	16.15	0.0	–
	PKS 0528+134	82.74	13.53	0.0	–
	PKS 1502+106	226.10	10.52	0.0	–
	3C 273	187.28	2.05	0.0	–
	3C279	194.05	-5.79	0.0	–
	HESS J1837-069	279.41	-6.95	4.5	0.01
	QSO 2022-077	306.42	-7.64	0.4	0.44
	PKS 1406-076	212.24	-7.87	0.0	–
	PKS 0727-11	112.58	-11.7	0.4	0.39
	QSO 1730-130	263.26	-13.08	3.3	0.03
PKS 0454-234	74.27	-23.43	0.0	–	
PKS 1622-297	246.53	-29.86	0.0	–	
PKS 1454-354	224.36	-35.65	0.0	–	
Starburst	M82	148.97	69.68	0.07	0.15
Radio Galaxies	NGC 1275	49.95	41.51	0.0	–
	Cyg A	299.87	40.73	0.9	0.03
	3C 123.0	69.27	29.67	0.0	–
	M87	187.71	12.39	0.0	–
	Cen A	201.37	-43.02	0.03	0.49
Seyfert	ESO 139-G12	264.41	-59.94	0.0	–

SUPPL. TABLE III. Catalog of 42 extragalactic sources, grouped according to their classification as BL Lac objects, Radio galaxies, Flat Spectrum Radio Quasars (FSRQ), Starburst galaxies, and Seyfert galaxies. A description of the information in the table can be found in Suppl. Tab. II.



SUPPL. FIG. 2. Arrival directions of the events (+ for shower events, × for track events) and test statistic (colors) in equatorial coordinates (J2000). The gray line denotes the galactic plane. This is an equatorial version of Fig. 5.

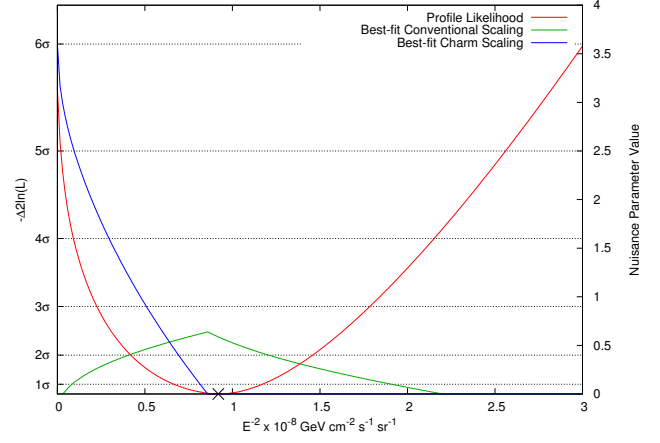


SUPPL. FIG. 3. Pre-trials p-value vs. width of galactic plane hypothesis. The width of the galactic plane is varied from $\pm 2.5^\circ$ to $\pm 30^\circ$ in steps of 2.5° . For each width, the pre-trials p-value is calculated by comparing the maximized likelihood to that from scrambled datasets. All results are consistent with the background-only hypothesis.

clustering along the galactic plane for each tested width of the plane.

Alternative Hypothesis Tests

The primary statistical test used in this article is based on optimization of a Poisson likelihood in zenith angle and deposited energy containing four components: penetrating muon background, atmospheric neutrinos from π/K decay, atmospheric neutrinos from charm decay, and an isotropic E^{-2} astrophysical test flux. The muon background was constrained by a Gaussian prior matching our veto efficiency measurement. To ensure maximum robustness, all neutrino rates were completely unconstrained beyond a non-negativity requirement.



SUPPL. FIG. 4. Profile likelihood scan of the normalization of the E^{-2} test flux for the unconstrained fit. The red line represents the likelihood difference (left axis) to the best-fit point (marked with ×). Nuisance parameters (right axis, blue and green lines) are fractions of, respectively, the 90% CL upper limit on prompt and best-fit conventional (π/K) atmospheric neutrino fluxes from [9] and show the best-fit values, without uncertainties, of the atmospheric flux for each choice of astrophysical flux. For very low astrophysical fluxes, large prompt atmospheric neutrino fluxes are required to explain the data (blue line) but even large values are in strong tension with the data (red line). Note that significances given on the left axis are approximate, although they coincide with results of Monte Carlo ensembles for the null hypothesis rejection (5.7σ).

To test the null hypothesis of no astrophysical flux, we compared the best global fit, with all components free, to the best fit when the astrophysical test flux was constrained to zero using the difference in likelihood as a test statistic. This rejected with a significance of 5.7σ the no-astrophysical case when compared to the best-fit alternative, which had a prompt flux (the hardest non-astrophysical component available to the fitter) 3.6 times above existing 90% CL limits [9] (Suppl. Fig. 4), which themselves are well above most common prompt flux predictions (e.g. [24]). Using the previous limits directly in the fit, through a Gaussian penalty function, would have increased the significance of the result to 6.8σ , tested against a best-fit prompt flux 1.6 times larger than the existing 90% CL limit.

In the first part of this study [11], we performed an additional test that does not include information on the spectrum or angular distribution of the penetrating muon background and has correspondingly much lower sensitivity. The construction of the test also does not allow incorporation of any non-statistical uncertainties in the atmospheric neutrino fluxes, in order to match the treatment and charm background model in [10]; it is presented here only for consistency with the previous result. Removing the two ~ 1 PeV events from the sample and incorporating them with the significance from [10] gives

4.8σ . Including all events directly in the test yields 5.2σ .

Comparisons of the properties of the events to model expectations are given in Suppl. Tab. IV and Suppl. Figs. 5 and 6.

Time Clustering Analysis

We performed two tests for clustering of events in time, following an identical procedure to that in [11]. The method is reviewed below. The first test looked for significant time clusters in all events (neglecting, like the point source search, events 28 and 32). A second searched for time clustering in eleven subsets of the events that formed possible spatial clusters of two or more events.

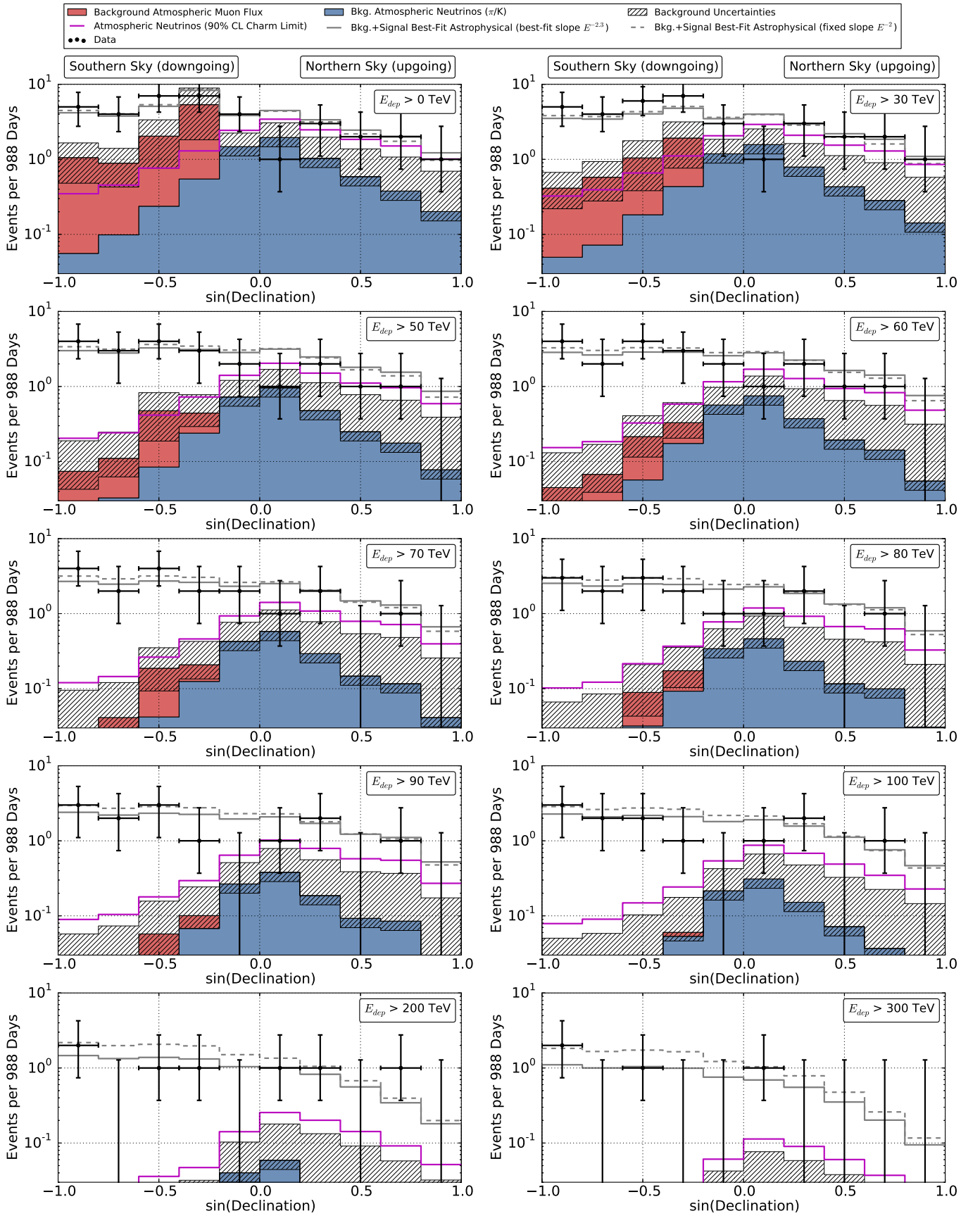
We applied an unbinned maximum likelihood method as in [34] to identify timing clusters relative to an assumed constant arrival rate in both the full sample and each spatial group. This selects the most significant time cluster over a discrete set of time windows (Δt_j), one for each possible pair of the 35 event times. Each event pair defines a start and end time (t_j^{\min} and t_j^{\max}), with a duration $\Delta t_j = t_j^{\max} - t_j^{\min}$. These quantities form the signal likelihood:

$$S_i^{\text{time}} = \frac{H(t_{\max} - t_j) \times H(t_j - t_{\min})}{t_{\max} - t_{\min}} \quad (\text{A.4})$$

where H is the Heaviside step function. For each Δt_j , the likelihood ratio to a flat alternative was used as a test statistic (TS_j) as in [34]. Significance was determined by comparing the highest TS with the distribution obtained for data sets scrambled in time.

Using all events, the most significant time cluster contained seven events (18, 19, 20, 21, 22, 23, 24). The fitted number of signal events (\hat{n}_s) is 6.09, with a duration of 27.3 days. The probability to observe a cluster this significant or better by chance is 11%.

The second test searched for time clustering among events found in several spatial groups. Within each group, the same scrambling approach and analysis was applied as to the full sample, but with fewer events. Results are shown in Suppl. Table V. The highest fluctuation observed corresponds to Cluster K with a pre-trial p-value 4.0%. Including trial factors due to the 11 spatial groups gives an overall post-trial p-value for this excess of 33%.



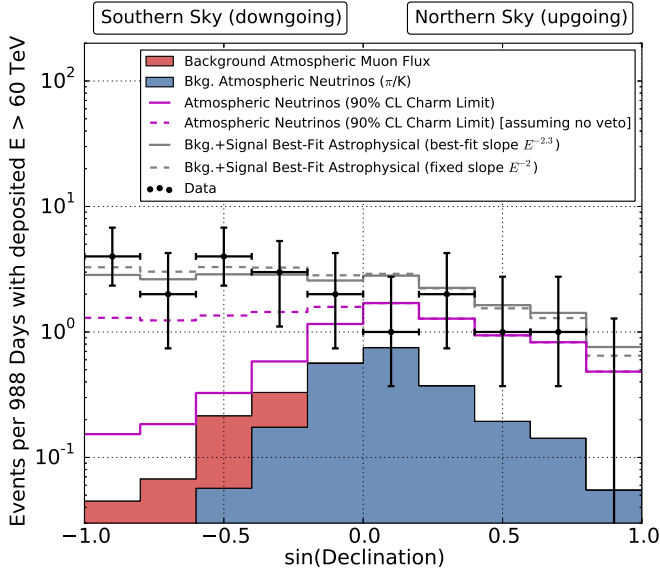
SUPPL. FIG. 5. Expected and observed distribution of events in declination for various cuts in deposited energy. The solid gray line ($E^{-2.3}$ added to backgrounds) provides a better fit to the data than the E^{-2} benchmark (dashed) at the 1σ level.

all energies								
	Muons	π/K atm. ν	Prompt atm. ν	E^{-2} (best-fit)	$E^{-2.3}$ (best-fit)	Sum (E^{-2})	Sum ($E^{-2.3}$)	Data
Tot. Events	8.4 ± 4.2	$6.6^{+2.2}_{-1.6}$	< 9.0 (90% CL)	23.8	23.7	38.8	38.7	37 (36)
Up	0	4.2	< 6.1	8.3	9.4	12.4	13.5	9
Down	8.4	2.4	< 2.9	15.5	14.4	26.3	25.2	27
Track	~ 7.6	4.5	< 1.7	4.6	4.3	16.7	16.4	8
Shower	~ 0.8	2.1	< 7.2	19.2	19.5	22.1	22.4	28
Fraction Up	0%	63%	68%	35%	40%	32%	35%	25%
Fraction Down	100%	37%	32%	65%	60%	68%	65%	75%
Fraction Tracks	$> 90\%$	69%	19%	19%	18%	43%	42%	24%
Fraction Showers	$< 10\%$	31%	81%	81%	82%	57%	58%	76%

$E_{\text{dep}} < 60$ TeV								
	Muons	π/K atm. ν	Prompt atm. ν	E^{-2} (best-fit)	$E^{-2.3}$ (best-fit)	Sum (E^{-2})	Sum ($E^{-2.3}$)	Data
Tot. Events	8.0	4.2	< 3.7	2.2	3.8	14.5	16.1	16
Up	0	2.6	< 2.4	1.2	2.0	3.7	4.7	4
Down	8.0	1.6	< 1.3	1.1	1.8	10.7	11.4	12
Track	~ 7.2	2.9	< 0.7	0.4	0.6	10.5	10.7	4
Shower	~ 0.8	1.4	< 3.0	1.8	3.2	4.0	5.3	12
Fraction Up	0%	63%	65%	52%	53%	26%	29%	25%
Fraction Down	100%	37%	35%	48%	47%	74%	71%	75%
Fraction Tracks	$> 90\%$	68%	19%	19%	17%	72%	67%	25%
Fraction Showers	$< 10\%$	32%	81%	81%	83%	28%	33%	75%

60 TeV $< E_{\text{dep}} < 3$ PeV								
	Muons	π/K atm. ν	Prompt atm. ν	E^{-2} (best-fit)	$E^{-2.3}$ (best-fit)	Sum (E^{-2})	Sum ($E^{-2.3}$)	Data
Tot. Events	0.4	2.4	< 5.3	18.2	18.6	21.0	21.4	20
Up	0	1.5	< 3.7	6.7	7.2	8.2	8.7	5
Down	0.4	0.8	< 1.6	11.6	11.4	12.8	12.7	15
Track	~ 0.4	1.7	< 1.0	3.8	3.5	5.8	5.5	4
Shower	~ 0.0	0.7	< 4.2	14.4	15.1	15.2	15.8	16
Fraction Up	0%	64%	70%	37%	39%	39%	41%	25%
Fraction Down	100%	36%	30%	63%	61%	61%	59%	75%
Fraction Tracks	$> 90\%$	71%	20%	21%	19%	28%	26%	20%
Fraction Showers	$< 10\%$	29%	80%	79%	81%	72%	74%	80%

SUPPL. TABLE IV. Properties of events and models. Limits on the prompt flux are from [9]. The best-fit per-flavor E^{-2} normalization is $E^2\Phi_\nu(E) = 0.95 \cdot 10^{-8} \text{ GeV cm}^{-2} \text{ s}^{-1} \text{ sr}^{-1}$. The global best-fit spectrum is $E^2\phi(E) = 1.5 \times 10^{-8} (E/100\text{TeV})^{-0.3} \text{ GeV cm}^{-2} \text{ s}^{-1} \text{ sr}^{-1}$. As event 32, a set of coincident muons, is not reconstructable, it is excluded from all but the first row of the table. Fractions for up/down and shower/track classifications are provided at the bottom; shower/track fractions for the muon background are estimates based on examination of lower-energy events. Note that the total track rate here is dominated by the highly uncertain muon background rate. The column labeled *Sum* shows the sum of all predictions given their nominal values and does not include any uncertainties in its constituent rates or the results of the best-fit background rates, which were slightly below expectations (Suppl. Fig. 4). A graphical presentation of the evolution of the up/down ratio with energy can be found in Suppl. Fig. 5. The track to cascade ratio is a strong function of spectrum due to threshold effects [11] that give higher efficiency in the threshold region for ν_e CC. This causes the near equality between this ratio for the E^{-2} test flux and the substantially softer charm background.

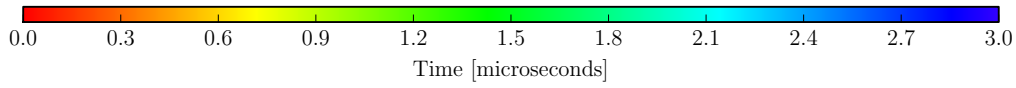
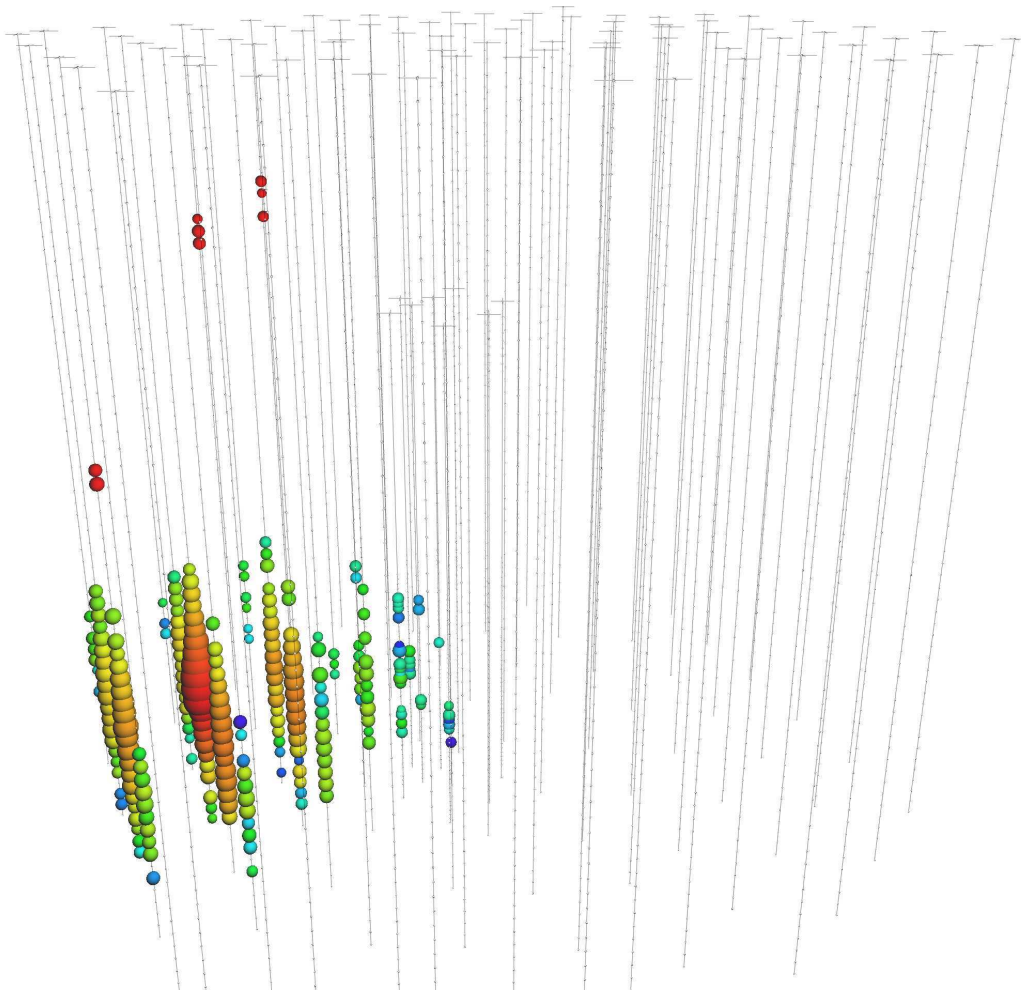
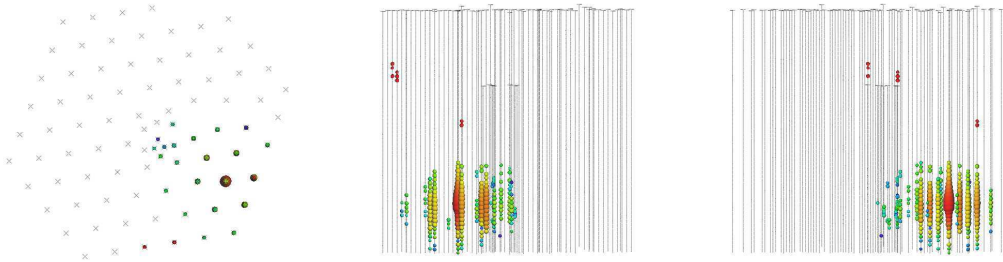


SUPPL. FIG. 6. Comparison of zenith distributions for atmospheric neutrino flux with charm saturating previous limits [9] before (dashed purple line) and after (solid purple line) removal of events accompanied into the detector by muons from the neutrinos’ parent air shower [27, 28].

	no. of events	event IDs	\hat{n}_s	$\Delta t_{cl.}$	p-value
Cluster A	6	2, 14, 22, 24, 25, 33	2.9	25	17%
Cluster B	2	15, 12	2.0	44	9%
Cluster C	2	10, 21	2.0	241	38%
Cluster D	3	3, 6, 27	3.0	558	62%
Cluster E	2	9, 26	2.0	294	50%
Cluster F	2	16, 23	2.0	151	24%
Cluster G	2	8, 16	2.0	190	32%
Cluster H	3	19, 20, 30	2.0	4	8%
Cluster I	2	4, 35	2.0	788	94%
Cluster J	2	17, 36	2.0	508	72%
Cluster K	3	29, 33, 34	3.0	120	4%

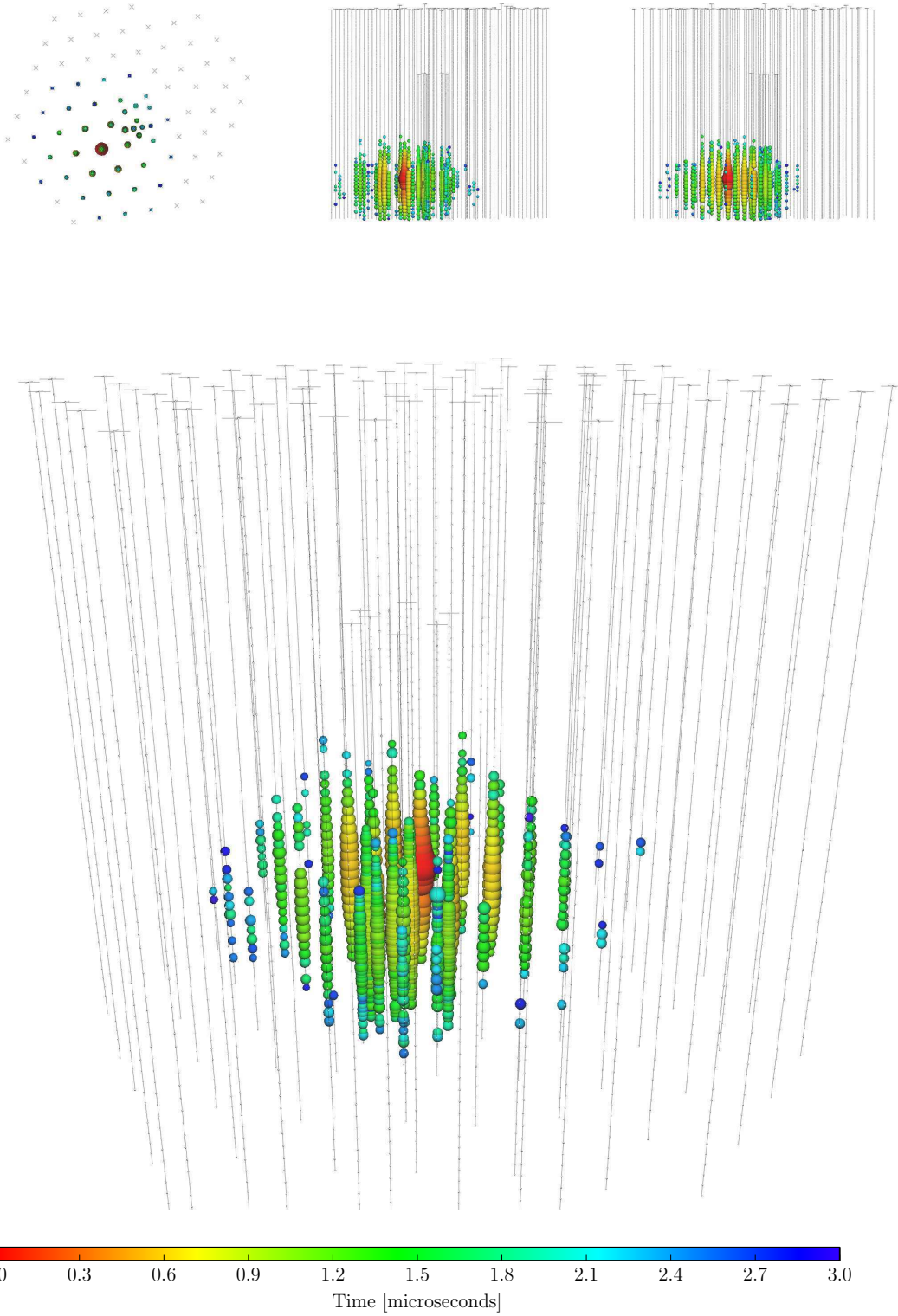
SUPPL. TABLE V. Time clustering of 11 spatially clustered event groups. All p-values are pre-trial. $\Delta t_{cl.}$, the best-fit duration, is in units of days.

EVENT 29



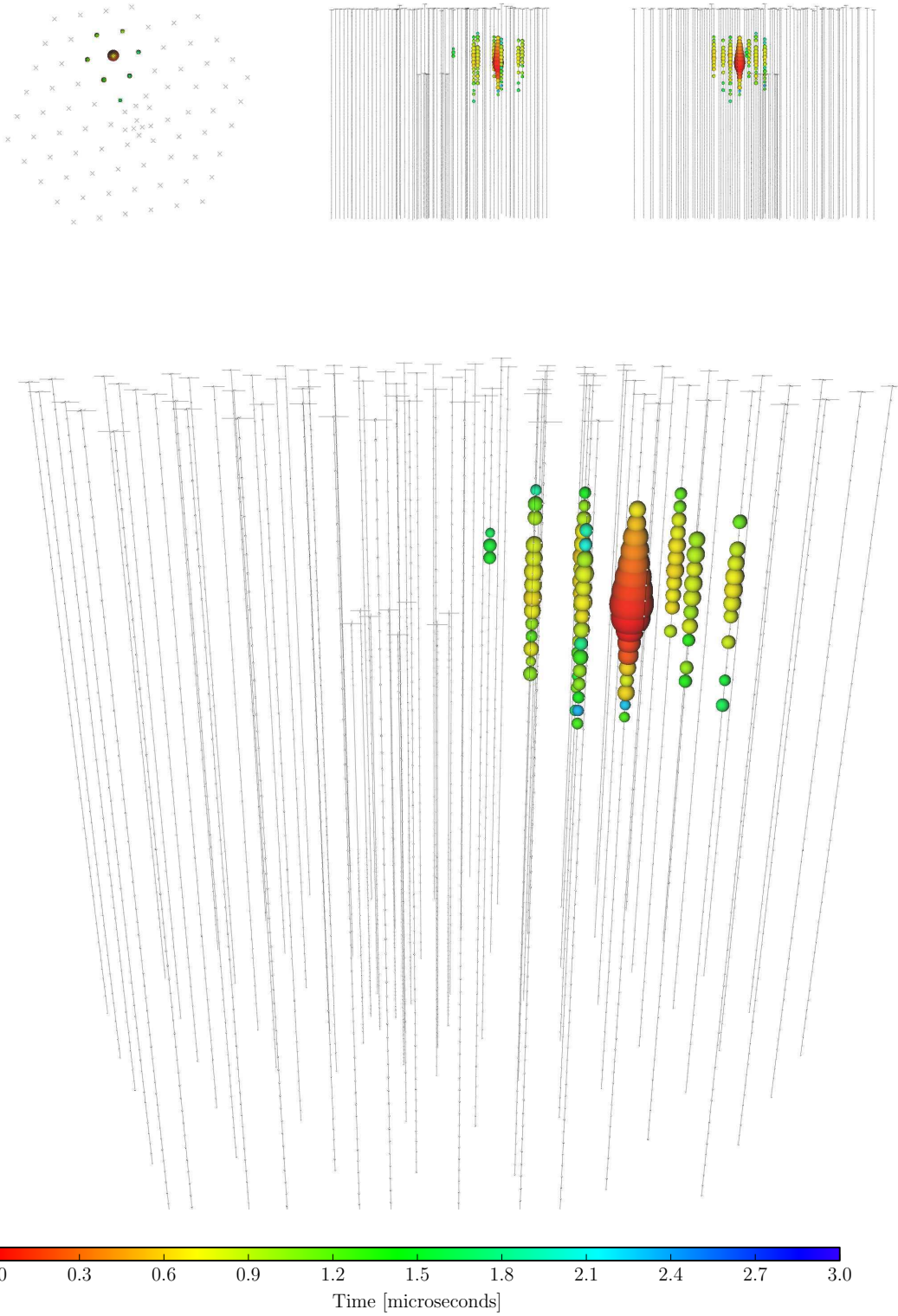
Deposited Energy (TeV)	Time (MJD)	Declination (deg.)	RA (deg.)	Med. Ang. Resolution (deg.)	Topology
$32.7^{+3.2}_{-2.9}$	56108.2572046	41.0	298.1	7.4	Shower

EVENT 30



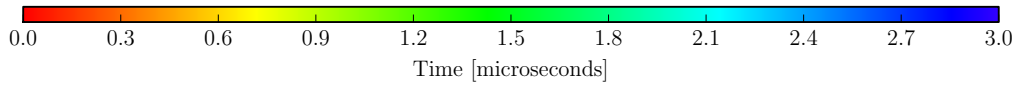
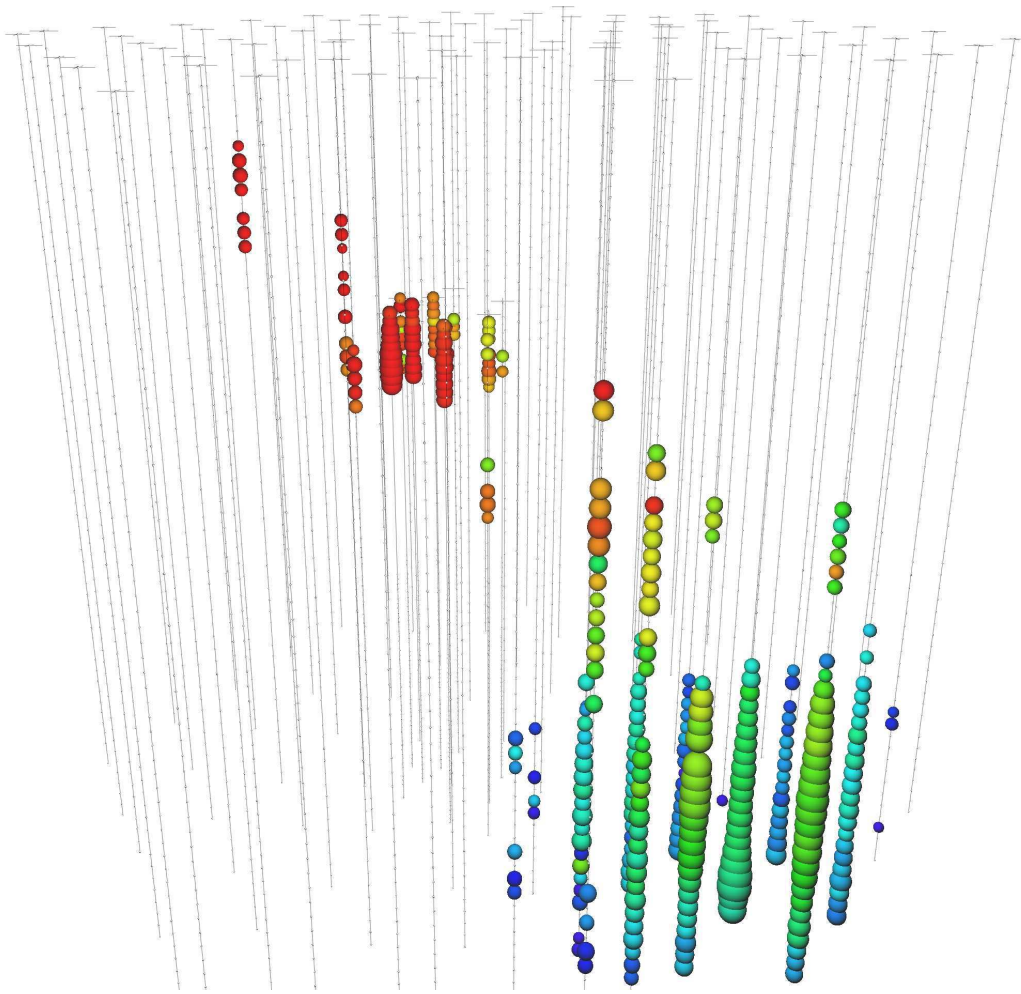
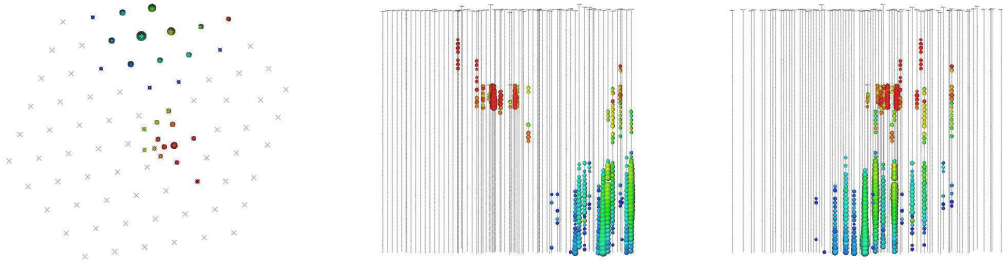
Deposited Energy (TeV)	Time (MJD)	Declination (deg.)	RA (deg.)	Med. Ang. Resolution (deg.)	Topology
129^{+14}_{-12}	56115.7283574	-82.7	103.2	8.0	Shower

EVENT 31



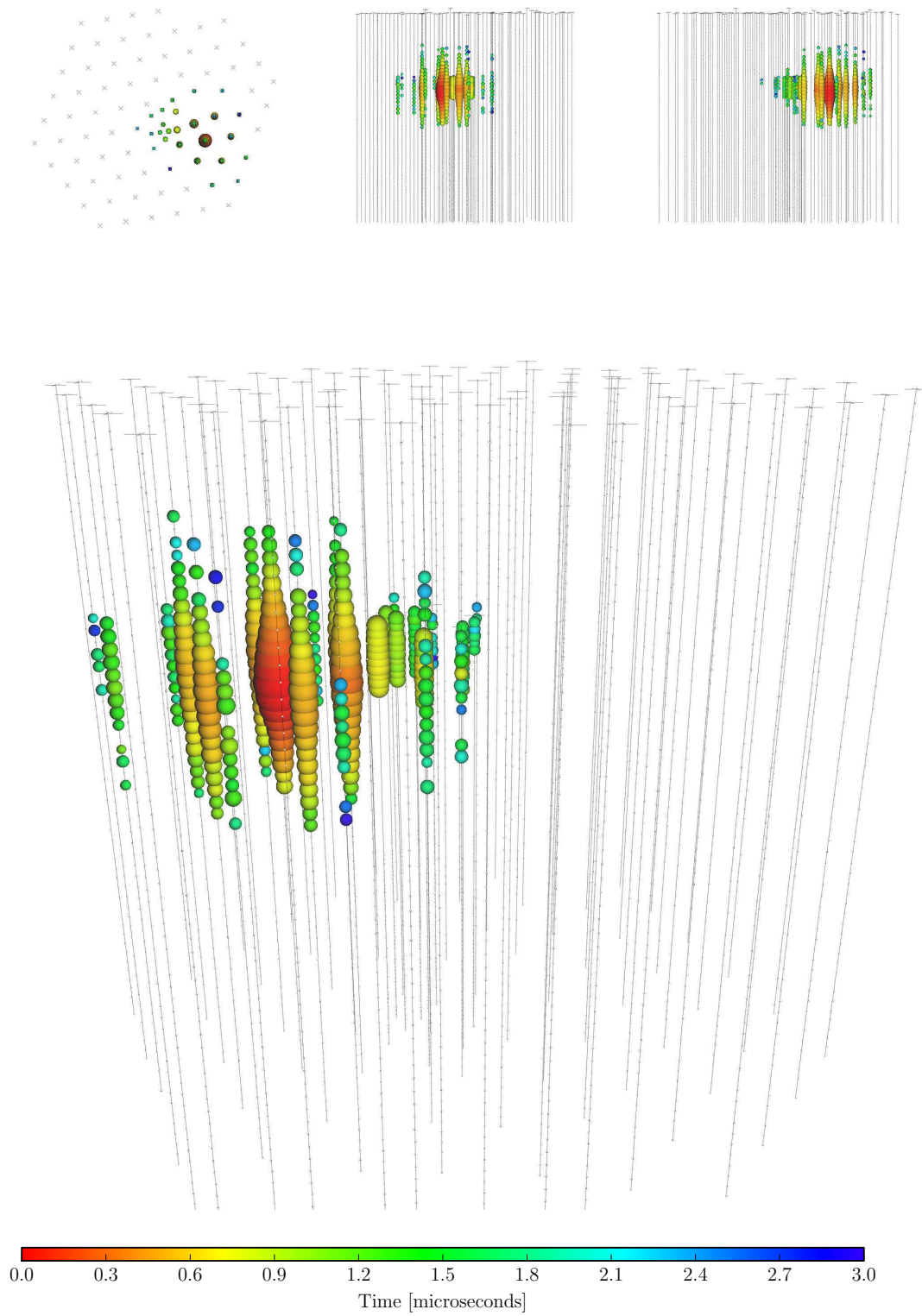
Deposited Energy (TeV)	Time (MJD)	Declination (deg.)	RA (deg.)	Med. Ang. Resolution (deg.)	Topology
$42.5^{+5.4}_{-5.7}$	56176.3914143	78.3	146.1	26.0	Shower

EVENT 32



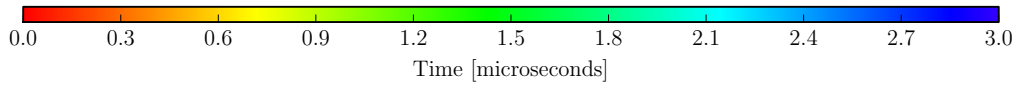
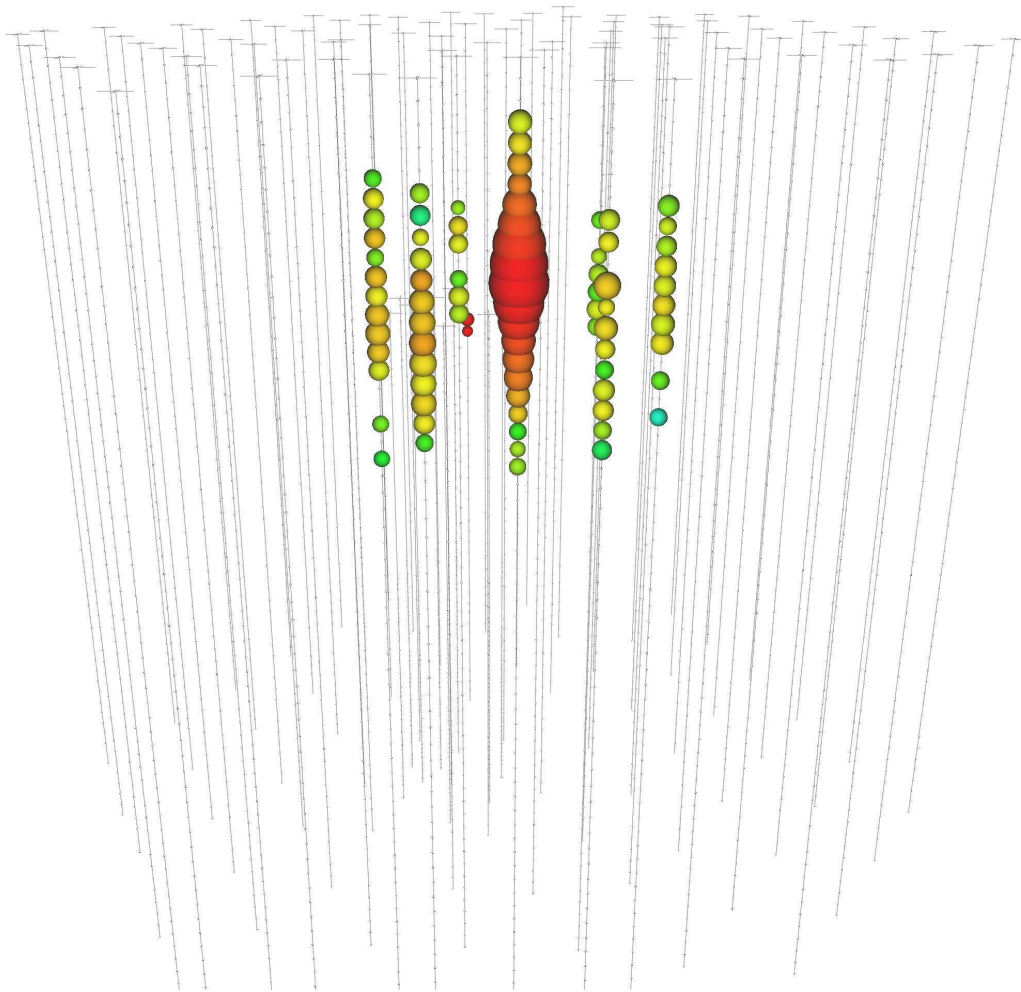
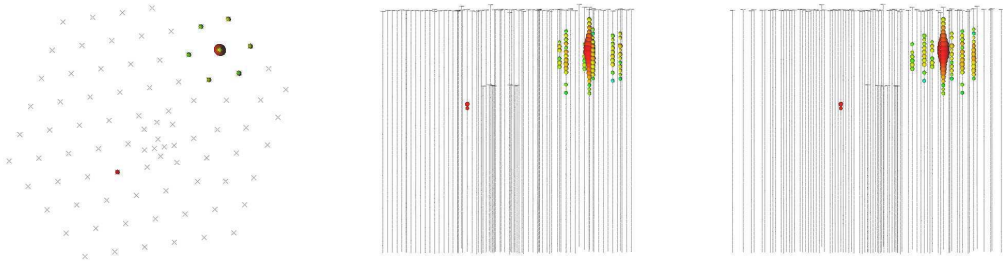
Deposited Energy (TeV)	Time (MJD)	Declination (deg.)	RA (deg.)	Med. Ang. Resolution (deg.)	Topology
—	56211.7401231	—	—	—	Coincident

EVENT 33



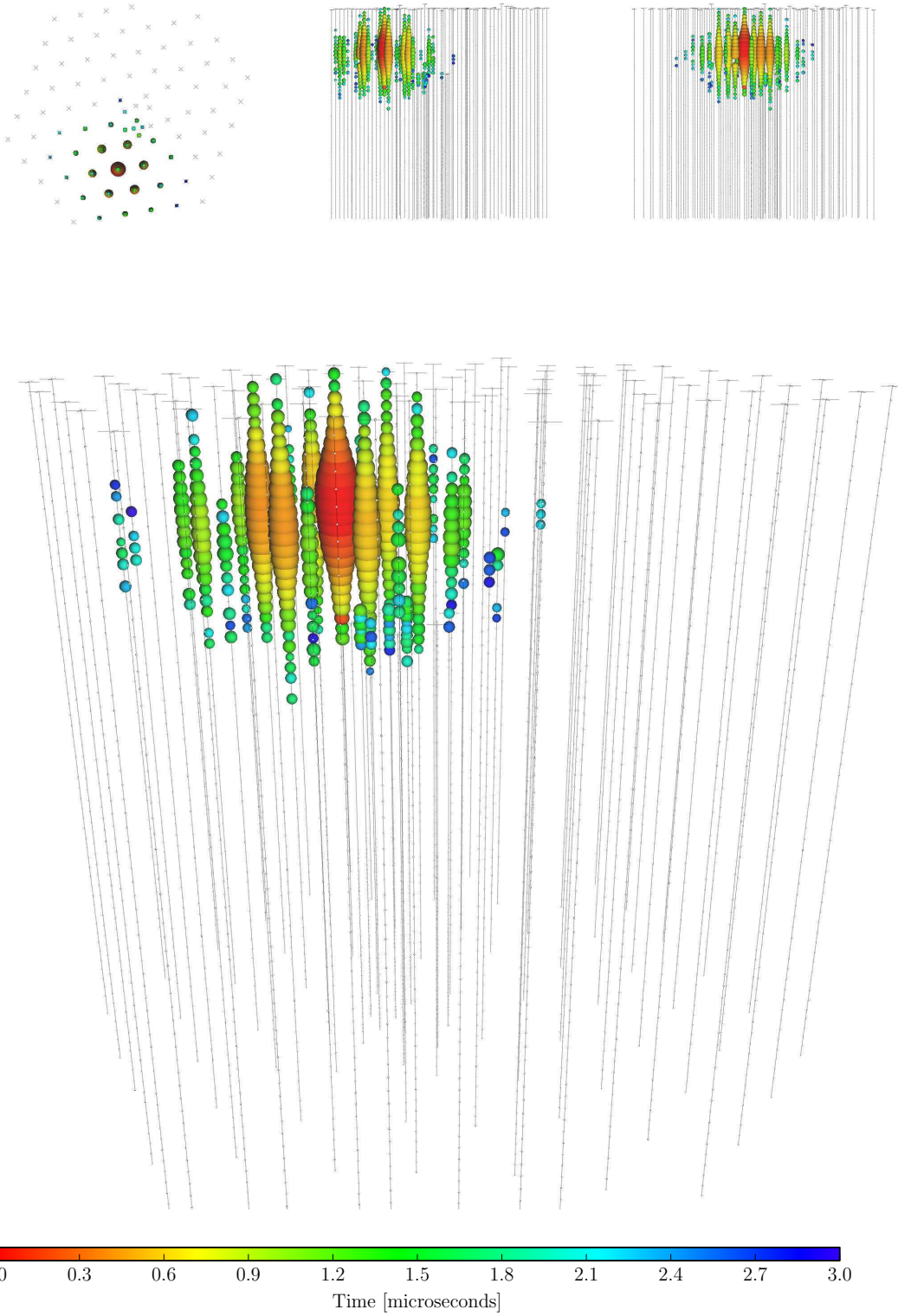
Deposited Energy (TeV)	Time (MJD)	Declination (deg.)	RA (deg.)	Med. Ang. Resolution (deg.)	Topology
385^{+46}_{-49}	56221.3424023	7.8	292.5	13.5	Shower

EVENT 34



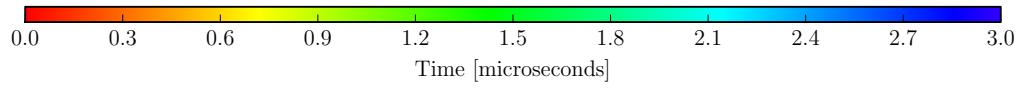
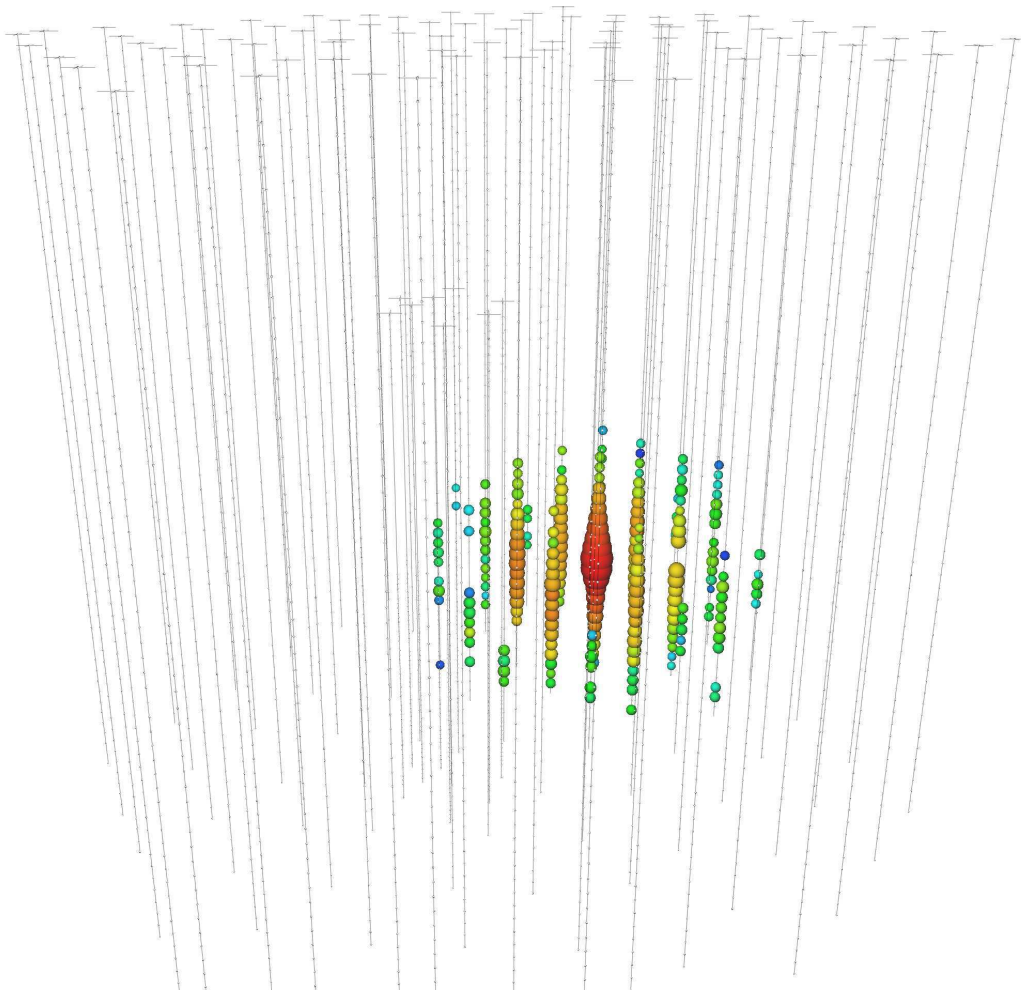
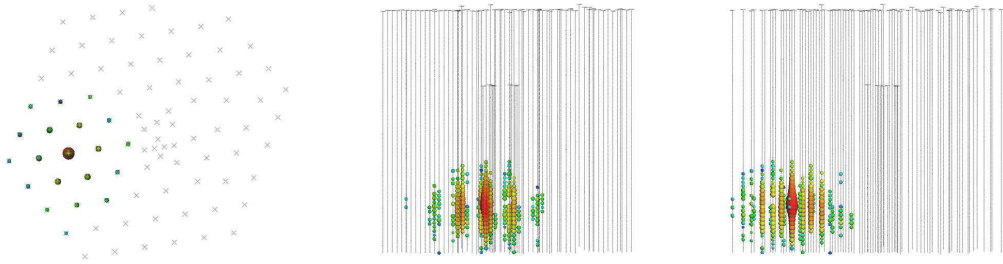
Deposited Energy (TeV)	Time (MJD)	Declination (deg.)	RA (deg.)	Med. Ang. Resolution (deg.)	Topology
$42.1^{+6.5}_{-6.3}$	56228.6055226	31.3	323.4	42.7	Shower

EVENT 35



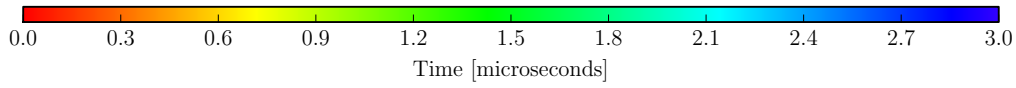
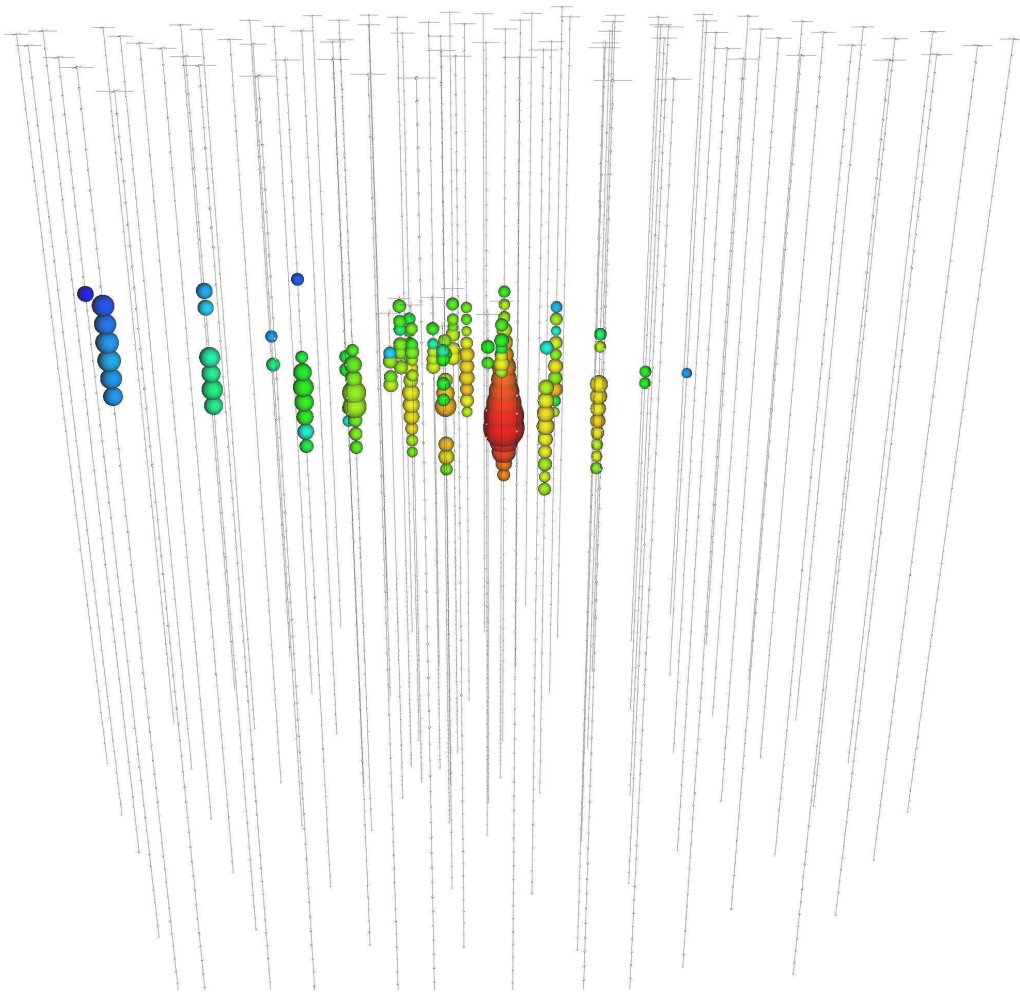
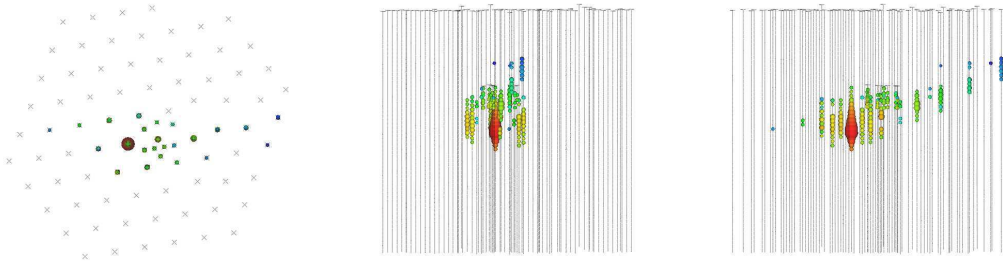
Deposited Energy (TeV)	Time (MJD)	Declination (deg.)	RA (deg.)	Med. Ang. Resolution (deg.)	Topology
2004^{+236}_{-262}	56265.1338677	-55.8	208.4	15.9	Shower

EVENT 36



Deposited Energy (TeV)	Time (MJD)	Declination (deg.)	RA (deg.)	Med. Ang. Resolution (deg.)	Topology
$28.9^{+3.0}_{-2.6}$	56308.1642740	-3.0	257.7	11.7	Shower

EVENT 37



Deposited Energy (TeV)	Time (MJD)	Declination (deg.)	RA (deg.)	Med. Ang. Resolution (deg.)	Topology
$30.8^{+3.3}_{-3.5}$	56390.1887627	20.7	167.3	$\lesssim 1.2$	Track

An absence of neutrinos associated with cosmic-ray acceleration in γ -ray bursts

IceCube Collaboration*

Very energetic astrophysical events are required to accelerate cosmic rays to above 10^{18} electronvolts. GRBs (γ -ray bursts) have been proposed as possible candidate sources^{1–3}. In the GRB ‘fireball’ model, cosmic-ray acceleration should be accompanied by neutrinos produced in the decay of charged pions created in interactions between the high-energy cosmic-ray protons and γ -rays⁴. Previous searches for such neutrinos found none, but the constraints were weak because the sensitivity was at best approximately equal to the predicted flux^{5–7}. Here we report an upper limit on the flux of energetic neutrinos associated with GRBs that is at least a factor of 3.7 below the predictions^{4,8–10}. This implies either that GRBs are not the only sources of cosmic rays with energies exceeding 10^{18} electronvolts or that the efficiency of neutrino production is much lower than has been predicted.

Neutrinos from GRBs are produced in the decay of charged pions produced in interactions between high-energy protons and the intense γ -ray background within the GRB fireball, for example in the Δ -resonance process $p + \gamma \rightarrow \Delta^+ \rightarrow n + \pi^+$ (p , proton; γ , photon (here γ -ray); Δ^+ , delta baryon; n , neutron; π^+ , pion). When these pions decay via $\pi^+ \rightarrow \mu^+ \nu_\mu$ and $\mu^+ \rightarrow e^+ \nu_e \bar{\nu}_\mu$, they produce a flux of high-energy muon neutrinos (ν_μ) and electron neutrinos (ν_e), coincident with the γ -rays, and peaking at energies of several hundred tera-electronvolts (TeV)^{4,11} (μ^+ , antimuon; e^+ , positron). Such a flux should be detectable using km³-scale instruments like the IceCube neutrino telescope^{12,13} (Supplementary Fig. 1). Owing to maximal mixing between muon neutrinos and tau neutrinos, neutrinos from pion decay in and around GRBs will arrive at Earth in an equal mixture of flavours. We focus here only on muons produced in ν_μ charged-current interactions. As the downgoing cosmic-ray muon background presents challenges for the identification of neutrino-induced muons, we achieve our highest sensitivity for upgoing neutrinos (from sources in the northern sky). However, the tight constraint of spatial and temporal coincidence with a GRB allows some sensitivity even in the southern sky. One of the two analyses presented here therefore includes Southern Hemisphere GRBs during the 2009–10 IceCube run.

The results presented here were obtained while IceCube was under construction, using 40 and 59 of the 86 photomultiplier strings of the final detector (Supplementary Fig. 1), which took data from April 2008 to May 2009 and from May 2009 until May 2010, respectively. During the 59-string data-taking period, 190 GRBs were observed and reported by γ -ray observatory satellites via the GRB Coordinates Network¹⁴, with 105 in the northern sky. Of those GRBs, 9 were not included in our catalogue owing to detector downtime associated with construction and calibration. Two additional GRBs were included from test runs before the start of the official 59-string run. 117 northern-sky GRBs were included from the 40-string period⁷ to compute the final combined result. GRB positions were taken from the satellite with the smallest reported error, which is typically smaller than the IceCube resolution. The GRB γ -ray emission start (T_{start}) and stop (T_{stop}) times were taken by finding the earliest and latest time reported for γ -ray emission.

As in our previous study⁷, we conducted two analyses of the IceCube data. In a model-dependent search, we examine data during the period of γ -ray emission reported by any satellite for neutrinos with the energy spectrum predicted from the γ -ray spectra of individual GRBs^{6,9}. The model-independent analysis searches more generically for neutrinos on wider timescales, up to the limit of sensitivity to small numbers of events at ± 1 day, or with different spectra. Both analyses follow the methods used in our previous work⁷, with the exception of slightly changed event selection and the addition of the Southern Hemisphere to the model-independent search. Owing to the large background of downgoing muons from the southern sky, the Southern Hemisphere analysis is sensitive mainly to higher-energy events (Supplementary Fig. 3). Systematic uncertainties from detector effects have been included in the reported limits from both analyses, and were estimated by varying the simulated detector response and recomputing the limit, with the dominant factor being the efficiency of the detector’s optical sensors.

In the 59-string portion of the model-dependent analysis, no events were found to be both on-source and on time (within 10° of a GRB and between T_{start} and T_{stop}). From the individual burst spectra^{6,9} with an assumed ratio of energy in protons to energy in electrons $\epsilon_p/\epsilon_e = 10$ (ref. 6), 8.4 signal events were predicted from the combined 2-year data set and a final upper limit (90% confidence) of 0.27 times the predicted flux can be set (Fig. 1). This corresponds to a 90% upper limit on ϵ_p/ϵ_e of 2.7, with other parameters held fixed, and includes a 6% systematic uncertainty from detector effects.

In the model-independent analysis, two candidate events were observed at low significance, one 30 s after GRB 091026A (event 1) and another 14 h before GRB 091230A (most theories predict neutrinos within a few minutes of the burst). Subsequent examination showed they had both triggered several tanks in the IceTop surface air shower array, and are thus very probably muons from cosmic-ray air showers. In Fig. 2 are shown limits from this analysis on the normalization of generic power-law muon neutrino spectra expected from shock acceleration at Earth as a function of the size of the time window $|\Delta t|$, which is the difference between the neutrino arrival time and the first reported satellite trigger time. As a cross-check on both results, the limit from this analysis on the average individual burst spectra^{6,9} during the time window corresponding to the median duration of the bursts in the sample (28 s) was 0.24 times the predicted flux, within 10% of the model-dependent analysis.

Assuming that the GRBs in our catalogue are a representative sample of a total of 667 per year (ref. 7), we can scale the emission from our catalogue to the emission of all GRBs. The resulting limits can then be compared to the expected neutrino rates from models that assume that GRBs are the main sources of ultra-high-energy cosmic rays^{4,8,10}, with sampling biases of the same order as model uncertainties in the flux predictions^{15,16}. Limits from the model-independent analysis on fluxes of this type are shown in Fig. 3.

These limits exclude all tested models^{4,8–10} with their standard parameters and uncertainties on those parameters (Figs 1, 3). The models are different formulations of the same fireball phenomenology,

*Lists of participants and their affiliations appear at the end of the paper.

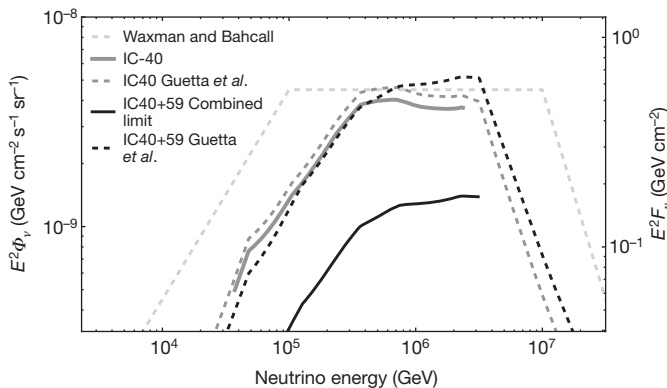


Figure 1 | Comparison of results to predictions based on observed γ -ray spectra. The summed flux predictions normalized to γ -ray spectra^{6,9,19} are shown as a function of neutrino energy (E) in dashed lines, with the dark grey dashed line labelled ‘IC40 Guetta *et al.*’ showing the flux prediction for the 40-string portion of the analysis, and the black dashed line labelled ‘IC40+59 Guetta *et al.*’ showing the prediction for the full two-year dataset. The cosmic ray normalized Waxman-Bahcall flux^{4,20} is also shown for reference as the pale grey dashed line. 90% confidence upper limits on these spectra are shown as solid lines, with the grey line labelled ‘IC40 limit’ showing the previous IceCube result⁶ and the black ‘IC40+IC59 Combined’ line showing the result from the full dataset (this work). The predicted neutrino flux, when normalized to the γ -rays^{6,9}, is proportional to the ratio of energy in protons to that in electrons, which are presumed responsible for the γ -ray emission (ϵ_p/ϵ_e , here the standard 10). The flux shown is slightly modified⁶ from the original calculation⁹. Φ_ν (left vertical axis) is the average neutrino flux at Earth, obtained by scaling the summed predictions from the bursts in our sample (F_ν , right vertical axis) by the global GRB rate (here 667 bursts yr^{-1} ; ref. 7). The first break in the neutrino spectrum is related to the break in the photon spectrum measured by the satellites, and the threshold for photo-pion production, whereas the second break corresponds to the onset of synchrotron losses of muons and pions. Not all of the parameters used in the neutrino spectrum calculation are measurable from every burst. In such cases, benchmark values⁷ were used for the unmeasured parameters. Data shown here were taken from the result of the model-dependent analysis.

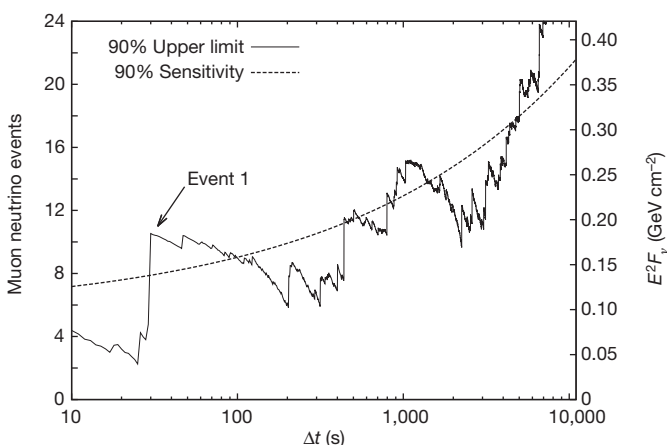


Figure 2 | Upper limits on E^{-2} power-law muon neutrino fluxes. Limits were calculated using the Feldman-Cousins method²¹ from the results of the model-independent analysis. The left-hand y-axis shows the total number of expected ν_μ events, while the right-hand y-axis (F_ν) is the same as in Fig. 1. A time window of Δt implies observed events arriving between t seconds before the burst and t afterward. The variation of the upper limit (solid line labelled ‘90% Upper limit’) with Δt reflects statistical fluctuations in the observed background rate, as well as the presence of individual events of varying quality. The dashed line labelled ‘90% Sensitivity’ shows the upper limit that would have been obtained with exactly the mean expected background. The event at 30 s (event 1) is consistent with background and believed to be a cosmic-ray air shower.

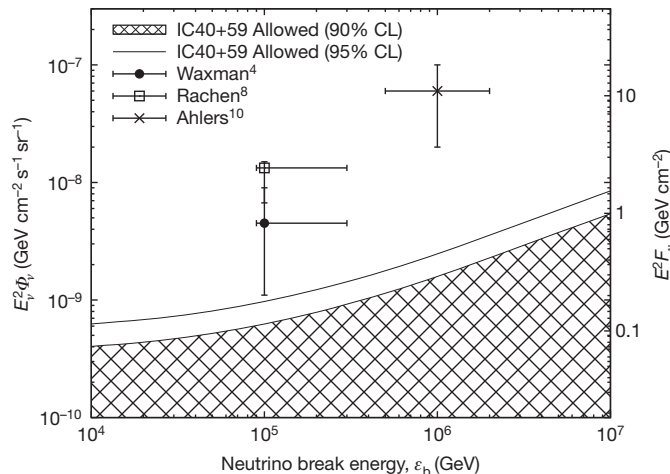


Figure 3 | Compatibility of some neutrino flux predictions based on cosmic ray production in GRBs with observations. The cross-hatched area (‘IC40+59 Allowed 90% CL’) shows the 90% confidence allowed values of the neutrino flux (vertical axes, as in Fig. 1) versus the neutrino break energy (ϵ_b) in comparison to model predictions with estimated uncertainties (points); the solid line labelled ‘IC50+59 Allowed 95% CL’ shows the upper bound of the 95% confidence allowed region. Data were taken from the model-independent analysis from the time window corresponding to the median duration of the GRBs in our catalogue ($|\Delta t| = 28$ s). Spectra are represented here as broken power laws ($\Phi_\nu \cdot \{E^{-1}/\epsilon_b, E < \epsilon_b; E^{-2}, E > \epsilon_b\}$) with a break energy ϵ_b corresponding to the Δ resonance for p - γ interactions in the frame of the shock. The muon flux in IceCube is dominated by neutrinos with energies around the first break (ϵ_b). As such, the upper break, due to synchrotron losses of π^+ , has been neglected here, as its presence or absence does not contribute significantly to the muon flux and thus does not have a significant effect on the presented limits. ϵ_b is related to the bulk Lorentz factor Γ ($\epsilon_b \propto \Gamma^2$); all of the models shown assume $\Gamma \approx 300$. The value of Γ corresponding to 10^7 GeV is $>1,000$ for all models. Vertical axes are related to the accelerated proton flux by the model-dependent constant of proportionality f_π . For models assuming a neutron-decay origin of cosmic rays (ref. 8 and ref. 10) f_π is independent of Γ ; for others (ref. 4) $f_\pi \propto \Gamma^{-4}$. Error bars on model predictions are approximate and were taken either from the original papers, where included¹⁰, or from the best-available source in the literature¹⁵ otherwise. The errors are due to uncertainties in f_π and in fits to the cosmic-ray spectrum. Waxman-Bahcall⁴ (circle) and Rachen⁸ (box) fluxes were calculated using a cosmic-ray density of $(1.5\text{--}3) \times 10^{44}$ $\text{erg Mpc}^{-3} \text{yr}^{-1}$, with 3×10^{44} the central value²⁰. The Ahlers¹⁰ model is shown with a cross. CL, confidence level.

producing neutrinos at proton–photon (p - γ) interactions in internal shocks. The remaining parameter spaces available to each model therefore have similar characteristics: either a low density of high-energy protons, below that required to explain the cosmic rays, or a low efficiency of neutrino production.

In the GRB fireball, protons are believed to be accelerated stochastically in collisions of internal shocks in the expanding GRB. The neutrino flux is proportional to the rate of p - γ interactions, and so to the proton content of the burst by a model-dependent factor. Assuming a model-dependent proton ejection efficiency, the proton content can in turn be related to the measured flux of high-energy cosmic rays if GRBs are the cosmic-ray sources. Limits on the neutrino flux for cosmic-ray-normalized models are shown in Fig. 3; each model prediction has been normalized to a value consistent with the observed ultra-high-energy cosmic-ray flux. The proton density can also be expressed as a fraction of the observed burst energy, directly limiting the average proton content of the bursts in our catalogue (Fig. 4).

An alternative is to reduce the neutrino production efficiency, for example by modifying the physics included in the predictions^{16,17} or by increasing the bulk Lorentz boost factor, Γ . Increasing Γ increases the proton energy threshold for pion production in the observer frame, thereby reducing the neutrino flux owing to the lower proton density at higher energies. Astrophysical lower limits on Γ are established by pair

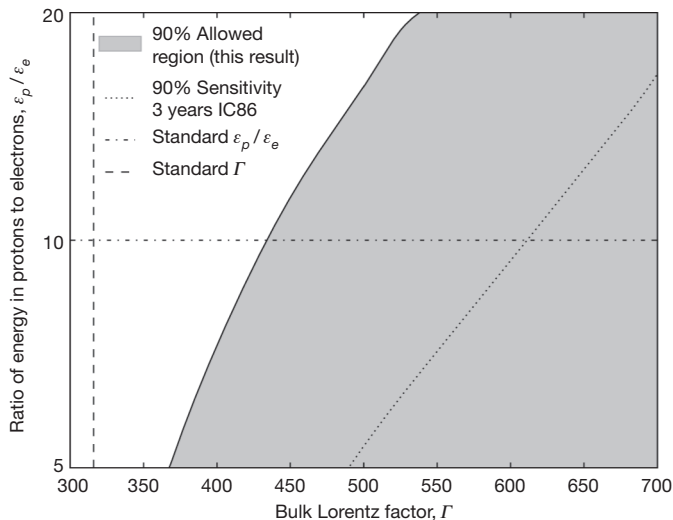


Figure 4 | Constraints on fireball parameters. The shaded region, based on the result of the model dependent analysis, shows the values of GRB energy in protons and the average fireball bulk Lorentz factor for modelled fireballs^{6,9} allowed by this result at the 90% confidence level. The dotted line indicates the values of the parameters to which the completed IceCube detector (IC86) is expected to be sensitive after 3 years of data. The standard values considered⁹ are shown as dashed-dotted and dashed lines and are excluded by this analysis. Note that the quantities shown here are model-dependent.

production arguments⁹, but the upper limit is less clear. Although it is possible that Γ may take values of up to 1,000 in some unusual bursts, the average value is probably lower (usually assumed^{6,9} to be around 300) and the non-thermal γ -ray spectra from the bursts set a weak constraint that $\Gamma \lesssim 2,000$ (ref. 18). For all considered models, with uniform fixed proton content, very high average values of Γ are required to be compatible with our limits (Figs 3, 4).

In the case of models where cosmic rays escape from the GRB fireball as neutrons^{8,10}, the neutrons and neutrinos are created in the same $p-\gamma$ interactions, directly relating the cosmic-ray and neutrino fluxes and removing many uncertainties in the flux calculation. In these models, Γ also sets the threshold energy for production of cosmic rays. The requirement that the extragalactic cosmic rays be produced in GRBs therefore does set a strong upper limit on Γ : increasing it beyond $\sim 3,000$ causes the proton flux from GRBs to disagree with the measured cosmic-ray flux above 4×10^{18} eV, where extragalactic cosmic rays are believed to be dominant. Limits on Γ in neutron-origin models from this analysis ($\gtrsim 2000$, Fig. 3) are very close to this point, and as a result all such models—in which all extragalactic cosmic rays are emitted from GRBs as neutrons—are now largely ruled out.

Although the precise constraints are model-dependent, the general conclusion is the same for all the versions of fireball phenomenology we have considered here: either the proton density in GRB fireballs is substantially below the level required to explain the highest-energy cosmic rays or the physics in GRB shocks is significantly different from that included in current models. In either case, our current theories of cosmic-ray and neutrino production in GRBs will need to be revisited.

Received 6 January; accepted 8 March 2012.

1. Waxman, E. Cosmological gamma-ray bursts and the highest energy cosmic rays. *Phys. Rev. Lett.* **75**, 386–389 (1995).
2. Vietri, M. The acceleration of ultra-high-energy cosmic rays in gamma-ray bursts. *Astrophys. J.* **453**, 883–889 (1995).
3. Milgrom, M. & Usov, V. Possible association of ultra-high-energy cosmic-ray events with strong gamma-ray bursts. *Astrophys. J.* **449**, L37 (1995).
4. Waxman, E. & Bahcall, J. High energy neutrinos from cosmological gamma-ray burst fireballs. *Phys. Rev. Lett.* **78**, 2292–2295 (1997).
5. Avrorin, A. V. *et al.* Search for neutrinos from gamma-ray bursts with the Baikal neutrino telescope NT200. *Astron. Lett.* **37**, 692–698 (2011).
6. Abbasi, R. *et al.* Search for muon neutrinos from gamma-ray bursts with the IceCube neutrino telescope. *Astrophys. J.* **710**, 346–359 (2010).

7. Abbasi, R. *et al.* Limits on neutrino emission from gamma-ray bursts with the 40 string IceCube detector. *Phys. Rev. Lett.* **106**, 141101 (2011).
8. Rachen, J. P. & Mészáros, P. in *Fourth Huntsville Gamma-Ray Burst Symposium* (eds Meegan, C. A., Preece, R. D. & Koshut, T. M.) 776–780 (American Institute of Physics Conference Proceedings Vol. 428, 1998).
9. Guetta, D., Hooper, D., Alvarez-Muñiz, J., Halzen, F. & Reuveni, E. Neutrinos from individual gamma-ray bursts in the BATSE catalog. *Astropart. Phys.* **20**, 429–455 (2004).
10. Ahlers, M., Gonzalez-Garcia, M. C. & Halzen, F. GRBs on probation: testing the UHE CR paradigm with IceCube. *Astropart. Phys.* **35**, 87–94 (2011).
11. Becker, J. K. High-energy neutrinos in the context of multimessenger astrophysics. *Phys. Rep.* **458**, 173–246 (2008).
12. Abbasi, R. *et al.* The IceCube data acquisition system: signal capture, digitization, and timestamping. *Nucl. Instrum. Methods Phys. Res. A* **601**, 294–316 (2009).
13. Ahrens, J. *et al.* Muon track reconstruction and data selection techniques in AMANDA. *Nucl. Instrum. Methods Phys. Res. A* **524**, 169–194 (2004).
14. GCN: The Gamma-ray Coordinates Network. <http://gcn.gsfc.nasa.gov>.
15. Guetta, D., Spada, M. & Waxman, E. On the neutrino flux from gamma-ray bursts. *Astrophys. J.* **559**, 101–109 (2001).
16. Baerwald, P., Hümmer, S. & Winter, W. Systematics in aggregated neutrino fluxes and flavor ratios from gamma-ray bursts. *Astropart. Phys.* **35**, 508–529 (2012).
17. Hümmer, S., Baerwald, P. & Winter, W. Neutrino emission from gamma-ray burst fireballs, revised. Preprint at <http://arXiv.org/abs/1112.1076> (2011).
18. Mészáros, P. Gamma-ray bursts. *Rep. Prog. Phys.* **69**, 2259–2321 (2006).
19. Becker, J. K., Stamatikos, M., Halzen, F. & Rhode, W. Coincident GRB neutrino flux predictions: implications for experimental UHE neutrino physics. *Astropart. Phys.* **25**, 118–128 (2006).
20. Waxman, E. Astrophysical sources of high energy neutrinos. *Nucl. Phys. B Proc., Suppl.* **118**, 353–362 (2003).
21. Feldman, G. J. & Cousins, R. D. Unified approach to the classical statistical analysis of small signals. *Phys. Rev. D* **57**, 3873–3889 (1998).

Supplementary Information is linked to the online version of the paper at www.nature.com/nature.

Acknowledgements We acknowledge support from the following agencies: US NSF, Office of Polar Programs, and US NSF, Physics Division; University of Wisconsin Alumni Research Foundation; the GLOW and OSG grids; US DOE, NERSC; the LONI grid; NSERC, Canada; Swedish Research Council, Swedish Polar Research Secretariat, SNIC, K. and A. Wallenberg Foundation, Sweden; German Ministry for Education and Research, Deutsche Forschungsgemeinschaft; Research Department of Plasmas with Complex Interactions (Bochum), Germany; FSR, FWO Odysseus, IWT, BELSPO, Belgium; University of Oxford, UK; Marsden Fund, New Zealand; Australian Research Council; JSPS, Japan; SNSF, Switzerland. J.P.R. was supported by the Capes Foundation, Brazil; N.W. by the NSF GRFP. We thank S. Hümmer, E. Waxman and W. Winter for discussions.

Author Contributions The IceCube observatory was designed and constructed by the IceCube Collaboration and the IceCube Project. It is operated by the IceCube Collaboration, who set science goals. Data processing and calibration, Monte Carlo simulations of the detector and of theoretical models, and data analyses were performed by a large number of IceCube members who also discussed and approved the scientific results. This manuscript was written by P.R. and N.W. and subjected to an internal collaboration-wide review process. All authors approved the final version of the manuscript.

Author Information Reprints and permissions information is available at www.nature.com/reprints. The authors declare no competing financial interests. Readers are welcome to comment on the online version of this article at www.nature.com/nature. Correspondence and requests for materials should be addressed to N.W. (nwhitehorn@icecube.wisc.edu) or to P.R. (redlpete@icecube.umd.edu).

IceCube Collaboration R. Abbasi¹, Y. Abdou², T. Abu-Zayyad³, M. Ackermann⁴, J. Adams⁵, J. A. Aguilar⁶, M. Ahlers¹, D. Altman⁷, K. Andeen¹, J. Auffenberg¹, X. Bai^{8,9}, M. Baker¹, S. W. Barwick¹⁰, R. Bay¹¹, J. L. Bazo Alba⁴, K. Beattie¹², J. J. Beatty^{13,14}, S. Bechet¹⁵, J. K. Becker¹⁶, K.-H. Becker¹⁷, M. Bell¹⁸, M. L. Benabderrahmane⁴, S. BenZvi¹, J. Berdermann⁴, P. Berghaus⁸, D. Berley¹⁹, E. Bernardini⁴, D. Bertrand¹⁵, D. Z. Besson²⁰, D. Bindig¹⁷, M. Bissok⁴, E. Blaufuss¹⁹, J. Blumenthal⁷, D. J. Boersma⁷, C. Boehm²¹, D. Bose²², S. Böse²³, O. Botner²⁴, L. Braye²², A. M. Brown⁵, S. Buhtink²², K. S. Caballero-Mora¹⁸, M. Carson², M. Casier²², D. Chirkin¹, B. Christy¹⁹, F. Clevermann²⁵, S. Cohen²⁶, C. Colnard²⁷, D. F. Cowen^{18,28}, A. H. Cruz Silva⁴, M. V. D'Agostino¹¹, M. Danninger²¹, J. Daughhetee²⁹, J. C. Davis¹³, C. De Clercq²², T. Degner²³, F. Descamps², P. Desiati¹, G. de Vries-Uiterweerd², T. DeYoung¹⁸, J. C. Díaz-Vélez¹, M. Dierckx¹⁵, J. Dreyer¹⁶, J. P. Dum¹, M. Dunkman¹⁸, J. Eisch¹, R. W. Ellsworth¹⁹, O. Engdegård²⁴, S. Euler⁷, P. A. Evenson⁸, O. Fadiran¹, A. R. Fazely³⁰, A. Fedynitch¹⁶, J. Feintzeig¹, T. Feusels², K. Filimonov¹¹, C. Finley²¹, T. Fischer-Wasels¹⁷, S. Flis²¹, A. Franckowiak²³, R. Franke⁴, T. K. Gaisser³, J. Gallagher³¹, L. Gerhardt^{11,12}, L. Gladstone¹, T. Glüsenkamp⁴, A. Goldschmidt¹², J. A. Goodman¹⁹, D. Góra⁴, D. Grant³², T. Griesel³³, A. Groß²⁷, S. Grullon¹, M. Gurtner¹⁷, C. Ha^{11,12}, A. Haj Ismail², A. Hallgren²⁴, F. Halzen¹, K. Han⁴, K. Hanson¹⁵, D. Heereman¹⁵, D. Heinen⁷, K. Helbing¹⁷, R. Hellauer¹⁹, S. Hickford⁵, G. C. Hill³⁴, K. D. Hoffman¹⁹, B. Hoffmann⁷, A. Homeier²³, K. Hoshina¹, W. Huelsnitz^{19,35}, J.-P. Hülþ⁷, P. O. Hulth²¹, K. Hultqvist²¹, S. Hussain⁸, A. Ishihara³⁶, E. Jacob⁴, J. Jacobsen¹, G. S. Japaridze³⁷, H. Johansson²¹, A. Kappes³⁸, T. Karg¹⁷, A. Karle¹, J. Kiryluk³⁹, F. Kislak⁴, S. R. Klein^{11,12}, J.-H. Köhne²⁵, G. Köhnen⁴⁰, H. Kolanoski³⁸, L. Köpke³³, S. Kopper¹⁷, D. J.

Koskinen¹⁸, M. Kowalski²³, T. Kowarik³³, M. Krasberg¹, G. Kroll³³, J. Kunnen²², N. Kurahashi¹, T. Kuwabara⁸, M. Labare²², K. Laihem⁷, H. Landsman¹, M. J. Larson¹⁸, R. Lauer⁴, J. Lünemann³³, J. Madsen³, A. Marotta¹⁵, R. Maruyama¹, K. Mase³⁶, H. S. Matis¹², K. Meagher¹⁹, M. Merck¹, P. Mészáros^{18,28}, T. Meures¹⁵, S. Miarecki^{11,12}, E. Middell⁴, N. Milke²⁵, J. Miller²⁴, T. Montaruli^{6,41}, R. Morse¹, S. M. Movit²⁸, R. Nahnhauser⁴, J. W. Nam¹⁰, U. Naumann¹⁷, S. C. Nowicki³², D. R. Nygren¹², S. Odrowski²⁷, A. Olivas¹⁹, M. Olivo¹⁶, A. O'Murchadha¹, S. Panknin²³, L. Paul⁷, C. Pérez de los Heros²⁴, A. Piegsa³³, D. Pieloth²⁵, J. Posselt¹⁷, P. B. Price¹¹, G. T. Przybylski¹², K. Rawlins⁴², P. Redl¹⁹, E. Resconi^{27,43}, W. Rhode²⁵, M. Ribordy²⁶, M. Richman¹⁹, B. Riedel¹, A. Rizzo²², J. P. Rodrigues¹, F. Rothmaier³³, C. Rott¹³, T. Ruhe²⁵, D. Rutledge¹⁸, B. Ruzybayev⁸, D. Ryckbosch², H.-G. Sander³³, M. Santander¹, S. Sarkar⁴⁴, K. Schatto³³, T. Schmidt¹⁹, S. Schöneberg¹⁶, A. Schönwald⁴, A. Schukraft⁷, L. Schulte²³, A. Schultes¹⁷, O. Schulz^{27,43}, M. Schunck¹, D. Seckel⁸, B. Semburg¹⁷, S. H. Seo²¹, Y. Sestayo²⁷, S. Seunarine⁴⁵, A. Silvestri¹⁰, M. W. E. Smith¹⁸, G. M. Spiczak³, C. Spiering⁴, M. Stamatikos^{13,46}, T. Stanev⁸, T. Stezelberger¹², R. G. Stokstad¹², A. Stöbl⁴, E. A. Strahler²², R. Ström²⁴, M. Stürer²³, G. W. Sullivan¹⁹, H. Taavola²⁴, I. Taboada²⁹, A. Tamburro⁸, S. Ter-Antonyan³⁰, S. Tilav⁸, P. A. Toale⁴⁷, S. Toscano¹, D. Tosi⁴, N. van Eijndhoven²², A. Van Overloop², J. van Santen¹, M. Vehring⁷, M. Voge²³, C. Walck²¹, T. Waldenmaier³⁸, M. Wallraff⁷, M. Walter⁴, R. Wasserman¹⁸, Ch. Weaver¹, C. Wendt¹, S. Westerhoff¹, N. Whitehorn¹, K. Wiebe³³, C. H. Wiebusch², D. R. Williams⁴⁷, R. Wischniewski⁴, H. Wissing¹⁹, M. Wolf²¹, T. R. Wood³², K. Woschnagg¹¹, C. Xu⁸, D. L. Xu⁴⁷, X. W. Xu³⁰, J. P. Yanez⁴, G. Yodh¹⁰, S. Yoshida³⁶, P. Zarzhitsky⁴⁷ & M. Zol²¹

¹Department of Physics, University of Wisconsin, Madison, Wisconsin 53706, USA.

²Department of Physics and Astronomy, University of Gent, B-9000 Gent, Belgium.

³Department of Physics, University of Wisconsin, River Falls, Wisconsin 54022, USA.

⁴DESY, D-15735 Zeuthen, Germany. ⁵Department of Physics and Astronomy, University of Canterbury, Private Bag 4800, Christchurch, New Zealand. ⁶Département de physique nucléaire et corpusculaire, Université de Genève, CH-1211 Genève, Switzerland. ⁷Ill. Physikalisches Institut, RWTH Aachen University, D-52056 Aachen, Germany. ⁸Bartol Research Institute and Department of Physics and Astronomy, University of Delaware, Newark, Delaware 19716, USA. ⁹Department of Physics, South Dakota School of Mines and Technology, Rapid City, South Dakota 57701, USA. ¹⁰Department of Physics and Astronomy, University of California, Irvine, California 92697, USA. ¹¹Department of Physics, University of California, Berkeley, California 94720, USA. ¹²Lawrence Berkeley National Laboratory, Berkeley, California 94720, USA. ¹³Department of Physics and

Center for Cosmology and Astro-Particle Physics, Ohio State University, Columbus, Ohio 43210, USA. ¹⁴Department of Astronomy, Ohio State University, Columbus, Ohio 43210, USA. ¹⁵Université Libre de Bruxelles, Science Faculty CP230, B-1050 Brussels, Belgium.

¹⁶Fakultät für Physik & Astronomie, Ruhr-Universität Bochum, D-44780 Bochum, Germany. ¹⁷Department of Physics, University of Wuppertal, D-42119 Wuppertal, Germany. ¹⁸Department of Physics, Pennsylvania State University, University Park, Pennsylvania 16802, USA. ¹⁹Department of Physics, University of Maryland, College Park, Maryland 20742, USA. ²⁰Department of Physics and Astronomy, University of Kansas, Lawrence, Kansas 66045, USA. ²¹Oskar Klein Centre and Department of Physics, Stockholm University, SE-10691 Stockholm, Sweden. ²²Vrije Universiteit Brussel, Dienst ELEM, B-1050 Brussels, Belgium. ²³Physikalisches Institut, Universität Bonn, Nussallee 12, D-53115 Bonn, Germany. ²⁴Department of Physics and Astronomy, Uppsala University, Box 516, S-75120 Uppsala, Sweden. ²⁵Department of Physics, TU Dortmund University, D-44221 Dortmund, Germany. ²⁶Laboratory for High Energy Physics, École Polytechnique Fédérale, CH-1015 Lausanne, Switzerland. ²⁷Max-Planck-Institut für Kernphysik, D-69177 Heidelberg, Germany. ²⁸Department of Astronomy and Astrophysics, Pennsylvania State University, University Park, Pennsylvania 16802, USA. ²⁹School of Physics and Center for Relativistic Astrophysics, Georgia Institute of Technology, Atlanta, Georgia 30332, USA. ³⁰Department of Physics, Southern University, Baton Rouge, Louisiana 70813, USA. ³¹Department of Astronomy, University of Wisconsin, Madison, Wisconsin 53706, USA. ³²Department of Physics, University of Alberta, Edmonton, Alberta, Canada T6G 2G7. ³³Institute of Physics, University of Mainz, Staudinger Weg 7, D-55099 Mainz, Germany. ³⁴School of Chemistry & Physics, University of Adelaide, Adelaide 5005, South Australia, Australia. ³⁵Los Alamos National Laboratory, Los Alamos, New Mexico 87545, USA. ³⁶Department of Physics, Chiba University, Chiba 263-8522, Japan. ³⁷CTSPPS, Clark-Atlanta University, Atlanta, Georgia 30314, USA.

³⁸Institut für Physik, Humboldt-Universität zu Berlin, D-12489 Berlin, Germany. ³⁹Department of Physics and Astronomy, Stony Brook University, Stony Brook, New York 11794-3800, USA. ⁴⁰Université de Mons, 7000 Mons, Belgium. ⁴¹Dipartimento di Fisica, Sezione INFN, I-70126, Bari, Italy. ⁴²Department of Physics and Astronomy, University of Alaska Anchorage, 3211 Providence Drive, Anchorage, Alaska 99508, USA. ⁴³Technische Universität München, D-85748 Garching, Germany. ⁴⁴Department of Physics, University of Oxford, 1 Keble Road, Oxford OX1 3NP, UK. ⁴⁵Department of Physics, University of the West Indies, Cave Hill Campus, Bridgetown BB11000, Barbados. ⁴⁶NASA Goddard Space Flight Center, Greenbelt, Maryland 20771, USA. ⁴⁷Department of Physics and Astronomy, University of Alabama, Tuscaloosa, Alabama 35487, USA.

Evidence for High-Energy Extraterrestrial Neutrinos at the IceCube Detector

IceCube Collaboration*

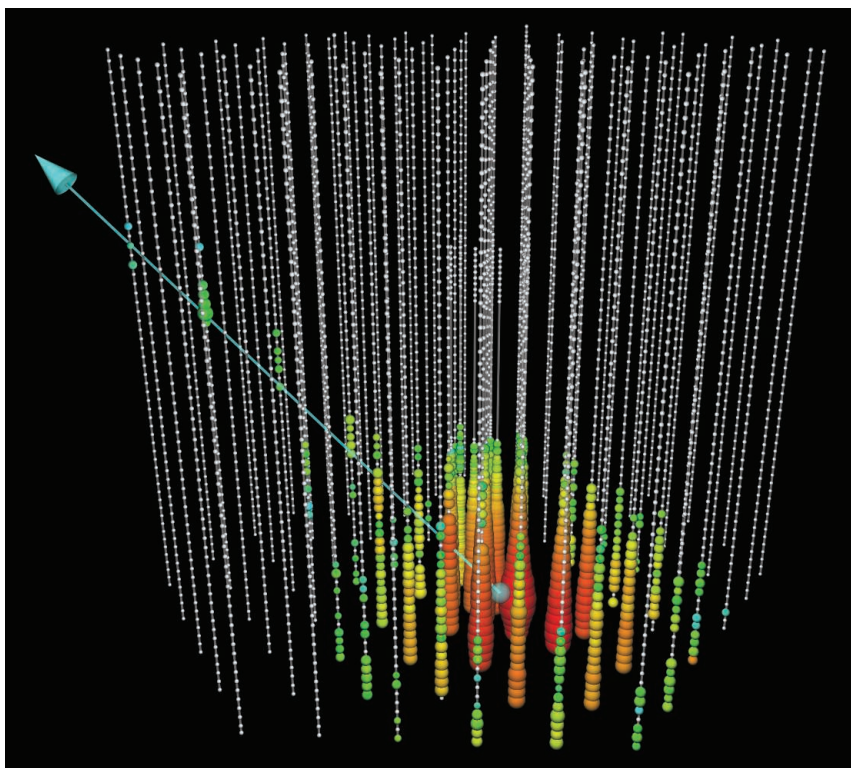
Introduction: Neutrino observations are a unique probe of the universe's highest-energy phenomena: Neutrinos are able to escape from dense astrophysical environments that photons cannot and are unambiguous tracers of cosmic ray acceleration. As protons and nuclei are accelerated, they interact with gas and background light near the source to produce subatomic particles such as charged pions and kaons, which then decay, emitting neutrinos. We report on results of an all-sky search for these neutrinos at energies above 30 TeV in the cubic kilometer Antarctic IceCube observatory between May 2010 and May 2012.

Methods: We have isolated a sample of neutrinos by rejecting background muons from cosmic ray showers in the atmosphere, selecting only those neutrino candidates that are first observed in the detector interior rather than on the detector boundary. This search is primarily sensitive to neutrinos from all directions above 60 TeV, at which the lower-energy background atmospheric neutrinos become rare, with some sensitivity down to energies of 30 TeV. Penetrating muon backgrounds were evaluated using an in-data control sample, with atmospheric neutrino predictions based on theoretical modeling and extrapolation from previous lower-energy measurements.

Results: We observed 28 neutrino candidate events (two previously reported), substantially more than the $10.6^{+5.0}_{-3.6}$ expected from atmospheric backgrounds, and ranging in energy from 30 to 1200 TeV. With the current level of statistics, we did not observe significant clustering of these events in time or space, preventing the identification of their sources at this time.

Discussion: The data contain a mixture of neutrino flavors compatible with flavor equipartition, originate primarily from the Southern Hemisphere where high-energy neutrinos are not absorbed by Earth, and have a hard energy spectrum compatible with that expected from cosmic ray accelerators. Within our present knowledge, the directions, energies, and topologies of these events are not compatible with expectations for terrestrial processes, deviating at the 4σ level from standard assumptions for the atmospheric background. These properties, in particular the north-south asymmetry, generically disfavor any purely atmospheric explanation for the data. Although not compatible with an atmospheric explanation, the data do match expectations for an origin in unidentified high-energy galactic or extragalactic neutrino accelerators.

A 250 TeV neutrino interaction in IceCube. At the neutrino interaction point (bottom), a large particle shower is visible, with a muon produced in the interaction leaving up and to the left. The direction of the muon indicates the direction of the original neutrino.



READ THE FULL ARTICLE ONLINE

<http://dx.doi.org/10.1126/science.1242856>

Cite this article as IceCube Collaboration, *Science* 342, 1242856 (2013). DOI: 10.1126/science.1242856

FIGURES IN THE FULL ARTICLE

Fig. 1. Drawing of the IceCube array.

Fig. 2. Distribution of best-fit deposited energies and declinations.

Fig. 3. Coordinates of the first detected light from each event in the final sample.

Fig. 4. Distributions of the deposited energies and declination angles of the observed events compared to model predictions.

Fig. 5. Sky map in equatorial coordinates of the TS value from the maximum likelihood point source analysis.

Fig. 6. Distribution of deposited PMT charges (Q_{tot}).

Fig. 7. Neutrino effective area and volume.

SUPPLEMENTARY MATERIALS

Materials and Methods
Event Displays 1 to 28
Neutrino Effective Areas

*The list of author affiliations is available in the full article online.

Corresponding authors: C. Kopper (ckopper@icecube.wisc.edu); N. Kurahashi (naoko@icecube.wisc.edu); N. Whitehorn (nwhitehorn@icecube.wisc.edu)

Evidence for High-Energy Extraterrestrial Neutrinos at the IceCube Detector

IceCube Collaboration*

We report on results of an all-sky search for high-energy neutrino events interacting within the IceCube neutrino detector conducted between May 2010 and May 2012. The search follows up on the previous detection of two PeV neutrino events, with improved sensitivity and extended energy coverage down to about 30 TeV. Twenty-six additional events were observed, substantially more than expected from atmospheric backgrounds. Combined, both searches reject a purely atmospheric origin for the 28 events at the 4σ level. These 28 events, which include the highest energy neutrinos ever observed, have flavors, directions, and energies inconsistent with those expected from the atmospheric muon and neutrino backgrounds. These properties are, however, consistent with generic predictions for an additional component of extraterrestrial origin.

High-energy neutrino observations can provide insight into the long-standing problem of the origins and acceleration mechanisms of high-energy cosmic rays. As cosmic ray protons and nuclei are accelerated, they interact with gas and background light to produce charged pions and kaons, which then decay, emitting neutrinos with energies proportional to the energies of the high-energy protons that produced them. These neutrinos can be detected on Earth in large underground detectors by the production of secondary leptons and hadronic showers when they interact with the detector material. IceCube, a large-volume Cherenkov detector (1) made of 5160 photomultipliers (PMTs) at depths between 1450 and 2450 m in natural Antarctic ice (Fig. 1), has been designed to detect these neutrinos at TeV-PeV energies. Recently, the Fermi collaboration presented evidence for acceleration of low-energy (GeV) cosmic ray protons in supernova remnants (2); neutrino observations with IceCube would probe sources of cosmic rays at far higher energies.

A recent IceCube search for neutrinos of EeV (10^6 TeV) energy found two events at energies of 1 PeV (10^3 TeV), above what is generally expected from atmospheric backgrounds and a possible hint of an extraterrestrial source (3). Although that analysis had some sensitivity to neutrino events of all flavors above 1 PeV, it was most sensitive to ν_μ events above 10 PeV from the region around the horizon, above which the energy threshold increased sharply to 100 PeV. As a result, it had only limited sensitivity to the type of events found, which were typical of either ν_e or neutral current events and at the bottom of the detectable energy range, preventing a detailed understanding of the population from which they arose and an answer to the question of their origin.

Here, we present a follow-up analysis designed to characterize the flux responsible for these

events by conducting an exploratory search for neutrinos at lower energies with interaction vertices well contained within the detector volume, discarding events containing muon tracks originating outside of IceCube (Fig. 1). This event selection (see Materials and Methods) allows the resulting search to have approximately equal sensitivity to neutrinos of all flavors and from all directions. We obtained nearly full efficiency for interacting neutrinos above several hundred TeV, with some sensitivity extending to neutrino energies as low as 30 TeV (see Materials and Methods). The data-taking period is shared with the earlier

high-energy analysis: Data shown were taken during the first season running with the completed IceCube array (86 strings, between May 2011 and May 2012) and the preceding construction season (79 strings, between May 2010 and May 2011), with a total combined live time of 662 days.

Results

In the 2-year data set, 28 events with in-detector deposited energies between 30 and 1200 TeV were observed (Fig. 2 and Table 1) on an expected background of $10.6^{+5.0}_{-3.6}$ events from atmospheric muons and neutrinos (see Materials and Methods). The two most energetic of these were the previously reported PeV events (3). Seven events contained clearly identifiable muon tracks, whereas the remaining 21 were showerlike, consistent with neutrino interactions other than ν_μ charged current. Events containing muon tracks in general have better angular resolution, typically of better than 1 degree (4), compared to the 10 to 15 degrees typical of events without visible muons (see Materials and Methods). Four of the low-energy tracklike events started near the detector boundary and were down-going, consistent with the properties of the expected 6.0 ± 3.4 background atmospheric muons, as measured from a control sample of penetrating muons in data. One of these—the only such event in the sample—had hits in the IceTop surface air shower array compatible with its arrival time and direction in IceCube (event 28). The points at which the remaining events were first observed were uniformly distributed throughout the detector (Fig. 3). This is consistent with expectations for neutrino

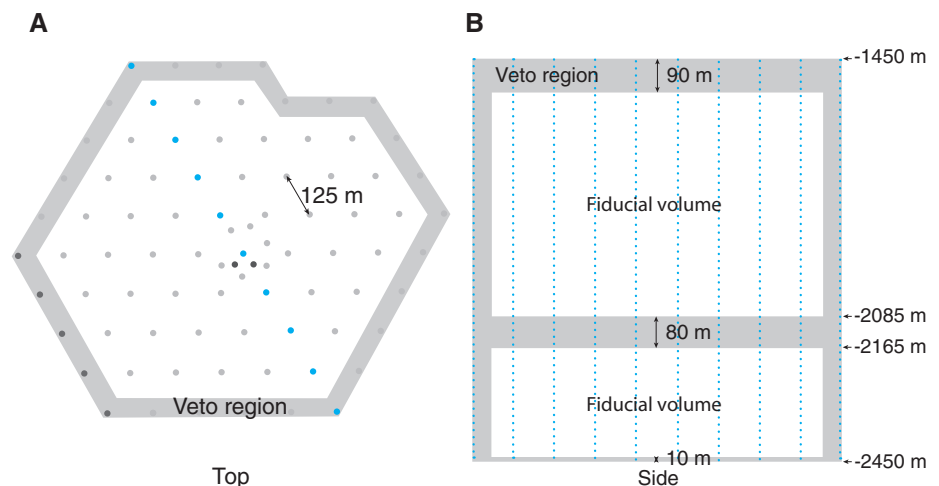


Fig. 1. Drawing of the IceCube array. Results are from the complete pictured detector for 2011 to 2012 and from a partial detector missing the dark gray strings in the bottom left corner for the 2010 to 2011 season. (A and B) The side view (B) shows a cross section of the detector indicated in the top view (A) in blue. Events producing first light in the veto region (shaded area) were discarded as entering tracks (usually from cosmic ray muons entering the detector). Most background events are nearly vertical, requiring a thick veto cap at the top of the detector. The shaded region in the middle contains ice of high dust concentration (24). Because of the high degree of light absorption in this region, near horizontal events could have entered here without being tagged at the sides of the detector without a dedicated tagging region.

*Full author list after Acknowledgments.

events and inconsistent with backgrounds from penetrating muons or with detector artifacts, which would have been expected to trace the locations of either the fiducial volume boundary or the positions of the instrumentation.

As part of our blind analysis, we tested a pre-defined fixed atmospheric-only neutrino flux

model (5), including a benchmark charm component (6), reevaluated using current measurements of the cosmic ray spectrum in this energy range (7, 8). This adds an additional 1.5 charm neutrinos to our mean background estimate and predicts, on average, 6.1 (π/K and charm) background neutrinos on top of the 6.0 ± 3.4 back-

ground muon events. Significance was evaluated on the basis of the number of events, the total collected PMT charge of each, and the events' reconstructed energies and directions (see Materials and Methods). Our procedure does not allow us to separately incorporate uncertainties on the various background components. To nevertheless obtain an indication of the range of possible significances, we calculated values relative to background-only hypotheses with charm at the level called "standard" in (6) as a benchmark flux as well as at the level of our current 90% confidence level (CL) experimental bounds (8) (corresponding to 3.8 times standard). To prevent possible confirmation bias, we split the data set into two samples. For the 26 new events reported here, using the benchmark flux, we obtain a significance of 3.3σ (one-sided). Combined using Fisher's method with the 2.8σ observation of the earlier analysis where the two highest energy events were originally reported (3), and which uses the same benchmark atmospheric neutrino flux model, we obtain a final significance for the entire data set of 28 events of 4.1σ . The same calculation performed a posteriori on all 28 events gives 4.8σ . These two final significances would be reduced to

Fig. 2. Distribution of best-fit deposited energies and declinations.

Seven of the events contain muons (crosses) with an angular resolution of about 1° , whereas the remainder are either electromagnetic (EM) or hadronic showers (filled circles) with an energy-dependent resolution of about 15° . Error bars are 68% confidence intervals including both statistical and systematic uncertainties. Energies shown are the energy deposited in the detector, assuming that all light emission is from electromagnetic showers. For ν_e charged-current events, this equals the neutrino energy; otherwise, it is a lower limit on the neutrino energy. The gap in E_{dep} between 300 TeV and 1 PeV does not appear to be significant: Gaps of this size or larger appear in 28% of realizations of the best-fit continuous power-law flux.

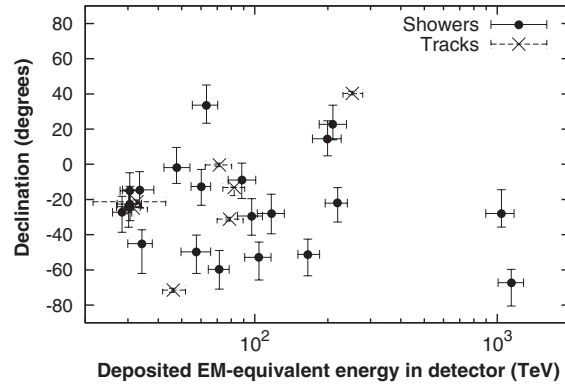


Table 1. Properties of the 28 events. Shown are the deposited electromagnetic-equivalent energy (the energy deposited by the events in IceCube assuming all light was made in electromagnetic showers), as well as the arrival time and direction of each event and its topology (track- or showerlike). The energy shown is equal to the neutrino energy for ν_e charged-current events, within experimental uncertainties, and is otherwise a lower limit on the neutrino energy because

of exiting muons or neutrinos. Errors on energy and the angle include both statistical and systematic effects. Systematic uncertainties on directions for showerlike events were determined on an individual basis; track systematic uncertainties here are equal to 1° , which is an upper limit from studies of the cosmic ray shadow of the moon (4). Additional per-event information, including event displays, can be found in the supplementary materials.

ID	Deposited energy (TeV)	Time (modified Julian date)	Declination (degrees)	Right ascension (degrees)	Median angular error (degrees)	Event type
1	$47.6^{+6.5}_{-5.4}$	55,351	-1.8	35.2	16.3	Shower
2	117^{+15}_{-15}	55,351	-28.0	282.6	25.4	Shower
3	$78.7^{+10.8}_{-8.7}$	55,451	-31.2	127.9	≤ 1.4	Track
4	165^{+20}_{-15}	55,477	-51.2	169.5	7.1	Shower
5	$71.4^{+9.0}_{-9.0}$	55,513	-0.4	110.6	≤ 1.2	Track
6	$28.4^{+2.7}_{-2.5}$	55,568	-27.2	133.9	9.8	Shower
7	$34.3^{+3.5}_{-4.3}$	55,571	-45.1	15.6	24.1	Shower
8	$32.6^{+10.3}_{-11.1}$	55,609	-21.2	182.4	≤ 1.3	Track
9	$63.2^{+7.1}_{-8.0}$	55,686	33.6	151.3	16.5	Shower
10	$97.2^{+10.4}_{-12.4}$	55,695	-29.4	5.0	8.1	Shower
11	$88.4^{+12.5}_{-10.7}$	55,715	-8.9	155.3	16.7	Shower
12	104^{+13}_{-13}	55,739	-52.8	296.1	9.8	Shower
13	253^{+26}_{-22}	55,756	40.3	67.9	≤ 1.2	Track
14	1041^{+132}_{-144}	55,783	-27.9	265.6	13.2	Shower
15	$57.5^{+8.3}_{-7.8}$	55,783	-49.7	287.3	19.7	Shower
16	$30.6^{+3.6}_{-3.5}$	55,799	-22.6	192.1	19.4	Shower
17	200^{+27}_{-27}	55,800	14.5	247.4	11.6	Shower
18	$31.5^{+4.6}_{-3.3}$	55,924	-24.8	345.6	≤ 1.3	Track
19	$71.5^{+7.0}_{-7.2}$	55,926	-59.7	76.9	9.7	Shower
20	1141^{+143}_{-133}	55,929	-67.2	38.3	10.7	Shower
21	$30.2^{+3.5}_{-3.3}$	55,937	-24.0	9.0	20.9	Shower
22	220^{+21}_{-24}	55,942	-22.1	293.7	12.1	Shower
23	$82.2^{+8.6}_{-8.4}$	55,950	-13.2	208.7	≤ 1.9	Track
24	$30.5^{+3.2}_{-2.6}$	55,951	-15.1	282.2	15.5	Shower
25	$33.5^{+4.9}_{-5.0}$	55,967	-14.5	286.0	46.3	Shower
26	210^{+29}_{-26}	55,979	22.7	143.4	11.8	Shower
27	$60.2^{+5.6}_{-5.6}$	56,009	-12.6	121.7	6.6	Shower
28	$46.1^{+5.7}_{-4.4}$	56,049	-71.5	164.8	≤ 1.3	Track

3.6σ and 4.5σ , respectively, using charm at the level of our current 90% CL experimental bound.

Discussion

Although there is some uncertainty in the expected atmospheric background rates, in particular for the contribution from charmed meson decays, the energy spectrum, zenith distribution, and shower to muon track ratio of the observed events strongly constrain the possibility that our events are entirely of atmospheric origin. Almost all of the observed excess is in showers rather than muon tracks, ruling out an increase in penetrating muon background to the level required. Atmo-

spheric neutrinos are a poor fit to the data for a variety of reasons. The observed events are much higher in energy, with a harder spectrum (Fig. 4) than expected from an extrapolation of the well-measured π/K atmospheric background at lower energies (8–10): Nine had reconstructed deposited energies above 100 TeV, with two events above 1 PeV, relative to an expected background from π/K atmospheric neutrinos of about one event above 100 TeV. Raising the normalization of this flux both violates previous limits and, because of ν_μ bias in π and K decay, predicts too many muon tracks in our data (two-thirds of tracks versus one-fourth observed).

Another possibility is that the high-energy events result from charmed meson production in air showers (6, 11). These produce higher-energy events with equal parts ν_e and ν_μ , matching our observed muon track fraction reasonably well. However, our event rates are substantially higher than even optimistic models (11) and the energy spectrum from charm production is too soft to explain the data. Increasing charm production to the level required to explain our observations violates existing experimental bounds (8). Because atmospheric neutrinos produced by any mechanism are made in cosmic ray air showers, down-going atmospheric neutrinos from the southern sky will, in general, be accompanied into IceCube by muons produced in the same parent air shower. These accompanying muons will trigger our muon veto, removing most of these events from the sample and biasing atmospheric neutrinos to the Northern Hemisphere. Most of our events, however, arrive from the south. This places a strong model-independent constraint on any atmospheric neutrino production mechanism as an explanation for our data.

By comparison, a neutrino flux produced in extraterrestrial sources would, like our data, be heavily biased toward showers because neutrino oscillations over astronomical baselines tend to equalize neutrino flavors (12, 13). An equal-flavor E^{-2} neutrino flux, for example, would be expected to produce only one-fifth of track events (see

Fig. 3. Coordinates of the first detected light from each event in the final sample. Penetrating muon events are first detected predominantly at the detector boundaries (top and right sides), where they first make light after crossing the veto layer. Neutrino events should interact uniformly throughout the approximately cylindrical detector volume, forming a uniform distribution in (r^2, z) , with the exception of interactions in the less transparent ice region marked “Dust layer,” which is treated as part of the detector boundary for purposes of our event selection. The observed events are consistent with a uniform distribution.

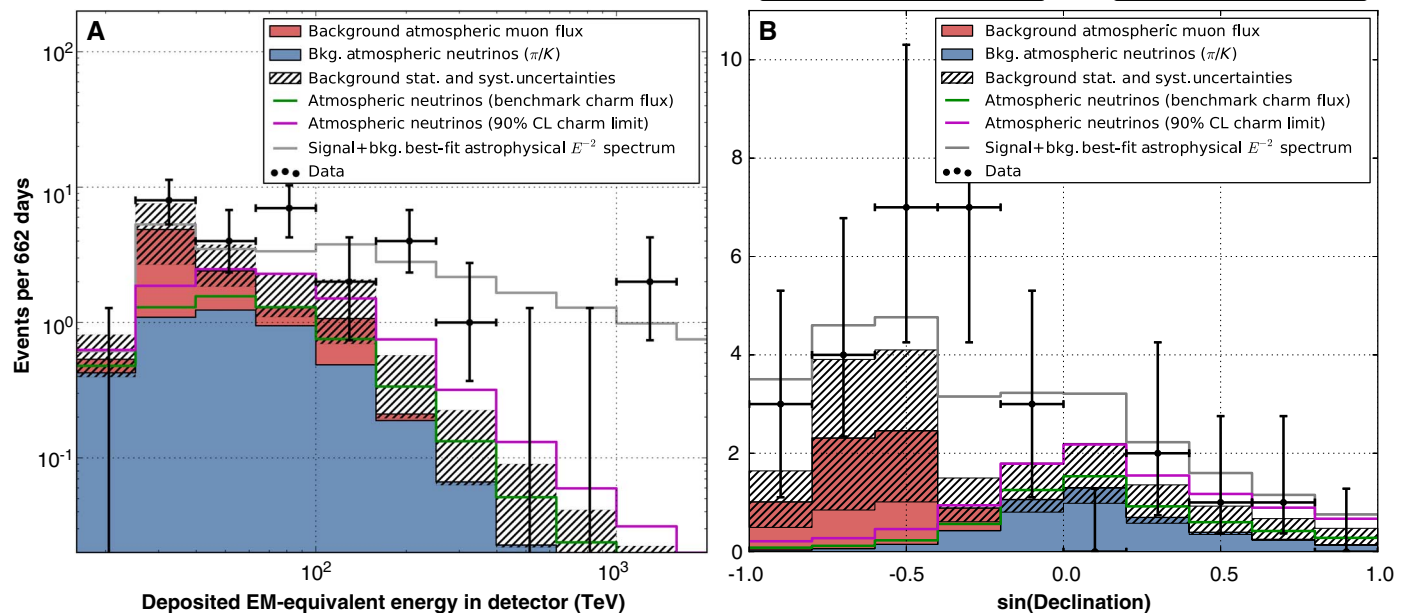
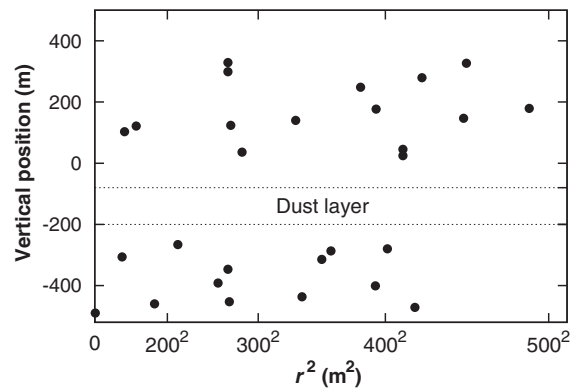


Fig. 4. Distributions of the deposited energies and declination angles of the observed events compared to model predictions. (A and B) Zenith angle entries for data (B) are the best-fit zenith position for each of the 28 events; a small number of events (Table 1) have zenith uncertainties larger than the bin widths in this figure. Energies plotted (A) are reconstructed in-detector visible energies, which are lower limits on the neutrino energy. Note that deposited energy spectra are always harder than the spectrum of the neutrinos that produced them because of the neutrino cross section increasing with energy. The expected rate of atmospheric neutrinos is shown in blue, with

atmospheric muons in red. The green line shows our benchmark atmospheric neutrino flux (see the text), and the magenta line shows the experimental 90% bound. Because of a lack of statistics from data far above our cut threshold, the shape of the distributions from muons in this figure has been determined using Monte Carlo simulations with total rate normalized to the estimate obtained from our in-data control sample. Combined statistical and systematic uncertainties on the sum of backgrounds are indicated with a hatched area. The gray line shows the best-fit E^{-2} astrophysical spectrum with a per-flavor normalization (1:1:1) of $E^2\Phi_\nu(E) = 1.2 \times 10^{-8} \text{ GeV cm}^{-2} \text{ s}^{-1} \text{ sr}^{-1}$.

Materials and Methods). The observed zenith distribution is also typical of such a flux: As a result of absorption in Earth above tens of TeV energy, most events (about 60%, depending on the energy spectrum) from even an isotropic high-energy extraterrestrial population would be expected to appear in the Southern Hemisphere. Although the zenith distribution is well explained (Fig. 4) by an isotropic flux, a slight southern excess remains, which could be explained either as a statistical fluctuation or by a source population that is either relatively small or unevenly distributed through the sky.

This discussion can be quantified by a global fit of the data to a combination of the π/K atmospheric neutrino background, atmospheric neutrinos from charmed meson decays, and an isotropic equal-flavor extraterrestrial power-law flux. With the normalizations of all components free to float, this model was fit to the two-dimensional deposited energy and zenith distribution of the data (Fig. 2) in the range of $60 \text{ TeV} < E_{\text{dep}} < 2 \text{ PeV}$, above most of the expected background (Fig. 4). The data are well described in this energy range by an E^{-2} neutrino spectrum with a per-flavor normalization of $E^2\Phi(E) = (1.2 \pm 0.4) \times 10^{-8} \text{ GeV cm}^{-2} \text{ s}^{-1} \text{ sr}^{-1}$. Although it is difficult to substantively constrain the shape of the spectrum with our current limited statistics, a flux at this level would have been expected to generate an additional three to six events in the 2 to 10 PeV range; the lack of such events in the sample may indicate either a softer spectrum (the best fit is $E^{-2.2 \pm 0.4}$) or the presence of a break or cutoff at PeV energies. When limited to only atmospheric neutrinos, the best fit to the data would require a charm flux 4.5 times larger than the current experimental 90% CL upper bounds (8) and even then is disfavored at 4σ with respect to a fit allowing an extraterrestrial contribution.

Search for Neutrino Sources

To search for spatial clustering, indicating possible neutrino sources, we conducted a maximum likelihood point source analysis (14). At each point in the sky, we tested a point source hypothesis based on full-sky uncertainty maps for each event obtained from the reconstruction. This yields a sky map of test statistic values [$\text{TS} = 2\log(L/L_0)$, where L is the maximized likelihood and L_0 is the likelihood under the null hypothesis], which reflects any excess concentration of events relative to a flat background distribution (Fig. 5). To account for trials due to searching the whole sky, we estimate the significance of the highest TS observed by performing the same analysis on the data with the right ascension of the events randomized. The final significance is then the fraction of these randomized maps that have a TS value anywhere in the sky as high or higher than that observed in data. The chance probability calculated this way is independent of Monte Carlo simulation. Therefore, the significance obtained is against the hypothesis that all events in this sample are uniformly distributed in right ascen-

sion, rather than the significance of a cluster of events above predicted backgrounds. Note that because muon tracks have much smaller angular uncertainties than showers, their presence can skew the highest TS values and overshadow clusters of shower events. To correct for this effect, and because muon events are more likely to be atmospheric background, we repeated every clustering analysis described here twice: once with the full 28 events and once with only the 21 shower events.

When using all events, the likelihood map reveals no significant clustering compared to randomized maps. For the shower events, the coordinates with the highest TS are at right ascension = 281° , declination = -23° (galactic longitude $l = +12^\circ$, latitude $b = -9^\circ$). Five events, including the second highest energy event in the sample, contribute to the main part of the excess with two others nearby. The fraction of randomized data sets that yield a similar or higher TS at this exact spot is 0.2%. (At the exact location of the galactic center, the fraction is 5.4%.) The final significance, estimated as the fraction of randomized maps with a similar or higher TS anywhere in the sky, is 8%. This degree of clustering may be compatible with a source or sources in the galactic center region, but the poor angular resolution for showers and the wide distribution of the events do not allow the identification of any sources at this time.

Two other spatial clustering analyses were defined a priori. We performed a galactic plane correlation study using the full directional reconstruction uncertainty for each event to define the degree of overlap with the plane. The plane width was chosen to be $\pm 2.5^\circ$ on the basis of TeV gamma-ray observations (15). A multicluster search using the sum of log-likelihood values at every

local maximum in the likelihood map was also conducted. Neither of these analyses yielded significant results.

In addition to clustering of events in space, we performed two tests for clustering of events in time that calculate significances by comparing the actual arrival times to event times drawn from a random uniform distribution throughout the live time. Because many sources (16–18) are expected to produce neutrinos in bursts, identification of such a time cluster could allow association with a source without reference to the limited angular resolution of most of the observed neutrinos. When using all events, no significant time cluster was observed. Furthermore, each spatial cluster in Fig. 5 containing more than one event was tested individually for evidence of time clustering. Of the eight regions tested, the most significant was a pair that includes the highest energy shower in the sample, but was still compatible with random fluctuations. The five shower events of the densest cluster show no significant overall time clustering.

Materials and Methods

Event Selection

Backgrounds for cosmic neutrino searches arise entirely from interactions of cosmic rays in Earth's atmosphere. These produce secondary muons that penetrate into underground neutrino detectors from above, as well as atmospheric neutrinos that reach the detector from all directions because of the low neutrino cross section, which allows them to penetrate Earth from the opposite hemisphere. These particles are produced in the decays of secondary π and K mesons; at high energies, a flux from the prompt decay of charmed mesons

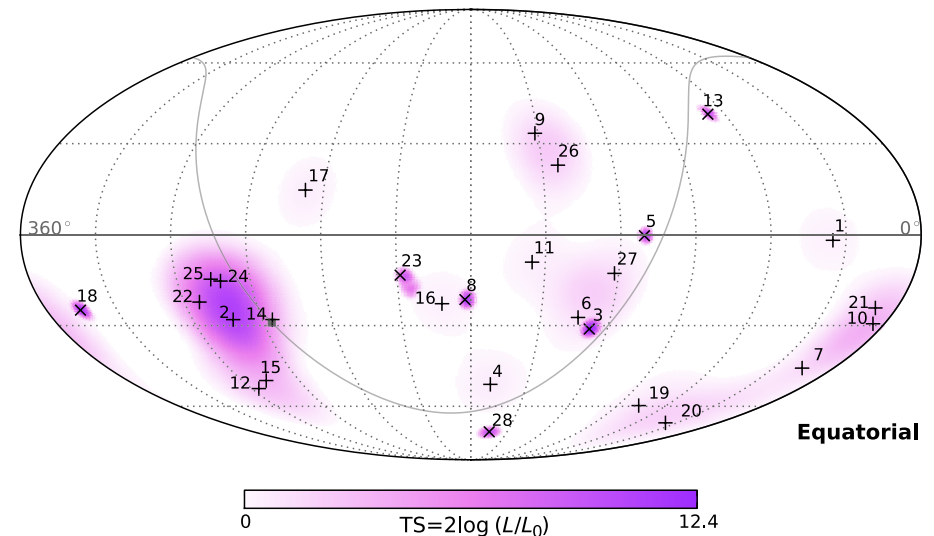


Fig. 5. Sky map in equatorial coordinates of the TS value from the maximum likelihood point source analysis. The most significant cluster consists of five events—all showers and including the second highest energy event in the sample—with a final significance of 8%. This is not sufficient to identify any neutrino sources from the clustering study. The galactic plane is shown as a curved gray line with the galactic center at the bottom left denoted by a filled gray square. Best-fit locations of individual events (listed in Table 1) are indicated with vertical crosses (+) for showers and angled crosses (x) for muon tracks.

(19) has been anticipated, although not yet observed. Cosmic ray muons are the dominant background in IceCube because of their high rate of 3 kHz. These can be removed from the sample either by using only up-going events, by limiting searches to events at very high energies (above ~ 1 PeV) (20, 21), or, as here, by requiring an observation of the neutrino interaction vertex using the detector boundary to detect and veto entering muon tracks.

Neutrino candidates were selected by finding events that originated within the detector interior. Included were those events that produced their first light within the fiducial volume (Fig. 1) and were of sufficiently high energy such that an entering muon track would have been reliably identified if present. In particular, we required that each event have fewer than three of its first 250 observed photoelectrons detected in the veto region. In addition, we required that the event produce at least 6000 photoelectrons overall to

ensure that statistical fluctuations in the light yield were low enough for entering muons to reliably produce light in the veto region. This event selection rejects 99.999% of the muon background above 6000 photoelectrons (Fig. 6) while retaining nearly all neutrino events interacting within the fiducial volume at energies above a few hundred TeV (Fig. 7). This selection is largely independent of neutrino flavor, event topology, or arrival direction. It also removes 70% of atmospheric neutrinos (22) in the Southern Hemisphere, where atmospheric neutrinos are usually accompanied into the detector by muons produced in the same parent air shower. To prevent confirmation bias, we conducted a blind analysis designed on a subsample of 10% of the full data set.

Event Reconstruction

Neutrino interactions in IceCube have two primary topologies: showers and muon tracks. Showers are created by secondary leptons and hadronic

fragmentation in ν_e and ν_τ charged-current interactions and by neutral-current interactions of neutrinos of all flavors. At the relevant energies (≥ 50 TeV), showers, including tracks left by τ leptons, have a length of roughly 10 m in ice and are, to a good approximation, point sources of light (23). Secondary muon tracks are created primarily in ν_μ charged-current interactions along with a hadronic shower at the neutrino interaction vertex, and have a typical range on the order of kilometers, larger than the dimensions of the detector. Note that, for a flux consisting of a mixture of flavors, this implies that showers will be the dominant topology because ν_μ CC represents only a small fraction of the total event rate: For an equally mixed E^{-2} spectrum, about 80% of the observed events would appear as showers.

Although the distribution of hit PMTs in the detector is approximately spherical for shower events, the detailed timing patterns of the photons in the individual PMTs retain the memory of the direction of the primary lepton. Comparison of these distributions with expectations from simulated showers yields a typical median angular resolution of 10° to 15° . Resolution on deposited energy, from the recorded waveform amplitudes, is typically 10 to 15%. In events with a muon track, the extension of the track in the detector provides a much tighter constraint on direction than the shapes of the waveforms alone, improving angular resolution greatly to better than 1° (4). Energy reconstruction only yields a lower limit on neutrino energy as a result of the energy removed from the detector by escaping muons and neutrinos. All quoted directional and energy reconstruction uncertainties are dominated by a systematic component arising from uncertainties in the optical properties of the ice (24) and the optical sensitivity of the PMTs (25).

Atmospheric Muon Background

Remaining atmospheric muon background comes from tracks that produce too little light at the edge of the detector to be vetoed and instead emit their first detected photons in the interior volume, mimicking a starting neutrino. These events usually produce an observable muon track in the detector like that from a ν_μ charged-current event. Much more rarely, catastrophic energy loss processes such as muon bremsstrahlung can create a showerlike signal, especially in the corners of the detector where the exiting muon track may not be observed.

The veto passing rate for throughgoing muons, and therefore the total muon background in the analysis, can be evaluated directly from the data by implementing a two-layer anticoincidence detector. Entering events can be tagged with high efficiency using the outer layer of IceCube; the rate of these tagged events that pass the next veto layer can be used as a control sample to evaluate the rate at which muons are detected by a single detector layer as a function of observed light yield. This per-layer probability can be used to estimate the final background rate after application

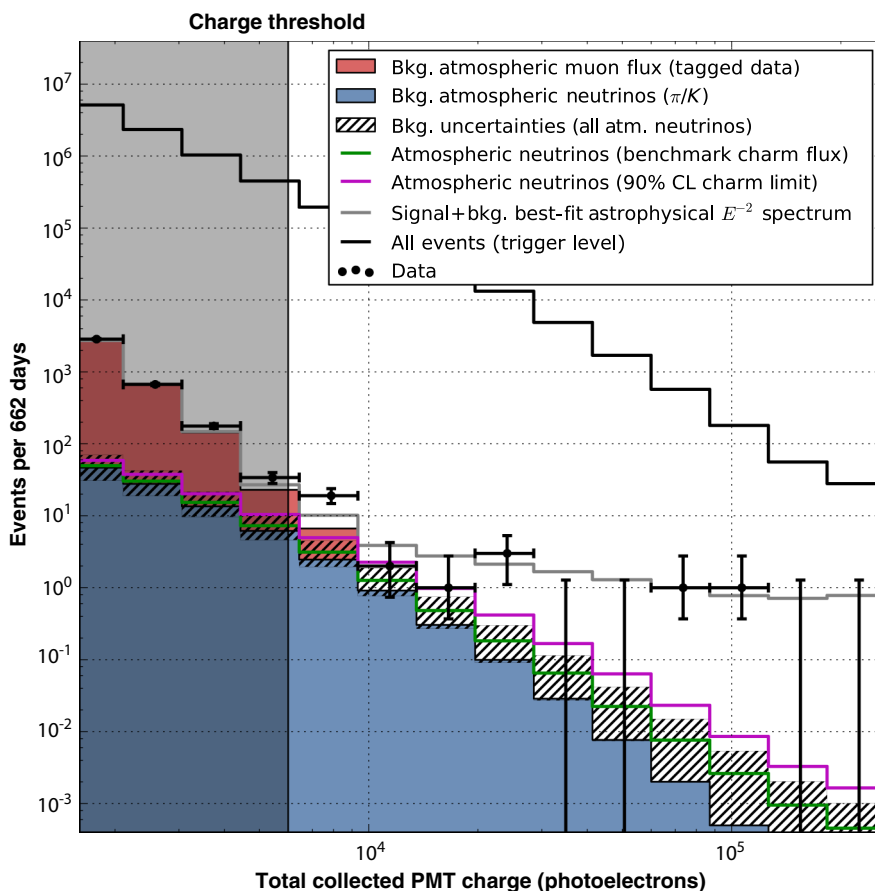


Fig. 6. Distribution of deposited PMT charges (Q_{tot}). Muons at higher total charges are less likely to pass the veto layer undetected, causing the muon background (red, estimated from data) to fall faster than the overall trigger rate (uppermost line). The data events in the unshaded region, at $Q_{\text{tot}} > 6000$, are the events reported in this work, with error bars indicating 68% Feldman-Cousins intervals. The best-fit E^{-2} astrophysical spectrum (gray line) and atmospheric neutrino flux (blue) have been determined using Monte Carlo simulations, with the hatched region showing current experimental uncertainties on the atmospheric neutrino background. The largest of these uncertainties is neutrinos from charmed meson decays, a flux that has yet to be observed and is thus not included in the blue region; the hatched region includes the best experimental 1σ upper limit (8). For scale, two specific charm levels are also shown: a benchmark theoretical model (6) (green line) and the experimental 90% CL upper bound (8) (magenta line).

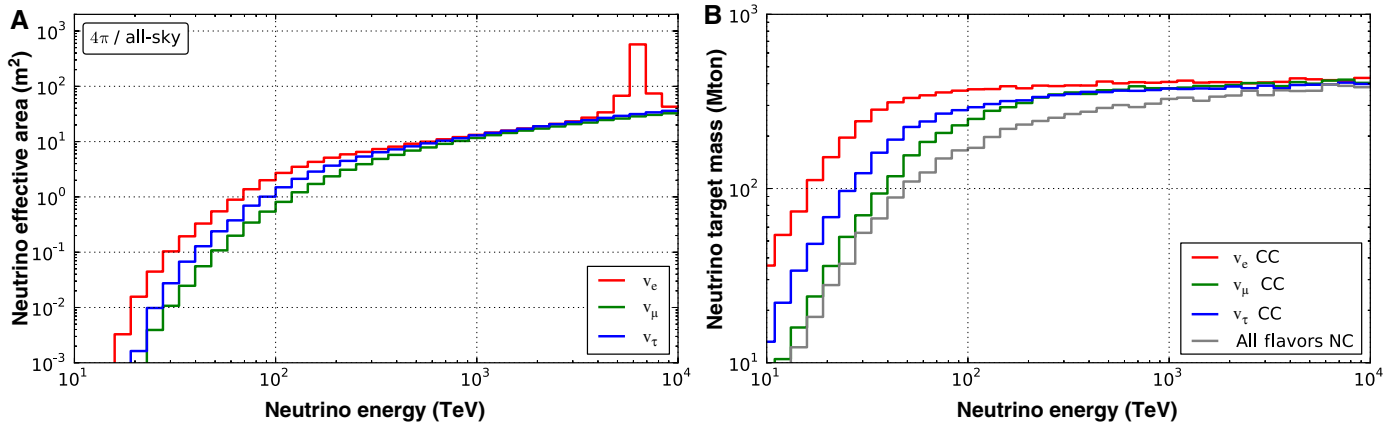


Fig. 7. Neutrino effective area and volume. Event rates can be obtained by multiplying the effective areas by 4π , by the sum of ν and $\bar{\nu}$ fluxes, and by the live time of 662 days. **(A)** Neutrino effective areas for each flavor assuming an equal flux of neutrinos and antineutrinos and averaged over all arrival angles. At 6.3 PeV, resonant W production on atomic electrons increases sensitivity to ν_e . The effective area includes effects from attenuation of

neutrinos in Earth (28), relevant at energies above 100 TeV. **(B)** Effective target mass as a function of energy. The deposited energy threshold in this search causes some flavor bias at low energies because of missing energy in escaping particles from ν_μ and ν_τ charged-current events. For ν_e charged-current events, where all the neutrino energy is visible in the detector, full efficiency is reached above 100 TeV.

of a geometrical correction factor of ~ 2 for the larger size of the analysis fiducial volume compared to the deep interior fiducial volume (after two veto layers). The resulting predicted veto passing rate agrees well with data at low energies, where we expect the event rate to be background-dominated (Fig. 6). In our signal region above 6000 photoelectrons, we observed three tagged events passing the inner veto and so predict 6.0 ± 3.4 veto-penetrating muon events in the 2-year data set.

Atmospheric Neutrinos

Atmospheric neutrino backgrounds, including an as-yet unobserved component from charmed meson decays, were estimated on the basis of a parametrization of the atmospheric neutrino flux (5, 7), consistent with previous IceCube measurements of the Northern Hemisphere muon neutrinos (8). We have also included a suppression of the atmospheric neutrino background from the Southern Hemisphere, resulting from the fact that accompanying high-energy muons produced in the same air shower can trigger our muon veto if they penetrate to the depth of the detector. Here, we have extended previous analytic calculations (22) of this suppression factor using the CORSIKA (26) air shower simulation to determine the fraction of atmospheric neutrinos accompanied at depth by muons above 10 TeV, at which they will be reliably detected by our muon veto. This factor is a strong function of neutrino energy and angle, with the strongest suppression expected at high energies and most downward angles. The suppression factor, bounded above at 90% to cover uncertainties in hadronic interaction models, was then folded with the Northern Hemisphere spectrum to predict the Southern Hemisphere event rate.

This produces an estimate of the atmospheric neutrino background of $4.6^{+3.7}_{-1.2}$ events in the 662-day live time. These events would be concentrated near the energy threshold of the anal-

ysis because of the steeply falling atmospheric neutrino spectrum. Uncertainties in the atmospheric neutrino background are dominated by the flux from charmed meson decays, which is too small to have been observed thus far and is currently bounded above experimentally by a 1σ upper limit of 3.4 events (8). The spectrum and composition of cosmic rays and models of hadronic interactions contribute a rate uncertainty at the relevant energies of $^{+30\%}_{-20\%}$, which dominates the uncertainties in the π/K component of the spectrum (27). The measured 5% uncertainty in the electromagnetic energy scale and detector linearity contributes a proportional $\pm 15\%$ uncertainty to the atmospheric background rates. Given the charge threshold, uncertainty in the light yield of hadronic showers, which is less well constrained, can affect the estimated background neutrino rate. However, the light yield for a hadronic shower is smaller than the well-known light yield for an electromagnetic shower at the same energy, limiting any resulting increase in the background rate to no larger than 30%.

Blind Calculation of Significance

We evaluated the significance of the excess over atmospheric backgrounds on the basis of both the total rate and properties of the observed events. From each event, the total deposited PMT charge, reconstructed energy, and direction were used to compute tail probabilities relative to the atmospheric muon and neutrino backgrounds. Overall significance was computed using the product of the per-event probabilities as a test statistic.

The muon background probability was computed as the fraction of the expected background with deposited charge greater than observed. Above the highest charge event in the control sample, we set an upper limit on the passing rate by assuming a constant veto efficiency. Similarly, the likelihood ratio between an isotropic E^{-2} astrophysical flux and the expected atmospheric neutrino back-

ground in declination and deposited energy was calculated for each event after folding with the observed reconstruction uncertainties, and the probability for an atmospheric neutrino event to have a larger value than observed was computed. Because our control sample of background muon events has limited statistics, we cannot produce a detailed map of the energies and angles of the penetrating muon background. For this reason, the muon and neutrino background probabilities were combined by taking the maximum of the two as the statistic for each event, which will somewhat underestimate the significance of any excess.

References and Notes

- IceCube Collaboration, First year performance of the IceCube neutrino telescope. *Astropart. Phys.* **26**, 155–173 (2006). doi: [10.1016/j.astropartphys.2006.06.007](https://doi.org/10.1016/j.astropartphys.2006.06.007)
- Fermi-LAT Collaboration, Detection of the characteristic pion-decay signature in supernova remnants. *Science* **339**, 807–811 (2013). doi: [10.1126/science.1231160](https://doi.org/10.1126/science.1231160) PMID: [23413352](https://pubmed.ncbi.nlm.nih.gov/23413352/)
- IceCube Collaboration, First observation of PeV-energy neutrinos with IceCube. *Phys. Rev. Lett.* **111**, 021103 (2013). doi: [10.1103/PhysRevLett.111.021103](https://doi.org/10.1103/PhysRevLett.111.021103) PMID: [23889381](https://pubmed.ncbi.nlm.nih.gov/23889381/)
- IceCube Collaboration, Observation of the cosmic-ray shadow of the Moon with IceCube arXiv:1305.6811 (2013). <http://arxiv.org/abs/1305.6811>
- M. Honda, T. Kajita, K. Kasahara, S. Midorikawa, T. Sanuki, Calculation of atmospheric neutrino flux using the interaction model calibrated with atmospheric muon data. *Phys. Rev. D* **75**, 043006 (2007). doi: [10.1103/PhysRevD.75.043006](https://doi.org/10.1103/PhysRevD.75.043006)
- R. Enberg, M. H. Reno, I. Sarcevic, Prompt neutrino fluxes from atmospheric charm. *Phys. Rev. D* **78**, 043005 (2008). doi: [10.1103/PhysRevD.78.043005](https://doi.org/10.1103/PhysRevD.78.043005)
- T. K. Gaisser, Spectrum of cosmic-ray nucleons, kaon production, and the atmospheric muon charge ratio. *Astropart. Phys.* **35**, 801–806 (2012). doi: [10.1016/j.astropartphys.2012.02.010](https://doi.org/10.1016/j.astropartphys.2012.02.010)
- IceCube Collaboration, A view of prompt atmospheric neutrinos with IceCube. *Nucl. Phys. B (Proc. Suppl.)* **237–238**, 266–268 (2013). doi: [10.1016/j.nuclphysbs.2013.04.105](https://doi.org/10.1016/j.nuclphysbs.2013.04.105)
- IceCube Collaboration, Search for a diffuse flux of astrophysical muon neutrinos with the IceCube

- 40-string detector. *Phys. Rev. D* **84**, 082001 (2011). doi: [10.1103/PhysRevD.84.082001](https://doi.org/10.1103/PhysRevD.84.082001)
10. IceCube Collaboration, Measurement of the atmospheric ν_e flux in IceCube. *Phys. Rev. Lett.* **110**, 151105 (2013). doi: [10.1103/PhysRevLett.110.151105](https://doi.org/10.1103/PhysRevLett.110.151105)
11. E. V. Bugaev, V. A. Naumov, S. I. Sinegovsky, E. S. Zaslavskaya, Prompt leptons in cosmic rays. *Nuov. Cim.* **12**, 41–73 (1989). doi: [10.1007/BF02509070](https://doi.org/10.1007/BF02509070)
12. S. Choubey, W. Rodejohann, Flavor composition of ultrahigh energy neutrinos at source and at neutrino telescopes. *Phys. Rev. D* **80**, 113006 (2009). doi: [10.1103/PhysRevD.80.113006](https://doi.org/10.1103/PhysRevD.80.113006)
13. S. Pakvasa, W. Rodejohann, T. J. Weiler, Flavor ratios of astrophysical neutrinos: Implications for precision measurements. *J. High Energy Phys.* **2**, 005 (2008). doi: [10.1088/1126-6708/2008/02/005](https://doi.org/10.1088/1126-6708/2008/02/005)
14. J. Braun *et al.*, Methods for point source analysis in high energy neutrino telescopes. *Astropart. Phys.* **29**, 299–305 (2008). doi: [10.1016/j.astropartphys.2008.02.007](https://doi.org/10.1016/j.astropartphys.2008.02.007)
15. A. A. Abdo *et al.*, A measurement of the spatial distribution of diffuse TeV gamma-ray emission from the Galactic plane with Milagro. *Astrophys. J.* **688**, 1078 (2008). doi: [10.1086/592213](https://doi.org/10.1086/592213)
16. E. Waxman, J. Bahcall, High energy neutrinos from cosmological gamma-ray burst fireballs. *Phys. Rev. Lett.* **78**, 2292–2295 (1997). doi: [10.1103/PhysRevLett.78.2292](https://doi.org/10.1103/PhysRevLett.78.2292)
17. K. Ioka, S. Razzaque, S. Kobayashi, P. Mészáros, TeV–PeV neutrinos from giant flares of magnetars and the case of SGR 1806–20. *Astrophys. J.* **633**, 1013 (2005). doi: [10.1086/466514](https://doi.org/10.1086/466514)
18. IceCube Collaboration, Neutrino analysis of the 2010 September Crab Nebula flare and time-integrated constraints on neutrino emission from the Crab using IceCube. *Astrophys. J.* **745**, 45 (2012). doi: [10.1088/0004-637X/745/1/A5](https://doi.org/10.1088/0004-637X/745/1/A5)
19. T. K. Gaisser, Atmospheric leptons, the search for a prompt component. *High Energy Phys. Phenomenol.* arXiv:1303.1431 (2013). <http://arxiv.org/abs/1303.1431>
20. IceCube Collaboration, Extending the search for neutrino point sources with IceCube above the horizon. *Phys. Rev. Lett.* **103**, 221102 (2009). doi: [10.1103/PhysRevLett.103.221102](https://doi.org/10.1103/PhysRevLett.103.221102); pmid: [20366087](https://pubmed.ncbi.nlm.nih.gov/20366087/)
21. IceCube Collaboration, Constraints on the extremely-high energy cosmic neutrino flux with the IceCube 2008–2009 data. *Phys. Rev. D* **83**, 092003 (2011). doi: [10.1103/PhysRevD.83.092003](https://doi.org/10.1103/PhysRevD.83.092003)
22. S. Schönert, T. K. Gaisser, E. Resconi, O. Schulz, Vetoing atmospheric neutrinos in a high energy neutrino telescope. *Phys. Rev. D* **79**, 043009 (2009). doi: [10.1103/PhysRevD.79.043009](https://doi.org/10.1103/PhysRevD.79.043009)
23. L. Rädcl, C. Wiebusch, Calculation of the Cherenkov light yield from electromagnetic cascades in ice with Geant4. *Astropart. Phys.* **44**, 102–113 (2013). doi: [10.1016/j.astropartphys.2013.01.015](https://doi.org/10.1016/j.astropartphys.2013.01.015)
24. IceCube Collaboration, Measurement of South Pole ice transparency with the IceCube LED calibration system. *Nucl. Instr. Meth. Phys. Res. A* **711**, 73–89 (2013). doi: [10.1016/j.nima.2013.01.054](https://doi.org/10.1016/j.nima.2013.01.054)
25. IceCube Collaboration, Calibration and characterization of the IceCube photomultiplier tube. *Nucl. Instr. Meth. Phys. Res. A* **618**, 139–152 (2010). doi: [10.1016/j.nima.2010.03.102](https://doi.org/10.1016/j.nima.2010.03.102)
26. D. Heck, J. Knapp, J. Capdevielle, G. Schatz, T. Thouw, *CORSIKA: A Monte Carlo Code to Simulate Extensive Air Showers* (Forschungszentrum Karlsruhe GmbH, Karlsruhe, Germany, 1998).
27. A. Fedynitch, J. Becker Tjus, P. Desiati, Influence of hadronic interaction models and the cosmic ray spectrum on the high energy atmospheric muon and neutrino flux. *Phys. Rev. D* **86**, 114024 (2012). doi: [10.1103/PhysRevD.86.114024](https://doi.org/10.1103/PhysRevD.86.114024)
28. A. Cooper-Sarkar, S. Sarkar, Predictions for high energy neutrino cross-sections from the ZEUS global PDF fits. *J. High Energy Phys.* **1**, 075 (2008). doi: [10.1088/1126-6708/2008/01/075](https://doi.org/10.1088/1126-6708/2008/01/075)

Acknowledgments: We acknowledge support from the following agencies: U.S. National Science Foundation—Office of Polar Programs, U.S. National Science Foundation—Physics Division, University of Wisconsin Alumni Research Foundation, the Grid Laboratory of Wisconsin (GLOW) grid infrastructure at the University of Wisconsin—Madison, and the Open Science Grid (OSG) grid infrastructure; U.S. Department of Energy, National Energy Research Scientific Computing Center, and the Louisiana Optical Network Initiative (LONI) grid computing resources; Natural Sciences and Engineering Research Council of Canada, WestGrid, and Compute/Calcul Canada; Swedish Research Council, Swedish Polar Research Secretariat, Swedish National Infrastructure for Computing (SNIC), and Knut and Alice Wallenberg Foundation, Sweden; German Ministry for Education and Research (BMBF), Deutsche Forschungsgemeinschaft (DFG), Helmholtz Alliance for Astroparticle Physics (HAP), and Research Department of Plasmas with Complex Interactions (Bochum), Germany; Fund for Scientific Research (FNRS-FWO), FWO Odysseus programme, Flanders Institute to encourage scientific and technological research in industry (IWT), and Belgian Federal Science Policy Office (Belspo); University of Oxford, UK; Marsden Fund, New Zealand; Australian Research Council; Japan Society for Promotion of Science (JSPS); the Swiss National Science Foundation (SNSF), Switzerland; and National Research Foundation of Korea (NRF). Additional data and resources are available in the supplementary materials. These include displays of the neutrino candidate events and list precise arrival times, as well as machine-readable tabular neutrino effective areas (Fig. 7). IceCube data are archived at <http://www.icecube.wisc.edu/science/data>.

IceCube Collaboration:

M. G. Aartsen,² R. Abbasi,²⁷ Y. Abdou,²² M. Ackermann,⁴² J. Adams,¹⁵ J. A. Aguilar,²¹ M. Ahlers,²⁷ D. Altmann,⁹ J. Auffenberg,²⁷ X. Bai,³¹ M. Baker,²⁷ S. W. Barwick,²³ V. Baum,²⁸ R. Bay,⁷ J. J. Beatty,^{17,18} S. Bechet,¹² J. Becker Tjus,¹⁰ K.-H. Becker,⁴² M. L. Benabderrahmane,⁴² S. BenZvi,²⁷ P. Berghaus,⁴² D. Berley,¹⁶ E. Bernardini,⁴² A. Bernhard,³⁰ D. Bertrand,¹² D. Z. Besson,²⁵ G. Binder,^{8,7} D. Bindig,⁴¹ M. Bissok,¹ E. Blaufuss,¹⁶ J. Blumenthal,¹ D. J. Boersma,⁴⁰ S. Bohaichuk,²⁰ C. Bohm,³⁴ D. Bose,¹³ S. Böser,¹¹ O. Botner,⁴⁰ L. Brayer,¹³ H.-P. Bretz,⁴² A. M. Brown,¹⁵ R. Brujin,²⁴ J. Brunner,²⁴ M. Carson,²⁷ J. Casey,⁵ M. Casier,¹³ D. Chirkin,²⁷ A. Christov,²¹ B. Christy,¹⁶ K. Clark,³⁹ F. Cleverman,¹⁹ S. Coenders,⁵ S. Cohen,²⁴ D. F. Cowen,^{39,38} A. H. Cruz Silva,⁴² M. Danning,³⁴ J. Daughhete,⁵ J. C. Davis,¹⁷ M. Day,²⁷ C. De Clercq,¹³ S. De Ridder,²² P. Desiati,²⁷ K. D. de Vries,¹³ M. de With,⁹ T. DeYoung,³⁹ J. C. Díaz-Vélez,²⁷ M. Dunkman,³⁹ R. Eagan,¹⁶ B. Eberhardt,²⁸ B. Eichmann,¹⁰ J. Eisch,²⁷ R. W. Ellsworth,¹⁶ S. Euler,¹ P. A. Evenson,²¹ O. Fadiran,²⁷ A. R. Fazley,⁶ A. Fedynitch,¹⁰ J. Feintzeig,²⁷ T. Feusels,²² K. Filimonov,⁷ C. Finley,³⁴ T. Fischer-Wasels,⁴¹ S. Flis,³⁴ A. Franckowiak,¹¹ K. Frantzen,¹⁹ T. Fuchs,¹⁹ T. K. Gaisser,³¹ J. Gallagher,²⁶ L. Gerhardt,^{8,7} L. Gladstone,²⁷ T. Glüsienkamp,⁴² A. Goldschmidt,⁸ G. Golup,¹³ J. G. Gonzalez,³¹ J. A. Goodman,¹⁶ D. Góra,⁴² D. T. Grandmont,²⁰ D. Grant,²⁰ A. Groß,³⁰ C. Ha,^{8,7} A. Hai Ismail,²² P. Hallen,¹¹ A. Hallgren,⁴⁰ F. Halzen,²⁷ K. Hanson,¹² D. Heereman,¹² D. Heinen,¹ K. Helbing,⁴¹ R. Hellauer,¹⁶ S. Hickford,¹⁵ G. C. Hill,² K. D. Hoffman,¹⁶ R. Hoffmann,⁴¹ A. Homeier,¹¹ K. Hoshina,²⁷ W. Huelsnitz,¹⁶ P. O. Hulth,³⁴ K. Hultqvist,³⁴ S. Hussain,³¹ A. Ishihara,¹⁴ E. Jacobi,⁴² J. Jacobsen,²⁷ K. Jagielski,¹ G. S. Japaridze,⁴ K. Jero,²⁷ O. Jlelat,²² B. Kaminsky,⁴² A. Kappes,⁹ T. Karg,⁴² A. Karle,²⁷ J. L. Kelley,²⁷ J. Kiryuk,³⁵ J. Kläs,⁴³ S. R. Klein,^{8,7} J.-H. Köhne,¹⁹ G. Kohonen,²⁹ H. Kolanoski,⁹ K. Köpke,²⁸ C. Kopper,²⁷ S. Kopper,⁴¹ D. J. Koskinen,³⁹ M. Kowalski,¹¹ M. Krasberg,²⁷ K. Krings,¹ G. Kroll,²⁸ J. Kunnen,¹³ N. Kurahashi,²⁷ T. Kuwabara,³¹ M. Labare,²² H. Landsman,²⁷ M. J. Larson,³⁷ M. Lesiak-Bzdak,³⁵ M. Leuermann,¹ J. Leite,³⁰ J. Linemann,²⁸ J. Madsen,³³ G. Maggi,¹³ R. Maruyama,²⁷ K. Mase,¹⁴ H. S. Matis,⁸ F. McNally,²⁷ K. Meagher,¹⁶ M. Merck,²⁷ T. Meures,¹² S. Miarecki,^{8,7} E. Middell,⁴² N. Milke,¹⁹ J. Miller,¹³ L. Mohrmann,⁴² T. Montaruli,²¹ R. Morse,²⁷ R. Nahnhauser,⁴² U. Naumann,⁴¹ H. Niederhausen,³⁵ S. C. Nowicki,²⁰ D. R. Nygren,⁸ A. Obertacke,⁴¹ S. Odrowski,²⁰ A. Olivas,¹⁶ A. O’Murchadha,¹² L. Paul,¹ J. A. Pepper,³⁷ C. Pérez de los Heros,⁴⁰ C. Pfendner,¹⁹ E. Resconi,³⁰ W. Rhode,¹⁹ M. Ribordy,²⁴ M. Richman,¹⁶ G. T. Przybylski,⁸ L. Rädcl,¹ M. Rameez,²¹ K. Rawlins,³ P. Redl,¹⁶ R. Reimann,¹ E. Resconi,³⁰ W. Rhode,¹⁹ M. Ribordy,²⁴ M. Richman,¹⁶ B. Riedel,²⁷ J. P. Rodrigues,²⁷ C. Rott,³⁶ T. Ruhe,¹⁹ B. Ruzybayev,³¹ D. Ryckbosch,²² S. M. Saba,¹⁰ T. Salameh,³⁹ H.-G. Sander,²⁸ M. Santarini,²⁷ S. Sarkar,³² K. Schatto,²⁸ F. Scheriau,¹⁹ T. Schmidt,¹⁶ M. Schmitz,¹⁹ S. Schoenen,¹ S. Schöneberg,¹⁰ A. Schönwald,⁴² A. Schukraft,¹ L. Schulte,¹¹ O. Schulz,³⁰ D. Seckel,³¹ Y. Sestayo,³⁰ S. Seunarine,³³ R. Shanidze,⁴² C. Sheremata,²⁰ M. W. E. Smith,³⁹ D. Soldin,⁴¹

G. M. Spiczak,³³ C. Spiering,⁴² M. Stamatikos,¹⁷ T. Stanew,³¹ A. Stasik,¹¹ T. Stezelberger,⁸ R. G. Stokstad,⁸ A. Stößl,⁴² E. A. Strahler,¹³ R. Ström,⁴⁰ G. W. Sullivan,¹⁶ H. Taavola,⁴⁰ I. Taboada,⁵ A. Tamburro,³¹ A. Tepe,⁴¹ S. Ter-Antonyan,⁹ G. Tešić,³⁹ S. Tilav,³⁴ P. A. Toale,³⁷ S. Toscano,²⁷ E. Unger,¹⁰ M. Usner,¹¹ N. van Eijndhoven,¹³ A. Van Overloop,²² J. van Santen,²⁷ M. Vehringer,¹ M. Voge,¹¹ M. Vraeghe,²² C. Walck,³⁴ T. Waldenmaier,⁹ M. Wallraff,¹ Ch. Weaver,²⁷ M. Wellons,²⁷ C. Wendt,²⁷ S. Westerhoff,²⁷ N. Whitehorn,²⁷ K. Wiebe,²⁸ C. H. Wiebusch,¹ D. R. Williams,¹⁷ H. Wissing,¹⁶ M. Wolf,³⁴ T. R. Wood,²⁰ K. Woschnagg,⁷ D. L. Xu,³⁷ X. W. Xu,⁶ J. P. Yanez,⁴² G. Yodanis,⁴² G. Yodanis,⁴² P. Zarzhitsky,³⁷ J. Ziemann,¹⁹ S. Zierke,¹ M. Zoll³⁴

¹III. Physikalisches Institut, RWTH Aachen University, D-52056 Aachen, Germany. ²School of Chemistry and Physics, University of Adelaide, Adelaide, South Australia 5005, Australia. ³Department of Physics and Astronomy, University of Alaska Anchorage, 3211 Providence Drive, Anchorage, AK 99508, USA. ⁴CTS/PS, Clark-Atlanta University, Atlanta, GA 30314, USA. ⁵School of Physics and Center for Relativistic Astrophysics, Georgia Institute of Technology, Atlanta, GA 30332, USA. ⁶Department of Physics, Southern University, Baton Rouge, LA 70813, USA. ⁷Department of Physics, University of California, Berkeley, Berkeley, CA 94720, USA. ⁸Lawrence Berkeley National Laboratory, Berkeley, CA 94720, USA. ⁹Institut für Physik, Humboldt-Universität zu Berlin, D-12489 Berlin, Germany. ¹⁰Fakultät für Physik und Astronomie, Ruhr-Universität Bochum, D-44780 Bochum, Germany. ¹¹Physikalisches Institut, Universität Bonn, Nussallee 12, D-53115 Bonn, Germany. ¹²Université Libre de Bruxelles, Science Faculty CP230, B-1050 Brussels, Belgium. ¹³Vrije Universiteit Brussel, Dienst ELEM, B-1050 Brussels, Belgium. ¹⁴Department of Physics, Chiba University, Chiba 263-8522, Japan. ¹⁵Department of Physics and Astronomy, University of Canterbury, Private Bag 4800, Christchurch, New Zealand. ¹⁶Department of Physics, University of Maryland, College Park, MD 20742, USA. ¹⁷Department of Physics and Center for Cosmology and Astroparticle Physics, Ohio State University, Columbus, OH 43210, USA. ¹⁸Department of Astronomy, Ohio State University, Columbus, OH 43210, USA. ¹⁹Department of Physics, TU Dortmund University, D-44221 Dortmund, Germany. ²⁰Department of Physics, University of Alberta, Edmonton, Alberta T6G 2E1, Canada. ²¹Département de physique nucléaire et corpusculaire, Université de Genève, CH-1211 Genève, Switzerland. ²²Department of Physics and Astronomy, University of Gent, B-9000 Gent, Belgium. ²³Department of Physics and Astronomy, University of California, Irvine, Irvine, CA 92697, USA. ²⁴Laboratory for High Energy Physics, École Polytechnique Fédérale, CH-1015 Lausanne, Switzerland. ²⁵Department of Physics and Astronomy, University of Kansas, Lawrence, KS 66045, USA. ²⁶Department of Astronomy, University of Wisconsin, Madison, WI 53706, USA. ²⁷Department of Physics and Wisconsin IceCube Particle Astrophysics Center, University of Wisconsin, Madison, WI 53706, USA. ²⁸Institute of Physics, University of Mainz, Staudinger Weg 7, D-55099 Mainz, Germany. ²⁹Université de Mons, 7000 Mons, Belgium. ³⁰T.U. Munich, D-85748 Garching, Germany. ³¹Bartol Research Institute and Department of Physics and Astronomy, University of Delaware, Newark, DE 19716, USA. ³²Department of Physics, University of Oxford, 1 Keble Road, Oxford OX1 3NP, UK. ³³Department of Physics, University of Wisconsin, River Falls, WI 54022, USA. ³⁴Oskar Klein Centre and Department of Physics, Stockholm University, SE-10691 Stockholm, Sweden. ³⁵Department of Physics and Astronomy, Stony Brook University, Stony Brook, NY 11794–3800, USA. ³⁶Department of Physics, Sungkyunkwan University, Suwon 440-746, Korea. ³⁷Department of Physics and Astronomy, University of Alabama, Tuscaloosa, AL 35487, USA. ³⁸Department of Astronomy and Astrophysics, Pennsylvania State University, University Park, PA 16802, USA. ³⁹Department of Physics, Pennsylvania State University, University Park, PA 16802, USA. ⁴⁰Department of Physics and Astronomy, Uppsala University, Box 516, S-75120 Uppsala, Sweden. ⁴¹Department of Physics, University of Wuppertal, D-42119 Wuppertal, Germany. ⁴²DESY, D-15735 Zeuthen, Germany.

*Corresponding author. E-mail: ckopper@icecube.wisc.edu (C.K.); naoko@icecube.wisc.edu (N.K.); nwhitehorn@icecube.wisc.edu (N.W.)

Supplementary Materials

www.sciencemag.org/content/342/6161/1242856/suppl/DC1
Event Displays 1 to 28
Neutrino Effective Areas

8 July 2013; accepted 8 October 2013
[10.1126/science.1242856](https://doi.org/10.1126/science.1242856)

EXTENDED PDF FORMAT
SPONSORED BY



Evidence for High-Energy Extraterrestrial Neutrinos at the IceCube Detector

IceCube Collaboration (November 21, 2013)
Science **342** (6161), . [doi: 10.1126/science.1242856]

Editor's Summary

Extraterrestrial Neutrinos

Neutrinos are thought to be produced in astrophysical sources outside our solar system but, up until recently, they had only been observed from one supernova in 1987. **Aartsen *et al.*** (10.1126/science.1242856; see the cover) report data obtained between 2010 and 2012 with the IceCube neutrino detector that reveal the presence of a high-energy neutrino flux containing the most energetic neutrinos ever observed, including 28 events at energies between 30 and 1200 TeV. Although the origin of this flux is unknown, the findings are consistent with expectations for a neutrino population with origins outside the solar system.

This copy is for your personal, non-commercial use only.

- Article Tools** Visit the online version of this article to access the personalization and article tools:
<http://science.sciencemag.org/content/342/6161/1242856>
- Permissions** Obtain information about reproducing this article:
<http://www.sciencemag.org/about/permissions.dtl>

Science (print ISSN 0036-8075; online ISSN 1095-9203) is published weekly, except the last week in December, by the American Association for the Advancement of Science, 1200 New York Avenue NW, Washington, DC 20005. Copyright 2016 by the American Association for the Advancement of Science; all rights reserved. The title *Science* is a registered trademark of AAAS.

Short CV of Prof. Dr. Stijn Buitink

(4/11/2016)



Personal information

Name: Dr. Buitink, S. (Stijn)

Researcher unique identifier: <http://inspirehep.net/author/profile/S.Buitink.1>
<http://orcid.org/0000-0002-6177-497X>

Date of Birth: 11 June 1980

Nationality: Netherlands

Education

2009	PhD “ <i>Radio Emission From Cosmic Particle Cascades</i> ” Department of Astrophysics/IMAPP, Radboud University Nijmegen, Netherlands
2004	Master “ <i>Unravelling Pulsar Profiles</i> ” Department of Astrophysics/IMAPP, Radboud University Nijmegen, Netherlands

Current position

2014 - present	Assistant Professor Astrophysics Department, Vrije Universiteit Brussel, Belgium
----------------	---

Previous positions

2012 - 2014	VENI researcher Department of Astrophysics/IMAPP, Radboud University Nijmegen, Netherlands KVI, University of Groningen, Netherlands
2011 - 2012	Post-doctoral researcher Interuniversity Institute for High Energies, Vrije Universiteit Brussel, Belgium
2009 - 2011	Post-doctoral researcher Lawrence Berkeley National Laboratory, Berkeley CA, USA
2004 - 2009	PhD student Radboud University Nijmegen, Netherlands

Grants and awards

2014	PI, ERC Starting Grant (1.5 M€) European Research Council
2012	co-PI, FOM projectruimte grant “Cosmic Lightning” (550 k€) Foundation for Fundamental Research on Matter (FOM)
2011	PI, VENI grant, Innovational Research Incentives Scheme (250 k€) Netherlands Organisation for Scientific Research (NWO)

Scientific Track Record

Author on 148 papers and a total of 4285 citations, h-index: 33. Source:inspire (4/11/2016)

Supervision of graduate students and postdoctoral fellows

2015 - present | Supervising 2 postdocs and 1 PhD student

Teaching activities

2014 - present	2 Master and 1 Bachelor course, Vrije Universiteit Brussel, Belgium
2013	Lecturer (undergraduate level, optics) Kernfysisch Versneller Instituut, University of Groningen, Netherlands
2011	Assistant lecturer Interuniversity Institute for High Energies, Vrije Universiteit Brussel, Belgium
2004 - 2009	Assistant lecturer Department of Astrophysics/IMAPP, Radboud University Nijmegen, Netherlands
2004 - 2009	Outreach lectures for amateur astronomers

Invited presentations (international):

2016	Annual Meeting of the German Astronomical Society, Bochum, Germany
2016	Acoustic and Radio EeV Neutrino Detection Activities (ARENA), Groningen, Netherlands
2016	KICP workshop “Next-Generation Techniques for UHE Astroparticle Physics”, Chicago, USA
2014	JSI workshop “Multi-Messenger Astronomy in the Era of PeV Neutrinos”, Annapolis, USA
2013	Lawrence Berkeley National Laboratory, USA
2013	TeV Particle Astrophysics (TeVPA) conference Irvine, USA
2010	UC Santa Barbara, USA
2010	Penn State U., USA
2010	CalTech, USA
2009	UC Berkeley, USA

Organization of Scientific Meetings

2016	ARENA meeting (member of LOC)
2014	LOFAR Air Shower Radio Simulation Workshop (organiser)

Major Collaborations

2014 - present	Pierre Auger Observatory
2012 - present	LOFAR Cosmic Ray Key Science Project (Co-PI)
2009 - 2013	IceCube
2004 - 2012	LOPES

List of 10 most important publications Prof. Dr. Stijn Buitink (2011-2016)

Five key publications marked with *

Buitink, S. et al., A large light-mass component of cosmic rays at $10^{17} - 10^{17.5}$ electronvolts from radio observations, *Nature* **531**, 70 (2016). *

Aab, A. et al. (Buitink, S.) Measurement of the Radiation Energy in the Radio Signal of Extensive Air Showers as a Universal Estimator of Cosmic-Ray Energy, *Phys. Rev. Lett.* **116**, 241101 (2016).

Nelles, A. et al. (Buitink, S.), Measuring a Cherenkov ring in the radio emission from air showers at 110-190 MHz with LOFAR, *Astropart. Phys.* **65**, 11 (2015).

Corstanje, A. et al. (Buitink, S.), The shape of the radio wavefront of extensive air showers as measured with LOFAR, *Astropart. Phys.* **61**, 22 (2015).

Schellart, P. et al., (Buitink, S.), Probing Atmospheric Electric Fields in Thunderstorms through Radio Emission from Cosmic-Ray-Induced Air Showers, *Phys. Rev. Lett.* **114**, 165001 (2015). *

Buitink, S. et al., Method for high precision reconstruction of air shower X_{max} using two-dimensional radio intensity profiles, *Phys. Rev. D* **90**, 082003 (2014). *

Schellart, P. et al. (Buitink, S.), Polarized radio emission from extensive air showers measured with LOFAR, *JCAP* **1410**, 014 (2014).

Schellart, P. et al., (Buitink, S.), Detecting Cosmic Rays with the LOFAR radio telescope, *Astron. & Astrophys* **560**, A98 (2013). *

Aartsen, M.G. et al. (Buitink S.), Search for Galactic PeV Gamma Rays with the IceCube Neutrino Observatory, *Phys. Rev. D* **87**, 062002 (2013). *

Abbasi, R. et al. (Buitink, S.), An absence of neutrinos associated with cosmic-ray acceleration in γ -ray bursts, *Nature* **484**, 351-353 (2012).

Applications for international research funding

I have received an ERC Starting Grant under the European Union's Horizon 2020 research and innovation programme (grant agreement n. 640130). The budget of 1500 kEuro is used for hiring PhD students and postdocs as well as a hardware upgrade for LOFAR.

Realisations of valorisation efforts

- Around 15 talks for amateur astronomer organizations in Belgium and the Netherlands
- Several articles in newspapers and magazines in response to press releases of publications (including De Morgen, De Standaard en EOS Wetenschap).
- Contributions to science blog Wtnschp.be and Dutch astronomy magazine.
- Telescope excursions for general public at University of Nijmegen.

Detecting cosmic rays with the LOFAR radio telescope

P. Schellart¹, A. Nelles^{1,2}, S. Buitink^{5,1}, A. Corstanje¹, J. E. Enriquez¹, H. Falcke^{1,2,3,4}, W. Frieswijk³, J. R. Hörandel^{1,2}, A. Horneffer⁴, C. W. James⁶, M. Krause¹, M. Mevius^{3,8}, O. Scholten⁵, S. ter Veen¹, S. Thoudam¹, M. van den Akker¹, A. Alexov^{33,7}, J. Anderson⁴, I. M. Avruch²³, L. Bähren¹, R. Beck⁴, M. E. Bell²⁶, P. Bennema³, M. J. Bantum³, G. Bernardi^{29,30}, P. Best¹⁶, J. Bregman³, F. Breitling¹⁹, M. Brentjens³, J. Broderick¹², M. Brügger²⁷, B. Ciardi¹³, A. Coolen³, F. de Gasperin²⁷, E. de Geus³, A. de Jong³, M. de Vos³, S. Duscha³, J. Eisloffel²⁰, R. A. Fallows³, C. Ferrari³², M. A. Garrett^{3,9}, J. Griebmeier²², T. Grit³, J. P. Hamaker³, T. E. Hassall^{12,10}, G. Heald³, J. W. T. Hessels^{3,7}, M. Hoefft²⁰, H. A. Holties³, M. Iacobelli⁹, E. Juette²¹, A. Karastergiou¹¹, W. Klijn³, J. Kohler⁴, V. I. Kondratiev^{3,28}, M. Kramer^{4,10}, M. Kuniyoshi⁴, G. Kuper³, P. Maat³, G. Macario³², G. Mann¹⁹, S. Markoff⁷, D. McKay-Bukowski^{34,15}, J. P. McKean³, J. C. A. Miller-Jones^{14,7}, J. D. Mol³, D. D. Mulcahy⁴, H. Munk³, R. Nijboer³, M. J. Norden³, E. Orru³, R. Overeem³, H. Paas²⁴, M. Pandey-Pommier²⁵, R. Pizzo³, A. G. Polatidis³, A. Renting³, J. W. Romein³, H. Röttgering⁹, A. Schoenmakers³, D. Schwarz³⁶, J. Sluman³, O. Smirnov^{29,30}, C. Sobey⁴, B. W. Stappers¹⁰, M. Steinmetz¹⁹, J. Swinbank⁷, Y. Tang³, C. Tasse¹⁷, C. Toribio³, J. van Leeuwen^{3,7}, R. van Nieuwpoort^{35,3}, R. J. van Weeren³¹, N. Vermaas³, R. Vermeulen³, C. Vocks¹⁹, C. Vogt³, R. A. M. J. Wijers⁷, S. J. Wijnholds³, M. W. Wise^{3,7}, O. Wucknitz^{18,4}, S. Yatawatta³, P. Zarka¹⁷, and A. Zensus⁴

(Affiliations can be found after the references)

Received 16 September 2013 / Accepted 4 November 2013

ABSTRACT

The low frequency array (LOFAR), is the first radio telescope designed with the capability to measure radio emission from cosmic-ray induced air showers in parallel with interferometric observations. In the first ~ 2 years of observing, 405 cosmic-ray events in the energy range of 10^{16} – 10^{18} eV have been detected in the band from 30–80 MHz. Each of these air showers is registered with up to ~ 1000 independent antennas resulting in measurements of the radio emission with unprecedented detail. This article describes the dataset, as well as the analysis pipeline, and serves as a reference for future papers based on these data. All steps necessary to achieve a full reconstruction of the electric field at every antenna position are explained, including removal of radio frequency interference, correcting for the antenna response and identification of the pulsed signal.

Key words. astroparticle physics – methods: data analysis – instrumentation: interferometers

1. Introduction

With the development of ever faster electronics and the increase in computational power, the construction of radio telescopes as large interferometric arrays of rather simple antennas opens a new window for observations. The low frequency array (LOFAR; van Haarlem et al. 2013), is the first large-scale implementation of this technique. In addition to producing the first high quality images at these low frequencies of 10–240 MHz, LOFAR was designed to study short, pulsed signals in the time-domain. With a vast array of antennas observing the whole sky simultaneously, observations are not limited to a predefined direction, therefore providing optimal conditions for cosmic-ray detection.

Cosmic rays, accelerated charged particles from astrophysical sources, can be observed over several decades of energy. When cosmic rays of high energies reach the Earth, they do not reach the surface as primary particles, but instead interact with atmospheric nuclei. Thereby, a cascade of particles is created, consisting mostly of photons and a significant fraction of charged particles. While propagating through the atmosphere, the charged particles of this extensive air shower emit electromagnetic radiation, which adds up coherently for wavelengths comparable to the dimensions of the shower front (Huege 2013).

Already in the 1960s it was proven that cosmic ray-induced air showers emit nanosecond duration pulses with significant power in the MHz radio frequency range (Jelley et al. 1965; Allan & Jones 1966), but due to lack of sufficiently sophisticated and fast electronics the technique was not pursued further. Only in the past decade interest in the detection technique was rekindled and successfully applied (Falcke et al. 2008). The proof of principle and large progress in the understanding of the emission was made at the LOFAR Prototype Experimental Station (LOPES; Falcke et al. 2005; Huege et al. 2012) and further refined by measurements at the CODALEMA experiment (Ardouin et al. 2005).

Similar to optical measurements of the fluorescence emission from atoms excited by interaction with the air shower, radio emission directly traces the longitudinal shower development, which is closely related to the type of the primary particle. Unlike optical fluorescence measurements, radio emission measurements are less dependent on observing conditions and can operate day and night matching the duty cycle of particle detector measurements.

Due to the very steep energy spectrum, measuring the highest-energy cosmic rays requires vast detector areas. Cost constraints therefore limit the density of detectors within this area giving a wide spacing between the individual antennas.

Theoretical models describing the different emission mechanisms at play point to a very detailed and non-symmetrical emission pattern at ground level (Werner et al. 2012; Alvarez-Muñiz et al. 2012; Marin & Revenu 2012; Huege et al. 2013). Testing these models therefore requires dense sampling of the electric field over a sufficiently large area.

LOFAR offers a high number of antennas clustered on an irregular grid, with increasingly large spacing between antenna clusters further away from the center. In the core of the array about 2300 antennas are installed within about 4 km², which allows air showers to be measured with unprecedented spatial resolution. These measurements will contribute significantly to conclusively confirm theoretical models for the radio emission on a shower by shower basis, a goal previously unattainable due to lack of sufficiently high quality data.

Measurements and converging theoretical predictions of the expected radio signal from a cosmic-ray induced air shower give a short, nanosecond time-scale bi-polar pulse, which is mostly linearly polarized. This article describes the detection set-up and automated processing pipeline used at LOFAR to measure and identify these signals.

Starting with a description of the instrumental set-up at LOFAR in Sect. 2, an overview of the data reduction pipeline is given in Sect. 3. Finally, Sect. 4 describes the characteristics of the dataset obtained between June 2011 and April 2013.

The LOFAR dataset will be used in forthcoming publications to verify existing models for radio emission from air showers and to develop new techniques that use radio emission to measure important characteristics of the incoming particle, such as energy and mass.

2. LOFAR

LOFAR is a distributed radio telescope. Its antennas are distributed over northern Europe with the densest concentration in the north of the Netherlands, in the Province of Drenthe. The observation support center and processing facilities are also located near this central core. The antennas of LOFAR are grouped into *stations*, each station taking the role of a single dish in a traditional radio interferometer array. A station consists of a number of low-band antennas (LBAs, 10–90 MHz) and high-band antennas (HBAs, 110–240 MHz). The 24 stations within the ~2 km wide core are distributed in an irregular pattern that maximizes *uv*-coverage, or spatial frequencies for standard interferometric observations. The 16 additional Dutch remote stations are distributed with increasing distance to the core. International stations are currently located in Germany, France, the United Kingdom, and Sweden, giving LOFAR a maximum baseline of 1292 km for interferometric observations. Core stations and remote stations consist of 96 LBAs plus 48 HBAs. International stations have 96 LBAs and 96 HBAs. At the center of the LOFAR core six stations are located in a roughly 320 m diameter area, called the *Superterp*, providing both the shortest baselines for interferometric observations and the densest population of antennas ideal for cosmic-ray observations. While every LOFAR station is equipped with the necessary electronics to observe cosmic rays, the current data set is taken with the central 24 stations, where additional information from particle detectors is available (see Sect. 2.3). The positions of the antennas of the seven most central LOFAR stations are shown in Fig. 1.

2.1. The antennas

The LBAs are the main tool for cosmic-ray detection. An LBA consists of two orthogonal inverted V-shaped dipoles, each with

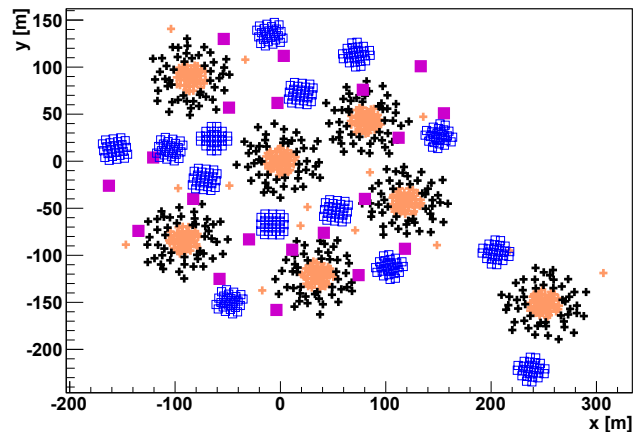


Fig. 1. Layout of the center of LOFAR. The six stations to the left form the Superterp. The crosses indicate the LBA inner and outer antenna sets, respectively. The open squares show the positions of the HBA tiles, which are split into two groups per station. The filled squares indicate the positions of the LORA particle detectors.



Fig. 2. Low-band antennas at the central core of LOFAR, the Superterp. In the background the black box of a LORA particle detector can be seen.

a length of 1.38 m. These are supported by a central PVC¹ pole, which holds the low-noise amplifier and guides the signal cables, as shown in Fig. 2. The dipoles *X* and *Y*, that make up each antenna, are oriented northeast to southwest (NE-SW) and northwest to southeast (NW-SE), as can be seen in Fig. 3.

The low-noise amplifier has an intentional impedance mismatch with the antenna. This mismatch, combined with the characteristic length of the dipoles, makes the system sensitive in a broad band from 10–90 MHz. In principle, this allows observations from the ionospheric cutoff up to the start of the commercial FM radio band. For most observations the frequency range is limited by a combination of selectable hardware and software filters to 30–80 MHz to suppress strong Radio Frequency Interference (RFI) in the outer bands. The LBAs are designed to be sky noise limited after RFI has been removed (van Cappellen et al. 2007). After amplification the signals from the individual dipoles are transmitted through coaxial cables to the electronics cabinet located at every station.

The HBAs have been optimized for a frequency band of 110–240 MHz. The design clusters 16 antenna elements into a *tile*, the signals from these elements are amplified and combined in an analog beam-former. This means that while the LBAs

¹ Polyvinyl chloride.

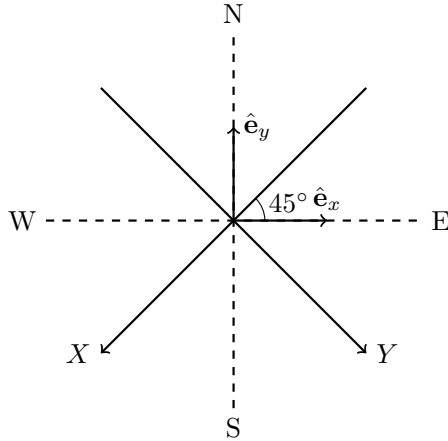


Fig. 3. Geometry of the LBA. The X and Y dipoles are oriented NE-SW and NW-SE respectively. This is rotated by 225 degrees with respect to the standard local Cartesian coordinate system used in Sect. 3.4.

are sensitive to the whole sky the HBAs are most sensitive within the $\sim 20^\circ$ of the tile-beam, of which the direction is chosen at the start of every observation. This results in a smaller effective area for cosmic-ray observations, as the measurement will only be optimal if the direction of the cosmic ray happens to coincide with the beam direction of the observation. Therefore, the analysis of HBA data and their interesting higher frequency range requires a different approach for cosmic-ray studies. Results of these measurements will be described in a later publication.

2.2. The transient buffer boards

After being forwarded to the electronics cabinet the signals of the LBAs are again amplified, filtered, and digitized by a 12 bit A/D converter with a sampling frequency of 200 MHz². Due to signal path limitations in the Dutch stations only 48 dual-polarized or 96 single-polarized antennas can be processed at a given time. For the dual-polarized option the antennas are grouped into an inner and an outer set, which has to be chosen before an observation.

For astronomical observations the data are then beamformed and sent to the central processing facility. In addition, there is the possibility to store a snapshot of the original data. Every station is equipped with ring-buffers, the so called Transient Buffer Boards (TBBs). These continuously store the last 1.3 s of raw data (an extension to 5 s is currently being deployed). When triggered, the contents of the TBBs are frozen, read out via the Wide Area Network and stored on disk for further analysis. The trigger can be generated based on various parameters in an FPGA³ at the local receiver unit. Alternatively, the trigger can be generated by an array of particle detectors (see Sect. 2.3) or received from outside of LOFAR. Currently, the main trigger for cosmic-ray observation is provided by the particle detectors. Later, a radio self-trigger will be implemented, using the current dataset as a training set to deduce trigger criteria, so that the FPGA trigger can be run independently at every LOFAR station. These criteria have to reduce false triggers to limit the data rate. Using every LOFAR station individually will dramatically increase the effective area.

Essential for measuring cosmic rays with LOFAR as a radio telescope is that the whole process of triggering and storing

² A 160 MHz clock is also available.

³ Field Programmable Gate Array.

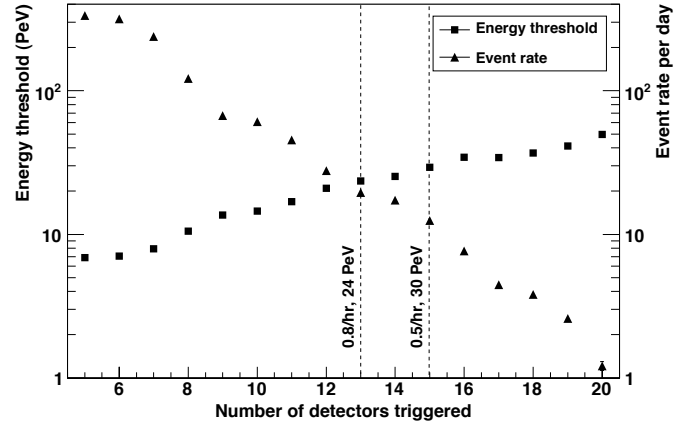


Fig. 4. Energy threshold in PeV (*left*) and the event rate per day (*right*) are shown as a function of the number of triggered particle detectors. Two possible trigger conditions are indicated with the dotted lines.

radio-pulse data can take place without interfering with the ongoing observations.

2.3. The LOFAR Radboud Air Shower Array

LORA, the LOFAR Radboud Air Shower Array, is an array of particle detectors co-located with the center of LOFAR. The array provides a reconstruction of basic parameters of recorded air showers, such as the direction and the position of impact, as well as the energy of the incoming cosmic ray (Thoudam et al., in prep.). It also provides the time of arrival, which is used to trigger the read-out of the radio antennas.

LORA consists of 20 detector units distributed on the Superterp, as shown in Fig. 1. Each detector contains two scintillators (0.45 m^2 , type: NE 114), which are individually read out through a photomultiplier tube. The detectors are inside weather-proof shelters and have been tested to not create any interference at radio frequencies.

Conditions at which triggers are sent to LOFAR can be adjusted to match the desired energy threshold. There are two constraints on the desired rate: the rate of events interesting for radio observations has to be maximized, while the network load on the LOFAR system has to be kept low in order to avoid interfering with the primary observation. A trigger in a single detector is generated when a particle signal of more than 4σ above the noise is registered. In order to only detect air showers a coincidence of several detectors is needed. Events of less than 10^{16} eV have a very low probability to be observable in radio above the sky-noise level. The energy threshold and the corresponding event rate are shown in Fig. 4 as the function of the number of triggered detectors. Requiring triggers in 13 detectors yields a threshold energy of $2.4 \times 10^{16} \text{ eV}$, with an average trigger-rate of 0.8 events/h. This trigger rate has been selected as the optimal setting for the observations.

2.4. Observations

After the commissioning phase LOFAR is to be used on a proposal-based schedule. Proposals are open to the community for imaging or beamformed observations, as well as TBB observations. Some fraction of the observing time is reserved for participating consortia and key science projects. The LOFAR cosmic ray key science project (CRKSP) is one of six LOFAR key science projects.

To maximize the duty cycle TBB observations can be run in the background of all other observations that do not need the full network bandwidth. This does however mean that the array configuration is determined by the primary observation, therefore the amount of data in a specific array configuration (such as the selection of LBA or HBA antenna type) available for analysis is not determined by the cosmic-ray project itself, except when LOFAR is otherwise idle and the observing configuration can be chosen freely.

During the observation, triggers from LORA are received by the LOFAR control system. The system checks whether a dump from the TBBs is allowed. If so, the ring-buffers are frozen and a specified block of data around the trigger time is dumped to disk. For each cosmic-ray event 2.1 ms of radio data are stored, which corresponds to 77 MB per station. This provides sufficient frequency resolution for high quality RFI cleaning while minimizing data transfer and storage requirements.

Every evening, the data-files are archived at LOFAR and compressed for transport. They are stored in the Long Term Archive (van Haarlem et al. 2013), from where they can be retrieved for data analysis.

3. Reconstruction of cosmic-ray data

All newly recorded data are processed every evening, after having been copied via the network to the processing cluster of the Astrophysics department at the Radboud University Nijmegen. In addition to the HDF5⁴ files, containing the data of one LOFAR station each, the recorded data from the particle detectors and a trigger log file are transferred. With this information an automated pipeline is run. The pipeline is based on the task oriented PyCRTools framework consisting of fast low-level C++ routines embedded in Python for maximum flexibility. All results are stored in a PostgreSQL database for subsequent data mining analysis. The goal of the processing pipeline is to autonomously identify a full set of physics quantities for each air shower detected with LOFAR. The pipeline is optimized to identify those nanosecond pulses that are not generated by terrestrial sources.

All data are first processed per station, i.e. per file. The set of files received for a single trigger form an *event*. When the data from one station pass the criteria for containing a cosmic-ray signal (see Sect. 3.3), the corresponding event is called a *cosmic-ray event*. It is not necessary to observe a pulse in all stations, only the stations with a significant signal are used in a combined analysis.

3.1. Pipeline structure

The reconstruction pipeline comprises a number of steps that will be individually explained in the following sections. An overview of the steps and the overall structure is depicted in Fig. 5.

3.2. Preparing the data

Before proceeding to extract the cosmic-ray signal from the data, some preparatory steps have to be performed. Knowledge about the system is applied in the form of calibration procedures, the data are cleaned of narrowband-transmitters, and antennas that show malfunctions are flagged.

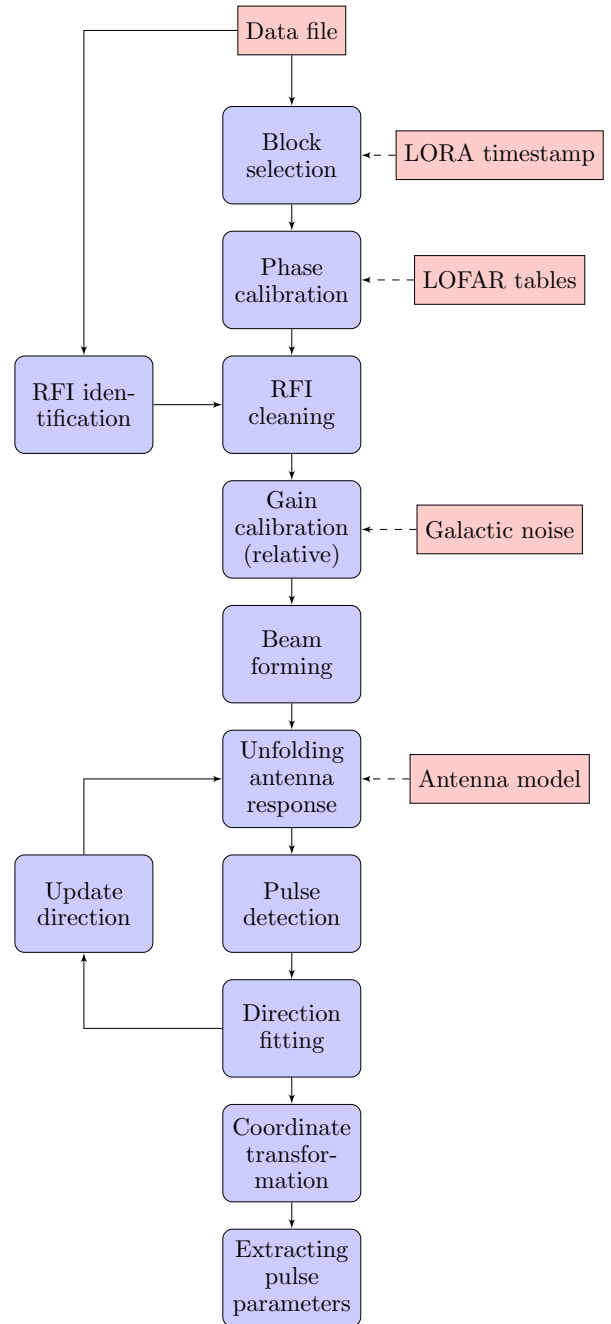


Fig. 5. General structure of the analysis pipeline. Rectangles represent input and rounded squares are processing steps.

3.2.1. Timing offsets and phase calibration

There are known signal path differences between the LOFAR antennas. Measured differences of cable lengths between the antennas are corrected for up to the 5 ns sample level already at the stations before the data are written to disk. Additionally, relative time offsets between the antennas are corrected for at sub-sample accuracy using standard LOFAR calibration tables. These tables are generated by phase-calibrating on the strongest astronomical radio sources and are regularly tested and updated if necessary (van Haarlem et al. 2013). Sub-sample corrections are applied as phase offsets to the Fourier transformed signal in the cosmic-ray pipeline, before processing it in the data analysis.

⁴ A tree-like file format (Alexov et al. 2012).

3.2.2. RFI cleaning

Narrow-band RFI in the time series signal can be revealed by making an average power spectrum. An example is shown in the top panel of Fig. 6, where most of the strong RFI is visible outside the 30–80 MHz range. The average power spectrum is created by averaging the square of the absolute value of the Fourier transform over several blocks of data. The block size can be freely chosen within the full data length to obtain a desired frequency resolution; here 2^{16} samples are used, giving a resolution of ~ 3 kHz, enough to resolve most RFI lines. A reasonable data length is needed for this procedure to produce a stable average, which sets the limit for the chosen block length to be stored from the TBBs, as mentioned in Sect. 2.4. In order to minimize artificial side lobes a half-Hann window is applied to the first and last 10% of each trace prior to the Fourier transformation.

The standard approach to RFI cleaning (or RFI flagging) is to identify peaks sticking out significantly above the overall spectral shape, also called the *baseline*, and set the corresponding Fourier component amplitudes to zero. However, this requires a priori knowledge of the baseline. While the baseline can be obtained through a smoothing or fitting procedure, this is often not stable in the presence of strong RFI, requiring an iterative approach.

An alternative approach to RFI cleaning uses the phase information in the complex-valued spectrum instead. If an RFI transmitter is measured in all antennas, the phase difference, or relative phase, between each pair of antennas will be a constant value as function of time with a small non constant random noise contribution. Note that the exact value of the constant, which only depends on the geometric delay between antennas, is not relevant, only its non time-varying nature. When no transmitter is present, the relative phase is expected to be both random and time varying, as the signal then consists of the added signals from many incoherent sources on the sky with additional random noise. Therefore, RFI can be identified by looking at the stability of phase differences between antennas over time. For each antenna-dipole $j = 0, 1, \dots, 95$ in a station and data block k , the phase spectrum is calculated as

$$\phi_{j,k}(\omega) = \arg(x_{j,k}(\omega)), \quad (1)$$

where $x_{j,k}(\omega)$ is the complex frequency component ω of the spectrum.

Subtracting the phase of one of the antennas as reference antenna gives the relative phases and results in a set of phases for every frequency channel, one for each block of data. Only one reference antenna is used and this is taken to be the one with median power to avoid selecting a broken antenna.

The average phase is defined as

$$\bar{\phi}_j(\omega) = \arg\left(\sum_{k=0}^{N-1} \exp(i\phi_{j,k}(\omega))\right), \quad (2)$$

and the phase variance as

$$s_j(\omega) = 1 - \frac{1}{N} \left| \sum_{k=0}^{N-1} \exp(i\phi_{j,k}(\omega)) \right|, \quad (3)$$

where N is the number of data blocks.

For completely random phases one expects $s_j(\omega) \approx 1$ as opposed to $s_j(\omega) = 0$ when all phases are equal. The phase variance per frequency channel will now either be at a value close to 1, including some random noise, or at a significantly lower level.

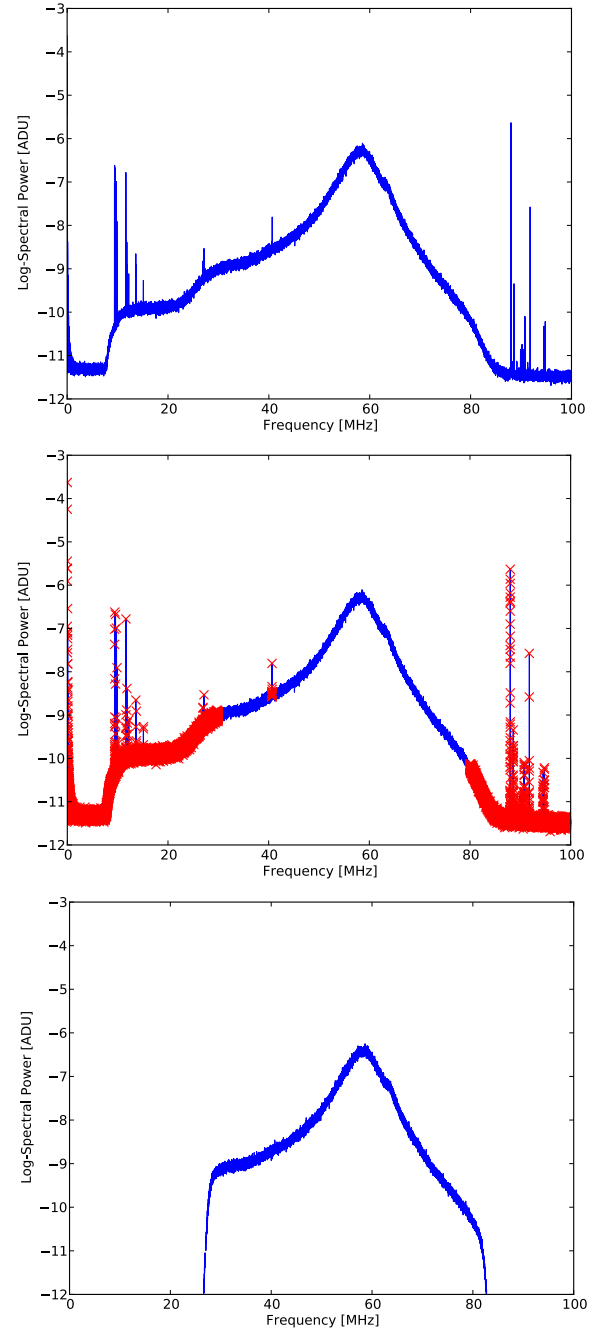


Fig. 6. The average spectrum of a typical LBA event. The raw data (*top*), with flagged contaminated channels (*middle*), cleaned and clipped to 30–80 MHz (*bottom*).

The latter reveals the presence of a radio transmitter, as shown in Fig. 7, where a contaminated part of the spectrum is shown with the corresponding phase variance.

Since RFI lines will result in peaks toward smaller values of the phase variance, and noise has no preferred peak direction, calculating the standard deviation σ in this plot only for values above the median will ensure a stable result. All frequencies that have a phase variance of at least 5σ below the median⁵ are flagged as containing RFI. Additionally a 30–80 MHz band-pass filter is applied, flagging the most heavily RFI polluted

⁵ Assuming a Gaussian distribution, σ can be estimated by sorting the data points, and comparing the value at 95 percentile to the median. This difference amounts to $\sim 1.64\sigma$.

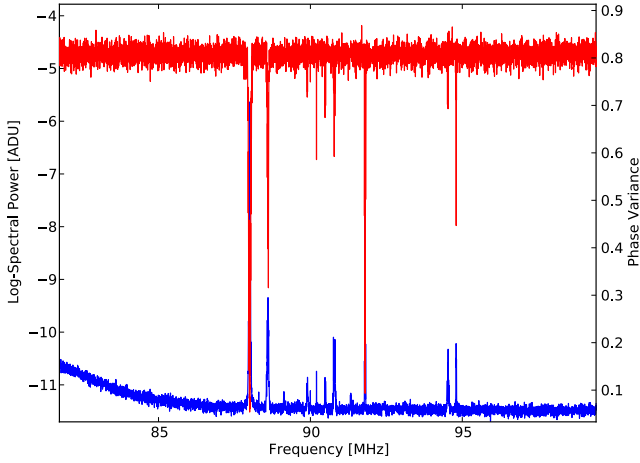


Fig. 7. Average LBA spectrum (bottom, left axis) with the corresponding phase variance (top, right axis). RFI lines can clearly be identified in the phase variance with peaks toward lower values, representing more stable phase differences between antennas over time.

low and high frequency parts of the bandwidth by default. To prevent pulse-ringing the 30–80 MHz block filter is first convolved with a, $\sigma_{\text{tapering}} = 2.5$ MHz, Gaussian⁶. After removing the flagged channels, the resulting cleaned spectrum is shown in the bottom panel of Fig. 6.

In general, there is very little RFI at the LOFAR Superterp. A lot of effort has been made to remove local sources that could disturb the LOFAR measurements and a protected zone has even been established (Offringa et al. 2013). This relative quietness is illustrated in Fig. 8. It shows the result of the RFI cleaning for all events for all frequencies. While every event has some RFI, no single RFI line is present in every event. Within the 30–80 MHz band, there are only two lines that are present in more than 40% of the events. In total there are rarely events with more than 2% flagged channels out of the more than 32 000 frequency channels in a block of data. This is shown in Fig. 9, where the total fraction of events is plotted against the number of flagged channels.

3.2.3. Flagging bad antennas

Occasionally, one or more antennas give invalid signals, e.g. due to hardware malfunction. To identify these *bad antennas* the integrated spectral power is calculated

$$P = \int_{30\text{ MHz}}^{80\text{ MHz}} |x(\omega)|^2 d\omega, \quad (4)$$

where $x(\omega)$ is the ω frequency component of the cleaned spectrum. The power in every antenna is required to be in the range of one half to two times the median power from all antennas. Antennas outside this range are marked as bad and excluded from further analysis.

3.2.4. Absolute gain calibration

There are ongoing efforts for an absolute calibration of the voltage traces of LOFAR and therefore the reconstructed electric

⁶ This effect also occurs when flagging large blocks of RFI but this does not happen in practice and so no tapering window is applied for this case.

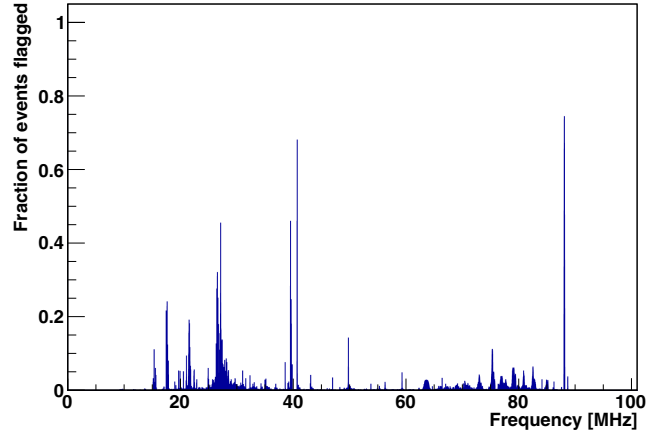


Fig. 8. Fraction of events that is affected by narrow-band RFI in each of the ~ 3 kHz frequency channels as function of frequency.

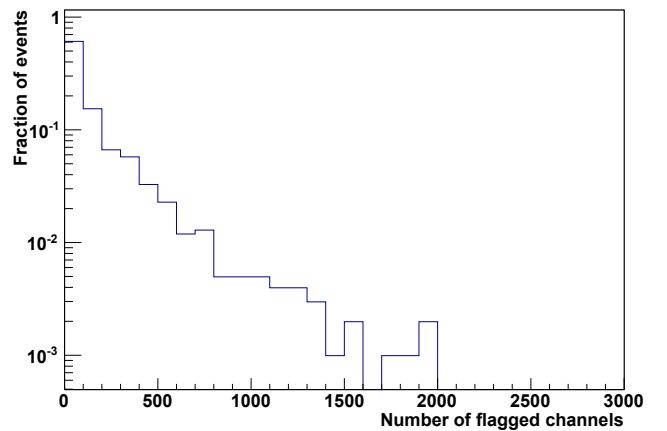


Fig. 9. Relative fraction of events with a certain number of flagged channels. Over 60% of the events have less than 100 channels (≈ 300 kHz) flagged out of the full used bandwidth of more than 16 000 channels.

field. Those efforts will be described in a forthcoming publication and include calibration on astronomical sources, terrestrial transmitters, and already conducted dedicated measurement campaigns, similar to those performed at other experiments, e.g. Nehls et al. (2008). Once implemented, the reconstruction pipeline will deliver calibrated electric field strengths and their polarization components for all events. However, significant progress in understanding the mechanisms of radio emission in air showers can already be made with a relative calibration.

3.2.5. Relative gain calibration

The LBA measurement is dominated by sky noise, which in turn is dominated by the Galaxy moving through the antenna beam pattern. Therefore, the noise as seen by each antenna is a function of the Local Sidereal Time (LST) and can be used to correct for differences in gain between antennas. Instead of correcting all antennas at all times to a fixed value, which would be over- or underestimating the noise at certain times, the received power can be normalized to a LST-dependent reference value. In Fig. 10 the integrated spectral power (Eq. (4)), after RFI cleaning, is given as a function of LST for the instrumental polarization X and Y . The data have been retrieved from all cosmic-ray events measured within the first year of data-taking. One can define a reference value for the integrated spectral power as a

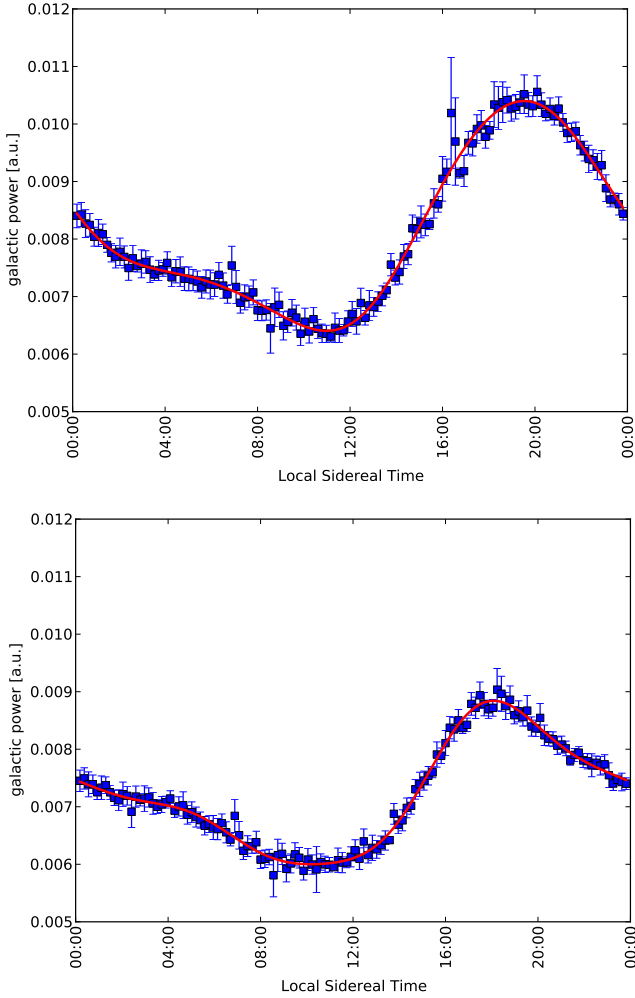


Fig. 10. Integrated spectral power normalized to the bandwidth, after RFI cleaning, as a function of local sidereal time for the X (NE-SW) (*top*) and Y (NW-SE) (*bottom*) instrumental antenna polarizations. Also shown is the fitted second order Fourier transform (solid line). The uncertainties on the data still include systematic effects due to the set-up itself, as well as possible artifacts of the RFI cleaning, when having certain frequencies that are contaminated in a significant fraction of the data.

function of LST by fitting a function to these data points. Since the movement of the Galaxy through the antenna beam pattern is periodic by nature it is fitted with the 2nd order Fourier series

$$P_{\text{ref}}(t) = \frac{a_0}{2} + \sum_{n=1}^2 a_n \sin(nt) + b_n \cos(nt), \quad (5)$$

thereby avoiding artificial jumps in the fit at 0:00 LST. The time t is given in units of radian here. This results in a gain correction for each antenna as

$$x'(\omega) = \sqrt{\frac{P_{\text{ref}}(t)}{P(t)}} x(\omega), \quad (6)$$

where the square root is needed, because the correction is applied to the amplitude spectrum.

3.3. Identifying cosmic-ray signals

After cleaning and calibration of the data, the central element of the pipeline is the identification and characterization of the radio pulse as the signal of the air shower.

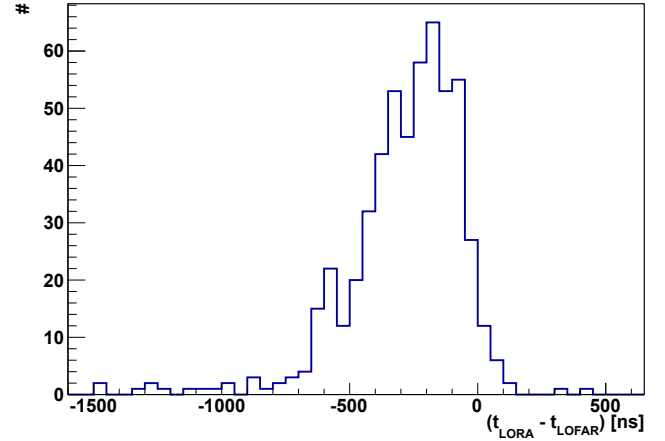


Fig. 11. Difference in time between the time of a pulse identified in the radio signal and the trigger time set by the signal in the particle detectors. This plot shows the distribution summed over all Superterp stations.

3.3.1. Using information from the particle detectors

In order to restrict the search for the radio pulse to a smaller region in the trace, the information from the trigger time of the particle detectors is used. Figure 11 shows the difference in time between the trigger from the particle detectors and the pulse location in the radio data obtained from a search with a large window. The distribution shows a clear peak at the region of the coincidences at an offset of 253 ± 168 ns. In absolute timing the offset between LORA and LOFAR is 10 253 ns, of which 10 000 ns are already accounted for in the triggering system.

Average offset is obtained by fitting a Gaussian to the distribution of pulse positions with respect to the trigger time. This is only an approximation, as the real offset per event depends on the position of the core and the incoming direction of the air shower. Also, effects due to the propagation of particles and radiation in the atmosphere can play a role. The overall difference is due to the fact that both detectors operate independently on different timing systems. Both are based on GPS timing, but correct for drifts (<20 ns) in different ways and have a differing absolute time. The spread on the differences is however sufficiently small for Superterp stations to not require additional synchronization of the two systems. Stations further away can have larger offsets due to the signal travel time, which can be corrected for after a reconstruction of the shower.

These measurements allow for the pulse search to be restricted to a small fraction of the full time trace, limiting the chance to pick up random noise fluctuations.

3.3.2. Finding candidate events

The trigger threshold of the scintillator array is chosen to be lower than the threshold to detect a radio signal. This ensures a full sample, but also makes it necessary to identify in a first quality check whether there is a detectable signal present. Therefore, per antenna polarization, the signals are first *beamformed* in the direction reconstructed from the data of the particle detectors. This direction is given in the local Cartesian coordinate frame of the station by \mathbf{n} and the position of each antenna j is given by \mathbf{r}_j . A planar wavefront arriving at the phase center $(0, 0, 0)$ at time $t = 0$ will arrive at antenna j with a delay given by

$$\Delta t_j = -\frac{1}{c} \frac{\mathbf{n} \cdot \mathbf{r}_j}{|\mathbf{n}|} = -\frac{1}{c} \hat{\mathbf{e}}_n \cdot \mathbf{r}_j, \quad (7)$$

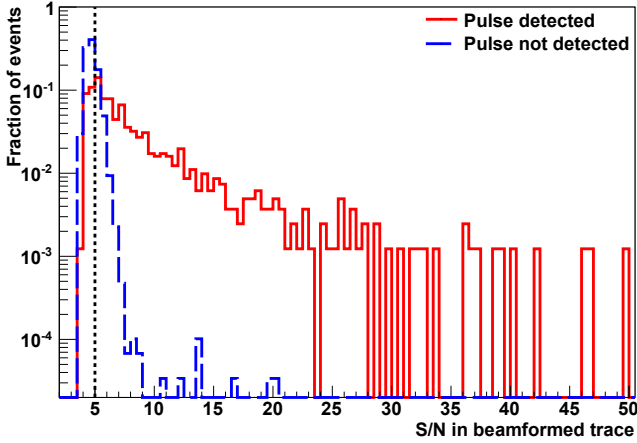


Fig. 12. Distribution of the signal-to-noise ratio (S/N) in initial beamforming. The S/N is defined the ratio of the peak amplitude of the beamformed trace and the RMS of this trace. Two cases are separated: a cosmic-ray event was ultimately detected by the pipeline (solid line) or not (dashed line). The initial cut, which is applied in the pipeline, is indicated by the dotted line.

where c is the speed of light. The beamformed signal, in frequency space, in this direction is then given by

$$x_{\text{br}}(\omega) = \sum_{j=0}^{N_a} x_j(\omega) e^{2\pi i \omega \Delta t_j}, \quad (8)$$

where $x_j(\omega)$ is frequency component ω of the Fourier transform of the signal from antenna j and N_a is the number of antennas. The inverse Fourier transform gives the beamformed time series signal. Due to beamforming any signal coming from the direction of the air shower is amplified by a factor N_a in amplitude while uncorrelated noise is only amplified by a factor $\sqrt{N_a}$. Therefore, if no significant signal is detected in the beamformed trace, the event very unlikely contains a cosmic-ray signal strong enough to be detected at single dipole level by the rest of the pipeline. Thus, the analysis of the data of that station is aborted.

To test this assumption, Fig. 12 shows the distribution of the peak amplitude in the beamformed signal per station, distinguishing between events in which ultimately a cosmic-ray was identified and those in which there was not. The peak amplitude is normalized by the root mean square of the trace, as a proxy for the noise contribution. From this it can be seen that the fraction of events where a strong signal is observed in the beamformed trace is significantly higher for stations where eventually a cosmic-ray signal is detected. All events in the tail of the non-detected distribution were visually inspected and identified as broad-band RFI, with pulses differing significantly in shape from those of cosmic rays and directions ultimately deviating significantly from the direction as measured with the particle detectors. This distribution shows that an initial filtering based on a moderate signal-to-noise of beamformed pulses is a quick and effective way to filter out those events that are potentially interesting, as well as further narrowing the search window per antenna reducing false positives for pulse detection.

3.3.3. Correction for the antenna response

The sensitivity of the LOFAR LBA is a complex function of both frequency and direction. Correcting for this *antenna pattern*, i.e. unfolding, requires an initial guess for the pulse direction and in turn may influence the position of the pulse in time and thus

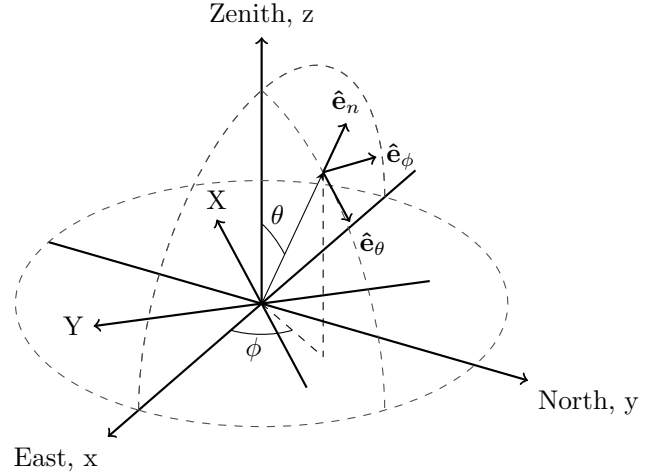


Fig. 13. On-sky polarization coordinate frame ($\hat{e}_\theta, \hat{e}_\phi, \hat{e}_n$). Also depicted is the (north, east, zenith) coordinate frame of the simulations, where the unit vectors ($\hat{e}_x, \hat{e}_y, \hat{e}_z$) correspond to the x, y and z -axis, respectively. Furthermore the dipole antennas X and Y are shown.

the direction by changing the phase at which each frequency arrives. Therefore the correction has to be done in an iterative loop as indicated in Fig. 5. Each iteration starts with an increasingly accurate signal direction and proceeds by unfolding the antenna pattern, pulse detection, and direction fitting. The loop is concluded when the direction no longer significantly changes, which usually happens in less than ~ 5 iterations.

For the antenna pattern of the LBA a simulation is used, which is made using the software WIPL-D (Kolundzija 2011) and a customized software model of the electronics chain.

From the impedance and radiation pattern in a transmitting situation the open circuit voltage is calculated as a function of frequency and direction for an incoming plane wave with an electric field strength of 1 V/m. The equivalent circuit of the antenna in a receiving situation is a voltage source with an internal resistance equal to the antenna impedance. This is combined with measured data of the amplifier directly behind the antenna. The result of the model is the output voltage of the amplifier over a 75Ω resistor⁷.

Any wave coming from a direction \hat{e}_n can be seen as a linear superposition of monochromatic plane waves, polarized in the \hat{e}_ϕ and \hat{e}_θ direction. Here ϕ and θ are the standard spherical coordinate angles with the x and z axis respectively, e.g.

$$\mathbf{E}(t) = \sum_{\omega} (E_{\theta, \omega} \hat{e}_\theta + E_{\phi, \omega} \hat{e}_\phi) e^{-i(kn \cdot x + \omega t)}. \quad (9)$$

This geometry can be seen in Fig. 13.

These terms are related to the output voltage of the amplifier for each dipole, and for each frequency, via the Jones matrix \mathbf{J} (Jones 1941; Hamaker et al. 1996) of the antenna model

$$\begin{pmatrix} V_X \\ V_Y \end{pmatrix} = \begin{pmatrix} J_{X\theta} & J_{X\phi} \\ J_{Y\theta} & J_{Y\phi} \end{pmatrix} \begin{pmatrix} E_\theta \\ E_\phi \end{pmatrix}, \quad (10)$$

where $J_{X\theta}$ is the complex response of the antenna and amplifier of the X -dipole to a wave purely polarized in the \hat{e}_θ direction.

Therefore, in order to both correct for the antenna response and convert from output voltage to electric field strength in the on-sky frame (see Sect. 3.4), each pair of Fourier components

⁷ Matched to the impedance of the coaxial cables connecting the antenna to the station electronics cabinet.

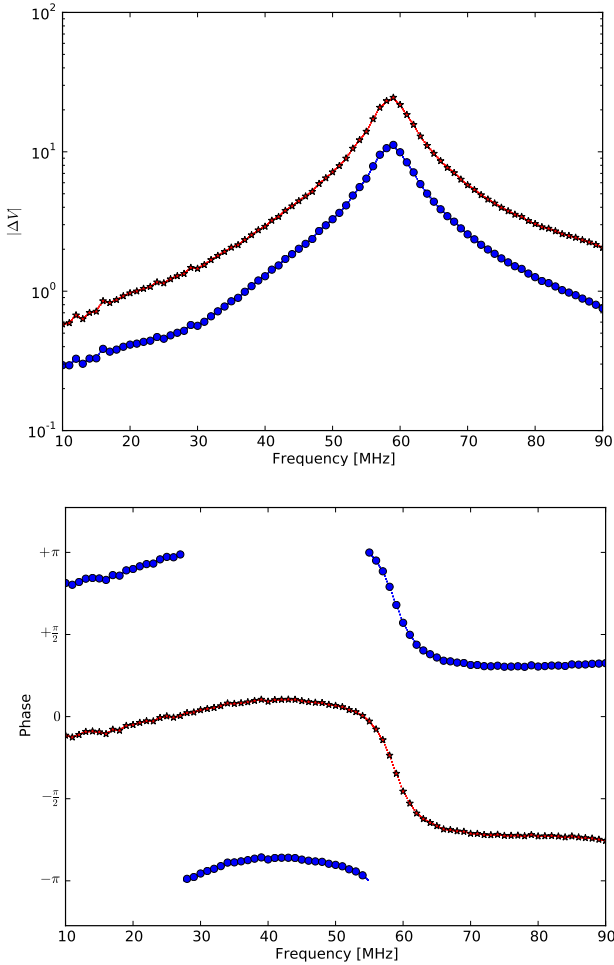


Fig. 14. Jones matrix components of the antenna model amplitudes (*top*) and phases (*bottom*) for a dipole receiving a wave polarized in the \hat{e}_θ direction (circles) and a wave polarized in the \hat{e}_ϕ direction (stars) for an arrival direction of $\phi = 345^\circ$, $\theta = 50^\circ$. Also plotted, as the dotted line, are the interpolated values.

from the signal in the two instrumental polarizations (X, Y) is multiplied by the inverse Jones matrix, followed by an inverse Fourier transform back to the time domain.

The components of the Jones matrix of the antenna model are simulated on a grid with steps of 1 MHz in frequency, 5° in θ and 10° in ϕ . In order to obtain the components at the frequency and direction of observation, trilinear interpolation is performed on the real and imaginary parts of the complex table when needed. Examples of the response are depicted as a function of frequency in Fig. 14 and as a function of direction in Fig. 15.

3.3.4. Pulse detection

Estimating the direction of the incoming air shower, see Sect. 3.3.5, can either be done using beamforming or through pulse timing. Beamforming was found to be very sensitive to the optimization algorithm used, essentially requiring a grid search to avoid getting stuck in a local minimum. This is computationally very expensive, moreover it only provides relative time differences between any two antennas rather than an absolute time needed for extraction of relevant physical parameters (see Sect. 3.4).

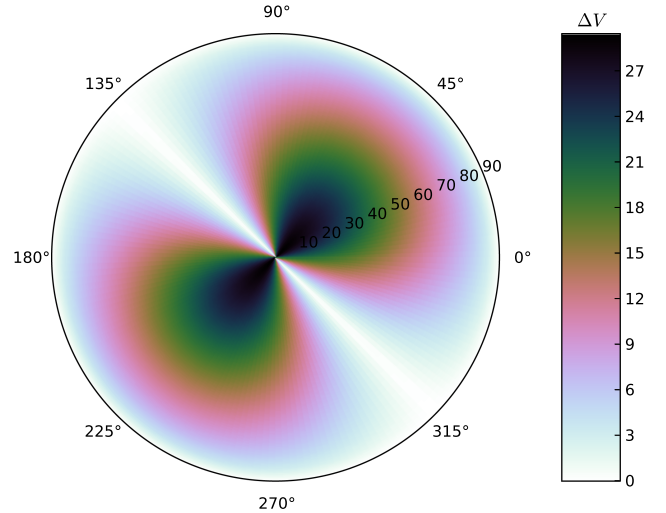


Fig. 15. An example Jones matrix component describing the dipole response, at 60 MHz, $|J_{X,\theta}|$ in the form of the output Voltage (ΔV) as a function of direction for an incoming wave that is purely linearly polarized in the \hat{e}_θ direction.

In order to use pulse timing, individual pulses have to be identified. This can be done by using the cross-correlation method, where one looks for the maximum in the cross correlation of the signals between all antennas. This however has the same drawback as beamforming, as only relative timing is calculated. A method to retrieve the absolute pulse timing is through the use of the *Hilbert envelope*, which is used in this pipeline. A detailed comparison of the methods is given in Sect. 3.3.5.

A sensible definition of the pulse arrival time is the measured arrival time of the maximum of the electric field strength. In practice, however, using directly $\max(|x(t)|^2)$ is highly dependent on the filter characteristics of the receiving system and the sampling used. Therefore, the arrival time is defined as the position of the maximum in the amplitude envelope of the analytic signal, also called the Hilbert envelope

$$A(t) = \sqrt{x^2(t) + \hat{x}^2(t)} \quad (11)$$

where $\hat{x}(t)$ is the *Hilbert transform*, or imaginary propagation, of the signal $x(t)$ defined by

$$\mathcal{F}(\hat{x}(t))(\omega) = -i \cdot \text{sgn}(\omega) \cdot \mathcal{F}(x(t))(\omega) \quad (12)$$

where \mathcal{F} denotes the Fourier transform.

In order to find the pulse maximum with subsample precision, the signal is first up-sampled by a factor 16, such that the maximum search will not be the limiting factor in the timing resolution. Subsequently, a simple maximum search is performed on the envelope. In addition, the signal-to-noise ratio is calculated where the signal is defined as the maximum and the noise as the root mean square of the envelope. An example can be seen in Fig. 16.

This maximum search is performed on each of the on-sky polarizations $E_\theta(t)$ and $E_\phi(t)$ separately and any pulse with a signal to noise greater than three is marked as a possible cosmic-ray signal to be used for direction fitting. Because the pulse is expected to be intrinsically stronger in one of the two polarizations, depending on the angle between the shower axis and the geomagnetic field, the polarization with the highest average signal to noise (over all antennas) is first identified and only its maximum positions are used for the subsequent direction fit.

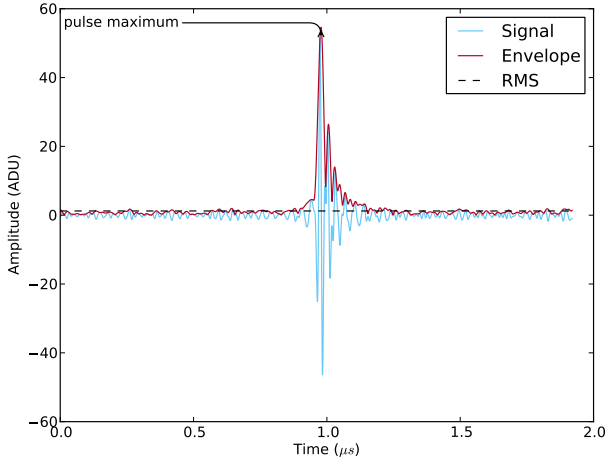


Fig. 16. The solid light line shows the up-sampled signal. Overlaid is the Hilbert envelope and the RMS noise in black dashes. A pulse is accepted whenever the signal to noise ratio exceeds three.

3.3.5. Arrival direction fitting

As described above, every station is processed separately, meaning that the data do not provide a large lever arm for direction fitting. However, it also means that the actual shape of the shower front is an insignificant factor in the direction fitting. For a measurement with a single station, which has a maximum baseline of 80 m, the shower front can be approximated by a plane wave. Thus, to determine the arrival direction of the cosmic ray a planar wavefront is fit to the arrival times of the pulses.

This method assumes that essentially all antennas are on a single plane, which certainly holds for all LOFAR stations as the ground was flattened during construction. Given a vector of arrival times t , and the vectors x and y for the coordinates of the antennas, the best fitting solution for a plane wave:

$$ct = Ax + By + C, \quad (13)$$

can be found using a standard least squares approach. From A and B the Cartesian directions ϕ , θ can be extracted as:

$$A = \sin(\theta) \sin(\phi), \quad (14)$$

$$B = \sin(\theta) \cos(\phi). \quad (15)$$

The plane wave fit itself is done in several iterations. After a fit is performed the residual delays are investigated and those antennas that have residual delays larger than 3 times the standard deviation on the residual delays, are removed from the set and the data are refitted. The fit is terminated when there are less than four antennas left in the set or if no further antennas need to be removed. For this best direction all residual delays, including those of removed antennas, are calculated again and used for quality cuts later.

There are several quality criteria in the pipeline related to the plane wave fit. If the fit fails, a station is not considered further. In addition, a cut is made on the remaining average residual delays with respect to the expectation of the best fit. This cut can be derived from the distribution of all occurring plane wave residual delays, as shown in the top panel of Fig. 17. The first peak with events of an average residual delay of less than 10 ns corresponds to excellent events, in which a clear cosmic-ray pulse can be identified in all antennas. The largest peak corresponds to all those events in which random noise fluctuations are identified as a pulse. This can be illustrated by a small Monte Carlo simulation. A random sample is picked from the range of the search window and its residual to the middle of the search window

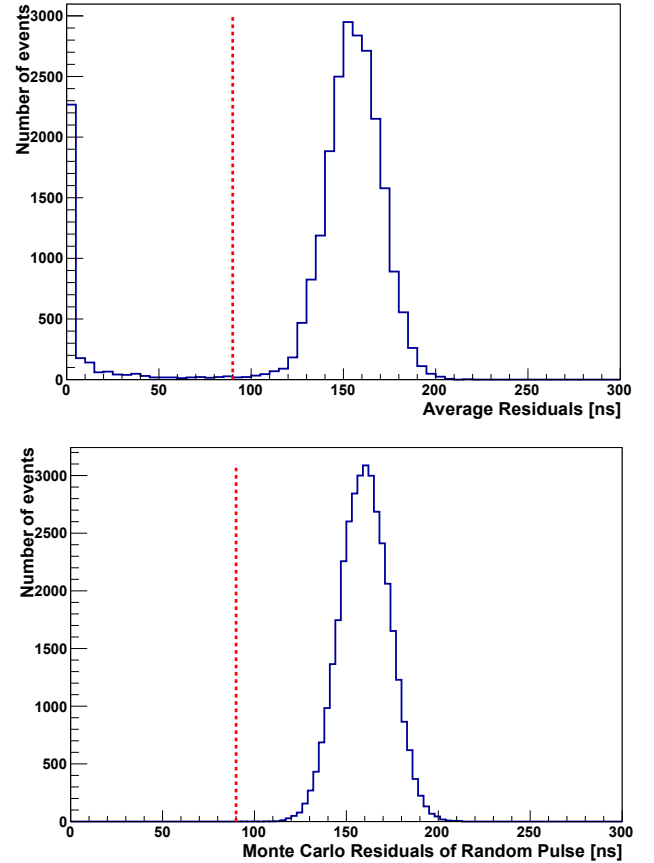


Fig. 17. Average residual delays derived from a plane-fit to data (*top*) and from random samples in the search window with respect to a horizontal shower front (*bottom*). The vertical line indicates the cut value derived from the simulated distribution, which is applied to the data.

(corresponding to a vertical shower) is calculated. This results in the distribution in the bottom panel of Fig. 17. The peak in the distribution obtained from data and the Monte Carlo distribution are centered around the same value and can therefore be identified with each other. Second order effects, being the directions of the air showers and non-infinite sampling, can influence the shape of the peak. The longer tail of the first peak (up to about 50 ns) corresponds to events that have some antennas with correctly identified pulses and varying numbers of outliers, i.e. antennas where a random pulse is identified.

Therefore one can safely choose the value 90 ns as a first cut for good cosmic-ray events. Further cuts for higher quality events or stations can be applied in later analyses.

The plane wave fit results now also allow for a justification of the choice of the Hilbert envelope as the method for pulse timing, as opposed to cross correlation. Figure 18 shows the ratio of the number of antennas in which a pulse has been identified by either method with respect to the remaining residuals on a test-set of randomly chosen events that contain a cosmic-ray signal. The distribution clearly shows that the Hilbert envelope finds significantly more signals in the first bin, i.e. in the correct bin with small residuals. In general, cross correlating is expected to be better for pulses with lower signal-to-noise ratio. For pulses with a high signal-to-noise, however, the Hilbert transform performs more accurately. When using the Hilbert envelope, the position of the maximum is only determined by the recorded individual pulse, whereas the peak of the cross correlation is determined by the degree to which two signals correlate. This degree of correlation can be influenced by correlations in the noise (for instance

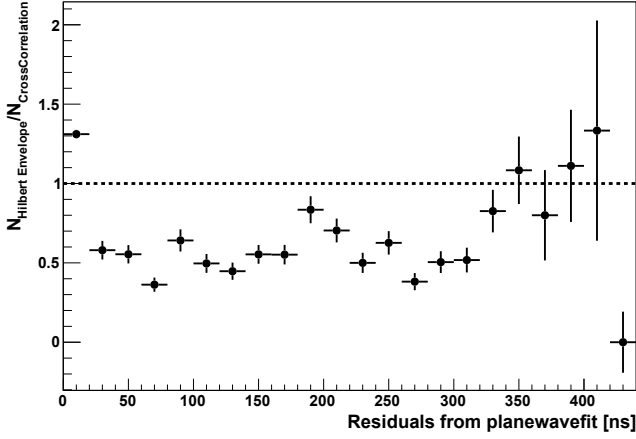


Fig. 18. Difference in reconstruction between Hilbert Envelope and Cross Correlation. The different quality of the reconstruction is illustrated by plotting the fraction of the numbers of antennas N , identified by each method, with respect to the residual that was found in the plane wave reconstruction. For values above one the Hilbert Envelope identified more antennas, which is the case for the desired correctly identified signals, which can be found below 20 ns.

residual RFI) or lacking similarity of the pulse shape between antennas, thereby making the cross-correlation less accurate for timing of pulses with a high signal-to-noise ratio.

3.4. Coordinate transformation

After the antenna pattern unfolding cycle completes with a successful direction fit for a given station, the electric field components in on-sky polarizations $E_\theta(t)$, $E_\phi(t)$, and the shower arrival direction \mathbf{n} are known. However, to compare measured data to air-shower simulations the three-dimensional electric field at ground level

$$\mathbf{E}(t) = E_x(t)\hat{\mathbf{e}}_x + E_y(t)\hat{\mathbf{e}}_y + E_z(t)\hat{\mathbf{e}}_z \quad (16)$$

is needed, where $\hat{\mathbf{e}}_x$, $\hat{\mathbf{e}}_y$ and $\hat{\mathbf{e}}_z$ form the right handed coordinate system pointing east, north and up, respectively. This geometry can also be seen in Fig. 13.

Assuming the signal has no electric field component in the propagation direction $-\hat{\mathbf{e}}_n$, this follows from a simple rotation $(E_x, E_y, E_z)^T = \mathbf{R} \cdot (E_\theta, E_\phi, 0)^T$, with the rotation matrix

$$\mathbf{R} = \begin{pmatrix} \cos \theta \cos \phi & -\sin \phi & \sin \theta \cos \phi \\ \cos \theta \sin \phi & \cos \phi & \sin \theta \sin \phi \\ -\sin \theta & 0 & \cos \theta \end{pmatrix}. \quad (17)$$

Note that this assumption is only an approximation, since the signal is measured in the near field of the shower and the source is moving. However, these are second order effects and the $E_\theta(t)$ and $E_\phi(t)$ components are expected to dominate over the $E_n(t)$ component (Huege 2013). Moreover, since LOFAR uses a dual polarization set-up it is not possible to extract the $E_n(t)$ component of a linearly polarized signal.

The pipeline concludes by storing pulse parameters for each antenna in the projected directions.

3.5. Extracting pulse parameters

In addition to the shower arrival direction, obtained from pulse timing, two more parameters are extracted: for each antenna the peak amplitude and integrated power of the pulse are calculated.

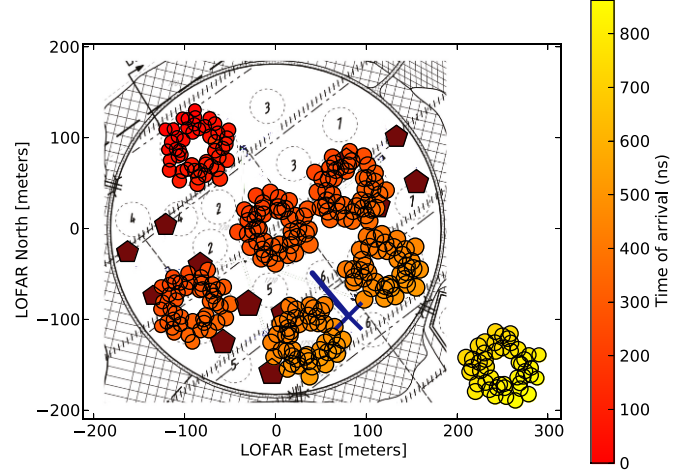


Fig. 19. Footprint of an air shower measured with LOFAR. The signal strength (peak amplitude of the radio signal) is encoded logarithmically in the size of the marker and the color shows the time of arrival. The pentagons represent the positions of the particle detectors, their size is proportional to the number of recorded particles. The reconstructed shower axis is indicated by the blue cross for the core position and the line for the projected arrival direction.

Without multiplicative unit conversion factors, ignored for current lack of absolute calibration, the integrated pulse power is defined through the integration of the instantaneous Poynting vector and the electric field strength as:

$$P = \sum_k P_k \propto \sum_k \int_{\Delta t} |E_k(t)|^2 dt, \quad (18)$$

where $k = (x, y, z)$ are the polarization components of the electric field and Δt is taken as a symmetric window around the pulse maximum.

This is calculated in discrete sampling x_i as

$$P_k = \frac{1}{f} \left(\sum_{\text{signal}} |x_i|^2 - \frac{N_{\text{signal}}}{N_{\text{noise}}} \sum_{\text{noise}} |x_i|^2 \right), \quad (19)$$

where $f = 200$ MHz is the sampling frequency and N_{signal} and N_{noise} are the number of samples in the signal and noise windows respectively. The noise window consists of the full 327 680 ns block excluding the pulse window.

3.6. A measured air shower

The result of the reconstruction pipeline is a full three-dimensional electric field vector per antenna position as a function of time. There are various ways in which this result can be visualized. The shower footprint, Fig. 19, shows the signal strength (peak amplitude of the radio signal) at the measured antenna locations as well as the time of arrival. Here, one can see that both the radio signal strength and the arrival times are consistent with the air-shower direction and core position as determined by the scintillator array. Both effects are distinctive properties of radio emission from air showers and are not produced by RFI.

Another common way to visualize the result is in the form of the lateral distribution, shown in Fig. 20. Here the radio signal strength, in all three polarization components, is shown as a function of projected distance to the shower axis. This projection retains the spatial distribution of the antennas (i.e. stations

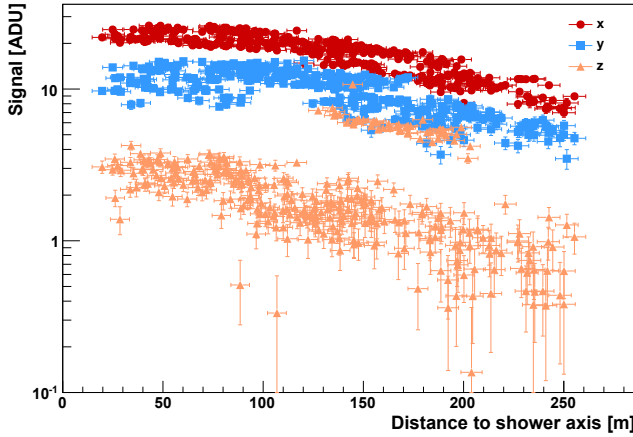


Fig. 20. Distribution of radio signals (peak amplitude in arbitrary units) with respect to the distance from the shower axis as reconstructed from the scintillator data. Shown are the three components of the reconstructed electric field.

can be seen as groups), but azimuthal symmetry in the shower plane is assumed. This rather complicated looking distribution can be explained using detailed models of the radio emission, which also include non-rotational symmetrical effects. Further details of event by event characteristics will be reported in forthcoming publications.

4. Properties of reconstructed air showers

In order to verify the data quality and the method of reconstruction a short overview of the first data taken with LOFAR is given. The data set used here (June 2011 until April 2013) contains 3341 recorded triggers, of which 1597 pass the strict quality cut for a good data reconstruction of the particle measurement. Of all triggers, 405 events contain signals of cosmic rays as identified by the pipeline, with a threshold energy of 5×10^{15} eV.

4.1. Triggers from the array of particle detectors

On the reconstruction of air showers from the particle data quality cuts are applied. The reconstruction is considered reliable, when the reconstructed shower core is contained within the array, the shower is not too horizontal ($\theta < 50^\circ$) and the reconstructed Molière radius⁸ falls in the range of 20–100 m. After cuts, the lowest energy of a shower that triggered a read-out of the LOFAR buffers is 1.8×10^{15} eV and the highest is 1.9×10^{18} eV. The LORA scintillator array becomes fully efficient above 2×10^{16} eV.

All triggers sent by the scintillator array follow a nearly uniform distribution in azimuth and a $\sin(\theta)\cos(\theta)$ -distribution in zenith angle as it is expected from the geometry for a horizontal array with flat detectors.

The number of events with a detectable radio signal increases with the number of triggered particle detectors, as can be seen in Fig. 21, where the fraction of triggered events, with and without a detected radio signal, is plotted against the number of particle detectors per event. The fraction is clearly increasing with the number of triggered detectors, as shown by a fitted straight line. According to this fit, at a threshold of 13 detectors about 10% of the events contain a cosmic-ray signal.

⁸ Characteristic transverse size of an air shower.

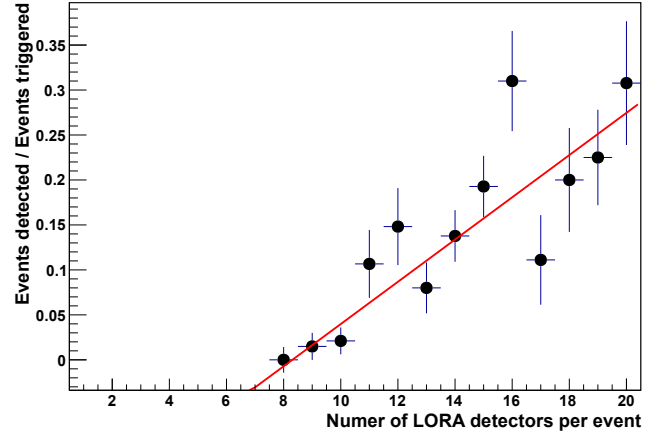


Fig. 21. Fraction of air showers with a detectable radio signal over the number of air showers triggered with a scintillator signal is plotted against the number of particle detectors above threshold in an event. The red straight line is a fit to the data.

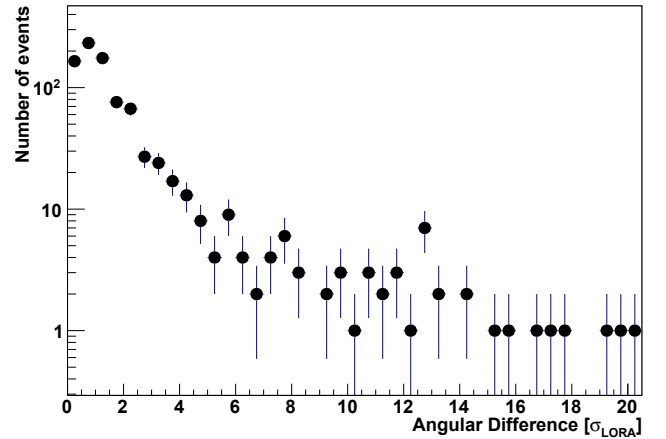


Fig. 22. Angular difference between the shower axis reconstructed from the particle data and the direction estimate from the radio signal. To make the events comparable, the difference is scaled with the uncertainty of the individual reconstruction σ_{LORA} .

4.2. Event rates and sensitivity

For a first estimate all reconstructed triggers are considered valid events which show radio pulses coming from a direction that agrees to 10° angular distance with the direction that was reconstructed from the arrival times measured with the particle detectors. This choice is based on the results shown in Fig. 22. This figure shows the angular difference between the two reconstructed axes for all events. A steep fall-off in number of events with an increasing angular difference can be seen. Any event that deviates more than $10\sigma_{\text{LORA}}$ certainly lies outside the correct distribution. The shower axis is on average reconstructed with an uncertainty $\sigma_{\text{LORA}} \sim 1^\circ$ from the data of the particle detectors. Thus, a quality cut of 10° is chosen.

Figure 23 shows all 405 cosmic-ray events successfully detected with the LBAs as distributed on the local sky. Visible is a clear north-south asymmetry, where 276 events arrive from the northern hemisphere. This corresponds to a probability $p = 0.68 \pm 0.02$ for a detected event to arrive from the north. As the magnetic field at LOFAR is parallel to the north-south axis this is expected, if the main contribution to the signal is of geomagnetic origin (Falcke et al. 2005; Ardouin et al. 2009).

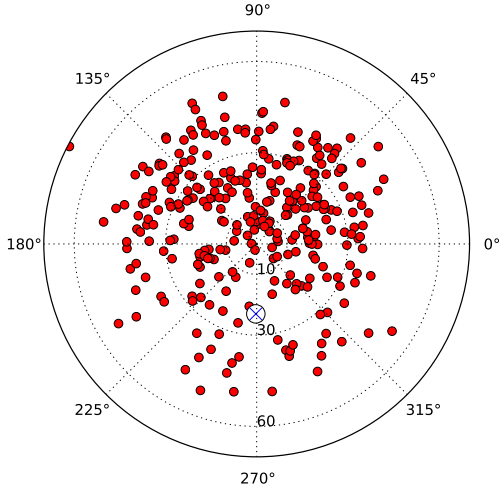


Fig. 23. Arrival directions of the cosmic-ray events detected with LOFAR from June 2011 until April 2013. East is 0° and north corresponds to 90°. Also indicated (cross) is the direction of the magnetic field at LOFAR.

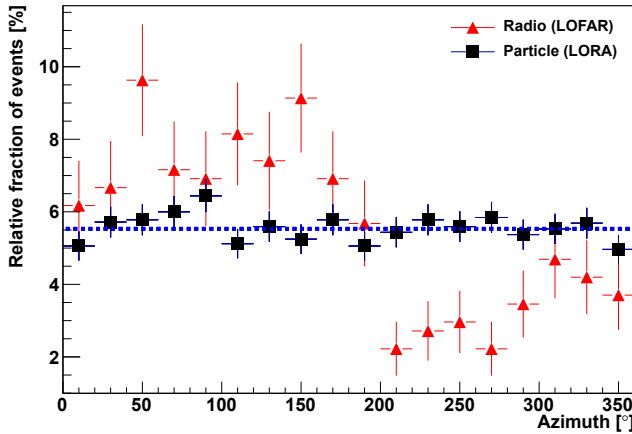


Fig. 24. Binned distribution of the azimuth angles of all events measured with the particle detectors (black squares) and those in coincidence of particle detectors and radio antennas (red triangles). The best fit of a straight line to the particle data is also shown. The fit has a $\chi^2/\text{nd.o.f.} = 0.9$.

The effect is also illustrated in Fig. 24, which shows the fraction of detected air showers as a function of azimuth angle for the events with radio signal, as well as for all LORA triggers sent. While the events registered with the LORA detectors are uniformly distributed in azimuth, the radio events show a clear deficit from the south. Due to the orientation of the LOFAR antennas and thereby the reduced sensitivity for purely east-west polarized signals, events arriving directly from the north are not necessarily preferred, as their signal is expected to be mainly polarized in the east-west direction (Huege 2013). The detection efficiency as a function of direction follows from a deconvolution of the expected emission strength with the antenna pattern and will not be discussed in detail here.

The energies of the air showers with a detectable radio signal are shown in Fig. 25. The depicted energy is the one reconstructed from the corresponding particle data. This reconstruction has an overall systematic uncertainty of 27% and varying event by event uncertainties (Thoudam et al., in prep.). One clearly sees that below $\sim 10^{17}$ eV the detection of air showers through their radio signal is not fully efficient, as the strength

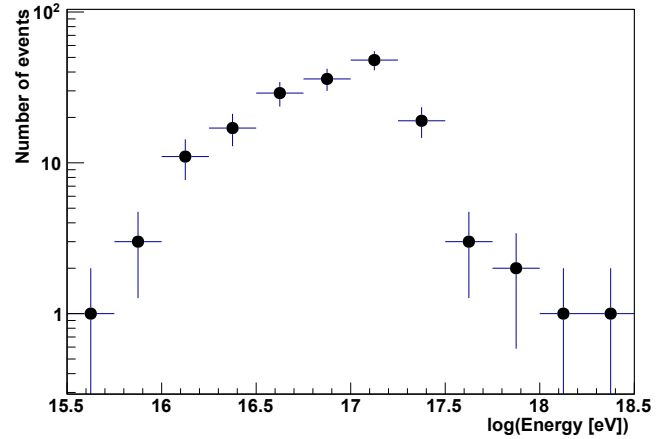


Fig. 25. Distribution of the energies of the cosmic rays which had a measurable radio signal in the LOFAR data. The depicted energy is the one reconstructed from the corresponding particle data. The quality cuts, as described in Sect. 4.1, are applied.

of the radio signal scales with the energy of the shower. Higher energies in this distribution are constrained by the steeply falling cosmic-ray energy spectrum and limited size of the detector array, which leads to limited event statistics at the highest energies. There are significant hints that showers of higher energies have been measured with LOFAR (especially when including the stations outside the Superterp), but these events are not well enough constrained by the data from the particle detectors in order to have a reference energy of the necessary accuracy. After a calibration of the energy of the radio measurements, those events will be used in a radio-stand-alone reconstruction.

5. Conclusions

At LOFAR cosmic-ray induced air showers are regularly measured with an array of particle detectors, LORA, and a large array of radio antennas. The cosmic-ray pipeline is routinely finding their distinctive radio signatures in the measurements and a full three-dimensional electric field vector is reconstructed for every antenna position.

A large dataset has been gathered with hundreds of identified cosmic-ray events in data from the LBAs. With up to a thousand antennas per events, these are the first highly detailed measurement of the radio signal of air showers. These measurements will be used for a detailed characterization of the shower shape and will be the benchmark data for comparison with models of radio emission in air showers.

Acknowledgements. The LOFAR cosmic ray key science project very much acknowledges the scientific and technical support from ASTRON, especially in constructing the LORA particle detectors. We thank the KASCADE Collaboration for providing the scintillator detectors. Furthermore, we acknowledge financial support from the Netherlands Research School for Astronomy (NOVA), the Samenwerkingsverband Noord-Nederland (SNN) and the Foundation for Fundamental Research on Matter (FOM) as well as support from the Netherlands Organization for Scientific Research (NWO), VENI grant 639-041-130. We acknowledge funding from an Advanced Grant of the European Research Council under the European Union's Seventh Framework Program (FP/2007-2013) / ERC Grant Agreement n. 227610. LOFAR, the Low Frequency Array designed and constructed by ASTRON, has facilities in several countries, that are owned by various parties (each with their own funding sources), and that are collectively operated by the International LOFAR Telescope (ILT) foundation under a joint scientific policy. The authors would like to thank both the internal and external referees for carefully reading the manuscript. Chiara Ferrari and Giulia Macario acknowledge financial support by the "Agence Nationale de la Recherche" through grant ANR-09-JCJC-0001-01.

References

- Alexov, A., Schellart, P., ter Veen, S., et al. 2012, in *Astronomical Data Analysis Software and Systems XXI*, eds. P. Ballester, D. Egret, & N. P. F. Lorente, ASP Conf. Ser., 461, 283
- Allan, H., & Jones, J. 1966, *Nature*, 212, 129
- Alvarez-Muñiz, J., Carvalho, W. R., & Zas, E. 2012, *Astropart. Phys.*, 35, 325
- Ardouin, D., Belletoile, A., Charrier, D., et al. 2005, *Int. J. Mod. Phys. A*, 20, 6869
- Ardouin, D., Belletoile, A., Berat, C., et al. 2009, *Astropart. Phys.*, 31, 192
- Falcke, H., Apel, W. D., Badea, A. F., et al. 2005, *Nature*, 435, 313
- Falcke, H., et al. 2008, in *ICRC Merida, Vol. Rapporteur*, 30th Int. Cosmic Ray Conf.
- Hamaker, J. P., Bregman, J. D., & Sault, R. J. 1996, *A&AS*, 117, 137
- Huege, T. 2013, *ARENA 2012*, AIP Conf. Proc. 1535, 121
- Huege, T., Apel, W. D., Arteaga, J. C., et al. 2012, *Nucl. Instr. Meth. Phys. Res. A*, 662, 72
- Huege, T., Ludwig, M., & James, C. W. 2013, *ARENA 2012*, AIP Conf. Proc. 1535, 128
- Jelley, J., Fruin, J., Porter, N., et al. 1965, *Nature*, 205, 327
- Jones, R. C. 1941, *Journal of the Optical Society of America*, 31, 488
- Kolundzija, B. 2011, in *Proc. of the 5th European Conference on Antennas and Propagation (EUCAP)*
- Marin, V., & Revenu, B. 2012, *Astropart. Phys.*, 35, 733
- Nehls, S., Hakenjos, A., Arts, M. J., et al. 2008, *Nucl. Inst. Meth. A*, 589, 350
- Offringa, A. R., de Bruyn, A. G., Zaroubi, S., et al. 2013, *A&A*, 549, A11
- van Cappellen, W., Rüter, M., & Kant, G. 2007, *LOFAR-ASTRON-ADD-009*
- van Haarlem, M. P., Wise, M. W., Gunst, A. W., et al. 2013, *A&A*, 556, A2
- Werner, K., de Vries, K. D., & Scholten, O. 2012, *Astropart. Phys.*, 37, 5
- ¹³ Max Planck Institute for Astrophysics, Karl Schwarzschild Str. 1, 85741 Garching, Germany
- ¹⁴ International Centre for Radio Astronomy Research – Curtin University, GPO Box U1987, WA 6845 Perth, Australia
- ¹⁵ STFC Rutherford Appleton Laboratory, Harwell Science and Innovation Campus, Didcot OX11 0QX, UK
- ¹⁶ Institute for Astronomy, University of Edinburgh, Royal Observatory of Edinburgh, Blackford Hill, Edinburgh EH9 3HJ, UK
- ¹⁷ LESIA, UMR CNRS 8109, Observatoire de Paris, 92195 Meudon, France
- ¹⁸ Argelander-Institut für Astronomie, University of Bonn, Auf dem Hügel 71, 53121 Bonn, Germany
- ¹⁹ Leibniz-Institut für Astrophysik Potsdam (AIP), An der Sternwarte 16, 14482 Potsdam, Germany
- ²⁰ Thüringer Landessternwarte, Sternwarte 5, 07778 Tautenburg, Germany
- ²¹ Astronomisches Institut der Ruhr-Universität Bochum, Universitätsstrasse 150, 44780 Bochum, Germany
- ²² Laboratoire de Physique et Chimie de l'Environnement et de l'Espace, LPC2E UMR 7328 CNRS, 45071 Orléans Cedex 02, France
- ²³ SRON Netherlands Institute for Space Research, PO Box 800, 9700 AV Groningen, The Netherlands
- ²⁴ Center for Information Technology (CIT), University of Groningen, The Netherlands
- ²⁵ Centre de Recherche Astrophysique de Lyon, Observatoire de Lyon, 9 av Charles André, 69561 Saint Genis Laval Cedex, France
- ²⁶ ARC Centre of Excellence for All-sky astrophysics (CAASTRO), Sydney Institute of Astronomy, University of Sydney, Australia
- ²⁷ University of Hamburg, Gojenbergsweg 112, 21029 Hamburg, Germany
- ²⁸ Astro Space Center of the Lebedev Physical Institute, Profsoyuznaya str. 84/32, 117997 Moscow, Russia
- ²⁹ Centre for Radio Astronomy Techniques & Technologies (RATT), Department of Physics and Electronics, Rhodes University, PO Box 94, 6140 Grahamstown, South Africa
- ³⁰ SKA South Africa, 3rd Floor, The Park, Park Road, 7405 Pinelands, South Africa
- ³¹ Harvard-Smithsonian Center for Astrophysics, 60 Garden Street, Cambridge, MA 02138, USA
- ³² Laboratoire Lagrange, UMR7293, Université de Nice Sophia-Antipolis, CNRS, Observatoire de la Côte d'Azur, 06300 Nice, France
- ³³ Space Telescope Science Institute, 3700 San Martin Drive, Baltimore, MD 21218, USA
- ³⁴ Sodankylä Geophysical Observatory, University of Oulu, Tähteläntie 62, 99600 Sodankylä, Finland
- ³⁵ Netherlands eScience Center, Science Park 140, 1098 XG Amsterdam, The Netherlands
- ³⁶ Fakultät für Physik, Universität Bielefeld, Postfach 100131, 33501 Bielefeld, Germany

A large light-mass component of cosmic rays at 10^{17} – $10^{17.5}$ electronvolts from radio observations

S. Buitink^{1,2}, A. Corstanje², H. Falcke^{2,3,4,5}, J. R. Hörandel^{2,4}, T. Huege⁶, A. Nelles^{2,7}, J. P. Rachen², L. Rossetto², P. Schellart², O. Scholten^{8,9}, S. ter Veen³, S. Thoudam², T. N. G. Trinh⁸, J. Anderson¹⁰, A. Asgekar^{3,11}, I. M. Avruch^{12,13}, M. E. Bell¹⁴, M. J. Bentum^{3,15}, G. Bernardi^{16,17}, P. Best¹⁸, A. Bonafede¹⁹, F. Breitling²⁰, J. W. Broderick²¹, W. N. Brouw^{3,13}, M. Brügger¹⁹, H. R. Butcher²², D. Carbone²³, B. Ciardi²⁴, J. E. Conway²⁵, F. de Gasperin¹⁹, E. de Geus^{3,26}, A. Deller³, R.-J. Dettmar²⁷, G. van Diepen³, S. Duscha³, J. Eislöffel²⁸, D. Engels²⁹, J. E. Enriquez³, R. A. Fallows³, R. Fender³⁰, C. Ferrari³¹, W. Frieswijk³, M. A. Garrett^{3,32}, J. M. Grießmeier^{33,34}, A. W. Gunst³, M. P. van Haarlem³, T. E. Hassall²¹, G. Heald^{3,13}, J. W. T. Hessels^{3,23}, M. Hoefl²⁸, A. Horneffer⁵, M. Iacobelli³, H. Intema^{32,35}, E. Juette²⁷, A. Karastergiou³⁰, V. I. Kondratiev^{3,36}, M. Kramer^{5,37}, M. Kuniyoshi³⁸, G. Kuper³, J. van Leeuwen^{3,23}, G. M. Loose³, P. Maat³, G. Mann²⁰, S. Markoff²³, R. McFadden³, D. McKay-Bukowski^{39,40}, J. P. McKean^{3,13}, M. Mevius^{3,13}, D. D. Mulcahy²¹, H. Munk³, M. J. Norden³, E. Orru³, H. Paas⁴¹, M. Pandey-Pommier⁴², V. N. Pandey³, M. Pietka³⁰, R. Pizzo³, A. G. Polatidis³, W. Reich⁵, H. J. A. Röttgering³², A. M. M. Scaife²¹, D. J. Schwarz⁴³, M. Serylak³⁰, J. Sluman³, O. Smirnov^{17,44}, B. W. Stappers³⁷, M. Steinmetz²⁰, A. Stewart³⁰, J. Swinbank^{23,45}, M. Tagger³³, Y. Tang³, C. Tasse^{44,46}, M. C. Toribio^{3,32}, R. Vermeulen³, C. Vocks²⁰, C. Vogt³, R. J. van Weeren¹⁶, R. A. M. J. Wijers²³, S. J. Wijnholds³, M. W. Wise^{3,23}, O. Wucknitz⁵, S. Yatawatta³, P. Zarka⁴⁷ & J. A. Zensus⁵

Cosmic rays are the highest-energy particles found in nature. Measurements of the mass composition of cosmic rays with energies of 10^{17} – 10^{18} electronvolts are essential to understanding whether they have galactic or extragalactic sources. It has also been proposed that the astrophysical neutrino signal¹ comes from accelerators capable of producing cosmic rays of these energies². Cosmic rays initiate air showers—cascades of secondary particles in the atmosphere—and their masses can be inferred from measurements of the atmospheric depth of the shower maximum³ (X_{max} ; the depth of the air shower when it contains the most particles) or of the composition of shower particles reaching the ground⁴. Current measurements⁵ have either high uncertainty, or a low duty cycle and a high energy threshold. Radio detection of cosmic rays^{6–8} is a rapidly developing technique⁹ for determining X_{max} (refs 10, 11) with a duty cycle of, in principle, nearly 100 per cent. The radiation is generated by the separation of relativistic electrons and positrons in the geomagnetic field and a negative charge excess in the shower front^{6,12}. Here we report radio measurements of X_{max} with a mean uncertainty of 16 grams per square centimetre for air showers

initiated by cosmic rays with energies of 10^{17} – $10^{17.5}$ electronvolts. This high resolution in X_{max} enables us to determine the mass spectrum of the cosmic rays: we find a mixed composition, with a light-mass fraction (protons and helium nuclei) of about 80 per cent. Unless, contrary to current expectations, the extragalactic component of cosmic rays contributes substantially to the total flux below $10^{17.5}$ electronvolts, our measurements indicate the existence of an additional galactic component, to account for the light composition that we measured in the 10^{17} – $10^{17.5}$ electronvolt range.

Observations were made with the Low Frequency Array (LOFAR¹³), a radio telescope consisting of thousands of crossed dipoles with built-in air-shower-detection capability¹⁴. LOFAR continuously records the radio signals from air showers, while simultaneously running astronomical observations. It comprises a scintillator array (LORA) that triggers the read-out of buffers, storing the full waveforms received by all antennas.

We selected air showers from the period June 2011 to January 2015 with radio pulses detected in at least 192 antennas. The total uptime was about 150 days, limited by construction and commissioning of the

¹Astrophysical Institute, Vrije Universiteit Brussel, Pleinlaan 2, 1050 Brussels, Belgium. ²Department of Astrophysics/IMAPP, Radboud University Nijmegen, PO Box 9010, 6500 GL Nijmegen, The Netherlands. ³ASTRON, Netherlands Institute for Radio Astronomy, Postbus 2, 7990 AA Dwingeloo, The Netherlands. ⁴Nikhef, Science Park Amsterdam, 1098 XG Amsterdam, The Netherlands. ⁵Max-Planck-Institut für Radioastronomie, Auf dem Hügel 69, 53121 Bonn, Germany. ⁶Institute for Nuclear Physics (IKP), Karlsruhe Institute of Technology (KIT), Postfach 3640, 76021 Karlsruhe, Germany. ⁷Department of Physics and Astronomy, University of California Irvine, Irvine, California 92697, USA. ⁸KVI Center for Advanced Radiation Technology, University of Groningen, 9747 AA Groningen, The Netherlands. ⁹Vrije Universiteit Brussel, Dienst ELEM, B-1050 Brussels, Belgium. ¹⁰Helmholtz-Zentrum Potsdam, Deutsches GeoForschungsZentrum GFZ, Department 1, Geodesy and Remote Sensing, Telegrafenberg A17, 14473 Potsdam, Germany. ¹¹Shell Technology Center, 560 048 Bangalore, India. ¹²SRON Netherlands Institute for Space Research, PO Box 800, 9700 AV Groningen, The Netherlands. ¹³Kapteyn Astronomical Institute, PO Box 800, 9700 AV Groningen, The Netherlands. ¹⁴CSIRO Australia Telescope National Facility, PO Box 76, Epping, New South Wales 1710, Australia. ¹⁵University of Twente, PO Box 217, 7500 AE Enschede, The Netherlands. ¹⁶Harvard-Smithsonian Center for Astrophysics, 60 Garden Street, Cambridge, Massachusetts 02138, USA. ¹⁷Square Kilometre Array (SKA) South Africa, 3rd Floor, The Park, Park Road, Pinelands 7405, South Africa. ¹⁸Institute for Astronomy, University of Edinburgh, Royal Observatory of Edinburgh, Blackford Hill, Edinburgh EH9 3HJ, UK. ¹⁹University of Hamburg, Gojenbergsweg 112, 21029 Hamburg, Germany. ²⁰Leibniz-Institut für Astrophysik Potsdam (AIP), An der Sternwarte 16, 14482 Potsdam, Germany. ²¹School of Physics and Astronomy, University of Southampton, Southampton SO17 1BJ, UK. ²²Research School of Astronomy and Astrophysics, Australian National University, Canberra, Australian Capital Territory 2611, Australia. ²³Anton Pannekoek Institute for Astronomy, University of Amsterdam, Science Park 904, 1098 XH Amsterdam, The Netherlands. ²⁴Max Planck Institute for Astrophysics, Karl Schwarzschild Strasse 1, 85741 Garching, Germany. ²⁵Onsala Space Observatory, Department of Earth and Space Sciences, Chalmers University of Technology, SE-43392 Onsala, Sweden. ²⁶SmarterVision BV, Oostersingel 5, 9401 JX Assen, The Netherlands. ²⁷Astronomisches Institut der Ruhr-Universität Bochum, Universitätsstrasse 150, 44780 Bochum, Germany. ²⁸Thüringer Landessternwarte, Sternwarte 5, D-07778 Tautenburg, Germany. ²⁹Hamburger Sternwarte, Gojenbergsweg 112, D-21029 Hamburg. ³⁰Department of Astrophysics, University of Oxford, Denys Wilkinson Building, Keble Road, Oxford OX1 3RH, UK. ³¹Laboratoire Lagrange, Université Côte d'Azur, Observatoire de la Côte d'Azur, CNRS, Boulevard de l'Observatoire, CS 34229, 06304 Nice Cedex 4, France. ³²Leiden Observatory, Leiden University, PO Box 9513, 2300 RA Leiden, The Netherlands. ³³LPC2E - Université d'Orléans/CNRS, 45071 Orléans Cedex 2, France. ³⁴Station de Radioastronomie de Nancy, Observatoire de Paris - CNRS/INSU, USR 704 - Université Orléans, OSUC, route de Souesmes, 18330 Nançay, France. ³⁵National Radio Astronomy Observatory, 1003 Lopezville Road, Socorro, New Mexico 87801-0387, USA. ³⁶Astro Space Center of the Lebedev Physical Institute, Profsoyuznaya street 84/32, Moscow 117997, Russia. ³⁷Jodrell Bank Centre for Astrophysics, School of Physics and Astronomy, University of Manchester, Manchester M13 9PL, UK. ³⁸National Astronomical Observatory of Japan, Tokyo 181-8588, Japan. ³⁹Sodankylä Geophysical Observatory, University of Oulu, Tähteläntie 62, 99600 Sodankylä, Finland. ⁴⁰STFC Rutherford Appleton Laboratory, Harwell Science and Innovation Campus, Didcot OX11 0QX, UK. ⁴¹Center for Information Technology (CIT), University of Groningen, PO Box 72, 9700 AB Groningen, The Netherlands. ⁴²Centre de Recherche Astrophysique de Lyon, Observatoire de Lyon, 9 avenue Charles André, 69561 Saint Genis Laval Cedex, France. ⁴³Fakultät für Physik, Universität Bielefeld, Postfach 100131, D-33501 Bielefeld, Germany. ⁴⁴Department of Physics and Electronics, Rhodes University, PO Box 94, Grahamstown 6140, South Africa. ⁴⁵Department of Astrophysical Sciences, Princeton University, Princeton, New Jersey 08544, USA. ⁴⁶GEPi, Observatoire de Paris, CNRS, Université Paris Diderot, 5 place Jules Janssen, 92190 Meudon, France. ⁴⁷LESIA, Observatoire de Paris, CNRS, UPMC, Université Paris Diderot, 5 place Jules Janssen, 92190 Meudon, France.

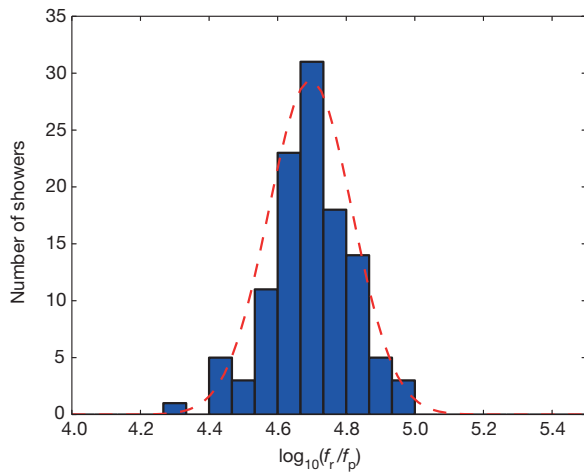


Figure 1 | Energy resolution. The distribution of f_r/f_p (blue bars) is fitted with a Gaussian (red dashed curve), yielding a standard deviation of $\sigma = 0.12$ on a logarithmic scale, which corresponds to an energy resolution of 32%; this value is the quadratic sum of the energy resolution of the radio and particle resolutions. In this analysis, there was no absolute calibration for the received radio power, so f_r has an arbitrary scale.

telescope. Showers that occurred within an hour of lightning activity or that have a polarization pattern that is indicative of influences from atmospheric electric fields are excluded from the sample¹⁵.

Radio intensity patterns from air showers are asymmetric, owing to the interference between geomagnetic and charge-excess radiation. These patterns are reproduced from first principles by summing the radio contributions of all electrons and positrons in the shower. We use the radio simulation code CoREAS¹⁶, a plug-in of CORSIKA¹⁷, which follows this approach.

It has been shown that X_{\max} , the atmospheric depth of the shower maximum, can be accurately reconstructed from densely sampled radio measurements¹⁸. (The atmospheric depth is the air density integrated over the path that the particle has travelled, starting at the top of the atmosphere.) We use a hybrid approach that involves simultaneously fitting the radio and particle data. The radio component is very sensitive to X_{\max} , whereas the particle component is used for the energy measurement.

The fit contains four free parameters: the shower core position (x, y), and scaling factors for the particle density (f_p) and the radio power (f_r). If f_p deviates substantially from unity, then the reconstructed energy does not match the simulation and a new set of simulations is produced. This procedure is repeated until the energies agree within the chosen uncertainties. The ratio of f_r and f_p should be the same for all showers, and is used to derive the energy resolution of 32% (see Fig. 1).

The radio intensity fits have reduced χ^2 values ranging from 0.9 to 2.9. All features in the data are well reproduced by the simulation (see Extended Data Figs 1–5), which demonstrates that the radiation mechanism is well understood. The reduced χ^2 values that exceed unity could indicate uncertainties in the antenna response or the atmospheric properties that were not already accounted for, or limitations of the simulation software.

Radio detection becomes more efficient for higher-altitude showers that have larger footprints (that is, larger areas on the ground in which the radio pulse can be detected). However, the particle trigger becomes less efficient because the number of particles reaching the ground decreases. To avoid a bias, we require that all the simulations produced for a shower satisfy a trigger criterion (see Methods). Above 10^{17} eV, this requirement removes four showers from the sample. At lower energies, the number of showers excluded increases rapidly, and so we exclude all showers with energies less than 10^{17} eV from our analysis.

Furthermore, we evaluate the reconstructed core positions of all simulated showers. Showers with a mean reconstruction error greater

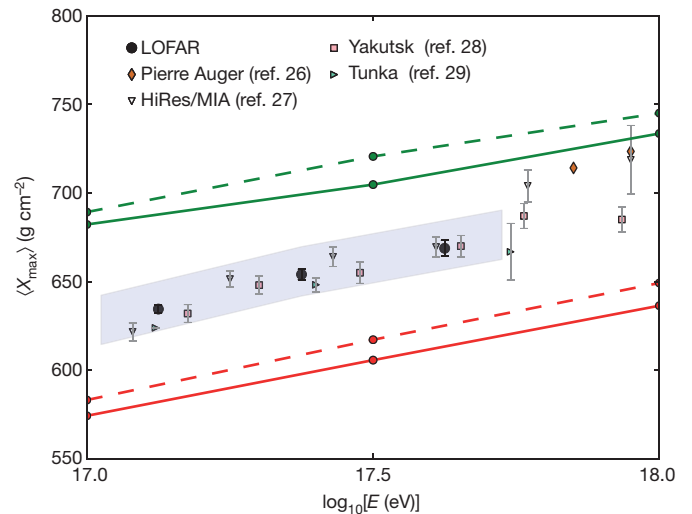


Figure 2 | Measurements of $\langle X_{\max} \rangle$. Mean depth of the shower maximum X_{\max} as a function of energy E for LOFAR, and for previous experiments that used different techniques^{26–29}. Error bars indicate 1σ uncertainties. The systematic uncertainties are $^{+14}_{-10}$ g cm⁻² on $\langle X_{\max} \rangle$ and 27% on E , as indicated by the shaded band. The Pierre Auger Observatory²⁶ measures the fluorescent light emitted by atmospheric molecules excited by air-shower particles. HiRes/MIA²⁷ used a combination of this fluorescence technique and muon detection. The Yakutsk²⁸ and Tunka²⁹ arrays use non-imaging Cherenkov detectors. The green (upper) lines indicate $\langle X_{\max} \rangle$ for proton showers simulated using QGSJETII.04 (solid) and EPOS-LHC (dashed); the red (lower) lines are for showers initiated by iron nuclei.

than 5 m are rejected. This criterion does not introduce a composition bias because it is based on the sets of simulated showers, not on the data. The final event sample contains 118 showers.

The uncertainty in X_{\max} is determined independently for all showers¹⁸, and has a mean value of 16 g cm⁻² (see Extended Data Fig. 6). Figure 2 shows our measurements of the average X_{\max} , $\langle X_{\max} \rangle$, which are consistent with earlier experiments using different methods. The high resolution for X_{\max} per shower allows us to derive more information about the composition of cosmic rays, by studying the shape of the X_{\max} distribution. For each shower, we calculate a mass-dependent parameter:

$$a = \frac{\langle X_{\text{proton}} \rangle - X_{\text{shower}}}{\langle X_{\text{proton}} \rangle - \langle X_{\text{iron}} \rangle} \quad (1)$$

in which X_{shower} is the reconstructed X_{\max} , and $\langle X_{\text{proton}} \rangle$ and $\langle X_{\text{iron}} \rangle$ are mean values of X_{\max} for proton and iron showers, respectively, predicted by the hadronic interaction code QGSJETII.04¹⁹.

The cumulative probability density function (CDF) for all showers is plotted in Fig. 3. First, we fit a two-component model of protons and iron nuclei (p and Fe), with the mixing ratio as the only free parameter. To calculate the corresponding CDFs we use a parameterization of the X_{\max} distribution fitted to simulations based on QGSJETII.04. The best fit is found for a proton fraction of 62%, but this fit describes the data poorly, with $p = 1.1 \times 10^{-6}$. (The test statistic for this fit is the maximum deviation between the data and the model CDFs, and p represents the probability of observing this deviation, or a larger one, assuming the fitted composition model; see Methods.)

A better fit is achieved with a four-component model of protons and helium, nitrogen and iron nuclei (p, He, N and Fe), yielding $p = 0.17$. Although the best fit is found for a helium fraction of 80%, the fit quality deteriorates slowly when replacing helium nuclei with protons. This is demonstrated in Fig. 4, in which p is plotted for four-component fits for which the fractions of helium nuclei and protons are fixed, and the ratio of nitrogen and iron nuclei is the only free parameter. The total fraction of light elements (p and He) is in the range [0.38, 0.98] at a 99% confidence level, with a best-fit value of 0.8. The heaviest

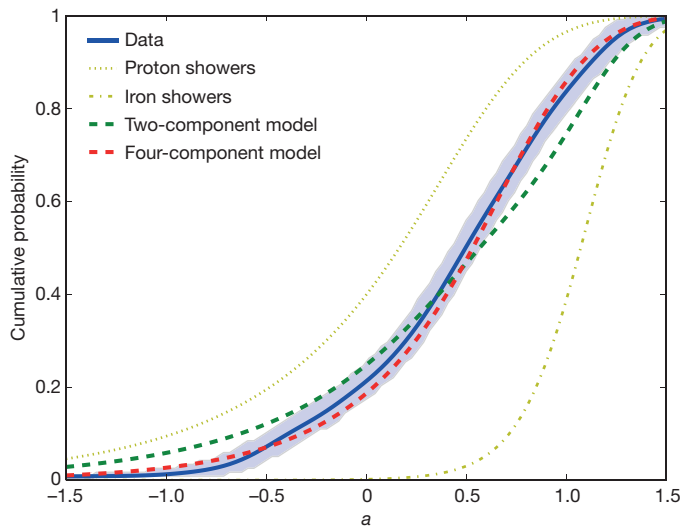


Figure 3 | Composition model fits. The cumulative probability density of the parameter a (see equation (1)) determined from the data (blue line; shading indicates the range in which $p > 0.01$) and several models, on the basis of QGSJETII.04 simulations. The set that contains only proton showers is centred around $a = 0$ and has a large spread (yellow dotted line), whereas iron showers give a distribution with a small spread centred around $a = 1$ (yellow dash-dotted line). A two-component model (p and Fe; green dashed line) yields the best fit for a proton fraction of 62%, but does not describe the data well ($p = 1.1 \times 10^{-6}$). A four-component model (p, He, N and Fe; red dashed line) gives the best fit with 0% protons, 79% helium, 19% nitrogen and 2% iron, with $p = 0.17$. The uncertainty on these values is presented in Fig. 4.

composition that is allowed within systematic uncertainties has a best-fit light-element fraction of 0.6 and a 99% confidence interval of [0.18, 0.82]. For information about the systematic uncertainties and the statistical analysis, see Methods.

The abundances of individual elements depend on the hadronic interaction model. The X_{\max} values predicted by EPOS-LHC²⁰ are, on average, 15–20 g cm^{-2} higher than those predicted by QGSJETII.04 (see Fig. 2). This coincides with the separation in $\langle X_{\max} \rangle$ between, for example, protons and deuterium or between helium and beryllium. Therefore, we present our result as a total fraction of light elements, to avoid placing too much emphasis on individual elements.

Recent results from the Pierre Auger Observatory³ indicate that the composition of cosmic rays at 10^{18} eV, just below the ‘ankle’ (a hardening of the all-particle cosmic-ray spectrum), can be fitted with a mixture of protons and either helium (QGSJET.II04) or nitrogen (EPOS-LHC). As the energy decreases, the proton fraction of the cosmic-ray composition decreases while the helium (or nitrogen) fraction increases, down to the threshold energy of 7×10^{17} eV. An extrapolation of this trend to our mean energy of 3×10^{17} eV connects smoothly to our best-fitting solution in which helium dominates.

An ‘ankle’-like feature in the cosmic-ray energy spectrum at $10^{17.1}$ eV has been measured⁴ at the KASCADE-Grande experiment, at which the spectral index for light elements changes to $\gamma = -2.79 \pm 0.08$. However, the light particle (p and He) fraction is found to be less than 30% at 3×10^{17} eV (on the basis of figure 4 in ref. 4), which is considerably lower than our value. In contrast to LOFAR, the composition measurements presented in ref. 4 are based on the muon/electron ratio. A muon excess compared to all commonly used hadronic interaction models was reported²¹. Inaccurate predictions of muon production, or $\langle X_{\max} \rangle$, could be the cause of the discrepancy in the fraction of light particles predicted by LOFAR and KASCADE-Grande.

If the ‘knee’ in the all-particle cosmic-ray spectrum (a steepening near 3×10^{15} eV) corresponds to the proton or helium cut-off of the main galactic cosmic-ray population, then the corresponding iron cut-off would lie at an energy of at most 26 times larger. If the main

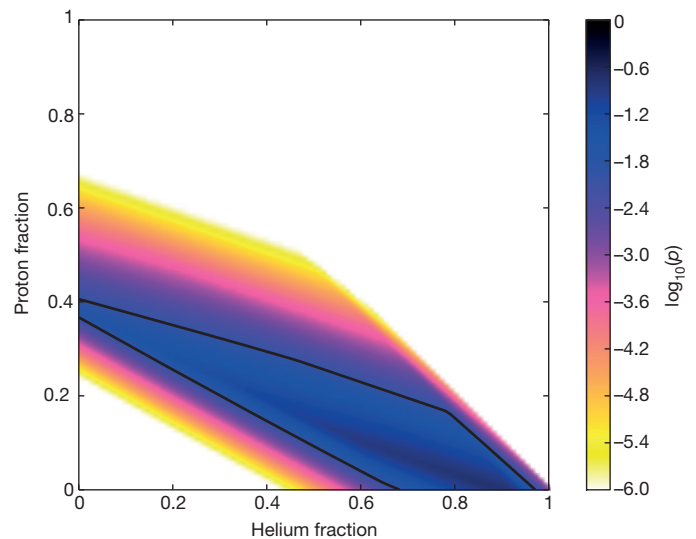


Figure 4 | p -value distribution for the four-component model. The four-component model is explored further by fixing the proton and helium fractions at all possible combinations, and solving for the nitrogen/iron ratio. The p value (see Fig. 3) is plotted as a function of the proton and helium fractions. The optimal fit (largest p value) is found for 0% protons and 79% helium ($p = 0.17$), but the deviation deteriorates slowly when replacing helium with protons. The black contour line bounds all combinations for which $p > 0.01$. At this significance level, the total fraction of light elements (p and He) lies between 0.38 and 0.98.

population of galactic cosmic-ray sources still dominates at 10^{17} eV, then the mass composition of the cosmic rays should be dominated by heavy elements at that energy. Therefore, the large component of light elements observed with LOFAR must have another origin.

In principle, it is possible that we observe an extragalactic component. In that case, the ‘ankle’ in the cosmic-ray spectrum, at energies slightly greater than 10^{18} eV, does not indicate the transition from galactic to extragalactic origin. Instead, it can be explained as the imprint of pair production on the cosmic microwave background on an extragalactic proton spectrum²². However, because this feature only appears for a proton-dominated flux it is contrary to our data that indicate a mixture of light elements.

A second galactic component, dominating around 10^{17} eV, could be produced by a class of extremely energetic sources (galactic exatrons), such as the explosions of Wolf Rayet stars into their stellar winds²³ or past galactic gamma-ray bursts²⁴. Alternatively, the original galactic population could be reaccelerated by the galactic-wind-termination shock²⁵. Such scenarios predict mixtures of light elements, consistent with our results.

Online Content Methods, along with any additional Extended Data display items and Source Data, are available in the online version of the paper; references unique to these sections appear only in the online paper.

Received 19 March 2014; accepted 29 December 2015.

- IceCube Collaboration. Evidence for high-energy extraterrestrial neutrinos at the IceCube detector. *Science* **342**, 1242856 (2013).
- Murase, K., Ahlers, M. & Lacki, B. Testing the hadronuclear origin of PeV neutrinos observed with IceCube. *Phys. Rev. D* **88**, 121301 (2013).
- Aab, A. *et al.* Depth of maximum of air-shower profiles at the Pierre Auger Observatory. II. Composition implications. *Phys. Rev. D* **90**, 122006 (2014).
- Apel, W. *et al.* Ankle-like feature in the energy spectrum of light elements of cosmic rays observed with KASCADE-Grande. *Phys. Rev. D* **87**, 081101 (2013).
- Kampert, K.-H. & Unger, M. Measurements of the cosmic ray composition with air shower experiments. *Astropart. Phys.* **35**, 660–678 (2012).
- Allan, H. R. in *Progress in Elementary Particle and Cosmic Ray Physics* Vol. 10 (eds Wilson, J. G. & Wouthuysen, S. A.) 171–302 (North-Holland Pub. Co., 1971).
- Falcke, H. & Gorham, P. W. Detecting radio emission from cosmic ray air showers and neutrinos with a digital radio telescope. *Astropart. Phys.* **19**, 477–494 (2003).
- Falcke, H. *et al.* Detection and imaging of atmospheric radio flashes from cosmic ray air showers. *Nature* **435**, 313–316 (2005).

9. Huege, T. The renaissance of radio detection of cosmic rays. *Braz. J. Phys.* **44**, 520–529 (2014).
10. Apel, W. *et al.* Reconstruction of the energy and depth of maximum of cosmic-ray air showers from LOPES radio measurements. *Phys. Rev. D* **90**, 062001 (2014).
11. Belov, K. *et al.* Towards determining the energy of the UHECRs observed by the ANITA detector. *AIP Conf. Proc.* **1535**, 209–213 (2013).
12. Werner, K. & Scholten, O. Macroscopic treatment of radio emission from cosmic ray air showers based on shower simulations. *Astropart. Phys.* **29**, 393–411 (2008).
13. van Haarlem, M. *et al.* LOFAR: the LOw-Frequency ARray. *Astron. Astrophys.* **556**, A2 (2013).
14. Schellart, P. *et al.* Detecting cosmic rays with the LOFAR radio telescope. *Astron. Astrophys.* **560**, A98 (2013).
15. Schellart, P. *et al.* Probing atmospheric electric fields in thunderstorms through radio emission from cosmic-ray-induced air showers. *Phys. Rev. Lett.* **114**, 165001 (2015).
16. Huege, T., Ludwig, M. & James, C. Simulating radio emission from air showers with CoREAS. *AIP Conf. Proc.* **1535**, 128–132 (2013).
17. Heck, D., Knapp, J., Capdevielle, J. N., Schatz, G. & Thouw, T. *CORSIKA: a Monte Carlo code to simulate extensive air showers*. Report No. FZKA 6019 (Forschungszentrum Karlsruhe, 1998).
18. Buitink, S. *et al.* Method for high precision reconstruction of air shower X_{max} using two-dimensional radio intensity profiles. *Phys. Rev. D* **90**, 082003 (2014).
19. Ostapchenko, S. QGSJET-II: results for extensive air showers. *Nucl. Phys. B* **151**, 147–150 (2006).
20. Pierog, T. & Werner, K. EPOS model and ultra high energy cosmic rays. *Nucl. Phys. B* **196**, 102–105 (2009).
21. Aab, A. *et al.* Muons in air showers at the Pierre Auger Observatory: mean number in highly inclined events. *Phys. Rev. D* **91**, 032003 (2015).
22. Aloisio, R. *et al.* A dip in the UHECR spectrum and the transition from galactic to extragalactic cosmic rays. *Astropart. Phys.* **27**, 76–91 (2007).
23. Stanev, T., Biermann, P. & Gaisser, T. Cosmic rays. IV. The spectrum and chemical composition above 10 GeV. *Astron. Astrophys.* **274**, 902–915 (1993).
24. Calvez, A., Kusenko, S. & Nagataki, S. Role of galactic sources and magnetic fields in forming the observed energy-dependent composition of ultrahigh-energy cosmic rays. *Phys. Rev. Lett.* **105**, 091101 (2010).
25. Jokipii, J. R. & Morfill, G. Ultra-high-energy cosmic rays in a galactic wind and its termination shock. *Astrophys. J.* **312**, 170–177 (1987).
26. Letessier-Selvon, A. *et al.* Highlights from the Pierre Auger Observatory. *Braz. J. Phys.* **44**, 560–570 (2014).
27. Abu-Zayyad, T. *et al.* Measurement of the cosmic-ray energy spectrum and composition from 10^{17} to $10^{18.3}$ eV using a hybrid technique. *Astrophys. J.* **557**, 686–699 (2001).
28. Knurenko, S. & Sabourov, A. The depth of maximum shower development and its fluctuations: cosmic ray mass composition at $E_0 \geq 10^{17}$ eV. *Astrophys. Space Sci. Trans.* **7**, 251–255 (2011).
29. Berezhnev, S. F. *et al.* Tunka-133: primary cosmic ray mass composition in the energy range $6 \cdot 10^{15}$ – 10^{18} eV. *Proc. 32nd Int. Cosmic Ray Conf.* **1**, 209–212 (2011).

Acknowledgements We acknowledge financial support from the Netherlands Organization for Scientific Research (NWO), VENI grant 639-041-130, the Netherlands Research School for Astronomy (NOVA), the Samenwerkingsverband Noord-Nederland (SNN) and the Foundation for Fundamental Research on Matter (FOM). We acknowledge funding from the European Research Council under the European Union's Seventh Framework Programme (FP/2007-2013)/ERC (grant agreement no. 227610) and under the European Union's Horizon 2020 research and innovation programme (grant agreement no. 640130). LOFAR, the Low Frequency Array designed and constructed by ASTRON, has facilities in several countries that are owned by various parties (each with their own funding sources) and that are collectively operated by the International LOFAR Telescope (ILT) foundation under a joint scientific policy.

Author Contributions All authors are part of the LOFAR collaboration and have contributed to the design, construction, calibration and maintenance of LOFAR and/or LORA. The first thirteen authors constitute the Cosmic Ray Key Science Project and have contributed to the acquisition, calibration and analysis of cosmic-ray radio data and LORA data. The manuscript was written by S.B. and subjected to an internal collaboration-wide review process. All authors approved the final version of the manuscript.

Author Information Reprints and permissions information is available at www.nature.com/reprints. The authors declare no competing financial interests. Readers are welcome to comment on the online version of the paper. Correspondence and requests for materials should be addressed to S.B. (Stijn.Buitink@vub.ac.be).

METHODS

Event selection. Cosmic ray detection at LOFAR runs continuously in the background during astronomical observations. When 16 out of the 20 scintillator stations of the LORA particle array detect a signal, a ‘trigger’ is issued and the ring buffers of all active antennas within about a 1-km radius are stored for offline analysis¹⁴. Which antennas are active depends on the settings of the astronomical observation. For this analysis, we selected showers that were measured with at least four antenna stations (corresponding to at least 192 antennas) in the low band (30–80 MHz after filtering).

The trigger and selection criteria introduce a composition bias. This bias is removed by excluding certain showers on the basis of dedicated sets of simulations that are produced for each observed shower. Each of these sets contains 50 proton and 25 iron showers that span the whole range of possible shower depths. A shower is only accepted if all simulations in its set satisfy the trigger and selection criteria. This anti-bias exclusion removes many showers below 10^{17} eV, but only four above that energy. Consequently, we restrict our analysis to the higher-energy showers, imposing a minimum bound on the reconstructed shower energy of $E_{\text{reco}} = 10^{17}$ eV.

Imposing this energy bound introduces another potential source of compositional bias, because the reconstructed energy might depend on the depth of the shower. However, in our reconstruction approach, this effect is very small because energy and X_{max} are fitted simultaneously. Extended Data Fig. 7 shows distributions of the ratio between true and reconstructed energy for proton and iron simulations. The systematic offset between the two particle types is of the order of 1%.

We used data from the Royal Netherlands Meteorological Institute to check for lightning-storm conditions during our observations. When lightning strikes were detected in the north of the Netherlands within an hour from a detection, the event is flagged and excluded from the analysis. The presence of electric fields in the clouds can severely alter the radio emission even in the absence of lightning discharges³⁰. The polarization angle of the radio pulse is very sensitive to the nature of the emission mechanism^{15,31} and is used as an additional veto against strong field conditions.

Finally, a quality criterion is imposed on the sample so that only showers that have a core position and arrival direction that allows accurate reconstruction are included. We use the dedicated sets of simulations produced for each shower to derive uncertainties on core position, energy and X_{max} . These three values are highly correlated, so a single criterion based on the core uncertainty of $\sigma_{\text{core}} < 5$ m is sufficient.

The quality criterion is based on the dedicated sets of simulations. These sets are produced for a specific combination of core position and arrival direction. Therefore, the quality criterion is effectively a criterion on position and direction, and does not introduce a composition bias.

There is no criterion on the quality of the reconstruction of the actual data. By applying the criteria described above we obtain a sample of 118 showers that are fitted to the simulation yielding reduced χ^2 values in the range 0.9–2.9. Deviations from unity can be ascribed to uncertainties in antenna response, atmospheric properties such as the index of refraction, or limitations of the simulation software.

Reconstruction. The energy and X_{max} of the shower are reconstructed with the technique described in ref. 18.

Statistical uncertainty. The statistical uncertainty on the power measurements of individual antennas includes three contributions. First, there is contribution from the background noise, which is a combination of system noise and the galactic background. Second, there is a contribution from uncertainties in the antenna response model. There can be differences between the responses of antennas, either because of antenna properties (for example, cross-talk between nearby antennas) or because of signal properties (for example, polarization). Because these fluctuations are different for each shower core position and arrival direction, they are essentially random and so are included as a 10% statistical uncertainty on the power. Third, there is a contribution due to the error introduced by interpolating the simulated pulse power. Strictly speaking this is not a measurement uncertainty, but it must be taken into account when fitting the data to simulation. The interpolation error is of the order of 2.5% of the maximum power¹⁸. The three contributions are added in quadrature and produce the 1σ error bars shown in Extended Data Figs 1–5.

The statistical uncertainty on X_{max} is given by the quadratic sum of the uncertainties due to the reconstruction technique and the atmospheric correction. The former is found by applying our analysis to simulated events with added Gaussian noise, where the noise level is determined from the data.

In the CORSIKA simulations, the standard US atmosphere model was used. The reconstructed shower depth is corrected for variations in the atmosphere using data from the Global Data Assimilation System (GDAS) of the NOAA National Climatic Data Center. We follow a previously developed procedure³², which typically leads to adjustments of the order of 5–20 g cm⁻². The remaining uncertainty after correction is of the order of 1 g cm⁻².

The refractive index of air is a function of temperature, air pressure and relative humidity. Using local weather information, the final data were split in two groups of equal size, corresponding to conditions with relatively high or low refractive index. The mean reconstructed X_{max} of these two subsets deviate from that of the total sample by ± 5 g cm⁻²; we adopt this value as an additional statistical uncertainty. Because the refractivity used in simulation corresponds to dry air, there is also an associated systematic error (see below).

The total statistical uncertainty on X_{max} is found by adding the above factors in quadrature. A distribution of the uncertainty for the showers in our final sample is shown in Extended Data Fig. 6.

The energy resolution is 32% and is found by comparing energy scaling factors of the radio power and particle density fit (see Fig. 1).

Systematic effects. The data have been subjected to several tests (outlined below) to determine the systematic uncertainty on the reconstructed values for X_{max} .

Zenith-angle dependence. The final data are split into two groups of equal size by selecting showers with a zenith angle below or above 32°. For both groups, the mean reconstructed X_{max} is calculated, yielding deviations from the mean value of the complete sample of ± 8 g cm⁻². This spread is larger than is expected from random fluctuations alone and is included as a systematic uncertainty. The dependence on zenith angle may be related to atmospheric uncertainties (see below).

Refractive index of air. As explained above, the refractive index changes because of differences in atmospheric conditions. Fluctuations in X_{max} due to changing humidity are of the order of 5 g cm⁻² with respect to the mean. However, the refractive index that was used in the radio simulations corresponds to dry air, and is a lower bound on the actual value. Therefore, the real value of X_{max} can be higher than the reconstructed value, but not lower; we adopt an asymmetric systematic uncertainty of +10 g cm⁻².

Hadronic interaction model. Because the reconstruction technique is based on full Monte Carlo simulations, it is sensitive to the choice of hadronic interaction model that is used. A comparison between QGSJETII.04, SYBILL 2.1 and EPOS-LHC, revealed that the uncertainty due to model dependence is about 5 g cm⁻². The uncertainty on the composition due to different models (in other words, on how to interpret the measured X_{max} values) is larger.

Radiation code. For this analysis we used the radiation code CoREAS, in which the contributions of all individual charges to radiation field are added together. The advantage of this microscopic approach is that it is completely model-independent and based on first principles. ZHAireS³³ is another microscopic code, which gives very similar results³⁴. To calculate the emission, CoREAS uses the end-point formalism³⁵, whereas ZHAireS is based on the ZHS algorithm³⁶. Both formalisms are derived directly from Maxwell’s equations and have been shown to be equivalent³⁷. The other difference between CoREAS and ZHAireS is that they take the particle distribution from different air-shower propagation codes (CORSIKA and AIRES, respectively) that internally use different hadronic interaction models. Because the radiation formalisms themselves are equivalent, small differences between CoREAS and ZHAireS are probably due to differences in the hadronic interaction models used to simulate the particle interactions. Therefore, the choice of radiation code does not introduce additional systematic uncertainty on top of the uncertainty due to hadronic interaction models that is already included. A comparison study with LOFAR data did not show any evidence for a systematic offset between the codes (S.B. *et al.*, in preparation).

The remaining small dependence of X_{max} on zenith angle is possibly related to the refractive index. Showers with different inclination angles have their shower maximum at different altitudes and, therefore, different local air pressures and refractive indices. Consequently, increasing the refractive index used in simulations will result in a zenith-dependent change in reconstructed X_{max} . This could potentially remove the observed dependence of the composition on zenith angle. Correctly taking into account a complete atmospheric model for the profile of the refractivity of air is subject of further study. Here, we treat the effect conservatively by linearly adding the first two contributions to the uncertainty. The other two contributions are independent and are added in quadrature, yielding a total systematic uncertainty of $^{+14}_{-10}$ g cm⁻².

The systematic uncertainty in the energy reconstruction with the LORA particle detector array is 27%, which includes effects due to detector calibration, hadronic interaction models and the assumed slope of the primary cosmic-ray spectrum in the CORSIKA simulations^{38,39}.

Statistical analysis. For each observed shower, we calculate a using equation (1):

$$a = \frac{\langle X_{\text{proton}} \rangle - X_{\text{shower}}}{\langle X_{\text{proton}} \rangle - \langle X_{\text{iron}} \rangle}$$

in which X_{shower} is the reconstructed X_{max} , and $\langle X_{\text{proton}} \rangle$ and $\langle X_{\text{iron}} \rangle$ are mean values predicted by QGSJETII.04¹⁹. Therefore, a is an energy-independent parameter that is mass sensitive. A pure proton composition results in a wide distribution of a

centred around zero, whereas a pure iron composition would result in a narrower distribution centred around one.

From the measurements we construct a cumulative distribution function (CDF) using the following Monte Carlo approach. A realization of the data is made by taking the measured values for the energy and X_{\max} , adding random fluctuations based on the statistical uncertainty of these parameters, and calculating a and the corresponding CDF. By constructing a large number of realizations with different random fluctuations, we calculate the mean CDF and the region that contains 99% of all realizations. These are indicated in Fig. 3 as the solid blue line and the shaded region, respectively.

We fit theoretical CDFs on the basis of compositions with two or four mass components to the data. The test statistic in the fit is the maximum deviation between the data and the model CDFs. The p value represents the probability of observing this deviation, or a larger one, assuming the fitted composition model.

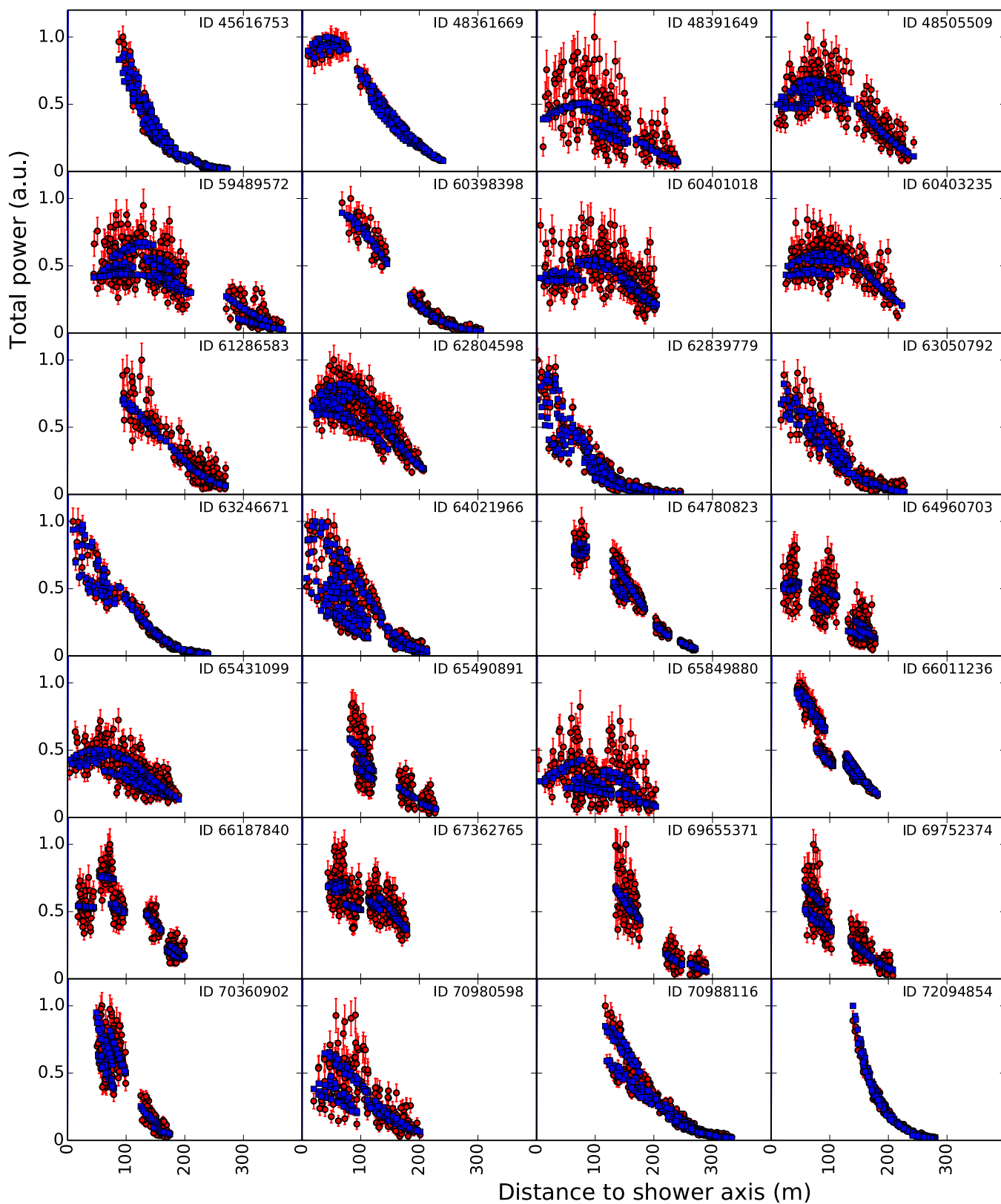
We first use a two-component model of proton and iron nuclei, in which the mixing ratio is the only free parameter. The best fit is found for a proton fraction of 62%, but it describes the data poorly, with p value of 1.1×10^{-6} .

A better fit is achieved with a four-component model (p, He, N and Fe), yielding $p = 0.17$. Although the best fit is found for a helium fraction of 80%, the fit quality deteriorates slowly when replacing helium by protons. This is demonstrated in Fig. 4, in which p is plotted for four-component fits with the fractions of helium and proton fixed, and the ratio between nitrogen and iron is the only free parameter. The solid line in Fig. 4 bounds the parameter space in which $p > 0.01$. We construct a 99% confidence interval on the total fraction of light elements (p and He) by finding the two extreme values of this fraction that lie within the $p > 0.01$ region.

The total fraction of light elements (p and He) is in the range [0.38, 0.98] at the 99% confidence level, with a best fit value of 0.8. The heaviest composition that is allowed within systematic uncertainties (see above) has a best-fit p + He fraction of 0.6 and a 99% confidence interval of [0.18, 0.82].

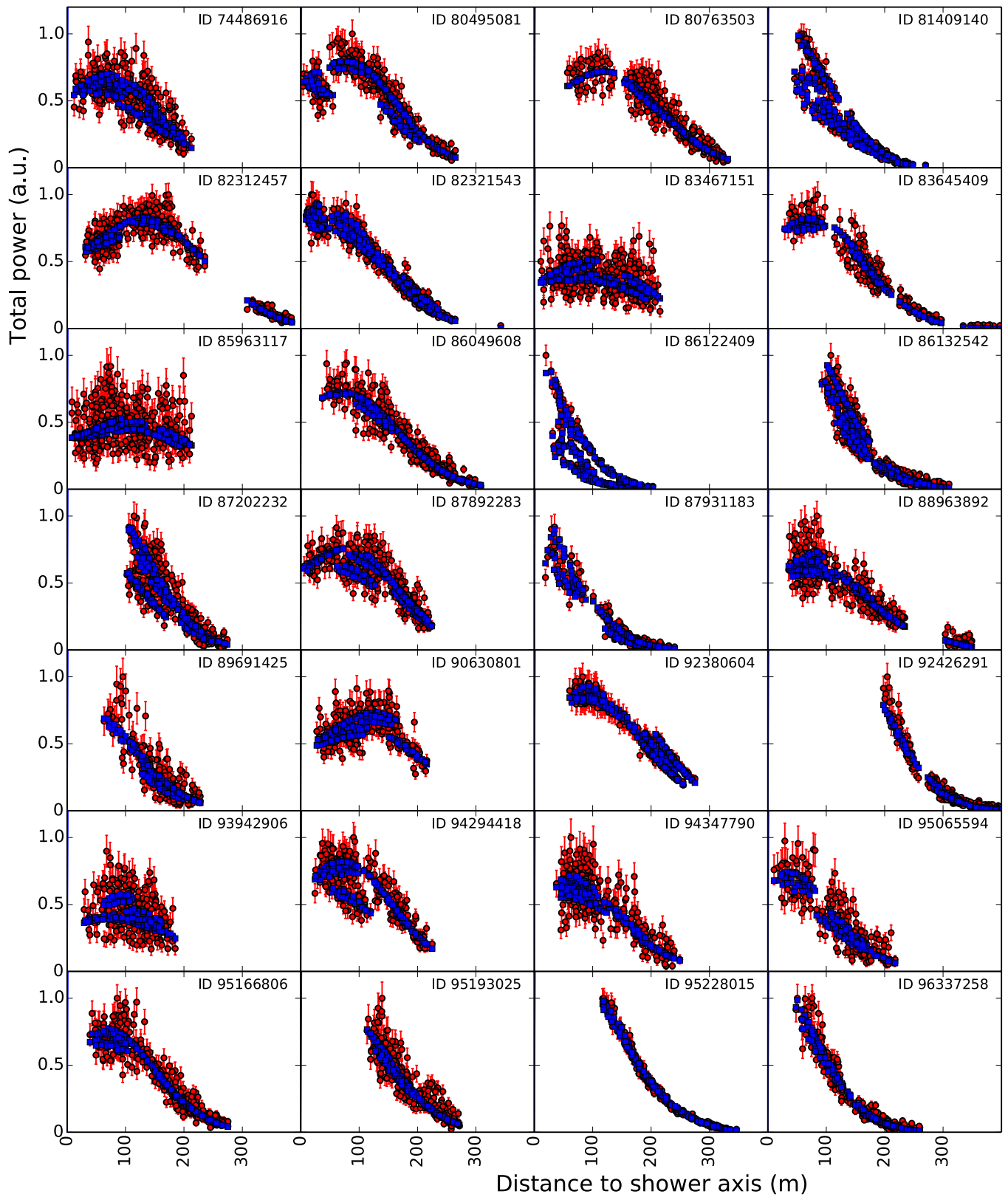
Code availability. Data analysis was done with PyCRTTools. PyCRTTools is free software, available from <http://usg.lofar.org/svn/code/trunk/src/PyCRTTools>, which can be redistributed and/or modified under the terms of the GNU General Public License as published by the Free Software Foundation, either version 3 of the License or any later version.

30. Buitink, S. *et al.* Amplified radio emission from cosmic ray air showers in thunderstorms. *Astron. Astrophys.* **467**, 385–394 (2007).
31. Schellart, P. *et al.* Polarized radio emission from extensive air showers measured with LOFAR. *J. Cosmol. Astropart. Phys.* **10**, 014 (2014).
32. The Pierre Auger Collaboration. Description of atmospheric conditions at the Pierre Auger Observatory using the Global Data Assimilation System (GDAS). *Astropart. Phys.* **35**, 591–607 (2012).
33. Alvarez-Muñiz, J. *et al.* Monte Carlo simulations of radio pulses in atmospheric showers using ZHAireS. *Astropart. Phys.* **35**, 325–341 (2012).
34. Huege, T. *et al.* The convergence of EAS radio emission models and a detailed comparison of REAS3 and MGMR simulations. *Nucl. Instrum. Methods Phys. Res. A* **662** (Suppl.) S179–S186 (2012).
35. James, C., Falcke, H., Huege, T. & Ludwig, M. General description of electromagnetic radiation processes based on instantaneous charge acceleration in “endpoints”. *Phys. Rev. E* **84**, 056602 (2011).
36. Zas, E., Halzen, F. & Stanev, T. Electromagnetic pulses from high-energy showers: implications for neutrino detection. *Phys. Rev. D* **45**, 362–376 (1992).
37. Belov, K. *et al.* Accelerator measurements of magnetically induced radio emission from particle cascades with applications to cosmic-ray air showers. *Phys. Rev. Lett.* (in the press). Preprint at <http://arXiv.org/abs/1507.07296> (2015).
38. Thoudam, S. *et al.* LORA: a scintillator array for LOFAR to measure extensive air showers. *Nucl. Instrum. Methods Phys. Res. A* **767**, 339–346 (2014).
39. Thoudam, S. *et al.* Measurement of the cosmic-ray energy spectrum above 10^{16} eV with the LOFAR Radboud Air Shower Array. *Astropart. Phys.* **73**, 34–43 (2016).

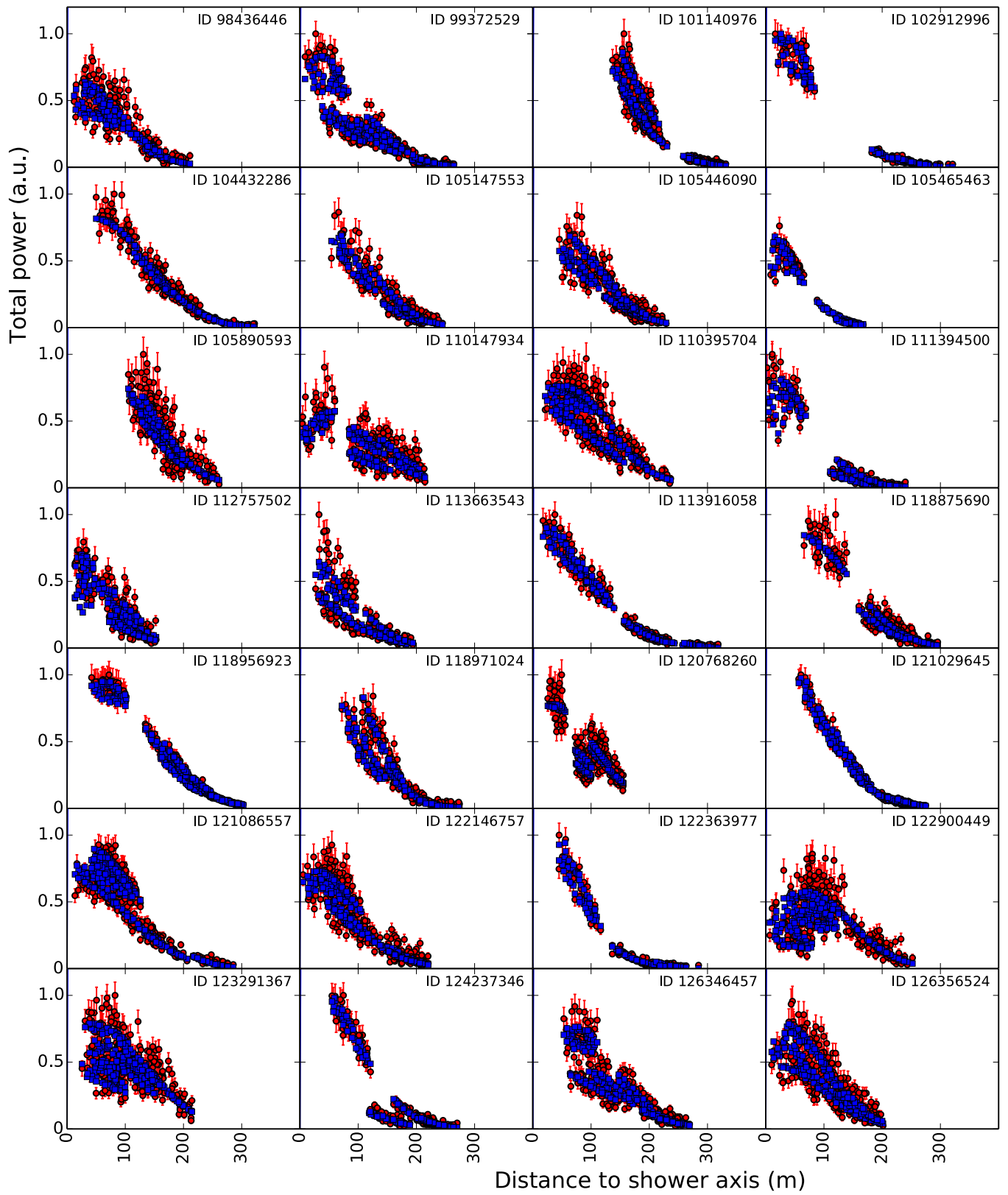


Extended Data Figure 1 | Fitted lateral distributions. Lateral distribution of radio-pulse power for all 118 measured showers (red circles) and the corresponding best-fitting CoREAS simulation (blue squares). The distance to the shower axis is the distance between the antenna and the

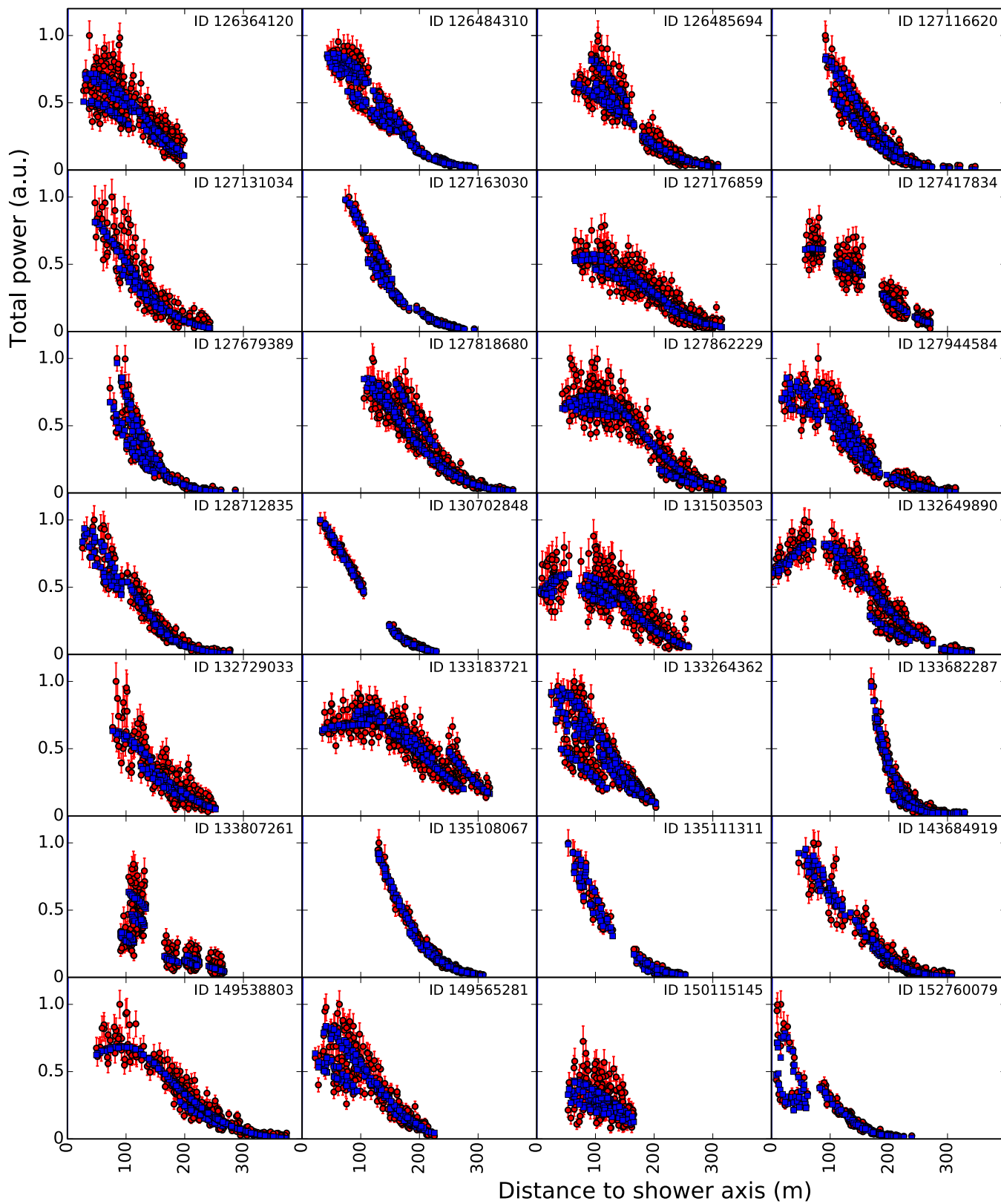
axis of the air shower. Therefore, a value of 0 corresponds to an antenna that is located at the position where the shower axis reaches the ground. The ID numbers are unique values that are used to label the detected air showers. a.u., arbitrary units.



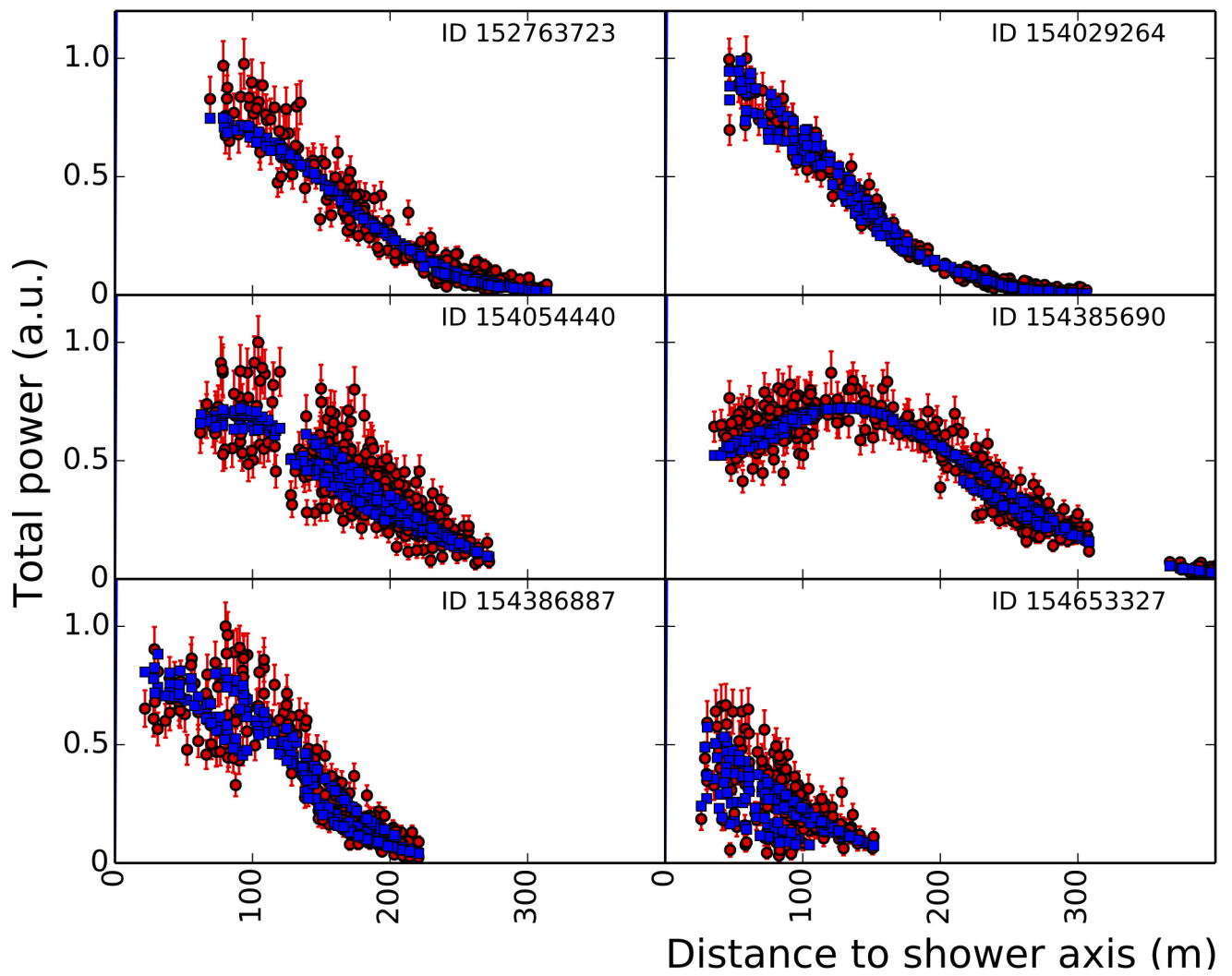
Extended Data Figure 2 | Fitted lateral distributions. Continuation of Extended Data Fig. 1.



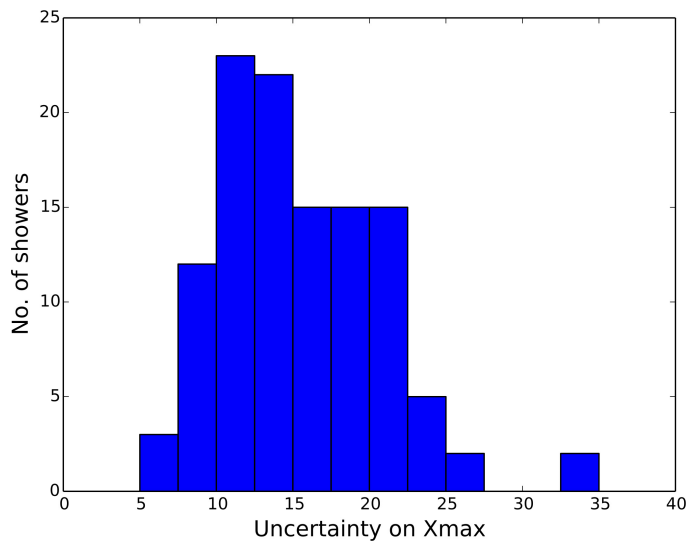
Extended Data Figure 3 | Fitted lateral distributions. Continuation of Extended Data Fig. 2.



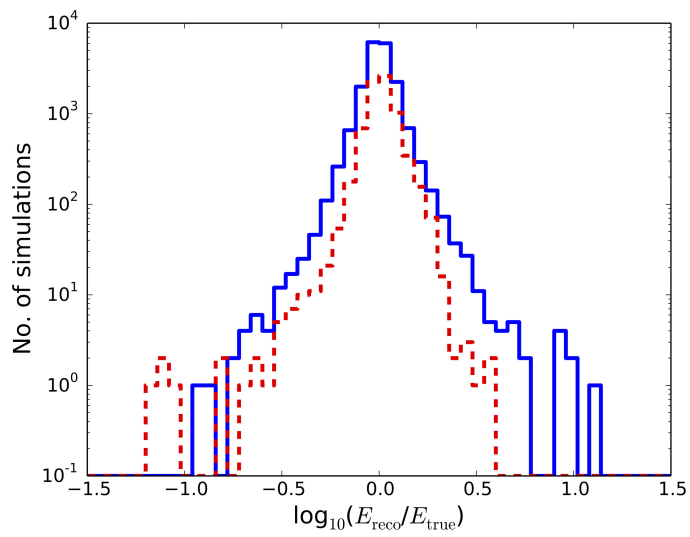
Extended Data Figure 4 | Fitted lateral distributions. Continuation of Extended Data Fig. 3.



Extended Data Figure 5 | Fitted lateral distributions. Continuation of Extended Data Fig. 4.



Extended Data Figure 6 | Distribution of uncertainty on X_{\max} . The distribution of the uncertainty on X_{\max} for all showers used in this analysis. The mean value is 16 g cm^{-2} .



Extended Data Figure 7 | Energy reconstruction. Distributions of the ratio between true (E_{true}) and reconstructed (E_{reco}) energy for proton (blue solid line) and iron (red dashed line) showers. The two types of showers have a systematic offset of the order of 1%.

Search for Galactic PeV gamma rays with the IceCube Neutrino Observatory

M. G. Aartsen,² R. Abbasi,²⁷ Y. Abdou,²² M. Ackermann,⁴¹ J. Adams,¹⁵ J. A. Aguilar,²¹ M. Ahlers,²⁷ D. Altmann,⁹ K. Andeen,²⁷ J. Auffenberg,²⁷ X. Bai,^{31,*} M. Baker,²⁷ S. W. Barwick,²³ V. Baum,²⁸ R. Bay,⁷ K. Beattie,⁸ J. J. Beatty,^{17,18} S. Bechet,¹² J. Becker Tjus,¹⁰ K.-H. Becker,⁴⁰ M. Bell,³⁸ M. L. Benabderrahmane,⁴¹ S. BenZvi,²⁷ J. Berdermann,⁴¹ P. Berghaus,⁴¹ D. Berley,¹⁶ E. Bernardini,⁴¹ D. Bertrand,¹² D. Z. Besson,²⁵ D. Bindig,⁴⁰ M. Bissok,¹ E. Blaufuss,¹⁶ J. Blumenthal,¹ D. J. Boersma,^{39,1} S. Bohaichuk,²⁰ C. Bohm,³⁴ D. Bose,¹³ S. Böser,¹¹ O. Botner,³⁹ L. Brayer,¹³ A. M. Brown,¹⁵ R. Bruijn,²⁴ J. Brunner,⁴¹ S. Buitink,^{13,†} M. Carson,²² J. Casey,⁵ M. Casier,¹³ D. Chirkin,²⁷ B. Christy,¹⁶ K. Clark,³⁸ F. Clevermann,¹⁹ S. Cohen,²⁴ D. F. Cowen,^{38,37} A. H. Cruz Silva,⁴¹ M. Danninger,³⁴ J. Daughhetee,⁵ J. C. Davis,¹⁷ C. De Clercq,¹³ S. De Ridder,²² F. Descamps,²⁷ P. Desiati,²⁷ G. de Vries-Uiterweerd,²² T. DeYoung,³⁸ J. C. Díaz-Vélez,²⁷ J. Dreyer,¹⁰ J. P. Dumm,²⁷ M. Dunkman,³⁸ R. Eagan,³⁸ J. Eisch,²⁷ R. W. Ellsworth,¹⁶ O. Engdegård,³⁹ S. Euler,¹ P. A. Evenson,³¹ O. Fadiran,²⁷ A. R. Fazely,⁶ A. Fedynitch,¹⁰ J. Feintzeig,²⁷ T. Feusels,²² K. Filimonov,⁷ C. Finley,³⁴ T. Fischer-Wasels,⁴⁰ S. Flis,³⁴ A. Franckowiak,¹¹ R. Franke,⁴¹ K. Frantzen,¹⁹ T. Fuchs,¹⁹ T. K. Gaisser,³¹ J. Gallagher,²⁶ L. Gerhardt,^{8,7} L. Gladstone,²⁷ T. Glüsenkamp,⁴¹ A. Goldschmidt,⁸ G. Golup,¹³ J. A. Goodman,¹⁶ D. Góra,⁴¹ D. Grant,²⁰ A. Groß,³⁰ S. Grullon,²⁷ M. Gurtner,⁴⁰ C. Ha,^{8,7} A. Haj Ismail,²² A. Hallgren,³⁹ F. Halzen,²⁷ K. Hanson,¹² D. Heereman,¹² P. Heimann,¹ D. Heinen,¹ K. Helbing,⁴⁰ R. Hellauer,¹⁶ S. Hickford,¹⁵ G. C. Hill,² K. D. Hoffman,¹⁶ R. Hoffmann,⁴⁰ A. Homeier,¹¹ K. Hoshina,²⁷ W. Huelsnitz,^{16,‡} P. O. Hulth,³⁴ K. Hultqvist,³⁴ S. Hussain,³¹ A. Ishihara,¹⁴ E. Jacobi,⁴¹ J. Jacobsen,²⁷ G. S. Japaridze,⁴ O. Jelati,²² A. Kappes,⁹ T. Karg,⁴¹ A. Karle,²⁷ J. Kiryluk,³⁵ F. Kislak,⁴¹ J. Kläs,⁴⁰ S. R. Klein,^{8,7} J.-H. Köhne,¹⁹ G. Kohnen,²⁹ H. Kolanoski,⁹ L. Köpke,²⁸ C. Kopper,²⁷ S. Kopper,⁴⁰ D. J. Koskinen,³⁸ M. Kowalski,¹¹ M. Krasberg,²⁷ G. Kroll,²⁸ J. Kunnen,¹³ N. Kurahashi,²⁷ T. Kuwabara,³¹ M. Labare,¹³ H. Landsman,²⁷ M. J. Larson,³⁶ R. Lauer,⁴¹ M. Lesiak-Bzdak,³⁵ J. Lünemann,²⁸ J. Madsen,³³ R. Maruyama,²⁷ K. Mase,¹⁴ H. S. Matis,⁸ F. McNally,²⁷ K. Meagher,¹⁶ M. Merck,²⁷ P. Mészáros,^{37,38} T. Meures,¹² S. Miarecki,^{8,7} E. Middell,⁴¹ N. Milke,¹⁹ J. Miller,¹³ L. Mohrmann,⁴¹ T. Montaruli,^{21,§} R. Morse,²⁷ R. Nahnauer,⁴¹ U. Naumann,⁴⁰ S. C. Nowicki,²⁰ D. R. Nygren,⁸ A. Obertacke,⁴⁰ S. Odrowski,³⁰ A. Olivas,¹⁶ M. Olivo,¹⁰ A. O'Murchadha,¹² S. Panknin,¹¹ L. Paul,¹ J. A. Pepper,³⁶ C. Pérez de los Heros,³⁹ D. Pieloth,¹⁹ N. Pirk,⁴¹ J. Posselt,⁴⁰ P. B. Price,⁷ G. T. Przybylski,⁸ L. Rädcl,¹ K. Rawlins,³ P. Redl,¹⁶ E. Resconi,³⁰ W. Rhode,¹⁹ M. Ribordy,²⁴ M. Richman,¹⁶ B. Riedel,²⁷ J. P. Rodrigues,²⁷ F. Rothmaier,²⁸ C. Rott,¹⁷ T. Ruhe,¹⁹ B. Ruzybayev,³¹ D. Ryckbosch,²² S. M. Saba,¹⁰ T. Salameh,³⁸ H.-G. Sander,²⁸ M. Santander,²⁷ S. Sarkar,³² K. Schatto,²⁸ M. Scheel,¹ F. Scheriau,¹⁹ T. Schmidt,¹⁶ M. Schmitz,¹⁹ S. Schoenen,¹ S. Schöneberg,¹⁰ L. Schönherr,¹ A. Schönwald,⁴¹ A. Schukraft,¹ L. Schulte,¹¹ O. Schulz,³⁰ D. Seckel,³¹ S. H. Seo,³⁴ Y. Sestayo,³⁰ S. Seunarine,³³ C. Sheremata,²⁰ M. W. E. Smith,³⁸ M. Soiron,¹ D. Soldin,⁴⁰ G. M. Spiczak,³³ C. Spiering,⁴¹ M. Stamatikos,^{17,¶} T. Stanev,³¹ A. Stasik,¹¹ T. Stezelberger,⁸ R. G. Stokstad,⁸ A. Stößl,⁴¹ E. A. Strahler,¹³ R. Ström,³⁹ G. W. Sullivan,¹⁶ H. Taavola,³⁹ I. Taboada,⁵ A. Tamburro,³¹ S. Ter-Antonyan,⁶ S. Tilav,³¹ P. A. Toale,³⁶ S. Toscano,²⁷ M. Usner,¹¹ D. van der Drift,^{8,7} N. van Eijndhoven,¹³ A. Van Overloop,²² J. van Santen,²⁷ M. Vehrung,¹ M. Voge,¹¹ M. Vraeghe,²² C. Walck,³⁴ T. Waldenmaier,⁹ M. Wallraff,¹ M. Walter,⁴¹ R. Wasserman,³⁸ Ch. Weaver,²⁷ C. Wendt,²⁷ S. Westerhoff,²⁷ N. Whitehorn,²⁷ K. Wiebe,²⁸ C. H. Wiebusch,¹ D. R. Williams,³⁶ H. Wissing,¹⁶ M. Wolf,³⁴ T. R. Wood,²⁰ K. Woschnagg,⁷ C. Xu,³¹ D. L. Xu,³⁶ X. W. Xu,⁶ J. P. Yanez,⁴¹ G. Yodh,²³ S. Yoshida,¹⁴ P. Zarzhitsky,³⁶ J. Ziemann,¹⁹ S. Zierke,¹ A. Zilles,¹ and M. Zoll³⁴

(IceCube Collaboration)

¹*III. Physikalisches Institut, RWTH Aachen University, D-52056 Aachen, Germany*²*School of Chemistry and Physics, University of Adelaide, Adelaide, South Australia 5005, Australia*³*Department of Physics and Astronomy, University of Alaska Anchorage, 3211 Providence Drive, Anchorage, Alaska 99508, USA*⁴*CTSPS, Clark-Atlanta University, Atlanta, Georgia 30314, USA*⁵*School of Physics and Center for Relativistic Astrophysics, Georgia Institute of Technology, Atlanta, Georgia 30332, USA*⁶*Department of Physics, Southern University, Baton Rouge, Louisiana 70813, USA*⁷*Department of Physics, University of California, Berkeley, California 94720, USA*⁸*Lawrence Berkeley National Laboratory, Berkeley, California 94720, USA*⁹*Institut für Physik, Humboldt-Universität zu Berlin, D-12489 Berlin, Germany*¹⁰*Fakultät für Physik and Astronomie, Ruhr-Universität Bochum, D-44780 Bochum, Germany*¹¹*Physikalisches Institut, Universität Bonn, Nussallee 12, D-53115 Bonn, Germany*

- ¹²*Université Libre de Bruxelles, Science Faculty CP230, B-1050 Brussels, Belgium*
¹³*Vrije Universiteit Brussel, Dienst ELEM, B-1050 Brussels, Belgium*
¹⁴*Department of Physics, Chiba University, Chiba 263-8522, Japan*
¹⁵*Department of Physics and Astronomy, University of Canterbury, Private Bag 4800, Christchurch, New Zealand*
¹⁶*Department of Physics, University of Maryland, College Park, Maryland 20742, USA*
¹⁷*Department of Physics and Center for Cosmology and Astro-Particle Physics, Ohio State University, Columbus, Ohio 43210, USA*
¹⁸*Department of Astronomy, Ohio State University, Columbus, Ohio 43210, USA*
¹⁹*Department of Physics, TU Dortmund University, D-44221 Dortmund, Germany*
²⁰*Department of Physics, University of Alberta, Edmonton, Alberta, Canada T6G 2G7*
²¹*Département de physique nucléaire et corpusculaire, Université de Genève, CH-1211 Genève, Switzerland*
²²*Department of Physics and Astronomy, University of Gent, B-9000 Gent, Belgium*
²³*Department of Physics and Astronomy, University of California, Irvine, California 92697, USA*
²⁴*Laboratory for High Energy Physics, École Polytechnique Fédérale, CH-1015 Lausanne, Switzerland*
²⁵*Department of Physics and Astronomy, University of Kansas, Lawrence, Kansas 66045, USA*
²⁶*Department of Astronomy, University of Wisconsin, Madison, Wisconsin 53706, USA*
²⁷*Department of Physics and Wisconsin IceCube Particle Astrophysics Center, University of Wisconsin, Madison, Wisconsin 53706, USA*
²⁸*Institute of Physics, University of Mainz, Staudinger Weg 7, D-55099 Mainz, Germany*
²⁹*Université de Mons, 7000 Mons, Belgium*
³⁰*T.U. Munich, D-85748 Garching, Germany*
³¹*Bartol Research Institute and Department of Physics and Astronomy, University of Delaware, Newark, Delaware 19716, USA*
³²*Department of Physics, University of Oxford, 1 Keble Road, Oxford OX1 3NP, United Kingdom*
³³*Department of Physics, University of Wisconsin, River Falls, Wisconsin 54022, USA*
³⁴*Oskar Klein Centre and Department of Physics, Stockholm University, SE-10691 Stockholm, Sweden*
³⁵*Department of Physics and Astronomy, Stony Brook University, Stony Brook, New York 11794-3800, USA*
³⁶*Department of Physics and Astronomy, University of Alabama, Tuscaloosa, Alabama 35487, USA*
³⁷*Department of Astronomy and Astrophysics, Pennsylvania State University, University Park, Pennsylvania 16802, USA*
³⁸*Department of Physics, Pennsylvania State University, University Park, Pennsylvania 16802, USA*
³⁹*Department of Physics and Astronomy, Uppsala University, Box 516, S-75120 Uppsala, Sweden*
⁴⁰*Department of Physics, University of Wuppertal, D-42119 Wuppertal, Germany*
⁴¹*DESY, D-15735 Zeuthen, Germany*

(Received 30 October 2012; published 20 March 2013)

Gamma-ray induced air showers are notable for their lack of muons, compared to hadronic showers. Hence, air shower arrays with large underground muon detectors can select a sample greatly enriched in photon showers by rejecting showers containing muons. IceCube is sensitive to muons with energies above ~ 500 GeV at the surface, which provides an efficient veto system for hadronic air showers with energies above 1 PeV. One year of data from the 40-string IceCube configuration was used to perform a search for point sources and a Galactic diffuse signal. No sources were found, resulting in a 90% C.L. upper limit on the ratio of gamma rays to cosmic rays of 1.2×10^{-3} for the flux coming from the Galactic plane region ($-80^\circ \leq l \leq -30^\circ$; $-10^\circ \leq b \leq 5^\circ$) in the energy range 1.2–6.0 PeV. In the same energy range, point source fluxes with E^{-2} spectra have been excluded at a level of $(E/\text{TeV})^2 d\Phi/dE \sim 10^{-12} - 10^{-11} \text{ cm}^{-2} \text{ s}^{-1} \text{ TeV}^{-1}$ depending on source declination. The complete IceCube detector will have a better sensitivity (due to the larger detector size), improved reconstruction, and vetoing techniques. Preliminary data from the nearly final IceCube detector configuration have been used to estimate the 5-yr sensitivity of the full detector. It is found to be more than an order of magnitude better, allowing the search for PeV extensions of known TeV gamma-ray emitters.

DOI: [10.1103/PhysRevD.87.062002](https://doi.org/10.1103/PhysRevD.87.062002)

PACS numbers: 95.55.Vj, 95.55.Ka, 95.85.Pw, 96.50.sd

* Also at Physics Department, South Dakota School of Mines and Technology, Rapid City, SD 57701, USA.

† Also at KVI, University of Groningen, Zernikelaan 25, 9747 AA Groningen, The Netherlands.

Corresponding author.

s.j.buitink@rug.nl

‡ Also at Los Alamos National Laboratory, Los Alamos, NM 87545, USA.

§ Also at Sezione INFN, Dipartimento di Fisica, I-70126, Bari, Italy.

¶ Also at NASA Goddard Space Flight Center, Greenbelt, MD 20771, USA.

I. INTRODUCTION

Gamma rays are an important tool for studying the cosmos; unlike cosmic rays (CRs), they point back to their sources and can identify remote acceleration regions. Air Cherenkov telescopes have identified numerous sources of high-energy ($E > 1$ TeV) gamma rays (see, e.g., Ref. [1]): within our galaxy, gamma rays have been observed coming from supernova remnants, pulsar wind nebulae (PWNe), binary systems, and the Galactic center. Extragalactic sources include starburst galaxies and active Galactic nuclei. Surface air-shower arrays like Milagro have performed all-sky searches for TeV gamma rays. Although these detectors are less sensitive to point sources than Air Cherenkov telescopes, they have identified several Galactic pointlike and extended sources [2]. Interactions of CRs with interstellar matter and radiation in the Galaxy produce a diffuse flux. Hadrons interacting with matter produce neutral pions, which decay into gamma rays, while CR electrons produce gamma rays via inverse Compton scattering on the radiation field. Milagro has measured this diffuse Galactic flux in the TeV energy range with a median energy of 15 TeV and reported an excess in the Cygnus region, which might originate from CRs from local sources interacting with interstellar dust clouds [3]. IceCube's predecessor AMANDA-II has also looked for TeV photons from a giant flare from SGR 1806-20, using 100 GeV muons. AMANDA's large muon collection area compensated for the small cross section for photons to produce muons [4].

At higher energies, extragalactic sources are unlikely to be visible because more energetic photons are predicted to interact with cosmic microwave background radiation and with infrared starlight from early galaxies, producing e^+e^- pairs [5]. At 1 PeV, for example, photon propagation is limited to a range of about 10 kpc. It is unknown whether Galactic accelerators exist that can produce gamma rays of such high energy, but an expected flux results from interaction of (extragalactic) CRs with the interstellar medium and dense molecular clouds.

To date, the best statistics on photons with energies in the range from ~ 300 TeV to several PeVs come from the Chicago Air Shower Array-Michigan Muon Array (CASA-MIA), built at the Dugway Proving Ground in Utah. CASA consisted of 1089 scintillation detectors placed on a square array with 15 m spacing. MIA consisted of 1024 scintillation counters buried under about 3 m of earth, covering an area of 2500 m². It served as a muon veto, with a threshold of about 0.8 GeV.

CASA-MIA set a limit on the fraction of photons in the cosmic-ray flux of 10^{-4} at energies above 600 TeV [6]. The experiment also sets a limit of 2.4×10^{-5} on the fraction of photons in the CR flux coming from within 5° of the galactic disk [7] at 310 TeV. This is near the theoretical expectation due to cosmic-ray interactions with the interstellar medium. For a northern hemisphere site like

CASA-MIA, Ref. [8] predicts a gamma-ray fraction of 2×10^{-5} for the average gas column density.

In this work, we present a new approach for detecting astrophysical PeV gamma rays, based on data of the surface component, IceTop, and the in-ice array of IceCube. IceTop measures the electromagnetic component of air showers, while the in-ice array is sensitive to muons that penetrate the ice with energies above 500 GeV. While most CR showers above 1 PeV contain many muons above this threshold, only a small fraction of PeV gamma-ray showers carry muons that are energetic enough to reach the in-ice array. Therefore, gamma-ray candidates are selected among muon-poor air showers detected with IceTop and in which the axis is reconstructed as passing through the in-ice array.

This approach of selecting muon-poor showers as gamma-ray candidates is fundamentally different from the earlier AMANDA-II gamma-ray search described above, which was only sensitive to gamma-ray showers that *do* contain high energy muons (> 100 GeV).

We present a limit on the gamma-ray flux coming from the Galactic plane, based on one year of data with half of the IceCube strings and surface stations installed. We also discuss the sensitivity of the completed detector.

II. THE ICECUBE DETECTOR

IceCube (see Fig. 1) is a particle detector located at the geographic South Pole. The in-ice portion consists of 86 strings that reach 2450 m deep into the ice. Most of the strings are arranged in a hexagonal grid, separated by ~ 125 m. Each of these strings holds 60 digital optical modules (DOMs) separated by ~ 17 m covering the range from 1450 to 2450 m depth. Eight strings form a denser instrumented area called DeepCore. The DOMs detect Cherenkov light produced by downward-going muons in cosmic-ray air showers and from charged particles produced in neutrino interactions. The data used in this analysis was collected in 2008/2009, when the 40 strings shown in Fig. 2 were operational.

Each DOM is a complete detector system, comprising a 25 cm diameter Hamamatsu R7081-02 phototube [9], shaping and digitizing electronics [10], calibration hardware, plus control electronics and power supply. Most of the buried photomultiplier tubes (PMTs) are run at a gain of 10^7 . Digitization is initiated by a discriminator, with a threshold set to 0.25 times the typical peak amplitude of a single photoelectron waveform. Each DOM contains two separate digitizing systems; the analog transient waveform digitizer records 400 ns of data at 300 megasamples/s, with a 14 bit dynamic range (divided among three parallel channels), while the fast analog-to-digital converter (fADC) records 6.4 μ s of data at 40 megasamples/s, with 10 bits of dynamic range. A system transmits timing signals between the surface and each DOM, providing timing calibrations across the entire array of about 2 ns [11,12].

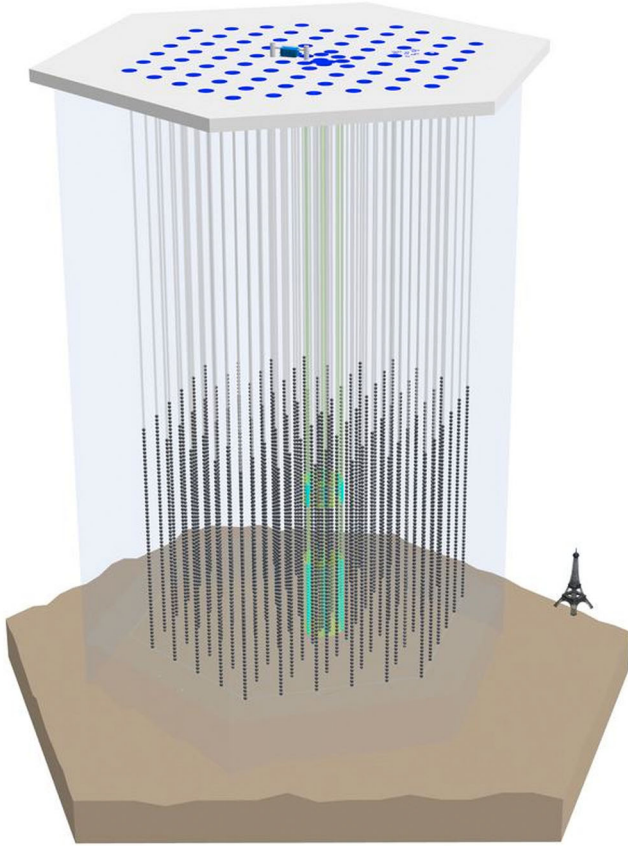


FIG. 1 (color online). IceCube consists of a $\sim\text{km}^2$ surface air-shower array and 86 strings holding 60 optical modules each, filling a physical volume of km^3 . The region in the center of the buried detector is more densely instrumented. See text for details.

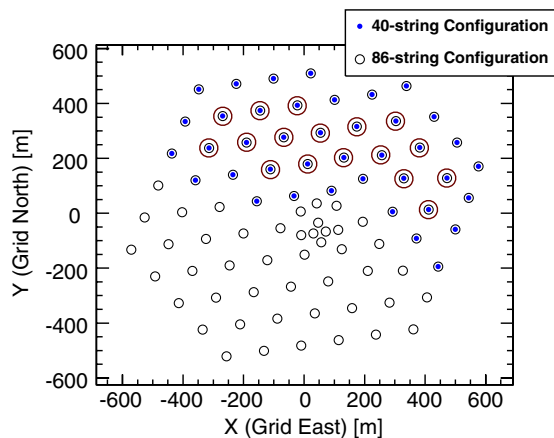


FIG. 2 (color online). Map of the locations of all 86 strings of the completed IceCube detector. The blue dots represent the 40-string configuration that is used for this analysis. At the surface level, each of these 40 strings is complemented by an IceTop station consisting of two tanks. The large (red) circles indicate the “inner strings” of the IceCube40 configuration.

The IceTop surface array [13] is located on the surface directly above the in-ice detectors. It consists of 81 stations, each consisting of two ice-filled tanks, about 5 m apart. For the 2008 data used here, 40 stations were operational [IceCube data with a configuration of 40 strings and 40 surface stations (IC40); see Fig. 2]. Each tank is 1.8 m in diameter, filled with ice to a depth of about 90 cm. The tanks are initially filled with water, and the freezing of the water is controlled to minimize air bubbles and preserve the optical clarity of the ice. Each tank is instrumented with two DOMs: a high-gain DOM run at a PMT gain of 5×10^6 , and a low-gain DOM, with a PMT gain of 5×10^5 . The two different gains were chosen to maximize dynamic range; the system is quite linear over a range from 1 to 10^5 photoelectrons. A station is considered hit when a low-gain DOM in one tank fires in coincidence with a high-gain DOM in the other; the thresholds are set to about 20 photoelectrons.

When an in-ice DOM is triggered, it sends a local coincidence (LC) message to its nearest two neighbors above and nearest two neighbors below. If the DOM also receives an LC message from one of its neighbors within 1μ , it is in hard local coincidence (HLC). In that case, the full waveform information of both the analog transient waveform digitizer and fADC chip is stored. For IC40 and earlier configurations, isolated or soft local coincidence (SLC) hits were discarded. In newer configurations, the SLC hits are stored, albeit with limited information. Keeping the full waveforms would require too much bandwidth, since the rate of isolated hits per DOM due to noise is ~ 500 Hz. Instead, only the three fADC bins with the highest values and their hit times are stored.

In Sec. IV, we present a gamma-ray analysis of the IC40 data set. In Sec. VI we study the expected sensitivity of the full IceCube detector and discuss how the inclusion of SLC hits increases the background rejection.

III. DETECTION PRINCIPLE

We create a sample of gamma-ray candidates by selecting air showers that have been successfully reconstructed by IceTop and have a shower axis that passes through the IceCube instrumented volume. The geometry limits this sample to showers having a maximum zenith angle of $\sim 30^\circ$. Since IceCube is located at the geographic South Pole, the field of view (FOV) is roughly constrained to the declination range of -60° to -90° , as shown in Fig. 3. This FOV includes the Magellanic clouds and part of the Galactic plane. Gamma rays at PeV energies are strongly attenuated over extragalactic distances, thus limiting the observable sources to those localized in our galaxy. At distances of ~ 50 kpc and ~ 60 kpc, the PeV gamma-ray flux from the large and small Magellanic cloud is suppressed by several orders of magnitude.

The contours in the background of Fig. 3 are the integrated neutral atomic hydrogen (HI) column densities

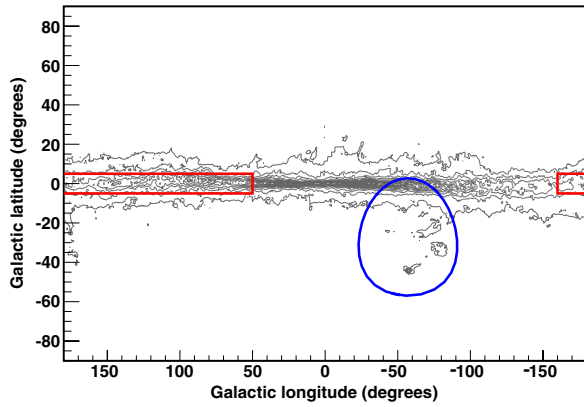


FIG. 3 (color online). Contours of HI column densities [14] in Galactic coordinates (flat projection). The blue circle indicates the gamma-ray FOV for IceCube in the present IC40 analysis. The red rectangles indicate the regions for which CASA-MIA [6] has set an upper limit on the Galactic diffuse photon flux in the 100 TeV–1 PeV energy range. IceCube’s FOV is smaller but covers a different part of the Galactic plane, close to the Galactic center.

under the assumption of optical transparency based on data from the Leiden-Argentine-Bonn survey [14]. These densities are not incorporated into the analysis and are only plotted to indicate the Galactic plane. We do expect, however, that gamma-ray sources are correlated with the HI column density. First, Galactic CR accelerators are more abundant in the high-density regions of the Galaxy. Secondly, the gamma-ray flux of (extra)galactic CRs interacting with the interstellar medium naturally correlates with the column density. However, it has to be noticed that this correlation is not linear, because of the attenuation of gamma rays over a 10-kpc distance scale. Furthermore, the column densities do not include molecular hydrogen, which can also act as a target for CRs.

The gamma-ray candidate events are searched for in a background of CR showers that have exceptionally few muons or are directionally misreconstructed. In the latter case, the muon bundle reaches kilometers deep into the ice but misses the instrumented volume. This background is hard to predict with Monte Carlo (MC) simulations. Cosmic-ray showers at PeV energies and with a low number of energetic muons are rare. For example, at 1 PeV, less than 0.2% of the simulated showers contain no muons with an energy above 500 GeV (see Fig. 4), approximately what is needed to reach the detector in the deep ice when traveling vertically. Determining how many hadronic showers produce a signal in a buried DOM would require an enormous amount of MC data to reach sufficient statistics, plus very strong control of the systematic uncertainties due to muon production, propagation of muons and Cherenkov photons through the ice, and the absolute detector efficiencies. It would also have to be able to accurately predict the errors in air-shower reconstruction parameters. For example, this analysis is very sensitive to the tails of the distribution of the error on the angular

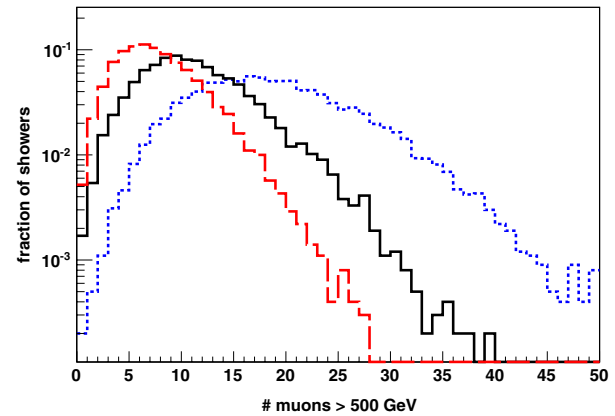


FIG. 4 (color online). Distribution of the number of muons with $E > 500$ GeV at 3 km altitude in samples of simulated showers of 0.6 PeV (red, dashed), 1 PeV (black, solid), and 2 PeV (blue, dotted). Each of the samples consists of 10,000 showers simulated with CORSIKA (using QGSJETII) with zenith angle $< 30^\circ$. The 1-PeV sample contains only 17 showers that contain no muons with energy above 500 GeV.

reconstruction of IceTop. Even MC sets that are large enough to populate these tails are not expected to properly describe them.

To avoid these issues, we determine the background directly from data. As a result, we are not able to measure a possible isotropic contribution to the gamma-ray flux because these gamma rays would be regarded as background. Instead, we search for localized excesses in the gamma-ray flux.

We search for a correlation of the arrival directions of the candidate events with the Galactic plane and scan for point sources. The acceptance of IceTop-40 is a complex function of azimuth and zenith due to its elongated shape and the requirement that the axis of the detected shower passes through IC40 (with the same elongated shape). However, since the arrival time is random (there are no systematic gaps in detector uptime with respect to sidereal time), the reconstructed right ascension (RA) of an isotropic flux of CR showers is uniform. The correct declination distribution of the background is very sensitive to the number of background showers introduced by errors in the IceTop angular reconstruction of the air shower as a function of the zenith angle and is taken to be unknown. However, the flat distribution of background over RA is enough to allow for a search for gamma-ray sources.

Recently, IceCube found an anisotropy in the arrival direction of CRs on the southern hemisphere [15]. These deviations with RA have been established for samples of CRs with median energies of 20 and 400 TeV. The two energy ranges show a very different shape of the anisotropy, but the level of the fractional variations in flux is at a part-per-thousand level for both [16]. An anisotropy with comparable magnitude in the PeV energy range is too small to affect this analysis (the IC40 final sample contains 268 events).

IV. IC40 ANALYSIS

A. Event selection

IC40 has taken data between April 5, 2008, and May 20, 2009, IC40, using several trigger conditions based on different signal topologies. This analysis uses the eight-station surface trigger, which requires a signal above threshold in both tanks of at least eight IceTop stations. An additional signal in IceCube is not required for this trigger, but all HLC hits in the deep detector within a time window of 10 μ before and after the surface trigger are recorded.

The air-shower parameters are reconstructed from the IceTop hits with a series of likelihood-maximization methods. The core position is found by fitting the lateral distribution of the signal, using

$$S(r) = S_{\text{ref}} \left(\frac{r}{R_{\text{ref}}} \right)^{-\beta - \kappa \log_{10} \left(\frac{r}{R_{\text{ref}}} \right)}, \quad (1)$$

where S is the signal strength, r is the distance to the shower axis, S_{ref} is the fitted signal strength at the reference distance $R_{\text{ref}} = 125$ m, β is the slope parameter reflecting the shower age, and $\kappa = 0.303$ is a constant determined from simulation [13,17]. Signal times are used to find the arrival direction of the air shower. The time delay due to the shape of the shower plane is described by the sum of a Gaussian function and a parabola, both centered at the shower core, which yields a resolution of 1.5° for IC40. The relationship between the reconstructed energy E_{reco} and S_{ref} is based on MC simulations for proton showers and depends on the zenith angle.

IceCube data is processed in different stages. In the first two levels, the raw data is calibrated and filtered, and various fitting algorithms are applied, of which only the IceTop reconstruction described above is used in this analysis. In the selection of photon-shower candidates from the data sample, we distinguish two more steps: level three (L3) and level four (L4). L3 includes all the conditions on reconstruction quality, geometry, and energy that make no distinction between gamma-ray showers and CR showers. The L4 cut is designed to separate gamma rays from CRs.

Two parameters are used to constrain the geometry and ensure the shower axis passes through the instrumented volume of IceCube. The IceTop containment parameter C_{IT} is a measure for how centralized the core location is in IceTop. When the core is exactly in the center of the array, $C_{\text{IT}} = 0$, while $C_{\text{IT}} = 1$ means that it is exactly on the edge of the array. More precisely, $C_{\text{IT}} = x$ means that the core would have been on the edge of the array if the array would be x times its actual size. The string distance parameter d_{str} is the distance between the point where the shower reaches the depth of the first level of DOMs and the closest inner string. Inner string, in this sense, means a string which is not on the border of the detector configuration. IC40 has 17 inner strings (see Fig. 2). The L3 cuts are:

- (i) Quality cut on lateral distribution fit: $1.55 < \beta < 4.95$ (cf. Eq. (1))
- (ii) Geometry cut: $C_{\text{IT}} < C_{\text{max}}$
- (iii) Geometry cut: $d_{\text{str}} < d_{\text{max}}$
- (iv) Energy cut: $E_{\text{reco}} > E_{\text{min}}$

The energy and geometry cuts are optimized in a later stage (Sec. IV C).

The L4 stage imposes only one extra criterion to the event: there should be no HLC hits in IceCube. This removes most of the CR showers, if E_{min} is chosen sufficiently high. The remaining background consists of CR showers with low muon content and misreconstructed showers, the high energy muons from which do not actually pass through IceCube.

The event sample after the L4 cut might be dominated by remaining background, but it can be used to set an upper limit to the number of gamma rays in the sample. Since the event sample after L3 cuts is certainly dominated by CRs, the ratio between the number of events after L4 and L3 cuts can be used to calculate an upper limit to the ratio of gamma-ray-to-CR showers.

The remaining set of candidate gamma-ray events is tested for a correlation with the Galactic plane (Sec. IV C) and the presence of pointlike sources (Sec. IV D). First, the results of simulations are presented, which provide several quantities needed for sensitivity calculations.

B. Simulation

Although we determine the background from data only, simulations are needed to investigate systematic differences in the detector response to gamma-ray showers and cosmic-ray showers. More specifically, we are interested in the energy reconstruction of gamma-ray showers, the fraction of gamma-ray showers that is rejected by the muon veto system, and a possible difference in effective detector area between both types of showers.

Gamma-ray and proton showers are simulated with CORSIKA v6.900, using the interaction models FLUKA 2008 and SYBILL 2.1 for low- and high-energy hadronic interactions, respectively. For both primaries, 10,000 showers are generated within an energy range of 800 TeV to 3 PeV with an E^{-1} spectrum. Because the shower axes are required to pass through IceCube, the zenith angle is restricted to a maximum of 35° . The observation altitude for IceTop is 2835 m. The atmospheric model MSIS-90-E is used, which is the South Pole atmosphere for July 01, 1997. Seasonal variations in the event rate are of the order of 10% [18].

The detector simulation is done with the IceTray software package. Each simulated shower is fed into the detector simulation ten times with different core positions and azimuthal arrival direction, for a total of 100,000 events for both gamma rays and protons. This resampling of showers is a useful technique for increasing the statistics when examining quantities like the resolution of the energy

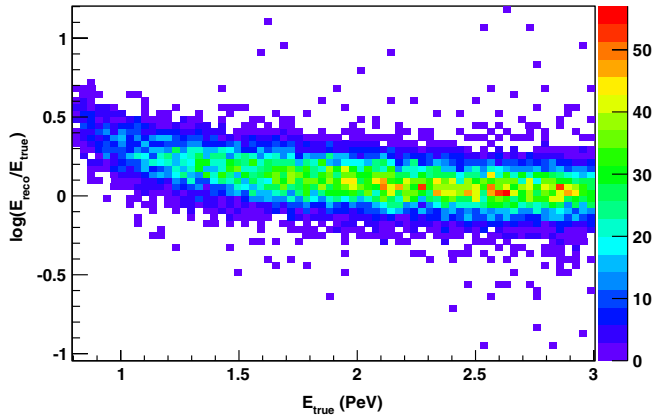


FIG. 5 (color online). Ratio between reconstructed and true energy of simulated gamma-ray showers as a function of their true energy. At low energies, the overestimation of the gamma-ray energy is largely due to a bias effect of the eight-station filter. At higher energies, this overestimation decreases.

reconstruction of IceTop. However, it cannot be used for quantities with large shower-to-shower variations, such as the number of high-energy muons.

The energy of gamma-ray showers is overestimated by the reconstruction algorithm. Fig. 5 shows the distribution of the logarithm of the ratio between the reconstructed and true primary energy as function of true energy, weighted to an $E^{-2.7}$ spectrum. There are two reasons for the energy offset. First, there is a selection effect of the eight-station filter, which has a bias (below a few PeV) toward showers that produce relatively large signals in the IceTop tanks. This also affects the reconstructed energy of CR showers. At higher energies, the offset decreases, but the reconstructed energy of gamma-ray showers is still slightly overestimated because the energy calibration of IceTop is performed with respect to proton showers.

Figure 6 shows the distribution of true energies of gamma-ray and proton showers for the energy cut $E_{\text{reco}} > 1.4$ PeV (which will be adopted in Sec. IV C). After this

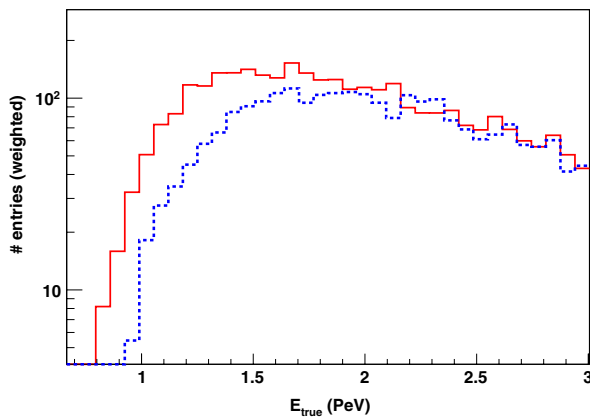


FIG. 6 (color online). Distribution of true energy of gamma-ray (red, solid) and proton (blue, dotted) showers for an energy cut at $E_{\text{reco}} > 1.4$ PeV, weighted to an $E^{-2.7}$ spectrum.

cut, 95% of the gamma-ray showers have a true energy above 1.2 PeV, while 95% of the proton showers have an energy above 1.3 PeV.

The fraction of gamma-ray showers that is falsely rejected because the showers contain muons that produce a signal in IceCube is found by applying the cuts to the MC simulation.

After applying the L3 cuts (defined in Sec. IV C) to the simulated gamma-ray sample, there are 737 events left in the sample, of which 121 produce a signal in IceCube. Taking into account an energy weighting of $E^{-2.7}$, this corresponds to 16%.

Showers that have no energetic muons can still be rejected if an unrelated signal is detected by IceCube. This could be caused by noise hits or unrelated muon tracks that fall inside the time window. This noise rate is determined directly from the data and leads to 14% signal loss. The total fraction of gamma-ray showers that is falsely rejected is therefore 28%.

Finally, because the composition, shower size, and evolution of gamma-ray and CR showers are different, one might expect a difference in the number of triggered stations and the quality of the reconstruction, which could lead to different effective areas. Such an effect would be of importance when calculating the relative contribution of gamma rays to the total received flux. We compare the effective area for gamma rays and protons by counting the number of events that are present at L3. We compensate for the energy reconstruction offset by reducing the reconstructed gamma-ray energy by a factor 1.16. The ratio of the effective area for gamma rays to that for protons is then found to be 0.99.

It should be emphasized that we do not use the simulation to determine the number of muons and their energy distribution from CR showers. This would require a simulation set that includes heavier nuclei instead of protons only. Moreover, various hadronic interaction models generate significantly different muon fluxes [19]. Instead, this analysis estimates the rate of CR showers that do not trigger IceCube using the data itself.

C. Galactic Plane test

The IC40 data set consists of 368 days of combined IceCube and IceTop measurements. The data from August 2009 are used as a burn sample, which means that they are used to tune the parameters of the analysis. After this tuning, the burn sample is discarded, and the remaining data is used for the analysis.

IceCube is sensitive to gamma rays above 1 PeV. Earlier searches by CASA-MIA in a slightly lower energy range (100 TeV–1 PeV) with better sensitivity have not established a correlation of gamma rays with the Galactic plane (see Fig. 15). For a Galactic diffuse flux below the CASA-MIA limit [6], no gamma rays are expected in the IC40 burn sample. However, IceCube observes a different part of

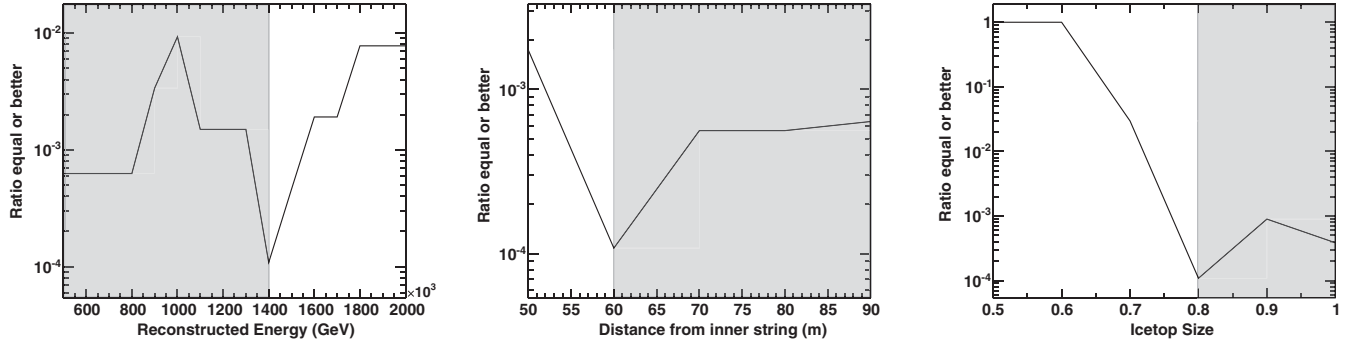


FIG. 7. Optimization scans for cut parameters E_{\min} , d_{\max} , and C_{\max} . The fraction of scrambled data sets that perform equal or better than the real data set is plotted against cut value. For each plot, the other 2 parameters are kept constant at their optimal value. The actual scan was done three dimensionally. For each plot, the shaded region indicates the parameter space that is excluded by the optimized cuts.

the Galactic plane (see Fig. 3), close to the Galactic center, so the possibility exists that previously undetected sources or local enhancements in CR and dust densities create an increase in the flux from that part of the sky.

In order to find a possible correlation of candidate events in our burn sample to the Galactic plane, different sets of L3 cut parameters are applied to find a set that produces the most significant correlation. Afterward, the cut parameters are fixed, and the burn sample is discarded. The fixed cut parameters are then used in the analysis of the rest of the IC40 data set to test whether the correlation is still present. Note that these cuts are applied at L3, so they affect both the event samples after L3 and L4 cuts. This is important because the ratio between the number of events after L4 and L3 cuts is used to calculate the ratio between gamma-ray and CR showers.

There are three cut parameters that are optimized by using the burn sample: E_{\min} , C_{\max} , and d_{\max} . This is done by scanning through all combinations of parameters within the following range: $600 \text{ TeV} \leq E_{\min} \leq 2 \text{ PeV}$ with steps of 100 TeV, $0.5 \leq C_{\max} \leq 1.0$ with steps of 0.1, and $50 \text{ m} \leq d_{\max} \leq 90 \text{ m}$ with steps of 10 m. For each combination, the number of events N_S in the burn sample after the L4 cut, located in the source region, is counted. The source region is defined as within 10° of the Galactic plane. Then, the data set is scrambled multiple times by randomizing the RA of each data point. For each scrambled data set, the number of events in the source region is again counted. The best combination of cut parameters is the set which has the lowest fraction of scrambled data sets for which this number is equal to or higher than N_S .

The result of the scan is given in the three panels of Fig. 7. For each cut parameter, the fraction of scrambled data sets that has a number of events in the source region equal to or exceeding the amount in the original data set is plotted for different cut values. For each plot, the values of the other two cut parameters are kept constant at their optimal value. The actual search is done in three dimensions. The ratio is lowest for $E > 1.4 \text{ PeV}$, $C_{\text{IT}} < 0.8$, and $d_{\text{str}} < 60 \text{ m}$. With

this combination of cuts, only 0.011% of the scrambled data sets produce an equal or higher number of events in the source region.

Note that while this procedure of optimizing cuts should be effective in the presence of a sufficient signal, the small fraction obtained here is consistent with fluctuations of the background CR distribution alone, given the large number of possible cut combinations that were scanned. These fluctuations are also responsible for the erratic behavior of the fraction with changing cut values. Nonetheless, the cut parameter values found with this procedure seem very reasonable (similar values are found with an alternative method, see Sec. VI).

The optimized cuts are applied to the complete IC40 data set minus the burn sample. There are 268 candidate events, of which 28 are located in the source region. Figure 8 is a map of the sky showing all 268 events. The colors in the background indicate the integrated HI column densities, cf. Fig. 3 (see the discussion in Sec. III). These are meant to guide the eye and are not part of the analysis.

The significance of the correlation with the Galactic plane is tested by producing data sets with scrambled RA. An equal or higher number of source region events is found in 21% of the scrambled data sets, corresponding to a nonsignificant excess of $+0.9\sigma$.

We follow the procedure of Feldman and Cousins [20] to construct an upper limit for the ratio of gamma rays to CRs. The background is determined by selecting a range of RA that does not contain the source region. Within this range, the data points are scrambled multiple times, and for each scrambled set, the number of events in a predefined region of the same shape and size as the source region is counted. This yields a mean background of 24.13 events for the source region. Using a 90% confidence interval, the upper limit on the number of excess gamma rays from this region is 14.

Since 28% of gamma-ray showers is rejected by the veto from the buried detector, the maximum number of excess gamma rays from the Galactic plane is $14/0.72 = 19.4$.

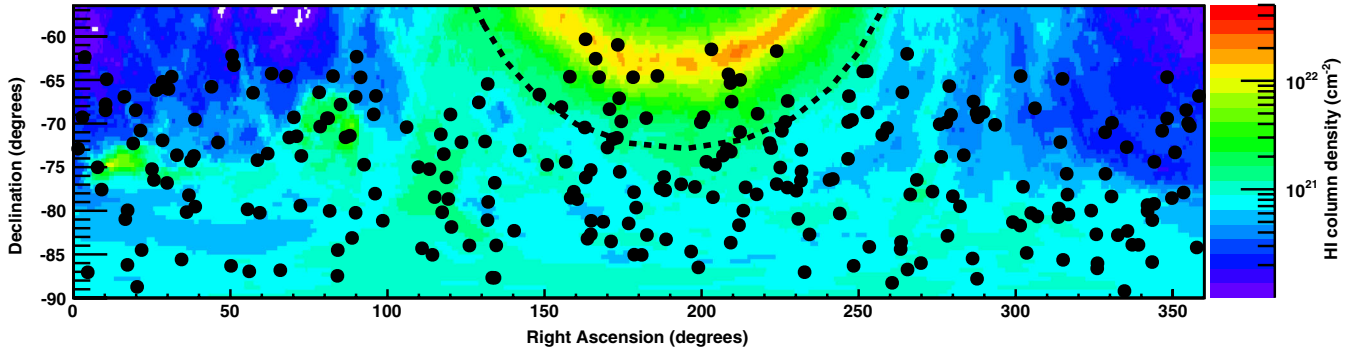


FIG. 8 (color online). Equatorial map of the 268 candidate gamma-ray events of the IC40 data set superimposed on HI column densities based on Ref. [14]. The dotted black curve encloses the source region, defined as within 10° of the Galactic plane.

From Fig. 6, it is known that the energy cut corresponds to a threshold of 1.2 PeV for gamma rays and 1.3 PeV for protons. Given that, at L3, the sample is dominated by CR showers and assuming a CR and gamma-ray power law of $\gamma = -2.7$, a 90% C.L. upper limit of 1.2×10^{-3} on the ratio of gamma-ray showers to CR showers in the source region can be derived in the energy range 1.2–6.0 PeV. The upper bound of 6.0 PeV is the value for which 90% of the events are inside the energy range. This value falls outside the range for which gamma-ray showers were simulated. However, there is no indication that the energy relation plotted in Fig. 5 behaves erratically above 3 PeV.

This is a limit on the average excess of the ratio of gamma rays to CRs in the source region with respect to the rest of the sky, i.e., a limit on the Galactic component of the total gamma-ray flux. A possible isotropic component is not included. Systematic uncertainties lead to a 18% variation of the upper limit, as determined in Sec. V.

D. Unbinned point source search

An additional search for pointlike sources tests the possibility that a single source dominates the PeV gamma-ray sky. This source does not necessarily lie close to the Galactic plane. An unbinned point source search is performed on the sky within the declination range of -85° to -60° , using a method that follows [21]. The region within 5° around the zenith is omitted because the method relies on scrambled data sets that are produced by randomizing the RA of the events. Close to the zenith, this randomization scheme fails due to the small number of events.

The data is described by an unknown amount of signal events on top of a flat distribution of background events. In an unbinned search, a dense grid of points in the sky is scanned. For each point, a maximum-likelihood fit is performed for the relative contribution of source events over background events.

For a particular event i , the probability density function (PDF) is given by

$$P_i(n_S) = \frac{n_S}{N} S_i + \left(1 - \frac{n_S}{N}\right) B_i, \quad (2)$$

where n_S is the number of events that is associated to the source, B_i is the background PDF, and

$$S_i = \frac{1}{2\pi\sigma^2} \exp\left(-\frac{\Delta\Psi^2}{2\sigma^2}\right) \quad (3)$$

is the two-dimensional Gaussian source PDF, in which $\Delta\Psi$ is the space angle between the event and the source location and $\sigma = 1.5^\circ$ is the angular resolution of IceTop. The background PDF B_i is only dependent on the zenith angle and is derived from the zenith distribution of the data. For each point in the sky, there is a likelihood function

$$L(n_S) = \prod_i P_i(n_S) \quad (4)$$

and associated test statistic

$$\lambda = -2(\log(L(0)) - \log(L(n_S))), \quad (5)$$

which is maximized for n_S . In the optimization procedure, n_S is allowed to have a negative value, which mathematically corresponds to a local flux deficit.

The procedure is similar to the search method for the neutrino point sources with IceCube [22], except that the source and background PDF do not contain an energy term. Because the range of energies in the event sample is relatively small (90% of the events have an energy between 1 and 6 PeV), an energy PDF is unlikely to improve the sensitivity.

Figure 9 displays a map of the sky with declination between -85° and -60° showing the events in this region and contours of the test statistic λ . The maximum value is $\lambda = 2.1$ at $\delta = -65.4^\circ$ and RA = 28.7° , corresponding to a fit of $n_S = 3.5$ signal events. The overall significance of this value for λ is found by producing 10,000 scrambled data sets by randomizing the RA of each event. Figure 10 shows the distribution of λ associated to the hottest spot in each scrambled data set. The median test statistic value for the hottest spot in the scrambled data sets is $\lambda = 2.7$, so the actual data set is consistent with a flat background.

Upper limits on the gamma-ray flux can be derived for each point in the sky by assuming that all events are gamma rays. Since many events are in fact muon-poor or

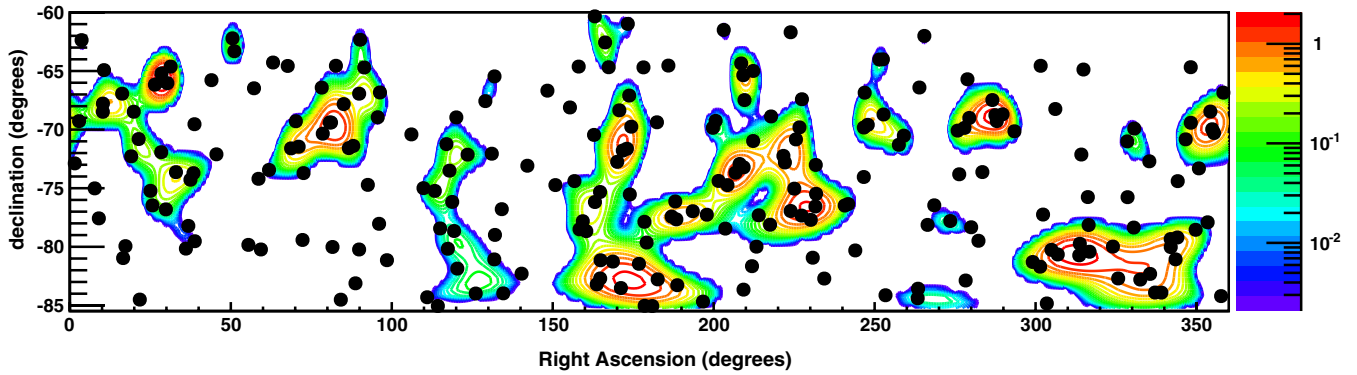


FIG. 9 (color online). Equatorial map of the part of the sky for which an unbinned point source search is performed. The contours indicate the value of λ , and the black dots are the candidate events.

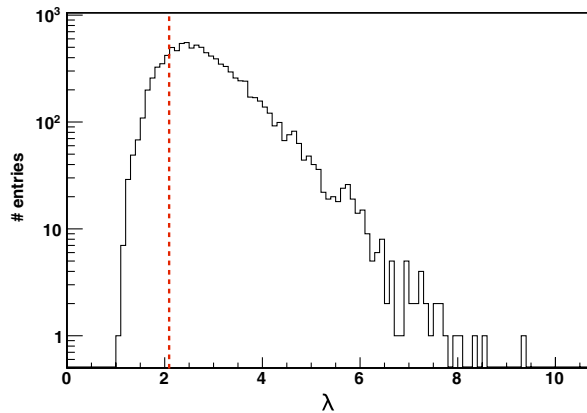


FIG. 10 (color online). Distribution of the largest value of λ observed in each scrambled data set. The red dotted line indicates the value for λ that corresponds to the hottest spot in the data.

misreconstructed showers, this leads to a conservative upper limit. Because the acceptance of IC40 decreases as a function of declination (see Fig. 14), the limit is more constraining at a lower declination. Figure 11 is a sky map of the 90% C.L. upper limit in the energy range $E = 1.2\text{--}6.0$ PeV for the E^{-2} source spectra. Point source

fluxes are excluded at a level of $(E/\text{TeV})^2 d\Phi/dE \sim 10^{-12}\text{--}10^{-11} \text{ cm}^{-2} \text{ s}^{-1} \text{ TeV}^{-1}$ depending on source declination. Corrections for signal efficiency and detector noise are taken into account. Systematic uncertainties lead to a 18% variation of the upper limit.

V. SYSTEMATIC ERRORS

Since this analysis derives the background from data, the systematic uncertainties due to the background estimation are small. The previously discussed cosmic-ray anisotropy measurement (see Sec. III and Ref. [16]) is too small to have an impact on this analysis. Since there are no systematic gaps in detector up time with respect to the sidereal time of day in our sample, the coverage of RA is homogeneous.

Therefore, we focus on the systematic uncertainties in the signal efficiency, due to uncertainties in the surface detector sensitivity, and in the muon production rate for photon showers.

The uncertainty in the surface detector sensitivity is studied in Ref. [17]; Table 2 there gives the uncertainties for hadronic showers as a function of shower energy and zenith angle. Although there are differences between hadronic and electromagnetic showers, most factors that

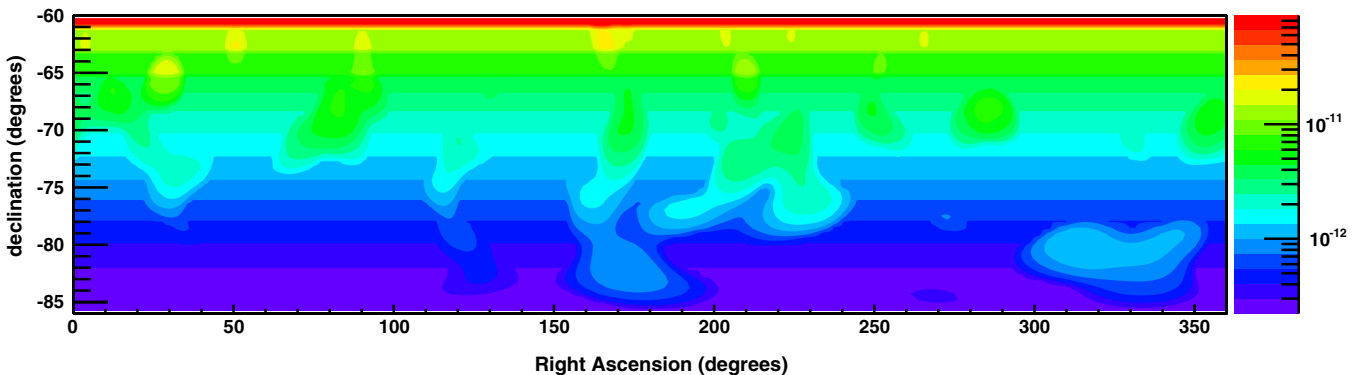


FIG. 11 (color online). Sky map of 90% C.L. upper limits on point source flux $(E/\text{TeV})^2 d\Phi/dE$ in $\text{cm}^{-2} \text{ s}^{-1} \text{ TeV}^{-1}$ for E^{-2} source spectra in the energy range $E = 1.2\text{--}6.0$ PeV. The limit is typically more constraining at low declinations where the effective area is largest.

contribute to this figure apply to both types of showers. Strongly contributing factors include atmospheric fluctuations, calibration stability, and uncertainties in response of detector electronics (PMT saturation and droop). The contribution from the uncertainty in modeling the hadronic interaction is clearly different for electromagnetic showers and is discussed below. For $E < 10$ PeV and zenith angle less than 30° , there is a 6.0% systematic uncertainty in energy and a 3.5% systematic uncertainty in flux. For an $E^{-2.7}$ spectrum, a 6.0% uncertainty in energy translates into a 17.0% uncertainty in flux, or, adding in quadrature, 17.4% flux uncertainty.

The uncertainty in the muon production from hadronic showers emerges from theoretical uncertainties. It depends on the hadronic photoproduction and electroproduction cross sections for energies between 10 TeV and 6 PeV. Figure 1 of Ref. [23] compares two cross sections from two different photoproduction models and finds (for water with a similar atomic number and mass number as air) a difference that rises from about 20% at 10 TeV to 60% at 1 PeV. The bulk of the particles in the shower are at lower energies, so we adopt a 20% uncertainty on the muon production rate via photoproduction. In addition, there is also a contribution of muon pair creation. To reach the in-ice DOMs, muons need at least 500 GeV. At 1 TeV, the fractional contribution of muon pair creation is $\sim 10\%$ [24]. Since muon pair production is not included in SYBILL 2.1, we arrive at 30% uncertainty in the total muon production rate. This uncertainty is applied to the 16% of photon showers that are lost because they contain muons for a final 4.8% uncertainty in sensitivity due to the unknown muon production cross section.

We add the uncertainties due to detector response and muon production in quadrature and arrive at an overall 18% uncertainty in sensitivity.

VI. ICECUBE 5-YR SENSITIVITY

The sensitivity of the full IceCube detector to a gamma-ray flux from the Galactic plane benefits from multiple improvements that can be made with respect to the analysis presented above. In this section, we use preliminary data from the IceCube79 (IC79) configuration (79 strings, 73 surface stations, 2010/2011) to estimate the sensitivity that the full IceCube detector can reach in 5 yr. Since the full detector [IceCube86 (IC86): 86 strings and 81 surface stations) is slightly larger than the IC79 configuration, the predicted sensitivity will be slightly underestimated. Also, the new cuts proposed below are not yet optimized, as this would require the actual IC86 data set.

A. Air-shower reconstruction

This analysis is very sensitive to the quality of the core reconstruction. If the shower core is not reconstructed accurately, a muon bundle that passes outside the in-ice array might be incorrectly assumed to be aimed at the detector. Because of the absence of a signal in the in-ice DOMs, the event is then misinterpreted as a gamma-ray candidate. A more accurate core reconstruction algorithm has been developed for IceTop and will improve the CR rejection in post-IC40 analyses. In addition, the angular resolution of the larger array is improved, increasing the sensitivity to point sources.

B. Isolated hits

The SLC mode [which has been available since IceCube59 (IC59), see Sec. II] increases the sensitivity to CR showers with low muon content. A muon with just enough energy to reach IceCube might not emit enough Cherenkov light to trigger multiple neighboring DOMs. By tightening the L4 cut so that no SLC hits are allowed to be

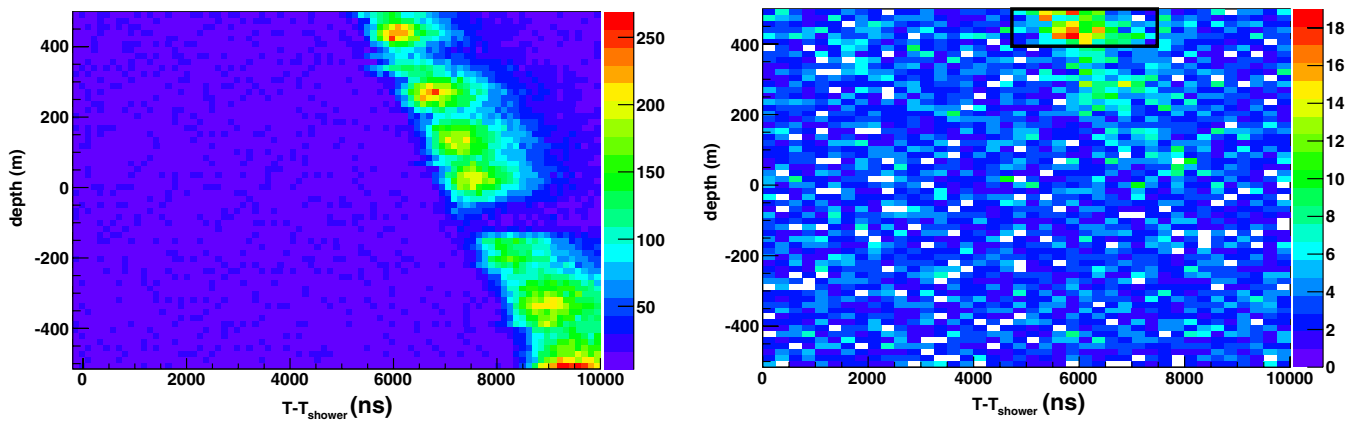


FIG. 12 (color online). Observed time of isolated hits (SLC) relative to the arrival time of the air-shower front measured by IceTop. The left plot shows the distribution of SLC hits for all events; the right plot is the same but restricted to the subset of events which have only SLC hits and no HLC hits. There is an excess of SLC hits in the region where a muon signal associated to the shower is expected. This allows an additional cut to separate gamma-ray showers from hadronic showers. The black box indicates the region in which an SLC hit counts as a veto (see text for details). The variation in the number of hits as a function of depth in the left plot is due to variations in the optical properties of the ice.

present in the data, the efficiency with which CR showers can be rejected increases. At the same time, actual gamma-ray showers may be rejected in the case of a noise hit in a single DOM. To keep this chance low, SLC hits only count as veto hits if they can be associated to the shower muon bundle both spatially and temporally.

Figure 12 shows the distribution of isolated hits in the complete detector as a function of time relative to the arrival time of the air shower as measured by IceTop. The plots show data at the L3 level, applying the same cut values as in the IC40 analysis. The left plot shows the distribution of SLC hits for all events, while the right plot shows the same distribution but restricted to the subset of events which contain *only* SLC hits, i.e., events with no HLC hits. Hits associated with the muon bundle are seen throughout the detector, although the number of hits varies with depth because of variations in the optical properties of the ice due to naturally varying levels of contaminants, such as dust, which attenuate Cherenkov photons. The large number of isolated hits in the two bottom rows is an edge effect: the DOMs have fewer neighbors, so the chance for a hit to be isolated increases. In principle, the same effect could occur at the top two rows. However, the muon bundle deposits more energy in this region, and the probability for any hit to have neighbor hits is larger here.

The muon-poor showers that produce no HLC hits (right-hand plot) can still cause some isolated hits in the top of the detector. These events can be removed with an additional cut on SLC hits. Because isolated hits can also be produced by noise, only a small area is selected in which SLC hits are used as a veto. A simple additional L4 cut is that all events are removed that have an SLC hit meeting the following three criteria:

- (i) it is within 200 m from the reconstructed shower axis,
- (ii) it is within a time window of 4.8–7.5 μ after the shower arrival time, and
- (iii) it is in one of the six top layers of DOMs (spanning a vertical extent of 85 m).

Note that the lower bound of the time window (4.8 μ) corresponds to the time it takes for a muon traveling

vertically to reach the top layer of in-ice DOMs starting from the surface. Muons from an inclined shower will arrive even later. The number of background events that are discarded in the L4 cut is increased by $\sim 30\%$, while the SLC noise rate in the data implies a decrease in signal efficiency of $\sim 5\%$.

With the completed detector, it will be possible to optimize the SLC cuts further by making the time window dependent on zenith angle and DOM depth. The effect of this optimization was not yet studied here.

C. Reoptimization of cuts

For the IC40 analysis, the cut parameters were optimized to increase the detection probability of a possible correlation of gamma rays with the Galactic plane. To increase the sensitivity of future searches with the completed IC86 configuration, the cut values were reevaluated to increase the number of candidate events without losing background rejection power. This was achieved by evaluating the ratio between the number of events after the L3 and L4 cuts.

While the L3 event sample is completely dominated by CRs, the L4 sample is a combination of possible gamma-ray showers, muon-poor CR showers, and misreconstructed CR showers. The fraction of gamma rays and muon-poor CRs in the detected events is independent from the cuts on geometry parameters d_{str} and C_{IT} . The number of misreconstructed CR showers, on the other hand, will increase if the geometry cut values are chosen too loosely. Therefore, the ratio between the number of L4 and L3 events as a function of the cut parameter should be flat up to some maximum value after which it starts to increase. This maximum value is the preferred cut value since it maximizes the number of candidate events without lowering the background rejection power. It also maximizes the FOV, as looser geometry cuts imply a larger maximum zenith angle.

Figure 13 shows the number of L3 (red) and L4 (blue) events together with their ratio (black dotted line; right-hand axis) as a function of the three main cut parameters (with the other cut parameters kept constant at their final value).

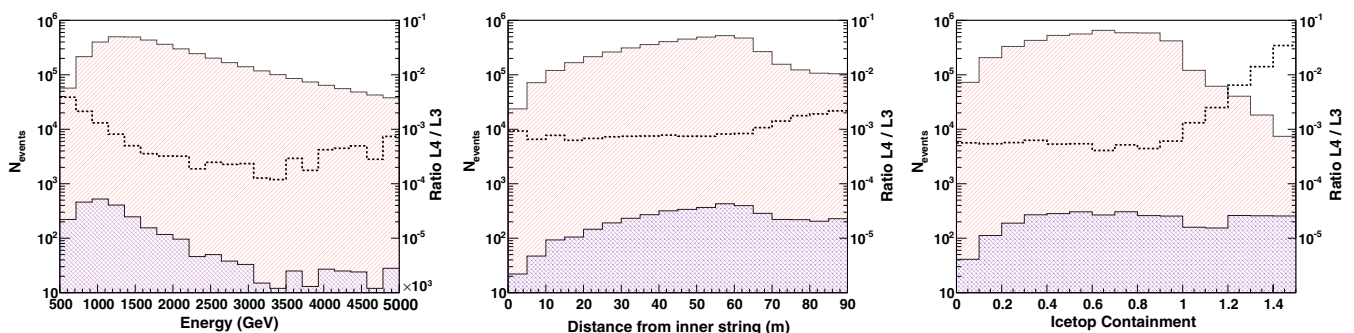


FIG. 13 (color online). The number of L3 (red) and L4 (blue) events in the data as a function of the three main cut parameters. The ratio of the number of L4 to L3 events is given by the black dotted line, for which the corresponding axis is drawn on the right-hand side of the plot.

The rejection efficiency for d_{str} is fairly stable up to 60 m. The number of events rapidly decreases above this value, while the rejection becomes worse. In this case, the alternative method of optimization yields the same result as the method used in the IC40 analysis. For the containment size C_{IT} , the ratio remains stable up to the edge of the array ($C_{\text{IT}} = 1$), after which it starts to rise. It appears the cut can be relaxed with respect to the IC40 analysis. In the following, we will use $d_{\text{str}} < 60$ m and $C_{\text{IT}} < 1.0$.

The efficiency of the energy cut increases, as expected, with increasing energy, leveling off around ~ 2.0 PeV. Since the total number of events falls off rapidly for increasing energy, the most sensitive region will be $\sim 2\text{--}3$ PeV. However, since the spectra of possible sources in this energy regime are unknown, it is not clear what energy cut would produce the optimal sensitivity. Instead, the sensitivity is calculated for ten energy bins in the range of 1–10 PeV (see Fig. 15).

D. Increased acceptance

With a larger array, the acceptance, defined here as the effective area integrated over the solid angle of each 1° bin in the zenith angle, increases considerably. Because of the condition that the shower axis has to be inside the instrumented area of both IceCube and IceTop, the increase is especially dramatic at larger zenith angles. Figure 14 shows the acceptance for IC40 with $C_{\text{IT}} < 0.8$ and the complete IC86 array with $C_{\text{IT}} < 1.0$. Not only does the acceptance increase at large zenith angles, but the range of possible zenith angles is also extended (to $\approx 45^\circ$). This extends the FOV to cover a larger part of the Galactic plane and probe an area closer to the Galactic center. The Galactic center itself is still outside the FOV at $\delta \approx -29^\circ$, corresponding to a zenith angle of 61° .

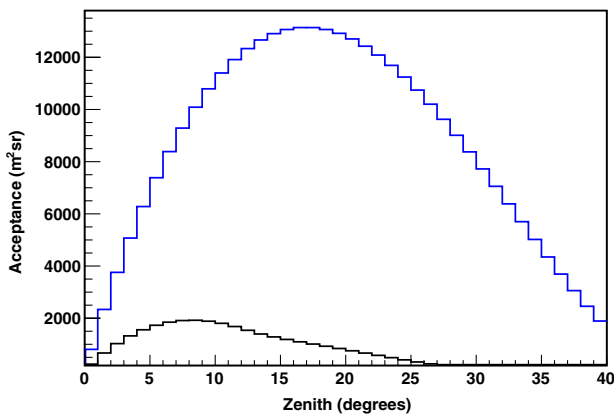


FIG. 14 (color online). Acceptance (effective area integrated over solid angle) for showers with an axis through both IceTop and IceCube for IC40, $C_{\text{IT}} = 0.8$ (black/lower line), and IC86, $C_{\text{IT}} = 1.0$ (blue/upper line).

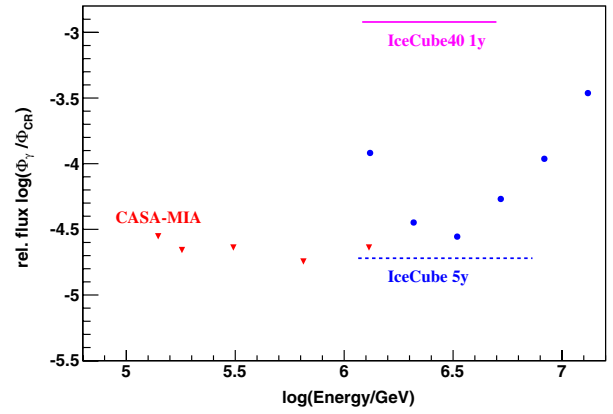


FIG. 15 (color online). Existing limits (red triangles for CASA-MIA and purple line for the present IC40 analysis) and IceCube sensitivity to a diffuse gamma-ray flux from a region within 10° from the Galactic plane. The blue dashed line indicates the 5-yr sensitivity of the completed detector, while the blue dots represent the sensitivity in smaller energy bins.

E. Sensitivity

The sensitivity that can be reached with 5 yr of data from the completed IceCube configuration can be estimated with preliminary data from IC79. It is assumed that the fraction of gamma rays that are missed due to noise hits is the same as in the IC40 analysis. The full detector obviously has more noise hits, but this can be compensated by refining the in-ice cut by only allowing vetoes from DOMs that can be associated to the shower muon bundle in space and time (cf., the SLC cut described above). The sensitivity is calculated by producing scrambled data sets with randomized RA. Figure 15 shows the 90% C.L. sensitivity to a diffuse flux from within 10° of the Galactic plane that can

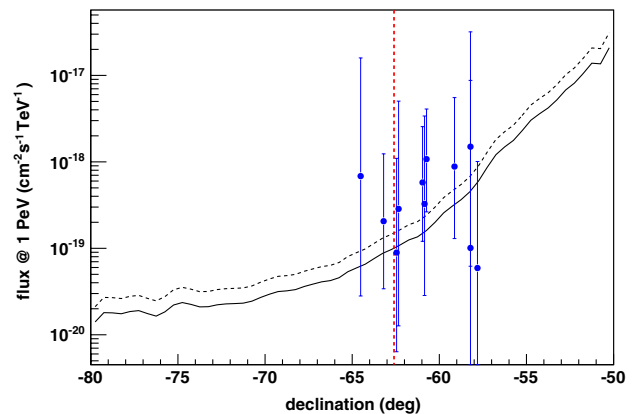


FIG. 16 (color online). IceCube 5-yr sensitivity to point sources as a function of declination. The solid (dashed) black line indicates the sensitivity to an E^{-2} ($E^{-2.5}$) flux. The dashed red line indicates the lowest declination reached by the Galactic plane. The blue points indicate the flux at 1 PeV with extrapolated uncertainties of the sources listed in Table I in the absence of a cutoff.

TABLE I. List of H.E.S.S. sources in IceCube gamma-ray FOV. For those values that have two error margins, the first indicates the statistical error, while the second indicates the systematic error.

Source	RA	decl.	Flux at 1 TeV ($\text{cm}^{-2} \text{s}^{-1} \text{TeV}^{-1}$)	Γ	Classification
H.E.S.S. J1356-645	13 ^h 56 ^m 00 ^s	−64° 30′ 00″	$(2.7 \pm 0.9 \pm 0.4) \times 10^{-12}$	$2.2 \pm 0.2 \pm 0.2$	PWN [27]
H.E.S.S. J1303-631	13 ^h 03 ^m 00 ^s	−63° 11′ 55″	$(4.3 \pm 0.3) \times 10^{-12}$	$2.44 \pm 0.05 \pm 0.2$	PWN [28]
RCW 86	14 ^h 42 ^m 43 ^s	−62° 28′ 48″	$(3.72 \pm 0.5 \pm 0.8) \times 10^{-12}$	$2.54 \pm 0.12 \pm 0.2$	shell-type supernova remnants [29]
H.E.S.S. J1507-622	15 ^h 06 ^m 53 ^s	−62° 21′ 00″	$(1.5 \pm 0.4 \pm 0.3) \times 10^{-12}$	$2.24 \pm 0.16 \pm 0.2$	no ID [30]
Kookaburra (Rabbit)	14 ^h 18 ^m 04 ^s	−60° 58′ 31″	$(2.64 \pm 0.2 \pm 0.53) \times 10^{-12}$	$2.22 \pm 0.08 \pm 0.1$	PWN [31]
H.E.S.S. J1427-608	14 ^h 27 ^m 52 ^s	−60° 51′ 00″	$(1.3 \pm 0.4) \times 10^{-12}$	$2.2 \pm 0.1 \pm 0.2$	no ID [32]
Kookaburra (PWN)	14 ^h 20 ^m 09 ^s	−60° 45′ 36″	$(3.48 \pm 0.2 \pm 0.7) \times 10^{-12}$	$2.17 \pm 0.06 \pm 0.1$	PWN [31]
MSH 15–52	15 ^h 14 ^m 07 ^s	−59° 09′ 27″	$(5.7 \pm 0.2 \pm 1.4) \times 10^{-12}$	$2.27 \pm 0.03 \pm 0.2$	PWN [33]
H.E.S.S. J1503-582	15 ^h 03 ^m 38 ^s	−58° 13′ 45″	$(1.6 \pm 0.6) \times 10^{-12}$	$2.4 \pm 0.4 \pm 0.2$	dark (Forbidden-Velocity-Wing?) [34]
H.E.S.S. J1026-582	10 ^h 26 ^m 38 ^s	−58° 12′ 00″	$(0.99 \pm 0.34) \times 10^{-12}$	$1.94 \pm 0.2 \pm 0.2$	PWN [35]
Westerlund 2	10 ^h 23 ^m 24 ^s	−57° 47′ 24″	$(3.25 \pm 0.5) \times 10^{-12}$	$2.58 \pm 0.19 \pm 0.2$	massive star cluster [35]

be achieved with 5 yr of full detector data. The blue dashed line indicates the integrated limit between 1 and 10 PeV, while the blue dots indicate the sensitivity in six smaller energy bins. The upper limits found by CASA-MIA and IC40 (present work) are also included in the plot. The KASCADE [25] results are not included since they set a limit on the all-sky gamma-ray flux.

Figure 16 shows the sensitivity to point sources that is possible with 5 yr of IceCube data. The sensitivity is a strong function of declination because the acceptance decreases at larger zenith angles. Point sources are expected to lie close to the Galactic plane, which reaches its lowest declination at -63° . Within the IceCube field of view, there are several PWNe and other gamma-ray sources detected by H.E.S.S. [26], listed in Table I. For these sources no significant cutoff was observed up to the maximum energy of 10 TeV, where statistics gets low. The blue dots indicate the flux that these sources would have at 1 PeV if their spectrum remains unchanged up to that energy. No correction for gamma-ray attenuation between the source and observer has been applied in this calculation. The extrapolation over two orders of magnitude causes large uncertainties in the gamma-ray flux due to propagation of the errors on the spectral indices.

VII. CONCLUSIONS

We have presented a new method of searching for high-energy gamma rays using the IceCube detector and its surface array IceTop. One year of data from IC40 was used to perform a search for point sources and a Galactic diffuse signal. No sources were found, resulting in a 90% C.L. upper limit on the ratio of gamma rays to cosmic rays of 1.2×10^{-3} for the flux coming from the Galactic plane region ($-80^\circ \lesssim l \lesssim -30^\circ$; $-10^\circ \lesssim b \lesssim 5^\circ$) in the energy range 1.2–6.0 PeV. Point source fluxes with E^{-2} spectra have been excluded at a level of $(E/\text{TeV})^2 d\Phi/dE \sim 10^{-12} - 10^{-11} \text{cm}^{-2} \text{s}^{-1} \text{TeV}^{-1}$ depending on source

declination. The full detector was shown to be much more sensitive because of its larger size, improved reconstruction techniques, and the possibility to record isolated hits.

This analysis offers interesting observation possibilities. IceCube can search for a diffuse Galactic gamma-ray flux with a sensitivity comparable to CASA-MIA, but at higher energies. This sensitivity is reached, however, by studying a much smaller part of the Galactic plane than CASA-MIA. IceCube is, therefore, especially sensitive to localized sources, which might be Galactic accelerators or dense targets for extragalactic CRs.

The H.E.S.S. and CANGAROO-III [36] telescopes have found several high-energy gamma-ray sources in IceCube’s FOV. Most of these sources are identified as or correlated with PWNe. Their energy spectrum has been measured up to a couple of tens of TeV. At this energy, statistics become low, and for most sources, no cutoff has been established. If these spectra extend to PeV energies without a break, IceCube will be able to detect them. It is also possible that an additional spectral component in the PeV energy range is present if a nearby dense molecular cloud acts as a target for the PWN beam [37]. IceCube will be able to study these systems and place constraints on their behavior at very high energies or possibly detect PeV gamma rays for the first time.

ACKNOWLEDGMENTS

We acknowledge the support from the following agencies: U.S. National Science Foundation-Office of Polar Programs, U.S. National Science Foundation-Physics Division, University of Wisconsin Alumni Research Foundation, the Grid Laboratory Of Wisconsin (GLOW) grid infrastructure at the University of Wisconsin-Madison, the Open Science Grid (OSG) grid infrastructure; U.S. Department of Energy, and National Energy Research Scientific Computing Center, the Louisiana Optical Network Initiative (LONI) grid computing resources;

National Science and Engineering Research Council of Canada; Swedish Research Council, Swedish Polar Research Secretariat, Swedish National Infrastructure for Computing (SNIC), and Knut and Alice Wallenberg Foundation, Sweden; German Ministry for Education and Research (BMBF), Deutsche Forschungsgemeinschaft (DFG), Research Department of Plasmas with Complex Interactions (Bochum), Germany; Fund for Scientific

Research (FNRS-FWO), FWO Odysseus programme, Flanders Institute to encourage scientific and technological research in industry (IWT), Belgian Federal Science Policy Office (Belspo); University of Oxford, United Kingdom; Marsden Fund, New Zealand; Australian Research Council; Japan Society for Promotion of Science (JSPS); and the Swiss National Science Foundation (SNSF), Switzerland.

-
- [1] F. Aharonian, J. Buckley, T. Kifune, and G. Sinnis, *Rep. Prog. Phys.* **71**, 096901 (2008).
- [2] A. A. Abdo *et al.* (Milagro Collaboration), *Astrophys. J.* **700**, L127 (2009).
- [3] A. A. Abdo *et al.* (Milagro Collaboration), *Astrophys. J.* **688**, 1078 (2008).
- [4] A. Achterberg *et al.* (IceCube Collaboration), *Phys. Rev. Lett.* **97**, 221101 (2006).
- [5] R. J. Gould and G. Schröder, *Phys. Rev. Lett.* **16**, 252 (1966).
- [6] M. C. Chantell *et al.* (CASA-MIA Collaboration), *Phys. Rev. Lett.* **79**, 1805 (1997).
- [7] A. Borione, M. A. Catanese, M. C. Chantell, C. E. Covault, J. W. Cronin, B. E. Fick, L. F. Fortson, J. Fowler *et al.*, *Astrophys. J.* **493**, 175 (1998).
- [8] F. A. Aharonian, *Astrophys. Space Sci.* **180**, 305 (1991).
- [9] R. Abbasi *et al.* (IceCube Collaboration), *Nucl. Instrum. Methods Phys. Res., Sect. A* **618**, 139 (2010).
- [10] R. Abbasi *et al.* (IceCube Collaboration), *Nucl. Instrum. Methods Phys. Res., Sect. A* **601**, 294 (2009).
- [11] A. Achterberg *et al.* (IceCube Collaboration), *Astropart. Phys.* **26**, 155 (2006).
- [12] F. Halzen and S. R. Klein, *Rev. Sci. Instrum.* **81**, 081101 (2010).
- [13] R. Abbasi *et al.* (IceCube Collaboration), *Nucl. Instrum. Methods Phys. Res., Sect. A* **700**, 188 (2013).
- [14] P. M. Kalberla, W. B. Burton, D. Hartmann, E. M. Arnal, E. Bajaja, R. Morras, and W. G. L. Pöppel, *Astron. Astrophys.* **440**, 775 (2005).
- [15] R. Abbasi *et al.* (IceCube Collaboration), *Astrophys. J.* **740**, 16 (2011).
- [16] R. Abbasi *et al.* (IceCube Collaboration), *Astrophys. J.* **746**, 33 (2012).
- [17] R. Abbasi *et al.* (IceCube Collaboration), [arXiv:1202.3039](https://arxiv.org/abs/1202.3039).
- [18] S. Tilav *et al.* (IceCube Collaboration), in *Proceedings of the 31st ICRC, Lodz, 2009*, <http://icrc2009.uni.lodz.pl/proc/pdf/icrc1398.pdf>.
- [19] T. Pierog and K. Werner, *Phys. Rev. Lett.* **101**, 171101 (2008).
- [20] G. Feldman and D. Cousins, *Phys. Rev. D* **57**, 3873 (1998).
- [21] J. Braun, J. Dumm, F. De Palma, C. Finley, A. Karle, and T. Montaruli, *Astropart. Phys.* **29**, 299 (2008).
- [22] R. Abbasi *et al.* (IceCube Collaboration), *Astrophys. J.* **732**, 18 (2011).
- [23] E. Couderc and S. Klein, *Phys. Rev. Lett.* **103**, 062504 (2009); L. Gerhardt and S. Klein, *Phys. Rev. D* **82**, 074017 (2010).
- [24] T. Stanev, C. Vankov, and F. Halzen, *Phys. Lett.* **158B**, 75 (1985).
- [25] G. Schatz *et al.*, in *Proceedings of 28th International Cosmic Ray Conference, Trukuba, Japan, 2003*, Vol. 4, p. 2293.
- [26] G. Rowell *et al.* (HESS Collaboration), *J. Phys. Conf. Ser.* **47**, 21 (2006).
- [27] A. Abramowski *et al.* (HESS Collaboration), *Astron. Astrophys.* **533**, A103 (2011).
- [28] F. Aharonian *et al.* (HESS Collaboration), *Astron. Astrophys.* **439**, 1013 (2005).
- [29] F. Aharonian *et al.* (HESS Collaboration), *Astrophys. J.* **692**, 1500 (2009).
- [30] F. Acero *et al.* (HESS Collaboration), *Astron. Astrophys.* **525**, A45 (2011).
- [31] F. Aharonian *et al.* (HESS Collaboration), *Astron. Astrophys.* **456**, 245 (2006).
- [32] F. Aharonian *et al.* (HESS Collaboration), *Astron. Astrophys.* **477**, 353 (2008).
- [33] F. Aharonian *et al.* (HESS Collaboration), *Astron. Astrophys.* **435**, L17 (2005).
- [34] M. Renaud *et al.* (HESS Collaboration), *AIP Conf. Proc.* **1085**, 281 (2008).
- [35] A. Abramowski *et al.* (HESS Collaboration), *Astron. Astrophys.* **525**, A46 (2011).
- [36] T. Mizukami *et al.*, *Astrophys. J.* **740**, 78 (2011).
- [37] H. Bartko and W. Bednarek, *Mon. Not. R. Astron. Soc.* **385**, 1105 (2008).

Method for high precision reconstruction of air shower X_{\max} using two-dimensional radio intensity profiles

S. Buitink,¹ A. Corstanje,¹ J. E. Enriquez,¹ H. Falcke,^{1,2,3,4} J. R. Hörandel,^{1,3} T. Huege,⁵ A. Nelles,¹ J. P. Rachen,¹ P. Schellart,¹ O. Scholten,⁶ S. ter Veen,¹ S. Thoudam,¹ and T. N. G. Trinh⁶

¹*Department of Astrophysics/IMAPP, Radboud University Nijmegen, 6500 GL Nijmegen, Netherlands*

²*Netherlands Institute for Radio Astronomy (ASTRON), Postbus 2, 7990 AA Dwingeloo, Netherlands*

³*Nikhef, Science Park Amsterdam, 1098 XG Amsterdam, Netherlands*

⁴*Max-Planck-Institut für Radioastronomie, Auf dem Hügel 69, 53121 Bonn, Germany*

⁵*IKP, Karlsruhe Institute of Technology (KIT), Postfach 3640, 76021 Karlsruhe, Germany*

⁶*KVI CART, University of Groningen, 9747 AA Groningen, Netherlands*

(Received 28 August 2014; published 17 October 2014)

The mass composition of cosmic rays contains important clues about their origin. Accurate measurements are needed to resolve longstanding issues such as the transition from Galactic to extra-Galactic origin and the nature of the cutoff observed at the highest energies. Composition can be studied by measuring the atmospheric depth of the shower maximum X_{\max} of air showers generated by high-energy cosmic rays hitting the Earth's atmosphere. We present a new method to reconstruct X_{\max} based on radio measurements. The radio emission mechanism of air showers is a complex process that creates an asymmetric intensity pattern on the ground. The shape of this pattern strongly depends on the longitudinal development of the shower. We reconstruct X_{\max} by fitting two-dimensional intensity profiles, simulated with CoREAS, to data from the Low Frequency Array (LOFAR) radio telescope. In the dense LOFAR core, air showers are detected by hundreds of antennas simultaneously. The simulations fit the data very well, indicating that the radiation mechanism is now well understood. The typical uncertainty on the reconstruction of X_{\max} for LOFAR showers is 17 g/cm^2 .

DOI: [10.1103/PhysRevD.90.082003](https://doi.org/10.1103/PhysRevD.90.082003)

PACS numbers: 95.55.Jz, 95.55.Vj, 95.85.Ry, 95.85.Bh

I. INTRODUCTION

High-energy cosmic rays are routinely measured by experiments around the world, yet there are still many urgent questions about their origin. Cosmic rays below 10^{16} eV are expected to be of Galactic origin, while the highest-energy cosmic rays are likely to come from extra-Galactic sources. However, it is not known how and at what energy this transition takes place. Another important question is whether the cutoff at the end of the spectrum [1,2] is due to interactions of cosmic-ray protons with the cosmic microwave background [3,4] or marks the highest energy that cosmic accelerators can reach. Accurate measurements of the cosmic-ray mass composition can resolve these questions [5]. In addition, a clean separation between protons and heavy nuclei above $6 \times 10^{19} \text{ eV}$ will greatly improve the search for a correlation between cosmic-ray arrival directions and their sources [6]. The fluorescence detection technique yields an excellent precision of $\sim 20 \text{ g/cm}^2$ [7,8], but its low duty cycle limits the detection rate at the highest energies.

Several techniques exist to measure mass-sensitive shower parameters. Particle detector arrays like KASCADE-Grande [9] and IceTop [10] measure the electron-to-muon ratio of the secondary shower particles at ground level. This ratio depends on the mass of the primary particle but also on the age of the shower, which makes the technique susceptible to shower-to-shower fluctuations.

The mass composition can also be inferred from the distribution of X_{\max} , the atmospheric depth of the shower maximum. At the Pierre Auger observatory, the longitudinal shower profile is measured by observing the fluorescence light that is emitted by air molecules that were excited by shower particles [7]. Alternatively, X_{\max} can be inferred by measuring the optical Cherenkov light emitted by the shower particles with arrays like Tunka [11]. Both techniques require dark nights and are therefore severely limited in duty cycle (below 15%). The fluorescence technique yields the best precision on X_{\max} of $\sim 20 \text{ g/cm}^2$.

Here, we propose a new technique that has the same precision but has a duty cycle of almost 100%, based on the radio emission produced by air showers. Like fluorescence light, the radio signal carries information of the complete longitudinal development of the shower [12]. It is therefore possible to reconstruct X_{\max} from the radio signal [13]. The method presented here requires measurements with many radio antennas simultaneously, in order to adequately sample the radiation profile. We apply this technique to data from the Low Frequency Array (LOFAR) radio telescope [14–16].

Our reconstruction technique requires precise simulations of the radio emission. The theory of air-shower radio emission has developed rapidly in the last decade, and simulation codes based on different approaches are now converging toward similar results [17]. In this work, we use

the CoREAS simulation package [18], which is a plugin for CORSIKA [19] that computes the radio pulse by adding the contribution of all individual electrons and positrons in the shower. We demonstrate that simulations are in excellent agreement with the LOFAR measurements, which sample the radio emission with hundreds of antennas per individual shower.

Section II gives a brief introduction to the LOFAR radio telescope array. In Sec. III, we describe the simulation tools and settings. The new reconstruction technique is explained in Secs. IV and V contains a review of systematic effects in the reconstruction. Conclusions are given in the final section.

II. LOFAR

LOFAR is a new-generation radio telescope constructed in the north of the Netherlands with satellite stations across Europe. It consists of thousands of dipole antennas, sensitive in the frequency range of 10–240 MHz. LOFAR has a flexible design that allows many different observation modes, some of which can run simultaneously. The raw electromagnetic waveform as it is measured by the dipoles is stored for 5 sec on ring buffers for each active antenna.

LOFAR is organized in stations, each containing 96 low-band antennas (LBAs; 10–90 MHz) and 48 high-band antennas (HBAs; 110–240 MHz). In the center of LOFAR, six of these stations are placed close together on a small artificial island, called the *superterp* (see Fig. 1). Other stations are placed around this island at increasing distances. A total of 24 stations form the LOFAR core, which has a diameter of ~ 2 km. For cosmic-ray detection, we focus on this dense core region.

The core is augmented with the LOFAR Radboud Air Shower Array (LORA) [20], which comprises 20 particle detectors. They cover the superterp area and are an essential part of the cosmic-ray measurement capability. LORA detects air showers above 10^{16} eV and provides a trigger for the radio antennas. It reconstructs the arrival direction, core position and gives a first energy estimate of the shower. Radio pulses can unambiguously be associated to air showers when their arrival time and direction coincides with the LORA reconstruction. Triggering on the radio pulse itself is technically possible, but an online filter is needed to distinguish cosmic-ray pulses from anthropogenic background noise. This is a subject of future study.

When a LORA trigger is received, a 2 ms trace is read out from the ring buffers of all active antennas and stored for offline processing [15]. A radio signal is typically found in hundreds of antennas. Depending on the mode of the current astronomical observations, either LBA or HBA data are available. Since HBA data are more challenging to analyze [21], we only consider LBA data in this study.

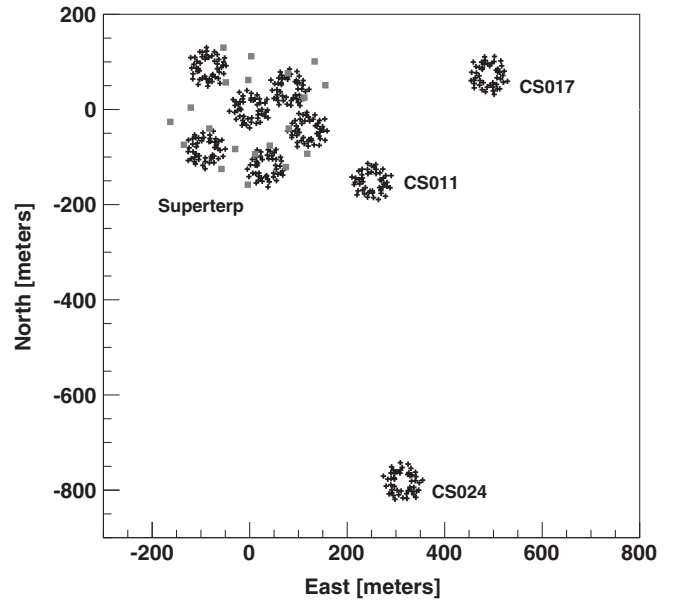


FIG. 1. Part of the LOFAR core. The “+” signs indicate the positions of antennas that are arranged in stations. Only the LBA antennas in the outer rings of each station are plotted. The inner parts of the LBA stations and the HBA stations, which are not used in this study, are not included in the plot. The central six stations form the superterp. Other core stations lie at increasingly larger distances from this cluster, three of which are visible in the map. The grey squares indicate the positions of LORA detectors.

III. RADIO EMISSION SIMULATIONS

A. Emission mechanism

The dominant component of the radio emission of air showers is driven by the geomagnetic field [16,22]. The electrons and positrons are deflected in opposite directions by the Lorentz force, and their drift creates a current perpendicular to the shower axis. As the shower develops, this current first grows and then decays, producing radio emission. The radiation is linearly polarized in the $\mathbf{v} \times \mathbf{B}$ direction, where \mathbf{v} is the velocity of the shower front and \mathbf{B} is the Earth’s magnetic field.

As the shower propagates through the atmosphere, it also develops an excess of negative charge, due to knockout electrons from atmospheric molecules joining the shower and the annihilation of positrons. The growth and subsequent decay of the charge excess give rise to a secondary emission component [23]. Charge excess radiation is also linearly polarized, but in a different direction, pointing radially outward from the shower axis. The relative contribution of charge excess to the total emission depends on the geometry (angle to the geomagnetic field, zenith angle, observer position, etc.) and has typical values of 5%–20% of the total pulse amplitude [24–26].

Because geomagnetic and charge excess radiation are polarized in different directions, the total emission is found by adding these contributions vectorially. The radiation

profile can be easiest understood when it is plotted in the shower plane, with axes in the direction of $\mathbf{v} \times \mathbf{B}$ and $\mathbf{v} \times (\mathbf{v} \times \mathbf{B})$ (see Fig. 3). In this frame, there is total constructive interference between the two components along the $\mathbf{v} \times \mathbf{B}$ axis in the positive direction, while the interference is most destructive in the negative direction along the same axis. Along the $\mathbf{v} \times (\mathbf{v} \times \mathbf{B})$ axis, the two components are polarized orthogonally and add in quadrature.

The resulting interference pattern is not rotationally symmetric and is typically bean shaped. Evidently, the lateral distribution of the radio pulse power is not a one-dimensional function of the distance to the shower axis. The radio profile can only be accurately described in two dimensions.

The bulk of the shower particles is confined to the shower front, a thin disk that travels toward the Earth at relativistic speed. For wavelengths exceeding the disk thickness (several meters), the radiation will be coherent (up to ~ 100 MHz). However, the propagation of the radio emission in a dielectric medium (air has an index of refraction of $n \approx 1.0003$ at sea level) produces Cherenkov-like effects, which must be included to properly describe the radiation [27]. At the Cherenkov angle, the radio pulse is compressed, and the emission is coherent up to GHz frequencies.

B. Experimental status

Radio pulses from air showers were already detected in the 1960s [28], but progress halted due to hardware limitations and a lack of proper understanding of the radiation mechanism. It was also feared that atmospheric electric fields would have a significant and unpredictable effect on the pulse strength.

In the last decade, the interest in radio detection was revived and pursued with modern electronics [29]. LOPES demonstrated that the emission mechanism is coherent and dominantly geomagnetic in nature [30] and that only the strong electric fields inside thunderstorms can significantly affect the radiation [31].

Proof for a contribution of charge excess was found by CODALEMA [32] and later by polarization studies of AERA [25] and LOFAR [26]. CROME [33] and ANITA [34] detected GHz emission at the Cherenkov angle, which can be interpreted as relativistic compression of the air-shower radio emission. Full Cherenkov rings were found by LOFAR in the 110–190 MHz range [21].

It has been shown by LOPES that the lateral distribution of the radio signal can be used to determine X_{\max} [13]. Their approach was based on a one-dimensional approximation of the radio profile, which yields a reconstruction resolution of 50 g/cm² for simulations and 95 g/cm² for LOPES data. Here, we show that a much better resolution can be achieved by using a two-dimensional profile and that modern radio simulation codes like CoREAS can accurately predict the complete radiation profile as measured by LOFAR with hundreds of antennas per individual

event, providing further proof that the emission mechanism is now understood to very high detail.

C. CoREAS and CORSIKA

In this work, we use the radio simulation code CoREAS [18], which is a plugin for the particle simulation code CORSIKA [19]. CoREAS is based on a microscopic description of the radiation mechanism; i.e., it computes the contributions of each electron and positron in the shower based on the “end-point” formalism [35]. In this formalism, the radiation produced by the acceleration of a particle at the start and end point of a particle track is calculated from first principles. By summing the contributions of all particle tracks, the total emission can be calculated without making any assumptions on the type of radiation. In other words, while the radiation is best understood when explained in terms of geomagnetic and charge excess contributions, CoREAS does not simulate these components separately. Instead, it produces the complete radiation field that is generated by the distribution of charged particles simulated by CORSIKA.

We use CORSIKA 7.400, with hadronic interaction models FLUKA 2011.2b [36] and QGSJETII.04 [37]. A comparison to other interaction models is made in Sec. VB. Thinning is applied at a level of 10^{-6} with optimized weight limitation [38].

A GEANT4 [39] simulation of the LORA detectors [20] is used to convert the CORSIKA particle output into the deposited energy as a function of distance to the shower axis. The particle lateral distribution function and radio profile will be fitted to the data simultaneously.

D. Two-dimensional profiles

As explained above, the radiation profile is not rotationally symmetric and can only be accurately described by a two-dimensional intensity map. The CoREAS code computes the radio pulse for specific observer positions on the ground. A LOFAR antenna model is applied to these pulses to simulate measured waveforms. This includes applying a frequency filter (10–90 MHz) and downsampling of the signal to 200 Msamples/s. In this analysis, we use the pulse power integrated over a 55 ns time window centered at the pulse peak.

To derive a two-dimensional map, we run simulations for 160 ground positions and reconstruct the full profile by interpolation. For robust interpolation, it is necessary to choose these positions such that they cover the locations where the interference between the two radiation components reaches its minimum and maximum. This is achieved by defining a star-shaped pattern in the shower plane with eight arms, two of which are aligned with the $\mathbf{v} \times \mathbf{B}$ axis, and projecting it onto the ground. Each arm contains 20 antennas, with a spacing of 25 m in the shower plane.

In Fig. 2, the interpolation technique is demonstrated. The simulated antenna positions are marked by large

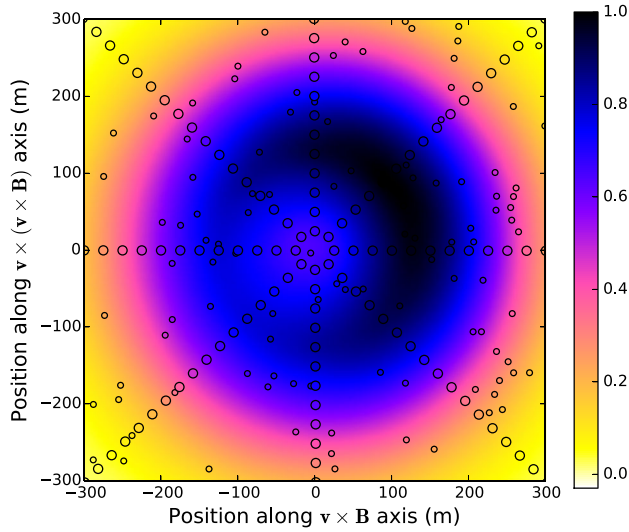


FIG. 2 (color online). Two-dimensional profile of the received power integrated over a 55 ns window. The large circles indicate the positions for which CoREAS simulations have been generated, while the full map in the background is created by interpolation. The smaller circles indicate test positions for which simulated values are compared to interpolated values.

circles, arranged in a regular pattern. Their color reflects the total power of the pulse as received by the antenna. The interpolated radio map is indicated by the background colors. By design, the interpolated map exactly matches the values at the simulated positions. To probe the error introduced by the interpolation, we run the same simulation for two hundred additional random positions, indicated by the smaller circles. The difference between the simulated

and interpolated total power is always smaller than 2.5% of the maximum power. This error is smaller than typical uncertainties in measured power for observations with LOFAR.

Figure 3 shows the radio profiles for two showers that have been simulated with CoREAS. Both showers have a zenith angle of 49° , an azimuth angle of 171° (i.e., coming from the northwest), and an energy of 2.3×10^8 GeV. The left panel displays the radiation profile of a proton shower that has penetrated deeply into the atmosphere, while the right panel shows the profile of a much shallower iron shower. In Fig. 4, the one-dimensional lateral distribution of the power is plotted for observers along the $\mathbf{v} \times \mathbf{B}$ and $\mathbf{v} \times (\mathbf{v} \times \mathbf{B})$ axes.

Obviously, the profiles are very different. A general feature is that the power falls off more rapidly with distance for deeper showers, which is clearly seen in Fig. 4. The X_{\max} reconstruction method used for LOPES is based on this feature [13,40].

However, there are also more subtle differences, like the amount of asymmetry and the position where the radiation reaches its maximum value. The method described in this paper makes use of all features of the radiation pattern by fitting the complete two-dimensional profile instead of a one-dimensional approximation.

The asymmetry along the $\mathbf{v} \times \mathbf{B}$ axis can be understood as the effect of the charge excess component. It is interesting to note that there also exists some asymmetry along the $\mathbf{v} \times (\mathbf{v} \times \mathbf{B})$ axis. This is not expected from radiation physics reviewed in Sec. III A. Indeed, when we plot the total “physical” pulse power as predicted by CoREAS, there is no asymmetry along the $\mathbf{v} \times (\mathbf{v} \times \mathbf{B})$ axis. It only appears once

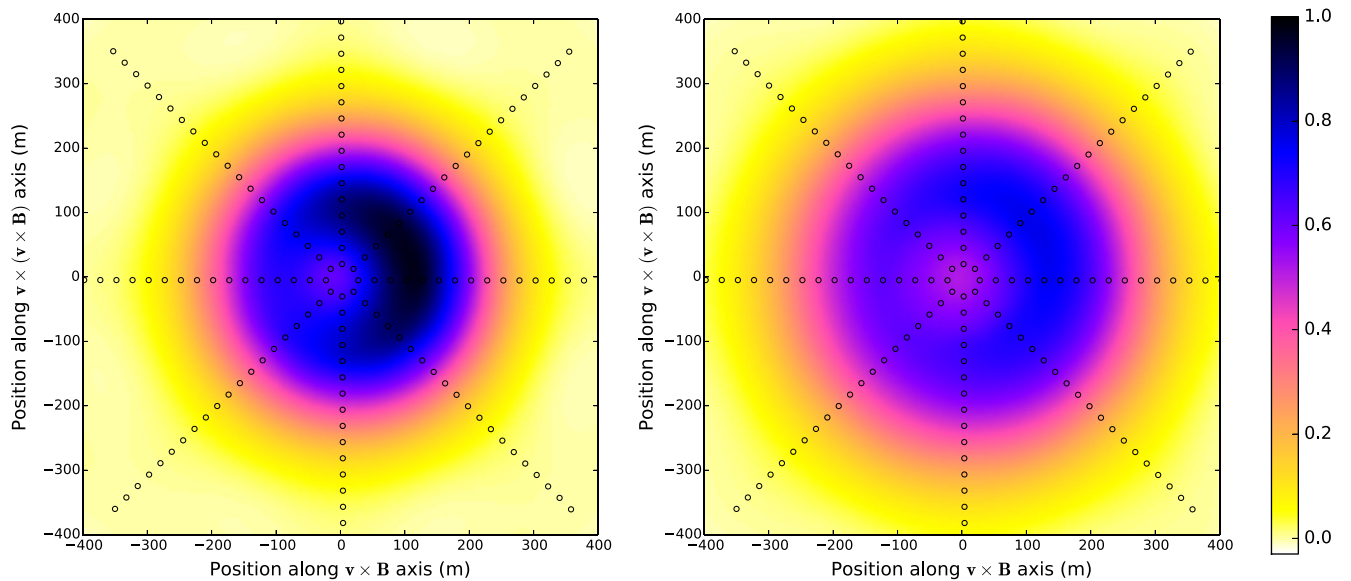


FIG. 3 (color online). Radiation profiles of a proton shower with $X_{\max} = 794 \text{ g/cm}^2$ (left panel) and an iron shower with $X_{\max} = 573 \text{ g/cm}^2$ (right panel). Both showers have an energy of 2.3×10^8 GeV and a zenith angle of 49° . The circles indicate the positions that have been simulated. The full background map is created by interpolation.

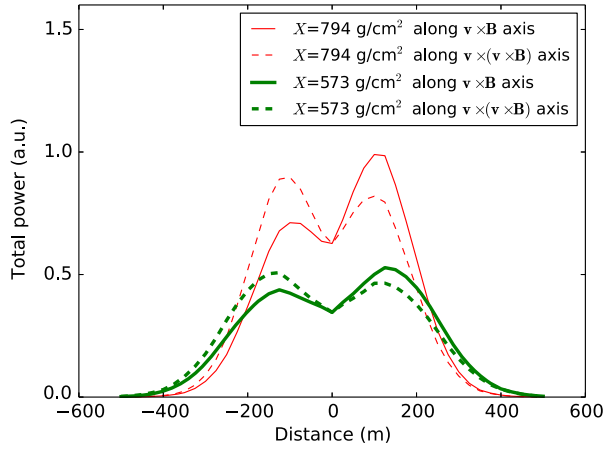


FIG. 4 (color online). The pulse power as a function of position along the axes for the proton (red, thin) and iron (green, thick) showers shown in Fig. 3.

the antenna response model is applied to the simulated pulses to calculate the total received power. The reason for this is that for observers at different locations the radiation has a different polarization. Since the antenna gain depends on the polarization, the power received by the antenna can be different even when the original pulse power is the same. In other words, different antennas pick up a different fraction of the total pulse power.

From Figs. 3 and 4, it is clear that the shape of the radiation profile strongly depends on the atmospheric depth of the shower maximum X_{\max} . However, it is reasonable to assume that other variations in the longitudinal and lateral distribution of the shower also have an influence on the radiation pattern. Below, we will demonstrate that the patterns are much more sensitive to X_{\max} than any other features of the shower development that vary from shower to shower. They do, however, limit the accuracy of the determination of X_{\max} .

E. Simulation set for LOFAR

We have developed a reconstruction technique in which simulated two-dimensional radio profiles are fitted to data. We run dedicated simulations for each shower detected by LOFAR. The shower arrival direction is reconstructed based on the arrival time of the radio pulses at all antennas [15]. An energy estimate is provided by a LORA shower reconstruction [20]. Since the shower core is often located outside the LORA array, this estimate is not accurate, and a better energy reconstruction is done at a later stage in the analysis. The core position itself is not needed as input for the simulation, since we use the star-shaped pattern of observer positions described above, instead of actual antenna positions.

For each shower in the set, we run 25 proton showers and 15 iron showers. With this amount of showers, we obtain a large range of X_{\max} values that reflects the natural spread.

IV. HYBRID RECONSTRUCTION TECHNIQUE

A. Fit procedure

For each simulation, we fit the two-dimensional radiation map and the one-dimensional particle lateral distribution function to the data simultaneously, by minimizing

$$\chi^2 = \sum_{\text{antennas}} \left(\frac{P_{\text{ant}} - f_r^2 P_{\text{sim}}(x_{\text{ant}} - x_0, y_{\text{ant}} - y_0)}{\sigma_{\text{ant}}} \right)^2 + \sum_{\text{particle detectors}} \left(\frac{d_{\text{det}} - f_p d_{\text{sim}}(x_{\text{det}} - x_0, y_{\text{det}} - y_0)}{\sigma_{\text{det}}} \right)^2, \quad (1)$$

where P_{ant} is the measured power integrated over a 55 ns window at an antenna at location $(x_{\text{ant}}, y_{\text{ant}})$ with noise level σ_{ant} , P_{sim} is the simulated power, d_{det} is the deposited energy as measured by a LORA detector at location $(x_{\text{det}}, y_{\text{det}})$ with noise σ_{det} , and d_{sim} is the simulated deposited energy. The fit contains four free parameters, two of which describe the location of the shower axis (x_0, y_0) . A scaling parameter f_p for the particle lateral distribution function is needed to correct the energy scale, while a scaling parameter for the radio power f_r^2 is needed because the antennas do not yet have an absolute calibration. The radio power is approximately proportional to the square of the cosmic-ray primary energy [41], so both f_r and f_p scale linearly with energy.

B. Application to LOFAR data

Figure 5 contains the fit results for three different showers. The left panels display the radiation pattern in the shower plane. The background colors indicate the simulated radio map, while the circles indicate the measurements of the LOFAR antennas. The color of the circle represents the received power at the antenna, so the fit is of high quality when the colors of the circles blend into the background. Note that the antennas are grouped in rings: the LOFAR stations. All these showers have been detected by all six superterp stations. In addition, emission from the shower in the top row was also found in three other core stations (CS024, CS011, and CS017 in Fig. 1), and the shower in the middle row was detected by one additional station outside the superterp (CS011). For very inclined events, the antenna rings appear flattened in the event display because of the projection onto the shower plane. As explained above, for each detected shower, a total of 40 simulations is produced. The results shown here are for the simulation that yielded the fit with the lowest χ^2 .

The right-hand panels of Fig. 5 show the same result in one dimension. For each antenna, the measured and simulated power is plotted as a function of distance to the shower axis. From all three examples, it is clear that the radio power is not a single-valued function of distance. Some distribution functions contain oval structures (middle and bottom row) that are reminiscent of the

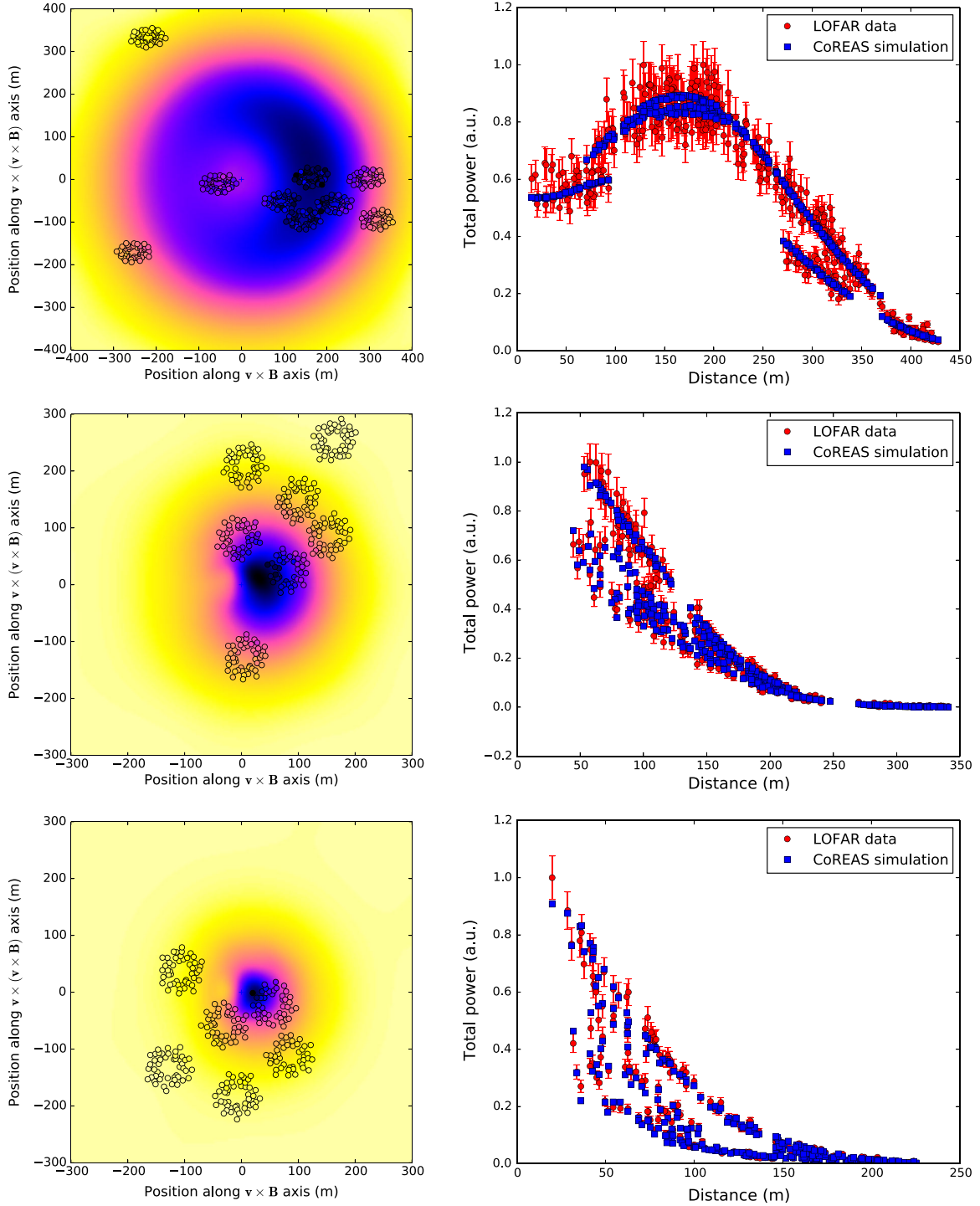


FIG. 5 (color online). Two-dimensional radio air-shower reconstructions. The measured power for three different showers (top, middle, and bottom) is fitted to a simulated radio map (left panels). The one-dimensional lateral distribution functions (right panels) are not single-valued functions of distance to the shower axis.

ring structure of the LOFAR stations. From the shower in the top row, it is clear that the position where the radio power reaches its maximum can be far from the shower axis (in this case ~ 150 m). As explained in Sec. III A, this is due to the interference between geomagnetic and

charge excess radiation, and Cherenkov-like propagation effects.

The fits displayed in Fig. 5 correspond to the simulation that yielded the lowest χ^2 . The reduced χ^2 values for all 40 simulations that are performed per detected shower are

plotted in Fig. 6 as a function of the slanted atmospheric depth of the shower maximum X_{\max} . While X_{\max} is not the only shower parameter that is different between simulations because of shower-to-shower fluctuations, it is clearly the parameter that most strongly determines the quality of the fit. However, smaller effects due to other variations in the shower development introduce a “jitter.” It is therefore not expected that the data points in Fig. 6 lie on a completely smooth curve.

The blue circles represent proton simulations, and the magenta squares stand for iron simulations. Proton showers on average penetrate deeper into the atmosphere than iron showers and have larger shower-to-shower fluctuations. Indeed, the proton showers cover a larger range of higher X_{\max} values than the iron showers. Interestingly, in the region of overlap, the data points of the different primaries follow the same curve, at least within the uncertainty of the above-mentioned jitter. We therefore conclude that showers with the same X_{\max} produce a very similar radiation pattern regardless of the mass of the cosmic-ray primary.

We fit a parabola to the data points within a 200 g/cm^2 range centered around the best-fitting simulation and regard its extremum as the reconstructed value for X_{\max} . The uncertainty on this reconstructed value is determined with a Monte Carlo study (see the next section) and is different for each shower. It is tempting to derive the uncertainty from the width of the fitted parabola. However, this is only possible if the data points really follow a smooth curve. The jitter on the χ^2 values introduced by shower-to-shower fluctuations affects the shape of the parabola and therefore renders it impossible to use the width of the parabola to find the uncertainty.

C. Uncertainty on X_{\max}

For each measured shower, the uncertainty on the reconstructed value for X_{\max} is found by applying the following procedure to the set of simulated showers. First, one simulation is singled out, and “fake” data are produced by evaluating the radio map at the position of each LOFAR antenna and adding Gaussian noise of the same level as found in the original data. For the position of each LORA particle detector, the total deposited energy as simulated with GEANT4 is determined, and again appropriate noise is added to the signal. Then, the remaining 39 simulated showers are fitted to the fake data set using the same fitting procedure as described in Sec. IV. This yields a value X_{reco} that can be compared to the actual X_{real} of the simulated shower. Finally, the procedure is repeated for all 40 simulated showers (each time taking care that the simulation that is used to produce the fake data set is excluded from the set of simulations that is used for reconstruction).

Figure 7 shows the distribution of the $|X_{\text{reco}} - X_{\text{real}}|$ for the 40 simulations corresponding to one particular shower. We define the 1σ uncertainty as the value of $|X_{\text{reco}} - X_{\text{real}}|$ that contains 68% of the histogram. The uncertainty that is

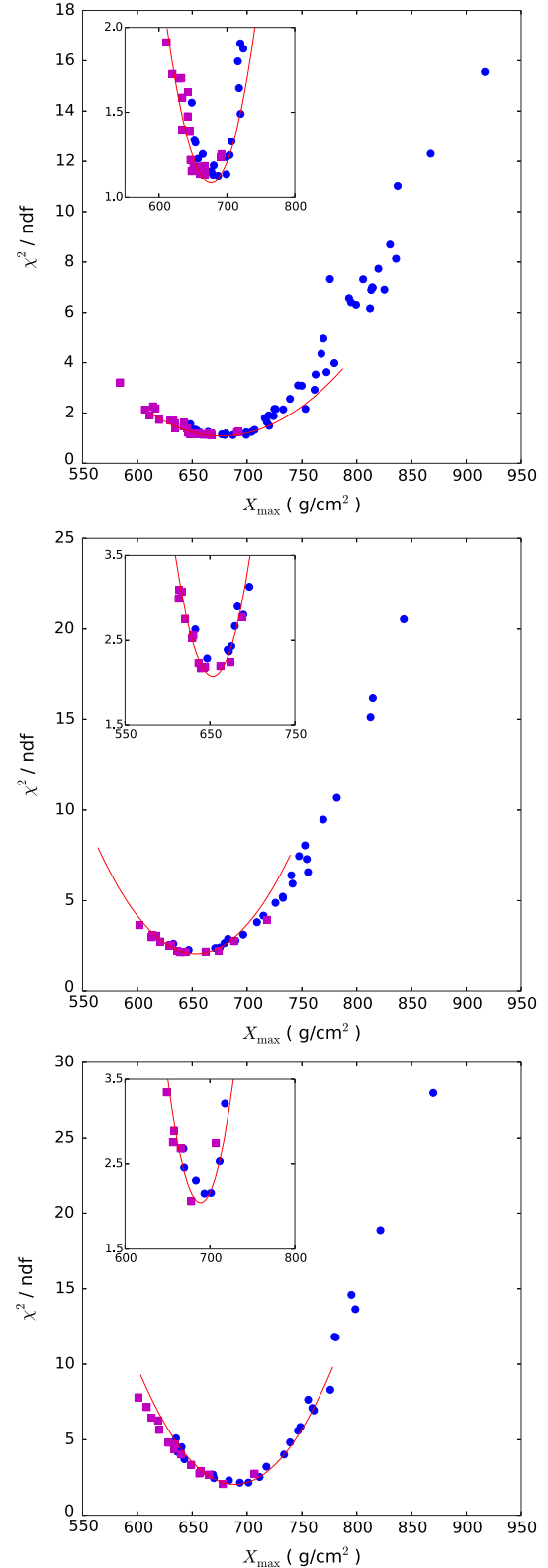


FIG. 6 (color online). Reduced χ^2 as a function of X_{\max} for the same three showers as Fig. 5. The proton simulations (blue circles) and iron simulations (magenta squares) lie on the same curve, at least within the scatter. A parabola (red line) is fitted to the data points near the minimum to reconstruct X_{\max} . The insets zoom in on this region.

found this way is the uncertainty due to the method σ_{meth} . There is an additional uncertainty due to the fact that the density profile of the atmosphere at the time of measurement is different from the atmospheric profile used in the CORSIKA simulation.

To correct for the atmosphere, we extract the local atmospheric density profile at the time of measurement from the Global Data Assimilation System (GDAS) [42]. We follow the approach that is used by the Pierre Auger Collaboration as described by Abreu *et al.* [43] This work also contains comparisons of atmospheric depth profiles predicted by GDAS and *in situ* measurements with weather balloons. The differences are typically smaller than 1 g/cm^2 , except for altitudes very close to the ground. Since global atmospheric models typically work better in the Northern hemisphere where more weather data are available, and the geography of the northern Netherlands is rather unremarkable, we assume that the uncertainty introduced by the atmospheric model is also not worse than 1 g/cm^2 at the LOFAR site.

Because the reconstruction of X_{max} based on the radio emission profile is essentially a geometrical technique, simulations that are produced with a standard atmosphere yield the correct geometrical altitude h . The corresponding atmospheric depth is now found by evaluating

$$X(h) = \frac{1}{\cos \theta} \int_h^\infty \rho_{\text{GDAS}}(h') dh', \quad (2)$$

where ρ_{GDAS} is the atmospheric density profile as predicted by GDAS and θ is the zenith angle of the shower. Corrections are typically of the order of $\sim 10 \text{ g/cm}^2$.

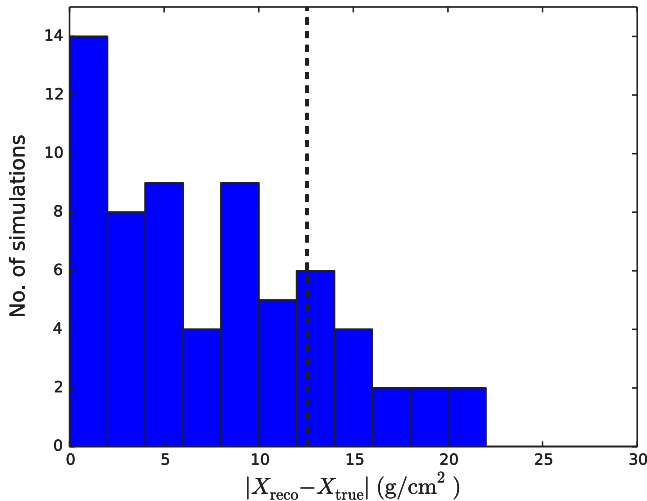


FIG. 7 (color online). The uncertainty on X_{max} for a particular shower is found by reconstructing many simulated showers and evaluating the histogram of the reconstruction error shown here. The black dotted line indicates the value that contains 68% of the histogram and is taken as the one sigma uncertainty on X_{max} .

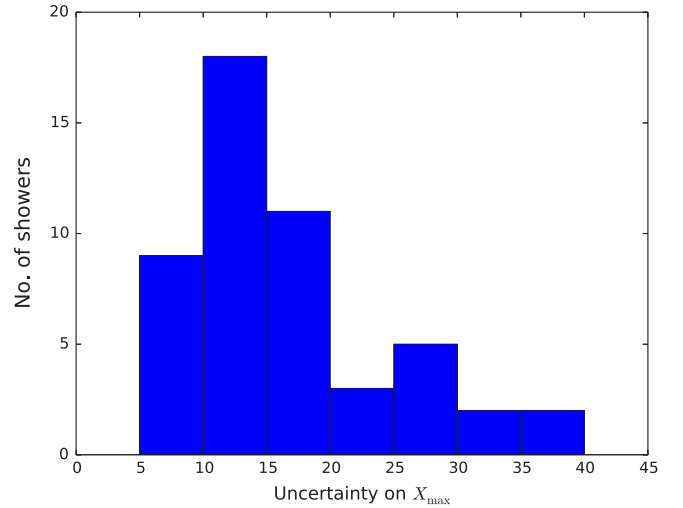


FIG. 8 (color online). Histogram of uncertainties on X_{max} for 50 sets of simulated LOFAR showers. The mean value is 17 g/cm^2 .

A third contribution to the uncertainty on X_{max} comes from the uncertainty in the direction reconstruction. In this analysis, we have used a plane wave approximation that has an angular resolution of $\sim 1^\circ$, which translates into an uncertainty of $\sim 2 \text{ g/cm}^2$ depending on zenith angle and shower depth. Using a more realistic reconstruction based on hyperbolic wavefront shapes, the accuracy increases to $\sim 0.1^\circ$ [44].

Simulation sets were generated for 50 showers (each set consisting of 25 proton and 15 iron showers). The uncertainties on X_{max} for these showers, as has been evaluated with the technique described above, are plotted in the histogram in Fig. 8. They range from 7.5 to 37.5 g/cm^2 , depending on the geometry of the event, with a mean value of 17 g/cm^2 .

V. SYSTEMATIC EFFECTS

In this section, we study the possible systematic effects that are introduced by the reconstruction method and the choice of models used for simulation.

A. Multivariate fit procedure

The shower simulations are fitted to the data using Eq. (1), which has four free parameters: two for the core location, one scaling factor for the radio power f_r^2 , and one scaling factor for the deposited energy in the particle detectors f_p . A multivariate fit can introduce systematic biases in one or more of the fit parameters. We study this using the same approach as described in Sec. IV C. Each simulated shower is used to construct a fake data set that is reconstructed using the 39 remaining simulations made for that particular shower. For each reconstruction, the fit parameters are compared to the actual values of the simulated event. This is done for a total of 50 showers.

The results are shown in Fig. 9. The top two panels show the offset of the reconstructed core position with respect to the real core position. The left panel is a two-dimensional histogram of the core offset in which it can be seen that the core offset has no preferred direction. Hence, there is no systematic effect on the core position due to the fit procedure. The absolute value of the core offset is histogrammed in the right-hand panel. The core position is reconstructed with an accuracy of within 5 m.

The bottom panels of Fig. 9 display the distribution of the logarithm of the scaling parameters f_p and f_r^2 . Since all 40 simulations of a specific shower have the same primary energy, both factors are unity when the reconstruction is perfect. Indeed, the histograms of both scaling factors are symmetric around unity. The maximum energy resolution that can be achieved with this method is given by the width of the distributions and is 15%–20%. The resolution of the radio energy scaling is slightly better than the particle energy scaling.

B. Choice of hadronic interaction model

The longitudinal development of air showers is sensitive to high-energy hadronic interactions. Hadronic cross sections, elasticities, and multiplicities cannot be calculated from first principles. Instead, phenomenological hadronic interaction models are used, which are fine-tuned to available accelerator data, but extrapolated to regimes in energy and phase space far beyond the reach of any Earth-based accelerator [45].

Differences in high-energy cross sections between models result in systematically different values for X_{\max} given a certain primary mass and energy. For example, the difference in the mean atmospheric depth of the shower maximum for proton primaries as predicted by QGSJETII-04 and EPOS-LHC is of the order of 20 g/cm² at 10¹⁸ eV [46]. Since the measurement of X_{\max} using the radio profile is a geometrical measurement (like fluorescence measurements), it can be argued that there is no systematic effect on the reconstructed

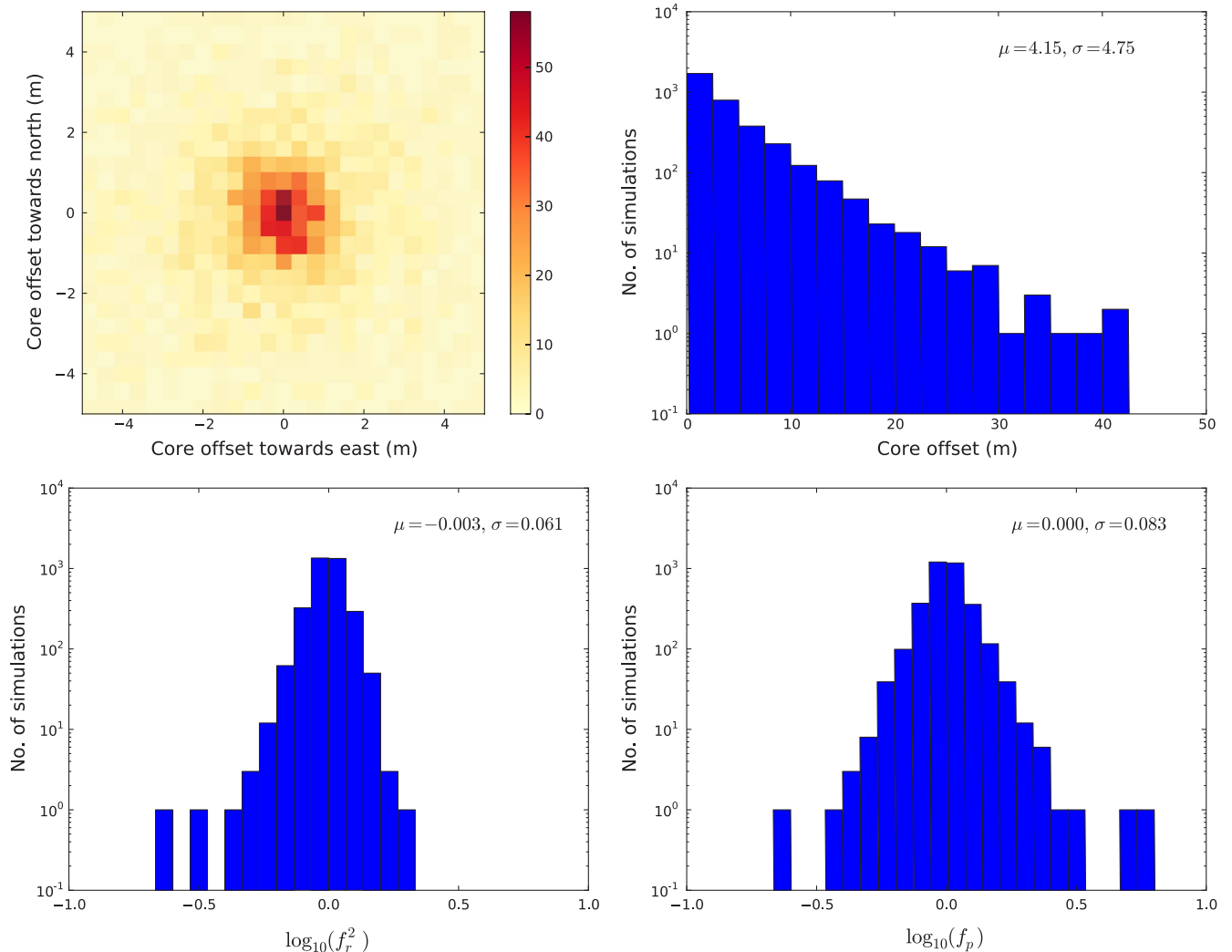


FIG. 9 (color online). Histograms of fitting parameters for 50 showers with 40 simulations each. Top row: distribution of core offset in one and two dimensions. Bottom row: distribution of the logarithm of the scaling parameters f_r^2 and f_p .

depth due to the choice of hadronic model and that this choice only becomes essential when interpreting the data, i.e., when deriving primary mass composition from X_{\max} measurements.

However, it is possible that the reconstructed value of X_{\max} systematically shifts when the shapes of the longitudinal development of actual showers are different from those of the simulated showers. To evaluate this effect, we have generated shower simulations based on EPOS-LHC and SIBYLL 2.1 for ten showers and reconstructed their X_{\max} values using QGSJETII-04 simulations.

The results are shown in Fig. 10. The largest systematic offset of 4.3 g/cm^2 is found for showers simulated with EPOS-LHC. Note, however, that current experimental constraints on hadronic interactions may very well allow parameter values that produce larger differences than those observed between these three particular models.

C. Choice of radio simulation code

There are currently four advanced codes that calculate the radio emission from air showers. CoREAS and ZHAireS [47] are both microscopic codes; i.e., they sum the contribution of individual electrons and positrons to obtain the total radio pulse. CoREAS is based on CORSIKA and the end-point formalism, while ZHAireS is based on Aires and the ZHS algorithm [48]. Still, both codes produce very similar results [17].

Selfas2 [49] and EVA [50] follow a more macroscopic approach, in which shower simulation codes are used to obtain histograms or parametrizations of the total charge distribution of the shower. The radiation is then calculated in a second step. A disadvantage of this approach is that the use of histograms or parametrizations may lead to the loss of information about the charge distribution. An advantage, however, is that such codes can provide a better qualitative understanding of the radiation mechanism. They can, for example, be used to calculate specific components of the total radiation (geomagnetic or charge excess), whereas the microscopic approach is oblivious to such distinctions as it calculates the radiation from first principles.

A detailed comparison of these four codes with LOFAR data is currently being made and will be the subject of a future publication. For now, we emphasize that for the example events shown here the CoREAS simulations reproduce all features observed in the data and are able to fit the data with excellent reduced χ^2 values and that CoREAS and ZHAireS produce very comparable results.

Finally, it should be understood that the correct simulation of the radio signal is mainly a numerical challenge, since the laws of electrodynamics are well known. This is in sharp contrast with the uncertainties introduced by the high-energy hadronic interactions, which can currently not be derived from first principles.

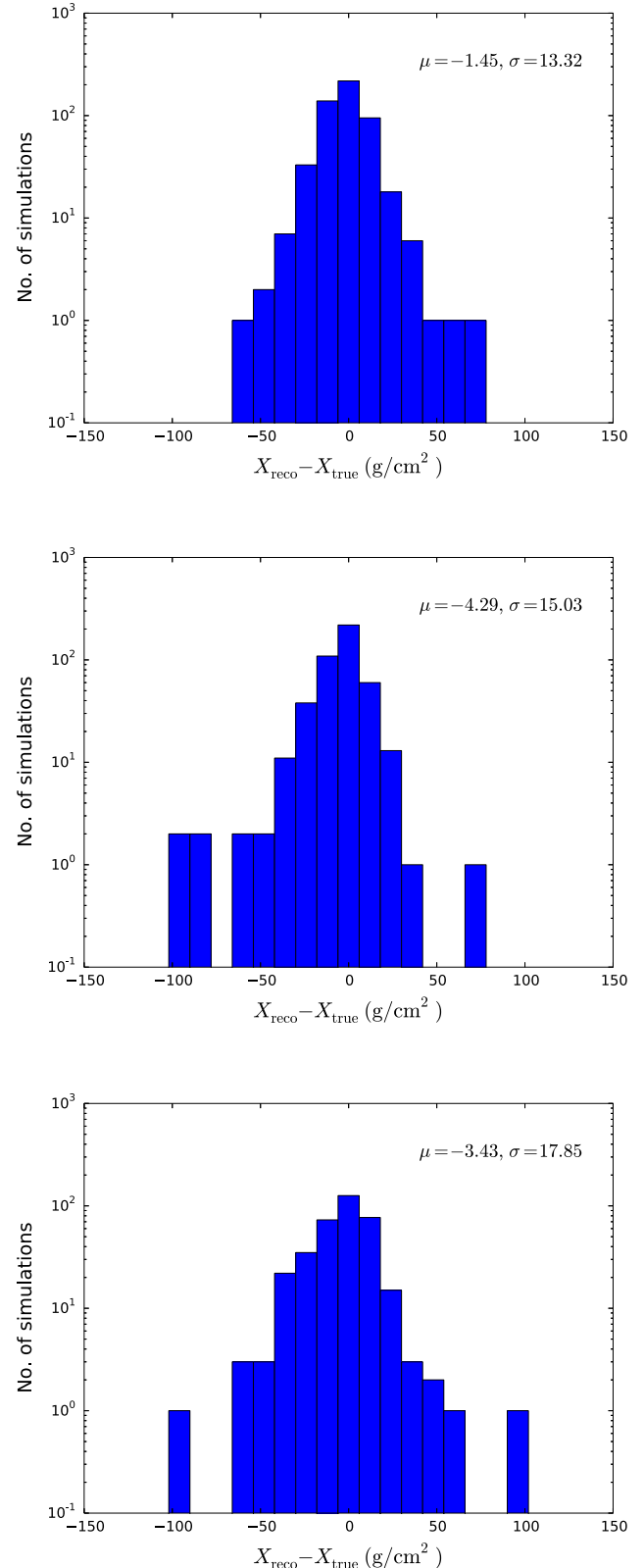


FIG. 10 (color online). Distribution of the error on the reconstructed value of X_{\max} for simulations based on different hadronic interaction models (top: QGSJETII.04, middle: EPOS-LHC, bottom: SIBYLL 2.1). In each case, the reconstruction was done with a sample of QGSJETII.04 showers.

VI. CONCLUSION

We have presented a new method to reconstruct the atmospheric depth of the shower maximum X_{\max} with radio measurements. It is based on the complete two-dimensional distribution of the emitted radio power that strongly depends on the longitudinal development of the shower. Application of the technique to LOFAR data yields very accurate reconstructions of typically 17 g/cm^2 . This makes LOFAR an excellent observatory to study the cosmic-ray composition in the energy regime around 10^{17} eV , which may harbor the transition from a Galactic to extra-Galactic origin. We are studying the possibility of performing air-shower radio detection with the Square Kilometer Array, allowing composition study up to 10^{18} eV , as well as measurements of the p-air cross section at energies beyond the LHC scale [51].

The HEAT extension of Auger [52] performs fluorescence measurements of X_{\max} in the 10^{17} – 10^{18} eV range. In this regime, radio measurements with LOFAR (and SKA) will provide a second observation method that is completely independent. Compared to fluorescence detection, radio measurements depend on more complicated signal simulation and analysis techniques but suffer from fewer systematic uncertainties due to signal propagation in the atmosphere (aerosols, etc.). The techniques are thus complementary, and a combination of them potentially leads to increased precision.

The radiation profiles that are produced with the CoREAS radio simulation code fit the data extremely well. All features in the complicated, asymmetric profiles are reproduced, and we find low reduced χ^2 values for showers that were observed with hundreds of antennas simultaneously. This inspires confidence that the radiation mechanism is now well understood and can be accurately simulated. The performance of other radio simulation codes is currently being studied and will be published separately.

We have followed a hybrid approach that combines the total radio power and particle measurements in a single fit. Because of the large number of antennas, the radio data give the dominant contribution to the fit of the shower core position. However, by including the particle detector data in

the fit, we have made sure that the shower reconstruction is fully consistent with all available data.

It is possible to extend the technique to incorporate information of the radio pulse that is currently not used. The polarization and spectrum of the pulse both depend on the antenna position relative to the shower axis, and pulse arrival times can be used to fit the shower front shape leading to a higher angular accuracy.

Producing large sets of radio simulations for each detected shower requires a large amount of computational resources. The process can be streamlined by making use of a two-dimensional parametrization of the radiation profile [53,54].

Radio detection of air showers provides a new way of accurately measuring X_{\max} . In contrast to fluorescence detection, it has a duty cycle of nearly 100% and may therefore be an interesting method for cosmic-ray composition studies at the highest energies. The main challenge lies in the size of the radio footprint, which is smaller than the particle footprint and requires a relatively dense antenna array. The technique itself, however, has matured and now produces accurate and robust results.

ACKNOWLEDGMENTS

We acknowledge financial support from the Netherlands Organization for Scientific Research (NWO), VENI Grant No. 639-041-130, the Netherlands Research School for Astronomy (NOVA), the Samenwerkingsverband Noord-Nederland (SNN), and the Foundation for Fundamental Research on Matter (FOM). We acknowledge funding from an Advanced Grant of the European Research Council under the European Unions Seventh Framework Program (Grant No. FP/2007-2013)/ERC Grant No. 227610. Part of this work was supported by Grant No. VH-NG-413 of the Helmholtz Association. LOFAR, the Low Frequency Array designed and constructed by ASTRON, has facilities in several countries that are owned by various parties (each with their own funding sources) and that are collectively operated by the International LOFAR Telescope (ILT) foundation under a joint scientific policy.

-
- [1] J. Abraham *et al.* (Pierre Auger Collaboration), *Phys. Rev. Lett.* **101**, 061101 (2008).
 - [2] R. U. Abbasi *et al.* (HiRes collaboration), *Phys. Rev. Lett.* **100**, 101101 (2008).
 - [3] K. Greisen, *Phys. Rev. Lett.* **16**, 748 (1966).
 - [4] G. Zatsepin and V. Kuzmin, *JETP Lett.* **4**, 78 (1966).
 - [5] K.-H. Kampert and M. Unger, *Astropart. Phys.* **35**, 660 (2012).
 - [6] J. Abraham *et al.* (Pierre Auger Collaboration), *Science* **318**, 938 (2007).
 - [7] J. Abraham *et al.* (Pierre Auger Collaboration), *Nucl. Instrum. Methods Phys. Res., Sect. A* **620**, 227 (2010).
 - [8] H. Tokuno *et al.* (Telescope Array Collaboration), *Nucl. Instrum. Methods Phys. Res., Sect. A* **676**, 54 (2012).
 - [9] W. Apel *et al.* (KASCADE-Grande Collaboration), *Phys. Rev. D* **87**, 081101 (2013).

- [10] M. G. Aartsen *et al.* (IceCube Collaboration), *Phys. Rev. D* **88**, 042004 (2013).
- [11] S. F. Bereznev *et al.* (Tunka Collaboration), in *Proceedings of the 32nd International Cosmic Ray Conference (ICRC2011), 2011, Beijing, China*, Vol. 1, p. 209, http://www.ihep.ac.cn/english/conference/icrc2011/paper/proc/v1/v1_0250.pdf.
- [12] W. Apel *et al.* (LOPES Collaboration), *Phys. Rev. D* **85**, 071101 (2012).
- [13] W. Apel *et al.* (LOPES Collaboration), *Phys. Rev. D* **90**, 062001 (2014).
- [14] M. P. van Haarlem *et al.* (LOFAR Collaboration), *Astron. Astrophys.* **556**, A2 (2013).
- [15] P. Schellart *et al.* (LOFAR Collaboration), *Astron. Astrophys.* **560**, A98 (2013).
- [16] H. Falcke and P. W. Gorham, *Astropart. Phys.* **19**, 477 (2003).
- [17] T. Huege, M. Ludwig, O. Scholten, and K. D. de Vries, *Nucl. Instrum. Methods Phys. Res., Sect. A* **662**, S179 (2012).
- [18] T. Huege, M. Ludwig, and C. W. James, *AIP Conf. Proc.* **1535**, 128 (2013).
- [19] D. Heck, J. Knapp, J. N. Capdevielle, G. Schatz, and T. Thouw, https://web.ikp.kit.edu/corsika/physics_description/corsika_phys.html.
- [20] S. Thoudam *et al.* (LOFAR Collaboration), [arXiv:1408.4469](https://arxiv.org/abs/1408.4469).
- [21] A. Nelles *et al.* (LOFAR Collaboration) (to be published).
- [22] F. D. Kahn and I. Lerche, *Proc. R. Soc. A* **289**, 206 (1966).
- [23] G. A. Askaryan, *J. Exp. Theor. Phys.* **14**, 441 (1962).
- [24] K. D. de Vries, O. Scholten, and K. Werner, *Astropart. Phys.* **45**, 23 (2013).
- [25] A. Aab *et al.* (Pierre Auger Collaboration), *Phys. Rev. D* **89**, 052002 (2014).
- [26] P. Schellart *et al.* (LOFAR Collaboration), *J. Cosmol. Astropart. Phys.* (to be published).
- [27] K. D. de Vries, O. Scholten, and K. Werner, *Astropart. Phys.* **45**, 23 (2013).
- [28] J. V. Jelley, J. H. Fruin, N. A. Porter, T. C. Weekes, F. G. Smith, and R. A. Porter, *Nature (London)* **205**, 327 (1965).
- [29] T. Huege, *Braz. J. Phys.* (to be published).
- [30] H. Falcke *et al.*, *Nature (London)* **435**, 313 (2005).
- [31] S. Buitink *et al.* (LOPES collaboration), *Astron. Astrophys.* **467**, 385 (2007).
- [32] V. Marin *et al.* (CODALEMA Collaboration), in *Proceedings of the 32nd International Cosmic Ray Conference (ICRC2011), 2011, Beijing, China*, Vol. 1, p. 291.
- [33] R. Šmída *et al.* (CROME Collaboration), *EPJ Web Conf.* **53**, 08010 (2013).
- [34] S. Hoover *et al.* (ANITA Collaboration), *Phys. Rev. Lett.* **105**, 151101 (2010).
- [35] C. James, H. Falcke, T. Huege, and M. Ludwig, *Phys. Rev. E* **84**, 056602 (2011).
- [36] G. Battistoni, F. Cerutti, A. Fassò, A. Ferrari, S. Muraro, J. Ranft, S. Roesler, and P. R. Sala, *AIP Conf. Proc.* **896**, 31 (2007).
- [37] S. Ostapchenko, *Nucl. Phys. B Proc. Suppl.* **151**, 147 (2006).
- [38] M. Kobał *et al.* (Pierre Auger Collaboration), *Astropart. Phys.* **15**, 259 (2001).
- [39] S. Agostinelli *et al.*, *Nucl. Instrum. Methods Phys. Res., Sect. A* **506**, 250 (2003).
- [40] T. Huege, R. Ulrich, and R. Engel, *Astropart. Phys.* **30**, 96 (2008).
- [41] T. Huege and H. Falcke, *Astropart. Phys.* **24**, 116 (2005).
- [42] NOAA Air Resources Laboratory (ARL), Global Data Assimilation System (GDAS1) Archive Information, Tech. Rep. (2004).
- [43] P. Abreu *et al.* (Pierre Auger Collaboration), *Astropart. Phys.* **35**, 591 (2012).
- [44] A. Corstanje *et al.*, *Astropart. Phys.* **61**, 22 (2015).
- [45] R. Ulrich, R. Engel, and M. Unger, *Phys. Rev. D* **83**, 054026 (2011).
- [46] T. Pierog, *J. Phys. Conf. Ser.* **409**, 012008 (2013).
- [47] J. Alvarez-Muñiz, W. R. Carvalho, and E. Zas, *Astropart. Phys.* **35**, 325 (2012).
- [48] E. Zas, F. Halzen, and T. Stanev, *Phys. Rev. D* **45**, 362 (1992).
- [49] V. Marin and R. Benoît, *Nucl. Instrum. Methods Phys. Res., Sect. A* **662**, S171 (2012).
- [50] O. Scholten, K. Werner, and F. Ruydy, *Astropart. Phys.* **29**, 94 (2008).
- [51] T. Huege *et al.*, [arXiv:1408.5288](https://arxiv.org/abs/1408.5288).
- [52] E. Varela *et al.* (Pierre Auger Collaboration), *J. Phys. Conf. Ser.* **468**, 012013 (2013).
- [53] A. Nelles, S. Buitink, H. Falcke, J. R. Hörandel, T. Huege, and P. Schellart, *Astropart. Phys.* **60**, 13 (2015).
- [54] J. Alvarez-Muñiz, W. Carvalho, H. Schoorlemmer, and E. Zas, *Astropart. Phys.* **59**, 29 (2014).



Probing Atmospheric Electric Fields in Thunderstorms through Radio Emission from Cosmic-Ray-Induced Air Showers

P. Schellart,^{1,*} T. N. G. Trinh,² S. Buitink,^{3,1} A. Corstanje,¹ J. E. Enriquez,¹ H. Falcke,^{1,4,5,6} J. R. Hörandel,^{1,4} A. Nelles,¹ J. P. Rachen,¹ L. Rossetto,¹ O. Scholten,^{2,7} S. ter Veen,^{1,5} S. Thoudam,¹ U. Ebert,^{8,9} C. Koehn,⁸ C. Rutjes,⁸ A. Alexov,¹⁰ J. M. Anderson,¹¹ I. M. Avruch,^{12,13} M. J. Bentum,^{5,14} G. Bernardi,¹⁵ P. Best,¹⁶ A. Bonafede,¹⁷ F. Breitling,¹⁸ J. W. Broderick,^{19,20} M. Brügger,¹⁷ H. R. Butcher,²¹ B. Ciardi,²² E. de Geus,^{5,23} M. de Vos,⁵ S. Duscha,⁵ J. Eislöffel,²⁴ R. A. Fallows,⁵ W. Frieswijk,⁵ M. A. Garrett,^{5,25} J. Grießmeier,^{26,27} A. W. Gunst,⁵ G. Heald,^{5,13} J. W. T. Hessels,^{5,28} M. Hoeft,²⁴ H. A. Holties,⁵ E. Juette,²⁹ V. I. Kondratiev,^{5,30} M. Kuniyoshi,³¹ G. Kuper,⁵ G. Mann,¹⁸ R. McFadden,⁵ D. McKay-Bukowski,^{32,33} J. P. McKean,^{5,13} M. Mevius,^{5,13} J. Moldon,⁵ M. J. Norden,⁵ E. Orru,⁵ H. Paas,³⁴ M. Pandey-Pommier,³⁵ R. Pizzo,⁵ A. G. Polatidis,⁵ W. Reich,⁶ H. Röttgering,²⁵ A. M. M. Scaife,²⁰ D. J. Schwarz,³⁶ M. Serylak,¹⁹ O. Smirnov,^{37,38} M. Steinmetz,¹⁸ J. Swinbank,²⁸ M. Tagger,²⁶ C. Tasse,³⁹ M. C. Toribio,⁵ R. J. van Weeren,¹⁵ R. Vermeulen,⁵ C. Vocks,¹⁸ M. W. Wise,^{5,28} O. Wucknitz,⁶ and P. Zarka³⁹

¹*Department of Astrophysics/IMAPP, Radboud University Nijmegen, PO Box 9010, 6500 GL Nijmegen, The Netherlands*

²*University of Groningen, KVI Center for Advanced Radiation Technology, 9700 AB Groningen, The Netherlands*

³*Astrophysical Institute, Vrije Universiteit Brussel, Pleinlaan 2, 1050 Brussels, Belgium*

⁴*Nikhef, Science Park Amsterdam, 1098 XG Amsterdam, The Netherlands*

⁵*ASTRON, Netherlands Institute for Radio Astronomy, Postbus 2, 7990 AA Dwingeloo, The Netherlands*

⁶*Max-Planck-Institut für Radioastronomie, Auf dem Hügel 69, 53121 Bonn, Germany*

⁷*Vrije Universiteit Brussel, Dienst ELEM, B-1050 Brussels, Belgium*

⁸*Center for Mathematics and Computer Science (CWI), PO Box 94079, 1090 GB Amsterdam, The Netherlands*

⁹*Eindhoven University of Technology (TU/e), PO Box 513, 5600 MB Eindhoven, The Netherlands*

¹⁰*Space Telescope Science Institute, 3700 San Martin Drive, Baltimore, Maryland 21218, USA*

¹¹*Helmholtz-Zentrum Potsdam, DeutschesGeoForschungsZentrum GFZ, Department 1: Geodesy and Remote Sensing, Telegrafenberg, A17, 14473 Potsdam, Germany*

¹²*SRON Netherlands Institute for Space Research, PO Box 800, 9700 AV Groningen, The Netherlands*

¹³*Kapteyn Astronomical Institute, PO Box 800, 9700 AV Groningen, The Netherlands*

¹⁴*University of Twente, PO Box 217, 7500 AE Enschede, The Netherlands*

¹⁵*Harvard-Smithsonian Center for Astrophysics, 60 Garden Street, Cambridge, Massachusetts 02138, USA*

¹⁶*Institute for Astronomy, University of Edinburgh, Royal Observatory of Edinburgh, Blackford Hill, Edinburgh EH9 3HJ, United Kingdom*

¹⁷*University of Hamburg, Gojenbergsweg 112, 21029 Hamburg, Germany*

¹⁸*Leibniz-Institut für Astrophysik Potsdam (AIP), An der Sternwarte 16, 14482 Potsdam, Germany*

¹⁹*Astrophysics, University of Oxford, Denys Wilkinson Building, Keble Road, Oxford OX1 3RH, United Kingdom*

²⁰*School of Physics and Astronomy, University of Southampton, Southampton SO17 1BJ, United Kingdom*

²¹*Research School of Astronomy and Astrophysics, Australian National University, Mt. Stromlo Observatory, via Cotter Road, Weston, Australian Capital Territory 2611, Australia*

²²*Max Planck Institute for Astrophysics, Karl Schwarzschild Straße 1, 85741 Garching, Germany*

²³*SmarterVision BV, Oostersingel 5, 9401 JX Assen, The Netherlands*

²⁴*Thüringer Landessternwarte, Sternwarte 5, D-07778 Tautenburg, Germany*

²⁵*Leiden Observatory, Leiden University, PO Box 9513, 2300 RA Leiden, The Netherlands*

²⁶*LPC2E, Université d'Orleans/CNRS, 45071 Orleans Cedex 2, France*

²⁷*Station de Radioastronomie de Nancay, Observatoire de Paris, CNRS/INSU, USR 704, Université Orleans, OSUC, Route de Souesmes, 18330 Nancay, France*

²⁸*Anton Pannekoek Institute, University of Amsterdam, Postbus 94249, 1090 GE Amsterdam, The Netherlands*

²⁹*Astronomisches Institut der Ruhr-Universität Bochum, Universitaetsstrasse 150, 44780 Bochum, Germany*

³⁰*Astro Space Center of the Lebedev Physical Institute, Profsoyuznaya Street 84/32, Moscow 117997, Russia*

³¹*National Astronomical Observatory of Japan, Tokyo 181-8588, Japan*

³²*Sodankylä Geophysical Observatory, University of Oulu, Tähteläntie 62, 99600 Sodankylä, Finland*

³³*STFC Rutherford Appleton Laboratory, Harwell Science and Innovation Campus, Didcot OX11 0QX, United Kingdom*

³⁴*Center for Information Technology (CIT), University of Groningen, PO Box 72, 9700 AB Groningen, The Netherlands*

³⁵*Centre de Recherche Astrophysique de Lyon, Observatoire de Lyon, 9 Avenue Charles André, 69561 Saint Genis Laval Cedex, France*

³⁶*Fakultät für Physik, Universität Bielefeld, Postfach 100131, D-33501 Bielefeld, Germany*

³⁷*Department of Physics and Electronics, Rhodes University, PO Box 94, Grahamstown 6140, South Africa*

³⁸*SKA South Africa, 3rd Floor, The Park, Park Road, Pinelands 7405, South Africa*

³⁹*LESIA, UMR CNRS 8109, Observatoire de Paris, 92195 Meudon, France*

(Received 23 January 2015; published 24 April 2015)

We present measurements of radio emission from cosmic ray air showers that took place during thunderstorms. The intensity and polarization patterns of these air showers are radically different from those measured during fair-weather conditions. With the use of a simple two-layer model for the atmospheric electric field, these patterns can be well reproduced by state-of-the-art simulation codes. This in turn provides a novel way to study atmospheric electric fields.

DOI: [10.1103/PhysRevLett.114.165001](https://doi.org/10.1103/PhysRevLett.114.165001)

PACS numbers: 92.60.Pw, 95.85.Ry, 96.50.sd

One of the important open questions in atmospheric physics concerns the physical mechanism that initiates lightning in thunderclouds [1]. Crucial to the answer is knowledge of atmospheric electric fields. Existing *in situ* measurements, from balloons or airplanes, are limited due to the violent nature of thunderstorms. Furthermore, they are limited to balloon trajectories or perturbed by the presence of the aircraft. Here, we present a new method to probe atmospheric electric fields through their influence on the pattern of polarized radio emission emitted by cosmic-ray-induced extensive air showers.

The main mechanism for driving radio-wave emission from air showers is that the relativistic electrons and positrons in the electromagnetic part of the shower are accelerated in opposite directions by the Lorentz force exerted by Earth's magnetic field. This produces a short, nanosecond time scale, coherent pulse of radio emission mostly at megahertz frequencies. The emission generated by this geomagnetic mechanism is unidirectionally polarized in the $\hat{\mathbf{e}}_{\mathbf{v} \times \mathbf{B}}$ direction. Here, \mathbf{v} is the propagation velocity vector of the shower and \mathbf{B} represents Earth's magnetic field [2–4].

A secondary emission mechanism, contributing between ~3%–20% to the signal amplitude depending on distance to the shower axis and the arrival direction of the shower [5,6], results from a negative charge excess in the shower front. This consists of electrons knocked out of air molecules by the air shower. This also produces a short radio pulse but now polarized radially with respect to the shower symmetry axis.

The emission from both processes is strongly beamed in the forward direction, due to the relativistic velocities of the particles. Additionally, the nonunity refractive index of the air causes relativistic time-compression effects leading to enhanced emission from parts of the shower seen at the Cherenkov angle [7,8]. Interference between the differently polarized emission from both components leads to a complex and highly asymmetric *intensity pattern* [9]. In contrast, time-compression effects do not alter the direction of the polarization vector of the emission. The *polarization pattern* of the radio emission thus points predominantly in the $\hat{\mathbf{e}}_{\mathbf{v} \times \mathbf{B}}$ direction with a minor radial deviation. Strong atmospheric electric fields will influence the motions of the electrons and positrons in air showers. This is expected to be visible in the polarization patterns of the recorded emission [10]. Therefore, we analyze air showers recorded during thunderstorms.

Data for this analysis were recorded with the low-band, 10–90 MHz, dual-polarized crossed dipole antennas located in the inner, ~2 km radius, core of the the LOw-Frequency ARray (LOFAR) radio telescope [11]. These antennas are grouped into circular stations that act as dishes for standard interferometric astronomical observations. For the purpose of air shower measurements, all antennas are equipped with ring buffers that can store up to 5 s of raw voltage data sampled every 5 ns. A dedicated scintillator array, the LOfar Radboud air shower Array (LORA), is located at the center of LOFAR to provide an independent trigger whenever an air shower with an estimated primary energy of $\geq 2 \times 10^{16}$ eV is detected [12]. When a trigger is received, 2 ms of raw voltage data around the trigger time are stored for every active antenna.

These data are processed in an off-line analysis [13] from which a number of physical parameters are extracted and stored. These include the estimated energy of the air shower (as reconstructed from the particle detector data), the arrival direction of the air shower (as reconstructed from the arrival times of the radio pulses in all antennas), and for each antenna polarization information in the form of the Stokes parameters: I (intensity), Q , U , and V . The orientation of the polarization vector is reconstructed from Stokes Q and U [6].

Over the period between June 2011 and September 2014, LOFAR recorded a total of 762 air showers. The complex radio intensity pattern on the ground of almost all measured showers can be well reproduced by state-of-the-art air shower simulation codes [14]. These codes augment well-tested Monte Carlo air shower simulations with radio emission calculated from first principles at the microscopic level [15,16]. In this analysis, we use the COREAS plug in of CORSIKA [17] with QGSJETII [18] and FLUKA [19] as the hadronic interaction models. It was previously found that the exact shape of the intensity pattern depends on the atmospheric depth where the number of shower particles is largest, X_{\max} , and that the absolute field strength of the radio emission scales with the energy of the primary particle.

The radio footprints of 58 of the 762 air showers are very different from those predicted by simulations. Of these, 27 air showers have a measured signal-to-noise ratio below 10 in amplitude—too low to get a reliable reconstruction. The polarization patterns of the other 31 showers differ significantly from those of “normal” fair-weather air showers. This can be seen in the middle and bottom panels of Fig. 1 where the polarization direction is clearly coherent

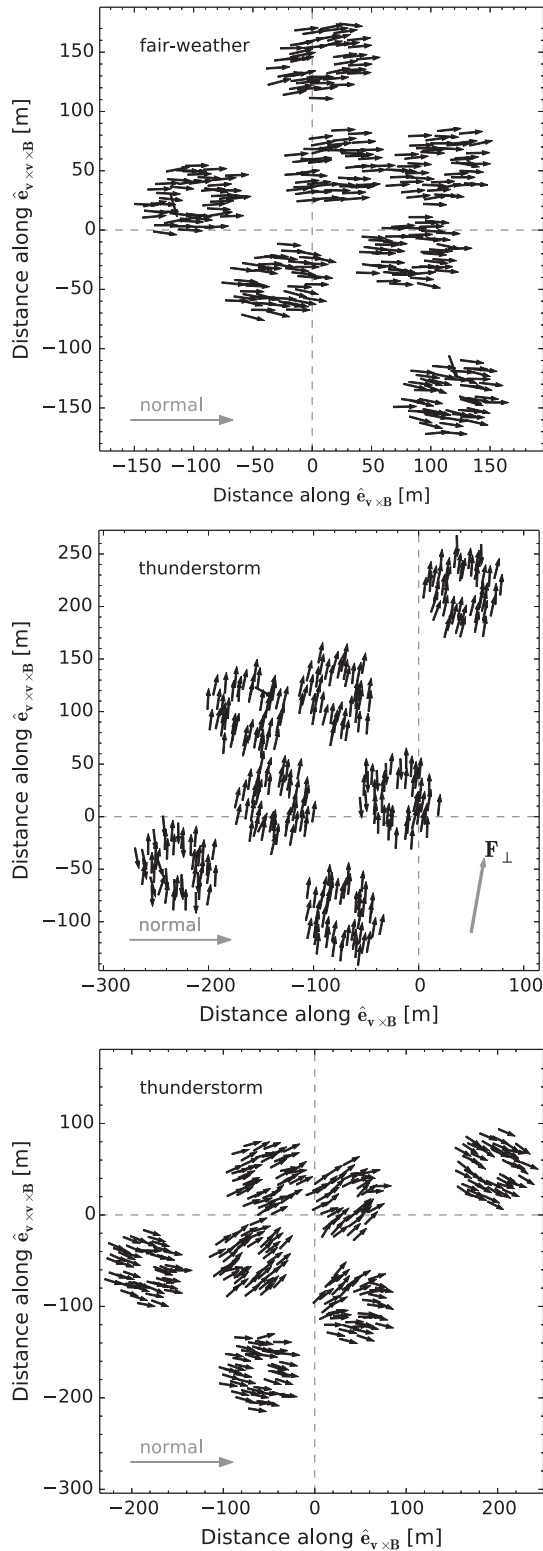


FIG. 1. Polarization as measured with individual LOFAR antennas (arrows) in the shower plane for three measured air showers. LOFAR antennas are grouped into circular stations, of which seven are depicted. The expected polarization direction for fair-weather air showers is indicated with “normal.” The position of the shower axis, orthogonal to the shower plane, is indicated by the intersection of the dashed lines.

(i.e., nonrandom) over all antennas but no longer in the expected $\hat{e}_{\mathbf{v} \times \mathbf{B}}$ direction. In addition, for some of these showers the intensity of the radio signal at low 10–90 MHz frequencies is strongest on a ring around the shower axis with a radius of approximately 100 m (see also Fig. 2). This “ring structure” in the intensity pattern is not present in normal fair-weather air showers that all lack rotational symmetry in the intensity pattern and instead show a single maximum that is displaced in the $\hat{e}_{\mathbf{v} \times \mathbf{B}}$ direction from the shower axis [14,20]. Twenty of these 31 showers occur within 2 h of lightning strikes recorded within ~ 150 km distance from LOFAR by the Royal Dutch Meteorological Institute. Given the similarity of the polarization patterns of the remaining showers where no lightning strikes were

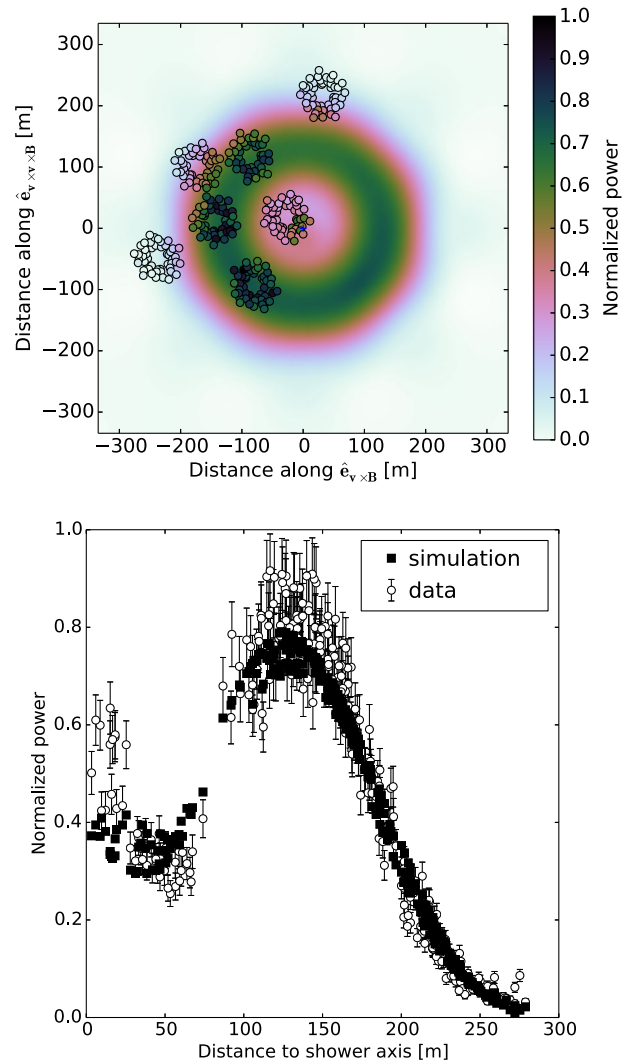


FIG. 2 (color online). Radio intensity pattern during a thunderstorm. Top: the circles represent antenna positions. Their color reflects measured pulse power. The best-fitting COREAS simulation is shown in color scale in the background. Where the colors of the circles match the background, a good fit is achieved. Bottom: measured (circles) and simulated pulse power (squares) as a function of distance to the shower axis.

measured, it is plausible that at these times the atmospheric electric field was also strong albeit not strong enough to initiate lightning. An electric field meter has since been installed at LOFAR that will provide independent verification for future measurements.

For the shower in the middle panel of Fig. 1, recorded during thunderstorm conditions, the pattern is unidirectional for the entire footprint. A second more complicated type is depicted in the bottom panel. Here, the pattern is more “wavy.” The analysis presented here focusses on an air shower of the first type where also a ring structure is visible and a strong signal is measured by the LORA particle detectors. All air showers of this type can be reconstructed with similar accuracy. For showers of the wavy type, a more complex analysis is currently being developed.

We propose that the influence of atmospheric electric fields on air shower radio emission can be understood in the following way.

The electric field, in the region of the cloud traversed by the air shower, can be decomposed into components perpendicular \mathbf{E}_\perp and parallel \mathbf{E}_\parallel to the shower symmetry axis. The perpendicular component of the field changes the net transverse force acting on the particles

$$\mathbf{F} = q(\mathbf{E}_\perp + \mathbf{v} \times \mathbf{B}). \quad (1)$$

This changes both the magnitude and the polarization of the radiation that follow \mathbf{F} .

During shower development, the air shower particles lose energy. The parallel component of the atmospheric electric field partially compensates this energy loss. Therefore, the total number of particles within a given energy range in the shower increases. Because the fractional gain of energy is greatest for lower energy particles, these are the most affected. However, low-energy particles do not contribute much to the total radio emission because they lag behind the shower front and their emission is not coherent for frequencies above 10 MHz. Thus, it is the perpendicular component of the electric field that determines the measured intensity and polarization direction.

In order to test these hypotheses, atmospheric electric fields were inserted into COREAS air shower simulations. By the comparison of fields acting purely parallel and purely perpendicular to the shower axis it was found that the effect of \mathbf{E}_\perp on the radio emission is indeed much stronger and will dominate in most shower configurations where both components are present. This will be discussed in greater detail in a forthcoming publication.

Having understood the basic effects of atmospheric electric fields on air shower radio emission, we proceed with a full reconstruction of LOFAR measurements. We follow the method developed by Buitink *et al.* [14] to fit COREAS simulations to LOFAR measurements. An atmospheric electric field is inserted into the simulations with the

perpendicular component chosen such that the net force is in the measured average polarization direction (as indicated in the middle panel of Fig. 1). The parallel component is set to zero since its influence on the received radiation intensity and polarization pattern is negligible.

The simplest electric field configuration that can reproduce the main features in both the measured intensity and polarization patterns is composed of two electric field layers. The upper layer, with strength $|\mathbf{E}_U|$, starts at a height h_U above the ground and extends down to a height h_L at which the lower layer starts, the direction of the net force changes by 180° , and the field strength decreases to $|\mathbf{E}_L|$. Two layers are needed because with one layer the ring structure seen in the measurements is not reproducible.

In Fig. 2 the reconstruction is shown for the air shower for which the polarization pattern is depicted in the middle panel of Fig. 1. The reconstruction is optimal for $h_U = 8$ km, $h_L = 2.9$ km, $|\mathbf{E}_U| = 50$ kV m $^{-1}$, and $|\mathbf{E}_L|/|\mathbf{E}_U| = 0.53$. For these values $\chi^2/\text{ndf} = 3.2$ as obtained for a joined fit to both the radio and particle data. A perfect fit of $\chi^2/\text{ndf} \approx 1$, as is often found for fair-weather showers, is likely not attainable with a simplified electric field model. However, all the main features of the intensity and polarization pattern (namely the overall polarization direction and ring structure) are already correctly reproduced.

The fit quality is sensitive to changes in the relative field strength and h_L as well as X_{max} . This can be seen in Fig. 3, where each parameter is varied while keeping the others fixed at their optimum values. This fixing is not possible for X_{max} in the CORSIKA software, because it is an outcome of the simulation rather than an input parameter. Therefore, simulations were selected where X_{max} differs by no more than 20 g cm $^{-2}$. The fit quality reaches its optimum value for $h_U = 8$ km and is not sensitive to a further increase. This is expected because above this altitude the air shower is not yet fully developed and there are relatively few particles contributing to the emission.

For fair-weather air showers, the measured radio intensity is related to the simulated values through a constant scaling factor [14] given the energy of the primary particle. This energy is derived from the particle density on the ground, as measured with LORA, combined with the information on X_{max} , as determined from the radio fit. For the air shower measured during thunderstorm conditions, the measured intensity is higher than the normally expected value, as the absolute electric field strength influences the radio intensity. However, the simulated intensity increases only until the atmospheric electric field strength reaches $|\mathbf{E}_U| \geq 50$ kV m $^{-1}$. When the field strength is increased further, the radio intensity stays constant. This saturation of the radio intensity appears to be related to the coherent nature of the emission but is still under investigation.

Measuring radio emission from extensive air showers during thunderstorm conditions thus provides a unique new

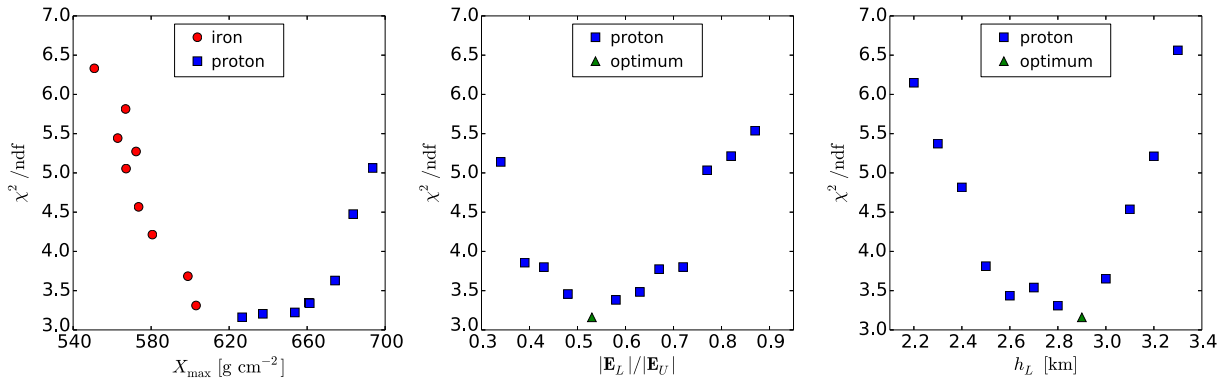


FIG. 3 (color online). Sensitivity of the fit quality to variations in the atmospheric depth of shower maximum X_{\max} (left panel), the relative field strength (middle panel), and the field reversal altitude h_2 (right panel). The optimal proton simulation is the same for all plots. The electric field strength, in the upper layer, for all simulations is $|\mathbf{E}_U| = 50 \text{ kV m}^{-1}$.

tool to probe the atmospheric electric fields present in thunderclouds. Unlimited by violent wind conditions and sensitive to a large fraction of the cloud, this technique may help answer the long-standing question “how is lightning initiated in thunderclouds?” It has been suggested by Gurevich *et al.* [21,22] that cosmic-ray-induced air showers in combination with runaway breakdown may initiate lightning. If this is indeed true then LOFAR with its combination of particle detectors and radio antennas is well positioned to measure it.

The LOFAR key science project cosmic rays acknowledges financial support from NOVA, SNN, and FOM as well as from NWO, VENI Grant No. 639-041-130. We acknowledge funding from an Advanced Grant of the European Research Council (FP/2007-2013)/ERC Grant Agreement No. 227610. We also acknowledge funding from the FOM-project 12PR3041 “Cosmic Lightning”. LOFAR, the Low Frequency Array designed and constructed by ASTRON, has facilities in several countries that are owned by various parties (each with their own funding sources) and that are collectively operated by the International LOFAR Telescope foundation under a joint scientific policy.

*P.Schellart@astro.ru.nl

- [1] J. R. Dwyer and M. A. Uman, *Phys. Rep.* **534**, 147 (2014).
- [2] F. D. Kahn and I. Lerche, *Proc. R. Soc. A* **289**, 206 (1966).
- [3] H. Falcke *et al.*, *Nature (London)* **435**, 313 (2005).
- [4] D. Ardouin *et al.*, *Astropart. Phys.* **31**, 192 (2009).
- [5] A. Aab *et al.*, *Phys. Rev. D* **89**, 052002 (2014).
- [6] P. Schellart, S. Buitink, A. Corstanje, J. E. Enriquez, H. Falcke, J. R. Hörandel, M. Krause, A. Nelles, J. P. Rachen, O. Scholten, S. ter Veen, S. Thoudam, and T. N. G. Trinh, *J. Cosmol. Astropart. Phys.* **14** (2014) 10.
- [7] K. D. de Vries, A. M. van den Berg, O. Scholten, and K. Werner, *Phys. Rev. Lett.* **107**, 061101 (2011).
- [8] A. Nelles, P. Schellart *et al.*, *Astropart. Phys.* **65**, 11 (2015).
- [9] K. D. de Vries, A. M. van den Berg, O. Scholten, and K. Werner, *Astropart. Phys.* **34**, 267 (2010).
- [10] S. Buitink, T. Huege, H. Falcke, and J. Kuijpers, *Astropart. Phys.* **33**, 296 (2010).
- [11] M. P. van Haarlem *et al.*, *Astron. Astrophys.* **556**, A2 (2013).
- [12] S. Thoudam, S. Buitink, A. Corstanje, J. E. Enriquez, H. Falcke, W. Frieswijk, J. R. Hörandel, A. Horneffer, M. Krause, A. Nelles, P. Schellart, O. Scholten, S. ter Veen, and M. van den Akker, *Nucl. Instrum. Methods Phys. Res., Sect. A* **767**, 339 (2014).
- [13] P. Schellart, A. Nelles *et al.*, *Astron. Astrophys.* **560**, A98 (2013).
- [14] S. Buitink, A. Corstanje, J. E. Enriquez, H. Falcke, J. R. Hörandel, T. Huege, A. Nelles, J. P. Rachen, P. Schellart, O. Scholten, S. ter Veen, S. Thoudam, and T. N. G. Trinh, *Phys. Rev. D* **90**, 082003 (2014).
- [15] T. Huege, M. Ludwig, and C. W. James, *AIP Conf. Proc.* **1535**, 128 (2013).
- [16] J. Alvarez-Muñiz, W. R. Carvalho, and E. Zas, *Astropart. Phys.* **35**, 325 (2012).
- [17] D. Heck, J. Knapp, J. N. Capdevielle, G. Schatz, and T. Thouw, *CORSIKA: a Monte Carlo Code to Simulate Extensive Air Showers* (Forschungszentrum Karlsruhe GmbH, Karlsruhe, Germany, 1998).
- [18] S. Ostapchenko, *Nucl. Phys. B, Proc. Suppl.* **151**, 143 (2006).
- [19] G. Battistoni, F. Cerutti, A. Fassò, A. Ferrari, S. Muraro, J. Ranft, S. Roesler, and P. R. Sala, in *Hadronic Shower Simulation Workshop*, edited by M. Albrow and R. Raja, AIP Conference Series, Vol. 896 (AIP, New York, 2007), pp. 31–49.
- [20] A. Nelles, S. Buitink, H. Falcke, J. R. Hörandel, T. Huege, and P. Schellart, *Astropart. Phys.* **60**, 13 (2015).
- [21] A. V. Gurevich, K. P. Zybin, and R. A. Roussel-Dupre, *Phys. Lett. A* **254**, 79 (1999).
- [22] A. V. Gurevich and A. N. Karashtin, *Phys. Rev. Lett.* **110**, 185005 (2013).